PAL POHANG ACCELERATOR LABORATORY
KAERI Korea Atomic Energy Research Institute
RAON

IBIC 2021

International Beam Instrumentation Conference

13-17, Sep., 2021
Virtual Conference

PROCEEDINGS

Topics

- Beam Charge and Current Monitors
- Beam Loss Monitors and Machine Protection
- Beam Position Monitors
- Transverse Profile and Emittance Monitors
- Longitudinal Diagnostics and Synchronization
- Feedback Systems and Beam Stability
- Data Acquisition and Processing Platforms
- Machine Parameter Measurements
- Overview and Commissioning

Scientific Program Committee

Solaris	Adriana Wawrzyniak	ANL	Nicholas Sereno
PAL	Changbum Kim	Soleil	Nicolas Hubert
LNLS	Daniel Tavares	SLAC	Patrick Krejcik
BNL	David Gassner	SLRI	Prapong Klysubun
PAL	Garam Hahn	FRIB	Steven Lidia
SPring-8	Hirokazu Maesaka	CERN	Thibaut Lefevre
LBNL	Jonah Weber	ESS	Thomas Shea
IHEP	Junhui Yue	ALBA	Ubaldo Iriso
DESY	Kay Wittenburg	FNAL	Victor Scarpine
J-PARK	Kenichirou Satou	PSI	Volker Schlott
JLab	Kevin Jordan	ORNL	Willem Blokland
Diamond	Lorraine Bobb	SSRF/SARI	Yongbin Leng
Elettra	Mario Ferianis		

pal.postech.ac.kr/ibic2021

Dear Colleagues,

The 10th international Beam Instrumentation Conference (IBIC 2021) was held as a virtual conference from September 13th to 16th 2021.

IBIC is a fruitful and successful gathering of the world's beam instrumentation community and it reflects the maturity of international collaboration in the field of beam instrumentation for accelerators. IBIC is dedicated to exploring the physics and engineering challenges of beam diagnostics and measurement techniques for particle accelerators worldwide.

IBIC 2021 was hosted by the PAL, which is operating two large-scale facilities: PLS-II and PAL-XFEL. PLS-II is the first 3rd generation synchrotron radiation facility in Korea, providing more than 4,800 hours of beam time per year. PAL-XFEL is the 3rd hard X-ray free-electron laser user facility in the world which was opened to the user in 2017.

Total 225 participants from 20 countries registered for IBIC 2021 including 34 student grants and 6 industrial registrations. 19 invited talks (including 1 tutorial talk), 13 contributed talks, and 113 posters were presented during 4 days of the conference. The organizing committee greatly appreciates them for their enthusiastic participation.

In addition to the participants, we would like to express our special thanks to the Scientific Committee who guided the conference and made an interesting scientific programme, the Editorial Team who worked hard to present the proceedings, and the Local Organizing Committee who made this conference possible.

Changbum Kim
IBIC 2021 Conference Chair

Scientific Program Committee (SPC)

Adriana Wawrzyniak		Solaris	Poland
Changbum Kim	**SPC Chair**	PAL	South Korea
Daniel Tavares		LNLS	Brazil
David Gassner		BNL	USA
Garam Hahn		PAL	South Korea
Hirokazu Maesaka		Spring-8	Japan
Jonah Weber		LBNL	USA
Junhui Yue		IHEP	China
Kay Wittenburg		DESY	Germany
Kenichirou Satou		J-PARK/KEK	Japan
Kevin Jordan		JLab	USA
Lorraine Bobb		Diamond	Great Britain
Mario Ferianis		Elettra	Italy
Nicholas Sereno		ANL	USA
Nicolas Hubert		Soleil	France
Patrick Krejcik		SLAC	USA
Prapong Klysubun		SLRI	Thailand
Steven Lidia		FRIB	USA
Thibaut Lefevre		CERN	Switzerland
Thomas Shea		ESS	Sweden
Ubaldo Iriso		ALBA	Spain
Victor Scarpine		FNAL	USA
Volker Schlott		PSI	Switzerland
Willem Blokland		ORNL	USA
Yongbin Leng		SSRF/SARI	China

Local Organizing Committee (LOC)

Changbum Kim	PAL	South Korea
Dong-Eon Kim	PAL	South Korea
Do Tae Kim	PAL	South Korea
Dongjin Kim	PAL	South Korea
Garam Han	PAL	South Korea
Hyojeong Hyun	PAL	South Korea
Jaeyu Lee	PAL	South Korea
Jinju Ko	PAL	South Korea
Sukhyun Jin	PAL	South Korea

JACoW Editorial & Support Team (JEST)

Dong-Eon Kim	**Editor-in-Chief**	PAL	South Korea
Jan Chrin		PSI	Switzerland
Jaeyu Lee		PAL	South Korea
Michaela Marx		DESY	Germany
Volker RW Schaa	**Technical Editor**	GSI	Germany

Contents

ISBN: 978-3-95450-230-1 ISSN: 2673-5350 doi:10.18429/JACoW-IBIC2021-MOOB01

ULTRA-FAST LINE-CAMERA KALYPSO FOR fs-LASER-BASED ELECTRON BEAM DIAGNOSTICS

M. M. Patil*, M. Caselle, E. Bründermann, G. Niehues, A. Ebersoldt, M. J. Nasse, M. Reißig,
A. Kopmann, J. L. Steinmann, S. Funkner, C. Widmann, T. Dritschler, S. Chilingarayan,
M. Weber and A.-S. Müller
Karlsruhe Institute of Technology, Karlsruhe, Germany

Abstract

A very common bottleneck to study short electron bunch dynamics in accelerators is a detection scheme that can deal with high repetition rates in the MHz range. The KIT electron storage ring KARA (Karlsruhe Research Accelerator) is the first storage ring with a near-field single-shot electro-optical (EO) bunch profile monitor installed for the measurement of electron bunch dynamics in the longitudinal phase-space. Using electro-optical spectral decoding (EOSD) it is possible to imprint the bunch profile on chirped laser pulses subsequently read out by a spectrometer and a camera. However, commercially available cameras have a drawback in their acquisition rate, which is limited to a few hundred kHz. Hence, we have developed KALYPSO, an ultra-fast line camera capable of operating in the MHz regime. Its modular approach allows the installation of several sensors e.g. Si, InGaAs, PbS, PbSe to cover a wide range of spectral sensitivities. In this contribution, an overview of the EOSD experimental setup and the detector system installed for longitudinal bunch studies will be presented.

INTRODUCTION

In an electron storage ring, investigation of ultra-fast dynamics in short electron bunches of a few ps length requires diagnostic methods that allow non-destructive measurements (e.g. longitudinal bunch profile of the electron bunches) at MHz repetition rate. Most commonly used methods involving the measurement of synchrotron radiation with a streak camera. This method is not capable of single-shot acquisitions, as this diagnostic tool averages the bunch profile over a few turns. On the other hand commercial line array cameras have a disadvantage of being slow with readout rate in the kHz range. In this paper, a diagnostic method based on EOSD combined with a novel line array camera KALYPSO (KArlsruhe Linear arraY detector for MHz rePetition-rate SpectrOscopy) developed at KIT will be presented. Electro-optic techniques are based on the so-called Pockels effect [1]. This effect leads to a phase or polarization modulation of the laser pulse passing through an electro-optic active crystal, e.g. gallium phosphide (GaP), in the presence of an external electric field. The phase modulation can be effectively converted to intensity modulation via a detection scheme based on one of different polarization-based methods [2].

EOSD is a well-known technique in THz spectroscopy. It dates back as early as 1998, when this method was used for the measurement of freely propagating sub-ps electromagnetic pulses using a linearly chirped optical beam [3]. Near-field EO measurements of sub-ps relativistic electron bunches were demonstrated for the first time at the linear accelerator FELIX, a free electron laser facility in the Netherlands [4]. Since then, several facilities have implemented this technique for characterizing electron bunches [5–12]. At the KIT storage ring KARA, far-field EO sampling measurements for the detection of CSR (Coherent Synchrotron Radiation) emitted by short electron bunches were pioneered in 2009 [13]. However, it was in 2013 when the first single-shot measurements based on near-field EO were performed in a storage ring [14].

Such measurements of the near-field in a storage ring are challenging due to the high repetition rate with a requirement for a single-shot non-destructive method without averaging. Another challenge is the deposited heat load on the EO crystal, especially on its coatings. The EOSD technique allows for the direct measurement of the Coulomb field, which gives additional insights into micro-bunching instabilities in storage rings [15].

While this method allows for single shot measurements of electron bunch profiles, the technological limitations posed by commercially available data acquisition systems (DAQs), e.g. low repetition rate of a few kHz, do not allow for the continuous study of the evolution of electron bunch dynamics. Hence, to overcome these challenges, a novel FPGA-based DAQ system combined with an ultra-fast line array camera was developed, KALYPSO [16, 17]. This line array camera offers a modular approach, allowing for the use of different micro-strip sensors based on Si, InGaAs, PbS, and PbSe depending on the required wavelength range. It has a maximum frame rate of 2.7 MHz, but a version operating at 12 MHz is currently being commissioned. In the further sections of this paper, the EOSD setup installed at KARA, the working principle of KALYPSO, data analysis and results from the experiment will be explained.

NEAR-FIELD EOSD SETUP

The measurements were carried out during single bunch operation at the storage ring KARA accelerator at a beam energy of 1.3 GeV. In order to study the micro-bunching instability, a low-alpha optics setup was used to compress the longitudinal bunch length to a few ps. The experimental setup is illustrated in Fig. 1.

First, chirped laser pulses generated by a self-built ytterbium-doped fiber laser (emitting around 1060 nm) are

---

* meghana.patil@kit.edu

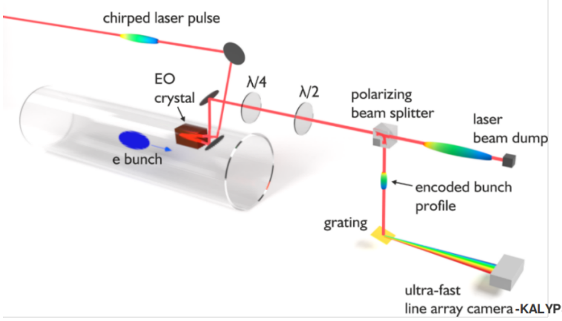

Figure 1: The near-field electro-optic spectral decoding setup for the measurement of longitudinal bunch profile of short electron bunches.

propagated into the storage ring with a 35-meter-long fiber which behaves like a pulse stretcher. The laser pulse passes the EO crystal located inside the beam pipe close to the electron bunch and is reflected at its back side. As the electron bunch and laser pulse are co-propagating, a transient birefringence is induced proportional to the electric field (Pockels effect). Thus, the bunch profile is imprinted on the spectral components of the laser pulse by turning the polarization from linear to elliptical. For decoding the information, the laser pulse is sent through polarization optics: a $\lambda/4$-waveplate is used for compensating the intrinsic birefringence of the crystal, a $\lambda/2$-waveplate and a polarizing beam splitter are used in almost crossed configuration. Therefore, changes of the polarization due to the Pockels effect in the crystal result in an intensity modulation of the spectral components. This can be measured with a spectrometer.

It is necessary to find the temporal overlap of the laser pulses and the electron bunches when they pass through the EO crystal. To adjust the temporal overlap between the laser and the electron bunch, the position of the laser peak intensity modulation is determined with a fast fiber-coupled photodiode. This configuration is then used for subsequent measurements. An oscilloscope is used to acquire the average peak signal of the photodiode (averaged over 100 sweeps) for EO sampling measurements. This signal is dependent on the relative time delay between the laser and the electron bunch, which can be modified by a vector modulator (VM). The readout of the oscilloscope and the VM are both controlled by a MATLAB script that has direct access to the oscilloscope and may access the EO setup control blocks of the accelerator control system (EPICS). Figure 2 shows an example of such a measurement.

For the final step, in order to measure the spectral intensity modulation, the laser pulses are sent through a grating setup and focused onto the Si-sensor of KALYPSO using a lens. The system is operated at a frame rate that is equal to and synchronized with revolution frequency of 2.7 MHz at KARA.

Table 1 shows the beam parameters at the time of the measurements performed for the data presented in this paper.

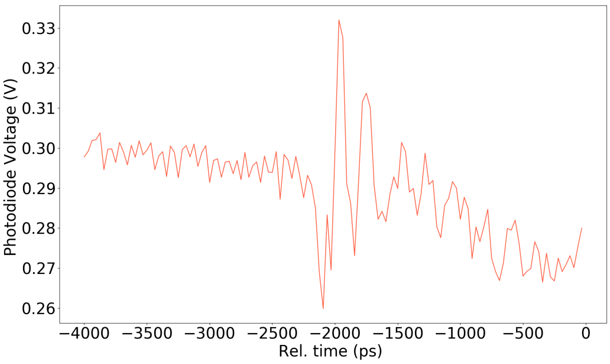

Figure 2: EO sampling traces measured using a fast photodiode combined with an oscilloscope clearly shows the wakefield of the electron bunches. The X axis corresponds to the phase steps of the VM and the Y axis to the maximum photodiode amplitude measured by the oscilloscope.

Table 1: KARA Beam Parameters in Short Bunch Mode Used During the Measurements

Energy (E)	1.3 GeV
Beam current (I_b)	1.13 mA
RF frequency (f_{RF})	499.744 MHz
Synchrotron frequency (f_s)	10.2 kHz
Momentum compaction factor (α_c)	6.5×10^{-4}

KALYPSO

KALYPSO is a line array detector that performs at a maximum frame rate of 12 MHz. KALYPSO's primary advantage over other detectors is its data streaming mode, which captures continuous data at MHz repetition rates and analyzes it with very little latency. Figure 3 depicts the most recent KALYPSO detector card developed and produced at KIT. The detector card comprises of a semiconductor based fine-pitch line-array sensor. A silicon (Si) sensor with an anti-reflection

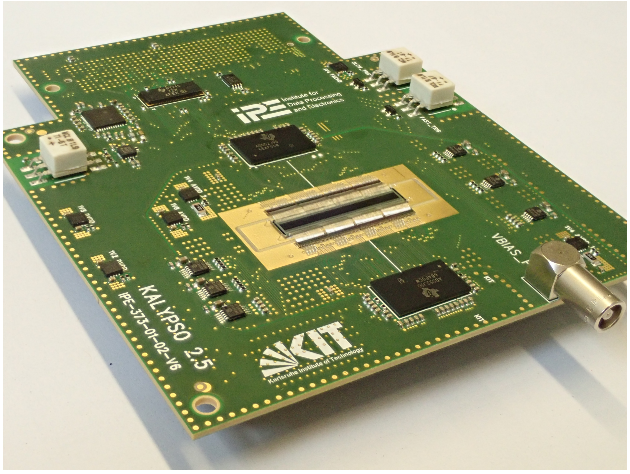

Figure 3: A fully assembled KALYPSO board with Si sensor and optimized sensitivity towards visible light.

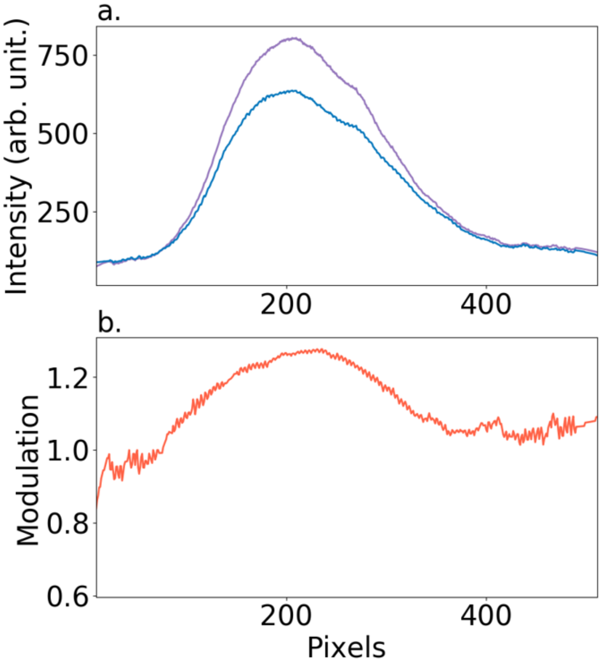

Figure 4: Laser pulse spectra measured using KALYPSO, a: modulated signal (purple) and unmodulated signal (blue), b: calculated EOSD signal (red).

coating (ARC) layer is used for applications requiring spectral sensitivity between 350 nm and 1050 nm [18]. Line arrays based on indium gallium arsenide (InGaAs), lead sellenide (PbSe), or lead sulphide (PbS) can be placed to detect wavelengths greater than 1050 nm. The sensor is read with a low-noise, highly linear front-end electronics ASIC, known as Gotthard-KIT, developed at KIT and PSI in UMC 110 nm CMOS technology [19]. The ASIC's analog outputs are digitized using a high-speed ADC-ADS52J90 linked via a JESD204b subclass 2 interface standard [20].

Additionally, the card has digital-to-analog converters (DACs) for voltage and current biasing the GOTTHARD ASIC, as well as low-jitter clock conditioners for on-board clock distribution. The KALYPSO detector card is connected to the HighFlex FPGA-based readout card through a VITA 57.1 FMC connector. The HighFlex is a KIT-developed FPGA-based readout card equipped with a Xilinx Virtex 7 FPGA, 4 GB DDR3 memory, and a PCIe Gen3 interface [21]. Streamed data can be processed on either a CPU or a GPU.

DATA ANALYSIS AND RESULTS

To calculate the bunch profile, we begin by determining the line array's background signal through laser beam blocking. The signal from the laser pulses propagating through the EO (GaP) crystal, without overlap with the electron bunch is then recorded in the following stage. To do this, the phase of the laser synchronization mechanism is altered such that the laser pulse gets to the EO crystal before the electron bunch. We remove the sensor background signal from both, the overlapped and non-overlapping samples to produce the modulated and unmodulated signals. Figure 4a. the modulated and unmodulated signals and Fig. 4b. the calculated EOSD signal, which is the quotient of Fig. 4a. Furthermore, a time calibration is then needed to convert the pixels to time.

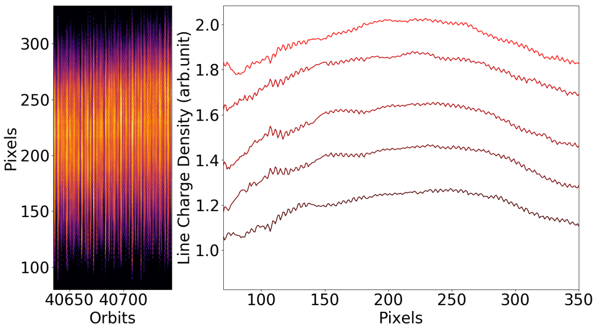

Figure 5: Evolution of the bunch profile in a time window of 40.48 µs. The data representation as a revolution plot allows for comparing different time frames and identify patterns in electron bunch dynamics at various time ranges. For example, the revolution plot of the 100 consecutive measurements indicate the shift in the center of bunch profiles towards higher pixel numbers. This shift can be seen in Fig. 6 as a part of the synchrotron oscillation equivalent to 10.2 kHz.

The unprecedented frame rate provided by the novel DAQ system KALYPSO allows for the precise recording of every single turn, up to a maximum of 10,000,000 turns corresponding to a time period of 3.67 s [22]. Figure 5 shows a small window with the centroid drifting of the bunch profiles, a part of the synchrotron oscillation, which gives an insight into measuring short-term bunch dynamics.

On the other hand, the long acquisition time at a framerate up to 12 MHz provided by the DAQ allows the revelation of dynamics such as the oscillation seen in Fig. 6 with an oscillation frequency of around 10.2 kHz. This matches the synchrotron oscillation frequency measured by the bunch-by-bunch feedback system of the KARA storage ring.

OUTLOOK AND FUTURE WORK

We have repeatedly proven the method's potential for studying longitudinal beam dynamics in this experiment by measuring the near-field of a squeezed relativistic electron bunch in a storage ring using single-shot EOSD. In combination with KALYPSO, we have been successful in obtaining single-shot measurements with high frame-rates over long time periods to study the short-term and long-term evolution of the longitudinal bunch and beam dynamics [23, 24].

The data acquired from such an experiment has also been used to study the bursting behavior of electron bunches by reconstructing the phase space distribution of the electron bunches using phase space tomography and also validated with the Vlasov-Fokker-Planck solver Inovesa [25, 26].

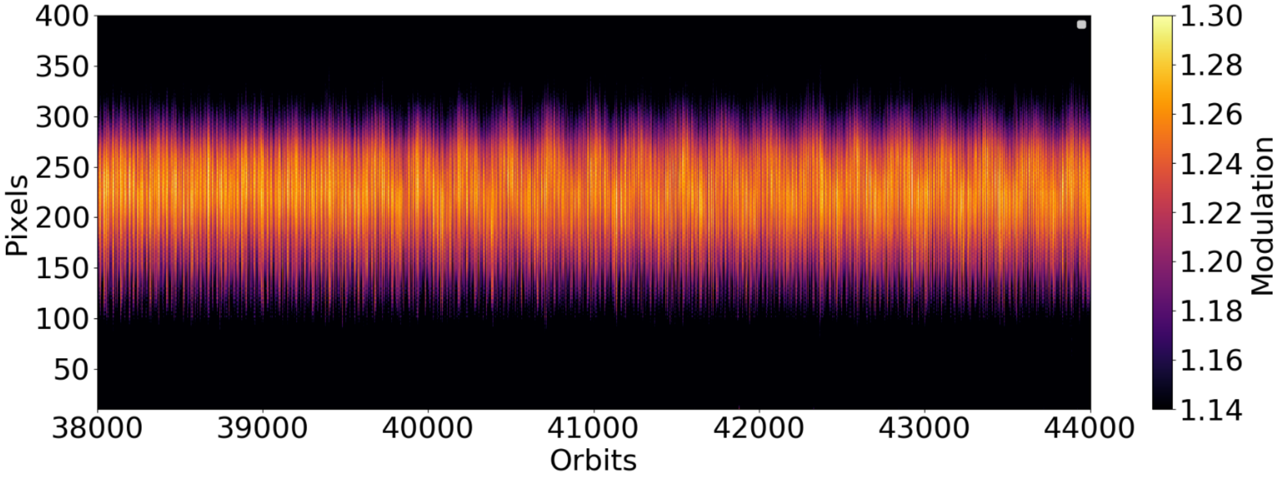

Figure 6: A section of 5,500 samples of the 100,000 continuously acquired bunch profiles spanning a total time period of 36.7 ms. On the X-axis an orbit corresponds to a single revolution with a time of 367 ns and the Y-axis corresponds to the modulation calculated from Fig. 4.

An experimental setup based on electro-optical spectral decoding (EOSD) is now under commission to measure the temporal profile of CSR at the KIT storage ring KARA. The EOSD approach enables for turn-by-turn observations of far-field radiation at MHz rates. Thus, the THz radiation from bunch evolution dynamics, e.g. microbunching, may be studied with high temporal resolution [27].

We have developed KALYPSO, an ultra-fast line array camera, for wide spectral range applications currently operating with frame rates up to 2.7 MHz. The detector has been installed in several experiments in KARA and other accelerator facilities [28, 29]. The detector presented in this paper is the latest version and is currently being commissioned at the EOSD experiment as well as at the energy spread measurement experiment at the visible light diagnostic port at KARA [30, 31]. The next version of this detector, capable of working up to 12 MHz, is in its final stages and will soon be available for measurements.

In an ongoing research towards harnessing high THz radiation, stable coherent synchrotron emission is required. Thus, a feedback loop based on reinforcement learning implemented with an FPGA-based readout card is being investigated. Initial efforts have shown promising results towards a machine learning based feedback system [32].

ACKNOWLEDGEMENTS

The authors would like to thank the former colleagues Nicole Hiller, Patrik Schönfeldt, Lorenzo Rota, and Benjamin Kehrer for their contribution towards the EOSD diagnostic installation at KARA. The authors would like to thank Pia Steck, Simon Hans Jürgen, and Alexander Dierlamm for their constant support in the integration of the ASICs and sensors. Aldo Mozzanica and Roberto Dinapoli for the support in ASIC development. M. M. P. acknowledges the support by the DFG-funded Doctoral School „Karlsruhe School of Elementary and Astroparticle Physics: Science and Technology“. The work is in part supported by the BMBF project 05K19VKD (Federal Ministry of Education and Research).

REFERENCES

[1] S. Casalbuoni, H. Schlarb, B. Schmidt, B. Steffen, P. Schmüser, and A. Winter, “Numerical studies on the electro-optic sampling of relativistic electron bunches,” TESLA Report 2005-01, 2005. `https://flash.desy.de/sites2009/site_vuvfel/content/e403/e1644/e1173/e1174/infoboxContent1175/tesla2005-01.pdf`

[2] B. Steffen, “Electro-Optic Methods for Longitudinal Bunch Diagnostics at FLASH,” Ph.D. thesis, University of Hamburg, Hamburg, Germany, 2007.

[3] Z. Jiang and X.-C. Zhang, “Electro-optic measurement of THz field pulses with a chirped optical beam,” *Appl. Phys. Lett.*, vol. 72, no. 16, pp. 1945–1947, 1998. `doi:10.1063/1.1212318`

[4] I. Wilke, A. M. MacLeod, W. A. Gillespie, G. Berden, G. M. H. Knippels, and A. F. G. Van Der Meer, “Single-Shot Electron-Beam Bunch Length Measurements,” *Phys. Rev. Lett.*, vol. 88, p. 124801, 2002. `doi:10.1103/PhysRevLett.88.124801`

[5] T. Tsang, V. Castillo, R. Larsen, D. M. Lazarus, D. Nikas, C. Ozben, Y. K. Semertzidis, T. Srinivasan-Rao, and L. Kowalski, “Electro-optical measurements of picosecond bunch length of a 45 MeV electron beam,” *J. Appl. Phys.*, vol. 89, pp. 4921–4926, 2001. `doi:10.1063/1.1358322`

[6] M. J. Fitch, A. C. Melissinos, P. L. Colestock, J.-P. Carneiro, H. T. Edwards, and W. H. Hartung, “Electro-optic Measurement of the Wake Fields of a Relativistic Electron Beam,” *Phys. Rev. Lett.*, vol. 87, p. 034801, June 2001. `doi:10.1103/PhysRevLett.87.034801`

[7] H. Loos, A. Doyuran, J. B. Murphy, J. Rose, T. Shaftan, B. Sheehy, Y. Shen, J. Skaritka, X. J. Wang, Z. Wu, and

L. H. Yu, “Electro-optic longitudinal electron beam diagnostic at SDL,” in *Proc. PAC'03*, Portland, OR, USA, vol. 4, pp. 2455–2457, 2003. `doi:10.1109/PAC.2003.1289152`

[8] A. Winter, M. Tonutti, S. Casalbuoni, P. Schmüser, S. Simrock, B. Steffen, T. Korhonen, T. Schilcher, V. Schlott, and H. Sigg, “Bunch length measurements at the SLS linac using electro-optical techniques,” in *Proc. EPAC'04*, Lucerne, Switzerland, pp. 253-255, 2004. `https://jacow.org/e04/PAPERS/THOALH01.PDF`

[9] B. Steffen, S. Casalbuoni, E.-A. Knabbe, H. Schlarb, B. Schmidt, P. Schmüser, and A. Winter, “Electro Optic Bunch Length Measurements at the VUV-FEL at DESY,” in *Proc. PAC'05*, pp. 3111–3113, Knoxville, TN, USA, 2005. `doi:10.1109/PAC.2005.1591381`

[10] I. Katayama, H. Shimosato, M. Bito, K. Furusawa, M. Adachi, M. Shimada, Heishun Zen, S.-i. Kimura, N. Yamamoto, M. Hosaka, M. Katoh, and M. Ashida, “THz Field Detection of the Coherent Synchrotron Radiation Produced by Laser Bunch Slicing,” in *Conference on Lasers and Electro-Optics 2010*, p. CMF6, 2010. `doi:10.1364/CLEO.2010.CMF6`

[11] C. Kaya, C. Schneider, A. Al-Shemmary, W. Seidel, M. Kuntzsch, J. Bhattacharyya, M. Mittendorff, P. Evtushenko, S. Winnerl, and G. Staats, “Phase sensitive monitoring of electron bunch form and arrival time in superconducting linear accelerators,” *Appl. Phys. Lett.*, vol. 100, pp. 141103–141103, 2012. `doi:10.1063/1.3699025`

[12] F. L. Müller, “Electro-Optical Bunch Length Measurements at the Swiss Light Source,” Ph.D. thesis, University of Bern, Bern, Switzerland, 2011.

[13] A. Plech, S. Casalbuoni, B. Gasharova, E. Huttel, Y.L. Mathis, A.-S. Müller, K. Sonnad, A. Bartels, and R. Weigel, “Electro-optical sampling of terahertz radiation emitted by short bunches in the ANKA synchrotron,” in *Proc. PAC'09*, Vancouver, Canada, 2009. `https://jacow.org/PAC2009/papers/tu5rfp026.pdf`

[14] N. Hiller, A. Borysenko, E. Hertle, E. Huttel, V. Judin, B. Kehrer, S. Marsching, A.-S. Müller, M. J. Nasse, A. Plech, M. Schuh, and N. Smale, “Electro-optical Bunch Length Measurements at the ANKA Storage Ring,” in *Proc. IPAC'13*, Shanghai, China, pp. 500–502, paper MOPME014, 2013. `https://jacow.org/IPAC2013/papers/mopme014.pdf`

[15] M. Brosi, J. L. Steinmann, E. Blomley, T. Boltz, E. Bründermann, J. Gethmann, B. Kehrer, Y.-L. Mathis, A. Papash, M. Schedler, P. Schönfeldt, P. Schreiber, M. Schuh, M. Schwarz, A.-S. Müller, M. Caselle, L. Rota, M. Weber, and P. Kuske, “Systematic studies of the microbunching instability at very low bunch charges,” *Phys. Rev. Accel. Beams*, vol. 22, p. 020701, 2019. `doi:10.1103/PhysRevAccelBeams.22.020701`

[16] L. Rota, M. Caselle, M. Balzer, M. Weber, A. Mozzanica, N. Hiller, M. J. Nasse, G. Niehues, P. Schonfeldt, C. Gerth, B. Steffen, D. Makowski, and A. Mielczarek, “KALYPSO: A Mfps Linear Array Detector for Visible to NIR Radiation,” in *Proc. IBIC'16*, Barcelona, Spain, Sep. 2016, pp. 740–743. `doi:10.18429/JACoW-IBIC2016-WEPG46`

[17] M. Caselle, L. Rota, A. Kopmann, S. A. Chilingaryan, M. M. Patil, W. Wang, E. Bründermann, S. Funkner, M. Nasse, G. Niehues, M. N. Balzer, M. Weber, A.-S. Müller, and S. Bielawski, “Ultra-fast detector for wide range spectral measurements,” in *Proc. SPIE 10937, Optical Data Science II*, vol. 1093704, 2019. `doi:10.1117/12.2508451`

[18] M. M. Patil, M. Caselle, L. Rota, A. Dierlamm, M. Baselga Bacardit, G. Niehues, E. Bründermann, M. Weber, A.-S. Müller, G. Borghi, and M. Boscardin, “Novel Si-Sensor technology for high resolution and high repetition-rate experiments at accelerator facilities,” in *Proc. TWEPP2018*, vol. 343, p. 045, 2019. `doi:10.22323/1.343.0045`

[19] L. Rota, M. Caselle, M. N. Balzer, M. Weber, A. Mozzanica, and B. Schmitt, *“Development of a Front-End ASIC for 1D Detectors with 12 MHz Frame-Rate,”* in *Proc. TWEPP-17*, vol. 313, p. 033, 2018. `doi:10.22323/1.313.0033`

[20] H. Saheb and S. Haider, “Scalable high speed serial interface for data converters: Using the JESD204B industry standard,” in *2014, 9th International Design and Test Symposium (IDT)*, pp. 6-11, 2014. `doi:10.1109/IDT.2014.7038577`

[21] M. Caselle, L. E. A. Perez, M. Balzer, T. Dritschler, A. Kopmann, H. Mohr, L. Rota, M. Vogelgesang, and M. Weber, “A high-speed DAQ framework for future high-level trigger and event building clusters,” *J. Instrum.*, vol. 12, p. C03015, 2017. `doi:10.1088/1748-0221/12/03/C03015`

[22] S. Funkner, M. Brosi, E. Bründermann, M. Caselle, M. J. Nasse, G. Niehues, L. Rota, P. Schönfeldt, M. Weber, and A.-S. Müller, “Long-Term Turn-by-Turn Measurements of Electron bunch Profiles at MHz Repetition Rates in a Storage Ring with Single-Shot Electro-Optical Sampling,” in *Proc. IRMMW-THz 2018, 43rd International Conference on Infrared, Millimeter, and Terahertz Waves*, pp. Fr-A2-1b-4, 2018. `doi:10.1109/IRMMW-THz.2018.8510080`

[23] S. Funkner, E. Blomley, E. Bründermann, M. Caselle, N. Hiller, M. J. Nasse, G. Niehues, L. Rota, P. Schönfeldt, S. Walther, M. Weber, and A.-S. Müller, “High throughput data streaming of individual longitudinal electron bunch profiles,” *Phys. Rev. Accel. Beams*, vol. 22, p. 022801, 2019. `doi:10.1103/PhysRevAccelBeams.22.022801`

[24] G. Niehues, E. Blomley, M. Brosi, E. Bründermann, M. Caselle, S. Funkner, M. J. Nasse, L. Rota, P. Schönfeldt, M. Schuh, M. Weber, and A.-S. Müller, “High Repetition Rate, Single-Shot Electro-Optical Monitoring Of Longitudinal Electron Bunch Dynamics Using the linear array detector Kalypso,” in *Proc. IPAC'18*, Vancouver, BC, Canada, Apr.-May 2018, pp. 2216–2218. `doi:10.18429/JACoW-IPAC2018-WEPAL026`

[25] S. Funkner, G. Niehues, M. J. Nasse, E. Bründermann, M. Caselle, B. Kehrer, L. Rota, P. Schönfeldt, M. Schuh, B. Steffen, J. L. Steinmann, M. Weber, and A.-S. Müller, “Revealing the dynamics of ultrarelativistic non-equilibrium many-electron systems with phase space tomography,” *Accelerator Physics*, 2019. `arXiv:1912.01323`

[26] P. Schönfeldt, M. Brosi, M. Schwarz, J. L. Steinmann, and A.-S. Müller, “Parallelized Vlasov-Fokker-Planck solver for desktop personal computers,” *Phys. Rev. Accel. Beams*, vol. 20, p. 030704, 2017. `doi:10.1103/PhysRevAccelBeams.20.030704`

[27] C. Widmann, E. Bründermann, M. Caselle, S. Funkner, M. J. Nasse, G. Niehues, M. M. Patil, C. Sax, J. L. Steinmann, M. Weber, A.-S. Müller, and C. Mai, “Implementing Electro-Optical Diagnostics for Measuring the

CSR Far-Field at KARA", in *Proc. IPAC'21*, Campinas, SP, Brazil, May 2021, pp. 931–934. `doi:10.18429/JACoW-IPAC2021-MOPAB294`

[28] B. Steffen, Ch. Gerth, M. Caselle, M. Felber, T. Kozak, D. R. Makowski, U. Mavrič, A. Mielczarek, P. Peier, K. Przygoda, and L. Rota, "Compact single-shot electro-optic detection system for THz pulses with femtosecond time resolution at MHz repetition rates," *Rev. Sci. Instrum.*, vol. 91, p. 045123, 2020. `doi:10.1063/1.5142833`

[29] C. Gerth, G. Brenner, M. Caselle, S. Dusterer, D. Haack, D. Makowski, A. Mielczarek, S. Palutke, L. Rota, V. Rybnikov, C. Schmidt, B. Steffen, and K. Tiedtke, "Linear array detector for online diagnostics of spectral distributions at MHz repetition rates," *J. Synchrotron Rad.*, vol. 26, pp. 1514-1522, 2019. `doi:10.1107/S1600577519007835`

[30] M.M. Patil, E. Bründermann, M. Caselle, A. Ebersoldt, S. Funkner, B. Kehrer, A.-S. Müller, M.J. Nasse, G. Niehues, J.L. Steinmann, W. Wang, M. Weber, and C. Widmann, "Modern Ultra-Fast Detectors for Online Beam Diagnostics," in *Proc. IPAC'21*, Campinas, SP, Brazil, May 2021, pp. 4540–4544. `doi:10.18429/JACoW-IPAC2021-FRXC03`

[31] B. Kehrer, M. Brosi, E. Bründermann, S. Funkner, G. Niehues, M. M. Patil, M. Schuh, J. Steinmann, A.-S. Müller, and L. Rota, "Turn-by-Turn Horizontal Bunch Size and Energy Spread Studies at KARA," in *Proc. IPAC'19*, Melbourne, Australia, May 2019, pp. 2498–2500, `doi:10.18429/JACoW-IPAC2019-WEPGW016`

[32] W. Wang, M. Caselle, T. Boltz, E. Blomley, M. Brosi, T. Dritschler, A. Ebersoldt, A. Kopmann, A. Santamaria Garcia, P. Schreiber, E. Bründermann, M. Weber, A.-S. Müller, Y. Fang, "Accelerated Deep Reinforcement Learning for Fast Feedback of Beam Dynamics at KARA," *IEEE Trans. Nucl. Sci.*, vol. 68, pp. 1794-1800, 2021. `doi:10.1109/TNS.2021.3084515`

ISBN: 978-3-95450-230-1 ISSN: 2673-5350 doi:10.18429/JACoW-IBIC2021-MOOB02

RECOMMISSIONING OF THE CERN INJECTOR COMPLEX BEAM INSTRUMENTATION

R. Veness*, European Organisation for Nuclear Research (CERN), Geneva, Switzerland

Abstract

During the last two years, the CERN injector complex has been completely renovated with the aim of providing high intensity and smaller emittance beams to the LHC.

A new Linac providing H- has been constructed and major upgrades in the Proton Synchrotrons (PS Booster ring, PS ring and Super PS ring) have been performed. A full suite of new beam diagnostics has been implemented and commissioned. This includes fast wire scanners, beam gas ionization monitors, quadrupolar pick-ups and diamond beam loss detectors. New radiation-hard beam position monitoring system was also successfully deployed in the SPS. This talk will present an overview of the performance of the newly built instruments.

INTRODUCTION

The LHC injectors are the heart of the CERN accelerator complex, producing and accelerating proton and ion beams upto LHC injection energies, as well as producing beams for fixed-target and other facilities on the site.

2019–2020 saw the second major shutdown of the whole CERN accelerator complex since the start of LHC operations, called LS2. This was required principally to complete the LHC Injectors Upgrade (LIU) project [1], with changes across the whole injection chain to produce brighter, more intense beams in preparation for the High-Luminosity LHC (HL-LHC) upgrade [2]. Table 1 shows the target beam parameters for this upgrade at the time of the instrumentation conceptual design in 2014.

Table 1: Achievable LIU Proton Beam Characteristics at Injection

Machine		PSB	PS	SPS	LHC
Kinematic energy	[GeV]	0.16	2	25	449
Number of bunches		1/ring	29.6	1.5	650
Bunch separation	[ns]	-	284	25	25
Bunch intensity	[10^{10} p/b]	29.6	28.1	2.2	2
Transverse emittance	[µs]	1.5	1.6	1.7	1.9
Bunch length	[ns]	650	205	4.2	1.65

The major change has been the construction of a new LINAC (LINAC4) which produces hydrogen ions (H-) at 160 MeV, rather than the 50 MeV protons from the previous LINAC2. These are stripped to p+ with carbon foils and accelerated in the existing Proton Synchrotron Booster (PSB) to 2 GeV. The existing Proton Synchrotron (PS) ring takes this new higher energy injection and accelerates into the Super Proton Synchroton (SPS) at 26 GeV which gives the final boost to 450 GeV for LHC injection.

In parallel with the LIU project, LS2 has also seen a significant consolidation project (called CONS) of the injector systems, taking advantage of the unprecedented access to machines, with the aim of ensuring reliable operations for the HL-LHC era. The injectors have been operating for, in some cases, more than 60 years and were historically separated by machine in instrument design and operations. One of the strategic goals of the Beam Instrumentation group was to use this major upgrade to standardize whole instrument groups across the injector complex, replacing mechanics, electronics and software where possible with the aims of decreasing commissioning time, improving maintainability and coping with reductions in expert manpower.

These LIU and CONS projects have led to a number of new in-vacuum beam instrumentation requirements, coming from the completely new LINAC4 and its injection into the PSB, instruments with a new specification due to the increased energies and intensities in the rings and for the consolidation of obsolete instruments, many of which were 30+ years old. The numbers are summarized in Table 2.

Table 2: In-vacuum Instruments Newly Commissioned Post-LS2

Machine / Complex	'New for old' Replacements	Additional Instruments
LINAC4	–	36
PSB	20	12
PS	9	2
SPS	4	3
LHC	3	1
ISOLDE / HIE	20	11
ELENA	–	31
TOTALS	56	96

A total of 152 in-vacuum instruments were built and newly commissioned post-LS2, plus some 348 new BLM channels. Not all of this work will be covered in this paper, in particular, there are two significant new installations, ELENA, the extra-low energy ion ring and an extension to the High Energy and Intensity isotope separator, HIE-ISOLDE, which have between them 42 new instruments. However, these are not part of the LHC injector chain so will be presented elsewhere. The paper will also cover the new acquisition system for SPS beam positioning system that has been designed, deployed and successfully commissioned with beam.

---

* raymond.veness@cern.ch

ISBN: 978-3-95450-230-1 ISSN: 2673-5350 doi:10.18429/JACoW-IBIC2021-MOOB02

LINAC4

Construction of the new LINAC4 started in 2008 and the commissioning of the machine and associated beam instrumentation has progressed in stages [3]. Although LINAC4 has been extensively used for testing and reliability, LS2 has seen the final stage of commissioning, with the connection of the LINAC to the new PSB injection and the subsequent recommissioning as the source of protons for all CERN machines from late 2020. The focus since the re-start has been on tuning the RF structures and optimizing beam transmission while preserving longitudinal and transverse emittance. Key to this has been the Time-of-Flight (ToF) and Beam Shape (BSM) monitoring systems [4].

The ToF system [5] was extensively used to tune each RF cavity to its nominal level of acceleration and precisely determine the beam kinetic energy. The method is based on the measurement of the signal phase shift difference while passing through pairs of strip lines Beam Position Monitors (BPMs), during an RF phase scan. Over the last year the robustness and automation of the whole monitoring system was highly improved [6].

The BSM system allows the reconstruction of the beam longitudinal distribution by converting it into a transverse distribution of low energy secondary electrons emitted by a beam-intercepting tungsten wire [7]. Two BSM monitors are in use, one at end of the LINAC and a second one installed in 2020, at the end of the LINAC transfer line. Following an initial period for the RF set-up, they are now regularly used to check the RF stability and to prepare the different H- beam types required by the PSB, with an example given in Fig. 1.

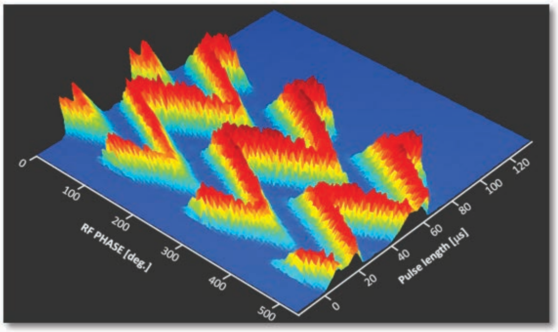

Figure 1: BSM output image showing energy modulation around 160 MeV. Courtesy of [4]

At low beam intensities, transverse emittance is inferred from wire grids and scanners. For beam pulse lengths longer than ~100 µm these instruments are restricted due to wire damage. A newly developed “laser stripping emittance meter” [7], which is minimally-invasive, intercepting only around 7% of particles has been developed and is under commissioning for these measurements.

NEW BOOSTER INJECTION REGION

The region between LINAC4 and PSB was completely re-built during LS2 to accommodate the new H- injection at 160 MeV. The carbon stripping foils which strip H- to p+ are instrumented with insertable observation screens (BTVs) to monitor the process. Improperly stripped particles are absorbed by a dedicated dump. This is instrumented with a “H0/H- monitor” consisting of 4 titanium plates. These measure the charge of partially stripped (H0) and non-stripped (H-) particles to monitor degradation of the stripping foils and interlock the maximum sustainable intensity on the dump [8]. Due to the complexities of the electronics and influence of secondary emission from plates, these monitors were calibrated against beam current transformers (BCTs) and a calibration factor was obtained. These are now fully commissioned and able to resolve stripping inefficiencies below 1%, with a stable error of below 1.5% for all plates in the four PSB rings (see Fig. 2).

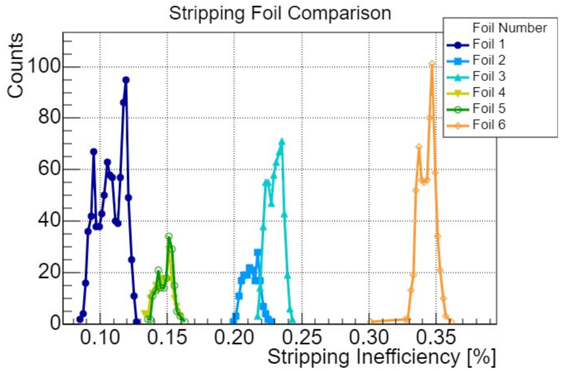

Figure 2: Stripping inefficiency as measured by the H0H-monitor in the PSB Ring 3 during dedicated studies with different foil types (preliminary results). Courtesy of [8]

The renewing of this injection region, with good access to areas that are normally tightly packed with equipment (see Fig. 3) and highly activated due to the injection losses was also the opportunity to replace 17 obsolete BTV monitors which are required for the set-up and commission the injection and extraction lines. These were replaced with a new, common design based on magnetically coupled bellows-free movements. Reliable installation and test before commissioning was important as these instruments were required to transfer the beams into the PSB with a completely new optics layout. The plan is now to re-use this standard BTV design wherever possible in the injector complex.

PROTON SYNCHROTRON

A new ionization profile monitor (called a Beam-Gas Ionisation (BGI) monitor) has been designed and installed in the PS. This, as depicted in Fig. 4, uses Timepix3 hybrid pixel detectors to image beam-gas ionisation electrons. The ionisation electrons are accelerated onto the detector by an electrostatic field inside a 0.2 T dipole field used to maintain the transverse position. A prototype was installed in 2017,

Figure 3: Four BTVs installed in the PSB.

but extensively re-designed and re-installed along with a second device in the vertical plane in 2021. It is the first use of active silicon detectors in the beam vacuum of an injector at CERN and as such has seen extensive off-line testing, both for performance and machine compatibility.

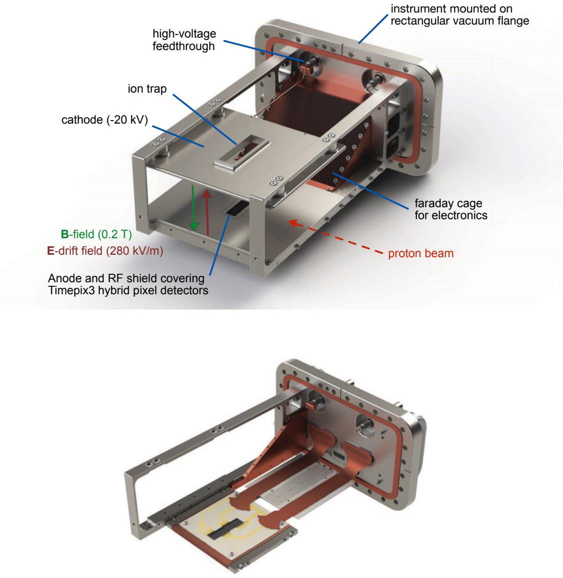

Figure 4: Design of the Timepix3 beam gas ionization monitor.

The instruments and software were available from first beam in the PS commissioning [9]. The fast 2 ms integration time allows for 600 profiles to be registered along the 1.2 s of a single PS beam cycle. The waterfall plot of Fig. 5 shows this complete beam size evolution across a machine cycle. The only significant issue during the commissioning was due to unexpected beam losses in the sector which was tracked down to an unwanted sextupolar field component in the compensation dipole. Magnet simulations have found a corrective shielding plate modification which will be applied in a future shutdown, with a short-term corrective fix in place using other lattice magnets.

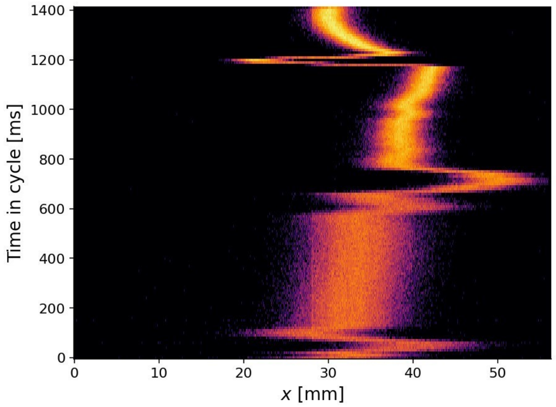

Figure 5: Waterfall plot evolution of the horizontal beam profile and position of a LHC-type bunch along the 1.2 s long PS cycle. Courtesy [9]

The PS ring also saw a number of other instrumentation changes, including a new Secondary Emission Monitor (SEM) grid for setting up the injection and the replacement of three obsolete SEM grids used for emittance measurement during set-up and now also equipped with fast electronics for turn-by-turn injection matching studies.

SUPER PROTON SYNCHROTRON

New Orbit Control Electronics (ALPS)

The SPS orbit system electronics for the 240 Beam Position Monitors (BPMs) in the SPS machine was completely replaced during LS2 [10]. The system, based on the use of logarithmic amplifiers, was specified to cover ~90 dB with a resolution in the order of 0.01 dB. The previous electronics were replaced by radiation tolerant analogue and digital front-ends connected by fibers to 60 back-end boards using the 'VME FMC Carrier' (VFC). This was to be the first major use of the new VFC board developed at CERN [11] and since rolled-out to a number of other new systems such as the new fast wire scanners, diamond BLMs, BCTs and tune measurement.

As the BPM system was considered a fundamental requirement for restarting the machine, extensive preparations were made to ensure operability. Components that were radiation tolerant by design were used wherever possible, and all cards underwent burn-in tests and calibration in the lab.

A number of dry runs with the system were also organized and performed with the accelerator operations team. These allowed a user-level test and debug of the system, but also built confidence, both in the system and in the team. The system worked from first beam in the SPS, giving orbit correction sufficient to start RF commissioning. This in turn allowed the use of the orbit acquisition mode to further commission the machine. Figure 6 shows an image of the SPS operational software showing the first successful injection in the accelerator captured by ALPS.

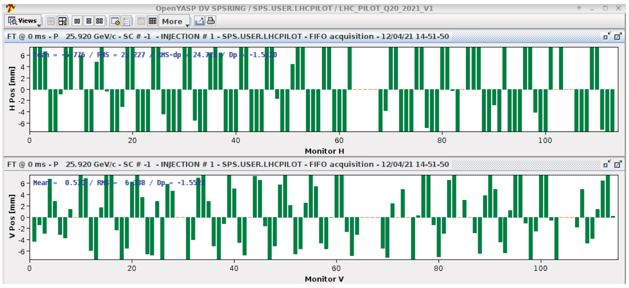

Figure 6: Screen capture of SPS-ALPS operational software. Courtesy of [10]

Based on logarithmic amplifiers with a settling time of 100 ns, the resolution of the system is expected to be worse for single bunch than for train of bunches, due to averaging. It was measured with beams in both configurations, and after a Singular Value Decomposition (SVD) analysis [12] resolutions of 140 µm and 7 µm have been demonstrated for single bunch and bunch train length of 10 µs respectively. Close collaboration between electronics, software and operations teams from early specification, through test and finally commissioning was key to the success of this project.

New Beam Dump and Instrumentation

Another major project executed in the SPS during LS2 has been the installation of a new SPS Beam Dump System (SBDS). This involved the relocation, design civil works and installation of a completely new 'in-line' beam dump to accommodate the higher brightness LIU beams in accordance with modern radio-protection standards. This has involved a complete re-distribution of beam instrumentation in two of the six SPS sectors, but more significantly the design of a new imaging system directly in front of the new dump [13].

Due to the exceptional 100% availability requirement and harsh radiation environment, the system was designed around a fixed Chromox screen intercepting the ejected but not circulating beam. The light passes along a 17 m optical line with 5 fixed mirrors to a radiation-shielded bunker containing the digital camera. The acquisition system takes advantage of the long decay time of Chromox to capture multiple images of the same event and perform on-line selection to provide an unsaturated image over a wide range of intensities.

The system was working from first beam and extensively used to evaluate dump kicker and diluter performance. An operational GUI is used in the control room with data showing the 'painting' of the beam on the dump, with an example given in Fig. 7.

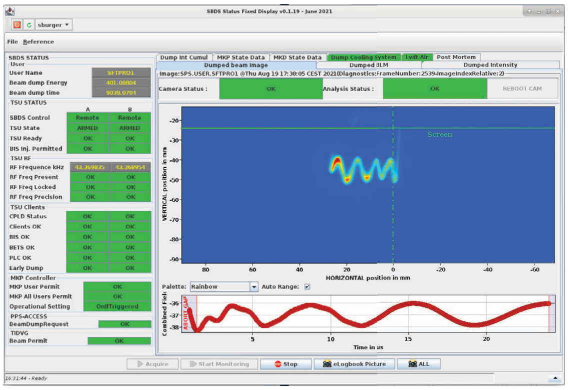

Image:SPS.USER.SFTPRO1 @Thu Aug 19 17:38:05 CEST 2021(Diagnostics:FrameNumber:2539-ImageIndexRelative:2)

Camera Status : OK
Analysis Status : OK

SBDS STATUS

User
User Name SFTPRO1
Beam dump Energy 401.08804
Beam dump time 9039.0704

TSU STATUS	A	B
SBDS Control	Remote	Remote
TSU State	ARMED	ARMED
TSU Ready	OK	OK
BIS Inj. Permitted	OK	OK
TSU RF		
RF Frequence kHz	43.369835	43.368954
RF Freq Present	OK	OK
RF Freq Locked	OK	OK
RF Freq Precision	OK	OK
TSU Clients		
CPLD Status	OK	OK
Clients OK	OK	OK
BIS OK	OK	OK
BETS OK	OK	OK
PLC OK	OK	OK
Early Dump	OK	OK

MKP Controller
MKP User Permit OK
MKP All Users Permit OK
Operational Setting OnlTriggered
PPS-ACCESS
BeamDumpRequest OK
TIDVG
Beam Permit OK

Palette: Rainbow
Auto Range: ☑

16:31:44 - Ready

Figure 7: SBDS operational display. Courtesy of [13]

NEW WIRE SCANNERS

Before the shutdown there were three different designs of wire scanners (BWS) operating in the injectors with maximum scan speeds of between 1 and 20 m.s^{-1}. All were obsolete mechanically, unreliable in electronics and software and not compatible with the smaller, higher brightness LIU beams. A major project saw one new 20 m.s^{-1} device designed and installed, with new control electronics, acquisition and software layer, in 17 locations across the 3 rings [14].

Prototype devices were installed in all three injector rings in the operation years preceding LS2 allowing for test and development of the mechanical instrument and acquisition as well the design of the control system. An emphasis was placed on system testability and maintainability during the design phase, with redundant, easily-accessible mechanics and controls hardware and mechanics designed for rapid diagnosis and validation [15].

During the so-called Individual System Tests (ISTs) periods, it was possible to test and validate all kinematic units without beam. The first instruments to see beam in the PSB required an intense period of firmware and software tests, which, as well as for the DAQ of the secondary shower detectors, were not possible to perform before. At this stage, the benefits of system standardization became apparent as the subsequent PS and SPS commissioning were much smoother, with scans made on the first day of beam, benefiting from the debugging in the PSB. Figure 8 shows data from the operational logbook from the SPS showing beam size and transverse emittance measured over 120 bunches.

Studies and optimisation of this complex instrument are still ongoing in parallel with operation, in particular for optimisation of the acquisition and implementation of the lower scanning speeds needed for the smallest beam sizes in the SPS. These small, high intensity beams will remain a technological limit for this device until improved wires are developed [16].

ISBN: 978-3-95450-230-1 ISSN: 2673-5350 doi:10.18429/JACoW-IBIC2021-MOOB02

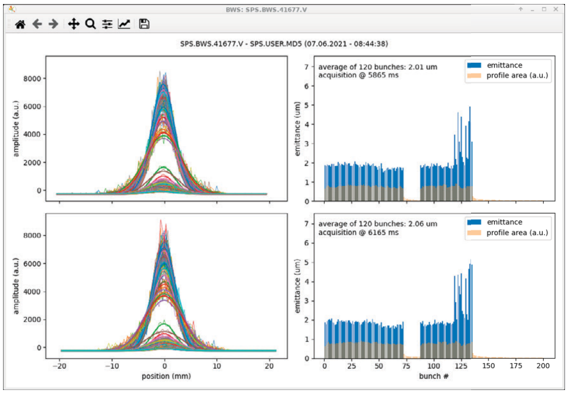

Figure 8: BWS Operational display from the SPS. Courtesy of [15]

BEAM LOSS UPGRADES

2021 sees the global commissioning of a new beam-loss monitoring (BLM) system [17]. The system provides automatic protection to accelerator equipment in case of unexpected beam losses as well as serving as a diagnostic tool for adjustment of machine parameters.

The system consists of 322 detectors of two different ionization chamber designs mounted ex-vacuum along the whole injector chain. Each detector has a dedicated HV power supply and customized coaxial cables to maximize reliability for these accelerator-critical diagnostics. The acquisition control system consists of 14 racks with custom-designed back-plane connecting up to 64 channels. There are two overlapping measurement techniques covering the $2x10^{10}$ input range with a measurement frequency of up to 2 µs.

Installation and commissioning was distributed over 6 years, starting with prototyping in the PSB in 2015. The LINAC4 system was the first to be fully operational and extensively used in the commissioning. The PSB and PS systems were then fully installed and the legacy units decommissioned during LS2. Figure 9 shows a BLM chamber installed in the PSB and illustrates the challenges of retrofitting such instruments into an existing machine.

Full commissioning was in three phases. Firstly ISTs were used for hardware and connection tests. This was followed by a full system dry-run without beam, testing overall modulation and triggering beam interlocks as well as training operators. The final tests with beam included generating intentional losses to trigger interlocks and measurement of loss signals.

The systems were operational from first beam in all machines and were important in the rapid re-start of the complex. Measurement data from the systems are used to calculate the deposited energy and the ambient radiation, and provide input to dosimetry and FLUKA simulations. Some localized issues of EMI have been observed, both synchronous and asynchronous with the beam, and have been attributed to nearby power cables. Ongoing commissioning activities include the refinement of thresholds for interlocks and mitigation of EM noise. In the longer term, automation of system checks will be made to further enhance reliability.

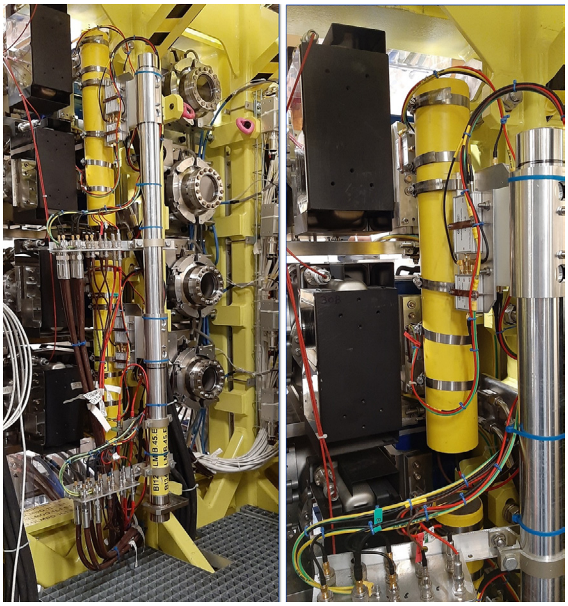

Figure 9: BLM ionisation chambers installed in the PSB.

CONCLUSIONS

The LHC injector complex re-started in January 2021 after two years of the most significant upgrade in it’s 60-year history. One hundred and fifty-two new in-vacuum instruments were designed and built and have been commissioned. Major instruments classes such as the fast wire scanners and SPS orbit system have been completely rebuilt along with the addition of innovative new instruments such as the BGI.

Major steps have been taken in the direction of standarisation of hardware and software which will pay-off in the future with reduced expert manpower and spares inventory, partly compensating the increase in the instrument park under the responsibility of the group.

Recommissioning has been a major undertaking due to the many changes, not only to instrumentation, but the layouts and energies of the machines and associated RF and magnet systems. However, all key instruments were available when needed by operations. This can be attributed to a number of factors: whenever possible, prototypes were installed and operated with beam in the run before the start of the shutdown, allowing for the few final design changes which led to major time and cost savings overall; dry-runs both with and without beam using combined BI and operations teams helped gain confidence in startup-critical systems; in the end, global schedule delays due to COVID stretched the final installation and early commissioning periods. This led to less conflict of expert resources in the key times when the same people are needed both in the tunnel and in the control room, often also in more than one machine.

Many lessons will always be learned from this kind of major project. For BI in LS2, the re-start has been relatively smooth to-date and so the lessons not so painful. EM noise, probably due to the inappropriate routing of power and signal cables has caused issues across several instrument classes and some corrective actions will be needed. Finally, restart schedules will always be tight, but dedicated schedule time for commissioning with beam needs to be defended if expectations of good early instrument availability are to be maintained.

ACKNOWLEDGEMENTS

The author would like to thank the members of the Beam Instrumentation group, our colleagues at CERN and our many collaborators in institutes around the world who worked hard on the design, test installation and commissioning of these systems.

This is a summary paper, relying heavily on the work presented in six other papers at this conference (as well as in earlier conferences) on the commissioning of new instruments. The author would like to thank these others for their support and for sharing their pre-prints.

REFERENCES

[1] High Luminosity LHC Project, `http://hilumilhc.web.cern.ch`

[2] "LHC Injectors Upgrade, Technical Design Report, Vol. I: Protons", CERN, Geneva, Switzerland, Rep. CERN-ACC-2014-0337, 2014.

[3] U. Raich, "Performance of Linac-4 Instrumentation During Commissioning", in *Proc. HB'16*, Malmö, Sweden, 2016, paper WEPM1X01, pp. 385–390. `doi:10.18429/JACoW-HB2016-WEPM1X01`

[4] F. Roncarolo *et al.*, "Commissioning the New CERN Beam Instrumentation Following the Upgrade of the LHC Injector Chain", in *Proc. IPAC'21*, Campinas, SP, Brazil, May 2021, pp. 976–979. `doi:10.18429/JACoW-IPAC2021-MOPAB316`

[5] M. Bozzolan, "BPM Time of Flight Measurements for Setting-up the RF Cavities of the CERN Linac4", in *Proc. LINAC'18*, Beijing, China, Sep. 2018, pp. 879–881. `doi:10.18429/JACoW-LINAC2018-THPO084`

[6] J. Tan, "LINAC4 diagnostics experience during commissioning", *ARIES workshop on Experiencies During Hadron LINAC Commissioning*, 2021. `https://agenda.ciemat.es/event/1229/contributions/2276/`

[7] A.V. Feschenko, "Technique and instrumentation for bunch shape measurements", in *Proc. RUPAC'12*, Saint Petersburg, Russia, Oct. 2012, pp. 181-185. `https://jacow.org/rupac2012/papers/frxor01.pdf`

[8] A. Navarro and F. Roncarolo, "PSB H0-H- Monitor Calibration and Commissioning", presented at IBIC'21, Gyeong-ju, Rep. of Korea, virt. conference, Sep. 2021, paper WEPP24, this conference.

[9] H. Sandberg *et al*, "Commissioning of Timepix3 based Beam Gas Ionisation Profile Monitors for the CERN Proton Synchrotron", presented at IBIC'21, Gyeong-ju, Rep. of Korea, virt. conference, Sep. 2021, paper TUOA05, this conference.

[10] A. Boccardi *et al.*, "The Commissioning of ALPS, the new Beam Position Monitoring System of CERNs Super Proton Synchrotron", presented at IBIC'21, Gyeong-ju, Rep. of Korea, virt. conference, Sep. 2021, paper MOPP23, this conference.

[11] A. Boccardi *et al.*, "A Modular Approach to Acquisition Systems for the Future CERN Beam Instrumentation Developments", in *Proc. ICALEPCS'15*, Melbourne, Australia, Oct. 2015, pp. 1103–1106. `doi:10.18429/JACoW-ICALEPCS2015-THHB2O02`

[12] J. Irwin *et al.*, "Model independent analysis with BPM correlation matrices", in *Proc. EPAC'98*, Stockholm, Sweden, Jun 1998, paper WEP21G, pp. 1644–1646. `https://jacow.org/e98/PAPERS/WEP21G.PDF`

[13] S. Burger *et al.*, "New CERN SPS Beam Dump Imaging System", presented at IBIC'21, Gyeong-ju, Rep. of Korea, virt. conference, Sep. 2021, paper TUPP22, this conference.

[14] R.Veness *et al.*, "Installation and Test of Pre-Series Wire Scanners for the LHC Injector Upgrade Project at CERN", in *Proc. IPAC'17*, Copenhagen, Denmark, May 2017, pp. 412–414. `doi:10.18429/JACoW-IPAC2017-MOPAB121`

[15] J. Emery *et al.*, "Commissioning of the LHC Injectors BWS Upgrade", presented at IBIC'21, Gyeong-ju, Rep. of Korea, virt. conference, Sep. 2021, paper TUPP18, this conference.

[16] A. Mariet and R. Veness, "Selection of Wires for the New Generation of Fast Wire Scanners at CERN", in *Proc. IBIC'18*, Shanghai, China, Sep. 2018, pp. 523–526. `doi:10.18429/JACoW-IBIC2018-WEPC19`

[17] M. Saccani, W. Vigano, and C. Zamantzasm "The Beam Loss Monitoring System after LHC Injectors Upgrade at CERN", presented at IBIC'21, Gyeong-ju, Rep. of Korea, virt. conference, Sep. 2021, paper TUPP32, this conference.

ISBN: 978-3-95450-230-1 ISSN: 2673-5350 doi:10.18429/JACoW-IBIC2021-MOOB03

OVERVIEW OF RAON BEAM INSTRUMENTATION SYSTEM AND CONSTRUCTION STATUS OF THE LOW-ENERGY LINAC*

Y. S. Chung†, H. J. Woo, G. D. Kim, J. W. Kwon, E. H. Lim[1],
Institute for Basic Science, Daejeon 3400, Korea,
[1]also at Korea University, Sejong City, Korea

Abstract

RAON is a heavy ion accelerator for researches using Rare Isotopes (RI) as a major research facility in Korea. RAON uses both In-flight Fragmentation and Isotope Separation On-Line methods to provide various RI beams. The ultimate goal of the driver Linac of RAON is to accelerate uranium and proton beams up to 200 MeV/u and 600 MeV, with a maximum beam currents of 8.3 pμA and 660 pμA, respectively. After 9 years of RAON construction, commissioning of the low-energy Linac front-end system that consists of 14.5 GHz ion source, low energy beam transport, a 500 keV/u radio frequency quadrupole, and medium energy beam transport has been carried out since late 2020. And beam injection to the low-energy superconducting Linac is planned to start in December 2021. Here, we introduce RAON beam instrumentation and diagnostics systems as well as the construction status of the low-energy Linac.

INTRODUCTION

RAON is a heavy ion accelerator facility to accelerate both stable and rare isotope (RI) beams up to the power of 400 kW with an energy higher than 200 MeV/u [1]. This facility is planned to have both Isotope Separation On-Line (ISOL) and In-Flight (IF) fragmentation method [2,3] to produce RI beams. Using both ISOL and IF method, this facility can provide the high intensity and quality RI beams to the experiment.

RAON accelerator is composed of an injector system and the superconducting linear accelerator. An injector system accelerates a heavy ion beam to 500 keV/u and creates the desired bunch structure for injection into the superconducting Linac. The injector system comprises two electron cyclotron resonance ion sources (ECR-IS), a low energy beam transport (LEBT), a radio frequency quadrupole (RFQ), and a medium energy beam transport (MEBT). The superconducting linear accelerator is divided into two sections, the low-energy superconducting Linac (SCL3) and the high-energy superconducting Linac (SCL2). Two superconducting Linac sections are connected by a Post-accelerator to Driver Linac (P2DT) which consists of a charge stripper and 180 degree bending system.

This article is to document the construction status of RAON. Beam instrumentation system and the early results of beam commissioning of the injector system will also be briefly discussed.

CONSTRUCTION STATUS OF RAON

Recently RAON construction project was evaluated thoroughly and it was decided that the whole construction project would be staged to two phases. The low-energy Linac section which consists of injector, SCL3 and low experimental system will be completed in the phase 1. ISOL system and high-energy experimental system are also constructed in the phase 1 as well. The high-energy superconducting Linac, SCL2 will be constructed in the 2nd phase launched in 2022.

The installation of injector system (14.5 GHz ECR-IS, LEBT, RFQ, and MEBT) was completed in October 2020, and immediately followed by the beam commissioning.

The superconducting cryomodule is being installed in the SCL3 tunnel since April 2020. As of August 2021, 22 QWR cryomodules, 13 HWR type-A (2 cavities) cryomodules, and 10 HWR type-B (4 cavities) cryomodules were installed in the SCL3 tunnel as shown in Fig. 1. The first beam injection to the SCL3 is planned to be in December 2021.

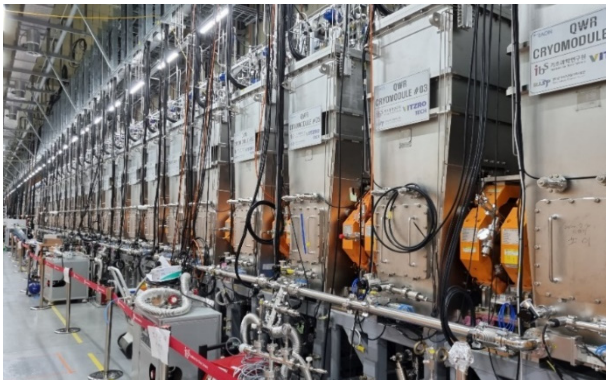

Figure 1: A photograph of SCL3 tunnel.

BEAM INSTRUMENTATION SYSTEM

For initial beam commissioning and component tuning, we will use $^{40}Ar^{9+}$ beam with ~30 eμA, 100 μsec pulse width, and a repetition rate of 1 Hz. Faraday Cup (FC), Wire Scanner (WS), Beam Viewer (BV), AC-Current Transformer (ACCT), and Beam Position Monitor (BPM) are properly used for beam tuning. During normal operation, on-line device such as BPM, ACCT, and Beam Loss Monitor (BLM) are used to monitor beam transport and acceleration function without destructing beam. The ACCT is to measure a beam current and transmission, and Differential Beam Current Measurement (DBCM) using ACCT networks is to primary detect beam loss in a certain section. Every BLM and the DBCM outputs will be linked to the RAON Fast Machine Protection System (MPS). Those on-

---

* Work supported by the IBS/RISP funded by the Ministry of Science and ICT and the National Research Foundation of the Republic of Korea under Contract 2013M7A1A1075764

† yschung@ibs.re.kr

line devices are designed to measure a beam current between typically 1 μA and 1 mA. We also install the 2D Emittance Meter (Allison Type); Strip-line Fast Faraday Cup (SFFC), and Beam Attenuator to measure beam emittance, bunch length, and reduce beam intensity, respectively.

The layout of RAON beam diagnostics is shown in Fig. 2. ISOL beam line is designed to transport the low energy and low intensity RI beam, therefore WS, FC, Plastic Detector (PD), Secondary Electron-BPM are main beam diagnostics devices. The diagnostics devices available in the injector are as follows: (i) 4 WSs, 3 FCs, 2 BVs, an ACCT in the LEBT. (ii) 4 WSs, 2 FCs, 6 BPMs, and 2 ACCTs in the MEBT (see Fig. 5). The WS consists of three 0.1 mm tungsten wires of horizontal, vertical, and 45 degree angled. The ACCT is the non-interceptive current transformer manufactured by the Bergoz Instrumentation [4]. Every warm section of the low-energy superconducting Linac, SCL3, a BPM and a BLM are installed. Also 4 WSs in 4 consecutive warm section (QWR 2~5, HWR-A 2~5, HWR-B 2~5) and 1 FC are installed to measure beam properties precisely. The high-energy superconducting linac, SCL2, has a similar configuration to SCL3.

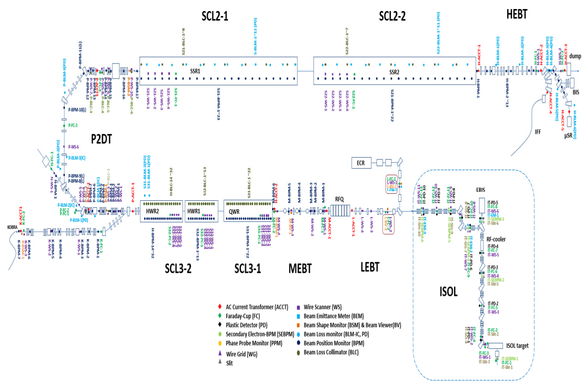

Figure 2: Layout of RAON beam diagnostics.

The BPM with 4 button-type electrodes is the non-interceptive position measurement device [5]. The BPM provides the beam phase as well as the beam position, and the beam induced phase information from two BPMs paired can be used to derive the absolute beam energy. A button (curved & square shape) BPM in SCL3, a large button (bent & square shape) BPM in P2DT, and a 150 mm long strip-line (curved & square shape) BPM in SCL2 are fabricated as shown in Fig. 3. All of SCL3 BPM were calibrated at wire test bench [6] and most of SCL3 BPM was installed in the tunnel.

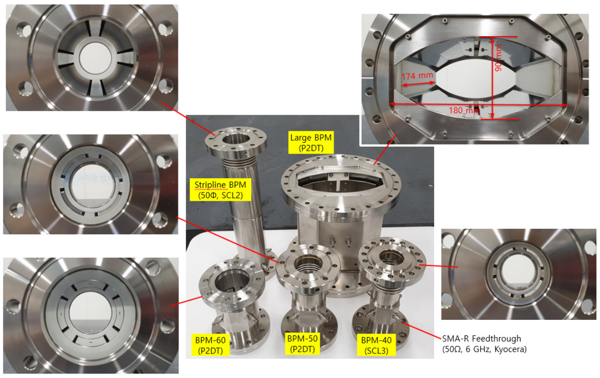

Figure 3: RAON Beam Position Monitor.

Both SCL3 and SCL2 adopt normal conducting quadrupole doublet focusing lattice in the warm section, where two quadrupole magnets are located between every cryomodules for beam focusing. The BPM in each warm section is mechanically aligned to the quadrupole magnet. Each beam diagnostics (or vacuum) chamber in the warm section has an inner diameter of 36 mm niobium ring, called as Beam Loss Collector (BLC) to directly collect any halo or strayed beam. The ring-type BLC in the warm section chamber is the main BLM in the SCL3 and combination of BLC, plastic detector, and proportional counter will be the BLM in P2DT, SCL2, and beam lines. However the DBCM with ACCT networks as described earlier will be utilized as the primary beam loss detection system.

Figure 4 shows the diagnostics DAQ system. BPM controller is designed and fabricated through domestic company [7]. The 8 channel pico-ammeter AMC board [8] in μTCA format is adopted to measure currents from WS, FC, and BLM (BLC). A standalone 1u chassis unit (upgrade of the previous cRIO system) is designed to measure ACCT outputs as well as DBCM processing which requires 100 MS/sec with 14 bit 4 ADC channels in the low-energy Linac. Those all three kinds of DAQ systems based on EPICS control support RAON global timing system, trigger, and interlock, etc.

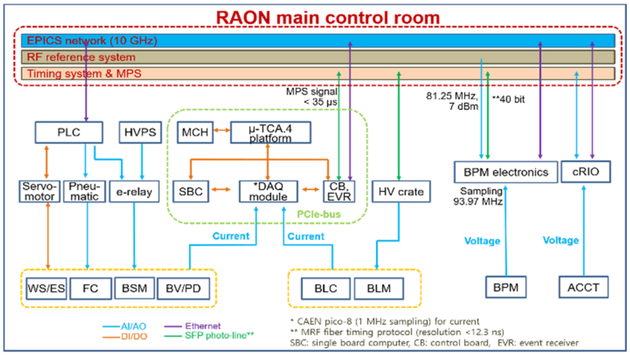

Figure 4: Diagnostics DAQ System.

INJECTOR BEAM COMMISSIONING

The 14.5 GHz ECR-IS is a compact permanent magnet ion source manufactured by the Pantechnik, France [9]. The 28 GHz superconducting ECR-IS is in the process of improving its performance. The LEBT is designed to transport and match ion beams extracted from the ECR-IS to the RFQ. Electrostatic quadrupoles were chosen rather than the magnetic quadrupoles for transport and focusing because these would be a more suitable for low velocities beams at LEBT. About 5 m long RFQ with 4-vane structure is designed to accelerate ion beams from 10 keV/u to 500 keV/u and it runs at 81.25 MHz of resonance frequency. The MEBT is to transport and to match ion beams accelerated from the RFQ to the low energy superconducting linac, SCL3. A total of eleven room temperature quadrupole magnets are chosen to transport and focus beams at MEBT. Four bunching cavities which run at 81.25 MHz of resonance frequency are also arranged to match the longitudinal beam size to the SCL3. Figure 5 shows the layout of the injector and diagnostics system.

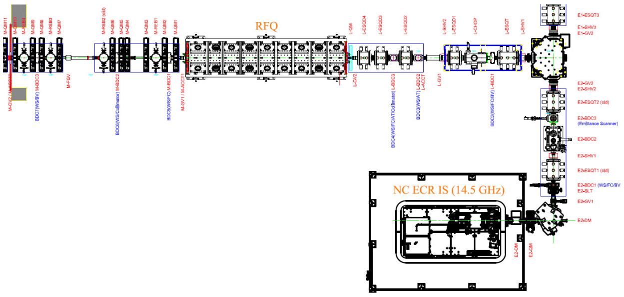

Figure 5: Instrumentation for Injector System.

The 14.5 GHz ECR-IS was commissioned with Argon and Oxygen, and proton beams and it could provide ion beams to the injector system from September 2020. The beam commissioning of the injector system has been started since October 2020. The $^{40}Ar^{9+}$ beam was successfully transmitted through LEBT, accelerated by RFQ, and transported to the end of MEBT. In the beam commissioning, a peak current of ~30 eμA continuous beam at LEBT was transported and an electrostatic chopper in the LEBT was used to generate a pulsed beam with a pulse length of 100 μsec and a repetition rate of 1 Hz. Figure 6 shows the BV image at LEBT and BPM signal at MEBT measured with 25 GHz sampling rate oscilloscope during beam commissioning in March, 2021.

SUMMARY

Construction project of RAON is staged to two phases. The low-energy Linac, ISOL system, and high energy experimental system will be completed in the phase 1. Construction of the high-energy superconducting Linac, SCL2 is pushed to construct in the 2nd phase. The injector system for low-energy Linac is in the beam commissioning stage since October 2020. During beam commissioning, it was confirmed that each component and beam instrumentations of injector was functioning as designed and was working properly in an integrated fashion.

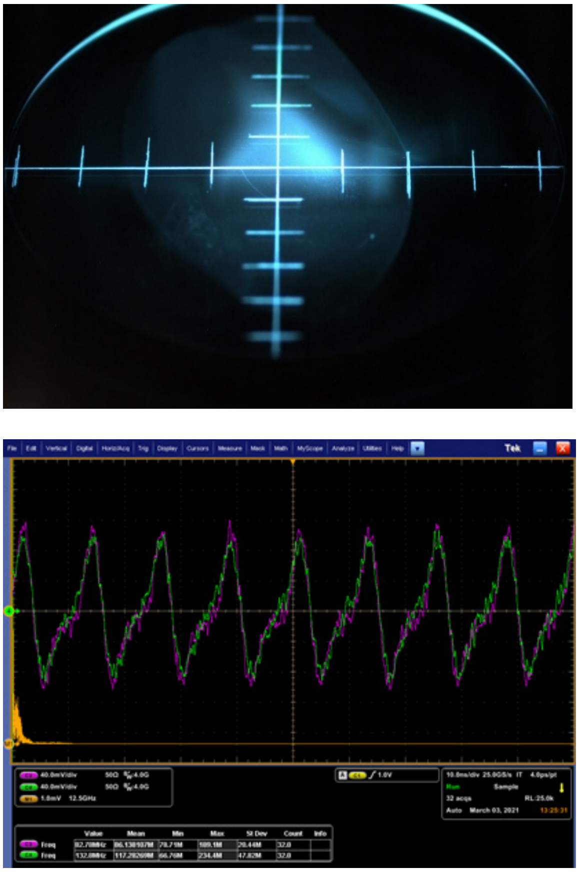

Figure 6: BV Image (Top) and BPM Signal (Bottom).

REFERENCES

[1] D. Jeon *et al.*, "Design of the RAON accelerator systems", *J. Korean Phys. Soc.*, vol. 65, pp. 1010-1019, 2014.

[2] K. Tshoo *et al.*, "Experimental systems overview of the Rare Isotope Science Project in Korea" *Nucl. Instrum. Methods Phys. Res., B*, vol. 317, pp 242-247, 2013.

[3] S. Taeksu *et al.*, "Rare Isotope Production and Experimental Systems of RAON", *New Physics : Sae Mulli*, vol. 66, pp. 1500-1510, 2016

[4] Bergoz Instrumentation, https://www.bergoz.com/.

[5] J. W. Kwon, H. J. Woo, G. D. Kim, Y. S. Chung, E.-S. Kim, "Beam position monitor for superconducting post-linac in RAON", *Nucl. Instrum. Methods Phys. Res., A*, vol. 908, pp. 136-142, 2018.

[6] J.W. Kwon, "Development of Beam Position Monitor system for RAON heavy ion accelerator", Ph.D. Thesis, Korea University, Sejong, Korea, 2020.

[7] mobiis, https://www.mobiis.com/.

[8] CAENels, https://www.caenels.com/.

[9] Pantechnik, https://www.pantechnik.com/.

SUMMARY OF THE ARIES WORKSHOP ON MATERIALS AND ENGINEERING TECHNOLOGIES FOR PARTICLE ACCELERATOR BEAM DIAGNOSTIC INSTRUMENTS*

R. Veness, R. Jones, CERN, Geneva, Switzerland
U. Iriso, ALBA-CELLS Synchrotron, Cerdanyola del Vallès, Spain
G. Kube, K. Wittenburg, Deutsches Elektronen-Synchrotron DESY, Hamburg, Germany
P. Forck, GSI, Darmstadt, Germany
V. Schlott, PSI, Villigen, Switzerland
D. Eakins, University of Oxford, Oxford, UK

Abstract

ARIES is an EU-sponsored programme for accelerator research and innovation. An international workshop was held online as part of this programme in June 2021 on the topic of 'Materials and Engineering Technologies for Particle Accelerator Beam Diagnostic Instruments'. The aim of the workshop was to bring together instrument designers, experts and industry and research groups to review the state of the art in the field, present designs and discuss future challenges, whilst also developing and strengthening collaborations between groups. There were sessions covering 'Instrument design and operation', 'Novel materials and applications' and 'New technology and components' over the three half-days of the online meeting. This paper reviews the key topics presented at the workshop.

INTRODUCTION

Over the years 2017 to 2021 the EU-funded ARIES programme [1] is funding a number of topical meetings on specific areas of interest to the accelerator beam instrumentation community through the work-package ARIES-ADA [2,3]. The workshop [4] under consideration within this publication was targeted at design and technology of physical instruments – an area which receives relatively little coverage in the literature. It was originally planned as a face-to-face meeting at Wadham College, Oxford but was postponed and finally re-structured as a remote meeting in June 2021 with a programme of 20 talks, reduced from the original 32. This included four talks from European industry, demonstrating close links to science in the field.

There were 205 participants registered from around the globe resulting in lively online discussions performed in dedicated break-out rooms for each talk.

BEAM INSTRUMENT DESIGN, PRODUCTION & OPERATION

Thibaut Lefevre (CERN) opened the scientific part of the workshop introducing the current beam instrumentation highlights from CERN. He showed how the trends in particle physics accelerators, both on the energy/brightness frontier and in areas such as antimatter and rare isotope physics are creating new challenges for beam instrumentation. CERN has just completed a major upgrade to the LHC injector complex. This required new instrument designs for highly radioactive environments, such as the BTV in the SPS synchrotron [5] as well as new simulation-driven designs for the mitigation of impedance heating. Designs for beam-intercepting devices such as screens and wire scanners have been upgraded with modern thermally resistant materials and faster movements. However, most innovation for current and future machines is related to non-invasive beam profile devices. New devices based on laser stripping of the LINAC4 H^- beams [6] and beam-gas ionisation in the Proton Synchrotron [7] are now operational at CERN whilst upgraded devices using synchrotron light and diffraction radiation are developed for the future High Luminosity LHC.

Gian Luca Orlandi (PSI) presented a collaboration between the Paul Scherrer Institut and Sincrotrone Trieste on electron beam lithography fabricated, freestanding wire scanners [8]. The project aims for minimally invasive electron beam profile measurements with sub-micron resolution. Applications are for FEL user operation and ultra-high precision, transverse beam diagnostics at novel laser and plasma driven accelerators. PSI produced 800 nm and 500 nm wide Au wires of 2 µm thickness and 2 mm beam clearance. FERMI manufactured a set of wires consisting of 3 µm thick sandwiches made of Au (1 µm) and Si_3N_4 (2 µm) and a Ti (20 nm) middle layer with a width of 0.7 µm, 0.8 µm, 1 µm and 2 µm, respectively [9, 10]. Beam tests were successfully conducted at SwissFEL, where a 300 MeV, low charge (1 pC), and low emittance ($\varepsilon_y \sim$ 55 nm) beam can be focused to transverse beam sizes of < 500 nm, see Fig. 1 and [11].

William Andreazza (CERN) presented a new generation of fast wire scanners built for the LHC Injector Upgrade project at CERN and the European Spallation Source in Lund, Sweden [12]. The high power beams require a wide

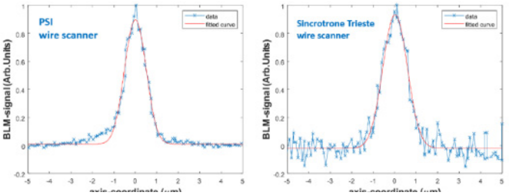

Figure 1: Vertical beam profiles at SwissFEL taken with single shot data acquisitions.The measured beam sizes are 434 ± 7 nm (PSI wire scanner) and 443 ± 33 nm (Sincrotrone Trieste wire scanner).

---

* This project has received funding from the European Union's Horizon 2020 Research and Innovation programme under Grant Agreement No 730871.

range of measurement speeds (5 m/s to 20 m/s) and a position accuracy in the order of 1 µm. Key components are an in-vacuum drive system without kinematic links, a vacuum-compatible frameless electrical motor, a high precision optical encoder (mark width of 6 µm at a pitch of 40 µm) and a metal wire fork fabricated by 3D additive machining technology. Prototypes were extensively tested in all CERN injector rings, and the full series of wire scanners has been delivered to CERN accelerators and ESS.

The contribution by Serena Psoroulas (PSI) focused on the definition of requirements on beam monitoring for clinical applications at the medical cyclotron. The ICRU report (2007) and the IEC standard (60601-2-64, 2014) regulates patient-relevant beam quantities and requires that proton range, dose uniformity, and absolute delivered dose are determined permanently. The monitoring chain of PSI Gantry 1 is based on ionisation chambers for dose and position measurement and Hall probe detectors for position and energy monitoring. To avoid drawbacks caused by ionisation chambers, particularly at high beam currents [13], a new resonant position and current monitor prototype is being investigated [14].

Benjamin Moser (CERN) showed the recently developed production procedure for SEM-Grids at CERN as depicted in Fig. 2. The PCB substrate for the wire support consists of alumina (Al_2O_3) with a purity of 96-97 %. It is equipped with 1 MΩ SMD resistors to verify the condition of the wires without beam. For the electrical connection between the feedthrough and the wire support, PICAL NP polyimide film is used as a base for flex-PCBs. The properties of an improved winding machine were discussed. This machine allows for efficient preparation of the wires. CERN brought forward "sticking wires" as a topic for discussion. A potential solution has already been designed but has not yet been tested in the machine. The discussion at the end mainly revolved around different ways to maintain tension in wires lost due to thermal expansion from by beam heating.

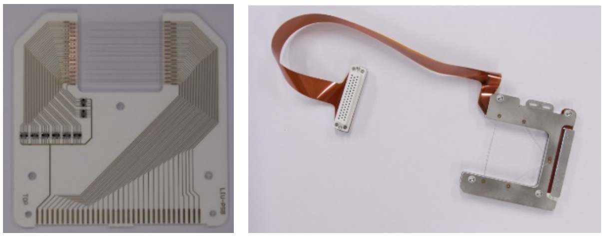

Figure 2: CERN standard SEM-Grid: Left: Alumina PCB with wires and resistors; right: assembly with Flex-PCB.

The contribution by Dirk Lipka (DESY) described a formalised approach for the realisation of a diagnostics system from design up to implementation of a large-scale accelerator, using the example of a button BPM [15, 16]. All requirements and conditions have to be collected, and subsequently, these conditions have to be divided into required sub-systems, e.g. mechanics and electronics. Here simulation tools speed up the design time as the tools can predict the behaviour with high precision. Attention has to be taken to the correct use of simulation tools, e.g. meshing and convergence. The design phase is completed with tolerance studies to prepare the construction. For a large number of items, initial pre-series are required to train companies for the final production. During the series production, the pieces should be checked to optimise the results and production process. In parallel, electronics should be developed and produced. Finally, the system has to be installed, calibrated and commissioned.

Alun Morgen (DSL) reported on a dedicated workshop on button BPM production held in May 2019 [17] and reported recently [18]. The topic is of great relevance due to the large quantity installed at any light source. Glass sealing technology is attracting increased interest, with several facilities receiving of prototype buttons to gain experience with this technology. Communication with the supplier at all stages of the process was identified as key to success. Particular care needed to be taken when the design is handed from one sub group to another e.g. subcontractors, or moving from design engineers to machinists. An increase in the in-house testing capability of facilities will be needed to establish and maintain the level of quality and tolerancing required for the successful operation of our diagnostics devices. In order to enable that and allow the tracking of individual components through the testing and validation processes, laser marking is being investigated.

Magnetically coupled drives are recently developed and commercially available for ultra-high vacuum applications, as Nick Clark (from the UHV-Design company) reported. There are several features: Non-polymer and without dry lubricant, all-metal and ceramic push-pulls for the lowest outgassing and lowest friction; high speed and high precision pneumatic and ball screw driven actuators designed explicitly for beam diagnostics. Different designs for the magnet assemblies exist, providing high coupling forces or torque and minimal external stray magnetic fields. Case studies are executed in collaboration between industry (here UHV-Design) and major institutes like BNL, CERN, Diamond and PSI, such as fast wire scanners.

NOVEL MATERIALS & APPLICATIONS

John Huber's team at University of Oxford, together with the CERN beam instrumentation group, explored different candidates for wire materials which could be viable for fast wire scanners, as current materials are expected to be unsuitable due to the associated temperatures and mechanical loads. Using the concepts behind Ashby diagrams [19, 20], a merit index was developed for selecting the wire material as depicted in Fig. 3 [21]. It suggested the best materials would be carbon-based, such as carbon nanotubes (CNT) and CNT ropes. Nearby competitor materials including beryllium and boron carbide were also identified. The force displacement response was measured for candidate materials including CNT ropes of different thicknesses. Combining this with thermal properties and density data, it was possible to identify CNT ropes on the Ashby diagram and confirm their superior performance. The group had also examined failure mechanisms in some of the wires, identifying the CNT ropes as preferable to ordinary carbon fibres due to having less statistical variation in breaking strength.

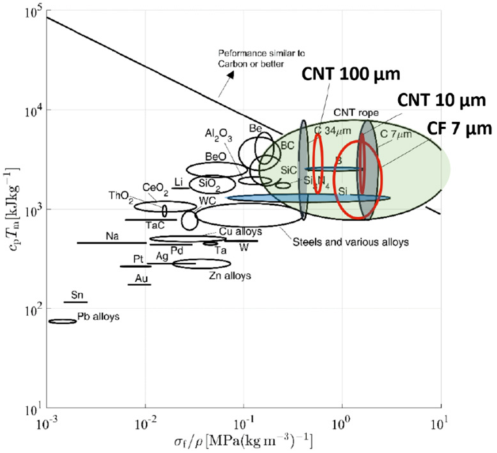

Figure 3: Ashby map showing the thermal and mechanical performance for potential wire scanner materials [21].

Alexandre Mariet (CERN) extended the discussion of carbon-based wire materials. For intense beam interactions local overheating can lead to sublimation, and hence premature failure during subsequent usage. He provided the properties of different CNT allotropes. These included both individual CNTs as well as wound strand CNT. A novel process for manufacturing the CNT wires was presented. Subsequent examination confirmed the presence of only carbon, indicating a material of high quality. In particular, Alexandre contrasted the mechanical behaviour and performance of 30 µm diameter CNTs and CNT wires, showing clear differences in their mode of failure.

Mike Barnes (CERN) discussed the design and optimisation of ferrite-based materials used for kickers, and the challenges posed by the high temperatures that can be developed due to beam-induced current. For the specific work described, hot-isostatic pressing (HIP) was employed to manufacture a bulk ferrite material from constituent powder, resulting in a near net dense compact. HIP exhibited a noticeable improvement in thermal properties, while the frequency-dependent magnetic permeability limits the rise-time to a few hundred ns. Adding a thin protective buffer to the magnet (e.g., 3 µm Ti), resulted in shifting its activation time by ~100 ns. These measurements were shown to be in good agreement with a thermal model which includes radiation transport.

Kevin Jordan (JLAB) talked about the use of boron nitride nanotubes (BNNT) as scintillators. In recent years, several studies were carried out at BNL, GSI and JLAB using BN as a scintillator, showing outstanding performance with electrons between 1.6 MeV and 7.4 GeV, and Au ions at 4.8 MeV/u. The presentation showed BN nanotubes of 2-6 nm diameter, providing mechanical properties (like tensile strength, Young modulus), as well as scintillator properties: decay time in the order of ns, photon yield four times lower than Chromox, and peak emission wavelength below 500 nm. The material can withstand high beam powers, and studies for its lifetime and resolution were presented.

Silke Vilcins (DESY) talked about changes to 316LN ESR material properties after high-temperature treatment. She provided practical advice and pragmatic solutions based on experience over the last 30 years. Processes like welding, brazing and stress relief heat treatments require special attention because they affect material properties like hardness, permittivity, grain structure or nitride concentration. At temperatures below 300ºC, there is almost no outgassing because the thermal energy is too low. Between 500ºC and 900ºC, there is the formation of M23C6 and possibly s-phase intergranular corrosion and grain disintegration. A vacuum annealing treatment, which leads to a low outgassing rate with constant hardness, appears challenging. Finally, a new material called ‘Alloy 50’ was presented as an alternative due to its superior hardness limits, low permittivity, good weldability.

Ivo Wevers (CERN) described the outgassing rate of four common polymers used in accelerators: PEEK, Kapton, Mylar and Vespel. The description was based on theoretical models and experimental results, and the measurements are well fitted with a 3-step model. At room temperature, the outgassing is initially very high but decays rapidly after a certain amount of time $\tau/2$, depending mainly on the thickness. Higher moisture content causes higher outgassing rates during all stages of the pump-down, while a greater diffusion coefficient (although increasing the initial outgassing rates) results in overall lower outgassing rates, particularly for pumping times beyond $\tau/2$. Finally, it was shown that storing polymeric parts with dried silica gel granules can effectively reduce their outgassing rates, but exposure to air during installation must be minimized.

Coming from a private company, Klaus Bergner (company VACOM) shared his experience of adequately defining the quality requirements. The focus was set on surface cleanliness in the manufacturing of vacuum components. In this regard, the specifications should be given for the total outgassing rate in the assembly and quantitatively so that the user can test and validate them. Thus, continuous communication between user and supplier is essential.

NEW TECHNOLOGIES & COMPONENTS

Gerhard Schneider (CERN) reported on his experience with viewports and mirrors. About 250 window flanges are installed on the CERN accelerator complex, either made of borosilicate glass (Kodial) or fused silica (quartz) glass. CERN has experienced failures of brand-new window flanges, mainly with fused silica material. Investigating the cause, they found out that window flange manufacturers used elastomer seals during leak tests, different from the use-case with non-annealed copper gaskets. The failure analyses led to a new technical specification requiring 100% of the window flanges to be tested with CERN supplied gaskets and baked to the nominal temperature. Metal flange parts and windows are usually procured by the window flange manufacturer from a sub-contractor. The real expertise of the manufacturer is solely the connection from the glass window to the weld ring and the welding of the

ISBN: 978-3-95450-230-1 ISSN: 2673-5350 doi:10.18429/JACoW-IBIC2021-MOOB04

ring to the base flange material. Weld rings must carefully be chosen, considering radiation and magnetic parameters and possible oxidation and low differential thermal expansion coefficient versus the optical window.

Slava Grishin (ESS ERIC) shared his experience on 16 years of collaborative work between CERN and IHEP (Protvino), where more than 5000 beam loss monitor (BLM) detectors of various types have been produced. The manufacturing process was under the responsibility of IHEP, using industry-produced components [22, 23]. For the success of such a collaborative project, crucial points are generally design optimisation and organisation of the collaboration between both partners particularly for specification and selection of industrial suppliers and components. The production of prototypes (with a pre-series for a large number of items), continuous material verification, continuous monitoring of the production schedule, several tests before, during and after production, final installation, and final control of detector performance are all key to success. Driven by the system complexity, no compromise should be allowed in some details, however, a high focus should be placed on quality assurance.

Ben Jensen (company Surrey NanoSystems) presented coatings for UHV instrument stray light suppression. Such coatings should have high absorbance at specific instrumentation wavelengths, both good Total Integrated Scattering (TIS) values and spectral Bidirectional Reflectance Distribution Function (BRDF) and low outgassing at chamber operational temperatures. They should be compatible with UHV bake-out and experience no degradation from long term UV exposure, be tolerant to radiation exposure, thermally stable and electrically conductive. Based on company experience in space technology applications, super-black coatings were developed (brand name Vantablack). Two such coatings were discussed, which were already tested at CERN: S-VIS and CX2 (a beta phase development coating). While both materials are spray applied, S-VIS requires vacuum post-processing (activation) to create the required absorbing cavities. This coating shows good UV-THz performance and seems to be well suited for applications in an accelerator environment.

Additive Manufacturing (AM) in Beam Instrumentation was presented by Ana Miarnau (CERN): A brief description of the techniques of AM was given. The "Selective Laser Melting" technique is used at CERN for the production of vacuum parts. Some mechanical constraints such as roughness, tolerances and vacuum constraints like impurities and porosity were reported. However, outgassing tests at CERN showed a typically clean and unbaked metal pump-down curve without significant contamination. Some examples from CERN were discussed [24].

The Easy Alignment System (EASy) was described by Ufuk Akkaya (DESY). New High-Precision 6-Axes-Positioning devices, the EASy-family, was developed at DESY to meet the needs of accelerators/experiments for high precision and stiffness. It has the advantage of combining compactness and a carrying capacity between 10 kg to > 5000 kg with a precision of weight-dependent positioning 1 to 20 µm. A standardised motor control unit will ensure integration in control systems whilst manual operation is also possible.

A sealing technology for high precision wide open vacuum flanges and waveguide connections was presented by Martin Lemke (DESY). The traditional metal sealing technology for large vacuum flanges requires a mirror-like surface. The new concept introduces small grooves on the sealing surface with about 50 µm depth and distance from each other of about 25 µm; an example is depicted in Fig. 4. This concept also reduces the requirements of the flange surface by some factors. No vacuum leaks were discovered during tests and installations at DESY and BESSY.

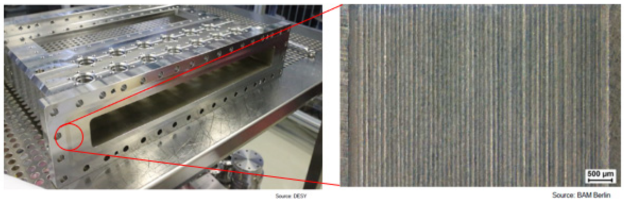

Figure 4: A large flange vacuum chamber with the grooves. The zoom shows a high magnification photo of one of the first test pieces.

CONCLUSION

The workshop took place with a lively atmosphere even despite the absence of a face-to-face contact. Each session was followed by a breakout room session, with one virtual room per speaker. This gave a more informal environment where detailed questions and discussions could be held and proved very successful, with some discussions, in particular those not discussed in regular conferences, lasting for an hour after the end of the programme.

Raymond Veness (CERN) chaired the final wrap-up session. He summarised some subjects of general interest to be followed-up by the community. These included:

- The use of nanotubes (carbon, boron nitride) for beam intercepting and other instrumentation uses
- Particle-free and low particle count devices and environments
- Development of a new generation of precision linear wire scanners
- The usage of magnetically coupled drives for UHV applications
- Novel methods of black coatings for optical light absorption.

Beam instrumentation experts from laboratories around the world were keen to share knowledge and best-practice in these areas, and it was agreed to make e-mail groups for the interested parties.

ACKNOWLEDGEMENTS

We like to thank Madeleine Catin and Dmitry Gudkov from CERN for their important contributions to making this a smooth and successful workshop.

This project has received funding from the European Union's Horizon 2020 Research and Innovation programme under Grant Agreement No 730871.

ISBN: 978-3-95450-230-1 ISSN: 2673-5350 doi:10.18429/JACoW-IBIC2021-MOOB04

REFERENCES

[1] Accelerator Research and Innovation for European Science and Society ARIES, `https://aries.web.cern.ch/`.

[2] Advanced Diagnostics at Accelerators ADA, `https://aries.web.cern.ch/wp8`

[3] P. Forck *et al.*, "ARIES-ADA: An R&D Network for Advanced Diagnostics at Accelerators", in *Proc. 7th Int. Beam Instrumentation Conf. (IBIC'18)*, Shanghai, China, Sep. 2018, pp. 71-74. `doi:10.18429/JACoW-IBIC2018-MOPB02`

[4] `https://indico.cern.ch/event/1031708/`.

[5] D. Celeste, E. Bravin, S. Burger, and F. Roncarolo, "Development and Test of a Beam Imaging System Based on Radiation Tolerant Optical Fiber Bundles", in *Proc. 10th Int. Particle Accelerator Conf. (IPAC'19)*, Melbourne, Australia, May 2019, pp. 2658-2660. `doi:10.18429/JACoW-IPAC2019-WEPGW078`

[6] T. Hofmann, G. E. Boorman, A. Bosco, S. M. Gibson, and F. Roncarolo, "A low-power laserwire profile monitor for H^- beams: Design and experimental results", *Nucl. Inst. and Meth. in Phys. Res. Section A,* vol. 903, pp. 140-146, 2018. `doi:10.1016/j.nima.2018.06.035`

[7] H. S. Sandberg *et al.*, "Commissioning of Timepix3 Based Beam Gas Ionisation Profile Monitors for the CERN Proton Synchrotron", presented at the 9th Int. Beam Instrumentation Conf. (IBIC'21), Pohang, Korea, Sep. 2021, paper TUOA05, this conference.

[8] G.L. Orlandi *et al.*, "Nanofabricated freestanding wire scanners for beam diagnostics with sub micrometer resolution", *Phys. Rev. Accel. Beams*, vol. 23, p. 042802, 2020. `doi:10.1103/PhysRevAccelBeams.23.042802`

[9] M. Veronese *et al.*, "A nanofabricated wire scanner with free standing wires: Design, fabrication and experimental results", *Nucl. Inst. and Meth. in Phys. Res. Section A*, vol. 891, pp. 32-36, 2018. `doi:10.1016/j.nima.2018.02.040`

[10] S. Borrelli *et al.*, "Generation and Measurement of Sub-Micrometer Relativistic Electron Beams", *Communications Physics-Nature*, vol. 1, p. 52, 2018. `doi:10.1038/s42005-018-0048-x`

[11] B. Hermann *et al.*,"Electron beam transverse phase space tomography using nanofabricated wire scanners with sub-micrometer resolution", *Phys. Rev. Accel. Beams,* vol. 24, p. 022802, 2021. `doi:10.1103/PhysRevAccelBeams.24.022802`

[12] J. Emery *et al.*, "Laboratory and Beam Based Studies for Assessing the Performance of the New Fast Wire Scanners for the CERN Injector Complex", in *Proc. 8th Int. Beam Instrumentation Conf. (IBIC'19)*, Malmö, Sweden, Sep. 2019, pp. 392-396. `doi:10.18429/JACoW-IBIC2019-TUPP033`

[13] R. Dölling *et al.*, "Ionisation Chambers and Secondary Emission Monitors at the PROSCAN Beam Lines", in *AIP Conference Proceedings* vol. 868, p. 271, 2006. `doi:10.1063/1.2401414`

[14] S. Srinivasan *et al.*, "Beamline characterization of a dielectric-filled re-entrant cavity resonator as beam current monitor for a medical cyclotron facility", *Pysica Medica* vol. 78, p. 101, 2020, `doi:10.1016/j.ejmp.2020.09.006`

[15] D. Lipka and S. Vilcins, "BPMs from Design to Real Measurement", in *Proc. 5th Int. Particle Accelerator Conf. (IPAC'14)*, Dresden, Germany, Jun. 2014, pp. 2774-2778. `doi:10.18429/JACoW-IPAC2014-THXA01`

[16] S. Vilcins and D. Lipka, "Mechanical Design of Cryogenic Vacuum Feedthroughs for X-FEL Button BPMs", in *Proc. IBIC'14*, Monterey, CA, USA, Sep. 2014, paper TUPF11, pp. 332-336.

[17] `https://www.dia-mond.ac.uk/Home/Events/2019/BPM-button-design-and-manufacturing-workshop.html`

[18] A. F. D. Morgan, "Technological Review of Beam Position Button Design and Manufacture", in *Proc. 8th Int. Beam Instrumentation Conf. (IBIC'19)*, Malmö, Sweden, Sep. 2019, pp. 448-452. `doi:10.18429/JACoW-IBIC2019-WEAO01`

[19] M. F. Ashby, "Overview No. 80: On the engineering properties of materials", *Acta Metall.* vol. 37, p. 1273, 1989. `doi:10.1016/0001-6160(89)90158-2`

[20] M. F. Ashby, *Materials selection in mechanical design, 3rd ed.*, Oxford, UK: Butterworth-Heinemann, 2005.

[21] H. Bigland, J. E. Huber, R. Veness, and A. C. F. Cocks, "Wire Materials for Scanners in the Large Hadron Collider: An Unusual Materials Selection Problem", *Adv. Eng. Mater.*, vol. 22, p. 1900927, 2020. `doi:10.1002/adem.201900927`

[22] V. Grishin *et al.*, "Ionization Chambers as Beam Loss Monitors for ESS Linear Accelerator", in *Proc. IBIC'17*, Grand Rapids, MI, USA, Aug. 2017, pp. 454-457. `doi:10.18429/JACoW-IBIC2017-WEPWC03`

[23] M. Saccani, W. Viganò, and C. Zamantzas, "The Beam Loss Monitoring System after LHC Injectors Upgrade at CERN", presented at IBIC'21, Pohang, Korea, Sep. 2021, paper TUPP32, this conference.

[24] R. Veness *et al.*, "Metal 3D Additive Machining for in-Vacuum Beam Instrumentation", in *Proc. MEDSI'18*, Paris, France, Jun. 2018, pp. 121-124. `doi:10.18429/JACoW-MEDSI2018-TUPH36`

ISBN: 978-3-95450-230-1 ISSN: 2673-5350 doi:10.18429/JACoW-IBIC2021-MOOC02

AN EXPERIMENTAL COMPARISON OF SINGLE CRYSTAL CVD DIAMOND AND 4H-SiC SYNCHROTRON X-RAY BEAM DIAGNOSTICS

C. Houghton*, C. Bloomer, L. Bobb, Diamond Light Source, OX11 0DE, Didcot, United Kingdom

Abstract

As synchrotron beamlines increasingly use micro-focus techniques with detectors sampling at kHz rates, the need for real-time monitoring of the beam position at similar bandwidths is vital. Commercially available single-crystal CVD diamond X-ray diagnostics are well established as excellent non-destructive monitors for synchrotron X-ray beamlines. Silicon carbide (4H-SiC) X-ray beam position monitors (XBPMs) are a recent development with the potential to provide the same benefits as their diamond counterparts with larger usable apertures and lower cost. At Diamond Light Source a comparison between single-crystal CVD diamond and 4H-SiC XBPMs has been carried out. The sc-diamond and 4H-SiC beam position monitors are mounted in-line along the beam path, so that synchronous kHz measurements of the synchrotron X-ray beam motion can be measured. Several tests of the two position monitors performance are presented: comparing kHz beam position measurements from the detectors, temporal response, and signal uniformity across the face of the detectors. Each test is performed with varying bias voltages applied to the detectors. A discussion of the benefits and limitations of 4H-SiC and diamond detectors is included.

INTRODUCTION

With the recent upgrades to synchrotron beamline optics that allow for sub-micron X-ray beam sizes at the sample point, and beamline detectors with operating frequencies in the kHz range, the need for accurate beam position monitoring at similar bandwidths is essential. Destructive X-ray beam position diagnostics such as fluorescent screens can not be used during experimental data collection as the transmission of X-rays through the materials used for these screens is low. For example 50 µm of LuAG scintillator has a transmission of just 7 % at 9 keV [1]. Modern beamlines require real-time non-destructive beam position monitoring to ensure the micro-focus beam is stable throughout any data collection. This demand led to the research and development of diamond X-ray Beam Position Monitors (XBPMs) due to their excellent transparency, radiation hardness, and thermal conductivity.

Early experiments with polycrystalline diamond [2,3] have led to modern, commercially available single-crystal chemical vapour deposition (scCVD) diamond XBPMs with beam position resolutions of a few 10 nm [4]. These XBPMs perform as excellent non-destructive monitors for synchrotron X-ray beamlines.

Silicon carbide (4H-SiC)[1] XBPMs are a more recent development that have the potential to provide the same benefits as their diamond counterparts with the added benefit of larger usable apertures and potentially lower cost [5]. In this paper a direct comparison of these two devices is conducted on a synchrotron X-ray beamline.

EXPERIMENTAL SET-UP

The experiment was conducted on the I18 [6] beamline at Diamond Light Source. The two XBPMs used in this experiment were a 10.5 µm thick 4H-SiC detector and a 50 µm thick single-crystal CVD diamond, referred to as sc-diamond. The thicknesses of these devices were chosen such that the two detector plates have similar X-ray transmission at typical synchrotron beamline photon energies. For example, the following experiments were conducted at 9 keV, where transmission is 95 % and 90 % for the sc-diamond and 4H-SiC XBPM respectively [1].

As shown in Fig. 1, the 4H-SiC detector was mounted in front of the sc-diamond as the sc-diamond XBPM has a smaller transparent aperture. These were placed in a nitrogen environment. Behind both the XBPMs was a fluorescent screen CMOS imaging system, used to capture beam images at 700 Hz for independent verification of beam motion. The three devices were secured to a X-Y motion stage just upstream of the sample point, allowing for the X-ray beam to be moved across the surface of the XBPMs. The applied bias voltages and the flux, by use of filters, could be changed throughout the experiment. Generally a 25 µm Al filter was

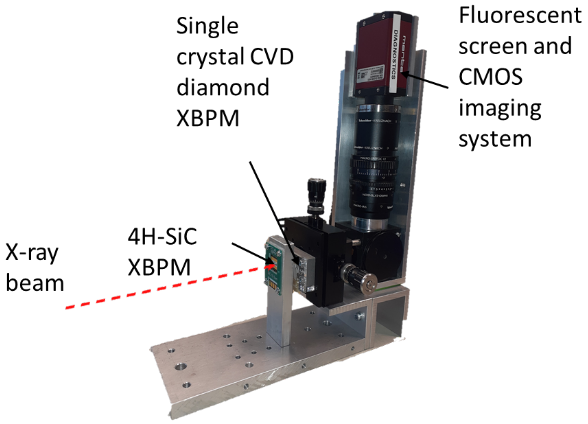

Figure 1: Image of the mounting stage used for the direct comparison of a 4H-SiC XBPM with a sc-diamond XBPM, complete with a CMOS camera imaging system.

---

* claire.houghton@diamond.ac.uk

[1] 4H-SiC refers to the polytype of silicon carbide

in place and the applied bias voltages were 10 V and 5 V for the sc-diamond and 4H-SiC XBPMs respectively.

RESULTS

Signal Uniformity

The motion stage upon which the XBPM and imaging system were mounted could be accurately positioned to within 2 µm. This allowed for two-dimensional raster scans to be completed. Figures 2 and 3 show the signal currents obtained during these scans.

One of the main benefits of using 4H-SiC for X-ray beam position measurements is the possibility for larger active regions, meaning larger beam size beamlines can have accurate position data in situ given that larger X-ray beams can be transmitted through the detector. This is demonstrated clearly in Fig. 2, where a 4.5 mm x 4.5 mm 2-dimensional scan was completed. The signal current generated from each quadrant is shown as a function of the position of the motion stage. The sc-diamond active region is 3 mm x 3 mm square whereas for 4H-SiC this region is 9 mm x 3 mm. Both devices show good signal uniformity across the surface. In Fig. 2 the 4H-SiC's four rectangular quadrants are visible, along with a strip of surface metallisation extending from each. This strip is used to carry the signal currents closer to the edge of the SiC plate, to reduce the need for long a delicate wire bonds.

The uniformity of the signal across both devices is further demonstrated in Fig. 3 where a finer detail 0.17 mm × 0.17 mm raster scan was completed. The current measured by the first quadrant (A) for both devices is shown. Visually the signal uniformity of two devices is indistinguishable.

Temporal Response

An experiment to determine the resolution limitations and the temporal response of the detectors was carried out. The aim of this measurement was to determine whether the beam motion measured on both of the XBPMs when the beam is centred on the quadrants is 'real' beam motion rather than intrinsic noise from the detector or acquisition electronics. To verify the beam motion a fluorescent screen CMOS imaging system was used. The images from the CMOS camera were

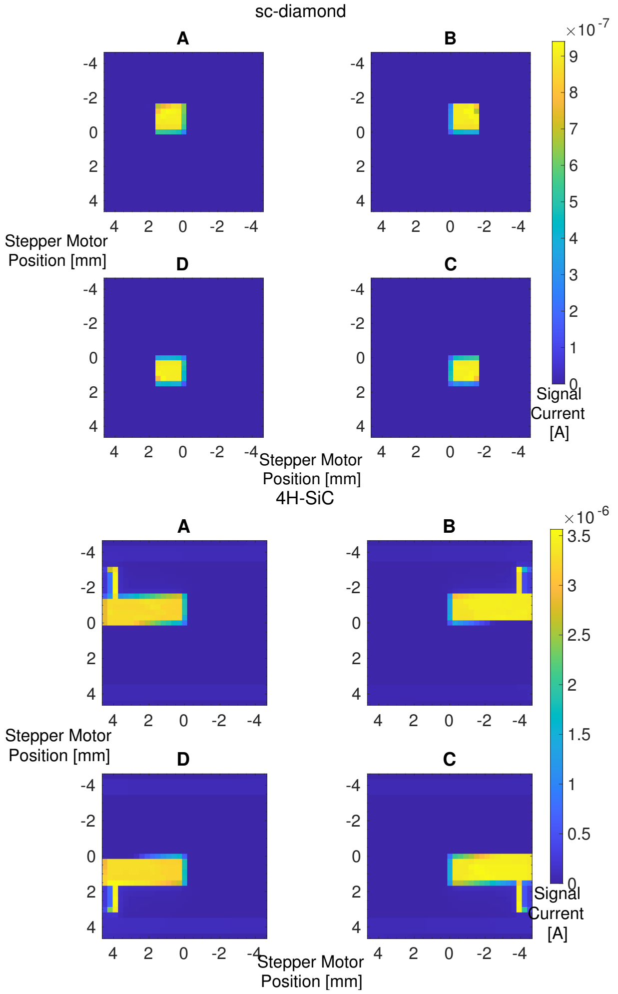

Figure 2: Two-dimensional 4.5 mm raster scan across the surface of (top) a 50 µm thick sc-diamond XBPM, and (bottom) a 10.5 µm thick 4H-SiC XBPMs.

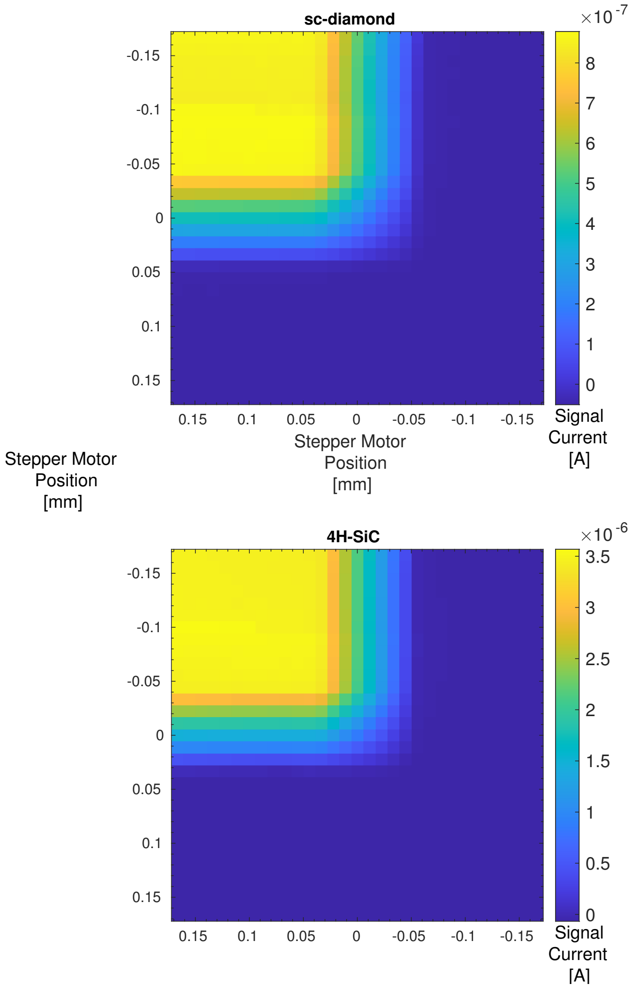

Figure 3: Two-dimensional 0.17 mm raster a single quadrant, A, of the surface of (Top) 10.5 µm thick 4H-SiC XBPM and (Bottom) 50 µm thick sc-diamond XBPMs.

analysed using a 2D Gaussian fit to provide independent beam position measurements. The frame rate of the camera was 700 Hz, much lower than the 20 kHz data collected by the XBPMs. However, it is still a good benchmark to corroborate the beam movement.

Presented in Fig. 4 are the intensity measurements for both the sc-diamond XBPM and 4H-SiC XBPM over 200 ms. The beam intensity measured from the sum of all pixels from the CMOS camera data has been plotted with the XBPM intensity measurement. The data has been normalised to the mean intensity for each device, and shows clear correlation. Therefore the 4H-SiC XBPM can work as a good non-destructive intensity monitor on beamlines, equally as responsive on ~ 10 ms timescales as a traditional sc-diamond XBPM.

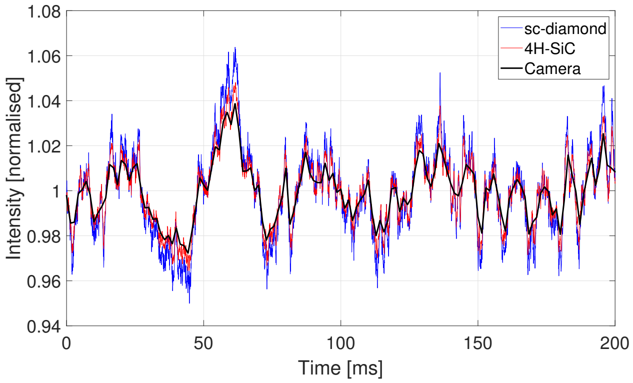

Figure 4: The X-ray beam intensity synchronously recorded by a sc-diamond and 4H-SiC XBPMs at 20 kHz. Intensity is calculated by the summing of all four XBPM quadrants. Also shown, as an independent measurement of intensity from a CMOS camera running at 700 Hz.

In addition, the position measurements for both XBPM devices are plotted in Fig. 5. The horizontal and vertical beam positions, x and y respectively can be determined from the XBPM 4 quadrant signals, Equation (1)

$$x = K_x \frac{(I_A + I_D) - (I_C + I_B)}{I_A + I_B + I_C + I_D} \tag{1a}$$

$$y = K_y \frac{(I_A + I_B) - (I_C + I_D)}{I_A + I_B + I_C + I_D} \tag{1b}$$

where $I_{(A,B,C,D)}$ are the currents through the four XBPM quadrants (A = top-left; B = top-right; C = bottom-right; D = bottom-left), and K_x and K_y are the scale factors for horizontal and vertical respectively.

Figure 5 shows vertical beam position over 200 ms for the 4H-SiC, sc-diamond XBPMs, and the camera. With a scale factor K_y of 100 µm and 50 µm for 4H-SiC and sc-diamond respectively. A 2D Gaussian fit was applied to the camera images where the calculated centroid is taken as the beam position. The small intrinsic beam motion present at the sample point due to the monochromator, slits and other optical elements can be seen on all of the devices. It is clear the camera does not have the temporal resolution to pick up some of the motion of the beam which both the XBPMs can measure. However, the two XBPM measurements show good agreement.

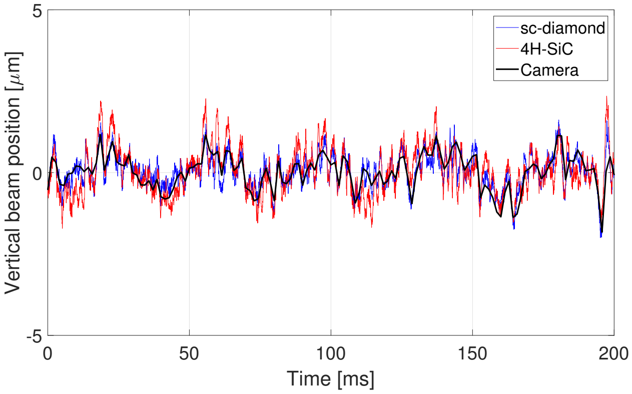

Figure 5: The vertical beam position synchronously recorded by a sc-diamond and 4H-SiC XBPMs at 20 kHz. Also shown, as an independent measurement of beam position from a CMOS camera running at 700 Hz.

Flux Linearity

Both sc-diamond and 4H-SiC detector materials use the same fundamental detection mechanism, where absorbed ionizing radiation excites electrons from the atomic valance band into the conduction band. The resulting signal current is proportional to the number of charge carriers that are excited, and proportional to the energy absorbed within the detector material. For diamond detectors it has been verified that for a given photon energy the signal current is extremely linear with respect to incident flux, over many orders of magnitude [7].

A measure of the flux linearity of the 4H-SiC detector with respect to the diamond XBPM was carried out. The I18 beamline at DLS has the ability to attenuate the incident beam by using various thickness of filter material. Figure 6 shows the resultant plot, with the results for the 4H-SiC XBPM plotted against the sc-diamond producing the expected linear plot. The small discrepancy observed at ~ 1 nA is likely a result of errors in the measuring equipment, rather than differences in signal generation. As it is already well established that sc-diamond XBPMs are linear with incident flux it is possible to conclude that the 4H-SiC XBPM is also linear with flux over the evaluated intensity range.

Bias Requirements

The sensitivity of single-crystal diamond detectors can be influenced by the magnitude of the bias voltage applied across the bulk diamond [7]. With higher voltage more of the charge carriers will be collected at the measurement electrodes, and there is less time for diffusion of the charge carriers leading to a more accurate beam profile measurement [8].

The 4H-SiC detectors are doped so as to operate as a p–n junction diode [5]. The result is an effective ‘built-in’

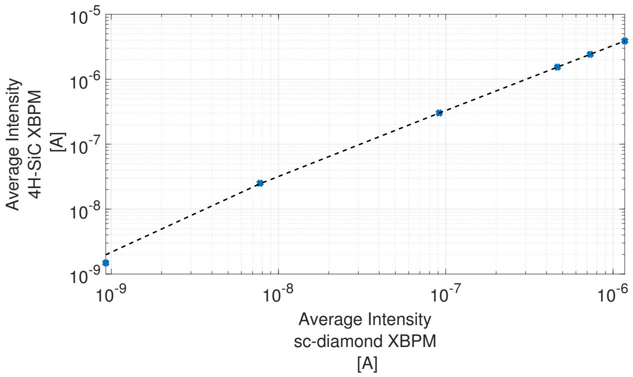

Figure 6: The average intensity of the 4H-SiC XBPM, calculated by summing all 4 quadrants, plotted against the same variable for the sc-diamond XBPM in a log-log plot. Dotted Line: The linear fit of the data points shown as blue dots.

electric field that enables operation of the 4H-SiC device at zero bias voltage. In contrast, due to the difficulty in doping sc-diamond [9, 10], virtually all commercial sc-diamond detectors require an external bias voltage to be supplied.

Figure 7 shows the measured current on two of the quadrants as a one-dimensional stepper motor scan was taken. On the left portion of the scan only quadrant ‘A’ is illuminated, and on the right only quadrant ‘D’ is illuminated. This shows the cross over between the two quadrants, which in both XBPMs is visually symmetrical. As expected the sc-diamond XBPM requires a minimum of 0.5 V in order to achieve something close to full charge collection. However, the 4H-SiC XBPM appears to need no applied bias in order to achieve similar charge collection efficiencies. There is little difference between the currents seen with 0 V and 5 V for the 4H-SiC XBPM, suggesting the detector could be run without the need for a bias voltage supply.

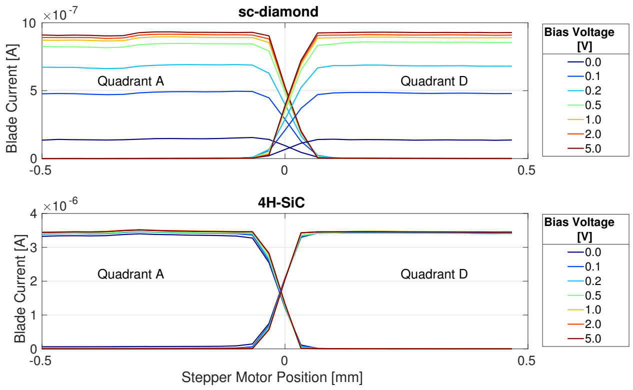

Figure 7: The results of 1D scans of the X-ray beam moving across the face of the detectors, with varying bias voltages applied. Top: 50 µm thick single-crystal diamond. Bottom: 10.5 µm thick 4H-SiC.

Additionally, the beam intensity was calculated as the sum of all the quadrants. An integration period of 1 seconds was used. The charge collection efficiency (CCE) was calculated and is presented in Fig. 8. A charge collection of 100 % is assumed to have occurred with an applied bias of 5 V. This further confirms the results seen in Fig. 7 the efficiency of the 4H-SiC XBPM does not drop below 90 %, conversely a minimum voltage of 0.5 V is required for the sc-diamond XBPM to reach efficiencies of the same level. Both detectors have the same CCE with bias voltages above 2 V.

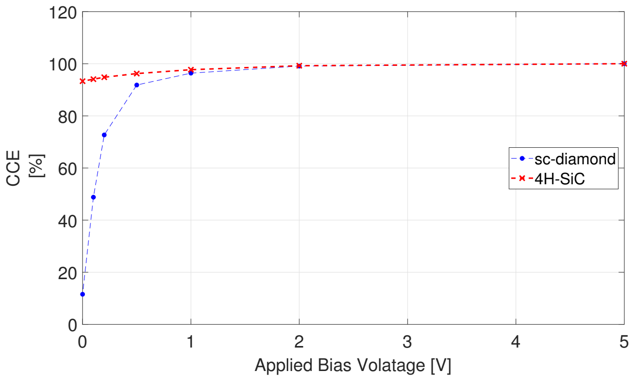

Figure 8: The Charge Carrier Efficiency (CCE) for sc-diamond and 4H-SiC XBPMs with bias voltage, using the average intensity from 30 seconds of 20 kHz data.

CONCLUSION

An experimental comparison between the existing commercially available sc-diamond and a new 4H-SiC non-destructive X-ray beam position monitor has been conducted in a nitrogen environment. The 4H-SiC XBPM has equivalent operational performance to the sc-diamond XBPM in signal uniformity, temporal resolution and flux linearity. 4H-SiC XBPMs can be operated without a bias voltage simplifying the installation on beamlines. In addition, the 4H-SiC can be produced with a larger clear aperture. This is beneficial for beamlines with larger beam sizes where the use of the smaller aperture sc-diamond XBPM would limit performance. Through appropriate choice of 4H-SiC thickness, 4H-SiC detectors can offer comparable transmission to sc-diamond XBPMs for in situ beam position measurements. Based on these results the 4H-SiC should be considered an option for non-destructive monitors for synchrotron X-ray beamlines in the future.

ACKNOWLEDGEMENTS

The authors of this paper would like to thank Konstantin Ignatyev and I18 for the beam time necessary for this experiment. We would also like to thank Cordutza Dragu for the synchronous trigger system used and Graham Cook for his work on the mounting system. Thank you for the support of STLab who provided the 4H-SiC detector for testing.

REFERENCES

[1] B.L. Henke, E.M. Gullikson, and J.C. Davis, “X-ray interactions: photoabsorption, scattering, transmission, and reflection at E=50-30000 eV, Z=1-92”, *At. Data Nucl. Data Tables*, vol. 54, no. 2, pp. 181-342, July 1993.

[2] D. Shu, T.M. Kuzay, Y. Fang, J. Barraza, and T. Cundiff, “Synthetic diamond-based position-sensitive photoconductive detector development for the Advanced Photon Source”, *J. Synchrotron Rad.*, vol. 5, pp. 636-638, 1998. `doi:10.1107/S0909049597019778`

[3] H. Sakae *et al.*, “Diamond Beam-Position Monitor for Undulator Radiation and Tests at the Tristan Super Light Facility”, *J. Synchrotron Rad.*, vol. 4, pp. 204–209, July 1997. `doi:10.1107/S090904959700561X`

[4] E. Griesmayer, P. Kavrigin, C. Weiss, and S. Kalbfleisch, “Applications of single-crystal CVD diamond XBPM detectors with nanometre x-ray beams”, *AIP Conference Proceedings*, vol. 2054, pp. 060052, 2019. `doi:10.1063/1.5084683`

[5] S. Nida *et al.*, “Silicon carbide X-ray beam position monitors for synchrotron applications”, *J. Synchrotron Rad.*, vol. 26, pp. 28–35, 2019. `doi:10.1107/S1600577518014248`

[6] JF. Mosselmans *et al.*, “I18–the microfocus spectroscopy beamline at the Diamond Light Source”, *J. Synchrotron Rad.*, vol. 16, pp. 818–824, 2009. `doi:10.1107/S0909049509032282`

[7] J. Bohon, E. Muller, and J. Smedley, “Development of diamond-based X-ray detection for high-flux beamline diagnostics”, *J. Synchrotron Rad.*, vol. 17, pp. 711-718, 2010. `doi:10.1107/S0909049510031420`

[8] C. Bloomer and G. Rehm, “The Use of single-crystal CVD diamond X-ray beam diagnostics for synchrotron beamline commissioning and operation at diamond light source Ltd”, *2016 IEEE Nuclear Science Symposium, Medical Imaging Conference and Room-Temperature Semiconductor Detector Workshop (NSS/MIC/RTSD)*, pp. 1-7, 2016. `doi:10.1109/NSSMIC.2016.8069893`

[9] J. Achard, V. Jacques, and A. Tallaire, “CVD diamond single crystals with NV centres: a review of material synthesis and technology for quantum sensing applications”, *J. Phys. D: Appl. Phys.*, vol. 53, pp. 313001, 2020. `doi:10.1088/1361-6463/ab81d1`

[10] S. Koizumi, C.E. Nebel, and M. Nesladek, Eds., Weinheim, “Theoretical Models for Doping Diamond for Semiconductor Applications”, in *Physics and Applications of CVD Diamond*, Germany: Wiley-VCH Verlag, 2008, pp. 200-236.

ISBN: 978-3-95450-230-1 ISSN: 2673-5350 doi:10.18429/JACoW-IBIC2021-MOPP03

SOLEIL UPGRADE PROJECT AND FORESEEN BEAM INSTRUMENTATION

N. Hubert, A. Bence, R. Broucquart, M. El-Ajjouri, M. Labat, D. Pédeau, J-P. Ricaud
Synchrotron SOLEIL, Gif-Sur-Yvette, France

Abstract

SOLEIL Synchrotron has an upgrade plan to replace its storage ring by a new one based on multi-bend (7/4BA) achromat lattice. The Conceptual Design Report (CDR) has been published recently and the Technical Design Report (TDR) phase should be finished for the end of 2023.

For the beam instrumentation, most of the equipment will have to be replaced, to overcome cases of electronics obsolescence and to fulfil the new tight requirements. Among them, the most challenging ones are the micron resolution transverse beam size measurement, the beam position monitoring and the stability feedbacks. The present machine will be used to validate some prototypes and it is planned to upgrade part of the diagnostics ahead of the dark period to speed-up the commissioning of the new storage ring.

This paper presents the diagnostics systems that are foreseen for the SOLEIL upgrade project.

SOLEIL UPGRADE

SOLEIL Synchrotron is a third-generation light source in operation since 2006. The 2.75 GeV storage ring based on a Double-Bend achromat (DBA) lattice provides a broad spectrum of photon ranging from the far infra-red to hard X-rays to 29 beamlines.

SOLEIL is working on an upgrade project plan based on Multi-Bend Achromat (MBA) lattice. The Conceptual Design Report (CDR) has been published [1] and the Technical Design Report (TDR) phase has started recently. The CDR reference lattice is based on 20 non-standard alternating 7BA and 4BA Higher-Order Achromat (HOA) cells reaching a horizontal natural emittance of about 80 pm.rad at the energy of 2.75 GeV and equal horizontal and vertical β-functions of between 1.5 to 1.0 m at the center of all Insertion Device (ID) straight sections [2]. Figure 1 compares the arrangement of the magnets in the 7BA cell of this new lattice and the one in the Double Bend Achromat (DBA) cell of the existing machine.

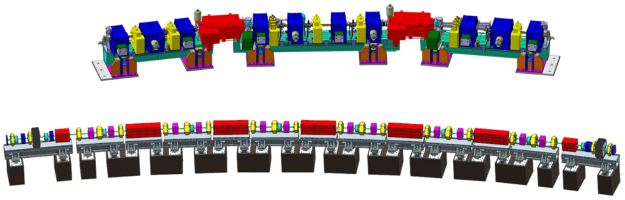

Figure 1: Engineering layout of the 7BA cell type of the new MBA-ARC (bottom) and the SOLEIL DBA-ARC cell (top).

The new machine implementation should minimize the impact on the ID source point position and reuse the existing tunnels and their radiation shielding walls [3].

The achieved natural horizontal emittance is about 50 times smaller than that of the existing SR (Fig. 2) and the effective emittance calculated in the straight section source points would be about 100 times smaller than the average value in those of the current SR.

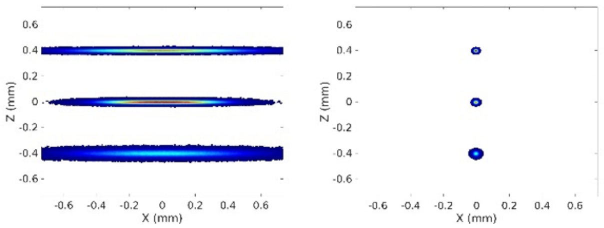

Figure 2: Comparison of the transverse beam profiles of the present SOLEIL (left) for the three straight sections with 1% coupling and SOLEIL Upgrade CDR reference lattice (right) with 50 pm.rad emittance in each plane.

With appropriate low gap IDs, this emittance reduction will improve the brilliance and coherent flux by more than two order of magnitudes [2].

FORESEEN BEAM INSTRUMENTATION

Most of the SOLEIL present diagnostics systems will have to be renewed to fit the new technical specifications of the upgrade (Table 1), but also to overcome obsolescence of the electronics.

Table 1: Current and Future Beam and Machine Parameters

	SOLEIL	**SOLEIL-Upgrade**
H. Emit. [pm.rad]	4000	80
V. Emit. [pm.rad]	20.3	80
H. Beam Size (min value at source point) [µm rms]	180	7.4
V. Beam Size (min value at source point) [µm rms]	8	2.8
BPM Aperture [mm]	84x25	16
Pos. and Angle Stability (wrt size and divergence)	10%	2-3%
Orbit Feedback Efficiency	200 Hz	1 kHz

Horizontal beam size reduction, compacity of the equipment and overall stability are the main new challenges to be overcome.

Transverse Beam Size

The electron beam transverse emittance is expected to be close to 50 pm.rad in both planes (with IDs) in the full coupling mode and could be reduced to 1 pm.rad in the vertical plane for coupling correction (machine optimization). This corresponds to electron transverse beam sizes between 2 and 20 µm-rms depending on the location around the storage ring. This small transverse emittance being one of the critical parameters of the future machine, it must be accurately (with sub-micron resolution on the beam size) as well as rapidly (~ 100 Hz repetition rate) measured. The robustness of the device is also a crucial point to decide the type of instrument to be implemented since the resulting measurement will be used as input for a beam size feedback. The chosen strategy is the use of two different technics on the same Xray extraction port. Depending on the required performance (high resolution/high speed) we can switch between the two following measurements:

- Pinhole Camera: this well-known system already in use at SOLEIL could achieve a 5 µm RMS resolution measurement with enough flux to allow high speed acquisition rates.
- Fresnel Diffraction: adding a spectral filter on the beam path and slightly increasing the pinhole size, the beam size could be inferred from the Fresnel diffraction pattern with a 1 µm RMS resolution however with a slower (~10 Hz) repetition rate (due to the reduction of flux from spectral filtering).

A high repetition rate measurement requires a high field dipole. To achieve 100 Hz the dipole source must be around 3 T (simulations performed at 50 keV). To ensure highest availability of the measurement, two identical (redundant) systems will be implemented downstream two dedicated 3 T superbends.

In addition to X-ray measurements, an additional one in the visible range is foreseen, taking benefit of the visible light extraction port that will be designed for other purposes (length and filling pattern monitors). Direct imaging or diffraction in sigma/pi polarization would give 2-5 µm RMS resolution measurements (at 200 nm).

To validate the proposed solutions for transverse beam monitoring, different prototypes will be tested on the current machine:

- A new visible light extraction mirror (with improved cooling capacities) has been designed and is planned to be installed in January 2022. This new mirror will make possible visible range beam size measurements in slit mode even at full current during user operation.
- A setup for Fresnel diffraction measurement should also be mounted on one of the two X-ray extraction port of the current machine for validation of this technic.
- A test bench to acquire and process video stream in hardware with the objective of reducing the latency and processing time compared to current software processing.

Beam Position

CDR lattice has 176 RF-Beam Position Monitors (RF-BPM) located at the start and end of each matching section and next to each focusing sextupole in the arcs [3]. The RF-BPM are the fixed points of the vacuum chamber, standing on low thermal expansion supports. At least one bellow positioned between two RF-BPM will ensure the absorption of the vacuum chamber mechanical stress. Table 2 summarizes the main specifications for the RF-BPM system.

Table 2: BPM Specifications (Rms Values)

	Bandwidth	**Specification**
Resolution	10 Hz	1µm @ 0.1 mA
	2 kHz	50 nm @ 500 mA
	TbT	100 µm @ 0.1 mA
	TbT	1 µm @ 500 mA
Beam current dep.	-	10 µm
Absolute accuracy	-	< 500 µm
Stability	One day	500 nm
	One week	1 µm
Temperature dep.	-	500 nm/°C
Latency (FOFB)	-	50 µs

The RF-BPM block has a circular shape with enlarged 16 mm inner diameter (compared with the 12 mm of the other vacuum chambers) to keep it in the shadow of the upstream synchrotron radiation. The button shape is being optimized to find the best compromise between amplitude of the collected signal and impedance budget on the machine [4]. A prototype is being manufactured with 5 mm diameter buttons (Fig. 3).

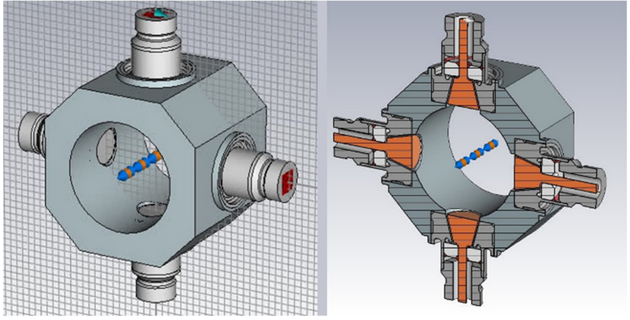

Figure 3: First drawings of the beam position monitor for SOLEIL-Upgrade. Internal BPM diameter is 16 mm, button diameter is 5 mm.

The RF-BPM electronics will be renewed since its components are already obsolete but also to fit the new specifications. In particular, the resolution and the dependencies (to beam current and temperature) must be improved (Table 1). The reduction (by a factor 10) of the latency of the data used for the fast orbit correction is also a strong objective. This latency is currently the main limitation for the Fast Orbit Feedback (FOFB) bandwidth which could then be pushed up to 1 kHz. Extensive beam-based tests are conducted to evaluate and compare the performances of the two possible compensation mechanism that are the switching (currently in used at SOLEIL) and the pilot tone [5]. The upgrade of the RF-BPM electronics will be performed ahead of the machine shutdown in order to have a fully ready and tested system for the commissioning of the future machine.

Most of the SOLEIL beamline frontends are currently equipped with tungsten/copper blade X-BPMs based on photo-emission principle. Those devices are reliable on dipole-based beamlines and on planar undulator but hardly usable downstream helical undulators. Moreover, some drawbacks due to this technology are painful for the operation like their sensitivity to low energies (including upstream dipole radiation), but also the apparition with time of increasing leakage currents. The strategy for the upgrade would be to have two different kinds of X-BPM:

- Diamond blades X-BPM operated in photoconductive mode for the planar sources (dipoles, wigglers and planar undulators). Those devices are less sensitive to low energy photons. Since the mechanical principle is close to our current X-BPM design (4 blades holder), the in-place X-BPM heads could be eventually refurbished.
- Diamond imaging for helical magnetic devices. An envisioned solution would be to insert a diamond disk in the photon beam to allow a quasi-imaging of the complex photon beam distribution.

Those two new X-BPM types must be validated on the machine by prototypes during the TDR phase.

Fast Orbit Feedback

The FOFB system is currently embedded on the BPM electronics. With the upgrade of the latter, the FOFB must be previously moved to a new external platform. This future implementation, to be deployed in the next two years, must already fulfil the specifications for the future machine and in particular (with the objective of increasing the loop bandwidth) the reduction of the data transfer latency by a factor 10. The new architecture will be versatile, being able to deal with both old and new BPM electronics and their respective data rate and communication protocols (10 kHz distributed with the Diamond Communication Controller [6] for the current system, and ~100 kHz on a protocol still to be defined for the new one).

The prototype under development for the FOFB is a flexible platform based on a µTCA crate embedding an FPGA board with System on Chip and FMC cards for the interfaces (SFPs for the data distribution and serial links for the command of the correctors). This platform will serve as a cell gateway to aggregate the BPM data and drive the correctors (Fig. 4). The processing will be computed on a central platform to allow more complex controller scheme (mode control) and will give the possibility to add additional measurement data (photon BPMs, injection events…). The corrector settings will be distributed back to cells on the same dedicated network. Corrector set points will also be archived in addition to the BPM data at the FOFB rate.

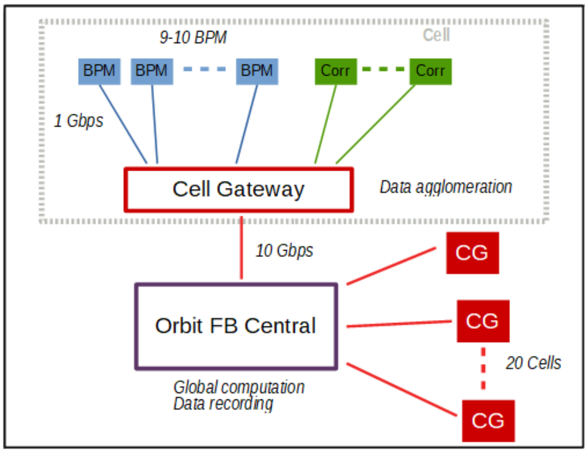

Figure 4: FOFB network topology.

The bandwidth of the correctors (and vacuum chamber) used for the FOFB must be higher than 1 kHz. The type of correctors that will be used and the number of sets (slow/fast) is still to be defined during the TDR. An architecture, similar to the one currently in operation [7], with two different sets of correctors (slow ones located in the arcs and fast ones installed upstream/downstream of each straight section) should fit SOLEIL Upgrade needs.

Beam Loss Monitors

Beam Loss Monitors (BLM) will be a key diagnostic system for the commissioning of SOLEIL Upgrade and its small aperture vacuum chambers (12 mm diameter). The 80 freshly installed monitors [8] will be reused and extended (on the injector) for the upgrade. They are made of plastic scintillators combined with fast photosensor modules (Fig. 5) and a dedicated commercial acquisition electronics. With a very high sensitivity and short temporal resolution this system will ease a lot the detection of potential obstacle and the optimization of the future machine.

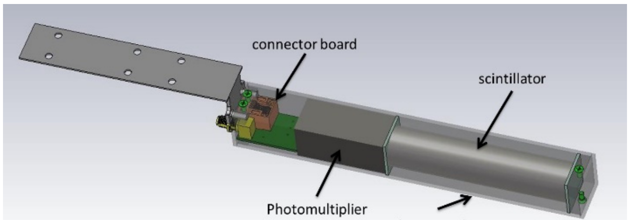

Figure 5: Beam Loss Detector made of plastic scintillator and a fast photosensor module.

Thanks to a careful relative calibration of the monitors, the radioprotection group will also use the BLM measurements on the current accelerator to crosscheck the results given by their simulation codes for SOLEIL Upgrade.

Beam Charge

Beam current will be monitored by two (for redundancy) commercial DCCT associated to a newly developed acquisition electronics [9].

The bunch distribution will be either detected on a combined/splitted BPM signal or on the visible light with an Avalanche Photo Diode (APD) installed in a dedicated path of the visible light diagnostics line. Downstream a fast acquisition (>8 GHz) of those signals will give a relative distribution of the beam charge into the 416 buckets.

The bunch purity will use the statistical Time Correlated Single Photon Counting method on another APD, this time in the X-ray path of the synchrotron radiation (more precisely in the fluorescence emission of the PHC copper absorber). For both distribution and purity, the acquisition electronics will have to be renewed due to obsolescence of the current ones.

Other Diagnostics

Table 3 summarizes the diagnostic systems that are foreseen for SOLEIL Upgrade:

Table 3: SOLEIL Upgrade Diagnostic Systems

Parameter	Type	Quantity
Emittance	X-ray: PHCs/Fresnel	2
	Visible: Interferometry/Pol.	1
Position	RF-BPM	~176
	X-BPM	~30
Current	DCCT	2
Filling	BPM + fast digitizer	1
	APD + fast digitizer	1
Purity	APD +TCSPC	2
Length	Streak Camera	1
Losses	Scintillators + PMT	~80
Dosimetry	RadFET	~40
Tune	BPM + Shaker Magnet	1

CONCLUSION

Cutting-edge instrumentation must be designed to answer the SOLEIL Upgrade tight specifications. On such a compact machine the mechanical integration of the diagnostics will also be a challenge and must be anticipated (beam extraction, pinhole integration as close as possible to the source, etc…). In order to ease and speed-up the commissioning of the new machine the FOFB and the BPM electronics will be upgraded ahead of the machine shutdown. The current machine will also be used as a testbench to validate concepts of Fresnel diffraction and adjustable pinholes for beam size measurements, and the BPM feedthrough prototypes.

REFERENCES

[1] Conceptual Design Report: Synchrotron SOLEIL Upgrade, 2021, `https://www.synchrotron-soleil.fr/fr/file/13803/download?token=OUzsp46P`

[2] A. Nadji, “Synchrotron SOLEIL Upgrade Project”, presented at the 12th Int. Particle Accelerator Conf. (IPAC'21), Campinas, Brazil, May 2021, paper MOBAP131.

[3] A. Loulergue *et al.*, “CDR Baseline Lattice for the Upgrade of SOLEIL”, presented at the 12th Int. Particle Accelerator Conf. (IPAC'21), Campinas, Brazil, May 2021, paper TUPAB054.

[4] M. El Ajjouri, F. Alves, A. Gamelin, and N. Hubert, “Preliminary Studies for the SOLEIL Upgrade Beam Position Monitors”, presented at the 9th Int. Beam Instrumentation Conf. (IBIC'21), Pohang, Korea, Sep. 2021, paper MOPP31.

[5] M. Cargnelutti *et al.*, “Stability Tests with Pilot-Tone Based Elettra BPM RF Front End and Libera Electronics”, in *Proc. 7th Int. Beam Instrumentation Conf. (IBIC’18)*, Shanghai, China, Sep. 2018. `doi:10.18429/JACoW-IBIC2018-TUPB13`

[6] I. S. Uzun *et al.*, “Initial Design of the Fast Orbit Feedback System for DIAMOND Light Source”, in *Proc. 10th Int. Conf. on Accelerator and Large Experimental Physics Control Systems (ICALEPCS'05)*, Geneva, Switzerland, Oct. 2005, paper P3_030.

[7] N. Hubert, L. Cassinari, J. Denard, A. Nadji, and L. S. Nadolski, “Global Fast Orbit Feedback System Down to DC using Fast and Slow Correctors”, in *Proc. 9th European Workshop on Beam Diagnostics and Instrumentation for Particle Accelerators (DIPAC'09)*, Basel, Switzerland, May 2009, paper MOOC01, pp. 27-31.

[8] N. Hubert, M. El Ajjouri, and D. Pédeau, “New Beam Loss Monitor System at SOLEIL”, in *Proc. 8th Int. Beam Instrumentation Conf. (IBIC'19)*, Malmö, Sweden, Sep. 2019, pp. 118-121. `doi:10.18429/JACoW-IBIC2019-MOPP017`

[9] R. Broucquart, “CIEL: Current Injection Efficiency and Lifetime”, presented at DEELS2020, `https://indico.cern.ch/event/892013/contributions/3881574/`.

CONCEPTUAL DESIGN OVERVIEW OF THE ELECTRON ION COLLIDER INSTRUMENTATION*

D. M. Gassner†, J. Bellon, M. Blaskiewicz, A. Blednykh, K. A. Drees, T. Hayes, C. Hetzel,
D. Holmes, R. Hulsart, P. Inacker, C. Liu, R. Michnoff, M. Minty, C. Montag, D. Padrazo Jr,
M. Paniccia, V. Ptitsyn, V. Ranjbar, M. Sangroula, T. Shaftan, P. Thieberger, E. Wang, F. Willeke
Brookhaven National Laboratory, Upton, NY, USA
L. Dalesio, Osprey DCS LLC, Ocean City, USA

Abstract

A new high-luminosity Electron Ion Collider (EIC) is being developed at Brookhaven National Laboratory (BNL). The conceptual design [1] has recently been completed. The EIC will be realized in the existing RHIC facility. In addition to improving the existing hadron storage ring instrumentation, new electron accelerators that include a 350 keV gun, 400 MeV Linac, a rapid-cycling synchrotron, an electron storage ring, and a strong hadron cooling facility will all have new instrumentation systems. An overview of the conceptual design of the beam instrumentation will be presented.

INTRODUCTION

The EIC [1, 2] will be realized in the existing Relativistic Heavy Ion Collider (RHIC) facility, the primary additions will be a chain of electron accelerators and systems that will reside inside the RHIC tunnel and service buildings. The well-established beam parameters of the present RHIC facility are close to what is required for the highest performance of the EIC, except for the total hadron beam current which will be increased by a factor of approximately three by increasing the number of bunches. A strong hadron cooling facility will utilize 100 mA of 150 MeV electrons to reduce the hadron beam emittance and control emittance growth due to intrabeam scattering. Polarized electrons will be generated in a new 350 keV DC gun from a strained superlattice GaAs photocathode and will be accelerated to 400 MeV in an S-band normal conducting Linac. The 3.8 km rapid cycling synchrotron (RCS) then increases the electron energy to 5, 10 or 18 GeV in 100 - 200 ms, then fills the electron storage ring (ESR). The 3.8 km ESR will provide ~70% polarized electron beams at 5, 10 or 18 GeV for collisions with the polarized protons or heavy ions in the hadron storage ring (HSR) at 41, 100 and 275 GeV. To maintain high spin polarization, each of the ESR electron bunches will be replaced every one to three minutes.

ELECTRON PRE-INJECTOR LINAC

Beam instrumentation (shown in Table 1) for the 350 keV DC gun and the 400 MeV electron LINAC [3] will be designed to measure beam properties at a repetition frequency of 1 Hz with single-bunch charge ranging from 100 pC to the design charge of 10 nC per bunch. Beam position monitors will measure the trajectory of the beam that has a bunch length range of 2 ns to 4.5 ps with better than 100 µm resolution. A pair of selected BPMs will provide time-of-flight measurements to determine the beam energy.

Table 1: Electron Pre-Injector Instrumentation

Type	Quantity
Beam Position Monitors	9
Beam Loss Monitors	5
Fast Current transformers	1
Integrating Current transformers	7
Faraday Cups	4
YAG/OTR Screen profile monitors	9
Longitudinal Profile Monitors	2
Mott Polarimeters	2
Slit scanner	1
Wire scanners	7

Transverse profile monitors using plunging YAG/OTR screens will be located throughout the beamlines. Slit scanners and wire scanners will be used to measure beam emittance. Longitudinal bunch profiles will be measured with a plunging radiator at low energy, and using synchrotron light emitted downstream of a bending magnet at 400 MeV, with a shared streak camera. Relative bunch lengths will be non-destructively measured using a ceramic gap with waveguide-coupled fast diodes downstream of the 4.5 ps bunching section. Mott polarimeters will be installed at the cathode preparation system (100 eV) and in the first diagnostic beamline upstream of the Linac (350 keV). Scintillators coupled to photo-multiplier tubes (PMTs) and/or Geiger counters, used to detect X-ray and gamma ray, will be placed after the gun, after the first dipole, in the bunching sections and between the acceleration sections to localize beam loss. Additionally, a long optical-fiber beam loss monitor will be used between the gun and the entrance of the Linac. All EIC current and charge monitors (DCCT, ICT, FCT) will be commercially provided [4].

RAPID CYCLING SYNCHROTRON

The EIC RCS [5] will accelerate two batches of four 7 nC bunches in adjacent buckets that are 1.69 ns apart that will subsequently be merged into two 28 nC electron bunches that are 2.43 µs apart by means of two steps of pairwise merging on a 1 GeV porch using the 591 MHz,

---

* Work supported by Brookhaven Science Associates, LLC under Contract No. DE-SC0012704 with the U.S. Department of Energy.

† gassner@bnl.gov

ISBN: 978-3-95450-230-1 ISSN: 2673-5350 doi:10.18429/JACoW-IBIC2021-MOPP04

295 MHz and 148 MHz RF systems. Once per second, new electron bunches are injected and accelerated (in 100 ms or 200 ms) to a beam energy of up to 18 GeV and injected into the fixed-energy ESR and brought into collisions with the hadron beam. The RCS BPM pickups will be in a rotated button arrangement. There will be one dual plane BPM at each of the 576 quadrupoles, located in a 32.8 mm diameter round beam pipe. The bunch intensity range is 1 to 28 nC, with a bunch length range between 16 – 91 ps. The required BPM resolution is on the order of 100 µm for the injected bunch and 10 µm for average orbits over many turns.

To facilitate commissioning and for re-establishing beam in the RCS, 7 plunging fluorescent screen transverse profile monitors will be installed, one after the injection septum and one in each of the 6 sectors. The screen profile monitor design will have similarities to the ones used in the NSLS-II storage ring with careful attention given to the impedance characteristics. See Table 2.

Table 2: RCS Instrumentation

Type	Quantity
Beam Position Monitors	576
Synchrotron Light Monitor	1
DCCT	1
Fast Current Transformer	1
Tune Monitor	1
Fluorescent Screens	7

The betatron tunes will be monitored at injection using BPMs to measure injection oscillations and during acceleration using turn-by-turn BPMs with beam excitation applied using fast strip-line kickers. A synchrotron light monitor (SLM) will be used for transverse profile measurements in the RCS using synchrotron radiation emitted from a bending magnet. The synchrotron radiation will be extracted through a dedicated optical beamline to a remotely located experimental room. The measured profiles will be used, together with modelled or measured beam optics, to infer the beam emittances and energy spread. Turn-by-turn measurements using gated cameras will provide measurements of injection matching, evaluate beam size evolution and beam position stability during acceleration. A streak camera will provide measurements of the bunch length and longitudinal profiles. A wide-band longitudinal bunch length monitor will be used to provide data for a mountain range display to show the bunch merging evolution.

TRANSFER LINE INSTRUMENTATION

Instrumentation in the two electron transfer beam lines (as shown in Table 3) will provide measurements for beam commissioning, regular monitoring, and optimization of routine beam operations. The BPMs will measure the single-bunch trajectories at a 1 Hz rate and will be used as input for trajectory correction and/or feedback to optimize beam transmission efficiency. In addition, the BPMs will be used to measure the beam energy and characterize the accelerator lattice. BPMs located in high dispersion regions will monitor relative changes in the beam energy. The orbit response matrix will be measured and monitored using the BPMs, to localize lattice errors. The electron transfer lines will also include multiple plunging YAG/OTR screens. These will provide position and profile measurements for beams with low (YAG) and high (OTR) bunch charge. A YAG/OTR station at a dispersive location will be used to determine the beam energy spread. Multiple, strategically located YAG/OTR stations will be used in combination for beam emittance measurements. The ion injection to the HSR will be changed from sector 6 for RHIC, to sector 4 for the EIC. The instrumentation in the new single pass beam line in the tunnel from sector 6 to sector 4 will be similar to the existing devices in the much longer AGS to RHIC transport.

Table 3: Transfer beamline Instrumentation

Type	Quantity
Linac to RCS transfer	
Beam Position Monitors	15
YAG/OTR Screens	7
Integrating Current Transformer	1
Fast Current Transformer	1
RCS to ESR transfer	
Beam Position Monitors	14
YAG/OTR Screens	3
Integrating Current Transformer	1
Fast Current Transformer	1
Sector 6 to HSR ion transfer	
Beam Position Monitors	6
Screen Profile Monitors	6
Integrating Current Transformers	2
Beam Loss Monitors	10

ELECTRON STORAGE RING

The ESR BPM button pickups will be in a planar arrangement, similar to those found in many light source storage rings. There will be one dual plane BPM pick-up at each of the 494 quadrupoles, located in a 36 x 80 mm multipole chamber beam pipe. The bunch intensity range is 2 to 28 nC, with bunch lengths between 7 – 9 mm, and bunch numbers between 290 – 1160 with respective bunch spacing of 40.7 – 10.2 ns, with a maximum current of 2.5 Amps. The most challenging position measurement will be made using the first 20 BPMs after the injection septum to ensure an acceptable injection orbit trajectory. The required resolution of 10 µm horizontal and 5 µm vertical is needed for the single newly injected replacement bunch during operations with 1160 circulating stored bunches in the ring. The average position resolution requirement of the stored beam is on the order of 1 um over many turns.

Two SLMs imaging visible radiation will be located near bending magnets. Water-cooled, in-vacuum mirrors will be used to transport the light out of the vacuum chamber. Several mirrors with good surface quality (< lambda/10) will guide the light to a remotely located experimental room containing a CCD/CMOS camera, a gated camera, and a streak camera. An X-ray pin hole monitor will provide a higher resolution (~5 µm) beam profile measurement, compared with the visible SLMs (~60 µm) which are limited by diffraction. This beamline will also allow independent measurements of the energy spread and horizontal and vertical emittance. See Table 4.

Table 4: Electron Storage Ring Instrumentation

Type	Quantity
Beam Position Monitors	494
Beam Loss Monitors	30
Synchrotron Light Monitors	2
X-ray Pin-Hole Monitor	1
DCCT	1
Fast Current Transformer	1
Compton Polarimeter	1
Longitudinal BbB feedback	1
Transverse BbB feedback	1
Slow orbit feedback	1
Tune Monitor	1

BLMs will be located only at strategic locations that include injection and at collimators. A Compton polarimeter will be installed to make a 1% (statistics) measurement of the beam polarization for an individual electron bunch. Both transverse and longitudinal bunch-by-bunch feedback systems are required to damp coupled-bunch instabilities. A tune monitor will utilize a transverse strip-line kicker and BPMs to measure the fractional betatron tunes.

HADRON STORAGE RING

The majority of existing RHIC instrumentation [6] devices in the superconducting HSR will be replaced with improved versions that have better impedance characteristics for operations with the EIC beams. See Table 5.

Table 5: Hadron Ring Instrumentation

Type	Quantity
Beam Position Monitors	276
Beam Loss Monitors	200
Ionization Profile Monitors	2
DCCT	1
Longitudinal Profile Monitor	1
HF Schottky	1
LF Schottky	1
Polarimeters	2
Tune Meter kicker	1
Base-Band Tune Meter	1
Longitudinal Damper	1
Injection Damper	1
Gap Cleaner	1
Head-Tail Pick-up	1

The HSR bunch intensity range is 1 to 30 nC, with bunch lengths between 6 - 7.5 cm, and bunch numbers between 290–1160 with respective bunch spacing of 40.7–10.2 ns, with a maximum current of 1 Amp. The existing 279 RHIC cold BPM striplines will be covered with a screen/sleeve and not used, new cold button pick-ups will be installed nearby each one. The BPM resolution requirement is on the order of 100 µm for the injected bunches and 10 µm for average orbit over many turns. Absolute polarization measurements will be made using a polarized atomic hydrogen jet, similar to the method used in RHIC. For relative polarization measurements, materials analysis of the carbon ribbon targets used in the existing RHIC proton-carbon (pC) polarimeter indicates that the higher proton beam currents at the EIC will induce heating to temperatures causing the targets to break after only a few seconds in the beam. A search for alternative target materials or methods has been initiated. The existing RHIC resistive wall current monitor will be replaced with a wider bandwidth electro-optical detector that can better resolve the longitudinal characteristics of the 6 cm (180 ps) ion bunches [7].

ELECTRON COOLING

To achieve a luminosity of 10^{34} $cm^{-2}s^{-1}$ in the EIC during long collision runs, it is desirable to cool the hadron beams to balance emittance growth rates due to intrabeam scattering thereby allowing the same hadron beam to be kept for long collision runs (~24 hours). A dedicated strong hadron cooling facility [8] with ~ 400 meters of beam transport will provide the 150 MeV, 100 mA electron beam that will co-propagate with the ions in the modulator and kicker regions, then return to an Energy Recovery Linac so the beam can be dumped at low energy. The button BPMs will measure average positions of the 100 pC – 1 nC bunches with 10-100 µm resolution in the transport beamlines. The co-propagating e-ion transverse alignment needs to be <5% of the ~0.7mm RMS beam size in the modulator and kicker.

Table 6: Strong Hadron Cooling Instrumentation

Type	Quantity
Beam Position Monitors	110
Beam Loss Monitors	88
Synchrotron Light Monitors	4
DCCT	2
Integrating Current Transformers	8
Fast Current Transformers	8
Faraday Cup/Dump Monitors	12
Screen Profile Monitors	35
Emittance Slit Monitors	7
Wire Scanners	9
Collimators	4
Relative Bunch Alignment	1
Beam Pipe Temperature Monitors	70

ISBN: 978-3-95450-230-1 ISSN: 2673-5350 doi:10.18429/JACoW-IBIC2021-MOPP04

Transverse profiles of the few mm sized beam will be measured with plunging YAG/OTR screens in the beam transports. A streak camera will image synchrotron light emitted from dipoles to measure the expected ~40 ps longitudinal profiles. The synchrotron light will also be used to measure and ensure the slice energy spread stays $<10^{-4}$ which is necessary for cooling. Slit and wire scanners will be used to measure the 1.9 - 2.8 µm RMS normalized emittance. Beam losses will be measured using fiber-optic cables coupled with photomultiplier tubes and pin-diode BLMs. The beam pipe temperature will be monitored at critical locations to sense beam scraping. See Table 6.

To ensure the amplified imprint of the ion beam on the cooling electrons interacts with the same part of the ion bunch in the kicker region that the electrons encountered in the modulator, a 1 micron stability for the longitudinal alignment is required in the kicker region. The primary source of instability will be from particle path length changes due to beam line transport magnetic field ripple. Determining a method to make this challenging longitudinal relative alignment is being studied.

INTERACTION REGION

The instrumentation in the IR regions [9] will assist in establishing and maintaining optimum collision configuration, protecting critical devices, and monitoring beam parameters. The electron and hadron beams collide at the interaction point with a 25 mrad crossing angle. To maintain luminosity, a global and local IR orbit feedback system controlling both beams will be implemented to compensate for ~10 Hz variations in the hadron ring arising from triplet magnet oscillations, and excitations in the range from 2 to 30 Hz in the ESR. Four dual-plane beam position monitors (BPMs), two for each beam, will be installed near the interaction points. For fast correction, 12 air-core steering magnets (8 for the vertical plane and 4 for the horizontal plane) will be used in the ESR. Of the 8 magnets, 4 provide position and angle trajectory control and the remaining 4 magnets cancel the dispersion introduced by the trajectory correction. Four vertical steering magnets, of the same type as the magnets used in the existing RHIC 10 Hz feedback system, will be designed for the IR of the hadron ring.

Table 7: Interaction Region Instrumentation

Type	Quantity
Beam Position Monitors	78
Beam Loss Monitors	30
Crab Tilt Monitor	1
IP Orbit Correction	2
Beam Pipe Temperature Monitors	40

Beam loss detectors will be installed near radiation-sensitive devices and at potential high loss regions in the IR to monitor both the hadron and electron beams. See Table 7.

Crabbing Angle Measurements

The electron and hadron bunches will be rotated horizontally by superconducting crab cavities to compensate the loss of luminosity due to the crossing angle inherent in the geometry of the IR. The crabbing angle of the bunches will be measured to setup and monitor these crab cavities. Even though the crabbing angle is confined between the cavities on either side of the IR during normal operations, the measurement can be carried out at a place with proper phase advance in other regions of the ring. Crab cavities placed on one side of the IP will perform the rotation of bunches, and crab cavities on the other side will restore the nominal orientation. To setup the crab cavities, the crabbing angle will be measured for the following cases: with cavities off as a baseline, with cavities at only one side of the IP turned on, and with cavities on both sides of the IP turned on.

An ion bunch tilted by the crab cavities will traverse a horizontal button BPM near the IP and produce signals on opposite pickup electrodes that will have different degrees of distortion depending on the tilt angle. This distortion can be viewed on a fast oscilloscope. In particular, the zero-crossing time difference between the two signals will be approximately proportional to the tilt angle. Simulations were performed to study this effect as a possible diagnostic tool for measuring the crabbing angles of hadron beam for the EIC. A dedicated ion crab tilt BPM will be installed close enough to the IP so that it can see the 12.5 mrad design ion tilt angle [10]. The electro-optic longitudinal profile monitor in the ESR can also be used to monitor the crabbing angle outside of the IR.

The electron beam crabbing angle will be monitored using a streak camera imaging synchrotron light generated at a location outside of the IR with minimal horizontal dispersion and optimal crabbing angle phase advance. The streak camera detects a horizontal beam profile which is tilted from vertical by an amount proportional to the crabbing angle when only the crab cavities on one side of IP are turned on. The tilt angle will be tuned to zero using the streak camera measurement as the phase of the crab cavities on the other side of the IP is optimized. The optimal phase advance from IP to the SLM will be a multiple of pi for maximum sensitivity to the tilt angle in the x-z profile.

COMMON ELECTRONICS PLATFORM

An FPGA based common platform for EIC electronics is planned for use in many systems that include instrumentation, power supply and low-level RF. The conceptual design is envisioned to have a carrier board with the capability for 2 customizable daughter/function cards and be packaged in a 1U chassis. Also under consideration is the use of a multi-slot chassis for high quantity systems, primarily the BPMs. The basic hardware architecture will be common for all systems, the packaging may include a few different versions. The carrier board will be available in both standard and high-performance configurations and have capabilities that include Gigabit ethernet, RS-232, and timing/clock generation. Each daughter card will have ~8” width and provide digital I/O, ADC, DAC and multi-Gigabit serial links to the Carrier FPGA. Electronics for one BPM can be serviced by one daughter card.

REFERENCES

[1] F. Willeke *et al.*, "Electron Ion Collider Conceptual Design Report 2021", BNL, NY, USA, BNL-221006-2021-FORE, 2021.

[2] C. Montag *et al.*, "Design Status Update of the Electron-Ion Collider", presented at the 12th Int. Particle Accelerator Conf. (IPAC'21), Campinas, Brazil, May 2021, paper WEPAB005.

[3] E. Wang *et al.*, "The Design of a High Charge Polarized Pre-injector for the Electron-Ion Collider", presented at the 12th Int. Particle Accelerator Conf. (IPAC'21), Campinas, Brazil, May 2021, paper TUPAB037.

[4] Bergoz Instrumentation, `http://www.bergoz.com`

[5] V. H. Ranjbar *et al.*, "The RCS Design Status for the Electron Ion Collider", presented at the 12th Int. Particle Accelerator Conf. (IPAC'21), Campinas, Brazil, May 2021, paper WEXA04.

[6] P. Cameron *et al.*, "Overview of RHIC Beam Instrumentation and First Experience from Operation", Invited talk at DIPAC 2001, ESRF, Grenoble, France, paper IT09.

[7] S. M. Gibson, A. Arteche, A. Bosco, S. E. Bashforth, M. Krupa, and T. Lefevre, "Enhanced Bunch Monitoring by Interferometric Electro-Optic Methods", in Proc. 9th Int. Particle Accelerator *Conf. (IPAC'18)*, Vancouver, Canada, Apr.-May 2018, pp. 2353-2356. `doi:10.18429/JACoW-IPAC2018-WEPAL073`

[8] E. Wang *et al.*, "The Accelerator Design Progress for EIC Strong Hadron Cooling", presented at the 12th Int. Particle Accelerator Conf. (IPAC'21), Campinas, Brazil, May 2021, paper TUPAB036.

[9] H. Witte *et al.*, "The Interaction Region of the Electron-Ion Collider EIC", presented at the 12th Int. Particle Accelerator Conf. (IPAC'21), Campinas, Brazil, May 2021, paper WEPAB002.

[10] P. Thieberger, M. G. Minty, and C. Montag, "Proposed BPM-Based Bunch Crabbing Angle Monitor", in *Proc. 9th Int. Particle Accelerator Conf. (IPAC'18)*, Vancouver, Canada, Apr.-May 2018, pp. 1860-1863. `doi:10.18429/JACoW-IPAC2018-WEPAF018`

ISBN: 978-3-95450-230-1 ISSN: 2673-5350 doi:10.18429/JACoW-IBIC2021-MOPP05

THE FRASCATI BEAM TEST FACILITY NEW LINE: FROM DESIGN TO BEAM COMMISSIONING

B. Buonomo, F. Cardelli, C. Di Giulio*, D. Di Giovenale, L. G. Foggetta,
on behalf of the BTF Upgrade team†, INFN-LNF, Frascati, Italy

Abstract

The request of beam time for long-time experiments and contemporary the need to provide beam time to the detector developers community, drive the INFN to invest in the commissioning of a new beam line test facility. In this work we describe the necessary steps followed from the design to the commissioning of the new beam line in the Frascati Beam Test Facility.

INTRODUCTION

In the development of the detectors for the high energy physics (HEP) and astro-particles physics, the test beam and irradiation facilities are the key enabling infrastructures.

From 2005 the Beam-Test Facility (BTF) of the DAΦNE accelerator complex in the Frascati laboratory of the Italian National Institute of Nuclear Physics (INFN) has gained an important role in the European infrastructures devoted to the development and testing of particle detectors [1–3].

The presented proposal in 2016 aimed at improving the performance of the facility extending the range of application for the LINAC beam extracted to the BTF lines, in the directions of hosting fundamental physics long term experiments [4] and providing electron irradiation also for industrial users.

To achieve this, it was requested to double the BTF beamlines, in order to cope with the significant increase of users due to the much wider range of applications.

The original BTF line is in operation since 2002 [5, 6], and from 2004 operates in opportunistic mode [7] during the running of the DAΦNE electron-positron collider. The full LINAC beam can also be extracted towards the BTF line without being intercepted by the target (within the 3×10^{10} particles/s limit established radio-protection rules for the current shielding configuration).

In the next paragraphs the steps from the Conceptual Design Report presented in 2016 [8] to the commissioning of the new line are described. The issues necessary to be discussed for the reconstruction of the first line of the BTF (BTF1) for a long term experiment and the processing difficulties of the commissioning of the second line of BTF (BTF2) are described.

THE DESIGN OF THE NEW BTF LINE

The main requirements from the users concerning the detector testing beam-test activities can be easily summarized:

- Good quality beam, in particular from the point of view of beam size, divergence and background, down to the low end of the BTF energy range, i.e., few tens of MeV. This requirement is particularly difficult to match if the setup is in air, downstream of the exit window.
- Extending the energy range towards higher energies: tracking and efficiency studies suffer from the Coulomb scattering of electrons, which scales as 1/p. Higher energies are also very useful for extending the range for the calibration of calorimeters.

The Beam-Test Facility (BTF) is an extraction and transport line, to produce electrons or positrons in a wide range of intensity, energy, beam spot dimensions and divergence, starting from the primary beam of the DAΦNE LINAC. The LINAC accelerate 50 pulses/s, one transported in the spectrometer, the other can be either transported to a small ring for emittance damping (and from there injected into the collider rings), or to the BTF line, by means of pulsed dipoles. A variable depth target (from 1.7 to 2.3 X_0) spreads the momentum distribution of the incoming beam, then secondary electrons (or positrons) are momentum selected by means of a 45 degree bending dipole and collimators (in the horizontal plane). The beam intensity is thus greatly reduced, depending on the chosen secondary beam energy central value (from about 30 MeV up to almost the primary beam energy) and spread (typically better than 1 percent at higher energy, depending on the collimators settings). The beam is then transported to the experimental hall and focused by means of two quadrupole FODO doublets. The layout of the beam selection and transport line is shown in Fig. 1, together with the shielded experimental area.

The original idea for the new layout consists in a beam-splitting dipole, wrapped around a double-exit pipe, that can drive beam pulses from the upstream BTF beam-line alternatively to the two new lines [9]. In case, the dipole can be connected to a pulsed power supply for a fast switch between the two lines. The first line drives the beam in the existing experimental hall (“BTF 1”), also profiting of the existing concrete block-house, while the second will transport the beam, with three additional dipoles, in the area previously used as BTF control room (“BTF 2”), with few civil engineering work. A complete optimization of the new lines optics has been performed, in order to define the

---

* claudio.digiulio@lnf.infn.it

† D. Alesini, M. Belli, B. Bolli, B. Buonomo, S. Cantarella, F. Cardelli, P. Carinci, G. Catuscielli, R. Ceccarelli, A. Cecchinelli, O. Cerafogli, P. Ciuffetti, M. Chiti, R. Clementi, O. Coiro, D. Di Giovenale, C. Di Giulio, E. Di Pasquale, R. Donghia, A. Esposito, O. Frasciello, L. G. Foggetta, F. Galletti, A. Ghigo, S. Incremona, F. Iungo, S. Lauciani, A. Liedl, V. Lollo, R. Mascio, M. Martini, A. Michelotti, M. Paris, L. Pellegrino, G. Piermarini, F. Putino, L. Sabbatini, F. Sardone, G. Sensolini, A. Stecchi, R. Ricci, L. A. Rossi, U. Rotundo, A. Stella, S. Strabioli, A. Vannozzi, R. Zarlenga (INFN Laboratori Nazionali di Frascati); P. Valente (INFN Roma)

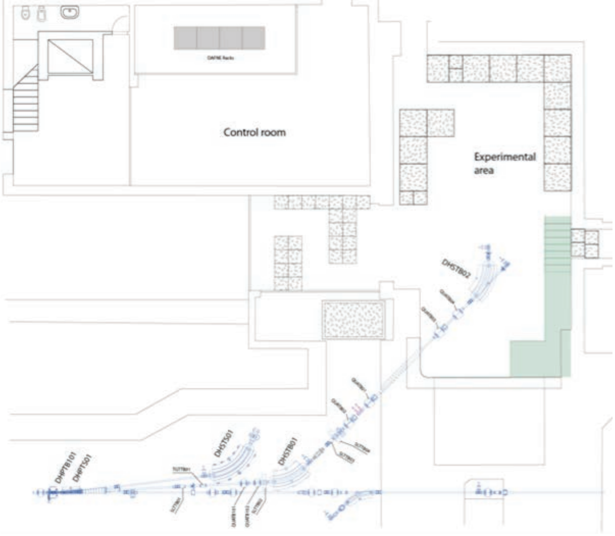

Figure 1: The BTF layout until 2017.

new beam elements requirements, both using G4beamline and MADX [10]. The original idea of a fast magnet for a 45 degree bending angle was excluded, so the design was changed for a fast 15 degree dipole magnet and a new design of the facility is shown in Fig. 2. The new magnetic line to transport the beam in the BTF2 experimental hall after the 15 degree pulsed magnet consists by 6 quadrupoles two 45 degree bending magnet and one 35 degree magnet.

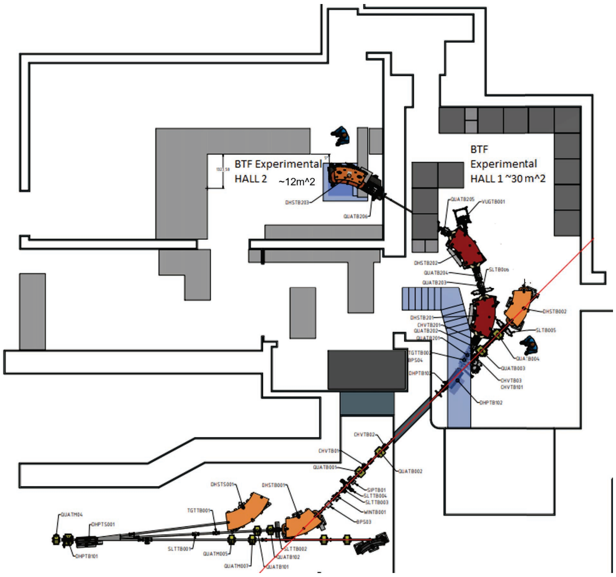

Figure 2: The BTF2 new layout.

THE NECESSARY STEPS FROM THE DESIGN TO THE COMMISSIONING

The budget The financial aspect of the project was shown in the conceptual design report presented in 2016. After review of the INFN Machine Advisory Committee the budget for all the project was available from March 2018.

The law authorizations All the requested legislation steps for start a new activity in the building 54 of the laboratory was submitted to the relative authorities and government agencies to obtain the permission. The agencies that request clarification on the environment aspect of the activity receive the answers in the request time thanks to the effort coordinated effort of the Safety Division, Technical Division, Radio-Protection Division, Administrative Division and Accelerator Division of the Laboratory.

The civil engineering activities After a first step where the general requirements from the Technical Division was collected related to the, building, cooling systems, power supplies, electrical and interlock systems, a continue feedback loop with the designer of the Accelerator Division was necessary, to produce the right actions to mitigate the risks that could present this upgrade project in a 50 year old building with a lack of documentation of the status of the building and auxiliary system.

The building 54 of the laboratory was modified for adding the new radio-protection shielding for the BTF2, a new entrance was realized and the building was modified to receive all the auxiliary systems as the new electric distribution and the required cooling system distribution for the magnets elements with their interlocks and for the experimental area. A new room of the roof of the BTF2 for the power supplies was prepared considering all the necessary auxiliary systems (network, cooling, controls). The new control room of BTF, far away 60 m from the experimental halls, was prepared in 2018 with all the auxiliary systems to accommodate the users.

The design and commissioning of the magnetic elements During the design phase was evident that the main constrain for the installation of the new BTF line was the space limitation. The Magnetic Service of the Accelerator Division has collected the requirement for a 20 T/m magnetic fields for the six quadrupoles and the requirements for the different dipoles, the fast pulse dipoles, the 2 H-type bending dipoles and the last 35 degree C-type bending dipole. The Magnetic Service has provided the Magnetic design to the Mechanical Engineering Service of the Accelerator Division that has produced the mechanical design for the bids. All the magnets delivered are characterized with their power supplies by the Magnet Service in the new measurement magnet area. More details on the magnetic elements are in [11].

The design and commissioning of the vacuum elements The requirement to adapt the BTF1 for long term experiment and the needs to remove all the Beryllium windows, drive the development of a safety system to protect the LINAC vacuum from the accidentally events that could happening during the installation of experience in both BTF lines.

The vacuum system has been designed by the Vacuum Service of the Accelerator Division in order to allow the

ISBN: 978-3-95450-230-1 ISSN: 2673-5350 doi:10.18429/JACoW-IBIC2021-MOPP05

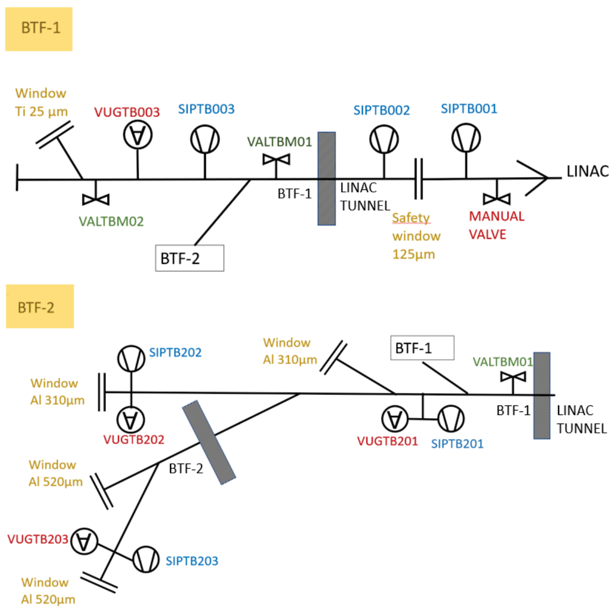

Figure 3: The BTF Vacuum system layout.

installation of elements in the transfer line without exposing the LINAC vacuum to risks. It is compose by fast valves, vacuum measurement systems, pumping devices, collimators for beam manipulation, beam stopper for safety procedure, thin Mylar windows for vacuum LINAC separation and thin Titanium (25 um) and Aluminium windows at the end of the lines as shown in Fig. 3.

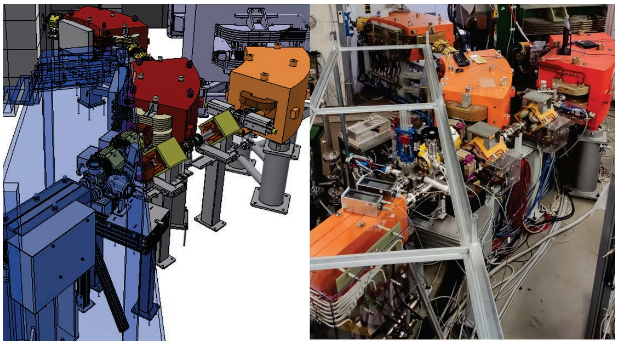

Figure 4: On the left the 3D design and on the right the commissioned BTF line.

The design and commissioning of the mechanics elements Most of the magnets and auxiliary mechanics system drawings are produced by the Mechanical Service of the Accelerator Division. They produce different 3D mapping of the BTF areas to reduce the installation time and the risk of the interference during the installation of all the elements as shown in in Fig. 4. Thanks to this method a detailed schedule of the activities has provided the tools to optimize the resources.

The radio protection system The radio-protection Service has followed all the procedure for the authorizations and provides the guidelines for the search procedure of the BTF2 area. The installation of the safety system for the BTF2 is shown in Fig. 5. Thanks to their support the beam commissioning of the new line is ongoing. The radio-protection limit for BTF2 is 10^6 particle/s with an energy of 730 MeV.

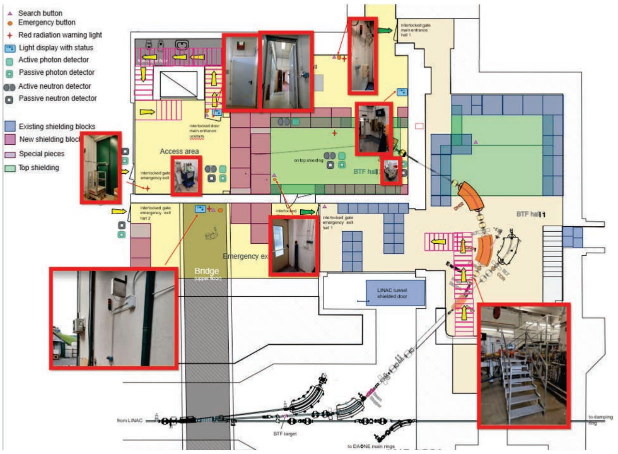

Figure 5: The layout of the BTF2 safety system.

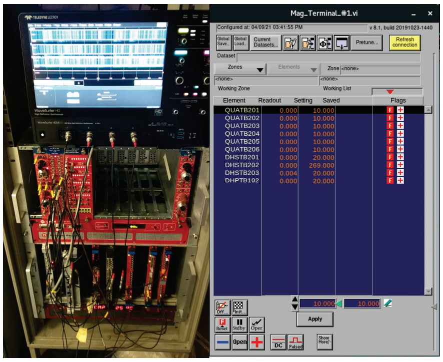

Configured at: 04/09/21 03:41:55 PM
v 8.1, build 20191023-1440

Element	Readout	Setting	Saved	Flags
QUATB201	0.000	10.000		F +
QUATB202	0.000	10.000		F +
QUATB203	0.000	10.000		F +
QUATB204	0.000	10.000		F +
QUATB205	0.000	10.000		F +
QUATB206	0.000	10.000		F +
DHSTB201	0.000	20.000		F +
DHSTB202	0.000	269.000		F +
DHSTB203	0.004	20.000		F +
DHPTB102	0.000	20.000		F +

Figure 6: On the left the new BTF2 DAQ system under test, on the right the controls of the new magnets implemented in DCS.

The control system As shown in Fig. 6, all the new magnetic elements power supplies controls are implemented into the DAΦNE Control System (DCS) [12] thanks to the support of the Control Service of the Accelerator division, and a BTF2 Data Acquisition System based on SIS3153 Ethernet-VMEbus interface was developed, installed and tested as shown in Fig. 6 during the test phase, where the SCALER, QDCs, PIO, TDCs and the Timing Unit are visible on the left.

THE FIRST BEAM COMMISSIONING IN BTF2

Driven by simulations and thanks to the possibility to check the beam at the straight exit of each dipole in the new transfer line, the first beam was transported at the exit of the new line in few working hours. The diagnostic used for this

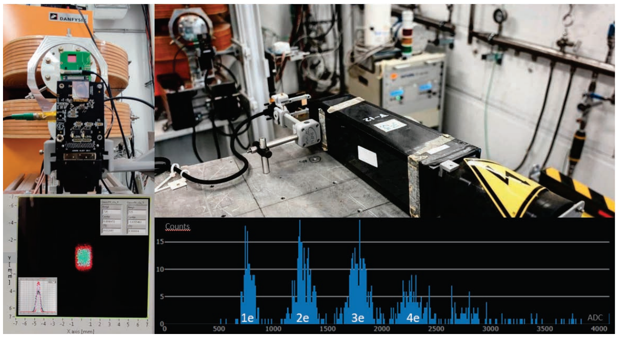

Figure 7: On the left high the pixel detectors low the cumulative distribution, on the right the lead glass calorimeter and low the particle count identification by the ADC counts (thanks to !CHAOS [13] integration of BTF DAQ).

test is a silicon pixel detector for details see [14–18] and a lead glass calorimiter as shown in Fig. 7.

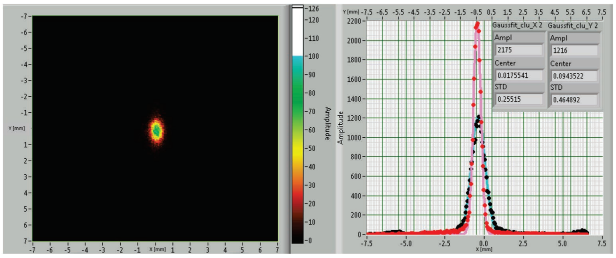

Figure 8: On the left the beam spot accumulated for about 2000 bunches with single particle detected by silicon pixel detector, on the right the Gaussian fit of the cumulative distribution ($\sigma_x = 0.25$ mm, $\sigma_y = 0.46$ mm).

After few days of optimization of the line parameters we obtain the best focused beam at the exit of the BTF2 for a 450 MeV electron beam bunch with single particle for bunch is shown in Fig. 8.

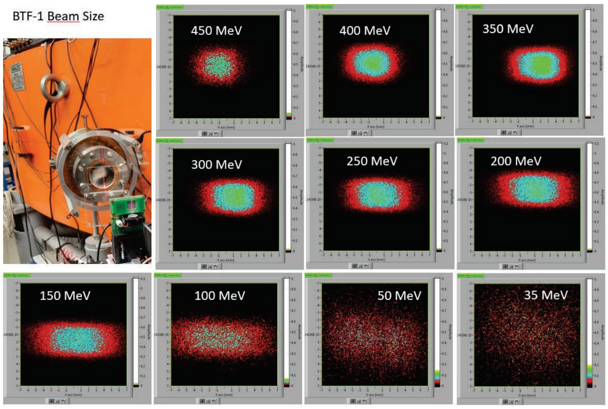

Figure 9: The BTF1 straight exit windows and the measured beam spot at various energy.

We test the possibility to transfer the beam between the two lines simply turning on and off the 15 degree pulsed magnet to find the best beam possible for the two lines. The measurements of the beam spot with silicon pixel detector are shown for an energy range from 450 MeV to 35 MeV in Fig. 9 for BTF1 and Fig. 10 for BTF2.

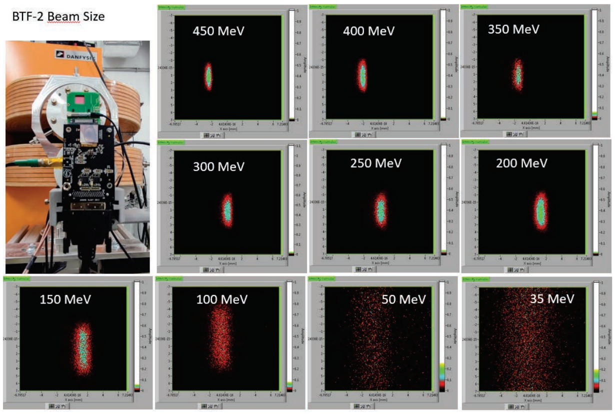

Figure 10: The BTF2 exit windows and the measured beam spot at various energy.

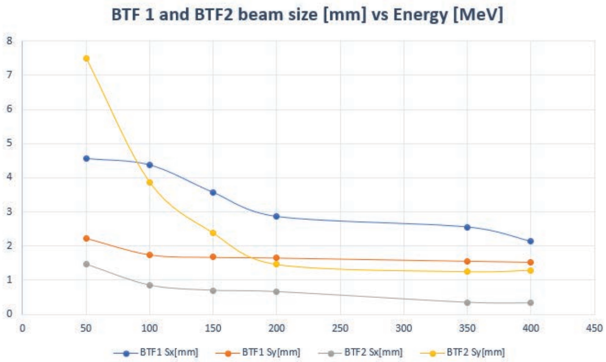

Figure 11: The plot of the measured BTF2 and BTF1 beam size vs Energy.

For the BTF2 a pretune of the magnet provide the possibility to check the beam quality for different energy of electron, as shown in Fig. 11.

CONCLUSION

The commissioning of the BTF2 line will continue in the next months to scan all the possibility and to provides to the users the parameters of the facility. The call for the users is scheduled to be published at the begin of 2022.

REFERENCES

[1] A. Rocchi *et al.*, "Linearity and rate capability measurements of RPC with semi-insulating crystalline electrodes operating in avalanche mode," *J. Instrum*, vol. 15, no. 12, C12004, 2020. `doi:10.1088/1748-0221/15/12/C12004`

[2] V. C. Antochi *et al.*, "Performance of an optically read out time projection chamber with ultra-relativistic electrons," *Nucl. Instrum. Meth. A*, vol. 999, p. 165209, 2021. `doi:10.1016/j.nima.2021.165209`

[3] E. Diociaiuti, "Study of the Mu2e sensitivity to the $\mu^- \rightarrow e^+$ conversion process," Thesis, FNAL, USA. `doi:10.2172/1605578`

[4] F. Oliva, “Performance of the charged particle detectors of the PADME experiment,” *J. Instrum*, vol. 15, no. 06, C06017, 2020. `doi:10.1088/1748-0221/15/06/C06017`

[5] A. Ghigo and F. Sannibale, “Single electron operation mode in DAPHNE BTF,” *Conf. Proc. C*, vol. 940627, pp. 2444-2446, 1995.

[6] A. Ghigo, G. Mazzitelli, F. Sannibale, P. Valente and G. Vignola, “Commissioning of the DAFNE beam test facility,” *Nucl. Instrum. Meth. A*, vol. 515, pp. 524-542, 2003. `doi:10.1016/j.nima.2003.07.017`

[7] B. Buonomo, G. Mazzitelli and P. Valente, “Performance and upgrade of the DAFNE Beam Test Facility (BTF),” *IEEE Trans. Nucl. Sci.*, vol.52, pp. 824-829, 2005. `doi:10.1109/TNS.2005.852704`

[8] P. Valente *et al.*, “Linear Accelerator Test Facility at LNF: Conceptual Design Report,” [arXiv:1603.05651 [physics.acc-ph]].

[9] B. Buonomo, C. Di Giulio, L. Foggetta and P. Valente, “The Frascati LINAC beam test facility performances and upgrades,” *Nuovo Cim. C*, vol. 40, no. 1, 69, 2017. `doi:10.1393/ncc/i2017-17069-6`

[10] B. Buonomo, C. Di Giulio, L. Foggetta and P. Valente, “Studies of the doubling of the Frascati Beam-Test Facility (BTF) line”, CERN, Geneva, Switzerland, Rep. AIDA-2020-NOTE-2016-002, 2016.

[11] L. Sabbatini *et al.*, “Fast Ramped Dipole and DC Quadrupoles Design for the Beam Test Facility Upgrade”, in *Proc. 9th Int. Particle Accelerator Conf. (IPAC’18)*, Vancouver, Canada, Apr.-May 2018, pp. 3638–3640. `doi:10.18429/JACoW-IPAC2018-THPAL011`

[12] G. Di Pirro, C. Milardi, A. Stecchi, L. Trasatti, “DANTE: control system for DAΦNE based on Macintosh and LabVIEW”, vol. 352, p. 455, Oct. 2002. `doi:10.1016/0168-9002(94)91568-7`

[13] A. Stecchi *et al.*, “!CHAOS General Status Report”, in *Proc. 12th International Workshop on Personal Computers and Particle Accelerator Controls (PCaPAC’18)*, Hsinchu City, Taiwan, Oct. 2018, pp. 17–21. `doi:10.18429/JACoW-PCaPAC2018-WEC5`

[14] L. G. Foggetta, B. Buonomo and P. Valente, “Evolution of Diagnostics and Services of the DANE Beam Test Facility”, in *Proc. 6th Int. Particle Accelerator Conf. (IPAC’15)*, Richmond, VA, USA, May 2015, pp. 904–906. `doi:10.18429/JACoW-IPAC2015-MOPHA049`

[15] B. Buonomo, C. Di Giulio, L. G. Foggetta and P. Valente, “The Frascati LINAC Beam-Test Facility (BTF) Performance and Upgrades”, in *Proc. 5th Int. Beam Instrumentation Conf. (IBIC’16)*, Barcelona, Spain, Sep. 2016, pp. 395–398. `doi:10.18429/JACoW-IBIC2016-TUPG29`

[16] P. Valente, B. Buonomo, C. Di Giulio and L. G. Foggetta, “Frascati Beam-Test Facility (BTF) High Resolution Beam Spot Diagnostics”, in *Proc. 5th Int. Beam Instrumentation Conf. (IBIC’16)*, Barcelona, Spain, Sep. 2016, pp. 221–224. `doi:10.18429/JACoW-IBIC2016-MOPG65`

[17] B. Buonomo, C. Di Giulio, L. G. Foggetta and P. Valente, “A Hardware and Software Overview on the New BTF Transverse Profile Monitor”, in *Proc. 5th Int. Beam Instrumentation Conf. (IBIC’16)*, Barcelona, Spain, Sep. 2016, pp. 818–821. `doi:10.18429/JACoW-IBIC2016-WEPG73`

[18] P. Valente, B. Buonomo, C. Di Giulio and L. G. Foggetta, “DANE BTF Improvements of the Transverse Beam Diagnostics”, in *Proc. 8th Int. Particle Accelerator Conf. (IPAC’17)*, Copenhagen, Denmark, May 2017, pp. 250–252. `doi:10.18429/JACoW-IPAC2017-MOPAB061`

ISBN: 978-3-95450-230-1 ISSN: 2673-5350 doi:10.18429/JACoW-IBIC2021-MOPP07

BEAM POSITION MONITOR FOR MYRRHA 17-100 MeV SECTION*

M. Ben Abdillah†, F. Fournier, University Paris-Saclay, CNRS/IN2P3, IJClab, France

Abstract

MYRRHA (Multi-Purpose Hybrid Research Reactor for High-Tech Applications) aims to demonstrate the feasibility of high-level nuclear waste transmutation at industrial scale. MYRRHA Facility aims to accelerate 4 mA proton beam up to 600 MeV. The accurate tuning of LINAC is essential for the operation of MYRRHA and requires measurement of the beam transverse position and shape, the phase of the beam with respect to the radiofrequency voltage with the help of Beam Position Monitor (BPM) system. MINERVA is the first phase of MYRRHA. It includes several sections allowing beam acceleration up to 100 MeV. A BPM prototype was realized for the single spoke section (17 MeV-100 MeV). This paper addresses the design, realization, and calibration of this BPMs and its associated electronics. The characterization of the beam shape is performed by means of a test bench allowing a position mapping with a resolution of 0.02 mm.

GENERAL DESCRIPTION OF MYRRHA

MYRRHA is a high power proton accelerator with strongly enhanced reliability performances. The conceptual design is on-going for more than 15 years. The adopted LINAC scheme to fulfil the reliability goal is based on 2 distinct sections, as illustrated in Fig. 1

The first phase (MINERVA) currently ongoing until 2026 aims at demonstrating the fault compensation strategy for the 600 MeV linac on a 100 MeV linac. The MYRRHA phase 1 accelerator will deliver a 100 MeV, 4 mA CW proton beam. The accelerated beam will be sent to a PTF (Proton Target Facility) for various applications including fusion research and isotope production.

MINERVA addresses the topics that have been identified as priority ones to successfully pursue the research, design and development of the MYRRHA accelerator and prepare for its actual construction. Among the topics, beam characterization would deliver data of fundamental importance in all beam dynamics simulation tools.

Beam Position Monitor (BPM) is a non-destructive beam diagnostic system, it measures beam position, phase shift regarding the accelerating signal and also gives an indication on the beam transverse shape. IJClab is in charge of the realization of a BPM prototype in order to contribute to the characterization of the beam along 17-100 MeV section that accelerates the beam from 17 MeV to 100 MeV. This document details the steps of design, fabrication and qualification of this prototype.

GENERAL DESCRIPTION OF BPM

BPMs allow measuring the vertical and horizontal coordinates of the center of gravity of the beam position and assessing the transverse size of the beam. Capacitive BPM is used. Each BPM is equipped with 4 probes formed by a sealed 50 Ohm feedthroughs attached to an electrode. The probes (feedthrough + electrode) should be as identical as possible and they should be symmetrical regarding the center of the BPM.

BPM must meet a set of constraints (vacuum, magnetism, positioning, steaming, resistance to ionizing radiation) in order to ensure its integration into the machine.

The beam induces electrical signal on each electrode, beam position, transverse shape and energy are induced from these electrical signals. The electronic module provides the following information by processing the electrical signals delivered by the electrodes:

- The horizontal and vertical position of the center of gravity of the beam.
- The phase of the beam with respect to the main Radio Frequency reference signal. Beam velocity and energy are processed from this measurement.
- Beam Ellipticity figuring in the second order moment of the beam transverse distribution.

BPM SPECIFICATIONS

Table 1 summarizes beam properties and BPM specifications for 17-100 MeV section of the MINERVA project.

- The precision on the position should be less than 100 µm on both axes. The phase shift relative to the accelerating signal should be measured with a precision less than 1degree. The beam ellipticity should be less than 1.6 mm² for circular beam while it should be measured within 20% precision for elliptical beams.

Table 1: Beam Parameters and BPM Specifications

Parameter	Range	Precision
Energy E	17 MeV-100 MeV	
Current I	0.1 mA-4 mA	
Duty cycle	2.10^{-4} to 0.125	
Bunch length @17 MeV	15°; 230 ps	
Bunch length @100 MeV	5°; 80 ps	
F_{acc}	176.1 MHz	
Beam pipe	28 mm	
Measured Position	±5 mm	100µm
Measured Phase	360degrees	1degree
Measured Ellipticity	±5 mm	Max (1.6mm²;20%)

---

* Work supported by SCK-CEN

† sidi-mohammed.ben-abdillah@ijclab.in2p3.fr

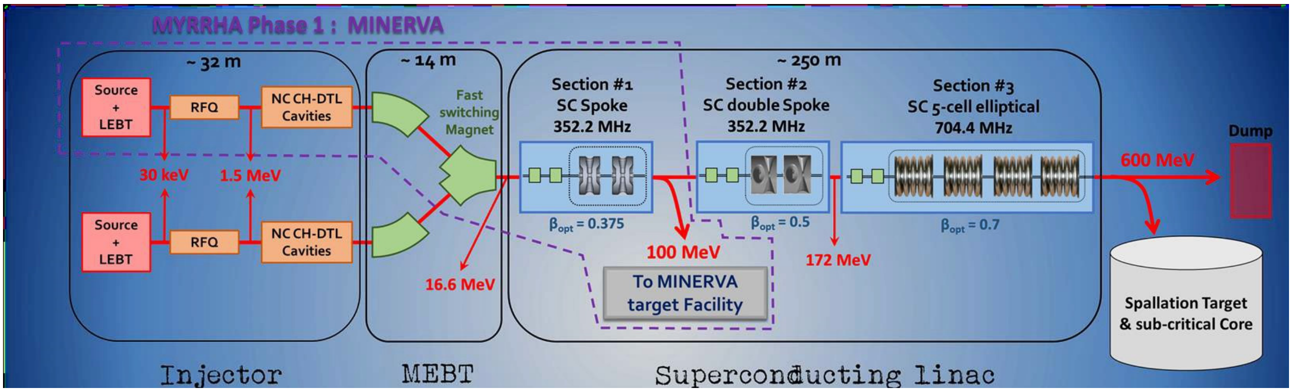

Figure 1: Conceptual design of MYRRHA with MINERVA outlined.

BPM DESIGN

Experience with SPIRAL2 BPMs [1] was of a great help. The relatively similar properties between the beams of MYRRHA and SPIRAL2 led us naturally to match the design of SPIRAL2 BPMs to MYRRHA and also improve this design.

The BPM probe is considered as a capacitance that is charged by the beam and discharged through a resistance connected to ground. The probe has a high-pass-filter characteristic with cutoff frequency $F_c=1/2\pi RC$.

High frequency information from the BPM is sometimes required to estimate bunch length or shape characteristics, or for the monitoring of the beam phase/time-of-flight. However, there are irregularities and resonant effects at very high frequencies due to mismatching between beam pipe and BPM, it is also difficult to match four electronics channels in gain and high impedance. Therefore, it is advised to operate the BPM at low frequencies ($F_{acc} < F_c$).

In the MYRRHA scope (beam energies between 17 and 100 MeV/u), the 2nd and upper harmonics of the beam image current are important. Consequently, Readout electronics must operate at f_{acc} and upper harmonics. Readout electronics processing high tones (above 0.5 GHz) are expensive and cumbersome; therefore, only 1^{st} and 2^{nd} harmonic tones of the BPM received signals are processed.

Regarding BPM design, emphasis is then put on 1^{st} and 2^{nd} harmonic tones of the BPM received signals.

The BPM design should succeed the following criteria for 17-100 MeV section of MYRRHA project:

- A strong output signal at each electrode (strong signal to noise ratio) particularly at the two first harmonics (f_{acc} and 2 f_{acc}). This would limit complications in the design of acquisition electronics.
- A strong sensitivity to the beam displacement
- Robust design: the BPM will be subject to numerous manipulations (tests, calibrations …)
- Simple design: at least 30 BPMs might be fabricated for 17-100 MeV section, therefore the fabrication should be made as simple as possible.
- The feed through resistance should be equal to 50 Ohm in order to match the impedance if the cables routing the received signal to the readout electronics.

BPM SIMULATIONS

The influence of the electrode dimensions on the signal level and harmonic content for different beams was calculated.

BPM diameter is set to D=56 mm

BPM model is depicted in Fig. 2.

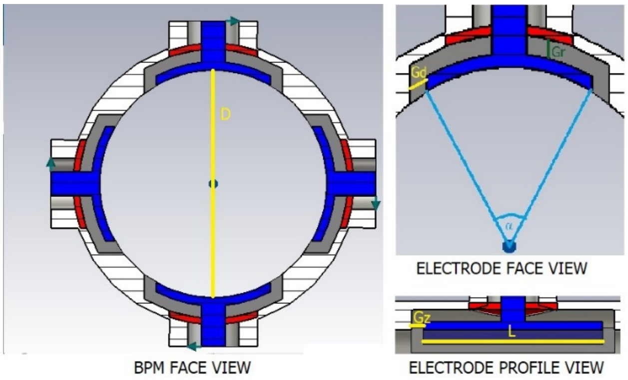

Figure 2: Design parameters.

The following parameters are optimized in BPM design

- Electrode angular width α: The wider α is the stronger the electrode output signal is however the sensitivity to beam displacement is slightly reduced. However, it is advisable to respect α<70° to reduce mutual impedance between electrodes.
- Electrode length L: the longer the electrode is, the stronger is the electrode output signal is. The sensitivity to beam displacement remains unchanged. However, long electrode is not that rigid only with soldering in its center.
- The gaps Gr, Gd, Gz and the relative permittivity ε_r are chosen in order to operate the BPM below or around its cutoff frequency.

CST is used for BPM simulations, it estimates the levels of the induced electrode voltage at frequency harmonics (first and second). BPM simulations are run with a beam current equal to 4 mA. Electrode length and angular width are kept low in order to maintain a feasible electrode stability and concentricity. The optimization on the parameters mentioned above led to the following result: L=45 mm, α=45deg, Gr=Gz=Gd=4 mm.

- For a beam current I=4 mA, the expected BPM output signal amplitude and BPM position and ellipticity sensitivities are mentioned in Tables 2 and 3.

Table 2: Expected Parameters at F_{acc}

Energy	Parameter	Value
Section start	Output amplitude (centered beam)	24 mV
	Position sensitivity	1.25 dB/mm
	Ellipticity sensitivity	0.19 dB/mm²
Section end	Output amplitude (centered beam)	11 mV
	Position sensitivity	1.22 dB/mm
	Ellipticity sensitivity	0.11 dB/mm²

Table 3: Expected Parameters at $2F_{acc}$

Energy	Parameter	Value
Section start	Output amplitude (Centered beam)	27 mV
	Position sensitivity	1.38 dB/mm
	Ellipticity sensitivity	0.13 dB/mm²
Section end	Output amplitude (Centered beam)	16 mV
	Position sensitivity	1.24 dB/mm
	Ellipticity sensitivity	0.11 dB/mm²

With a beam intensity of 100 µA, the level is 34dB lower; the cables bringing the BPM signals to electronics rack (about 30 m long) would bring an extra 3dB lost. The signals strengths at the electronics inputs are close -60 dBm.

BPM FABRICATION

The feedthrough pin is fragile and brazing it to a large electrode is subject to errors in electrodes positioning and concentricity over the 4 electrodes of the BPM. It would be even more difficult to repeat this operation properly over more than 100 electrodes.

SOLCERA*, which already provided BPMs for SPIRAL 2 LINAC, suggests reinforcing the feedthrough pin with a molybdenum spacer around it assuring though a better positioning and concentricity of the electrodes.

MYRTE BPM [2] realization steps were repeated for MYRRHA 17-100 MeV section BPM. The following issues were noticed during this realization.

Feedthrough Realization

10 feedthroughs were tested. Due to brazing, the external diameter of feedthroughs is higher than expected. However, it doesn't affect the BPM operation as all the feedthroughs suffer from the same default. The length of the connector before the joint is not the same over the 10 feedthroughs. Though, 2 samples were not accepted. Four feedthrough are chosen as the difference between their capacitances is less than 0.01 pF and their TDR responses are close to identical.

BPM Block Realization

Once the needed feed-through matched, the BPM block was fabricated and delivered, the controls had shown a deviation over reference faces higher than the precision requested. This has a direct effect on the alignment of the BPM inside the LINAC: the offset between the BPM and the beam pipe revolution axes is increased. However, this offset could be measured with precision at IJClab test bench and taken into account in BPM operation.

BPM CHARACTERIZATION

BPM Position Parameters

The BPM position coordinates are related to the electrodes received signals through the following equations:

$$\left(\frac{R}{L}\right)_{dB} = \left(1+G(\beta,f)\right)S_x(f) * \left(X-\Delta_x(\omega)\right)$$

$$\left(\frac{T}{B}\right)_{dB} = \left(1+G(\beta,f)\right)S_y(f) * \left(Y-\Delta_y(\omega)\right)$$

(X, Y) are the beam position coordinates. β the beam relative velocity; f the electrodes output signal acquisition frequency. S_x and S_y the position sensitivity at β=1.

Δ_x and Δ_y the position offsets at β=1.

G(β,f) is a correction factor set by Shafer [3] depending on β and f. G (1, f) =0.

The equations above operate properly for beam positions close to beam pipe central axis.

Position sensitivity changes with the beam position. Full interest is put on positions close to the beam pipe central axis. The goal is to measure beam position offset and sensitivity.

- The approach used for MYRTE BPM [2] is repeated. The results of the measurements of BPM electrical offsets and position sensitivity (with relative velocity β≈1) are summarized in Table 4.

Table 4: BPM Position Parameters

Frequency	Position offset	Position sensitivity
F_{acc}	(76 µm; -162 µm)	1.19 dB/mm
$2F_{acc}$	(71 µm; 98 µm)	1. 2dB/mm

The measured position sensitivity is applied at any position in the beam pipe. Therefore, the error between the measured position and the beam position is increased away from the beam axis. This error is measured for positions covering a 20 mm*20 mm square centered at the BPM electrical center. The results are mentioned in Fig. 3.

ISBN: 978-3-95450-230-1 ISSN: 2673-5350 doi:10.18429/JACoW-IBIC2021-MOPP07

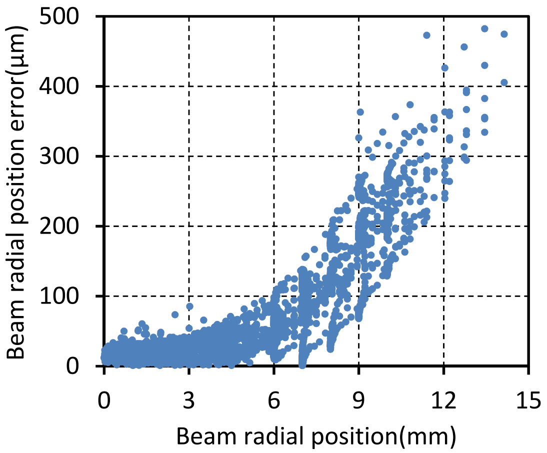

Figure 3: Position error.

The error is within 100 µm for radial position up to 6 mm, which satisfies the BPM specifications.

BPM Ellipticity Parameters

The ellipticity offsets emphasizes the case of centered beam with an elliptical transverse shape; the said beam induced equal signals on opposite electrodes but not the same signal on the 4 electrodes of the BPM.

For a beam with a circular transverse shape, the BPM ellipticity is related to the electrodes received signals through the following equation:

$$\left(\frac{R*L}{T*B}\right)_{dB} = \left(1+G_E(\beta,f)\right)S_E(f) * \ (X^2-Y^2)-\Delta_E(f)$$

(X, Y) are the beam position coordinates. S_E is the ellipticity sensitivity at β=1. Δ_E is the ellipticity offset at β=1 at the BPM electrical center. $G_E(\beta,f)$ is a correction factor mentioned in [4].

An experiment was run using the test bench in IJClab. A sweep over the Y axis (from -1 mm to 1 mm with a 50 µm step) is performed. The wire transverse shape is circular. The experiment results are sketched in Table 5.

Table 5: BPM Ellipticity Parameters

Frequency	Ellipticity offset	Ellipticity sensitivity
F_{acc}	0.2dB	0.033dB/mm²
$2F_{acc}$	0.1dB	0.033dB/mm²

Regarding the ellipticity offset, the ellipticity error is 0.01dB which corresponds to 0.3 mm².

The ellipticity sensitivity is measured close to the center. It is though applied at any position in the beam pipe. Therefore, the error between the measured ellipticity and the beam ellipticity is increased away from the beam axis. The said error is measured for positions covering a 5 mm*5 mm square centered at the BPM electrical center. The results are mentioned in Fig. 4.

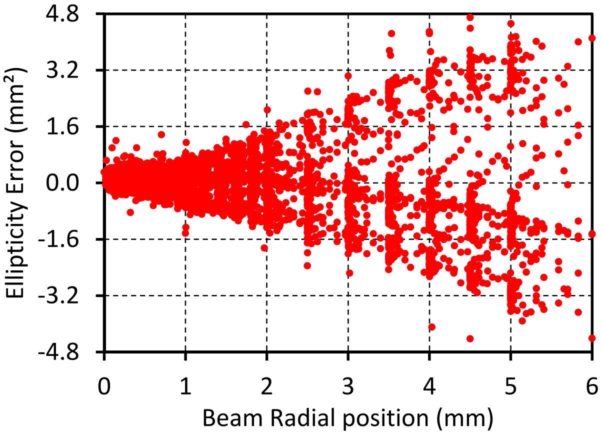

Figure 4: Ellipticity error.

The error is within 1.6 mm² for radial position up to 2 mm, which is quite less than desired in specifications.

CONCLUSION

MYRRHA 17-100 MeV section BPM prototype is presented in this paper. The mechanical fabrication is offering stable and reproducible BPM. BPM Characterization shows that beam position measurement is satisfied within specifications. Beam ellipticity is measured properly for a limited range of beam positions, a better mapping of ellipticity sensitivity is needed to match specifications on that point.

REFERENCES

[1] M. Ben Abdillah *et al.*, “Development of the beam position monitors for the SPIRAL2 Linac”, in *Proc. 1st Int. Beam Instrumentation Conf. (IBIC’12)*, Tsukuba, Japan, October 2012, TUPA18, pp.374-377.

[2] M. Ben Abdillah, P. Blache, F. Fournier, and H. Kraft, “Development of a Low-beta BPM for MYRTE Project”, in *Proc. IBIC’19*, Malmö, Sweden, Sep. 2019, WEPP002, pp. 504-507.

[3] R.E. Shafer, “Beam position monitor sensitivity for low beta beams”, in *Proc. 1994 Int. Linac Conf.*, Tsukuba, Japan, 1994, pp. 905-907.

[4] M. Ben Abdillah, “Novel electrostatic beam position monitors with enhanced sensitivity”, in *Proc. 5th Int. Beam Instrumentation Conf. (IBIC’16), Barcelona, Spain, September* 2016, TUPG09, pp. 335-337.

ISBN: 978-3-95450-230-1 ISSN: 2673-5350 doi:10.18429/JACoW-IBIC2021-MOPP08

DESIGN OF A CAVITY BEAM POSITION MONITOR FOR THE FLASH 2020+ UNDULATOR INTERSECTION PROJECT AT DESY

D. Lipka*, Deutsches Elektronen-Synchrotron DESY, Hamburg, Germany

Abstract

The FLASH 1 beamline at DESY will be upgraded from fixed to variable gap undulators in the next years. For this the vacuum beamline has to be adapted. This reduces the inner diameter compared to the existing chamber. The vacuum components should fit to the new dimension to minimize transitions and therefore reduce wakefields which could interact with the electron beam and disturb the SASE effect. The electron beam position in the intersection of the undulators should be detected with a high resolution and a large charge dynamic range. Cavity BPMs are known to fulfill these requirements. The existing design with 10 mm inner diameter for the European XFEL is reduced to 6 mm. Additional improvements are: widening of the dipole resonator waveguide to adapt to the dipole mode and antenna transmission. The resonator frequency of 3.3 GHz and loaded quality factor of 70 are maintained to use electronic synergies to other projects. The design considerations and simulation results of the cavity BPM are presented.

MOTIVATION

The superconducting free-electron laser user facility FLASH [1] at DESY in Hamburg routinely delivers several thousand high brilliance XUV and soft X-ray photon pulses per second. The user facility FLASH is in operation since 2005 and since 2014 the bunch train from the superconducting linac can be split between the original FLASH 1 undulator beamline and a new second beamline FLASH 2. In 2016 a significant Mid Term Refurbishment Program was started for FLASH. Its program will persist for the next years. As part of the DESY strategy process DESY 2030 [2] that was initiated 2016, a second substantial upgrade, FLASH 2020+ was proposed [3]. In April 2019 the internal conceptual design report (CDR) for FLASH 2020+ [4] was finalized. The mid and long term upgrades are described in [5].

There are several key aspects of the upgrade in 2024: the important one is in order to enhance the independence of the two beamlines and their over all operability, FLASH 1 needs to be equipped with variable gap undulators. To be able to close the undulators further a smaller inner vacuum chamber is proposed. This implies a reduction of the available Cavity Beam Position Monitor (CBPM) design from the European XFEL with an inner vacuum diameter of 10 mm [6] to 6 mm. The reduction of the diameter minimizes transition of the vacuum boundaries and therefore the impact of reduce wakefields which would interact with the electron beam and disturb the SASE production. Many institutes are developing such CBPM [7–19] to provide the beam position with the best resolution which consists of a dipole and a reference resonator. In this contribution the design considerations of both resonators are described.

DESIGN

For the general design the resonance frequency and quality factor have to be chosen for the dipole and reference resonator of the CBPM. Both parameters should be similar for the dipole and reference resonator to simplify the signal processing. Since the inner tube diameter is 6 mm with a cut-off frequency of 29 GHz this high cut-off this is not a limitation. To provide synergies for the already developed electronics the resonance frequency of $f = 3.3$ GHz is defined. The repetitive bunch frequency of 1 MHz allow only for a fast decaying signal, therefore a low loaded quality factor of $Q_L = 70$ is chosen which results in a bandwidth of 47 MHz. This allows a monitor production in stainless steel. The basic design is depicted from the SACLA facility [7] which was modified for the European XFEL [6]; in addition a design for the SINBAD accelerator with 34 mm diameter was developed in 2018 [19]. The quality factor and resonance frequency of the new design for FLASH 1 are similar to the European XFEL and SINBAD CBPMs for synergy but with other tube diameters and resonator thicknesses.

Dipole Resonator

The TM$_{11}$ mode of the dipole resonator provides a signal proportional to beam offset and charge. The amplitude sensitivity is $S = \pi f\sqrt{\frac{Z}{Q_{ext}}\left(\frac{R}{Q}\right)}$ [19,20], with the line impedance $Z = 50\,\Omega$ and the normalized shunt impedance $\left(\frac{R}{Q}\right)$ and the external quality factor Q_{ext}. The antenna position defines the value of the external quality factor; a small value dominates the loaded quality factor because $\frac{1}{Q_L} = \frac{1}{Q_{ext}} + \frac{1}{Q_0}$ with Q_0 the internal quality factor (which is still relative large compared to Q_{ext} for stainless steel) and therefore increases the sensitivity too. To obtain a larger sensitivity the normalized shunt impedance can be increased by using a large resonator thickness l because $\left(\frac{R}{Q}\right) \propto l$ [21], in this design $l = 5$ mm is applied. The Eigenmode solver of the simulation tool CST [22] is used to design and investigate the resonator properties. The resulting geometry is shown in Figures 1 and 2.

The resonator has a kink to decrease the resonator diameter which bends the dipole field. This is an advantage for a smaller overall monitor transverse size. The dipole field is propagating into the four slots where the dominating monopole field TM$_{01}$ can not propagate due to the geometry and is therefore in comparison with the dipole signal negligible at the antenna positions [23]. The thickness of the slots are increased compared to [6, 19] to provide the low external quality factor shown in Table 1.

---

* dirk.lipka@desy.de

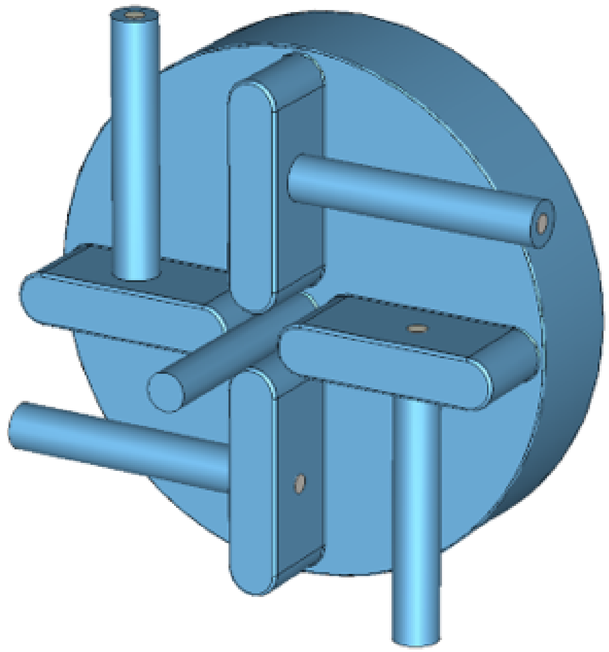

Figure 1: 3-dimensional simulation view of the vacuum design of the dipole resonator.

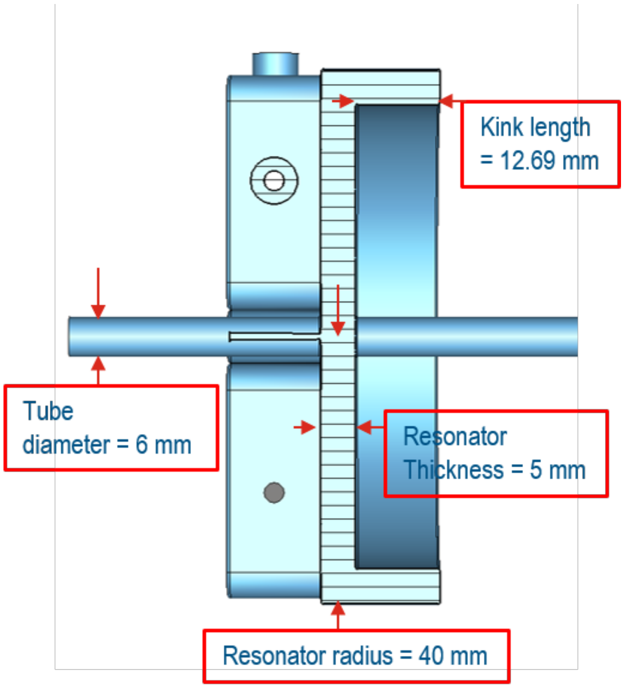

Figure 2: Cut view of the simulated dipole resonator with main design parameters.

Table 1: Dipole Resonator Property Results

f	(3299.6 ± 9.4) MHz
Q_L	70.2 ± 2.3
Q_0	585 (Stainless steel)
Q_{ext}	79.7
S	3.42 V/(nC mm)

An additional signal is generated when the beam is not parallel to the CBPM axis with a phase difference of 90° compared to the offset signal, this signal will increase with the resonator thickness [24]. To simulate the beam angle signal, the "particle in cell" (PIC) solver of CST [22] is used. The resulting relative angle compared to the offset amplitude results to be 0.62 mm/rad, this means that a beam angle of 1 rad results in the same signal amplitude as a beam offset of 0.62 mm. This value is even smaller compared to the European XFEL design with 10 mm tube diameter and 3 mm resonator thickness with the same resonance frequency and quality factor results in 0.9 mm/rad; the influence of the smaller diameter to the signal caused by the angle seems to be not negligible.

In Table 1 the property results are summarized. The resonance frequency and loaded quality factor are investigated with mechanical tolerances. When all geometric tolerances are taken into account and will add linearly to a difference of the design value, a maximum deviation is obtained; the results are shown in Table 1 too. The values show that the deviation of the resonance frequency is expected to be small compared to the bandwidth and therefore no tuners are necessary for the production of the resonator.

Reference Resonator

The reference resonator is used to measure a charge dependent signal to normalize the dipole signal and define the direction of the offset by RF phase comparison between both resonators. For proper data processing the phase of the dipole and reference resonator signals the resonance frequency and loaded quality factors should be similar. Therefore the goal values of the resonator are equal to the dipole resonator. The design of the reference resonator is shown in Figures 3 and 4.

Two antennas are foreseen to add a symmetry to the design and be able to get a second charge output. A kink is used for the reference resonator too; this bends the monopole mode into it and the antenna can transfer the signal to a perpendicular port (compared to the beam direction). This is useful for a compact longitudinal mechanical size of the CBPM. The size of the antenna is adapted to the inner diameters of a N-connector to avoid reflections from the feedthrough and minimize influences from the antenna to the external quality factor. The kink high is smaller compared to the resonator thickness to decrease the external quality factor to the desired value.

In Table 2 the resulting reference resonator properties are summarized. The resonance frequency and loaded quality factors are almost the same as for the dipole resonator. Tolerance studies with the expected mechanical deviations result in maximum possible deviations of the resonance frequency and quality factor. Here the deviations are comparable to the dipole resonator. Therefore this design can be produced without tuners for the reference resonator as well.

ISBN: 978-3-95450-230-1 ISSN: 2673-5350 doi:10.18429/JACoW-IBIC2021-MOPP08

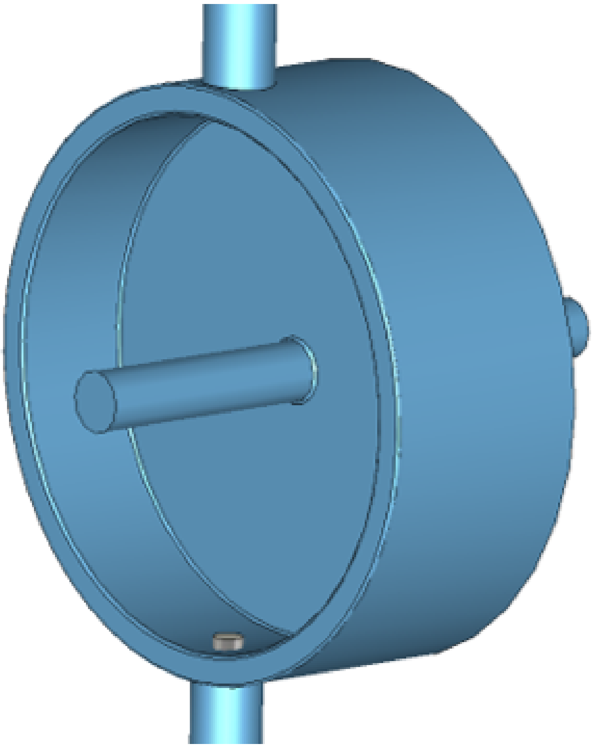

Figure 3: 3-dimensional simulation view of the vacuum design of the reference resonator.

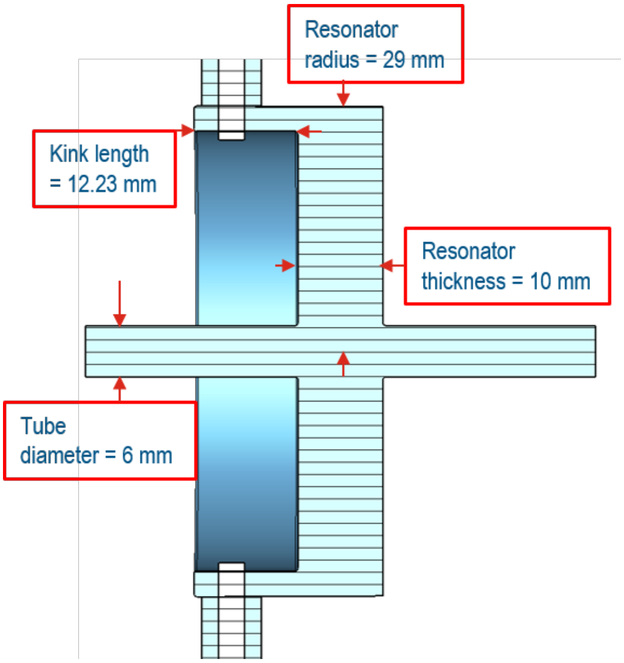

Figure 4: Cut view of the simulated reference resonator with main design parameters.

Compound of Both Resonators

Joining both resonators results in the complete CBPM. But the strong monopole field of the reference resonator at the same resonance frequency can influence the dipole field. To minimize this influence the distance between both resonators has to be specified. Assume that the dipole field is negligible when the resulting offset is below 0.1 µm; this corresponds to a sensitivity of $S_{dipole}(0.1\mu\text{m}) = 0.342\,\text{mV/nC}$, see Table 1. The ratio $20\log_{10}(S_{dipole}(0.1\mu\text{m})/S_{reference}) = -106.9\,\text{dB}$ defines the maximum transmission for any combination between the ports of both resonators. Since the dipole antennas are not arranged in a symmetry plane, the transmission to the reference resonator are not the same for all antennas. Here one needs to identify the plane with the highest influence. In the present design the maximum transmission requirement is fulfilled even with the shortest distance between both resonators due to the small diameter of the pipe, see Figure 5.

Table 2: Reference Resonator Property Results

f	(3300.0 ± 9.3) MHz
Q_L	70.0 ± 2.9
Q_0	551 (Stainless steel)
Q_{ext}	80.2
S	75.8 V/nC

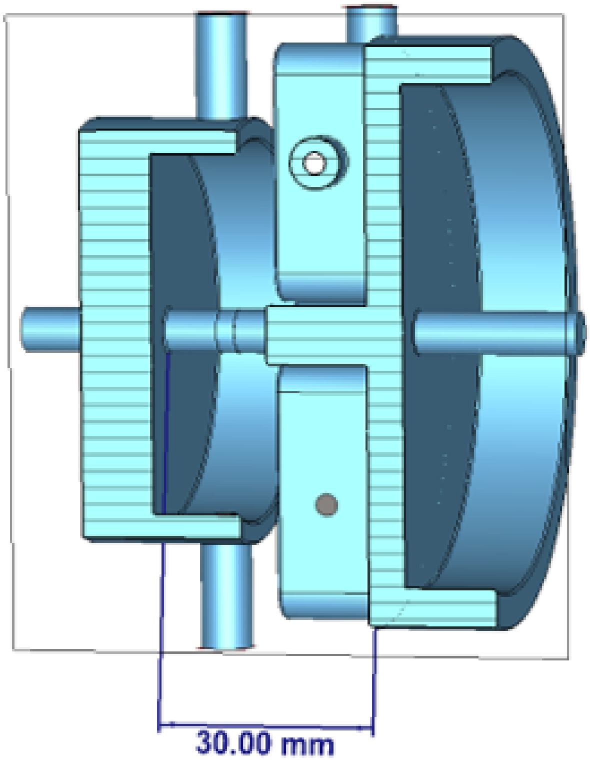

Figure 5: 3-dimensional simulation view of the vacuum design of both resonators with their proposed distance.

SUMMARY

The CBPM is designed for the FLASH 2020+ Undulator Intersection Project. In comparison to former designs the dipole resonator got a larger slot thickness to match with the small external quality factor and the antenna dimensions are similar to N-connectors to avoid additional reflection since small deviation in the feedthrough would influence the resonator properties. Tolerance studies are performed and show that the required resonance frequencies and loaded quality factors can be achieved without tuners.

REFERENCES

[1] W. Ackermann *et al.*, “Operation of a free-electron laser from the extreme ultraviolet to the water window”, *Nature Photonics*, vol. 1, no. 6, pp. 336–342, Jun. 2007. `doi:10.1038/nphoton.2007.76`

[2] H. Dosch *et al.*, Eds., “DESY 2030 — our strategy for the future”, internal DESY publication, Mar. 2018. `http://www.desy.de/sites2009/site_www-desy/content/e264024/e271297/DESY_2030_Broschuere_2018_ENG_ehs_WEB_eng.pdf`

[3] R. Röhlsberger *et al.*, “Light Source Upgrades at DESY: PETRA IV and FLASH2020+”, *Synchrotron Radiation News*, vol. 32, no. 1, pp. 27–31, 2019. `doi:10.1080/08940886.2019.1559605`

[4] M. Beye *et al.*, “FLASH2020+: Making FLASH brighter, faster and more flexible: Conceptual Design Report”, `https://bib-pubdb1.desy.de/record/434950`

[5] M. Vogt, K. Honkavaara, J. Rönsch-Schulenburg, S. Schreiber, and J. Zemella, “Upgrade Plans for FLASH for the Years After 2020”, in *Proc. 10th Int. Particle Accelerator Conf. (IPAC’19)*, Melbourne, Australia, May 2019, pp. 1748–1751. `doi:10.18429/JACoW-IPAC2019-TUPRB027`

[6] D. Lipka, D. Nölle, M. Siemens, and S. Vilcins, “Development of Cavity BPM for the European XFEL”, in *Proc. 25th Linear Accelerator Conf. (LINAC’10)*, Tsukuba, Japan, Sep. 2010, paper TUP094, pp. 629–631.

[7] H. Maesaka *et al.*, “Development of the RF Cavity BPM of XFEL/SPring-8”, in *Proc. 9th European Workshop on Beam Diagnostics and Instrumentation for Particle Accelerators (DIPAC’09)*, Basel, Switzerland, May 2009, paper MOPD07, pp. 56–58.

[8] S. W. Jang, H. Hayano, and E.-S. Kim, “Development of L-band Cavity BPM for STF”, in *Proc. 10th Int. Particle Accelerator Conf. (IPAC’19)*, Melbourne, Australia, May 2019, pp. 2547–2549. `doi:10.18429/JACoW-IPAC2019-WEPGW034`

[9] J. Q. Li, Q. S. Chen, K. Fan, K. Tang, and P. Tian, “Design and Simulation of a Cavity BPM for HUST Proton Therapy Facility”, in *Proc. 8th Int. Beam Instrumentation Conf. (IBIC’19)*, Malmö, Sweden, Sep. 2019, pp. 530–533. `doi:10.18429/JACoW-IBIC2019-WEPP010`

[10] L. Yang *et al.*, “Low Q Cavity BPM Study for the Beam Position Measurement of Nanosecond Spaced Electron Bunches”, in *Proc. 9th Int. Particle Accelerator Conf. (IPAC’18)*, Vancouver, Canada, Apr.-May 2018, pp. 1881–1883. `doi:10.18429/JACoW-IPAC2018-WEPAF027`

[11] J. Chen, Y. B. Leng, R. X. Yuan, L. W. Lai, and S. S. Cao, “Development of the Prototype of the Cavity BPM System for SHINE”, presented at the 12th Int. Particle Accelerator Conf. (IPAC’21), Campinas, Brazil, May 2021, paper FRXC06.

[12] Sh. Bilanishvili, “Design of Cavity BPM Pickup for EuPRAXIA@SPARC_LAB”, presented at the 12th Int. Particle Accelerator Conf. (IPAC’21), Campinas, Brazil, May 2021, paper MOPAB291.

[13] S. J. Lee *et al.*, “PAL-XFEL Cavity BPM Prototype Beam Test at ITF”, in *Proc. 37th Int. Free Electron Laser Conf. (FEL’15)*, Daejeon, Korea, Aug. 2015, pp. 468–470. `doi:10.18429/JACoW-FEL2015-TUP043`

[14] J. R. Towler, T. Lefevre, M. Wendt, S. T. Boogert, A. Lyapin, and B. J. Fellenz, “Development and Test of High Resolution Cavity BPMs for the CLIC Main Beam Linac”, in *Proc. 4th Int. Beam Instrumentation Conf. (IBIC’15)*, Melbourne, Australia, Sep. 2015, pp. 474–478. `doi:10.18429/JACoW-IBIC2015-TUPB060`

[15] S. W. Jang *et al.*, “The High Position Resolution Cavity BPM Developments and Measurement for ILC Final Focus System”, in *Proc. 5th Int. Particle Accelerator Conf. (IPAC’14)*, Dresden, Germany, Jun. 2014, pp. 3599–3601. `doi:10.18429/JACoW-IPAC2014-THPME147`

[16] F. Marcellini *et al.*, “Design of Cavity BPM Pickups for SwissFEL”, in *Proc. 1st Int. Beam Instrumentation Conf. (IBIC’12)*, Tsukuba, Japan, Oct. 2012, paper TUPA24, pp. 390–393.

[17] Y. I. Kim *et al.*, “Cavity Beam Position Monitor at Interaction Point Region of Accelerator Test Facility 2”, in *Proc. 4th Int. Particle Accelerator Conf. (IPAC’13)*, Shanghai, China, May 2013, paper MOPWA058, pp. 807–809.

[18] S. Walston *et al.*, “Resolution of a High Performance Cavity Beam Position Monitor System”, in *Proc. 22nd Particle Accelerator Conf. (PAC’07)*, Albuquerque, NM, USA, Jun. 2007, paper FRPMS049, pp. 4090–4092.

[19] D. Lipka, M. Dohlus, M. Marx, S. Vilcins, and M. Werner, “Design of a Cavity Beam Position Monitor for the ARES Accelerator at DESY”, in *Proc. 7th Int. Beam Instrumentation Conf. (IBIC’18)*, Shanghai, China, Sep. 2018, pp. 269–272. `doi:10.18429/JACoW-IBIC2018-TUPB05`

[20] S. Walston *et al.*, “Performance of a high resolution cavity beam position monitor system”, *Nuclear Instruments and Methods in Physics Research Section A: Accelerators, Spectrometers, Detectors and Associated Equipment*, vol. 578, no. 1, pp. 1-22, 2007.

[21] R. Lorenz, “Cavity beam position monitors”, in *Proc. 8th Beam Instrumentation Conf. (BIW’98)*, Stanford, USA, AIP Conference Proceedings 451, p. 53, 1998. `doi:10.1063/1.57039`

[22] Computer Simulation Technology, `http://www.cst.com`

[23] V. Balakin *et al.*, “Experimental results from a microwave cavity beam position monitor”, in *Proc. 18th Particle Accelerator Conf. (PAC’99)*, New York, USA, March 1999,pp. 461–464. `doi:10.1109/PAC.1999.795732`

[24] T. Slaton, G. Mazaheri, and T. Shintake, “Development of Nanometer Resolution C-Band Radio Frequency Beam Position Monitors in the Final Focus Test Beam”, in *Proc. 19th Int. Linac Conf. (LINAC’98)*, Chicago, IL, USA, Aug. 1998, paper TH4064, pp. 911–913.

ISBN: 978-3-95450-230-1 ISSN: 2673-5350 doi:10.18429/JACoW-IBIC2021-MOPP09

RESEARCH ON THE OPTIMAL AMPLITUDE EXTRACTION ALGORITHM FOR CAVITY BPM*

J. Chen†, S. S. Cao, Y. B. Leng#, T. Wu, Y. M. Zhou, B. Gao
Shanghai Advanced Research Institute, CAS, Shanghai, China

Abstract

The wake field of different modes of cavity BPM carries different bunch information, the amplitude and phase of the signals of different modes can be extracted through the signal processing method to obtain the characteristic parameters of the source bunch. In the application of bunch charge and position measurement, the accurate amplitude extraction method for cavity BPM signal is the primary issue to be considered when designing the data acquisition and processing system. In this paper, through theoretical analysis and numerical simulation, it is proved that the optimal algorithm of amplitude extraction for CBPM exists, and the dependence between the data processing window size and the decay time of the cavity BPM under the optimal design is given. In addition, the relationship between the optimized amplitude extraction uncertainty and the noise-to-signal ratio, sampling rate of data acquisition and processing system, and the decay time of the cavity BPM is also proposed, which can also provide clear guidance for the design and optimization of the CBPM system.

INTRODUCTION

Cavity BPM (CBPM) adopting a resonant cavity structure and using the characteristic modes excited by the electron beam to measure the beam parameters, has the advantage of high resolution and is widely used in FEL facilities and Linear Colliders. A typical CBPM system is composed of a cavity pickup, a radio frequency signal conditioning front end, and a data acquisition and processing electronic. The factors that affect system performance mainly include the signal-to-noise ratio (SNR) of the cavity pickup, crosstalk between different modes, beam trajectory with a finite angle, noise figure of RF front-end, performance of Analog to Digital Converter (ADC) and digital signal processing algorithms.

For cavity BPM pickups, it can be divided into low-Q (Quality factor) and high-Q from the Q value of the pickup. In theory, as long as the ADC sampling rate and number of bits are high enough, the multi-point sampling of the signal can always obtain a processing gain greater than 1. Therefore, the best signal acquisition and processing method must be the amplitude and phase extraction after full waveform sampling.

However, in the actual measurement system, due to the limitation of sampling rate and effective number of bits of ADC, when the Q value is exceedingly small, the duration time of signal is short, the data acquisition and processing schemes mostly choose analog IQ demodulation combined with peak sampling of phase locked. However, since this paper discusses general rules, technical limitations of ADC are not specifically considered.

As for the high-Q cavity BPM system, in terms of data acquisition and processing methods, the conventional method is to sample and quantize the full waveform of the IF signal conditioned by the RF front-end. And then the amplitude and phase information were extracted in the digital domain by the algorithm such as digital down-conversion (DDC), time-domain fitting, harmonic analysis, etc. In general, all waveform data are used in digital signal processing, and there is no systematic research on the optimal signal processing method. In addition, for the design and optimization of the system, there is also have no clear guiding formula for the parameters selection among the various components of the CBPM system.

In this paper, based on theoretical analysis and numerical simulation, the optimal algorithm of amplitude extraction for CBPM is discussed, and the guidance formula about the optimized amplitude extraction uncertainty and the parameters of CBPM system is also studied.

THEORETICAL ANALYSIS

The output signal of the cavity BPM can be expressed by the Eq. (1):

$$V_{port}(t) = A \cdot e^{-\frac{t}{\tau}} \cdot \sin(\omega t + \varphi). \tag{1}$$

So, the envelope of the signal can be expressed by:

$$y_{sig} = A \cdot e^{-t/\tau}. \tag{2}$$

Assume the white gaussian noise level of the signal can be expressed by:

$$y_n = A \cdot \sigma. \tag{3}$$

Where σ represents the relative noise-to-signal ratio.

The number of data points of the signal waveform after being quantized by ADC is represented by *N*, and the sampling rate of ADC is represented by *Fs*, when taking *N* points for digital signal processing, the total signal can be written as:

$$y_{signal} = \sum_{n=1}^{N} A \cdot e^{-\frac{n}{F_s \cdot \tau}}. \tag{4}$$

---

*Work supported by National Natural Science Foundation of China (2016YFA0401903) and Ten Thousand Talent Program and Chinese Academy of Sciences Key Technology Talent Program
† chenjian@zjlab.org.cn
# lengyongbin@sinap.ac.cn

Since noise is superimposed incoherently, the total noise can be written as:

$$y_{noise} = A \cdot \sigma \cdot \sqrt{N} \, . \tag{5}$$

So, when selecting N points of waveform data for digital signal processing, the relative amplitude extraction uncertainty can be expressed as:

$$\frac{y_{noise}}{y_{signal}} = \frac{A \cdot \sigma \cdot \sqrt{N}}{\sum_{n=1}^{N} A \cdot e^{-\frac{n}{F_s \cdot \tau}}} \approx \frac{\sigma \cdot \sqrt{N}}{\tau \cdot F_s \cdot (1 - e^{-\frac{N}{F_s \cdot \tau}})} \, . \tag{6}$$

Denote N by T and Fs, the Eq. (6) can be simplified to:

$$\frac{y_{noise}}{y_{signal}} = \frac{\sigma \cdot \sqrt{T}}{\tau \cdot \sqrt{F_s} \cdot (1 - e^{-\frac{T}{\tau}})} \, . \tag{7}$$

Therefore, take the derivative of Eq. (7), the relationship between the T and each parameter under the minimized amplitude extraction uncertainty can be found, the result is reduced as:

$$(\frac{2T}{\tau} + 1) \cdot e^{-\frac{T}{\tau}} = 1 \, . \tag{8}$$

After solving, we get that the relationship between the optimal data processing window size (T) and the signal decay time (τ) under the minimized amplitude extraction uncertainty is:

$$T = 1.257 \cdot \tau \, . \tag{9}$$

The theoretical analysis results show that the optimal data processing window size of the cavity BPM signal exists, and irrelevant to the sampling rate, effective bits of the ADC and the noise-to-signal ratio of the signal, but only with the decay time (loaded Q value) of the cavity BPM. This is the balance between the noise-to-signal and the signal processing gain, which minimizes the amplitude extraction uncertainty.

Substituting Eq. (9) into Eq. (7), so that the relationship between the amplitude extraction uncertainty and the relative noise-to-signal ratio (σ), sampling rate of data acquisition and processing system (Fs), and the decay time of the cavity pickup (τ) under the optimization algorithm can be obtained, expressed by Eq. (10), which also has an important guiding sense for the design and optimization of the Cavity BPM system.

$$R = 1.567 \cdot \frac{\sigma}{\sqrt{\tau \cdot F_s}} \, . \tag{10}$$

BEAM EXPERIMENT

Shanghai Soft X-ray FEL (SXFEL) is the first coherent X-ray light source in China, and cavity BPMs are installed for measure the beam position precisely. Based on the theoretical analysis mentioned above, in order to verify the relationship between the system parameters and the best window size under beam conditions, some experiments are designed, and cavity BPMs and BAMs with different parameters were selected at the SXFEL. The parameters of cavity pickups are listed in Table 1.

Table 1: Parameters of Cavity Pickups at SXFEL

	CBPM1-X	CBPM1-REF	BAM1	BAM2
Resonant frequency (MHz)	4681.8	4696.0	4720.3	4685.2
Decay time (ns)	320	144	300	298

The signals excited by the X and REF cavities of CBPM1 with different decay time are compared to verify the quantitative relationship between decay tine and the best window size. The power divider is used to divide the IF signal of REF and X and then be quantized by the ADC with resolution of 16 bit and sampling rate of 476 MHz, so as to remove the effect of bunch charge jitter. As shown in Fig. 1, the best window sizes of REF cavity and X cavity with different decay time are 1.27 times and 1.29 times of their respective decay time, it is in good agreement with the theoretical analysis and simulation results, and the corresponding amplitude extraction uncertainty has also been greatly improved. In addition, in order to evaluate the impact of sampling rate and number of bits of ADC on the best window size, the REF cavity of CBPM1 was selected, and using the same evaluation method but different DAQ system for data acquisition, including home-made Digital BPM (DBPM) processor[1] and QT7135, Libera digit-500 and NI's 5772. The parameters of different DAQs and the corresponding normalized best window sizes are listed in Table 2. The beam experiment results show that within the calculation error range, the best window size is irrelevant with the sampling rate and number of bits of ADC.

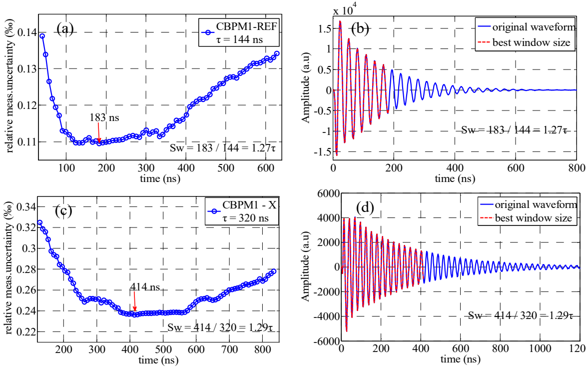

Figure 1: (a) Relationship between data window size and relative measurement uncertainty of REF cavity. (b) waveform of best window size and original data. (c) Relationship between data window size and relative measurement uncertainty of X cavity. (d) waveform of best window size and original data.

Table 2: Comparison Results of DAQ with Different Parameters (CBPM1 REF τ = 144 ns)

	DBPM	Libera digit 500	NI-5772	QT 7135	
Sampling rate (MHz)	119	476	476	476	952
Resolution (bits)	16	14	12	16	16
Best window size	1.28 τ	1.31 τ	1.30 τ	1.27 τ	1.28 τ

Adjust the parameters of the electron gun, the bunch charge was changed from 15 pC to 180 pC, and the signal coupled by two adjacent BAM pickups with similar decay time but different resonant frequencies [2]. Under different bunch charges, the signal of BAM pickups has different SNR. The local oscillator signal of 4654.2 MHz down-converts the RF signals of BAM1 and BAM2 to IF about 66.1 MHz and 31 MHz, respectively. which can evaluate the effects of different SNR and different signal frequency on the best window size. The results of the beam experiment are shown in Fig. 2. The best window size is about 1.29 times the decay time of the cavity under different bunch charges, which has no obvious dependence on the SNR of the signal and the frequency of the IF signal.

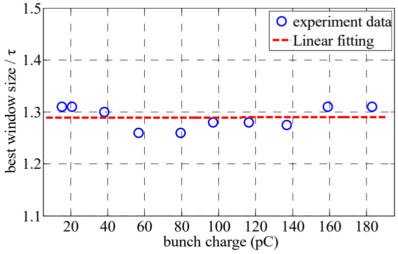

Figure 2: Normalized best window size at different bunch charge.

APPLICATION IN CBPM OF SXFEL

For the SXFEL, in order to provide accurate measurement of the beam orbit and use it for orbit correction to find the ideal orbit of the electron beam, a cavity BPM system consisting of a C-band cavity pickup, a single-stage down-conversion RF front-end and a dedicated digital BPM processor (DBPM) were developed. The system schematic of the cavity BPM system is shown in Fig. 3.

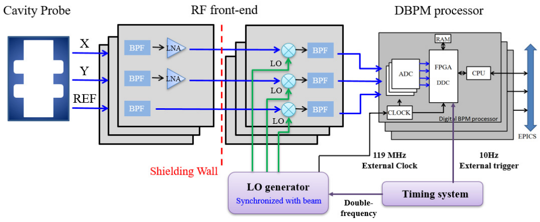

Figure 3: System schematic of the cavity BPM system.

When designing the cavity, to greatly reduce the influence of crosstalk between cavities, the resonant frequency of the position cavities and the reference cavity are designed slightly different [3, 4], and the corresponding loaded Q is also different. The RF front-end with low noise-figure and phase-locked with reference clock to down-converted the RF signal to low IF about 35 MHz and adjust the amplitude to be close to the full scale of the ADC. The data acquisition and signal processing use the home-made DBPM processor, the analog bandwidth is 650 MHz, the resolution is 16 bit, and the maximum sampling rate is 125 MHz.

Three adjacent CBPM pickups were installed at the drift section to evaluate the performance of the system. In the experiment, about 600 sets of data with original data length of 4.2 µs were sampled by the DBPM and processed offline. For the evaluation data we sampled, compare the position resolution results calculated by the typical all waveform data and the method of introducing the best window size into the algorithm. As shown in Fig. 4, the blue lines are the original waveform data of the Y direction of the three CBPMs and the REF channel of CBPM1, and the red lines is the best window size of the corresponding channels at the best resolution obtained. And Fig. 5 show the results of the system position resolution evaluated under the original waveform data and the best window size, respectively.

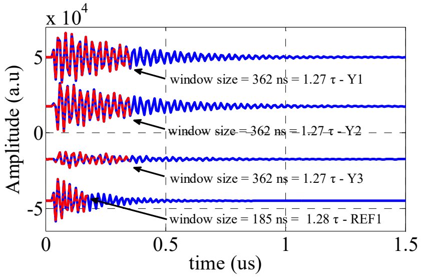

Figure 4: The original waveform and the best window size of the corresponding channels at the best resolution.

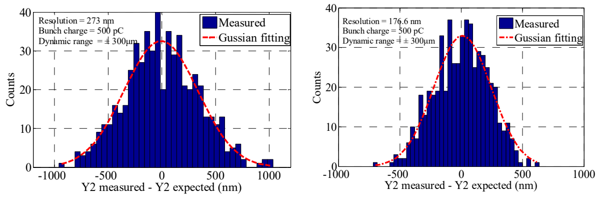

Figure 5: (left) Position resolution of the system at original waveform data. (right) position resolution at best window size.

It can be seen that the best data window sizes are about 1.27 and 1.28 times the decay time of the respective cavities, which is consistent with the theoretical analysis results, and on the other hand, it also verified that the best window size has no dependence on the SNR of source signal or the noise figure of RF front-end. Under the best window size, the calculated beam position resolution of Y direction can reach 177 nm @500 pC·±300 µm. Compared with the 273 nm calculated from the original waveform data, the performance is improved by nearly 30%, so this algorithm can be applied in online CBPM system for further performance optimization.

CONCLUSION

Cavity BPM is widely used in FEL facilities for accurate measurement of beam position. The accurate amplitude extraction method for cavity BPM signal is particularly important to the performance of the system. This research proposes an optimal amplitude extraction algorithm for the data processing of cavity BPM signal, and the guidance formula about the optimized amplitude extraction uncertainty and the parameters of CBPM system is also studied for the first time. Based on theoretical analysis and numerical simulation methods, the general solution of the best window size was determined to be about 1.26 times the decay time. The beam experiment results on SXFEL also verified the superiority and practicality of this algorithm, and be expected to be applied in SXFEL user facility and the SHINE for further performance optimization.

REFERENCES

[1] Y. B. Leng, G. Q. Huang, L. W. Lai, Y. B. Yan, and X. Yi, “Online Evaluation of New DBPM Processors at SINAP”, in *Proc. 13th Int. Conf. on Accelerator and Large Experimental Physics Control Systems (ICALEPCS'11)*, Grenoble, France, Oct. 2011, paper WEPMS028, pp. 1041-1043.

[2] S. Cao *et al.*, “Optimization of beam arrival and flight time measurement system based on cavity monitors at the SXFEL”, *IEEE Trans. Nucl. Sci.*, vol. 68, pp. 2-8, 2021. `doi:10.1109/TNS.2020.3034337`

[3] J. Chen *et al.*, “Beam test results of high Q CBPM prototype for SXFEL”, *Nuclear Sci. Tech.*, vol. 28, p. 51, 2017. `doi:10.1007/s41365-017-0195-x`

[4] J. Chen *et al.*, “Study of the crosstalk evaluation for cavity BPM”, *Nuclear Sci. Tech.*, vol. 29, p. 83, 2018. `doi:10.1007/s41365-018-0418-9`

ISBN: 978-3-95450-230-1 ISSN: 2673-5350 doi:10.18429/JACoW-IBIC2021-MOPP10

OBSERVATION OF WAKEFIELD EFFECTS WITH WIDEBAND FEEDTHROUGH-BPM AT THE POSITRON CAPTURE SECTION OF THE SuperKEKB INJECTOR LINAC

M. A. Rehman*, T. Suwada
High Energy Accelerator Research Organization (KEK), Tsukuba, Japan

Abstract

At the SuperKEKB injector linac, positrons are generated by striking electron beam at tungsten target. The secondary electrons are also produced during positron creation and accelerated in the positron capture section. A new wideband feedthrough–beam position monitor (BPM) system was developed for synchronous detection of secondary produced e^- and e^+ beams with temporal separation of about 180 ps. When e^+/e^- bunches pass through the accelerating structure or vacuum duct of different radius, they generate wakefields. These wakefields can be directly observed with the feedthrough-BPM. A simulation study has also been carried to validate the observed wakefield effects with the feedthrough-BPM. The effects of wakefields on beam parameters will be reported in this paper.

INTRODUCTION

The SuperKEKB (SKEKB) [1, 2] is an electron and positron collider with asymmetric energies to study CP violation in B mesons and also to search for new physics beyond the Standard Model, with the target luminosity of 8×10^{35} cm^{-2}s^{-1}, which is 40 time higher than its predecessor KEKB [3]. The SKEKB collider consists of e^- and e^+ rings of energy 7 GeV (HER) and 4 GeV (LER) with the stored beam current of 2.6 A and 3.6 A, respectively.

The SKEKB injector linac generates e^-/e^+ bunches of 5 nC and 4 nC to directly inject into HER and LER, respectively, at their designed energy. The low emittance e^- beam is produced by a RF–photocathode gun. The e^+ beam is produced by striking the e^- beam of energy 3.5 GeV and bunch charge of 10 nC at a tungsten target. The positrons are generated as secondary particles and have a large transverse emittance. To capture a large amount of positrons, a pulsed solenoid called flux concentrator and a large aperture S–band (LAS) accelerating structures [4] are placed in the downstream of the e^+ target. The secondary electrons are also produced in a similar amount of charges during the e^+ creation process and accelerated in the capture section. Because of phase slipping process in the capture section, the time interval between secondary produced e^- and e^+ bunches is about only 135 ps under nominal operation.

Due to low frequency response and high–frequency cable losses, conventional beam monitors, i.e., stripline beam position monitors, are difficult to detect such closely spaced and opposite polarities bunches in the capture section. For this reason in the past capture section there were no beam monitoring devices. As a result of a lack of information about the beam properties such as transverse positions, bunch lengths and, bunch charges, the e^+ beam suffers some amounts of beam loss after the capture section.

Therefore, a new wideband feedthrough type BPM was developed to overcome the above–mentioned challenges. This new monitor can synchronously detect e^- and e^+ bunch properties, i.e., transverse positions, bunch lengths, time interval, and bunch charges. It provides an opportunity to enhance positron beam transport through the capture section. The detailed analysis of bunch properties is reported in [5,6]. The modal analysis of electromagnetic coupling between SMA-feedthrough and beam is described in [7]. The effect of wakefields induced by the passage of e^-/e^+ bunches through the end of the accelerating structure on the BPM signal will be discussed in detail in this report.

WIDEBAND FEEDTHROUGH BEAM POSITION MONITOR

The feedthrough–BPM consists of a vacuum pipe of length 431 mm which has an inner diameter of 38 mm, four SMA-type feedthroughs having inner conductor made of Kovar with $\pi/2$ rotational symmetry are installed at the upstream direction of the vacuum pipe. The diameter of the central connector pin of feedthroughs is 1.8 mm, and they extend 1 mm to the center of the beam pipe from the inner surface of the vacuum pipe. The vacuum pipe of BPM also has bellows mounted at the downstream and upstream direction for flexible installation. The upstream bellow is shielded in order to any suppress unwanted wakefields. In the upstream direction, BPM is attached with the LAS accelerating structure. The 3-D model of the new wideband feedthrough–BPM with LAS structure is shown in Fig. 1 (a). Figure 1 (b) shows the front view of the new monitor with dimensions. Two new feedthrough–BPMs were installed in the positron capture section. The horizontal and vertical steering coils are also installed at the same locations in the capture section to optimize the e^+ transmission through the capture section. The entire capture section is enclosed in the DC solenoid coils for efficient transmission of large emittance e^+ beam. For the sake of simplicity, they have been omitted from Fig. 1. The details can be found elsewhere [2,5].

The SMA connectors of the feedthroughs are first connected to 2 m–long semirigid coaxial cable due to its protection against a high radiation environment. Later the semirigid cable was connected to 15 m–long 10D and 2 m–long RG223 coaxial cable [8]. The RG223 coaxial cables are then connected to a real–time keysight oscilloscope of bandwidth

---

* rehman@post.kek.jp

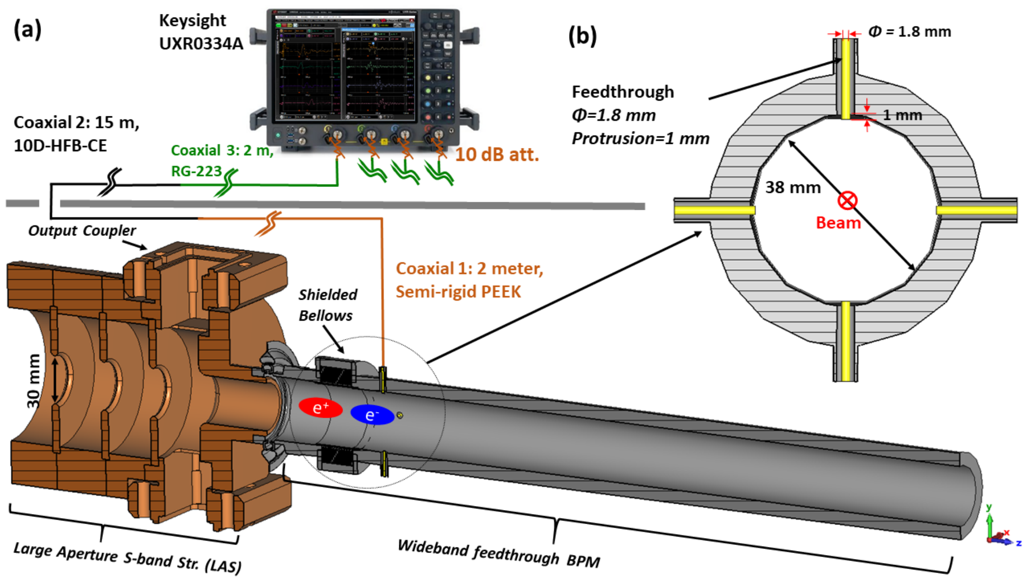

Figure 1: (a) The mechanical model of the feedthrough–BPM with LAS accelerating structure (only last three structures and output coupler). The cabling and connections of feedthrough-BPM to wideband oscilloscope are also shown. (b) Front view of the feedthrough-BPM.

33 GHz and a sampling rate of 128 GS/s [9] with a 10-dB attenuator. The cable losses have been measured in advance by a vector network analyzer [10] and are de-embedded from the feedthrough–BPM signals by the oscilloscope.

WAKEFIELD SIMULATION OF WIDEBAND FEEDTHROUGH–BPM

When a charged particle travels through any obstacle (i.e., accelerating structure, beam pipe of different radii, etc.), it generates electromagnetic (EM) fields that are left behind the particle. This EM field is called wakefield [11]. These wakefields can act on subsequent bunches (long–range wakefield) and can also act on trailing particles of the same driving bunch (short–range wakefield). In order to understand the wakefield field effect on the feedthrough-BPM signal, a time-domain simulation in CST-wakefield solver [12] has been done. In this section, simulation of single and double bunch beams and their effects for the feedthrough–BPM signals will be described.

The 3-D model used in the simulation is shown in Fig. 1 (a). Figures 2 (a) and 2 (b) present the simulation results of a single bunch e^- beam through the new monitor with and without accelerating structure, respectively. For the simulation the e^- bunch length (1σ) was assumed 10 ps with the bunch charge of 5 nC. Since the cutoff frequency in the experiment was chosen to 10 GHz by applying a 4th–order Bessel filter. Therefore, a Bessel filter with the cutoff frequency of 10 GHz is also applied to simulation results. In Fig. 2 (a) the typical bipolar signal from the feedthrough–BPM [13] (without accelerating structure) appears and after the passage of high–energy e^- bunch, a small noise appears due to the wakefield produced by the protrusion of feedthrough.

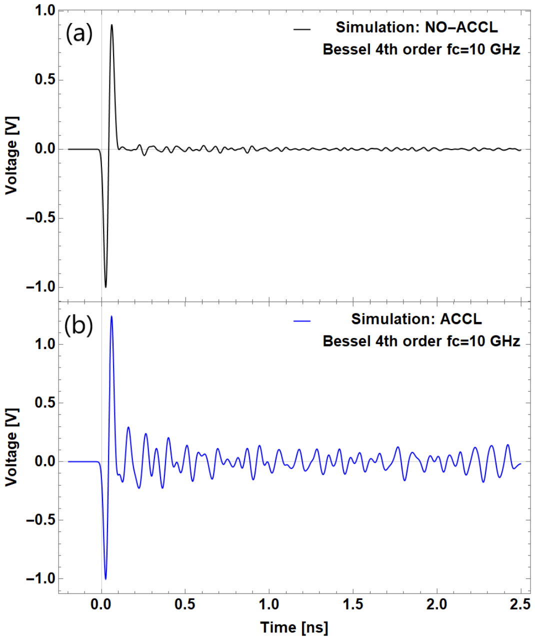

Figure 2: (a) The CST-wakefield simulation of the high–energy e^- single bunch of the feedthrough–BPM without LAS structure. No large ringing signal appears after the bipolar signal from the feedthrough–BPM. A very small noise appears only due to the 1 mm protrusion of the feedthroughs toward the center of the vacuum duct. (b) The CST-wakefield simulation of the feedthrough–BPM with the last three cavities and output coupler of LAS structure. The large ringing signal immediately appears after the bipolar signal of the e^- beam.

Whereas in the case of a simulation with the accelerating structure, a large ringing signal appears after the main bipo-

ISBN: 978-3-95450-230-1 ISSN: 2673-5350 doi:10.18429/JACoW-IBIC2021-MOPP10

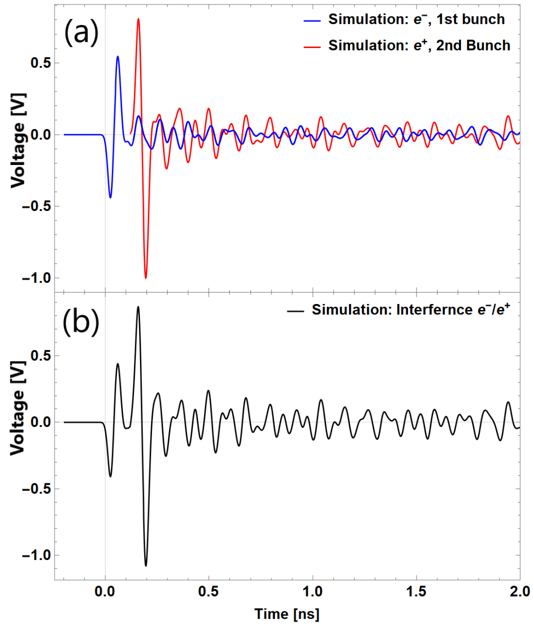

Figure 3: (a) The independent simulated signals of secondary e^- and e^+ bunches. (b) The interference of secondary e^- and e^+ signals.

lar signal as shown in Fig. 2 (b). The long–range wakefield generated by the passage of e^- bunch through the accelerating structure will reach to the feedthrough–BPM much later. Moreover, the output coupler of the accelerating structure also acts as a dumper for the higher-order modes of wakefield.

When e^- bunch passes through the end duct of accelerating structure, which has an inner diameter of 30 mm, to the feedthrough-BPM with the inner diameter of 38 mm, a wakefield produced due to this abrupt change of vacuum duct diameter. This short–range wakefield travels with the speed of light and emerges as an immediate ringing signal after the beam signal, as shown in Fig. 2 (b). Therefore, the area and bunch width for the second lobe of the bipolar signal differ with some errors from the bipolar signal without accelerating structure.

Since it is not possible to simulate the double bunch structure with the opposite polarities in the CST wakefield solver,e^- and e^+ bunches were considered independently and superimposed on each other to find the total wakefield effect. Figure 3 (a) shows the e^- and e^+ bunches independently in blue and red colors, respectively. In the nominal operation, the intensity of e^+ charges is about twice of secondary e^-, therefore e^+ intensity was assumed higher than that of the e^- bunch. The time interval between the electron and positron bunch was taken 135 ps. Figure 3 (b) shows the superposition of e^- and e^+ bunches. The e^- bunch (first bunch) exposed to only short-range wakefield, whereas the e^+ bunch experiences the wakefield generated by the e^- bunch and also self-generated wakefields. The area, bunch width, and time interval for the e^+ bunch's first lobe of the bipolar signal differ with some errors from the bipolar signal without accelerating structure.

EXPERIMENTAL RESULTS

In order to estimate the effect of the wakefield on the experimental signal of the double bunch, it is assumed that the wakefield–induced voltage oscillates and decays [14] as follows:

$$V(t) = \sum_n a_n \sin[\omega_n t + \phi_n] e^{\frac{-\omega_n}{2Q_n} t}, \tag{1}$$

where $V(t)$ is the induced voltage by the wakefields, n represents the mode number, ω_n resonant angular frequency of the accelerating structure, Q_n is the quality factor, and ϕ_n shows the phase delay between different excited modes.

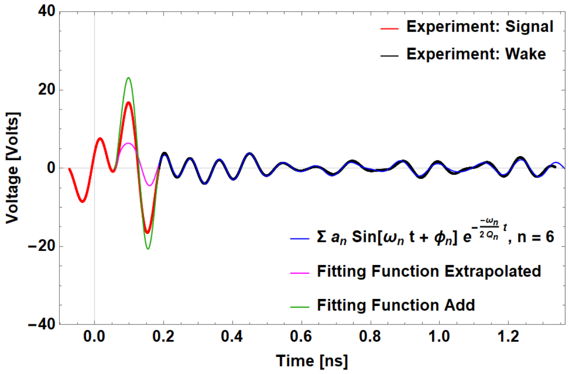

Figure 4: The synchronous signal of e^-(first)/e^+(second) bunch at nominal accelerating phase from the new feedthrough–BPM, the cutoff frequency was set to $f_c = 10$ GHz. The fast oscillation and decay signal arises due to the wakefields of the e^-/e^+ bunches.

The model described in eq. (1) is used to fit the experimental data and then extrapolated it on the bipolar signal to estimate the effect of the wakefields on the beam parameters. Figure 4 shows the synchronous signal of e^-(first)/e^+(second) at nominal accelerating phase from the new feedthrough–BPM, the cutoff frequency was set to $f_c = 10$ GHz. The red curve in Fig. 4 is a double bipolar signal from the e^- and e^+ bunches, whereas the curve shown in black presents induced voltage on the feedthrough–BPM due to the wakefield, which exhibits fast oscillation and decay. These wakefields induced voltages were fitted by using eq. (1) as shown in blue color in Fig. 4.

The induced voltages by the passage of the e^-/e^+ bunches through the different radius of vacuum duct are a superposition of the several higher–order modes excited by the wakefields. Therefore, fitting to experimental data was done with the different values of n. Figure 5 shows the variation in reduced χ^2 to experimental data as a function of the higher–order modes "n". It can clearly be seen at the value of $n = 6$ the reduced χ^2 value becomes ~ 1. Therefore, $n = 6$ was chosen for the fitting function.

The fitting function is also a superposition of the wakefield of e^- and e^+ bunches, as the e^- bunch is ahead of the

e^+ bunch therefore, the e^- bunch does not witness any wakefields by the e^+ bunch. For this reason, the fitting function was extrapolated only to the bipolar signal of the e^+ bunch. In Fig. 4 the magenta curve is the extrapolation of the fitting function to the e^+ bipolar signal. The green curve in Fig. 4 shows the constructive interference of the extrapolated fitting function to the e^+ bunch. The interference of the wakefields induced voltages on the e^+ bipolar signal contributes to errors in area, bunch width, and time interval with taking into account the phase, respectively for the e^+ bunch's first lobe of the bipolar signal. The comparison of the wakefield errors for the beam parameters between experiment and simulation is summarized in Table 1. The estimated wakefield errors for the beam parameters are consistent in experiment and simulation.

Table 1: Comparison of the Wakefield Errors for Beam Parameters Between Experiment and Simulation

Wakefield Errors		
Beam Parameters	**Experiment**	**Simulation**
Area	41%	38%
Bunch width	1.2 ps	0.72 ps
Time Interval	2.5 ps	2.4 ps

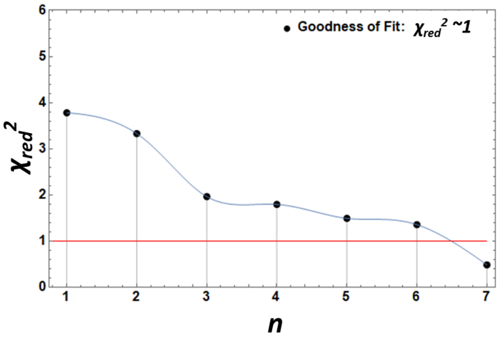

Figure 5: Variation in the reduced χ^2 of the fitting function to the ringing signal of e^-/e^+ bunch. For $n = 6$ reduced χ^2 becomes ~ 1.

SUMMARY

The short–range wakefield has been observed as a ringing signal after a double bipolar signal in synchronous measurements of the e^- and e^+ bunches with the wideband feedthrough-BPM system at the e^+ capture section of the SuperKEKB factory. A simulation study and analytical function fitting on experimental data have been successfully carried out to estimate the effect of the wakefield on the beam parameters measured by the new beam monitor.

ACKNOWLEDGMENTS

We thank Profs. Toshiyasu Higo and Tetsuo Abe for their generous support and guidance for this project.

REFERENCES

[1] K. Akai *et al.*, "SuperKEKB collider", *Nucl. Instrum. Methods Phys. Res. A*, vol. 907, p. 188, 2018. `doi:10.1016/j.nima.2018.08.017`

[2] Y. Ohnishi *et al.*, "Accelerator design at SuperKEKB", *Prog. Theor. Exp. Phys.*, vol. 2013, 03A011, 2013. `doi:10.1093/ptep/pts083`

[3] T. Abe *et al.*, "Achievements of KEKB", *Prog. Theor. Exp. Phys.*, vol. 2013, 03A001, 2013. `doi:10.1093/ptep/pts102`

[4] S. Matsumoto, T. Higo, K. Kakihara, T. Kamitani, and M. Tanaka, "Large-aperture Travelling-wave Accelerator Structure for Positron Capture of SuperKEKB Injector Linac", in *Proc. 5th Int. Particle Accelerator Conf. (IPAC'14)*, Dresden, Germany, Jun. 2014, pp. 3872–3874. `doi:10.18429/JACoW-IPAC2014-THPRI047`

[5] Tsuyoshi Suwada, Muhammad Abdul Rehman, Fusashi Miyahara, "First Simultaneous Detection of Electron and Positron Bunches at the Positron Capture Section of the SuperKEKB Factory", *Sci. Rep.* 11, 12751, 2021. `doi:10.1038/s41598-021-91707-0`

[6] M. A. Rehman, T. Suwada, and F. Miyahara, "First Synchronous Measurement of Single-Bunched Electron and Positron Beams with a Wideband Feedthrough-BPM at the Positron Capture Section of the SuperKEKB Injector Linac", presented at the 12th Int. Particle Accelerator Conf. (IPAC'21), Campinas, Brazil, May 2021, paper MOPAB163.

[7] Tsuyoshi Suwada, "Modal Analysis of Electromagnetic Couplings Between SMA-Feedthrough Electrode and Beam for Wideband Beam Monitor", presented at the 9th Int. Beam Instrumentation Conf. (IBIC'21), Pohang, Korea, Sep. 2021, paper WEPP12.

[8] Catalog of high-frequency coaxial cables, `https://www.fujikura-dia.co.jp/`.

[9] Keysight Technologies, Inc., UXR0334A Infiniium UXR-Series, `https://www.keysight.com/en/`.

[10] Keysight Technologies, Inc., N5230A PNA-L Network Analyzer, `https://www.keysight.com/en/`.

[11] M. Ferrario *et al.*, "Wakefields and Instabilities in Linear accelerators", *Proc. CAS-CERN Accel. Sch. Adv. Accel. Physics*, Trondheim, Norway, August 2013, edited by W. Herr (CERN-2014-009).

[12] CST STUDIO SUITE, `http://www.cst.com/`.

[13] R. E. Shafer, "Beam Position Monitoring", *AIP Conf. Proc.*, vol. 249, p. 601, 1992. `doi:10.1063/1.41980`

[14] A. Chao, K. H. Mess, M. Tigner and F. Zimmermann, "Handbook of Accelerator Physics and Engineering", World Scientific, 2013, pp. 264-265. `doi:10.1142/8543`

ISBN: 978-3-95450-230-1 ISSN: 2673-5350 doi:10.18429/JACoW-IBIC2021-MOPP12

DEVELOPMENT OF AN X-BAND CBPM PROTOTYPE FOR SHINE*

S. S. Cao†, Y. B. Leng*, R. X. Yuan, R. T. Jiang
Shanghai Advanced Research Institute, Chinese Academy of Sciences, Shanghai, China

Abstract

SHINE (Shanghai High repetition rate XFEL aNd Extreme light facility) is a newly proposed high-repetition-rate X-ray FEL facility and will be used to generate brilliant X-rays between 0.4 and 0.25 keV. To guarantee the high performance of FEL light pulses, it is required to precisely monitoring the trajectory of the electron bunch. The position resolution of each bunch at the undulator section is required to be better than 200 nm at a bunch charge of 100 pC and 10 μm at a bunch charge of 10 pC. Since the cavity beam position monitor (CBPM) is widely used in FEL facilities for its unique high resolution and high sensitivity and the output signals of an ideal pillbox cavity are proportional to the resonant frequency, thus the X-band CBPM is preferred because it is expected to obtain better results at low bunch charge compared with the C-band CBPM. Therefore, an X-band CBPM prototype is also developed for SHINE. This paper will focus on the design and production process of the X-CBPM.

INTRODUCTION

SHINE is designed to become one of the most efficient and advanced free electron laser user facilities in the world and provide an ultra-powerful tool for cutting-edge research. The facility is composed of a superconducting linear accelerator, 3 underlines, 3 optical beam lines, and the first 10 experimental stations[1, 2]. The facility is designed to operate at a maximum repetition rate of 1 MHz and the beam energy is 8 GeV. The bunch charge is ranging from 10 pC to 300 pC. The pulse length is only 20 to 50 fs.

To build such an ultra-high performance FEL facility, stringent requirements are placed on the beam position monitor system so as to establish and maintain precise beam trajectory and prevent emittance growth. At the undulator section, the bunch position resolution is required to be better than 200 nm at a bunch charge of 100 pC and 10 um at 10 pC bunch charge. Since the cavity beam position monitors (CBPM) can couple high signal-to-noise ratio (SNR) RF signals for high-resolution bunch position detection and the reported position resolution can even reach nm-scale, thus the CBPM is utilized in this section. Generally, the CBPM can work at S-band, C-band and X-band. In this research, the X-band CBPM is selected for three reasons. Firstly, the X-band CBPM has a more compact structure. Secondly, the X-band CBPM is expected to extract the RF signals with better SNR. Thirdly, it could test the machining techniques of the manufacturers.

This paper will mainly introduce the design and cold test of the X-CBPM as well as the high-bandwidth feedthrough.

REQUIREMENTS

As described in [3], the X-CBPM will operate at 11.483 GHz which has a 59.5 MHz deviation from the quadruple frequency of 2856 MHz. The bandwidth is ranging from 1.59 MHz to 3.18 MHz. Thus the decay time constant is ranging from 100 ns to 200 ns. In order to reduce the influence of beam jitter in the X/Y direction on the beam position measurement in the Y/X direction, the XY crosstalk is required to be smaller than -34 dB under a dynamic range of ±100 μm. The fundamental requirements of the X-CBPM have been summarized in Table 1.

Table 1: Requirements of X-CBPM

Parameters	Value	Unit
Frequency	11483	MHz
Decay time constant	100~200	ns
Qload	3611~7222	~
Bandwidth	1.59~3.18	MHz
XY crosstalk	<-34	dB
Crosstalk between Ref. and Pos. cavity	<-60	dB

DESIGN OF X-CBPM

The X-CBPM is composed of a position cavity and a reference cavity. The position cavity of X-CBPM is equipped with four rectangular waveguides and thus demands four high-bandwidth feedthroughs. The waveguides are mainly used to reject the TM010 mode and extract the TM110 mode. The structure of this cavity is shown in Fig. 1(a).

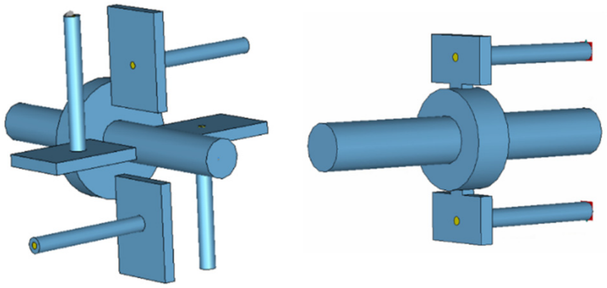

Figure 1: A 3-D view of X-CBPM vacuum parts: (a) position cavity; (b) reference cavity.

Unlike the previous CBPM reference cavity, the reference cavity of X-CBPM additionally contains two rectangular waveguides. This is mainly because of the limited space for installation of feedthrough. The diameters of the beam pipe and the reference cavity resonating at 11.483 GHz are 10 mm and 20 mm, respectively. Excluding the thickness of the cavity wall, the space left for installing feedthrough in the radial direction is less than

---

* Work supported by National Key Research and Development Program of China under Grant 2016YFA0401903.
† lengyongbin@zjlab.org.cn

4 mm. To solve this problem, a rectangular waveguide is added at both ends of the reference cavity, as shown in Fig. 1(b). The TM010 mode in the cylindrical cavity can enter the rectangular waveguide through magnetic coupling.

Using the computer simulation software (for example CST), the final CBPM model can be obtained through iterative optimization and calculation. The RF signals coupled from the X-CBPM are shown in Fig. 2. Among them, Fig. 2(a) and (c) show the waveforms generated in the reference cavity and position cavity, respectively; Fig. 2(b) and (d) present the frequency spectrum of the reference cavity and position cavity, respectively. The simulation results using CST can be summarized in Table 2. Both of the reference cavity and position cavity work at 11.483 GHz. The bandwidths of the reference cavity and position cavity are 1.81 MHz and 1.94 MHz, respectively.

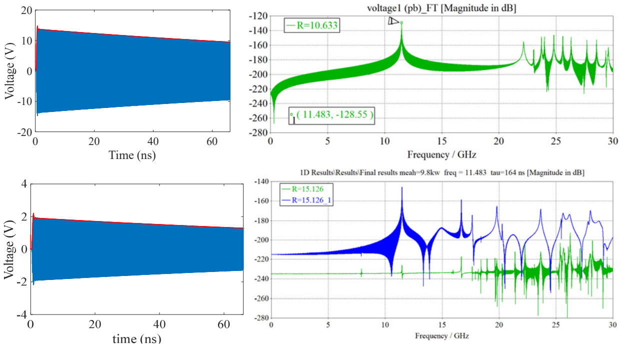

Figure 2: (a) The output signal waveform of reference cavity; (b) The frequency spectrum of reference cavity; (c) the output signal waveform of position cavity; (d) the frequency spectrum of position cavity.

Table 2: Simulation Results of X-CBPM

Parameters	Reference cavity	Position cavity
Frequency/GHz	11.483	11.483
Decay time constant/ns	164	176
Qload	6344	5919
Bandwidth/MHz	1.81	1.94
Sensitivity/(V/nC)	14	2@1 mm

TEST OF X-CBPM

In order to understand the characteristic of the X-CBPM, multiple tests have been performed during the production process with a broadband network analyzer. The X-CBPM has been manufactured last year, as shown in Fig. 3. The whole length of the X-CBPM is 144 mm. The distance between the reference cavity and position cavity is more than 60 mm to improve the isolation between the two cavities.

The first cold test results have been measured with a NA, as shown in Fig. 4. There are several unexpected modes that occurred in the frequency response of the reference cavity and position cavity. During the second test, we made some improvements to reduce the gap between the cavity parts by adding few circular rings between the gaps. The feedthroughs are further fixed. Moreover, the reference cavity and position cavity are tested seperatly, as shown in Fig. 5.

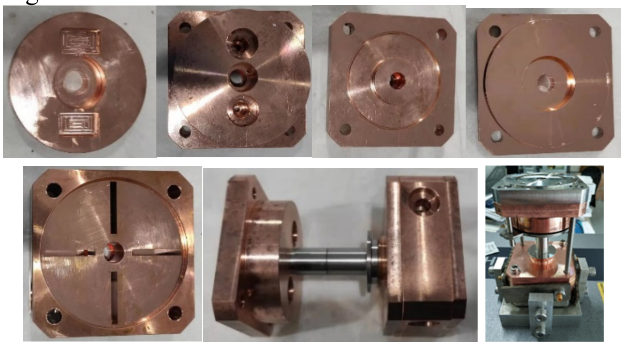

Figure 3: The photos of X-CBPM.

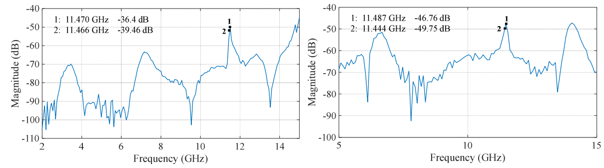

Figure 4: The first cold test result: (a) position cavity; (b) reference cavity.

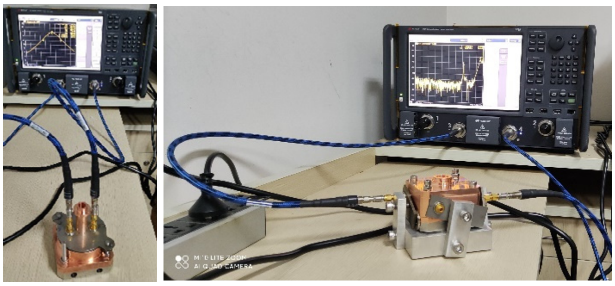

Figure 5: Photos of X-CBPM second test.

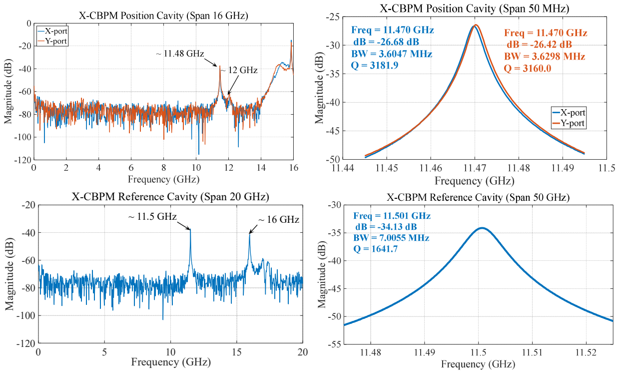

Figure 6: Frequency response of the second cold test: (a) Position cavity (span=15 GHz); (b) Position cavity (span=50 MHz); (c) Reference cavity (span=20 GHz); (d) Reference cavity (span=50 MHz).

The second cold test results are presented in Fig. 6. It is apparent that the frequency response of the position cavity and reference cavity in Fig. 6.(a) and (c) is quite different from that in Fig. 5. The unexpected modes in Fig. 5 have disappeared in Fig. 6. The tested frequency responses of the position cavity and reference cavity are almost consistent with simulation results. The measured frequencies

ISBN: 978-3-95450-230-1 ISSN: 2673-5350 doi:10.18429/JACoW-IBIC2021-MOPP12

of the position cavity and reference cavity are 11.470 GHz and 11.501 GHz, respectively. The measured bandwidths for position and reference cavity are 3.6 MHz and 7.0 MHz. However, there is an unanticipated mode operating at 12 GHz near the TM110 mode of the position cavity. The frequency response of the mode is related to the pressure on the cavity. Figure 7 shows two different frequency response under different pressure on the position cavity.

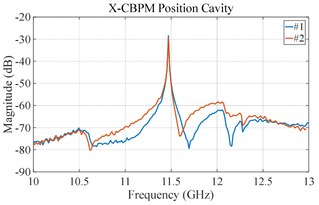

Figure 7: Frequency response under different pressure on the position cavity.

Finally, the physical photo of the cavity after brazing and argon arc welding is shown in Fig. 8. The cold test results are presented in Fig. 9. Among them, Fig. 9(a) shows the frequency response of reference cavity, position cavity-X, and position cavity-Y, respectively. The frequency response of the reference cavity is consistent with that in Fig. 6. The frequency response of the position cavity is slightly different from the second test result. The 12-GHz-mode has disappeared this time. The cold test results show that the frequency of the reference cavity is 11.506 GHz, which is 23 MHz larger than the simulation result of 11.483 GHz. The position cavity-X and position cavity-Y are 11.485 GHz and 11.486 GHz, respectively, which are quite close to the simulation frequency of 11.483 GHz. The measured bandwidth of the reference cavity is completely consistent with the simulation result, but the measured bandwidths of the position cavity-X and position cavity-Y are 0.6 and 0.4 MHz larger than the simulation result. The measured maximal XY crosstalk is -44 dB which can still satisfy the requirement. The final test results have summarized in Table 3.

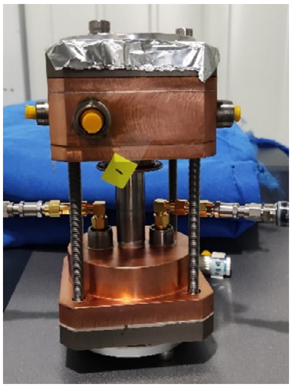

Figure 8: The physical photo of the X-CBPM.

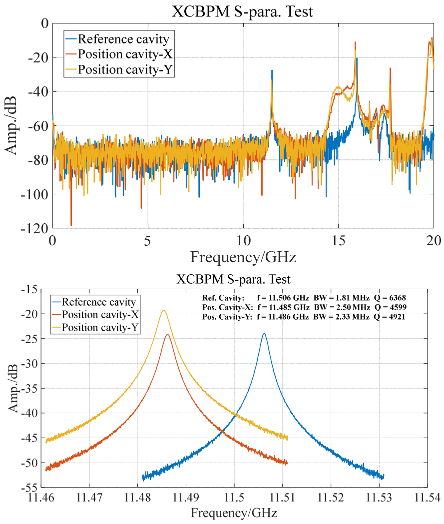

Figure 9: (a) Frequency response of X-CBPM (span=20 GHz); (b) Frequency response of X-CBPM (span=50 MHz).

Table 3: Final Cold Test Results of X-CBPM

Parameters	**Ref.**	**Pos-X**	**Pos-Y**
Frequency/GHz	11.506	11.485	11.486
Decay time constant/ns	176	127	138
Qload	6368	4599	4921
Bandwidth/MHz	1.81	2.5	2.3
XY crosstalk/dB	~	-44	

CONCLUSION

An X band cavity BPM prototype has been successfully developed. The results of multiple tests show good suppression of these unexpected modes so that there is no significant interference on the measurement of the dipole mode. An important experience is that reducing the cavity gap can help obtain effective cold test results before welding.

Plans are being made to construct two additional X-CBPM and test them in SXFEL as soon as possible. The important resolution can be obtained under beam conditions in the near future.

REFERENCES

[1] Feng. C. and Deng. H., “Review of fully coherent free-electron lasers”, *Nucl. Sci. Tech.*, vol. 29, p. 160, 2018. `doi:10.1007/s41365-018-0490-1`

[2] Z. Zhu, Z. T. Zhao, D. Wang, Z. H. Yang, and L. Yin, “SCLF: An 8-GeV CW SCRF Linac-Based X-Ray FEL Facility in Shanghai”, in *Proc. 38th Int. Free Electron Laser Conf. (FEL'17)*, Santa Fe, NM, USA, Aug. 2017, pp. 182-184. `doi:10.18429/JACoW-FEL2017-MOP055`

[3] S. S. Cao, R. Jiang, Y. B. Leng, and R. X. Yuan, “Design and Test of CBPM Prototypes for SHINE”, in *Proc. 9th Int. Beam Instrumentation Conf. (IBIC'20)*, Santos, Brazil, Sep. 2020, pp. 124-127. `doi:10.18429/JACoW-IBIC2020-WEPP13`

ISBN: 978-3-95450-230-1 ISSN: 2673-5350 doi:10.18429/JACoW-IBIC2021-MOPP13

DESIGN OF SUPPORT FOR BPM DISPLACEMENT MEASUREMENT SYSTEM FOR HALF AND EPICS CONNECTION*

C. H. Wang, T. Y. Zhou, L. L. Tang, P. Lu, B. G. Sun†
NSRL, University of Science and Technology of China, Hefei, Anhui, China

Abstract

The beam orbit stability is an important parameter to measure the stability of the synchrotron radiation source. As for the fourth-generation storage ring, the emittance and beam size continue to decrease and higher requirements are being put forward for beam orbit stability. There are two main factors that affect the stability of the beam orbit. One is the vibration of the ground and other systems, which requires highly mechanically stable support. The other is due to synchrotron radiation and changes in ambient temperature, which lead to the expansion and deformation of the vacuum chamber, causing BPM movement and misjudging the position of the beam orbit. The misjudging will introduce errors in the orbit feedback system and decrease the stability of the beam orbit. Therefore, a set of offline BPM (beam position monitor) displacement measurement system with high stability was built. However, considering the adverse effect of the INVAR36 on magnetic field and the drift of the displacement data [1], we added carbon fiber to the new support for BPM displacement measurement probes. Besides we realized the function of real-time reading BPM displacement data through EPICS. This article mainly introduces the support design and EPICS connection of the BPM displacement measurement system.

INTRODUCTION

The Hefei Advanced Light Facility (HALF), a fourth-generation diffraction-limited storage ring, has completed pre-research. For the fourth-generation storage ring, ultra-high beam orbit stability is essential. The beam orbit stability is generally required to be less than 10% of the beam size, and near the insert device, it's usually required to be less than 5% of the beam size [2]. For HALF, the minimum beam size in the horizontal and vertical directions is 5 µm and 2 µm, which means the stability of the beam orbit should be less than 500 nm in the horizontal direction and 200 nm in the vertical direction. In order to meet the stability of beam orbit, a high-precision, a high-precision displacement measurement system and a high stable support for the high-precision probe are needed. The vibration amplitude of the support is also expected to be less than 50 nm and 20 nm in the horizontal and vertical directions.

We choose CapaNCDT6200 series from Micro Epsilon to measure the displacement of BPMs. The CapaNCDT-6200 has a measuring range of 1 mm, a static resolution of 0.75 nm and a dynamic resolution of 20 nm.

DESIGN

A single-sided INVAR36 support has already been processed before. The data drift in the one-sided measurement of BPM displacement, as it is shown in Fig. 1. It is difficult to know whether the data drift is due to the movement of the BPM, the movement of the support or the thermal expansion of the BPM, so a new support was designed. We plan to measure the movement of BPM from both sides at the same time and change the material. The upper part is carbon fiber composite and the lower part still uses INVAR36 alloy. Based on these, the support is designed.

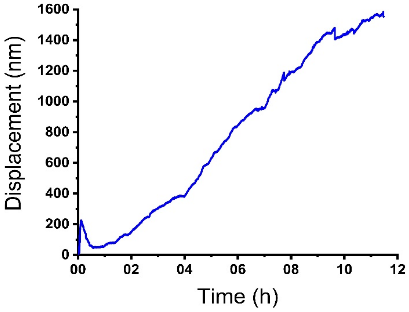

Figure 1: Data drift measured in the one-sided measurement of BPM displacement.

Analysis of Vibration Model

The support system can be simplified to the model [3] shown in Fig. 2, where k represents for stiffness and c represents for damping coefficient.

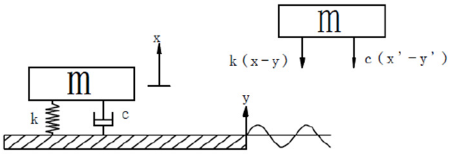

Figure 2: Vibration model.

The relationship between eigen-frequency ω_n and the support vibration amplitude X at the base vibration with amplitude Y and frequency ω can be expressed in Eq. (1) and shown in Fig. 3:

$$\beta = \frac{X}{Y} = \sqrt{\frac{1+\left(2\varsigma\frac{\omega}{\omega_n}\right)^2}{\left[1-\left(\frac{\omega}{\omega_n}\right)^2\right]^2+\left[2\varsigma\frac{\omega}{\omega_n}\right]^2}} \tag{1}$$

where $\varsigma = c/2\sqrt{km}$ represents for damping ratio and $\omega_n = \sqrt{k/m}$ represents for eigen-frequency, $\beta = X/Y$ represents for the vibration amplitude amplification factor of the support.

---

* Work supported by National Natural Science Foundation of China (Grant No. 12005223, 12075236) and the Fundamental Research Funds for the Central Universities (WK2310000080)

† bgsun@ustc.edu.cn

The underlying assumption is that the eigen-frequency ω_n is higher than the base vibration frequency ω. As shown in Fig. 3, a higher ω_n will get a smaller support vibration amplitude X.

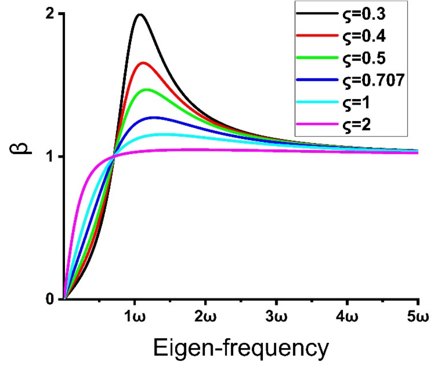

Figure 3: Relationship between amplification factor and eigen-frequency.

Design Requirement

The main considerations of the support designs are the size, the fixed method and the eigen-frequency.

The support of the BPM displacement measurement probe needs to be 400 mm in height and the longitudinal length is no more than 100 mm. And it needs a whole to fix the measuring probe with a diameter of 10 mm and a height of 21 mm.

The support needs to be fixed on the same platform as that of HALF. It is fixed on the platform with four screws, which will reduce the eigen-frequency of the support to a certain extent.

As it shown in Fig. 3, the eigen-frequency should be designed as high as we can. Figure 4 shows the vertical and horizontal PSD (power spectral density) of the platform vibration. The vibration can be divided into natural vibration and cultural vibration. The PSD of natural vibration is approximately proportional to $1/f^4$ and the cultural vibration mainly concentrated within 50 Hz [4]. From the perspective of resonance, the eigenfrequency if the design should also be as high as possible to avoid the peaks in the PSD.

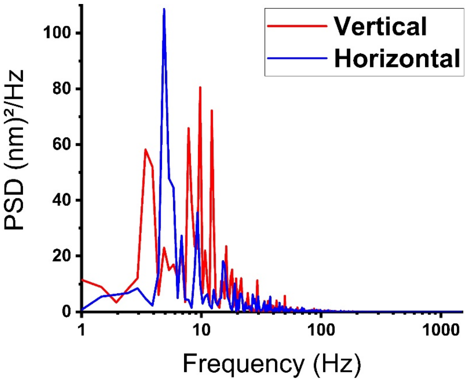

Figure 4: The vertical and horizontal PSD of the platform.

FEA and Optimization

According to the design requirements, the initial model of the support is shown in Fig. 5. Then the parameters of the support are optimized through FEA (finite element analysis). Finally, a size suitable for processing is selected near the optimal solution.

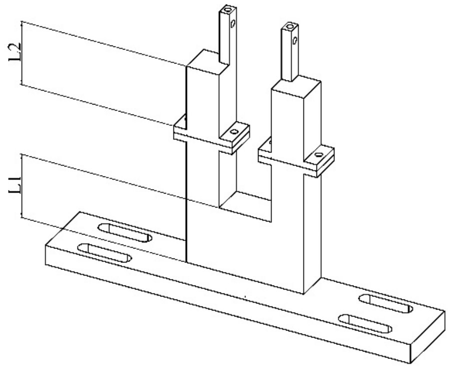

Figure 5: The initial model of the support.

In order to increase the eigen-frequency, the size of the carbon fiber composite and the size of invar36 alloy are optimized. The sizes of L1, L2 are changed continuously and obtain the corresponding eigen-frequency through FEA. Figure 6 shows the relationship between the eigen-frequency and L1, L2.

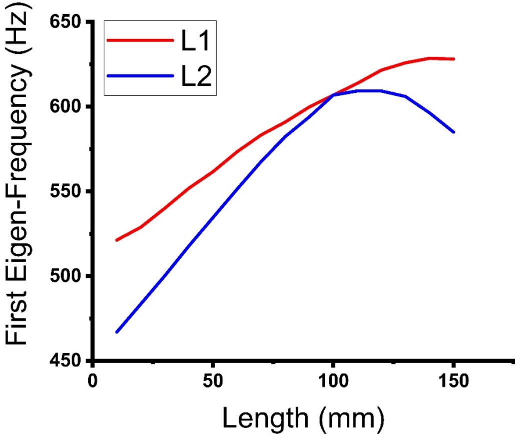

Figure 6: the relationship between the eigen-frequency and L1, L2.

The length of L1 determines the fixed difficulty. The longer L1 is, the harder the support is fixed. Although the first eigen-frequency increases with L1, we still choose L1 as 100 mm instead of 110 mm. There is little difference in the first eigen-frequency, when L2 is 100 mm or 110 mm. Considering the difficulty of carbon fiber processing, we also choose L2 as 100 mm.

Finally, considering the difficulty of processing, we choose the value of L1, L2 to be 100 mm and 100 mm. The simulation results of the first longitudinal and horizontal eigen-frequency are

$$f_{1z} = 606.81\,Hz, f_{1x} = 791.78\,Hz.$$

The z-direction is the longitudinal direction and the x-direction is the horizontal direction.

MEASUREMENT

In the process of testing, the constrained mode of the eigen-frequency and the vibration of the support are measured on the same platform as that of HALF.

Eigen-frequency by Hammer Method

A force hammer is used to hit the support. The frequency response curve is calculated by collecting the force of the hammer and the acceleration at the top of the support and then the eigen-frequency is obtained. Figure 7 is the horizontal and longitudinal frequency response of the constrained mode, which shows the first eigen-frequency in the longitudinal and horizontal directions are $f_{1z} = 252.9\ Hz$ and $f_{1x} = 470.7\ Hz$.

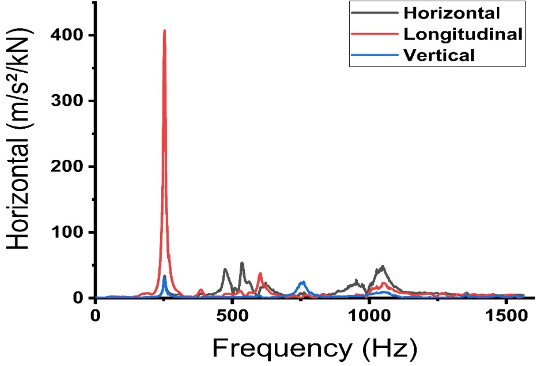

Figure 7: The horizontal and longitudinal frequency response of the constrained mode.

The difference between the simulation results and the measurement results is due to the fixing method of the carbon fiber and INVAR36 and the difference in the parameters between the ideal carbon fiber and the commercially available carbon fiber.

Vibration Measurement of the Support

Two voltage displacement sensors are used to measure the vibration on the support and the platform at the same time [5]. The RMS vibration amplitude on the support and the platform are listed in Table 1. The horizontal and vertical RMS vibrations on the top of the support were measured at 13.09 nm and 13.56 nm resulting in the amplification factors of 1.047 and 1.030.

Table 1: RMS of Vibration Amplitude on the Top and the Platform

Vibration amplitude RMS	Horizontal	Vertical
Top	13.09nm	13.56 nm
Platform	12.50 nm	13.16 nm
Target	50 nm	20nm
Amplification Factor	1.047	1.030

Measurement of the BPM Displacement

The BPM displacement is measured by CapaNCDT6200. Two probes are used to measure the displacement from both sides of the BPM. With reference to the vibration of the support measured above, the movement and the expansion of the BPM can be analyzed from the displacement data. The BPM displacement data measured by two probes is show in Fig. 8.

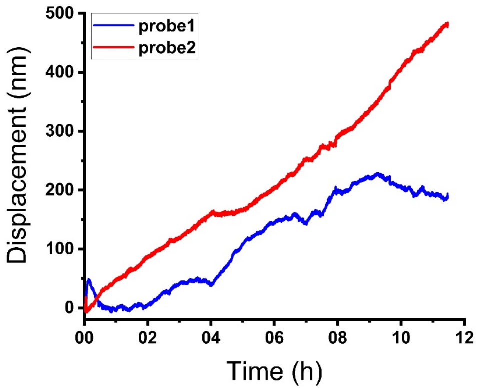

Figure 8: The displacement of BPM.

In Fig. 8, the curves moving in the same direction is due to the BPM thermal expansion and the two lines moving in the opposite direction is due to the BPM movement.

EPICS CONNECTION

In order to correct the error of the beam position induced by the movement of the vacuum chamber and the BPM, it is necessary to upload the BPM displacement data to the EPICS system in real time.

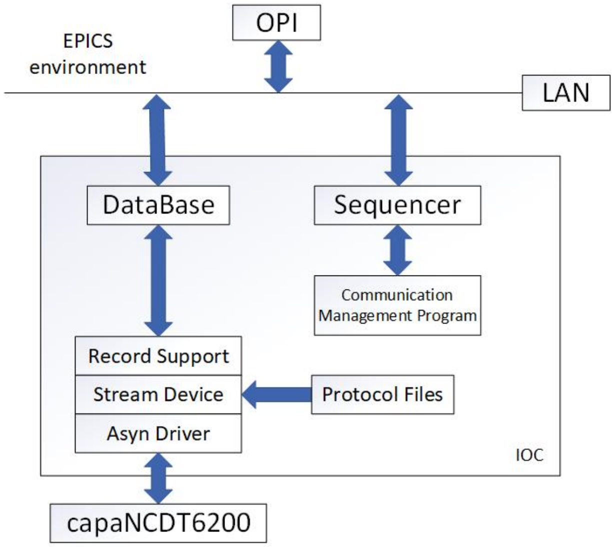

Figure 9: The EPICS architecture.

IOC mainly consists of run-time database, device driver and sequencer. The run-time database consists of all kinds of records. The device driver can be divided into three layers: record support, driver support and device support. StreamDevice is used as device support, and Asyn is used as driver support [6]. The EPICS support module [7] for capaNCDT6200 on GitHub is used to transfer data to EPICS. Figure 9 shows the EPICS architecture for the data transfer between the BPM displacement measurement system and OPI.

When the IOC is started, the BPM displacement data is read through the serial port, packaged into EPICS record and released to the local area network. The data can be obtained by accessing PV name through OPI. The data obtained by PV is shown in the Fig. 10, and the unit of these data is μm.

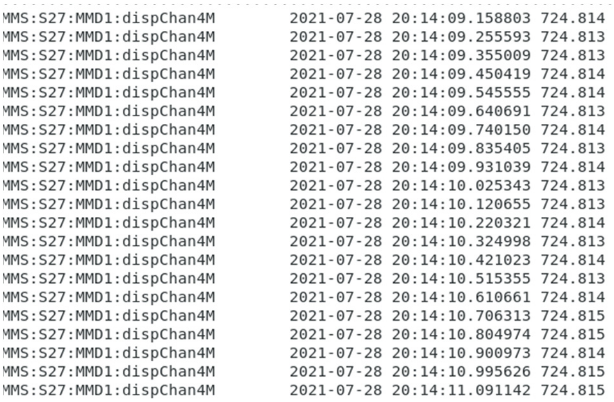

```
MMS:S27:MMD1:dispChan4M        2021-07-28 20:14:09.158803 724.814
MMS:S27:MMD1:dispChan4M        2021-07-28 20:14:09.255593 724.813
MMS:S27:MMD1:dispChan4M        2021-07-28 20:14:09.355009 724.813
MMS:S27:MMD1:dispChan4M        2021-07-28 20:14:09.450419 724.814
MMS:S27:MMD1:dispChan4M        2021-07-28 20:14:09.545555 724.814
MMS:S27:MMD1:dispChan4M        2021-07-28 20:14:09.640691 724.813
MMS:S27:MMD1:dispChan4M        2021-07-28 20:14:09.740150 724.814
MMS:S27:MMD1:dispChan4M        2021-07-28 20:14:09.835405 724.813
MMS:S27:MMD1:dispChan4M        2021-07-28 20:14:09.931039 724.814
MMS:S27:MMD1:dispChan4M        2021-07-28 20:14:10.025343 724.813
MMS:S27:MMD1:dispChan4M        2021-07-28 20:14:10.120655 724.813
MMS:S27:MMD1:dispChan4M        2021-07-28 20:14:10.220321 724.814
MMS:S27:MMD1:dispChan4M        2021-07-28 20:14:10.324998 724.813
MMS:S27:MMD1:dispChan4M        2021-07-28 20:14:10.421023 724.814
MMS:S27:MMD1:dispChan4M        2021-07-28 20:14:10.515355 724.813
MMS:S27:MMD1:dispChan4M        2021-07-28 20:14:10.610661 724.814
MMS:S27:MMD1:dispChan4M        2021-07-28 20:14:10.706313 724.815
MMS:S27:MMD1:dispChan4M        2021-07-28 20:14:10.804974 724.815
MMS:S27:MMD1:dispChan4M        2021-07-28 20:14:10.900973 724.814
MMS:S27:MMD1:dispChan4M        2021-07-28 20:14:10.995626 724.815
MMS:S27:MMD1:dispChan4M        2021-07-28 20:14:11.091142 724.815
```

Figure 10: Data obtained by PV disChan4M.

CONCLUSION

The new support has a high first eigen-frequency in the horizontal and longitudinal directions of 252.9 Hz and 470.7 Hz. The horizontal and vertical RMS vibration amplitude of the support are 13.09 nm and 13.56 nm, which meet requirements for beam orbit stability. The new support realizes the function of measuring the displacement from both sides, which explains the reason for the drift of BPM displacement data. In addition, the data transfer between the BPM displacement measurement system and EPICS is also realized, which is necessary for further realization of BPM data correction.

REFERENCE

[1] B. Kosciuk *et al.*, "Development and Testing of Carbon Fiber Vacuum Chamber Supports for NSLS-II", in *Proc. 24th Particle Accelerator Conf. (PAC'11)*, New York, NY, USA, Mar.-Apr. 2011, paper TUP286, pp. 1364-1366.

[2] R. Bartolini, H. C. Huang, J. Kay, and I. P. S. Martin, "Analysis of Beam Orbit Stability and Ground Vibrations at the Diamond Storage Ring", in *Proc. 11th European Particle Accelerator Conf. (EPAC'08)*, Genoa, Italy, Jun. 2008, paper WEPC002, pp. 1980-1982.

[3] W. T. Thomson and M. D. Dahleh, *Theory of vibration with applications*, Upper Saddle River, New Jersey, USA: Prentice Hall, 1998.

[4] Z. Z. Wang, J. S. Cao, J. He, H. Z. Ma, Y. F. Sui, and Z. Wang, "Study on Supports System of BPMs for HEPs", in *Proc. 8th Int. Particle Accelerator Conf. (IPAC'17)*, Copenhagen, Denmark, May 2017, pp. 322-324. `doi:10.18429/JACoW-IPAC2017-MOPAB087`

[5] A. X. Wang *et al.*, "Structural optimization design for beam position monitor support of High Energy Photon Source", *High Power Laser and Particle Beams*, vol. 33, pp. 044006-1-044006-9, 2021. `doi:10.11884/HPLPB202133.200297`

[6] S. Xu, G. Liu, Y. Song, and X. K. Sun, "Control System Design for Front End Devices of IRFEL", in *Proc. 9th Int. Particle Accelerator Conf. (IPAC'18)*, Vancouver, Canada, Apr.-May 2018, pp. 4920-4922. `doi:10.18429/JACoW-IPAC2018-THPML109`

[7] GitHub, `https://github.com/epics-modules/microEpsilon`

ISBN: 978-3-95450-230-1 ISSN: 2673-5350 doi:10.18429/JACoW-IBIC2021-MOPP14

PRECISE SINGLE BUNCH MEASUREMENTS USING FAST RF SWITCHES*

W. Cheng[#], A. Brill, Argonne National Laboratory, Lemont, IL 60439, USA

Abstract

To measure the swap-out injection/extraction bunches of the Advanced Photon Source Upgrade (APS-U) storage ring, single-pass Beam Position Monitor (BPM) electronics will be installed in the first sectors after the injection with fast RF switches. The fast RF switch will select a bunch signal to be processed by the single pass BPM electronics, and have the remaining bunches processed by the regular BPM electronics. In addition to measuring the swap-out bunch during injection, the setup will be able to carry out various other measurements of any selected single bunch (or bunches). This paper presents the performance of the fast RF switches and related electronics.

INTRODUCTION

APS-U is an ultimate low emittance storage ring [1] that is being constructed at Argonne National Laboratory. The machine has small dynamic aperture, hence swap-out injection will be used. It is of great interest to measure one selected bunch (like the swap-out bunch) during machine studies and operation. Precise 1-bunch measurement of the X/Y positions (and sum signals) in turn-by-turn (TBT) rate will supply important information to machine physicists. For example, it will make sure the swap-out bunch get pre-kicked; it allows single-turn trajectory measurement during the injection/extraction period; and it will be able to confirm that a fresh bunch is captured with a desired intensity.

Modern BPM electronics typically use 125 MHz, 16-bit ADC digitizers. There are band-pass filters (BPF) implemented in the analog front end to select button BPM signal around the RF frequency (or at its harmonics). For example, APS-U storage ring will be equipped with such BPM electronics [1], with +/-10 MHz BPF and ADC sampling at 108 MHz (revolution frequency × 398). Due to the BPF, the single bunch signal will be stretched to ~300 ns, making single-bunch position measurement impossible if the bunch-to-bunch spacing is less than that. For the APS-U machine, the bunch spacing will be either 11.4 ns (324-bunch mode) or 76.7 ns (48-bunch mode), both are small enough so that regular BPM electronics will not be able to measure individual bunches.

Wider band digitizers allow bunch-by-bunch (BxB) measurements. These new digitizers have been tested at various machines [2-4]. However, due to its wider bandwidth, there are limitations of the BxB position measurements:

- The BxB resolution is worse due to the wider bandwidth, and the ADC digitizer will have less resolution (8 to 12-bit for a broadband ADC vs. 16-bit for a regular BPM electronics).
- The number of turns that can be saved is limited.
- It is more difficult to process and stream out the data.
- The measurement may be sensitive to clock jitter, bunch lengths and synchronous phases, and depends on the algorithm to process the BxB positions.

As in many cases, it is good enough to measure one selected bunch at the TBT rate. Fast RF switches have been proposed to select the 1-bunch signals before sending them to regular BPM processing electronics. It has been demonstrated that the regular BPM electronics have very good single bunch TBT position resolution. The single-bunch BPM electronics setup is illustrated in Fig. 1. At each selected BPM pickup location, the four button signals (namely A/B/C/D) pass through a fast RF switch box. The fast RF switch will choose a single-bunch signal for the single pass BPM electronics, and the remaining bunch signals continue feed to the regular BPM electronics (Libera Brilliance+ or LB+). The fast RF switch unit (gray box on the left which includes four switch boxes; and a dedicated Spark BPM electronics (gray box on the bottom right) select and measure the one-bunch TBT positions/sum. The blue line box shows the regular LB+ electronics which measures the position of all bunches except one.

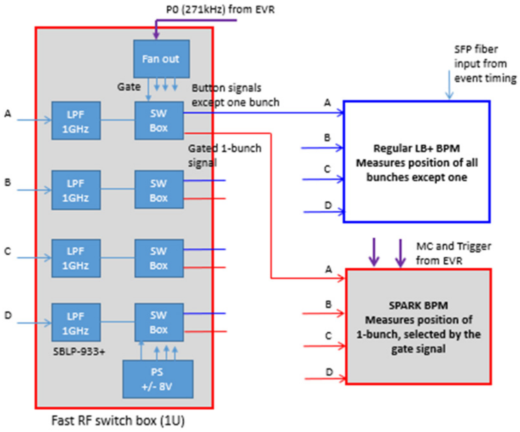

Figure 1: Schematic setup of the single pass BPM.

There will be about 20 BPMs (selected in the first three sectors right after injection) in the APS-U storage ring to be equipped with the single bunch TBT BPM electronics. Using these BPMs, the injected bunch phase space can be measured [5, 6]. Additionally, TBT position and sum signals from these BPMs will be useful to track the swap-out bucket for the pre-kick, extraction, and injection process. The idea of fast RF switches to select 1-bunch signal has been implemented in KEK's ATF and SuperKEKB [7, 8]. We report the procurement status and

---

*Work supported by DOE contract No: DE-AC02-06CH11357
[#] wcheng@anl.gov

beam test results of the RF switches, the single-pass BPM electronics (Libera Spark) and regular LB+ BPM electronics.

PRODUCTION STATUS

There are 560 LB+ BPM electronics ordered. All of these regular BPMs have been received, see details of the production status and performance at [9].

The fast RF switches and single pass BPM electronics (Libera Spark) had contract awards in April 2021. First article units have been received and tested in June/July. Production units are expected to be delivered in October 2021.

The fast RF switch first article units have been tested on the bench to characterize the input/output port VSWR, insertion loss, isolation, and switching noise. Figure 2 gives example of the measured insertion losses from the input port to the two outputs (input -> out1 which will be connected to LB+ with RF switch in "off" state; input -> out2 which will be connected to Spark with RF switch in "on" state). It's worth mentioning that there are Mini-circuits SBLP-933+ [10] low pass filters (LPF) added in front of the switch input port. The LPF is used to filter out the high frequency beam signals, and it may contribute part to the insertion losses especially for high frequencies. VSWR of the input port is affected by the LPF as well.

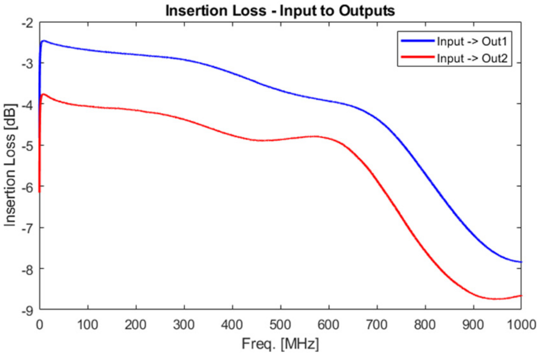

Figure 2: Typical measured insertion losses of the RF switches. At 352 MHz where the BPM electronics operate, the insertion losses are 3.07 dB and 4.58 dB, respectively.

A typical time domain response of the RF switches is shown in Fig. 3, where Ch1 is the gate signal with 10 ns width; the input 352 MHz signal was switched to out2 (Ch3) when the gate is on (-0.8 V) and out1 (Ch2) when the gate is off (0 V). The RF switches work well down to a width of 4-6 ns, which is well below the minimum bunch spacing of 11.4 ns. The RF switching noise was measured to be several mV with no input signal. The switching noise is much smaller than the typical beam induced signals.

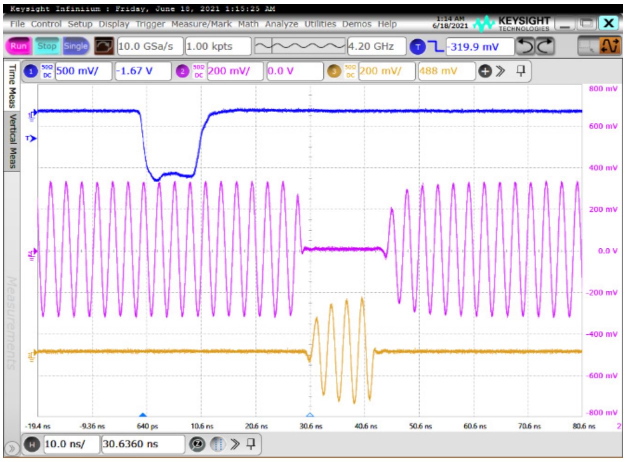

Figure 3: Typical response of the RF switches in time domain. 352 MHz CW signal was connected to the input port at 1 Vpp (+4 dBm). Ch1 (blue) – gate signal applied to the switches, 10 ns width; Ch2 (magenta) – out1 of the switch, this is the output signal outside of the gate; Ch3 (orange) – out2 of the switch, this is the output signal within the 10 ns gate.

Like the LB+, the received Spark electronics have been tested in the lab with good performance. Single bunch measurement resolution is more relevant for this application as the Spark electronics will normally measure 1-bunch signal. See the next section of beam measurement results at the APS storage ring.

APS BEAM TESTS

Beam Test Setup

The fast RF switch and Spark units, together with the LB+ electronics, have been installed in the APS machine for studies and parasitic monitoring during APS user operations. A dedicated BPM four-button signals were connected to the fast RF switches as shown in Fig. 1, the outputs of the switches fed to Spark and LB+ respectively. Timing signals have also been prepared to properly select the bunches. Figure 4 is a picture of the electronics installed at S27.

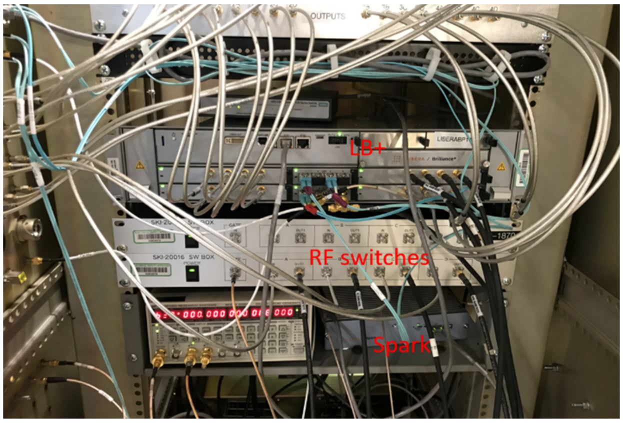

Figure 4: Beam test setup at S27 of the APS machine.

Existing APS button BPM signals were used (S27A:P3) for the beam tests. As compared to the APS-U button, the APS BPM has larger button sizes and transverse chamber profile. The button signals have been compared to be similar. With the same bunch lengths, button capacitance and beam current, the signal at 352 MHz (RF frequency) differs by ~0.7 dB. This means the measured results from the existing A:P3 BPM signals will be valid for the future APS-U BPM.

During regular 24-bunch, 102 mA APS top-up user operation, one bunch signal can be selected by the RF switches. As shown in Fig. 5, one of the 24 bunches (Ch3, orange) was gated out to be sent to the Spark BPM. The other 23-bunch signals (Ch2, magenta) were connected to LB+. A 10 ns gate width was used (Ch1, blue), and the delay was adjusted to select any of the 24 bunches. There was a 20 dB attenuator pad added at the RF switch input.

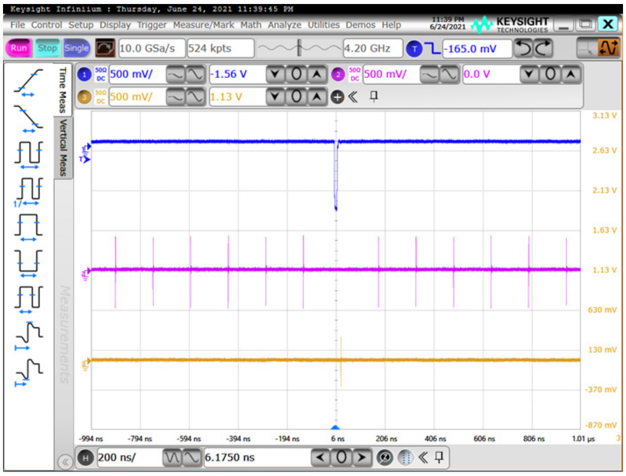

Figure 5: Button BPM signals of the fast RF switch output. The gate input (blue) is configured to select the signal from a single bunch (orange) to send to the single-bunch Spark BPM. The remaining 23 bunches (magenta) are measured by the standard LB+ BPM.

Single Bunch TBT Resolution

The Spark BPM TBT resolution has been measured at various single bunch currents. The results are plotted in Fig. 6. There were two Spark electronics connecting to S27A:P2 and S27A:P3 signals respectively. The Libera Spark electronics process the TBT data in DDC (Digital Down Convert) mode or TDP (Time Domain Process) mode, TDP mode gives better resolution for single bunch fill. With stored beam current above 1mA, the typical TBT resolution was measured to be around 1 um. The front-end attenuator was set to 0 dB for low currents (<1 mA) and adjusted for higher currents to avoid ADC saturation. It was not tested during the study, but the TBT resolution is expected to be further improved with proper mask.

Adding the RF switches will decrease the signal level 3-4 dB, as shown in Fig. 2. The single bunch TBT resolution was measured with the RF switches to be ~1 µm resolution with roughly 1 mA stored beam. The switching noise affects the TBT resolution at very low current (<0.2 mA), but the resolution is still well below the 30 µm specification.

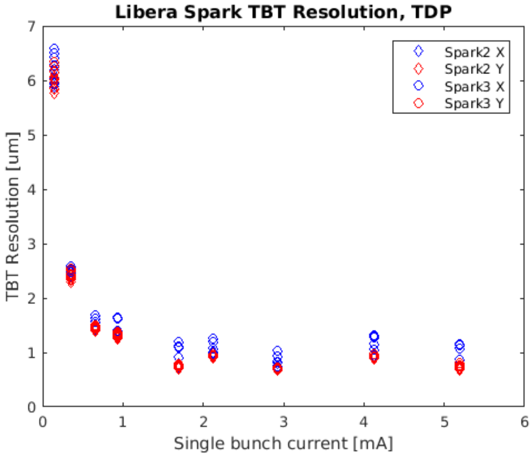

Figure 6: Libera Spark TBT resolution (in TDP mode), at various single bunch currents.

First-turn injected bunch resolution has been measured as well. With ~1 nC charge, the first turn position had RMS jitter of less than 10 µm.

Injection Transients

To further test the TBT dynamics measurements during injection, the RF switches and single bunch Spark electronics have been used to monitor APS top-up injections. One bunch signal was gated out by the RF switch and fed to the Spark, while the remaining 23-bunch signal was connected to the LB+. The gated 1-bunch was at bucket #432.

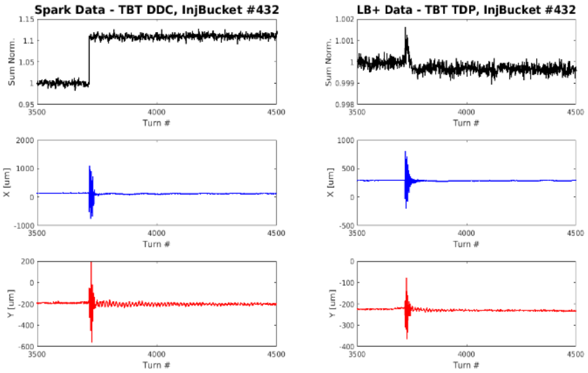

Figure 7: TBT data measured during APS 24-bunch top-up operation. Left side plots are for the gated 1-bunch measured with Spark electronics; right side plots are for the remaining 23 bunches measured by LB+.

Figure 7 shows the TBT sum and positions while the gated 1-bunch got a top-up injection. The bunch charge increased ~10% which is a clear indication that injected charge was captured. The sum signal measured on the remaining 23 bunches did not change, as expected. Both

BPMs see injection transients in the x/y positions. The event trigger occurs ~2700 turns before the injection, and BPM electronics are capable of acquiring TBT waveform data prior or post trigger with user-defined turn offsets. In the particular example, the offsets were set to -1000 turns. That was the reason that the actual injection took place at turn #3700. When injection was made to any of the 23 bunches monitored by the LB+, the sum signal for the LB+ increased and the Spark electronics didn't see any charge accumulation.

What is measured here is similar to the APS-U swap-out injection. The difference is that the APS storage ring uses accumulation injection, and for the future APS-U, the bucket will be totally refreshed with a new injecting bunch. With proper timing adjustments, the RF switches and electronics will be able to monitor the swap-out injection beam dynamics.

Effect on the Regular BPM

While the RF switches select different bunches, the measured positions on the other bunches shall not be affected. This has been checked during the APS 324-bunch operation. By gating a single bunch and adjusting the gate delay to select different bunches, the LB+ (measuring 323 bunches) position variation was less than 0.5 µm peak-to-peak. This included the actual beam drifting during the bunch scan, so the electronics effect is less than that.

SUMMARY

A single bunch TBT measurement system has been proposed and tested for the APS-U storage ring. The system allows precise TBT measurement of a selected bunch and proves to be important for the beam dynamics measurement of the swap-out bunch. This method shall be useful for other machines with similar swap-out injection scheme, or for existing storage rings with accumulating injection. Using commercially available RF switches and BPM electronics, a single bunch TBT resolution of 1 µm can be achieved. Beam tests at the APS machine demonstrate that the system will work well for the APS-U, with either 48-bunch mode or 324-bunch mode.

ACKNOWLEDGMENTS

The author acknowledges Dr. Tobiyama from KEK for fruitful discussion and his generous support by lending the RF switches for earlier evaluation. Support and encouragement from APSU/APS managers are greatly appreciated. Tony Pietryla and Ran Hong helped a lot to get the new APSU MRF timing signals for the test. Nick Sereno helped during the study shift to characterize the TBT resolution and injecting bunch resolution. Discussion with the vendors [11, 12] has been productive.

The work is supported by the U.S. Department of Energy, Office of Science, Office of Basic Energy Sciences, under Contract No. DE-AC02-06CH11357.

REFERENCES

[1] "Advanced Photon Source Upgrade Project – Final Design Report", APSU-2.01-RPT-003, May 2019.

[2] D. Padrazo *et. al.*, "Next Generation RF BPM Development at NSLS-II", presentation at the Next Generation Beam Position Acquisition and Feedback Systems Workshop, Nov 12-14, 2018.

[3] Z. C. Chen and Y. B. Leng, "Bunch-by-Bunch Study of the Transient State of Injection at the SSRF", in *Proc. 4th Int. Beam Instrumentation Conf. (IBIC'15)*, Melbourne, Australia, Sep. 2015, pp. 396-398. `doi:10.18429/JACoW-IBIC2015-TUPB035`

[4] Y. Yang, Y. B. Leng, Y. B. Yan, and N. Zhang, "Bunch-by-bunch Beam Position and Charge Monitor based on Broadband Scope in SSRF", in *Proc. 4th Int. Particle Accelerator Conf. (IPAC'13)*, Shanghai, China, May 2013, paper MOPME054, pp. 595-597.

[5] M. Borland, "Diagnostics for monitoring the APS-U swap-out process", Argonne Internal Technote AOP-TN-2019-066, 2019.

[6] M. Borland, "Determining APS-U injection coordinates using first-turn BPM", Argonne Internal Technote AOP-TN-2020-014, 2020.

[7] M. Tobiyama, H. Fukuma, H. Ishii, and K. Mori, "Development of Gated Turn-by-Turn Position Monitor System for the Optics Measurement During Collision of SuperKEKB", in *Proc. 2nd Int. Beam Instrumentation Conf. (IBIC'13)*, Oxford, UK, Sep. 2013, paper MOPF32, pp. 295-298.

[8] T. Naito *et al.*, "BEAM OSCILLATION MONITOR FOR THE MULTI-BUNCH BEAM", in *Proc. 4th Int. Particle Accelerator Conf. (IPAC'13)*, Shanghai, China, May 2013, paper MOPME018, pp. 506-508.

[9] J. Carwardine, "Upgraded Libera Brilliance+ instruments for the 560 beam position monitors of the APS Upgrade storage ring", Online Libera Workshop, 2021.

[10] `https://www.minicircuits.com/pdfs/SBLP-933+.pdf`

[11] `https://www.i-tech.si/`.

[12] `https://www.sf-elecoms.com/`.

WIRE TEST OF LARGE TYPE BPM FOR P2DT IN RAON

J. W. Kwon†, Y. S. Chung, G. D. Kim, H. J. Woo, E. H. Lim[1]
Institute for Basic Science, Daejeon 34000, Korea
[1]also at Department of Accelerator Science, Korea University, Sejong, 30019, Korea

Abstract

RAON (Rare isotope accelerator complex for On-line experiments) is accelerator to accelerate heavy ion such as uranium, oxygen, and proton. At P2DT(Post to Driver linac Transport line) section where is located between SCL3 and SCL2, particle beam would be higher charge state by stripper. In bending area in P2DT, BPM(Beam Position Monitor) should accept the beam that has large size (~10 cm) horizontally. Required BPM transverse position resolution is 150 μm. We simulated Large type BPM with CST particle studio. Fabricated LBPM was tested on the developed wire test bench that could move BPM for width of ±80 mm, height of ±40 mm with manual steering knob.

INTRODUCTION

Rare isotope Accelerator complex for ON-line experiments (RAON) include of superconducting linear accelerators, which comprise superconducting linac2 (SCL2) and superconducting linac 3 (SCL3) sections [1]. The extracted beam from ECR ion source of injector will be accelerated and transferred from SCL3 to SCL2 through P2DT section. The layout of the post linac to driver linac transport (P2DT) section of RAON is depicted in Fig.1. In the P2DT section, the charge state of the beam is changed to a higher charge state by charge stripper using carbon foil, and only the beam of a specific charge is transmitted by the Charge Selector. The beam selected by the charge selector is transmitted and accelerated to the experimental area through SCL2.

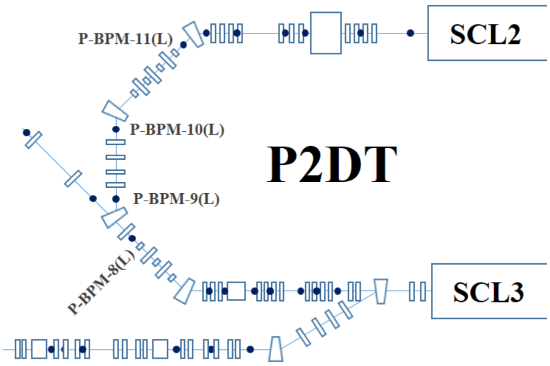

Figure 1: Layout of P2DT section of RAON, there are 4 large type BPMs for only P2DT section.

The P2DT section has four dipole magnets and 2 charge selector, which are used to select the design charge state for acceleration in the SCL2. As the beam passes through the charge stripper, particle beam has higher charge state and charge selector has a role of collimator to pass the beam that has charge state between 77+ and 81+.

In the P2DT region, the energy, and bunch length of a uranium beam are 18.5 MeV/u and 0.3 ns rms, respectively. The designed input beam pulse current of P2DT is 340 μA, and the output beam current is 660 μA

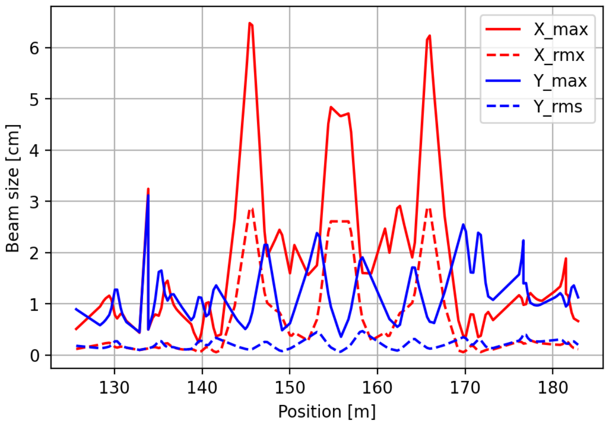

Figure 2: Beam size in P2DT section.

As the particle beam passes through a dipole magnet, the beam size increases horizontally. The increased beam size caused by multi charge state is greater than for single charge state beams. It is caused by different A/Q for same dipole magnetic field.

In the case of a uranium beam, the maximum beam size along the horizontal direction is greater than 6 cm after passing the first dipole magnet as depicted in Fig. 2. Four BPMs will be installed at the bending areas, which are placed between the four dipole magnets. The BPMs are required to accept large-size beams for measuring the positions and phases of the beams. For the bending areas where the BPMs are installed, the BPMs can be damaged because dipole magnet failure. Although MPS(machine protection system) is configured, we fundamentally want to avoid direct damage to the BPM electrode. In case of dipole magnet failure, an accelerating particle beam will hit the BPM electrode. The electrode of BPM has low heat capacity and the only place to dissipate heat is brazed feedthrough.

The required transverse position resolution is 150 μm at 81.25 MHz, that is the fundamental RF frequency and bunch repetition rate of the RAON. The formula of Δ/Σ will be used to calculate the position on the basis of the signal strength of BPM. We prepared an electronic system to calculate the signal strength and phase of all electrodes using the IQ method of 81.25 MHz [2]. BPM pickup signals were simulated using CST Particle Studio [3].

---

† jangwonk@ibs.re.kr

ISBN: 978-3-95450-230-1 ISSN: 2673-5350 doi:10.18429/JACoW-IBIC2021-MOPP15

DESIGN AND FABRICATION OF LARGE TYPE BPM

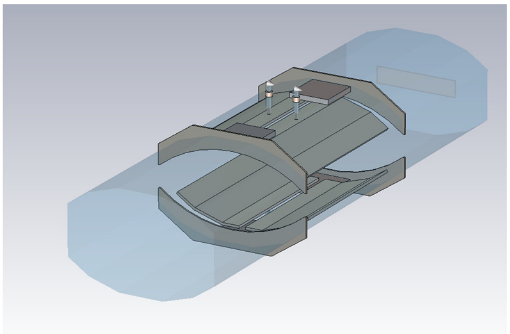

Figure 3: Design of large type BPM for CST simulation.

Two major design issues were considered while designing the BPM. First, the side regions were removed to avoid electrode damage due to machine failure. Second, the electrode plate was configured to have as high a signal strength of 81.25 MHz as possible. In Fig. 3, we depict the design while considering the design issues. A bent electrode shape was chosen to solve the design issues.

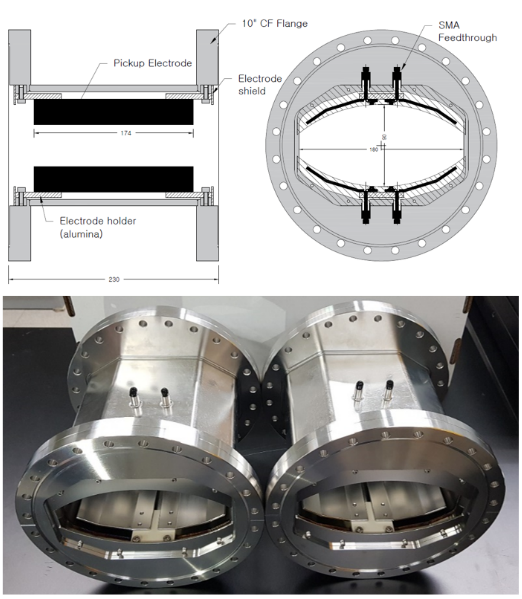

Figure 4: Drawing and fabricated of large type BPM.

The designed BPM has four large electrodes and four small feedthroughs. Ceramic parts are required to support the large plate to avoid overloading in the feedthrough. The fabricated large type BPM is depicted in Fig. 4. The rectangular bent electrode is bolted to special parts that were welded with Kyocera SMA-R feedthrough. The housing, electrode, collimator, and flange were fabricated using 316L stainless steel, which is a non-magnetic material. Alumina ceramic components were assembled to insulate and hold the electrodes.

WIRE TEST OF LARGE TYPE BPM

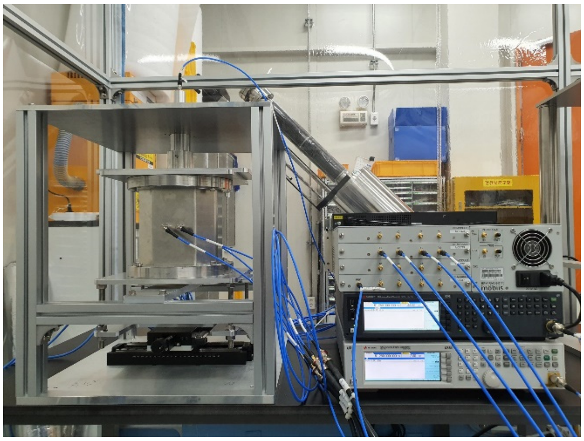

Figure 5: Setting of Wire test bench.

Wire test is a simple way to check the BPM performance without real beam. The developed wire test stand includes a stretched wire that can be installed through the BPM and a movable bench for 2D planes, as shown in Fig. 5. The wire test bench has the 2 movable stage for X and Y axis and it could move BPM for width of ±80 mm, height of ±40 mm with manual steering knob. The minimum scale of the stage is 20 µm and 10 µm in the X and Y directions, respectively. The input signal on the wire is set to measure the signal strength at the feedthrough of the BPM, which corresponds to a current of 300 µA. The case of a beam passing through the center of the beam pipe was simulated using the CST particle studio, and the component of 81.25 MHz was calculated as a value of -32dBm.

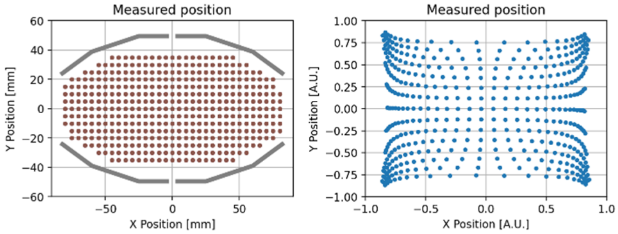

Figure 6: Measured position, (a)left : red dots show real wire positions, grey line show electrode plate (b)right : blue dots show measrued positions of BPM electronics.

The wire test was performed on an area that was as wide as possible measurable as shown in Fig. 6(a). The measured position with developed BPM electronics is depicted in Fig. 6(b). The measured position X_0, Y_0 have a value range of ± 1 [4]. Calibration factors is required to correct the position in mm dimension of the actual position. There are few calibration methods for BPM such as 1D linear, 1-D polynomial, 2-D-Polynomial [4]. We choose 1-D 3th polynomial method for large type BPM as express in Eq. (1).

$$X_{measured} = K_1X_0{}^3 + K_2X_0{}^2 + K_3X_0{}^1 + K_4X_0{}^0$$

$$Y_{measured} = L_1Y_0{}^3 + L_2Y_0{}^2 + L_3Y_0{}^1 + L_4Y_0{}^0 \tag{1}$$

Calibration factors were obtained from 1-D polynomial fit with measured position results on X, Y axis. After considering the calibration factors, all the measured data can be found to be meaningful in the position dimension. Fig. 7 shows the position calibrated in mm using the 1D polynomial calibration factors.

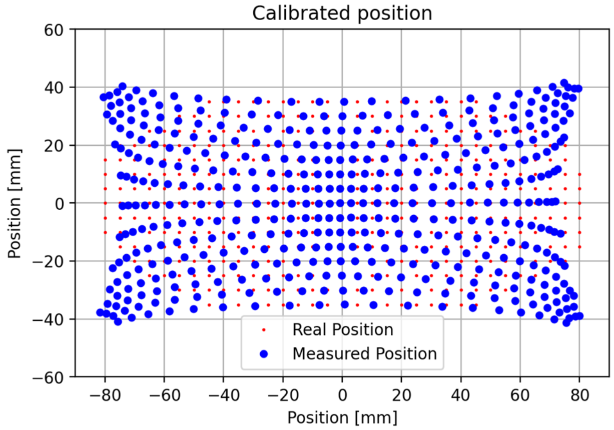

Figure 7: Calibrated position, red dots show real wire position and blue dots show calibrated position.

Figure 7 shows calibrated position with 1D 3th polynomial method. The farther the measurement position is in the X direction, the more it deviates from the actual position. This is because the closer to the electrode plate, the greater the distortion of the position measurement. And the accuracy, which means the difference in length between the actual position and the corrected position, is shown in Fig. 8. Accuracy is less than 10mm in most areas occupying a large area inside the rhombus-shaped BPM. Closer to the electrode plate, the accuracy values increase up to 30 mm.

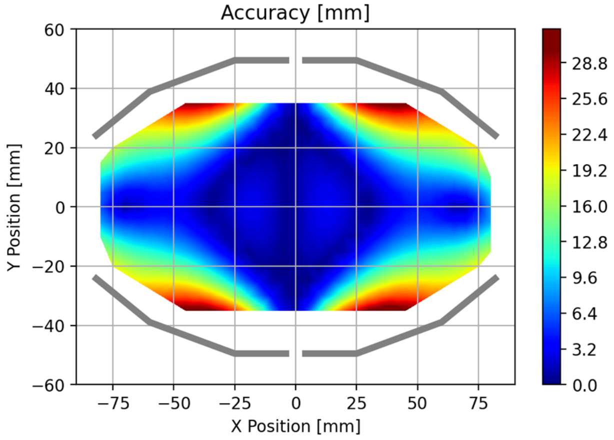

Figure 8: Accuracy in measured area.

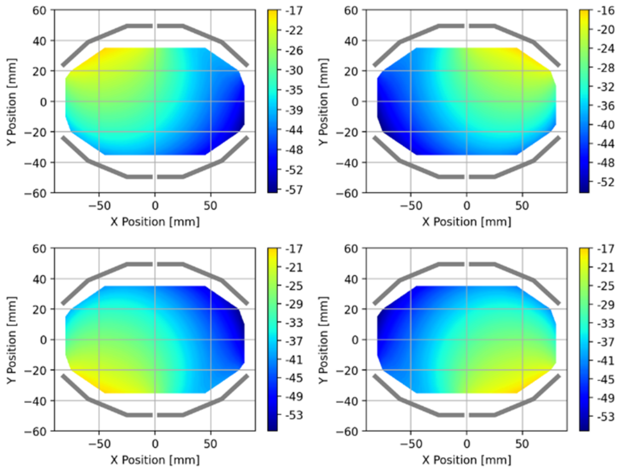

Figure 9: The amplitudes (dBm) of each measured electrode plate. Right-Up: (X-, Y+), Left-Up: (X+, Y+), Right-Down: (X-, Y-), Left-Down: (X+, Y-)

To obtain measured position 4 amplitudes is used from 4 electrode plate. The amplitudes of each measured electrode plate at the position where wire test performed is depicted in Fig. 9. Since the large type BPM has a symmetrical structure, the distribution of the measured signal strength measured on the electrode plate has a symmetrical shape. The amplitude values ranged from approximately -60dBm to -17dBm. Amplitude gain was calibrated prior to performing the BPM wire test. As the wire test results showed that the distorted area was close to the electrode plate, the strength measured near the electrode plate did not differ significantly as the position was changed. In addition, since the electrode has a diagonal direction to represent the X-Y plane, nonlinear measurement results are obtained.

CONCLUSION & DISCUSSION

To correct the beam trajectories, BPM is required to accept a large-size beam for the horizontal axis in the P2DT section. The BPM was designed to cover as much as possible and was fabricated using bent electrode plates of optimal length. We developed a wire test bench with two movable stages, ±40 mm in X direction and ±80 mm in Y direction with manual steering knobs. Fabricated large type BPM was performed at the wire test bench with signal strength for stretched wire corresponding to 300 µA beam current and a narrow beam. Accuracy and signal strength were obtained at each measurement location considering the correction factor obtained from the values measured on the X-axis and Y-axis of the wire test bench. In most areas, the accuracy value was less than 10 mm, and the signal strength of -60dbm to -17dbm was measured at each electrode.

Although large BPM was tested at wire test bench, it can explain in case of very narrow beam. The beam size, current, and charge state vary in the P2DT section during beam operation. There is charge stripper to strip electron from heavy-ion particle. At that time various stripped particle ion is produced and transport to SCL2 through large type

ISBN: 978-3-95450-230-1 ISSN: 2673-5350 doi:10.18429/JACoW-IBIC2021-MOPP15

BPM. To select charge state of particle beam, the beam size would be increased for X axis. Because BPM measures the center of charge, the measured position may change as the stripping efficiency changes. Of course, the calibrated position including calibration factor and real position measurement is differ depending various beam size.

ACKNOWLEDGMENT

This work was supported by the Rare Isotope Science Project of the Institute for Basic Science, funded by the Ministry of Science, ICT, and NRF of Korea (2013M7A1A1075764).

REFERENCE

[1] S. K. Kim *et al.*, ″Rare Isotope Science Project: Baseline Design Summary”, Institute for Basic Science, Daejeon, Korea, 2012.

[2] J. W. Kwon, H. J. Woo, G. D. Kim, Y. S. Chung, E.-S. Kim, “Beam position monitor for superconducting post-linac in RAON”, *Nucl. Instrum. Methods Phys. Res. A,* vol. 908, pp. 136-142, 2018.

[*3*] Computer simulation technology, `https://www.cst.com/`.

[4] J. W. Kwon, “Development of Beam Position Monitor system for RAON heavy ion accelerator”, Ph.D. Thesis, Korea University, Korea, 2020.

CURRENT STATUS OF ELETTRA 2.0 eBPM SYSTEM

G. Brajnik*, R. De Monte, Elettra-Sincrotrone Trieste, Trieste, Italy
M. Cargnelutti, P. Leban, P. Paglovec, B. Repič, Instrumentation Technologies, Solkan, Slovenia

Abstract

In the last years, there has been a growing interest in using the pilot-tone technique for long-term stabilization of electron beam position monitors in synchrotrons. At Elettra, after an internal development, the effectiveness of this approach was proven with tests in the laboratory and on the storage ring. The pilot-tone scheme will be adopted for the eBPMs that will equip Elettra 2.0, the low-emittance upgrade of the present machine. In order to support the development, industrialisation and production of the overall system, a partnership with Instrumentation Technologies has been signed. With the extensive experience with the Libera instruments, the company will be engaged in improving the BPM system developed by Elettra and getting it ready for serial production. This paper presents the current status of the BPM system, with an emphasis on the efforts done to improve the key performances of the system and to address its weaknesses (e.g. enhancing single bunch response and low currents sensitivity) within the industrialisation process, with the goal to get to a reliable system, easy to maintain and that meets the multiple project requirements for the new storage ring, the booster, the pre-injector and the transfer lines.

INTRODUCTION

Elettra 2.0 will be the new diffraction limited storage ring that will start serving the users at the end of 2026, replacing the current machine (Elettra). Even if the lattice length will remain more or less the same, the number of beam position monitors (BPMs) will increase to 147 [1]. In order to reduce costs and optimize resources, the same electronics will be used in preinjector, transfer lines, booster and storage ring. Thus, different operation modes are required for a correct behaviour: single pass (first turn) mode, gated mode, close orbit mode.

As a consequence of the excellent results obtained during the development of the overall prototype [2], the machine will be equipped with BPM controlled by electronics based on pilot tone. A modular approach was chosen, with analog front ends detached from the digital part (Figure 1). The front ends will be placed in machine tunnel, powered and controlled via Ethernet links, while the analog-to-digital conversion and processing unit will remain in accelerator service area (radiation safe), with sufficient computing power to manage two BPMs each. The required connections to machine infrastructure will be optical (e.g., 10 Gb Ethernet link for global orbit feedback data) or copper-based (interlock, synchronisation).

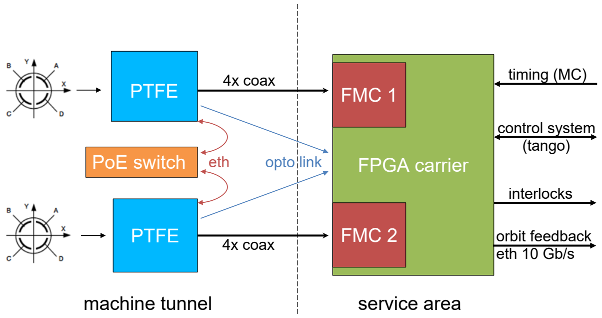

Figure 1: Block diagram of the system.

The process of building such a system for a high number of units (about 200 for the analog front ends, 100 for the digital platform) is not straightforward. Many aspects have to be considered, especially whose related to manufacturing, maintenance and reliability. For this reason, a partnership was signed with Instrumentation Technologies after a tender procedure, in order to industrialize and produce all the components of the system. In this way, Instrumentation Technologies' long-term experience in manufacturing diagnostic tools for particle accelerators will be combined with Elettra's knowledge of the overall aspects of a light source. This collaboration is already making improvements over the original prototype, and these results will be discussed in the following sections.

PILOT TONE FRONT END

The analog front end has been presented already at IBIC 2016 [3]: it consists of an RF analog processing chain with pilot tone injection. Compared to the first working prototype, we have made improvements on various aspects, both in terms of performance improvement and in terms of reliability and the production process.

Radiation Sensor

In order to compensate the overall signal path, the front end has to be installed in the machine tunnel, as near as possible to the pick-ups. This area presents unavoidable and unpredictable ionizing radiations due to multiple sources, that can damage the electronics and cause malfunctions. So, special care must be taken in correct positioning of the electronics, preferring low radiation zones. For this reason, a commercial radiation sensor (Teviso BG51 [4]) has been integrated in the front end (Figure 2). It is capable to detect beta radiation, gamma radiation and X-rays, in a measurement range of dose rate from 0.1 µSv/h to 100 mSv/h. The pulse count rate is about 5 cpm for 1 µSv/h, and the energy response ranges from 50 keV to above 2 MeV. Its output

---

* gabriele.brajnik@elettra.eu

ISBN: 978-3-95450-230-1 ISSN: 2673-5350 doi:10.18429/JACoW-IBIC2021-MOPP16

is directly connected to the internal microcontroller of the front end, that keeps track of the integrated dose over programmable time windows (last minute, entire life of the device or custom time window).

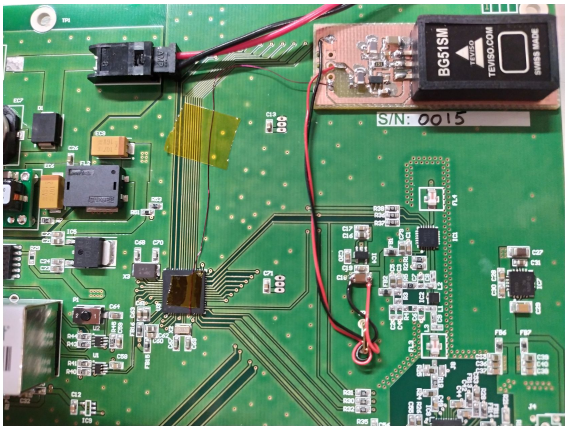

Figure 2: Radiation sensor on front end.

After a test at Elettra Radioprotection laboratory with Cs-137 and Co-60 radioactive sources, that confirmed the performances stated in the datasheet, the front end was installed in the machine, about 1 m below a BPM block. Figure 3 shows the radiations level reported by the sensor during a machine run of about one week, during three different operation modes: machine physics, 2.4 GeV with 150 mA and 2.0 GeV with 310 mA. As expected, the higher the current, the higher the radiation is. However, this addition is not intended to replace a beam loss monitor, but as a useful diagnostic tool to check the device health.

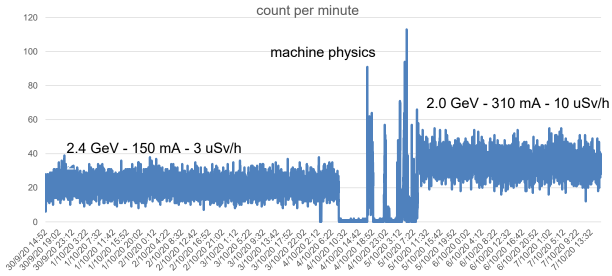

Figure 3: Detected radiation over a one week machine run.

Signal Conditioning Improvements

Glitch Trigger The procedure of changing the gain of the digital attenuators can require a significant amount of time, with a settling time of microseconds. During this time, glitches and spikes can occur on the output (Figure 4). These artefacts will reflect directly on the position calculated by the digital interface. Even if we proved that pilot tone compensation can greatly reduce them, a fiber optic phototransmitter (POF) has been added in order to communicate the gain switching event through a fiber optic link directly to the FPGA. The latter will tag the calculated positions during the switching phase, giving the user the possibility to decide whether to discard them or not.

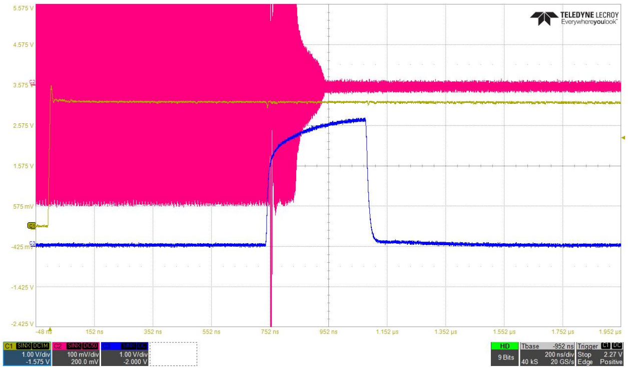

Figure 4: Attenuator spikes. Purple trace: RF signal output, blue trace: glitch trigger to phototransmitter.

Extra Gain Stage The overall gain of the filters, attenuators and amplifiers chain of the prototype front end, can be adjusted between −28 dB and +35 dB at 500 MHz frequency. With low currents (e.g. below 1 mA) and multibunch filling pattern, a resolution of 1 µm was measured. For this reason, we added an extra gain stage of 20 dB: the aim is not only to enhance performances at low currents, but also to ease the future commissioning of Elettra 2.0, where low currents will be injected in the initial stages.

Switchable filters The LC bandpass filter at 500 MHz was chosen for its frequency flatness over its 10 MHz bandwidth. This is essential to guarantee the proper operation of pilot tone compensation. Obviously, a wide bandwidth means a short impulse response over time, which was measured to be about 48 ns (Figure 5).

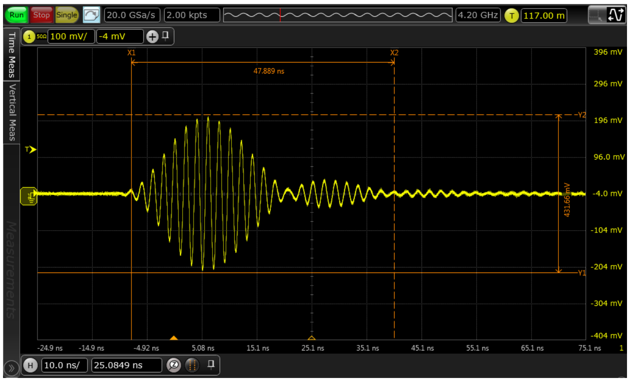

Figure 5: LC filter pulse response.

Considering that during single bunch and first turn operation, sampling the filter's impulse response is an effective way to calculate the position, we decided to extend the performances of the system with the possibility of switching the LC filter with a narrower SAW filter. In this case, with a typical bandwidth of about 1 MHz, the impulse response lasts longer (about 200 ns), and more samples can be collected, but losing the capability of the compensation (SAW filters frequency response is not suitable for pilot tone technique). This is a negligible drawback, since broadband noise dominates the improvements given by the compensation.

Industrialisation

The prototype front-end module was tested in machines with RF ranging from 352 MHz to 500 MHz. The module was controlled through the ethernet interface independent from the BPM electronics. The hardware design was then reviewed by the Instrumentation Technologies (I-Tech) company. The company has over 20 years experience in the accelerator field and established supply and production chains. The emphasis was put in the design for manufacturing which is essential for reproducible mass production.

The module's power supply has been changed from standard 12 V to Power-over-Ethernet (PoE) which reduces the number of cables and enables remote power cycle control. The prototype version was not optimized for special fill patterns, such as a "single bunch" fill pattern. The new module contains an additional RF path (selectable) with a SAW filter that stretches the short pulse to a usable filter ringing (200-250 ns) which is sufficient for a reliable position measurement. The original module was built from two PCBs connected over headers, while the new module is built from a single PCB which simplifies the mass production and eliminates failures associated with bad connection (Figure 6). From the installation point of view, the chassis and fittings were adapted to usually limited space in the tunnel and in order to facilitate the access for service. Nevertheless, thanks to MSP430 microcontroller bootloader, it is possible to reprogram its firmware through the Ethernet connection. A simple utility written in C (available through a GUI or CLI for batch updates) takes the binary file of the firmware, puts the microcontroller in bootloader mode and flashes it, checking the correctness of data.

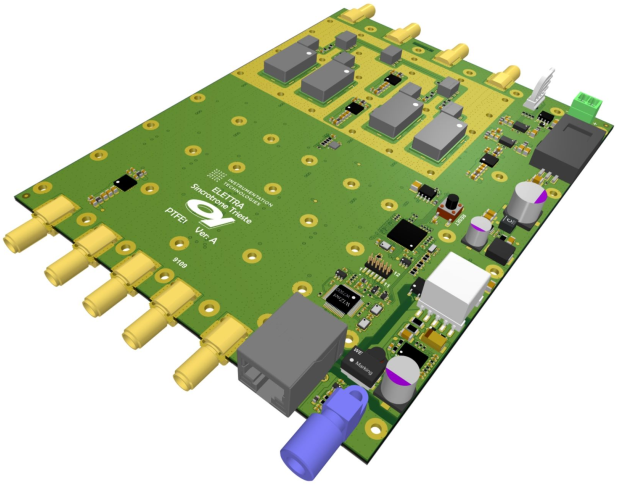

Figure 6: PCB rendering of the industrialized version.

DIGITAL ACQUISITION UNIT

After the first experience with a FPGA-based evaluation board [2], we decide to move on the in-house developed board based on Intel (formerly Altera) Arria 10 GX FPGA already presented [5]. The whole double digital receiver and demodulator, written in Verilog HDL, has been successfully ported on the new platform, adding several features. Now the system is capable to send data over 10-Gb Ethernet, thanks to SFP+ interfaces. This will allow continuous streaming of turn-by-turn data to the global orbit feedback. Also, the possibility to choose the output data rate with a variable filter (from turn-by-turn to 10 kHz) has been added.

However, we decided to go one step further: the final FPGA will be an Intel Arria 10 SX system-on-chip (SoC). The presence of an ARM hard processor assures more flexibility on higher level tasks, like system maintenance, configuration (remote firmware upgrade, diagnostic) and connection to the control system (Tango for Elettra).

Furthermore, the higher pin number of the future FPGA will allow to host two HPC FMC connectors, that means two beam position monitors per digital unit. In this case, a beam angle calculation can be performed between two consecutive BPMs, enabling an efficient beam position interlock to protect the vacuum chamber.

FMC Module

In order to use the new FPGA carrier board, we developed a 4-channel analog-to-digital conversion FMC card (Figure 7), based on Linear Technology LTC2107 ADCs, 16-bit, 210 MS/s. The input stage was carefully designed to handle 500 MHz signals, with a proper input impedance matching and an isolated balun for preventing ground loops. The clock tree relies on a Texas Instruments LMK04828 dual PLL, that generates and distributes to the four converters a clean sampling clock derived from machine revolution clock, with a fixed phase relationship.

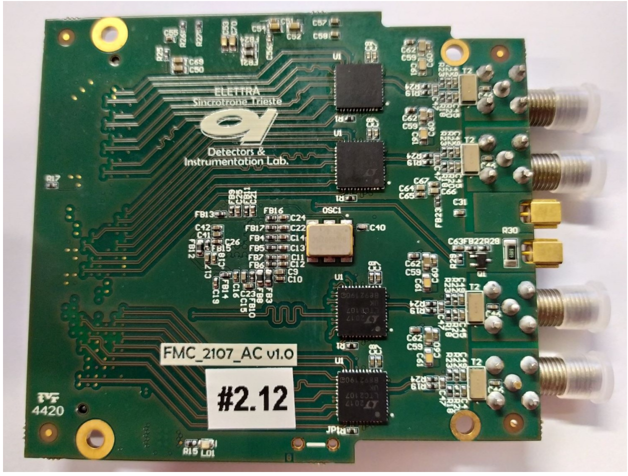

Figure 7: FMC card with 4 ADCs.

Mechanics

The prototype of the digital acquisition unit was built from multiple boards connected with cables. After I-Tech's hardware review, the design was simplified and made ready for mass production. Due to more active and power-hungry components, the unit requires active cooling, provided by three fans. The cool air enters the chassis on the lower part of the front panel. The fans force the air through the PCBs to the upper part of the chassis. The warm air exits at the upper part of the back panel. The 19" width chassis was designed to allow easy access to the fans on one side and to the PCB on the other side. Such design provides easy and quick service or maintenance (Figure 8).

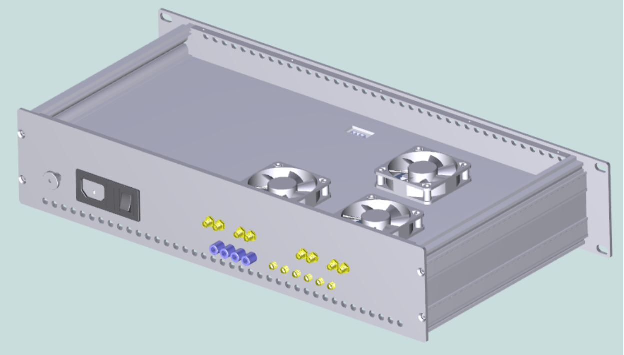

Figure 8: Rendering of digital platform.

CONCLUSION

The BPM system for Elettra 2.0 project was developed and updated over stages. The final prototype design was reviewed and further optimized for mass production. The collaboration between Elettra Sincrotrone Trieste and Instrumentation Technologies started in Spring 2021 with weekly review and development meetings. The meetings boosted the development pace which resulted in quick first articles production with expected deliveries still in year 2021 despite worldwide delay of components delivery. The mass production and final testing of the BPM system for Elettra 2.0 will be done by the Instrumentation Technologies with foreseen deliveries in year 2023.

REFERENCES

[1] E. Karantzoulis, A. Carniel, D. Castronovo, S. Di Mitri, B. Diviacco, S. Krecic, "Elettra and Elettra 2.0", presented at the 12th Int. Particle Accelerator Conf. (IPAC'21), Campinas, Brazil, May 2021, paper TUPAB051.

[2] G. Brajnik, S. Bassanese, G. Cautero, S. Cleva, and R. De Monte, "Integration of a Pilot-Tone Based BPM System Within the Global Orbit Feedback Environment of Elettra", in *Proc. IBIC'18*, Shanghai, China, Sep. 2018, pp. 190–195. `doi:10.18429/JACoW-IBIC2018-TUOC01`

[3] G. Brajnik, S. Bassanese, S. Carrato, G. Cautero, and R. De Monte, "A Novel Electron-BPM Front End With Sub-Micron Resolution Based on Pilot-Tone Compensation: Test Results With Beam", in *Proc. IBIC'16)*, Barcelona, Spain, Sep. 2016, pp. 308–311, `doi:10.18429/JACoW-IBIC2016-TUPG02`

[4] Teviso BG51 datasheet, `https://www.teviso.com/file/pdf/bg51-data-specification.pdf`

[5] G. Brajnik, S. Cleva, R. De Monte, and D. Giuressi, "A Common Diagnostic Platform for Elettra 2.0 and FERMI", in *Proc. IBIC'19*, Malmö, Sweden, Sep. 2019, pp. 280–282. `doi:10.18429/JACoW-IBIC2019-TUPP003`

BEAM POSITION DETECTION OF A SHORT ELECTRON BUNCH IN PRESENCE OF A LONGER AND MORE INTENSE PROTON BUNCH FOR THE AWAKE EXPERIMENT

Eugenio Senes*[1], P. N. Burrows[1,2], R. Corsini[1], W. Farabolini[1], T. Lefevre[1],
A. Gilardi [3], M. Krupa[1], S. Mazzoni[1], C. Pakuza [1,2], M. Wendt[1]

[1] CERN, Geneva, Switzerland
[2] JAI and University of Oxford, Oxford, United Kingdom
[3] Lawrence Berkeley National Laboratory, Berkeley, California, USA

Abstract

The AWAKE experiment studies the acceleration of electrons to multi-GeV levels driven by the plasma wakefield generated by an ultra-relativistic and high intensity proton bunch. The proton beam, being considerably more intense than the co-propagating electron bunch, perturbs the measurement of the electron beam position achieved via standard techniques. This contribution shows that the electrons position monitoring is possible by frequency discrimination, exploiting the large bunch length difference between the electron and proton beams. Simulations show that the measurement has to be carried out at a frequency of a few tens of GHz, which is far higher than the spectrum produced by the 1 ns long (4 sigma) proton bunch. As operating a conventional Beam Position Monitor (BPM) in this frequency range is problematic, an innovative approach based on the emission of coherent Cherenkov Diffraction Radiation (ChDR) in dielectrics is being studied. After describing the monitor concept and design, we will report about the results achieved with a prototype system at the CERN electron facility CLEAR.

INTRODUCTION

The AWAKE experiment successfully demonstrated the acceleration of an electron bunch in 10 meters of Rubidium plasma driven by a high energy proton bunch [1]. Due to the high accelerating gradients produced in the plasma, the research in this technology is promising for a new generation of compact high energy accelerators [2]. A new experimental run has started recently, the AWAKE Run 2, with the first protons delivered to the experiment during summer 2021. The AWAKE Run 2 is a new experimental program that aims to further study the proton-driven Plasma Wakefield Acceleration (PWFA) in the next decade, while finding technical solutions to apply the PWFA to operational accelerators. Among the copious experimental program, one finds the development of even stronger accelerating gradients, the conservation of the accelerated beam quality and the scalability of the acceleration scheme [3]. The present layout of the AWAKE experiment is shown in Fig. 1. A 400 GeV, 1 ns-long proton driver bunch is extracted from the SPS and reaches the AWAKE experiment through a dedicated transfer line. Few meters upstream to the plasma cell, it merges with a common beamline with the electron bunch and the plasma ionising laser pulse [4]. The electron bunch is considerably shorter and less intense than the proton bunch. The beam parameters are reported in Table 1. The two beams may travel with different trajectories, in order to select the merging point distance inside the plasma cell. The plasma is created out of rubidium vapour [5], ionised by a high power laser pulse [6]. Downstream the plasma cell, diagnostic devices can be inserted to analyse the beams [7]. The electrons are then sent to a spectrometer [8] to measure their energy, while the spent laser and proton beams are finally dumped.

Two different BPM systems measure the electron [9] and the proton [10] bunch transverse position, upstream the plasma cell. Due to the very different bunch structure of the electron and proton beam (see Table 1), the whole instrumentation installed in the common beamline is perturbed when both beams are present. This originates from the very different electromagnetic field of the proton bunch, that is considerably more intense than that of the electrons. As a result, the former overshadows the latter, limiting the possibility to measure the electron beam only n the absence of the proton beam. However, with shorter bunch length, the electron spectrum extends to higher frequencies compared to the proton spectrum and it would provide an opportunity to perform measurements on the electron beam in presence of the proton bunch. Currently, the experiment can operate either by setting up the two beams separately or by relying on the different repetition rate of the electron and proton beams. In fact, while the electrons are produced with a 10 Hz repetition rate, the protons are extracted every 30 s or more [11]. Therefore, during operation, the electron bunch position was extrapolated by the electron position in a number of shots before and after the proton pulse. This approach, although successful for a test experiment, may prove insufficient for an operational accelerator or to study beam-beam effects [12].

Table 1: AWAKE Beam Parameters

Beam	**proton**	**electron**
Charge [nC]	48	0.1 – 0.6
Length (1σ) [ps]	250	1 – 5
Energy [MeV]	4×10^5	16 – 20

---

[*] eugenio.senes@cern.ch

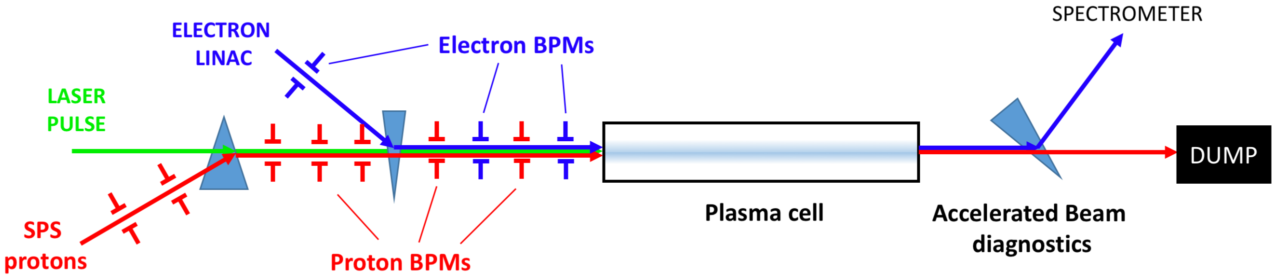

Figure 1: The present layout of the AWAKE experiment.

In fact, besides accelerating high quality beams, also the beam stability and reproducibility is essential.

POSITION DETECTION BASED ON THE BUNCH LENGTH DIFFERENCE

The bunch length difference of the electron and proton beam can be exploited in order to measure the position of both beams simultaneously. In fact, the bunch length difference translates in a different extension of the coherent beam spectrum in the frequency domain. Figure 2 shows the proton and electron beam spectra calculated for the AWAKE beams parameters mentioned in Table 1, under the approximation of Gaussian longitudinal bunch distributions. The detection frequency of the existing electron BPM system is also reported (vertical solid line). The proton and electron bunch present the same spectral power at a frequency of about 2 GHz. This explains why the present BPM system, working at 400 MHz, is not capable of measuring electrons when the two beams are present. It should however be possible to measure the electron beam position, provided that the detection is carried out at a sufficiently higher frequency where the proton signals would not be dominating the measurement.

Additional care must be taken in determining the target working frequency point for the new electron BPM system. The assumption of proton beams with a Gaussian longitudinal distribution is in fact not realistic, and imperfections or the presence of a sub-structure cause the proton spectrum to leak at higher frequency than the initial estimation. The presence of a sub-structure of the proton bunch has also been assessed via streak camera measurements of the light pulse from an optical transition radiation (OTR) screen. A series of investigations concluded that a safe operation frequency for the electron BPM system in presence of protons is of around the order of 30 GHz.

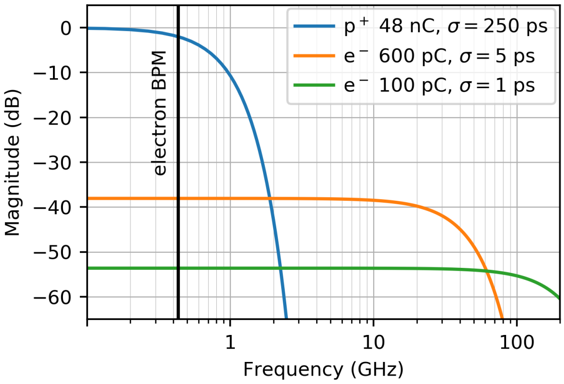

Figure 2: Bunch spectrum for the AWAKE beams assuming Gaussian bunch shape.

It should be noted that the rather large 60-mm-diameter beampipe presents a cutoff frequency of 2.93 GHz. It is therefore likely that any measurements performed above that frequency may become sensitive to the wakefield and electromagnetic fields in general propagating inside the beampipe.

A CHERENKOV DIFFRACTION RADIATION-BASED BPM

The Cherenkov Diffraction radiation (ChDR) is a particular type of polarization radiation that is produced in a dielectric material when a particle is passing in its vicinity while travelling faster than the speed of light in the dielectric [13]. The radiation is produced at the characteristic Cherenkov angle

$$\cos(\theta_{\mathrm{Ch}}) = \frac{1}{\beta n} \tag{1}$$

where θ_{Ch} is the angle of emission, β is the velocity of the particle in units of the speed of light in vacuum, and n is the index of refraction of the dielectric. Compared to other radiation production techniques, ChDR offers a higher photon fluence while being non-interceptive [14]. The possibility of realising non-intercepting beam diagnostic devices has drawn a considerable interest in the study of ChDR in recent years [15, 16].

In order to integrate the ChDR radiator in an accelerator, the dielectric target in which the radiation is produced needs to be integrated in the vacuum pipe. In the case of AWAKE, the choice of dielectric target fell onto cylindrical ceramic bars for fabrication convenience reasons. The dielectric bar is oriented at the Cherenkov angle to limit the internal reflections of the ChDR wavefront, and cut flush with the internal side of the beampipe. A longitudinal section of this device is

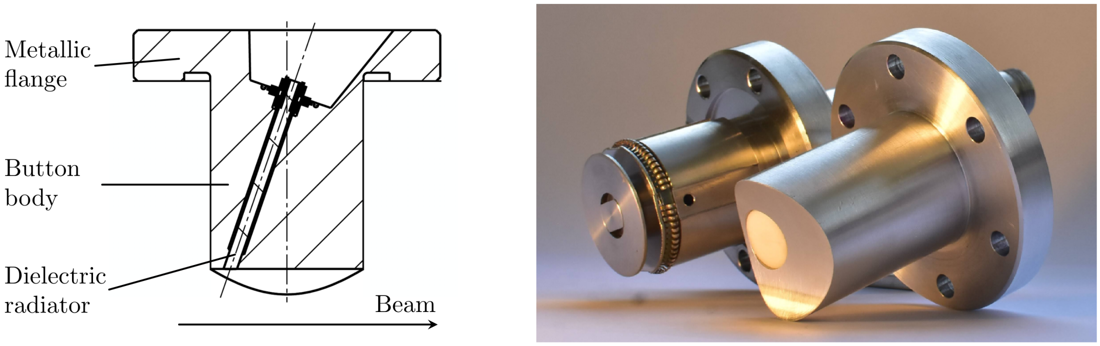

Figure 3: On the left, the longitudinal section of a ChDR button. The ceramic and metal part are indicated. On the right, a picture of a ChDR button (front), compared to a traditional capacitive BPM button (back). The white ring is the ceramic insert in the metal button.

shown in Fig. 3. The design of the button affects the properties of the radiation that is emitted at the end of the radiator. De facto, the dielectric bar enclosed in the metal structure is a loaded waveguide, where different electromagnetic modes can thus propagate through the radiator itself. Therefore, the radiator diameter would define the low cut-off frequency of the produced radiation. For a circular dielectric-loaded waveguide, the cut-off frequency of the fundamental mode is

$$f_c = 1.8412 \frac{c}{2\pi r} \frac{1}{\sqrt{\epsilon_r}} \tag{2}$$

where c is the speed of light, r is the radiator radius, and ϵ_r is the relative permittivity of the dielectric material [17]. As the radiator coupling to the beam field cannot be easily treated with analytical calculations, a simulation campaign was launched using CST Studio Suite [18]. Via numerical simulations, the radiator dimensions were selected to optimize the cut-off frequency and the power radiated [19, 20]. The impact of the change of radiator diameter on the spectrum of emission is shown in Fig. 4 for Polytetrafluoroethylene (PTFE) circular radiators ranging from 2 to 18 mm diameter. It is evident that the cut-off frequency is increased as the radiator diameter is reduced, as expected from waveguide theory. The vertical dashed lines mark the theoretical cutoff frequency for the base mode of a circular loaded waveguide of the same diameter (see Eq. (2)). In the specific case of AWAKE, the cut-off frequency, i.e. radiator diameter, can be set to reject the strong signal component of the protons below few GHz, while enabling the emission of the electrons at higher frequency.

EXPERIMENTAL TEST CAMPAIGN

A dedicated measurement campaign was carried out on a prototype in air at the CERN Linear Electron Accelerator for Research (CLEAR) [21], with the goal of studying the response of the beam position monitor. The prototype device was installed in the in-air test stand located at the end of the beamline, and equipped with motorized translation stages. The beam position is kept constant and stable, and it is monitored by a scintillating screen after the test device. The relative beam position in the BPM is varied by moving the test device around the beam. Electron bunches with charges ranging between 50 and 400 pC were used, and bunch length between 1.1 and 4.8 ps (1σ).

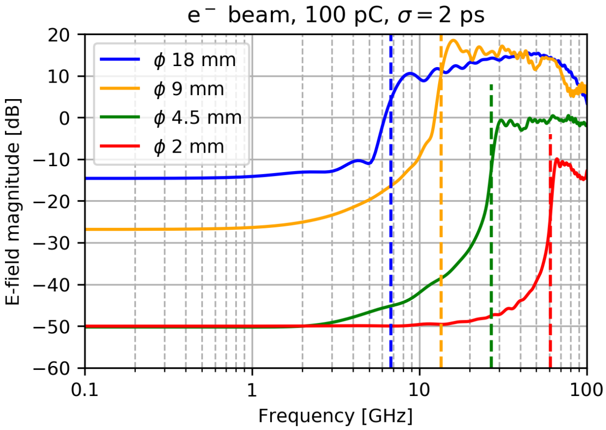

Figure 4: Spectrum of the ChDR emission at 1 cm from the radiator end calculated with CST Studio for different PTFE radiator diameters. The vertical dashed lines are the analytical base mode cutoff frequency of a dielectric-loaded circular waveguide with the same diameter.

The detection system is based on zero-bias Schottky diode RF detectors, working in the Ka band (26.5-40 GHz). The ChDR emission of two opposite ChDR radiators is coupled to the detection in the accelerator bunker by means of horn antennas. Downstream the antennas, two bandpass filters are installed with a central frequency of 30 GHz and a bandwidth of 300 MHz. The filtered signal is delivered to the detection outside the bunker through a 15 m-long WR28 waveguide network. The signal is appropriately attenuated before the diode detector to make sure that the diode is driven in the linear regime. The signal, demodulated by the diodes, is then amplified by a low noise amplifier, and sampled with an oscilloscope.

The sensitivity to the beam position is calculated by computing the Δ/Σ quantity, i.e. dividing the difference of the output voltage of each detection channel by the sum of the outputs. The measured sensitivity of the BPM is shown in Fig. 5. Per each position, 200 beam shots were acquired and averaged to compensate for the accelerator charge jitter. The image current model curve [22] is also shown for comparison with a traditional BPM ideal response. The measured sensitivity is roughly half the ideal sensitivity from the image current model. Partially, this can be attributed to the non optimized test detection system, that privileged flexibility over the absolute performance. In fact, direct Cherenkov radiation is produced in the air along the test-stand, contributing to the background. It would be eliminated by carrying out the tests in vacuum. Additionally, the horn antennas pointing and distancing from the radiators is a relevant source of asymmetry in the detection of different radiators, that can be limited by realizing a closed metallic transition between the radiator and the waveguide. Further performance improvements can be obtained by designing a specific superheterodyne-based detection system optimized for the AWAKE beam parameters.

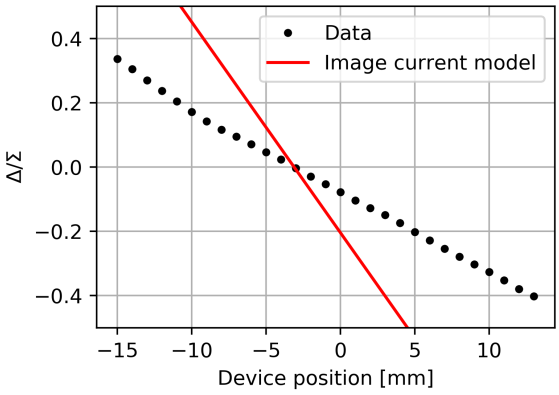

Figure 5: Beam position sensitivity of the test device compared to the image current theoretical model. A test beam of single bunches with a charge of 140 pC and a σ of 2 ps was used.

CONCLUSIONS AND FUTURE DEVELOPMENTS

For the AWAKE experiment, the challenges in the detection and characterization of proton and electron beams simultaneously have been described in this paper. The R&D efforts in the development of an electron beam position monitoring system that is functioning in the presence of an intense proton beam has been reported. Initial tests of a Cherenkov- Diffraction radiation dielectric pick-up have been performed on the CLEAR facility at CERN in order to assess the feasibility of the concept. Some limitations in providing a quantitative characterisation of the monitor were found and explained due to the fact that tests were performed in-air. A vacuum compatible Pick-up design is currently being manufactured, together with a custom based detection system at 30 GHz that would enable to provide an operational BPM based on ChDR. This new system should be tested on CLEAR again before its installation in the AWAKE experiment foreseen in 2022.

REFERENCES

[1] E. Adli *et al.* (AWAKE Collaboration), "Acceleration of electrons in the plasma wakefield of a proton bunch," *Nature*, vol. 561, no. 7723, pp. 363–367, 2018, doi:10.1038/s41586-018-0485-4

[2] M. Wing *et al.*, "Particle physics applications of the AWAKE acceleration scheme," CERN, Tech. Rep. CERN-PBC-REPORT-2018-004, 2018, https://cds.cern.ch/record/2651302

[3] P. Muggli, "Physics to plan AWAKE Run 2," *J. Phys. Conf. Ser.*, vol. 1596, p. 012 008, 2020, doi:10.1088/1742-6596/1596/1/012008

[4] C. Bracco, B. Goddard, E. Gschwendtner, M. Meddahi, A. Petrenko, and F. Velotti, "The Challenge of Interfacing the Primary Beam Lines for the AWAKE Project at CERN," in *Proc. IPAC'14*, Dresden, Germany, 2014, paper TUPME077, pp. 1534–1536, doi:10.18429/JACoW-IPAC2014-TUPME077

[5] G. Plyushchev, R. Kersevan, A. Petrenko, and P. Muggli, "A Rubidium Vapor Source for a Plasma Source for AWAKE," *J. Phys.*, vol. D51, p. 025 203, 2018, doi:10.1088/1361-6463/aa9dd7

[6] V. Fedosseev *et al.*, "Integration of a Terawatt Laser at the CERN SPS Beam for the AWAKE Experiment on Proton-Driven Plasma Wake Acceleration," in *Proc. IPAC'16*, Busan, Korea, 2016, paper WEPMY020, pp. 2592–2595, doi:10.18429/JACoW-IPAC2016-WEPMY020

[7] S. Mazzoni *et al.*, "Beam Instrumentation Developments for the Advanced Proton Driven Plasma Wakefield Acceleration Experiment at CERN," in *Proc. IPAC'17*, Copenhagen, Denmark, 2017, paper MOPAB119, pp. 404–407, doi:10.18429/JACoW-IPAC2017-MOPAB119

[8] J. Bauche *et al.*, "A magnetic spectrometer to measure electron bunches accelerated at AWAKE," *Nucl. Instrum. Meth.*, vol. A940, pp. 103–108, 2019, doi:10.1016/j.nima.2019.05.067

[9] S. Liu *et al.*, "The Installation and Commissioning of the AWAKE Stripline BPM," in *Proc. IBIC'18*, Shanghai, China, 2019, paper TUPB01, pp. 253–256, doi:10.18429/JACoW-IBIC2018-TUPB01

[10] M. Barros Marin *et al.*, "Performance of the AWAKE Proton Beam Line Beam Position Measurement System at CERN," in *Proc, IBIC'17*, Grand Rapids, MI, USA, 2018, paper TUPCF06, pp. 209–212, doi:10.18429/JACoW-IBIC2017-TUPCF06

[11] H. Damerau *et al.*, "RF Synchronization and Distribution for AWAKE at CERN," in *Proc. IPAC'16*, Busan, Korea, 2016, paper THPMY039, pp. 3743–3746, doi:10.18429/JACoW-IPAC2016-THPMY039

[12] U. Dorda, R. Aßmann, C. Bracco, J. Grebenyuk, A. Petrenko, and J. Schmidt, "Simulations of Electron-Proton Beam Interaction before Plasma in the AWAKE Experiment," in *Proc. IPAC'15*, Richmond, VA, USA, 2015, paper WEPWA003, pp. 2492–2495, doi:10.18429/JACoW-IPAC2015-WEPWA003

[13] M. V. Shevelev and A. S. Konkov, “Peculiarities of the generation of Vavilov-Cherenkov radiation induced by a charged particle moving past a dielectric target,” *J. Exp. Theor. Phys.*, vol. 118, pp. 501–511, 2014, `doi:10.1134/S1063776114030182`

[14] A. Curcio *et al.*, “Beam-based sub-thz source at the cern linac electron accelerator for research facility,” *Phys. Rev. Accel. Beams*, vol. 22, p. 020 402, 2 2019, `doi:10.1103/PhysRevAccelBeams.22.020402`

[15] D. Alves, M. Gąsior, and T. Lefèvre, “Analysis of Quadrupolar Measurements for Beam Size Determination in the LHC,” in *Proc. IBIC’19*, Malmö, Sweden, 2019, paper TUPP034, pp. 397–401, `doi:10.18429/JACoW-IBIC2019-TUPP034`

[16] S. Mazzoni *et al.*, “Non Invasive Bunch Length Measurements Exploiting Cherenkov Diffraction Radiation,” Campinas, SP, Brazil, unpublished, 2021.

[17] J. D. Jackson, *Classical electrodynamics; 3rd ed.* Wiley, 1999.

[18] CST Studio Suite, version 2018 and 2019. `https://www.3ds.com/products-services/simulia/products/cst-studio-suite/`

[19] C. Pakuza *et al.*, “Development of a Cherenkov Diffraction Radiation-based Beam Position Monitor for operation at the AWAKE experiment at CERN,” in *Proc. Joint APP, HEPP, NP conference 2021*, 2019, paper THAO01.

[20] E. Senes, “Development of a beam position monitor for co-propagating electron and proton beams,” Ph.D. dissertation, 2020.

[21] D. Gamba *et al.*, “The CLEAR user facility at CERN,” *Nucl. Instrum. Methods Phys. Res., Sect. A*, vol. 909, pp. 480–483, 2018, `doi:10.1016/j.nima.2017.11.080`

[22] R. E. Shafer, “Beam position monitoring,” *AIP Conference Proceedings*, vol. 601, 1992, `doi:10.1063/1.41980`

DEVELOPMENT OF A PASS-THROUGH DIAGNOSTIC FOR NEXT-GENERATION XFELs USING DIAMOND SENSORS*

I. Silva Torrecilla[†], B. Jacobson, J. MacArthur, D. Zhu
SLAC National Accelerator Laboratory, Menlo Park, California, USA
J. Bohon, D. Kim, J. Smedley, Los Alamos National Laboratory, Los Alamos, New Mexico, USA
E. Gonzalez, S. Kachiguine, F. Martinez-Mckinney, S. Mazza, M. Nizam, N. Norvell, R. Padilla, E. Potter, E. Ryan, B. Schumm, M. Tarka, M. Wilder, Santa Cruz Institute for Particle Physics and the University of California at Santa Cruz, Santa Cruz, California, USA
C. T. Harris, Sandia National Laboratory, Albuquerque, New Mexico, USA

Abstract

X-ray FELs deliver rapid pulses on the femtoseconds scale, and high peak intensities that fluctuate strongly on a pulse-to-pulse basis. The fast drift velocity, and high radiation tolerance properties of CVD (chemical vapor deposition) diamonds, make these crystals a good candidate material for developing a multi-hundred MHz pass-through diagnostic for the next generation of XFELs. Commercially available diamond sensors work as position-sensitive pass-through diagnostics for nJ-level pulses from synchrotrons. Supported by the University of California and the SLAC National Laboratory, a collaboration of UC campuses and National Laboratories have developed a new approach to the readout of diamond diagnostic sensors designed to facilitate operation for FEL-relevant uJ and mJ pulses. Single-crystal diamond detectors have been tested on the XPP end station of the Linac Coherent Light Source beam at SLAC. We present results on the linearity and charge collection characteristics as a function of the density of deposited charge.

INTRODUCTION

Monocrystalline diamonds are recognized to exhibit a number of properties that make them attractive options for a broad range of sensor applications. Superior radiation tolerance, a fast saturated drift velocity (approximately 200 μm/nsec) and superior thermal conductivity (2200 W/m-K) distinguish diamond among other semiconductor sensor materials such as silicon and gallium-arsenide.

Here, we explore the use of diamond sensors as a pass-through diagnostic for X-ray Free Electron Laser (XFEL) beams. For this application, involving intense X-ray beams being trained directly on the diagnostic sensor, diamond properties that might be disadvantageous for other applications provide additional advantages relative to other sensor materials. The low atomic number of carbon leads to a relatively small scattering cross section for X-ray above the carbon K-shell edge of 0.28 keV, limiting the absorption of the XFEL beam as it passes through the diagnostic. In addition, the large diamond band gap of 5.5 eV, and resulting pair excitation energy of 13.3 eV [1], limits the production of signal charge relative to other sensor materials.

In this study, we explored the characteristics of diamond-sensor charge collection in limits relevant to their application as pass-through diagnostics for high-intensity, high repetition-rate X-ray beams. These studies were performed at the XPP beamline of the Linac Coherent Light Source (LCLS) at the SLAC National Accelerator Laboratory on April 5-6, 2021. The studies made use of a monochromatic beam of 11.89 keV X-rays with individual pulse varying in energy from 1 μJ to nearly 100 μJ. Both the duration and efficiency of charge collection were studied as a function of the density of deposited charge within the diamond sensor.

SENSOR AND READOUT

The studies made use of a 4x4 mm^2 monocrystalline diamond substrate, provided by the Element Six corporation and thinned by Applied Diamond, Inc. The diamond was plated with planar platinum electrodes of area approximately 3.5x3.5 mm^2 and 25 nm thickness at the Center for Integrated Nanotechnologies (CINT) facility in Albuquerque, New Mexico, USA. The thickness of the diamond substrate was measured to be 37 ± 10 μm in the laboratory of the Santa Cruz Institute for Particle Physics (SCIPP) on the campus of the University of California at Santa Cruz.

The sensor was mounted on a printed-circuit board (PCB), produced by the SCIPP laboratory, featuring a low-impedance signal path designed to circulate large amounts of signal charge at high bandwidth. Figure 1 shows the details of the PCB signal path, including the loaded diamond sensor described above. To reduce inductive load associated with bond wires, the sensor is connected to the readout path through a metallic band composed of indium. This band carries signal charge to a series array of two resistors – a 1 Ω resistor followed by a 10 mΩ resistor, with contacts on the long side to minimize inductance – that shunt the signal current directly to ground. 50 Ω pick-off traces make contact with the sensor side of both the 1 Ω and 10 mΩ resistors, each of which terminates at an SMA connector close to the pickoff point, providing signals than can be digitized and recorded with a high-bandwidth digital storage oscilloscope. Figure 2 provides a larger-scale view of

---

* Work supported by the UC-National Laboratory Fees Research Program grant ID #LFR-20-653232, the U.S. Department of Energy, grant number DE-SC0010107 (SCIPP), contract 89233218CNA000001 (LANL), Contract DE-NA-0003525 (Sandia), Contract No. DE-AC02-76SF00515(SLAC).

[†] email address isleydys@slac.stanford.edu

the PCB, showing the signal-trace paths and SMA connector footprints. The AC signal return path is provided by a bank of 44 parallel 22 µF capacitors, amounting to a total capacitance of approximately 1 mF, between ground and the bias plane onto which the sensor is attached making use of Leitsilber Conductive Silver Cement. The redundant parallel paths reduce the overall inductance of the signal return path, while the large capacitance provides an ample reservoir of charge to support the large signal charges generated by the intense XFEL pulse.

It should be noted that the charge collection speed can be very fast for the sensor described above and shown in Fig. 1. With a saturated drift speed in diamond of approximately 200 µm/nsec, absent effects from space-charge and electronic impedance, the nominal charge collection time for the 37 µm thick sensor is less than 200 psec.

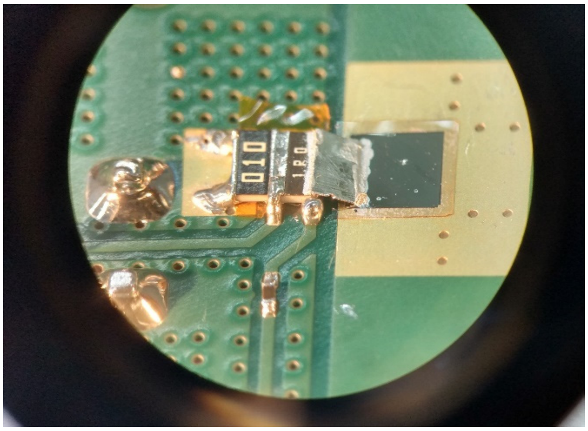

Figure 1: Detail of the readout PCB signal path showing the 37 µm thick diamond sensor, the low-impedance indium band connecting the sensor to the readout network, the series array of 1 Ω and 10 mΩ resistors that shunt the signal to ground, and the two 50 Ω pick-off traces.

DATA ACCUMULATION

The data used in this study was accumulated in the early morning of April 6, 2021. The monochromatized LCLS beam provided pulses of 11.89 keV X-rays with a falling energy spectrum (see Fig. 3) that ranged between 1 and 80 µJ. Making use of energy-attenuation coefficients from [2], approximately 1.3% of the beam energy was absorbed by the sensor as the pulse passed through it.

Data was accumulated with both the full beam as well as with a beam attenuated by 90% through the insertion of a physical attenuator upstream of the sensor assembly. The two signal pick-offs (1 Ω and 10 mΩ) were read out by a 25 GHz digital storage oscilloscope operating with a sampling rate of 40 Gs/S. High-bandwidth signal-path attenuation was used, as needed, to ensure that the pulses didn't saturated the dynamic range of the oscilloscope. Beam was provided both in un-focused (FWHM estimated to be 350 µm) and focused (FWHM estimated to be 43 µm) modes. Data were taken for sensor bias voltage ranging between 5.4 and 100 Volts. For each configuration of beam intensity, beam focus and bias voltage, runs of approximately 1000 pulses were accumulated. The signals from the 10 mΩ signal pick-off were found to be too noisy to use for the characterization of the detector response, and will not be made use of in the results that follow.

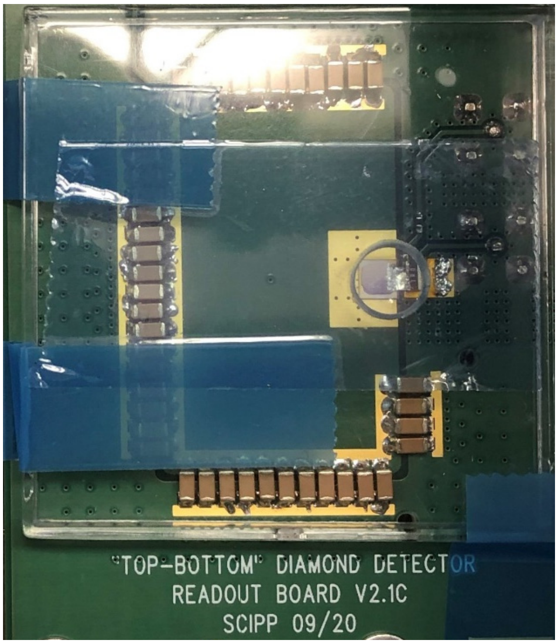

Figure 2: Full view of the readout PCB showing the AC return path provided by a highly parallelized array of 22 µF capacitors. Note that in this photograph, the assembly is rotated by 180 degrees relative to that of Fig. 1.

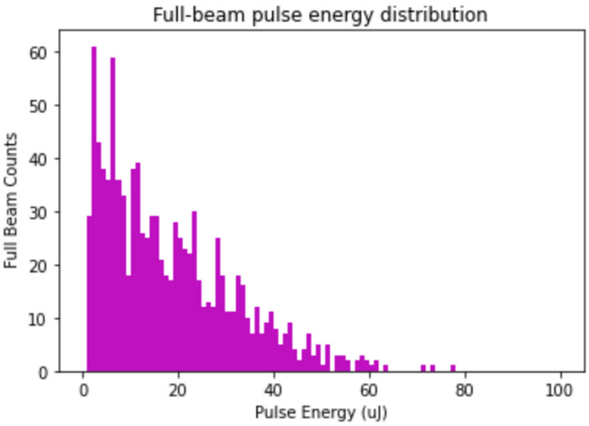

Figure 3: Typical distribution of pulse energies delivered by the LCLS during data accumulation.

ANALYSIS AND RESULTS

Charge collection current was estimated according to

$$I_{coll}(t) = V(t)/R_{eff}$$

where I_{coll} is the estimated charge-collection current, V is the measured signal voltage, and R_{eff} is the effective resistance of the signal path, including both the applicable shunt resistance and the 50 Ω termination resistance of the oscilloscope. For the 1 Ω signal pickoff, this parallel combination of 1.01 Ω and 50 Ω led to an effective resistance of $R_{eff} = 0.99$ Ω.

Total collected charge, as a function of collection time, was estimated by integrating, for signals within a given pulse-energy bin, the average charge collection current from the point of passage of the beam through the sensor (t=0) to the specified collection time:

$$Q_{coll}(t_{coll}) = \int_0^{t_{coll}} I_{coll}(t)\, dt\,.$$

Figures 4 and 5 show the collected charge as a function of time, estimated in this way, for signals arising from successive bins in delivered pulse energy, for unfocused and focused beam, respectively. The signals shown are those arising when the diamond sensor was biased to 100 V. In comparing the detector response between the cases of unfocused and focused beam, it should be noted that, in a given pulse energy bin, the total delivered charge is essentially identical; what differs between the two cases is the density of generated charge carriers created inside the diamond bulk, hereafter referred to as the "plasma density" ρ_P.

It is seen that the time required for full collection of the signal charge increases with total delivered charge, but also is significantly larger when, for a given pulse energy, the beam is focused. This suggests that characteristics of the charge collection, such as collection time and collection efficiency, may be characterized in terms of plasma density, a property internal to the diamond sensor itself, independent of the particular scheme employed to extract its signal.

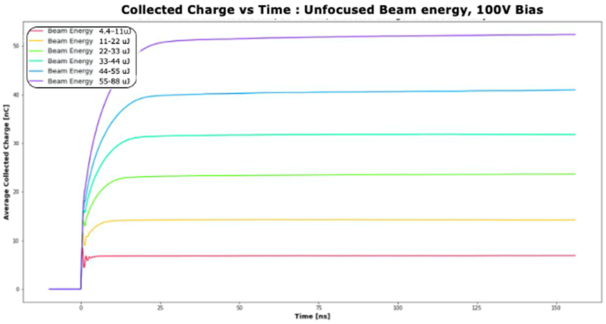

Figure 4: Collected charge as a function of collection time for a sensor bias of 100 V, with the beam focused to a FWHM of 350 µm.

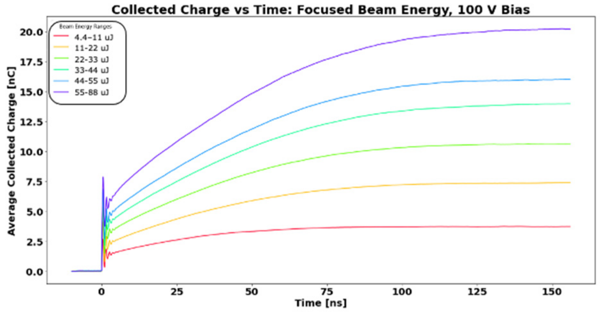

Figure 5: Collected charge as a function of collection time for a sensor bias of 100 V, with the beam focused to a FWHM of 43 µm.

In the following, we estimate plasma density ρ_P according to

$$\rho_P = 0.76\frac{Q_{dep}}{V}$$

where Q_{dep} is the charge deposited in the diamond bulk and $V = \pi T(d/2)^2$ is the volume occupied by the plasma, with T being the sensor thickness and d equal to the full-width at half-maximum quoted above for the unfocused and focused beams (350 and 43 µm, respectively). The factor of 0.76 represents the fraction of a gaussian beam contained within its FWHM.

The value of Q_{dep} in each pulse-energy bin is estimated by multiplying the mean delivered pulse energy in the given bin by a conversion factor of 0.931 nC/µJ. This factor is given by the ratio of $Q_{coll}(t\rightarrow\infty)$, the asymptotic value of the observed collected charge estimate, to the mean delivered pulse energy in the lowest pulse-energy bin of the 100%, 100 V bias, unfocused-beam running, for which the charge collection efficiency is assumed to be 100%. This assumption will be justified below.

Making use of this conversion factor, and the expression for plasma density, both the deposited charge and the plasma density can be estimated for any delivered pulse energy for any configuration of the experimental setup. By comparing $Q_{coll}(t\rightarrow\infty)$ with the deposited charge estimate (estimate of the charge generated by the beam passage), an estimate of the charge collection efficiency can be made as a function of plasma density. For the case of 100 V of applied bias, for which both full-energy and 90%-attenuated data was accumulated with unfocused beam, and full-energy data was accumulated for focused beam, the range of plasma density deposited in the sensor varied by nearly four orders of magnitude.

Figure 6 shows the estimated charge collection efficiency as a function of plasma density for the three bias voltages for which data was accumulated for both unfocused and focused beam: 20 V, 60 V and 100 V. The consistency of the estimated charge collection efficiency, albeit with limited statistics, for the 90%-attenuated running, at and below the plasma density associated with the lowest energy bin for the case of unfocused beam, supports the assumption that the charge collection efficiency is near 100% for that data. For the highest bias voltage (100 V, corresponding to a bias field of approximately 2.7 V/µm), charge collection efficiency loss is observed to occur for plasma densities above 10^{16} cm^{-3}. For the 60 V and 20 V (1.6 and 0.54 V/µm, respectively) bias running, charge collection efficiency worsens with lessening bias, with efficiency loss observed even for a plasma density as low as 10^{16} cm^{-3}, the lowest density explored for these lesser biases.

From the information shown in Figs 4 and 5, as well as corresponding information for running with sensor biases of 20 V and 60 V, the time required to accumulate a given fraction of the asymptotic value $Q_{coll}(t\rightarrow\infty)$ can be estimated as a function of plasma density. Values of this estimate for a fraction of 95% of $Q_{coll}(t\rightarrow\infty)$ are displayed in

Fig. 7 as a function of plasma density. The charge collection time, characterized in this way, depends strongly upon both plasma density and applied bias field, and approaches 100 ns even for the highest bias field (2.7 V/µm) explored in this study.

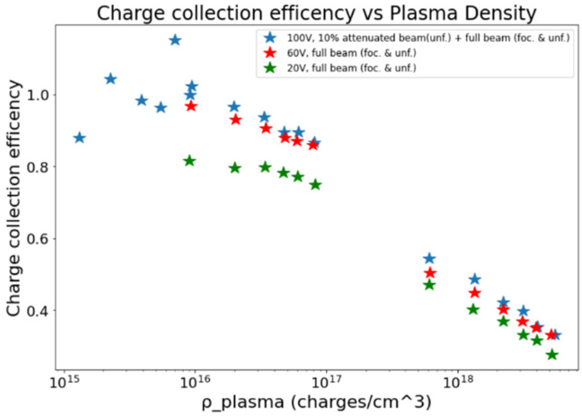

Figure 6: Estimated charge collection efficiency as a function of plasma density (cm^{-3}) for 100 V, 60 V and 20 V sensor bias.

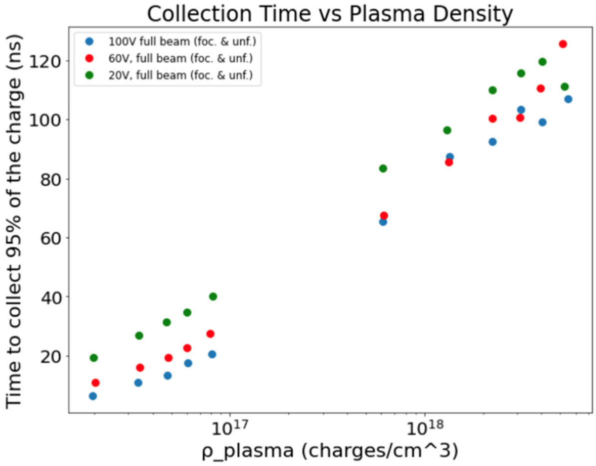

Figure 7: Time required to collect 95% of $Q_{coll}(t\to\infty)$, as a function of plasma density, for various detector biasing levels.

SUMMARY AND CONCLUSIONS

In a study to explore its suitability as a pass-through diagnostic for high-intensity X-ray beams, a thin diamond sensor, biased to fields as high as 2.7 V/µm, was exposed to XFEL pulses of 11.89 keV X-rays with energies of up to 80 µJ. For this highest bias voltage, charge collection efficiency was found to be maintained for plasma densities as high as 10^{16} cm^{-3}, with the charge collection efficiency worsening monotonically with applied bias voltage. Charge collection time, characterized by the amount of time required to accumulate 95% of the asymptotic value of collected charge, was also found to depend strongly on plasma density and detector bias voltage. While the results suggest that charge collection speed and efficiency may be improved by increasing the bias field above 2.7 V/µm (the maximum value used in the study), it seems that the intrinsic charge collection properties of monocrystalline diamond will present challenges to the development of pass-through diagnostics for high-intensity XFEL beams (which can approach several mJ), especially for high repetition-rate applications.

ACKNOWLEDGEMENTS

This work was supported by the UC-National Laboratory Fees Research Program grant ID #LFR-20-653232, and by the U.S. Department of Energy, grant number DE-SC0010107. This work was performed, in part, at the Center for Integrated Nanotechnologies, an Office of Science User Facility operated for the U.S. Department of Energy (DOE) Office of Science by Los Alamos National Laboratory (Contract 89233218CNA000001) and Sandia National Laboratories (Contract DE-NA-0003525). We also acknowledge the generous support of the SLAC National Accelerator Laboratory, through its provision of LCLS beam time and staff support. Use of the Linac Coherent Light Source (LCLS), SLAC National Accelerator Laboratory, is supported by the U.S. Department of Energy, Office of Science, Office of Basic Energy Sciences under Contract No. DE-AC02-76SF00515.

REFERENCES

[1] Jeffrey W. Keister and John Smedley, “Single Crystal Diamond Photodiode for Soft X-ray Radiometry”, *Nucl. Instrum. & Meth. A*, vol. 606, pp. 774-779, 2009.

[2] `https://physics.nist.gov/PhysRefData/Xray-MassCoef/ElemTab/z06.html`

BEAM POSITION MONITOR CALIBRATION BY RAPID CHANNEL SWITCHING*

R. Hulsart†, R. Michnoff, S. Seletskiy, P. Thieberger
Brookhaven National Laboratory, Upton, NY, USA

Abstract

One of the requirements for low-energy RHIC electron cooling (LEReC) is a small relative angle between the ion and electron beams as they co-propagate. In order to minimize relative electron-ion trajectories angle, BPM measurements of both beams must be very accurate. Achieving this requires good electronic calibration of the associated cables and RF components, due to their inherent imperfections. Unfortunately, these are typically frequency dependent, especially in the RF filter and amplifier stages. The spectral content of the ion vs. electron bunch signals varies significantly, presenting a calibration challenge, even when using the same sampling channels and electronics to measure both beams.

A scheme of rapidly swapping the BPM signals from the pickup electrodes between the two signal cables (and sampling channels), using switches installed near the BPM was implemented to combat these calibration issues. Bias in each signal path appears as an offset which has an equal and opposite component when the cables are reversed. Taking the average of the two measurements with the channels in normal and reverse positions reduces this offset error. Successful transverse cooling of the RHIC ion beam has been verified after using this switching technique to provide continuous calibration of the BPM electronics [1]. Details of the processing hardware and switch control methodology to achieve this result will be discussed.

INTRODUCTION

Beam position measurements in accelerators are commonly performed by sampling the induced signals on a pair of pickup electrodes mounted in the vacuum chamber. In order for them to be precise and accurate, small differences in signal amplitude need to be measured between these two sampling channels. In most BPM systems, separate analog signal paths consisting of cables, amplifiers, attenuators, and filters are used to process each signal before being sampled by an analog to digital convertor (ADC). Each of these circuit elements has inherent properties that can attenuate or reflect signals with a dependence on frequency.

Typically, a calibration procedure is followed by using a known test signal to match the gain and offset of each of these channels, in order to balance their response. In theory once these channels are matched the true position of the beam will be the only contributor to any difference. In reality, the circuit response due to the test signal can differ significantly from that produced by a real beam. There are also accelerators where the spectral content of the beam signal can change during operation due to variations in RF frequencies such as with rebucketing. The presence of two beams of different bunch length and/or structure also has the same effect of changing the response of the individual circuit elements of each sampling channel. This leads to a situation where a static calibration using a test signal is inadequate to remove the electronic offsets for all beam conditions. Another source of offsets that can't be removed with static calibrations is the presence of radiofrequency interference (RFI) at the bunch frequency or its harmonics picked up by the long cables and enhanced by ground-loops. Such RFI can vary with time and can produce offsets that are bunch-intensity dependent.

One method of removing these offsets is to periodically swap the channels that each of the pickup electrodes (PUE) is connected to. By placing a set of switches close the BPM, each PUE can be connected to either of the sampling channels, including cables, analog processing electronics, and ADC. When using a BPM with two PUE's, this will produce two separate position measurements, where the differences due to the sampling channels are equal and opposite in sign. By rapidly switching and averaging these two together, a true measurement is obtained that is free from the offsets produced by elements downstream of the point of switching.

SWITCHING TECHNIQUE

Theory of Operation

To simplify this description, we will consider a single plane BPM measurement derived from two PUE's. An enclosure containing an arrangement of solid-state transistor switches is placed close to the BPM and connected via short cables. We will call these PUE signals A and B and these are the inputs to the switch. The outputs will be labelled 1 and 2 and are connected via longer cables to the BPM processing electronics.

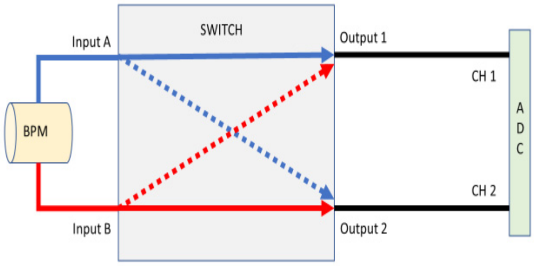

Figure 1: Switching Block Diagram.

The switch circuit is designed such that in the 'Normal' position, input A is connected to output 1 and B is connected to 2. When a control signal is applied to the switch,

---

* Work supported by BSA under DOE contract DE-AC02-98CH10886
† rhulsart@bnl.gov

it changes to the ‘Reverse’ condition, where input A goes to output 2, and B to 1. The resulting situation is that any difference between A and B gets inverted when the switch position is changed, however, any difference that appears after the switch between 1 and 2 will remain unaffected. Figure 1 illustrates this in block form.

Since the arrangement of PUE’s A and B are related to the sign convention of the accelerator, the calculated position needs to be inverted in sign when the switch is in the reverse position, because the PUEs are now reversed with respect to the beam direction through the BPM. By inverting the calculation when the switch is in the ‘Reverse’ position, the true position produced by the beam will remain correct in sign. The offset that exists due to differences between paths 1 and 2 will also change sign, and so appear as an equal but inverted offset when combined with the true position from the BPM. This has the effect of producing two positions, one equal to ‘true position + electronic offset’ and the other ‘true position – electronic offset’. By observing this envelope one can separate the beam position from the electronic offset. In addition, by rapidly switching back and forth, the mean of these two measurements will remove the offset, and only include the true position. A more complete derivation of this process is explored in a technical brief [2].

Switch Control Methods

A few considerations need to be accounted for in order to realize such a switching system. It is possible to separately control the switch position where the BPM electronics is not aware of the reversal. In this case the position data can be altered (inverted) manually or by separate software that is aware of the switch position. Such a system can still be useful for ‘slow’ calibrations that are periodically performed. In this case the calibration constants of the BPM channels would be adjusted such that there is no longer any difference between ‘Normal’ and ‘Reverse’. This type of application would have to be periodically checked to deal with dynamic beam spectral changes or changes due to thermal drifts over long time scales.

To provide continuous and automatic calibration, especially with high repetition rate beams, it is better to allow the BPM electronics itself to control the switching. In this case a control signal is provided as an output from the BPM processor, and the internal calculation will invert the measurement whenever the switch is in the ‘Reverse’ position. Such a system was realized for the LEReC project using the BNL designed V301 BPM processing electronics [3].

BPM SWITCHING FOR LEREC

The requirement to co-propagate ion and electron beams with minimal angle between electron and ion trajectories for the LEReC project was a driver for the realization of this type of BPM switching system. Even though the repetition rate of the ion and electron bunches were similar (9 MHz spacing), the spectral content of each were not, since the ion beam consisted of a train of single long bunches whereas the electron beam ‘macrobunch’ consisted of a series of 704 MHz spaced short bunches with an overall 9 MHz modulated structure. Due to these differences, the calibration coefficients needed to balance the offsets of the electronic channels are not the same for each case. In order to be able to use the same processor to measure both beams accurately, the switching system described herein was realized.

LEReC Switching Hardware

A custom hardware module was designed at BNL to perform the channel switching. A set of four GaAs FET RF switches (Analog Devices HMC349) are arranged in a manner which allows the input signals A and B to be swapped to either output, 1 or 2, simultaneously. Great care was taken in this PCB design to closely match each part of the circuit, for both IC placement and routing of the traces on the board. A single 5V control signal is common to all four switches, which causes them to change state in unison. Each of these switches has a small insertion loss which did not differ significantly from part to part. During testing of about 30 units, negligible offset contributions were measured from the switches themselves. See figure 2 for a circuit schematic. More details are also available in an earlier comprehensive LEReC BPM system description[4].

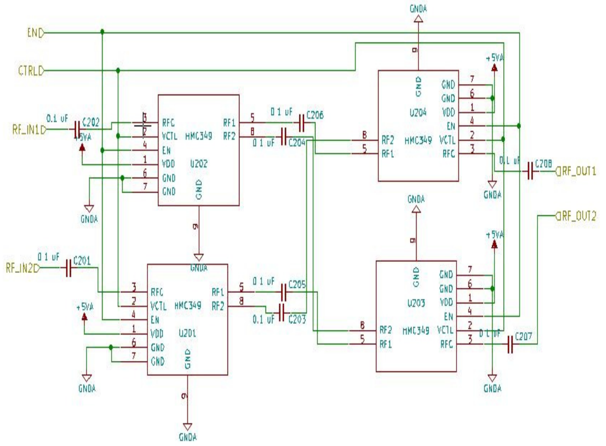

Figure 2: Switching Circuit Schematic.

LEReC Beam Measurements with Switching

During the commissioning of the LEReC the switching technique was carefully scrutinized. During assembly of the electron accelerator a test signal using a well-matched splitter was injected into each BPM signal path close to the BPM itself. The test signal used was a 704 MHz sine wave modulated at 9 MHz (similar to the electron beam macrobunch). Gain and offset coefficients were adjusted for each BPM to obtain a zero position reading.

Once electron beam was available in the ‘pulsed’ 1 Hz mode using only a few macrobunches, the switches were manually moved between the ‘Normal’ and ‘Reverse’ positions. As expected, many of the BPMs no longer appeared well calibrated (showing a change between the two switch positions), due to differences between the test signal and real beam signal. The calibration settings were then manually adjusted again to remove any differences. When ion beam was present in the same BPMs, the same proced-

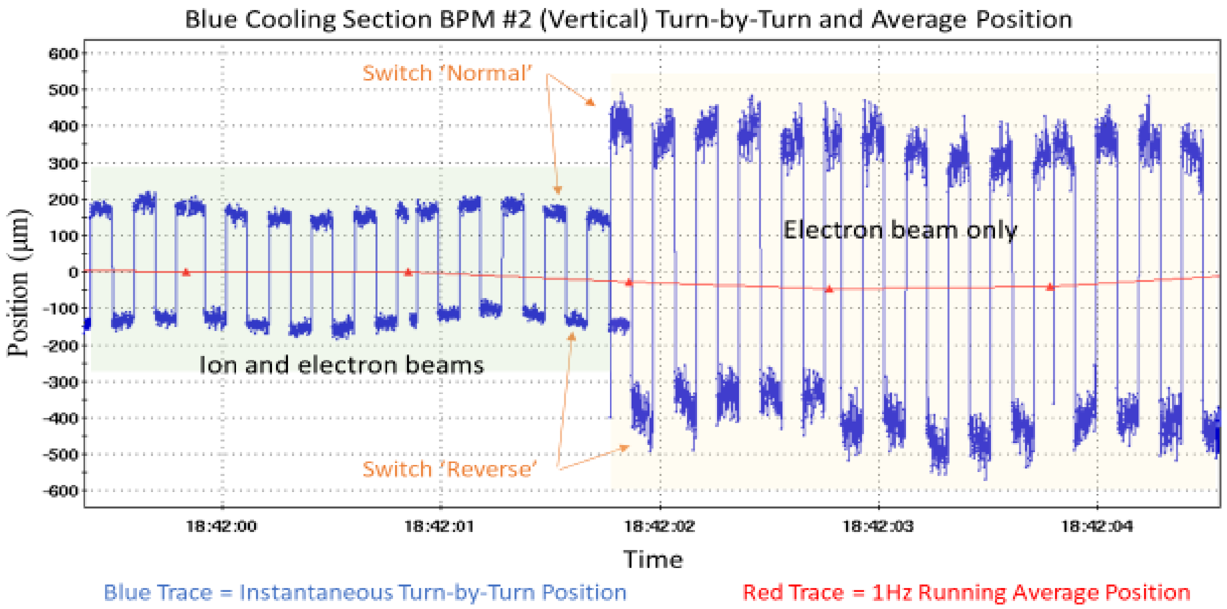

Figure 3: Calibration difference with ion and electron beam (left) vs. electron beam only (right).

ure was followed, and as expected, differences due to switch position were again present. The switches were then commanded to switch automatically every 100 RHIC turns (approximately a 760 Hz rate for a 76 kHz revolution frequency). A running average position was calculated by the BPM processor that had a cutoff frequency of a few Hz, thereby smoothing out the two positions derived from the switching. Regardless of the calibration values for each channel (to a reasonable magnitude) no artifact of the switching envelope remained, thereby providing a smooth and constantly calibrated position reading from the BPMs regardless if ions or electrons were being measured.

Figure 3 illustrates the differences in calibration very clearly during the moment that the ion beam in RHIC was removed. In this particular case the ion beam intensity was several times higher than the electron beam, so that it dominated the BPM response when both beams were present (therefore the response shown on the left is nearly identical with ion beam alone). When the ions were removed it is evident that the position appears to have shifted by ~200 µm when looking at the turn-by-turn data in either switch position. The average of these two positions remains the same however, which illustrates that this offset comes from a source downstream of the switches, and not the beams themselves. This was further verified by the fact that transverse cooling was evident (using other instrumentation) when the beams were aligned based on these BPM measurements. Note that the time axis in this figure is not continuous – only 1024 turns are reported each second, despite the revolution frequency of ~76 kHz. The jumps in the position correspond to changing the switches every 100 turns.

Drift Compensation

By running the switching in this continuous mode, long-term drifts due to thermal effects are also compensated for. Any changes in attenuation in the long cables running out of the tunnel due to temperature will be averaged out by this same method. In addition, thermal effects within the electronics, both in the filtering stages and amplifiers, also benefit from the same averaging. Figure 4 shows the result when a test signal was applied to a LEReC BPM where the envelope of the turn-by-turn data can be seen to change by ~40 µm as temperature is changing (top plot) by ~4°C due to air conditioner cycling in the equipment building. The average position (red trace) however remains almost unaffected.

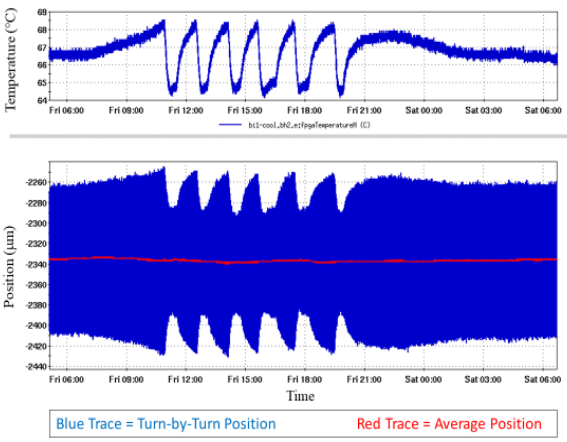

Figure 4: Drift over 24 hours due to temperature.

SWITCHING TRANSIENTS

One of the major issues presented by using FET solid-state switches to perform the channel switching is the presence of transients induced by the switches themselves each time they change state. This effect is also known as 'video feedthrough' and is an inherent effect of the FET device. There are other means of switching, such as using mechanical relays, that could be used as an alternative to solid-state devices, although there are other issues that these devices could present as well.

In this application, it was decided to deal with the transients produced by a mixture of filtering, averaging, and masking. The spectrum of these artifacts are broadband, but somewhat limited to frequencies below 100 MHz. Unfortunately, a long ‘tail’ of very low frequency was also evident that would not be able to be removed by the ~9 MHz low-pass filters used in one set of the electronics.

The ion bunch pattern of the RHIC accelerator includes an ‘abort gap’ of about 1 us duration where no beam signal is present. Since the electronics is usually timed to ignore samples acquired in this region, the timing of the switch control signal was adjusted such that the strongest part of the transient takes place within this gap. This alone prevented the strongest perturbations from affecting the position measurement.

In addition, a digital high-pass filter was implemented in the BPM electronics, centered around a 5 MHz cut-off frequency. This had the dual effect of both removing the low-frequency tail of the switch transient, and also removing other noise from sources in the accelerator complex.

Because of the high revolution frequency of the accelerator relative to the 1 Hz average measurement rate, the switching only needed to be performed about every 100 turns to still provide a stable signal when averaged down to a few Hz. This lower switching rate also had the benefit of reducing the overall impact of the transient on the running average, since the transient was only present for one out of every one hundred turns.

The combination of these techniques led to an almost complete removal of the transient effects of switching on the calculated BPM position.

CONCLUSION

The hardware required to realize the switching scheme described herein was relatively low in cost. The LEReC accelerator BPM system already had a requirement for amplifiers to be placed near the beamline, in order to improve the signal to noise ratio of the BPM signals at very low bunch intensity. A chassis and power supply were already necessary for these amplifiers, so adding the switching circuitry incurred a trivial cost.

Even in the case where there are no dynamic changes to the spectral content of the beam signal, BPM system designers usually strive to use well matched components in each of the sampling channels, especially in the filtering components. Procuring and testing these filters to verify their matching (usually in pairs) is a time consuming and sometimes a costly process. These costs of installing switching hardware should be compared to this in the sense that it relaxes the matching requirements for many of the circuit elements.

During the planning and design phase for LEReC, the idea of rapidly switching the BPM signals was extensively discussed [5]. This allowed ample time for experimentation and prototyping, which enabled us to develop a robust system and also allowed time to test the effects of both thermal drifts and signal shape on the position results, using simulated signals. It is sometimes difficult to determine the quality of BPM measurements in a real accelerator beam line, due to compounding uncertainties such as mechanical offsets, and dependence on data from other instrumentation systems about beam properties. Although many techniques such as beam based alignment can be used, the LEReC project had the unique quality that transverse cooling efficiency was closely related to the alignment of the interacting beams [1]. During the commissioning process of this experiment, it was shown that the switching of BPM signals was essential in providing the correct position measurements which then allowed transverse cooling to be optimized. The continual use of this technique then allowed long-term operational cooling [6] to take place over several months in order to achieve the RHIC low-energy experimental goals [7].

ACKNOWLEDGEMENTS

We thank Zach Sorrell for his excellent design work realizing the switching hardware. In addition, we are grateful for the steadfast support from Dmitry Kayran during the lengthy BPM commissioning efforts which spanned many shifts, and grateful of the overall project leadership provided by Alexei Fedotov that resulted in successful 3-D cooling of low energy ion beams [6].

REFERENCES

[1] S. Seletskiy *et al.*, “Obtaining transverse cooling with non-magnetized electron beam”, *Phys. Rev. Accel. Beams,* vol. 23, p. 110101, 2020.

[2] S. Seletskiy *et al.*, “Some Considerations about Switching BPM Channels”, BNL Report No. BNL-213694-2020-TECH, Feb. 2020.

[3] R. L. Hulsart, P. Cerniglia, N. M. Day, R. J. Michnoff, and Z. Sorrell, “A Versatile BPM Signal Processing System Based on the Xilinx Zynq SoC”, in *Proc. 5th Int. Beam Instrumentation Conf. (IBIC'16)*, Barcelona, Spain, Sep. 2016, pp. 646-649. `doi:10.18429/JACoW-IBIC2016-WEPG12`

[4] Z. Sorrell, P. Cerniglia, R. L. Hulsart, K. Mernick, and R. J. Michnoff, “Beam Position Monitors for LEReC”, in *Proc. 5th Int. Beam Instrumentation Conf. (IBIC'16)*, Barcelona, Spain, Sep. 2016, pp. 47-50. `doi:10.18429/JACoW-IBIC2016-MOPG08`

[5] P. Thieberger, “The LEReC BPM Challenges”, LEReC presentation, BNL, 2015.

[6] A. V. Fedotov *et al*, “Experimental Demonstration of Hadron Beam Cooling Using Radiofrequency Accelerated Electron Bunches”, *Phys. Rev. Lett.*, vol. 124, p. 084801, 2020.

[7] Grazyna Odyniec for the STAR Collaboration, “Beam Energy Scan Program at RHIC (BES I & BES II)”, `https://indico.cern.ch/event/760216/contributions/3153661/attachments/1721648/2779745/Odyniec_Corfu-2018.pdf`

RESEARCH ON RESOLUTION OF ORBIT BASED ON CLUSTERING ANALYSIS AND BP NETURAL NETWORK IN SSRF*

R. T. Jiang[†], N. Zhang, Y. M. Deng, Y. B.Leng[‡]
Shanghai Advanced Research Institute, Chinese Academy of Sciences, Shanghai, China

Abstract

Keeping the beam current's normal motion is an important mission for Shanghai Synchrotron Radiation Facility (SSRF). So the Orbit (rms)x/y is an main parameter for SSRF's running. However, the orbital resolution has been constrained by the accuracy of acquired data. To eliminate BPM's failure causing the inaccurate orbital resolution, the work based on clustering analysis and BP neural network to removed the abnormal BPM and recalculate the resolution of orbit. Experiment data came from the machine research. The analysis results showed that the rms value of orbit was 100.75 µm (x direction) and 14.9 µm (y direction) using all BPM's data but the recalculate value was 98.03 µm (x direction) and 2.6 µm (y direction) when eliminated the data of faulty BPM. The analysis result indicated that the method can optimize the resolution of orbit and next work is further to evaluate the orbital resolution with more operation data.

INTRODUCTION

The storage ring in SSRF is equipped with different machine parts located at 20 cells of the storage ring to monitor the beam dynamics [1]. Due to the accidental error of machine parts and the collimation error of each magnet, particles usually deviate from ideal orbit to form orbit and it can result in machine performance degradation or even failure. Good orbit is the foundation of accelerator operation, and orbit correction is the most basic of current accelerator beam adjustment. And it is also one of the most widely studied fields at present. As a beam monitoring system, the BPMs at the beam lines after the insertion devices (ID) or the bending magnets are also of great importance, because they also serve as the orbit feedback system to ensure stability of the electron Beams [2]. Meanwhile, the BPM confidence levels included in the feedback system can be used to estimate stability of the beam dynamics. The BPMs can monitor the stability of beam Orbit. Therefore, an abnormal BPM should be found and treated to avoid the deviation calculation for beam orbit.

A typical BPM system consists of the probe (button-type or stripline-type), electronics (Libra Electronics/ Brilliance in SSRF) and transferring component (cables and such). Ever since the SSRF commissioning in 2009, the BPM have occurred all kinds of malfunction. They were permanently damage of individual probe or corre-sponding cable, misaligned (position/angle) probes, high-frequency vibrations, electronics noise, and others. These faults mean totally useless of the signals from the BPM, which should be ignored until its replacement or repair. Hence, it is essential to find an effective method to detect the faulty BPM and revise the beam orbit.

With development in machine learning methods, a series of powerful analysis approaches make it possible for detecting beam position monitor's stability. Cluster analysis is one of machine learning methods. It is aimed at classifying elements into categories on the basis of their similarity [3]. Its applications range from astronomy to bioinformatics, bibliometric, and pattern recognition. Clustering by fast search and find of density peaks is an approach based on the idea that cluster centres are characterized by a higher density than their neighbours and by a relatively large distance from points with higher densities [4]. This idea forms the basis of a clustering procedure in which the number of clusters arises intuitively, outliers are automatically spotted and excluded from the analysis, and clusters are recognized regardless of their shape and of the dimensionality of the space in which they are embedded. In addition to, it is able to detect non-spherical clusters and to automatically find the correct number of clusters.

Based on the advantage of clustering by fast search and find of density peaks, this study located and removed the faulty BPM at SSRF. Through we removed the faulty BPMs, considering the beam integrity, the research work used the BP netural network to fit the beam position in all BPM's data (the removed BPMs's collected data were replaced the fitted data).

EXPERIMENTAL DATA AND ANALYSIS METHOD

Experimental Data and Acquisition System

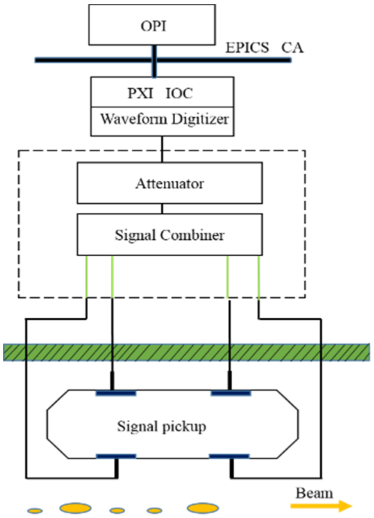

Figure 1: Acquisition system layout.

---

* Work supported by National Nature Science Foundation of China (No.11375255)

[†] jiangruitao@sinap.ac.cn
[‡] lengyongbin@sinap.ac.cn

In this study, the experimental data were collected from the BPM turn-by-turn (TBT) data. The acquisition system was shown in the Fig.1. By analysing the raw data, the study work extracted the data of of X and Y direction to research the resolution of beam orbit.

Multi-Dimensional Clustering Analysis Model and BP Netural Work

In this work, a multi-dimensional clustering analysis model was established. The created model based an assumption that cluster centres should be surrounded by neighbour points with lower local density and that they are at a relatively large distance from any points with a higher local density. For each data point i, it was computed two quantities: its local density ρi and its distance δi from points of higher density. Both these quantities depend only on the distances dij between data points, which are assumed to satisfy the triangular inequality. The local density ρi of data point i is defined as

$$\rho_i = \sum_j \chi(d_{ij} - d_c) \tag{1}$$

where χ (x) =1 if x < 0 and χ (x)=0 otherwise, and d_c is a cutoff distance. Basically, ρ_i is equal to the number of points that are closer than d_c to point *i*. The algorithm is sensitive only to the relative magnitude of ρ_i in different points, implying that, for large data sets, the results of the analysis are robust with respect to the choice of d_c. In this paper, the d_c is 0.02. On the other hand, δ_i is measured by computing the minimum distance between the point *i* and any other point with higher density:

$$\delta_i = \min_{j:\rho_j > \rho_i} (d_{ij}) \tag{2}$$

For the point with highest density, we conventionally take $\delta_i = \max_j (d_{ij})$. Note that δ_i is much larger than the typical nearest neighbour distance only for points that are local or global maxima in the density. Thus, cluster centres are recognized as points for which the value of δi is anomalously large. Generally, the value of δi and ρi represent whether the point is cluster centre, the typical characteristic of cluster centre is the value of δi and ρi are larger. Decision graph could depict the value of δ_i and ρi and show which points are cluster centre. By the multi-dimensional clustering analysis model, the study removed the faulty BPMs. Meanwhile, the work used the BP netural networks to fit the beam position in all BPM's data.

RESULTS AND DISCUSSION

To Verify the Effectiveness of Multi-Dimensional Clustering Analysis Model

The BPM's data has been acquired from the average signal of 140 ID* 3000 turns. The scatter diagram was shown in the Fig. 2. It could see that most of BPM are in together, means that BPMs acquisition signals are normal. The rest scattered were around the big group but the 75# and 68# BPM are away from the big group. Theoretically, the farther away the normalization value 1 for the transverse oscillation, the more easily anomaly for those BPMs. 75# and 68# BPMs may be the malfunction of BPMs, because they are far away the big group.

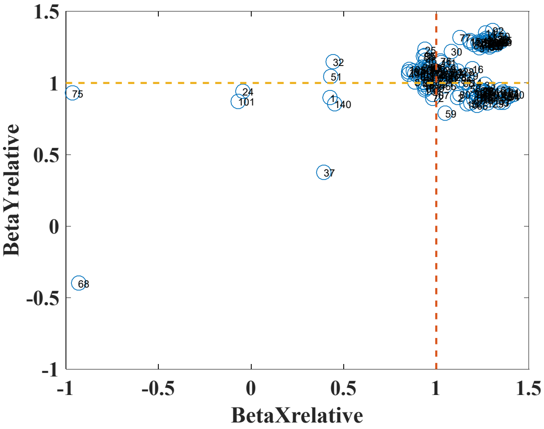

Figure 2: Scatter diagram based on β oscillation of X and Y direction.

The study use multi-dimensional clustering analysis model to analysis the beam running data to judge the working performance of all BPMs. Theoretically, when beam position monitors are isolated and away from group, they are probability faulty beam position monitors which faulty BPM corresponds to the smaller ρ and the larger δ. Base on the nature idea, the work calculated the decision graph that could show which BPM is the cluster centre and which is isolated. On the math, cluster center should be those surrounded by other point with lower local density ρi and they are at a relatively large distance from any points with a higher local density. The decision graph was shown in Fig. 3. The 68# and 75# has a relatively high δ and relatively low ρ, it can be considered as cluster which was composed of a single point (isolated), namely, meaning a faulty BPM. From the analysis results, in Fig. 4, most of BPMs are gather together; through it included three small group.

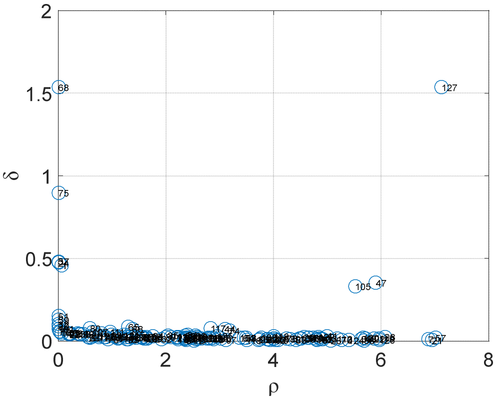

Figure 3: Decision graph.

ISBN: 978-3-95450-230-1 ISSN: 2673-5350 doi:10.18429/JACoW-IBIC2021-MOPP21

Through the above analysis, the multi-dimensional clustering analysis model could classify all BPMs with the input variable are β oscillation of X and Y directions. The abnormal and performs worse BPMs could be separated. The other BPMs were be classified into three small group.

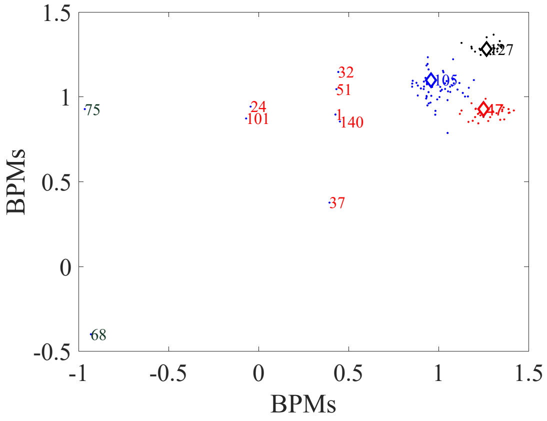

Figure 4: Clustering analysis results.

To Removed the Faulty BPMs and Refit the Beam Orbit

Based on the acquired data, the rms value of orbit is 100.75 µm (x direction) and 14.9 µm (y direction) using all BPM's data. Through the clustering analysis, the 75# and 68# were broken and the 24#, 32#, 1#,37#, 51# and 101# BPM were worse performance BPMs. So we remove these BPMs to recalculate the beam orbit. The BP netural network [5] were be used to fit the removed BPMs.

The result showed that the rms value of orbit is 98.03 µm (x direction) and 2.6 µm (y direction) in the Fig. 5 and Fig. 6. And the R value are 0.99421 and 0.9681, respectively. The analysis result indicated that the method can optimize the resolution of beam orbit and next work is further to evaluate the orbital resolution with more operation data.

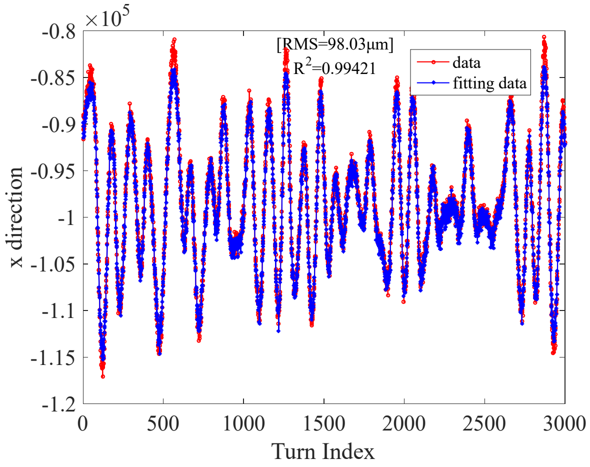

Figure 5: The beam orbit of X direction.

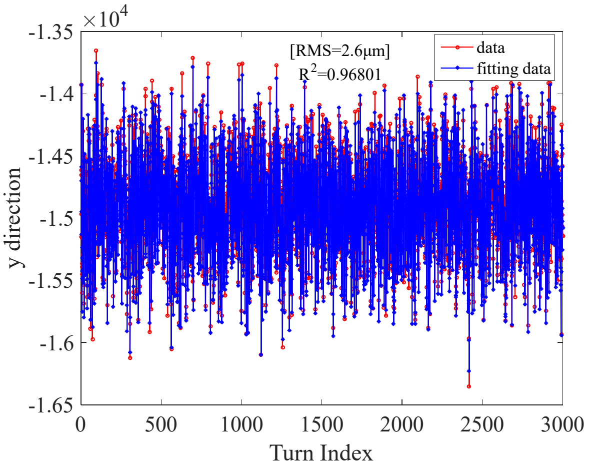

Figure 6: The beam orbit of Y direction.

CONCLUSION

As a user facility, beam stability is of utmost importance and high priority. High beam stability is one of the most fundamental processes used for beam control in accelerators. Improving its orbit stability can optimize the performance of the accelerator and promote the experimental output in machine research time. This work made use of the characteristics of many channels and large amount of data for the beam measuring system, develop a new method based on clustering analysis and BP netural network, explore the feasibility of the application in keeping the beam orbit stability.

The experimental results demonstrate that the proposed cluster analysis method could capture the faulty BPMs. Especially, the decision graph could be find more key information about BPMs. Meanwhile, the analysis results demonstrate the rms value of orbit is 98.03 µm (x direction) and 2.6 µm (y direction). The real beam orbit were corrected. But the validity needs more numbers to back it up.

REFERENCES

[1] Leng Y B *et al.*, "Beam position monitor system for SSRF storage ring", *Nucl Sci Tech*, vol. 33, no. 6, pp. 401–404, 2012

[2] Cheng Z C *et al.*, "Performance evaluation of BPM system in SSRF using PCA method", *Chin. Phys. C*, vol. 38, no. 6, pp. 112-116, 2014.

[3] P. O. Brown *et al.*, "Cluster analysis", *Qual. Quant.*, vol. 14, no. 1, pp. 75-100, 1980.

[4] Rodriguez *et al.*, "Clustering by fast search and find of density peaks", *Science*, vol. 344, no. 6191, p. 1492, 2014.

[5] A.L. Edelen *et al.*, "Neural networks for modeling and control of particle accelerators", *IEEE Trans. Nucl. Sci.*, vol. 63, no. 2, pp. 878–897, 2016.

ISBN: 978-3-95450-230-1 ISSN: 2673-5350 doi:10.18429/JACoW-IBIC2021-MOPP22

SIGNAL ANALYSIS AND DETECTION FOR THE BPMs OF THE LHC HOLLOW ELECTRON LENS

G. Bantemits, M. Gasior, A. Rossi, M. Wendt, CERN, Geneva, Switzerland

Abstract

The Large Hadron Collider (LHC) at CERN will be equipped with two hollow electron lenses (HEL) for the high luminosity upgrade, which allow for scraping of the LHC proton or ion beams transverse tails by overlapping a coaxial hollow electron beam over a 3 m length. A precise alignment of the two beams is essential for the HEL functionality, the bunched LHC hadron beam of up to 7 TeV beam energy, and the non-relativistic, DC-like electron hollow beam of 10 keV energy. The absolute and relative transverse positions of both beams will be monitored by two stripline beam position monitors (BPM), located in the HEL, and the pickup signal processed by a narrowband signal detection system. This paper summarizes the analysis of the expected proton and electron beam signals, including laboratory measurements, with aim of a narrowband diode-detection read-out electronics as BPM signal processor.

INTRODUCTION

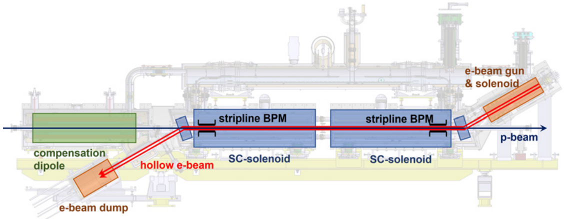

Figure 1: Sketch of the HL-LHC hollow electron lens (HEL).

A high-luminosity LHC upgrade project (HL-LHC) is in progress at CERN [1], with the goal to boost the yearly integrated luminosity from presently 50–65 fb^{-1} to > 250 fb^{-1} at the two collision experiments ATLAS and CMS. Among the many changes and improvements required, a new particle collimation strategy was developed to enhance the transverse beam halo depletion, which includes the use of a hollow electron lens (HEL) for each of the two circulating hadron beams [2]. It utilizes a "non-material" hollow electron beam scraper, placed coaxially around the proton beam, to increase the diffusion rate of protons or ions with large emittance. Figure 1 shows the schematic of the approximately 6-meter-long HEL system in a sectional view, which consists of a thermionic electron beam gun, accelerating a hollow electron beam of up to 5 A current to approximately 12 keV beam energy, before being bent onto the LHC proton beam orbit. The beam is controlled by two main superconducting solenoid magnets and a set of auxiliary solenoids and steering magnets, before being bent downwards to a beam dump. Inside the 120 mm warm bore of each superconducting solenoid, a beam position monitor (BPM) pickup with four symmetrically arranged electrodes is located. The horizontal and the vertical pairs of stripline electrodes of 400 mm length are used to monitor the beam position of both beams, i.e.the hollow electron beam and the counter-propagating proton beam, each detected separately at the upstream ends of the electrodes by a high-resolution BPM signal processor, enabling a precise relative alignment of both beams.

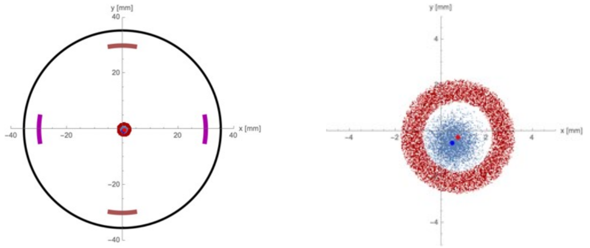

(a) (b)

Figure 2: Hollow electron beam position measurement with a BPM pickup (left), proton and hollow electron beam close-up (right).

Figure 2 (left) gives an idea of the BPM pickup of 60 mm diameter aperture in a cross-section view, indicating the beam pipe and the stripline electrodes, as well as both beams near the center. Figure 2 (right) illustrates a close-up cross-section view of the proton and the hollow electron beam in a non-optimized beam position, both beams should be perfectly centered to each other. Also indicated are their center-of-charges, by a blue dot (for the proton beam) and a red dot (for the hollow electron beam), as they would be monitored by the proposed BPM system. The proton and hollow electron beams to be detected have very different beam formats, see Table 1.

Table 1: Proton and Hollow Electron Beam Specifications

	Time structure	**Beam charge /current**	**Relativistic factor β**	**Transverse size**
Proton beam	2760 bunches ~ 1 ns (4σ)	$1 - 2.3e^{11}$ p/b	1	$\sigma_x \approx \sigma_y$ ≈ 0.3 – 1.2 mm
Hollow electron beam	"DC-like" 1.2 – 86 µs pulse duration	0.1 – 5 A	0.2 – 0.24	Inner diameter ≈ 2 – 8 mm Outer diameter ≈ 4 – 16 mm

Figure 3 illustrates the situation of the two beams at the location of the HEL stripline BPM in a longitudinal section view. Let's name the two symmetric stripline electrodes "A" and "B", either the horizontal, or the vertical pair of electrodes. With the help of a signal pre-processing scheme,

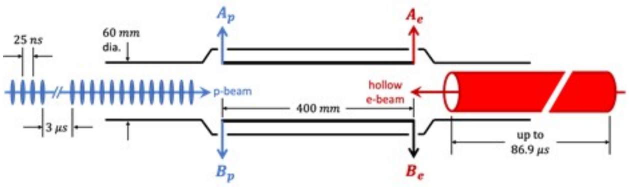

Figure 3: HEL beam position monitor.

it will be always the upstream electrode pair which senses the relevant beam type, indicated by the index “p” for the proton or ion beam and “e” for the hollow electron beam.

THE HEL STRIPLINE BPM PICKUP

While the final HEL BPM requires a 60 mm diameter beam pipe aperture, we use an existing larger model of 81 mm aperture for our test bench measurement, and for the initial beam test at the HEL test stand as well. This stripline type BPM pickup is equipped with four electrodes of 400 mm length, two per plane, each precisely tuned to a 50 Ω characteristic impedance. Each stripline covers a 0.307 rad azimuthal width, corresponding to a 17^0 covering angle.

For the RF characterization of the BPM a coaxial test setup was manufactured, which enables RF measurements over a wide range of frequencies. The particle beam is “replaced” by a tapered, coaxial center conductor of constant 50 Ω characteristic impedance, see Fig. 4. This bench setup will provide a TEM field configuration, similar to that of a particle beam travelling at a relativistic velocity near c.

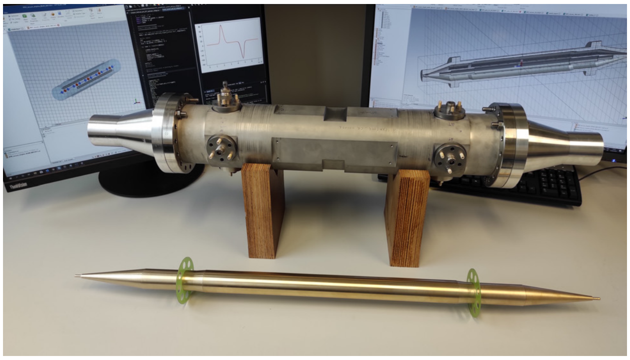

Figure 4: The stripline BPM between a tapered coaxial test bench structure with the inner and outer conductor.

Regarding the symmetry of this coaxial BPM test bench setup, we characterized the transfer impedance of 1-of-4 striplines w.r.t. the coaxial “beam” input, with the help of a vector network analyzer (VNA). Figure 5 (a) shows the magnitude response of the beam-to-electrode transfer function of the upstream (port 2: |S21(f)|) and of the downstream (port 3: |S31(f)|) stripline electrode w.r.t. the stimulus signal connected to the coaxial “beam” port, i.e. port 1. All unused ports of the setup have been terminated in their characteristic impedance. The S21 measurement depicted in Fig. 5 (a) matches the analytical analysis very well.

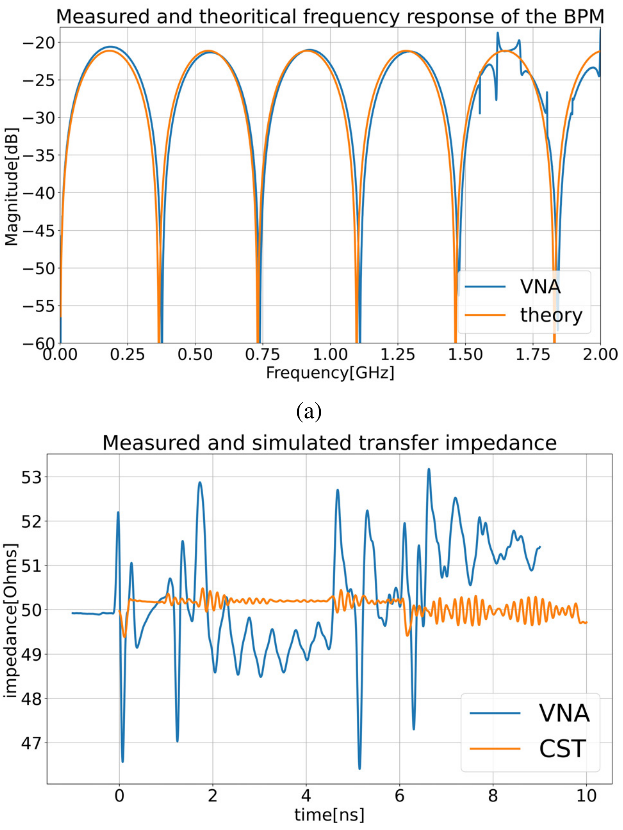

(a)

(b)

Figure 5: (a) The frequency response of the BPM stripline electrode, upstream port (S21) from measurement (VNA) and theory, and downstream port (S31). (b) Measured / simulated TDR of the BPM test bench setup.

We also verified the characteristic impedance of the coaxial setup using the time-domain reflectometry (TDR) option of the VNA. Figure 5 (b) compares the VNA-based TDR measurement with a numerical analysis performed with the commercial *CST Studio Suite software* [3]. While the agreement is not perfect, the 50 Ω characteristic impedance is still well-matched within ±5 % over the entire length of the coaxial line.

BPM SIGNAL ANALYSIS

The hollow electron lens BPM should measure the center of charge of both beams, separately for the proton and for the electron beam, and independently of their individual beam formats. As a first step, we analyse the expected beam signal from the BPM pickup electrodes:

Proton Signal Analysis

Up to 2760 proton beam bunches are circulating in the LHC at a relativistic velocity $\beta = v/c \approx 1$, with a spacing of ∼ 7.5 m ≡ 25 ns between them, see also Table 1. The up to 2.3×10^{11} protons (≡ 36.8 nC) within each bunch have an approximate Gaussian longitudinal distribution, with $\sigma_t \approx 250$ ps. In case of lead-ion beams, the bunch intensity is much lower, $\sim 5 \times 10^{10}\ Pb^{82+}$, also the ion bunches tend to be a little longer. For the measurements in the laboratory those values had to be limited to a bunch length equivalent of $\sigma_t \approx 420$ ps, and a maximum bunch intensity of 0.084 nC, by the maximum ratings of our available pulse signal source generator, see also Fig. 6 (a). This Gaussian-like, proton bunch equivalent pulse signal is fed into the coaxial BPM test bench setup, while the response signals produced at the upstream and downstream ports of one of the BPM stripline electrodes are measured with a broadband oscilloscope. Figure 6 summarizes the proton signal analysis, (a) shows the proton bunch equivalent voltage input signal, terminated with 50 Ω, (b) the time-domain voltage output signal at the upstream and downstream ports of the stripline electrode and (c) the simulated transfer-function frequency domain characterization |S21(f)| for both, the upstream and the downstream port. The time-domain measurements Fig. 6(a) and (b) have been compared with analytical estimations (theory), and with numerical simulations (CST), demonstrating a good agreement. Please note, for $\beta \approx 1$ the stripline electrode acts as a TEM directional coupler, and therefore any remaining signal at the downstream port is an unwanted error signal due to non-TEM field effects. From the measurements we can estimate the directivity as $v_{up}/v_{down} \approx 15 \equiv 24$ dB, which is also observed in the frequency-domain VNA analysis, Fig. 6(c).

Electron Signal Analysis

The electron gun of the hollow electron lens will produce a circular electron beam of approximately 10 keV energy, which corresponds to a relativistic velocity of $\beta = 0.2$, see also Table 1 [2]. The longitudinal distribution of the electrons is assumed to be uniform and correspond to a constant DC beam current with 5 A maximum. The extraction voltage between cathode and anode in the gun can be varied, with rise and fall times of ~ 200 ns, which allows to switch on-off the hollow electron beam during the 3 µs abort gap of the LHC hadron beam (see Fig. 3), or in the kicker-gap between batches. Therefore, the maximum duration of the hollow electron beam is 86.9 µs, while the repetition rate is equivalent to the LHC revolution time of 88.9 µs. Like for the proton signal analysis, the laboratory equipment limits the electron beam intensity to equivalent 0.1 A maximum (DC). Figure 7 (a) shows the inverted time-domain signal with 200 ns rise/fall times. Figure 7 (b) shows the corresponding output signal at the upstream stripline port w.r.t. the electron beam, which is basically a differentiated waveform of the input signal, Fig. 7 (a), as the stripline acts as capacitive coupled RC high-pass filter for these low frequencies (with $R = 50\ \Omega$).

The coaxial, air-transmission-line BPM test bench (Fig. 4) will always excite a Transverse Electro-Magnetic (TEM) field pattern with a signal velocity $\beta = 1$, also for the hollow electron beam equivalent current signal shown in Fig. 7 (a). However, the effects of the non-relativistic beam velocity of $\beta = 0.2$ on the output signals of the stripline was investigated through simulations with the “Particle-In-Cell” solver of CST. Figure 8 shows the result as magnitude spectrum in the frequency-domain of the stripline electrode output signal, which is the upstream port for the low-beta electron beam. Also shown in Fig. 8 is the residual error signal from the proton bunches (downstream proton port) due to the limited directivity of the striplines, see also Fig. 6 (c) (orange trace). To resolve this interference a frequency discrimination around ~ 15 MHz seems to be a viable option.

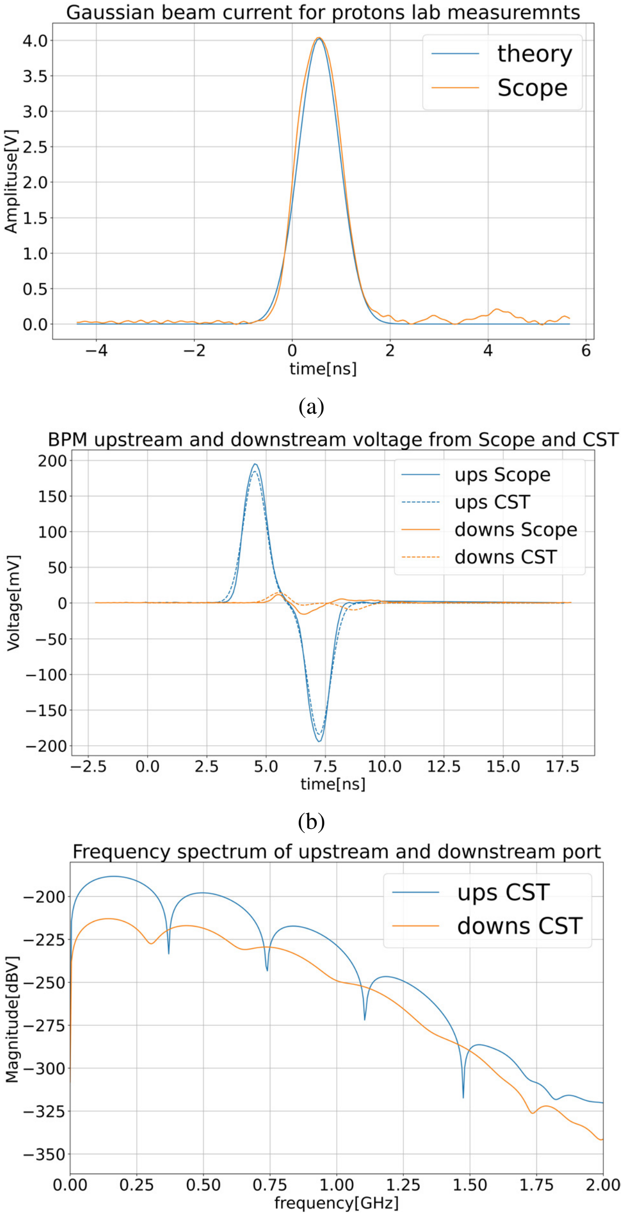

(a)

(b)

(c)

Figure 6: (a) Proton bunch signal, time-domain. (b) Stripline BPM response, TD, upstream and downstream ports (c) Stripline BPM response, FD, upstream and downstream ports.

ISBN: 978-3-95450-230-1 ISSN: 2673-5350 doi:10.18429/JACoW-IBIC2021-MOPP22

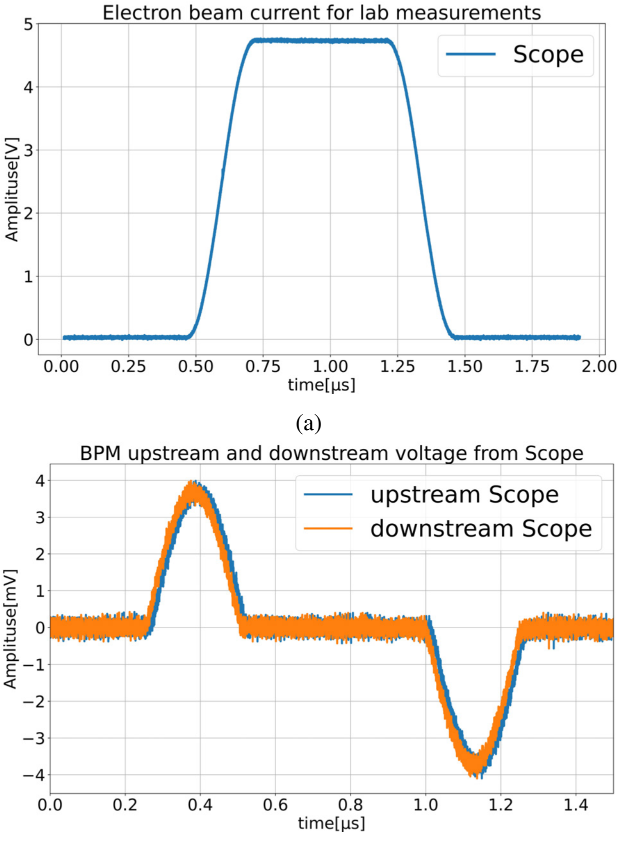

(a)

(b)

Figure 7: (a) Electron beam current for lab measurements and (b) measured output voltage at the upstream BPM port.

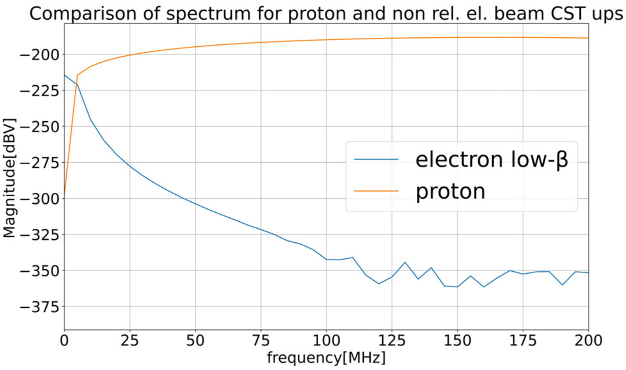

Figure 8: Frequency-domain magnitude spectrum for the low-beta electron beam signal, and the residual proton beam error signal.

Signal Detection and Frequency Discrimination

The proposed BPM signal processing for both beam signals is based on a time-domain signal peak detection scheme. This requires the time domain signals for the stripline electron ports A_e to be error free of the convoluted residual proton signal content, and vice versa the time domain signal on the proton ports A_p to ensure a pure proton signal without electron signal content. On the proton port A_p the residual electron signal, even with the maximum electron beam intensity of 5 A (DC), will have a peak value < 1 V calculated from simulations. In the same port the proton or ion signal with the minimum bunch charge of 5×10^{10} cpb will have a peak value of~ 15 V that is adequate to ensure a correct proton / ion signal measurement by the peak detection scheme. On the electron port A_e the maximum peak value of electron signal will be the same <1 V while the maximum residual proton signal on this port can reach ~ 6 V indicating the necessity of an additional signal pre-processing scheme that will suppress the higher proton peak value. Thus, a third order low pass non reflective filter with a cut-off frequency of 13.3 MHz (see Figure 8) was designed, which rejects the high frequency proton signal content and allows our peak detection scheme to detect the pure electron beam peak values.

BPM MEASUREMENT RESULTS

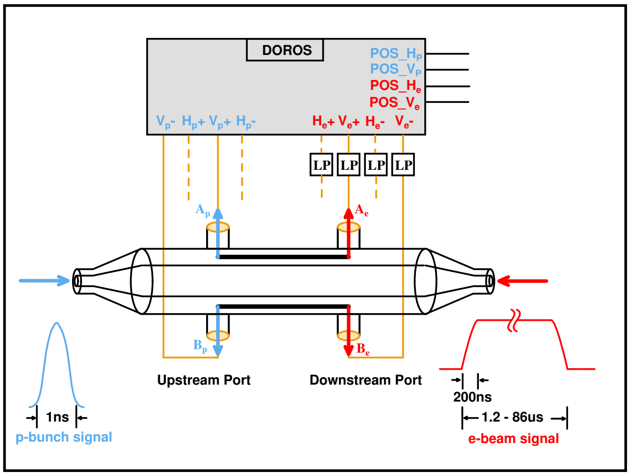

Figure 9: BPM measurement setup schematic.

The proposed architecture of the read-out front-end electronics for the BPM signals is sketched in Fig. 9. For our test in the laboratory, we used the stripline BPM test bench as shown in Fig. 4 and applied the electron and proton beam signals discussed in the previous section - simultaneously on both inputs, in counter-propagating manner, delivered by two synchronized pulse generators, however, with approximately 250× (protons) / 50× (electrons) lower intensity compared to the nominal proton / electron beam intensity. The BPM pickup signals from the upstream ports (w.r.t. the protons) are fed to 4 (out of 8) channels of the narrowband diode-detection read-out electronics system called DOROS[4]. The DOROS BPM signal processor detects the four peak signal levels and calculates the position of the bunched beam for the horizontal and vertical plane w.r.t. the center of the BPM. The four downstream BPM ports w.r.t. the protons, i.e., the electron signal upstream ports, are passed through a 3rd order, non-reflective low-pass filter with 13.3 MHz cut-off frequency, and then fed to the other four read-out channels of the same DOROS system. Figure 10 (a) and (b) summarizes the position measurement results for two different, 12-hour long laboratory measurement runs using our BPM test bench setup, performing one measurement per second. The mean value has been deducted from the original measurements for better visualization and comparison of the long-term drift effects. Both, the mean value and the variance of the measured data are displayed in the plots of Fig. 10 (a) and (b). The lower peak values of the electron signals result in a lower resolution, which is still < 0.15 µm. The long-term drift effects of the non-temperature stabilized BPM read-out electronics are ~ 1.5 µm, and fulfill the requirements of the HEL beam alignment during typical LHC luminosity runs.

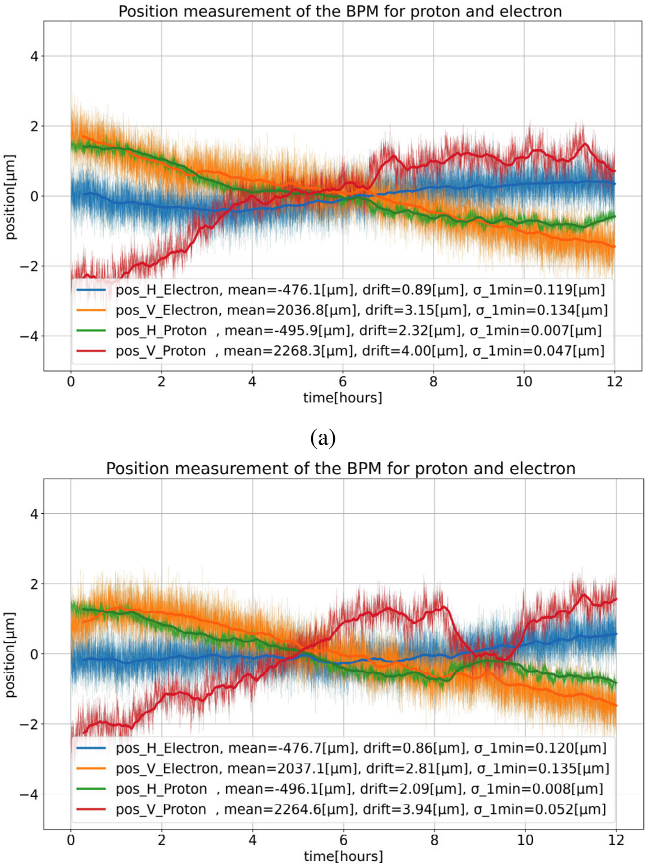

(a)

(b)

Figure 10: 12-hour long HEL BPM laboratory measurements with simulated beam signals.

CONCLUSION

A BPM measurement setup, developed to simultaneously measure the center of charge position of both, a quasi-DC, low-beta hollow electron beam and bunched hadron beam travelling at a relativistic velocity is presented. Numerical simulations and laboratory measurements demonstrate the feasibility of the system composed out of well-known components, a stripline-BPM pickup, low-pass filters, and a peak-detector signal processing system to fulfil the requirements for the beam alignment in the hollow electron lens of the HL-LHC.

REFERENCES

[1] I. Béjar Alonso, O. Brüning, P. Fessia, M. Lamont, L. Rossi, L. Tavian, M. Zerlauth, “High-Luminosity Large Hadron Collider (HL-LHC), Technical design report”, CERN, Geneva, Switzerland, CERN-2020-010, 2020. doi:10.23731/CYRM-2020-0010

[2] S. Redaelli *et al.*, “Hollow electron lenses for beam collimation at the High-Luminosity Large Hadron Collider (HL-LHC)”, *Journal of Instrumentation*, vol. 16, p. P03042, Mar. 2021. doi:10.1088/1748-0221/16/03/P03042

[3] see web site, http://www.cst.com

[4] M. Gasior, G. Baud, J. Olexa, and G. Valentino, “First Operational Experience with the LHC Diode ORbit and OScillation (DOROS) System”, in *Proc. 5th Int. Beam Instrumentation Conf. (IBIC'16)*, Barcelona, Spain, Sep. 2016, pp. 43–46. doi:10.18429/JACoW-IBIC2016-MOPG07

ISBN: 978-3-95450-230-1 ISSN: 2673-5350 doi:10.18429/JACoW-IBIC2021-MOPP23

COMMISSIONING OF ALPS, THE NEW BEAM POSITION MONITOR SYSTEM OF CERN'S SUPER PROTON SYNCHROTRON

A. Boccardi*, J. Albertone, M. Barros Marin, T. Bogey, V. Kain, K.S.B. Li,
P. A. Malinowska[1], A. Topaloudis, M. Wendt, CERN, Geneva, Switzerland
[1]also at AGH University of Science and Technology, Kraków, Poland

Abstract

The Super Proton Synchrotron (SPS) is both the final machine in the pre-accelerator chain of the Large Hadron Collider (LHC) at CERN and a machine providing several fixed target experiments with proton and ion beams. In the framework of CERN's LHC Injectors Upgrade (LIU) project, aimed at improving the performances of the pre-accelerators in view of the high-luminosity upgrade of the LHC, the Beam Position Monitor (BPM) system of the SPS was redesigned during Run 2 of the LHC and deployed during the subsequent Long Shutdown 2 (LS2). This new system is called ALPS (A Logarithmic Position System) and acquires the signals from some 240 BPMs. It is designed to improve the system's reliability and reduce the required maintenance with respect to its predecessor. During the restart of the SPS in 2021, the BPM system was a key element of the fast recommissioning of the machine, proving the validity of the chosen design approach and pre-beam commissioning strategy. This paper aims to illustrate the design choices made for ALPS, the strategy for commissioning it with beam in parallel with the machine restart, the commissioning procedure and the results obtained.

INTRODUCTION TO ALPS

The Super Proton Synchrotron (SPS) is the second largest accelerator in the CERN complex. It can accelerate both proton and ion beams to fill the Large Hadron Collider (LHC) but also provides beams to several fixed target experiments. The beams accelerated by the SPS may vary in bunch intensity from 5E8 up to 5E11 protons per bunch, but also in bunch spacing, from single bunch to trains spaced from 5 ns to 75 ns. Table 1 summarises the beam types accelerated in the SPS.

The majority of the pick-ups in the SPS are of the shoeboxe type, with very low sensitivity: 0.1 dB/mm and 0.2 dB/mm respectively for the horizontal and the vertical planes. Because of the limited BPM sensitivity, the system needs to cover the 70 dB dynamic range, mostly deriving from intensity (see Table 1), with an expected resolution in the order of 0.01 dB, corresponding to about 100 µm. ALPS (A Logarithmic Position System) uses logarithmic amplifiers to compress the dynamic range, as described in details in [1]. The chosen amplifiers have a dynamic range of about 40 dB, in which processing errors are acceptable for the system requirements. In order to cover the full 70 dB required, the electrode signal is split in 3 channels with different sensitivity ranges, each separated by about 15 dB [1]. The 3 channels are acquired in parallel and the online processing algorithm automatically selects the ranges which can be used for position calculation.

The logarithmic amplifiers only approximate the logarithm function, and the error function is specific for each amplifier. The mismatch between the error functions in the different channels, as well as the integral error, need to be compensated for in the processing chain to achieve a precision compatible with the target resolution, otherwise they would lead to position- and intensity-dependent systematic errors. This is achieved with a correction polynomial applied in the online processing chain, and computed from calibration measurements performed in the lab on each amplifier. Figure 1 illustrates the residual integral error of the measured power at the input of the front-end after the calibration. ALPS' front-end electronics, both analogue and digital, is indeed installed in the SPS tunnel and exposed to radiation but no digital processing is performed there after digitisation: the digitised signals are directly transmitted to the surface via optical fibres after packaging and serialisation. The front-end as a whole, as well as each of its active components individually, was qualified for radiation with the help of CERN's Radiation to Electronics (R2E) working group and, whenever possible, radiation-tolerant by design ASICs designed by the CERN PH-ESE group were used. As a result, the front-end electronics, installed in small crates located under the beamline itself, is expected to properly operate, i.e. without significant drifts, up to an integrated dose of 750 Gy [2].

The use of radiation-tolerant front-end electronics, with digitisation in the tunnel and optical transmission, eliminated the need for the long cables used in the previous system. Those cables were the main reason for maintenance interventions: due to the low sensitivity of the pick-ups, even small drifts in the cable characteristics had to be measured and compensated for between each run.

Table 1: SPS Beam Types

Spacing	Charges per bunch MAX	Charges per bunch MIN
5 ns	5e10	5e8
25 ns	3e11	1e9
50 ns	3e11	1e9
75 ns	3e11	1e9
single bunch	5e11	1e9

---

* andrea.boccardi@cern.ch

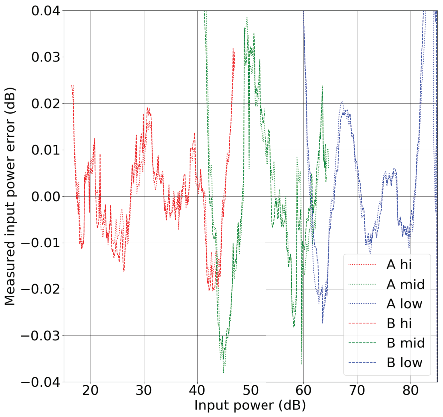

Figure 1: Plot of the residual error on the power level estimation at the input of one of the front-ends after applying the correction polynomials. In the plot, the different sensitivity ranges are depicted in different colours and the result for each of the electrodes is shown with a different line style. The horizontal axis is in dB with an arbitrary offset. It can be observed how the traces for the 2 electrodes overlap, and the absolute error is kept below 0.03dB.

COMMISSIONING CHALLENGES

The SPS was recommissioned in 2021 after a large upgrade program in which several operation-critical systems were totally replaced, including the accelerating radiofrequency system (RF). The BPM system is fundamental for the commissioning of an accelerator from day one: to thread the beam around the machine, to establish a first closed orbit and to perform the first beam-optic checks. For this reason, several of the ALPS acquisition modes were expected to work reliably from first injection. This was possible thanks to an extensive and successful dry run programme organised in collaboration with the SPS operation crew (SPS-OP). This improved not only the readiness of the system, but also SPS-OP's confidence in a system with which they were familiar before the first beam.

INSTALLATION, TEST AND DRY COMMISSIONING

The SPS has ~240 BPMs connected to the ALPS acquisition system. While the front-end electronics is distributed all along the ring, the back-end electronics is grouped in 6 surface buildings called BAs, each serving a sextant of the SPS. The basic building block of the back-end electronics is a VME [3] board called VME FMC Carrier (VFC), which is the standard readout board of CERN's Beam Instrumentation group (SY-BI) [4]. These boards are equipped with a Field Programmable Gate Array (FPGA) in which the samples coming from the front-end are processed in real time to obtain a pseudo position. The transfer function of the specific BPM being read out is required to translate this value, expressed as the difference between the signal amplitudes from 2 opposite electrodes, into an actual position. This operation is performed in software in a PC installed in the same VME crate as the VFCs.

Synchronisation with the machine cycle and events is achieved via the general machine timing (GMT), which is distributed to each VME PC, and the beam synchronous timing (BST), which is distributed to each VFC and embeds the revolution frequency and various triggers in a digital frame.

Each VFC receives the data from 4 front-ends and each crate is equipped with up to 10 VFCs for a total of up to 40 BPMs, covering the needs of a full sextant.

The first BA installation was finalised at the end of 2019, while the remaining 5 were completed and tested in the first half of 2020.

ALPS has several acquisition modes and processes and each of them had to be commissioned:

- **FIFO**: When this mode is activated, any valid position sample detected by the system is stored in a memory with 64 locations. This mode does not depend on timing and is therefore the main tool for the commissioning of the accelerator when the RF is not yet operational.
- **Injection trajectory**: This mode stores the position of each injected train of bunches, considered as a unit (i.e. no bunch-by-bunch information), for the first 64 turns.
- **Capture trajectory**: This mode stores the position of a selected group of bunches, considered as a unit for 1000 turns after it is triggered.
- **Global orbit**: This mode publishes the position of all the bunches averaged over 1 ms.
- **Synchronous orbit**: This mode implements the same logic as the global orbit, but the average is performed only on a selected group of bunches and therefore needs to be synchronised with the revolution frequency.
- **Snapshot**: This mode stores the raw ADC signals, their processed version, and most of the control and synchronisation signals while preserving their relative timings. It is used to measure and compensate for the delay resulting from the different cable lengths and the time of fly of the beam.
- **Trajectory interlock process**: This is not strictly an acquisition mode, but rather a process running in parallel that identifies possible beam instability by monitoring each position sample. If the process identifies a possible instability, the beam is dumped and several buffers intended to identify the beam behaviour that triggered the dump are stored for further analysis.
- **Orbit interlock process**: This is a software check running on the VME PC that monitors the orbit in the location where an extraction bump is prepared. If the orbit is not measured at the expected level after the bump has been prepared, the extraction kicker is not allowed to charge. The same test is performed a few ms before firing the kicker for a final validation. If either of the 2 checks fails, the extraction is not permitted and the beam is sent to the dump line instead.

Each of these modes was tested in the lab to verify the basic functionalities, but as soon as the first BA installation (including the associated front-end electronics) was complete, the tests were performed using the actual system and its embedded test circuitry, wherever possible in collaboration with SPS-OP. This approach was originally chosen in order to be able to test the integration of the system in the different software layers, but it also had the advantage of giving the operators more than one year to familiarise themselves with ALPS. This allowed SPS-OP to discover potential operational shortcomings and to look for solutions and improvements as a team with the BI developers, whether to adapt the instruments and the associated tools or to adjust the way they were used. For example, the complex interpretation of the injection trajectory post-mortem data, a group of buffers designed to help analyse the instabilities that caused the beam dump command, benefited from the dry runs and interaction between the two teams. Those interactions resulted in an optimisation of the data stored and better analysis tools.

BEAM COMMISSIONING AND ISSUES

The first beam after the long shutdown was injected in the SPS on 12 April 2021 and was immediately acquired by ALPS with the FIFO mode (see Fig. 2). The position measured made it possible to promptly correct the optics settings and store the beam for several turns, a necessary condition for the start of the RF commissioning.

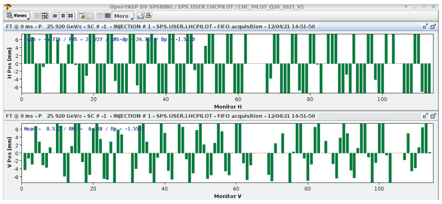

Figure 2: A screen capture of the SPS BPM operational software depicting the first successful injection in the accelerator as captured by ALPS in FIFO mode. The trajectory measured made it possible to promptly correct the optics settings.

Once the RF had captured the beam, making it possible to reliably distribute the BST and triggers, the other acquisition modes of ALPS could be used to further set up the beam. Thanks to the extensive dry runs, the commissioning of the system with beam did not require any dedicated beam time, and all the modes were immediately available.

ALPS' immediate availability and ease of use was such that SPS-OP declared that it enabled them to gain an enormous amount of time compared to previous start-ups.

The only significant issue encountered when testing the system in real conditions was linked to high-intensity single-bunch beams: when the injected intensity of the single-bunch beams was increased to above 1e11, the system started showing increased noise and, depending on the actual intensity, even wrong orbit readings.

It is important to note that the system uses a dedicated processing chain for single-bunch measurements. The analogue front-end does not reach a steady state when excited with a single state and therefore requires dedicated calibration settings; moreover, the sampling frequency of 40 MHz does not guarantee a sample close to the peak of the signal, so a digital up-sampling algorithm had to be implemented in the FPGA [1].

Fortunately, the system was able to reduce the signal levels at the input using the programmable attenuators originally foreseen for calibration purposes. This allowed the SPS commissioning to continue while the ALPS team was investigating the problem.

The issue was found in the programmable parameters used to determine the sample to select for the position measurement. It had not been possible with the laboratory setup, nor with the calibration circuit used for the dry runs, to reliably emulate intensities higher than 1e11, and it had been assumed that the shape of the signal would have been a simple scaling of that obtained for lower intensities. Unfortunately, due to saturation of some components in the channel with higher sensitivity, this assumption turned out to be wrong. Once the issue was identified thanks to analysis of the raw data via 'snapshot' acquisitions, it was easy to correct. The attenuators were nevertheless kept in the chain at their maximum level, 8 dB, as the system performed better than expected for low-intensity beams.

MEASURED RESOLUTION

The resolution of the system depends more on the beam time structure than on beam intensity, as long as the input remains in the calibrated range.

The resolution estimation was performed via Singular Value Decomposition (SVD) analysis [5]. Table 2 shows the estimated resolution for the 2 most common BPM types in the SPS: the shoeboxes BPH and BPV. The table indicates the estimated resolution before SVD analysis, with the data still affected by beam motion, and after removing the first 4 modes identified by the SVD decomposition. The data for this analysis, for a total of 5000 points of turn-by-turn data from each BPM, was acquired during normal operation of the SPS and not in dedicated runs. The multi-bunch beam used was a 10 µs train of proton bunches spaced 5 ns apart, for a total of 400 samples at 40 MHz. As a result, the

Table 2: Turn-by-turn resolution for a single-bunch and a 10us-long multi-bunch beam. The resolution varies with the BPM type due to the different aperture. For the purpose of the analysis, the first 4 modes obtained with SVD have been subtracted to remove the variations linked to the beam motion.

Beam type	**BPH**	**BPV**
Single-bunch: before SVD	600 µm	150 µm
Single-bunch: after SVD	290 µm	140 µm
Multi-bunch (10 µs): before SVD	250 µm	12 µm
Multi-bunch (10 µs): after SVD	80 µm	7 µm

ISBN: 978-3-95450-230-1 ISSN: 2673-5350 doi:10.18429/JACoW-IBIC2021-MOPP23

multi-bunch resolution is expected to be approximately 20 times better than the single-bunch resolution for the same BPM type, simply because of averaging. Another important factor is the different sensitivity of the horizontal and vertical BPMs: as a result, the vertical resolution after SVD should be 2 times better than the horizontal one.

For single-bunch beams, the factor 2 between vertical and horizontal resolution is respected after the subtraction of the beam motion (i.e. after SVD). For single- and multi-bunch beams, it can be observed that the SVD has minimal effect on the estimated resolution in the vertical plane, where the beam is very quiet, as expected, and, after the SVD analysis, the expected factor 20 between the resolution for single- and multi-bunch beams is respected.

In the horizontal plane (BPH), on the other hand, the resolution for the multi-bunch beam after SVD is not in line with expectations. Neither the factor 20 with respect to the single-bunch case, nor the factor 2 with respect to the vertical plane resolution, is respected. This last consideration in particular might suggest that, in this case, the SVD analysis did not succeed in removing all beam-motion components. Bearing in mind that the electronics is the same for the 2 planes, and that the only difference is the sensitivity of the 2 types of electrode (merely a consequence of their different apertures), it can be estimated that the real resolution is better than 24 µm, i.e. 2 times the resolution measured in the vertical plane before the SVD analysis.

CONCLUSIONS

ALPS commissioning started with dry runs one year before the first beam was injected in the SPS in 2021, in the middle of the Long Shutdown 2 (LS2), at a time when some of SPS-OP's software tools were still being developed and some acquisition modes were still being tested. This made it possible not only to test the integration of the system, but also to get the operators used to ALPS and how it should be operated.

The exchanges with SPS-OP during the dry runs highlighted possible use scenarios as well as the associated shortcomings of the system as a whole, leaving the developers on both sides enough time to adapt to and implement the changes required. During this process, SPS-OP had to deal with several iterations of error finding and debugging of the system following new releases, but this actually created a stronger team spirit between the operators and the beam instrumentation team working on ALPS. When the first beam was injected in April 2021, ALPS felt like a familiar system to the SPS-OP team, who already knew how to operate it and what to expect.

However, not everything could be tested without beam. In particular, high-intensity single-bunch beams could not be emulated, and the system's response to them was unexpected. This required a period of investigation, during which the issues linked to the higher intensity could only be mitigated with the use of programmable attenuators, luckily already present in the input line for calibration purposes. The investigation, carried out in parallel with the SPS commissioning, and mostly in parasitic mode, lasted approximately one week: the problem was identified in a set of parameters used to select the sample for the position computation and was easily solved.

The resolution measured in the vertical plane, after the use of SVD analysis is 140 µm for single-bunch beams in turn-by-turn mode and is in line with the estimations based on laboratory measurement. For multi-bunch beams, it has been verified that the resolution scales with the square root of the length of the bunch train measured in slots of 25 ns, proving also the effectiveness of the digital up-sampling and dedicated calibration for the more difficult single-bunch case. In the vertical plane, with the beam being very stable, the effect of SVD analysis is minimal for both single- and multi-bunch beams, but it was nevertheless important to apply it: without the SVD analysis the scaling of the resolution with the number of samples used per turn would not be respected.

In the horizontal plane, the resolution for the single-bunch beams in turn-by-turn mode is 290 µm, a factor 2 worse than in the vertical plane, but this was expected given that the BPM aperture in this plane is twice as big. For multi-bunch beams, on the other hand, the resolution even after SVD analysis remains a factor 5 worse than expected from scaling the single-bunch case. Given that the electronics is the same for both planes, it is believed that this mismatch is an artefact of the SVD analysis, which is not capable of effectively suppressing the strong beam movements in the horizontal plane. Other methods of estimating the resolution are still under investigation in order to confirm this hypothesis.

REFERENCES

[1] M. Wendt *et al.*, "Technology and First Beam Tests of the New CERN-SPS Beam Position System", in *Proc. IBIC'19*, Malmö, Sweden, Sep. 2019, pp. 655–659. `doi:10.18429/JACoW-IBIC2019-WEPP046`

[2] M. Barros Marin *et al.*, "The GBT-based Expandable Front-End (GEFE)", in *Proc. of the Topical Workshop on Electronics for Particle Physics (TWEPP 2015)*, Lisbon, Protugal, September 2015.

[3] ANSI/VITA, American National Standard for VME64, 1-1994 (R2002).

[4] A. Boccardi *et al.*, "A Modular Approach to Acquisition Systems for Future CERN Beam Instrumentation Developments", in *Proc. 15th Int. Conf. on Accelerator and Large Experimental Physics Control Systems (ICALEPCS'15)*, Melbourne, Australia, Oct. 2015, pp. 1103–1106. `doi:10.18429/JACoW-ICALEPCS2015-THHB2O02`

[5] J.Irwin *et al.*, "Model-Independent Analysis with BPM Correlation Matrices", in *Proc. 6th European Particle Accelerator Conf. (EPAC'98)*, Stockholm, Sweden, Jun. 1998, paper WEP21G, pp. 1644–1646.

ISBN: 978-3-95450-230-1 ISSN: 2673-5350 doi:10.18429/JACoW-IBIC2021-MOPP24

SIGNAL PROCESSING ARCHITECTURE FOR THE HL-LHC INTERACTION REGION BPMs

D. R. Bett*, University of Oxford, Oxford, UK
A. Boccardi, I. Degl'Innocenti, M. Krupa, CERN, Geneva, Switzerland

Abstract

In the HL-LHC era, the Interaction Regions around the ATLAS and CMS experiments will be equipped with 24 new Beam Position Monitors (BPM) measuring both counter-propagating beams in a common vacuum chamber. Numerical simulations proved that, despite using new high-directivity stripline BPMs, the required measurement accuracy cannot be guaranteed without bunch-by-bunch disentanglement of the signals induced by both beams. This contribution presents the proposed signal processing architecture, based on direct digitisation of RF waveforms, which optimises the necessary computing resources without a significant reduction of the measurement accuracy. To minimise the number of operations performed on a bunch-by-bunch basis in the FPGA, some of the processing takes place in the CPU using averaged data.

INTRODUCTION

The Large Hadron Collider (LHC) will undergo major upgrades in the context of the High Luminosity LHC (HL-LHC) project with the goal to deliver 3000 fb^{-1} of integrated luminosity over twelve years of operation from 2027 [1]. New Inner Triplets (IT) consisting of several high-gradient focusing magnets around ATLAS and CMS experiments will squeeze the proton beams to a 7.1 µm RMS beam size at the collision point [2]. In order to reliably collide such exceptionally small beams, each HL-LHC IT will feature six Beam Position Monitors (BPM) of two different types [3]. Since these BPMs will be installed in regions where both proton beams circulate in a common vacuum chamber, they must be able to clearly distinguish between the positions of the two counter-propagating particle beams.

The longitudinal positions of the BPMs were optimised to guarantee that the temporal separation between the two beams at each BPM location will always be greater than 3.9 ns, which is approximately 3 times longer than the bunch length. Nevertheless, using directional-coupler BPMs (also known as stripline BPMs) is unavoidable to reduce the inter-beam cross-talk. In such BPMs the passing beam couples to four long stripline electrodes parallel to the beam axis. Each electrode is connectorised on both ends but the beam couples predominantly to the upstream port with only a relatively small signal generated at the downstream port. This feature, referred to as directivity, allows both beams to be measured by a single array of electrodes. Figure 1 shows a 3D model of one of the HL-LHC stripline BPMs. Most of the HL-LHC IT BPMs incorporate four tungsten absorbers protecting the superconducting magnets from the high-energy collision debris [4]. As the absorbers must be placed in the horizontal and vertical plane, the BPM electrodes are installed at ±45° and ±135° significantly increasing the measurement non-linearity for large beam offsets.

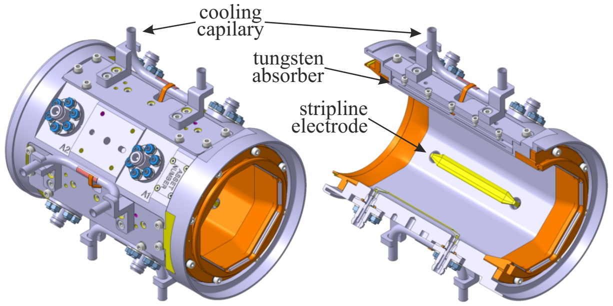

Figure 1: Tungsten-shielded cryogenic directional coupler BPM design for HL-LHC.

To cope with the very demanding requirements of precise beam position measurements near the experiments, a new state-of-the-art acquisition system for the HL-LHC IT BPMs is under development. It will be based on nearly-direct digitization by an RF System-on-Chip (RFSoC) [5]. This unique family of integrated circuits combines a set of Analogue-to-Digital Converters (ADC), Digital-to-Analogue Converters (DAC), Programmable Logic (PL) and several embedded CPUs, referred to as the Processing System (PS), on a single die. Each of the 8 ports of each BPM will be connected to a dedicated RFSoC 14 bit ADC channel sampling at 5 GSa s^{-1}. The acquisition electronics and signal processing software will use this raw data to compute the beam position applying a correction algorithm to minimize the parasitic contribution of the other beam as well as taking into account the BPM rotation, non-linearity and scaling factors.

ACQUISITION ELECTRONICS DESIGN CRITERIA

The final specification for the HL-LHC IT BPMs is not yet available but some preliminary design criteria have been set to guide the design of the future acquisition electronics.

The HL-LHC beam will consist of up to 2808 bunches spaced by multiples of 25 ns with intensities spanning close to two orders of magnitude from 5×10^9 up to 2.2×10^{11} charges. However, for most common operational scenarios it is assumed that the intensity of bunches within the same beam might vary by a factor of four, while the ratio of bunch intensity between the two beams can reach a factor of ten. HL-LHC bunches are not expected to be longer than 1.2 ns (4σ) but for some special operational modes the BPM system should be able to measure bunches as short as 0.5 ns.

---

* douglas.bett@physics.ox.ac.uk

The temporal separation between bunches of the counter-rotating beams is fixed at each BPM location and ranges from ±3.9 to ±10.5 ns. The beam position measurement range must cover half of the BPM aperture of approximately 120 mm.

The HL-LHC Inner Triplet BPM system will produce data in two main acquisition modes:

- **Trajectory mode**: on-demand bunch-by-bunch, turn-by-turn measurements over a finite number of turns;
- **Orbit mode**: continuous multi-bunch, multi-shot measurements with data-rate reduced through averaging.

Due to the very high sampling rate, synchronizing the ADC clock with the accelerator timing would be virtually impossible. The HL-LHC IT acquisition will therefore use a free-running clock and will detect the bunch windows automatically based on the sampled data.

Until a full specification is available, the following performance goals are considered at this stage of the project:

- **RMS resolution** (in trajectory mode): 15 µm;
- **Measurement reproducibility** (over 10 hours in orbit mode): ±5 µm;
- **Maximum two-beam disentanglement error** (in orbit mode): ±20 µm.

OVERVIEW OF SIGNAL PROCESSING

A CST Microwave Studio model of the BPM was used to calculate the signals generated on each BPM port by the passage of a single bunch of charged particles. For a Gaussian bunch (width $\sigma = 0.3$ ns, intensity $q = 2.3{\times}10^{11}$ particles) travelling along the BPM axis, the signals induced at opposite ends of a single stripline are shown in Fig. 2.

For each stripline, each beam produces an upstream signal at the entrance end of the BPM and a much smaller downstream signal at the other end; by analogy to a directional coupler, these signals will henceforth be referred to as the "coupled" and "isolated" signals respectively. For a given port, the beam that gives rise to the coupled signal is denoted the "main beam", while the beam travelling in the opposite direction generating the isolated signal is referred to as the "counter beam". The total signal observed on any given port is thus the sum of the coupled signal due to the main beam and the isolated signal due to the counter beam. The amplitude of each of the two sub-signals varies with the intensity and position of the corresponding beam, and the two sub-signals are separated in time by the bunch crossing timing for that particular BPM. The graphs presented in this paper are the results of a simulation framework developed in GNU Octave [6].

For the case of two beams of equal intensity, the isolated sub-signal accounts for a very small contribution to the total power observed on each port. However, in the worst case scenario, where there is a large imbalance in the intensity of the two bunches and a large difference in the orbits, the isolated sub-signal is comparable in magnitude to the coupled sub-signal. This is illustrated in Fig. 3.

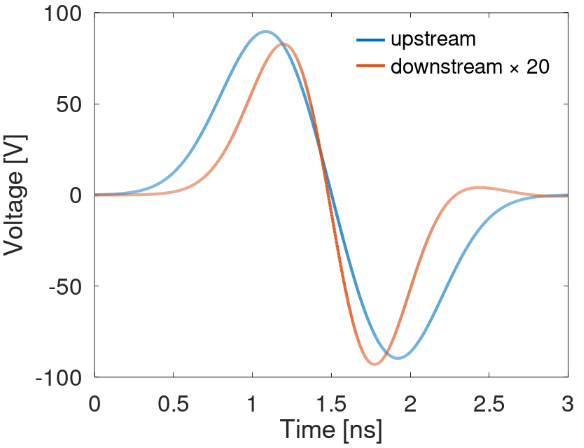

Figure 2: Simulated stripline signals from the CST model of the HL-LHC IT BPMs. The beam enters the upstream end of the BPM. The downstream signal has been amplified by a factor of 20.

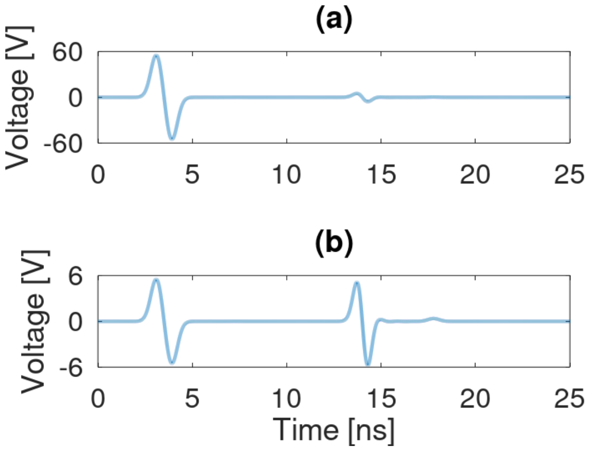

Figure 3: Simulated signal on a BPM port for the case of (a) two nominal-intensity ($q = 2.3 \times 10^{11}$ particles) beams; (b) a main beam with one-tenth of nominal intensity and a counter beam of nominal intensity. The position of the two beams corresponds to the presqueeze orbit of the CP BPM at IR 1 where the separation of the two beams in the vertical direction is more than 25 mm. Note that the main beam arrives first in this case.

Beam Disentanglement Algorithm

Since the presence of a counter beam may alter the measured position of the main beam, some method of "disentangling" the coupled and isolated sub-signals is required. The method proposed here is named the "power compensation" method as it attempts to subtract the power of the counter beam from the total power measured on each port.

Let's assume the BPM ports being numbered from 1 to 8, with the odd ports being upstream for beam 1 and sharing the stripline with the successively-numbered even port. Let $V_1[n]$ represent the waveform measured by the digitizer sampling port 1 of the BPM over a single 25 ns period. This waveform can be expressed as:

$$V_1[n] = \kappa_1 V_c[n] + \kappa_2 V_i[n] \tag{1}$$

where:

- $V_c[n]$ is the sequence of samples representing the coupled signal induced by an on-axis reference main beam with some nominal intensity and bunch length;
- $V_i[n]$ is the sequence of samples representing the isolated signal induced by a reference counter beam with the same parameters as the main beam;
- The κ scale factors set the amplitude of each sub-signal according to the actual intensity of each beam and their position in the BPM plane. $\kappa_1 = \rho_1 \cdot q_1$, where q_1 is the intensity of the actual beam 1 (expressed here as a multiple of the intensity of the reference main beam) and ρ_1 is a scaling factor accounting for the distance of beam 1 from the electrode with ports 1 and 2.

The signal's "power" can be calculated by taking the sum of squared samples for both sides of the equation:

$$\sum_{n=1}^{N} V_1[n]^2 = \kappa_1^2 \sum_{n=1}^{N} V_c[n]^2 + 2\kappa_1\kappa_2 \sum_{n=1}^{N} V_c[n] \cdot V_i[n] + \kappa_2^2 \sum_{n=1}^{N} V_i[n]^2$$

where N is the number of samples in a 25 ns window and $V_1[n]$ denotes the n-th sample of the V_1 waveform. By introducing some new notation, the above expression can be written as:

$$\psi_1 = \kappa_1^2 \psi_c + 2\kappa_1\kappa_2\chi + \kappa_2^2\psi_i \tag{2}$$

Note that the $\psi_{c,i}$ and χ parameters represent scalars calculated from the observed or reference waveform for the specific port, while the κ parameters are unknowns that we wish to calculate. Equation 2 can be trivially rearranged into the form of an equation quadratic in κ_1:

$$\kappa_1^2 + \left(2\frac{\chi}{\psi_c}\kappa_2\right)\kappa_1 + \left(\frac{\psi_i}{\psi_c}\kappa_2^2 - \frac{\psi_1}{\psi_c}\right) = 0 \tag{3}$$

By making the approximation $\kappa_2 \approx \sqrt{\frac{\psi_2}{\psi_c}}$, i.e. considering that the influence of beam 1 on port 2 is negligible for computing κ_1, the coefficients of this quadratic equation can be expressed solely in terms of a set of scalars that can be calculated in advance from the reference waveforms (ψ_c, ψ_i, χ) and a pair of scalars that must be calculated from the measured waveforms at both ends of a single stripline (ψ_1, ψ_2). The power compensation procedure thus amounts to calculating the coefficients of a single quadratic equation for each port, and then solving them.

Full Signal Processing Chain

The power compensation represents a single stage of the five-stage signal processing algorithm for converting a set of eight digitized waveforms to a horizontal and vertical position reading for each of the two beams.

1. Calculation of the sum of squared samples for each waveform, i.e. $\psi_{1..8}$.
2. Scaling of $\psi_{1..8}$. Variable attenuators will be used to match the signal level on each port to the input range of the ADC; this attenuation must be removed before any further processing takes place. The stability of the signals over a single fill (~10 hours) is also an issue of concern and a scheme where the onboard DACs are used to periodically monitor the symmetry of a given pair of channels is being developed. The measured result of such a self-calibration procedure would also be applied at this stage.
3. Power compensation. The values of $\psi_{n,n+1}$ calculated from the waveforms from the two ports of a single stripline are combined with the $\psi_{c,i}$ and χ values, precalculated from the reference waveforms for the specific port, to give the coefficients of a pair of quadratic equations that can be solved to give the amplitude of the main beam signal for each waveform.
4. Position calculation. The usual difference-over-sum method can be used with the main beam amplitudes for each pair of ports (top/bottom and left/right for both ends of the BPM) to give the horizontal and vertical positions of each beam in the BPM frame.
5. A polynomial correction will be applied to the measured horizontal and vertical position of each beam in order to account for the non-linearity and the 45° rotation of the BPM if required.

Expected Performance

Simulation results suggest that the performance goals will be challenging to achieve given the range of conditions the system must be able to accommodate. While the achieved RMS resolution in trajectory mode consistently works out in the 10-15 µm range, it is reasonable to expect the real system to under-perform relative to the model. To achieve the measurement reproducibility goal in orbit mode, it is calculated that the uncorrected imbalance in signal gain between a pair of ports must not exceed 0.01%. The exact details of the self-calibration scheme are still being worked out, so it is difficult to assess at this stage how feasible such an imbalance is. However, the results suggest that the maximum two-beam disentanglement error of 20 µm can be comfortably achieved using the power compensation procedure.

SYSTEM ARCHITECTURE

Due to the RFSoC's particular nature, it is possible to distribute the signal processing amongst 3 different systems:

1. The Programmable Logic (PL) of the RFSoC, i.e. the configurable logic blocks, the flip-flops and block RAMs typical of an FPGA;
2. The Processor System (PS) of the RFSoC, i.e. a group of embedded CPUs;
3. The Software (SW) running on a remote back-end computer in communication with the RFSoC.

Even though it would be possible to implement the whole signal processing within the programmable logic of the RFSoC, this would not be the most efficient use of the system.

The acquisition of all signals of one HL-LHC IT BPM requires 8 high-sampling-rate ADCs, one per signal. The PL will be used for fast signal processing. The internal Block RAM will be used for storing high-rate data (raw data for calibration and debugging) and for implementing the filters required for the orbit mode. The external DDR memory will store the high-volume data of the trajectory mode. The PS will control the acquisition, will implement the slow calibration and will be connected to the remote computer e.g. by Ethernet. Orbit mode data will be streamed out continuously at a slow rate (in the order of tens of hertz), while the trajectory mode data will be sent out on demand.

When all signal processing is performed within the RFSoC, the SW receives already calculated beam position data, in arbitrary units, to which it must apply only the calibration coefficients and the non-linearity polynomial correction. Alternatively, the back-end can receive the signal powers computed for each of the 8 BPM ports, after the two-beam compensation and averaging when required, and delegate the beam position calculation to the SW. The latter solution allows to save PL resources, at the cost of doubling the bandwidth and the required memory space. It also provides access to the independent port signals, granting the opportunity for more off-line analyses.

An estimation of the resources needed for the signal processing implementation in both cases is reported in Table 1. Each value is put in relation to the resources available on a Generation-3 RFSoC equipped with 4 GB of DDR4 memory, which are indicated in brackets. An estimation of the maximum rate with which trajectory mode data can be read-out is also given. The PL resources - Digital Signal Processing (DSP) slices, Look Up Tables (LUT) and Flip-Flops (FF) - are accounted only for the implementation of the algorithm and not of the full acquisition system. The available DDR bandwidth (BW) is estimated at about 70% of the declared peak performance in the datasheet of the RFSoC [5]. The required DDR BW is computed for the continuous write of the trajectory data; the read-out is on demand and sporadic. The read-out BW assumes an Ethernet protocol over a 1000 Mbps link running at 50% efficiency. The calculated bandwidth takes into account the back-end continuously reading orbit data from the RFSoC.

Table 1: Summary and comparison of the estimated resources needed when computing the beam position solely in the RFSoC and when a part of the computation is delegated to software (SW) running on a remote computer.

Available resources	**Position calculation in RFSoC**	**Position calculation in SW**
ADCs (8)	100%	100%
Block RAM (38 Mb)	3%	4%
PL DSP (4272)	6%	5%
PL LUT (4255280)	3%	2%
PL FF (850560)	3%	2%
DDR (32 Gb)	3%	6%
DDR BW (95 Gbps)	10%	18%
Read-out BW (500 Mbps)	3%	6%
Max trajectory rate	1.25 s^{-1}	0.55 s^{-1}

SUMMARY

Although the signal processing chain for the HL-LHC IT BPMs is still under development, the analysis performed so far indicates that an acquisition system using an RFSoC sampling the 8 BPM outputs could meet the basic performance goals without exceeding the available resources. The decision how to distribute the required processing steps between the RFSoC and the SW running on a back-end computer will be taken based on the experience gained with a proof-of-principle system foreseen for 2022.

ACKNOWLEDGEMENTS

The authors would like to thank Manfred Wendt from CERN for his continuous input to the project.

REFERENCES

[1] L. Rossi, O. Brüning, "Progress with the High Luminosity LHC Project at CERN", in *Proc. IPAC'19*, Melbourne, Australia, May 2019, pp. 17–22. doi:10.18429/JACoW-IPAC2019-MOYPLM3

[2] F. Bordry *et al.*, "Machine Parameters and Projected Luminosity Performance of Proposed Future Colliders at CERN", [arXiv:1810.13022 [physics.acc-ph]].

[3] M. Krupa, "Beam Instrumentation and Diagnostics for High Luminosity LHC", in *Proc. IBIC'19*, Malmö, Sweden, Sep. 2019, pp. 1–8. doi:10.18429/JACoW-IBIC2019-MOAO02

[4] L. S. Esposito *et al.*, "FLUKA Energy Deposition Studies for the HL-LHC", in *Proc. IPAC'13*, Shanghai, China, May 2013, paper TUPFI021, pp. 1379–1381.

[5] Xilinx, DS926 - Zynq UltraScale+ RFSoC Data Sheet: DC and AC Switching Characteristics (v1.8), https://www.xilinx.com/content/dam/xilinx/support/documentation/data_sheets/ds926-zynq-ultrascale-plus-rfsoc.pdf

[6] D. R. Bett *et al.*, "Simulation of the Signal Processing for the New Interaction Region BPMs of the High Luminosity LHC", in *Proc. IBIC'20*, Santos, Brazil, Sep. 2020, pp. 120–123. doi:10.18429/JACoW-IBIC2020-WEPP12

HARMONIC BASED BEAM POSITION MEASUREMENTS ON DEBUNCHED BEAMS

M. Bozzolan†, CERN, Geneva, Switzerland

Abstract

In some accelerator environments, e.g. in linear accelerator (LINAC), the beam position is measured with a BPM operating at one particular strong harmonic component present in the beam signal. This approach has limitations once the beam gets debunched and the harmonic components drops. Nevertheless, from a signal processing point of view the signal-to-noise ratio can be still acceptable with highly debunched beams, leading, in principle, to a reasonable, even if degraded, position measurement. A simplified beam transport model developed for the CERN BI transfer line between LINAC4 and the PS Booster demonstrates, that in some case, the harmonic component cannot be used anymore for position measurement despite the fact it is still significative in amplitude.

INTRODUCTION

Beam Position Monitors (BPMs) are one of the most used instruments in a particle accelerator. Their main functionality is the monitoring of the beam trajectory in linear accelerators (LINACs) and transfer lines and the closed orbit in circular machines. In addition, BPMs can provide other beam parameters such as beam intensity, kinetic energy and longitudinal distribution.

The basic idea of most BPM is to measure the image current flowing on the conducting beam pipe [1]. Typically, for the estimation of the transverse beam position, a set of two opposite electromagnetic pickups or electrodes is used, for the horizontal and the vertical plane.

Different types of BPM pickups exist and, depending on the machine and the required measurements, a specific BPM type is chosen accordingly.

The signals at the BPM electrodes can be degraded by electromagnetic interference of nearby devices. Also, depending on the BPM type, its signal can be corrupted by beam loss and secondary emitted particles. If the beam has a fixed pattern, this feature can be exploited in order to mitigate these effects. For example, in LINACs, where the acceleration process bunches the beam at a rate defined by the frequency of the accelerating cavities, the signals present strong components at the harmonics of the RF frequency. In this case, the receiver could be tuned at a single harmonic and use the envelope of the received signal for the position estimation.

CURRENT HARMONICS OF A GAUSSIAN BEAM

Assuming a train of bunches with a Gaussian longitudinal distribution [2], with individual bunch charge q, spaced by $T=1/f_{\mathrm{RF}}$, the beam current intensity is

$$I(t) = \frac{q}{\sqrt{2\pi}\sigma} \sum_{n=-\infty}^{+\infty} e^{-\frac{(t-nT)^2}{2\sigma^2}} \tag{1}$$

and the harmonics can made explicit by expanding the summation using the cosine series[§]

$$I(t) = I_0 \left[1 + \sum_{n=1}^{+\infty} K_n \cos\left(\frac{2\pi n t}{T}\right) \right] \tag{2}$$

where I_0 is the DC beam average current and

$$K_n = e^{-\left(\frac{\omega_{RF}\cdot n\cdot\sigma}{\sqrt{2}}\right)^2} \tag{3}$$

CURRENT HARMONICS OF A NON-GAUSSIAN BEAM

In the case of non-Gaussian longitudinal distribution, the same expansion in cosine series as with the Gaussian beam can be made, but with the difference that one or more harmonics can vanish and hence cannot be used.

For example, a train of rectangular square bunches of duration W and period $T=1/f_{\mathrm{RF}}$ is described by Eq. (2) with

$$K_n = sinc\left(\frac{n\pi W}{T}\right) = \frac{\sin\left(\frac{n\pi W}{T}\right)}{\frac{n\pi W}{T}} \tag{4}$$

vanishing for pulse duration W multiple of T/n [2]. This means that for specific bunch lengths the signal from the electrodes of a BPM pickup will not have the f_{RF} harmonic component

In practice this condition can be reached along the transfer line of LINACs where the beam energy spread associated with the non-relativistic beam energy, and space charge effect, results in increasing long bunches. This debunching process also modifies the shape of the longitudinal bunch distribution so that the harmonic vanishing can happen even if a Gaussian beam is injected into the line.

Furthermore, a so called “de-buncher cavity” can be present at the end of a LINAC in order to provide the energy spread demanded by the downstream machine, which causes the vanishing of the harmonic content at a range of locations depending on the settings of this cavity.

---

† michele.bozzolan@cern.ch

[§] Cosine series can only be used for even functions but it’s not reducing generality

CERN LINAC4 TO PSB TRANSFER LINE CASE

The CERN H⁻ transfer line from LINAC4 to PS Booster (PSB) is equipped with 13 dual plane (2+2 electrodes) stripline pickups. The BPM system operates at the 352.2 MHz LINAC4 frequency and a (de)buncher cavity is located at the beginning of the line.

LINAC4 produces beam in pulses at a rate of 1.2 seconds. The pulse length is in the order of several hundreds of microseconds. The downstream PS Booster is made of four vertically stacked synchrotron rings. Each LINAC4 pulse is composed of four time slices sequentially distributed to the four PSB rings at the end of the transfer line [3].

The BPM system reports four beam positions representing the average beam position along each time slice that is eventually sent to the destination PSB ring (Fig. 1).

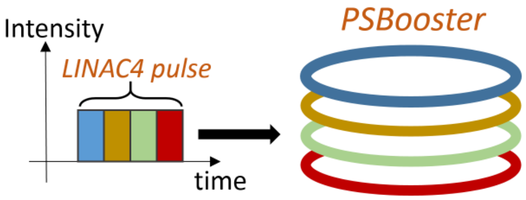

Figure 1: PS Booster injection scheme.

The setting of LINAC4 and the transport line are unchanged along the pulse, so, in principle, each slice should behave identically. When the (de)buncher cavity is not active (natural debunching) or is set to rebunch the beam, the BPM system works properly along all the beam line with stable reported positions. But if the (de)buncher cavity is active increasing the beam energy spread and debunching the beam, the measured positions in a specific region of the line are showing degraded performance from shot-to-shot and slice-to-slice variations.

By observing the BPM sum signal, representing the intensity of the 352 MHz component of the beam current at the BPM location, a notch is observed in the region where bad positions are reported (Fig. 2). The position instability could be caused by a too low signal-to-noise ratio, but this seems to be not the case as the observed position fluctuations are not compatible with the measured signal-to-noise levels.

SIMPLIFIED BEAM TRANSPORT MODELLING

In order to understand and explain the observed behaviour, a simplified beam transport model of the (de)buncher cavity and the following transport line has been written in Python. The assumptions of this model are:

1) Perfectly collimated beam moving ballistically straight with no magnetic fields
2) Zero transit time in the cavity.
3) Pure transverse electromagnetic field generated by the beam.
4) Constant energy spread along the line (no space charge or other collective effects).
5) Linear BPM response

The initial longitudinal bunch shape and energy spread are input parameters that originated from other simulations and/or specific measurements.

Despite several simplifying assumptions, the results are in good agreement with the measurements and with the precise simulation made with TraceWin (Fig. 2) [4].

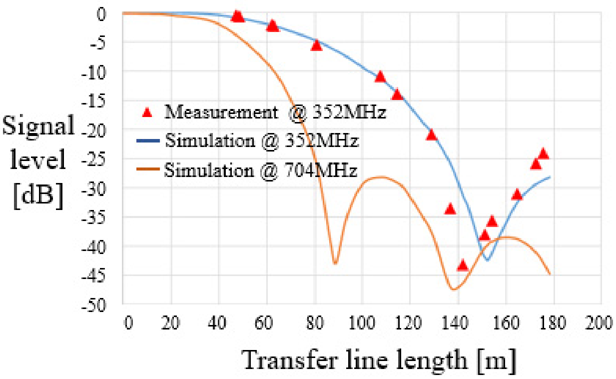

Figure 2: Signal level along the line for debunched beam.

The measured signal intensity notch at the location of about 140 m downstream the transfer line could be explained by the shape of a single bunch transported along the line. Figure 3 shows the expected longitudinal bunch distribution, which differs from a perfect Gaussian shape. Even in case of a Gaussian distribution at the beginning of the line, the beam would lose such a distribution while moving along the line, with the consequent possibility of developing intensity notches at specific locations depending on the harmonic component used for measurement.

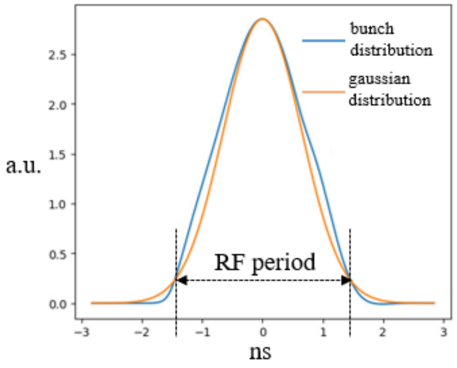

Figure 3: Longitudinal distribution of a transported bunch.

ISBN: 978-3-95450-230-1 ISSN: 2673-5350 doi:10.18429/JACoW-IBIC2021-MOPP25

POSITION MEASUREMENTS IN THE REGION OF THE NOTCH

In principle, any higher harmonic of the beam could be used by the BPM system, but in practice, for the CERN LINAC4 to PSB transfer line only the first (352 MHz) and the second harmonic (704 MHz) have a reasonable signal level following the losses of the long cable (>100 m) running from the tunnel to the electronics.

From the simulation in Fig. 2, the notch of the second harmonic is slightly shifted from the notch of the first harmonic. A comparison between the vertical positions measured at the first (Fig. 4) and at the second harmonic (Fig. 5) is made for a BPM pickup at a location close to the first harmonic notch of the transfer line at ~140 m.

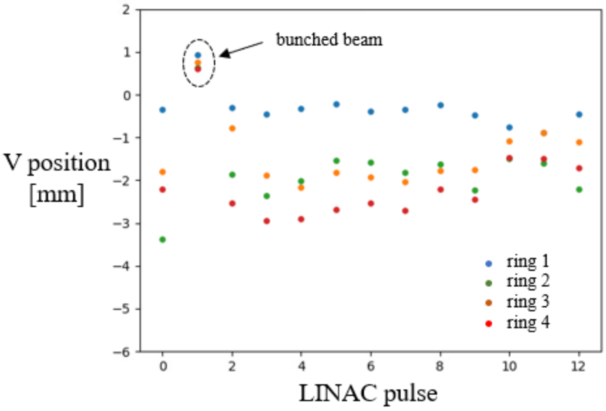

Figure 4: Debunched beam measured at 352 MHz.

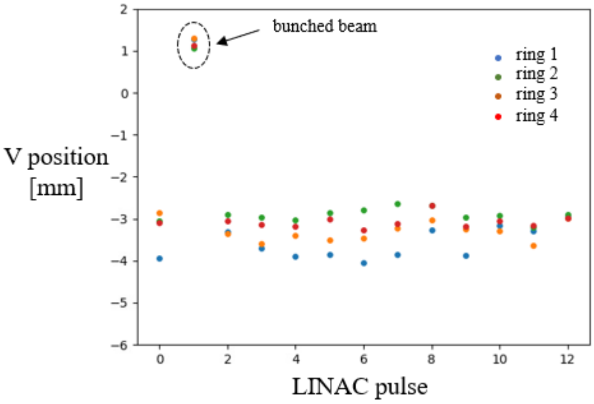

Figure 5: Debunched beam measured at 704 MHz.

The vertical position of the four slices injected in PSB (Fig. 1) for multiple LINAC4 pulses is plotted along with the pulse index in the horizontal axis. Measurements were performed simultaneously for the first and the second harmonic by splitting the electrode signals. To be noticed that the pulse #1 was a bunched beam and the position at both harmonics converges to a similar value for all slices which is the expected behaviour also for the debunched beam pulses. The different absolute position between the bunched and debunched beam pulses is not unexpected because of the different beam optics applied in the line for the two cases.

Using the second harmonic, the position stability slice-to-slice and shot-to-shot showed an improved reproducibility and uniformity, which is expected from the fact that the pickup location is not as close to a notch as for the first harmonic for this specific setting of the debuncher cavity. However, the results are still not satisfactory.

Since the LINAC4 beam is chopped at a 1 MHz rate (Fig. 6), a position measurement exploiting this feature, that will be called low frequency (LF), was used to confirm the artefacts of the high frequency (HF) measurements, based on the harmonics of the bunching frequency (Fig. 7).

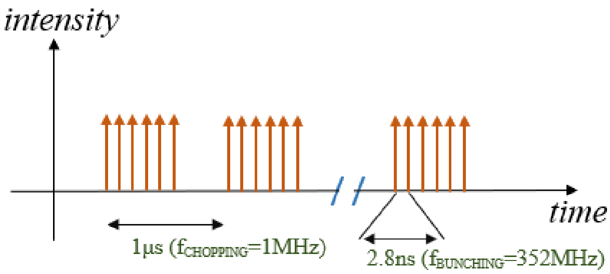

Figure 6: LINAC4 beam structure.

In this case the horizontal beam positions at LF and at 352 MHz (HF) were measured at the same time by splitting the electrode signals. For the LF measurement the electrode signals were low-pass filtered with 20 MHz cut-off frequency to completely remove the bunching frequency components and keep the chopping pattern contribution.

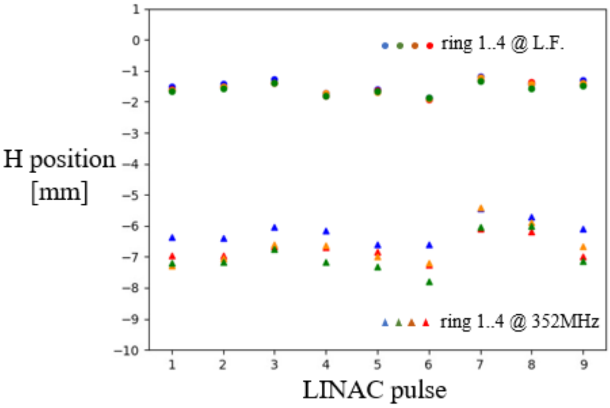

Figure 7: Debunched beam measured at LF and 352 MHz.

The improvement in the position stability is evident and coherent with the results in case of bunched beam in terms of shot-to-shot and bunch-to-bunch stability, proving the inconsistency of the debunched beam position measured using the harmonics of the bunching frequency at this location.

To confirm the consistency of the LF measurement, also bunched beam was measured simultaneously at LF and at 352 MHz, giving, as expected in this case, reported beam positions in very good agreement (Fig. 8).

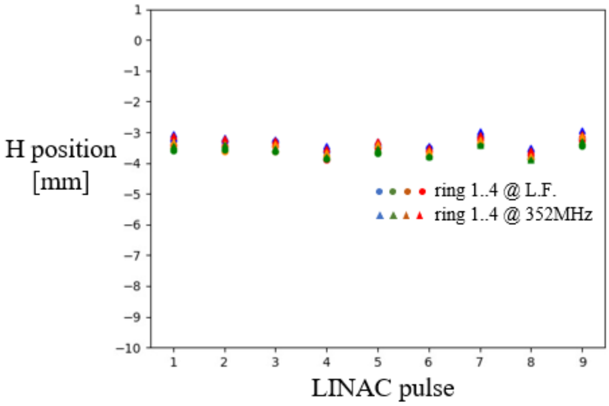

Figure 8: Bunched beam measured at LF and 352MHz.

Using the simplified model described before, an off-center beam position is calculated in the region of the signal intensity notch, depending on the transverse beam position along the bunch used as simulation parameter. Variation of this parameter along the LINAC4 beam pulse and from pulse to pulse could explain the measured fluctuations. However, this mechanism has not been verified by measurements or more comprehensive simulations.

CONCLUSION

In case of highly debunched beam, the use of BPM operating at harmonic components present in the signal must be carefully evaluated since the signal levels may have notches at specific locations along the beam line. In this region at the CERN LINAC4 to PS booster transfer line, the BPM system, both operating at the first and second harmonic of the LINAC, shows unacceptable fluctuations of the reported beam position.

Using a different harmonic can be in principle beneficial at some specific location, but in general more notches could appear along the line. This was tried and indeed did not solve the issue in the specific case described.

The presence of a low-frequency modulation (beam pulse chopping), with low in the sense that the period is much longer than the bunch distance, could potentially solve this accuracy degradation as demonstrated by initial measurements.

REFERENCES

[1] P. Forck, Joint University Accelerator School, Archamps, Lecture Notes on Beam Instrumentation and Diagnostics, `https://www-bd.gsi.de/conf/juas/juas_script.pdf`
[2] R. Shafer, “Beam Position Monitoring”, in *AIP Conf. Proceedings*, vol. 249, p. 601, 1992.
[3] F. Gerigk and M. Vretenar, “Linac4 Technical Design Report”, CERN, Geneva, Switzerland, Rep. CERN-AB-2006-08, 2006.
[4] J. B. Lallement, private communication.

PERFORMANCE OF BPM READOUT ELECTRONIC BASED ON PILOT-TONE GENERATOR AND A MODIFIED LIBERA SPARK AT ALBA

L. Torino*, U. Iriso, ALBA-CELLS, Cerdanyola del Vallès, Barcelona, Spain

Abstract

As many synchrotron radiation sources, ALBA is also going through an upgrade project. At the same time, the world of BPM electronic is evolving fast to keep up with the stringent requirement of new facilities. In order to follow the situation closely and develop know-how for the future, we decided to install and test in our storage ring a BPM readout system composed by a Pilot-Tone generator (developed by Elettra) and a modified Libera Spark (by Instrumentation Technologies). We compare position measurement results and stability with the ones obtained by our standard Libera Brilliance and a Libera Brilliance+ electronics.

INTRODUCTION

As other third generation Synchrotron Light Sources, ALBA [1] is also starting its upgrade project which will lead to the new ALBA-II machine [2]. In this frame, an upgrade of the BPMs readout system, composed nowadays by Liberas Brilliance [3], will be needed and, for this reason, alternative electronics are being studied. In particular, the system proposed by ELETTRA in collaboration with I-Tech has been tested at ALBA storage ring. The system is based on the idea of using a Pilot-Tone signal (PT) to calibrate online fluctuations related to external factor acting on cables and readout electronics [4].

This method is intended to avoid the use of quasi-crossbar switches which are now running in Libera Brilliance and Libera Brilliance+ electronics to minimize effects of the electronics on the beam measurement [3]. Main disadvantages of this compensation technique are that:

1. signal pollution due to cables is not kept into account for the compensation;
2. the switching mechanism generates glitches in the Fast Signal and might compromise the final position measurement.

Both these disadvantages may be solved using the PT method.

PILOT-TONE + LIBERA SPARK

The system is composed by a PT generator and a modified Libera Spark. The PT generator produces a sinusoidal RF signal at a frequency close to the RF frequency. The PT signal is injected after each BPM buttons in order to pass along all the electronics path.

The idea is that, since the beam and the PT frequencies are similar, any fluctuation induced by variation in the electronics path will be similar for both signals. Moreover, since frequencies are slightly different, it is possible to separate the responses of the two signals thanks to Fourier analysis, and to compensate the Raw Signal coming from the beam with using the one of the PT [5].

The PT generator, designed by ELETTRA, is optimized to produce frequencies close to the 499.65 MHz of ALBA RF frequency. It is powered over Ethernet and can easily be located inside the tunnel and controlled via a Tango device. The signal is splitted and added to the beam signal inside the generator. It is possible to regulate the amplitude of the PT signal in order to have it similar to the one produced by the beam. Also, individual output attenuator can be set for each channel.

The Libera Spark has been modified in order to be able to actually see the PT signal: to do so, saw filters at the entrance of the electronics were removed. As a downside, the removal of these saw filters makes impossible to perform measurements during single bunch operation. Saw filters, apart from filtering, also have the function of spreading the single bunch signal over several ADC samples. This allows the signal processing for this operation mode, which is not measurable using this technique nowadays.

Libera Spark software has been modified to separate beam and PT signal through Fourier analysis and to finally calculate the compensated data. The device server provided by I-Tech, shows:

- Raw Signal: Sum of PT and Beam signal as passing through the whole electronics.
- PT Signal: PT signal resulting after Fourier analysis of the Raw Signal inside the Libera.
- Compensated Signal: obtained by compensating the Raw Signal using the PT one.

At ALBA the RF frequency is 499.654 MHz. The PT frequency is set to be 501.41 MHz. The ADC of the modified Spark, adjusted for ALBA, under-samples these signals with a frequency of 118.2217 MHz. The resulting intermediate frequencies for the beam and the PT are $if_{RF} = 26.76$ MHz and $if_{PT} = 28.52$ MHz. The plot of the Fourier transform of the Raw Signal for each of the four BPMs buttons is presented in Fig. 1, two main peaks are present at if_{RF} and if_{PT}.

CONFIGURATION

The PT generator has been located in the tunnel and connected to a spare BPM. In order to have consistent results, data has been compared to the one obtained from a second and a third BPM connected respectively to a Libera Brilliance and a Libera Brilliance+.

---

* ltorino@cells.es

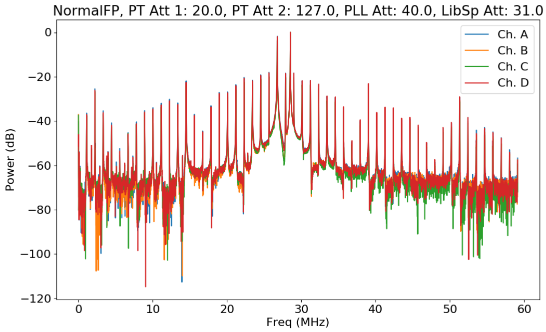

Figure 1: Spectrum of the signal read by the Libera Spark for each BPM button. Two main peaks are present: the beam intermediate frequency and the one of the PT signal.

All these BPMs are not in the Fast Orbit Feedback loop and are in the same sector (SR07). In particular BPMs connected to the Libera Brilliance+ and to the PT-Libera Spark (BPMSR0709 and BPMSR0710) are respectively before and after a free straight secsion, while the one connected to a Libera Brilliance is in the middle of the arc (BPMSR0704). One meter long cables are used to connect the BPM buttons to the PT generator while standard 20 m cables are used to bring the signal of all BPMs outside the tunnel. All electronics are located in the same rack where a temperature and humidity sensor is also present. A schematic of the configuration is presented in Fig. 2.

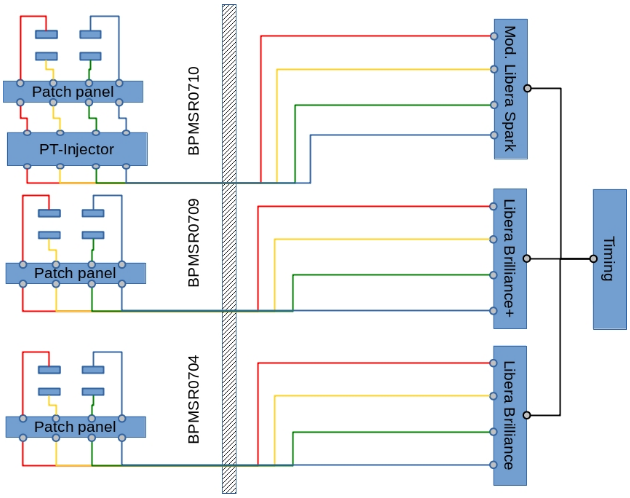

Figure 2: Schematic of the different readout system distribution.

Data is stored at 1 Hz during several user operation runs as well as during dedicated machine days. For each readout setup we save the raw data (VA, VB, VC, and VD) and horizontal and vertical position.

In case of the PT-Libera Spark system, Raw, PT, and Compensated data sets are saved.

STANDARD OPERATION

Data taken during standard operation are useful to verify the stability of the measurement and the capability of the PT technique of compensating drifts in the measurements not related with machine events.

Horizontal and vertical position data from an entire run of user operation is presented in Fig. 3: compensated data from the PT-Libera Spark system in blue, Libera Brilliance in red and Libera Brilliance+ in violet. Jumps in the Libera Brilliace horizontal positions (top plot) happen after machine days each Monday. This are due to different settings of the machine: the Libera Brilliance is connected to a BPM which is located in the middle of the girder in between different magnets and far from FOFB BPMs and correctors.

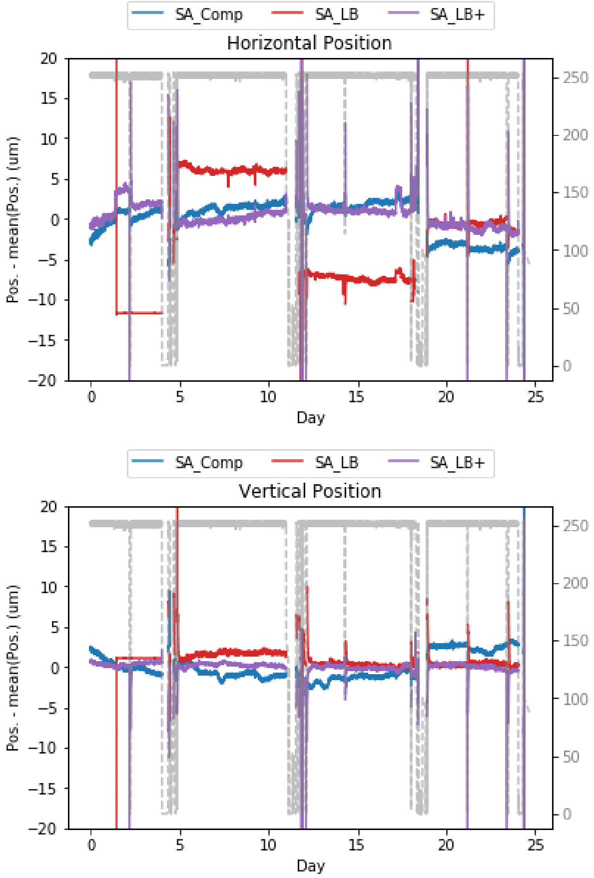

Figure 3: Horizontal (top) and vertical position (bottom) data from the PT-Libera Spark (blue), Libera Brilliance (red), Libera Brilliance+ (violet).

From the plot, it is possible to realize that the best long term stability is the one obtained with the Libera Brilliance+, while some drifts can be observed in data acquired using the PT-Libera Spark system. Since BPMs connected to this electronics are before and after an empty straight session, the behavior of position data should be the same. However, it is interesting to notice that the PT is well compensating fluctuation due to temperature in the rack. Considering the

PT Correction Signal for each button, one can notice a clear correlation with the temperature, as presented in Fig. 4.

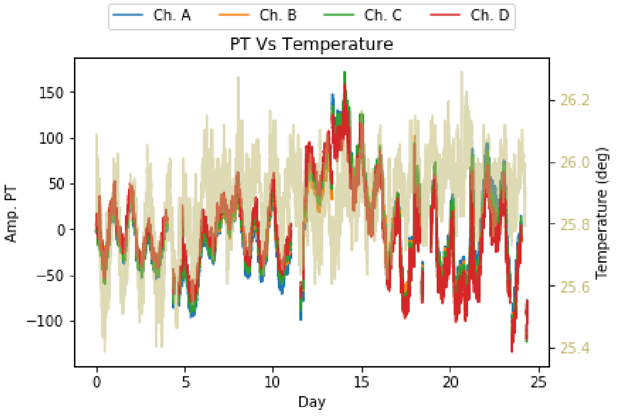

Figure 4: PT compensation data for each BPM button and temperature in the rack.

The work of the PT compensation can also be appreciated looking at the different kind of position data provided from the PT-Libera Spark system. As an example, vertical data during one day, presented in Fig. 5, shows a step in both Raw Signal (SA, in orange), and in the PT compensation (SA_PT, in green). As a results, the compensated data (SA_Comp, in blue) does not show any step.

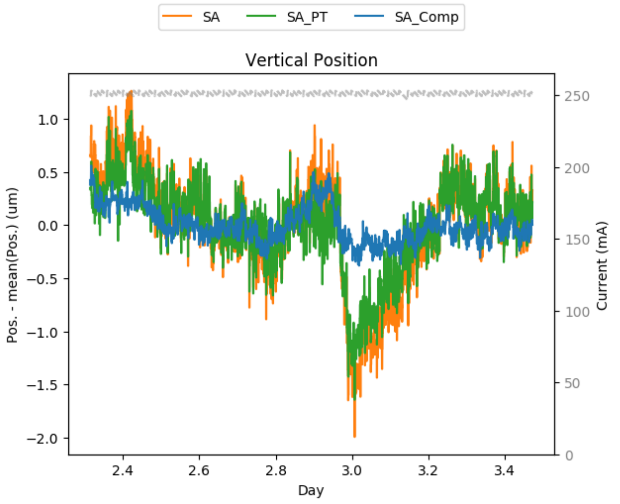

Figure 5: Vertical position data from the PT-Libera Spark system. Raw data (SA, in orange) are compensated by the PT compensation signal (SA_PT, green). The compensated data (SA_Comp, blue) does not show any perturbation.

Figure 6 shows instead the same set of data for the second week of the run presented in Fig. 3. An offset of 5 µm has been added to separate the curves. It is clear that compensated data have a smaller standard deviation with respect to uncompensated one. Also, some perturbations are present in the raw data (in orange) around day 4. The PT compensation (green) follows a similar behavior, meaning that the perturbation is not coming from the beam. Compensated data are then flat. On the other hand no compensation has been applied to the bump present between days 1 and 2. This might be related to beam motion.

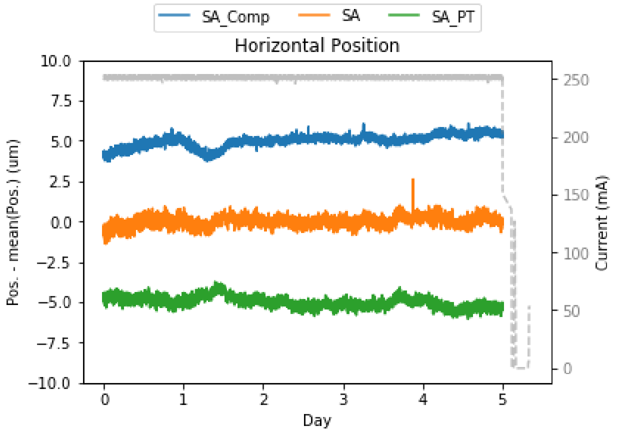

Figure 6: Horizontal position data from the PT-Libera Spark system. Note the PT actuating around day 4.

DIFFERENT FILLING PATTERNS

During machine dedicated time, different Filling Patterns (FPs) were injected in the storage ring. The idea was to see how the measured position and stability changed when changing the bunch distribution.

ALBA longitudinal structure is composed by 448 buckets. Three different FP were tested:

- Standard ALBA FP: First 440 buckets are filled and the last 48 are empty (98% of filled buckets);
- Eight trains: eight trains of 45 consecutive bunches, in between each train a gap of 11 empty buckets is present (80% of filled buckets);
- One-Third: Only 1/3 consecutive buckets are filled (33% of filled buckets).

As an example the ADC data of the One-Third FP is shown in Fig. 7. The buffer roughly covers three turns. It is clear that the gap is not empty but is filled by the PT-signal.

To have comparable data between different FPs, the current was fixed at 150 mA. The PT amplitude has been adjusted in order to maintain the same level of beam and PT signal.

For each FP, the position and the RMS over one hour data acquisition have been measured, after waiting for an additional hour to reach thermal stabilization. The position obtained using the standard FP has been used as a reference.

Figure 8 shows the position measured for each FP. Data shows a repetibility of the position measurement using different FP within 3 µm. The One-Third FP shows worst results for all electronics, this is due to the fact that only the 33% of buckets were filled, leading to a larger contribution of noise.

RMS of the position measurement, presented in Table 1, shows that, over the chosen time range, PT stability results

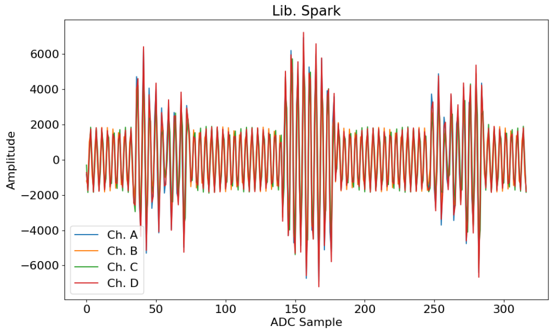

Figure 7: ADC data for the One-Third FP. The buffer covers three turns.

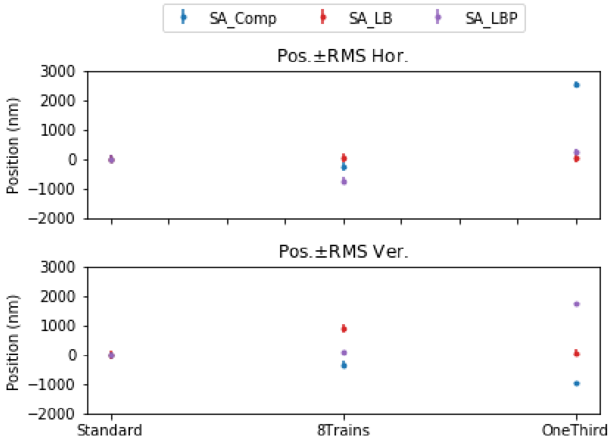

Figure 8: Positions for different FP measured with different electronics: PT-Libera Spark (blue), Libera Brilliance (red), Libera Brilliance+ (violet).

are comparable with the ones obtained with the Libera Brilliance+.

CONCLUSION

A PT-Libera Spark system has been installed and tested at the ALBA storage ring. Data taken during standard operation as well as in machine days proves that the PT compensation system is performing well to cure perturbation related with the cable/electronic path. Long term data indicates a slight tendency to drift in position while the position and stability obtained in the one hour time range show performances which are comparable to the one obtained with the Libera Brilliance+.

Table 1: SA Data RMS over One Hour Acquisition for Different FP

Fill. Pattern	**RMS (nm)**		
	Spark+PT	Brilliance	Brilliance+
Standard Hor.	121	141	123
Standard Ver.	92	143	70
8-Trains Hor.	149	147	125
8-Trains Ver.	115	153	61
1/3 Hor.	86	115	87
1/3 Ver.	70	116	82

ACKNOWLEDGEMENTS

Authors would like to thanks G. Brajnik (ELETTRA) and P. Leban (I-Tech) for the technical suport. Many thanks to R. Brouquart (Soleil) for providing the the PT generator device server.

REFERENCES

[1] F. Perez, “First Year Operation of the ALBA Synchrotron Light Source”, in *Proc. 4th Int. Particle Accelerator Conf. (IPAC’13)*, Shanghai, China, May 2013, paper MOPEA055, pp. 202–204.

[2] G. Benedetti, M. Carlà, U. Iriso, Z. Martí, and F. Perez, “A Distributed Sextupoles Lattice for the ALBA Low Emittance Upgrade”, presented at the 12th Int. Particle Accelerator Conf. (IPAC’21), Campinas, Brazil, May 2021, paper WEPAB074.

[3] P. Leban, “Libera Brilliance User Manual”, 2009.

[4] P. Leban, G. Brajnik, and R. De Monte, “Evaluation of Pilot-Tone Calibration Based BPM System at Elettra Sincrotrone Trieste”, in *Proc. 10th Int. Particle Accelerator Conf. (IPAC’19)*, Melbourne, Australia, May 2019, pp. 2638–2640. `doi:10.18429/JACoW-IPAC2019-WEPGW072`

[5] G. Brajnik, S. Carrato, S. Bassanese, G. Cautero, and R. De Monte, “A Novel Electron-BPM Front End With Sub-Micron Resolution Based on Pilot-Tone Compensation: Test Results With Beam”, in *Proc. 5th Int. Beam Instrumentation Conf. (IBIC’16)*, Barcelona, Spain, Sep. 2016, pp. 307–310. `doi:10.18429/JACoW-IBIC2016-TUPG02`

ISBN: 978-3-95450-230-1 ISSN: 2673-5350 doi:10.18429/JACoW-IBIC2021-MOPP27

EPU-PBPM WITH CVD-DIAMOND BLADE AT PLS-II

J. Ko*, D-T. Kim, G. Hahn, S. Shin and T. Ha
Pohang Accelerator Laboratory, POSTECH, Pohang, Republic of Korea

Abstract

All 18 photon beam position monitors (PBPM) installed on the PLS-II are tungsten blade types. The elliptical polarized undulator (EPU) has the characteristic that the spatial profile of the beam varies depending on the polarization mode. This is related to the thermal load of the blade and therefore changes in blade material are inevitable on fixed blades. In this paper, we analyze power density and flux density according to EPU mode and describe the process of installing new PBPM with CVD-diamond blades on the PLS-II EPU beamline for the first time.

INTRODUCTION

The Pohang Light Source II (PLS-II), a third-generation synchrotron-radiation source, has been operational since 2013, with electron-beam energy of 3 GeV and natural emittance of 5.8 nm-rad [1]. The maximum average beam current stored in the storage ring is 400 mA and operates in top-up mode to achieve stable electron-beam orbit as well as synchrotron-radiation flux. Currently, a total of 35 beamlines including 19 insertion-device beamlines are in operation for user service.

One of the major operational issues in electron-storage ring as a light source is the stability in the transverse position for the photon beam as well as the electron beam. To monitor the transverse position of the photon-beam the PLS-II installs 18 photon-beam position monitors (PBPM) at the font-end of the beamline. 13 of these operate on the planar undulator beamline and 5 on the bending magnet beamline. A pick-up usually has two or four blades. For beamlines using BM as a light source, it has two blades. For the blades, 0.5 mm-thick tungsten plates are used, which are installed on the top and bottom of the detector head [2].

For beamlines using an elliptically polarized undulator (EPU) as a light source a new type of PBPM is required. Because the spatial profile of the beam varies with the polarization of light, the blade can cut a large part of the photon beam from EPU. Thus, structural changes of the blades due to thermal loads could cause a problem because the existing blades are optimized for photon beams from bending magnets and planar undulators. Thus we built the new type of PBPM for EPU beamline (EPU-PBPM) invented by the Taiwan Light Source (TPS) [3]. In this paper, an analysis is described to verify that this EPU-PBPM satisfies the characteristics of the PLS-II EPU source.

DESIGN OF EPU-PBPM

Table 1 shows the parameters according to the polarization of EPU72 which is the light source of 10A1-Soft X-ray Nanoscopy beamline (BL10A) at PLS-II. EPU72 with a length of 2.6 m was divided into 72 mm intervals. Figure 1 shows a schematic diagram of the pick-up of EPU-PBPM, which is installed at the front-end 10 m away from EPU72. The blade spacing is 5 mm horizontally and 3 mm vertically. And the blades of EPU-PBPM were decoupled horizontally, this structure may be useful to suppress the cross-talk effect of scattered beams affecting the opposite blade.

Table 1: PLS-II BL10A EPU72 Parameters

	Hor. mode	Cir. mode	Ver. mode
$B_x(T)$	0	0.48	0.6
$B_y(T)$	0.79	0.48	0
K_x	0	3.24	4.09
K_y	5.33	3.24	0
Total power (kW)	3.30	2.44	1.94

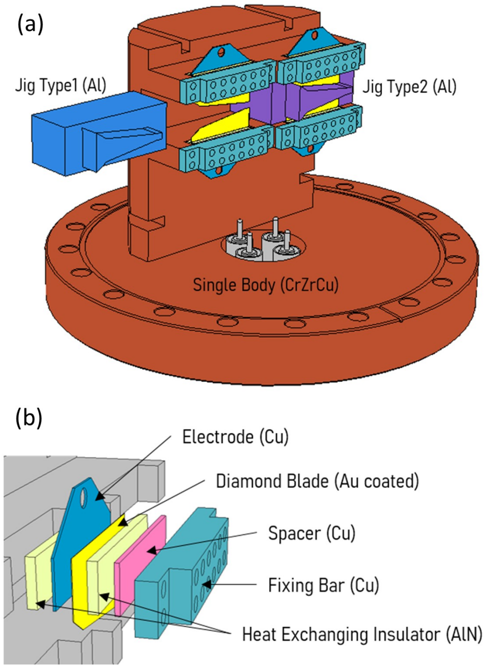

Figure 1: (a) A schematic diagram of the structure of the pick-up of EPU-PBPM. (b) Layered construction of blades.

ANALYSIS OF EPU-PBPM

Power Density

The power density according to the mode is shown in Figure 2. These properties were calculated using SPECTRA code [4]. Angular power density can evaluate the thermal

---

* kopearl@postech.ac.kr

load on the blades of the PBPM. Assuming that the beam passes through the center of the PBPM, the thermal load on the blades can be evaluated from the integral value in Fig. 2 (bottom).

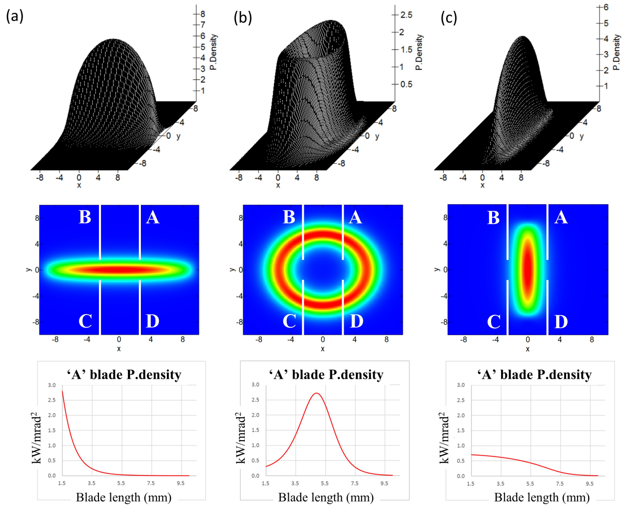

Figure 2: The power density according to the light polarization. (Top) 3D wire-frame. (Middle) 2D contour plot. (Bottom) Power density for 'A' balde. (a) is for horizontal linear mode, (b) is for circular mode, and (c) is for vertical linear mode.

The integral values are 2.3 for horizontal linear mode, 8.4 for circular mode, 3.1 for vertical linear mode, and we can see that the thermal load in circular mode is three times great than linear modes. Therefore, to cover these three modes with a fixed blade spacing of 5(H) x 3(V) mm, the blade material had to be changed to be effective for thermal loads.

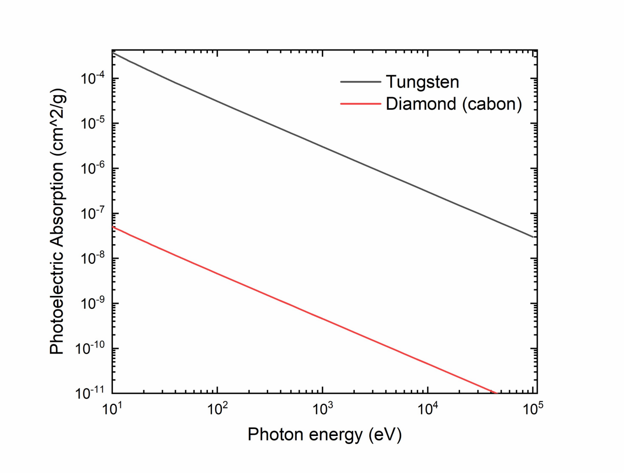

Figure 3: Comparison of photoelectric absorption of tungsten and diamond.

The diamond blade is more effective at thermal loads than the tungsten blade because it has a lower X-ray cross section. The energy domain of the synchrotron radiation we use mainly is 100 to 10000 eV. And in this region, the interaction between photons and materials is the photoelectric effect. Therefore the absorbed photons by the photoelectric effect are converted to heat, so if the photoelectric absorption cross section for X-ray [5] is small, the thermal load of the material is small. Figure 3 shows photoelectric absorption for tungsten and diamond. We can see that the photon absorption of diamond is 1/10,000 than that of tungsten. Therefore, CVD-diamond was adopted as a blade for EPU-PBPM.

Flux Density

The flux density for the three modes is shown in Fig. 4. It is also calculated using SPECTRA.

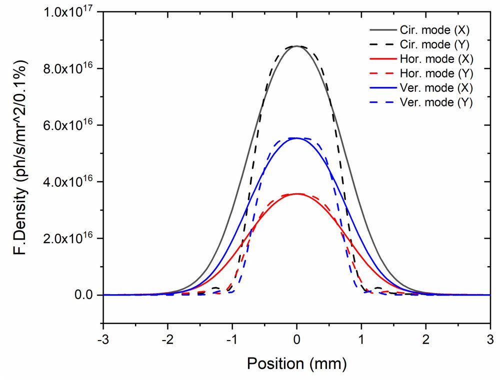

Figure 4: Flux density by polarization mode of EPU72.

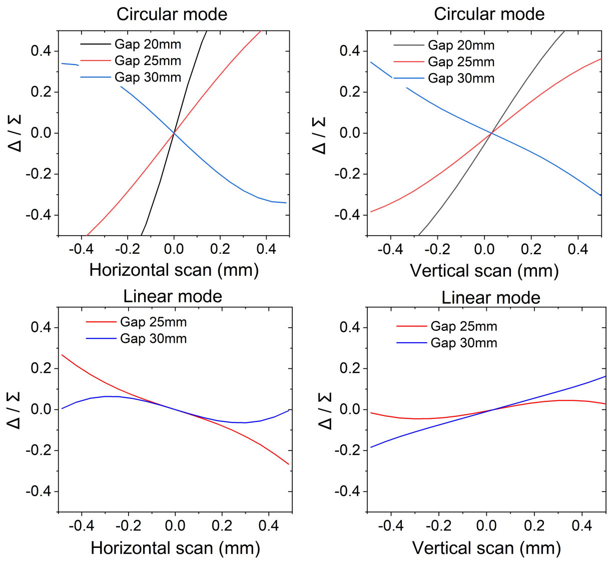

Figure 5: The position changes according to circular/linear polarization mode and undulator gap.

Flux density is used to evaluate whether EPU-PBPM can cover the positional changes of the three modes with fixed blade gap. Figure 5 and Table 2 show the rate of change in the position of the photon beam according to the pick-up stage and EPU gap. In all cases, linearity is obtained in the range of hundreds of micrometers and the slope is adjusted to 1 by adjusting the calibration factor K in the signal processor.

Table 2: The slope of linearity according to circular/linear polarization mode and undulator gap. Horizontal linear mode is used above 25 mm gap.

	Circular Mode X	Circular Mode Y	Hor. Linear Mode X	Hor. Linear Mode Y
Gap 20 mm	3.67	1.33	-	-
Gap 25 mm	1.45	0.70	0.37	0.16
Gap 30 mm	1.05	0.40	0.32	0.24

So, a CVD-diamond blade with a spacing of 5 (H)x3 (V) mm is considered suitable for thermal load and position measurement of the photon beam from the EPU72.

ASSEMBLY AND INSTALLATION

Figure 6 shows the assembly process of EPU-PBPM. A CVD-diamond is a commercial product of Applied Diamond, Inc. Four gold-plated CVD-diamond blades are inserted between insulators and mounted on copper blocks. During the assembly process, the electrical short and vacuum leakage tests are performed.

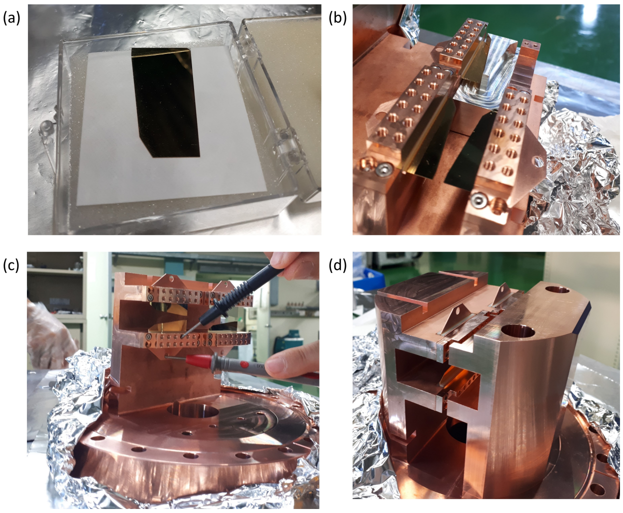

Figure 6: Assembly process for the EPU-PBPM. (a) A piece of CVD-diamond blade, (b) Utilizing jig, (c) Short test, (d) Complete basic configuration.

EPU-PBPM was installed at the front-end of BL10A during this summer maintenance (Figure 7) . Signal processing connection and calibration are the next steps, and will be applied to beam operation later this year.

CONCLUSION

A new type of EPU-PBPM has been installed on PLS-II for the first time. Although TPS XBPM was referenced for the pick-up design, an analysis of power density and flux density verifies that it is a photon beam position monitor that meets the characteristics of PLS-II EPU72. Furthermore, the horizontally decoupled blade structure is considered to be effective in suppressing the cross-talk effect shown in PBPM, which is currently operating on 18 beamlines. It will be used after thorough calibration and inspection, but particularly careful observation is required for the thermal load on diamond blades.

Figure 7: EPU-PBPM installation at the front-end of BL10A.

ACKNOWLEDGEMENTS

We would like to thank J.-Y. Chuang (NSRRC,TPS) for providing helpful information and the many useful discussions. This work was supported by the Basic Science Research Program through the National Research Foundation of Korea (NRF-2019R1C1C1003412) and by the Basic Science Research Program through the National Research Foundation of Korea (NRF-2019R1C2C1004862).

REFERENCES

[1] S. Shin *et al.*, “Commissioning of the PLS-II”, *J. Instrum.*, vol. 8, no .1, P01019, 2013. doi:10.1088/1748-0221/8/01/p01019

[2] C. Kim *et al.*, “Correlation study of a beam-position monitor and a photon-beam-position monitor in the PLS-II”, *J. Korean Phys. Soc.*, vol. 66, p. 167, 2015.

[3] J.-Y. Chuang *et al.*, “Discussion and improvement of a blade-type XBPM with coupling suppression by compensating calibration coefficients”, *Nucl. Instrum. Methods Phys. Res. A*, vol. 953, p. 163174, 2020. doi:10.1016/j.nima.2019.163174

[4] T. Tanaka and H. Kitamura, “SPECTRA: a synchrotron radiation calculation code”, *J. Synchrotron Rad.*, vol. 8, p. 1221, 2001. doi:10.1107/S090904950101425X

[5] https://www.nist.gov/pml/xcom-photon-cross-sections-database

DEVELOPMENT OF 8 STRIPLINE BPM FOR MEASUREMENT OF MOMENTUM SPREAD OF ELECTRON BEAM AT INJECTOR TEST FACILITY OF POHANG ACCELERATOR LABORATORY

C. Sung, S. Kim, B. Shin, M. Chung*
Ulsan National Institute of Science and Technology, Ulsan, Republic of Korea
I. Nam, C. Kim, Pohang Accelerator Laboratory, Pohang, Republic of Korea

Abstract

A stripline beam position monitor has been developed with 8 feedthroughs in order to nondestructively measure the momentum spread of beam. The beam momentum spread causes the variation of transverse beam width at a dispersive section and can be detected by the multipole moment based analysis of the beam-induced electromagnetic field. The feasibility of such a device will be tested with electron beam generated in the beamline of Injector Test Facility (ITF) at Pohang Accelerator Laboratory (PAL). The experimental preparation with electron beam test will be presented and the future plan for an application to bunch compressors at X-ray Free Electron Laser (XFEL) of PAL will be followed.

INTRODUCTION

A beam position monitor was proved that it enables to nondestructively measure an energy spread of an electron beam with multi-striplines by T. Suwada *et al.* [1]. At a dispersive section such as a bending point with dipole magnet, the transverse beam width is varied in the bending plane depending on a momentum spread of beam so that the quadrupole moment becomes non-negligible in the transverse plane. R. H. Miller demonstrated the beam position monitor can be used to measure the quadrupole moment [2].

The 8-stripline BPM has been developed to nondestructively control the momentum spread of electron beam for X-ray Free Electron Laser at Pohang Accelerator Laboratory (PAL-XFEL). The stiplines were designed to match the characteristic impedance as 50 Ω following [3, 4]. It is tested with a conducting wire and thin Cu sheet for the resolution to quadrupole moment before the electron beam test.

Beam dynamics simulations were also performed to predict the relation between the quadrupole moment and momentum spread of PAL-XFEL electron beam with the `ELEGANT` [5].

The deivce is implemented for the electron beam test at the Injector Test Facility (ITF) of PAL [6]. The PAL-ITF consists of a photocathode RF gun, a booster cavity (accelerates up to 70 MeV), dipole and quadrupole magnets within about 10 meter space [7].

MOMENTUM SPREAD AND MULTIPOLE MOMENT ANALYSIS

When the particle beam travels at a dispersive section such as a dipole magnet, the path length of particles differ with its longitudinal momentum so that the transverse distribution will be changed at the exit. For example, if a particle is bent in the horizontal plane (x), the particle position will be changed as

$$x_f = x_i + D_x\left(\Delta P_x/P_0\right). \tag{1}$$

with x_i, x_f for the initial and final horizontal positions. D_x is the dispersion function at dispersive section and $\left(\Delta P/P_0\right)$ is the fraction of momentum deviation to the total momentum, P_0.

The difference of squared RMS beam size defines a quadrupole moment and it can be written as

$$\sigma_x^2 - \sigma_y^2 = \beta_x\epsilon_x - \beta_y\epsilon_y + D_x^2\langle(\Delta P/P_0)^2\rangle. \tag{2}$$

where $\left(\sigma_x^2 - \sigma_y^2\right)$ in the L.H.S is the quadrupole moment. In the R.H.S, the β_x, β_y are the beta functions in x and y direction. ϵ_x, ϵ_y are the RMS emittances in x and y directions, respectively, and $\langle(\Delta P/P_0)^2\rangle$ is the RMS momentum spread.

The RMS momentum spread can be figured out by the measurement of quadrupole moment defined as above nondestructively with the stripline monitor.

Multipole Moment Analysis

A charged particle beam induces an image current on a surface of surrounding conducting chamber and the image current density is described by the series representation as below

$$\begin{aligned} J &= \frac{I_{\text{beam}}}{2\pi r}\left[1 + \frac{2\rho}{r}\cos(\theta - \phi)\right. \\ &+ \left.\frac{2\rho^2}{r^2}\cos(2\theta - 2\phi) + 2\frac{\sigma_x^2 - \sigma_y^2}{r^2}\cos(2\theta + 2\alpha)\right]. \end{aligned} \tag{3}$$

In the Eq.(3), the (r, θ) and (ρ, ϕ) represent the position of electrode and beam centroid, respectively, and the I_0 is the beam current and α is the skew angle of transverse beam distribution.

Thus, the quadrupole moment will be reconstructed from the measurement with multiple striplines (in this proceeding,

---

[*] mchung@unist.ac.kr

ISBN: 978-3-95450-230-1 ISSN: 2673-5350 doi:10.18429/JACoW-IBIC2021-MOPP28

8 were used), even though the quadrupole moment contributes very weakly to the total signal as it is inversely proportional to the square of the radius of chamber.

PARTICLE SIMULATION FOR RECONSTRUCTION OF QUADRUPOLE MOMENT

It is demonstrated in the particle simulation with the beam dynamics code `ELEGANT` [5] that there is a the feasibility of reconstructing the momentum spread from the quadrupole moment. The simulation aims to reconstruct the momentum spread at the bunch compressor of PAL-XFEL which consists of 4 dipole magnets as a chiance structure. In the bunch compressor, the transverse beam distribution is expected to be manipulated as the Fig. 1 in which the quadrupole moment is large because of the momentum spread.

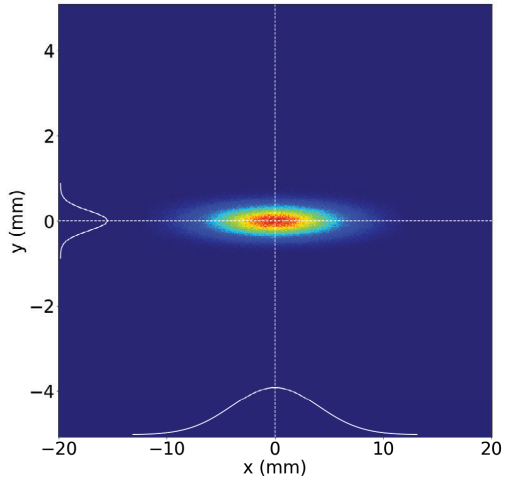

Figure 1: Transverse beam distribution after dispersive section.

In the simulation result (Fig. 2), it is expected that the multipole moment analysis enables to measure the momentum spread of around 0.2 ~ 0.4% for 200 pC electron beam of PAL-XFEL since the quadrupole moment is around a few squared milli-meter level.

FABRICATION AND BENCH TEST OF 8-STRIPLINE BPM

Design of Stripline BPM

Following P. Forck [4], the mechanical dimension of stripline is optimized to match the characteristic impedance to 50 Ω. In order to comply with the beamline dimension of PAL-XFEL, the structure is fabricated as the Fig. 3 with the dimensions as listed below and the design work is carried out with the `Computer Simulation Technology Particle Studio` (CST PS).

- Chamber diameter: 22 mm
- Stripline radius: 19 mm
- Opening angle of stripline: 23°
- Stripline thickness: 1 mm

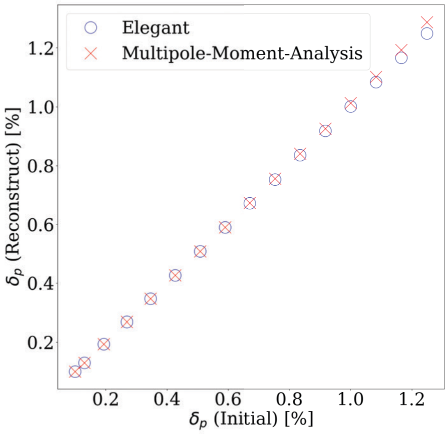

Figure 2: Momentum spread determined from quadrupole moment.

- Stripline length: 120 mm
- End-to-end length: 180 mm

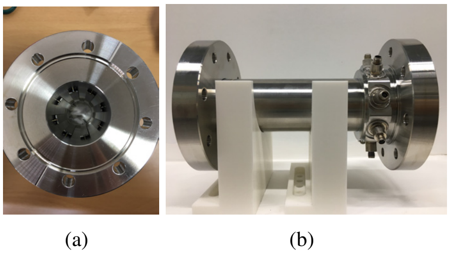

(a) (b)

Figure 3: Fabricated prototype BPM.

Time Domain Reflectometry

After the fabrication, it is tested with the time domain reflectometry to characterize the impedance of striplines. The results in the Fig. 4 show that the electrodes are designed to well match the characteristic impedance to 50 Ω with slight discrepancies.

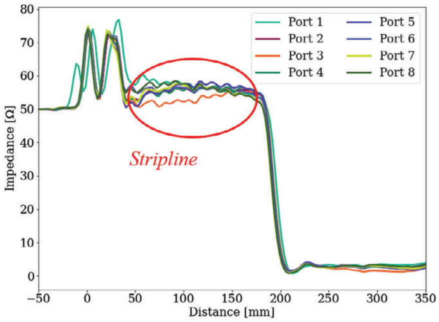

Figure 4: Result of Time Domain Reflectometry.

Bench Test

The stripline BPM is inserted by a conducting wire or a thin Cu sheet. Then, a pulsed signal is sent from the signal generator and the output data is transferred to the digital oscilloscope Fig. 5.

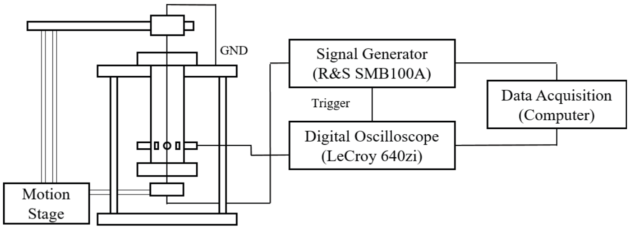

Figure 5: Schematic diagram of test stand.

Using the wire or Cu sheet, the device has been tested for the resolution of centroid position and skew angle. As a result, the resolutions were achieved as 1 milli-meter and 1 degree as shown in the Fig. 6. It will be further tested with electron beam at the Injector Test Facility of PAL, which provides 70 MeV electrons via an RF photocathode gun and an S-band cavity.

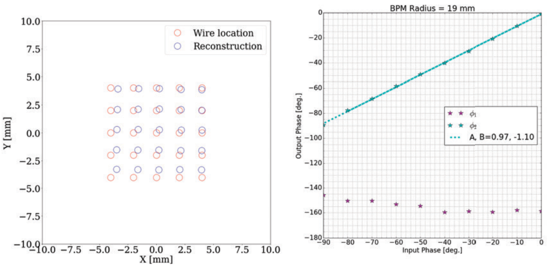

(a) Position (b) Skew angle

Figure 6: Resolution results of bench test.

Injector Test Facility of PAL

Figure 7 shows the ITF beamline where the RF photocathode gun is found in the bottom.

The RF photocathode gun is developed with 1.6 cell 2.856 GHz cavity. The electrons are emitted at the wall of gun first cell with a laser pulse driven by Ti:Sapphire laser system. After emitted from the cathode, the electrons are accelerated up to 70 MeV through a traveling wave structure for which the klystron and modulator provide an RF power [7]. The magnets and various instruments are followed by the accelerating cavity, for instance, the dipole and quadrupole magnets. Transverse deflecting cavity and many diagnostic systems are installed.

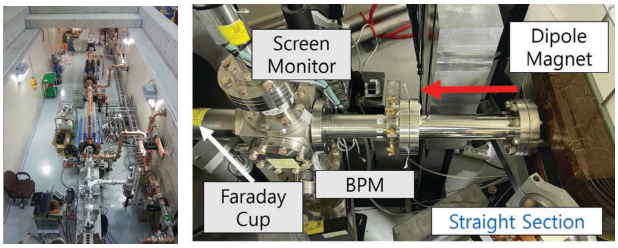

(a) (b)

Figure 7: PAL-ITF beamline.

The 8-stripline BPM is implemented at the behind of dipole magnet in the end of beamline as shown in Fig. 7(b). The electron beam will be measured with the stripline BPM and screen monitor, and dumped at the Faraday cup after controlled by the dipole and quadrupole magnets and the accelerating cavity.

CONCLUSION AND FUTURE PLAN

The stipline BPM has been developed with 8 feedthroughs in order to non-destructively measure the momentum spread of electron beam at PAL-XFEL. Following the particle simulation with the `ELEGANT`, it is shown that it can be applicable for the electron beam of PAL-XFEL with the resolution of 0.2 ~ 0.4% for the RMS momentum spread. After it was tested with the conducting wire and Cu sheet, it has been installed at the beamline of PAL-ITF for the further electron beam test.

REFERENCES

[1] T. Suwada *et al.*, “Nondestructive Beam Energy-Spread Monitor Using Multi-Strip-Line Electrodes”, *Phys. Rev. ST Accel. Beams*, vol. 6, p. 032801, March. 2003. doi:10.1103/PhysRevSTAB.6.032801

[2] R. H. Miller *et al.*, “Nonintercepting Emittance Monitoring”, in *Proc. HEAC’83*, Fermilab, Illinois, 1983, pp. 602-605.

[3] R. E. Shafer, “Beam Position Monitoring”, AIP *Conf. Proc.*, vol. 249, n. 1, pp. 601–636, 1992. doi:10.1063/1.41980

[4] P. Forck *et al.*, “Beam Position Monitors”, CERN Accelerator School (CAS), Dourdan, 2009, CERN-2009-005 p. 187.

[5] M. Borland, “A Flexible SDDS-Compliant Code for Accelerator Simulation”, Argonne, IL, USA, APS/LS-287, 2000.

[6] S. J. Park *et al.*, “Construction of Injector Test Facility (ITF) for the PAL XFEL”, in *Proc. IPAC’13*, Shanghai, China, May 2013, paper WEPWA043, pp. 2220–2222.

[7] J. H. Han *et al.*, “Injector Design for PAL-XFEL Project”, in *Proc. IPAC’12*, New Orleans, LA, USA, May 2012, paper TUPPP060, pp. 1732–1734.

ISBN: 978-3-95450-230-1 ISSN: 2673-5350 doi:10.18429/JACoW-IBIC2021-MOPP29

DESIGN AND OPTIMISATION OF BUTTON BEAM POSITION MONITOR FOR SPS-II STORAGE RING*

S. Naeosuphap†, P. Sudmuang, Synchrotron Light Research Institute, Nakhon Ratchasima, Thailand

Abstract

The Beam Position Monitors (BPMs) for the new Thailand synchrotron light source, Siam Photon Source II (SPS-II), has been designed utilizing as the essential tool for diagnosing the position of the beam in the storage ring. Its design with four-button type BPM has been optimized to obtain the high precision of position data in normal closed orbit and feedback mode as well as turn by turn information. We calculate feedthroughs capacitance, sensitivities, induced power on a 50 Ω load, and intrinsic resolution by using Matlab GUI developed by ALBA, to find the appropriate position, thickness, and gap of the BPM button. Extensive simulation with the electromagnetic simulation packages in CST Studio Suite was also performed to investigate the dependence of the induced BPM signal, wakefield, Time Domain Reflectometry (TDR), and power loss on different BPM geometry.

INTRODUCTION

Four-button pick up electrodes have designed for a stable and precise beam position monitor in the SPS-II storage ring. They are an essential part to provide information about the position of the beam in the vacuum chamber during machine commissioning, beam tuning and routine operation. The preliminary design of the button electrode is performed by using ALBA/DIAMOND Matlab tool [1]. The button diameter, thickness and the gap between button and chamber wall are necessary to optimize for archiving low power losses, high signal transmission, Time Domain Reflectometry (TDR), Thermal transferring and proper impedance matching. These simulations are performed by using simulation packages in CST Studio Suite. [2]. The model was used in the simulation shown in Fig. 1.

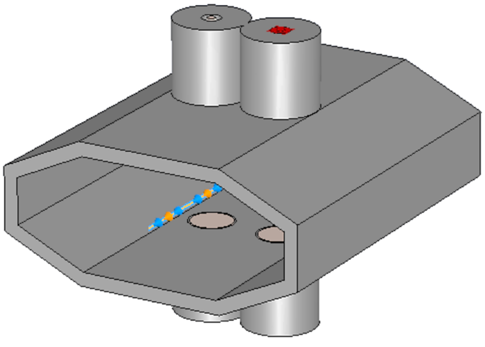

Figure 1: A simulation model of SPS-II storage ring BPM.

SPS-II BPM REQUIREMENT

The SPS-II storage ring consists of 14 Double Triple Bend Achromat (DTBA) cells and each cell is equipped with 10 BPMs. In total, there are 140 BPMS utilized for the machine operation. Since the beam size at the center of an IDs is approximately 2.6 μm, the beam position stability of 0.2 μm level needs to be obtained. The BPM button geometry, especially for button diameter has been considered to provide about 100 nm position resolution at 100 mA and 2 kHz bandwidth.

GENERAL CONSIDERATION OF BPM BUTTON

The BPM chamber has been modeled based on a standard storage ring vacuum chamber which is designed as an octagonal shape with a vertical inner aperture of 16 mm, a horizontal inner aperture of 40 mm and sides of 6.6 mm. To achieve the required resolution, the calculation of sensitivity, signal power and intrinsic resolution are performed by using Matlab tool. This software can study the basic geometries and related parameters of BPM at a preliminary design phase. The goal of this calculation is to optimize the button diameter, button gap and thickness, as well as the button separation on the storage ring vacuum chamber.

Mechanical Design

In order to achieve sufficient induced power, sensitivity, and mechanical limitation of the storage ring vacuum chamber the BPM button diameter is considered to be 6 mm. The gap size between button electrode and housing should be smallest as possible as a mechanical limitation, to increase the button capacitance and shifts the high order modes (HOM) resonances to higher frequencies [3]. The trapped HOMs can be caused by beam instabilities and will leak inside the button when the button thickness is too thin. To avoid this issue, we considered increasing the button thickness to be 4 mm. Design parameters of the SPS-II button pick up electrodes are shown in Table 1.

The simulation results of sensitivity, signal power and intrinsic resolution are shown in Fig. 2. To obtain the horizontal and vertical sensitivities (Sx and Sy), a Delta over Sum method is used [4], the slope at no beam displacement gives us the Sx and Sy is 0.1359 and 0.1343, respectively. Considering a bandwidth of 2 kHz, which is the expectation value for a fast orbit measurement system, the calculated intrinsic resolution of the BPM button at 100 mA beam current is 14.63 nm, which meets the specific requirements for the measurement resolution.

Table 1: Preliminary Design Parameters for the SPS-II BPM Button

Button calculation parameters (mm)	
Button diameter	6
Button thickness	4
Button gap	0.3
Button separation	10.5

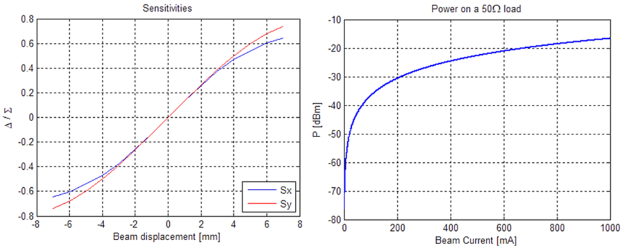

Figure 2: Calculated sensitivity and signal power of SPS-II storage ring BPM.

Optimisation of BPM Buttons Separations

Sensitivity is one of the important characteristics of a BPM system, which depends on the button diameter, the horizontal and the vertical separations of the buttons, and the distance from the button to the electron beam. In our case, the vertical button separation is fixed due to the chamber inner aperture of 16 mm. The length of horizontal button separation can be optimized with no more than 20 mm by combining button diameter and button gap between button and housing. Hence, the maximum button separation is 13.4 mm with considering the button diameter and button gap of 6 and 0.3 mm, respectively. We have calculated the sensitivity with different horizontal button separations from 10 mm to 12 mm to determine the proper horizontal button separation. The result is shown in Fig. 3. The horizontal button separation of 10.5 mm is chosen that both sensitivity Sx and Sy are approximately the same at 0.134.

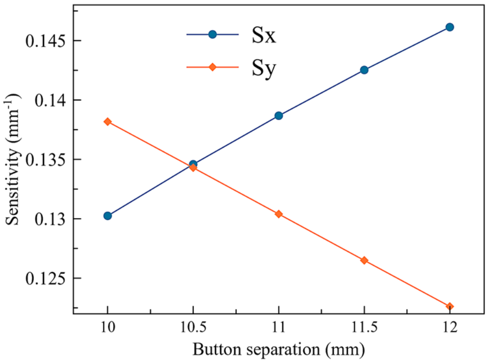

Figure 3: BPM sensitivities in the horizontal and vertical direction as a function of horizontal button separation.

Impedance Matching

The BPM button pick up electrode is defined as similar to a coaxial cable which has a characteristic impedance of 50 Ω. If it is matched well to 50 Ω, there will be no TEM-modes reflected in the chamber [5]. Thus, the diameter of ceramic, pin and feedthrough are optimized by using Eq.1.

$$Z_0 = \frac{1}{2\pi\varepsilon_0 c} \cdot \sqrt{\frac{1}{\varepsilon_r}} \cdot \ln\left(\frac{D}{d}\right), \qquad (1)$$

where Z_0 is characteristic impedance in Ω, ε_0 is vacuum permittivity, ε_r is the relative permittivity of the dielectric, c is the speed of light, D is the inner diameter of the outer conductor and d is the diameter of the inner conductor. The matching gives us the diameter of feedthrough, pin and ceramic diameter is 2.764 mm, 1.2 and 6.6 mm, respectively.

SIMULATION OF BPM BUTTON SIGNAL

The SPS-II button geometry as shown in Fig. 4 is based on button geometry implemented at ALBA [6]. The BPM housing and chamber are made of stainless steel 316L. The BPM button and central conductor are made of Molybdenum and form the central pin of a reverse-polarity female SMA connector. An insulator is located between the central conductor and the outer conductor for electric insulation and vacuum shielding and is made of aluminium oxide (Al_2O_3). There is an insert step button and an upper ceramic gap in the button structure which use to improve the time signal and shift HOM inside the button.

To check the BPM performance, we have simulated RF characteristics on the BPM button pick up electrodes such as induced voltage signal, wake impedance, Time Domain Reflectometry and power loss by using CST CST Studio Suite with three simulation packages consists of Wakefield solver, Time domain solver, and Thermal and Mechanics. The BPM model as shown in Fig. 1 and Fig. 4 are used in the CST simulation.

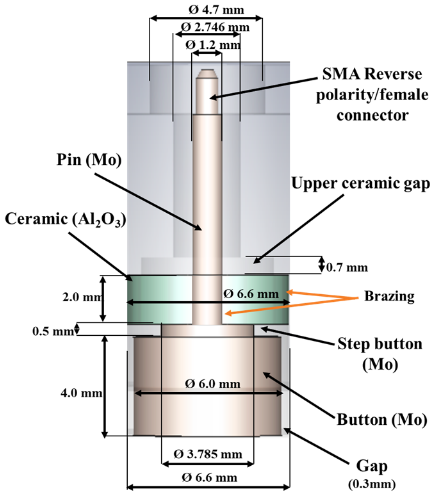

Figure 4: The designed BPM button electrode for the SPS-II storage ring.

Time Signal

An induced voltage signal for a single bunch electron beam obtained from the Wakefield simulation package in the CST Particle Studio is shown in Fig. 5.

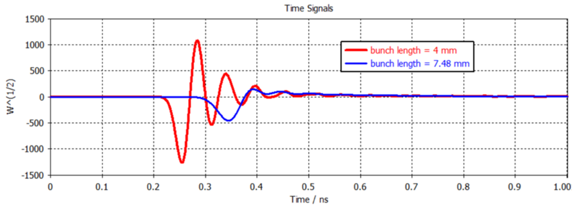

Figure 5: Simulation result of an induced voltage signal of BPM button as a function of time with different bunch lengths.

A signal waveform with bunch length (σ) 4 mm and 7.48 mm are also plotted for comparison. At the natural bunch length of 7.48 mm (24.9 ps), a bipolar oscillating impulse can be observed.

Wake Impedance

In the preliminary design, it is preferable to have the ceramic insulator of 1 mm thickness but the manufacturing might be an issue due to the brazing process with low thickness ceramic size. Thus, the effect of different ceramic thicknesses on the longitudinal wake impedance are also studied together with the effect of the step button and upper ceramic gap. For the 2 mm thickness ceramics, the first trapped mode arises at frequency 13.49 Hz, compared to the 1 and 1.5 mm thickness ceramics with arising at frequency 14.30 Hz and 13.87 Hz, respectively as shown in Fig. 6. This suggests that the low ceramic thickness should be chosen for shifting the first trapped mode to a higher frequency.

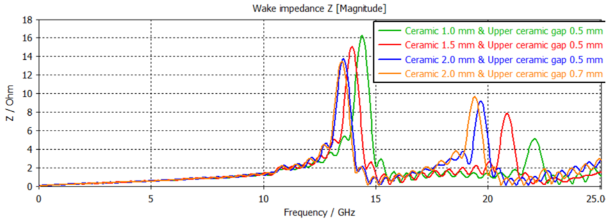

Figure 6: Simulation result of longitudinal wake impedance as a function of frequency with different ceramic thickness and upper ceramic gap thickness.

In the simulation results caused by an adjusting thickness of the upper ceramic gap, it was found that there is no strong effect on longitudinal wake impedance. With 0.5 mm thickness, the first trapped mode is slightly better than 0.7 mm thickness.

Time Domain Reflectometry (TDR)

TDR curve obtained by CST Time domain simulation is shown in Fig. 7. It can be seen a slightly mismatching in ceramic position at a time of 0.16 ns when the ceramic thickness is increased. While adjusting the thickness of the upper ceramic gap does not affect the TDR curve.

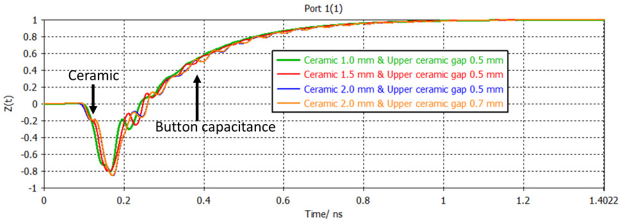

Figure 7: TDR simulation result.

In TDR simulation results, the button capacitance of 3.10 pF can also be obtained by fitting the curve with the equation of reflectivity as:

$$\rho = 1 - e^{-\frac{t-t_0}{\tau}} \tag{2}$$

$$\tau = R \cdot C_b,$$

where R is feedthrough characteristic impedance and C_b is button capacitance [7].

Power Loss

The loss factor due to a single bunch was calculated for all three different ceramic thicknesses by using the Wakefield solver. The wake loss factor (κ_{loss}) for the longitudinal wake component is calculated by:

$$\kappa_{loss} = -\int_{-\infty}^{\infty} \lambda(s) W_{||}(s) ds \tag{3}$$

where $\lambda(s)$ describes the normed charge distribution function over electron direction (s) and $W_{||}(s)$ is the longitudinal wake impedance. It is given in [V / pC] [8]. The power loss (P_{loss}) depends on the wake loss factor and bunch parameters, which can be defined as

$$P_{loss} = T_0 \frac{I_{av}^2}{M} \kappa_{loss}, \tag{4}$$

where I_{av} is the total average current, T_0 is the revolution period, and M is the number of bunches.

Summary results of the wake loss factor are shown in Table 2. The calculation results for bunch length (σ) of 4 mm and 7.48 mm are also shown for comparison. The power loss is found at 1 to 7 Watt, for σ = 7.48 mm and 4 mm respectively, at I_{av} = 300 mA in M =140 bunches and 1.2 µs revolution period. As shown in Table 2, the wake loss factor increases slightly when the thickness of the ceramic is increased.

Table 2: Summary Results of the Loss Factor for Different Ceramics Thickness

Ceramic (mm)	**κ_{loss} (mV/pC) (σ = 4 mm)**	**κ_{loss} (mV/pC) (σ = 7.48 mm**
1.0	9.301	1.441
1.5	9.358	1.485
2.0	9.369	1.519

THERMAL ANALYSIS OF BPM BUTTON

Thermal simulation of heat transfer for three different ceramic thicknesses was calculated by CST Thermal and Mechanics module. In the simulation, an ambient temperature of 30 °C and one watt heat source are applied to each button as a worst-case. The simulation results are shown in Fig. 8. It can be seen that increasing the ceramic thickness reduces the temperature difference between Button and Pin (ΔT = T_{button}-T_{pin}). The greatest temperature difference ΔT= 2.24 °C) is found on the BPM structure with 2.0 mm ceramic thickness. This is mainly due to the larger contact area between the button and ceramics.

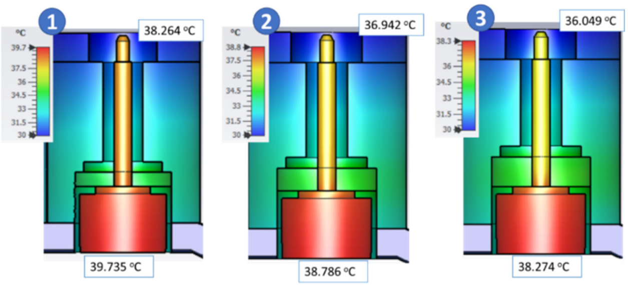

Figure 8: Thermostatic results for 1) Ceramic thickness 1 mm, 2) Ceramic thickness 1.5 mm, 3) Ceramic thickness 2 mm.

CONCLUSION

The SPS-II BPM is composed of the four-button pick up electrodes and the 50-Ω-matched SMA-type feedthrough mouthed on the octagon chamber. The button diameter, the button gap, and the horizontal separations of the buttons are designed as 6 mm, 0.3 mm, and 10.5 mm, respectively. This BPM design is sufficient to obtain 100 nm position resolution at 100 mA and 2 kHz bandwidth. In order to verify the BPM performance, the RF characteristics together with the thermal analysis on the BPM button are also performed by using the simulation packages in CST Studio Suite. The BPM capacitance, sensitivities obtained from CST simulation is in good agreement with the value calculated by the Matlab tool. The effect of different bunch lengths and different BPM button geometry on the induced voltage signal, wake impedance, wake loss, TDR and heat transfer have been analysed. It was found that these parameters need to be optimized together in order to determine the proper BPM geometry. Manufacturing of the SPS-II BPM button prototypes will be performed by choosing the BPM structure with the ceramic thickness of 1.5 mm and the upper gap thickness of 0.5 mm.

ACKNOWLEDGEMENTS

We would like to thank all the members of the SPS-II technical support team for their assistance, encouragement, and co-operation.

REFERENCES

[1] A. Olmos, F. Pérez, and G. Rehm, "Matlab code for BPM button geometry computation", in *Proc. 8th European Workshop on Beam Diagnostics and Instrumentation for Particle Accelerators (DIPAC'07)*, Venice, Italy, May 2007, paper TUPC19, pp. 186-188. `doi:10.1.1.611.4846`

[2] CST, `http://www.cst.com/`.

[3] M. Shafiee, S.A.H. Feghhi, and J. Rahighi, "Numerical analysis of the beam position monitor pickup for the Iranian light source facility", *Nuclear Instruments and Methods in Physics Research Section A*, vol. 874, pp. 162-170, 2017. `doi:10.1016/j.nima.2016.11.065`

[4] S.R. Smith, "Beam Position Monitor Engineering", in *Proc. 7th Beam Instrumentation Workshop*, Argonne, IL, USA, 6-9 May 1996, pp. 50-65. `doi:10.1063/1.52306`

[5] A. Blednykh *et al.*, "NSLS-II Storage Ring BPM Button Development", in *Proc. 6th Int. International Particle Accelerator Conf. (IPAC 2015)*, Richmond, Virginia, USA, May 2015, pp. 3-8. `doi:10.18429/JACoW-IPAC2015-MOPMN021`

[6] ALBA, `http://www.cells.es/Divisions/Accelerators/RF_Diagnostics/Diagnostics/OrbitPosition/BlocksAndButtons/SR/`.

[7] Y. T. Huang *et al.*, "Development of a Feedthrough with Small Reflection for the TPS BPM", in *Proc. 2nd Int. 2nd Int. Particle Accelerator Conf. (IPAC'11)*, San Sebastian, Spain, Sep. 2011, paper TUPS029, pp. 1593-1595.

[8] H. O. C. Duarte, S. R. Marques, and L. Sanfelici, "Design and Impedance Optimization of the SIRIUS BPM Button", in *Proc. 2th Int. Beam Instrumentation Conf. (IBIC'13)*, Oxford, UK, Sep. 2013, paper TUPC07, pp. 365-368.

ISBN: 978-3-95450-230-1 ISSN: 2673-5350 doi:10.18429/JACoW-IBIC2021-MOPP29

TESTS OF A NEW BPM LONG TERM DRIFT STABILIZATION SCHEME BASED ON EXTERNAL CROSSBAR SWITCHING AT PETRA III

G. Kube, F. Schmidt-Föhre, K. Wittenburg, Deutsches Elektronen-Synchrotron DESY, Germany
A. Bardorfer, L. Bogataj, M. Cargnelutti, P. Leban, P. Paglovec, B. Repič, I-Tech, Solkan, Slovenia

Abstract

For the new PETRA IV project at DESY, about 800 high resolution BPMs will be installed with the readout electronics system based on MTCA.4 as technical platform. In order to fulfill the requested long–term drift requirement to be less than 1 micron over a period of six days (one week of user operation), due to the machine–specific geometry the BPM cable paths have to be stabilized in addition. To achieve this demand, the well proven concept of crossbar switching was extended such that the analogue switching part is separated from the read–out electronics and brought as close as possible to the BPM pickup. This contribution summarizes first proof–of–principle measurements which were performed at PETRA III using a modified Libera Brilliance+ with external switching matrix. These measurements indicate that the concept of external switching works well and that the performance of this modified test setup fulfills the specifications.

INTRODUCTION

The PETRA IV project at DESY aims to upgrade the present synchrotron radiation source PETRA III into an ultralow-emittance source which will be diffraction limited up to X-rays of about 10 keV [1]. Using a hybrid six bend achromatic (H6BA) lattice with a unit cell providing an emittance of 45 pm rad, the target emittance of about 20 pm rad will be recovered by a large number of damping wigglers distributed in the short straights of the octants not equipped with user beamlines [2]. This small PETRA beam emittance translates directly into much smaller beam sizes of 7 μm in both planes at the insertion device source points, thus imposing stringent requirements on the machine stability. In order to measure beam positions and control orbit stability to the requisite level of accuracy, a high resolution BPM system will be installed which consists of about 800 individual monitors with the readout electronics based on MTCA.4 as technical platform.

In Table 1 the BPM readout specifications are summarized. As demonstrated already in Refs. [3, 4], the listed requirements are achievable with the commercial Libera Brilliance+ (LB+) system [5]. However, in order to fulfill the requested long-term drift requirement for the case of PETRA IV, the specific machine geometry has to be taken into account. Originally, PETRA was built in 1976 as an e^-/e^+ collider for high–energy physics, later on acting as pre–accelerator for the hadron–electron ring accelerator HERA, then converted into the 3^{rd} generation synchrotron light source PETRA III which started operation in 2009 [6]. Due to the history as high–energy physics collider, the PETRA machine circumference of 2304 m is much larger compared to light sources built in the last two decades, and the machine infrastructure is distributed in the former experimental halls with the result of long cable lengths between monitor and readout electronics. Driven by considerable cost saving, the plan for PETRA IV is to reuse again the existing ring tunnel in the areas between the experimental halls as shown in Fig. 1. However, the tunnel cross section is too small for housing all required cables, i.e. it will not be possible to interconnect BPM pickups in the accelerator with their corresponding readout electronics in an experimental hall using cable paths inside the accelerator tunnel. As consequence, additional cable access shafts will be required to minimize the arising load inside the tunnel, and it is not guaranteed that cable routing will be in a perfectly stabilized temperature and humidity environment, thus affecting the BPM position readings [7, 8]. Therefore, in order to fulfill the requested long–term drift stability the BPM cable paths have to be stabilized in addition.

Table 1: Readout electronics specifications. The single bunch / turn resolution holds for 0.5 mA bunch current, the closed orbit one for 1 kHz bandwidth, the beam current dependency for a 60 dB range with centered beam, and the long term stability should be measured over 6 days and a temperature span of ±1 deg within a stabilized rack.

Requirement	Value
single bunch / single turn	< 10 μm
closed orbit resolution	< 100 nm (rms)
beam current dependence	±2 μm
long term stability	< 1 μm

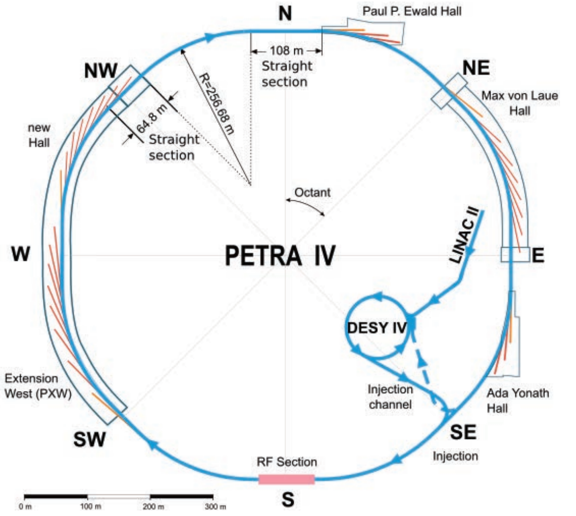

Figure 1: Layout of the PETRA IV facility.

ISBN: 978-3-95450-230-1 ISSN: 2673-5350 doi:10.18429/JACoW-IBIC2021-MOPP30

Different drift compensation schemes are available, the most popular one is the well proven concept of crossbar switching [9, 10] which is implemented in the *Libera* modules and stabilizes the analogue RF front–end part of the system. Another concept which has gained in popularity in recent years is the pilot tone (PT) compensation method where a sinusoidal PT signal with fixed frequency close to the carrier one is injected in the signal chain. This signal is used as reference for calibration and compensation, see e.g. Refs. [11–16]. If the PT signal is injected close to the BPM pickup before the cable, not only the front–end but also cable drifts can be compensated. However, the same effect can be achieved for crossbar switching if the analogue switching part is separated from the read–out electronics and brought as close as possible to the BPM pickup. In Ref. [17] both methods are discussed in detail and compared with each other. Based on this discussion and tests performed with the PT compensation scheme at PETRA III, it was decided to follow the idea with external crossbar switching.

This contribution summarizes first proof–of–principle measurements which were performed at PETRA III using a modified LB+ with an external switching matrix. These measurements indicate that the concept works well and that the performance of this modified test setup fulfills the specifications for PETRA IV.

TEST SETUP AT PETRA III

A sketch of the setup in use for the PETRA III studies is shown in Fig. 2. In order to get rid of the beam jitter, the four pickup signals from a test BPM in the tunnel are summed up with a combiner/splitter (MACOM DS-409-4), attenuated by a 500 MHz bandpass filter (Wainwright Instruments, WBK500-15-5SS), split again by the same type of combiner/splitter, and then fed to the switching matrix box. Outside the accelerator tunnel, the LB+ readout module is mounted in a rack located in an electronic hutch, the length of the interconnecting cables (3/8” Cellflex, LCF38-50JFN) is about 100 m. In order to synchronize the external analogue crossbar switching with the digital one inside the LB+, both deviced are interconnected via a UTP Cat 7A cable. While the temperature in the electronic hutch is stabilized to a level of ±1 deg, the accelerator tunnel at the BPM location is not stabilized and temperature drifts of more than 2 deg are possible throughout a week of operation. In order to measure the temperature at sensitive components, therefore both the external switching matrix and the bandpass filter are equipped with temperature sensors.

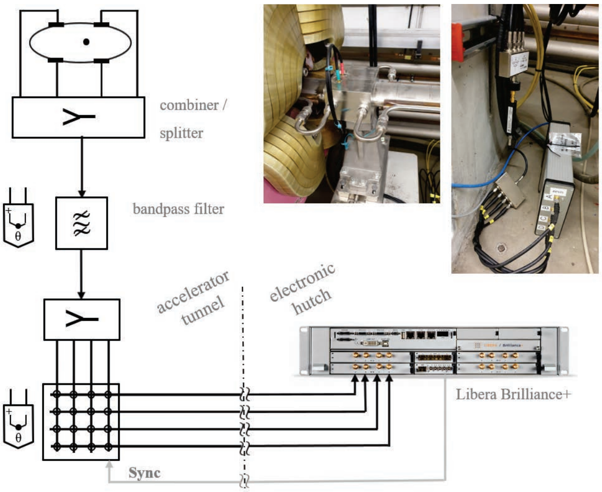

Figure 2: Principle scheme of the test setup. The photos show the setup in the tunnel: the BPM pickup (left) and the electronics part (right).

LONG TERM STABILITY STUDIES

Beginning from the end of April 2021 when the test setup was completed, a series of measurements was performed. Each measurement started at the end of a PETRA III maintenance day when beam was back in the machine, and stopped one week later at the beginning of the next maintenance day, i.e. the overall measurement time was about 160 h. As an example, Fig. 3 shows the temporal evolution of the beam current during one week of user run operation. About 50,000 data samples were recorded in Slow Acquisition (SA) mode of the readout electronics with 10 s wait time between consecutive samples. During the measurements, Digital Signal Conditioning (DSC) and crossbar switching were active in the LB+, the same holds for Automatic Gain Control (AGC).

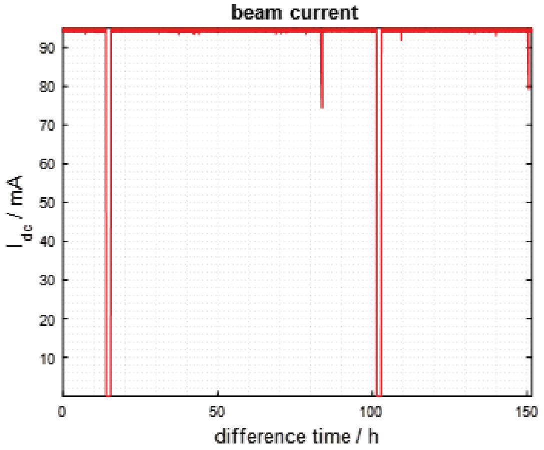

Figure 3: Beam current during one week of user operation end of May 2021. In this period PETRA III was operated with I_b = 95 mA in 40 bunches. In this week two total beam losses happened, and two times there was a delay in the top–up sequence.

Figure 4 represents the temperature profiles as measured with the two sensors mounted at switching box and bandpass filter. All data shown here and in the following were taken simultaneously to the ones in Fig. 3. As can be seen the tunnel temperature is not stable, in case of a beam loss it drops immediately by about 1 deg.

In Fig. 5 the position readout data from the SA data path are plotted. The monitor constant for data representation and beam position analysis amounts to $K_{x,y}$ = 10 mm throughout this report. In case of beam losses when there is no signal

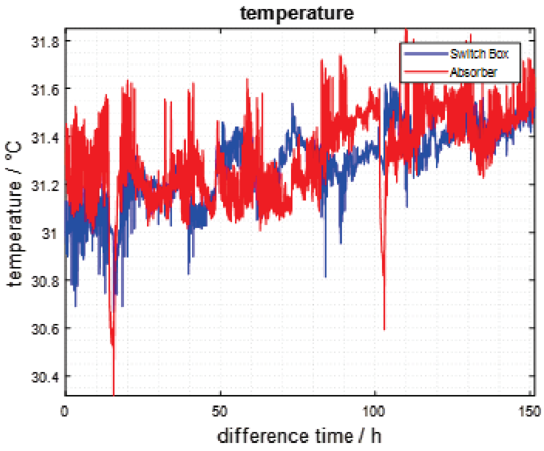

Figure 4: Temperature profiles measured at switching box and bandpass filter in the accelerator tunnel.

power at the input of the LB+, position readings are useless and a measure of the system noise. In order to exclude this distorting resolution influence, only data for $I_b \geq 25$ mA are considered for the data analysis.

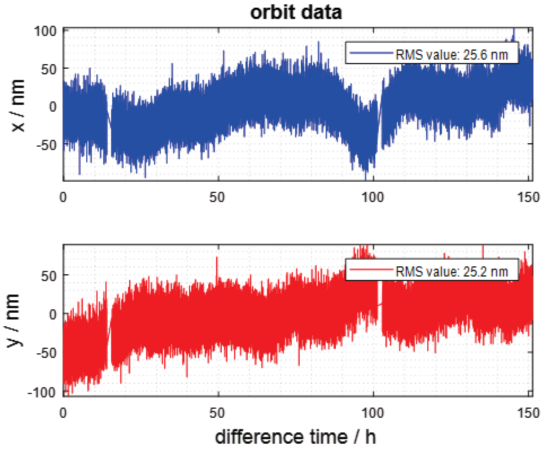

Figure 5: Position readings acquired from the SA data path. The monitor constant is $K_{x,y} = 10$ mm.

As can be seen from this figure, the long term stability of the position data is very good. The rms values amount to 25.6 nm horizontally and 25.2 nm vertically, the peak–to–peak readings are < 200 nm which is well below the requested specification of <1 µm. Furthermore, comparing Figs. 4 and 5 there is no obvious correlation between position readings and temperature profile, i.e. the compensation scheme by external crossbar switching works well and compensates temperature together with possible humidity changes on both readout electronics and interconnecting cables.

Figure 6 illustrates the temporal evolution of the DSC coefficients gain and phase which both characterize the complex channel gain. As can be seen, a change in the beam current (beam loss or delay in top–up sequence) is immediately visible in the gain, c.f. Fig. 3. However, after about 130 h all DSC gains show strong fluctuations which are neither directly correlated with a change in I_b nor with a temperature drift inside the accelerator tunnel. Correlating the rack temperature in the electronic hutch (not shown here) with the gain coefficients it was found that the rear door of the rack was opened at that time because of maintenance work, i.e. the DSC coefficients are very sensitive on environmental changes. However, it is important to note that no effect is visible in the position readings which means that this influence is well compensated.

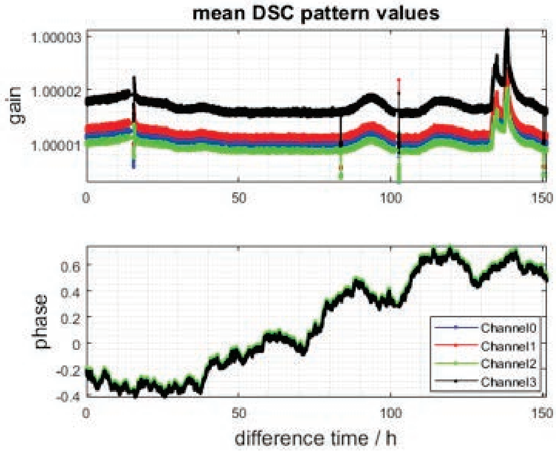

Figure 6: Temporal evolution of the DSC coefficients gain (top) and phase (bottom). Both parameters characterize the weighted average of the four data paths and represent a complex channel gain. More details about the theoretical background can be found in Ref. [9].

Besides the results presented here, other long term measurements were taken for both PETRA III operational modes (40 and 480 bunch filling pattern). All of them resulted in orbit rms values between 20 and 40 nm, thus giving confidence that the specification for the long term stability is fulfilled.

PERFORMANCE EVALUATION

Apart from the long term stability which is critical especially for PETRA IV due to the specific machine geometry, the remaining requirements listed in Table 1 were also subject of investigation. For the determination of the closed orbit resolution, 10 files of position readings were recorded both for Turn–by–Turn (TbT) and Fast Acquisition (FA) data path (PETRA III TbT frequency 130.1 kHz, FA data rate 10 kHz), each measurement consisting of 32768 consecutive samples. With knowledge of the sampling frequency, each position measurement was transformed in a corresponding Power Spectral Density (PSD), and taking into account that 10 data sets were recorded for each data path an averaged PSD was formed. Integrating the PSD over the frequency, the resolution can be determined as function of the bandwidth as shown in Fig. 7 for the FA data path. Below the first crossbar switching frequency at 3.3 kHz, the TbT measurement shows comparable results. As can be seen from this figure, at 1 kHz bandwidth the resolution is well below 100 nm, thus the specification is fulfilled.

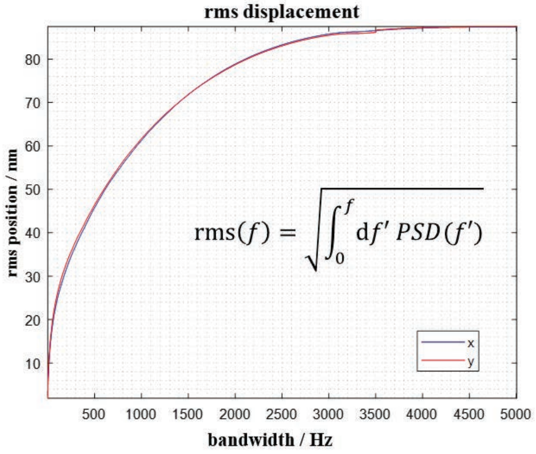

Figure 7: Closed orbit resolution as function of bandwidth for FA data path.

Figure 8 shows the single bunch (single turn) resolution as function of bunch current. For this measurement the data were collected from the Single Pass (SP) data path, i.e. in order to minimize resolution disturbing noise contributions a mask was set in the ADC spectrum which allowed to derive position information only from that region which contains bunch information. For the single turn measurement, a single bunch was injected in PETRA and dumped immediately after one passage. Each dot in the figure represents the rms from 100 consecutive shots. However, the bunch current from a single injection is not sufficient to test the specification at 0.5 mA. Therefore, single bunch measurements were also carried out with circulating beam at higher bunch currents using accumulation. As can be seen, for 0.1 mA bunch current both measurements agree well, therefore it is assumed that it is the case also for higher bunch currents, at least if no LB+ attenuator switching is involved which is the case for currents < 0.35 mA. While the resolution specification of <10 µm is reached already at this current, it is also the case for higher bunch charges.

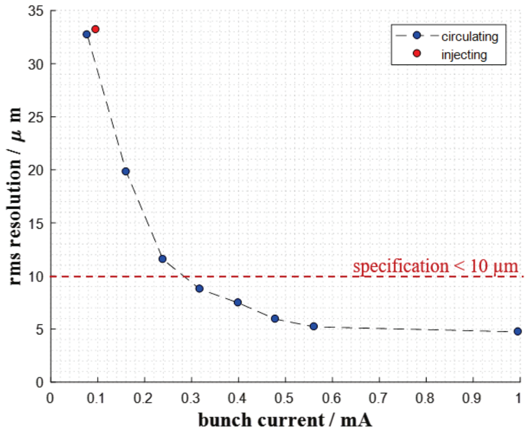

Figure 8: Single bunch resolution as function of bunch current for single turn (red dot) and circulating beam (blue dots).

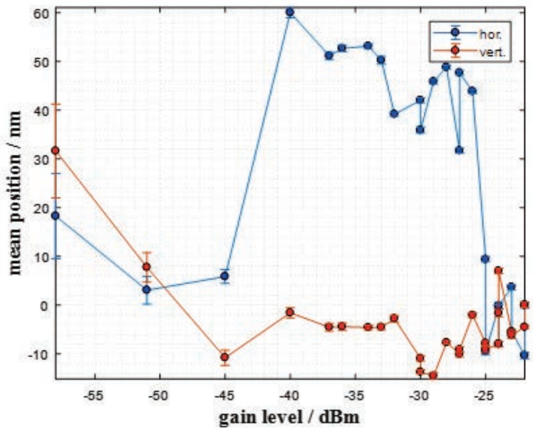

Figure 9: Beam position as function of input gain level (bunch current). Each dot represents the mean value from 500 SA position readings.

Finally the beam current dependency was investigated. PETRA III was filled with 120 mA in 480 bunches, then the beam current was reduced step by step by bringing collimator jaws closer to the beam. Position readings were recorded both in SA and TbT mode, Fig. 9 shows the result for the SA data path. As can be seen, the position variation is well below the specified ±2 µm level, the same holds for the TbT data not shown here. It should be noted that the gain variation with beam covers a range of only 40 dB and not 60 dB as specified. However, in order to protect the external crossbar switching matrix, higher gain levels were not possible. At the other hand, in the factory acceptance test without beam the same LB+ was investigated at higher power levels and demonstrating a similar performance, such that it can be concluded the same would be the case for a measurement with beam.

SUMMARY AND OUTLOOK

This paper summarizes first proof–of–principle measurements which were performed at PETRA III using a modified LB+ with external switching matrix. These measurements indicate that the concept works well, i.e. drifts in the RF front–end and from the interconnecting cables due to environmental changes are compensated to a high level. All long–term measurements performed so far indicate that the achieved readout stability is well below 50 nm (rms) over one week of operation, and independent from the bunch pattern. As demonstrated in laboratory measurements, the most temperature–drift critical element in the analogue signal chain is the external switching matrix itself: its temperature coefficient of about 72.5 nm/K dominates the temperature coefficient of the whole chain, therefore keeping the matrix at stable temperature is important. Furthermore, the overall performance of the readout electronics was investigated, indicating that it is comparable to a standard LB+ but with better long–term stability, thus meeting the specifications for PETRA IV. In the next step the readout system will be revised to be compliant with the MTCA.4 standard.

ISBN: 978-3-95450-230-1 ISSN: 2673-5350 doi:10.18429/JACoW-IBIC2021-MOPP30

REFERENCES

[1] C.G. Schroer *et al.*, *J. Synchrotron Rad.*, vol. 25, pp. 1277–1290, 2018.

[2] I. Agapov *et al.*, "PETRA IV Report", DESY, Hamburg, Germany, Rep. p4-WP201-re-0006, July 2021.

[3] S. Condamoor *et al.*, "Machine Studies with Libera Instruments at the SLAC Spear3 Accelerators", in *Proc. 7th Int. Beam Instrumentation Conf. (IBIC'18)*, Shanghai, China, Sep. 2018, pp. 284–288. `doi:10.18429/JACoW-IBIC2018-TUPB12`

[4] P. Leban *et al.*, "New RF BPM Electronics for the 560 Beam Position Monitors of the APS-U Storage Ring", presented at the 12th Int. Particle Accelerator Conf. (IPAC'21), Campinas, Brazil, May 2021, paper THPAB265.

[5] `https://www.i-tech.si/products/libera-brilliance-3/`.

[6] K. Balewski *et al.*, "PETRA III: a low emittance synchrotron radiation source",DESY, Hamburg, Germany, Tech. note DESY 2004-035, 2004.

[7] G. Rehm and C. Bloomer, "Impact of Relative Humidity on EBPM Readings", talk presented at 2nd Diagnostics Experts of European Light Sources Workshop (DEELS'15), Cerdanyola del Vallès, Spain, June 2015, `https://indico.cells.es/event/22/`.

[8] N. Hubert, "Test of BPM Cables vs Humidity and Temperature", talk presented at 6th Diagnostics Experts of European Light Sources Workshop (DEELS'19), Grenoble, France, June 2019, `https://indico.cern.ch/event/789811/`.

[9] U. Mavrič, "Innovative RF Design Unites Benefits of Multiplexed and Multi-channel System", in *Proc. 4th Beam Instrumentation Workshop (BIW'04)*, Knoxville, TN, USA, May 2004, pp. 373–378.

[10] A. Kosicek, "Libera Electron Beam Position Processor", in *Proc. 21st Particle Accelerator Conf. (PAC'05)*, Knoxville, TN, USA, May 2005, paper RPAT093, pp. 4284–4286.

[11] M. Dehler *et al.*, "New digital BPM system for the Swiss light source", in *Proc. 4th European Workshop on Beam Diagnostics and Instrumentation for Particle Accelerators (DIPAC'99)*, Chester, UK, May 1999, paper PT06, pp. 168–170.

[12] R. A. Baron, F. H. Cardoso, S. R. Marques, J. L. B. Neto, and J.-C. Denard, "Development of the RF Front End Electronics for the SIRIUS BPM System", in *Proc. 2nd Int. Beam Instrumentation Conf. (IBIC'13)*, Oxford, UK, Sep. 2013, paper WEPC07, pp. 670–673.

[13] J. Mead *et al.*, "NSLS-II RF Beam Position Monitor Comissioning Update", in *Proc. 3rd Int. Beam Instrumentation Conf. (IBIC'14)*, Monterey, CA, USA, Sep. 2014, paper WECYB2, pp. 500–504.

[14] G. Brajnik, S. Carrato, S. Bassanese, G. Cautero and R. De Monte, "Pilot tone as a key to improving the spatial resolution of eBPMs", in *Proc. AIP Conf.*, vol. 1741, 2016, Art. no. 020013. `doi:10.1063/1.4952792`

[15] M. Cargnelutti, S. Bassanese, G. Brajnik, S. Cleva, R. De Monte, and P. Leban, "Stability Tests with Pilot-Tone Based Elettra BPM RF Front End and Libera Electronics", in *Proc. 7th Int. Beam Instrumentation Conf. (IBIC'18)*, Shanghai, China, Sep. 2018, pp. 289–292. `doi:10.18429/JACoW-IBIC2018-TUPB13`

[16] G. Brajnik, B. Repič, "Current Status of Elettra 2.0 eBPM System", Libera Workshop 2021, `https://www.i-tech.si/wp-content/uploads/2021/06/8.-Gabriele-Brajnik_Elettra_compressed.pdf`

[17] F. Schmidt-Föhre, G. Kube, K. Wittenburg, "Comparison of two Long Term Drift Stabilization Schemes for BPM Systems", presented at the 10th Int. Beam Instrumentation Conf. (IBIC'21), Pohang, South Korea, Sep. 2021, paper MOPP36.

PRELIMINARY STUDIES FOR THE SOLEIL UPGRADE BPM

M. El Ajjouri, N. Hubert, A. Gamelin, P. Alves, Synchrotron SOLEIL, 91192 Saint-Aubin, France

Abstract

Synchrotron SOLEIL is currently preparing a machine upgrade based on multibend achromat lattice with a drastically reduced horizontal electron beam emittance (<100 pm•rad). Foreseen quadrupole and sextupole strengths will impose a small vacuum chamber diameter and the future Beam Position Monitors (BPM) will have a 16 mm inner diameter (circular shape). To minimise the BPM contribution to the longitudinal impedance, and induced heating on their mechanics, the feedthrough and button shapes must be optimised. This paper summarises the systematic electromagnetic simulations that have been carried on in order to distinguish the effect of single dimension changes (such as button thickness and shape, ceramic thickness and diameter) on the amplitudes and frequency position of the resonances. It also introduces the preliminary BPM design for the SOLEIL upgrade project.

INTRODUCTION

Synchrotron SOLEIL has recently published the Conceptual Design Report (CDR) of the SOLEIL Upgrade [1]. The specifications are challenging for the new beam parameters especially the beam size and emittance below 100 pm rad (Fig. 1). The energy will remain the same as today (2.75 GeV). The project includes considerable modification of the accelerator and especially the replacement of the storage ring for a new multi bend achromat lattice. Natural bunch length will be 9 ps RMS, lengthened to 30 ps RMS by a harmonic cavity to preserve the transverse emittance and beam lifetime.

The main parameters of the SOLEIL upgrade SR and the existing SOLEIL SR are compared in Table 1.

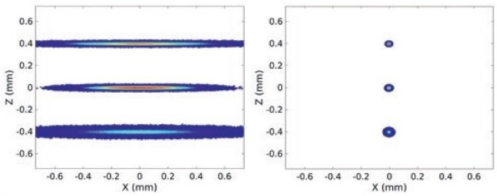

Figure 1: Comparison of the transverse beam profiles (x: horizontal, z: vertical plane) of the present SOLEIL (left) for 3 types of straight sections (short, medium and long / plots shifted for convenience) with 1% coupling and SOLEIL upgrade CDR reference lattice (right) with 50 pm.rad emittance.

Table 1: Main Parameters of the Present and CDR Reference Lattice

	SOLEIL	***SOLEIL Upgrade***
Circumference (m)	354.097	353.74
Beam energy (GeV)	2.75	2.75
maximum beam current (mA)	500	500
Natural emittance (pm.rad)	3900	80
Bunch length rms (ps)	15	9
BPM vacuum chamber (mm)	70/25	16
Number of BPM	122	~200

The SOLEIL upgrade project pushes the vacuum system conception to a new limit: the high gradient quadrupoles and the large strength of the sextupoles require the minimum size of the vacuum chamber inner diameter to be as low as 12 mm.

BPM SPECIFICATION AND CHALLENGING

The Beam Position Monitor (BPM) system is the largest (and one of the most critical) diagnostic systems for a synchrotron light source: about 200 position measurement units are considered in the CDR reference lattice. The system should deliver beam position measurement with a resolution of less than 50 nm RMS in closed orbit measurement (used for feedback loops). The measurement stability is also very important with a drift that must be below 1 µm over 24 hours. The BPM sensors for the SOLEIL upgrade will be the usual RF button pickups installed at 45° on the vacuum chamber. In order to protect the BPM from possible heating due to synchrotron radiation, its internal diameter is enlarged to 16 mm. The challenge will be the manufacturing of a small dimension pickup and its positioning on the BPM body with respect to tight tolerances in order to maintain an absolute position.

FIRST 2D SIMULATIONS

Preliminary studies have been carried out to design the future BPM pickups. With the usual delta over sum equation used to compute the position, the response is linear on a ± 1mm range around the BPM center with an on-axis error below 3 % (Fig. 2). We can consider a polynomial response to enlarge the linear range if needed for machine physics studies at large amplitude.

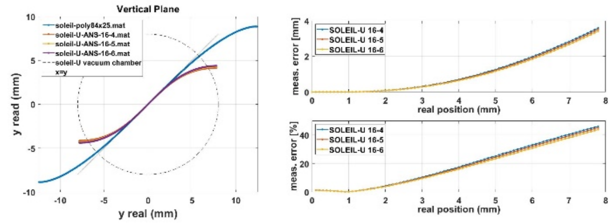

Figure 2: Linearity response for different button diameter (orange=4 mm, yellow=5 mm, purple=6 mm) compared to the current BPM in blue (left). Estimation of the error for the three diameters(right). BPMLab simulations [2].

The voltage collected on the antenna is related to the beam current by the Eq. (1) [3]:

$$U_{im}=Z_t(\omega,\beta)*I_{beam}=\left(\frac{1}{\beta c}\frac{A}{2\pi a}\right)*\frac{1}{C}*\frac{i\omega RC}{1+i\omega RC}*Ibeam \quad (1)$$

where a is the distance to the beam, A is the button area, β is the beam velocity and c is the speed of light.

The button capacitance to ground C and 50 Ω coaxial cable impedance R are equivalent to a high-pass filter with a cutoff frequency fcut =1/(2πRC). Hence the interest of maximising the value of the capacitance in order to have a lower cut-off frequency. The capacity C can be approximated by formula Eq. (2):

$$C=\frac{\pi\varepsilon_r t}{\ln(\frac{r_h}{r_b})}+\frac{\pi\varepsilon_r {r_b}^2}{d} \quad (2)$$

where t is the button thickness, ε_r is the dielectric permittivity, r_b and r_h the button and housing radius, and d is top button gap. The envisioned gap value of 200 µm is a compromise between the capacity and the constraints of mechanical manufacturing. The 3D numerical simulation computation with result using the CST electrostatic tool [4] allowed us to estimate the capacity of the button with complex design.

3D MODELISATION DESIGN AND OPTIMISATION

The power loss in the BPM block is one of the main parameters to be considered during its design. The BPM contribution to overall impedance budget has to be minimized and as well as the power deposited by the beam on the mechanics.

The power deposited by beam is given by formula Eq. (3) [5]:

$$P_{loss}=M*I_b^{2*}k_{loss} \quad (3)$$

where M is the number of bunches and I_b the beam current. The loss factor is given by Eq. (4):

$$k_{loss}=2M\sum_{p=0}^{\infty}R_e\left[Z_{||}(pM\omega_r)\right]*power\ spectrum(pM\omega_r) \quad (4)$$

where $\omega_r=2\pi f_{rev}$ and $R_e\left[Z_{||}(pM\omega_r)\right]$ is the real part of the longitudinal impedance.

The loss factor being the result of a convolution between the beam spectrum and the longitudinal impedance (see Fig. 3), it will be minimized by minimising amplitude of the impedance peaks or shifting them to high frequencies. Additional optimization can also be done avoiding that the impedance peaks falls at the same frequencies as the beam (discrete) spectrum.

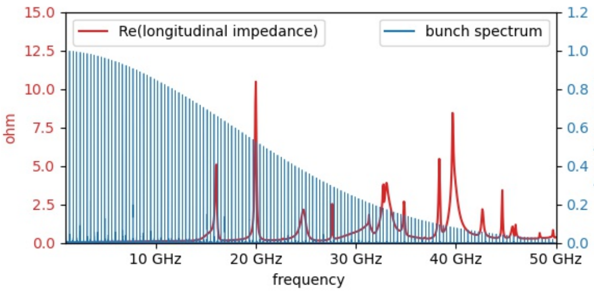

Figure 3: The longitudinal impedance (red) and beam spectrum (blue).

In this section we describe the main stages of optimisation of the different parts of the electrode to improve the longitudinal impedance, while preserving a maximum of signal transmitted by the button. Considered parameters for optimisation are presented in (Fig. 4)

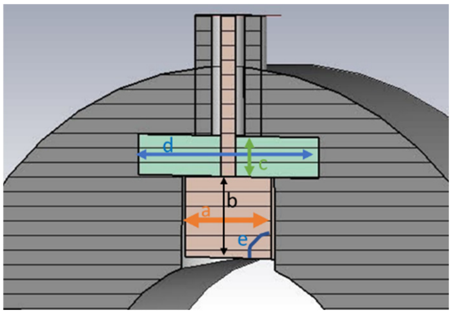

Figure 4: The parameters considered for optimisation: (a) button diameter, (b) button thickness, (c) dielectric thickness, (d) dielectric diameter and (e) button angle.

Button Diameter

Three button diameters are studied in order to find the best compromise between high signal collection (ie largest button surface) (Fig. 5) and lowest contribution to the longitudinal impedance (i.e. smallest diameter) (Fig. 6).

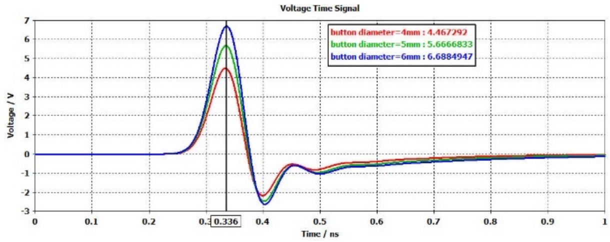

Figure 5: Voltage versus button diameter for bunch charge=1.44 nC and sigma =30 ps.

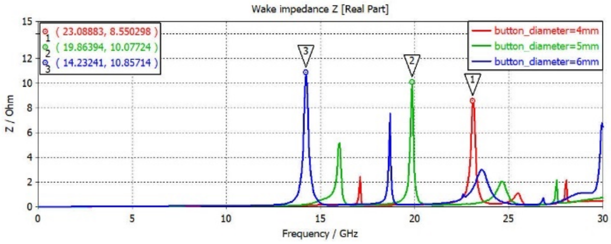

Figure 6: Real part of longitudinal impedance versus button diameter.

The first trapping mode, corresponding to the TE_{11}, mode is given by the Eq. (5) [6, 7], it depends on the diameter of the button, and it's housing.

$$f_c^{Hmp} = \frac{1}{\sqrt{\varepsilon_r}} * \frac{c}{\pi} * \frac{1}{r_b + r_h} \tag{5}$$

where ε_r is the dielectric permittivity, r_b and r_h the button and housing radius. This analytical evaluation of TE_{11} mode is compared to the CST simulation [2] in Table 2 for the three diameters considered.

Table 2: Comparison Between Analytical Model and the TE11 Mode Frequency Computing by CST

Button diameter (mm)	4	5	*6*
Analytical value (GHz)	22,72	18,35	*15,39*
Numerical computing (GHz)	23.14	19.85	*14.24*

Analytical value and numerical computing are in good agreement. The difference may come from the numerical model that takes into account the complete feedthrough and not only the button geometry.

The 5 mm diameter presents the good compromise between the signal amplitude and impedance contribution.

Button Thickness

We study the effect of the button thickness to reduce the heating induced by the beam on the BPM button. The observation of the impedance spectrum shows that the thickness of 2 mm presents a larger peak towards 15 GHz (Fig 7).

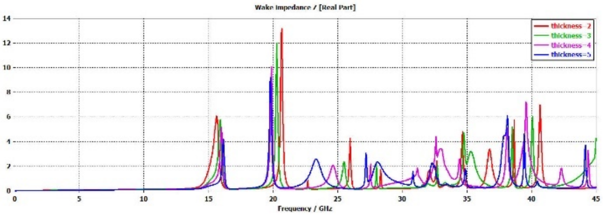

Figure 7: Real part of longitudinal impedance versus button thickness.

According to Eq. (3), the minimum power is obtain for 4 mm button thickness, as summarized in Table 3.

Table 3: Power Loss Versus Button Diameter (mm) for Sigma Beam Length = 9 ps rms

Button thickness (mm)	2	3	4	5
Power loss (W)	6,13	5.14	4.91	5.58

Dielectric Optimisation

The thickness, the relative permittivity, the diameter and the pin radius of the dielectric influence directly the frequency of trapped modes due to the ceramic (or other dielectric). The frequency of this mode can be estimated by Eq. (6) [7].

$$f^{Hm1p} = \frac{1}{\sqrt{\varepsilon r}} * \frac{c}{2\pi} * \sqrt{\left(\frac{2m}{r_p + r_d}\right)^2 + \left(\frac{\pi p}{t_d}\right)^2} \tag{6}$$

where ε_r is relative permittivity , r_d dielectric radius, r_p pin radius and t_d the dielectric thickness m and p=1,2,3….
In our case we consider Al_2O_3 alumina with ε_r=9.4.

We simulated several thicknesses of the dielectric. (Fig. 8) shows the longitudinal impedance for different thicknesses.

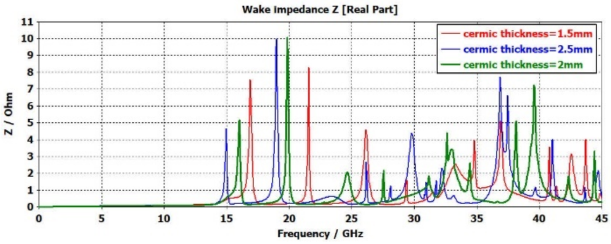

Figure 8: real part of longitudinal impedance vs. ceramic thickness. Red 1.5 mm, green 2 mm and blue 2.5 mm.

We expected that the thickness of the ceramic does not influence the first peak, which depends only on the geometry of the button. We see that all the spectrum shifts in high frequency when the thickness of the ceramic is reduced. This is also probably due to the fact that the numerical computing consider the whole feedthrough geometry and not only the part around the ceramic. The calculation of the beam power shows that a thickness of 2 mm is the best compromise and will be chosen for our design (see Table 4).

Table 4: H111 Mode Frequency Versus Ceramic Thickness

Ceramic thickness (mm)	1.5	2	2.5
Analytical value (GHz)	33.69	25.89	21.33
Numerical computing (GHz)	21.55	19.86	18.99
Power loss (W)	5,75	4,91	5,24

The dielectric diameter is usually adapted to the pin diameter to respect the 50 Ω impedance of the feedthrough and to optimise the signal transmission between button and coaxial cable. Such constraint would impose a big dielectric diameter, and a big feedthrough difficult to implement in the 16 mm BPM. Simulation on a mis adapted feedthrough (with smaller dielectric diameter) is possible and even improves a little bit the amplitude of the collected signal (Fig. 9).

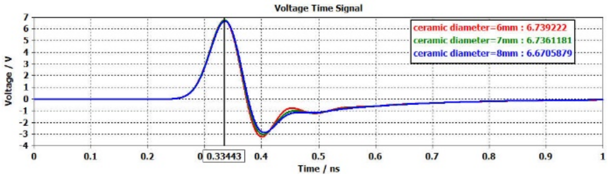

Figure 9: Time signal induced by with 30 ps rms bunch length and 1.44 pC bunch charge against ceramic diameter red 6 mm, blue 7 mm and green 8 mm.

Button Geometry Effect

Based on the work carried out on the optimisation of the BPM impedance of Sirius [7], we compared three shapes of buttons: with angles of 90°, 75°, and 65° (Fig. 10).

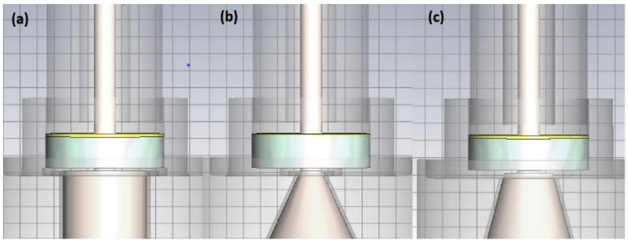

Figure 10: Button angle shape simulates (a) Button 90° (b) 65° conical button. (c) 75° conical button.

The conical shape of the button shifts the trapped mode in the high frequencies (Fig. 11).

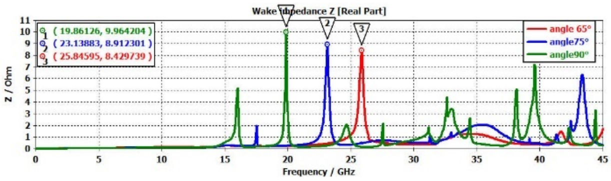

Figure 11 The real part of longitudinal impedance for different button geometry: green 90° button angle, blue 75° button angle, red 65° button angle.

As a consequence, the power deposed by the beam on the BPM block is decreased. With bunch length equals 9 ps rms, the power drops from 20% between the 90° button angle and the 65°button angle (see Table 5).

Table 5: Power Loss Versus Button Angle

Button angle in degree	65	75	90
power loss (w)	3,93	4.25	4.91

PROTOTYPING

In order to validate the mechanical integration of such a small design (initial internal diameter was even smaller at 10 mm) and BPM calibration procedure, we have realised a first prototype with commercially available feedthroughs (3 mm buttons) (see Fig. 12).

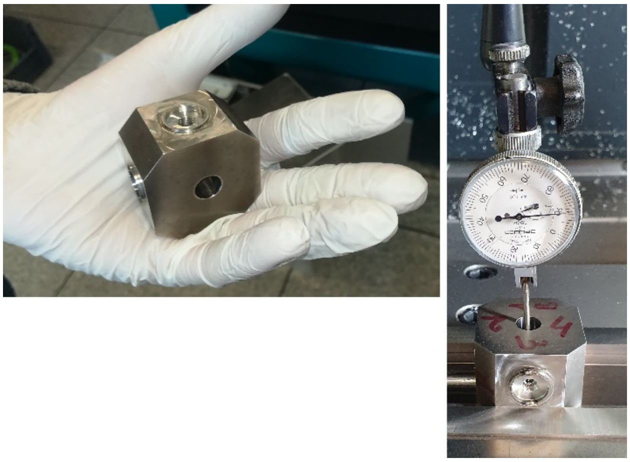

Figure 12: BPM prototype (left) and electrode positioning metrology (right).

Careful metrology has been carried on in order to optimize the mechanical tolerances to be defined for the BPM and feedthrough manufacturing.

PERSPECTIVES

A preliminary discussion with the button manufacturers made it possible to raise and resolve several blocking points such as the mechanical positioning of the buttons or the mechanical tolerances.

A new button design is being validated, and a new prototype is being manufactured. Thermal simulation has still to be conducted to decide the materials for the BPM body and button, and if a cooling system will be required.

CONCLUSION

Future BPMs for the SOLEIL upgrade are under design. The main challenge is the drastic reduction of the vacuum chamber circumference. Accurate electromagnetic simulations are ongoing to minimise impedance. Deposited power should also be estimated, and thermal simulation will help us to decide whether to have a water-cooling circuit around the body of the BPM.

REFERENCES

[1] Synchrotron SOLEIL “Conceptual Design Report”, `https://www.synchrotron-soleil.fr/en/file/13803/download?token=OUzsp46P`

[2] A. A. Nosych, U. Iriso, and J. Olle, “Electrostatic Finite-element Code to Study Geometrical Nonlinear Effects of BPMs in 2D”, in *Proc. 4th Int. Beam Instrumentation Conf. (IBIC'15)*, Melbourne, Australia, Sep. 2015, pp. 418-422. `doi:10.18429/JACoW-IBIC2015-TUPB047`

[3] P. Forck, P. Kowina, and D. Liakin, GSI, “Beam Position Monitors”, CAS, Dourdan, France, May 2008.

[4] `https://www.3ds.com/fr/produits-et-services/simulia/produits/cst-studio-suite`

[5] L. Teofili *et al.*, “A Multi-Physics Approach to Simulate the RF Heating 3D Power Map Induced by the Proton Beam in a Beam Intercepting Device”, in *Proc. 9th Int. Particle Accelerator Conf. (IPAC'18)*, Vancouver, Canada, Apr.-May 2018, pp. 3452-3455. `doi:10.18429/JACoW-IPAC2018-THPAK093`

[6] A. Blednykh *et al.*, "NSLS-II Storage Ring BPM Button Development", in *Proc. 6th Int. Particle Accelerator Conf. (IPAC'15)*, Richmond, VA, USA, May 2015, pp. 748-750. `doi:10.18429/JACoW-IPAC2015-MOPMN021`

[7] H. O. C. Duarte, S. R. Marques, and L. Sanfelici, "Design and Impedance Optimization of the SIRIUS BPM Button", in *Proc. 2nd Int. Beam Instrumentation Conf. (IBIC'13)*, Oxford, UK, Sep. 2013, paper TUPC07, pp. 365-368.

BPM SYSTEM FOR THE PIP-II INJECTOR TEST FACILITY*

N. Eddy#, J. Diamond, B. Fellenz, R. Santucci, A. Semenov, D. Slimmer, D. Voy,
Fermilab, Batavia, IL 60510, USA

Abstract

A new BPM system was used for commissioning and operation of the PIP2 Injector Test Facility. The system of 13 warm and 12 cold BPMs was based upon custom 250 MS/s digitizers controlled and readout over gigabit ethernet by a single multi-core rackmount server running linux. The system provided positions, intensity, and phase for each bpm as a pulse average or pulse waveform from 10 µs to 4.4 ms at a 20 Hz pulse repetition rate.

INTRODUCTION

The PIP-II Injector Test facility was developed to perform an integrated test for the front-end of the PIP-II linac upgrade project at Fermilab [1]. The beamline shown in Fig. 1 includes the warm front-end consisting of the ion source, low energy beam transport (LEBT), radio-frequency quadrupole (RFQ), and the medium energy beam transport (MEBT) sections. It also includes the first two superconducting cryomodules consisting of the half-wave resonator (HWR) module and the 1st single spoke resonator (SSR1) module which are followed a high energy beam transport (HEBT) section with diagnostics and beam dump. The PIP-II Injector provides bunched beam out of the RFQ at 162.5 MHz with pulse lengths from 10 µs to 4 ms at up to a 20 Hz pulse repetition rate with up to 10 mA instantaneous beam current.

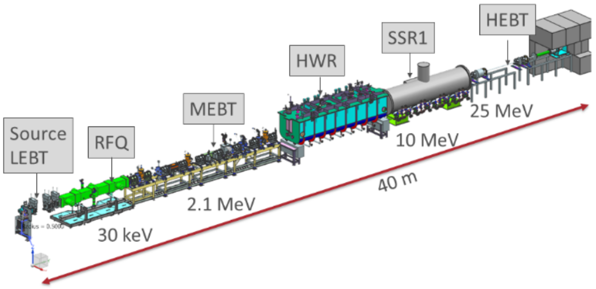

Figure 1: Beamline layout of the PIP-II Injector Test Facility.

After the RFQ, there are 9 warm button BPM pickups in the MEBT section, then 8 cold button BPM pickups in the HWR, 4 cold button BPM pickups in the SSR1, and 4 warm button BPMs in the HEBT. A completely new data acquisition system was developed for the final PIP-II Injector Test run in 2020.

BPM SYSTEM

The new readout electronics are shown in Fig. 2. The main components of the new system are analog signal conditioning modules, custom digitizer modules, a commodity rackmount PC, and Gigabit ethernet control and readback for the system via a standard Gigabit switch.

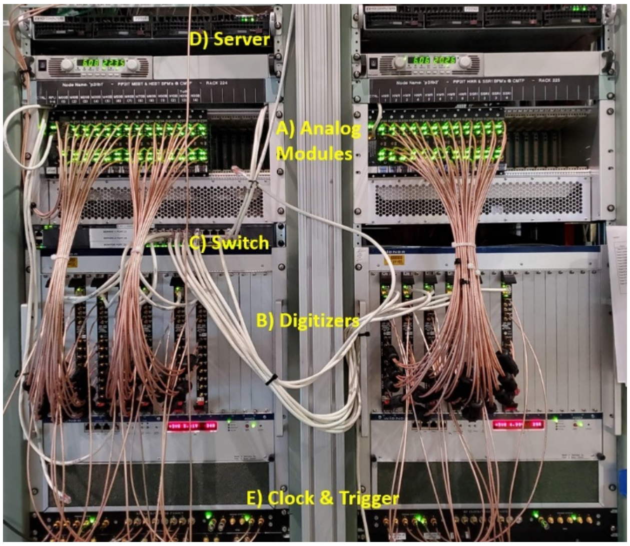

Figure 2: The PIP-II injector test BPM electronics.

Analog Signal Conditioning Module

The Analog Signal Conditioning Modules provide filtering and signal level control (see Fig. 3). There is a 500 MHz low pass filter and programmable 0-32db in 0.5db steps attenuator at the input. A removable daughter card handles the filtering. For PIP-II Injector Test, the daughter card splits the signal to provide band pass filters for both the 1st and 3rd beam harmonics at 162.5 MHz and 487.5 MHz. The daughter card also provides programmable high (26db) and low (6db) gain for each signal path. There is also a variable gain amplifier on the board output with 64 settings from 0-31db. The modules reside in two Eurocard crates which each have a controller board. All settings on each analog module are controlled via ethernet by a raspberry-pi module on the controller board.

---

* This work was supported by the DOE contract No.DEAC02-07CH11359 to the Fermi Research Alliance LLC.
# eddy@fnal.gov

ISBN: 978-3-95450-230-1 ISSN: 2673-5350 doi:10.18429/JACoW-IBIC2021-MOPP33

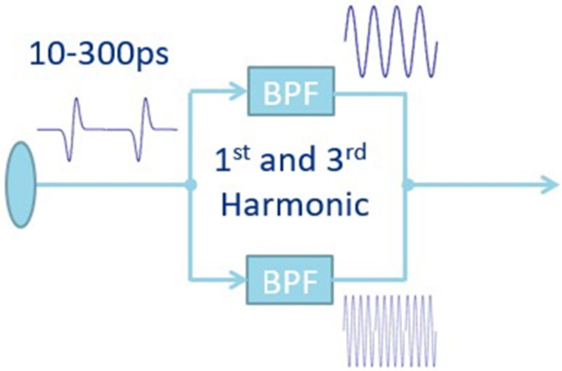

Figure 3: Analog signal conditioning.

Digitizer Modules

A block diagram of the custom digitizer module is shown in Fig. 4. The module was designed in a VME/VXS form factor. It has 8 250MS/s ADCs which interface to the Altera Aria V FPGA via the JESD204B fast serial standard. A dedicated clock chip provides all necessary clocks for the ADCs and FPGA. The clocks are all generated locked to an external 162.5 MHz reference from the low level RF system so that the entire system runs locked to the beam frequency. For PIP-II Injector Test, the module only used the VXS crate for power and cooling. All control and readout occurred over the front-panel Gigabit ethernet connection.

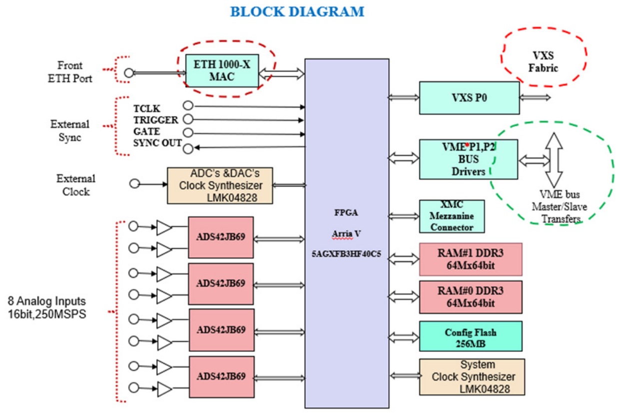

Figure 4: Block diagram for the custom digitizer.

The Digital Signal processing block diagram is shown in Fig. 5 along with the relevant frequencies as a function of the 162.5 MHz RF. The ADC sampling and NCO frequencies for the digital downconverters (DDC) are critical for the phase measurement. Each DDC decimates the signal down to a 1 MHz rate and has 250 kHz bandwidth. Up to 2048 I, Q pairs for each harmonic are stored for each ADC channel on each beam pulse. The data can be further averaged and decimated to record longer beam pulses.

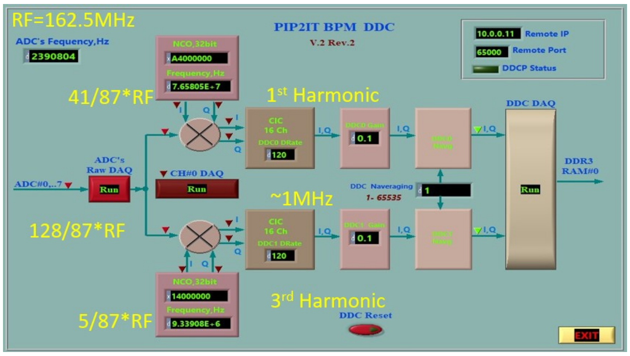

ADC's Fequency,Hz 2390804
NCO,32bit A4000000
Frequency,Hz 7.65805E+7
DDC0 DRate 120
DDC0 Gain 0.1
DDC Naveraging 1- 65535 1
DDC1 DRate 120
DDC1 Gain 0.1
NCO,32bit 14000000
Frequency,Hz 9.33908E+6
10.0.0.11 Remote IP
65000 Remote Port
DDCP Status

Figure 5: Block diagram for the DDC logic.

Frontend Readout and Controller

The most significant change to the system was moving from a crate CPU board to an external rackmount PC running linux. The rackmount PC interfaces to the digitizer modules via ethernet by way of a standard ethernet switch. The rackmount PC has two 10 Gigabit ethernet interface. One is connected to the switch to talk to the digitizer modules on a private network and the other is connected to the accelerator controls network. The rackmount sever PC has significantly more resources and power compared to the crate CPUs for a fraction of the cost. It is also able to take advantage of a wealth of standard code development tools and routines. The Gigabit ethernet readout achieved 100 MB/s which provides a factor of 10 rate improvement over previous VME implementations. The Gigabit ethernet interface was implemented using Distributed Direct Communication Protocol (DDCP) interface developed at Fermilab. This interface provides methods for talking to hardware including interrupt and streaming features. A block diagram of the interface architecture is shown in Fig. 6.

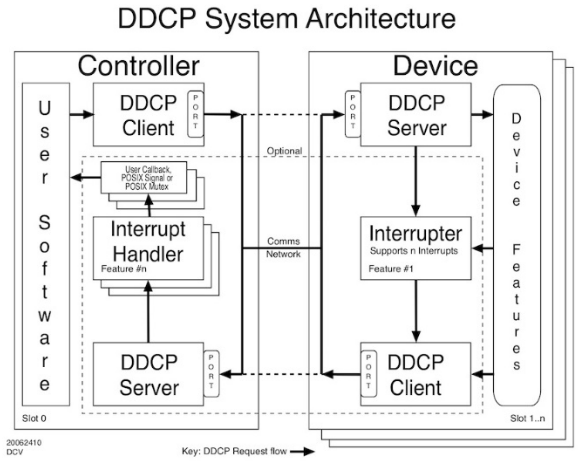

Figure 6: A block diagram of the DDCP architecture.

The frontend controller calculates positions, intensities, and phase from the I, Q data for each BPM. There are four ADC channels for each BPM corresponding to the four pickup electrodes. The digitizers generate I, Q pairs for both the 1st and 3rd beam harmonics for each channel. For PIP-II Injector Test run, 512 samples were readout on each beam pulse for a total of 16 kB per BPM. This allowed the data for all 25 BPMs to be easily readout over the Gigabit ethernet bus at 20 Hz.

BPM SYSTEM PERFORMANCE

The BPM system provides measurements of the beam position, intensity for each harmonic, and phase for each BPM. The horizontal and vertical positions are calculated from a 2D polynomial fit [2] to the magnitudes of the 1st harmonic for the four bpm electrodes. For the MEBT, a low β correction is also applied. On each beam pulse, the average as well as the waveform of positions across the beam pulse are available to the accelerator control system. For the nominal commissioning beam pulse of 10 µs and 2 mA, the BPM position resolution was 8 µm. The horizontal position along a 400 µs beam pulse is shown in the MEBT in Fig. 7. The variation at the front of the pulse was determined to be from the RFQ.

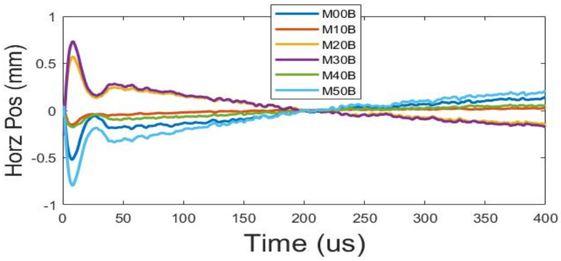

Figure 7: Horizontal positions for a 400 µs beam pulse in the MEBT.

The intensities for both the 1st and 3rd beam harmonic are calculated as the sum of the magnitudes from each BPM electrode. The ratio of the intensity for the two harmonics is related to the bunch length of the beam. Figure 8 shows a plot of the Bunch Factor defined as the ratio of the 3rd harmonic intensity to the 1st harmonic intensity for all 25 BPMs for beam accelerated to 16 MeV after SSR1.

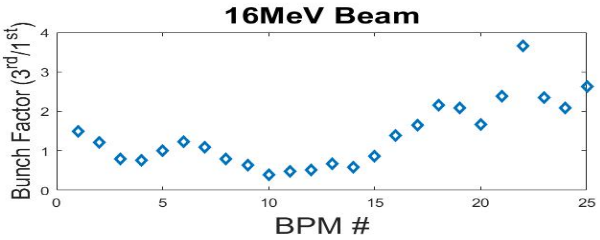

Figure 8: Bunch Factor from BPM intensities along the PIP-II Injector Test beamline for beam accelerated to 16 MeV.

The beam phase with respect to the RF reference is calculated from the 1st harmonic I & Q data. The phase measurement for a 10 µs 2 mA beam pulse was found to have 0.2° RMS. The phase measured for a 4.4 ms beam pulse in the MEBT is shown in Fig. 9. The observed phase oscillation was determined to be caused by the RFQ while the step in the last couple BPMs was caused by the last buncher cavity turning off.

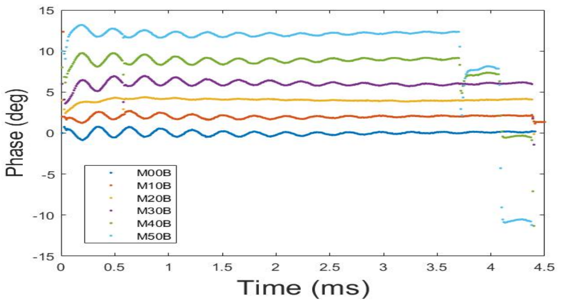

Figure 9: Measured phase along a 4.4 ms beam pulse in the MEBT.

The BPM phase measurement can be used to phase in the RF cavities and to calculate the beam energy as it is a measure of the time of arrival of the beam. To calculate the energy, a technique developed at FRIB was used [3]. This involves calibrating the phase response of each BPM by injecting the same known signal into each BPM cable in the tunnel. Once calibrated, the phase from 3 BPMs can be used to determine the energy. Using this method, the energy in the HEBT was measured with 0.2% resolution which was much better than the measurements obtained from a movable Time of Flight BPM which was over 1%.

SUMMARY

A completely new BPM readout system was installed and commissioned at the PIP-II Injector Test facility. The system imployed a new architecture based upon Gigabit ethernet for readout and control of the digitizer modules using a commodity rackmount server PC. The system was a key diagnostic for the operation of the facility.

REFERENCES

[1] PIP-II Conceptual Design Report, 2018, `http://pip2-docdb.fnal.gov/cgi-bin/ShowDocument?docid=113`

[2] C. Briegel *et al.*, "Status of the ATF Damping Ring BPM Upgrade Project", in *Proc. LCWS07 and ILC07*, pp. 810-816, 2007.

[3] S. Cogan, J. L. Crisp, T. M. Ford, and S. M. Lidia, "First Results of Button BPMs at FRIB", in *Proc. 7th Int. Beam Instrumentation Conf. (IBIC'18)*, Shanghai, China, Sep. 2018, pp. 311-313. `doi:10.18429/JACoW-IBIC2018-TUPC07`

PERFORMANCE OF THE SLAC-PAL-VITZROTECH X-BAND CAVITY BPMs IN THE LCLS-II UNDULATOR BEAM LINES*

Christopher Nantista†, Patrick Krejcik, Bobby McKee, Andrew Young, Sonya Hoobler, Dennis Martinez-Galarce and Michael Rowen, SLAC National Accelerator Laboratory, Menlo Park, U.S.A.
Changbum Kim, Pohang Accelerator Laboratory, Pohang, Korea

Abstract

The hard X-ray and soft X-ray undulator beamlines of the LCLS-II X-ray FEL incorporate 65 X-band cavity beam position monitors for accurate tracking of the electron beam trajectories and Beam-Based Alignment. For this crucial function, a design was jointly developed between PAL and SLAC, consisting of a monopole reference cavity and a dipole position cavity, with signals coupled out through coaxial vacuum feed-throughs. For the relatively large quantity needed, the production of completed units was contracted to the Korean company Vitzrotech, who developed the manufacturing process to successfully fabricate the needed quantity. Herein, an overview is given of the production experience, tuning, installation and performance of these devices.

INTRODUCTION

The LCLS-II free electron laser at SLAC requires monitoring of the beam position with sub-micron level resolution in both *x* and *y*. The device chosen by the project to achieve this is an X-band cavity beam position monitor, or RFBPM, of a unique configuration whose design was developed over the last couple of decades [1-3]. It consists of two independent resonant cavities, dipole and reference, with signals coupled out through coaxial vacuum feedthroughs. A distinguishing feature benefiting sensitivity is the magnetic coupling of the dipole cavity fields into side waveguide stubs in a way that shields the pickups from the monopole mode [4]. The design adopted had been recently deployed in the PAL-XFEL in Pohang, Korea. For production of the 65 units required in the soft X-ray and hard X-ray undulator beamlines of LCLS-II, the technology was transferred to the Korean industrial firm Vitzrotech in Gyeonggi-do. The full complement of RFBPMs was completed, installed and recently commissioned at SLAC.

DEVICE DESCRIPTION

Developed through a Cooperative Research and Development Agreement (CRADA), with final design by PAL, the 10 cm beamline device passes the beampipe through two resonant pillbox cavities (Fig. 1a). As sensitivity roughly scales with wavelength, an X-band cavity frequency of nominally 11.424 GHz was chosen, equal to four times that of the SLAC normal conducting and PAL S-band linacs. The main cavity operates in the TM_{110} mode. Each polarization component, excited by either an *x* or *y* offset of the beam, couples through its radial magnetic field into a pair of slot-coupled longitudinal waveguide stub resonators. Capacitive probes couple signal out through coaxial feedthroughs brazed into the sides of these in a pin-wheel pattern. The smaller second cavity, excited on axis in the fundamental TM_{010} mode, provides a phase reference for the sign of the position cavity signals and an amplitude reference for their bunch charge dependence. Its signal is coupled out through a pair of coaxial feedthroughs magnetically coupled through the edge of its end wall.

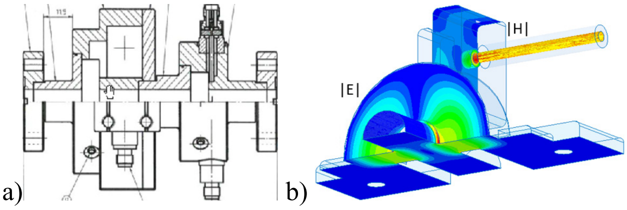

Figure 1: a) cutaway and external view of RFBPM geometry and b) field simulation of dipole cavity coupling.

Two feedthroughs couple to each of the three cavity modes. Each incorporates a ceramic coaxial vacuum window. Four threaded tuning pins are provided around the edge of each cavity at the 45° positions. Split-ring collars are used with special tuning tools to provide push-pull capability on these pins for fine-tuning of the cavity frequencies (Fig. 2b).

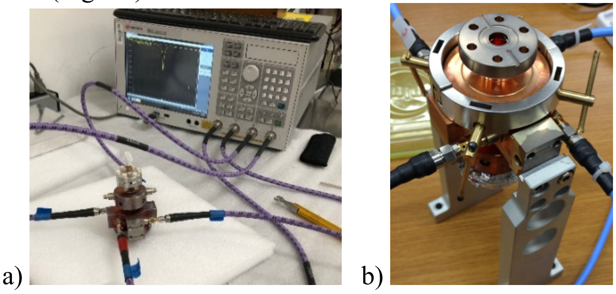

Figure 2: a) RF testing on 4-port network analyzer and b) fine tuning of cavity with tuning collar and tools.

PRODUCTION EXPERIENCE

After an initial 3 prototypes were received and one was beam tested, fabrication of production units began at Vitzrotech, in batches of about 15–25. Upon receipt of each batch, acceptance testing at SLAC would proceed via mechanical inspection, vacuum testing and RF characterization (Fig. 2a). Over the 2–3 year production span, with roughly a hundred units produced, problems were encountered and overcome by the vendor, with advisory input from SLAC and from PAL via regular video meetings and a couple of factory visits.

---

* Work supported by U.S. Department of Energy under Contract Numbers DE-AC02-06CH11357.

† nantista@slac.stanford.edu

Some units were lost or needed to be reworked due to learning curve issues with the complicated, multi-stage procedure of brazing together the multiple body parts, flanges, holding blocks, tuning pins and feed-throughs. These were addressed largely by adjustments to temperatures, jigging and the number and arrangement of units in the furnace.

Another issue that required attention was achieving the desired RF coupling, β. The sensitivity of the cavity β to the final brazed pin position was simulated to be on the order of 10% per 100 µms. With fairly broad specification ranges and improved consistency, this concern was overcome. Having two ports per cavity mode allows us to choose the better-coupled one in each pair for cabling, the other being terminated with a coax load.

Cross-talk in the dipole cavity, defined as the relative coupling between orthogonal ports and opposite ports (i.e. x-y vs. x-x or y-y) is required to be below -20 dB in order to independently resolve x and y beam position. Coupling can result from an asymmetry in the dipole cavity where the defining normal mode orientations are not perfectly aligned with the port axes. Some units were received out of specification, despite having passed the factory testing. Fortunately, our tuning procedure at SLAC allowed the coupling to be re-adjusted within specification, along with the mode frequencies themselves.

In addition to the specification of the cavity frequencies all being within 10 MHz of nominal, it is also required that the x and y resonances each be within a couple of megahertz of the reference cavity frequency, due to the effect on the commonly downmixed signal amplitudes. (Toward the end of the program, it became standard procedure to fine-tune the reference cavity during acceptance testing to midway between the dipole frequencies.) Though the dipole cavity frequency can be tuned and cross-talk suppressed, the arrangement of the tuning pins does not facilitate differential tuning along the x and y axes. A handful of units ended up being deemed unusable or held in reserve due to excessive x-y frequency spread.

By far the greatest obstacle encountered in the production was the reliability of the feedthrough vacuum windows. With six fragile SMA feedthroughs per RFBPM, this Achilles' heel led to quite a few units either failing acceptance or needing to be replaced due to vacuum leaks showing up during or after installation. Much attention and a number of meetings were focused on this problem, considering such issues as the ceramic braze and the connector pin depth. The infant mortality rate was reduced without significant design modification largely by a combination of a more selective feedthrough quality assurance protocol by Vitzrotech and a more delicate handling protocol at SLAC. The latter included leak-checking one unit at a time, adding straight or angled SMA connectors to the ports to avoid undue stress from multiple cable connections, transporting holder mounted units in a padded Pelican™ case and anchoring the signal cables with a base clamp at installation for stress relief and contact avoidance.

Though the above technical challenges faced in the course of this program are worth documenting, it should be noted that the vendor was always very professional, technically accomplished, accommodating and responsive to concerns. They were a pleasure to interact with on this extended scale production of a laboratory-developed design. It is worth noting to their credit that in the final batch of 18 units delivered not a single failure was encountered.

RF BENCH TESTING RESULTS

Each received RFBPM was cold tested at SLAC for comparison with the vendor factory test data. They were kept under vacuum during this process, which can make a difference on the order of 0.5 MHz in frequency). A 4-port network analyzer (Fig. 2a) facilitated measurement of return loss plots from each dipole port as well as all couplings between ports. The cavity frequencies are found from the dips in the plots, and the apparent port couplings β_{measN} from the standard VSWR technique (after level correction of feed-through round-trip loss, typically ~-0.15 dB. In this calculation, the power emitted from the opposite port is seen as indistinguishably combined with ohmic wall loss. Thus, for each pair of ports coupled to the same mode, the actual port couplings are then calculated as:

$$\beta_{p1} = \frac{1+\beta_{meas2}}{1-\beta_{meas1}\beta_{meas2}}\beta_{meas1}, \text{ and similarly for } \beta_{p2},$$

after which the total external coupling is determined from:

$$\beta_{tot} = \beta_{p1} + \beta_{p2} = \frac{\beta_{meas1}+\beta_{meas2}+2\beta_{meas1}\beta_{meas2}}{1-\beta_{meas1}\beta_{meas2}}.$$

The loaded quality factors are calculated from the 3 dB drop off points of the coupling plots between opposite ports from $Q_L = f_r/\Delta f_{3dB}$, and from these and the total couplings, Q_0 is determined. Table 1 lists the main parameter specifications along with the average values achieved and standard deviations based on data from 84 units.

Table 1: Parameter Specifications and Unit Statistics

Cavity	Param.	Specification	Average	SD
ref.	f_r (GHz)	11.424±0.010	11.4234	.0012
	Q_L	1,700–2,800	2,511	180
	β_{tot}	1.25–2.1	1.486	0.219
	Q_0	5,200–6,700	6,227	542
dipole	f_r (GHz)	11.424±0.010	11.4234	.0017
	Q_L	1,900–3,000	2,425	204
	β_{tot}	1.25–2.1	1.729	0.174
	Q_0	5,800–7,300	6,619	592

INSTALLATION

In preparation for each installation, an RFBPM that has passed all testing and received any required tuning was fitted with straight or an elbow SMA connectors in the orientation appropriate for the installation cable direction (for SXR or HXR), with termination loads on the opposite ports. It was then mounted in an adjustable beamline holder stand (see Fig. 3) integrated with other beamline interspace components, re-checked for vacuum integrity and installed on a girder.

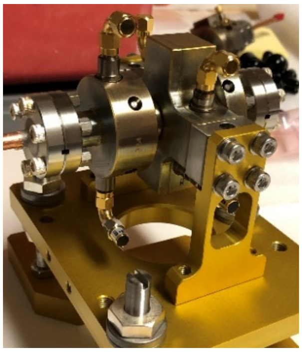

Figure 3: RFBPM ready for beamline integration.

After girder installation and under vacuum, the cavity BPM is measured again to determine the resonant frequencies. If tuning is needed for the front-end electronics, this is performed at this stage.

ELECTRONICS DESIGN

In order to achieve the required performance, the SLAC Technical Innovation Directorate has developed a common hardware and firmware platform for beam instrumentation based on the Advanced Telecommunication Computing Architecture (ATCA) platform with a SLAC built advanced mezzanine card (AMC) along with a common carrier FPGA board.

The cavity BPM signals are downmixed from 11.424 GHz to 40 MHz using a super heterodyne receiver as shown in the block diagram in Fig. 4. This technique has been used on LCLS-I, LCLS-II and PAL X-FEL. To meet the dynamic range requirement and maintain good linear response, there are digitally controlled attenuators that provide 30 dB of dynamic range.

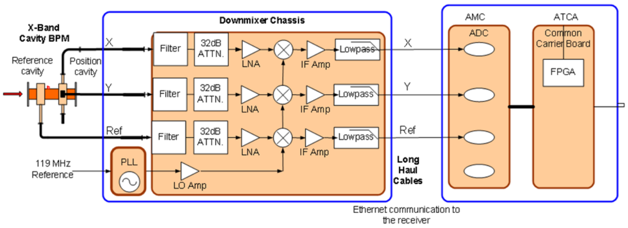

Figure 4: Block diagram of the cavity BPM electronics.

After the signals have been downmixed to the IF frequency, the signals are digitized using a TI-JESD 350 MHz digitizer. The BPM system uses a common carrier module containing an FPGA (Xilinx Kintex Ultrascale XCKU040 or XCKU060). It has serial connections to the backplane Ethernet, and to the RTM and AMC cards. JESD204b is used to the AMC cards. The carrier card also contains DC-DC power supplies from the -48 V to a variety of voltages used by the AMC cards. A slot of an ATCA crate consists of a carrier card, which supports two AMC cards and one, RTM card. The ATCA backplane features a dual-star network that provides 10 Gb Ethernet connectivity from each carrier module to a switch in slot 1. Timing data broadcasted from slot 2 to all carriers uses a proprietary protocol in order to support beam-synchronous data acquisition.

The BPM system is calibrated using the mover system on each girder. We instruct the movers to move ±100 µm steps with a total transverse distance of 1 mm. Using a Matlab script, we coordinate the move and the acquisition of the BPM reading. The Matlab program calculates the scale factors and polarity of the BPM electronics (see Fig. 5). We use the model to compensate for second order effects from the magnets due to the quadrupole offsets. Also, jitter correction is compensated by measuring orbit drifts of the upstream BPMs.

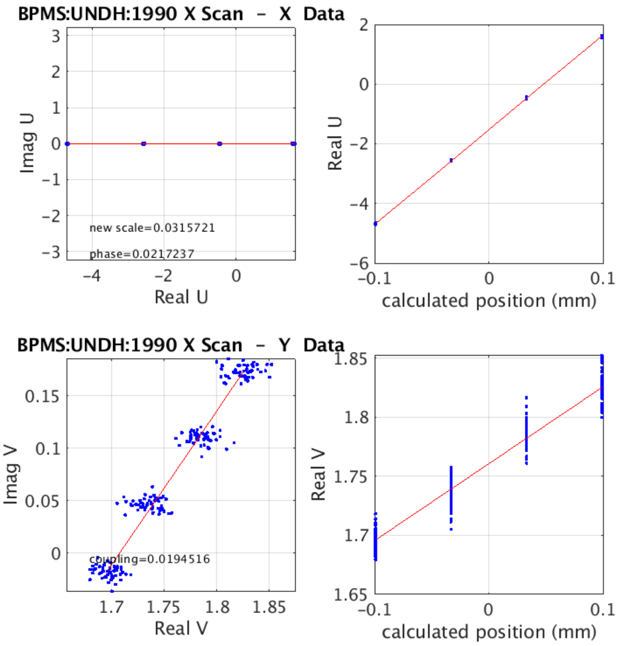

Figure 5: Calibration and Coupling measurement.

PERFORMANCE RESULTS

Using the beam-synchronous data acquisition features of the electronics and the intrinsic beam jitter we can determine the BPM resolution by predicting where the beam is supposed to be downstream and where it was measured to be using a linear predictor. The next set of figures illustrate the resolution at 165 pC, 82 pC and 26 pC. The BPM system show good linearity with respect to charge.

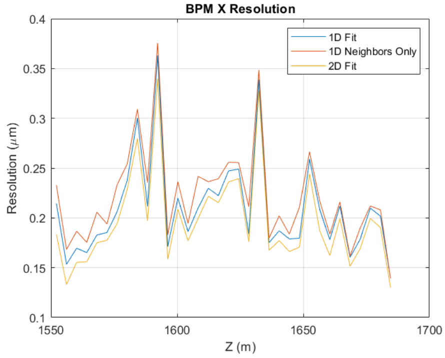

Figure 6: X-plane resolution for HXR undulator at 165 pC.

Figures 6 and 7 illustrate that most BPMs have a resolution of 200 nm in both X-Y plane. However, one BPM had a Y-plane resolution that was drastically worse. It was discovered this was due to an oscillation on the Monopole cavity electronics which has since been repaired. The next figures illustrate the resolution of 82 pC.

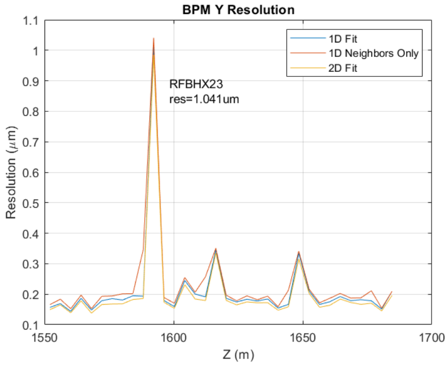

Figure 7: Y-plane resolution for HXR undulator at 165 pC.

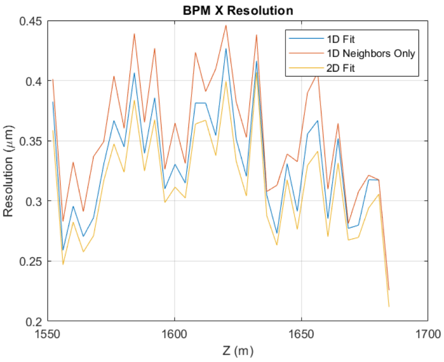

Figure 8: X-plane resolution for HXR undulator at 82 pC.

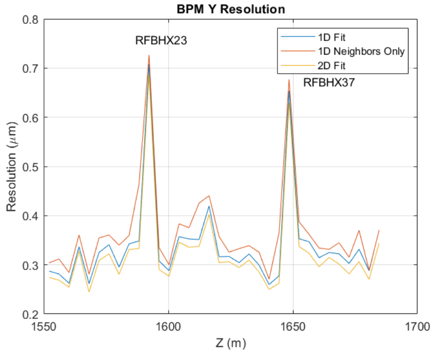

Figure 9: Y-plane resolution for HXR undulator at 82 pC.

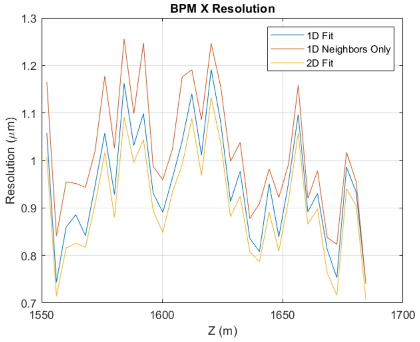

Figure 10: X-plane resolution for HXR undulator at 26 pC.

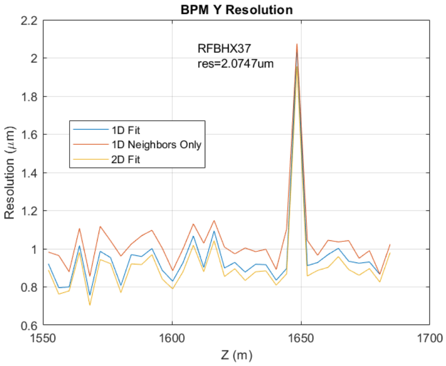

Figure 11: Y-plane resolution for HXR undulator at 26 pC.

At 26 pC the resolution for most BPMs is 1 μm. The data was taken with the electronics calibrated and optimized at 180 pC. Thus, some improvements can still be made to increase the resolution at low bunch charge.

CONCLUSION

The CRADA and industrial partnership with Pohang and Viztrotech has been very successful. We have installed 65 BPMs in LCLS-II HXR and SXR. LCLS-II cavity BPMs work as specified and are recording shot to shot data at 120 Hz. Future operations will include running at 1 MHz repetition rates.

ACKNOWLEDGEMENTS

We would like to thank members of the Vitzrotech technical team for fabricating and aiding in the design implementation of the cavity BPM structures.

REFERENCES

[1] R. Johnson, Z. Li, S. Smith, V. Smith Stanford Linear Accelerator, T. Naito, J. Rifkin, “An X-Band Cavity for a High Precision Beam Position Monitor”, in *Proc. 6th European Workshop on Beam Diagnostics and Instrumentation for Particle Accelerators (DIPAC'03)*, Mainz, Germany, May 2003, paper PT13, pp. 196-198.

[2] A. Young, J. E. Dusatko, S. L. Hoobler, J. J. Olsen, T. Straumann and C. Kim, “Performance Measurements of the New X-Band Cavity BPM Receiver”, in *Proc. 2nd Int. Beam Instrumentation Conf. (IBIC'13)*, Oxford, UK, Sep. 2013, paper WEPC24, pp. 735-738.

[3] S. J. Lee, Y. J. Park, C. Kim, S. H. Kim, D. C. Shin, H. S. Kang, J. H. Han, I. S. Ko, “PAL-XFEL Cavity BPM Prototype Beam Test at ITF”, in *Proc. 37th Int. Free Electron Laser Conf. (FEL'15)*, Daejeon, Korea, Aug. 2015, pp. 468-470. `doi:10.18429/JACoW-FEL2015-TUP043`

[4] Zenghai Li, Ronald Johnson, Stephen R. Smith, “Cavity BPM with Dipole-Mode-Selective Coupler,” in *Proc. 20th Particle Accelerator Conf. (PAC'03)*, Portland, OR, USA, May 2003, paper ROAB004.

COMMISSIONING AND RESULTS OF SPIRAL2 BPMs

C. Jamet, P. Legallois, GANIL, Caen, France

Abstract

Construction of a new accelerator is always an opportunity to face challenges and make new developments. The BPM diagnostics installed in the SPIRAL2 linac and the associated instrumentation are part of these developments. BPM instrumentations are, of course, used to measure positions and phases of ion beams but also transverse shapes, called ellipticity, as well as the beam velocity. Specifications involve knowing and calculating the sensitivities in position and in ellipticity as a function of the beam velocities. These impose small amplitude differences between channels, which require precise calibration of electronics. This paper describes the modelling and analysis of the BPM behaviour according to the beam velocity, the technical solutions, modifications and improvements. An analysis of the results and evolutions in progress are also presented.

INTRODUCTION

The SPIRAL2 accelerator is a new facility built on the GANIL site at Caen in France. The first ECR ion source produce ion beams, the second proton and deuteron beams. A CW RFQ accelerates beams with $A/Q \leq 3$ at energy of 0.74 MeV/A ($ß \approx 0.04$). The injector commissioning took place from end 2015 to 2019 [1] with the qualification of the diagnostic monitors [2].

A high power CW superconducting linac produces up to 5 mA beams with a maximum energy of 33 MeV for protons and 20 MeV/A for deuterons. The linac is composed of 19 cryomodules, 12 with one $ß = 0.07$ cavity and 7 with 2 $ß = 0.12$ cavities. The HEBT lines distribute the linac beam to a beam Dump, to NFS (Neutron For Science) or to S3 (Super Separator Spectrometer) experimental rooms [3]. A proton beam at 33 MeV, 5 mA and a power of 16 kW was produced in 2020.

BPMs are installed inside quadrupoles in the warm sections of the linac between cryomodules. BPMs are composed of 4 squared electrodes with a radius of 24 mm, a length of 39 mm and an electrode angle of 60°.

LINAC CAVITY TUNING

The ß values in the linac are from 0.04 up to 0.26 for the 33 MeV proton beam. The first cavity tuning step consists to tune the phase and amplitude of the cavities one by one at low beam power, the downstream cavities being detuned to avoid beam energy changes. Three BPM phase measurements, one before and two after the cavity to tune, allow to measure the beam velocity. After aligning the beam using the BPM positions, the cavity phase is scanned over 360° to find the buncher phase. Comparisons with theoretical values allow to compute the cavity voltage and phase to be applied. The second step is to match the beam to the linac with quadrupole tunings in the MEBT by an iterative process. The matching method uses the ellipticity values given by the BPMs. The last step is to gradually increase the beam power while monitoring beam losses.

BPM SPECIFICATIONS

The BPM specifications to tune the SC linac cavities are given in (Table 1).

Table 1: BPM Specifications

Parameter	Resolution	Range
Position	+/- 150 µm	+/-20 mm
Phase	+/-0.5 deg.	+/-180 deg.
Ellipticity	+/-20 % or +/- 1.2 mm^2	

At low velocities, sensitivities in position and ellipticity are function of the beam beta and the frequency harmonic [4]. One of our objectives was to find a formula to calculate the ellipticity sensitivity correction.

BPM MODEL

Equations

Beam bunches generate a periodical beam current represented by a Fourier series [4].

$$I_b(t) = \langle I_b \rangle \left[1 + 2 \sum_{n=1}^{\infty} A_n cos(n\omega_0 t + \phi_n) \right]$$

- I_b the beam intensity
- $<I_b>$ the average beam intensity
- A_n the Fourier component amplitudes
- ω_0 the fundamental pulsation
- ϕ_n the Fourier component phases

The wall current density $i_{w,}$ at frequency $n\omega_0/2pi$, induced by a pencil beam on the conducting cylindrical tube is given by the equation [5]:

$$i_w(n\omega_0, r, \theta, \phi_w) = \frac{A_n \langle I_b \rangle}{\pi a} \left[\frac{I_0(gr)}{I_0(ga)} + 2 \sum_{m=1}^{\infty} \frac{I_m(gr)}{I_m(ga)} cos\Big(m(\phi_w - \theta)\Big) \right]$$

- r the beam radius
- a the radius of the tube
- ϕ_ω the position angle on the cylindrical tube
- θ the beam angle
- $I_m()$ the modified Bessel function of order m

With

$$g = \frac{n\omega_0}{\beta\gamma c} = \frac{n\omega_0\sqrt{1-\beta^2}}{\beta c}$$

- λ the wave length
- γ the Lorentz factor
- $n\omega_0$ the pulsation

ISBN: 978-3-95450-230-1 ISSN: 2673-5350 doi:10.18429/JACoW-IBIC2021-MOPP35

With a Gaussian shape for the bunch longitudinal distribution, the instantaneous beam current is:

$$I_b(t) = \frac{\langle I_b \rangle}{\sqrt{2\pi}\sigma_{tp}} e^{-\frac{(t)^2}{2\sigma_{tp}^2}}$$

- $<I_b>$ the average beam intensity
- σ_{tp} the RMS length in time of the beam pulse

The Fourier component amplitudes A_n are:

$$A_n = e^{\left[\frac{-n^2\omega_0^2\sigma_{tp}^2}{2}\right]}$$

The wall current through the electrodes corresponds to the integration of the density on the electrode angles.

$$I_{w(r,l,u,d)}(n\omega_0, r, \theta) = \int_{angle_{elec}-}^{angle_{elec}+} i_w a d\phi_w$$

Wall current equations are simplified by taking only the Bessel coefficients of order 2 and with gr << 1. The formulas are then written for a large Gaussian beam.

$$I_{w(R,L,U,D)} = \int_{-\infty}^{\infty}\int_{-\infty}^{\infty} \frac{1}{\sigma_x\sqrt{2\pi}} \frac{1}{\sigma_y\sqrt{2\pi}} I_{w(r,l,u,d)}(x, y, X_0, Y_0) e^{\frac{-x^2}{2\sigma_x^2}} e^{\frac{-y^2}{2\sigma_y^2}} dxdy$$

$$I_{wR,L} = \frac{A_n\langle I_b \rangle}{\pi}\left[\frac{\phi_0}{I_0(ga)} \pm \frac{2g}{I_1(ga)} sin(\frac{\phi_0}{2})X_0 + \frac{g^2 sin(\phi_0)}{4I_2(ga)}\left((X_0^2 - Y_0^2) + (\sigma_x^2 - \sigma_y^2)\right)\right]$$

$$I_{wU,D} = \frac{A_n\langle I_b \rangle}{\pi}\left[\frac{\phi_0}{I_0(ga)} \pm \frac{2g}{I_1(ga)} sin(\frac{\phi_0}{2})Y_0 - \frac{g^2 sin(\phi_0)}{4I_2(ga)}\left((X_0^2 - Y_0^2) + (\sigma_x^2 - \sigma_y^2)\right)\right]$$

- A_n the Fourier component amplitudes
- ϕ_0 the electrode angular width
- X_0, Y_0 the horizontal and vertical positions (mm)
- ϕ_0 the angle of electrodes (radian)
- σ_x ,σ_y The horizontal and vertical RMS sizes (mm)
- I_0, I_1, I_2: Modified Bessel functions of order 0,1,2

The positions and ellipticity with a beam of transverse Gaussian distributions are defined taking into account the sensibility corrections.

$$X = \frac{K}{1+G}\frac{(I_{wR} - I_{wL})}{(I_{wR} + I_{wL} + I_{wU} + I_{wD})}$$

$$Y = \frac{K}{1+G}\frac{(I_{wU} - I_{wD})}{(I_{wR} + I_{wL} + I_{wU} + I_{wD})}$$

K, the position sensitivity, is function of the mechanical dimensions.

$$K = \frac{\phi_0 a}{2sin(\frac{\phi_0}{2})}$$

- ϕ_0 the angle of electrodes (radian)
- a the radius of the tube

Ellipticity is defined as $\sigma_x^2 - \sigma_y^2$ where σ_x and σ_y are the standard deviation of the transverse sizes of the beam. Ellipticity is calculated from the formula:

$$Ell = (\sigma_x^2 - \sigma_y^2) = \frac{S}{1+G_E}\frac{(I_{wR} + I_{wL}) - (I_{wU} + I_{wD})}{(I_{wR} + I_{wL} + I_{wU} + I_{wD})} - (X^2 - Y^2)$$

S, the ellipticity sensitivity, is also function of the radius and the electrode angle.

$$S = \frac{a^2\phi_0}{2sin(\phi_0)}$$

For SPIRAL2 BPMs, K = 25.1 mm, S = 348 mm^2

For gr << 1, the simplified equations of G, the correction coefficient of the position sensitivity, and GE the correction coefficient of the ellipticity sensitivity are:

$$1 + G \approx \frac{I_0(ga)}{I_1(ga)}\frac{ga}{2} \qquad (1 + G_E) \approx \frac{I_0(ga)(ga)^2}{8I_2(ga)}$$

Values of the corrected sensitivities in function of different beta in the linac are shown on the Table 2.

Table 2: SPIRAL2 BPM Corrected Sensitivities

beta	**Kh1 (mm)**	**Kh2 (mm)**	**Sh1 (mm^2)**	**Sh2 (mm^2)**
0.04	21.8	16.6	290	194
0.08	24.2	22	331	290
0.12	24.7	23.6	341	320
0.26	25.0	24.8	347	342

From the wall current, the wall density charges are calculated at a given $n\omega_0$.

$$\lambda_{R,L} \approx \frac{A_n < I_b >}{\pi\beta c}\left[\frac{\phi_0}{I_0(ga)} \pm \frac{2g}{I_1(ga)} sin(\frac{\phi_0}{2})X_0 + \frac{g^2 sin(\phi_0)}{4I_2(ga)}\left((X_0^2 - Y_0^2) + (\sigma_x^2 - \sigma_y^2)\right)\right]$$

$$\lambda_{U,D} \approx \frac{A_n < I_b >}{\pi\beta c}\left[\frac{\phi_0}{I_0(ga)} \pm \frac{2g}{I_1(ga)} sin(\frac{\phi_0}{2})Y_0 - \frac{g^2 sin(\phi_0)}{4I_2(ga)}\left((X_0^2 - Y_0^2) + (\sigma_x^2 - \sigma_y^2)\right)\right]$$

The integrations of the charge density over the electrode length can be written as the product of convolution of the charge density with a Heaviside step function at the electrode length.

$$Q_{elec}(t) = \beta c\lambda \otimes \mathcal{H}(t)$$

In the frequency domain, the Fourier transform of the charge is the product of the Fourier Transform of the charge density by the step function.

$$\tilde{Q}_{elec}(f) = \beta c\tilde{\lambda} \times \tilde{\mathcal{H}}(f)$$

The Fourier transform of the periodical charge signal is then:

$$\tilde{Q}_{elec}(f) = L_{elec} sinc(\pi\frac{L_{elec}}{\beta c}f)\lambda_{R,L,U,D}$$

The electrode intensity, the derivation of the charge, generates amplitude on Z_{rc}, the impedance of the resistor R in parallel with the electrode capacitance C. Electrode voltages are defined by:

$$\tilde{U}_{elec}(f) = 2\pi i f Z_{RC} sinc(\pi\frac{L_{elec}}{\beta c}f)L_{elec}\lambda_{R,L,U,D}$$

BPM electronic modules measure the electrode amplitudes at the first (h1, F_{acc} = 88.0525 MHz) and second (h2, 176.105 MHz) harmonics. The h1 and h2 electrode amplitudes are obtained from the Fourier Transform.

$$V_{h1_{eff}-(elec-R,L,U,D)} = \sqrt{2}|Z_{RC_{h1}}|I_{w(R,L,U,D)} sin(\pi \frac{L_{elec}}{L_{acc}})$$

$$V_{h2_{eff}-(elec-R,L,U,D)} = \sqrt{2}|Z_{RC_{h2}}|I_{w(R,L,U,D)} sin(2\pi \frac{L_{elec}}{L_{acc}})$$

$$|Z_{RC_{h1}}| = \frac{R}{\sqrt{1+(2\pi F_{acc}RC)^2}} \qquad |Z_{RC_{h2}}| = \frac{R}{\sqrt{1+(4\pi F_{acc}RC)^2}}$$

In this model, equations are function of σ_{tp} the standard deviation of the bunch in time (Fourier component terms "A_n"), the electric field enlargement is taken into account by the Bessel coefficients.

A vector summation of the 4 electrode signals is calculated by the electronic boards to give a vector-sum amplitude and phase. The sum of the charge density is proportional to the beam intensity.

$$I_{wR} + I_{wL} + I_{wU} + I_{wD} = \frac{4}{3}\frac{\langle I_b \rangle}{I_0(ga)} A_n$$

Considering that the phases of the 4 BPM signals are identical, the RMS amplitudes of the vector-sum h1 and h2 are:

$$V_{VS-h1_{eff}} = \frac{4\sqrt{2}}{3}|Z_{RC_{h1}}| sin(\pi \frac{L_{elec}}{L_{acc}}) \frac{\langle I_b \rangle}{I_0(g_{h1}a)} e^{-2\pi^2 \sigma_{tp}^2 F_{acc}^2}$$

$$V_{VS-h2_{eff}} = \frac{4\sqrt{2}}{3}|Z_{RC_{h2}}| sin(2\pi \frac{L_{elec}}{L_{acc}}) \frac{\langle I_b \rangle}{I_0(g_{h2}a)} e^{-8\pi^2 \sigma_{tp}^2 F_{acc}^2}$$

With

$$L_{acc} = \frac{\beta c}{F_{acc}}$$

The bunch length is calculated from the ratio of h1 and h2 vector-sum amplitudes.

$$\sigma_{tp} = \frac{1}{\sqrt{6}\pi F_{acc}} \sqrt{ln[2\frac{|Z_{RC_{h2}}|}{|Z_{RC_{h1}}|} cos(\pi \frac{L_{elec}}{L_{acc}}) \frac{I_0(g_{h1}a)}{I_0(g_{h2}a)} (\frac{V_{VS-h1_{eff}}}{V_{VS-h2_{eff}}})]}$$

BPM INSTRUMENTATION

BPM Electronic Boards

BPM electronic boards were designed and realized in the framework of collaboration between the BARC Indian laboratory and GANIL. The BPM system consists of a set of two VME64x based 6U boards, an Analog and Digital boards. BPM systems process signals either at the 88.0525 MHz fundamental frequency or at the second harmonic for both amplitude and phase measurements. Horizontal and vertical positions, ellipticity, amplitude and phase of the vector-sum are calculated from both h1 and h2 measurements. The input signal range is between -20 and -65 dBm with a variable gain from 13.5 to 60 dB.

The design of the BPM system is based on the scheme of auto-gain equalization using offset tone. In this scheme, the gain of the different channels is equalized with respect to the injected offset tone. The scheme consists to digitally generate an amplitude and phase stable offset tone having a small frequency shift with respect to the RF reference. This offset tone is added to each of the four incoming signals [6].

Calibration and Stabilisations

In order to obtain the required resolutions, 2 solutions were implemented in the electronic process, a very precise calibration and stabilizations of the 4 gains and phases. The calibration is used to correct the gain and phase deviations of signals and offset tone on the 4 channels at h1 and h2. Calibration signals around -20 dBm are send successively to the 4 channels. Correction coefficients are next memorized in a file used to initialize BPM boards during startup. Gain and phase stabilizations were designed to correct gain and phase deviations over the entire operating range. Deviations come from drift effects like temperature and from gain and phase differences of attenuators.

Calibration Results

After the calibration, tests are carried out with a generator to verify the results, maximum shifts in amplitudes between the four channels in function of the level (Fig. 1), shifts in phase (Fig. 2) are also measured.

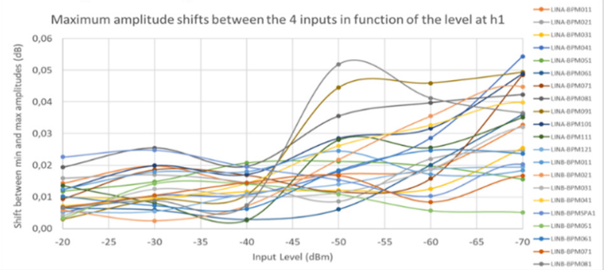

Figure 1: Max. amplitude shifts between the 4 channels.

Amplitude shifts generates +/- 0.03 mm position and +/- 0.5 mm2 ellipticity variations in function of the level from -20 dBm to -70 dBm. The maximum phase shift between channels is limited to 0.5° in this level range and the phase difference between boards is lower than +/- 0.5°.

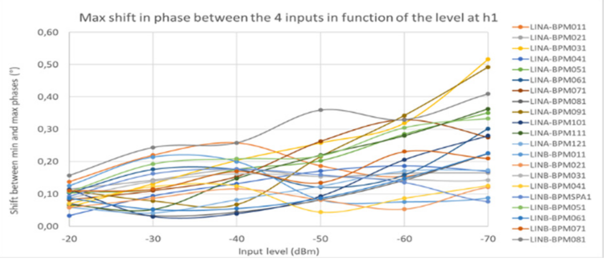

Figure 2: Max. phase shifts between the 4 channels.

MODIFICATIONS AND IMPROVEMENTS

Important precautions have been taken regarding the choice and installation of cables. After tests, the ACOME M5333Z cable was chosen for the BPMs to electronic cabinet connexions. Attenuations are 0.85 dB at h1 and 1.4 dB at h2 for cable lengths of 23 m +/- 10 mm. The 80 cables were grouped by 4 in function of their phase before installation. The lengths of small cables inside the 2 BPM cabinets were adjusted so that the overall phase of the cables is very close (+/- 0.4° shifts at 88.0525 MHz).

The BPM commissioning on the D-Plate, from 2016 to 2018, allows to learn how to use, calibrate, qualify and modify the BPM electronics [7]. The main modifications were to add shielding on the analog cards to reduce the coupling between certain channels and to limit the EMC disturbances on cabinets and cables.

The validation of position and ellipticity measurements with beams was more complicated due to difficulties to compare BPM measurements with other diagnostics and to know very precisely the beam characteristics at the BPM positions. However, the comparisons between h1 and h2 allowed us to understand that the differences in impedance matching of the 4 electronic board inputs disturbed the amplitude measurements. The required ellipticity measurement accuracy imposes severe constraints in terms of gain on the 4 channels (+/- 0.03 dB for +/- 1.2 mm^2). Early 2020, a 50 Ω matching was added on each BPM cable output. A small cable was also added on each output, with a length adjusted to have an open circuit as well as a SMA T adapter and a 50 Ω. The beam measurements are now made under the same matching conditions as the calibration.

RESULTS WITH BEAMS

In 2020, a 4.15 mA proton beam at 33 MeV, generated the BPM signals shown by Fig. 3. The h1 amplitudes (purple curve) gradually decrease when the velocity increase. The h2 amplitudes (orange curve) reach a maximum for a beta around.

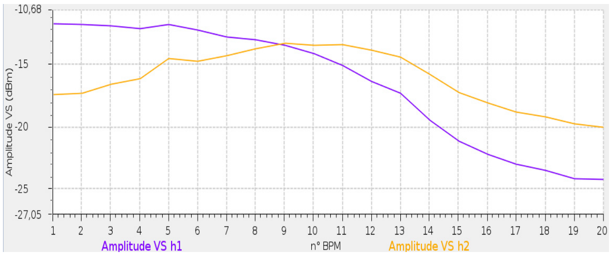

Figure 3: h1 and h2 amplitudes from the 20 BPMs.

Position and ellipticity values show a good agreement between h1 and h2 measurements and confirm the correctness of the formulas of the sensitivity coefficients. (Figs. 4 and 5).

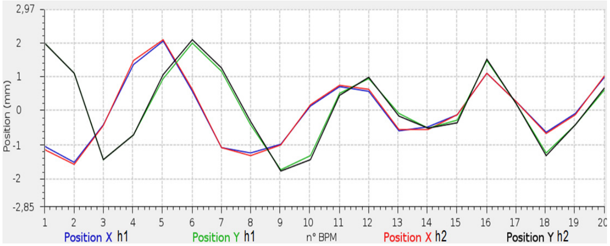

Figure 4: h1 and h2 positions from the 20 BPMs.

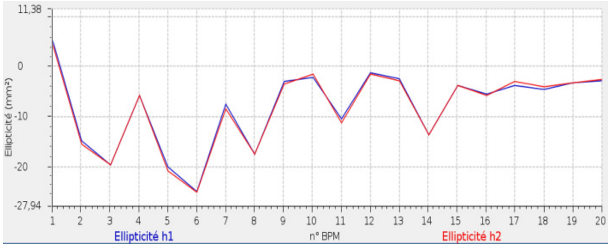

Figure 5: h1 and h2 ellipticities from the 20 BPMs.

Amplitude calculations taking the measured beam intensity with an ACCT and the bunch lengths given by the TraceWin code [8] are compared with the measured h1 and h2 vector-sum (VS) amplitudes. The calculated and measured curves are relatively close and validate the VS amplitude equations (Fig. 6).

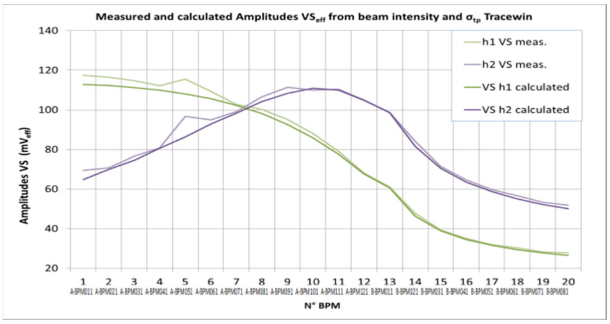

Figure 6: Measured and calculated VS amplitudes.

Bunch length calculations from the h1 and h2 vector-sum request precise measurements of the cable losses at both harmonics. Length values are actually very sensitives to low amplitudes variations, few % of differences on the h1/h2 ratio can generate important errors. Comparisons between calculated values from h1/h2 and length values from the TraceWin code did not give satisfactory results. More measurements will be done with different beams to better understand and improve this important measurement for linac tuning.

Early 2021, an improved cavity tuning procedure using beam energy measurements from the BPMs was tested. A new calibration procedure, taking into account the phase drift from BPM outputs, was applied to correct these phase shifts and have the same phase reference for the 20 BPM monitors.

In July 2021, with a helium beam at 40 MeV, beam energies were measured using the Time of Flight monitor (ToF) located at the linac exit to check the BPM measurements. Figure 7 shows that from cavity 12 the energy differences are relatively small, this validated the BPM phase accuracies and the calibration procedure.

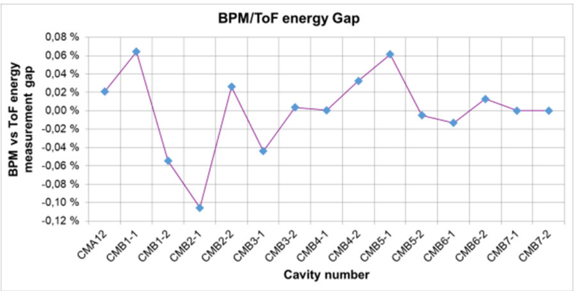

Figure 7: Energy differences between BPMs and ToF.

CONCLUSIONS

After various optimizations, the BPM systems meet the requirements and allow an optimal setting of the linac. The position and ellipticity sensitivities are calculated and applied for each new beam according to the theoretical velocity parameters. The calibration and stabilization systems allow to obtain a very good precision, big thanks to the BARC team which conceived and provided these systems. The next actions concern the development of a "Post-Mortem" system of data storage with an acquisition rate of 10 µs, an improvement of the bunch length measurements, an automation of the calibrations and an increase of the sensitivity towards the very low levels.

REFERENCES

[1] R. Ferdinand *et al.*, “Final Results of the SPIRAL2 Injector Commissioning”, in *Proc. 10th Int. Particle Accelerator Conf. (IPAC'19)*, Melbourne, Australia, May 2019, pp. 848-851. `doi:10.18429/JACoW-IPAC2019-MOPTS006`

[2] C. Jamet *et al.*, “SPIRAL2 Diagnostic qualifications with RFQ beams”, in *8th Int. Beam Instrumentation Conf. (IBIC’19)*, Malmö, Sweden, Sep. 2019. `doi:10.18429/JACoW-IBIC2019-MOPP036`

[3] P. Dolegieviez, R. Ferdinand, X. Ledoux, H. Savajols, and F. Varenne, “Status of the SPIRAL2 Project”, in *Proc. 10th Int. Particle Accelerator Conf. (IPAC'19)*, Melbourne, Australia, May 2019, pp. 844-847. `doi:10.18429/JACoW-IPAC2019-MOPTS005`

[4] R. E. Shafer, “Beam Position Monitor Sensitivity for Low-beta; Beams”, in *Proc. 1994 Linear Accelerator Conf. (LINAC'94)*, Tsukuba, Japan, Aug. 1994, paper TH-84, pp. 905-907.

[5] J. H Cupérus, “Monitoring of particle beam at high frequencies*”, Nuclear Instrument and Methods,* vol. 145*,* pp. 219-231, 1977.

[6] G. Joshi *et al.*, “An offset tone based gain stabilization technique for mixed-signal RF measurement systems”, *Nucl. Instr. Meth. A*, vol. 795, pp. 399-408, 2015. `doi:10.1016/j.nima.2015.06.015`

[7] P. Ausset *et al.*, “Operation of the Beam Position Monitor for the Spiral 2 Linac on the Test Bench of the RFQ”, in *Proc. 5th Int. Beam Instrumentation Conf. (IBIC'16)*, Barcelona, Spain, Sep. 2016, pp. 642-645. `doi:10.18429/JACoW-IBIC2016-WEPG11`

[8] D. Uriot and N. Pichoff, “Status of TraceWin Code”, in *Proc. 6th Int. Particle Accelerator Conf. (IPAC'15)*, Richmond, VA, USA, May 2015, pp. 92-94. `doi:10.18429/JACoW-IPAC2015-MOPWA008`

10th Int. Beam Instrum. Conf. IBIC2021, Pohang, Rep. of Korea JACoW Publishing
ISBN: 978-3-95450-230-1 ISSN: 2673-5350 doi:10.18429/JACoW-IBIC2021-MOPP36

COMPARISON OF TWO LONG TERM DRIFT STABILIZATION SCHEMES FOR BPM SYSTEMS

Frank Schmidt-Foehre, Gero Kube, Kay Wittenburg
Deutsches Elektronen-Synchrotron, 22607 Hamburg, Germany

Abstract

For the planned upgrade of synchrotron radiation sources PETRA (called PETRA IV) at DESY a much higher beam brilliance is requested. In order to measure according beam positions and to control orbit stability to the corresponding level of accuracy, a future high-resolution BPM system has to deliver the necessary requirements on machine stability. This needs to enable long-term drift requirements of even less than 1 micron beam position deviation per week. Such a specification goal requires an additional long-term drift stabilization of the beam position monitor (BPM) readout scheme for PETRA IV, which will include a compensation of BPM cable parameter drifts. This paper discusses a comparison of two common compensation schemes using different signal conditioning features, typically needed at machine topologies with long BPM cable paths. Certain critical aspects of the different schemes are discussed in this report, while existing successful measurements are referred in some references.

INTRODUCTION

Some 3rd generation synchrotron radiation sources like PETRA III at DESY are planned to be upgraded into 4th generation low-emittance synchrotron light sources over the next years [1]. These new machines require much smaller beam sizes at the insertion device source points for generation of high brilliant photon beams. In addition, improved long-term drift performance of BPM position measurement will be needed to cope with the corresponding level of accuracy for the required control orbit stability [2, 3].

A large amount of well-known high-resolution button BPM systems will be used as workhorses around such a ring for appropriate beam position measurement and stability control (orbit-feedbacks). PETRA IV will utilize considerably long frontend cables up to 100 m for the BPM system due to:

- avoiding radiation sensitive electronics in the tunnel
- the large accelerator circumference (2.3 km)
- space limitations inside the tunnel.

The cables connect the BPMs in the tunnel with their readout electronics outside the tunnel. Certain parts of the cable will be conducted outside the tunnel under harsh, unstable environmental conditions. Compensation schemes will be used, to control the environmental impact on BPM cable parameters, resulting in long-term drifts of the measured beam position, to a sufficiently low level. These long cables, carrying sensitive analog button RF-signals, are exposed to long-term deviation of critical signal propagation properties like the relative dielectric permittivity (epsilon r) through drifts of environmental parameters like temperature, humidity and mechanical stability [4, 5].

The compensated signal path has to incorporate as much of the BPM cable as possible to cope for parameter deviations along this cable segment. In consequence, this needs an electronic device for handling of the compensation scheme, located at the beginning (close to the BPM) and another one at the end of the compensated signal path (e.g. included in the BPM frontend).

Two main compensation concepts and their technical implementations will be discussed below, together with their common similarities and differences, their individual pro's and con's in comparison to the needs and preferences for use in the future PETRA VI synchrotron light source [2, 3].

COMPENSATION SCHEMES

Four years ago, a new BPM frontend compensation scheme was introduced for the ELETTRA storage ring at the Sincrotrone Trieste in Italy [6-8], which has been tested and is now in use at different accelerators [9]. Meanwhile, this system is manufactured in collaboration with the Instrumentation Technologies d. d. company at Solkan, Slovenia. It is mainly used in combination with the Libera Spark readout electronics of the same company [7, 10]. This compensation scheme uses an artificial pilot tone (PT), which is added into each BPM button signal chain inside an electronic box located at the foremost coupling opportunity just behind the button output connector as shown in Fig. 1 (signal combiner/splitter combination is used for equalization of button signals here). A pre-series PT frontend has been tested in a test setup as shown in Fig. 1 in combination with the non-switching Libera Spark readout electronics at the PETRA III ring at DESY in 2019 for performance comparison against other existing BPM readout electronics (Libera Brilliance+ and Libera Brilliance) [11].

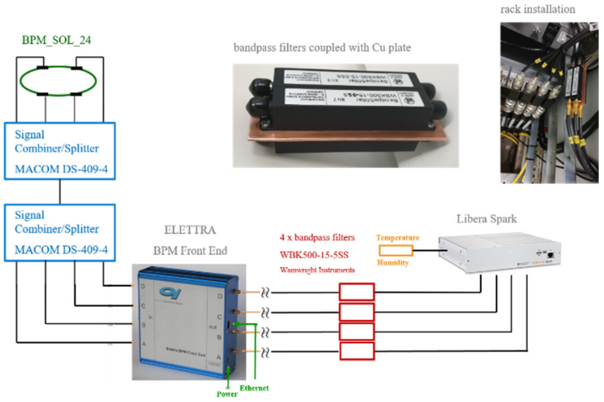

Figure 1: Button BPM setup with PT frontend and adapted Libera Spark readout electronics [11].

It's pilot-tone coupling as shown in Fig. 2, together with the compensation principle is explained and discussed in [12].

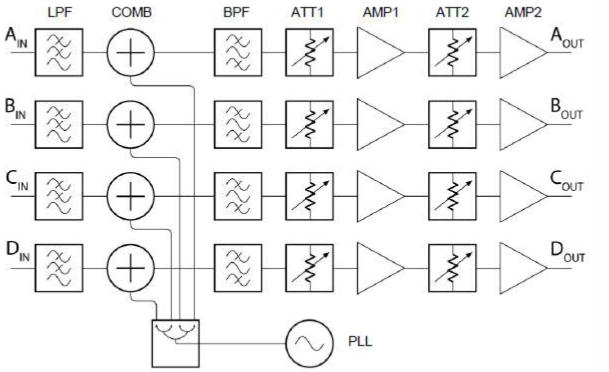

Figure 2: Coupling of pilot-tone inside PT frontend [12].

Another compensation scheme, developed by the Instrumentation Technologies d. d. company at Solkan, Slovenia 20 years ago for the SLS at PSI, Switzerland uses a continuously and synchronously-permuting crossbar-switching/de-switching scheme for all of the 4 BPM button RF input channels inside the readout electronics device. It enables real-time compensation of amplitude and phase at each BPM button signal channel in reference to the average of all 4 channels [13-15]. This contemporary crossbar-switching scheme is intended to work along the internal analog RF-frontend input signal paths. DESY has many years of operational experience with the Libera Brilliance BPM readout electronics used at PETRA III, which uses this device-internal crossbar-switching compensation scheme.

An adapted external switching scheme was suggested by DESY and others [16], which incorporates the BPM RF-cables in front of the readout-electronics inputs by shifting the electronical analog crossbar-switching part as far as possible towards the frontend of the signal chain close to the BPM chamber.

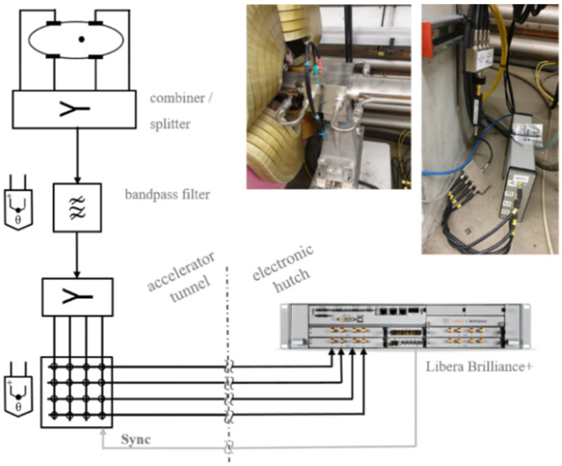

Figure 3: Button BPM setup with ECS frontend and adapted Libera Brilliance+ readout electronics [17, 18].

This extended crossbar-switching scheme is referred to as 'ECS' throughout this document. A first prototype of such ECS scheme was recently developed in a collaboration between DESY and Instrumentation Technologies d. d. and tested in a setup at PETRA III as shown in Fig. 3. First measurements with this prototype are presented in the MOPP30 paper at this conference [17].

SIMILARITIES AND DIFFERENCES

The main goal of a fast auto-compensation scheme like PT or ECS is, to reduce temporal drifts of hardware components, circuits and cabling in the whole analog BPM button RF-signal chain related to various effects, like e.g. drifts of environmental parameters, mechanical forces and aging.

Both compensation schemes (PT and ECS) correct for such signal drifts, resulting in an increased drift performance of the compensated BPM channel.

Both schemes can be set up statically via the control-system. These settings remain stable as long as the electrical boundary conditions remain.

As a common drawback, both auto-compensation schemes disturb the turn-by-turn (TbT) BPM measurements by their individually generated spectral artefacts. This has to be handled accordingly during measurement at beam operation. On the other hand, this will not be problematic within regular user operation, as TbT data is typically acquired on demand for 1st turn, commissioning and machine study measurements and might even serve as a mechanism for proof of function for the individual compensation scheme during normal operation. In addition, any data stream used for feedback applications shall be sufficiently free of residual compensation artefacts.

To cope with this task, both variants similarly add an electronic module to the signal chain in close vicinity of the BPM chamber and act upon the BPM button-signals at the earliest possible stage in the signal-chain behind the BPM, to minimize the length of uncompensated paths in the button signal chains. Nevertheless, both solutions leave short uncompensated signal-paths between the BPM buttons and this first electronic-boxes, that have to be drift-stabilized by other means (e. g. rigid cables, temperature-stabilized tunnel environment). Note that additional electronics near the beam need radiation hard designs and appropriate shielding. Radiation measurements under operational conditions shall clarify existing radiation hardness and enable estimations for ideal location and sufficient shielding of the frontend devices inside the tunnel.

Both schemes need an additional cable connection to carry support signals from the readout- to the additional frontend-electronics near the BPM inside the tunnel. These signals and cables increase the BPM channel cost and risk of errors due to EMI or electro-mechanical malfunction.

In case of irreversible failure of the compensation frontend-electronics, the remaining part of the compensation in the readout-electronic backend has to be deactivated accordingly, resulting in an intermediate drift of the BPM measurement until repair. As electronics inside the tunnel is not accessible in normal accelerator run periods, such

BPM can either be deactivated or has to be repaired (electronics frontend exchange) on short notice, depending on its individual position and functionality.

Main differences in the compensation schemes can be found in their functional concepts, the implementations and its operational consequences.

The PT scheme compensates for parameter drifts in the BPM button-signal measurement channel by measuring, comparing and compensating deviations of an artificial, discrete sinosoidal cw signal, that is located in direct spectral vicinity to the carrier frequency of the beam (example at the PETRA III test installation: ~1-5 MHz from beam center frequency at 30 MHz bandwidth). Figure 4 shows a typical amplitude spectrum of a PT setup as used for Petra III test measurements, carried out using different beam modes in 2019 [10].

As PT uses a single tone for signal propagation measurement and compensation, it is able to provide absolute measurements of signal attenuation at the used PT frequency. This measurement relies on a perfectly adjusted and stable pilot-tone signal (amplitude, frequency).

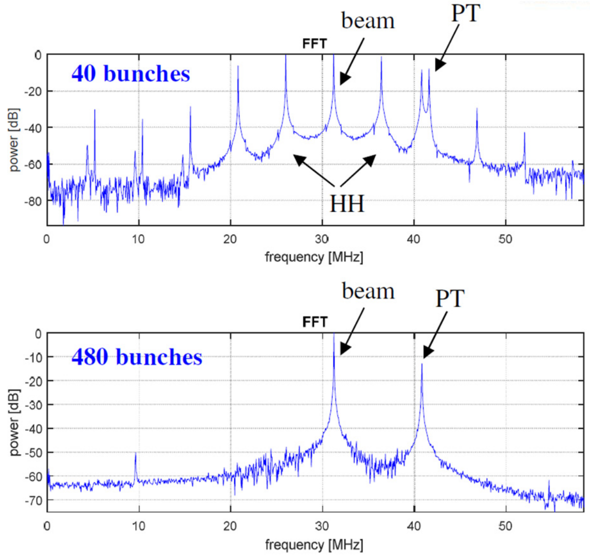

Figure 4: typical amplitude spectra of a PT system used for PETRA III test measurements at 40 bunch/100 mA and 480 bunches/120 mA beam modes (HH: higher harmonics) [11].

The pilot-tone signal is added to the button signal spectrum at the input of the transmission channel and selected at the other end of the channel for the recovery of the original transmitted BPM signals. As the pilot-tone has to be transmitted using the same channel settings as used for the original button signal, the separation process produces an impact on the spectrum of the useful button signals by the non-ideal side-lopes of the required filter. This effect is increased by analog filters in the PT frontend and the asynchronicity between pilot-tone frontend signal generation clock (PLL based on local crystal oscillator) and digital filter backend clock (local clock, synchronized to the accelerator timing system by PLL) with the ELETTRA PT implementation.

To the contrary, the ECS switches between the 4 BPM button signals, thus producing spurious lines in the original spectrum. These discrete switching frequencies (typically 3.3 kHz and higher harmonics for Libera Brilliance at PETRA III) are configured and adjusted such to reside far away from critical frequencies inside the BPM button signal spectrum. They can be filtered out efficiently through steep log-in notch filters, synchronized to the accelerators machine frequency. Residual spike-like imperfect switching artefacts are eliminated further by a synchronized, single data substitution algorithm for generation of low residue, broadband TbT data.

No more artificial spectral components are added to the original BPM button spectrum within the fully synchronous ECS scheme by design.

The impact of the parameter drifts in the analog signal transmission channels acts upon the full button-signal spectrum. In consequence, the compensation should also take the whole button-signal spectrum into account for compensation bandwidth. While the PT scheme relies only on the deviation representativity of a singular, un-synchronized cw pilot-tone signal, the ECS scheme uses the same full-spectrum BPM button-signal as a control-variable for the auto-compensation control-loop.

Finally, the PT concept needs a couple of additional analog and digital hardware components and circuits to add and extract the required pilot-tone signal into the spectrum and attenuation framework of the original BPM button signals.

The ECS scheme relies on the similar circuits and components as the contemporary readout-device-internal crossbar-switching. It only shifts the foremost readout-circuits including the crossbar-switch towards the BPM tunnel-frontend, while extending the slow, reduced-slope switch-control signal and power connection towards this frontend via a well-shielded, symmetrical twisted-pair (e.g. CAT-7) cable connection for low EMI susceptibility.

DISCUSSION

If the individual pilot-tone reference signal of a PT frontend is adjusted as a standard, the Pilot-Tone scheme offers auto-calibration against that standard reference signal, as well as auto-drift compensation. Due to the concept of PT scheme, the artificial pilot-tone signal disturbs the signal integrity of the original BPM button-signals and may produce spurious spectral lines. An off-centered pilot-tone RF-frequency generates an impact from the typical variation in the spectral properties of usable RF-bandpass-filters (production variance, temporal drift). This adds a device-individual artificial drift compensation error. External synchronization of the PT frontend clock with the machine clock may further improve the spectral performance. As dynamic errors of the pilot-tone may reduce the auto-compensation performance, static errors may reduce the auto-calibration accuracy. While auto-compensation affects amplitude drifts in the corresponding signal-path, phase drifts remain un-compensated within the PT scheme. As the PT reference signal-level dynamics are critical for overall measurement performance, they might need dynamic adaption and further optimization to achieve full system performance over the full dynamic measurement range.

ECS compensates the drifts in the raw electrical source signals from the individual BPM buttons and levels the impact from the main influencing environmental parameters to stabilize the derived position value. This scheme is deeply integrated into the readout electronics on both sides of the disturbed signal transmission channel and thus not advisable for retrofit of existing BPM installations for drift performance upgrade.

The concept of ECS compensation implies, that all other drifting parts of the compensated transmission channel segments (e. g. aging of components, thermo-mechanical drifts) will automatically also be compensated for at the source of their drifts by design. At ECS, the resulting compensated BPM button signal-transmission channels are free of drifts above a reasonably low level, determined by the granularity of the compensated drift parameters (amplitude, phase) as implemented in the respective digital acquisition system.

As the point of compensation impact is shifted maximally towards the BPM frontend inside the tunnel with both, the ECS and the PT compensation schemes, both of them will stabilize the drifts in the major part of the transmission channel.

PT compensates for drifts of calculated position signals, that are derived from all underlying disturbed raw button signal channels at once during the readout process. This compensation scheme is designed using clearly separated blocks in the frontend readout-electronics and the ELETTRA PT implementation uses an existing device-interface (Ethernet) for implementation of the required digital control and power path. This might offer usability of PT electronics and respective readout-electronics firmware update for drift performance upgrades at certain existing BPM installations. PT relies on the fact, that the drift of the dielectric cable permittivity (epsilon r) is constant over the frequency region-of-interest and similar to the value at PT signal frequency.

While the PT frontend conceptually needs memory to provide a stand-alone PT generator, it is susceptible to SEU as produced by Neutron irradiation, whereas the ECS frontend mainly uses passive components in addition to the semiconductor crossbar-switch without need for memory, which makes it conceptually radiation harder. Nevertheless, the ESC frontend has still to be proved for susceptibility against degradation due to irradiation.

As an ECS system does not add comparingly significant artificial signal parts to the useful button-signals, the resulting measurement represents mainly the original BPM signals.

Furthermore, the ECS utilizes the full usable bandwidth of the original button signals, thus providing ideal full-bandwidth loop control without neglecting any probably critical spectral parts of the compensated transmission channels.

CONCLUSION AND OUTLOOK

An ECS system offers simple and well-known building blocks, together with an intrinsically radiation hard design, which shall be confirmed by appropriate radiation measurements. As this compensation scheme compensates at the source of signal transmission drifts and does not add significant artificial parts to the useful button-signals, as well as utilizing the full usable bandwidth of the original BPM button signals for compensation, it seems to be conceptionally well suited for use in the planned PETRA IV project.

Radiation tolerance of the ECS and PT frontend boxes and compensable dynamic ranges of main environment parameters exposed to BPM cables shall be tested for implementation.

As both compensation schemes use electronics inside the tunnel, regular self-tests of the frontend electronics should be considered for device degradation and failure recognition in due time, to support preventive maintenance.

ACKNOWLEDGEMENTS

We thank P. Leban from Instrumentation Technologies d. d. and G. Brajnik from Sincrotrone Trieste for providing a Libera Spark and an ELETTRA Pilot-Tone frontend and their comprehensive support according to the measurements.

REFERENCES

[1] K. Balewski *et al.*, “PETRA III: a low emittance synchrotron radiation source”, Tech. note DESY 2004-035, 2004.

[2] C.G. Schroer *et al.*, “PETRA IV: the ultralow-emittance source project at DESYY”, *J. Synchrotron Rad.*, vol. 25, pp. 1277–1290, 2018.

[3] I. Agapov *et al.*, *PETRA IV Report* , p4-WP201-re-0006, July 2021.

[4] G. Rehm, C. Bloomer, “Impact of Relative Humidity on EBPM Readings”, talk presented at *2nd Diagnostics Experts of European Light Sources Workshop (DEELS’15)*, Barcelona, Spain, June 2015. `https://indico.cells.es/event/22/`.

[5] N. Hubert, “Test of BPM Cables vs Humidity and Temperature”, talk presented at *6th Diagnostics Experts of EuropeanLight Sources Workshop (DEELS’19)*, Grenoble, France, June 2019. `https://indico.cern.ch/event/789811/`.

[6] G. Brajnik, S. Carrato, S. Bassanese, G. Cautero and R. De Monte, “Pilot tone as a key to improving the spatial resolution of eBPMs”, in *Proc. AIP Conf.*, vol. 1741, p. 020013, 2016. `doi:10.1063/1.4952792`

[7] M. Cargnelutti *et al.*, “Stability Tests with Pilot-Tone Based Elettra BPM RF Front End and Libera Electronics”, in *Proc. 7th Int. Beam Instrumentation Conf. (IBIC’18)*, Shanghai, China, Sep. 2018, pp. 289–292. `doi:10.18429/JACoW-IBIC2018-TUPB13`

[8] G. Brajnik, B. Repič, “Current Status of Elettra 2.0 eBPM System”, Libera Workshop 2021, `https://www.i-tech.si/wp-content/uploads/2021/06/8.-Gabriele-Brajnik_Elettra_compressed.pdf`

[9] Overview of Talks Resources – Online Libera Workshop 2021, `https://www.i-tech.si/particle-accelerators/libera-workshop-2021-2/`.

[10] `https://www.i-tech.si/products/libera-spark-erxr/`.

[11] G. Kube, "BPM Studies in view of PETRA IV", 15th Libera Online Workshop, June 17, 2020, `https://www.i-tech.si/wp-content/uploads/2021/06/6.-Gero-Kube_DESY_compressed1.pdf`

[12] G. Brajnik, S. Carrato, S. Bassanese, G. Cautero, and R. De Monte, "A Novel Electron-BPM Front End With Sub-Micron Resolution Based on Pilot-Tone Compensation: Test Results With Beam", in *Proc. 5th Int. Beam Instrumentation Conf. (IBIC'16)*, Barcelona, Spain, Sep. 2016, pp. 307-310. `doi:10.18429/JACoW-IBIC2016-TUPG02`

[13] M. Dehler *et al.*, "New digital BPM system for the Swiss light source", in *Proc. 4th European Workshop on Beam Diagnostics and Instrumentation for Particle Accelerators (DIPAC'99)*, Chester, UK, May 1999, paper PT06, pp. 168–170.

[14] U. Mavrič, "Innovative RF Design Unites Benefits of Multiplexed and Multi-channel System", in *Proc. 4th Beam Instrumentation Workshop (BIW'04)*, Knoxville, TN, USA, May 2004, pp. 373–378.

[15] A. Kosicek, "Libera Electron Beam Position Processor", in *Proc. 21st Particle Accelerator Conf. (PAC'05)*, Knoxville, TN, USA, May 2005, paper RPAT093, pp. 4284–4286.

[16] G. J. Portmann, M. J. Chin, W. E. Norum, and J. M. Weber, "BPM Electronics With Self-Calibration at the ALS", in *Proc. 9th Int. Beam Instrumentation Conf. (IBIC'20)*, Santos, Brazil, Sep. 2020, paper FRAO03. `doi:10.18429/JACoW-IBIC2020-FRAO03`

[17] G. Kube *et al.*, "Tests of the New BPM Long Term Drift Stabilization Scheme Based on External Crossbar Switching at PETRA III", presented at the 9th Int. Beam Instrumentation Conf. (IBIC'21), Pohang, Korea, Sep. 2021, paper MOPP30.

[18] `https://www.i-tech.si/products/libera-brilliance-3/`.

AN AUTOMATIC FOCALIZATION SYSTEM FOR ENHANCED RADIOISOTOPE PRODUCTION WITH SOLID TARGETS*

P. Casolaro†, P. D. Häffner, G. Dellepiane, I. Mateu, P. Scampoli[1], N. Voeten, E. Zyaee, S. Braccini
Albert Einstein Center for Fundamental Physics, Laboratory for High Energy Physics,
University of Bern, Bern, Switzerland
[1]also at Department of Physics “Ettore Pancini”, University of Napoli Federico II,
Complesso Universitario di Monte S. Angelo, Napoli, Italy

Abstract

A research program aimed at the production of novel radioisotopes for theranostics is ongoing at the 18 MeV cyclotron laboratory in operation at the Bern University Hospital (Inselspital). A method based on the bombardment of isotope enriched materials in form of compressed 6 mm diameter pellets was developed. To accomplish this challenging goal, accurate knowledge of beam energy, positioning and focusing as well as production cross sections are crucial. Investigations are carried on to assess all these items. In particular, an automatic compact focalization system was conceived and constructed to optimize the irradiation procedure. It is based on a 0.5 m long magnetic system, embedding two quadrupoles and two steering magnets, and a non-destructive beam monitoring detector located in front of the target. The profiles measured by a fiber detector are elaborated by a feedback optimization algorithm that acts on the magnets and keeps the beam focused on target to enhance the production yield. Following the first successful functional tests, the preliminary results on the production of medical radioisotopes are presented.

INTRODUCTION

Medical cyclotrons for radiosiotope production are nowadays optimized for providing standard radioisotopes as the ^{18}F used in Positron Emisssion Tomography (PET) applications. Theranostics is a novel approach in cancer treatment based on the combined use of diagnostic (γ or β^+ emitters) and therapeutic (α or β^- emitters) radioisotopes. The production of radioisotopes for theranostics is currently a reserach topic. The University of Bern is equipped with an IBA 18/18 HC medical cyclotron for both routine production of radiopharmaceuticals and scientific research. Figure 1 shows a picture of the cyclotron and of its Beam Transfer Line (BTL), which ends in a separate bunker with independent access. Multidisciplinary research activities are carried out at the Bern cyclotron laboratory. These include the study of new radioisotopes for theranostics, radiation hardness, fundamental physics, radiation protection and particle detector physics [1].

Figure 1: The Bern medical cyclotron.

In particular, the production of novel radioisotopes for theranostics is performed by irradiating solid targets in form of 6 mm diameter pellets made of compressed powder [2, 3]. Beams extracted from medical cyclotrons for standard radioisotope production have a typical dimension of the order of 10 mm. Thus, in order to achieve a safe, reliable and optimized production for theranostics, the beam should be focused on target over the whole irradiation. However, the focused beam is very sensitive to any beam instability due, for example, to drifts of the main coil of the cyclotron caused by the temperature increase. To address these scientific requirements, a new Automatic Focalization System (AFS) has been developed. Its operating principle as well as first functional tests carried out on a AFS-prototype installed in the BTL are presented in this work.

MATERIALS AND METHODS

The production of non-conventional radioisotopes at the Bern medical cyclotron is carried out by irradiating solid targets contained in a specifically designed target coin. It is made of two halves, typically made of aluminum, held together by permanent magnets. The overall thickness of the target coin is 2 mm. A picture of the target coin with the permanent magnets and 6 mm diameter pellet is shown in Fig. 2.

A new beam line has been implemented to enhance the performance of the production of new radioisotopes for theranostics (Fig. 3). It is made of a Mini-PET Beamline (MBL), a UniBEaM detector and a IBA Nirta solid target station.

---

* Work partially supported by the Swiss National Science Foundation (SNSF). Grants: 200021_175749 and CRSII5_180352.

† pierluigi.casolaro@lhep.unibe.ch

ISBN: 978-3-95450-230-1 ISSN: 2673-5350 doi:10.18429/JACoW-IBIC2021-MOPP38

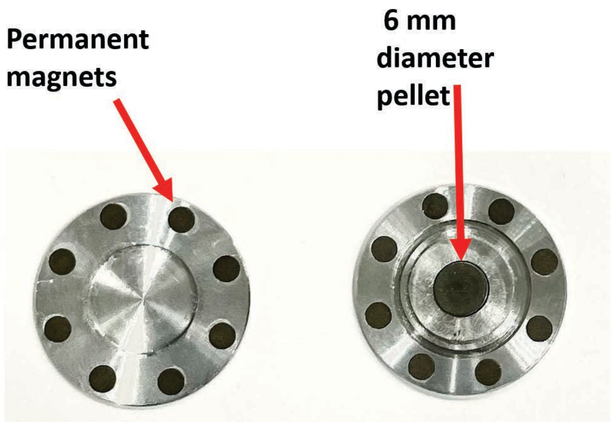

Figure 2: Target coin with permanent magnets and the 6 mm diameter pellet indicated by arrows.

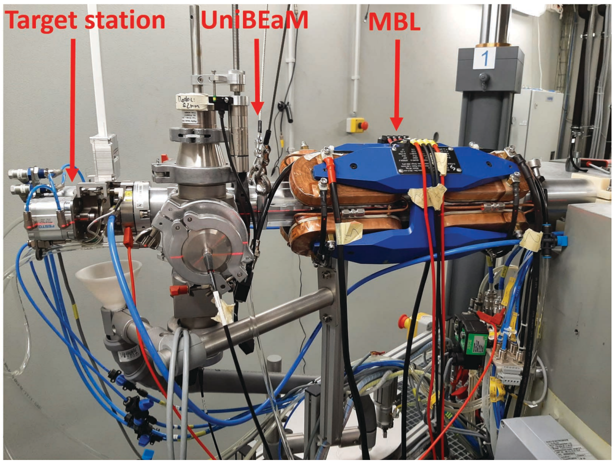

Figure 3: Beam line for the production of novel radioisotopes for theranostics at the Bern medical cyclotron.

The MBL is a 50 cm long structure with two quadrupole and two steerering magnets produced by the company D-Pace. The UniBEaM is a two-dimensional beam profiler based on scintillation optical fibers, developed by our group [4]. Specifically, two 250 µm diameter Ce^{3+} doped quartz scintillation fibers are moved across the beam pipe by two high-precision motors; the beam profile is determined by measuring the light intensity and the corresponding fiber position. The MBL focuses the beam on the target and beam profiles are measured by the UniBEaM. The new Automatic Focalization System (AFS) features a specific software which adjusts the MBL currents on the basis of the feedback provided by the UniBEaM detector. A schematic of the AFS main elements is shown in Fig. 4.

In detail, the operating principle of the AFS control system is the following:

1 UniBEaM X and Y profiles are recorded and optimization parameters are defined as functions of the centroid and FWHM for each profile.

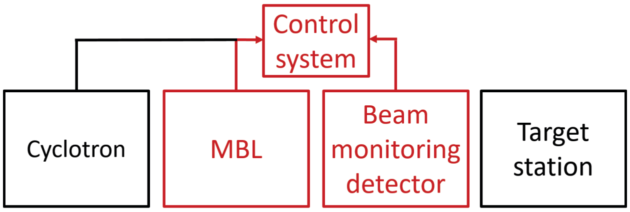

Figure 4: Schematic of the elements of the cyclotron for non-conventional radioisotope production. The part in red refers to the Automatic Focalisation system.

2 The optimization parameters are compared to those of the target region (i.e. the position of the pellet in the target station).

3 The MBL currents are varied and new optimization parameters are compared to those of the previous profile.

4 The automated procedure ends when the difference between the optimization parameters of two consecutive beam profiles is less than a defined tolerance.

A different detector was also used as beam monitor for the AFS. In particular, the π^2 detector, a yttrium orthosilicate coated aluminium foil read out by a CCD camera, has been used to assess the focusing capabilities of the new system. This detector was recently developed by our group [5]. The AFS has to withstand harsh conditions with irradiations of several hours and beam currents up to 30 µA.

RESULTS

The beam profiles measured by the UniBEaM are used by the Automatic Focalization System (AFS) to adjust the MBL currents and finally focus the beam on the target. However, the position of the UniBEaM is 30 cm far from that of the target. Thus, the beam profile on the target is evaluated starting from the measured UniBEaM profiles throughout beam dynamics calculations [6]. In particular, the scaling factor f for the beam divergence is defined as follows:

$$f = \frac{\sigma_{target}}{\sigma_{UB}} = \sqrt{L^2 \cdot \frac{\gamma_{UB}}{\beta_{UB}} - 2 \cdot L \cdot \frac{\alpha_{UB}}{\beta_{UB}} + 1}, \qquad (1)$$

where σ_{target} and σ_{UB} are the beam profile standard deviations at the position of the target and of the UniBEaM, L is the distance between the target and the UniBEaM. The Twiss parameters α_{UB}, β_{UB}, γ_{UB} are defined as a function of the two quadrupole currents at the position of the UniBEaM.

The displacement of the beam profile is derived from the Lorentz force equation as follows:

$$\Delta x = \frac{q(\int B(l)dl)c}{\sqrt{E_{kin}^2 + 2E_{kin}mc^2}} \cdot L, \qquad (2)$$

where m and q are the proton mass and elementary charge, $\int B(l)dl$ is the integral of the magnetic field along the beam axis, E_{kin} is the kinetic energy and c the speed of light. These calculations are performed by the optimization algorithm for the horizontal and vertical measured UniBEaM profiles to obtain the beam profile on the target. In order to verify the correctness of this evaluation, we measured the beam profile on the target with a second UniBEaM. The results, shown in Fig. 5, report an excellent agreement between the measured and calculated beam profiles.

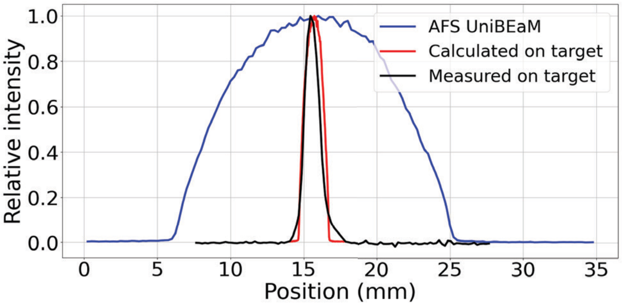

Figure 5: Beam profile measured by the AFS-UniBEaM (blue); calculated (red) and measured (black) beam profiles on the target position.

AFS focusing capabilities have been proved by comparing the beam spot of a focused (after the AFS) and unfocused (before the AFS) beam measured with the π^2 detector placed at the target position. Images of Fig. 6 demonstrate that the AFS is capable to focus the beam on a target region of 4×3 mm^2, which is less than the surface of the pellet (6 mm diameter).

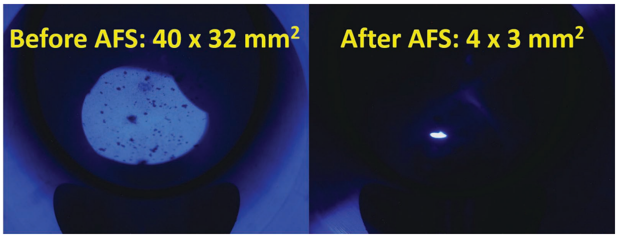

Figure 6: Beam spot before (left) and after (right) the optimization procedure.

To assess the capabilities of the new AFS in recovering the beam after a beam instability, we produced a slight perturbation of the beam by acting on the external magnetic steerers; thus, we ran the AFS. The results, reported in Fig. 7, show that the AFS is able to put back the beam in position following a 1.3 mm horizontal beam shift. Similar results have been obtained after a beam shift on the vertical axis. Finally we tested the enhancement of the AFS performance by irradiating two natural zinc targets, one with a flat beam and the other with an AFS optimized beam. For these two extreme cases, we found a gain factor in the produced ^{68}Ga and ^{67}Ga specific activities of about 20 [6].

CONCLUSIONS AND OUTLOOK

A new beam line has been implemented at the Bern medical cyclotron aimed to establish a reliable procedure for the irradiation of solid targets in view of the production of theranostics radioisotopes. A beam monitoring detector provides a fast feedback for the control system which automatically adjusts the currents of the quadrupoles and steerers to focus and position the beam on target. We successfully tested the AFS with the UniBEaM, a beam profiler based on scintillation optical fibers, and the π^2 detector, a beam monitor based on a scintillation foil and a CCD camera. In particular, we observed that the AFS is able to focus the beam on a surface smaller than that of the pellet of material for the production of theranostics radioisotopes as well as to automatically recover the optimized condition following an external perturbation. Being less than 1 meter, the compactness is a crucial aspect allowing the installation in facilities with limited space including the cyclotrons for radioisotope production. Follwing the tests with the BTL, the AFS was installed directly on the cyclotron and tests and optimization are ongoing.

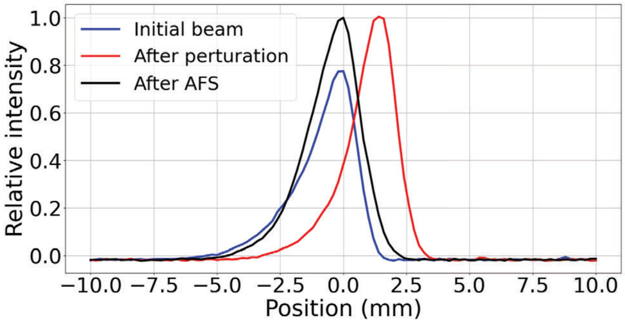

Figure 7: Automatic Foclisation Capabilities in recovering the beam after a perturbation on the focused beam.

ACKNOWLEDGEMENTS

We would like to acknowledge contributions from the LHEP engineering and technical staff. We thank SWAN Isotopen AG for the collaboration.

REFERENCES

[1] S. Braccini, “The new bern PET cyclotron, its research beam line, and the development of an innovative beam monitor detector”, in *AIP Conf. Proc.*, vol. 1525, pp. 144-150, 2013. `doi:10.1063/1.4802308`

[2] S. Braccini, C. Belver-Aguilar, T. S. Carzaniga, G. Dellepiane, P. Haeffner and P. Scampoli, “Novel Irradiation Methods for Theranostic Radioisotope Production with Solid Targets at the Bern Medical Cyclotron”, in *Proc. 22nd Int. Conf. on Cyclotrons and their Applications (Cyclotrons’19)*, Cape Town, South Africa, Sep. 2019, pp. 127–131. `doi:10.18429/JACoW-CYCLOTRONS2019-TUA02`

[3] G. Dellepiane, C. Belver-Aguilar, T. S. Carzaniga, P. Casolaro, P. D. Häffner, P. Scampoli, M. Schmid and S. Braccini, “Research on theranostic radioisotope production at the Bern medical cyclotron”, in *IL NUOVO CIMENTO*44 C, 130, 2021. `doi:10.1393/ncc/i2021-21130-6`

[4] M. Auger, S. Braccini, T. S. Carzaniga, A. Ereditato, K. P. Nesteruk, and P. Scampoli, “A detector based on silica fibers

for ion beam monitoring in a wide current range", *J. Instrum.*, vol. 11, p. 03027, 2016. `doi:10.1088/1748-0221/11/03/p03027`

[5] C. Belver-Aguilar, S. Braccini, T. S. Carzaniga, A. Gsponer, P. D. Häffner, P. Scampoli, M. Schmid, "A Novel Three-Dimensional Non-Destructive Beam-Monitoring Detector", *Applied Sciences*, vol. 10, no. 22, p. 8217, 2020. `doi:10.3390/app10228217`

[6] P. D. Häffner, C. Belver-Aguilar, P. Casolaro, G. Dellepiane, P. Scampoli and S. Braccini "An Active Irradiation System with Automatic Beam Positioning and Focusing for a Medical Cyclotron", *Applied Sciences*, vol. 11, no. 6, p. 2452, 2021. `doi:10.3390/app11062452`

ISBN: 978-3-95450-230-1 ISSN: 2673-5350 doi:10.18429/JACoW-IBIC2021-MOPP44

ANALYSIS OF MULTI-BUNCH INSTABILITIES AT ALBA USING A TRANSVERSE FEEDBACK SYSTEM

U. Iriso and T.F. Günzel
ALBA-CELLS Synchrotron, Cerdanyola del Vallès, Spain

Abstract

Since 2015 Alba is equipped with a transverse bunch by bunch feedback system, which not only damps the transverse coupled bunch instabilities in the machine, but also allows the impedance characterization of the storage ring. This characterization is produced by an internal sequence, which is programmed to excite and measure the growth and damping rates of each of the multi-bunch modes. This paper describes the measurement technique, presents the studies carried out to characterize the machine and different movable systems like the scrapers or in-vacuum undulators. Results are compared with the transverse impedance spectra obtained from computer simulations.

INTRODUCTION

Transverse betatron oscillations associated with beam instabilities limit the machine performance in current synchrotron light sources. These instabilities are driven by long range wakefields, usually trapped modes in cavity-like structures in the vacuum chamber, resistive wall (RW) impedances, and occasionally from multibunch ion instabilities when the machine vacuum is not the optimum.

Since 2015, ALBA uses the transverse bunch-by-bunch (BBB) feedback system described in [1] to damp these instabilities. It is based on the Libera BBB electronics (iTech) and controlled using the firmware and software developed at Diamond Light Source (DLS) [2,3]. This system not only allows to damp instabilities, but it also allows to program sequences that apply different control parameters at the same time as data acquisition. This is used to measure the growth rates of the individual multi-bunch modes, and so to 1) evaluate the ALBA impedance model, and 2) assess the most dangerous modes for the ALBA Storage Ring.

In this report, similarly to what is done in [4], we analyze the results of these scans for different machine configurations, like different chroms or different position of movable systems like scrapers or in-vacuum undulators (IVUs).

IMPEDANCE THEORY

For a beam with M bunches and N particles per bunch and non-zero chromaticity ξ, the complex frequency shift of mode (m,l) is [4,5]:

$$\Omega_{m,l}-\omega_\beta = -i\frac{MNr_0c}{2\gamma T_0^2\omega_\beta}\sum Z_\perp(\omega_{m,l}\cdot h_l(\omega_{m,l}-\omega_\xi)) \ , \quad (1)$$

where r_0 the classical radius of the electron, c is the speed of light, γ is the Lorentz factor, and T_0 is the revolution period. While the $\mathrm{Re}(\Omega_{m,l})$ corresponds to the coherent beam frequency shift, the $\mathrm{Im}(\Omega_{m,l})$ corresponds to the growth rate of mode (m,l), which we will measure experimentally using the BBB in the following sections.

The oscillation frequency of the discrete modes (m,l) is:

$$\omega_{m,l} = (pM+m)\omega_0 + \omega_\beta + l\omega_s \ , \quad (2)$$

with $p = [-\infty, +\infty]$, and ω_0, ω_β, ω_s the (angular) revolution, betatron and synchrotron frequencies. We note that the spectrum of a real signal is folded anti-symmetrically around half of the harmonic number, $h/2$, so that the peak at m_0 has its mirror at $(h-m_0)$ [4,5].

But to infer the beam growth rate of mode (m,l), it is crucial to have a good impedance model $Z_\perp$ in Eq. 1. At ALBA, the contribution of $Z_\perp$ is considered to be composed of two parts, namely the Resistive Wall (RW) $Z_\perp^{RW}$ contribution and the narrow-band resonators $\sum Z_\perp^{\mathrm{res}}$:

$$Z_\perp = Z_\perp^{RW} + \sum Z_\perp^{\mathrm{res}} \ . \quad (3)$$

These two contributions can be expressed as:

$$Z_\perp^{RW} = G_1 L\frac{\mathrm{sgn}(\omega)+i}{\pi b^3}\sqrt{\frac{Z_0\rho c}{2\omega}}, \quad \text{and} \quad (4)$$

$$Z_\perp^{\mathrm{res}} = \frac{R_S}{\frac{\omega}{\omega_r}+iQ\left(\left(\frac{\omega}{\omega_r}\right)^2-1\right)} \ . \quad (5)$$

Here, b is the chamber half-aperture, G_1 is the chamber form Yukoya factor, Z_0 is the vacuum impedance and ρ is the chamber resistivity, R_s is the resonator shunt impedance, Q its quality factor, and ω_r is the resonator eigenfrequency.

Next, we compare the BBB measurements with the impedance model assuming the contributions described by Eq. 3. For simplicity, we assume $l = 1$ and so we will refer to the excitation modes simply as mode m.

EXPERIMENTAL SETUP

We program the BBB to produce a "super-sequence" with the following steps:

- excite mode "m" during 250 turns at the frequency given by Eq. 2;
- leave the BBB inactive to characterize the evolution of mode "m" during the following 500 turns;
- switch the feedback "on" to damp the (possible) instability created by mode "m" for the next 500 turns.

The sequence is then repeated for mode "m+1" and a full characterization spans up to mode 448 (ALBA harmonic

ISBN: 978-3-95450-230-1 ISSN: 2673-5350 doi:10.18429/JACoW-IBIC2021-MOPP44

number), and it takes only few seconds. The number of turns at each step is optimized in a try-and-error method to obtain the growth rate fits more precisely.

Figure 1 shows the evolution of mode "m=255" for ξ=0 following the sequence described before: the beam is excited at mode "m=255" during the first 250 turns (blue points). Next, the excitation is stopped and we observe its growth rate (red points): in this case, since the evolution shows a positive slope, it indicates that this particular mode is unstable (on the contrary, a negative slope would indicate damping). The mode growth rate is obtained from the linear fit to the red points. Finally, we force the beam damping by activating the BBB feedback to stabilize the beam (green dots).

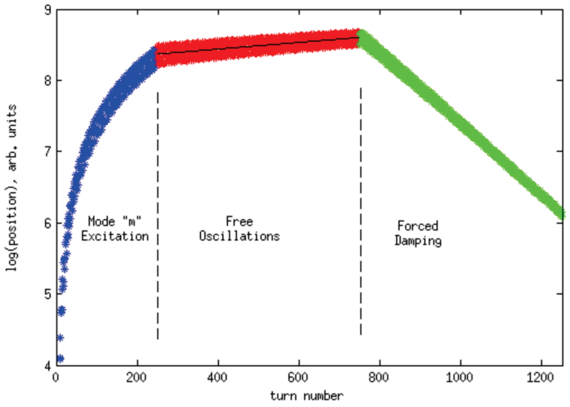

Figure 1: Amplitude evolution (log scale) during the acquisition sequence for mode m=255.

MODEL COMPARISON

In the following, we focus our analysis in the vertical plane, since this is the most critical plane in practice.

In order to evaluate the ALBA impedance model, ZAP simulations following the Zotter formalism [6] are performed. We assume a RW-based model, with Insertion Devices (IDs) closed, vertical chrom. $\xi = 0$, and a full-filling pattern (all possible bunches are filled, i.e. 448). Figure 2 (red curve) shows this simulation, with an additional resonator at $m = 255$ later identified with the vertical scraper) that has been added to match the BBB observations.

Using the BBB, a beam of 100 mA is stabilized in these conditions, and then we performed the mode scan shown in Fig. 2 (blue trace), where the contribution of the radiation damping has been removed to be compared with the ZAP simulations. While the central part is fitted reasonably well, the edges of the spectrum are not well fitted by the model. These differences are not well u nderstood. They point towards the RW-model used in this simulation, which might not be good enough due to: 1) improve the RW model, and 2) add BBR corresponding to the the geometrical impedance, as in Ref. [7] it is seen that this part contributes significantly to the impedance budget. We do not rule out even the possible noise in the BBB acquisition system.

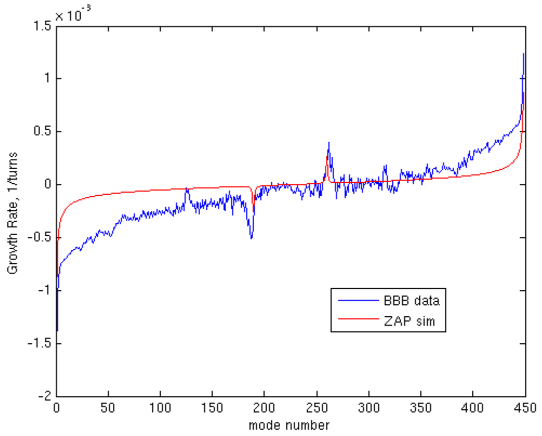

Figure 2: BBB mode spectra for different 100 mA (blue), and fit using ZAP simulations (red).

EFFECT OF VERTICAL CHROMATICITY

Figure 3 shows the growth rate for all possible modes when the vertical chromaticity is varied, all the Insertion Devices (IDs) are open, and the machine is filled with 250 mA in a 90% filling pattern.

Note that the curves in Fig. 3 for the different vertical chromaticities are almost parallel, and they are shifted down as we increase the chromaticity indicating a more stable beam due to headtail damping. In fact, by subtracting the difference in the growth rates for each mode in Fig. 3, we can evaluate the additional damping rate produced by a ξ step. If we call the growth rate at mode m as α^{ξ}_{m} the average growth rate per step of ξ can be inferred by:

$$\left\langle \frac{\Delta\alpha}{\Delta\xi} \right\rangle = \frac{1}{h}\sum_{m=1}^{h=448}\sum_{i} \frac{\alpha_m^{\xi_{i+1}}-\alpha_m^{\xi_i}}{\xi_{i+1}-\xi_i}\,, \qquad (6)$$

where i runs on the different ξ in Fig. 3. The distribution of the different components on the rhs of Eq. (6) is shown in Fig. 4: each chromaticity step produces an additional damping rate of $\langle \frac{\Delta\alpha}{\Delta\xi} \rangle = (1.5 \pm 0.3) \cdot 10^{-4}$ 1/turns.

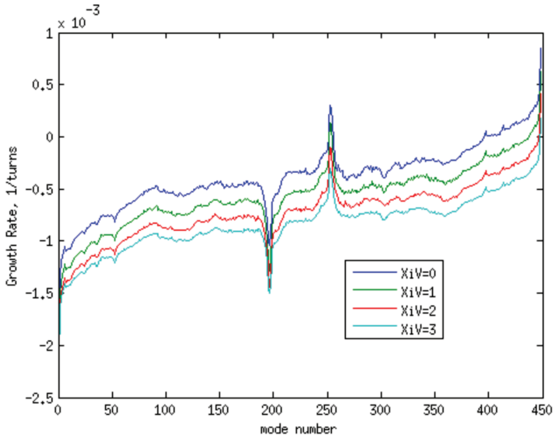

Figure 3: Mode spectra for different ver chroms and 250mA.

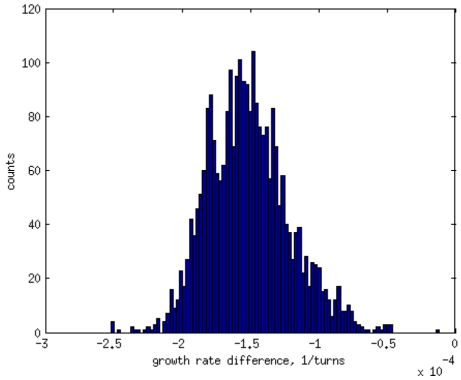

Figure 4: Histogram of $\langle\frac{\Delta\alpha}{\Delta\xi}\rangle$, growth rate difference per chromaticity step for all possible modes (see Eq. (6)).

VERTICAL SCRAPER

Figure 5 shows the scan for the different vertical scraper gaps. One can see that, as we close the scraper to narrower gaps, the peaks in Fig. 2 drift from $m_0 = 255$ for the scraper nominal gap (9.5 mm) towards larger mode numbers. Furthermore, the peak amplitude increases as we close the gap, going above zero (instability threshold) for gap ~8.0 mm. Note the clear anti-symmetry of the peaks around h/2=224, as it is characteristic of the impedance mode spectrum.

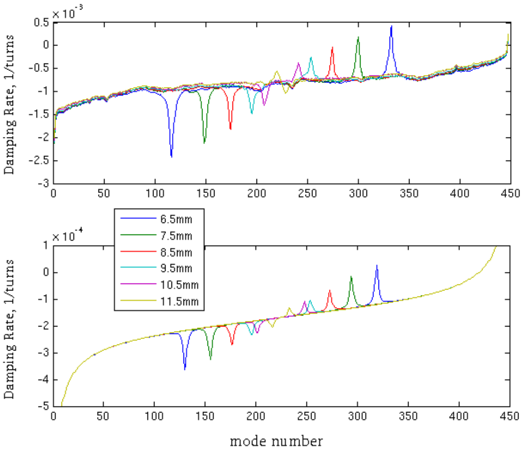

Figure 5: BBB mode spectra for different scraper gaps.

The behaviour of the scraper is reproduced with GdfidL simulations [8] using a simplified geometry of the vacuum chamber and the scraper jaws. The simulations reproduce very well the drift in the peak position vs the scraper gap (see Fig. 5). There is a difference of about 14 modes, which corresponds to a frequency of 15 MHz (recall f_{rev}=1.12 MHz at ALBA). On the other hand, the growth rate shows only a good qualitative agreement for the peak amplitude which corresponds to about a factor of 3. This discrepancy is due to the finite trailer used in the simulations, which has been shorten-up in order to speed up the CPU-time.

CHARACTERIZATION OF IVUS

ALBA disposes of two identical In-Vacuum Undulators (IVU), located in Sectors S11 (NCD beamline) and S13 (Xaloc). In order to increase the sensitivity of the method, we have performed mode spectrum measurements scanning the gap of both IVUs at the same time.

In Fig. 6, we identify the IVU modes as a triple-peak around modes m_{IVU}=100, 130 and 170. The peaks are clearly visible for the minimum gap (5.7 mm) and gradually decrease until for 9 mm the peaks almost disappear in the general RW curve. Even though the transverse impedance is anti-symmetric in the frequency domain, note that no mirror peaks appear at $(h - m_{\text{IVU}})$. This surprising effect was already observed in Diamond [4] , and further investigations are still being carried out to understand this behaviour.

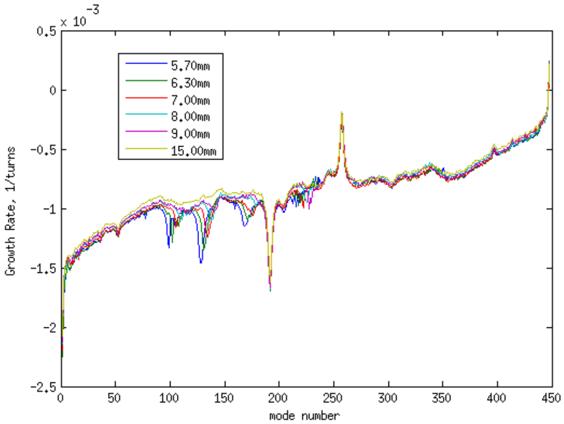

Figure 6: BBB mode spectra for different IVU gaps.

CONCLUSIONS

The transverse BBB feedback system is used to evaluate the growth rate of each of the multi-bunch modes at ALBA. This has been used to crosscheck the ALBA impedance model. It has been seen that the current RW-model shows some discrepancies with the measurements and further investigations are being carried out.

The narrow-band resonators have been identified as the vertical scraper and the in-vacuum undulators. While the peaks of the first one have been very well reproduced with ZAP simulations, the peaks of the IVUs are not well reproduced due to their non-symmetric behavior and further investigations are still being carried out.

ACKNOWLEDGEMENTS

The authors would like to acknowledge G.Rehm and M.Abbot from Diamond for their help with the BBB, and J.C. Giraldo for the engineering drawings.

REFERENCES

[1] A. Olmos, U. Iriso, J. Moldes, F. Perez, M. Abbott, G. Rehm, I. Uzun, "Integration of the Diamond Transverse Multibunch Feedback System at ALBA", in *Proc. IBIC'15*, Mel-

bourne, Australia, Sep. 2015, pp. 414–417. `doi:10.18429/JACoW-IBIC2015-TUPB046`

[2] A. Morgan, G. Rehm, and I. Uzun, “Performance and Features of the Diamond TMBF System”, in *Proc. EPAC’08*, Genoa, Italy, Jun. 2008, paper THPC126, pp. 3281–3283.

[3] G. Rehm, M.G. Abbott, A.F. Morgan, “New Features and Measurements using the Upgraded Transverse Multibunch Feedback at Diamond”, in *Proc. IBIC’14*, Monterey, CA, USA, Sep. 2014, paper WEPD24, pp. 696–699.

[4] R. Bartolini, R. Fielder, G. Rehm and V. Smaluk, “Analysis of Multi-bunch Instabilities at the Diamond Storage Ring”, in *Proc. IPAC’16*, Busan, Korea, May 2016, pp. 1685–1687. `doi:10.18429/JACoW-IPAC2016-TUPOR013`

[5] A. W. Chao, *Physics of Collective beam Instabilities in Accelerators*, New York, USA: Wiley, 1993.

[6] M. S. Zisman *et al.*, “ZAP User’s Manual”, LBL, Berkeley, USA, Rep. LBL-21270, 1986.

[7] T.Günzel and U. Iriso, “Revision of the Impedance Model for the Interpretation of the Single Bunch Measurements at ALBA”, in *Proc. IPAC’15*, Richmond, VA, USA, May 2015, pp. 330–333. `doi:10.18429/JACoW-IPAC2015-MOPJE026`

[8] `http://www.gdfidl.de`

ISBN: 978-3-95450-230-1 ISSN: 2673-5350 doi:10.18429/JACoW-IBIC2021-TUOA01

SINGLE-CRYSTAL DIAMOND PIXELATED RADIATION DETECTOR WITH BURIED GRAPHITIC ELECTRODES

C. Bloomer*[1], L. Bobb, Diamond Light Source Ltd, Didcot, UK
M. E. Newton, University of Warwick, Coventry, UK
[1]also at University of Warwick, Coventry, UK

Abstract

A new type of transmissive pixel detector has been developed for synchrotron radiation diagnostics at Diamond Light Source. A thin single-crystal CVD diamond plate is used as the detector material, and a pulsed-laser technique has been used to write conductive graphitic electrodes inside the diamond plate. Instead of using traditional electrodes formed from a layer of surface metallisation, the graphitic electrodes are buried under the surface of the diamond and result in an all-carbon imaging detector. Within the instrument's transmissive aperture there are no surface structures that could be damaged by exposure to radiation beams, and no surface metallization that could introduce unwanted absorption edges. The instrument has successfully been used to image the X-ray beam profile and measure the beam position to sub-micron accuracy at 100 FPS at Diamond Light Source. A novel modulation lock-in technique is used to read out all pixels simultaneously. Presented in this work are measurements of the detector's beam position resolution and intensity resolution. Initial measurements of the instrument's spread-function are also presented. Numerical simulations are used to identify potential improvements to the electrode geometry to improve the spatial resolution of similar future detectors. The instrument has applications in both synchrotron radiation instrumentation, where real-time monitoring of the beam profile is useful for beam diagnostics and fault-finding, and particle tracking at colliders, where the electrode geometries that buried graphitic tracks can provide increased the charge collection efficiency of the detector.

INTRODUCTION

Synchrotron light sources are particle accelerators which are used to generate highly intense beams of UV and X-ray light. At modern synchrotrons monochromatic photon beams of up to 1×10^{14} photons/s and of energies from a few 10 eV up to 100 keV are used to examine a range of biological, chemical, and physical samples. The light produced can be focused down to sub-micron spot sizes [1]. Experimental timescales range from picoseconds, up to years [2, 3].

Common to all the experiments conducted at synchrotrons globally is the requirement to monitor and maintain the stability of the photon beam incident upon the sample: in spatial position, in beam profile, in intensity, in photon energy; and to do so over the range of timescales utilised by the synchrotron users. The typically required photon beam stability at a 3rd generation synchrotron is $< 10\,\%$ of the beam size, $< 1\,\%$ of beam intensity, over kHz timescales [4, 5]. New 4th generation synchrotrons have even stricter stability requirements [6]. To provide this level of beam stability, the measurements of the incident photon beam must correspondingly be at least as accurate as these stringent requirements. It is also required that the instruments used to make beam stability measurements are minimally invasive, and mostly transparent to the incident light: a diagnostic instrument that makes a perfect measurement of the beam but does not transmit any of the incident photons through to the sample would not be acceptable! If measurements of the photon beam can be obtained then real-time optics adjustments can be made to keep the beam position stabilised at the sample, and to keep the X-ray intensity maximised.

Non-destructive X-ray beam profile monitoring is essential as synchtrotron and XFEL beamlines increasingly aim to deliver sub-micron beam sizes at their samples points. Significant effort is put into ensuring that precision optics can meet these requirements, from ex-situ measurement and optimisation [7], to in-situ beam profile monitoring and adaptive improvement [8]. It is increasingly common to consider real-time feedback and adaptive optics to ensure that the mirror performance is maintained [9]. The ability to reliably and non-destructively monitor the beam profile is an essential step in ensuring the reliability of the beamline optics.

DIAMOND DETECTORS

To fulfil these requirements for non-destructive monitoring, single crystal chemical vapour deposition (scCVD) diamond makes for an excellent non-invasive detector material: a 50 µm plate is mostly transparent to > 4 keV photons, radiation tolerant, and exhibits good detector properties. The

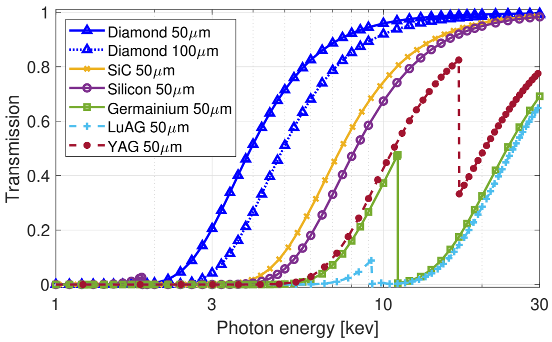

Figure 1: The X-ray transmissivity of scCVD diamond alongside other common solid-state detector materials for ionizing radiation, and common fluorescent materials.

---

* chris.bloomer@diamond.ac.uk

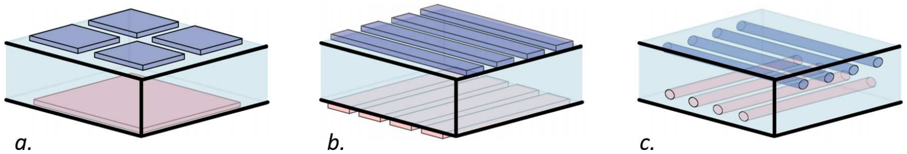

Figure 2: A sketch (not to scale) illustrating different detector electrode designs that are currently in use (*a*, *b*), and the electrode design presented in this paper (*c*). This figure is reproduced from [17].

X-ray transmission of scCVD diamond is presented alongside that of other common detector materials in Fig. 1, using data compiled from [10]. Diamond has superior transmissivity, and no absorption edges around common synchrotron experimental photon energies, 4 - 20 keV. Also included for comparison are the transmission of common fluorescent screen materials that a beamline may use to monitor the beam profile.

The ionizing radiation that is absorbed in the detector material generates electron-hole pairs. Under the influence of an electrical bias the electrons and holes migrate towards the external electrodes. An arrangement of four 'quadrant' electrodes can provide a position measurement in two dimensions, as depicted in Fig. 2 *a*. This design originated in the late 1990s using polycrystalline diamond [11], and was then improved upon through the use of single-crystal diamond [12]. Single-crystal diamond detectors are now available 'off the shelf' from multiple commercial suppliers. Such commercially available devices have the ability to provide 2-dimensional beam position measurements with precision at nanometer scales [13, 14]. However, this common design of instrument makes a number of trade-offs to obtain such precise 2-dimensional beam position measurements.

The first trade-off is the small position-sensitive region of the detector. Only when the X-ray beam footprint straddles two quadrants is a position measurement possible. When the incident X-ray beam falls wholly within one quadrant the instrument cannot provide an accurate position measurement. It can only be inferred that the beam is located *somewhere* within that one quadrant. The position of a 100 μm wide X-ray beam can only be accurately measured if it passes through the instrument within ± 100 μm of the quadrant gap.

The second trade-off is that since the position measurement for the smallest beamsizes can be limited by the gap between the quadrants, there is a strong motivation to make this isolating gap between the surface electrodes as small as possible, typically 2 - 5 μm [14]. This leads to delicate instruments with very small isolating gaps where surface contaminants, debris, or damage can easily 'short' two neighbouring electrodes and impair position measurement.

The third trade-off is the inability to obtain X-ray beam profile information. With only four pixels, or 'quadrants', the beam measurement is limited to a simple X- and Y-position. To tackle this third problem in particular, an approach using 'strip-electrodes' applied to the surface of the diamond has been developed, enabling beam profile information to be measured [15, 16]. A sketch illustrating this electrode configuration is depicted in Fig. 2 *b*. However, each additional electrode introduces another potential source of detector failure should an electrical short occur.

A new design of transparent X-ray diagnostic is presented in these proceedings. This detector aims to address the three drawbacks listed above. This detector utilises buried graphitic electrodes instead of surface strip-electrodes, as is illustrated in Fig. 2 *c*. The instrument has been successfully tested at Diamond Light Source, and is cable of transmissively measuring the beam profile in real time [17].

LASER-WRITING OF DIAMOND

The detector presented here makes use of recent developments in adaptive optics to laser-write graphitic tracks buried within bulk diamond. These are fabricated using an ultrashort pulse laser technique. At the laser focal point there is sufficient energy deposited into the diamond that a local phase transition can take place: electrically non-conductive diamond is converted into conductive graphite. In this section, a short history of the use of graphitic electrodes will be presented.

The technique was first demonstrated in the late 1990s as a method of electrically contacting doped layers within CVD grown diamond, using graphite columns that extended to the surface of the diamond [18]. Later work produced '3D diamond detectors' for ionizing radiation, with columnar graphitic electrodes embedded within the bulk diamond [19]. A square array of electrodes was written through the diamond plate at 200 μm intervals. Half of the columns were connected to the 'bias' supply and half of the columns were connected to the 'measurement' circuit. This 'interdigitated' electrode approach had a number of advantages over traditional top-and-bottom surface electrodes for radiation detectors: firstly it was shown to increase the radiation resistance of detectors to high energy particles; secondly the array of graphitic 'micro-channels' reduced the mean distance between electrodes, enabling greater charge collection efficiency. A useful summary of the first results obtained for particle tracking detectors is provided by [20].

The second half of the 2010s has seen further research into the use of scCVD diamond particle detectors with graphitic columns as electrodes: measurements of different charged particle beams [21, 22]; studying the effects of different hexagonal vs cubic column arrays [23]; modelling such detectors [24]; investigating the graphetization processes [25]; and investigating the effect that columnar electrodes have on the diamond stress and charge transport properties [26]. All of these papers are related to detector work for LHC and similar machines for particle tracking, where radiation tolerant diamond detectors are essential given the extremely high dose rates experienced.

As well as simple columnar electrodes, improvements in adaptive optics have enabled the writing of graphitic wires following arbitrary 3D paths within a diamond plate [27], or long electrodes running parallel to the surface of the plate [28]. The listed papers are not an exhaustive list of the research in this field, but are intended to give the reader a flavour of the work being carried out.

Buried graphitic electrodes provide protection from mechanical and chemical damage, and from conductive surface contaminants. Graphite is more transmissive to X-rays than an equivalent thickness of aluminium, titanium, or other traditional electrode material. Additionally, there is no danger of the electrode material introducing new absorption edges that may affect synchrotron experiments, as the K-edge in both graphite and diamond (carbon sp^2 and sp^3 respectively) differ by just a few eV [29].

X-RAY IMAGING MONITOR DESIGN

The detector design utilised in this work was first presented in [30]. The diamond plate was provided by *Element Six* for the purposes of this research and is described by the supplier as ‘Single Crystal Optical Plus’ grade material.

Figure 3 presents the layout of the detector. Two sets of 11 parallel ‘bias’ electrodes run under the surface of the diamond plate, orthogonal to two sets of 11 parallel ‘measurement’ electrodes. To identify the wires, the shorter of the sets of wires are referred as the ‘X’ electrodes, and the longer set of wires will be referred to as the ‘Y’ electrodes. This naming convention arose because in the experimental testing the ‘X’ wires were oriented horizontally and the ‘Y’ wires were oriented vertically.

The ‘X’ electrodes are located at a depth of 200 µm within the material, and the ‘Y’ electrodes are located at a depth of 100 µm, providing an electrode separation of 100 µm within the diamond. There is an in-plane spacing of 50 µm between each individual electrode within each array. Each electrode comprises of three parallel tracks laterally spaced by 2 µm.

The electrodes are connected to the surface by vertical graphitic columns referred to as ‘vias’. These are located at the edges of the diamond plate for the purpose of connecting the buried electrodes to a surface metallisation pad, well away from the centre of the detector where the beam would pass through.

The electrodes each comprise of three parallel tracks to improve conductivity, as can be observed in Fig. 4 A. The resistance of each of the buried graphitic electrodes was measured to be 31±6 kΩ / mm.

The repetition of two arrays of 11 ‘X’ electrodes and two arrays of ‘Y’ electrodes is to provide multiple potential 11 x 11-pixel imaging regions, each with a pixel pitch of 50 x 50 µm. This redundancy was built into the detector in case of a graphitic track or a surface contact being incomplete or non-conductive. Arrays of 11 x 11 pixels were chosen as this matched the number of signal acquisition hardware channels that were available to the authors at the time of this detector’s design.

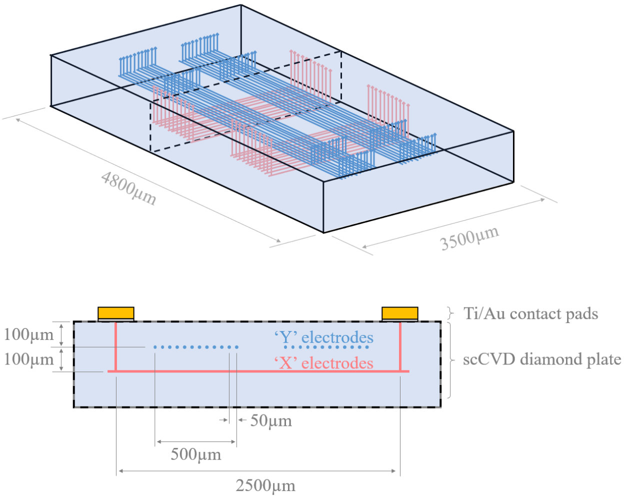

Figure 3: Top: A sketch (not to scale) of the wire layout within the diamond plate. A black dotted line indicates the region of the cross section presented. Bottom: The cross-section through the diamond plate. The location of the surface metallisation at the edge of the detector is shown. This figure is reproduced from [30].

The overall 0.6 mm thickness of the diamond plate was dictated only by the availability of material. The relatively large 100 µm separation between the ‘X’ and ‘Y’ electrodes within this prototype detector was chosen to increase X-ray absorption and charge carrier generation. The 100 µm separation between the surface of the diamond plate and the upper electrode array was arbitrarily chosen, and for a future detector could be ~ 5 µm.

Ideally, a transmissive detector would remain as thin as practical so as to minimise X-ray absorption. These relatively large inter-electrode spacing and large electrode-to-surface spacing was chosen only so as to ensure comfortable margin for any alignment errors that may have occurred during fabrication of this first prototype.

The design ensures that there is no surface metallisation, or indeed any surface features, present within the active region of the detector. The upward vias used to extract the signal are located at the edges of the diamond plate, at least 500 µm away from the centre of the interaction points.

EXPERIMENTAL RESULTS

To test the response of the detector to incident X-rays, it was installed in air at the sample point of the I18 beamline at Diamond Light Source [31]. The beamline was configured to deliver a collimated flux of up to 3×10^{11} ph / s at a tunable photon energy. The beam size at the detector could be altered from 20 µm up to 250 µm FWHM.

Also mounted along the beam path was an an ion chamber (beam intensity monitor), a traditional four-quadrant X-ray

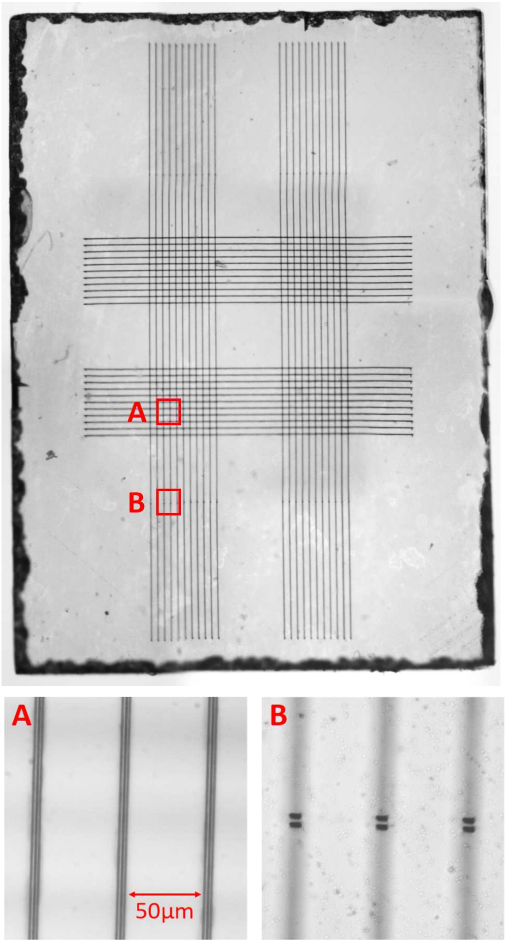

Figure 4: Top: A microscope image of the diamond plate showing the fabricated graphitic wires. Bottom left: A magnified view of the area shown in the red square marked 'A'. The upper electrodes can be seen in focus; the lower electrodes are out of the microscope focus. Bottom right: A magnified view of the area shown in the red square marked 'B'. The upwards 'vias' are visible in focus. This figure is reproduced from [17].

beam position monitor (XBPM)[1], and a CMOS camera system monitoring a cerium-doped lutetium-aluminium-garnet, LuAG:Ce, fluorescent screen. These were for the purposes of monitoring the incident beam with commonly used beamline instrumentation, so that the performance of this graphitic wire detector could be quantitatively compared. This apparatus was mounted together onto a support plate, and the whole assembly was bolted onto the a motorised X, Y stepper motor stage so that the detectors could be aligned to the beam path. A sketch showing the experimental set up at the I18 sample-point is presented in Fig. 5.

1-Dimensional Profile Measurements

A 1-dimensional beam profile can be obtained by applying a constant bias to each of the 11 measurement channels. With the beam centred upon one of the four imaging regions, a static bias of + 10 V was applied to all of the corresponding 'X' electrodes. Each 'Y' electrode was connected to a low-impedance electrometer which was used to record the resulting signal currents. The magnitude of the resulting signal currents is directly proportional to the absorbed photon power, providing a 1-dimensional profile of the X-ray beam. A comparison of the vertical X-ray beam profile measured by the detector and that obtained by the fluorescent screen and CMOS camera is presented in Fig. 6. This figure shows two examples of different beamsizes: 180 µm FWHM beam size (top), and 22 µm (bottom). The measurements of the X-ray beam profile using the graphitic wire detector show good agreement with that obtained from the camera. However, it is noted that the spatial resolution of the graphitic wire detector (the 'spread function') is limited to the 50 µm pixel pitch, and it cannot resolve the narrow, 22 µm beam profile.

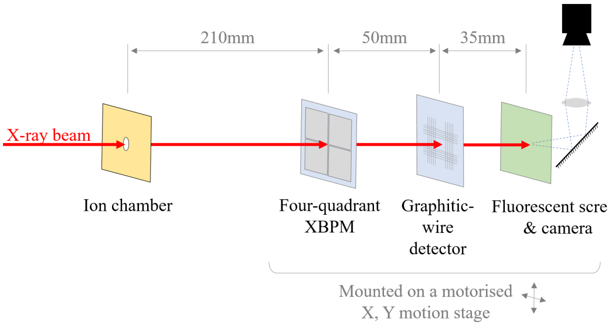

Figure 5: A sketch showing the layout of the detectors along the X-ray beam path.

Imaging Results

Readout of the individual pixels was achieved using a novel lock-in modulation technique. Rather than apply a static 'DC' bias to an individual electrode or to a set of electrodes, a modulated 'AC' bias was used. A different frequency was applied to each of the 11 'X' electrodes (1.1 kHz, 1.2 kHz, 1.3 kHz, ..., etc), with a modulation amplitude of 0.5 V around a DC level of 0 V.

The resulting signal currents were acquired at 20 kHz from the perpendicular electrodes with low impedance electrometers. A Fourier transform of the signal currents from each measurement electrode is carried out. The Fourier amplitude of the measured signal at a given frequency is proportional to the flux passing through the detector at the intersection between the measurement electrode and the bias electrode modulated by that frequency. An illustration of this approach is presented in Fig. 7.

Shown in Fig. 8 are an example of the 20 kHz measured signal currents obtained, shown in the time domain (top), and in the frequency domain (bottom). This acquisition frequency and modulation frequencies have been specifically chosen such that when acquiring a 10 ms acquisition (i.e. 100 FPS capture rate) each bin of the Fourier transform

---

[1] A *Sydor Technologies* diamond beam position monitor (DBPM).

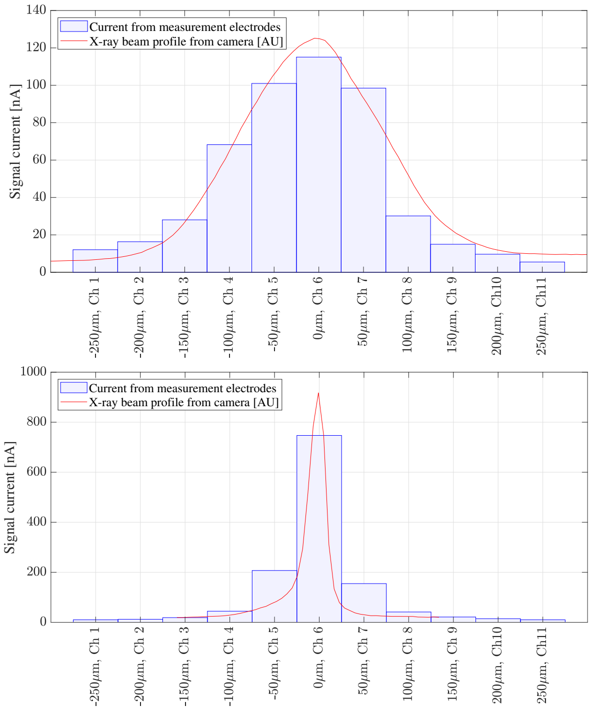

Figure 6: Vertical 1-dimensional beam profile measurements obtained using a static bias, compared to fluorescent screen camera image profiles. Top: 180 µm FWHM beam size. Bottom: 22 µm FWHM beam size.

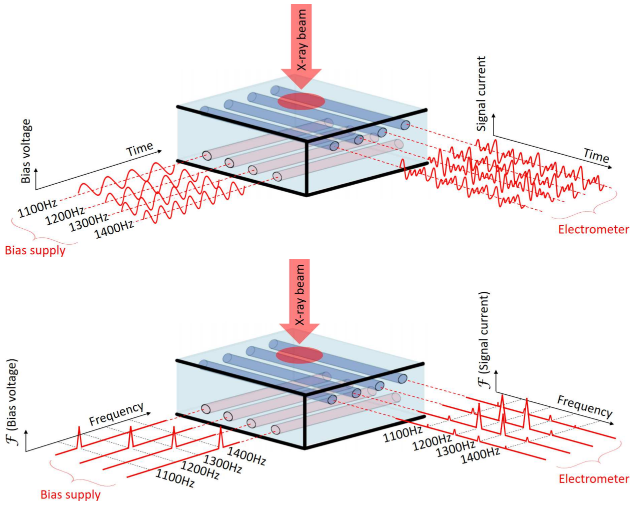

Figure 7: The readout scheme presented in this work utilises a different modulation frequency applied to each bias electrode. The individual modulation frequencies are detectable at the measurement electrodes. Top: A time-domain view of the modulation scheme. Bottom: A frequency-domain picture, showing how the individual modulation frequencies measured by the electrometer build up a picture of the beam profile upon the detector. This figure is reproduced from [17].

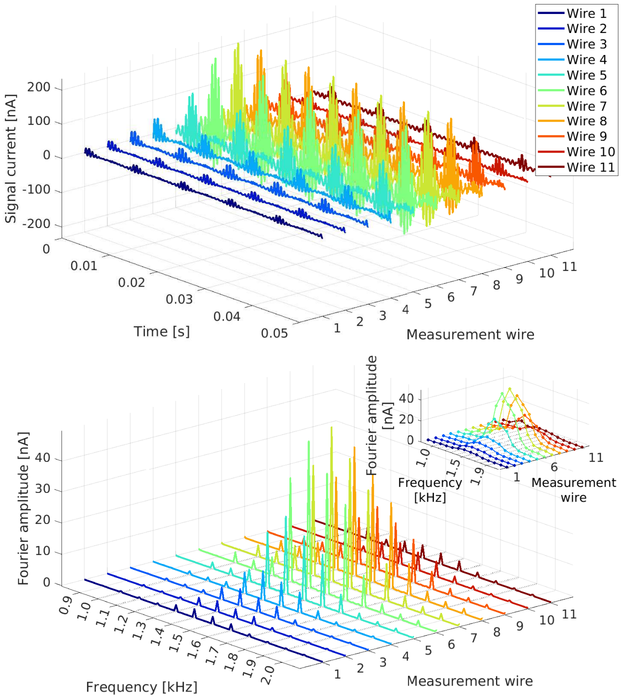

Figure 8: Top: The 20 kHz signals acquired from 11 measurement electrodes whilst the X-ray beam is illuminating the detector. Bottom: The Fourier transform of a 1 second long acquisition at 20 kHz signals. Inset: The Fourier transform of a 10 ms acquisition. These currents correspond to the leftmost image from Fig. 9.

corresponds to one modulation frequency, and thus one column of pixels on the detector.

Figure 9 presents the imaging results obtained during a scan of the beamline's mirror curvature, bringing the beam into focus at the location of the sample-point over the course of the sequence of images. The X-ray beam is focused from 180 µm down to 40 µm FWHM (from left to right). Each image shows a region 500 x 500 µm.

To determine the position-sensitivity of the detector, the beam profile was recorded as the instrument was stepped vertically through the X-ray beam. A 180 µm FWHM X-ray beam with an approximately Gaussian profile was used for these tests. At each position of the scan images were acquired at 100 FPS. A 2-dimensional Gaussian fitting routine is applied to the image to obtain the centroid position. Figure 10 presents the results of these scans. The error bars are the standard deviation in fitted beam position from the sequential detector images acquired at each scan position. They represent the uncertainty on the acquired beam position for the 180 µm FWHM X-ray beam, and provide an upper-bound on the beam position resolution. The mean standard deviation in position measurement was 600 nm, or 0.3 % of the vertical beam size, FWHM.

To determine the signal linearity that can be obtained while using this lock-in modulation acquisition method, a scan of beam intensity was carried out using a series of adjustable attenuation filters. These can be inserted into the

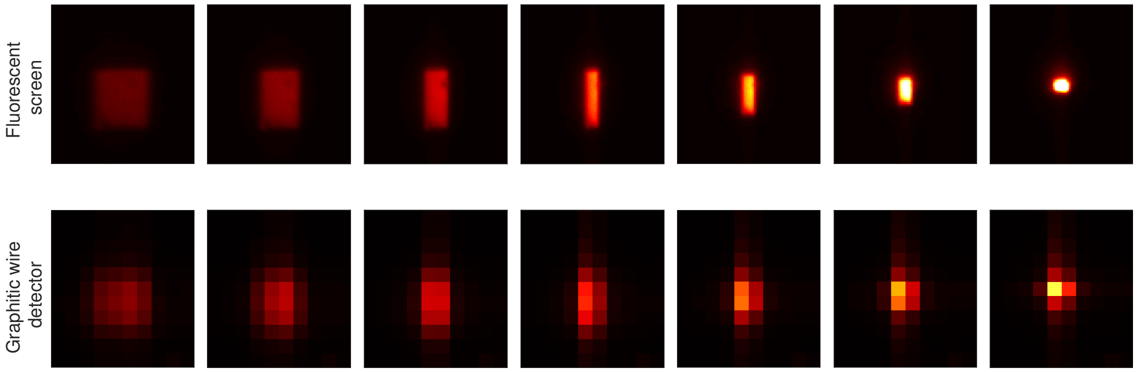

Figure 9: Images obtained during beam focusing from the fluorescent screen (top) and from the graphitic wire detector (bottom). In both cases the image size is 500 x 500 µm.

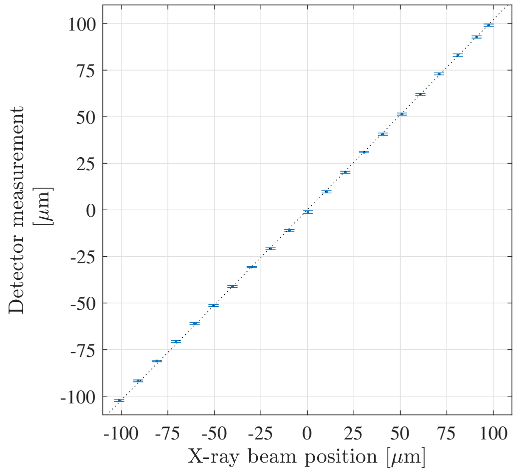

Figure 10: The detector is scanned across the incident X-ray beam in steps of 10 µm. At each point in the scan images are acquired at 100 FPS.

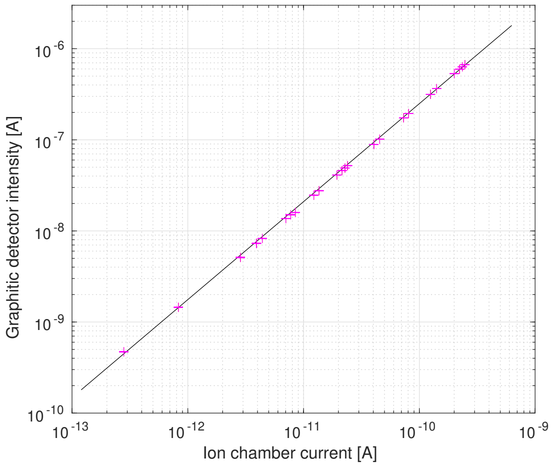

Figure 11: The signal linearity from the graphitic wire XBPM is plotted against that measured using the beamline's intensity monitor diode.

beam path to reduce the sample-point flux. The beamline's ion-chamber was used as the flux reference measurement. The output of the ion chamber is directly proportional to the absorbed power, which for a fixed photon energy is directly proportional to the incident flux.

The beam intensity measured by the graphitic wire detector was obtained by taking the sum of all pixels in the acquired image, i.e. the sum of the Fourier transform amplitudes. Figure 11 presents this intensity measurement as the incident flux is varied over 3-orders of magnitude. These results demonstrate that the signal linearity of the graphitic wire XBPM is at least as good as the beamline's ion chamber over 3-orders of magnitude of flux.

CHARGE CARRIER MODELLING

To help optimise the detector performance and evaluate different electrode geometries for future detectors, a simple model of carrier motion through the diamond plate has been produced. This section describes the carrier dynamics used in the model. This work is expanding upon similar modelling of silicon detectors carried out in [32], where Chapter 7 in particular contains useful information and equations to describe the motion of carriers through a crystal.

At room temperature, liberated charge carriers in diamond will diffuse randomly in space because of thermal energy. This is analogous to Brownian motion, and is modelled by the Wiener process. In this model individual atomistic effects are neglected, and only 'microscopic' net motions are be considered. The overall probability of finding a particle at location x after time t, given starting conditions of $x_0 = 0$ and $t_0 = 0$, is a Gaussian distribution given by Eq. (1):

$$p(t,x) = \frac{1}{\sqrt{4\pi D(t-t_0)}} \exp\left(-\frac{(x-x_0)^2}{4D(t-t_0)}\right) \quad (1)$$

The constant D is the Einstein diffusion coefficient:

$$D = \frac{\mu_q k_B T}{q} \quad (2)$$

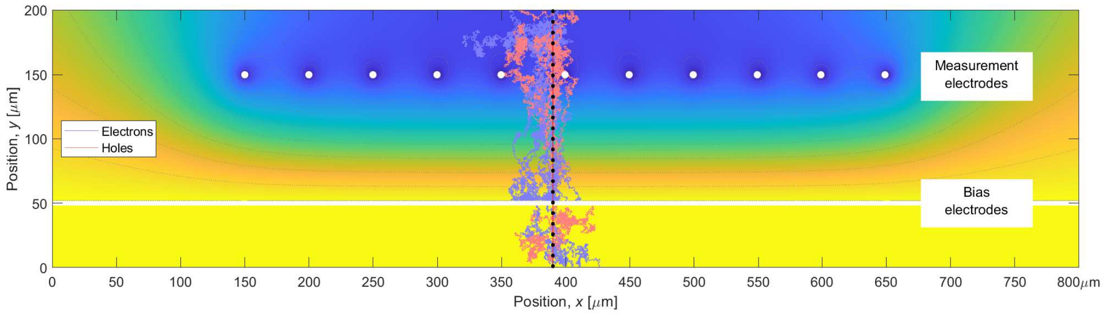

Figure 12: Simulated trajectories of 25 generated electron-hole pairs through a 800 x 200μm cross-section of detector. The electron-hole origins are marked by black dots along the path of the incident beam of ionizing radiation.

where μ_q is the mobility of the charge carrier; k_B is the Boltzmann constant; T is the absolute temperature; and q is the electrical charge of the particle.

In addition to the random diffusion of carriers they may also undergo a net drift under the influence of an external electric field. Their drift velocity is dependent on the electric field applied across the material. At high fields the velocity becomes limited due to collisions with atoms in the crystal lattice and energy loss through the generation of phonons. The resulting net carrier velocities, $\vec{v_q}$, are given by Eq. (3):

$$\vec{v_q} = \frac{\mu_q \vec{E}}{1 + \frac{\mu_q \vec{E}}{v_{q,s}}} \tag{3}$$

where $\vec{E}$ is the electric field strength; and $v_{q,s}$ is the saturation velocity of the charge carriers within the diamond.

The mean drift distances travelled by a carrier, $\vec{x_q}$, in a given time interval, t, is simply the carrier velocity multiplied by the time interval:

$$\vec{x_q}(t) = \vec{v_q}\, t \tag{4}$$

Using published values for the carrier mobilities, lifetimes, and saturation velocities typically found similar synthetic diamond plates [33], Eqs. (1) and (4) can be used to model the position of carriers after discrete time steps. The simulation uses time steps of 5 ps. This is a sufficiently large time step that quantum and atomistic effects can be neglected, but small enough to accurately reflect the motion of charge carriers through detector regions on micrometer scales. The carrier trajectories are modelled until either they reach an electrode or the carrier lifetime is reached. An example of this modelling is presented in Fig. 12.

Future work will concentrate on confirming the validity of this model by comparing it to experimental data. Comparison of the modelled charge collection efficiency and experimental data is useful in determining the quality of the diamond plates used for detectors, as dislocations and impurities affect the carrier dynamics [34, 35]. Accurate modelling of the lateral drift of charge carriers will allow limitations on the ultimate spatial resolution of the detector to be established.

CONCLUSIONS

The pixel detector presented in this work is demonstrated to be capable of transmissively imaging the synchrotron X-ray beam profile. A modulation lock-in readout technique has been developed which enables all pixels to be read simultaneously. Images of the beam profile can be obtained at up to 100 FPS.

Beam motions much smaller than the ‘pixel size’ can be easily resolved by applying 2D Gaussian fitting to determine the centroid, and the resolution of the position measurement is 600 nm for 10 ms acquisitions and 180 μm beam size FWHM. Intensity linearity is equivalent to a standard ion-chamber over 3-orders of magnitude of flux.

Ongoing modelling is being used to help optimise future detector design and electrode geometry, and probe possible constraints on spatial resolution of the detector due to lateral charge diffusion.

The single crystal diamond detector includes no metallisation in the beam path and introduces fewer absorption edges that may interfere with beamline experiments. Keeping the transmissive region of the sensor free from metallisation also reduces the danger of electrodes being damaged by high incident flux. The detector may be permanently installed in the X-ray beam path, offering significant advantages over fluorescent screens, or knife-edge scans which intercept a significant portion of the synchrotron flux or block it entirely.

ACKNOWLEDGEMENTS

The authors wish to acknowledge the support of many individuals and groups that aided in this research. The scCVD diamond plate used to create this detector was provided by Element Six. We wish to acknowledge the contributions of Patrick Salter for the graphitic electrode fabrication, at the University of Oxford. Ben Green carried out the metallisation, Frank Courtney carried out the wire bonding, and Yorck Ramachers provided useful input on charge carrier modelling, all at the University of Warwick. The X-ray measurements were conducted on the I18 beamline at Diamond Light Source, and we thank the I18 staff for their assistance. Finally, we wish to acknowledge the support of Guenther Rehm for his contributions to the project.

REFERENCES

[1] G. Ice *et al.*, "The Race to X-ray Microbeam and Nanobeam Science", *Science*, vol. 334, pp. 1234–1239, 2011. `doi:10.1126/science.1202366`

[2] J. Mosselmans *et al.*, "A time resolved microfocus XEOL facility at the Diamond Light Source", *Journal of Physics: Conference Series*, vol. 425, p. 182009, 2013. `doi:10.1088/1742-6596/425/18/182009`

[3] C. A. Murray *et al.*, "New Synchrotron Powder Diffraction Facility for Long Duration Experiments", *Applied Crystallography*, vol. 50, pp. 172–183, 2017. `doi:10.1107/S1600576716019750`

[4] B. Hettel, "Beam stability at light sources", *Review of Scientific Instruments*, vol. 73, pp. 1396–1401, 2002. `doi:10.1063/1.1435812`

[5] G. Decker, "Beam Stability in Synchrotron Light Sources", in *Proc. DIPAC'05*, Lyon, France, pp. 233–237, 2005.

[6] C. Steier, "Beam Stability Requirements for 4th Generation Synchrotron Light Sources Based on MBA Lattices", 1st BES Light Sources Beam Stability Workshop, 2018.

[7] S. Alcock *et al.*, "High-speed adaptive optics using bimorph deformable X-ray mirrors", *Review of Scientific Instruments*, vol. 90, p. 021712, 2019. `doi:10.1063/1.5060737`

[8] H. Mimura *et al.*, "Breaking the 10 nm barrier in hard-X-ray focusing", *Nature Physics*, vol. 6, pp. 122–125, 2010. `doi:10.1038/NPHYS1457`

[9] E. Abruna *et al.*, "Real-time feedback for X-ray adaptive optics with an interferometric absolute distance sensor array", *Proceedings of SPIE: Adaptive X-Ray Optics V*, vol. 10761, p. 107610H, 2018. `doi:10.1117/12.2323698`

[10] B. L. Henke *et al.*, "X-ray interactions: photoabsorption, scattering, transmission, and reflection at E=50-30000 eV, Z=1-92", *Atomic Data and Nuclear Data Tables*, vol. 54, pp. 181–342, 1993. `doi:10.1006/adnd.1993.1013`

[11] P. Bergonzo *et al.*, "Diamond-based semi-transparent beam-position monitor for synchrotron radiation applications", *Journal of Synchrotron Radiation*, vol. 6, pp. 1–5, 1999. `doi:10.1107/s090904959801509x`

[12] J. Morse *et al.*, "Single crystal CVD diamond as an X-ray beam monitor", *Diamond and Related Materials*, vol. 16, pp. 1049–1052, 2007. `doi:10.1016/j.diamond.2006.11.081`

[13] C. Bloomer *et al.*, "The use of single-crystal CVD diamond X-ray beam diagnostics for synchrotron beamline commissioning and operation at Diamond Light Source Ltd", *IEEE Nuclear Science Symposium Conference Record*, 2016. `doi:10.1109/NSSMIC.2016.8069893`

[14] E. Griesmayer *et al.*, "Applications of single-crystal CVD diamond XBPM detectors with nanometre X-ray beams", *AIP Conference Proceedings*, vol. 2054, p. 060052, 2019. `doi:10.1063/1.5084683`

[15] D. Shu *et al.*, "CVD-Diamond-Based Position Sensitive Photoconductive Detector for High-Flux X-Rays and Gamma Rays", in *Proc. PAC'99*, New York, USA, pp. 2090–2092, 1999. `doi:10.1109/PAC.1999.794382`

[16] T. Zhou *et al.*, "Pixelated transmission-mode diamond X-ray detector", *Journal of Synchrotron Radiation*, vol. 22, pp. 1396–1402, 2015. `doi:10.1107/S1600577515014824`

[17] C. Bloomer *et al.*, "A single-crystal diamond X-ray pixel detector with embedded graphitic electrodes", *Journal of Synchrotron Radiation*, vol. 27, pp. 599–607, 2016. `doi:10.1107/s160057752000140x`

[18] R. Walker *et al.*, "Formation of buried p-type conducting layers in diamond", *Applied Physics Letters*, vol. 71, pp. 1492–1494, 1997. `doi:10.1063/1.119946`

[19] A. Oh *et al.*, "A novel detector with graphitic electrodes in CVD diamond", *Diamond and Related Materials*, vol. 38, pp. 9–13, 2013. `doi:10.1016/j.diamond.2013.06.003`

[20] F. Bachmair *et al.*, "A 3D diamond detector for particle tracking", *Nuclear Instruments and Methods in Physics Research, Section A*, vol. 786, pp. 97–104, 2015. `doi:10.1016/j.nima.2015.03.033`

[21] G. Forcolin *et al.*, "Study of a 3D diamond detector with photon and proton micro-beams", *Diamond and Related Materials*, vol. 65, pp. 75–82, 2016. `doi:10.1016/j.diamond.2016.02.005`

[22] M. Girolami *et al.*, "Investigation with β-particles and protons of buried graphite pillars in single-crystal CVD diamond", *Diamond and Related Materials*, vol. 84, pp. 1–10, 2018. `doi:10.1016/j.diamond.2018.02.014`

[23] M. J. Booth *et al.*, "Study of cubic and hexagonal cell geometries of a 3D diamond detector with a proton micro-beam", *Diamond and Related Materials*, vol. 77, pp. 137–145, 2017. `doi:10.1016/j.diamond.2017.06.014`

[24] G. Forcolin *et al.*, "Simulation of 3D diamond detectors", *Nuclear Instruments and Methods in Physics Research, Section A*, vol. 845, pp. 72–75, 2017. `doi:10.1016/j.nima.2016.06.099`

[25] T. Lühmann *et al.*, "Investigation of the graphitization process of ion-beam irradiated diamond using ellipsometry, Raman spectroscopy and electrical transport measurements", *Carbon*, vol. 121, pp. 512–517, 2017. `doi:10.1016/j.carbon.2017.05.093`

[26] S. Salvatori *et al.*, "Diamond Detector with Laser-Formed Buried Graphitic Electrodes: Micron-Scale Mapping of Stress and Charge Collection Efficiency", *IEEE Sensors Journal*, vol. 19, pp. 11908–11917, 2019. `doi:10.1109/JSEN.2019.2939618`

[27] B. Sun *et al.*, "High conductivity micro-wires in diamond following arbitrary paths", *Applied Physics Letters*, vol. 105, p. 231105, 2014. `doi:10.1063/1.4902998`

[28] A. Khomich *et al.*, "Very long laser-induced graphitic pillars buried in single-crystal CVD-diamond for 3D detectors realization", *Diamond and Related Materials*, vol. 90, pp. 84–92, 2018. `doi:10.1016/j.diamond.2018.10.006`

[29] A. Hamon *et al.*, "ELNES study of carbon K-edge spectra of plasma deposited carbon films", *Journal of Materials Chemistry*, vol. 14, pp. 2030–2035, 2004. `doi:10.1039/b406468m`

[30] C. Bloomer *et al.*, "A Single Crystal CVD Diamond X-ray Beam Diagnostic with Embedded Graphitic Wire Electrodes", *Proceedings of the 13th International Conference on Synchrotron Radiation Instrumentation*, vol. 2054 p. 060058, 2018. `doi:10.1063/1.5084689`

[31] J. Mosselmans *et al.*, “I18 - the microfocus spectroscopy beamline at the Diamond Light Source”, *Journal of Synchrotron Radiation*, vol. 16, pp. 818–824, 2009. doi:10.1107/S0909049509032282

[32] J. Becker, “Signal development in silicon sensors used for radiation detection”, PhD Dissertation zur Erlangung des Doktorgrades des Department Physik der Universitat Hamburg, Germany, 2010.

[33] M. Pomorski *et al.*, “Charge transport properties of single crystal CVD-diamond particle detectors”, *Diamond and Related Materials*, vol. 16, pp. 1066–1069, 2007. doi:10.1016/j.diamond.2006.11.016

[34] A. Lohstroh *et al.*, “Effect of dislocations on charge carrier mobility–lifetime product in synthetic single crystal diamond”, *Applied Physics Letters*, vol. 90, p. 102111, 2007. doi:10.1063/1.2711754

[35] A. Tarun *et al.*, “Impact of impurities and crystal defects on the performance of CVD diamond detectors”, *Diamond and Related Materials*, vol. 63, pp. 169–174, 2016. doi:10.1016/j.diamond.2015.08.018

ISBN: 978-3-95450-230-1 ISSN: 2673-5350 doi:10.18429/JACoW-IBIC2021-TUOA03

TRANSVERSE BEAM EMITTANCE MEASUREMENT BY UNDULATOR RADIATION POWER NOISE*

I. Lobach†, The University of Chicago, Chicago, Illinois
K. J. Kim[1], ANL, Lemont, Illinois,
V. Lebedev, S. Nagaitsev[1], A. Romanov, G. Stancari, A. Valishev, Fermilab, Batavia, Illinois
A. Halavanau, Z. Huang, SLAC, Menlo Park, California
[1]also at The University of Chicago

Abstract

Generally, turn-to-turn power fluctuations of incoherent spontaneous synchrotron radiation in a storage ring depend on the 6D phase-space distribution of the electron bunch. In some cases, if only one parameter of the distribution is unknown, this parameter can be determined from the measured magnitude of these power fluctuations. In this contribution, we report the results of our experiment at the Integrable Optics Test Accelerator (IOTA) storage ring, where we carried out an absolute measurement (no free parameters or calibration) of a small vertical emittance (5–15 nm rms) of a flat beam by this new method, under conditions, when the small vertical emittance is unresolvable by a conventional synchrotron light beam size monitor. This technique may be particularly beneficial for existing state-of-the-art and next generation low-emittance high-brightness ultraviolet and x-ray synchrotron light sources.

Please see our Letter [1] for the details about our measurements of the transverse electron beam emittances using the turn-to-turn fluctuations of the undulator radiation power at the Integrable Optics Test Accelerator (IOTA) storage ring at Fermilab. The theoretical foundations of this method are described in Refs. [2, 3]. The design and the experimental program of the IOTA ring are described in Ref. [4].

REFERENCES

[1] I. Lobach *et al.*, "Transverse beam emittance measurement by undulator radiation power noise," *Phys. Rev. Lett.*, vol. 126, p. 134 802, 13 Apr. 2021. DOI: `10.1103/PhysRevLett.126.134802`. `https://link.aps.org/doi/10.1103/PhysRevLett.126.134802`

[2] I. Lobach *et al.*, "Measurements of undulator radiation power noise and comparison with ab initio calculations," *Phys. Rev. Accel. Beams*, vol. 24, p. 040 701, 4 Apr. 2021. DOI: `10.1103/PhysRevAccelBeams.24.040701`. `https://link.aps.org/doi/10.1103/PhysRevAccelBeams.24.040701`

[3] I. Lobach *et al.*, "Statistical properties of spontaneous synchrotron radiation with arbitrary degree of coherence," *Phys. Rev. Accel. Beams*, vol. 23, p. 090 703, 9 Sep. 2020. DOI: `10.1103/PhysRevAccelBeams.23.090703`. `https://link.aps.org/doi/10.1103/PhysRevAccelBeams.23.090703`

[4] S. Antipov *et al.*, "IOTA (Integrable Optics Test Accelerator): facility and experimental beam physics program," *J. Instrum.*, vol. 12, no. 03, T03002, 2017.

---

[*] This manuscript has been authored by Fermi Research Alliance, LLC under Contract No. DE-AC02-07CH11359 with the U.S. Department of Energy, Office of Science, Office of High Energy Physics.

[†] ilobach@uchicago.edu

MEASUREMENT AND RECONSTRUCTION OF A BEAM PROFILE USING A GAS SHEET MONITOR BY BEAM-INDUCED FLUORESCENCE DETECTION IN J-PARC

Ippei Yamada*[1], Motoi Wada
Graduate School of Science and Engineering, Doshisha University, Kyoto, Japan
Katsuhiro Moriya, Junichiro Kamiya, Michikazu Kinsho
Japan Atomic Energy Agency, J-PARC center, Ibaraki, Japan
[1]also at Japan Atomic Energy Agency, J-PARC center

Abstract

A non-destructive transverse beam profile monitor using interaction between a beam and a gas sheet has been developed and demonstrated in J-PARC. The gas sheet formed based on rarefied gas dynamics enables two-dimensional beam profile measurement by detection of induced fluorescence as a 2D image with a CCD camera. The relative-sensitivity spatial distribution of the developed monitor was measured to quantitatively reconstruct a beam profile from the captured image. The sensitivity distribution consists of the sheet-gas density spatial distribution, non-uniformity of the incident solid angle, and the detection efficiency distribution of the CCD camera. The J-PARC 3 MeV H^- beam profile was successfully reconstructed with deviation of 7% ± 2% by the integral equation derived from the monitor's principle with the sensitivity distribution.

INTRODUCTION

A non-destructive or a minimal destructive diagnostic system, which is advantageous for constant monitoring, plays an important role for high-intensity, high-energy beam accelerator operation. The system enables to minimize beam losses and radioactivations of the accelerator components. We have developed a non-destructive transverse beam profile monitor, *the gas sheet monitor*, using interaction between a beam and an injected sheet-shaped gas [1]. The gas sheet is formed based on a technique of rarefied gas dynamics to increase a local gas density. The sheet gas interacts with a high intensity beam and induces photons whose spatial distribution depends on the gas density spatial distribution and the beam intensity spatial distribution in transverse. The two-dimensional beam profile can be obtained by taking a picture of the fluorescence and applying a proper analysis considering the effect of the gas density distribution. Figure 1 shows the development flow of the gas sheet monitor. Development of the gas sheet monitor is separated into four components: (1) formation of gas sheet, (2) evaluation of the gas density spatial distribution, (3) test of the profile measurement using a high intensity beam, and (4) reconstruction of the beam profile. In this paper, we report the details of the beam profile measurement with the gas sheet monitor from the four viewpoints.

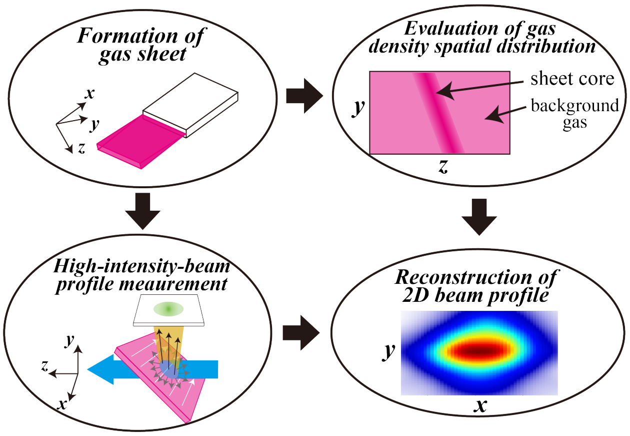

Figure 1: A development flow of the gas sheet beam profile monitor system.

PRINCIPLE

Gas Sheet Formation

The gas sheet is formed based on rarefied gas dynamics. When the mean free path of gas molecules is longer than the typical vacuum chamber dimension like in a beam pipe, the motion of gas molecules is determined not by intermolecular collisions but by the thermal motion and reflections with the chamber wall. The incident angle for reflections with a wall does not affect the reflection angle, and the probability distribution function of the reflection angle θ with respect to the normal direction of the wall is proportional to $\cos\theta$: cosine law. A long gas conduit of a thin cross section can form a gas sheet by increasing the number of reflections in the thickness direction for molecules to obtain a large angle. In this condition, the motion of gas molecules can be modeled by the individual motion of the constant velocity with reflections being subject to the cosine law, such as Molflow+ code [2].

Beam Profile Measurement

Figure 2 shows the gas sheet monitor consisting of a gas sheet flowing along x axis and a photon detector integrating fluorescence induced by beam-gas interaction along y axis. The high intensity beam passes through the gas sheet along z axis. The photons are induced by interaction between the beam and not only the gas sheet but also the background gas.

---

* ip_yamada@icloud.com

ISBN: 978-3-95450-230-1 ISSN: 2673-5350 doi:10.18429/JACoW-IBIC2021-TUOA04

The detected luminous intensity spatial distribution $g(x,z)$ is constructed by the produced photon spatial distribution, the detection efficiency spatial distribution of the image sensor array, and non-uniformity of the solid angle. The latter two effects are integrated as the detection efficiency spatial distribution of the gas sheet monitor, $\alpha(x,y,z)$. The relation among the detected luminous intensity spatial distribution $g(x,z)$, the transverse beam profile $F(x,y)$, the gas density spatial distribution $n(x,y,z)$, and the detection efficiency spatial distribution $\alpha(x,y,z)$ can be written as an integral equation,

$$g(x,z) = \int_D \alpha(x,y,z) \cdot n(x,y,z) \cdot F(x,y)\mathrm{d}y \qquad (1)$$

$$\equiv \int_D k(x,y,z) \cdot F(x,y)\mathrm{d}y \qquad (2)$$

where D is the integral region larger than the full beam width in y direction, such as a beam pipe. The distribution $k(x,y,z)$ is defined as the relative-sensitivity spatial distribution of the gas sheet monitor. The beam profile $F(x,y)$ can be reconstructed from the obtained luminous intensity distribution $g(x,z)$ by giving the relative-sensitivity distribution $k(x,y,z)$ and solving Eq. (2).

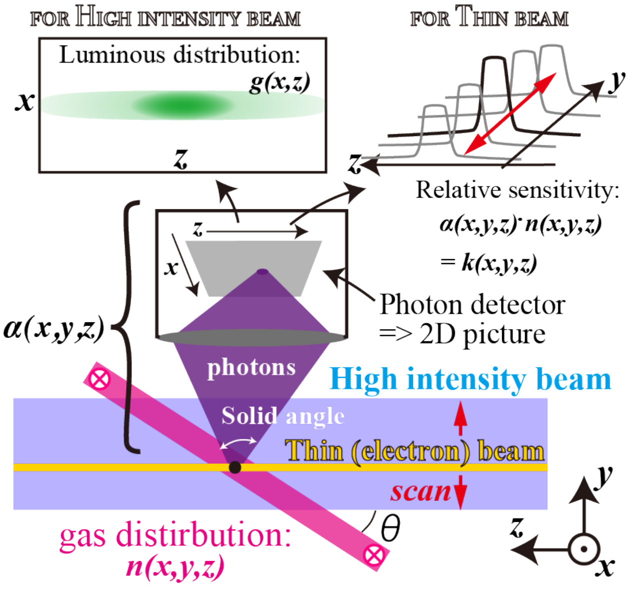

Figure 2: The principle of the gas sheet monitor.

The relative-sensitivity spatial distribution can be measured by injecting a thin beam into the gas sheet monitor. The center position of the thin beam, the beam widths, and the beam profile are defined as (x_0, y_0), Δx, Δy, and $F_{\mathrm{thin}}(x,y)$, respectively. A thin beam induces photons in a limited local volume,

$$g(x,z) = \int_{\Delta y} k(x,y,z) \cdot F_{\mathrm{thin}}(x,y)\mathrm{d}y. \qquad (3)$$

The measurement spatial resolutions are regarded as the thin beam widths Δx and Δy, and the luminous signal is integrated along x axis,

$$\int_{\Delta x} g(x,z)\mathrm{d}x = \int_{\Delta x}\int_{\Delta y} k(x,y,z) \cdot F_{\mathrm{thin}}(x,y)\mathrm{d}x\mathrm{d}y \qquad (4)$$

$$G(z) = \tilde{F}_{\mathrm{thin}} \cdot k(x_0, y_0, z) \qquad (5)$$

where $\tilde{F}_{\mathrm{thin}}$ is the luminous intensity coefficient for thin beam injection. The obtained distribution $G(z)$ is in proportion to the one-dimensional sensitivity spatial distribution. Scanning the thin beam position (x_0, y_0) gives the three-dimensional relative-sensitivity distribution, if the coefficient $\tilde{F}_{\mathrm{thin}}$ is constant over the scanned area.

DEVELOPED GAS SHEET MONITOR

The developed gas sheet monitor system consisting of a gas sheet generator, a cover chamber with a slit, a main chamber attached to a beam line, and a photon detector system is shown in Fig 3. The gas sheet generator is a cuboid conduit of 100 mm × 50 mm × 0.1 mm. A cover chamber having a rectangular slit of 50 mm × 0.5 mm with a turbomolecular pump which has a 420 ℓ/s pumping speed for N_2 surrounds the gas sheet generator to cut the gas-sheet distribution tail. Figure 4 shows the calculated gas flux spatial distribution along the thickness direction at the beam-gas interaction point for N_2 gas. The gas sheet with 0.5 mm thickness for full width at half maximum can be formed by the conduit, and the cover chamber with 420 ℓ/s pumping reduces the tali part intensity. The N_2 gas sheet entering the main chamber through the slit interacts with the beam and is evacuated by a turbomolecular pump and a cryo pump with the pumping speeds of 300 ℓ/s and 750 ℓ/s for N_2, respectively. The photon detector system consists of a set of optical lenses, an image intensifier, and a CCD camera. The diameter of the optical lenses is 50 mm and the distance from the beam-gas interaction point to the objective lens is 200 mm. The image intensifier increases the signal intensity up to 10^4 times. The CCD camera has 1920 × 1080 sensors of 16 bit.

RELATIVE-SENSITIVITY DISTRIBUTION

The relative-sensitivity spatial distribution was measured with a 3 keV, 10 µA, DC electron beam as a thin beam in Fig. 2. An example of the image captured by the sensitivity spatial distribution measurement is shown in Fig. 5. The total exposure time was 20 minutes (=120 s × 10 frames). The inlet pressure of the sheet generator was 100 Pa and the pressure of the main chamber was 5.7×10^{-5} Pa. The white part describes the photon signal produced by beam-gas interaction. The one-dimensional sensitivity distribution $k(x_0, y_0, z)$ can be constructed by integrating the luminous intensity along x axis in 1 mm. The two-dimensional relative-sensitivity distribution $k(x_0, y, z)$ constructed by scanning the electron beam position along y axis is shown in Fig. 6.

MEASUREMENT AND RECONSTRUCTION OF BEAM PROFILE

The high-intensity-beam profile was measured using the J-PARC 3 MeV, 60 mA H^- beam at the MEBT test stand [1,3].

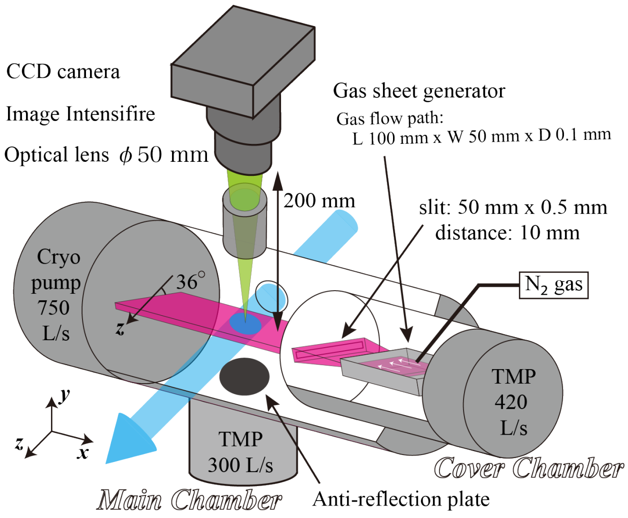

Figure 3: The developed gas sheet monitor system. The monitor system dimensions are 1,500 mm × 600 mm × 220 mm in x, y and z direction, respectively.

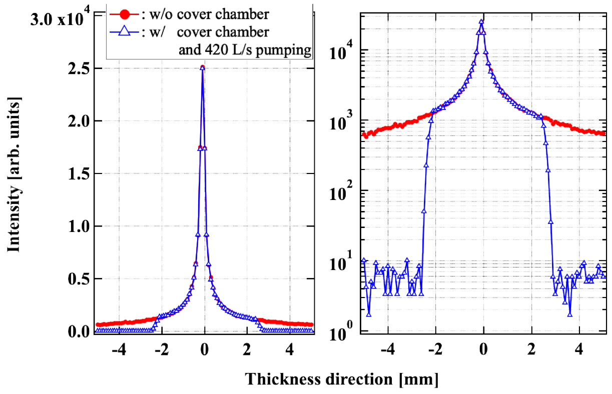

(a) linear plots (b) semi-log plots

Figure 4: The simulated gas flux spatial distribution along the sheet thickness direction at the beam-gas interaction point.

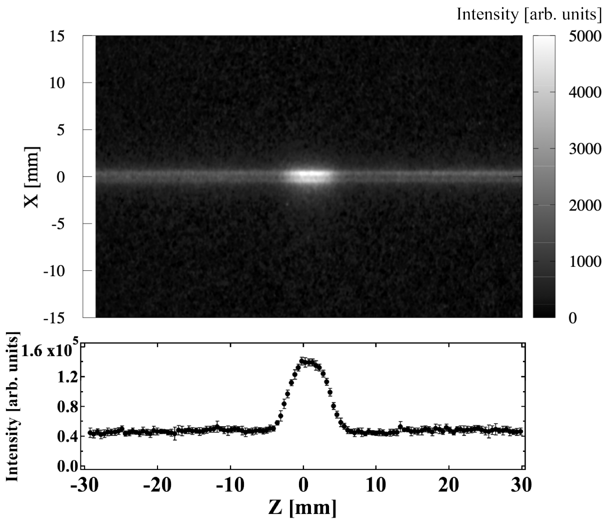

Figure 5: An example of the captured image of the photons produced by beam-gas interaction and the one-dimensional sensitivity distribution $k(x_0, y_0, z)$ constructed by integrating the luminous intensity along x direction.

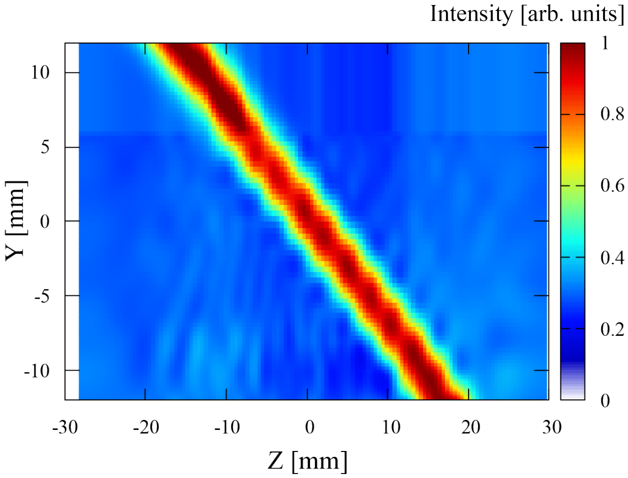

Figure 6: The two-dimensional relative-sensitivity spatial distribution in y-z plane: $k(x_0, y, z)$.

An example of the captured image is shown in Fig. 7. The image was captured using 1.7×10^{15} H^- particles/frame and was averaged over 80 frames. The inlet pressure of the sheet generator was 100 Pa and the pressure of the main chamber was 5.6×10^{-5} Pa. The image describes that the photon signals produced not only by the gas sheet core but also by the background gas are detected. The beam profile should be reconstructed from the image and the measured relative-sensitivity distribution with Eq. (2). Solving the integral equation numerically is not easy because the numerical method needs over 100-order-digit precision. Regarding the integral equation as an integral formula, the function $g_{\mathrm{int}}(x, z)$ is defined as an integral of the measured sensitivity distribution and an assumed beam profile. The distribution $g_{\mathrm{int}}(x, z)$ is compared with the distribution $g_{\mathrm{H^-}}(x, z)$ which is the image shown in Fig. 7 obtained by beam profile measurement. When these two distributions $g_{\mathrm{int}}(x, z)$ and $g_{\mathrm{H^-}}(x, z)$ agree each other, the assumed beam profile is considered to be the actual beam profile.

The beam profile is approximated with a set of 21 parameters $a = (a_0, a_1, \cdots, a_{10}), b = (b_1, b_2, \cdots, b_{10})$,

$$F(x_0, y; a, b) = \frac{a_0}{2} + \sum_{k=1}^{10} \left\{ a_k \cos\left(k\frac{\pi y}{L}\right) + b_k \sin\left(k\frac{\pi y}{L}\right) \right\} \tag{6}$$

where L is the half length of the beam-defined region. The beam profile assumed by Eq. (6) is optimized using the Nelder-Mead method [4]. The method optimizes the N parameters not by calculating the derivative of the objective function but by geometrically moving the parameters to minimize a simplex constructed from vertices of the objective function for $N + 1$ sets of the parameters. The objective func-

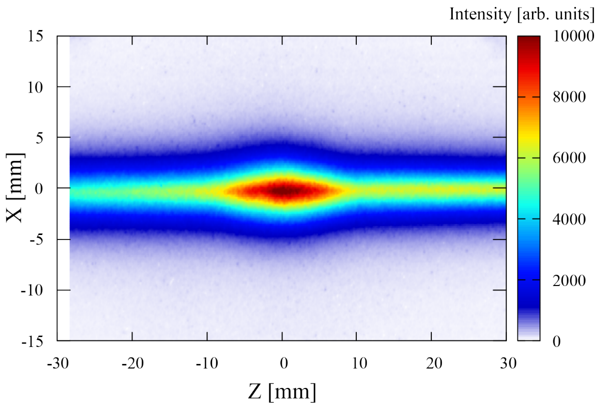

Figure 7: The image obtained by the high-intensity-beam profile measurement. This two-dimensional luminous intensity distribution is defined as $g_{\mathrm{H}^-}(x,z)$.

tion is defined as a deviation between $g_{\mathrm{int}}(x,z)$ and $g_{\mathrm{H}^-}(x,z)$:

$$s(a,b,x_0) = \sqrt{\frac{1}{M}\sum_{i=1}^{M}\left\{\frac{g_{\mathrm{H}^-}(x_0,z_i) - g_{\mathrm{int}}(x_0,z_i;a,b)}{g_{\mathrm{H}^-}(x_0,z_i)}\right\}^2}\,. \tag{7}$$

The 22 initial beam profiles are defined with Fourier series of Gaussian distributions whose σ are 2-4 mm. The reiteration of the optimization is terminated when the normalized simplex volume becomes smaller than some limit:

$$\frac{s_{\mathrm{max}} - s_{\mathrm{min}}}{\frac{1}{N+1}\sum_{i=1}^{N+1} s(a_i,b_i)} < T_h. \tag{8}$$

Figure 8 shows the result of the beam profile optimization with $T_h = 0.001$ at $x_0 = 3.0$ mm. The distributions $g_{\mathrm{H}^-}(x_0,z)$ and $g_{\mathrm{int}}(x_0,z)$ agree each other with the deviation defined as Eq. (7) of 3% ± 1%. The reconstructed (optimized) profile $F(x_0,y)$ is also shown in Fig. 8. Reconstructing the beam profiles $F(x_0,y)$ for each x and arraying the profiles for x direction yield the two-dimensional beam profile shown in Fig. 9 with the deviation of 7% ± 2% on average.

CONCLUSION

We demonstrated that the relative-sensitivity spatial distribution can be measured by injecting the thin electron beam into the gas sheet monitor and the high-intensity-beam profile can be quantitatively reconstructed using the devised integral equation with the measured sensitivity distribution. The proposed method from constructing a relative-sensitivity distribution to reconstructing a high-intensity-beam profile can be applied to any profile monitor based on beam-gas interaction. We are starting to use the gas sheet monitor for investigating time development of the beam profile in a beam pulse and investigating an effect of gas injection on the beam quality.

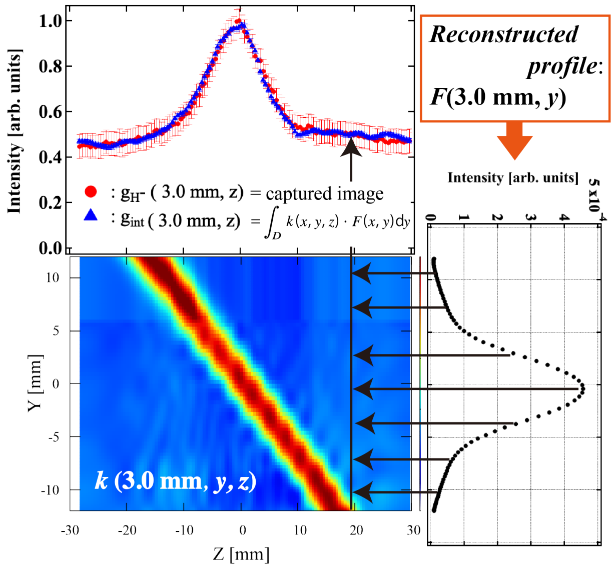

Figure 8: Reconstruction of the beam profile by comparing the distributions $g_{\mathrm{H}^-}(x_0,z)$ and $g_{\mathrm{int}}(x_0,z)$ which is calculated by Eq. (2) with the relative-sensitivity distribution $k(x_0,y,z)$ and the assumed beam profile $F(x_0,y)$. The error bars describe the standard deviation of the measurement.

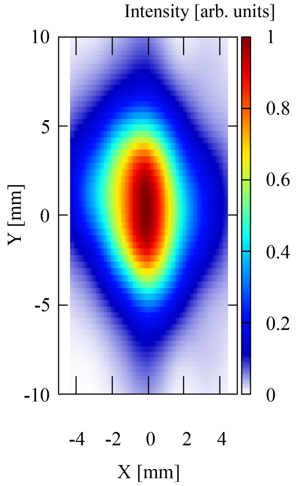

Figure 9: The reconstructed two-dimensional beam profile of the J-PARC 3MeV H$^-$ beam.

REFERENCES

[1] I. Yamada *et al.*, "High-intensity beam profile measurement using a gas sheet monitor by beam induced fluorescence detection", *Phys. Rev. Accel. Beams*, vol. 24, p. 042801, 2021.

[2] Molflow+, `http://molflow.we.cern.ch`

[3] Y. Kondo *et al.*, "Upgrade of the 3-MeV Linac for testing of Accelerator Components at J-PARC", *Journal of Physics: Conference Series*, vol. 1350, p. 012077, 2019.

[4] J. A. Nelder and R. Mead, "A simplex method for function minimization", *The Computer Journal*, vol. 7, p. 308313, 1965.

ISBN: 978-3-95450-230-1 ISSN: 2673-5350 doi:10.18429/JACoW-IBIC2021-TUOA05

COMMISSIONING OF TIMEPIX3 BASED BEAM GAS IONISATION PROFILE MONITORS FOR THE CERN PROTON SYNCHROTON

H. Sandberg*[1], W. Bertsche[2], D. Bodart[1], S. Jensen[1], S. Gibson[3], S. Levasseur[1], K. Satou[4],
G. Schneider[1], J.W. Storey[1], and R. Veness[1]
[1]CERN, Switzerland
[2]University of Manchester, Cockcroft Institute, UK
[3]Royal Holloway University of London, John Adams Institute, UK
[4]Accelerator Laboratory, KEK, Japan

Abstract

A pair of operational Beam Gas Ionisation (BGI) profile monitors was installed in the CERN Proton Synchrotron (PS) at the beginning of 2021. These instruments use Timepix3 hybrid pixel detectors to continuously measure the beam profile throughout the cycle in the horizontal and vertical planes. In the weeks following their installation, both BGI's were commissioned in situ by equalizing and tuning the thresholds of the Timepix3 detectors.

First measurements were taken during the beam commissioning period, demonstrating the operational readiness of the instruments. Sextupolar components originating from the magnetic shield in the vertical BGI magnet were later discovered and required compensation to reduce their effect on the PS beams. With the compensation in place, operational measurements could be started and provided new insights into the dynamics of the PS beam cycles.

INTRODUCTION

A novel BGI profile monitor design aims at providing continuous, bunch-by-bunch and turn-by-turn measurement of the transverse beam profile in the CERN PS [1]. This instrument design uses electric and magnetic fields to transport electrons from rest-gas ionisation to a Timepix3 [2] based detection system installed directly inside the beam vacuum. The beam profile is inferred from the transverse distribution of the detected electrons. In 2017 a prototype was successively installed in the CERN PS and was updated in 2018 with new detectors. It provided the first measurements of transverse horizontal beam profiles using this novel design and demonstrated the feasibility of the in-vacuum Timepix3 use [3, 4].

During the long shutdown 2 of the CERN accelerator complex, the prototype was replaced by an operational instrument and a second instrument was installed to measure the transverse beam profile in the vertical plane. The horizontal BGI reused the vacuum chamber, magnet and infrastructure from the prototype instrument, while the vertical BGI required the installation of a new vacuum chamber and a new 0.2 T triplet dipole magnet. Both instruments were ready for the first beam in the PS on March 2021.

DETECTOR SETUP AND EQUALISATION

A new generation of in-vacuum detector electronics was designed and manufactured for the operational vertical and horizontal instruments. This new design consist of an array of four modules each with one Timepix3 chip. This solves production yield issues discovered with the prototypes and improves the manufacturability and reliability of the detector. To ensure that the detectors were working as expected, each of them was tested twice, once in the lab prior to installation and once in the CERN PS after installation. The testing procedure consists of; measurements of the detector and sensor bias currents, temperature measurements, internal digital-to-analog converter (DAC) response scans, equalisation, threshold tuning and detection tests using radioactive sources. Equalisation and threshold tuning are the two most important step of the commissioning.

The equalisation process aims to create a uniform response of all pixels in the matrix by tuning 4-bit DACs that shifts the response of each pixel relative to a global threshold. All pixels have a slightly different response due to manufacturing process variations and for a fixed input signal some pixels are therefore below the threshold while others are above. The response is measured at the maximum and minimum range of the pixel DACs to find the ideal value for each pixel. Figure 1 presents the Timepix3 matrix response measurement before (two large distributions) and after equalisation (narrow central distribution). Equalisation

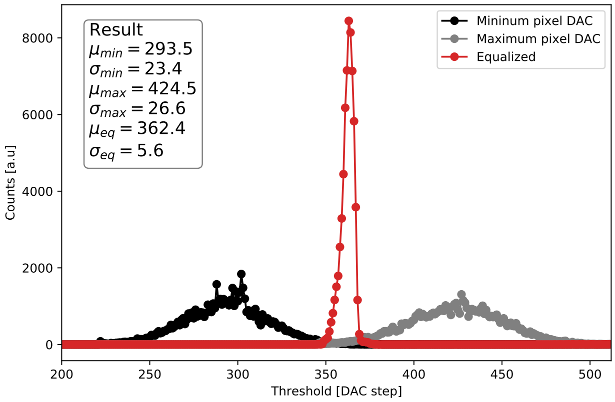

Figure 1: Equalisation result from a Timepix3 detector in the operational horizontal BGI instrument.

---

* hampus.sandberg@cern.ch

also allows to locate dead and noisy pixels as they fail to reach their equalisation target.

Threshold tuning consists of adjusting the detection threshold of each Timepix3 against a common signal source. This maximises the efficiency of ionisation electrons detection and eliminates differences in efficiency between the four detectors. A ^{55}Fe radiation source is used in the lab, while in the CERN PS, the remnant radiation background is used. A more detailed description of the detector setup and testing is given in [5]. After installation the detectors successfully passed the testing procedure and no significant difference was found when compared to the results of the lab tests.

FIRST BEAM MEASUREMENTS

As soon as the beam arrived in the PS in March 2021 the BGI instruments were switched on to start measuring the beam profile. The readout software had been integrated with the operational control system of the CERN accelerator complex during the long shutdown. Computers with dedicated software, called Front-End Software Architecture (FESA) device, control the BGI instruments and allow beam profiles to be read out and published to operational software applications, user created scripts and to the logging database. To synchronize the instruments with the accelerator there are hardware triggers connected to the readout electronics and the FESA devices. The readout has been designed to acquire up to 1024 beam profiles for any beam cycle in the PS with configurable integration time and repetition rate. The settings of the instrument are specific for each cycle, and this allows to measure each of them individually even when played one after the other in a programmed sequence called super cycle.

Figure 2 shows a pixel image from the four Timepix3 detectors in the horizontal BGI instrument acquired during the first week of March 2021 when the first beams were circulating in the PS. The image looks as expected with a uniform response along the direction of the beam (s) and a gradient along the transverse horizontal direction (x). The honeycomb shaped shadow is from an RF shield mounted above the detectors, which blocks the ionisation electrons, creating areas with lower count rate in the detector. A method to correct and ensure a uniform detection efficiency is discussed in [6] and was applied to the operational readout during the first weeks of the instrument commissioning period.

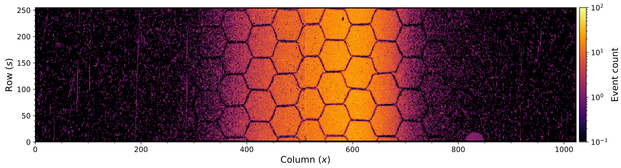

Figure 2: Pixel image of a single bunch beam cycle in the PS.

The pixel image in Fig. 2 is a 1.2 s integration of a full single bunch beam cycle. For beam profile measurements integration times in the order of 2 ms or less are used to capture the details of the beam dynamics within the cycle. An integration time of 2 ms for each beam profile results in a total of 600 profiles for this single bunch beam. In Fig. 3 all these beam profiles are shown in a waterfall plot with the first profile at the bottom and the last at the top. This shows the strength of the BGI instruments in that they can resolve the dynamic behavior of the beam from a single capture of a cycle. Single shot instruments, such as wire scanners, would require measurements of 600 cycles where the start trigger is stepped throughout the cycle.

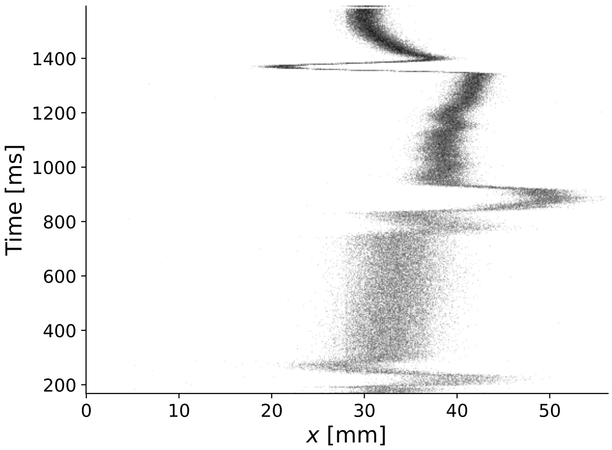

Figure 3: Waterfall plot of a single bunch LHC beam cycle.

The time evolution of the beam size and position throughout a cycle can be determined by fitting a Gaussian distribution to each beam profile, an example of this type of measurement is shown in Fig. 4. This is the intended operational mode of the BGI instruments as it facilitates quantification of the beam dynamics and performance.

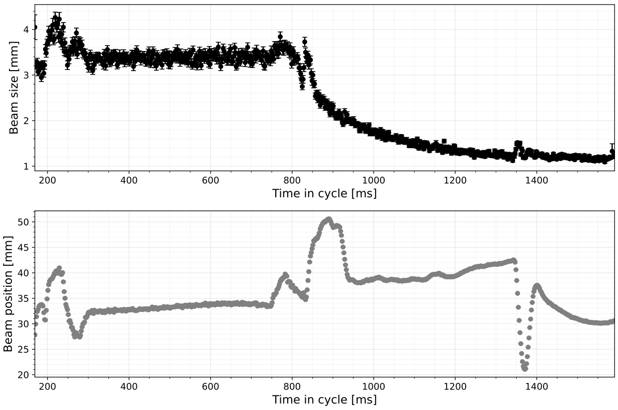

Figure 4: Evolution of the beam size (top) and position (bottom) of a single cycle.

OPERATIONAL ISSUES

During the beam commissioning period the operators had issues with beam losses and conducted a study to find the cause of it. After some time, it was discovered that the magnetic shield of the dipole magnet for the vertical BGI instrument, which was installed and had not been used in the accelerator yet, caused some unwanted sextupolar components and resonances in the beam. This was later confirmed by the magnet group through rigorous simulations and a permanent solution was found which requires adjustment to the shielding plates in the magnet. The fix has been scheduled for the next winter shutdown. In the meantime, the magnet activation is controlled by the operators and enabled only for selected cycles where its effect is compensated using the other magnets in the PS. The horizontal magnet does not have this issue and has been installed in the PS since 2017.

EXAMPLES OF OPERATIONAL MEASUREMENTS

In the following section examples of operational measurements will be shown that were kindly provided by M. Coly, M. Fraser and A. Huschauer from the CERN operational, accelerator beam transfer and physics groups. The discussion will be limited to the measurement setup and how the BGI instruments were used. Beam performance will not be analyzed or discussed.

Beamlets in Multi-turn Extraction Beam

The PS accelerator is producing beams with different properties for experimental areas and for further acceleration in the Super Proton Synchrotron (SPS). One of these beams going to the SPS is using a multi-turn extraction (MTE) technique, where the beam is split in the transverse phase space into several beamlets to be extracted individually [7]. After splitting, the beamlets can be observed with the BGI instrument as shown in Fig. 5, where five lines can be seen at different transverse positions. One of the beamlets, called the core, has a higher intensity and is identified by the more intense color in the figure. This difference in intensity can be detected by the BGI because the number of ionisation electrons is proportional to the number of particles in the beam. The dynamic behavior of the beamlets as a function of the time in the cycle is also visible and give insight to how they behave.

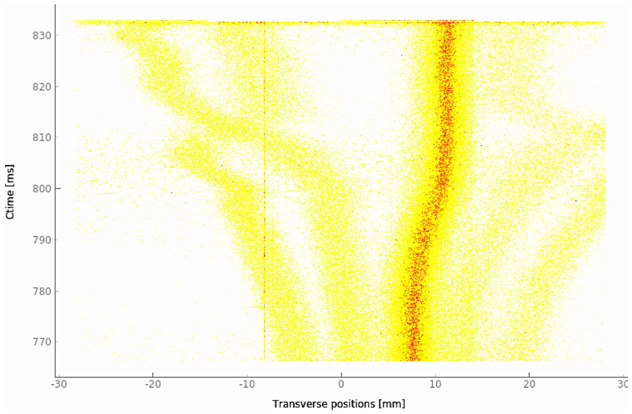

Figure 5: Beamlets of the MTE beam measured with the BGI.

Second Injection Beam Losses

The Timepix3 pixel detectors used in the BGI instruments detects not only ionisation electrons, but also particles originating from beam losses and activated material. The detectors are mounted in the primary vacuum of the accelerator, about 7 cm from the beam. During normal operation with stable beams in the PS the amount of beam loss is negligible and can be seen as an occasional track on the pixel image. In some specific cases the amount of losses can be greater and is usually distributed over the full detector sensor area. The cause of such losses detected by the BGI can then be investigated further.

Figure 6 is an example of a measurement where higher losses can be observed. At 1320 ms there is a wide band that extends outside the uniform beam profile at the center of the waterfall plot. At this time in the cycle a second injection of particles usually occurs, triggered by the injection kicker magnet kicking the beam from the transfer line into the PS, where particles are already circulating. During this specific measurement the kicker magnet was active but no particles were injected. The beam loss detected by the BGI is therefore correlated to a disturbance to the particles already in the PS beam pipe. Beam loss measurements with the BGI only show it at one location in the accelerator, in contrast to the beam loss monitoring (BLM) system that measure the losses around the whole accelerator.

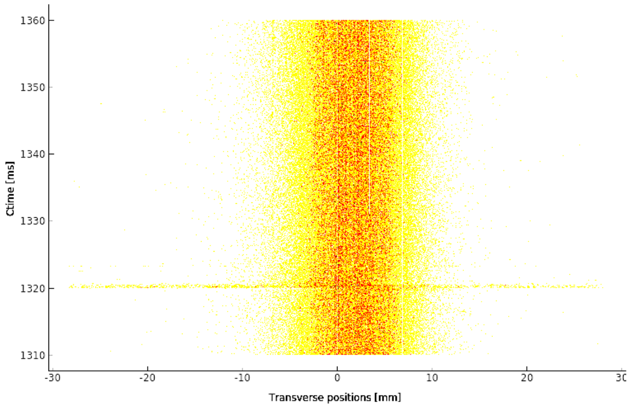

Figure 6: Second injection beam losses seen with the BGI.

Intermediate Plateau Beam Size Squeeze

When a full cycle is measured the BGI instrument provides the operator with an overview of how the beam evolves throughout the cycle in the transverse plane as shown earlier in Fig. 4. If the measurement shows an unexpected beam size or position evolution, the operator can further investigate it by programming a trigger for a more detailed measurement in that specific area of the cycle for the following cycles.

One such measurement is shown in Fig. 7 where there is a dip at 1450 ms in the beam size (σ) evolution. This happens in the so called intermediate plateau, a part of the cycle where the beam has been accelerated to an intermediate energy before the second injection. The longitudinal momentum spread was observed to decrease and increase during the acceleration, which couples to the horizontal beam size through dispersion, explaining what is observed with the BGI instrument. With up to 1024 beam profiles measured per cycle the BGI can detect rapid changes in the beam size as demonstrated here.

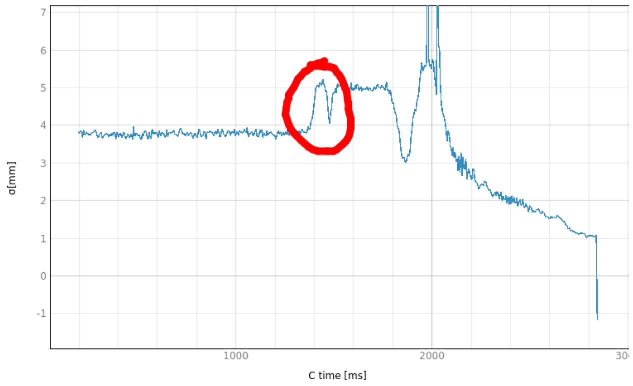

Figure 7: Beam size changes measured with the BGI due to rapid changes in the longitudinal momentum spread.

Injection Mismatch Oscillations

In [4] it was shown that the prototype BGI instrument was capable of resolving turn-by-turn beam profiles, but the period of a turn in the PS is 2.2 µs and with only residual gas in the BGI instrument there is not enough ionisation electrons detected to resolve the profile. For the prototype instrument a nearby vacuum pump was sublimated to create a localised pressure bump which was enough to create around 80 electrons per turn. Based on this measurement it was decided to equip the operational BGI instruments with dedicated argon gas injection systems, making it possible to increase the ionisation electron rate on demand.

An initial test of the gas injection system and turn-by-turn measurements using the operational horizontal instrument is shown in Fig. 8. This is currently a work-in-progress, but the first test shows that the expected beam size oscillations induced by an injection mismatch can be observed with the BGI. The operational processing of the Timepix3 events needs further development to ensure that each is assigned to the correct turn in the cycle.

CONCLUSION

Beam gas ionisation profile monitors have successfully been commissioned in the CERN PS for operational measurements of the transverse beam profiles in the horizontal and the vertical plane. The Timepix3 hybrid pixel detectors used in the instrument were tested and equalized in the lab prior to installation in the primary vacuum of the accelerator and the same process was repeated after installation. No significant discrepancies were found between the results obtained in lab and those obtained after installation for the same instrument. Both instruments were ready before the restart of the PS in March 2021 and could successfully measure the profile of the beam since the beginning of the run. Operational software was prepared and integrated with the CERN control system and accelerator timing signals and has been used by the operators and beam physicists. Examples of operational measurements have been shown where the non-invasive and continuous measurement technique of the Timepix3 based BGI instrument is highlighted.

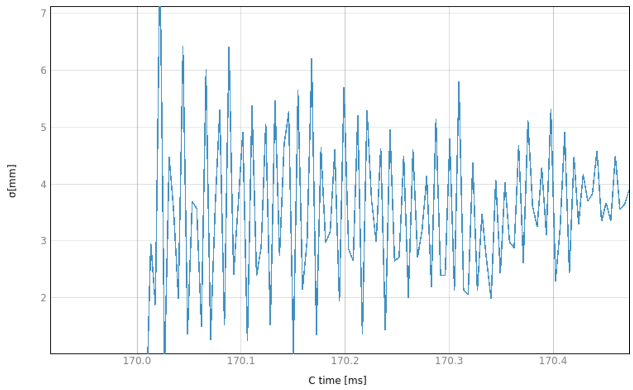

Figure 8: Forced injection mismatch induces beam size oscillations.

REFERENCES

[1] J. Storey *et al.*, "First Results From the Operation of a Rest Gas Ionisation Profile Monitor Based on a Hybrid Pixel Detector," WE2AB5. 5 p, 2018. DOI: `10.18429/JACoW-IBIC2017-WE2AB5`.
[2] T. Poikela *et al.*, "Timepix3: A 65k channel hybrid pixel readout chip with simultaneous ToA/ToT and sparse readout," *Journal of Instrumentation*, vol. 9, no. 05, pp. C05013–C05013, 2014. DOI: `10.1088/1748-0221/9/05/c05013`.
[3] S. Levasseur *et al.*, "Time-Resolved Transverse Beam Profile Measurements with a Rest Gas Ionisation Profile Monitor Based on Hybrid Pixel Detectors," WEPAL075. 4 p, 2018. DOI: `10.18429/JACoW-IPAC2018-WEPAL075`.
[4] H. Sandberg *et al.*, "Measuring the Beam Profile by Counting Ionization Electrons," in *Proc. IBIC'19*, (Malmö, Sweden), ser. International Beam Instrumentation Conference, pp. 252–255. DOI: `10.18429/JACoW-IBIC2019-TUBO04`.
[5] S. Levasseur, "Development of a hybrid pixel detector based transverse profile monitor for the cern proton synchrotron," PhD thesis, Royal Holloway University of London, 2020.
[6] H. Sandberg, "Development of a novel transverse beam profile and emittance monitor for the cern proton synchrotron," PhD thesis, The University of Manchester, 2020.
[7] P. Bourquin *et al.*, *The CERN PS multi-turn extraction based on beam splittting in stable islands of transverse phase space: Design Report*, CERN-2006-011. CERN, 2006.

TWO-DIMENSIONAL BEAM SIZE MEASUREMENTS WITH X-RAY HETERODYNE NEAR FIELD SPECKLES

M. Siano*, B. Paroli, M. A. C. Potenza, L. Teruzzi, Università degli Studi di Milano, Milan, Italy
U. Iriso, A. A. Nosych, E. Solano, L. Torino, ALBA-CELLS, Cerdanyola del Vallés, Spain
D. Butti, A. Goetz, T. Lefevre, S. Mazzoni, G. Trad, CERN, Geneva, Switzerland

Abstract

We report on 2D beam size measurements with a novel interferometric technique named Heterodyne Near Field Speckles, capable of resolving few-micrometer beam sizes. It relies on the interference between the weak spherical waves scattered by a colloidal suspension and the intense transilluminating X-ray beam. Fourier analysis of the resulting speckles enables full 2D coherence mapping of the incoming radiation, from which the beam sizes along the two orthogonal directions are retrieved. We show experimental results obtained with 12.4 keV X-rays at the NCD-SWEET undulator beamline at ALBA, where the vertical beam size has been changed between 4 and 14 micrometers by varying the beam coupling. The results agree well with the estimated beam sizes from the pinhole calculations. Finally, we discuss recent investigations on alternative targets aimed at improving the signal-to-noise ratio of the technique.

INTRODUCTION

Two-dimensional (2D) beam size measurements are of utmost importance for present and future accelerators. Knowledge of the beam sizes enables to assess the beam emittance in storage rings [1]. Furthermore, beam size ultimately affects the transverse coherence properties of the emitted synchrotron radiation in current and forthcoming Synchrotron Light Sources (SLS), thus impacting many research areas that rely on coherence-based techniques [2].

Non-invasive beam size measurement methods can be divided into two main categories: direct imaging techniques and interferometric methods. Direct imaging techniques such as the X-ray pinhole camera directly provide a 2D image of the source, though they are typically limited in resolution to beam sizes larger than 10 µm [3]. Contrarily, interferometric methods such as the Young's double-pinhole interferometer provide higher resolutions, but are limited to one-directional measurements only [3].

Here we report on recent 2D beam size measurements with a novel, non-conventional interferometric technique named Heterodyne Near Field Speckles (HNFS). We show that the technique is intrinsically 2D and that it can resolve beam sizes as small as a few micrometers. As in all interferometric techniques, what we actually measure is the Complex Coherence Function (CCF) of the synchrotron radiation

$$\mu(\Delta\mathbf{r}) = \frac{\langle e(\mathbf{r})e^*(\mathbf{r}+\Delta\mathbf{r})\rangle}{\sqrt{\langle i(\mathbf{r})\rangle\langle i(\mathbf{r}+\Delta\mathbf{r})\rangle}}\,, \tag{1}$$

from which the beam size is retrieved by means of Statistical Optics approaches. In Eq. (1), $e(\mathbf{r})$ is the electric field at a point $\mathbf{r}$ on the wavefront of the synchrotron light, $i(\mathbf{r}) = |e(\mathbf{r})|^2$ is the corresponding intensity and $\langle\cdot\rangle$ denotes ensemble average over many electron bunches. The radiation CCF $\mu(\Delta\mathbf{r})$ quantifies the correlations of the emitted electric field between two points across the wavefront of the synchrotron light separated by $\Delta\mathbf{r}$ [4, 5].

THE HETERODYNE NEAR FIELD SPECKLES TECHNIQUE

The HNFS technique relies on the interference between the incoming partially-coherent synchrotron light and the weak spherical waves scattered by nanospheres suspended in water.

In the ideal case of a single scatterer, the self-referencing interference between the intense transilluminating field and the weak scattered spherical wave generates circular fringes whose visibility decays according to the 2D CCF of the incoming radiation, as shown in Fig. 1(a). Here, vertically elongated coherence areas have been assumed as typically encountered in undulator sources.

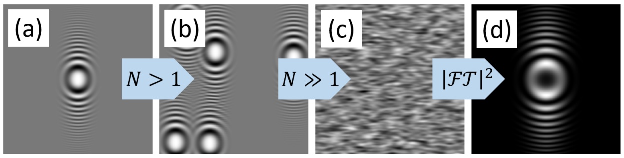

Figure 1: Fundamentals of the HNFS technique. (a) Single-particle interference image. Interference fringes are modulated by the 2D CCF of the synchrotron light. (b) and (c) Under heterodyne conditions, speckles are simply formed as the intensity sum of many equal single-particle interference patterns. (d) Power spectrum of heterodyne speckles, showing Talbot oscillations enveloped by the squared modulus of the 2D CCF.

Measurement of the visibility of the circular fringes as a function of the distance $\Delta\mathbf{r}$ from the center of the pattern allows to directly measure the 2D coherence properties of the incoming light. Furthermore, interference fringes are narrower at larger $\Delta\mathbf{r}$. This allows to introduce a one-to-one relation, known as the spatial scaling, between the spatial frequency of the interference fringes, $\mathbf{q}$, and transverse displacements, $\Delta\mathbf{r}$ [6–8]:

$$\Delta\mathbf{r} = z\frac{\mathbf{q}}{k}\,, \tag{2}$$

---

* mirko.siano@unimi.it

where z is the distance from the scattering particle and $k = 2\pi/\lambda$, being λ the radiation wavelength.

In the real case of a colloidal suspension composed by many particles, the observed intensity distribution is a random speckle pattern, as shown in Fig. 1(b,c). We assume heterodyne conditions, namely that the scattered light e_s is much weaker than the incoming field e_0: $|e_s| \ll |e_0|$ [6–8]. In practice, heterodyne conditions for X-rays are fulfilled by properly diluting the sample to volume concentrations of roughly 10%. Under these conditions, speckles are simply formed as the intensity sum of many equal single-particle interference images as depicted in Fig. 1(b,c) and Fourier analysis of the resulting speckle patterns enables 2D coherence mapping [6–8], as evidence in Fig. 1(d). The power spectrum $I(\mathbf{q}, z)$ of heterodyne speckles at a distance z from the sample exhibits peculiar oscillations, known as Talbot oscillations, enveloped by the squared modulus of the radiation CCF [6–8]:

$$I(\mathbf{q}, z) = T(q, z)C\left(z\frac{\mathbf{q}}{k}\right)H(\mathbf{q})S(\mathbf{q}) + P(\mathbf{q})\,, \qquad (3)$$

where $\mathbf{q}$ denotes spatial frequencies in Fourier space, $q = |\mathbf{q}|$, $T(q, z) = 2\sin[zq^2/(2k)]$ describes the Talbot oscillations and $C(\Delta\mathbf{r}) = |\mu(\Delta\mathbf{r})|^2$. Notice the same spatial scaling as in Eq. (2), which allows to map spatial frequencies (Fourier-space coordinates) into transverse displacements (direct-space coordinates). Terms $H(\mathbf{q})$ and $S(\mathbf{q})$ describe the additional contributions to the envelope of the Talbot oscillations due to the spatial frequency response of the detection system and the particle form factor, respectively. Finally, $P(\mathbf{q})$ describes the additive noise contribution mainly coming from shotnoise and readout noise.

THE EXPERIMENTAL SETUP AT THE NCD-SWEET BEAMLINE AT ALBA

We performed experiments at the hard X-ray undulator beamline NCD-SWEET at the ALBA Synchrotron Light Source. The experimental setup is sketched in Fig. 2.

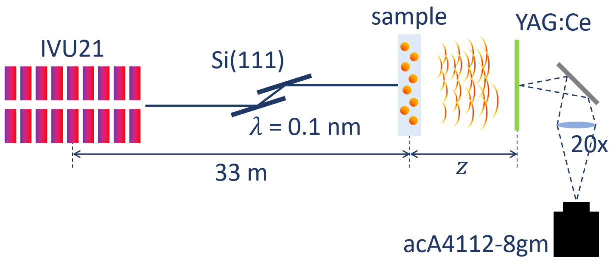

Figure 2: Experimental setup at the NCD-SWEET undulator beamline at ALBA.

A channel-cut Si(111) monochromator selects the photon energy $E = 12.4$ keV ($\lambda = 0.1$ nm), corresponding to the 7th harmonic of the IVU21 in-vacuum undulator. The X-rays impinge onto the sample consisting of a water suspension of silica spheres with diameter $d = 500$ nm, stored in 2-mm-thick capillaries at a distance $Z_0 = 33$ m downstream the undulator center. The volume concentration of the sample is roughly 10 %, which ensures heterodyne conditions as previously mentioned. One capillary is filled with only distilled water to characterize the noise contribution $P(\mathbf{q})$. Heterodyne speckles are recorded at distances z ranging from 2 cm up to 1.2 m downstream the sample. A YAG:Ce scintillator screen with thickness 50 µm is used to convert X-ray photons into visible light. A microscope objective with nominal magnification 20x projects the visible light onto the sensor (Basler acA4112-8gm, with a pixel size of 3.45 µm). A 45-deg mirror is inserted between the scintillator and the relay optics to avoid radiation damage onto the lenses and the sensor due to the transmitted X-ray photons. For each z, we acquire a stack of 50 images to improve statistics. The acquisition frame rate is set to 1 Hz and the random Brownian motions of the sample ensure statistical independence between consecutive speckle images. The main parameters of the NCD-SWEET experimental setup are summarized in Table 1.

Table 1: Main Parameters of the NCD-SWEET Beamline

Parameter	**Symbol**	**Value**
Electron beam energy	E_{beam}	2.98 GeV
Undulator number of periods	N_w	92
Undulator period length	λ_w	21.6 mm
Photon energy	E	12.4 keV
Monochromator bandwidth	$\Delta E/E$	10^{-4}
Radiation wavelength	λ	1 Å
Sample material		SiO_2
Particle diameter	d	500 nm
Distance from undulator center	Z_0	33 m
Sample-detector distance	z	2 cm - 1.2 m

EXPERIMENTAL RESULTS

During the experiments, the beam coupling was varied to test the sensitivity of the technique to different beam sizes. Four different values of the beam coupling were tested: $\kappa = 0.50$ %, $\kappa = 0.65$ % (nominal coupling during operations), $\kappa = 1.60$ % and $\kappa = 2.80$ %. Figure 3 shows an example of the 2D power spectra acquired at the same sample-detector distance under the four different beam configurations.

Power spectra are rotated by roughly 5 degrees due to a relative tilt between the electron beam and the sensor. Nevertheless, the intrinsic 2D nature of the HNFS technique allows to unambiguously identify the horizontal and vertical beam axes regardless of such misalignment.

Qualitatively, the horizontal width of the power spectra (i.e. the horizontal coherence) is always the same for all four coupling values. On the other hand, the vertical width of the power spectra (i.e. the vertical coherence) is progressively decreasing as the beam coupling is increased. We report a direct comparison of vertical profiles in Fig. 3(e) for visual purposes. In terms of beam sizes, this implies that the hor-

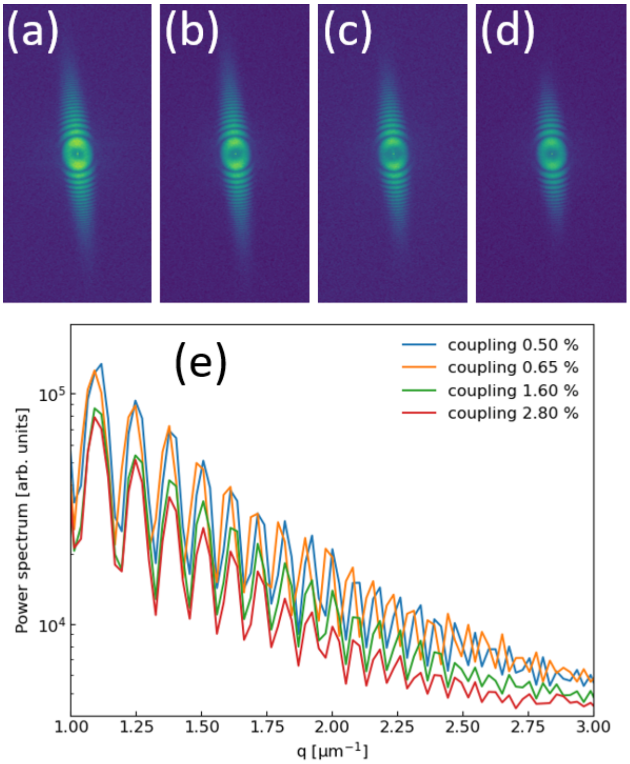

Figure 3: 2D power spectra of heterodyne speckles acquired at the same sample-detector distance under different beam couplings. (a) $\kappa = 0.50\,\%$, (b) $\kappa = 0.65\,\%$, (c) $\kappa = 1.60\,\%$, (d) $\kappa = 2.80\,\%$. (e) Direct comparison of vertical profiles.

izontal beam size is unchanged during the coupling scan, whereas the vertical beam size increases.

Quantitative information on the horizontal and vertical coherence is extracted from the corresponding profiles of 2D power spectra. Using Eq. (3), we characterize the Talbot oscillations as follows:

$$T(q,z)C\left(z\frac{q}{k}\right) = \frac{I(q,z) - P(q)}{H(q)S(q)}\,. \tag{4}$$

The noise term $P(q)$ is measured from the power spectrum of the capillary filled with only water. The contribution due to $H(q)S(q)$, which we will refer to as the calibration function, is determined from the envelope of the Talbot oscillations at the shortest distances. In fact, for $z \rightarrow 0$, $C(zq/k) \rightarrow C(0) = 1$, where the last equality directly comes from the definition of the radiation CCF given in Eq. (1). Therefore, from Eq. (3) we obtain

$$H(q)S(q) = \frac{I(q,z)_{z\rightarrow 0} - P(q)}{T(q,z)} \tag{5}$$

To avoid division by Talbot zeros in Eq. (5), we perform a piece-wise analysis and merge data from a few different distances, taking advantage of the fact that Talbot oscillations change with z.

Finally, coherence data from different sample-detector distances are merged upon the spatial scaling. As it can be noticed from Fig. 4, Talbot maxima and minima collapse onto unique curves when data are plotted as a function of transverse displacements. We refer to these curves as the upper and lower envelopes of the Talbot oscillations, and their decay is then fitted by assuming a Gaussian CCF. In terms of coherence measurements, we stress that the technique is fully self-consistent and the width of the Gaussian CCF, also known as the coherence length of the radiation, is the only free parameter in the entire data reduction procedure. Inversion of data from transverse coherence lengths σ^H_{coh} and σ^V_{coh} into horizontal and vertical beam sizes σ^H_{beam} and σ^V_{beam}, respectively, is done by means of pre-computed Look-Up Tables obtained via extensive simulations [9]. Results are reported in Fig. 5 and in Table 2.

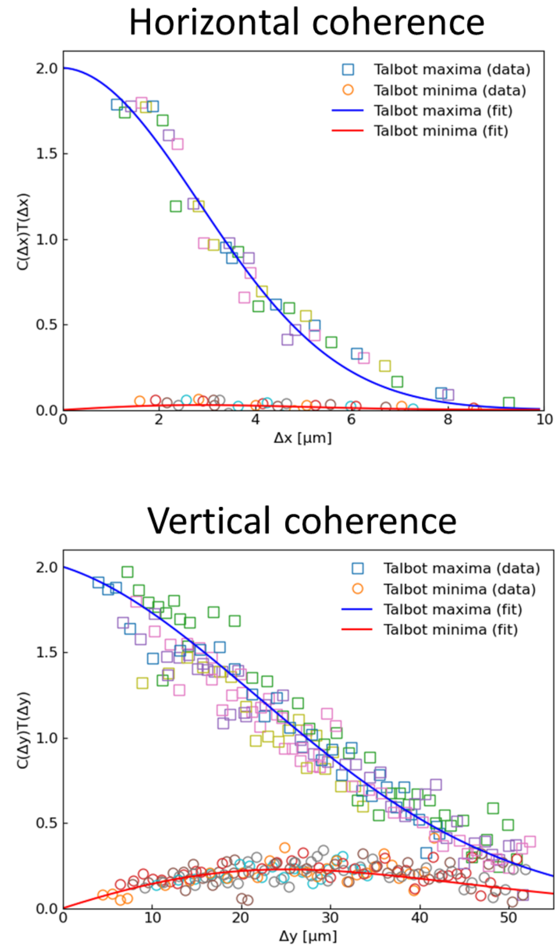

Figure 4: Talbot maxima and minima from different z collapse onto unique curves upon the spatial scaling (data refer to the case $\kappa = 2.80\,\%$). Their decay can be fitted assuming a Gaussian CCF to extract the coherence lengths of the radiation in the (top) horizontal and (bottom) vertical directions.

The measured horizontal beam sizes for the four different values of the beam coupling are all comparable within experimental uncertainties. The average value of 124 μm is in good agreement with the expected value of 129 μm

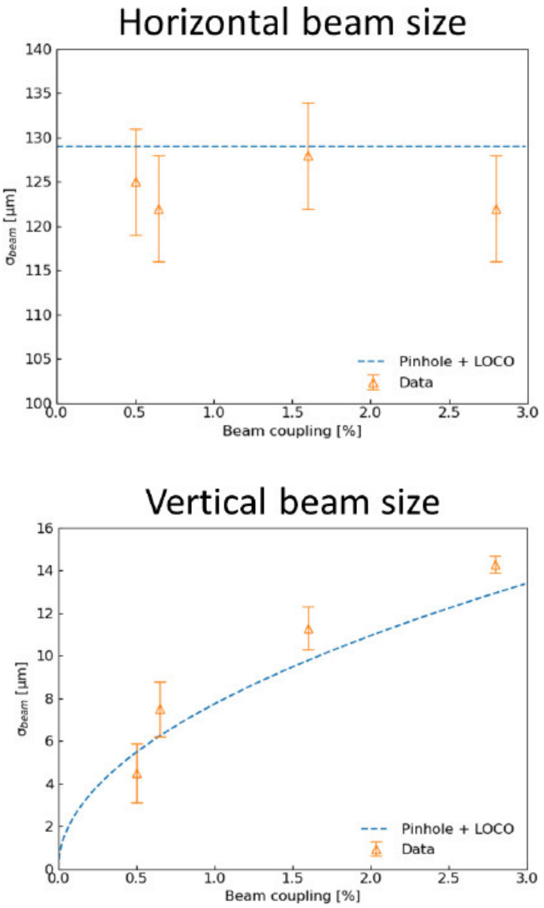

Figure 5: (Top) Horizontal and (bottom) vertical beam sizes as a function of the beam coupling.

from independent estimation based on pinhole and LOCO measurements.

At variance, the vertical beam size increases from roughly 4 µm at coupling 0.50 % to roughly 14 µm at coupling 2.80 %. Measured values are in good agreement with pinhole and LOCO estimations. Discrepancies between measured values and theoretical estimations are observed at the largest couplings, though being limited to less than 15 % (1.5 µm in absolute values). However, the model does not take into account effects, such as dispersion contributions, that might influence beam size predictions at the largest couplings. Finally, to reduce uncertainties on data at the smallest beam couplings, one should access larger sample-detector distances to better sample the high vertical coherence.

CONCLUSIONS

We have shown how the HNFS technique can be effectively used for two-dimensional electron beam size measurements. The method was tested at the NCD-SWEET undulator beamline at ALBA, where the vertical beam size was changed by varying the beam coupling in the storage ring. The measured horizontal beam size is unchanged during the coupling scan and the average value is 124 µm. Contrarily, the vertical beam size changes from roughly 4 µm to roughly 14 µm during the coupling scan. Results along both the horizontal and vertical directions are in good agreement with expectations based on independent pinhole and LOCO measurements. For future experiments, we plan to use some gold-based sample (colloidal gold, gold glass, nanoporous gold) to increse the amount of scattered signal with respect to the current sample, thus improving the overall SNR of the technique. However, unlike the case of the silica sample, effects from the particle form factor and sedimentation should be carefully taken into account and further investigations need to be done.

Table 2: Measured coherence lengths $\sigma_{\text{coh}}^{H,V}$, measured beam sizes $\sigma_{\text{beam}}^{H,V}$ and expected beam sizes $\sigma_{\text{beam, th}}^{H,V}$ based on pinhole and LOCO estimations.

	σ_{coh}^{H}	σ_{beam}^{H}	$\sigma_{\text{beam, th}}^{H}$
$\kappa = 0.50\,\%$	4.2 ± 0.2 µm	125 ± 6 µm	129 µm
$\kappa = 0.65\,\%$	4.3 ± 0.2 µm	122 ± 6 µm	129 µm
$\kappa = 1.60\,\%$	4.1 ± 0.2 µm	126 ± 6 µm	129 µm
$\kappa = 2.80\,\%$	4.3 ± 0.2 µm	122 ± 6 µm	129 µm
	σ_{coh}^{V}	σ_{beam}^{V}	$\sigma_{\text{beam, th}}^{V}$
$\kappa = 0.50\,\%$	105 ± 32 µm	4.5 ± 1.4 µm	5.5 µm
$\kappa = 0.65\,\%$	66 ± 11 µm	7.5 ± 1.3 µm	6.2 µm
$\kappa = 1.60\,\%$	44 ± 4 µm	11.3 ± 1.0 µm	9.8 µm
$\kappa = 2.80\,\%$	36 ± 1 µm	14.3 ± 0.4 µm	12.9 µm

REFERENCES

[1] L. Torino, U. Iriso, “Transverse beam profile reconstruction using synchrotron radiation interferometry”, *Phys. Rev. Accel. Beams.*, vol. 19, p. 122801, 2016.

[2] K. A. Nugent, “Coherent methods in the X-ray sciences”, *Adv. Phys.*, vol. 59, pp. 1–99, 2010.

[3] N. Samadi, X. Shi, L. Dallin, and D. Chapman, “Source size measurement options for low-emittance light sources”, *Phys. Rev. Accel. Beams*, vol. 23, p. 024801, 2020.

[4] J. W. Goodman, *Statistical Optics*, New York, USA, John Wiley and Sons Inc., 2000.

[5] L. Mandel, E. Wolf, *Optical Coherence and Quantum Optics*, Cambridge, UK, Cambridge University Press, 1995.

[6] R. Cerbino, L. Peverini, M. A. C. Potenza, A. Robert, P. Bosecke, and M. Giglio, “X-ray-scattering information obtained from near-field speckle”, *Nat. Phys.*, vol. 4, p. 238, 2008.

[7] M. D. Alaimo, M. A. C. Potenza, M. Manfredda, G. Geloni, M. Sztucki, T. Narayanan, and M. Giglio, “Probing the Transverse Coherence of an Undulator X-Ray Beam Using Brownian Particles”, *Phys. Rev. Lett.*, vol. 103, p. 194805, 2009.

[8] M. Siano, B. Paroli, and M. A. C. Potenza, “Heterodyne Near Field Speckles: from laser light to X-rays”, *Advances in Physics:X*, vol. 6, p. 1891001, 2021.

[9] G. Geloni, E. Saldin, E. Schneidmiller, and M. Yurkov, “Transverse coherence properties of X-ray beams in third-generation synchrotron radiation sources”, *Nucl. Instrum. Method Phys. Res. A*, vol. 588, p. 463, 2008.

STUDIES OF BEAM LOSS MONITORS AT THE CHINA SPALLATION NEUTRON SOURCE*

Tao Yang†,1, Jilei Sun, Jianmin Tian, Lei Zeng, Taoguang Xu, Weiling Huang, Fang Li,
Zhihong Xu, Ruiyang Qiu, Ming Meng, Anxin Wang, Mengyu Liu1, Xiaojun Nie
Institute of High Energy Physics, Chinese Academy of Sciences, Beijing, China
Spallation Neutron Source Science Center, Dongguan, China
1also at University of Chinese Academy of Sciences, Beijing, China

Abstract

Beam loss detection is essential for the machine protection and the fine-tuning of the accelerator to reduce the induced radioactivity. The beam loss monitors (BLM) at the China Spallation Neutron Source (CSNS) are mainly divided into the following types: the coaxial cylindrical ionization chamber (IC) filled with Ar/N_2 gas mixture, Xe, BF_3 gas, and the scintillator with photomultipliers, among which the Ar/N_2 IC is the main type. In the low-energy section of the linac (beam energy <20 MeV), the BF_3 BLMs enclosed by a high-density polyethylene (HDPE) moderator are utilized to detect the beam losses. The Monte Carlo program FLUKA is employed to perform the relevant simulations. This paper presents the summary of the beam-loss detection for the CSNS BLM system.

INTRODUCTION

The CSNS had generated the neutron beam by the spallation reaction of 1.6-GeV protons striking on the tungsten target in August 2017. At present, its beam power is 100 kW with a repetition rate of 25 Hz. In phase II of CSNS, the beam power will be raised to 500 kW and the remaining neutron instruments will be built. A schematic layout of the CSNS phase I complex is shown in Fig. 1. The CSNS accelerator is mainly comprised of a 50-keV H^- ion source, a 3-MeV radio frequency quadrupole (RFQ) accelerator, an 80-MeV drift tube linac (DTL), and a 1.6 GeV proton rapid cycle synchrotron (RCS) [1]. The main design parameters of CSNS are listed in Table 1.

Table 1: The Basic Design Parameters of the CSNS

Design parameter	**Value**
Beam power (kW)	100
Linac energy (MeV)	80
Beam current in the linac (mA)	15
Extraction energy (GeV)	1.6
Proton per pulse	1.56×10^{13}
Repetition rate (Hz)	25
Linac RF frequency (MHz)	324
Target material	Tungsten

Beam loss may bring out high energy deposition to damage the accelerator components or produce undesired radioactivation, so it is one of the most important issues during the running and commissioning of an accelerator facility [2-4]. Monitors based on the IC and plastic-scintillator with photomultipliers are the two types of BLMs used in the CSNS. There are 190 IC-type BLMs (preliminary and the subsequent newly added amount) along the entire beam line at the CSNS, mostly filled with Ar/N_2 mixture gas, several filled with Xe or BF_3 gas, and there are also 15 scintillator-based BLMs. IC is the main BLM type for the CSNS as well as other hadron machines due to its robustness to radiation damage, large dynamic range, little maintenance, and ease for calibration [5-8].

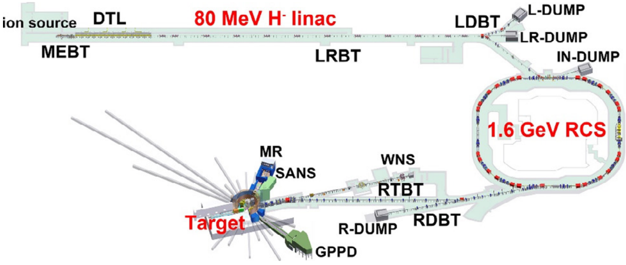

Figure 1: Schematics of the CSNS complex.

In this paper, the performance and some beam loss experiments of our IC BLMs are presented. The relevant Monte Carlo simulations with FLUKA are also executed to verify the experiments, simulates the induced current of different loss scenarios and then evaluates the suitability of electronics, and provide the basis of schemes for some special detections, e.g., the beam-loss detection in the low-energy section of linac for a proton accelerator based on the moderated secondary neutrons.

THE CSNS IC BLM

The schematic and the photograph of the CSNS IC BLM are shown in Fig. 2. The sensitive volume is the tube-like region enclosed by the outer and inner electrode with an effective length of 17.4 cm. The working gas is a mixture of argon and nitrogen with a volume ratio of 70:30 at a total pressure of 1 atm. The standard bias voltage is set to be -2100 V which falls well in the intermediate part of the plateau tested by the ^{60}Co source in our previous research [9]. The high voltage is applied on the outer electrode, while electrons are collected on the inner electrode. All electrodes and coverages of BLMs are made of stainless steel, and the insulators are made of alumina ceramics.

---

*This work is supported by the National Natural Science Foundation of China (Grants No. 11575219, No. 11705215, and No. 11805220).

† yangt@ihep.ac.cn

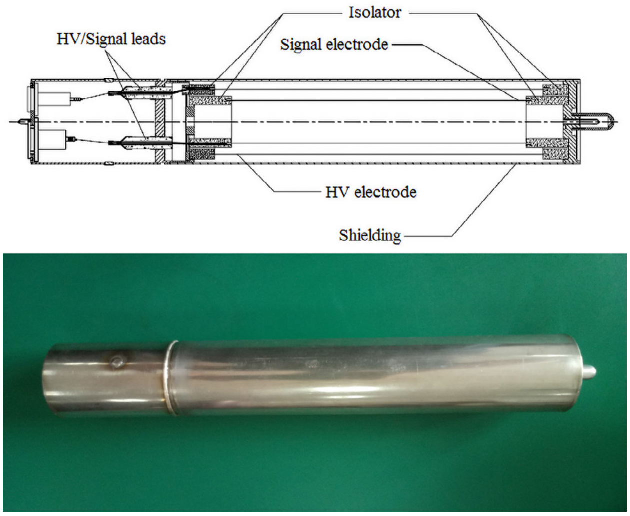

Figure 2: The schematic and the photograph of the CSNS IC BLM.

Beam losses can generally be categorized into the slow loss (regular loss) and fast loss (irregular loss) [3]. The slow losses can be caused by various effects: Touschek effect, collisions, transversal and longitudinal diffusion, residual gas scattering, beam instability, etc. The slow losses are typically not avoidable due to the intrinsic characteristics of beam transport. The fast losses are often caused by the beam misalignment or some operation failures, such as the fault of the rf or magnet power supply system, which may cause serious damage to accelerator components.

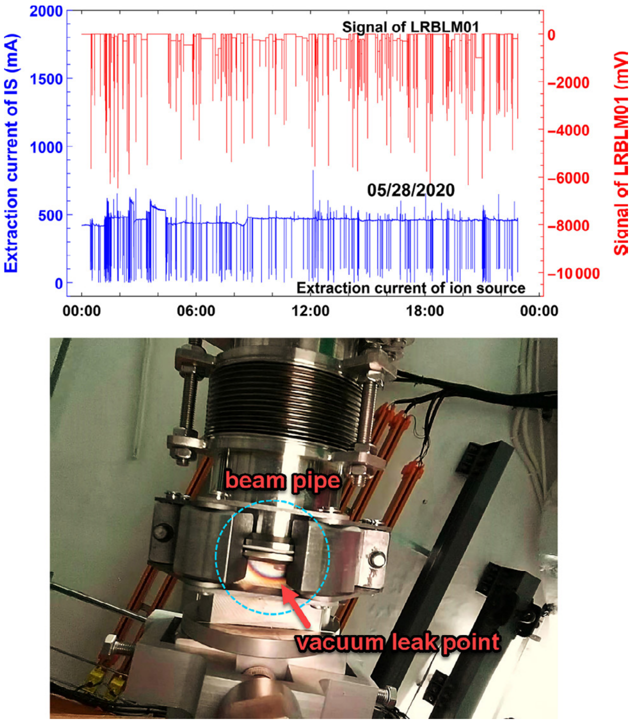

Figure 3: Two typical beam loss categories at the CSNS. The top plot depicts the regular loss caused by the beam instability originated from the sparking of the ion source, and the bottom photo shows an irregular beam loss event leading to a vacuum leak accident at the CSNS LRBT part.

According to the operation experiences at the CSNS, the most frequent causes of regular beam loss are beam instability, residual gas scattering, and space charge effects, while the most frequent cause of irregular loss is the failure of the magnet power supply system. Figure 3 shows two typical beam loss categories at the CSNS. The top plot presents a BLM signal versus the synchronous extraction-current signal of the ion source, which apparently reveals the time relevance of the BLM signal on the beam instability originated from the sparking of the ion source. The bottom photo shows an irregular beam loss event leading to a vacuum leak accident caused by the wrong setting of the switch magnet at the CSNS linac to ring beam transport line (LRBT), which caused a partial melting in the beam pipe and led to a vacuum leak accident.

THE BEAM LOSS EXPERIMENT IN THE MIXED RADIATION FIELD

A good way to validate Monte Carlo simulations and test the sensitivity of BLMs is to create an intentional controlled beam loss and record the monitor responses. Figure 4 depicts the experiment layout of the beam loss detection in the temporary beam diagnostic system during the project construction. The diagnostic system includes a double-slit type emittance monitor and a Faraday cup. The H^- beam energy was ~21.67 MeV, and the current was ~10 mA. Moving the emittance monitor could generate variable beam losses, and the lost beam current was obtained by the subtraction value of the currents measured by the forward and backward beam current transformers (CTs).

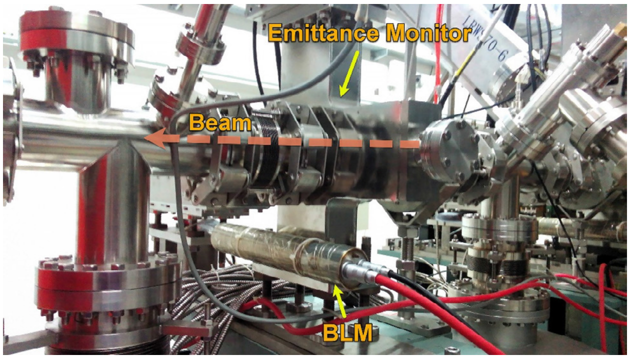

Figure 4: The experiment layout of the controlled beam loss detection using an emittance monitor in the temporary beam diagnostic system during the projection construction.

During the experiment, the emittance monitor was moved in the *x*-direction to intercept the beam. The simulation results of energy deposition in BLM are finally normalized to the ionization current according to the lost beam current. H^- ions cannot be defined in FLUKA, here we treat the H^- ion as proton in simulations because the two electrons energy of H^- ion (~11.9 keV) is rather small compared to the proton energy. The two electrons mainly undergo the ionization energy loss process nearby the loss location, and thus the contribution of stripped electrons to the BLM signal could be neglected.

ISBN: 978-3-95450-230-1 ISSN: 2673-5350 doi:10.18429/JACoW-IBIC2021-TUOB01

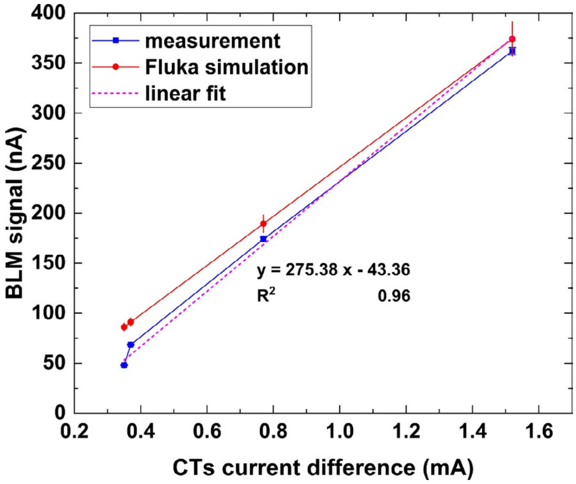

Figure 5: Experimental and simulated BLM signal in the mixed radiation field generated by the movable emittance monitor.

Figure 5 shows the experimental and simulated BLM signal, as can be seen, simulations are basically consistent with the experimental results, and both of which present an approximate linear relation with the lost beam current. Applying the two-steps method in FLUKA, the signal contribution of each particle can be obtained. The result indicates that the secondary photons induced by the beam loss dominate the signal (~85%) for this experiment configuration.

MONTE CARLO SIMULATIONS FOR THE BEAM LOSS RESPONSES

Different loss scenarios are assumed to evaluate the BLM responses, which mainly involves the beam loss on the drift tube in the linac part, loss on the beam pipe of the straight section, quadrupole, and dipole in the RCS part. The uniformly distributed and localized losses are assumed as the two main loss patterns in simulations. Figure 6 illustrates the loss scenarios. The impact angle takes the value of 1 mrad for the scenario I~V. Scenarios II and III simulate the BLM responses of uniform regular losses due to the residual gas scattering, space charge effect, or beam instability, etc. Scenario I, IV, and V simulate responses of localized losses due to aperture limitations. Scenario VI simulates responses of an irregular loss caused by a malfunction of the bending magnet. The lost-particle direction of scenario VI is parallel to the tangential direction of the beam orbit at the entrance of the dipole, which corresponds to an irregular beam loss caused by the beam misalignment or magnet malfunction. Beam energy ranges from 3~80 MeV in the linac part, and from 80~1600 MeV in the RCS part. The quadrupole and dipole magnet for simulations are the frequently used types (RCS206Q, RCS160B) in the RCS part of CSNS.

In order to obtain the macroscopic ionization current responses of BLMs in different scenarios, the responses per lost primary should be multiplied with the beam loss intensity. 1 W/m for a uniformly distributed beam loss is usually considered for most proton accelerators as a threshold. Consequently, the beam loss rate is assumed to be 1 W/m for scenario II and III corresponding to a uniform loss in the RCS part. While a 0.1% loss is assumed for scenarios I, IV, and V corresponding to a localized loss. The full loss of beam bunch for scenario VI is a hypothetical extreme case, which represents the worst possible accident caused by the failure of the bending-magnet power supply system.

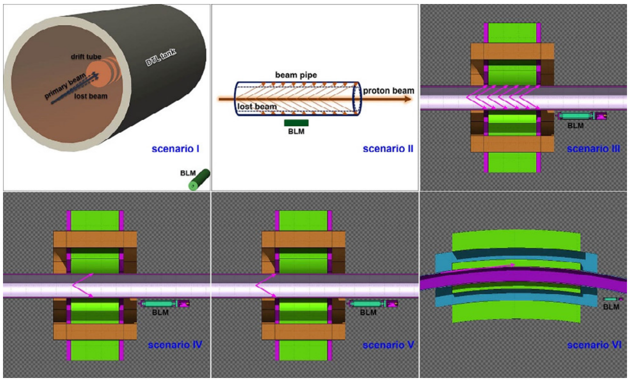

Figure 6: Calculation models of the assumed beam loss scenarios.

The simulated current results for different beam loss scenarios are shown in Fig. 7, and the dashed lines correspond to the corrected current due to the space charge effects. The current for 0.1% loss of scenario I increases with the beam energy and ranges from 0.25 to 2222.09 pA. Although simulations get a positive result for beam energy below 20 MeV, however, due to the sensitivity of electronics (200 pA~20 μA), this beam loss signal couldn't be efficiently detected if the loss rate is very low. In practice, beam loss can be hardly detected for beam energy below 20 MeV during the actual machine operation in CSNS, which is consistent with the simulated results.

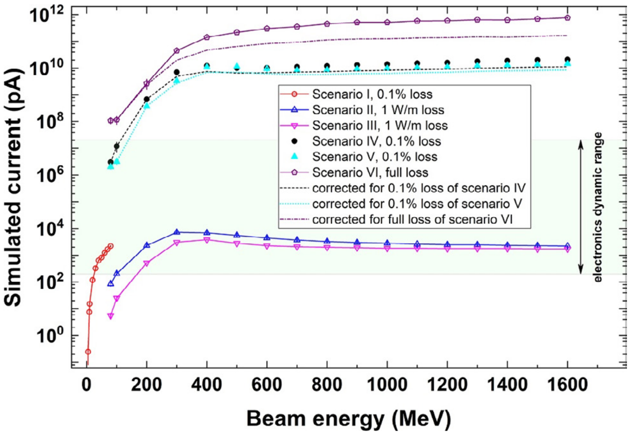

Figure 7: Simulated ionization current for scenarios with the corresponding loss rate. The dashed lines correspond to the corrected current due to the space charge effects.

Considering 200 pA~20 μA the dynamic range of the BLM electronics used in CSNS, BLMs could detect a 0.1% loss level in the CSNS DTL part for beam energy higher than 20 MeV. The simulated current for 1 W/m loss of scenario II~III increases first and then declines with the increase of beam energy, and the current range falls within the electronics dynamic range and in the order of nA except for the beam energy below ~200 MeV. The loss rate of 1W/m means fewer protons for higher beam energy, which corresponds to the slight decline tendency for the 1 W/m loss of scenario II~III. In addition, the ionization rates of scenario I~III with the respective loss rates are far below the critical value ~9.82×10^7 ions/(cm^3·μs) [9], so the current correction due to the space charge effect is needless.

Current responses increase first and then reach a plateau for 0.1% loss of scenario IV~V and full loss of scenario VI. The simulated current for scenario IV and V with 0.1% loss is far beyond the upper limit of input of electronics except for the beam energy below 200 MeV, which however is not a serious issue from a monitoring perspective since this over-threshold signal will trigger the machine protection system to shut down the beam. Disregarding the saturation of electronics, the ionization rate already exceeds the critical value for the three scenarios with the corresponding loss rates when the beam energy is greater than 200~300 MeV, meanwhile, space charge effects begin to play an important role. The dashed lines depict the corrected currents, the collection efficiency declines from 0.70 to 0.53 for scenario IV with 0.1% loss when the beam energy rises from 300 MeV to 1.6 GeV, and it declines from 0.85 to 0.59 for scenario V with 0.1% loss within the same energy range. While for the case of full loss of scenario VI, the collection efficiency declines from 0.89 at 200 MeV to 0.22 at 1.6 GeV. The loss rate on the order of ~10^{-5} in one bunch for scenario IV~VI will give a current within the electronics dynamic range, nevertheless, this loss rate would not bring about the space charge effects.

BEAM LOSS DETECTION IN THE LOW-ENERGY SECTION OF THE LINAC

Beam loss detection in the low energy section of CSNS linac (i.e., <20 MeV) is a difficult task using the Ar/N_2 IC since the thick DTL tank (~4.2 cm) has a significant shielding effect on the secondary particles. However, neutrons will leak out of the tank, which may be easier to be detected if suitable neutron converters are selected.

We design an easily assembled and validated scheme to do this research, which mainly employs an IC filled with BF_3 gas and a neutron moderator. Figure 8 depicts the experimental layout and the FLUKA geometric model of the two types of BLMs installed near the DTL tank. BLMs are installed at 2/3 of the first tank length where the nominal beam energy is about 15 MeV. The BF_3 (96%-enriched ^{10}B) monitor is enclosed by a 7.5-cm-thick HDPE moderator. The monitors' responses are acquired to validate the feasibility of the scheme.

The energy deposition in the sensitive volume of two BLMs given by FLUKA is respectively 0.1335 (±2.1%) eV/primary and 1.115×10^{-4} (±7.1%) eV/primary for the BF_3 and Ar/N_2 BLM. Thus the beam loss signal of the BF_3 monitor is about 1197 (±89) times that of Ar/N_2 BLM, which is a considerable increasement for the signal.

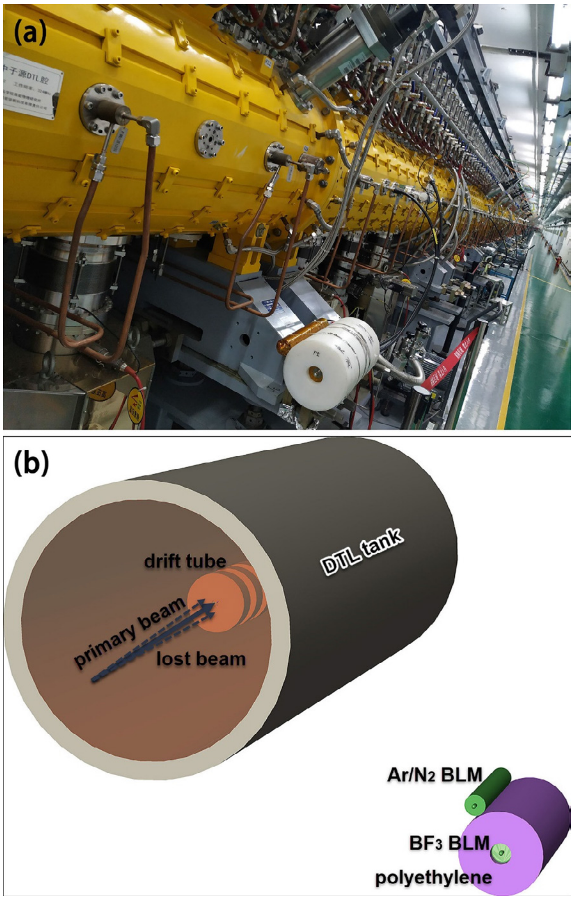

Figure 8: (a) Experimental layout of two types of BLM installed at the first tank of DTL, and (b) the geometric model implemented in FLUKA.

In order to validate the signal ratio of beam loss for the two types of BLM experimentally, we intentionally mismatch the magnet parameters to generate a beam-orbit distortion in a single-shot mode. The waveforms in a loss event are shown in Fig. 9. The Ar/N_2 monitor presents an observable beam loss signal, while the waveform of the BF_3 monitor reaches an oversaturated level. The saturation region of the BF_3 signal could be complemented using the CR-(RC)^n model [10]. The fitting amplitude is respectively 149.5 (±2.0) V for the BF_3 monitor and 91 (±0.87) mV for the Ar/N_2 monitor. The signal of the BF3 monitor is about 1642 (±27) times higher than that of the Ar/N_2 monitor, which is approximately consistent with the FLUKA simulation in the order of magnitude. The difference is caused by the uncertainty of the actual beam loss. Through simulations and experiments, it demonstrates that the detection of thermal neutrons is an effective way to detect the beam loss in the low energy section of a proton accelerator.

ISBN: 978-3-95450-230-1 ISSN: 2673-5350 doi:10.18429/JACoW-IBIC2021-TUOB01

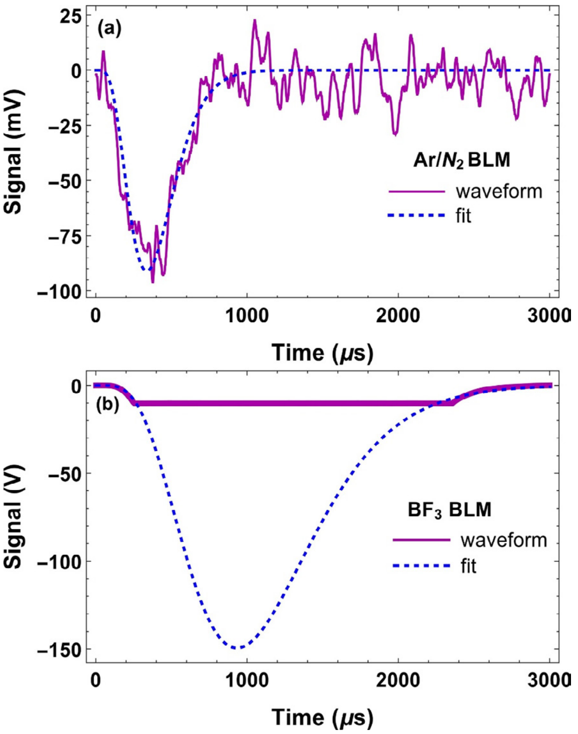

Figure 9: The experimental waveforms of the beam loss signal and the waveform fit in a controlled beam loss event for the (a) Ar/N_2 BLM and (b) BF_3 BLM.

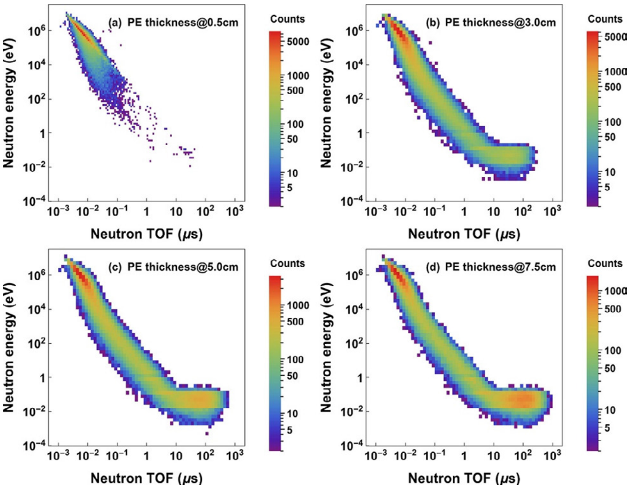

Figure 10: The number of neutrons arriving in the BF_3 monitor plotted versus the neutron TOF and energy in a 2D histogram. The amount of lost protons is 10^{11}.

Figure 10 illustrates a 2D histogram of neutron arriving in the BF3 monitor as a function of the neutron time of flight (TOF) and the neutron energy. A thermal neutron zone emerges as increasing the PE thickness as seen from Fig. 10, and the neutron TOF roughly ranges from ~ns to hundreds of μs depending on the HDPE thickness. Similar experimental results of the time responses have been reported for the slow-module of neutron sensitive BLM system in ESS, which also presents a maximum time-delay of a few hundreds of μs caused by the moderator layer [11]. The moderator has a delay effect on the beam loss signal, which is caused by the thermalization and migration process of neutrons [12], and a long delay time is unfavorable for the machine protection, so the moderator thickness should be optimized to balance the detection efficiency and the signal delay in the future applications.

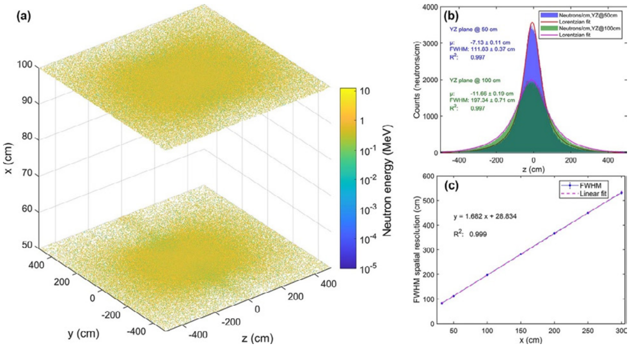

Figure 11: (a) The neutron hit maps on the YZ plane respectively at 50 and 100 cm for the number of lost particles set as 10^9, (b) the neutron one-dimensional distribution by projecting the 2D hit maps on the z-axis, and (c) the spatial resolution of neutron distribution vs the positions of YZ plane.

Multiple scattering of neutrons will lead to a nonnegligible uncertainty for the loss location by the detection of neutrons. Therefore, the spatial resolution of the source-position of beam loss should be investigated. The problem is simplified in simulation by placing several planes at different positions out of the linac DTL to score the neutron hit positions. The planes are perpendicular to the x-axis with a size of 10×10 m^2. The beam energy is set to be 15 MeV and the loss position is set at z=0 with a loss angle of 1 mrad. Figure 11 shows the hit maps of secondary neutrons induced by 10^9 lost primaries and the neutron distribution along the z-axis direction. Neutrons spread wider on the YZ plane at 100 cm compared to 50 cm, which implies that a better spatial resolution can be obtained for a neutron-sensitive BLM closer to the DTL tank. The full width at half maximum (FWHM) is adopted as the spatial resolution. The spatial resolution is respectively 111.83 cm and 197.34 cm for the YZ plane at 50 cm and 100 cm. Figure 11(c) reveals a linear relation of the spatial resolution with locations of the YZ plane. In our experimental configurations, the simulated spatial relation is ~2 m.

CONCLUSION

Beam loss detection is one of the most important issues in a proton accelerator. This paper presents the experimental and Monte Carlo studies for BLMs used in CSNS. We have executed the beam loss measurement in a mixed radiation field with a moveable slit-type emittance monitor on the temporary test stand during the CSNS project construction. The BLM responses in several assumed beam loss scenarios from the linac DTL to the RCS part in the CSNS are also performed, which gives a rough dynamic range of BLM and the signal tendency with the increase of beam energy. The ionization-current responses are obtained according to different loss scenarios and rates, and the space charge effects are also taken into account. In addition, we study the beam loss monitoring through detection of the moderated neutrons in the low energy section of the DTL part where the low fluences of secondary particles bring out the detection difficulty. The BF_3 monitor was adopted to detect neutrons in the secondary radiation field. Both simulation and experiment show the signal of the BF_3 monitor is about three orders of magnitude higher than that of Ar/N_2 monitor. Finally, the spatial resolution for the neutron-based beam loss detection is estimated from the distribution of secondary neutrons.

REFERENCES

[1] J. Wei *et al.*, “China Spallation Neutron Source: Design, R&D, and outlook”, *Nucl. Instrum. Methods Phys. Res., Sect. A*, vol. 600, pp. 10-13, 2009.

[2] A. Lechner *et al.*, “Energy Deposition Studies for Fast Losses during LHC Injection Failures”, in *Proc. 4th Int. Particle Accelerator Conf. (IPAC'13)*, Shanghai, China, May 2013, paper TUPFI027, pp. 1397-1399.

[3] K. Wittenburg, “Beam loss monitors”, CERN, Geneva, Switzerland, Rep. CERN-2009-005, 2009.

[4] A. Smolyakov, E. Mustafin, N. Pyka, and P. J. Spiller, “Radiation Damage Studies for the Slow Extraction from SIS100”, in *Proc. 11th European Particle Accelerator Conf. (EPAC'08)*, Genoa, Italy, Jun. 2008, paper THPP102, pp. 3602-3604.

[5] E. B. Holzer *et al.*, “Beam Loss Monitoring System for the LHC”, in *Proc. IEEE Nuclear Science Symposium*, Fajardo, PR, Oct. 2005, p. 1052.

[6] D. Gassner, P. Cameron, C. Mi, and R. L. Witkover, “Spallation Neutron Source Beam Loss Monitor System”, in *Proc. 20th Particle Accelerator Conf. (PAC'03)*, Portland, OR, USA, May 2003, paper WPPB017, p. 2447.

[7] L. Tchelidze, H. Hassanzadegan, A. Jansson, and M. Jarosz, “Beam Loss Monitoring at the European Spallation Source”, in *Proc. 2nd Int. Beam Instrumentation Conf. (IBIC'13)*, Oxford, UK, Sep. 2013, paper WEPC45, pp. 795-798.

[8] R. Witkover, E. Zitvogel, and R. Michnoff, “RHIC Beam Loss Monitor System Design”, in *Proc. 17th Particle Accelerator Conf. (PAC'97)*, Vancouver, Canada, May 1997, paper 8P067, p. 2218.

[9] T. Yang *et al.*, “Experimental studies and Monte Carlo simulations for beam loss monitors”, *Phys. Rev. Accel. Beams* vol. 24, p. 032804, 2021.

[10] G. F. Knoll, *Radiation Detection and Measurement*. New York, NY, USA: John Wiley & Sons, Inc., 2010.

[11] L. Segui *et al.*, “A Micromegas Based Neutron Detector for the ESS Beam Loss Monitoring”, in *Proc. 7th Int. Beam Instrumentation Conf. (IBIC'18)*, Shanghai, China, Sep. 2018, pp. 211-214. `doi:10.18429/JACoW-IBIC2018-TUPA02`

[12] D. G. Cacuci, *Handbook of Nuclear Engineering*. Boston, MA, USA: Springer, 2010.

ISBN: 978-3-95450-230-1 ISSN: 2673-5350 doi:10.18429/JACoW-IBIC2021-TUOB02

CMOS BASED BEAM LOSS MONITOR AT THE SLS

C. Ozkan Loch†, A. M. Stampfli, R. Ischebeck, Paul Scherrer Institute, Villigen, Switzerland

Abstract

For several years, the SLS storage ring was not equipped with loss monitors to observe loss patterns around the storage ring; hence, any understanding of the operational losses, accidental losses, or manual beam dumps was missing. Initially, a long quartz fibre (350 m) was installed around the ring to locate losses, and read out with a photomultiplier tube. With the long fibre, we garnered some understanding yet, it was not easy to locate the position of the losses. Hence, we opted for scintillator based fibre loss monitors, installed in choice locations. All the fibres are read out together with a single CMOS based 2.3 MP camera. A device was built with 28 channels. Ten fibres were connected and are located in the injection kicker in the BTRL and three arcs of the storage ring. With these loss monitors, we were able to detect and locate the position of losses due to injection and sudden beam dumps/losses.

In this paper, we will introduce the concept and the components of this monitor, and present the data processing algorithm that identifies the individual fibres in the images, allowing us to locate and track the losses in the SLS storage ring.

INTRODUCTION

At SLS 2.0 [1], loss monitors will be used to monitor beam losses from the Booster-to-Ring transfer line down to the storage ring and around it, to detect low charge on-axis injection and provide loss patterns around the storage ring during filling and top-up operation. For commissioning and daily operation of the storage ring and insertion device protection, loss monitors that can detect “fast” losses (~100 ms) from faults or beam perturbations from injection are needed. The fast losses can be correlated to sudden changes in lifetime. We also need to identify “slow” losses that influence lifetime during standard operation.

At SwissFEL, a beam loss monitor system based on plastic fibre scintillators and photomultiplier tubes as detectors was developed [2]. This system was custom built for the stringent requirements of SwissFEL, where hardware interface to the machine protection system was required for dynamic regulation of beam rate to ensure operability of the facility within the allowed limits.

For the SLS 2.0, we took the SwissFEL BLM approach of distributed scintillating fibres and exchanged the single photomultiplier tube (PMT) per fibre readout with a CMOS camera because the camera would allow observing multiple fibres, simultaneously. A proof of principle experiment was carried out at the end of the injection straight by losing single injected bunches into the SLS storage ring. The CMOS camera was able to detect losses from the scintillating fibres. A prototype BLM system was built in-house that can accommodate 28 fibres. Presented in this paper is the CMOS based BLM, the image processing and first results from the system installed in the SLS storage ring.

LOSS MONITOR SYSTEM

The beam losses cause scintillation light inside the scintillating fibres (Saint Gobain, BCF12 [3]), which is carried out of the tunnel with duplex plastic optical fibres (POF). One end of the POF is connected to an LED [4] for calibration purposes and the other end of the fibre is connected to the camera. The fibres from the tunnel connect to the front panel. The box that contains all the components of the system can be seen in Fig. 1a.

The beam loss system has the following functionalities:

- camera and LED control
- read the CMOS with a computer
- image the light from the fibres
- identify the individual fibres
- calibrate the fibres with LEDs
- display the measurements graphically
- archive the loss data

Hardware

The fibres that connect to the front panel are coupled to a bunch of short fibres inside the box. These fibres are arranged in a dense array by a holder that also serves to shield the fibres from each other and the external light (Fig. 1b). This holder also doubles as a polishing holder for the fibres. All fibre ends have been polished for improved light throughput.

The camera images the fibre holder with two objectives together in a tandem configuration. The focus of both objectives is set to infinity, such that the fibres, located at the flange focal distance of the first objective lens, are imaged onto the CMOS sensor located at the flange focal distance of the second lens. This system allows for a good light collection efficiency with two large-aperture, infinity-corrected objectives. The imaging ratio is the ratio of the focal lengths of the two lenses. We used objectives with f=50 mm and f=16 mm, respectively, resulting in a magnification of M = –1/3.125.

The image sensor is read out by a Jetson Nano [5] through a USB port. Software, written in Python, processes the images and makes the data available to the control system.

A fully functioning setup is installed in the rack at the SLS in a compact housing. All components inside the box and the front panels can be seen in Fig. 1.

---

† cigdem.ozkan@psi.ch

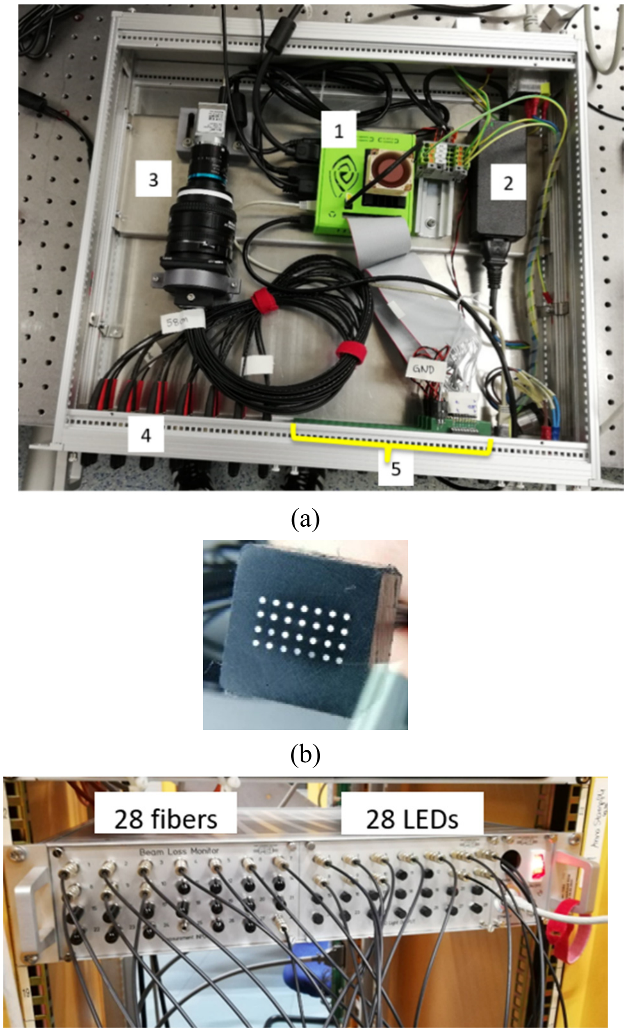

(a)

(b)

(c)

Figure 1: (a) Inside the BLM system, where 1 is the Jetson nano CPU to control system and process data, 2 is the Jetson nano's power supply, 3 is the camera with the objective lenses in tandem, 4 is where the fibres from the tunnel are connected, and 5 are the LEDs. (b) Shows the fibre holder that is imaged by the camera. (c) Front panel of the system mounted in an electronics rack at the SLS.

Image Analysis

The raw camera image is cropped around the fibres as this area is smaller than the entire field-of-view. Since the fibres are arranged in a rectangular pattern of 4x7, a grid can be placed over the image to check the exact alignment of the fibre holder.

All LEDs are switched on to create a bit. The bit mask is then multiplied to every image acquired with the camera mask (see Fig 2). The sum of the area of each fibre yields a value that indicates the light intensity from each fibre, or the loss detected.

All LEDs are imaged one-by-one with a short fibre, and the composite LED image is also used to normalize the variation of intensity between the LEDs (Fig. 3). Once the LED responses have been normalized, this "flat field" is used to normalize the fibre responses that connect from the LEDs, to the scintillators inside the tunnel and back to the front panel for imaging.

Once the fibre responses are "flattened", or normalized to the average intensity of the fibres, the images can be subtracted by the dark image (no beam) and fibre areas are integrated to track beam losses.

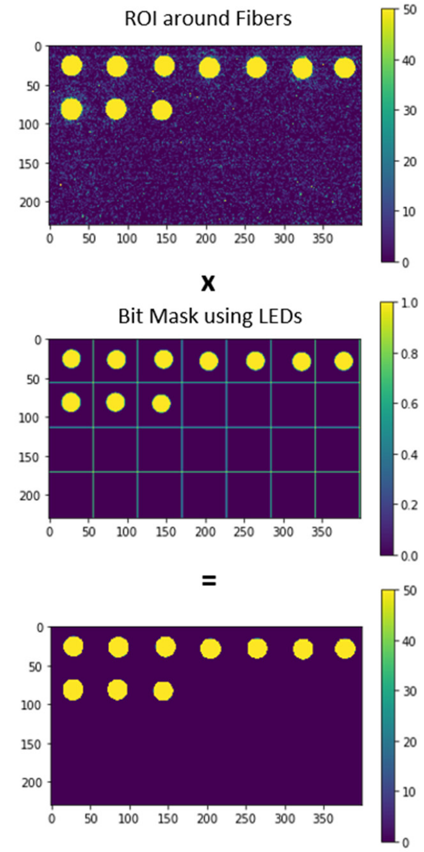

Figure 2: Figure shows how the fibres areas identified. The integrated fibre area gives the loss value.

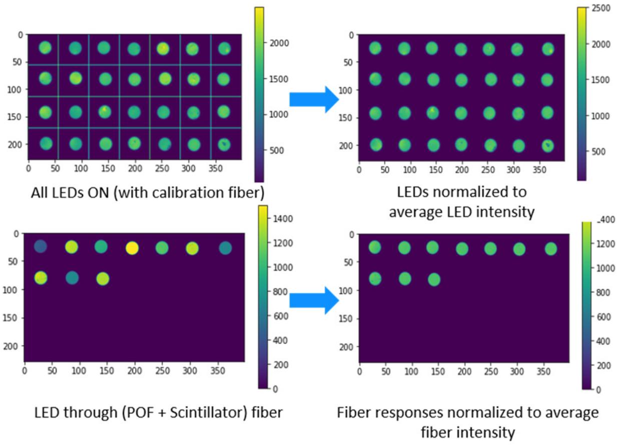

Figure 3: The LEDs are normalized to their average intensity with a short calibration fibre, and then the normalized LED response is used to normalize the response of the POF and scintillator fibres in the tunnel.

A dark image is calculated by averaging 100 dark images. The dark images are treated same as the raw images and the intensities are subtracted from the fibre intensity values from the raw images.

First Results with Beam

Ten POF duplex fibres, of about 48 m length, were installed at SLS to detect losses from a quarter of the machine. Scintillator coils were made from 2 m scintillator fibres and wrapped around 3D printed holders. An existing map of the radiation hotspots, provided by the radiation safety group, was used to install the scintillator coils in the locations with high probability of seeing losses (Fig. 4).

Data was taken during the filling of the SLS ring after a shutdown. On the day of the measurements, the SLS was experiencing problems with the Booster RF amplifier. Whenever the beam was lost, all the fibres scintillated and when the beam was manually dumped, two fibres scintillated strongly.

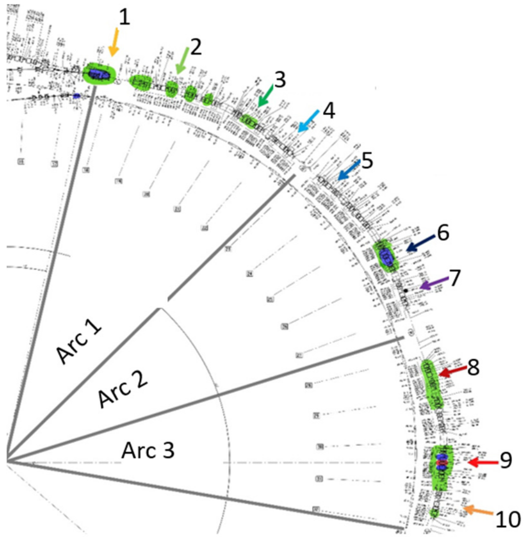

Figure 4: Partial map of SLS showing the locations of the radiation measurements and the ten scintillator fibres.

All disturbances as well as the manual beam dump were measured and can be seen in the plot in Fig. 5 as jumps in fibre intensities. The radiation hotspot corresponds to the last two fibres in the third arc (fibres 9 and 10). This location corresponds to the hotspot measured by the radiation protection group (downstream of second dipole in arc 3), and supports the conjecture that the beam is lost in one location.

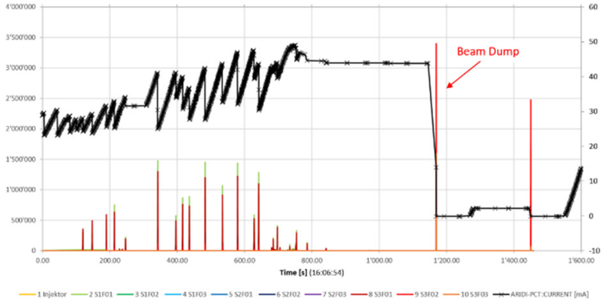

Figure 5: Losses seen over time during machine start up. Booster RF related problems were creating losses in the storage ring that were detected by all fibres. The manual beam dump was detected by two fibres (fibres 9 and 10) that match the hotspot.

CONCLUSION

CMOS based BLM system has proven useful in locating losses around the storage ring, hence, it is good for surveillance. Since a single system hosts 28 fibres, the spatial resolution in locating losses can be easily more than four locations per arc.

Due to the use of a single CMOS camera, this loss monitor system does not allow for turn-by-turn loss detection. However, it does detect injection losses. The CMOS camera makes the system cost effective for the purpose of locating losses.

This system shall be tested at an Undulator exit as a measure of sensitivity for Undulator alignment and protection.

REFERENCES

[1] Aiba M., *et. al.*, “SLS-2 Conceptual Design Report”, `https://www.dora.lib4ri.ch/psi/islandora/object/psi%3A34977/datastream/PDF/Streun-2017-SLS-2._Conceptual_design_report-%28published_version%29.pdf`

[2] C. Ozkan Loch *et. al.*, “Loss monitoring for undulator protection at SwissFEL”, *Phys. Rev. Accel. Beams*, vol. 23, p. 102804, 2020.

[3] Saint Gobain, Scintillating Fibres, `https://www.crystals.saint-gobain.com/products/scintillating-fiber`

[4] HFBR-1505AZ, `https://www.broadcom.com/products/fiber-optic-modules-components/industrial/industrial-control-general-purpose/sercos-fieldbus/hfbr-1505az`

[5] NVDIA Jetson Nano Development Kit B0, `https://developer.nvidia.com/embedded/jetson-nano-developer-kit`

PARTICLE AND PHOTON BEAM MEASUREMENTS BASED ON VIBRATING WIRE

S.G. Arutunian, G.S. Harutyunyan, E.G. Lazareva, A.V. Margaryan
Yerevan Physics Institute, 0036, Yerevan, Armenia
M. Chung, D. Kwak, Ulsan National Institute of Science and Technology, 44919, Ulsan, Korea

Abstract

The instrumentation introduced herein is based on high-quality vibrating wire resonator, in which the excitation of wire oscillation is made through the interaction of the wire current with a permanent magnetic field. The high sensitivity of the oscillation frequency to the wire temperature allows the resonator to be used for measuring charged-particle/X-ray/laser/neutron beam profiles with wide dynamic range. The beam flux falling on the wire increases its temperature from fractions of mK to hundreds of degrees. Another application method is to use the vibrating wire as a moving target, in which signals created at beam interaction with the wire are measured synchronously with the wire oscillation frequency. This method allows to effectively separate the background signals. Also, the well-defined (in space) and stable (in time) form of the wire oscillation allows the vibrating wire to be used directly as a miniature scanner for measuring thin beams. The latter two methods enable a significant reduction in scanning time compared to the original thermal-based method.

INTRODUCTION

Vibrating wire (VW) resonators have a number of attractive characteristics: high quality factor, long-term stability, practical absence of irreversible drifts caused by component aging. On the basis of such resonators, we have developed several instruments for measuring the profiles of beams of different nature (charged particles, electromagnetic radiation in a wide wavelength range, from infrared to hard gamma rays, neutrons). Three principles of operation of such instruments have been proposed. The first uses the dependence of the resonator frequency on the wire tension, which is determined by the flux of particles falling on the wire. The second one uses the signals of secondary particles in the interaction of the beam with the wire, and measurements are made synchronously with the string oscillations. In the third, the wire oscillations are used as a miniature scanner to scan beams in the micrometer size range.

THERMAL METHOD

The Vibrating Wire Monitor (VWM) on the thermal principle can be described as a wire stretched between two clips mounted on the basis. Part of the wire is placed in a magnetic field created by permanent magnets. The oscillations of the wire at natural frequency are excited by the interaction of the current flowing through the wire with the magnetic field. The wire is connected to the input of operational amplifier with positive feedback, which leads to autogeneration of natural oscillations of the wire (see [1] for details). The particles of the measured beam heat the wire, leading to a change in its tension and, accordingly, the frequency of oscillations, which serves as the output signal of the VWM. VWMs have good relative accuracy (several units per 1e-6), long-term stability (many months) and a large dynamic range (up to 6 orders of magnitude).

Let us describe the operation of the VWM using the example of a profiling station for the Cyclon18 proton accelerator with the particle energy of 18 MeV [2] (the results of studies will be published in more detail in [3]). Figure 1 shows the main units of such a station.

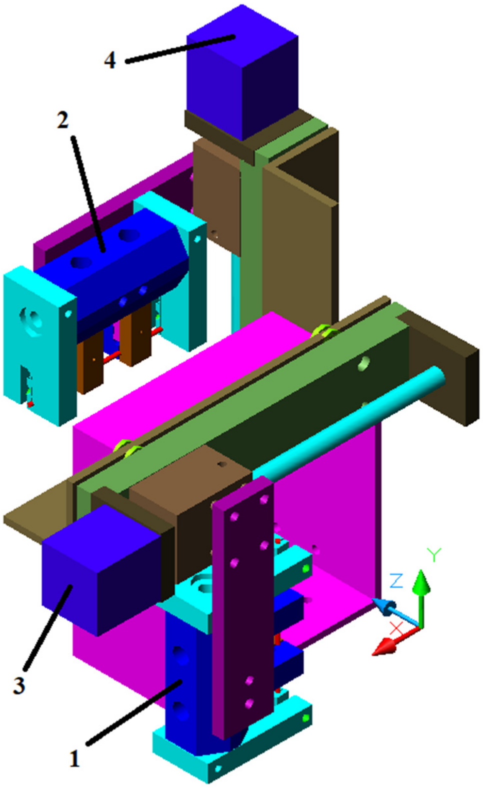

Figure 1: Profiling station for horizontal and vertical scanning, equipped with VWMs (1 and 2) and linear drive systems (3 and 4). Beam extends along the Z-axis.

Note that thermal monitors have response times ranging from fractions of a second to several seconds, depending on the wire material, the sensor geometry, and the atmosphere/vacuum in which the sensor is used. For the VWM used here (stainless steel string of length 56 mm, and 100 µm in diameter), this time is about 0.46 sec. The beam current was controlled by changing the current of the ion source located in the center of the cyclotron.

ISBN: 978-3-95450-230-1 ISSN: 2673-5350 doi:10.18429/JACoW-IBIC2021-TUPP03

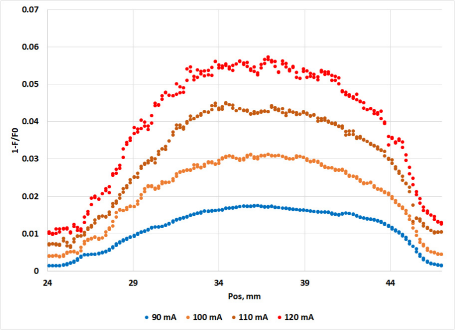

Figure 2: Vertical profiles of the proton beam for different values of ion source current (with scanning speed of 0.2 mm/s).

Figure 2 shows the results of vertical scans at ion source currents of 90 mA, 100 mA, 110 mA, and 120 mA.To estimate the beam current, we will use a formula that relates the relative frequency measurement to the current of particles exposed on the wire I_p [1]:

$$\frac{\Delta F}{F_0} = -\frac{E}{2\sigma_0}\frac{\alpha_W \varepsilon_{heat}(\delta_p I_p / e)}{\left[8\lambda S / L + 4\varepsilon\sigma_{ST\text{-}B} T_0^3 \pi dL + \alpha_{conv}\pi dL\right]}$$

where d, L, S, are wire diameter, length and cross-section; E, $\alpha_W, \lambda, \varepsilon$ are wire elasticity modulus, thermal expansion coefficient, thermal conductivity, and wire emissivity (set to 0.3); σ_0, F_0 are wire initial tension and corresponding frequency (second harmonic); α_{conv} is convection losses coefficient (set to 36 W/m^2/K), δ_p is proton ionization losses in wire (calculated by Bethe-Bloch formula and for d = 100 µm is about 1.3 MeV), ε_{heat} is coefficient of transfer ionization losses to heat (set to 0.3). Substituting the tabulated values for other parameters, we obtain that for an ion source current of 90 mA the total proton beam current is on the order of 1 µA (the corresponding distribution in Fig. 2 was fitted by a Gaussian function with an amplitude of 0.0175 and RMS distribution of 6.5 mm). Presented in Fig. 3 dependences of ion source current and proton current on maximum of obtained in Fig. 2 distributions allow to calibrate the proton beam current by values of ion source current.

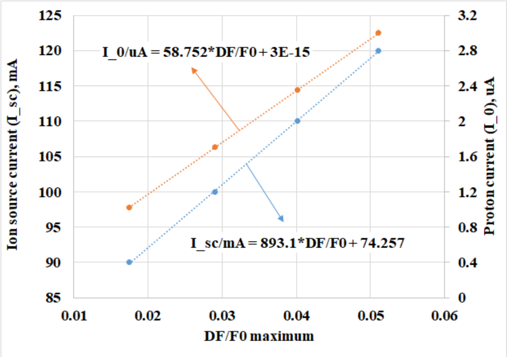

Figure 3: Dependences of ion source current and proton current on maximum distributions in Fig. 2.

VWM for Elastic Properties Investigation

VMWs can also be applied for measuring neutron fluxes penetrating the wire. It is proposed to use a vibrating wire exposed in the neutron flux, to observe the effect of neutron irradiation impact on the elastic properties of metals. The effect is caused by both neutron capture (mainly for neutrons with energy less than 1 MeV) and lattice disturbance during the atom-neutron collisions with energy more than 1 MeV. We suggest to use a two-wire monitor, in which wires are located in the same thermal space and are separated to significantly differentiate the exposure of neutrons to the wires. A prerequisite for a successful proposal is the long-term stability of VWM.

VW AS A RESONANCE TARGET

It is often necessary to produce a faster scanning of the beam. For this we proposed a hybrid method based on measurement of secondary particles during beam scattering on a wire (of traditional wire scanners), but using the vibrating wire as a target. Synchronous measurements with wire oscillations allow detecting only the signal generating from the scattering of the beam on the wire. This resonant method enables fast beam profiling in the presence of a high level of background. The concept was suggested in [4], and for photon beams it was realized in [5]. The method can be applied to different types of beams by simply choosing an appropriate detector for each case. For photon beams, fast photodiodes can be used, and for charged particles, scintillators combined with photomultipliers etc. (see Fig. 4).

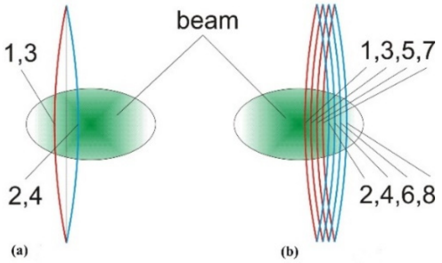

Figure 4: For odd indices the wire at its leftmost position, and for even indices the wire at its rightmost position: (a) the scanner is stationary; (b) the scanner is moving.

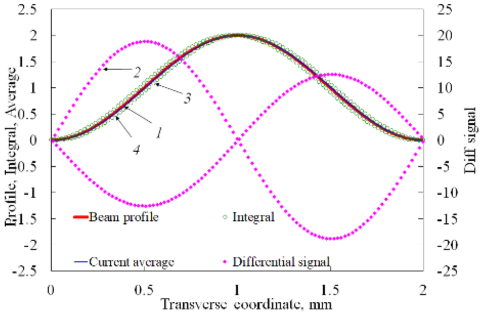

Figure 5: 1 - initial profile, 2 - differentiation of synchronized signal, 3 - integral of differential signal with sign inversing, 4 - current average of 3 practically recovers initial profile 1.

For a certain data processing algorithm, the scanning speed can significantly exceed the speed of the wire during its oscillations [6]. The algorithm is as follows: a differential signal on the extreme positions of the vibrating wire is calculated, this signal is integrated (with inversion of the sign on the half-periods of wire oscillation) and then the current average procedure is applied to it. An example of using such an algorithm is shown in Fig. 5 - here the speed of scanning is 10 times higher than the average speed of the wire on one half-period of oscillations. The method was successfully tested in the laser beam tomography experiment [7].

VW AS A MINIATURE SCANNER

The idea of using the motion of a vibrating wire as a miniature scanner has been suggested in [5]. The amplitude of vibrations of the developed resonators of the vibrating wire reaches a few hundred micrometers. Such a range of wire motion is well suited for profiling micrometer-size beams. The first experimental results were obtained and a criterion of reliability of the results was determined in [8]. The experimental technique with laser beams has been further improved in [9, 10].

To implement the method, it is essential to have a strictly defined motion of the wire in space. In particular, it is desirable to exclude the mixing of harmonics of transverse vibrations in two orthogonal planes. For this purpose, in [10], a new magnetic field system with single poles providing the flatness of oscillations was developed.

It was also important to ensure fast measurement of secondary particles (for laser radiation these are photons reflected from the string surface). Fast photodiodes and fast operational amplifiers were used in [10]. The time of one measurement was about 10 μs, which required the development of an algorithm for processing the primary experimental data, taking into account the time derivative of the signal (calculated as the slope coefficient of the linear regression for seven current data points).

The motion of the wire center in all noted works was assumed to be sinusoidal. Under the conditions of the scheme of autogeneration of natural oscillations, i.e., periodic influence of the electronic circuit on the oscillation process, this statement required a proof. For this purpose, the following experiment was carried out in [10]: the oscillation feeding circuit was abruptly cut off and the observation of oscillations of the wire, which passed to the mode of free oscillations with damping, was continued. The measurements showed that the structure of the signals reflected from the wire did not change.

In addition, in [10], a technique for stitching profiles at displaced positions of the vibrating wire resonator was developed. The comparison of such profiles made it possible to determine the absolute parameters of the wire motion and to reconstruct the beam profiles in absolute coordinates. In the experiments, the profile of the focused beam of the semiconductor laser was measured, and the supply voltage was chosen so that inhomogeneities appeared in the beam profile. The results of the measurements are shown in Fig. 6.

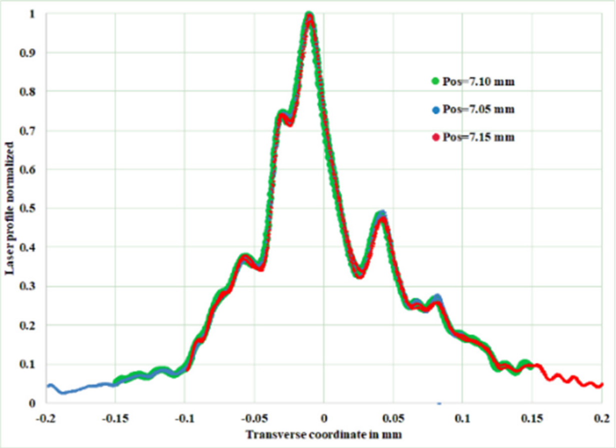

Figure 6: Reconstruction of the laser beam profile using the numerical differentiation of the primary photodiode signal.

Scanning of the profile in several positions of the vibrating wire monitor allowed us to restore the profile of the beam in absolute coordinates. The method of determining the laser beam profile by superimposing the overlapped profiles in several resonator positions of the vibrating wire is similar to the creation of a panoramic image by the stitching procedure. Image stitching is the process that combines images with overlapped areas to form an image with a wide view. Usually, after inputting a series of images with overlapped areas, feature matching is applied to find the corresponding points of the images for stitching, and then, translation is done to align them properly.

CONCLUSION

The beam diagnostic methods discussed above are united by the idea of using a vibrating wire as a sensitive element / resonant target / miniature scanner. Note that progress in one of these directions gives an opportunity to modify sensors for other methods of use. The unique properties of vibrating wire resonators allow one to search for more and more new possibilities for their use, such as studying the properties of neutron-irradiated wires.

ACKNOWLEDGMENTS

This work was supported by the RA MES SCS in the frame of project 20APP-2G001 and the Research Grants Support Program 2021 from UNIST Basic Science Institute.

REFERENCES

[1] S. G. Arutunian *et al.*, “Vibrating wire monitor: Versatile instrumentation for particle and photon beam measurements with wide dynamic range”, *Journal of Instrumentation*, vol. 16, no. R01001, pp. 1-33, 2021.

[2] `https://www.petct-armenia.am`

[3] M. Aginian *et al.*, “Vibrating wire station for horizontal and vertical profiling of proton beam of Cyclotron C18 in air”, *J. Cont. Phys.*, to be published.

[4] S. G. Arutunian and A. V. Margaryan, “Oscillating Wire as a ``Resonant Target'' for Beam Transversal Gradient Investigation”, in *Proc. 5th Int. Particle Accelerator Conf. (IPAC'14)*, Dresden, Germany, Jun. 2014, pp. 3412-3414. `doi:10.18429/JACoW-IPAC2014-THPME076`

[5] S. G. Arutunian *et al*., “Fast resonant target vibrating wire scanner for photon beam”, *Rev. Sci. Instrum.,* vol. 87, p. 023108, 2016.

[6] M. A. Aginian *et al*., “Development of New Algorithm in the Method of a Resonant Vibrating Target for Large Scanning Speeds”, *J. Cont. Phys*., vol. 54, p. 232, 2019.

[7] M. A. Aginian *et al.*, “New method in medical tomography based on vibrating wire: bench-test experiment on laser beam”, *IOP Journal of Physics: Conf. Series 826,* vol. 012016, pp. 1-11, 2017.

[8] E. G. Lazareva, “Vibrating wire for profile measurements of thin beams in particle accelerators: Preliminary tests using a laser beam”, *J. Cont. Phys*., vol. 53, p. 136, 2018.

[9] S. G. Arutunian *et al*., “A method for profile measurements of small transverse size beams by means of a vibrating wire”, *Rev. Sci. Instrum.*, vol. 90, p. 073302, 2019.

[10] S. G. Arutunian *et al.*, “Characterization of micron-size laser beam using a vibrating wire as a miniature scanner”, *Rev. Sci. Instrum.*, vol. 92, p. 033303, 2021.

SPACE-CHARGE AND OTHER EFFECTS IN FERMILAB BOOSTER AND IOTA RINGS' IONIZATION PROFILE MONITORS [*]

V. Shiltsev[†], Fermi Accelerator Laboratory, Batavia, IL, USA

Abstract

Ionization profile monitors (IPMs) are widely used in accelerators for non-destructive and fast diagnostics of high energy particle beams. At low beam intensities, initial velocities of the secondaries to collect (ions or electrons) result in the IPM profile smearing. At high beam intensities, the space-charge forces make the measured IPM profiles significantly different from those of the beams. We analyze dynamics of the secondaries in IPMs, describe an effective algorithm to reconstruct the beam sizes from the measured IPM profiles and apply it to the Fermilab 8 GeV proton Booster and 70 MeV/c IOTA ring IPMs.

INTRODUCTION

Particle accelerators heavily rely on precise diagnostics and control of critical beam parameters such as intensity, pulse structure, position, transverse and longitudinal beam sizes, halo, etc [1]. Ionization profile monitors (IPMs) [2–7] are fast and non-destructive diagnostic tools used in proton and ion linacs, colliders, and rapid cycling synchrotrons (RCS) [8–10]. They operate by collecting ions or electrons created after the ionization of residual vacuum molecules by high energy charged particle beams [1, 11], which are then guided to a detector by a uniform external electric field E_{ext}. The detector is usually made of many thin parallel strips, whose individual signals are registered to make the beam profile signal ready for processing – see Fig.1.

Space-charge forces of the primary beams make the measured IPM profiles different from those of the beams and must be correctly accounted for. Brute force numerical modeling [12, 13] can successfully reproduce experimentally measured IPM profiles but offer limited predictive physics insights. Several phenomenological fits were proposed to relate the measured beam size σ_m and the initial beam size σ_0 - see, e.g., [3, 12, 14, 15] - but despite acceptable data approximation, they are not based on clear physical reasons for as many four free parameters and exponents. Below we briefly describe an effective algorithm developed in [16] to reconstruct the beam sizes from measured IPM profiles and known key parameters, such as high-energy beam intensity N and IPM extracting field E_{ext} is the guiding electric field. Based on that theory, we discuss the Booster IPMs measurements and possible upgrades, as well as specifications for the IOTA ring IPMs.

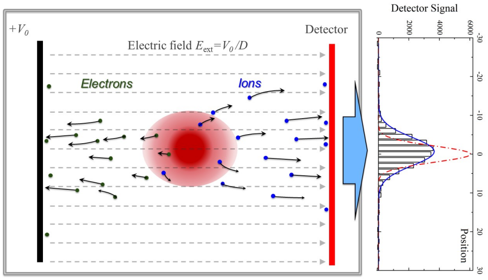

Figure 1: Transverse cross-section of a high energy beam (red) in vertical IPM and schematically shown motion of secondary ions (blue dots) and electrons (green dots) under the impact of horizontal extracting electric field E_{ext} and space-charge field of the primary beam. The diagram on the right shows the IPM detector signals at right before extraction of an intense beam of $N = 4.6 \cdot 10^{12}$ protons from the Fermilab Booster synchrotron. The actual rms proton vertical size of the proton beam is $\sigma_0 = 2.1$ mm - see dashed red curve, while the rms width of the IPM signal is σ_m =3.6 mm, see blue line for the Gaussian fit.

SPACE-CHARGE DRIVEN IPM PROFILE EXPANSION

Ref. [16] presents a final-form solution of the general equations of transverse motion of non-relativistic ions with charge Ze and mass M born in the acts of ionization of the residual gas molecules by a high energy proton beam passing through IPM with extracting external electric field $E_{\text{ext}} = V_0/D$ due to the voltage gradient V_0 across the IPM gap D. No guiding external magnetic field is assumed. IPMs usually operate with electric fields $E_{\text{ext}} \sim O$(100-1000 V/mm) which significantly exceed the space-charge field $E^{\text{SC}} \sim O$(1-10 V/mm) and that assumption helps to solve the equations of motion.

Important beam parameters of the high energy beam are its current $J(t)$, velocity v_p and rms transverse size σ_0. The space-charge potential of such beam is $U_{SC} = J/(4\pi\epsilon_0 v_p) \approx 30[\text{V/A}]J/\beta_p$, $\beta_p = v_p/c$, c is the speed of light, and ϵ_0 is the permittivity of vacuum [17]. Three characteristic times are of importance for the analysis: i) a characteristic time for the secondaries to get extracted out of the beam by the external electric field $\tau_0 = \sqrt{\frac{2M\sigma_0}{ZeE_{\text{ext}}}} = \tau_2\sqrt{\frac{\sigma_0}{d}}$; ii) time for secondary particle to reaches the IPM detector plane $\tau_2 = \sqrt{\frac{2Md}{ZeE_{\text{ext}}}}$, where d is the average distance from the beam center to the detector; and iii) a characteristic expansion time due to the space-charge $\tau_1 = \left(\frac{eZU_{SC}}{M\sigma_0^2}\right)^{-1/2}$.

Proton beam space-charge fields result in *proportional magnification of the IPM profile* of the distribution of the secondary particles, i.e., $\sigma_m = \sigma_0 \cdot h$. Under a reasonable

---

[*] This manuscript has been authored by Fermi Research Alliance, LLC under Contract No. DE-AC02-07CH11359 with the U.S. Department of Energy, Office of Science, Office of High Energy Physics.

[†] shiltsev@fnal.gov

assumption of DC or slow varying proton current $J(t) = J$, the rms transverse size of the IPM profile at the time when the secondary particle reaches the IPM detector $t = \tau_2 \gg \tau_0$ is found as:

$$\sigma_m = \sigma_0 \cdot h \approx \sigma_0 \cdot \Big[1 + \frac{2U_{SC}}{E_{\text{ext}}\sigma_0} \Big(\frac{\Gamma(\frac{1}{4})}{3} \sqrt{\frac{d}{\sigma_0}} - \frac{\sqrt{\pi}}{2} \Big) \Big] . \quad (1)$$

The gamma-function $\Gamma(\frac{1}{4}) \approx 3.625$. The space-charge magnification factor h is determined only by the space-charge potential U_{SC}, the primary beam size σ_0, the IPM extracting field E_{ext}, and the beam-to-MCP distance d but *it does not depend on the type of secondary species* (their mass and charge, etc). Equation (1) can be easily solved, and the original σ_0 can be found from σ_m with other IPM and beam parameters known.

A similar analysis for uniform, rather than Gaussian, primary proton beam current density distribution with radius a results in an exact solution in elementary functions that is very close to Eq. (1), with the numerical factor $2\Gamma(1/4)/3 \approx 2.42$ replaced by $(4\sqrt{2}/3) \approx 1.88$, and substitution of equivalent $\sigma_0 = a/2$.

The effect of the high-energy beam current $J(t)$ time structure, such as in bunched beams, depends on the rms bunch length τ_b and time between bunches t_b and can be approximated by substitution $U_{SC} \to U_{SC}(1 + t_b/\tau_0)$. See [16] for details as well analysis of the extreme case of short and rare bunches $\tau_b \ll (\tau_0, \tau_1, \tau_2) \ll t_b$.

The effect of the high energy beam size aspect ratio $R = \sigma_x/\sigma_y$ is relatively weak, too. Indeed, the space-charge factor $1/\tau_1^2$ scales as $2/(1+R)$ while the characteristic time $\tau_0 \propto \sqrt{R}$. Therefore, the magnification factor H – which is proportional to the product τ_0/τ_1^2 – scales as $2\sqrt{R}/(1+R)$. The latter is relatively small, i.e, 0.94 for $R = 0.5$, and can be safely neglected for most common cases of $h \leq 2$.

To account for initial velocities of the secondaries $v_{0,y}$, one can assume them to be random with the rms value of $\sqrt{2\mathscr{E}_i/M}$ and get in quadrature addition to Eq. (1):

$$\sigma_m^2 = \sigma_0^2 h^2 (U_{SC}, \sigma_0, E_{\text{ext}}, d) + \Big(\frac{4\mathscr{E}_i d}{ZeE_{\text{ext}}} \Big) . \quad (2)$$

The types of IPMs are distinguished by the species they collect - electrons or ions. The initial kinetic energy $\mathscr{E}_i$ for ionization electrons is about 35 eV needed on average for ion-electron pair production by protons in hydrogen [18]. Corresponding smearing Eq. (2) of the particle position measured by the IPM is about $\sigma_T = D\sqrt{2\mathscr{E}_i/ZeV_0}$, that is some 6 mm for a typical gap D = 100 mm and voltages as high as V_0 = 20 kV. That is absolutely unacceptable for millimeter-scale or smaller primary beam sizes and the electron-collecting IPMs usually have to use a focusing external magnetic field B_x, parallel to the extracting electric field, to suppress the smearing. Physics principles, advantage, and disadvantages of the IPMs with a magnetic field are discussed in [19].

As for ions, their initial kinetic energy is smaller and depends on their kind and the type of reaction. For diatomic gases, the most relevant process is dissociative ionization by the primary fast protons, i.e., $p + H_2 \to p + H + H^+$ with typical kinetic energy of the H^+ of the order of a few eV [20]. Corresponding smearing of the profile σ_T in the ion-collecting IPMs is $O(1\text{ mm})$ [21]. These IPMs do not require an external magnetic field and, therefore, are usually of smaller size, simpler design, and lower cost. Two such monitors – vertical and horizontal– are installed in the Fermilab Booster rapid cycling synchrotron (RCS) and we apply our analysis to their experimentally measured profiles [22, 23].

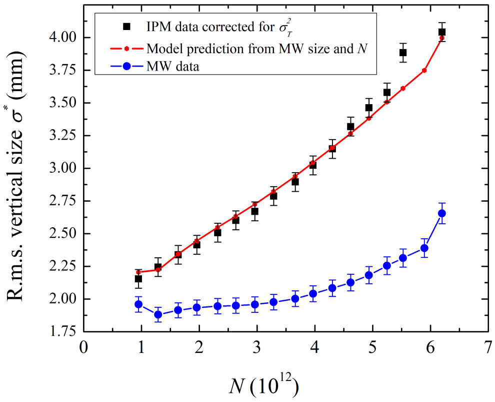

Figure 2: The Fermilab Booster IPM vertical rms beam size σ^* right before beam extraction (V_0 = 24 kV, D = 103 mm, black squares) [16, 22] vs the total proton beam intensity N. The theoretical predication of this paper's Eq. (1) (red line) is calculated using the initial beam sizes σ_0 as measured by the Multi-Wires emittance monitor (blue line). The measured IPM rms sizes σ_m are corrected for the intensity independent smearing $\sigma^* = \sqrt{\sigma_m^2(N) - \sigma_T^2}$, with $\sigma_T^2 = 2.7\text{ mm}^2$.

APPLICATION FOR FERMILAB BOOSTER IPM

The Fermilab Booster [24] is a 474 m circumference, alternating-gradient 15 Hz RCS accelerating protons from 0.4 GeV at injection to 8.0 GeV at extraction in 33.3 ms, or about 20,000 turns – half of the magnet cycle period. Correspondingly, all proton beam parameters (intensity, positions, bunch length, emittances) as well as accelerating RF frequencies and voltage significantly vary in the cycle. The typical total intensity of 84 circulating proton bunches is about $N = 4.6 \cdot 10^{12}$. The Booster proton beam dynamics is quite complex leading to the beam emittance growth and particle losses during the acceleration [22] which set limits on the high power operation of the entire Fermilab complex of accelerators for high energy neutrino physics [25, 26]. Fast diagnostics of the proton beam size is, therefore, of critical importance for the Booster operations and upgrades.

There are two types of instruments to measure beam sizes in the Booster – the Multi-Wires and IPMs. The Multi-Wires are intercepting devices installed in the Booster extraction beamline. The Multi-Wires (harps of 48 wires spaced by 1 mm) beam size measurements data are presumed to be intensity independent and accurate to some 2-3%. The IPMs operate in the ion collection mode and report the average rms beam sizes (determined by the Gaussian fits of the profiles) every turn (about 2 µs).

Besides the space-charge expansion and the effect of the initial ion velocities Eq. (2), the IPM intensity independent profile smearing can be caused by a finite separation between the individual IPM charge collection strips (total of 40, $\Delta = 1.5$ mm apart), angular misalignment of the long and narrow strips with respect to the high energy beam trajectory, and by non-uniformity of the extraction electric field in the operational IPM aperture and these effects can be taken into account by cross-calibration of low-intensity beam sizes measured by the IPM σ_m and by the Multi-Wires σ_{MW}, or by other appropriate beam size monitors [1, 9, 22, 27–30]. Comparison of the Booster IPM and Multi-Wires data at various beam intensities yields $\sigma_T^2 = \lim_{N\to 0}\left(\sigma_m^2(N) - \sigma_{MW}^2(N)\right) = 2.8 \pm 0.1\ \mathrm{mm}^2$ [22].

At high intensity, the average space-charge potential of the Booster proton beam is $U_{SC} \approx 14[\mathrm{V}]\cdot N/(4.6\cdot 10^{12})$. Typical rms proton bunch length and bunch-to-bunch spacing are $\tau_b \approx 2-3$ ns, $t_b \approx 19$ ns. Characteristic times for the IPM with $D = 103$ mm and $V_0 = 24$ kV are $\tau_b \approx 2-3$ ns, $t_b \approx 19$ ns, $\tau_0 \approx 22$ ns, $\tau_1 \approx 67$ ns (for $N = 6\cdot 10^{12}$) and $\tau_2 \approx 110$ ns. Therefore, the beam profile expansion factor h can be calculated by using Eq. (1) in which the original σ_0 is taken from the Multi-Wires data and with the beam-to-MCP distance $d \approx D/2 = 52$ mm. To take into account the time structure of the Booster bunched beam, the rms profile expansion coefficient h Eq. (1) needs to be augmented by a numerical factor $[1 + t_b/\tau_0]$. The resulting rms vertical IPM beam size estimates $h\sigma_0$ are found to be in excellent agreement with the measured IPM rms sizes $\sigma^* = \sqrt{\sigma_m^2(N) - \sigma_T^2}$ measured over a broad range of beam intensities as illustrated in Fig. 2. One can see that the space-charge induced IPM profile expansion of the extracted beam (8 GeV proton kinetic energy) grows with the beam intensity and become quite large, $h - 1 \simeq 0.7$, at the nominal N. The instrumental smearing σ_T adds another ~(10-15)%. For operational monitoring of the emittance evolution over the 33 ms acceleration ramp, it is important to account for : a) the beam obit motion as the space-charge expansion depends on the distance d from the beam orbit to the IPM collection plate; b) $O(10\%)$ variations of the beta-functions at the IPM locations during the ramp; c) significant changes in the beam bunching factor.

Knowing σ_T, N and the IPM extracting field V_0/D one can easily reverse Eq. (1) and find the original proton beam σ_0 from the measured and corrected σ^*, see, e.g., [22]. Figure 3 illustrates the result of such analysis for the measured profiles of the Booster beam with $N = 4.62\cdot 10^{12}$. There, the red curve is for the rms vertical beam size $\sigma_m(t)$ as measured by the IPM at each of 20 thousand turns of the Booster acceleration cycle; the black line represents the beam size after correction for the intensity independent smearing σ^*; and, finally, the true proton rms beam size σ_0 was reconstructed following the algorithm of Eqs. (1) and (2) and is represented by the blue line. One can see that the overall beam size correction is about 20% early in the Booster acceleration cycle when the true rms beam size σ_0 is about 5.3 mm. At the end of the acceleration cycle from 400 MeV to 8 GeV, accounting for the space-charge effect results in a very large correction from 3.7 mm to 2.2 mm rms. Also, one can see that the reconstructed IPM size at the end of the acceleration cycle matches well the extracted beam size measured by the Multi-Wires, as indicated by a black open circle with error bars at the right of Fig. 3.

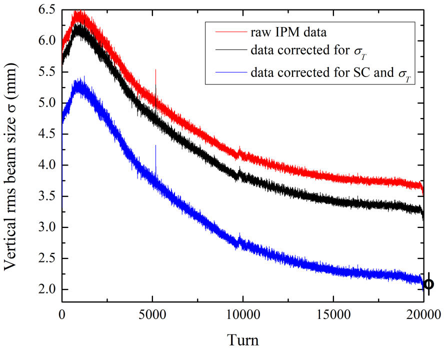

Figure 3: An example of reconstruction of vertical rms proton beam size in 33 ms (20000 turns) acceleration cycle of the Fermilab 8 GeV Booster synchrotron with the total beam intensity of $N = 4.6\cdot 10^{12}$: time dependence of the original IPM data (red), the data corrected for smearing effects due to σ_T (black) and the same data after additional correction for the space-charge expansion (blue). The open black circle with error bars at the left represents the measured Multi-Wires beam size of the extracted beam.

IPMS FOR BOOSTER UPGRADE AND IOTA

There are plans to further upgrade the Fermilab proton complex from the current world-leading level of ~840 kW of average 120 GeV proton beam power on the neutrino target to over 1.2 MW at the start of the LBNF/DUNE experiment in the second half of the 2020s via replacement of the existing 40 years old 400 MeV normal-conducting Linac with a modern CW-capable 800 MeV superconducting RF linear accelerator (PIP-II, see [31]). The corresponding upgrade of the Booster IPMs will be needed, too, for two reasons. First of all, the PIP-II linac will provide about 50% increase in the Booster beam intensity to some $N = 6.5\cdot 10^{12}$ and, consequently, the IPM space-charge expansion factor will grow to $h \approx 2.0$ making it very hard to account for it and correct. Secondly, recent experimental studies of the Booster losses and emittance evolution [22, 23, 32] indicate a very complicated dynamics of the proton beam that includes a complex interplay of impedance, instabilities, space-charge effect, and electron cloud effects, many of which are manifested in significant differences in the behavior of individual bunches. The existing Booster IPMs have limited frequency bandwidth and are capable of reporting only one-turn average beam profiles, i.e., they can not measure profiles of individual bunches or groups of 6-10 bunches (out of 81-84 total).

Table 1: Parameters of Fermilab IPMs

	Tevatron*	Booster	IOTA
Proton pc, GeV	980	0.95-8.9	0.07
N_p /bunch, 10^{10}	25	5.5	9
N_b	36	84	1 or 4
f_{rev}, µs	21	2.22	1.83
β_p	1	0.7-1	0.07
J_{avg}, mA	80	330	2-8
U_{SC}, V	2.4	14	2.5
t_b, ns	396	25-20	460-1800
σ_p at IPM, mm	1-0.3	5-2	1-4
IPM B, T	0.2	0	0
IPM V_0, kV	10	24	24
IPM D, mm	87	103	103
IPM pitch Δ, mm	0.25	1.5	0.5
IPM $h-1$, max.	~0.02	~0.7	~0.16

A possible way to address the above needs might be the employment of the Tevatron-style IPMs [7, 9, 33–35] - see Table 1. Two of those (vertical and horizontal) were used in 2006-2011 (now in storage), operated in the electron collection mode with external guiding magnetic field $B = 0.1 - 0.2$T, had fast electronics and were able to report profiles of individual proton and antiproton bunches separated by some 200 ns. The guiding magnetic field effectively suppresses the space charge IPM profile expansion which otherwise would be as high as $h \simeq 1.6$. The Larmor motion of electrons adds very little to the measured beam profile smearing, and the measured IMP beam profile was found to be very close, withing few %, to the real one with approximate relation $\sigma_m = \sqrt{\sigma_0^2 + \delta_L^2/B^2}$, where $\delta_L \approx 26\,\mu$m at $B = 1$ T [33]. For the such IPMs in the Booster, the field as low as $B = 0.02$ T will suffice to keep the IPM smearing under ~10%. To avoid beam orbit distortion due the IPMs, its integrated magnetic field $\int Bdl \simeq 4 \cdot 10^{-3}$ Tm can be easily compensated or corrected.

No magnetic field, Booster-type IPMs can be employed for proton beam diagnostics in the IOTA ring [36]. Major parameters of that facility for accelerator research are listed in Table 1. One can see that even for the highest proton beam current and the smallest beam size - parameters which usually anti-correlate - the space-charge IPM expansion parameter is at about 16% that leaves enough room for reasonably precise correction following recipes of Eq.(1) and the above analysis. The revolution frequency of IOTA is close to that of the Booster and the bandwidth of the existing Booster IPM electronics should be sufficient for turn-by-turn profile measurements in IOTA. Of course, for the rms beam size of about $\sigma_0 \simeq 1$ mm it would be very necessary to have a smaller pitch Δ (distance between stripes), preferably 1 to 0.5 mm or less as it adds to the measured size in quadrature approximately as $\sigma_m = \sqrt{\sigma_0^2 + \Delta^2/12}$. Another attractive opportunity for improvement can be a controlled leak of Xe or Kr – see Fig.4 – as IPM operation with such gases results in a smaller profile smearing [21, 37].

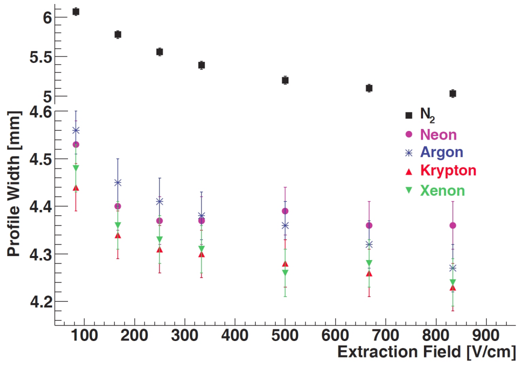

Figure 4: Measured GSI IPM profile width versus extraction field for different residual gases (from Ref. [37]).

SUMMARY

Theory and analysis of space-charge effects and intensity independent instrumental errors σ_T in the operation of ionization profile monitors for measurements of high-intensity beams [16] offer practical correction algorithms to reconstruct the original beam sizes. Being applied to the 8 GeV Fermilab Booster proton synchrotron, that allows some 10% accuracy in the determination of σ_0 from the rms sizes measured in the IPMs σ_m. Upcoming Booster beam intensity upgrade, besides expected increase in the IPM space-charge expansion factor up to ~2, rises concerns over multi-bunch proton dynamics effects - all that calls for the installation of faster IPMs which also employ some 0.02T guiding external magnetic field for electron collection. The Booster type (ion collecting) IPMs can be employed in the 70 MeV/c IOTA proton ring, especially if the pitch of the stripes can be reduced to 1 mm or less and the residual gas to ionize is set by calibrated Xe or Kr leaks.

The author would like to thank J. Eldred, V. Kapin, V. Lebedev, K. Seiya, and R. Thurman-Keup for useful discussions on various aspects of the Fermilab Booster IPM operation, fruitful cooperation, and valuable input.

REFERENCES

[1] P. Strehl, *Beam Instrumentation and Diagnostics, vol. 120*, Berlin, Germany: Springer, 2006.

[2] F. Hornstra, W. H. DeLuca, “Nondestructive beam profile detection systems for the Zero Gradient Synchrotron”, in *Proc. VI Conference on High Energy Acceleration*, Cambridge, MA, 1967, pp. 374–377.

[3] H. Weisberg *et al.*, “An ionization profile monitor for the Brookhaven AGS”, *IEEE Trans. Nucl. Sci.*, vol. 30, p. 2179, 1983. `doi:10.1109/TNS.1983.4332753`

[4] B. Hochadel *et al.*, “A residual-gas ionization beam profile monitor for the Heidelberg Test Storage Ring TSR”, *Nucl. Instr. Meth. A*, vol. 343, p. 401, 1994. `doi:10.1016/0168-9002(94)90217-8`

[5] R. Anne *et al.*, “A noninterceptive heavy ion beam profile monitor based on residual gas ionization”, *Nucl. Instr. Meth. A*, vol. 329, p. 21, 1993. `doi:10.1016/0168-9002(93)90918-8`

[6] R. Connolly *et al.*, “Beam profile measurements and transverse phase-space reconstruction on the Relativistic Heavy-Ion Collider”, *Nucl. Instr. Meth. A*, vol. 443, p. 2015, 2000. `doi:10.1016/S0168-9002(99)01162-6`

[7] A. Jansson *et al.*, “The Tevatron ionization profile monitors”, *AIP Conf. Proc.*, vol. 868, p. 159, 2006. `doi:10.1063/1.2401401`

[8] F. Benedetti *et al.*, “Design and development of ionization profile monitor for the cryogenic sections of the ESS Linac”, *EPJ Web of Conf.*, vol. 225, p. 01009, 2020. `doi:10.1051/epjconf/202022501009`

[9] R. S. Moore, A. Jansson, and V. Shiltsev, “Beam instrumentation for the Tevatron collider”, *J. Instrumentation*, vol. 4, no. 12, p. 12018, 2009. `doi:10.1088/1748-0221/4/12/P12018`

[10] S. Levasseur *et al.*, “Development of a rest gas ionisation profile monitor for the CERN Proton Synchrotron based on a Timepix3 pixel detector”, *J. Instrumentation*, vol. 12, no. 02, p. C02050, 2017. `doi:10.1088/1748-0221/12/02/C02050`

[11] K. Wittenburg, “Specific instrumentation and diagnostics for high-intensity hadron beams”, in *CAS - CERN Accelerator School: High Power Hadron Machines*, Mar. 2013, pp. 251–308. `doi:10.5170/CERN-2013-001.251`

[12] J. Amundson *et al.*, “Calibration of the FNAL Booster ionization profile monitor”, *Phys. Rev. ST Accel. Beams*, vol. 6, p. 102801, 2003. `doi:10.1103/PhysRevSTAB.6.102801`

[13] Workshop in Simulations, Design and Operational Experience of Ionisation Profile Monitors, `https://indico.gsi.de/event/5366`

[14] R. Thern, “Space charge distortion in the Brookhaven ionization profile monitor”, BNL, Upton, NY, USA, Rep. BNL-39487, Mar. 1987.

[15] W.S. Graves *et al.*, “A nondestructive fast beam profile monitor”, *Nucl. Instr. Meth. A*, vol. 364, p. 364, 1995. `doi:10.1016/0168-9002(95)00218-9`

[16] V. Shiltsev, “Space-charge effects in ionization beam profile monitors”, *Nucl. Instr. Meth. A*, vol. 986, p. 164744, 2021. `doi:10.1016/j.nima.2020.164744`

[17] M. Reiser, *Theory and Design of Charged Particle Beams*, New York, USA: John Wiley and Sons, 2008.

[18] C. Bakker and E. Segre, “Stopping power and energy loss for ion pair production for 340-Mev protons”, *Phys. Rev.*, vol. 81, p. 489, 1951. `doi:10.1103/PhysRev.81.489`

[19] D. Vilsmeier, M. Sapinski, and R. Singh, “Space-charge distortion of transverse profiles measured by electron-based ionization profile monitors and correction methods”, *Phys. Rev. Accel. Beams*, vol. 22, p. 052801, 2019. `doi:10.1103/PhysRevAccelBeams.22.052801`

[20] C. Dimopoulou *et al.*, “Dissociative ionization of H2 by fast protons: three-body break-up and molecular-frame electron emission”, *J. Phys. B: At. Mol. Opt. Phys.*, vol. 38, p. 593, 2005. `doi:10.1088/0953-4075/38/5/010`

[21] J. Egberts, “IFMIF-LIPAC beam diagnostics. Profiling and loss monitoring systems”, Ph.D. thesis, Universite Paris Sud, Orsay, France, 2012.

[22] J.Eldred *et al.*, “Beam intensity effects in Fermilab Booster synchrotron”, *Phys. Rev. Accel. Beams*, vol. 24, p. 044001, 2021. `doi:10.1103/PhysRevAccelBeams.24.044001`

[23] V. D. Shiltsev, J. S. Eldred, V. A. Lebedev, and K. Seiya, “Beam Losses and emittance growth studies at the Record high space-charge dQ_SC in the Booster”, presented at the 12th Int. Particle Accelerator Conf. (IPAC’21), Campinas, Brazil, May 2021, paper WEXB08.

[24] E. Hubbard *et al.*, “Booster Synchrotron”, FERMILAB, Batavia, IL, USA, Rep. FERMILAB-TM-405, 1973.

[25] V. Shiltsev, “Fermilab proton accelerator complex status and improvement plans”, *Modern Phys. Lett. A*, vol. 32, p. 1730012, 2017. `doi:10.1142/S0217732317300129`

[26] M. Convery *et al.*, “Fermilab accelerator complex: status and improvement plans”, FERMILAB, Batavia, IL, USA, Rep. FERMILAB-TM-2693, 2018.

[27] M. Minty, F. Zimmermann, *Measurement and Control of Charged Particle Beams*, Berlin, Germany: Springer Nature, 2003.

[28] E. Bravin, “Transverse beam profiles”, CERN, Geneva, Switzerland, May 2020. `arXiv:2005.07400`

[29] V. Lebedev and V. Shiltsev, *Accelerator Physics at the Tevatron Collider* Berlin, Germany: Springer, 2012.

[30] F. Roncarolo, “Accuracy of the Transverse Emittance Measurements of the CERN Large Hadron Collider”, Ph.D. thesis, Milan Polytechnic, Milan, Italy, 2005.

[31] V. Lebedev *et al.*, “The PIP-II conceptual design report”, FERMILAB, Batavia, IL, USA, Rep. FERMILAB-TM-2649-AD-APC, 2017.

[32] C.Y.Tan, “Ecloud in Booster”, Fermilab internal report beams-doc-9120 (Aug. 12, 2021), `https://beamdocs.fnal.gov/cgi-bin/sso/ShowDocument?docid=9120`

[33] A. Jansson *et al.*, “Ionization Profile Monitoring at the Tevatron,” in *Proc. 10th European Particle Accelerator Conf. (EPAC’06)*, Edinburgh, UK, Jun. 2006, paper THYFI01, pp.2777-2780.

[34] J. Zagel *et al.*,“Operational Use of Ionization Profile Monitors at Fermilab”, in *Proc. 14th Beam Instrumentation Workshop (BIW’10)*, Santa Fe, NM, USA, May 2010, paper TUPSM009, pp.111-115

[35] J. Zagel *et al.*, “Third generation residual gas ionization profile monitors at Fermilab”, `arXiv:1502.02703`.

[36] S. Antipov *et al.*, “IOTA (Integrable Optics Test Accelerator): facility and experimental beam physics program”, *Journal of Instrumentation*, vol. 12, T03002, 2017. `doi:10.1088/1748-0221/12/03/T03002`

[37] J. Egberts *et al.*, “Detailed Experimental Characterization of an Ionization Profile Monitor”, in *Proc. 10th European Workshop on Beam Diagnostics and Instrumentation for Particle Accelerators (DIPAC’11)*, Hamburg, Germany, May 2011, paper WEOA03, pp. 547–549.

ISBN: 978-3-95450-230-1 ISSN: 2673-5350 doi:10.18429/JACoW-IBIC2021-TUPP06

SIMULATION OF A QUAD-SLITS INTERFEROMETER FOR MEASURING THE TRANSVERSE BEAM SIZE IN HLS-II*

Sanshuang Jin, Yunkun Zhao, Jigang Wang†, Baogen Sun‡, Fangfang Wu, Leilei Tang, Tianyu Zhou
National Synchrotron Radiation Laboratory (NSRL),
University of Science and Technology of China (USTC), Hefei, China

Abstract

A quad-slits interferometer using visible light is designed to measure the transverse beam size of Hefei Light Source-II (HLS-II). According to the basic beam parameters of the B7 source point, the preliminary simulation results are obtained by using the Synchrotron Radiation Workshop (SRW) code. Furthermore, the core parameters of the quad-slits components in the interferometer are optimized. Among, the optimum slits-separations of d_H and d_V are acquired to be 6.0 and 10.0 mm, respectively. It is shown that the simulated results are consistent with the theoretical values, which provides a reference value for performing the related experimental measurement in the future.

INTRODUCTION

It is known that the synchrotron radiation (SR) refers to the electromagnetic wave radiated when the acceleration state of the charged particles changes. So far the SR light source has been widely used in the fields of condensed-matter physics, medical research, biochemistry, materials and advanced manufacturing processes due to its significant characteristics of high-brightness, high polarization and good stability. With the advancement of accelerator science and technology, the transverse beam size becomes smaller and smaller and reaches few dozens of micrometers. There is no doubt that it requires a huge engineering challenge to accurately measure such a small beam size. The current mainstream technology for the measurement of the transverse beam size is to employ the SR optical system. It is especially pointed out that this SR system has the excellent advantage of real-time and online measurement without damage to the stored bunched beam [1]. Up to now, the traditional methods for measuring the transverse beam size include FZP imaging [2], double-slits and quad-slits interferometry [3,4], pinhole imaging [5] and so on [6,7]. Among them, the FZP imaging method is considered as uneconomical because of the smaller beamline layout in HLS-II and the expensive optical diffractive element FZP. As for the pinhole imaging method, it is difficult to measure the small transverse beam size owning to the inevitable optical diffraction effect. In addition to the double-slits interferometer proposed by T. Mitsuhashi [8], which possesses high resolution that can be used in visible light and even X-ray bands. In combination with the remarkable merits of the optical interference measurement system, the B7 beamline of HLS-II has been achieved the online measurement of the transverse beam size. This previous double-slit interferometry occupies a large space and has a high maintenance cost. In order to further precisely obtain the beam size of B7 source point, we are devoted to designing a simple suitable quad-slits interferometer which can reduce the complexity of the optical system.

PRINCIPLE AND PHYSICAL DESIGN

HLS-II is a second-generation electron storage ring with low emittance of 36.4 nm·rad and with beam energy of 800 MeV. Note that a double-slits interferometer already has been applied to measure the transverse beam size of B7 source point. Then we are desired to design a new quad-slits interferometer for improving the measurement accuracy and system robustness. The parameters of B7 source point are clearly shown in Table 1.

Table 1: The Parameters of B7 Source Point

Parameters	**Value**
Electron beam energy E_e (GeV)	0.8
Beam current I (mA)	400
Circumference L (m)	66.1308
Radius of BM ρ (m)	2.1645
Vertical magnetic field of BM B (T)	1.2327
Transverse natural emittance ϵ (nm·rad)	36.4
Energy spread (RMS)	0.000 47
β_x (m)	1.7668
β_y (m)	12.3485
α_x (m)	−3.002
α_y (m)	2.1319
η_x (m)	0.1059
η_x'	−0.1990

According to the above parameters given in Table 1, the transverse beam size can be calculated by

$$\begin{cases} \sigma_x^2 = \varepsilon_x \beta_x + (\eta_x \frac{\Delta p}{p})^2 \\ \sigma_y^2 = \varepsilon_y \beta_y \end{cases} \tag{1}$$

where σ_x and σ_y are the horizontal and vertical beam size, respectively. ε_x and ε_y are the horizontal and vertical beam emittance, respectively. β_x and β_y are the horizontal and vertical beta function, respectively. Δp/p is the energy spread and η_x is dispersion function. Through the calculation we

---

* Work supported by the National Natural Science Foundation of China under Grant 12075236, Grant 11575181, Grant 51627901, Grant 11805204, and Grant 11705203, the Anhui Provincial Natural Science Foundation under Grant 1808085QA24, and the Fundamental Research Funds for the Central Universities under Grant WK2310000080

† wangjg@ustc.edu.cn
‡ bgsun@ustc.edu.cn

can know that the theoretical horizontal and vertical beam size of HLS-II are 255.98 and 93.88 µm, respectively. In terms of the Van Cittert-Zernike theorem, the coherence of two points in space can be expressed by the Fourier transform of the light source with a standard Gaussian distribution. The structure of the quad-slits interferometer designed using this principle is distinctly shown in Fig. 1.

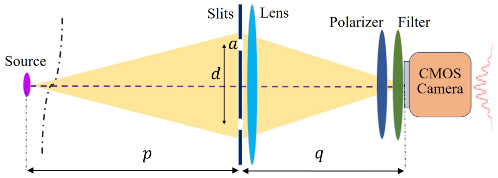

Figure 1: The particle trajectories under different RF phase modulation amplitudes (f_s=21.3 kHz and f_m=20.0 kHz).

In Fig. 1, p is the distance from the light source to the quad-slits component, and q is the distance from the quad-slits component to the CMOS camera. Here, the achromatic lens is used to modulate the wavefront of the light passing through the quad-slits component shown in Fig. 2. to stabilize the interference pattern on the CMOS camera surface. And the polarizer is utilized for obtaining the horizontal polarization light, and the filter is applied to obtain quasi-monochromatic light. It is necessary to use a monochromator instead of a filter to obtain quasi-monochromatic light when using shorter-wavelength light to measure the transverse beam size of the storage ring light source. In fact, we chose visible light of 500 nm as the detection source, which is mainly attributed to the high availability and the large coherence length of this wavelength band. In addition, it is easy to setup and adjust the optical path, which is more convenient for carrying out experiments.

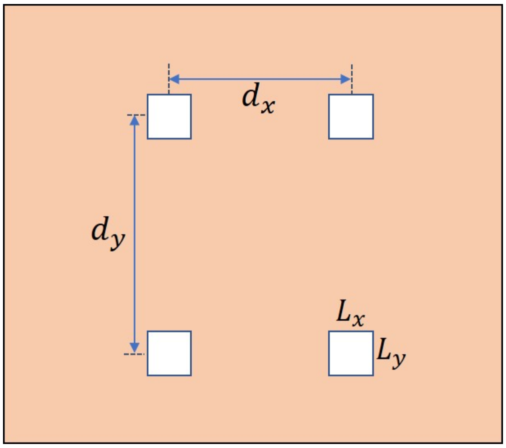

Figure 2: Schematic diagram of the experimental measurement system.

For the extended light source, the horizontal and vertical interference pattern with wavelength λ can be described by the formula [9,10]

$$\begin{cases} I_H(x) = 2I_0L_x^2L_y^2sinc^2(\frac{\pi ax}{\lambda f})(1+\gamma_H cos[\frac{2\pi d_x x}{\lambda f}]) \\ I_V(y) = 2I_0L_x^2L_y^2sinc^2(\frac{\pi ay}{\lambda f})(1+\gamma_V cos[\frac{2\pi d_y y}{\lambda f}]) \end{cases} \tag{2}$$

Here, I_H and I_V denote the horizontal and vertical intensity distribution, x and y denotes the horizontal and vertical coordinate, f denotes the focal length, L_x denotes the slit width, L_y denotes the slit height, d_x and d_y denote the horizontal and vertical slits-separation, respectively. γ_H and γ_V are the horizontal and vertical visibility of the quad-slits interference pattern, which can be expressed as

$$\gamma = \frac{I_{max} - I_{min}}{I_{max} + I_{min}} \tag{3}$$

In Eq. (3), I_max and I_min stand for the minimum and maximum intensity of the interferogram near the central position, respectively. In the quad-slits interferometer, the coherence of the quad-slits is equivalent to the visibility of the interference pattern on the CMOS camera. Assuming that the light source is spatially Gaussian distribution, yields

$$\gamma = exp(-\frac{2\pi^2d^2\sigma^2}{\lambda^2p^2}) \tag{4}$$

As a consequence, the beam size can be extracted from the measurement of γ, which can be expressed as

$$\sigma = \frac{\lambda q}{\pi d}\sqrt{\frac{1}{2}ln(\frac{1}{V})} \tag{5}$$

In order to measure more accurately in the actual measurement process, the visibility needs to be obtained by fitting the experimental data, rather than through a single point measurement. The fitting equation is described as follows

$$I(x) = a_0 + a_1sinc^2(a_2x + a_3[1 + a_4cos(a_5x + a_6)]) \tag{6}$$

Here, a_4 indicates the visibility of the interference pattern.

SIMULATION RESULTS

Compared with the previous double-slits interferometry, the newly designed quad-slits interferometry uses a higher resolution CMOS camera (2.5 µm×2.5 µm), and at the same time removes the zoom structure before the CMOS camera. Therefore, this quad-slits interferometry has a simpler optical path and eliminates various aberrations caused by the zoom structure. In the entire optical interference system we designed, the relevant parameters are as follows: p is 12.000 m, q is 1.091 m, the focal length f of the lens is 1.000 m, L_x is 2.0 mm, L_y is 2.0 mm, d_x is 6.0 mm, and d_y is 10.0 mm. According to the above designed parameters, the simulated result of the interference system using SRW code is shown in Fig. 3. By fitting the data of the horizontal and vertical interferogram as shown in Figs. 4 and 5 by Eq. (6), the corresponding visibilities are acquired to be 0.2915 and 0.6743, respectively. It is concluded that the horizontal beam size is 249.90 µm, and the vertical beam size is 84.78 µm. In general, the design of B7 quad-slits interferometry meets the current practical requirements.

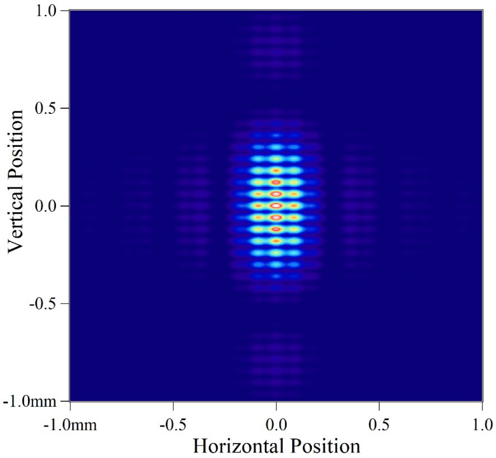

Figure 3: Simulated interferogram of the quad-slits interferometer.

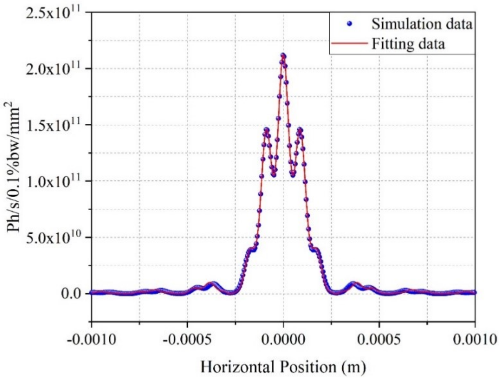

Figure 4: Data fitting in the middle of the horizontal interferogram.

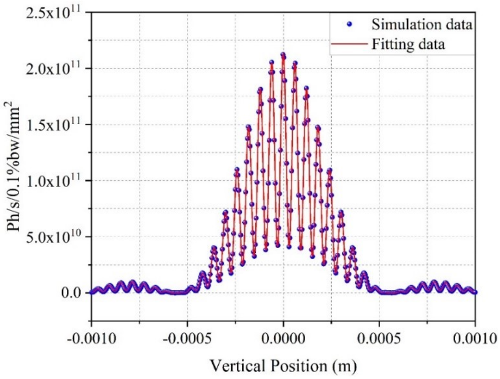

Figure 5: Data fitting in the middle of the vertical interferogram.

CONCLUSION

In this paper, a quad-slits interferometer using visible light was proposed according to the characteristics of the light source. And then, the SRW code is used to obtain the intensity distribution of B7 source point based on the relevant machine parameters of HLS-II. The simulation results of the horizontal and vertical size are obtained as 249.90 and 84.78 µm, respectively. This is of guiding significance to the subsequent optimization and improvement of the experimental measurement system performance. In the next research work, we will further verify the reliability and applicability of the designed interference measurement system.

ACKNOWLEDGEMENTS

This work was supported in part by the National Natural Science Foundation of China under Grant 12075236, Grant 11575181, Grant 51627901, Grant 11805204, and Grant 11705203, the Anhui Provincial Natural Science Foundation under Grant 1808085QA24, and the Fundamental Research Funds for the Central Universities under Grant WK2310000080.

REFERENCES

[1] K. Tang *et al.*, "Transverse beam size measurement system using visible synchrotron radiation at HLS II," *Chinese Phys. C*, vol. 40, no. 9, p. 097002, 2016. doi:10.1088/1674-1137/40/9/097002

[2] H. Sakai *et al.*, "Improvement of Fresnel zone plate beam-profile monitor and application to ultralow emittance beam profile measurements," *Phys. Rev. Spec. Top. Accel. Beams*, vol. 10, p. 042801, 2007. doi:10.1103/PhysRevSTAB.10.042801

[3] T. Naito *et al.*, "Very small beam-size measurement by a reflective synchrotron radiation interferometer," *Phys. Rev. Spec. Top. Accel. Beams*, vol. 9, p. 122802, 2006. doi:10.1103/PhysRevSTAB.9.122802

[4] M. L. Chen *et al.*, "Measurement of beam size with a SR interferometer in TPS," in *Proc. 7th Int. Particle Accelerator Conf. (IPAC'16)*, Busan, Korea, May 2016, pp. 313–315. doi:10.18429/JACoW-IPAC2016-MOPMR032

[5] C. Thomas *et al.*, "X-ray pinhole camera resolution and emittance measurement," *Phys. Rev. Spec. Top. Accel. Beams*, vol. 13, p. 022805, 2010.

[6] T. Mitsuhashi *et al.*, "Spatial coherency of the synchrotron radiation at the visible light region and its application for the electron beam profile measurement," in *Proc. 17th Particle Accelerator Conf. (PAC'97)*, Vancouver, Canada, May 1997, paper 3V016, pp. 766–768.

[7] A.D. Garg *et al.*, "Design of synchrotron radiation interferometer (SRI) for beam size measurement at visible diagnostics beamline in Indus-2 SRS" *Nucl. Instrum. Methods Phys. Res. A*, vol. 902, pp. 164–172, 2018.

[8] N. Samadi *et al.*, "Source size measurement options for low-emittance light sources," *Phys. Rev. Accel. Beams*, vol. 23, p. 024801, 2020. doi:10.1103/PhysRevAccelBeams.23.024801

[9] K. Changbum *et al.*, "Two-dimensional SR Interferometer for PLS-II," *J. Korean. Phys. Soc*, vol. 58, no. 4, pp. 725–729, 2011.

[10] M. Mitsuhiro *et al.*, "Two-dimensional visible synchrotron light interferometry for transverse beam-profile measurement at the SPring-8 storage ring," *J. Synchrotron Rad*, vol. 10, pp. 295–302, 2003.

ISBN: 978-3-95450-230-1 ISSN: 2673-5350 doi:10.18429/JACoW-IBIC2021-TUPP07

DEVELOPMENT OF A MULTI-CAMERA SYSTEM FOR TOMOGRAPHY IN BEAM DIAGNOSTICS

A. Ateş [*], G. Blank, U. Ratzinger and C. Wagner
Institute of Applied Physics, Goethe University, Frankfurt, Germany

Abstract

Embedded visual systems in industry led to advancements of single board computers and single board cameras. Due to the lower power consumption and high flexibility of these miniature devices, a multi-camera system can be developed more effectively. A prototype of a beam-induced residual gas fluorescence monitor (BIF) has been developed and successfully tested at the Institute of Applied Physics (IAP) of the Goethe University Frankfurt. This BIF is based on a single-board camera inserted into the vacuum. The previous promising results led to the development of a multi-camera system with 10 cameras. One of the advantages of such a system is the miniature design, allowing this detector to be integrated within the vacuum and in regions that are difficult to access. The overall goal is to study the beam with tomography algorithms at a low energy beam transport section. We hope to reconstruct an arbitrary beam profile intensity distribution without assuming a Gaussian beam.

INTRODUCTION

Beam-induced fluorescence (BIF) monitors are standard detectors at accelerator facilities [1]. For ultrahigh vacuum beam diagnostics, scientific cameras are commonly used in combination with MCP photon amplifiers to determine the beam position and profile. New BIF monitors have been successfully tested at the low-energy beamline of the Frankfurt Neutron Source at the Stern Gerlach Center [2,3]. These developments lead to new ways to study the beam. One idea is to view the beam from multiple angles. This allows the use of tomography algorithms to reconstruct the intensity distribution of the transverse beam profile. Beam tomography has previously been studied using a camera and a rotating vacuum chamber to rotate the camera and obtain any number of views. Another approach is to view the beam through viewing windows.

Our goal is to maximize the number of viewing angles and develop a fast tomographic detector with a minimal form factor to be as flexible as possible. Our approach is to use non-scientific single-board cameras with single-board computers and to put as many cameras as possible in the vacuum. Figure 1 shows a photo of the cameras mounted on the holder. It is designed to fit into a vacuum vessel with a diameter of 200 mm and a length of 300 mm.

The detector is built for low energy beam transport sections in high vacuum regions of about 10^{-7} mbar. To increase the emitted light, it is possible to introduce a buffer gas during image acquisition. We tested the cameras at a residual argon gas pressure down to 1×10^{-4} mbar. There were several challenges to overcome in developing such a detector. One challenge was to get all cameras in parallel into full operation and retrieve all data. Another challenge was to align each of the cameras so that their center of field of view matched. The following sections present our approaches to solving these challenges.

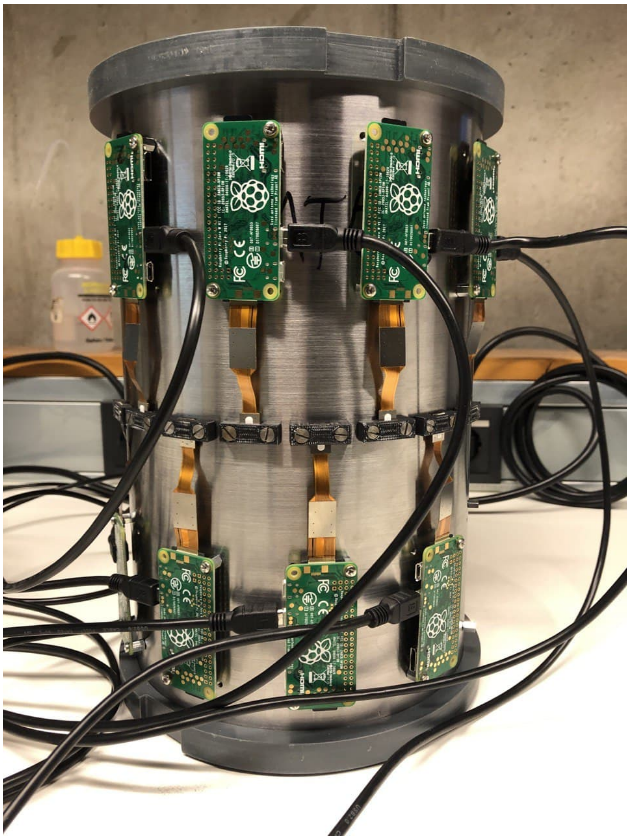

Figure 1: The picture shows a photo of the tomography detector with the Raspberry Pi Zero and its camera modules attached to a stainless steel pipe.

HARDWARE SET UP

Raspberry Pi Zero and its Camera

The cameras you see in Fig. 1 are single-board cameras with so-called raspberry pi zero single-board computers. The Raspberry Pi Zero is the Raspberry Pi with the smallest dimensions among the Raspberry Pi computer models. The Raspberry Pi and especially its camera are gaining more and more attention not only in the Maker scene, but also in the scientific community [4]. Due to its compact dimensions and low power consumption of about 15 mW, they are predestined for projects like drones, robots or any mobile

---

[*] ates@iap.uni-frankfurt.de

ISBN: 978-3-95450-230-1 ISSN: 2673-5350 doi:10.18429/JACoW-IBIC2021-TUPP07

devices. The camera consists of a 5 MP high resolution Omnivision OV5647 CMOS image sensor. The sensor size is 3.76 mm × 2.74 mm and has a pixel size of 1.4 m × 1.4 m. It has a focal length (3.6 mm) with a single aperture (F2.9). The sensor sensitivity can be varied between ISO values from 100 to 800, and it is possible to vary the analogue gain of the ADC for the blue and red color pixels, i.e. to change the white balance manually. The camera has been tested in high vacuum up to 1×10^{-7} mbar and in strong magnetic field (up to 0.6 T) [5].

Powering the Cameras

To supply the cameras with 5 V and at least 300 mA, we used a USB hub. This is also integrated into the vacuum. Its power management unit was suitable to supply all ten Raspberry Pis. With this solution, only one power and ground vacuum feedthrough pin was required. Figure 2 shows a wiring diagram of the cabling.

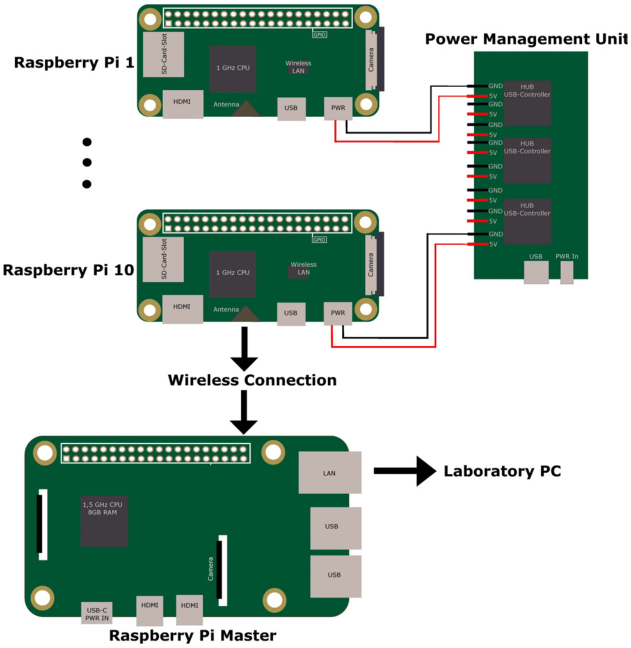

Figure 2: Ten Raspberry Pi Zeros are connected to the power supply unit of the USB hub in the vacuum.

Retrieving the Data and Controlling the Cameras

We used a wireless connection to control the cameras. A master Raspberry Pi with an external WIFI antenna was installed as an access point. All ten cameras connect wirelessly to the access point. The master sends the command to capture the image and the slaves send the image back to the master. At this point, initial image processing can be performed before all images are sent to the main laboratory computer for further processing and application of tomographic reconstruction algorithms. The main computer is not located inside the vacuum, only the external antenna. Therefore, only two pins for the power supply and five pins for the USB connection were needed to control the tomography detector.

CALIBRATION

Scaling

The first step was to align the cameras to the center of the beam path and determine the focal point for sharp images. The cameras are equipped with a board lens or officially with an $M12 \times 0.5$ mm lens. A ruler with 0.5 mm steps was used for initial adjustment and a 0.1 mm thread was used for fine adjustment. The camera sensors were attached to the mount with two screws. Perfect alignment was not possible. It was decided to align the cameras as best as possible by hand and then match the images by software.

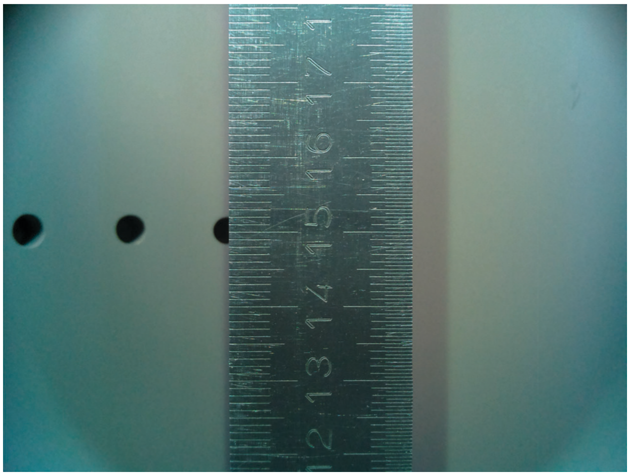

Figure 3: This ruler, which was placed in the center of the beam path at a distance of 0.5 mm, was used for scaling.

For the (mm/px) scaling, a ruler was placed in the center of the beam path (Fig. 3). The scaling of the cameras is approximately 0.03 mm/px or 31 px/mm. There is an individual scaling lookup table for each camera. A calibration wire was used to determine the beam path center (Fig. 4). Two wire holders were attached to the end flanges of the detector. The wire holders were aligned with a matching ring to the flanges. The position relative to the beam path center or line of side was determined using the Taylor-Hobson telescope at the end of the beam line.

Multi-Camera Image Matching

As already mentioned, the cameras are only aligned with two screws. In addition, all camera lenses have an offset. The fields of view of the individual cameras must match each other. For this purpose, the image of the first camera was selected as a reference and all other camera images were matched to it. A stick with a black and white pattern was placed in the center (Fig. 5). Using this pattern, one can select a set of three points in each image and match these sets of points to the reference camera by affine image transformation.

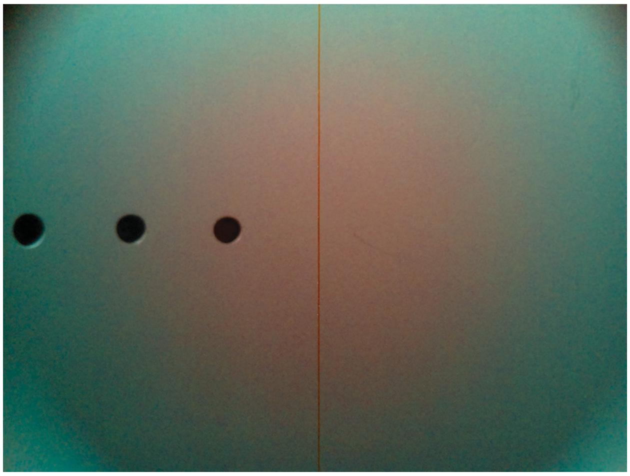

Figure 4: The calibration wire with a diameter of 0.25 mm has a gold layer that is reflective. A white thread was not reflective enough to distinguish it against the background.

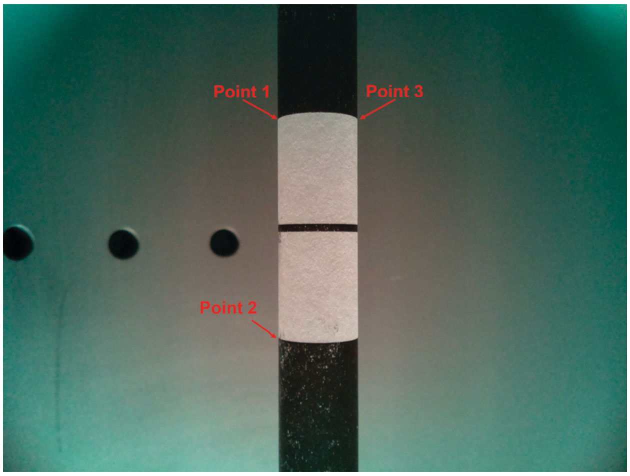

Figure 5: A 10 mm diameter rod with a pattern on it was held in the center of the detector. Three points were determined that matched the images from each camera.

TOMOGRAPHIC RECONSTRUCTION

Image Pre-processing

To evaluate the calibration and test the tomographic reconstruction algorithm, the images must be pre-processed. After affine transformation, each image was normalized and converted to grayscale. A Canny edge detection algorithm was used to highlight the contour of the calibration bar. Finally, the image was converted to black and white. These conversions are the best prerequisite for optimal reconstruction and detection of alignment errors. The result of the pre-processing is shown in Fig. 6.

Tomographic Algorithm

The development of tomographic reconstruction algorithms, especially in accelerator facilities, is a current scientific topic [6]. Time and resource efficient software has been developed in different laboratories. Here we use the python-based software toolbox Tomopy [7]. Most of the commonly used tomographic reconstruction algorithms such as Algebraic Reconstruction Tomography (ART) or Filtered Back Projection (FBP) are implemented here. Unlike the usual detectors with an X-ray source rotating over the object and creating as many profiles as necessary, here we have limited viewing angles. The ART algorithm was developed for iterative reconstruction of objects examined at a particular viewing angle [8]. In contrast, the filtered back projection is better suited for unlimited viewing angles. For this reason, the ART algorithm was used to evaluate detector calibration for an initial test.

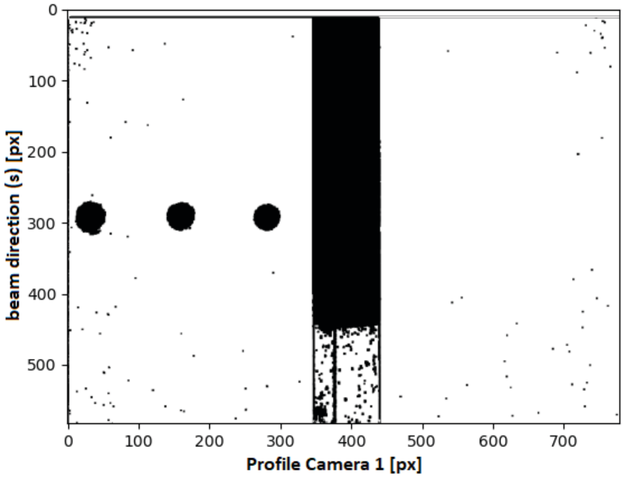

Figure 6: Result after pre-processing the image in Fig. 5.

Figure 7 shows one reconstructed slice of the calibration rod.

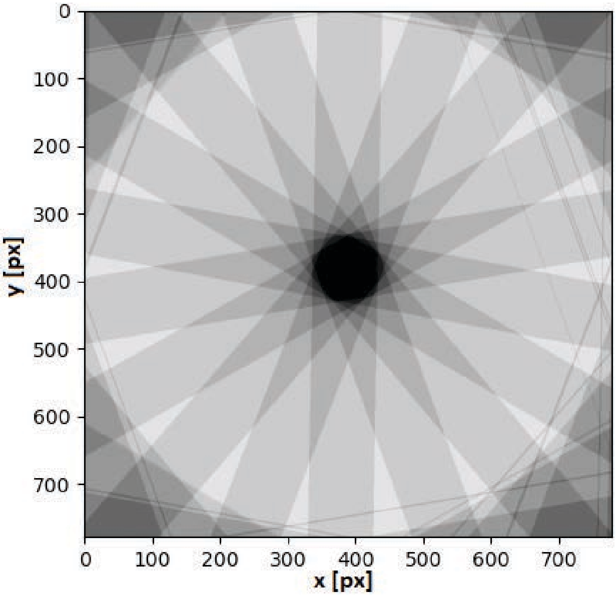

Figure 7: One slice of the tomographic reconstruction of the calibration rod.

Tomopy Software Toolbox has also integrated an effective image post-processing algorithm. The result of post-processing is shown in Fig. 8.

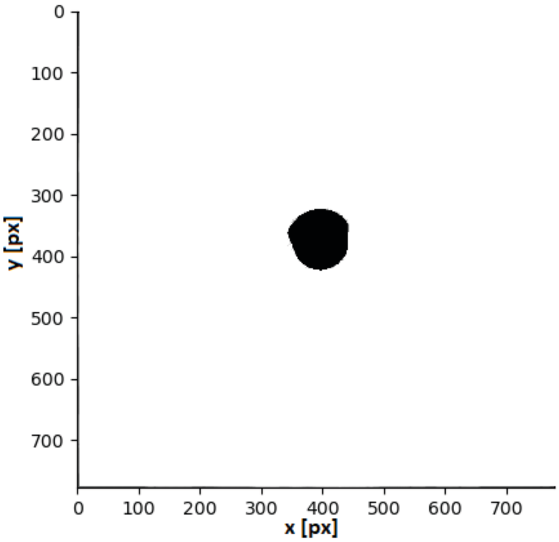

Figure 8: After image post-processing of the reconstruction.

Fig. 8 shows a asymmetrically shaped reconstruction of the calibration rod. There could be two reasons for this. One is a misalignment of the cameras, the other could be a problem in the pre- and post-processing. To investigate the misalignment of the cameras, the calibration wire from Fig. 4 was used. Figure 9 shows the tomographic reconstruction of the calibration wire of 0.25 mm thickness. One can see the misalignment, which could not be corrected yet.

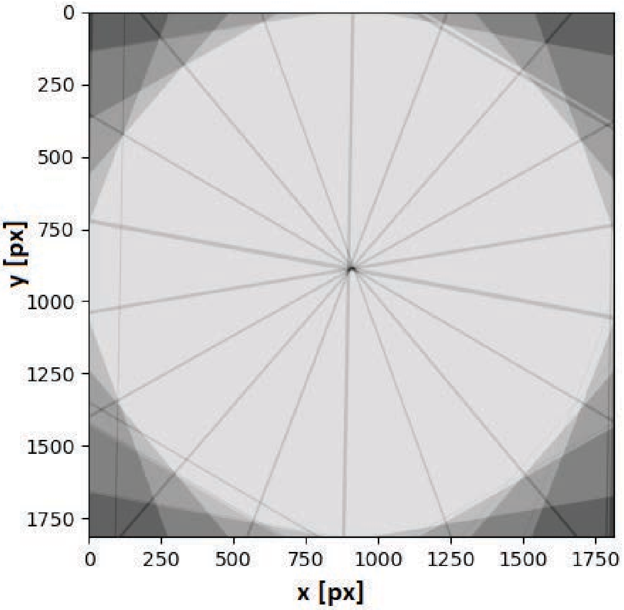

Figure 9: Tomographic reconstruction of the calibration wire from Fig. 4.

CONCLUSION

In this paper, a tomographic BIF detector for ion beam investigations is presented. This BIF is based on ten single-board cameras on a tube concentrically aligned to the beam axis and hold by the outer vacuum pipe. Several challenges had to be overcome. Data communication was provided by an edge device serving as a WiFi access point and master control unit. Camera calibration for real-world scaling was performed using a ruler placed in the center of the detector. The detector was aligned to the center of the beam path using a calibration wire and a Taylor-Hopson telescope. The problem of matching the fields of view of the cameras has not yet been perfectly solved. Reconstruction by the tomographic algorithms showed misalignment that could not yet be corrected. Further investigations will be performed using the python-based Tomopy software toolbox. The toolbox contains image pre- and post-processing that can be integrated. It also implements other reconstruction algorithms that may be better suited for this purpose. The tomography detector is installed in the beamline at IAP and will be tested with a 25 mA, 30 keV proton beam in the near future.

REFERENCES

[1] P. Forck *et al.*, “Profile Measurement by Beam Induced Fluorescence for 60 MeV/u to 750 MeV/u Heavy Ion Beams”, in *Proc. 10th European Particle Accelerator Conf. (EPAC’06)*, Edinburgh, UK, Jun. 2006, paper TUPCH010, p. 1013.

[2] S. Alzubaidi *et al.*, “The Frankfurt neutron source FRANZ”, *Eur. Phys. J. Plus*, vol. 131, p. 124, 2016. `doi:10.1140/epjp/i2016-16124-5`

[3] A. Ates *et al.*, “Development of a Multi-Camera System for Non-Invasive Intense Ion Beam Investigations”, presented at the 12th Int. Particle Accelerator Conf. (IPAC’21), Campinas, Brazil, May 2021, paper MOPAB282

[4] M. Pagnutti *et al.*, “Laying the foundation to use Raspberry Pi 3 V2 camera module imagery for scientific and engineering purposes”, *J. Electron. Imaging*, vol .26, no. 1, p. 013014, 2017. `doi:10.1117/1.JEI.26.1.013014`

[5] A. Ates *et al.*, “Non-invasive diagnostics of ion beams in strong toroidal magnetic fields with standard CMOS cameras”, *Nucl. Instr. Phys. Res. A*, vol. 877, pp. 69–73, 2018. `doi.org/10.1016/j.nima.2017.09.020`

[6] D. M. Pelt *et al.*, “Integration of TomoPy and the ASTRA toolbox for advanced processing and reconstruction of tomographic synchrotron data”, *J. Synchrotron Radiation*, vol. 23, pp. 842–849, 2016. `doi:10.1107S1600577516005658`

[7] D. Gürsoy *et al.*,“TomoPy: a framework for the analysis of synchrotron tomographic data”, *J. Synchrotron Radiation*, vol. 21, pp. 1188-1193, 2014. `doi:10.1107/S1600577514013939`

[8] J. S. Fraser, “Beam Tomography or Art in Accelerator Physics”, Los Alamos, USA, Los Alamos Scientific Laboratory Report LA-7498-MS, 1978.

10th Int. Beam Instrum. Conf. IBIC2021, Pohang, Rep. of Korea JACoW Publishing
ISBN: 978-3-95450-230-1 ISSN: 2673-5350 doi:10.18429/JACoW-IBIC2021-TUPP10

DEVELOPMENT OF A BEAM HALO MONITOR USING VISIBLE SYNCHROTRON RADIATION AT DIAMOND LIGHT SOURCE

E. Howling*, L. Bobb, Diamond Light Source, Oxford, UK

Abstract

A Beam Halo Monitor (BHM) has been developed at Diamond Light Source (DLS). It is an optical system that uses visible synchrotron radiation (SR) to image the beam halo. In this paper, the design of the monitor is presented, including the introduction of a Lyot stop system to reduce diffraction effects. The BHM was used to take images of a source point of visible SR from a dipole at DLS. These images were analysed to investigate the beam halo and determine the limitations of the monitor. These results will help inform the design of the visible light extraction system and any future BHMs for Diamond-II.

INTRODUCTION

Diamond Light Source (DLS) is a third generation synchrotron light source. In the storage ring, most electrons in the beam reside in the beam core. Due to Touschek and gas scattering some are offset from the core and form a beam halo [1].

Synchrotron radiation from bending magnet sourcepoints at visible and X-ray wavelengths is commonly used for beam diagnostics. X-ray pinhole cameras are used to image the beam core for transverse profile measurements [2]. However, these do not have a great enough dynamic range to image the beam halo, as the halo is approximately 10^{-5} times as bright as the core. Furthermore, the beam core cannot be imaged using visible SR due to the diffraction limit. However, the beam halo is large enough to be imaged with visible SR [3].

A Beam Halo Monitor (BHM) has been developed to better understand the formation and properties of the beam halo. In circular colliders, damping rings and synchrotron light sources, beam halo is one of the critical issues limiting the performance as well as potentially causing component damage and activation [1]. In the case of synchrotron light sources, the beam core determines characteristic parameters such as brightness for beamlines. Therefore a significant beam halo is undesirable. This becomes all the more important upon considering planned synchrotron upgrades, such as Diamond-II [4], where increased brightness for beamline experiments is a key performance indicator.

Given the reduced emittance in Diamond-II, the beam core will be focused to a greater particle density and therefore will exhibit a greater rate of Touschek scattering [5]. These properties of the Diamond-II storage ring mean the beam halo is likely to be more significant than in the current machine. Thus it is beneficial to understand how we expect the beam halo to behave and how it could be observed.

Similar projects have previously been undertaken, including the successful development of a coronagraph BHM at KEK [3]. A similar design was tested at CERN, where it was able to distinguish the halo from the core of a test lamp with a dynamic range of 10^7 [6]. A coronograph BHM was also designed using a micro mirror array to mask the beam core and tested at the University of Maryland Electron Ring [7, 8] and at DLS in collaboration with The Cockcroft Institute.

THE BEAM HALO MONITOR

Stage 1: Design and Installation

A BHM was designed to use visible SR emitted from a dipole magnet to image the beam halo, as shown in Fig. 1. The objective lens is a BORG77EDII apochromat, the characteristics of which are given in Table 1.

Table 1: Characteristics of the BORG77EDII Lens [10]

Parameter	Value
Aperture	77 mm
Focal length	510 mm
F ratio	6.6

Table 2: Properties of the Mako G-319B Camera with a Sony IMX265 Progressive Scan CMOS Sensor [11]

Parameter	Value
Pixels (H × V)	2048 × 1544
Pixel size (H × V)	3.45 × 3.45 µm
Sensing area (H × V)	7.1 × 5.3 mm
Pixel depth	8/12 bit
Shutter type	global
Resolution	3.20 MegaPixels
Max frame rate	37.50 fps

An image of the sourcepoint is formed on a Mako G-319B camera, which uses a Complementary Metal-Oxide-Semiconductor (CMOS) sensor, the properties of which are given in Table 2. Using a CMOS sensor allows the pixels imaging the beam core to saturate without blooming effects ruining the image [9]. The visible SR is a direct representation of the distribution of the electrons at the sourcepoint.

The monitor was built and tested in the lab. A system of mirrors was set up to replicate the 7.37 m optical path from the sourcepoint to the lens, and images taken of a 1951 USAF target were used to characterise the system. Using QuickMTF software [12], the modulation transfer function (MTF) of the system was measured. The properties of the stage 1 beam halo monitor are shown in Table 3.

The monitor was installed in the storage ring, next to the visible light extraction line. Reference images of the

---

* Emily.Howling.2017@live.rhul.ac.uk

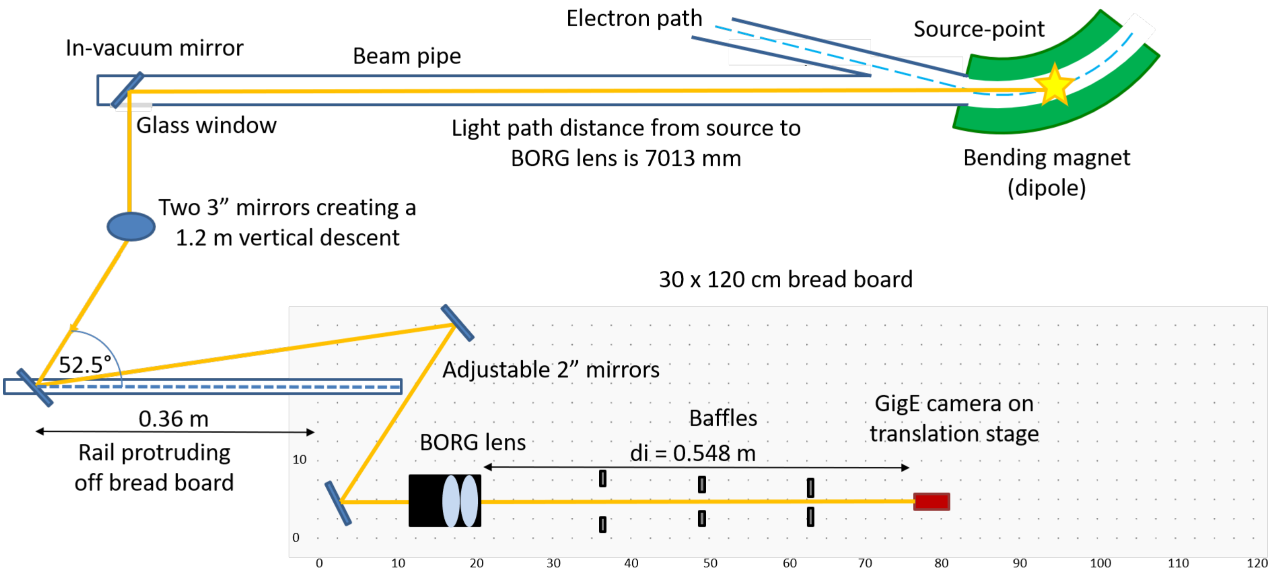

Figure 1: Schematic showing the set up of the stage 1 BHM in the storage ring, not to scale.

Table 3: Table Showing the Properties of the Stage 1 Beam Halo Monitor, as Characterised in the Lab

Parameter	Value
Magnification	−0.0743
Clear aperture	19.8 mm
FOV (H × V)	(56 × 52) ±2 mm
MTF50	0.10587 c/p
MTF10	0.26114 c/p
Depth of focus	0.6864 mm

In-Vacuum Mirror (IVM) were taken using ambient illumination through the viewport. From these images, the orientation of the sourcepoint image relative to the global horizontal and vertical axes of the storage ring could be identified, as shown in Fig. 2.

Stage 1: Results

A longitudinal scan of the camera on the 100 mm translation stage was used to determine the optimal position for imaging at constant camera gain and exposure. The optimal position is taken to be that with the maximum intensity.

Images of the sourcepoint were taken at a range of exposures. An example is shown in Fig. 3 where a significant diffraction pattern is observed. The cross shape of the pattern suggests diffraction from a rectangular aperture. Given that the IVM is the only element with a rectangular aperture in the optical path, it was concluded that the diffraction pattern was caused by the this element. Since this mirror cannot be altered, ways to mitigate the diffraction contribution were explored.

Stage 2: Including a Lyot Stop

It is preferable to minimise the diffraction contribution to the acquired image, rather than opting for complex background subtraction via post-processing. To reduce the diffraction contribution using hardware, a Lyot stop system was incorporated into the BHM. A Lyot stop system uses an objective lens to image the source, followed by a field lens to

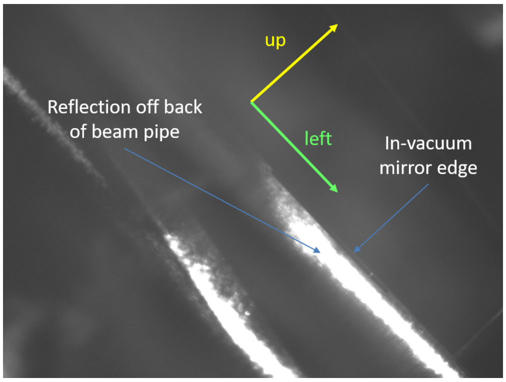

Figure 2: Reference image of the in-vacuum mirror taken using the stage 1 beam halo monitor.

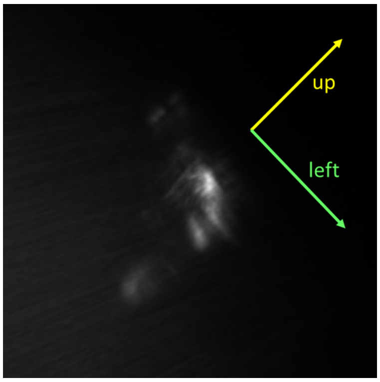

Figure 3: Image of the sourcepoint, region of interest, taken using the stage 1 beam halo monitor with camera gain of 4 dB and a camera exposure time of 893 µs. There is a diffraction pattern below and to the right of the beam core caused by the in-vacuum mirror edges.

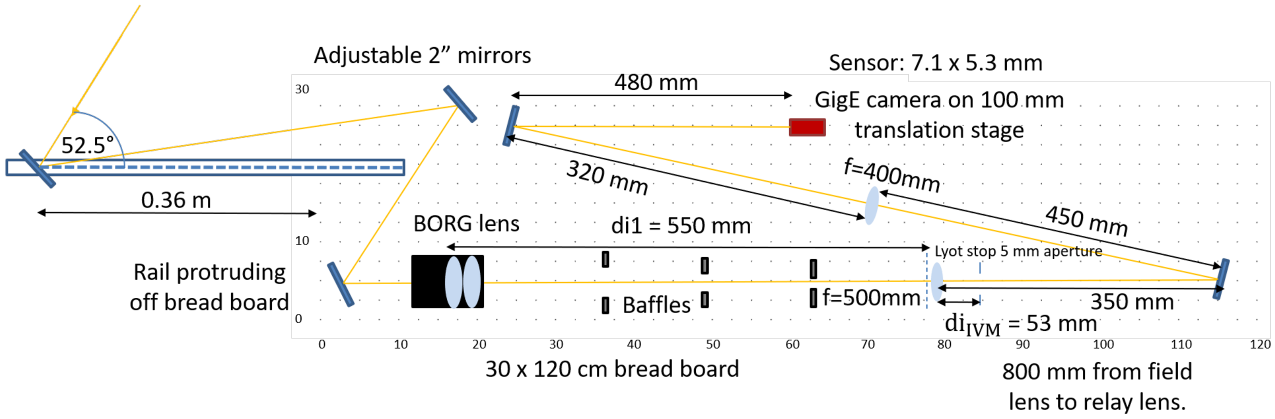

Figure 4: Schematic of the stage 2 beam halo monitor.

image the element causing the diffraction, which is usually the objective lens [3]. This essentially pushes the diffraction pattern to the edge of the image of the diffracting aperture. A Lyot stop is an aperture that then blocks the diffraction pattern. Finally, a relay lens relays the image of the source to the camera. This principle is summarised in the schematic shown in Fig. 5.

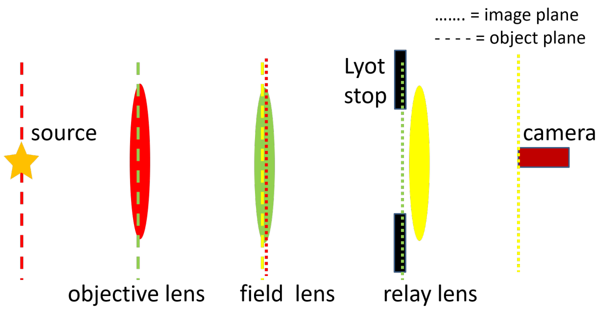

Figure 5: Schematic showing the principle of a Lyot stop system.

At DLS, the diffraction observed in the BHM is not predominately caused by the objective lens, but by the IVM which is 3.13 m upstream of the objective lens. Therefore an adapted Lyot stop was incorporated to suppress the diffraction contribution from the IVM. A schematic of the design for the stage 2 BHM is shown in Fig. 4.

The BHM was upgraded from stage 1 to stage 2 in-situ within the storage ring tunnel. Figure 6 shows an image taken by the stage 2 BHM. Images taken with stage 2 showed a significant suppression of the point spread function from diffraction at the IVM. However, the remaining diffraction pattern is still a major contribution to the background.

ANALYSIS

Images of the sourcepoint were taken at different exposures. The electron beam current was 300±2 mA. The electron beam core had a Gaussian distribution with horizontal and vertical beam sizes of 44.7 µm and 19.5 µm respectively.

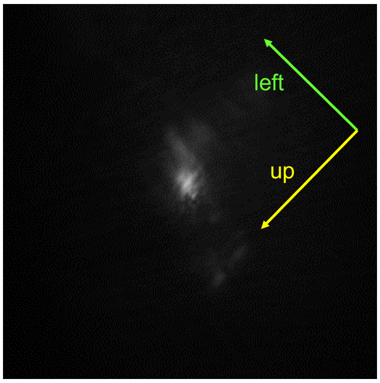

Figure 6: Image of the sourcepoint, region of interest, taken by the stage 2 BHM, with camera gain of 4 dB and a camera exposure time of 893 µs. It shows a signification reduction in the point spread function caused by diffraction from the IVM compared to Fig. 3.

These images were analysed using Matlab [13]. The 'makehdr' function was used to combine the images acquired over a range of camera exposures into High Dynamic Range (HDR) images, allowing both the beam core and the beam halo to be resolved. Cross sections through the centre of the sourcepoint in the HDR images were taken, as shown in Fig. 7. The cross sections were taken in the horizontal and vertical planes, as close as possible to the centre of the beam core, whilst also avoiding the areas of the image most significantly affected by the diffraction pattern caused by the IVM. The cross sections showed a Gaussian beam core and tails either side caused by the beam halo. However the background, predominately caused by the diffraction from the IVM is still too significant to reach meaningful conclusions about the extent of the beam halo.

CONCLUSION

A beam halo monitor has been developed at DLS to investigate whether the beam halo caused by gas and Touschek scattering can be imaged, as a possible diagnostic to investigate these phenomena. This has particular relevance for future lower emittance machines like Diamond-II in which

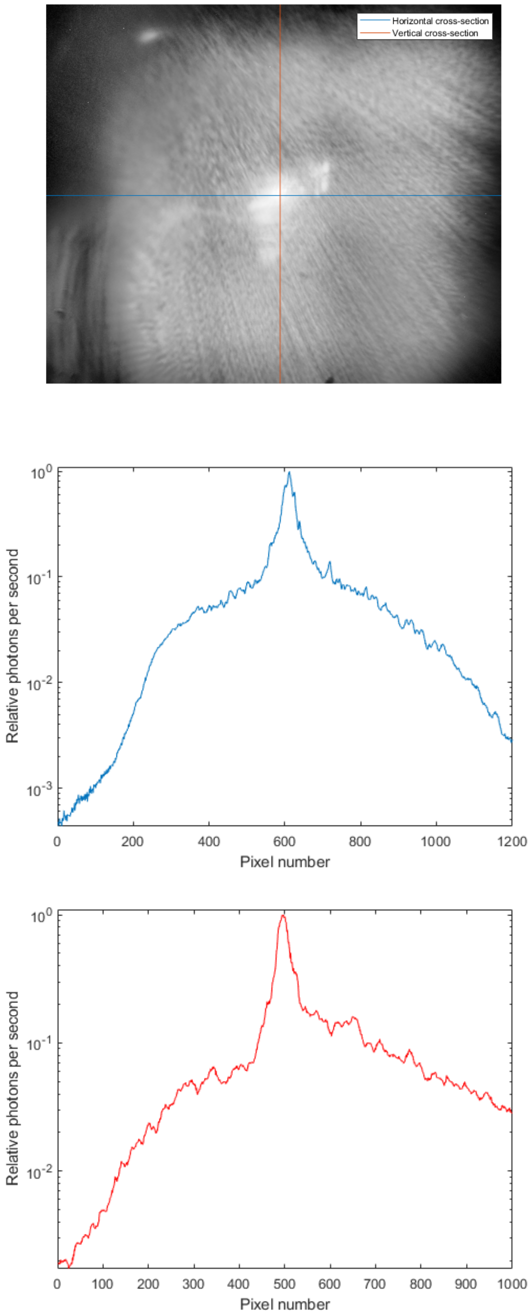

Figure 7: High dynamic range image (top), horizontal (centre) and vertical (bottom) cross-sections of the source point taken with stage 2 of the beam halo monitor using a 5 mm diameter Lyot stop.

losses will be higher than at present. First measurements have shown that the in-vacuum mirror causes a significant diffraction pattern to the bema halo images. An upgraded system featuring a Lyot stop demonstrated the diffraction contribution from the IVM can be significantly reduced, but not completely eliminated. Therefore further development is needed to confidently identify the degree of beam halo. For an improved beam halo monitor for Diamond-II, this work highlights that the IVM should be designed with minimal diffraction. Further improvements also include the use of post-processing to remove the remaining diffraction contribution from acquired images or the incorporation a micro mirror array to further suppress the point spread function. Further analysis could be done by comparing cross sections from the BHM with scraper measurements and simulations.

ACKNOWLEDGEMENTS

The authors would like to thank the Year in Industry programme at Diamond Light Source which funded this studentship.

REFERENCES

[1] R. Yang *et al.*, “Evaluation of beam halo from beam-gas scattering at the KEK Accelerator Test Facility”, *Phys. Rev. Accel. Beams*, vol. 21, p. 051001, 2018. `doi:10.1103/PhysRevAccelBeams.21.051001`

[2] C. Thomas *et al.*, “X-ray pinhole camera resolution and emittance measurement”, *Phys. Rev. ST Accel. Beams*, vol. 13, p. 022805, 2010. `doi:10.1103/PhysRevSTAB.13.022805`

[3] T. Mitsuhashi, “Beam Halo Observation by Coronagraph”, in *Proc. DIPAC’05*, Lyon, France, Jun. 2005, paper ITMM03, pp. 7–11. `https://jacow.org/d05/papers/ITMM03.pdf`

[4] L.C. Chapon *et al.*, “Diamond-II Conceptual Design Report”, May 2019. `https://www.diamond.ac.uk/Home/About/Vision/Diamond-II.html`

[5] A. Piwinski, “The Touschek Effect in Strong Focusing Storage Rings”, DESY, pp. 98-179, 1999. `arXiv:physics/9903034v1`

[6] A. Goldblatt *et al.*, “Design and Performance of Coronagraph for for Beam Halo Measurments in the LHC”, in *Proc. IBIC’16*, Barcelona, Spain, Sep. 2016, pp. 253–256. `doi:10.18429/JACoW-IBIC2016-MOPG74`

[7] J. Egberts and P. Welsch, “Flexible core masking technique for beam halo measurement swith high dynamic range”, *J. Instrum.*, vol. 5, p. P04010, 2010. `doi:10.1088/1748-0221/5/04/p04010`

[8] H. D. Zhang *et al.*, “Beam halo imaging with a digital optical mask”, *Phys. Rev. ST Accel. Beams*, vol. 15, p. 072803, 2012. `doi:10.1103/PhysRevSTAB.15.072803`

[9] J. Chouinard, “CCD vs CMOS industrial cameras”, 2018. `https://www.1stvision.com/machine-vision-solutions/2018/06/ccd-vs-cmos-industrial-cameras-excel-in-allied`

[10] Black BORG Series, 2014. `https://sciencecenter.net/hutech/catalog/bborg.pdf` (accessed 3 September 2021)

[11] Edmund Optics Inc, “Allied Vision Mako G-319 1/1.8" Monochrome CMOS Camera”, `https://www.edmundoptics.com/p/allied-vision-mako-g-319-1-18-inch-monochrome-cmos-camera/33093/`.

[12] QuickMTF, “Quick MTF, an image quality testing application”, `http://www.quickmtf.com/`.

[13] MathWorks MATLAB, `https://www.mathworks.com/products/matlab.html`

EMITTANCE MEASUREMENT ALGORITHM AND APPLICATION TO HIMM CYCLOTRON*

Yong Chun Feng[†,1], Rui Shi Mao[1], Xiao Juan Wei
Institute of Modern Physics, Chinese Academy of Sciences, 730000 Lanzhou, China
[1]also at Lanzhou Kejintaiji Corporation, LTD, 730000 Lanzhou, China

Abstract

HIMM, a Heavy Ion Medical Machine, developed by Institute of Modern Physics, has been in operation since April 2020. The beam emittance of the cyclotron exit is measured with the most often used techniques, i.e. slit-grid, Q-scan and 3-grid at a dedicated beam line which is not the actual HIMM optical line. The high speed data acquisition architecture is based on FPGA, and motion control system is constructed based on the NI module.

The data post processing and emittance calculation is based on Python code with self-developed algorithm, including Levenberg–Marquardt optimization algorithm, thick lens model, dispersion effect correction, error bar fit, mismatch check, image denoise and “Zero-thresholding” calculation. The algorithm description and simulation are discussed in detail. The application of the algorithm to HIMM cyclotron is presented in this paper as well.

INTRODUCTION

The heavy ion medical machine (HIMM) is developed by the Institute of Modern Physics (IMP), which consists of two electron cyclotron resonance (ECR) ion sources, a cyclotron, a synchrotron ring and five nozzles [1]. The synchrotron has a compact structure with a circumference of 56.2 m. The layout of the HIMM complex is shown in Fig. 1. Up to now, the slow-extraction efficiency of HIMM has reached nearly 90% for all energies from 120 to 400 MeV/u. The spill duty factor has exceeded 90% at a sample rate of 10 kHz with the feedback-based slow-extraction technique applied [2, 3].

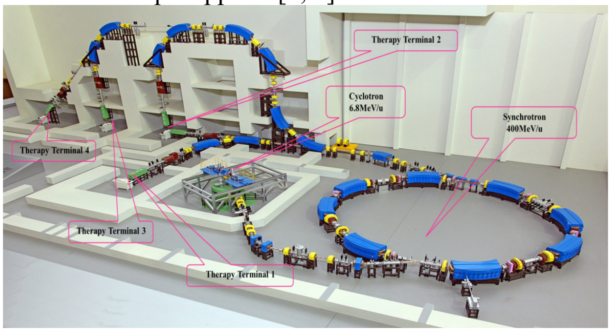

Figure 1: Layout of the HIMM complex.

Cyclotron, as the injector, plays a critical role in HIMM complex, which delivers the high quality beam to the ring through the MEBT (median energy beam transport line). The emittance and TWISS parameters measurement at the exit of the cyclotron are essential. Before integrating the cyclotron into HIMM, a dedicated beam line is constructed temporarily at the laboratory, and the measurement of emittance is performed along it.

The emittance and TWISS parameters at the exit of the cyclotron are measured using three most commonly used methods, slit–grid [4-6], Q-scan [7-9] and 3-grid [8-10]. A cross-check is of capability to validate this measurement.

In this paper, optimizition algorithm for Q-scan and 3-grid is introduced, in which dispersion correction and thick lens model fit are of the most importance in improving the reconstruction accuracy of the emittance. In addition, slit-grid algorithm, especially denoising in reconstrucing the beam phase space is interpreted also. Both the optimizition algorithm and denoising process can result in a positive improvement for emittance calculation from the view point of simulation and analytic derivation. Finally, the measurement results of the cyclotron are presented.

ALGORITHM DESCRIPTION AND SIMULATION

Optimizition Algorithm for Q-scan and 3-grid

In the approximation of linear, beam transport along a lattice can be expressed in the form of matrix, which indicate how the transfer elements impose a function to the beam. From the view of matrix point, a transfer matrix can be formulated as

$$M = \begin{pmatrix} a & b \\ c & d \end{pmatrix} \tag{1}$$

without the loss of generality. The matrix must be symplectic, which is a remarkable property of a Hamiltonian system. After the implementation of the matrix, the squared distribution in the real space at the exit of the lattice element can be written as

$$\Sigma_{11}^{f} = a^2\left(\langle x_\beta^2\rangle + D^2\langle\delta^2\rangle\right) + 2ab\left(\langle x_\beta x'_\beta\rangle + DD'\langle\delta^2\rangle\right) + b^2\left(\langle x'^2_\beta\rangle + D'^2\langle\delta^2\rangle\right) \tag{2}$$

, with the dispersion considered and chromaticity ignored. For a typical configuration of focus lens followed by a drift, the a and b can be expressed as

$$\begin{aligned} a(k) &= \cos\sqrt{k}l - \sqrt{k}L\sin\sqrt{k}l \\ b(k) &= \tfrac{1}{\sqrt{k}}\sin\sqrt{k}l + L\cos\sqrt{k}l \end{aligned} \tag{3}$$

with L the drift length, $k = B'/B\rho$, $B'l = C_1 + C_2 I$, C_1 and C_2 for calibrated coefficient of magnet. For Q-scan scheme, the desired values, i.e., $\langle x_\beta^2\rangle$, $\langle x_\beta x'_\beta\rangle$, $\langle x'^2_\beta\rangle$, can be

---

* Work supported by NSFC (Nos.12105336), NSFC (Nos. 11775281) , NSFC (Nos. 11905271) and the Natural Science Foundation of Gansu Province (No. 20JR10RA115)

† fengyongchun@impcas.ac.cn

ISBN: 978-3-95450-230-1 ISSN: 2673-5350 doi:10.18429/JACoW-IBIC2021-TUPP11

obtained via solving a non-linear least squares problem with the objective function given as follows

$$\Sigma_{11}^{f}(\boldsymbol{I},\boldsymbol{\alpha};D,D',\delta)=\Sigma_{11}^{f} \tag{4}$$

, in which, $\boldsymbol{\alpha}=\left(\langle x_\beta^2\rangle,\langle x_\beta x'_\beta\rangle,\langle x'^2_\beta\rangle\right)$. To find a solution, the following minimization procedure would be implemented,

$$\boldsymbol{\alpha}=\arg\min_{\boldsymbol{\alpha}} S(\boldsymbol{\alpha}) \tag{5}$$

where $S(\boldsymbol{\alpha})=\sum_{i=1}^{n}\left[y_i-\sqrt{\Sigma_{11}^{f}(\boldsymbol{I},\boldsymbol{\alpha};D,D',\delta)}\right]^2$.

If data uncertainties involved, the minimization may be scaled with a weighting factor ε_i that refers to the uncertainties of the profile y_i,

$$\boldsymbol{\alpha}=\arg\min_{\boldsymbol{\alpha}}\sum_{i=1}^{n}\left[\frac{y_i-\sqrt{\Sigma_{11}^{f}(\boldsymbol{I},\boldsymbol{\alpha};D,D',\delta)}}{\varepsilon_i}\right]^2 \tag{6}$$

The most widely used optimization algorithm for this is the so called Levenberg–Marquardt algorithm (LMA or just LM), which can be thought of a combination of the method of gradient descent and the Gauss-Newton algorithm (GNA), both of which are the most classical optimization algorithm. Thus, LMA adapts the advantages of both of the two algorithm, and hence has high performance as expected [11-13].

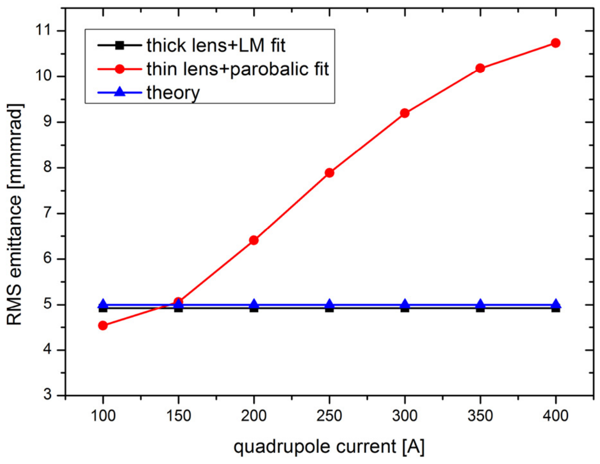

Figure 2: The difference between parabolic fit based thin lens model and LMA fit based thick lens model. Red dot-line is parabolic fit based thin lens model. Black dot-line is LMA fit based thick lens model, which agrees well with the theoretical emittance depicted by blue dot-line.

If (D,D',δ) are given at the measurement point beforehand, the TWISS parameters can be extracted with a high accuracy. For the case of unknown (D,D',δ), to extract the whole parameters including (D,D',δ) simultaneously , at least one dipole must be involved along the transport line.

For 3-grid scheme, the variable would be drift length L instead, hence, the objective function will be

$$\Sigma_{11}^{f}(\boldsymbol{L},\boldsymbol{\alpha};D,D',\delta) \tag{7}$$

LMA is an iterative approach with trust-region searching strategy. For each iteration, the Jacobian matrix $\boldsymbol{J}=\partial\boldsymbol{r}/\partial\boldsymbol{\alpha}$ is given as the first step, and then the advance of $\boldsymbol{\alpha}$, $\Delta\boldsymbol{\alpha}$, is found by solving the following linear equation

$$(\boldsymbol{J}^T\boldsymbol{J}+\lambda\boldsymbol{I})\Delta\boldsymbol{\alpha}=-\boldsymbol{J}^T\boldsymbol{r} \tag{8}$$

Where $\boldsymbol{I}$ is the identity matrix and λ is a damping parameter to control the solution $\Delta\boldsymbol{\alpha}$ brings $\boldsymbol{r}^T\boldsymbol{r}$ down hill how fast. The error of the fitting parameters is estimated by the covariance matrix defined as $\boldsymbol{C}=\boldsymbol{J}^T\boldsymbol{J}$ and then the 1σ error bar is $\sigma_i=\sqrt{C_{ii}}$ for the i’th paremeter [14].

A simulaton is performed based on the discussion above. First, the dispersion-free beam line is tracked, comparision between parabolic fit based thin lens model and LMA fit based thick lens model is presented in Fig. 2. With thin lens model and parabolic fit applied, the solutions don’t converge to the actual one, and a visible difference is observed as expected. Highly overestimated results occur at high current cases, which can be inferred from the fact that thin lens approximation is reasonable only when the quadrupole current is low. LMA fit based thick lens model gives the desired results in comparison to the actual one with a deviation of 1.56%.

Typically, dispersion can result in overestimated measurement of emittance from the enlarged beam width. The typical treatment for dispersion is to subtract its contribution from the measured beam width [15], like that $\langle x_\beta^2\rangle=\sqrt{\langle x_{meas}^2\rangle-D^2\langle\delta^2\rangle}$. However, this procedure is sometimes error-prone and of less robustness since the dispersion has to be evaluated explicitly as a function of quadrupole settings. An alternative is to take account of it as the fixed parameters in the fit model, which is more reasonable if the dispersion is given at the initial position as the first time, as interpreted in Eq. (5).

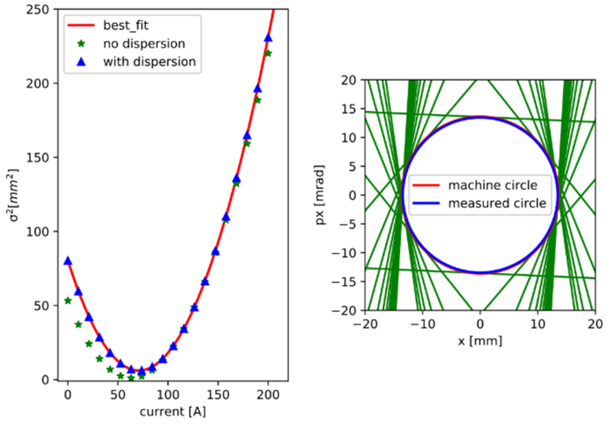

Figure 3: Left: non-zero dispersion induced beam width change. (green star) Diagnostics section is dispersion-free. (blue angle) Residual dispersion D = 5 m at the entrance of quadrupole. (red line) Fit using thick lens model with dispersion correction algorithm applied. Right: reconstructed phase space plotted in normalized coordinates frame, which displays the mismatch qualitatively.

The simulation results of emittance change induced by dispersion are shown in Figs. 3 and 4. The beam width change induced by a non-zero dispersion can be observed from Fig. 3 left. With the increase of dispersion, the reconstructed emittance is overestimated more and more, especially when the derivative of dispersion is positive, as presented in Fig. 4. If fit model treats dispersion as known parameters as formulated in Eq. (5), the dispersion-free TWISS parameters can be achieved with a good accuracy. This can be observed alternatively from the normalized phase space illustrated in the right plot of Fig. 3. which displays the mismatch between the designed (machine circle) and measured phase space (measured circle). A mismatch factor can be calculated as described in [16, 17],

$$\xi = \frac{1}{2}(\gamma_D\beta - 2\alpha_D\alpha + \beta_D\gamma) \tag{9}$$

if the designed TWISS (β_D, γ_D) is equal to the measured one (β, γ), the beam is matched to the machine optical, otherwise the mismatch is indicated by ξ.

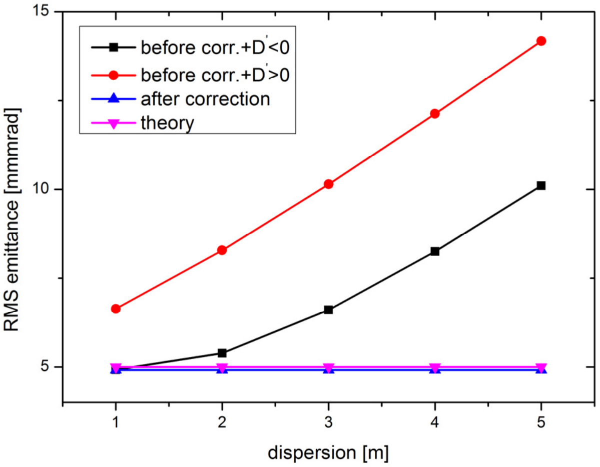

Figure 4: The comparison between with and without dispersion correction applied. Before correction and dispersion derivative $D' > 0$ (red), before correction and dispersion derivative $D' < 0$ (black), after correction (blue), theoretical one (purple).

'Zero-Thresholding' Approach for Slit-Grid Technique

The slit-grid measurement would generate a 2D phase space that is the area the emittance calculation launched. From which, the RMS emittance can be retrieved statistically. To simplify the calculation, the data index of the phase space matrix are used instead of the data itself [18]. The RMS emittance is defined as

$$\varepsilon_{rms} = \sigma_{n_x}\sigma_{n_{px}}\Delta x\Delta x'\sqrt{1-\rho^2} \tag{10}$$

the notation is the same with the reference [18].

Typically, the data are noisy owing to disturbances from the MW electronics and the environment. It is, therefore, necessary to denoise the data before performing the calculation. A systematic procedure to complete the emittance evaluation is given in [19], in which, a method called 'zero-thresholding' approach is proposed. For the method, the beam phase space is processed following a systematic procedure, including ad hoc-based interpolation, wavelet-based denoising, threshold-based ROI selection, and "zero-thresholding"-based emittance extraction. From the simulation, the quantized error decreases with the increased interpolation number, and a deviation of below 4% is reached when interpolation number 4 is given. The theory supporting the "zero-thresholding"based emittance extraction is given in APPENDANCE.

APPLYING ALGORITHM TO HIMM CYCLOTRON

The emittance of the HIMM cyclotron is measured and the data processing is finished. Three techniques are employed to complete this procedure, and the algorithm disscused above is applyed. The results are shown in Table 1, Figs. 5-7.

The results of these measurements agree well with each other for the vertical plane. There is a discrepancy for the horizontal plane, however. Based on our deductions, this is attributed to the nonzero dispersion contribution. The dispersion and its derivative are not known with a high accuracy in the horizontal plane at the exit of cyclotron, and the temporal beam line is not designed to be dispersion-free in the diagnostics section.

Table 1: Emittance Summary at the Exit of HIMM Cyclotron Measured Using Three Techniques

	Slit-grid	**Q_scan**	**3-grid**
Horizontal(95%) [mm*mrad]	45.32	51.5	56.93
Vertical (95%) [mm*mrad]	37.56	31.8	38.15

APPENDANCE

For simplicity, assumping the real space distributuion obeys 1D Gaussian function with zero mean, that is $x \sim \mathcal{N}(x;0,\sigma)$. The probability density function can be formulated as

$$f(x;\sigma) = \frac{1}{\sqrt{2\pi}\sigma}\exp\left(-\frac{x^2}{2\sigma^2}\right). \tag{A1}$$

The maximum intensity locates at $x = 0$, and the value is $I_{max} = f(0) = 1/\sqrt{2\pi}\sigma$. Assumping the threshold is $I_{th} = \chi I_{max}$, in which, $\chi \in (0,1)$ means the proportion of the signal the threshold occupied. A larger χ is corresponding to a smaller phase space, and hence a cleaner phase space. The phase space coordinates x_{th} corresponding to the threshold I_{th} can be evaluated by $f(x_{th}) = I_{th}$, which gives

$$x_{th} = \pm\sqrt{-2ln(\chi\sigma)}. \tag{A2}$$

If beam phase space is not cut by the threshold, that is $\chi = 0$ or $x_{th} = \pm\infty$, the statistic deviation of the distribution is σ exactly. However, when it is cut, the new statistic deviation should be evaluated via the definition as

$$\sigma_{th}^2 = \langle(x - \langle x\rangle)^2\rangle = \frac{\int_{-x_{th}}^{x_{th}} x^2 f(x)dx}{\int_{-x_{th}}^{x_{th}} f(x)dx} = \frac{-2\chi\sigma^2\left[iDaw\left(i\sqrt{-ln\chi}\right)+\sqrt{-ln\chi}\right]}{\sqrt{\pi}Erf\left(\sqrt{-ln\chi}\right)} \tag{A3}$$

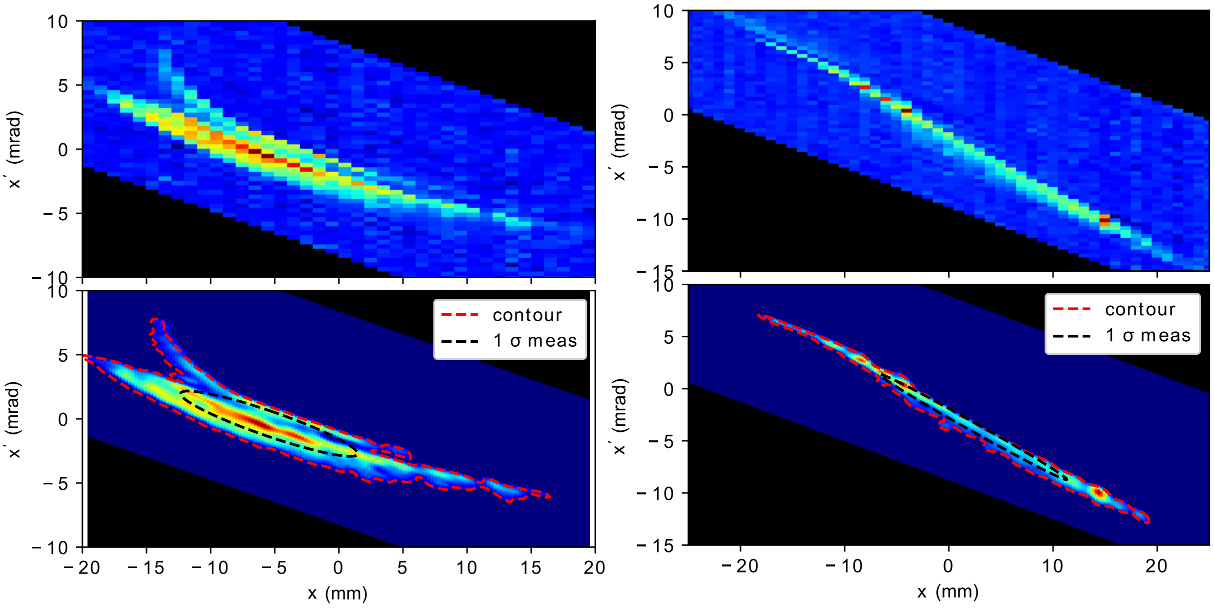

Figure 5: Phase space distribution obtained from slit-grid technique. Left: the horizontal plane, Right: the vertical plane. Top: the raw phase space, bottom: the denoised phase space, the red dashed line is the contour line with a contour level of 10%, and the black dashed line is the measured 1σ phase ellipse.

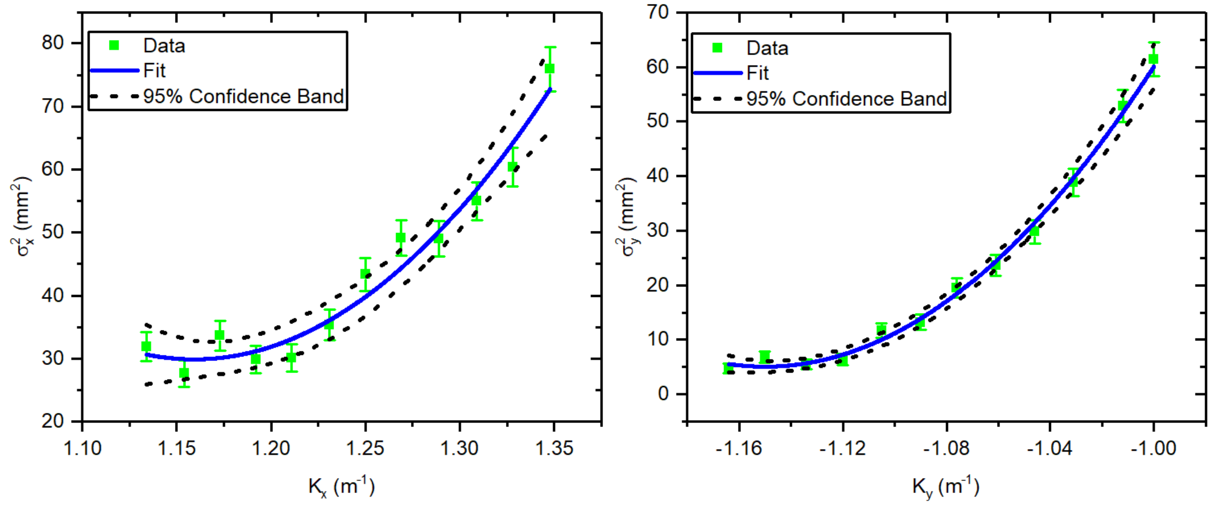

Figure 6: Q-scan data and fit. Left: the horizontal plane; Right: the vertical plane.

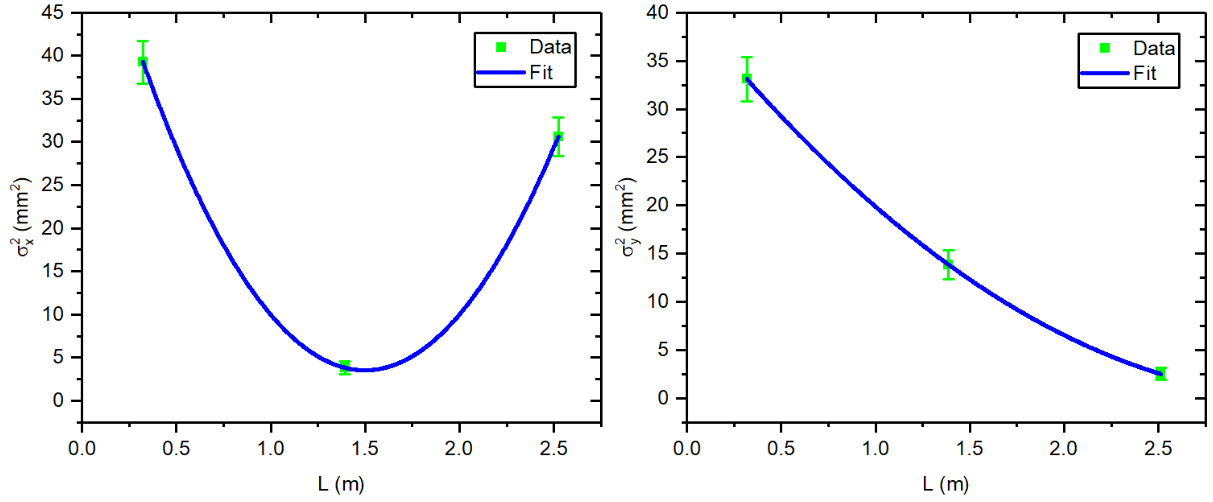

Figure 7: 3-grid data and fit. Left: the horizontal plane; Right: the vertical plane.

, in which i is the complex, $Daw(x) \equiv \exp(-x^2)\int_0^x \exp(t^2)dt$ is the Dawson's integral, $Erf(z) \equiv \frac{2}{\sqrt{\pi}}\int_0^z \exp(-t^2)dt$ is the Error function. The ratio between σ_{th} and σ is

$$\delta^2(\chi) = \frac{\sigma_{th}^2}{\sigma^2} = \frac{-2\chi\left[iDaw\left(i\sqrt{-ln\chi}\right)+\sqrt{-ln\chi}\right]}{\sqrt{\pi}Erf\left(\sqrt{-ln\chi}\right)}. \qquad (A4)$$

The evolution of δ^2 with χ is shown in Fig. 8. It is a monotonic decreasing function. The limit of $\delta^2(\chi)$ near the $\chi = 0$ is

$$\lim_{\chi\to 0} \delta^2(\chi) = 1 \qquad (A5)$$

, which indicates that σ_{th} approaches σ when χ approaches 0. It geives the correctness of the formulation Eq. (A4). With the increase of χ, a linear section occurs, which gives the possibility to approximate the σ with σ_{th} linearly. Series expansion of $\delta^2(\chi)$ at far away from $\chi = 0$ is

$$\begin{aligned}\delta^2(\chi) = 0.823 - 1.453(\chi - 0.1)\\ +\mathcal{O}((\chi - 0.1)^2).\end{aligned} \qquad (A6)$$

Linear approximation gives a good estimation of σ, as depicted in Fig. 8. Therein the dotted red line is a linear approximation of $\delta^2(\chi)$. The deviation is large somewhat near the $\chi = 0$. The maximum deviation is 0.03, and the maximum deviation in terms of statistic deviation σ is less than 2%.

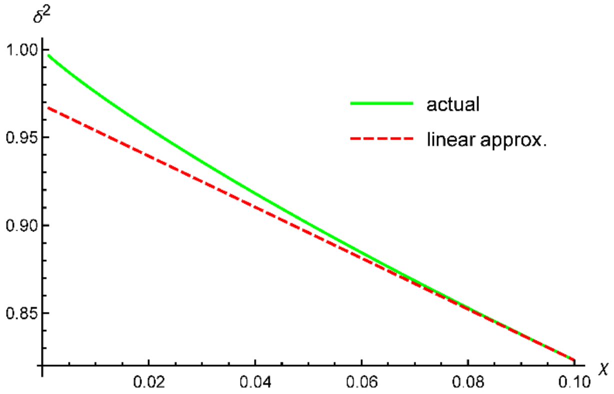

Figure 8: The evolution of δ^2 with χ. Green line is $\delta^2(\chi)$, dotted red line is a linear approximation.

REFERENCES

[1] J. Yang *et al.*, "Design of a compact structurecancer therapy synchrotron", *Nucl. Instrum. Meth.* A, vol. 756, pp. 19–22, 2014. `https://doi.org/10.1016/j.nima.2014.04.050`

[2] J. Shi *et al.*, "Heavy ion medical machine (HIMM) slow extraction commissioning", *Nucl. Instrum. Meth. A*, vol. 918, pp. 76–81, 2019. `doi:10.1016/j.nima. .2018.11.014`

[3] Y. C. Chen *et al.*, "Optimization and Upgrade of Slow Extraction Control System for HIRFL CSR Main Ring", in *Proc. 16th Int. Conf. on Accelerator and Large Experimental Physics Control Systems (ICALEPCS'17)*, Barcelona, Spain, Oct. 2017, pp. 1663-1665. `doi:10.18429/JACoW-ICALEPCS2017-THPHA122`

[4] J. Montano *et al.*, "Off-line emittance measurements of the SPES ion source at LNL", *Nucl. Instrum. Meth. A*, vol. 648, pp. 238–245, 2011. `doi:10.1016/j.nima.2011.05.038`

[5] X.H. Wang, Z.G. He, and J. Fang, "Slit-based emittance measurement system for high-brightness injector at Hefei light source", *High Power Laser Part. Beams*, vol. 24, pp. 457–462, 2012. `doi:10.3788/HPLPB20122402.0457`

[6] C. Xiao *et al.*, "Measurement of the transverse four-dimensional beam rms-emittance of an intense uranium beam at 11.4MeV/u", *Nucl. Instrum. Meth. A,* vol. 820, pp. 14-22, 2016. `doi:10.1016/j.nima.2016.02.090`

[7] F. Lohl *et al.*, "Measurements of the transverse emittance at the FLASH injector at DESY", *Phys. Rev. Spec. Top. Accel. Beams,* vol. 9, p. 092802, 2006. `doi:10. 1103/PhysRevSTAB.9.092802`

[8] M. Olvegard and V. Ziemann, "Effect of large momentum spread on emittance measurements", *Nucl. Instrum. Meth. A,* vol. 707, pp. 114–119, 2013. `doi:10.1016/j.nima.2012.12.114`

[9] Z. Zhang and X.G. Jiang, "Pulsed intense electron beam emittance measurement", *Nucl. Sci. Tech.*, vol. 25, p. 060201, 2014. `doi:10.13538/j.1001-8042/nst.25.060201`

[10] L.Y. Zhang and J.J. Zhuang, "Calculation of two-screen emittance measurement", *Nucl. Instrum. Meth. A*, vol. 407, pp. 356–358, 1998. `doi:10.1016/S0168-9002(98)00049-7`

[11] K. Levenberg, "A Method for the Solution of Certain Non-Linear Problems in Least Squares", *The Quarterly of Applied Mathematics*, vol. 2, pp. 164-168, 1944.

[12] D.W. Marquardt, "An algorithm for least-squares estimation of nonlinear parameters", *Journal of the Society for Industrial and Applied Mathematics*, vol. 11(2), pp. 431-441, 1963.

[13] Mark K. Transtrum and James P. Sethna, "Improvements to the Levenberg-Marquardt algorithm for nonlinear least-squares minimization", arXiv:1201.5885v1 [physics.data-an].

[14] X. Huang, S. Y. Lee, K. Y. Ng, and Y. Su, "Emittance measurement and modeling for the fermilab booster", *Phys. Rev. ST Accel. Beams*, vol. 9 p. 014202, 2006. `doi:10.1103/PhysRevSTAB.9.014202`

[15] K. Holldack, J. Feikes, and W. Peatman, "Source size and emittance monitoring on BESSY II", *Nucl. Instrum. Meth. A*, vol. 467, pp. 235-238, 2001. `doi:10.1016/S0168-9002(01)00555-1`

[16] M. G. Minty and F. Zimmermann, *Measurement and Control of Charged Particle Beams*, Springer-Verlag Berlin Heidelberg New York: Springer, 2003

[17] S. Y. Lee, *Accelerator Physics (3thd Edition)*, Singapore: World Scientific, 2011.

[18] A. W. Chao *et al.*, "Heavy Ion Linacs—Emittance Measurements P. Forck, P. Strehl", in *Handbook Of Accelerator Physics And Engineering (2nd Edition)*, Singapore: World Scientific, 2013, pp. 702-704.

[19] Y.-C. Feng *et al.*, "Transverse emittance measurement for the heavy ion medical machine cyclotron", *Nucl. Sci. Tech.*, vol. 30(12), pp. 184, 2019. `doi:10.1007/s41365-019-0699-7`

ISBN: 978-3-95450-230-1 ISSN: 2673-5350 doi:10.18429/JACoW-IBIC2021-TUPP12

DEVELOPMENT OF A PEPPER POT EMITTANCE MEASUREMENT DEVICE FOR THE HIT-LEBT

R. Cee*, C. Dorn[1], E. Feldmeier, T. Haberer, A. Peters, J. Schreiner, T. Winkelmann,
Heidelberg Ion Beam Therapy Centre, Heidelberg, Germany
[1]also at GSI Helmholtzzentrum für Schwerionenforschung GmbH, Darmstadt, Germany

Abstract

The Heidelberg Ion Beam Therapy Centre (HIT) is a synchrotron based medical accelerator facility for the treatment of cancer patients with ions. Since the first treatment in November 2009 about 7000 patients have been irradiated with protons or carbon ions and, since July 2021, also with helium ions. In 2010 HIT started the operation of a test bench with a setup comparable to the LEBT at the accelerator. Since 2013 the test bench serves as a common low energy beamline of Siemens Healthcare and HIT with components from both partners. In parallel to ion source and RFQ research and development we have experimented with our proprietary pepper pot device. We plan to install the final version of the pepper pot into the LEBT section and use the measured beam distributions for the design of a new RFQ. With the recent redesign of the mask-target assembly we have increased the active area of the device and generated a possibility for an accurate pixel calibration by a specialised calibration mask. Our tool PePE (Pepper Pot Emittance Evaluation) offers different approaches for the reconstruction of the 4D emittance parameters from the raw image. The evaluation process was validated by a pepper pot image generated from a simulated beam with known properties.

INTRODUCTION

For reliable beam dynamics simulation and accelerator design the knowledge of the phase space occupied by the beam is of major importance. The pepper pot device is particularly suitable for characterizing the output beam of the ion source. Its vital component is the mask, a metal sheet with a regular grid of holes, reminding of the lid of a pepper pot thus giving the instrument its name. When inserted into the beam the mask cuts out a set of beamlets which are made, after a drift, visible on a scintillating screen. A digital camera records the light spots in a raw image which has to be processed with respect to the location and intensity of the beamlets. The beamlets have to be related to the holes giving not only the position but also the angle coordinate, the latter from the small difference between the beamlet position on the screen and the hole position on the mask. The hole spacing has to be chosen *small* enough to fulfil the demands on spatial resolution but *big* enough to avoid overlapping of the beamlets, leading to unfeasible images.

The resolution will in most cases be lower compared to e.g. a slit-grid-assembly but the major benefits of the pepper pot are the fast data acquisition (single shot) and the 4D information including not only the real space (x-y) and the pure phase spaces (x-x' and y-y') but also the momentum space (x'-y') and the mixed phase spaces (x-y' and y-x').

TEST BENCH

The HIT test bench has its origin in 2010 when it was set up as a test facility for the third ion source branch for our low energy beam transport system (LEBT) [1]. After installation of the source and most of the beam line components into the productive accelerator, we continued to operate the test bench with alternating components. The exploratory focus is now on ion source optimisation, emittance measurement and RFQ characterisation.

The HIT test bench in its current state represents a LEBT with a subsequent RFQ accelerator (see Fig. 1). The ECR ion source for the production of ${}^{12}C^{4+}$, H_3^+ and ${}^{4}He^{2+}$ ions is directly coupled to a spectrometer dipole and followed by a dual stroke round aperture (⌀10 mm, ⌀20 mm or out) for charge separation. The beam line behind the dipole comprises a triplet, a chopper for pulsed beam operation and a solenoid for the final matching of the beam into the RFQ. For beam alignment three steerer pairs are installed. The beam line is well equipped with beam diagnostic devices such as Faraday cups, beam transformers and profile grids. The pepper pot emittance meter with a mask, a quartz target, a mirror and a camera is located in a diagnostics chamber between chopper and solenoid. The diagnostic line downstream the RFQ contains three capacitive phase probes for time-of-flight resp. energy measurements.

The last subject of investigation has been the pepper pot device, which was, in its original form, developed in 2010 [2]. After having collected a number of measurement data for all available ions, we could draw our conclusions of how to improve the device. A couple of optimisations, described in the following section, have already been put into effect and measurements are in progress.

PEPPER POT HARDWARE

The pepper pot equipment is attached to two distinct actuators both mounted to the same diagnostics chamber: one holding the mask and the screen, the other one the mirror directing the light through a glass window to the camera installed on the flange. The distance between mask and screen is adjustable, realised by a fixed screen and a displaceable mask. The most important properties of mask and screen are summarised in Table 1.

---

* rainer.cee@med.uni-heidelberg.de

ISBN: 978-3-95450-230-1 ISSN: 2673-5350 doi:10.18429/JACoW-IBIC2021-TUPP12

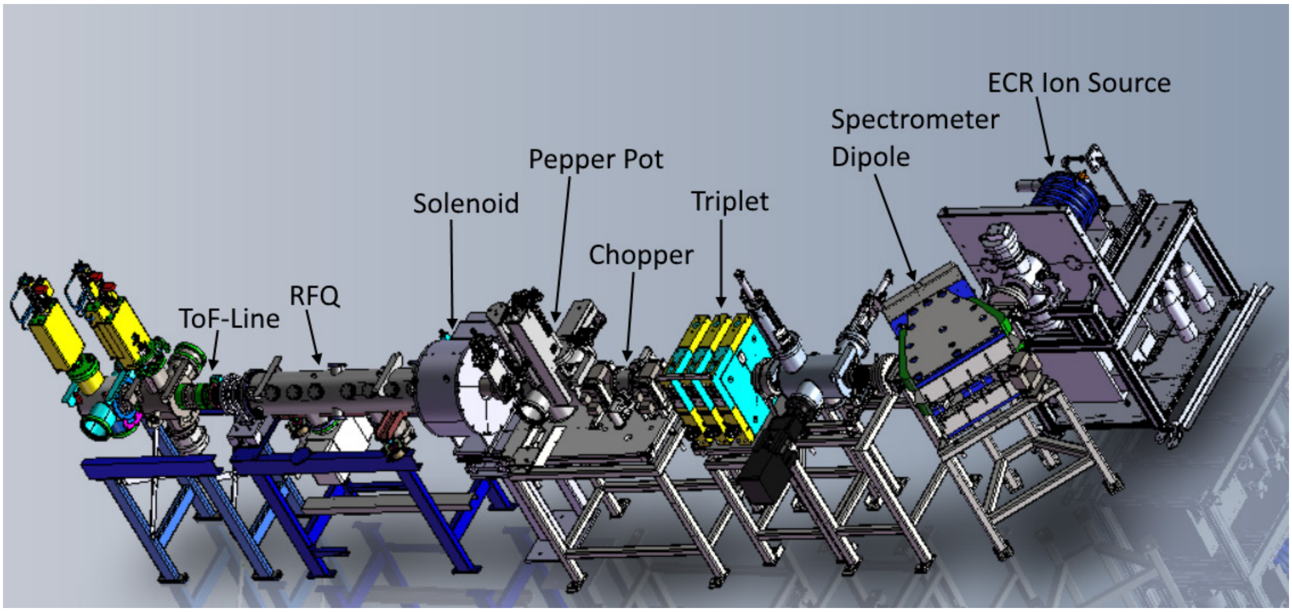

Figure 1: Test bench setup with an overall length of approx. 8 m.

Table 1: Main Pepper Pot Characteristics

Mask		**Screen**	
material	tungsten	material	quartz glass
thickness	100 µm	supplier	QGH [3]
hole spacing	1.5 mm	product	Herasil 3
hole diameter	100 µm	thickness	200 µm

The camera in use is a Prosilica GT from Allied Vision [4] with 16 bit colour depth (monochrome) and a maximum image size of 2464 × 2056 (5.1 megapixel). During our first sets of measurements at the test bench we recognized that the beams do not fit on the 45 mm × 45 mm mask, when no aperture was inserted upstream. We further estimated from profile measurements in the LEBT that the mask will also be too small in its final place in the medical accelerator. We consequently designed a new pepper pot layout with a larger, round mask with an active area of now 72 mm in diameter. The formerly 60 mm (effectively 55 mm) diameter quartz glass disk was increased to a 80 mm (effectively 74 mm) keeping material and thickness. The mask-screen distance is now realised in steps of 5 mm instead of being floating improving the accuracy. The new setup with round mask and round screen is shown in Fig. 2.

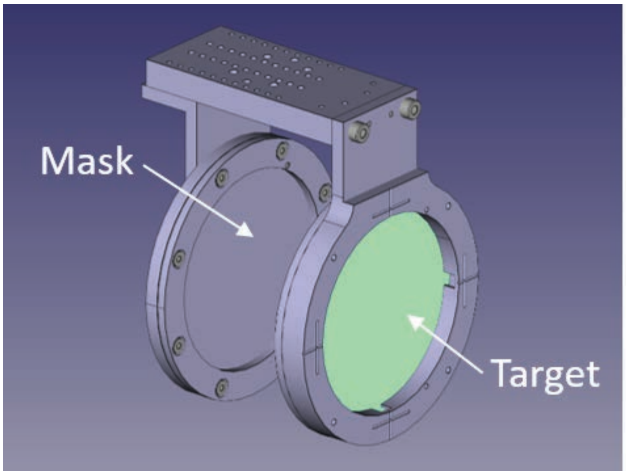

Figure 2: New pepper pot assembly with round mask and target (screen).

PIXEL CALIBRATION

Pixel calibration. i.e. the translation of pixels into millimetres, is an important detail of the pepper pot measurement. It depends on the optics and has to be performed for the plane of the screen (not the mask!). We formerly used the support ring of the screen to do the pixel calibration. For the enhanced design we came up with a new method using a calibration mask. This mask has nine holes arranged as a cross and can be placed at the location of the screen.

MEASUREMENT SEQUENCE

A pepper pot measurement essentially means to take an image of the viewing screen, showing a number of light spots. This raw image (in our case tif-format) has then to be evaluated with respect to its local brightness maxima. To ensure a robust functioning of the search algorithm the image is first processed applying the following steps:

- **subtraction of the dark image** (if available)**:** this eliminates defective pixels and effects from interfering light
- **selection of the relevant area:** this cuts off artefacts at the edge of the image, e.g. caused by (intentionally) larger edge holes and reduces calculation time

- **smoothing with a Gaussian filter:** this suppresses the presence of local maxima connected to noise
- **subtraction of the background:** a user defined value can be subtracted from the entire image
- **noise reduction:** by zeroing pixels below a certain brightness threshold, the beamlets can be clearly confined from each other; the threshold can be changed by the user during the evaluation and allows for the iteratively optimisation on the basis of the visual result

The found beamlets are assigned to the closest hole in the mask, with the hole coordinates defining the x- and y-position of the beamlet. The angle in both directions is determined by the beamlet-to-hole difference and the distance between mask and screen. The final emittance calculation can then be made by using all non-zero pixels (PIX-method, most accurate, but slow), the maxima-pixel only (MAX-method, fast, but less accurate) or by a centre-of-mass algorithm based on Voronoi-cells. The latter has been discarded as it has, in the current realisation, not passed the validation process.

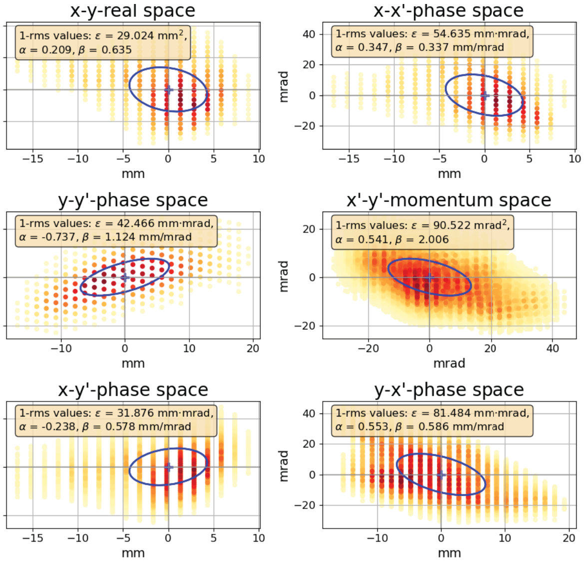

Figure 3: Pepper pot result of a 126 µA carbon beam (dual stroke at ⌀20 mm) at the HIT test bench using the PIX-method.

All described steps are implemented in a Python code we call PePE (**Pe**pper **P**ot Emittance **E**valuation). The result of a data evaluation with this tool is displayed in Fig. 3. It shows the six 2D-subspaces of a 126 µA carbon beam (dual stroke at ⌀20 mm) at the HIT test bench based on the PIX-method. These data have been recorded with the original quadratic mask.

VALIDATION BEAM

A validation of the evaluation algorithm can be performed by comparison with other emittance meters known for giving well established results. Another possibility is to generate a particle distribution of predefined properties (Twiss parameters) as validation beam [5].

The procedure consists of the following steps:

- **Particle generation:** in the presented case 2.5 millions uniformly distributed particles correlated in the horizontal (convergent) and vertical phase space (divergent), uncorrelated in the mixed phase spaces
- **Masking:** particles not passing the mask holes are filtered out; the remaining ~11 000 particles are plotted in Fig. 4
- **Drift:** particle drift from the mask to the screen (here 15 mm)
- **Image generation:** from a 2D histogram of the particles a tif-image is generated, which is evaluated as it was a real measurement

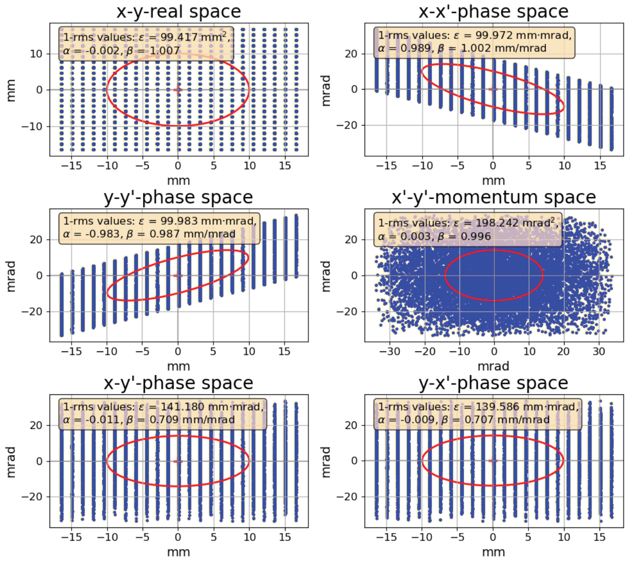

Figure 4: Validation beam after masking (~11 000 particles).

The image generated as described was analysed with the two evaluation methods PIX (all pixels are taken into account) and MAX (only pixels with local intensity maxima are taken into account). The results are summarised in Table 2 (1-rms-values). For the pixelwise evaluation all Twiss parameters are confirmed within an accuracy of ~3 %, the emittance remaining within a limit of 1.5 %. Regarding the evaluation of the intensity maxima only, the deviation of the ellipse parameters reaches up to 16 %, whereas the values for the emittance reveal a systematic underestimation of max. -8.5 %.

This investigation validates the PIX-method, whereas the result of the MAX-method stills remains within tolerable errors considering the fact that a substantial part of the data is discarded. Of course the explicit numbers in Table. 2 depend on statistics and my vary with the number of simulated particles but this does not affect the conclusion.

Table 2: Evaluation and Comparison of the Validation Beam

Parameter [Unit]	**Input**	**Result (two methods)**	
		PIX	**MAX**
α_x [1]	0.989	0.981 (-0.8 %)	1.030 (+4.1 %)
β_x [mm/mrad]	1.002	0.971 (-3.1 %)	1.025 (+2.3 %)
ϵ_x [mm mrad]	99.97	101.5 (+1.5 %)	95.3 (-4.7 %)
α_y [1]	-0.983	-0.979 (-0.4 %)	-1.140 (+16 %)
β_y[mm/mrad]	0.987	0.964 (-2.3 %)	1.056 (+7.0 %)
ϵ_y[mm mrad]	99.98	100.2 (+0.2 %)	91.5 (-8.5 %)

LEBT INTEGRATION

Emittance measurements at the end of our LEBT have been performed in the frame of the initial commissioning with a mobile slit-grid arrangement [6]. For daily operation emittance measurements were not foreseen in the design.

Provided tests of the new pepper pot layout are successful, we will integrate the device in our LEBT to give us the possibility to measure the emittance of the production beam at any time. As space is limited we plan to free two sockets in a diagnostics chamber right behind the switching magnet (red magnet in Fig. 5). The upper socket will house the actuator with mask and screen, whereas the horizontal socket will hold the mirror and the camera.

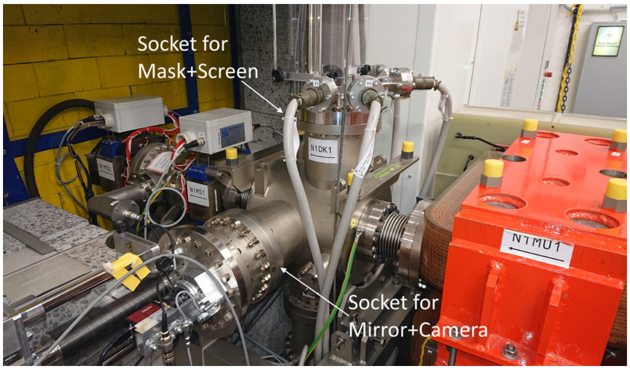

Figure 5: Designated place of installation of the pepper pot in the LEBT behind the switching magnet (red magnet).

CONCLUSION AND OUTLOOK

At HIT, a pepper pot emittance meter was constructed which recently got a new design with a larger active area. In parallel, an evaluation tool was developed giving us the correlations of all 2D subspaces. We found a way to validate the algorithm by the generation and evaluation of an artificial pepper pot image.

In a next step we are going to repeat earlier measurements with the new mask-screen layout. The resulting particle distributions are an important ingredient for our ongoing project of designing a new RFQ with the goal of transmission optimisation.

ACKNOWLEDGEMENTS

This work wouldn't have been possible without the contribution of Siemens Healthcare GmbH, Erlangen, Germany, represented by A. Robin, to the test bench. They have provided the ECR source and most of the magnets. Specials thanks goes to Eckelmann AG, Wiesbaden, Germany, for the integration of the test control system.

REFERENCES

[1] T. W. Winkelmann *et al.*, "Integration of a Third Ion Source for Heavy Ion Radiotherapy at HIT", in *Proc. ECRIS'12*, Sydney, Australia, Sep. 2012, paper TUPP03, pp. 46–48.

[2] M. Ripert *et al.*, "A Low Energy Ion Beam Pepper Pot Emittance Device", in *Proc. BIW'10*, Santa Fe, NM, USA, May 2010, paper TUPSM060, pp. 297–301.

[3] Aachener Quarzglas-Technologie Heinrich GmbH & Co. KG, Im Süsterfeld 4, 52072 Aachen, Germany, `https://www.quarzglas-heinrich.de`

[4] Allied Vision Technologies GmbH, Taschenweg 2A, 07646 Stadtroda, Germany, `https://www.alliedvision.com`

[5] Personal communications, I. Bustinduy, ESS Bilbao, Spain, Feb. 2021.

[6] M. T. Maier *et al.*, "Status of the Linac-commissioning for the Heavy Ion Cancer Therapy Facility HIT", in *Proc. EPAC'06*, Edinburgh, UK, Jun. 2006, paper TUPLS036, pp. 1571–1573.

ISBN: 978-3-95450-230-1 ISSN: 2673-5350 doi:10.18429/JACoW-IBIC2021-TUPP13

BEAM PROFILE MONITOR DESIGN FOR A MULTIPURPOSE BEAM DIAGNOSTICS SYSTEM

A. R. Najafiyan†, F. Abbasi, Shahid Beheshti University, Tehran, Iran
Sh. Sanaye Hajari, F. Ghasemi, Physics and Accelerator Research School,
Nuclear Science and Technology Research Institute (NSTRI), Tehran, Iran

Abstract

Beam diagnostic tools are the key component of any accelerator. They provide the way to measure beam parameters in order to monitor the accelerator performance. The beam profile is a bridge to other beam parameters such as transverse position, size, divergence and emittance. Depending on the characteristics of the beam, there are different tools and methods for beam profile monitoring. A suitable diagnostic tool for measuring the beam profile with high resolution is scintillator view screens which are the oldest and most precise tools. This paper presents the beam profile monitor design for a multipurpose beam diagnostic system. This system is aimed to measure the beam profile, transverse parameter, momentum spectrum and current. The concerning issues in the beam profile monitor design such as image resolution, radiation damage and scintillator temperature distribution have been discussed.

INTRODUCTION

Diagnostic instruments are a set of equipment used to measure the various parameters of the particle beam in accelerators. A suitable diagnostic tool for high-resolution profile monitoring are scintillation screens that utilize the mechanism of the scintillation phenomenon. In this method, according to Fig. 1, the scintillation light is recorded by an optical system and processed in order to extract the beam parameters. We designed a scintillation screen monitor using YAG for a multipurpose beam diagnostics system that will be able to measure proton beams up to 200 keV energy and electron beams up to 10 MeV.

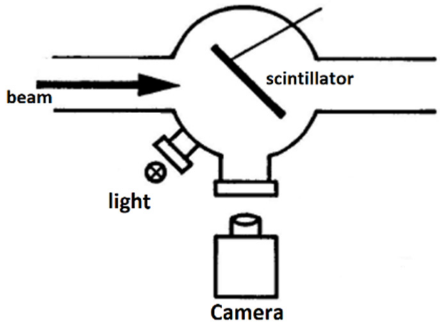

Figure 1: Layout of beam profile diagnostic system.

In this paper, the concerning issues in the beam profile monitor design such as image resolution, radiation damage, temperature distribution and charge accumulation on the scintillator have been discussed. Specially, using the Geant4 Monte Carlo code, we have estimated the resolution of the scintillator view screen and the temperature distribution of the scintillator is simulated using Comsol software and its effect on measured beam profile has been addressed.

PROFILE MONITORING DESIGN

The design procedure includes, scintillator material selection, handling the thermal and charge accumulation issues and estimation and improvement of the measurement resolution.

Selection of Scintillation Material

For the scintillation material high light yield, resistance to radiation damage, vacuum compatibility, linear response and lower temperature sensitivity is demanded, YAG:Ce is a trade-off choice since it presents good scintillation yield and radiation damage resistance and low temperature dependence as discussed below [1].

Radiation Damage

Cavity and atomic displacement are the main types of radiation damage in scintillation crystals [2]. These lattice damage alters the energy of the crystal bond. As a result, optical parameters such as the yield and frequency of scintillation output light change [3]. Radiation damage is directly related to LET (the amount of energy that an ionizing particle transfers to the material per unit distance) of incident radiation, and the LET of each beam is directly related to its mass and charge and inversely related to its energy [4]. Therefore, the damage of the electron beams is generally small compared to the ion beams due to their mass.

---

† alireza.najafiyan2@gmail.com

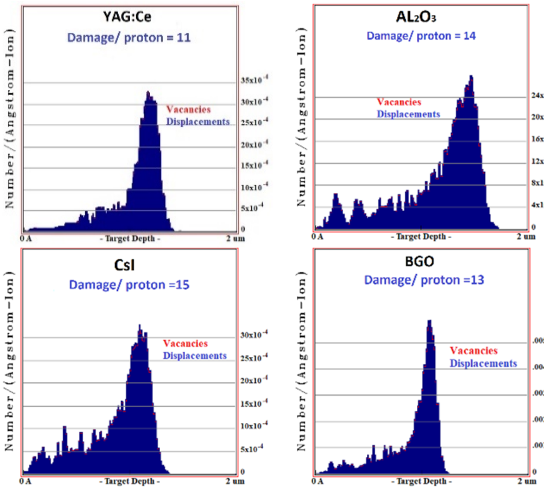

Figure 2: Comparison of radiation damage of scintillators caused by a 200 keV proton.

The scintillation damage caused by a 200 keV proton beam in conventional scintillators are simulated using TRIM software. According to the Fig. 2, the YAG scintillator is the most resistant material to be used as a beam diagnostic tool with the minimum amount of cavities and displacement created (11 damage per collision).

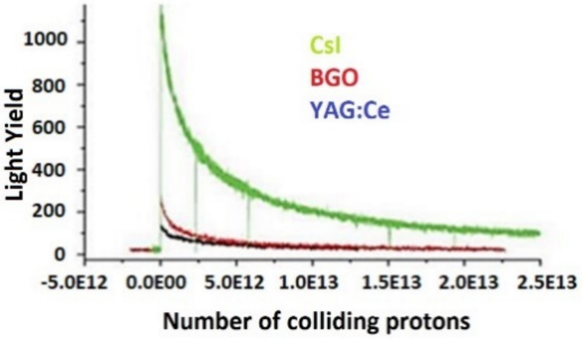

Figure 3: Changes in the optical response of the YAG, BGO and CsI scintillation against radiation damage [5].

This result is consistent with the experimental data obtained by Simon *et al.* (Fig. 3), which emphasizes the high resistance of the YAG scintillation to proton radiation [5]. As shown in Fig. 3, the optical response of CsI and BGO after irradiation of 5,000 billion protons is about 20% and 16% of the initial value, respectively, while for the case of YAG, it is 31%.

Temperature Distribution

As the proton beam strikes the surface of the scintillator, its temperature increases and resulting in degradation of its optical response.

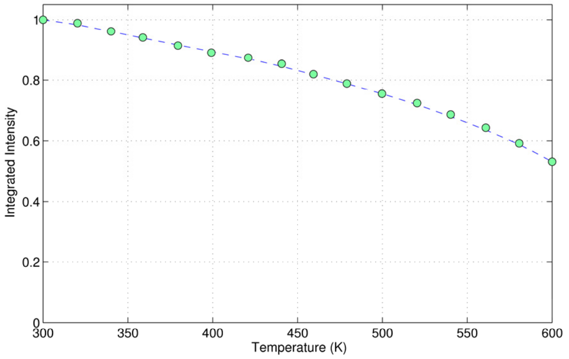

Figure 4: The temperature dependence of YAG yield [3, 6].

Bachmann *et al.* calculated the effect of temperature changes on the intensity of the YAG scintillation yield [3].The results are shown in Fig. 4, where the light intensity of YAG is reduced by about half the maximum value at a temperature of about 600 K ($T_{1/2}$). This temperature is conventionally selected as the maximum allowable temperature of the scintillator. To calculate the final temperature of the scintillator, we simulated the temperature distribution using Comsol software (as shown in Fig. 5) and obtained the final temperature of the YAG: Ce scintillator for different beam powers. Information about the simulated problem is given in Table 1.

Table 1: Simulated Problem Information

YAG (30*30mm*50 um)	scintillator
Al (30*30mm*10 mm)	substrate
Copper cylinder (R=5 m , h=200 mm)	holder
10 mm	Beam radius
From 0.1 to 10 W	Beam power

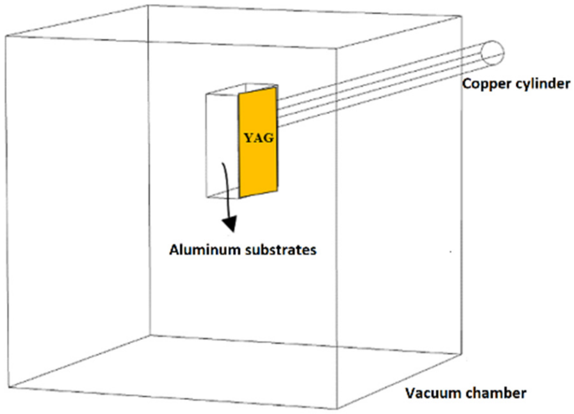

Figure 5: Schematic of the simulated problem.

If the scintillator has no substrate, the scintillator temperature at high powers will reach to 600 K ($T_{1/2}$). The average final scintillation temperature for different beam powers is shown in Fig. 6.

ISBN: 978-3-95450-230-1 ISSN: 2673-5350 doi:10.18429/JACoW-IBIC2021-TUPP13

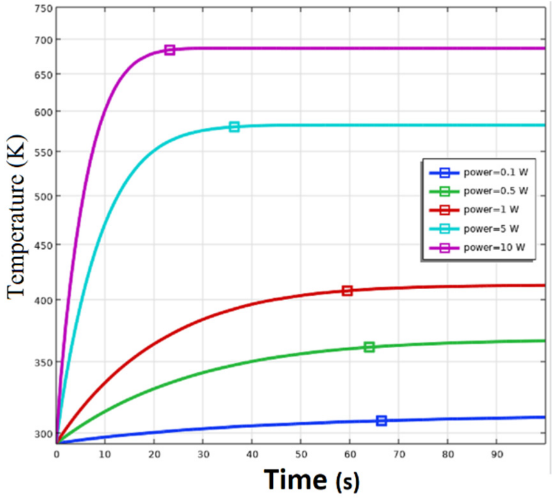

Figure 6: Simulation of the final temperature of the YAG for different beam powers using Comsol software.

As you can see in Fig. 7, at a beam power of 5 W, the temperature of the scintillator has reached above the $T_{1/2}$, also the temperature difference between the center of the scintillator and the sides reaches 300 K which affects the linearity of the scintillator response. In fact, the presence of temperature differences leads to changes in the optical efficiency of different points of the scintillator compared to the ideal state and this can disrupt the beam profile [6].

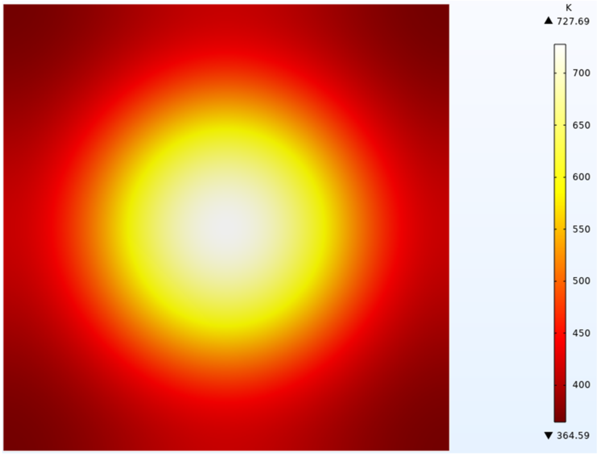

Figure 7: Temperature profile of YAG for 5 W beam power.

Using MATLAB software, we simulated the change of the beam profile for different powers of the input beam. An example of a one-dimensional beam profile for a 5 W beam power is shown in Fig. 8. The presence of a temperature difference of 300 K between the center of the scintillator and the sides increases the width (RMS) of the beam.

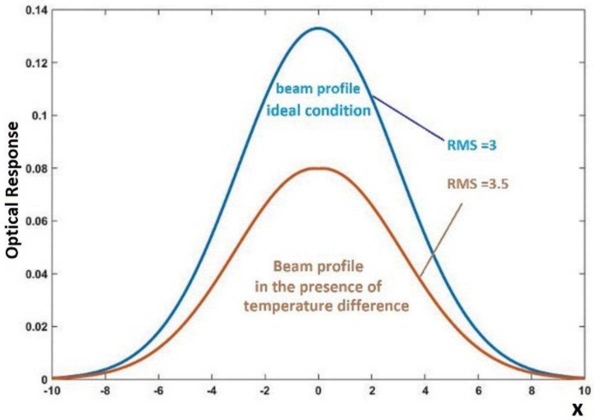

Figure 8: 1D beam profile for 5 W beam power (blue diagram: no temperature difference in scintillation, brown diagram: 300 K temperature difference).

According to Fig. 8, the presence of a temperature difference causes a 17% increase in the width (RMS) of the beam. As a result, the profile of the measured beam has changed and the final shape of the beam has been disturbed. Arrangements must be made to minimize this temperature difference. To do this, we place a 10 mm thick aluminum substrate with a copper holder behind the scintillator. The addition of an aluminum substrate and a copper improves the heat transfer process, thus minimizing the temperature difference of the scintillator at different points.

According to the simulation results shown in Fig. 9, by placing the aluminum substrate and copper holder, better heat transfer has taken place in the scintillator and the temperature of the scintillator has reached below the allowable temperature ($T_{1/2}$) . On the other hand, the temperature difference between the center of the scintillator and the sides is reduced significantly (temperature difference is less than 1 K), and therefore there is no significant change in the ratio of the light output of the scintillator and the width of the beam.

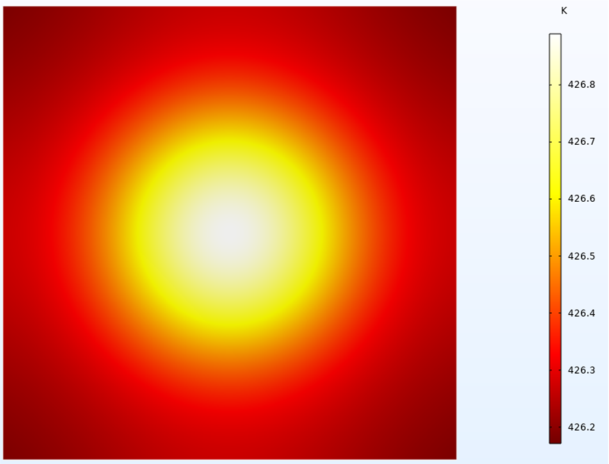

Figure 9: Temperature profile of YAG for 5 W beam power in the presence of aluminum substrate.

ISBN: 978-3-95450-230-1 ISSN: 2673-5350 doi:10.18429/JACoW-IBIC2021-TUPP13

Also, by connecting the aluminum substrate to the ground (as shown in Fig. 10), the charge accumulation in the scintillator and damage caused by sparks to the scintillator is prevented.

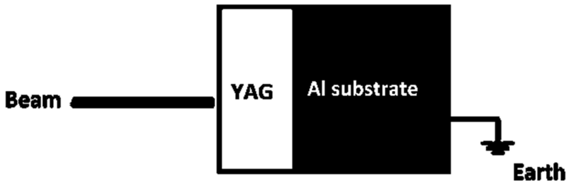

Figure 10: Schematic of the connection of the aluminum substrate to the ground to prevent sparks.

Image Resolution

In order to estimate the image resolution limits due to coulomb scattering, the Geant 4 Monte Carlo code is used. We simulate the collision of an ideal zero-dimensional beam with the YAG scintillator screen. Due to multiple scattering within the scintillator, an area of the scintillator is illuminated. Figure 11 shows the scattering of protons in the YAG scintillator. The dimensions of this area is a measure of the resolution of the scintillator.

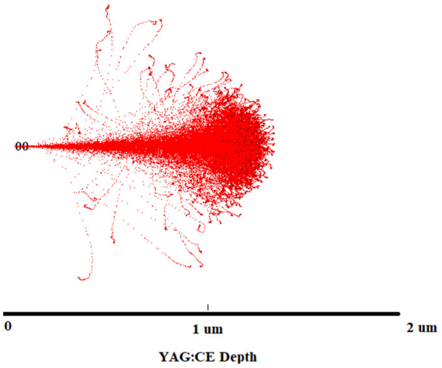

Figure 11: Multiple scattering of proton beam in YAG scintillator (Srim simulation).

Figure 12 shows the transverse distribution of the profile of this ideal beam in both x and y directions with its 2D profile. By calculating the RMS (size) of the beam profile, a measure of the scintillation resolution can be obtained.

As shown in the Fig. 12, the RMS for a 200 keV proton beam is less than 0.1 µm (RMS =72 nm) with an error of less than 2%, which indicates the very high resolution of the YAG scintillator. To benchmark the results, we simulated the problem with the MCNP code, which resulted in a difference of less than 2% compared to the Geant4 code. This difference is due to the different methods of problem solving by the codes.

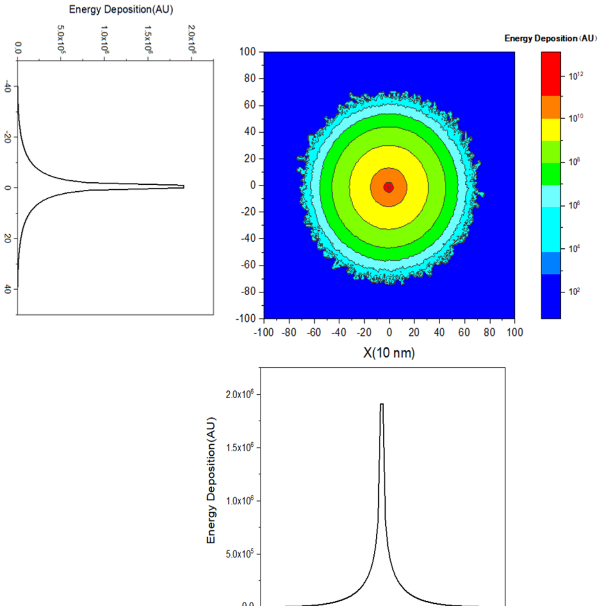

Figure 12: The profile of the 200keV proton beam on the YAG scintillation target.

CONCLUSION

In this paper, the design procedure such as scintillator material selection, handling the thermal and charge accumulation issues and estimation and improvement of the measurement resolution have been studied. In order to select the resistant scintillator material, the scintillation damage caused by a 200 keV proton beam in conventional scintillators are simulated using TRIM software and the YAG scintillator was the most resistant material to be used as a beam diagnostic tool with the minimum amount of cavities and displacement created (11 damage per collision). The effects of scintillation temperature changes on the beam profile were also investigated. At 5 W, the temperature difference between different points of the scintillation, affects the linearity of the scintillator response and causes a 17% increase in the width (RMS) of the beam. To reduce these damaging effects on the beam profile, it was suggested to place an aluminium substrate behind the scintillator. Finally, using Geant 4 Monte Carlo code, we simulated the collision of an ideal 200 kV proton beam with the YAG: Ce scintillator and obtained the beam transverse distribution (beam profile). By calculating the RMS (root mean square) of the beam profile, we obtained a measure of the resolution of the YAG: Ce scintillator, which was less than 0.1 microns, and confirmed the proper resolution of the YAG: Ce scintillator for use as diagnostic tool.

REFERENCES

[1] T. Naito and T. M. Mitsuhashi, “YAG:Ce Screen Monitor Using a Gated CCD Camera”, in *Proc. 3rd Int. Beam Instrumentation Conf. (IBIC'14)*, Monterey, CA, USA, Sep. 2014, paper TUPD08, pp. 426-429.

[2] S. J. Russell, Z.-F. Wang, W. B. Haynes, B. E. Carlsten, and L. M. Earley, “Optical beam profile diagnostic for low

energy, long pulse, moderate current electron beams", *Review of scientific instruments,* vol. 77, no. 3, p. 033302, 2006.

[3] V. Bachmann, C. Ronda, and A. Meijerink, "Temperature quenching of yellow Ce3+ luminescence in YAG: Ce, " *Chemistry of Materials*, vol. 21, no. 10, pp. 2077-2084, 2009.

[4] H. Feng *et al.*, "Temperature dependence of luminescence characteristics of Lu 2 (1− x) Y 2 x SiO 5: Ce 3+ scintillator grown by the Czochralski method", *Journal of applied physics*, vol. 108, no. 3, p. 033519, 2010.

[5] C. Simon *et al.*, "Scintillating Screens Investigations with Proton Beams at 30 keV and 3 MeV", in *Proc. 5th Int. Beam Instrumentation Conf. (IBIC'16)*, Barcelona, Spain, Sep. 2016, pp. 273-276.
`doi:10.18429/JACoW-IBIC2016-MOPG79`

[6] D. W. Storey, "A view screen beam profile monitor for the ARIEL e-linac at TRIUMF", 2011.

ISBN: 978-3-95450-230-1 ISSN: 2673-5350 doi:10.18429/JACoW-IBIC2021-TUPP14

COMMISSIONING OF THE SEM-GRID MONITORs FOR ELENA

M. McLean*, J. Cenede, G. Tranquille, CERN, Geneva, Switzerland
M. Hori, Max-Planck-Institut für Quantenoptik, Garching, Germany

Abstract

The Extra Low ENergy Antiproton ring (ELENA) is a compact ring for the further deceleration and cooling of the 5.3 MeV antiprotons delivered by the CERN Antiproton Decelerator. It decelerates antiprotons to a minimum energy of 100 keV, creating special challenges for the beam instrumentation. These challenges have been addressed by an extremely sensitive SEM-Grid (Secondary Emission Monitor) monitor which is also compatible with the Ultra High Vacuum (UHV) requirements of ELENA. Since November 2019, ELENA's H^- ion source has been used to test the SEM-Grid monitors and, since July 2020, the monitors have been used to commission the ELENA transfer lines. In this paper, a summary of the features of the SEM-Grid will be given together with an overview of its commissioning activities. An ingenious technique for testing the integrity of the grid wires which are not directly accessible will also be described.

INTRODUCTION

ELENA [1,2] is a small synchrotron of 30.4 m circumference constructed recently at CERN and sketched in Fig. 1. The purpose of the machine is to decelerate antiprotons coming from the Antiproton Decelerator (AD) [3] at 5.3 MeV beam energy down to 100 keV. Multiple branching electrostatic transfer lines lead to the experimental zones. All the transfer lines are equipped with multiple SEM-Grid Profile Monitors to enable accurate and automated steering of the beam.

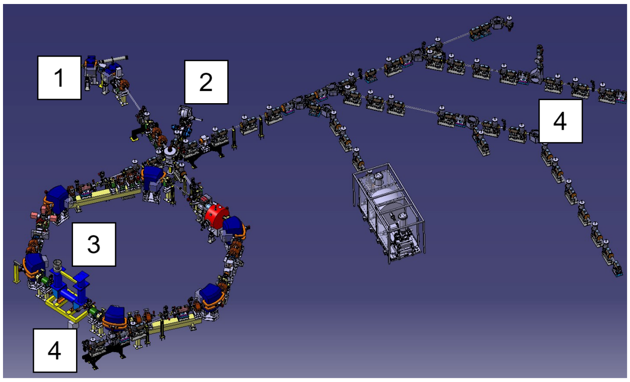

Figure 1: ELENA ring and transfer lines.
1 - Injection from AD
2 - H^- source
3 - ELENA ring with electron cooler
4 - Transfer lines

These monitors and electronics were initially developed by the ASACUSA collaboration based on an earlier design [4] used in the radiofrequency quadrupole decelerator facility, and then productionised, assembled, installed, and commissioned by CERN. Numerous issues were resolved during this process. The monitors were installed to observe protons, antiprotons and H^- ions at 100 keV to 5.3 MeV.

MONITOR OVERVIEW AND COMMISSIONING

Each monitor is composed of five stacked grids; one sensor grid for each plane (horizontal and vertical), sandwiched between three anode grids to attract any liberated electrons. The sense grids use 47 wires of Ø20 µm, while the anode grids use 43 wires of Ø12 µm. The sense wires are bigger to optimise the charge collection, while the anode wires are a compromise between mechanical strength and beam attenuation. The sense wires are on a 500 µm pitch in the central region and 3 mm pitch at the sides, they are at ground potential. The anode wires are on a 1.5 mm pitch under a bias voltage of 60 V. When a particle hits one of the sensor grid wires, a few electrons are liberated and attracted to the anode wires. A charge then flows into the sensor wire to replace the lost electrons, and this charge is measured. Each monitor absorbs about 10% of the beam, therefore it is mounted on a pneumatic in-out mechanism so it can be removed from the beam path when not required. Figure 2 shows the different components of the SEM-Grid monitor.

A total 43 SEM-Grid Monitors are planned to be installed in the ELENA transfer lines. The installation has been progressing since early 2020, as the transfer lines were completed and as the parts to assemble the monitors became available.

Mechanics

The grids are supported by a guided bellows and connected to the electronics by two 50-way vacuum feedthroughs. All the in-vacuum parts of the monitor were designed to be compliant to stringent vacuum requirements regarding the materials used, the surface treatment and cleanliness, this is especially relevant to the detector grid which utilises a ceramic PCB. The guide rods have a vacuum compatible treatment of molybdenum disulfide (MoS_2) to avoid sticking.

Installation The monitor is assembled in a clean environment and placed in a spare tank to protect the grid during transport. The vertical position of the grid is measured in a metrology laboratory, and any offset is then corrected by a custom spacer. The monitor is then installed in a bake-out

---

[*] mark.mclean@cern.ch

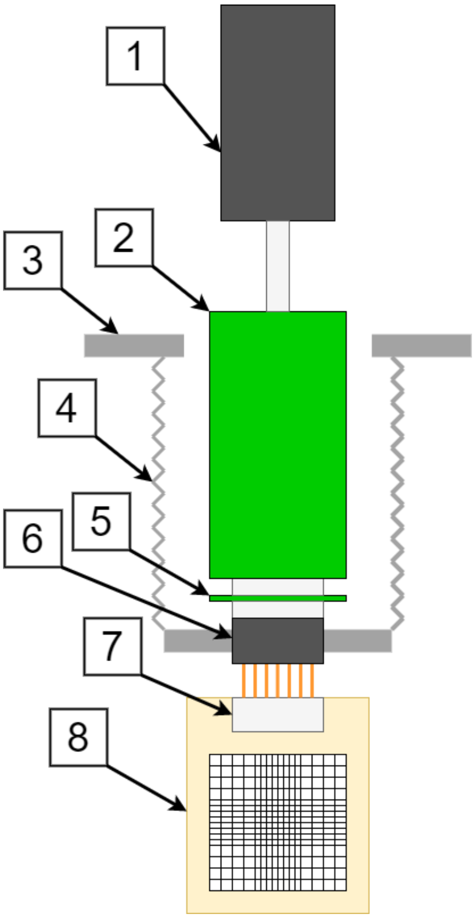

Figure 2: SEM-Grid detector overview. The pneumatic cylinder (1) moves the detector assembly in or out of the beam, while the flange (3) and bellows (4) maintain the vacuum tightness. The front-end boards (2) digitise the extremely weak signals from the detector grid (8), which are connected via an adapter PCB (5), a vacuum feed-through (6) and a D connector (7).

rig and the wires are checked using Time Domain Reflectometry (TDR), described below. If the TDR results are sufficiently good (generally fewer than five non-adjacent bad pairs), the monitor is baked-out at 180 °C for 24 hours under a vacuum. After the bake-out, the temperature is reduced to room temperature and then the pressure should fall to 1×10^{-10} mbar for the monitor to be accepted. The pressure is continuously monitored to detect any leaks and out-gassing must not exceed 2×10^{-8} mbar l/s. Importantly, the temperature is ramped up and down over a period of one day, in order to minimize thermal stress on the delicate sensor grids. Then the TDR test is repeated, and if the results are still acceptable the monitor is ready to be installed.

Key challenges A major challenge with the monitors has been the electrical connections inside the ultra-high-vacuum. The range of available materials is strictly limited, excluding solder flux and conductive epoxy, leaving fluxless soldering or mechanical fastening as the only permitted techniques. The grid is based on a ceramic Printed Circuit Board (PCB) and the wires are attached by resistance welding. Occasionally a wire may break but this is unusual. The bigger problem, illustrated by Fig. 3, has been the connection of the connector pins to the PCB, this is currently done by vacuum brazing with a fluxless solder with a lead-to-tin ratio of 95%:5% and a melting temperature between $T = 301$–314°C. We found that the brazing alloy does not adhere very well to the platinum-palladium-gold conductor [6] of the PCB and can fail during the following vacuum bake-out at temperature $T = 180$–200°C which typically lasts up to a few days. Oxidization and leaching of the metal alloys at the interface surfaces are assumed to be the primary reasons. No flux can be used during the vacuum brazing to alleviate this problem, as the flux can later contaminate the non-evaporable getter (NEG) pumps of the ELENA beamlines during bake-out. R&D with other fluxless soldering alloys is ongoing to address this problem.

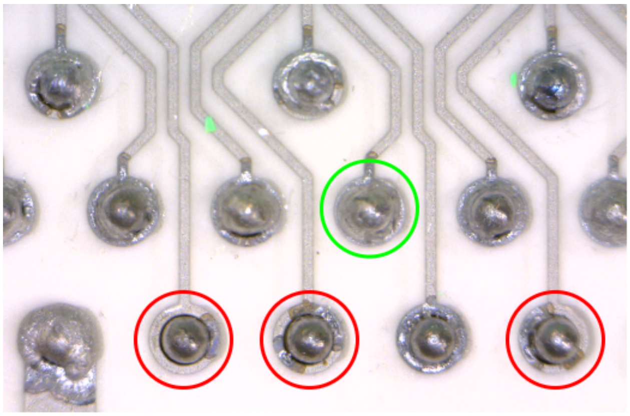

Figure 3: Poor reflow of the fluxless solder indicated by red circles.

Electronics

There is a front-end board for the read-out of each plane. This includes a 64 channel charge sensitive amplifier ASIC (the IDE1140 from IDEAS [5]) which amplifies the signals from all 47 sense wires and simultaneously latches their values in an array of sample-and-holds on receipt of a trigger from the ELENA timing system. These analogue voltages are then converted by a 14 bit ADC under the control of an Field Programmable Gate Array (FPGA). See Figure 4.

Figure 4: Block diagram of the Front-End.

As shown in Fig. 5, the system is divided in three parts: the front-end boards, a local crate and a VME crate. The front-end boards interface directly to the grids and contain the electronics that amplify and digitise the detector signals. Data and control is exchanged between both front-end boards

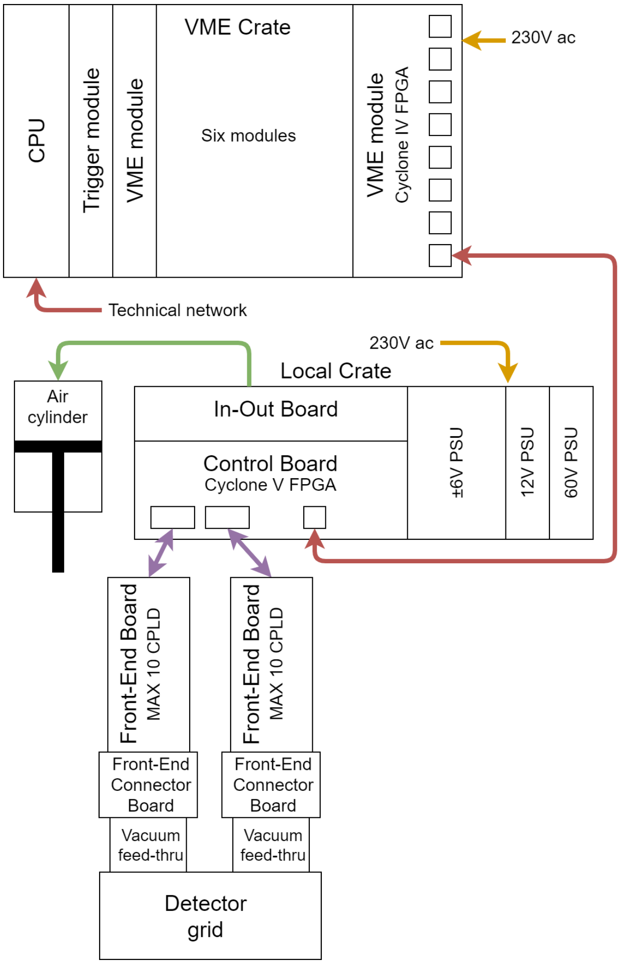

Figure 5: Block diagram of the System.

and the control board in the local crate. In addition, this crate houses the power supplies and the control electronics for the in-out mechanism. From here the data is sent via a fibre-optic cable to a module in a VME crate, where a FESA class (Front-End Software Architecture, the lowest level of CERN's acquisition software stack) provides an interface to the operator's Graphical User Interface (GUI). Each VME module communicates with up to eight monitors. The results are then displayed as horizontal and vertical beam profiles, as shown in Fig. 6, with a Gaussian fit superimposed.

Sensitivity With the H^- source configured to produce small, low-energy bunches, a typical bunch contains about 5×10^6 particles. The sense wires are Ø20 µm on a 500 µm pitch, so 4% of the beam hits a sense wire of each plane. A well focused beam has a diameter of 5 mm and so hits about ten wires. Therefore there are about 20,000 beam interactions per wire. A proton of energy $E = 100$ keV striking the Au surface of a sense wire is expected to liberate around 2 secondary electrons [7], which provides a total charge of approximately 6 fC for 20,000 protons. The ASIC (Application Specific Integrated Circuit) noise is about 0.06 fC and the amplifier and ADC (Analogue to Digital Converter) do not add significantly to this. Therefore the expected signal-to-noise ratio is of order 100:1, which correlates well to what has been observed. Tests indicate a similar sensitivity between H⁻ ions and antiprotons, but the mechanisms by which electrons are liberated in the antiproton case are not fully understood. Besides the contributions from charged pions and nuclear fragments that emerge from antiproton annihilations, there are expected to be some Auger electrons.

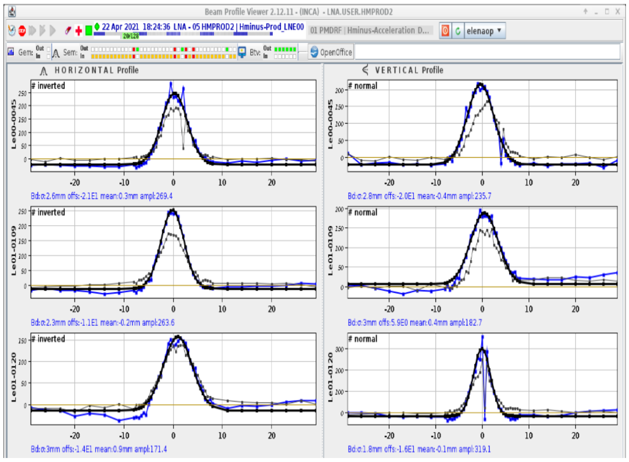

Figure 6: Examples of H^- ion beam profiles.

There is an offset in the measured signal from each wire, but this offset is stable and the acquisition software records it in the absence of beam and then subtracts it from subsequent readings.

Triggering Timing of the acquisition to better than 500 ns is essential to obtaining a good and repeatable beam profile. Triggers are provided from the H^- source, the injection from the AD, and the two extraction kickers. Once the beam has circulated in ELENA it is split into four bunches. For each monitor, the trigger source and target bunch number can be selected, and there is a programmable delay after which the sample-and-hold circuits of the ASIC are triggered. To tune the delay, a longitudinal acquisition mode is provided in which a single grid wire is sampled continuously at up to 10 MHz. When the results are displayed it is easy to see any adjustment that may be needed to the timing. Figure 7 shows a correctly adjusted delay with the signal peak aligned to time 0. During operation, different bunches may be sent to different transfer lines, so the beam server software updates the bunch number at the start of each cycle.

TIME DOMAIN REFLECTOMETRY (TDR) TESTING OF SENSOR WIRES

One of the recurring challenges during the installation of the SEM-Grids was to verify the condition of the grids when it was not possible to send beam to the monitor. For example, many monitors were installed before the source and ion-switch were fully operational. It was also helpful to be able to verify the grid before the installation of the monitor. In collaboration with our colleagues in the Beam Position Monitoring section we used a handheld Radio-Frequency

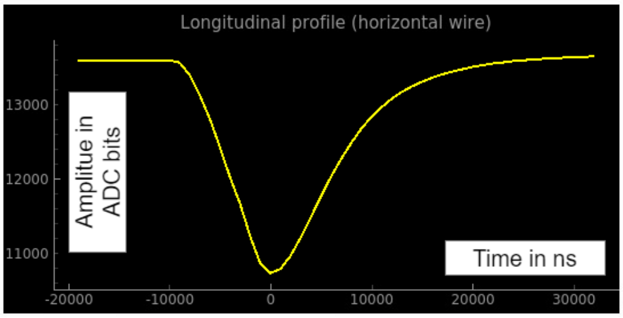

Figure 7: Longitudinal acquisition mode.

(RF) Analyser (the Agilent Fieldfox N9917A) to measure the impedance along an adjacent pair of sensor wires. This was facilitated by a specially designed PCB which routed the sensor wires in pairs from the vacuum feed-through to a matrix of SMA connectors. The impedance of the connection to each pair of sensor wires was then controlled and repeatable. The RF Analyser transmitted a signal at a rapidly swept frequency into the pair of wires, and analysed the echoes returned from each change of impedance. Thus it was possible to compare the impedance of a grid under test with a "known good" grid and easily detect any anomalies in the sensor wire impedance, even for a grid which was installed and under vacuum. This technique could not determine which of the pair of wires was faulty, but it provides a report of how many pairs were faulty. Figure 8 shows an example of data from a grid with a single faulty pair. The early increase of impedance of the orange line is clearly visible.

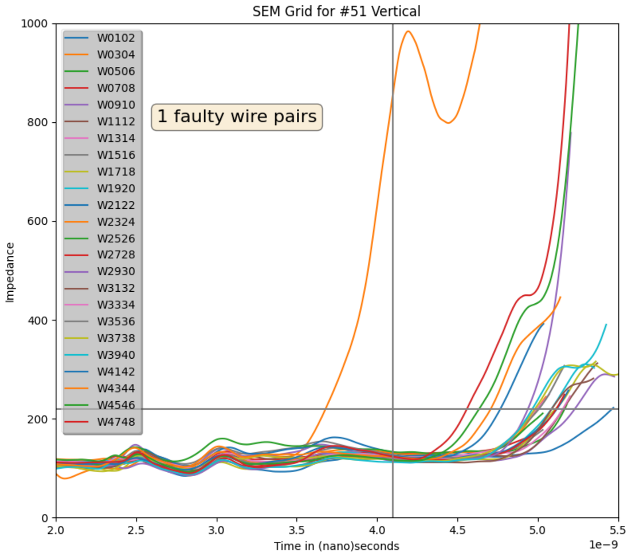

Figure 8: Measurement of impedance against time (=distance) to classify the wire pairs as good or bad.

CONCLUSION

Almost the full complement of SEM-Grid Monitors have now been installed in the ELENA transfer lines and tested with H^- ions. The CERN accelerator complex has restarted this summer and the devices are already providing the ELENA operators with antiproton beam profiles, allowing them to steer the beam to the experiments that will study the symmetry between matter and antimatter.

ACKNOWLEDGEMENTS

None of this would have been possible without the help and support of: Arkadiusz Jedrzej Lis and Stephane Bart Pedersen of the SY-BI-SW software section; Alexander Sinturel of TE-VSC vacuum group; Laurette Ponce, Davide Gamba and the rest of the BE-OP-AD operations team; Stephane Deschamps, Wilfried Devauchelle and the rest of the SY-BI-XEI section; Christian Carli and Francois Butin who kept us focused.

REFERENCES

[1] V. Chohan *et al.*, "Extra Low ENergy Antiproton (ELENA) ring and its Transfer Lines", CERN, Geneva, Switzerland, Rep. CERN-2014-002, April 2014.

[2] C. Carli *et al.*, "ELENA Commissioning and Status", presented at the 12th Int. Particle Accelerator Conf. (IPAC'21), Campinas, Brazil, May 2021, paper MOPAB177.

[3] Antiproton decelerator, `https://home.cern/science/accelerators/antiproton-decelerator/`.

[4] M. Hori, "Photocathode microwire monitor for nondestructive and highly sensitive spatial profile measurements of ultraviolet, x-ray, and charged particle beams", *Rev. Sci. Instrum.*, vol. 75, p. 113303, 2005.

[5] Integrated Detector Electronics AS, `http://ideas.no/products/ide1140/`.

[6] Dupont 4597R, `https://www.dupont.com/content/dam/dupont/amer/us/en/transportation-industrial/public/documents/en/4597R.pdf`

[7] D. Hasselkamp, K.G. Lang, A. Scharmann, N. Stiller, "Ion induced electron emission from metal surfaces", *Nucl. Instrum. Methods*, vol. 180, p. 349, 1981.

4D BEAM TOMOGRAPHY AT THE UCLA PEGASUS LABORATORY

V. Guo*, P. Denham, P. Musumeci, A. Ody, and Y. Park,
UCLA Department of Physics and Astronomy, Los Angeles, CA, USA

Abstract

We present an algorithm to tomographically reconstruct the 4D phase space of a beam distribution of a high brightness electron beam, based on the use of two fluorescent screens separated by a beamline containing a quadrupole triplet which can be used to impart arbitrary rotations to the beam phase space. The reconstruction method is based on generating a macroparticle distribution which matches the initial profile and then it is iteratively updated using the beam projections on the second screen until convergence is achieved. This process is repeated for many quadrupole current settings. The algorithm is benchmarked against GPT simulations, and then implemented at the UCLA Pegasus beamline to measure the phase space distribution for an upcoming high speed electron microscope experiment.

INTRODUCTION

In high brightness electron accelerators, the beam dynamics and transport is strongly influenced by the space charge fields associated with the details of the electronic distribution and its evolution along the beamline, which depends on each particle position and velocity [1]. In linear beam dynamics, it is sufficient to monitor the second order moments of the distribution which has a constant shape along the beamline, but as soon as non-linear forces (either external or internal) are applied, the distribution will evolve and change along the beamline. Having an accurate representation of the beam transverse phase space is then critical to predict and then optimize the beam behavior in many setups. For example in single-shot time-resolved electron microscopy, it has been pointed out that different electronic distribution can originate different space-charge induced aberrations and greatly affect the spatial resolution of the instrument [2].

While it is of great interest to know the shape of the transverse phase space distribution function, the experimental measurement of this quantity poses some challenges as beam profile monitors only record the spatial beam distribution (i.e. the projection of the 4D phase space volume onto the x-y plane) while the angular or transverse velocity distribution is harder to access.

Tomography is a well developed imaging technique that uses a set of projections to reconstruct a distribution in a space with higher dimensions. Typically, tomography is used to reconstruct the shape of an object in 3D from a complete set of 2D projections along different angles as for example in CAT scans. Applied to beam physics, tomography can be used to reconstruct the 4D phase space distribution from an appropriately chosen set 2D transverse beam profile (projections) [3–6].

In this paper, we present the development of such a technique at the UCLA Pegasus Laboratory [7, 8] where fluorescent screens are used to record the spatial projections of a high brightness beams before and after a set of three quadrupoles with adjustable currents to change the rotation angles of the transverse phase space and enable a tomographic reconstruction. Importantly, the transformation of the phase space in these measurements does not provide projections for the entire range of rotation angles due to the limitation in the quadrupole currents or placement of the beamline components. Therefore, while usual tomography reconstructs the source volume from complete set of projections over the entire range of possible angles [9, 10], the algorithm for beam phase space reconstruction should be tolerant of this incomplete set of projections. We present here the MATLAB algorithm we used in the reconstruction which is based on sampling the 4D beam transverse phase space with a macroparticle distribution. The algorithm is shown to work well both on simulation and experimental data and is eventually expected to be used in a feedback loop to optimize the photocathode illumination to generate ideally shaped 4D transverse phase space distributions to improve spatial resolution in single shot time-resolved electron microscopy.

DATA COLLECTION

In order to perform a tomographic reconstruction, sufficient access to different rotation angles is needed. While the technique can be generalized and applied to other beamlines, in the following we focus on the setup currently installed at the UCLA Pegasus laboratory shown in Fig. 1. The measurement takes place in the area highlighted by the red square. The initial spatial distribution is recorded on screen 4 and the various projections are obtained changing the currents in the green quadrupoles with the beam profile recorded on the final YAG screen.

The current settings for the quadrupoles are chosen in order to maximize the range of angles the phase space rotates before hitting the final screen.

In order to do this, we write the beam transport matrix as a function of current settings on each of the quadrupole (I_1, I_2, I_3) using a smooth approximation for the quadrupole field gradient profile $G(z)$ along the axis:

$$G(I,z) = \frac{CI}{2}\left[\tanh\left(\frac{b}{2}\left(\frac{L}{2}-z\right)\right)+\tanh\left(\frac{b}{2}\left(\frac{L}{2}+z\right)\right)\right]$$

where L is the effective length of the quadrupole, b is the steepness parameter of the edges, and the nominal magnetic field gradient CI is simply proportional to the current setting of the quadrupole. For the quadrupoles used in the experiment $L = 0.078\,\mathrm{m}$, $b = 135\,\mathrm{m}^{-1}$ and $C = 0.45\,\mathrm{T m^{-1} A^{-1}}$.

---

[*] vgwr618@g.ucla.edu

ISBN: 978-3-95450-230-1 ISSN: 2673-5350 doi:10.18429/JACoW-IBIC2021-TUPP15

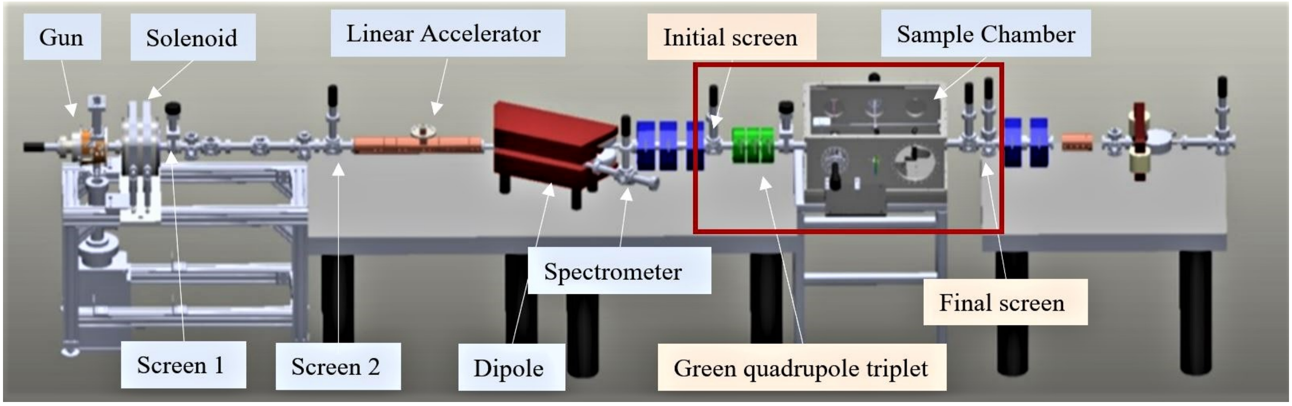

Figure 1: Schematic of the UCLA Pegasus beamline. Initial screen projection is collected at screen 4. The green quadrupole triplets perform rotations on the beam. Spatial projection images after rotation are collected at the final screen. The red box shows where the experiment takes place.

The overall gradient function for our beamline can be obtained by the superposition of $G_I(z)$ for each quadrupole. The locations of the screens and the quadrupoles along the beamline are given in Table 1.

Table 1: Locations of the Screens and the Quadrupoles Along the UCLA Pegasus Beamline

Beamline Component	**Position**
Screen 4	3.191 m
Green Quadrupole 4	3.295 m
Green Quadrupole 5	3.381 m
Green Quadrupole 6	3.466 m
Final Screen	4.500 m

The matrix transport is checked to match the General Particle Tracer (GPT) simulation of the beam envelope evolution as shown in Fig. 2.

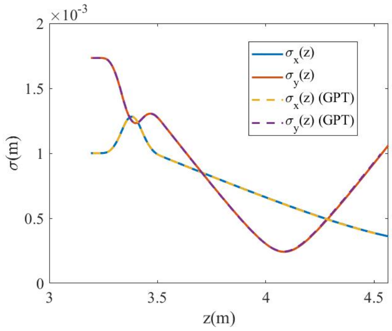

Figure 2: The envelope evolution of a Gaussian beam under quadrupole current settings 1.41 A, -2.39 A, and 1.17 A. The dashed lines shows the evolution under GPT simulation and the solid lines shows the evolution using the step transport matrices.

For uncoupled transport, the 2D transport matrix can also be defined by affine transformation $M = SER$, where S, E, and R are the shear, expansion, and rotation matrix respectively:

$$M = \begin{pmatrix} 1 & 0 \\ k & 1 \end{pmatrix} \begin{pmatrix} e_1 & 0 \\ 0 & \frac{1}{e_1} \end{pmatrix} \begin{pmatrix} \cos(\theta) & -\sin(\theta) \\ \sin(\theta) & \cos(\theta) \end{pmatrix}.$$

We can then obtain the overall rotation angles θ_x and θ_y from the beam transport matrix,

$$\theta_x = \arccos\left(\frac{M_{1,1}}{\sqrt{M_{1,1}^2 + M_{1,2}^2}}\right), \; \theta_y = \arccos\left(\frac{M_{3,3}}{\sqrt{M_{3,3}^2 + M_{3,4}^2}}\right),$$

which is dependent on the current settings. Setting goal x- and y- rotations from 0 to π, the desired quadrupole current settings can be computed using a nonlinear least square optimization. The obtained current settings are used to collect final screen images under different rotations.

Accessible angles are limited to the middle of the rotation space due to the quadrupole and screen positions as well as the current setting limits. In addition the final screen has a diameter of 8 mm which also poses a limit on the available rotation angles. The rotation angles used in the simulations and experiments discussed below are shown in Fig. 3.

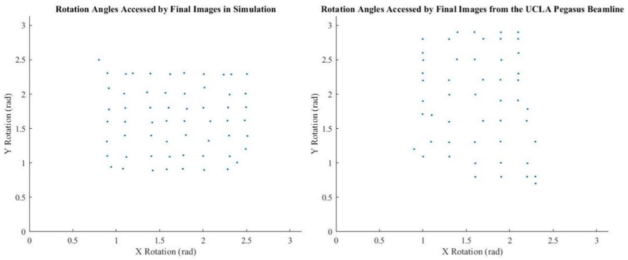

Figure 3: On the left is the x- and y- rotation angles of each set of quadrupole settings used in simulation. On the right is the x- and y- rotation angles of each set of quadrupole settings used in the Pegasus beamline experiment.

RECONSTRUCTION ALGORITHM

To reconstruct the 4D transverse phase space (x, x', y, y'), we developed an algorithm that starts from the spatial projection as measured by screen 4 and attempts to match the projections on the final screen resulting after applying rotations using three quadrupoles.

We begin by initializing a number N of macroparticles using the image at the initial screen as the probability distribution for the x-y coordinates. A random uniform momentum distribution is then assigned to the ensemble, which gives us an initial guess 4D distribution (x_i, x_i', y_i, y_i').

For each set of quadrupole settings, the guess ensemble is transported to the final screen using the beam transport matrix. The phase space distribution so obtained is then projected onto the $x - y$ plane and then compared with the data image at the final screen. Particles that landed in pixels having excess charge compared to the measured image are marked as candidates to be respawned. After the marking process is repeated through all the quadrupole settings in the data sets, particles that failed to land in the correct pixels for more than k images are respawned with values from a 4D normal distribution centered at 0 with standard deviation from the second-order moment matrix of the particles that survived the marking process. The algorithm terminates when the number of particles that need to be respawned is less than p% of the total number of macroparticles used. The convergence parameters k and p can be altered based on need for precision.

Reconstruction of Simulation

To test the reconstruction algorithm, we generated a test data set using GPT formed by an initial screen image and 59 final screen images with different quadrupole current settings. The algorithm then reconstructs the test distribution using those images.

The test beam we chose is Gaussian in its spatial distribution with a double Gaussian momentum distribution. This choice is made to demonstrate the algorithm's ability to converge towards a momentum space with a complicated inner pattern. The distribution to be reconstructed is shown in Fig. 4.

Setting the convergence parameters to be $k = 1$ and $p = 1$, the algorithm was able to reconstruct the full 4D phase space in 7.46 s on a standard personal laptop using four cores. The momentum reassignment loop stopped after 22 iterations when the particles that landed in an over-dense region in more than one image is less than 1% of the total number of particles used.

While the reconstructed phase space shown in Fig. 5 can give a good idea of the ability of the algorithm to reconstruct the initial distribution we can also compare the second order moment matrix which is found to agree within 10% of the initial beam matrix.

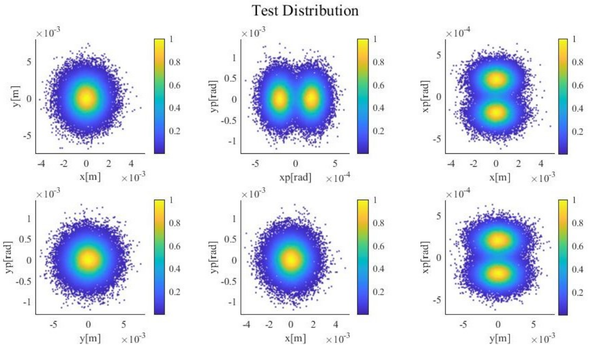

Figure 4: Simulated test distribution to be reconstructed.

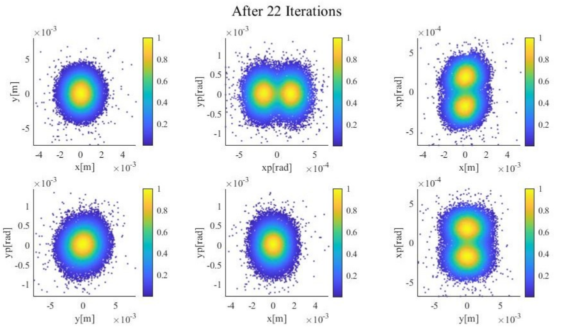

Figure 5: The reconstructed 4D phase space after 22 iterations of momentum reassignment.

Reconstruction of Experimental Data

The algorithm was then used on experimental data collected from the UCLA Pegasus laboratory. The beam energy for these measurements was 8.7 MeV and the beam charge was 2 pC. An initial screen image was taken at screen 4 and used as a probabilistic intensity mask to obtain the initial spatial distribution as shown in Fig. 7. A guess Gaussian momentum distribution with $\sigma_x = 4 \times 10^{-4}$ rad and $\sigma_y = 3 \times 10^{-4}$ rad is initialized with this spatial distribution to create a guess initial 4D distribution. The number of macroparticles used to simulate the distribution is 50,000.

The initial 4D distribution is then transported to the final screen position using the beam transport matrices based on each set of quadrupole current settings and compared against 50 data images from the beamline. Setting the algorithm hyper-parameters to be $k = 5$ and $p = 15$, the runtime is 361.78 s using four cores on a personal laptop. Figure 6 shows the comparison between the data images and the reconstructed phase space projections. The point-spread function used in the displayed trial is 18.63 µm. In order to take into account for the Poissonian statistics associated with the limited number of macroparticles used to sample the beam distribution, the noise parameter from image filtering is set as 0.5 so that a particle will be marked to be respawned if $p_r - p_t > 0.5 \cdot \sqrt{p_t}$ where p_r is the count value of the pixel the particle lands in and p_t is the corresponding value from the same pixel in the target data image. The reconstructed

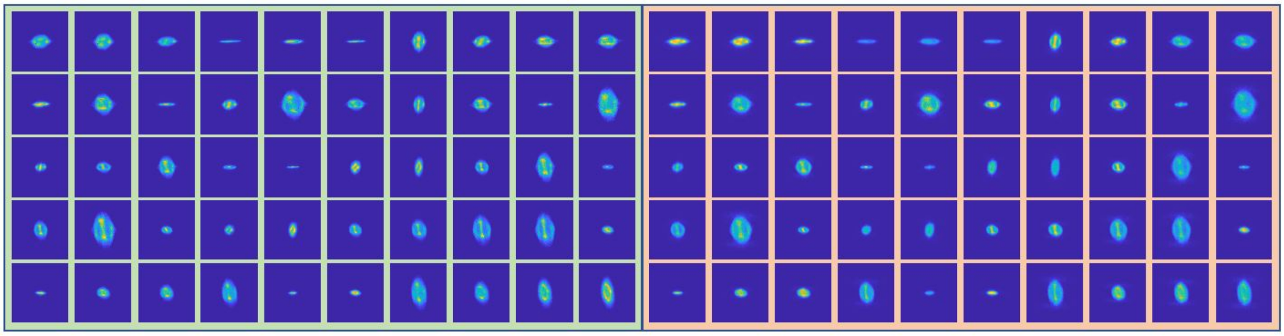

Figure 6: The left box contains 50 final images from the UCLA Pegasus beamline. The right box are the corresponding final images based on the reconstructed 4D phase space.

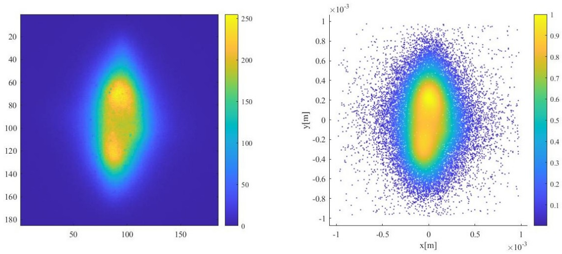

Figure 7: The left shows the initial screen 4 image collected from the UCLA Pegasus beamline. The right shows the spatial distribution the algorithm initializes based on the screen image.

distribution has a beam geometric emittance of 41 nm. The distribution is shown in Fig. 8.

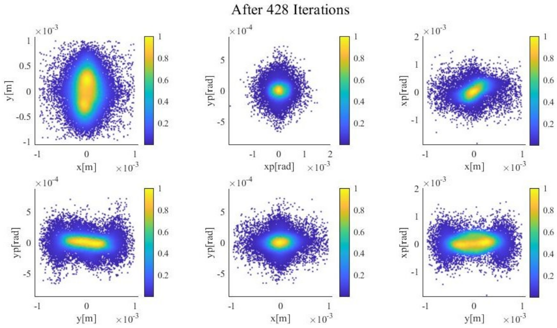

Figure 8: The reconstructed 4D phase space after 428 iterations of momentum reassignment.

In comparison with the simulation case, reconstruction using experimental data is much more difficult due to noise and image quality. The reconstruction time increases with the number of images used. Additionally, tighter parameter control–i.e. allowing smaller number of images to be missed, stopping at lower number of particles to be respawned, or decreasing the noise parameter–can all result in a longer reconstruction time.

CONCLUSION

We have presented a method to tomographically reconstruct the full 4D transverse phase space distribution. The method uses one initial screen projection, three quadrupoles for beam rotation, and a final screen for spatial projections of the beam's final distribution. Sufficient access to the rotation angles in both x and y is needed in order to get an accurate reconstruction. Using an iterative momentum reassignment algorithm, the method can reconstruct the full 4D phase space with reasonable computational time. We have verified the algorithm by applying it to a simulated distribution. Using collected images from GPT, the algorithm was able to reconstruct complicated inner patterns within the momentum space. The reconstructed distribution closely matches the original distribution.

The algorithm is tested on data images collected from the UCLA Pegasus beamline. Although the reconstruction time is higher than in simulation, the algorithm is able to reconstruct a 4D transverse phase space that produces images that well match the final spatial projections of the actual beam under 50 quadrupole-controlled rotations. Potential future improvements that could be made include understanding the role of the space charge fields in the measurements, decreasing the reconstruction time, optimizing image processing method to reduce noise, and improving reconstruction accuracy.

ACKNOWLEDGMENTS

This work has been supported by the National Science Foundation under Grant No. PHY-1549132 and grant PHY-1734215 and DOE grant No. DE-SC0009914. PD was supported by National Science Foundation under Grant No. DMR-1548924.

REFERENCES

[1] P. Musumeci, J. G. Navarro, J. Rosenzweig, L. Cultrera, I. Bazarov, J. Maxson, S. Karkare, and H. Padmore, "Advances in bright electron sources," *Nuclear Instruments and Methods in Physics Research Section A: Accelerators, Spectrometers, Detectors and Associated Equipment*, vol. 907, pp. 209–220, 2018.

[2] P. Denham and P. Musumeci, "Space-charge aberrations in single-shot time-resolved transmission electron microscopy," *Physical Review Applied*, vol. 15, no. 2, p. 024050, 2021.

[3] B. Hermann, V. A. Guzenko, O. R. Hürzeler, A. Kirchner, G. L. Orlandi, E. Prat, and R. Ischebeck, "Electron beam transverse phase space tomography using nanofabricated wire scanners with submicrometer resolution," *Physical Review Accelerators and Beams*, vol. 24, no. 2, p. 022802, 2021.

[4] F. Hannon, I. Bazarov, B. Dunham, Y. Li, and X. Liu, "Phase Space Tomography Using the Cornell ERL DC Gun", in *Proc. 11th European Particle Accelerator Conf. (EPAC'08)*, Genoa, Italy, Jun. 2008, paper TUPC032, pp. 1119–1121.

[5] K. Hock, M. Ibison, D. Holder, A. Wolski, and B. Muratori, "Beam tomography in transverse normalised phase space," *Nuclear Instruments and Methods in Physics Research Section A: Accelerators, Spectrometers, Detectors and Associated Equipment*, vol. 642, no. 1, pp. 36–44, 2011.

[6] D. Xiang, Y.-C. Du, L.-X. Yan, R.-K. Li, W.-H. Huang, C.-X. Tang, and Y.-Z. Lin, "Transverse phase space tomography using a solenoid applied to a thermal emittance measurement," *Physical Review Special Topics-Accelerators and Beams*, vol. 12, no. 2, p. 022801, 2009.

[7] D. Alesini, A. Battisti, M. Ferrario, L. Foggetta, V. Lollo, L. Ficcadenti, V. Pettinacci, S. Custodio, E. Pirez, P. Musumeci, *et al.*, "New technology based on clamping for high gradient radio frequency photogun," *Physical Review Special Topics-Accelerators and Beams*, vol. 18, no. 9, p. 092001, 2015.

[8] J. Maxson, D. Cesar, G. Calmasini, A. Ody, P. Musumeci, and D. Alesini, "Direct measurement of sub-10 fs relativistic electron beams with ultralow emittance," *Physical Review Letters*, vol. 118, no. 15, p. 154802, 2017.

[9] V. Yakimenko, M. Babzien, I. Ben-Zvi, R. Malone, and X.-J. Wang, "Electron beam phase-space measurement using a high-precision tomography technique," *Physical Review Special Topics-Accelerators and Beams*, vol. 6, no. 12, p. 122801, 2003.

[10] C. McKee, P. O'Shea, and J. Madey, "Phase space tomography of relativistic electron beams," *Nuclear Instruments and Methods in Physics Research Section A: Accelerators, Spectrometers, Detectors and Associated Equipment*, vol. 358, no. 1-3, pp. 264–267, 1995.

ISBN: 978-3-95450-230-1 ISSN: 2673-5350 doi:10.18429/JACoW-IBIC2021-TUPP16

THE FIRST BEAM EXPERIMENT RESULT OF THE PROTYPE OF WIRE SCANNER FOR SHINE *

F. Z. Chen†, B. Gao, J. Chen, Y.B. Leng
Shanghai Advanced Research Institute, Chinese Academy of Sciences, Shanghai, China
J. Wan, Shanghai Institute of Applied Physics, Chinese Academy of Sciences, Shanghai, China

Abstract

As a kind of quasi-non-destructive beam size monitoring, SHINE will employ dozens of wire scanners. The preliminary study is confronted with motion control difficulty. To reduce the ultrahigh coordinate about wire movement with beam loss data acquisition, a new method has been proposed in the SXFEL test platform. The strategy is utilizing the beam jitter, which is of the same magnitude with the beam size. Combine with the jitter of the beam position, we move tungsten wires in a few of different position to realize the measurement. This paper will present our experiment design as well as a furthermore plans about the prototyping design.

INTRODUCTION

As a quasi-non-destructive beam size and emittance measurement system, wire scanner is widely used in linear accelerators worldwide [1]. As a classic beam size measurement system, the measurement principle of wire scanner is very simple. It is assumed that the downstream secondary product flow is proportional to the intensity of the electron beam passing through the tungsten wire [2]. The secondary products mainly include high-energy electrons, gamma rays and secondary currents generated on tungsten wires. Therefore, the signal detected by the downstream photomultiplier is positive correlation with the beam intensity, and the size of the beam can be measured by accurately measuring the distance of the tungsten wire movement. In addition to the application of the wire scanner for accurate beam size measurement, one or several sets of such detectors can also be used to complete offline or online beam emittance measurement and energy dispersion measurement.

In this article, we discuss the hardware and software structure of the SHINE wire scanner prototype and the first beam experiment results.

IDEA

The initial setting is to use wire scanner to scan the beam transversal section at a uniform speed [3]. Take advantage of the high repetition frequency of the SHINE, the position of the wire and the beam interaction can be obtained. Combining the beam loss data, we can calculate the beam size using Gaussian fit.

Since the SHINE is still under construction, our wire scanner prototype is installed in the SXFEL facilty for testing at present. It is differ from the hard X-ray free electron laser facility with high repetition frequency(up to 1MHz), the current repetition frequency of the SXFEL facilty just 2 Hz. Under the circumstances, the fast scan method requires high precision for the timing system, also the movement speed requirement for linear motor uniform scanning is too low. After the first preliminary experiment, we acquired that the beam size of the SXFEL is in the magnitude of several hundred microns, and the jitter of the beam position is about the same order of magnitude. This will introduce a noticeable uncertainty of measurement using the fast scan mode. However, it provides a new idea for the SXFEL experiment adopt a static testing method. We can make use of the beam jitter, acquire a step-by-step scanning method in the SXFEL wire scanner prototype principal verification stage.

The basic idea is fixing the position of the wire target, changing the original wire scanning motion mode of the wire sweeping the beam to the beam sweeping wire. We can get the beam loss signal and beam position signal in different beam positions due to beam jitter. The step-by-step static testing is using the CBPM to acquire the accuracy position(position resolution up to 200nm). The data acquisition system using external clock and external trigger come from electronic chamber, which can guarantee the synchronization of the beam loss and the impact point.

SYSTEM SETUP

The wire scanner system is comprised of the mechanical execution structure and the beam loss detector in the tunnel, the upper computer and the data acquisition board outside the tunnel. Figure 1 is the installation photo in the tunnel. From nearest to farthest, CBPM is upstream the mechanical execution structure, the beam loss detector is installed downstream parallel to the vacuum pipe.

After the tensile test of 10 µm tungsten wire and 20 µm tungsten wire, we chose 20 µm tungsten wire as the test wire for the first version of the prototype. The tungsten wire is mounted on the customized fork connected to the linear motor, it was distributed in three directions testing the beam size in the horizontal direction, the vertical direction and the oblique 45 degrees(see Fig. 2).

We use the linear motor of LinMot to drive the wire target. The main motion modes of the motor are as follows:

- Step by step test: In this mode, the scanner will move to the user defined position for several test, after that, it will move to another position. The sample interval is defined by the beam jitter.

---

* Work supported by National Nature Science Foundation of China(No.11375255)
† chenfz@sari.ac.cn

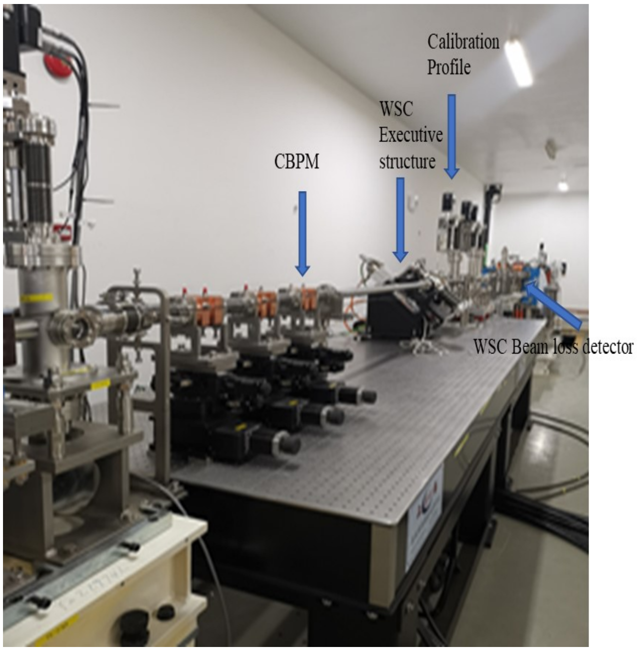

Figure 1: Installation photo in the tunnel.

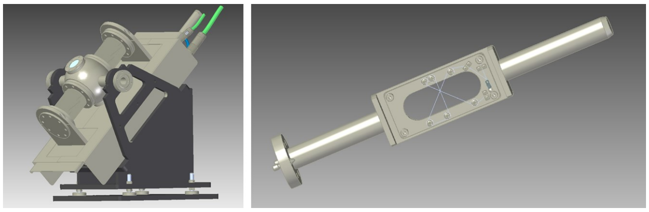

Figure 2: The Prototype Wire Scanner Executive Structure & the wire structure.

- Fast scan: This is intended to execute a motor pattern download in server, which defined the velocity, accelerated velocity and stroke.
- User scan: The operator independently adjusts the motor position according to the current position, the control panel has a variety of operation options, and the motor server controls the motor according to demand.

In order to better evaluate the mechanical execution structure and make a backup at the same time, we also installed the same 20 µm tungsten wire on the adjacent proflie calibration screen(see Fig. 3).

The following Fig. 4 is the wiring diagram of the wire scan prototype. We introduce the timing signal from the timing system as the trigger signal of the data acquisition board. At the same time, we use the frequency synthesizer multiplication timing signal as the clock signal. The four channels of the data acquisition board are collected respectively. Loss signal, two position signals of CBPM horizontal direction and vertical direction and CBPM reference cavity signal used for normalized charge.

Figure 5 is the linear drive module.The grey part is the linear motor, the green part is the package structure, it can provide mechanical alignment for linear motor installation. The white part is the linear encoders, we choose the Heidenhain LIC411 which position resolution is 0.1 µm.

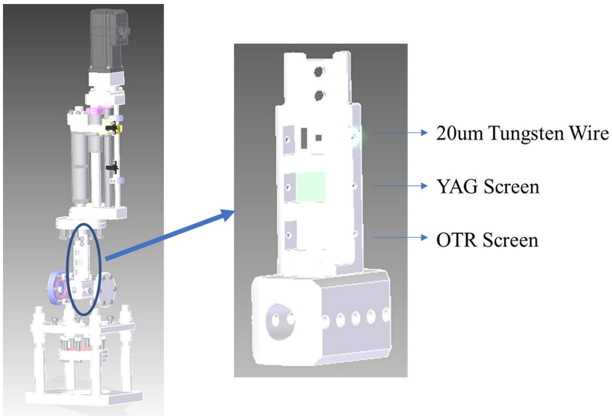

Figure 3: The Prototype Profile Structure & the screen formation.

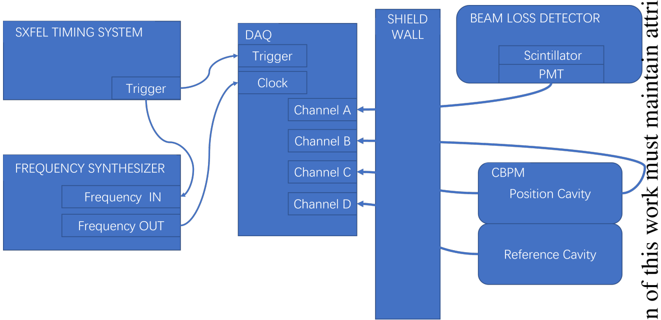

Figure 4: The diagram of the wiring connection.

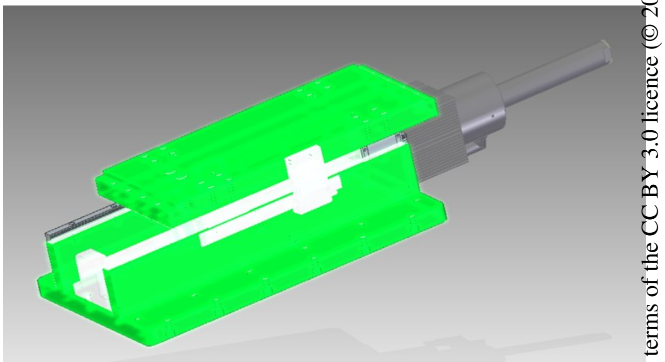

Figure 5: Linear drive module. The grey part is the linear motor, the green part is the package structure, and the white part is the linear encoders.

EXPERIMENT RUSULTS

After the software and hardware installation was completed, we carried out the beam current experiment in the SXFEL facility. First, with the YAG screen of the profile near the wire scanner, we verified that all three directions of the tungsten wire can interact with the beam, Figure 6 shows the images caught by the CCD camera when passing through the beam. The images illustrate the beam interation with the tungsten wire.

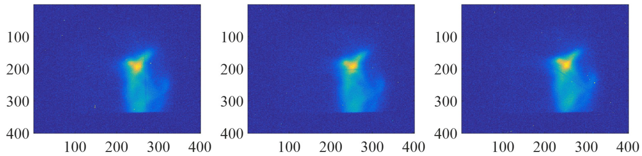

Figure 6: Three directions of tungsten wire and beam interaction diagram.

Use the data acquisition board to synchronously collect the beam position signal and the beam loss signal. The CBPM reference cavity signal can be used to normalize the charge amount of the position and beam loss signals. Figure 7 shows the signal received by the beam loss detector under the interaction between the wire and the beam, and the normal wireless state. The figure shows that the noise floor has a large peak, which is suspected that the beam interact with the remaining air molecules in the vacuum tube. More supplementary experiments will be arranged later.

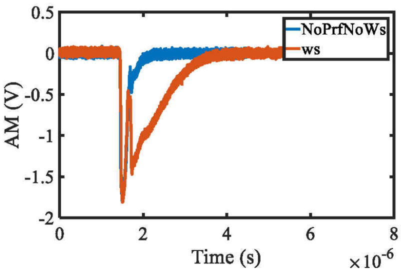

Figure 7: Beam loss signal.

In view of the complexity of the noise background, our system resolution is not ideal for the beam loss signal represented by the peak signal after deducting the noise floor. Although the overall trend of the data fits the Gaussian distribution(see Fig. 8). The calculated beam spot size is larger than the profile test result.

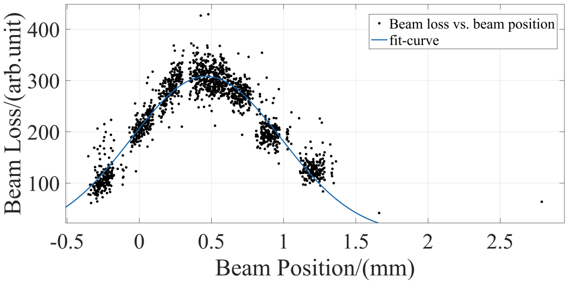

Figure 8: Beam loss vs beam position.

CONCLUSION

Wire scanner system are keeping update. In the next step, we will try to adjust the execution structure and the position of the beam loss detector, adjust the detector installation position and other methods to improve the beam loss signal reception efficiency and improve the system resolution. At the same time, to ensure that the mechanical execution structure can operate stably in the free electron laser facility with high repetition frequency, we will conduct some destructive experiments to verify it in the later stage.

ACKNOWLEDGEMENTS

The authors wish to express their thanks to the SXFEL commissioning team for providing the experimental conditions and constant support. We gratefully acknowledge the participation of mechanical group for installation of the vacuum installation.

REFERENCES

[1] G. L. Orlandi *et al.*, "Design and Test of Wire-Scanners for SwissFEL", in *Proc. FEL'14*, Basel, Switzerland, Aug. 2014, paper THP091, pp. 948–951.

[2] Alexander Novokhatski *et al.*, "A simple method for a very short X-ray pulse production and attosecond diagnostic at LCLS", *Nucl. Instrum. Methods Phys. Res., Sect. A*, vol. 921, pp. 57-64, 2019. `doi:10.1016/j.nima.2018.12.017`

[3] J. Wan *et al.*, "Prototype Design of Wire Scanner for SHINE", in *Proc. IBIC'20*, Santos, Brazil, Sep. 2020, pp. 285–287. `doi:10.18429/JACoW-IBIC2020-THPP36`

ISBN: 978-3-95450-230-1 ISSN: 2673-5350 doi:10.18429/JACoW-IBIC2021-TUPP17

FAST MEASUREMENTS OF THE ELECTRON BEAM TRANSVERSE SIZE AND POSITION ON SOLEIL STORAGE RING

M. Labat*, A. Bence, N. Hubert, D. Pédeau, Synchrotron SOLEIL, Gif-sur-Yvette, France
M. M. Patil, M. Caselle, A. Ebersoldt, E. Bründermann,
Karlsruhe Institute of Technology, Karlsruhe, Germany

Abstract

On SOLEIL storage ring, three beamlines are dedicated to electron beam diagnostics: two in the X-ray range and one in the visible range. The visible range beamline uses the synchrotron radiation which is emitted in one of the ring dipoles and further extracted by a slotted mirror operated in surf-mode (surfing on the upper part of the synchrotron layer). The radiation in the visible range is then transported towards a diagnostic hutch in the experimental hall, allowing electron beam imaging at the source point onto a standard CCD camera. In the perspective of prototyping works for the eventually forthcoming upgrade of SOLEIL, and for the on-going commissioning of a new Multipole Injection Kicker (MIK), we recently installed in this hutch two new branches ended by two new cameras (a KALYPSO system and a standard CMOS camera). We report in this paper the first results obtained on those branches.

INTRODUCTION

SOLEIL storage ring presently delivers synchrotron radiation to 29 beamlines. The stability of the delivered photon beams, a main figure of merit for users, relies on an accurate monitoring of the electron beam orbit and electron beam size / emittance at users source points. The electron beam size / emittance is measured independantly by two pinhole camera (PHC) systems, located at two different places of the ring. One of the PHC measurement is used in a feedback loop to maintain the vertical emittance within +/-5 %. However, with typical exposure times of 50–100 ms, those systems cannot follow fast beam dynamics features at the turn-by-turn scale for instance.

The installation of a new injection magnet and the perspective of an upgrade for SOLEIL recently revealed the need for an additionnal beam size diagnostic with a faster response.

We therefore decided to upgrade our visible range MRSV (*Moniteur de Rayonnement Synchrotron Visible*) beamline with two new branches. This work presents the preliminar results obtained on those branches.

EXPERIMENTAL SETUP

The experimental layout of the MRSV beamline is presented in Fig. 1. The synchrotron radiation of one of the ring dipoles (ANS-C01) is extracted using a slotted mirror operated in *surf–insertion* mode: the mirror is surfing on top of the synchrotron radiation layer to catch visible range photons. Because of heat load issues, we can't operate the mirror in *slot–insertion* mode, i.e. centered on the beam axis with synchrotron radiation X–rays going through the slot, at high current. The synchrotron radiation is then transported via a set of mirrors down to a hutch in the experimental hall. On the beam path inside the tunnel are succesivly placed: a motorized slit to define the horizontal collection angle θ_x of the beamline and a spherical lens for refocussing. At the arrival on the optical bench in the hutch, the synchrotron radiation is splitted into several branches.

Initially, three branches were implemented (see pink boxes in Fig. 1): one with a fast diode for filling pattern measurement, one with a Streak Camera for bunch length measurement and one with a standard ethernet camera for a coarse imaging of the beam at the source point. We added two new branches to test higher resolution / higher speed imaging systems for beam size retrieval.

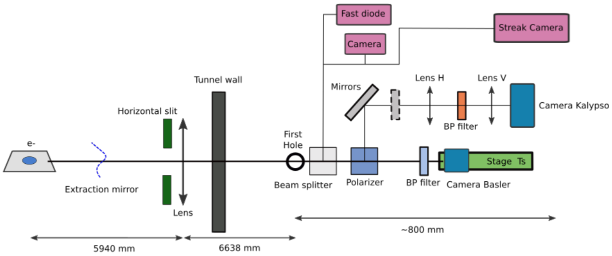

Figure 1: Layout of the MRSV beamline with its three initial branches in pink, and its two new branches.

BEAMLINE MODELING

To achieve an accurate imaging, an accurate modeling of the beamline is mandatory. We used for that the SRW (*Synchrotron Radiation Workshop*) code [1]. In Fig. 2 is first presented the simulated effect of using the extraction mirror in *surf* rather than in *full* (or *slot*) –insertion mode. Because of the disymmetry of the extraction, there is nearly no more difference between the polarization components of the radiation.

After a first attempt of comparison between measured and simulated intensity distributions in the image plane of the MRSV beamline, we realized that the beamline was suffering from strong stigmatism: the image plane in y was few tens of centimeters downstream the image plane in x. Because the focussing lens in the tunnel is spherical, we immediatly suspected the extraction mirror to introduce this stigmatism. To verify this interpretation, we simulated the effect of a

---

* marie.labat@synchrotron-soleil.fr

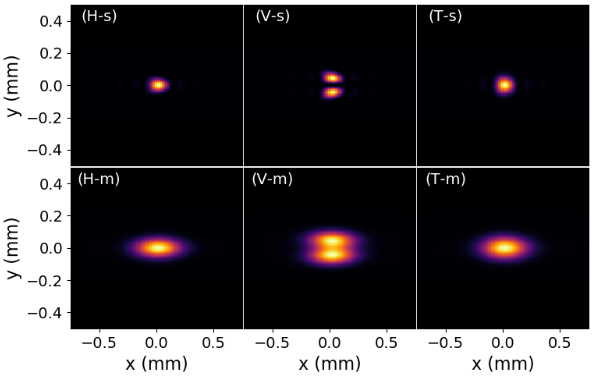

(a) Full–insertion mode

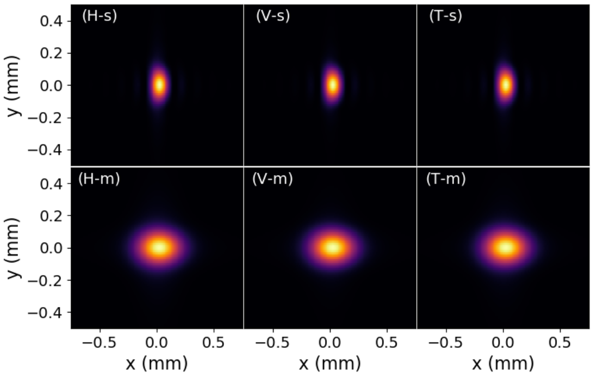

(b) Surf–insertion mode

Figure 2: Intensity distribution in the image plane simulated with SRW using an extraction mirror in (a) full–insertion and (b) surf–insertion mode. Polarization is (left) Horizontal, (middle) Vertical and (Right) Total, using (top line) single–electron, (bottom line) multi–electron mode. Other parameters: λ=400 nm, f_{xy}=3.21 m, D=6.984 m, θ_x=3.5 mrad, θ_y=10 mrad.

double focussing: an astigmatic one from the spherical lens together with a stigmatic one (only along vertical dimension) from the extraction mirror. The result is an effective focal length f_x along x and f_y along y where $f_x \neq f_y$. Fitting the experimental observations of the intensity distributions versus D the distance from lens to camera for several wavelengths led to f_x=3.21 m and f_y=3.4 m at 400 nm. The good agreement between model and simulation confirmed that under heat load, the extraction mirror becomes slightly convex in the y direction, introducing an additionnal focussing in this direction. In Fig. 3 is presented the result of the simulated effect of this stigmatic focussing on the beam distribution in the x image plane. The image distribution is further distorted along y.

In Fig. 4, we finally present the simulated and measured effect of the distance D from lens to camera for a wide horizontal collection angle θ_x. Even though images are displayed in logarythmic scale, the agreement between simulation and experiment remains reasonnable.

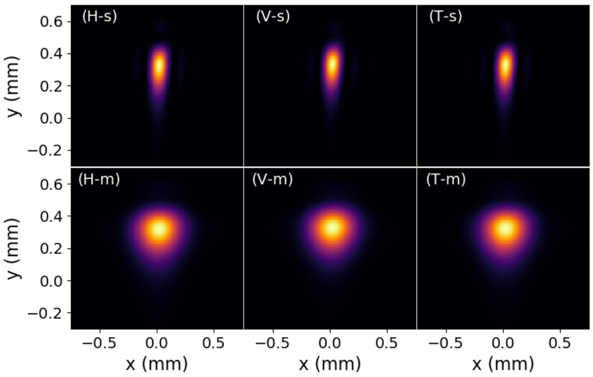

Figure 3: Intensity distribution in the image plane simulated with SRW using an extraction mirror in surf–insertion mode withf_x=3.21 m and f_y=3.4 m. Other parameters as in Fig. 2.

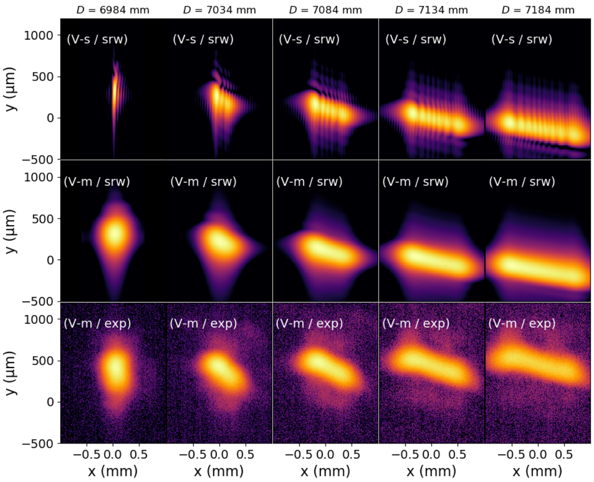

Figure 4: Intensity distribution in the image plane simulated with SRW (first line in single–electron, second line in multi–electron mode) and experimentally measured (third line) versus D. Extraction mirror in surf–insertion mode with f_x=3.21 m and f_y=3.4 m, θ_x=θ_y=10 mrad, λ=400 nm, vertical polarization. Images in logarythmic scale. Camera for experiment: Basler ace1920.

FIRST NEW BRANCH: NB#1

Confident in the modeling of the beamline, we then used SRW simulations to optimize the distance D, the observation wavelength λ and the horizontal collection angle θ_x to get the highest contrast between the single–electron spot size (PSF) and the multi–electron spot size. The higher indeed will be this contrast, the more sensitive should be the final beam size measurement. The best result was obtained at the shortest reachable wavelength (400 nm) with the maximum collection angle (10 mrad) in the x image plane. We implemented the first new branch NB#1 accordingly. The radiation is spectrally filtered using a bandpass filter centered at 400 nm with 10 nm bandwidth, for the sake of simplicty the vertically polarized component is retained using a polarizing beamsplitter cube (see Fig. 1), while an ace1920

CMOS camera from Basler is used to record the images with a 5.6 μm pixel pitch.

We then investigated on the beam size retrieval method from the experimental images. For nearly Gaussian PSF profiles, beam size retrieval can simply be achieved by fitting the beam profiles in the image plane with Gaussian functions, and then quadratically substract the widths of the PSF to those fitted widths. But in our case of imaging with a surf–inserted mirror, a chromatic focussing and a large horizontal collection angle, the PSF functions are far from being Gaussian. We therefore tried, as a first step, to fit the beam profiles in the image plane with the convolution of the SRW simulated PSFs with Gaussian functions of width S_x, S_y. (S_x, S_y would correspond to the *real* beam size in the image plane, i.e. beam size at source point σ_x, σ_y magnified by M the beamline magnification). The results were not satisfactory in the y direction because images are recorded in the x image plane, not in the y plane. We then tried to compute a pseudo–PSF for the y plane, making the deconvolution of the SRW simulated beam profile with a Gaussian function of width $S_y = M \times \sigma_y$, where σ_y is the beam vertical size at source point used as input in the simulation. However, this method was still leading to beam size at the source point several times larger than the expected one. This was essentially due to the fact that we could not reach a perfect agreement between SRW simulation and measurement of the beam distribution in the image plane probably because of complicated mirror surface distortions. We finally tried to convolute the previous pseudo–PSF with a Gaussian error function. The width of this function was manually adjusted to match the beam size retrieved with the beam size expected. Beam size retrieval with this method is illustrated in Fig. 5. Up to now, this is the best method we could set.

In order to test the sensitivity of our mesurement, we then simultaneously recorded the vertical beam sizes measured on NB#1, PHC#1 and PHC#3 as a function of the vertical emittance. The results are shown in Fig. 6. This measurement first reveal the high level of fluctuation on NB#1 (more than 100% fluctuation in the beam size measurement). While the exposure time for PHCs is in the 50–100 ms range, the exposure time on NB#1 is 30 μs, i.e. nearly three orders of magnitude, so we expected of course more fluctuations on NB#1. But the main source of fluctuation is most probably due to the radiation transport in air, over more than 10 meters and passing via differently air conditionned areas. The amplitude of the fluctuations is indeed far above the possible *physical* ones, of the order of a few microns.

SECOND NEW BRANCH: NB#2

The polarizer at the entrance of the optical bench splits the synchrotron radiation in one vertically polarized component going straight to NB#1, and one horizontally polarized component deflected by 90 degrees. This component of the synchrotron radiation is the one used for our second branch NB#2. The radiation on NB#2 is transported with mirrors down to a Kalypso camera [2]. This camera was provided by KIT. It consists of a linear array detector with an ultrafast reading electronics. This system is described in details in [2]. To match the linear array geometry, the photon beam is refocussed with a pair of cylindrical lenses (f=100 mm). To obtain a reasonnable resolution with the maximum flux, a bandpass filter of 80 nm bandwidth centered at 600 nm is used.

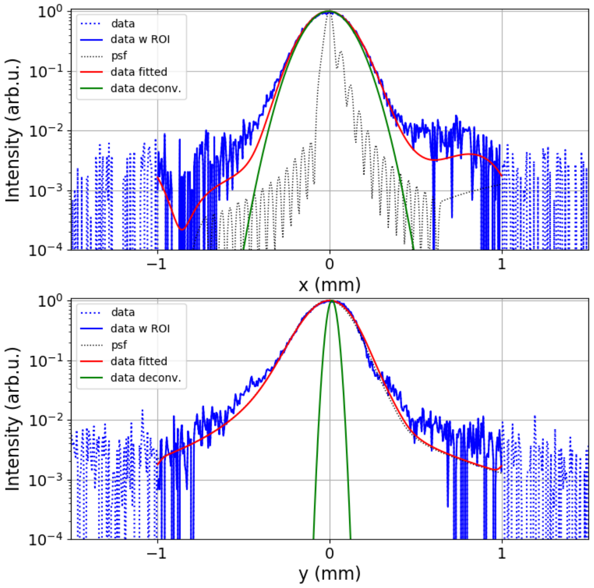

Figure 5: Example of beam size retrieval from measured images. (data) experimental profiles corresponding to line cuts of 2 pixels at maximum intensity lcoation. (data w roi) data restricted to a ROI of ±1 mm. (psf) Point Spreaf Function simulated with SRW and eventually corrected. (data fitted) Experimental profiles restricted to ROI fitted by convolution of a Gaussian profile with the PSF function. (data deconv.) Gaussian profile obtained from fit. D=6.994 m, θ_x=θ_y=10 mrad, λ=400 nm, polarization is vertical.

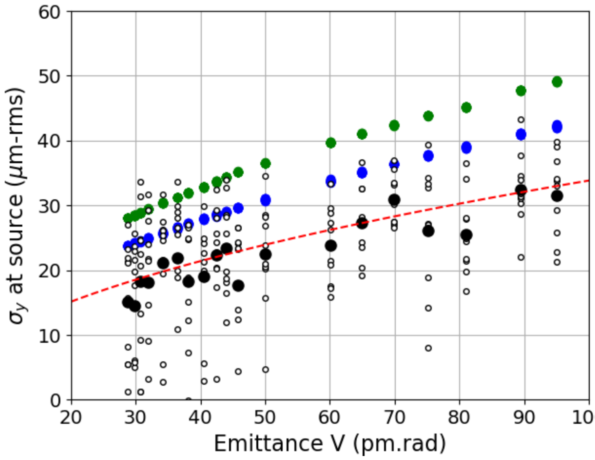

Figure 6: Vertical beam size measured versus vertical emittance by (green dot) PHC#1, (blue dot) PHC#3, (o) MRSV HR branch single shot, (•) MRSV HR branch average of the 10 single shots. D=6.994 m, θ_x=θ_y=10 mrad, λ=400 nm, polarzation is vertical.

A typical example of a Kalypso image is presented in Fig. 7(a). Each vertical line of the image corresponds to one record of the light distribution along the linear array. In the example, it is the vertical distribution of the beam which is captured. Along the image horizontal axis are displayed the successive records. Each record can be externally or internally triggered up to 3 MHz which offers outstanding opportunities for machine physics studies. In the example, the records were triggered by the turn-by-turn clock (846 kHz), so that each record corresponds to the imaging of the same portion of the bunch train turn after turn.

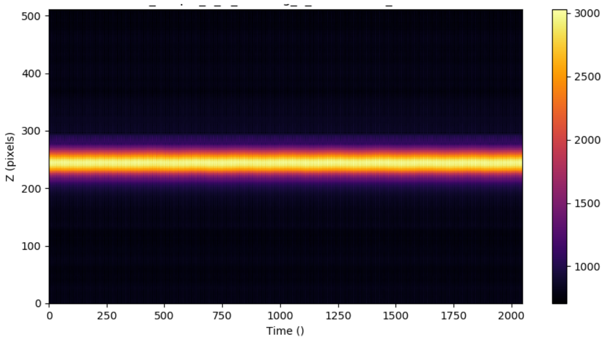

(a) Image

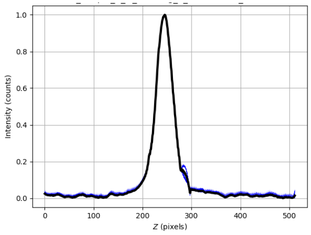

(b) Normalized vertical intensity profile

Figure 7: (a) Example of a Kalypso camera image in users operation at 500 mA. (b) Normalized projection of the (a) image along the horizontal axis to provide with the beam distribution along the vertical axis.

The Kalypso system is still under commissioning on NB#2. But we could already perform an interesting machine physics experiment. We used indeed the Kalypso camera to follow the effect of the injection on the stored beam during the operation of SOLEIL. To maintain a constant current, top–up injection is performed into the storage ring. Every few minutes, 4 kickers are used to create a bump on the stored beam orbit, allowing the injection of few additionnal mA. Because the bump is not perfectly closed, we can observe on the beam position monitors a transient displacement of the beam in both the horizontal and the vertical planes. Launching the acquisition of the Kalypso camera slightly before the injection time, and using an external turn–by–turn trigger, we could record the images presented in Fig. 8. The top image shows the horizontal beam distribution and the bottom image shows the vertical beam distribution. We can change the imaging plane using a crossed or non–crossed periscope on the photon beam path. In both planes, we clearly observe the kick given at the injection time, but we can also follow the evolution of the beam back to its equilibrium on a real turn–by–turn basis. The beam oscillates as expected in both planes at the synchrotron frequency with a damping time significantly shorter in the vertical than in the horizontal plane.

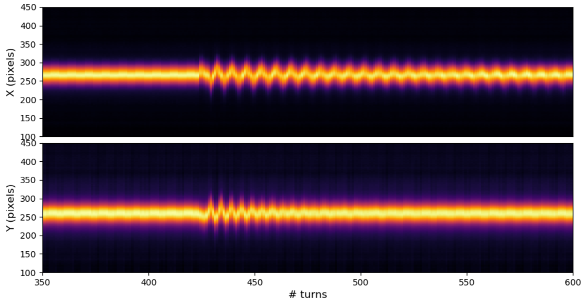

Figure 8: Kalypso images recorded on MRSV beamline. Recording launched a few hundred turns before injection time. Imaging of (Top) the horizontal and (bottom) the vertical distribution of the beam.

CONCLUSION

We presented here recent results obtained on the two new branches NB#1 and 2 of our visible range MRSV beamline.

We made significant efforts to obtain a satisfactory modeling of our beamline relying on SRW simulations. We managed to include the effect of the surf–insertion mode and of a stigmatic focussing induced by the mirror. Unfortunatly, some discrepancies remain between simulation and measurement, so that up to now, we can only retrieve the beam sizes at the source point including, in addition to the PSF, an additionnal arbitrary –but constant– contribution to the beam size. Next January, the extraction system for the MRSV beamline will be upgraded (new extraction mirror and new cooling system). This should enable to improove the accuracy of the imaging on NB#1 in surf–insertion mode, but also to work in the slot–insertion mode in users operation.

The preliminar results obtained on NB#2 are very encouraging. The ultra–high repetition rate of the camera enabled already to follow the beam dynamics at injection in one single image. By the end of 2021, we plan to improve the focussing on the camera and to calibrate the magnification on NB#2 to have an aboslute beam size measurement.

Both NB#1 and 2 strongly suffer from a very high level of fluctuations most probably due to the long in–air transport. We'll try to upgrade the beamline to move it under-vacuum along 2022.

REFERENCES

[1] O. Chubar, P. Elleaume, "Accurate and Efficient Computation of Synchrotron Radiation in the Near Field Region", in *Proc. 6th European Particle Accelerator Conf. (EPAC'98)*, Stockholm, Sweden, Jun. 1998, paper THP01G, p.1177-1179.

[2] M. Caselle *et al.*, "Ultrafast linear array detector for real-time imaging", *Proc. of SPIE*, vol. 10937, 1093704-1, 2019.

10th Int. Beam Instrum. Conf. IBIC2021, Pohang, Rep. of Korea JACoW Publishing
ISBN: 978-3-95450-230-1 ISSN: 2673-5350 doi:10.18429/JACoW-IBIC2021-TUPP18

COMMISSIONING OF THE LHC INJECTORS BWS UPGRADE

J. Emery*, W. Andreazza, D. Belohrad, S. Di Carlo, J.C. Esteban Felipe, A. Goldblatt,
D. Gudkov, A. Guerrero, S. Jackson, G.O. Lacarrere, M. Martin Nieto,
A.T. Rinaldi, F. Roncarolo, C. Schillinger, R. Veness,
European Organization for Nuclear Research (CERN), Geneva, Switzerland

Abstract

A novel generation of fast Beam Wire Scanners (BWS), developed in the framework of the LHC Injectors Upgrade (LIU), has been recently deployed in the 3 LHC injector synchrotrons, accelerating protons from 160 MeV to 450 GeV, during the 2019-2020 LHC long shutdown. The monitors feature high precision motor controllers, high resolution wire position monitoring and wide dynamic range secondary particles detectors. This contribution will document the commissioning of the 17 new systems during the accelerator complex restart in 2021, which is an exciting and challenging phase in the life cycle of an instrument. A summary of the so far achieved levels of reliability, reproducibility, detectors/DAQ bandwidth, and overall accuracy, will be used to revisit the options for further improving the systems' performance in the future.

INTRODUCTION

The LHC Injectors Upgrade (LIU) Beam Wire Scanner (BWS) achieves high performances and reliability with completely new engineering concepts. After more than a decade of research and development within the instrumentation group at CERN [1–5], seventeen systems have been installed in the injectors complex during the second LHC long shutdown (LS2). The commissioning has been following the restart of the injectors in 2021, starting with the Proton Synchrotron Booster (PSB) with eight systems, Proton Synchrotron (PS) with five and Super Proton Synchrotron (SPS) with four. This paper, after introducing the new system features, will focus on the various commissioning stages that allowed to hand over the systems to the various accelerators operation crews.

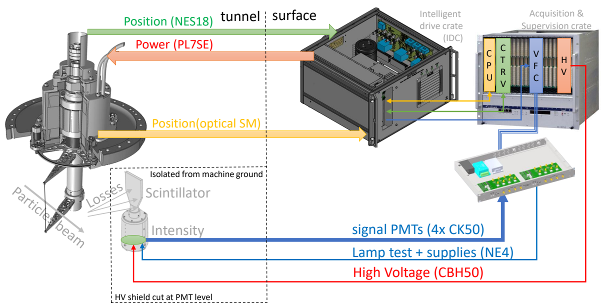

Figure 1: LIU BWS with its electronics at the surface (right) while mechanics and detectors are on the beam line (left).

INSTRUMENT DESCRIPTION

A wire-scanner monitor is based on a very thin carbon wire made crossing the particle beam at high velocity [6]. This interaction produces a shower of secondary particles, which correlated to the wire position, allows reconstructing the transverse beam profile.

The new BWS features key innovations, with the kinematic unit having moving parts only in vacuum, using magnetic and optical means to transfer power and signaling from and to the air side. The position of the shaft is measured by a solid rotor resolver for trajectory control [7] and by a high accuracy optical encoder, developed in-house, to precisely infer the fork and wire position during a scan [8]. The encoder is based on the analysis of a laser beam focused on and then reflected by reflective and anti-reflective tracks engraved on the optical disc mounted on the shaft. Due to the high acceleration felt by the carbon wire the calibration of this system is essential to compensate for uncertainties of the wire trajectory for predefined speeds [9]. The secondary particle shower detection uses one scintillator coupled to four detectors equipped with different neutral density filters to cover the large dynamic range of beam energies and intensities across the LHC injectors [10]. The output signals are digitised simultaneously at high speed and processed to provide profile measurements for each particle bunch.

Figure 1 shows the instrument architecture. The kinematic unit and particle detectors (left side) are located in the accelerator tunnel. The stand-alone control unit and the VME acquisition system (right side) are in the surface service area. The communication from tunnel to surface is done with cables and optical fibers, with lengths above 150 m in some cases.

Hardware Test Procedures

Emphasis was made on the system testability when designing the LIU wire-scanner. Multiple procedures were implemented to quickly validate the systems after installation and any time a diagnosis is required.

The Open Loop Test (OLT) verifies the cabling, electronics and sub parts of the kinematic unit. The three phases motor is powered without current and position feedback, i.e. in open loop, similar to stepper motors. The scanner moves forward and backward by 3.14 rad in steps and an example of the measured motor currents (blue, green, orange) and shaft angle (red) is shown in Fig. 2. The levels are compared to references to detect any non-conformity. With this procedure, the system hardware commissioning can be carried out from the surface without the need of tunnel access to

---

* jonathan.emery@cern.ch

connect test scanner outside the vacuum, as necessary with legacy systems.

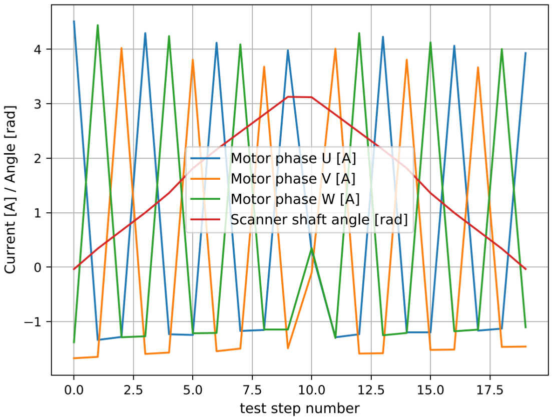

Figure 2: Motor currents and shaft angle of scanner PS.64.V during an Open Loop Test (OLT) checking the scanner connectivity and kinematic unit rotation.

The Scan Without Motion (SWM) performs all the scan procedure without the need for moving the wire in the beam. As during a standard scan, the PMT acquisition is triggered at a predetermined shaft angle, but in this test the angle is simulated with predefined tables. The test generates data from all sensors, from the motor currents to the PMT signals.

The PMT Lamp Test (PLT) uses the incandescent lamp in front of PMTs controlled from the surface and allows verifying the high voltage supply, tunnel pre-amplifier and signal cables to the surface.

The Optical Encoder Test (OET) consist in the optical encoder laser power scans allowing defining the optimal and stable level.

INDIVIDUAL SYSTEM TESTS

The Individual System Tests (IST) at CERN are the overall verification by experts of a system before the HW and Beam commissioning carried out by the accelerator operation crew. This was the opportunity to adjust the wire scanners' settings after their final installation in the various machines. These tests were performed using expert software tools managing the final version of the stand-alone control unit . This allowed performing OLTs and OETs for all systems, thus validating the connections and mechanics under vacuum. A series of 100 scans per scanner was performed to study the trajectory stability. As an example, Figure 3 shows the motion pattern reproducibility for two SPS scanners, as they move through the beam axis and back. One of the two is less reproducible. Even if there is no evidence that a larger angular spread reduces the overall instrument performance, it is valuable to keep track of it, since it may lead to long term reliability issues with the kinematic unit. Table 1 summaries the Trajectory Reproducibility Error (TRE) for all scanners in mrad/s, indicating at which rate reproducibility degrades.

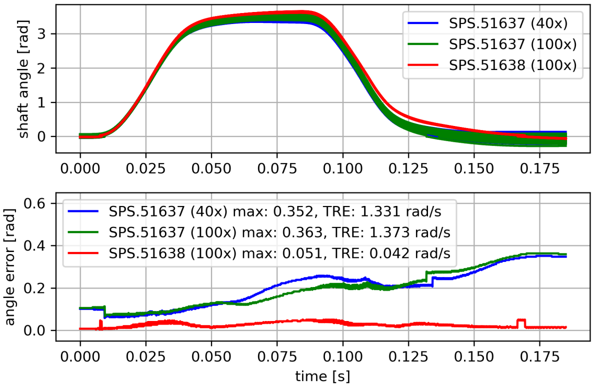

Figure 3: Kinematic unit angular trajectory for sets of scans (top) and the scan to scan variation within the set (bottom).

Table 1: LIU BWS name (N), accelerator (A), cabling length [m] (L), trajectory reproducibility error [mrad/s] (TRE), PMT noise [bin] (N1) noise @16 kHz [V^2/Hz] (N2).

N	A	L	TRE	N1	N2	scan*
R1H	PSB	60	21	171	0.02	2047
R2H	PSB	60	21	158	0.00	1361
R3H	PSB	60	697	88	0.00	4528
R4H	PSB	60	21	133	0.00	1572
R1V	PSB	55	232	144	0.01	1681
R2V	PSB	55	85	145	0.00	1261
R3V	PSB	55	63	95	0.00	6499
R4V	PSB	55	845	126	0.01	1431
54H	PS	185	63	1706	44.1	2866
64V	PS	230	63	901	8.04	2797
65H	PS	232	106	492	1.04	1028
68H	PS	215	21	522	2.15	331
85V	PS	216	85	1634	19.2	497
41677V	SPS	170	169	487	0.36	4517
41678V	SPS	170	63	155	0.12	325
51637H	SPS	150	1373	378	0.63	2040
51638H	SPS	150	42	2526	0.88	1095

*Total of 35'876 scans (up to 01.09.2021)

All secondary shower detection systems were validated using the PLT procedure.

COMMISSIONING WITH BEAM

The BWS development before the 2019-2020 Long Shutdown (LS2) included the test of various prototypes with beam in the PSB, PS an SPS [3, 11, 12]. The commissioning with beam of the final systems in 2021 took several weeks in the PSB, especially to fully deploy and validate the latest FW and SW versions. On the other hand, in the PS and SPS, thanks to the experience in the PSB and benefiting of the systems' standardization, it was possible to acquire beam profiles from the first day of beam operation.

Figure 4 shows an example of a LHC-type beam with 25 ns bunch separation measured in the SPS with the LIU

ISBN: 978-3-95450-230-1 ISSN: 2673-5350 doi:10.18429/JACoW-IBIC2021-TUPP18

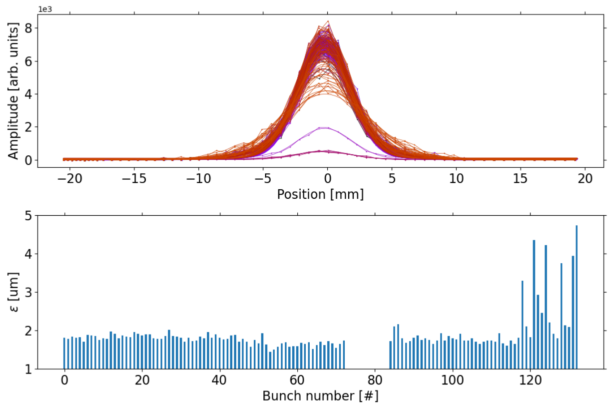

Figure 4: SPS.BWS.41677.V measurement (top) of 25 ns separated bunches (LHC Type beam). The beam emittance growth at the end of the train is due to the electron cloud effect (bottom).

scanner 41677V (top). The growth of the beam emittance at the end of the train is due to the electron cloud effect (bottom).

With the first milestone of handing over all systems to operation, the challenging phase of maximizing availability and optimizing the overall systems' accuracy is ongoing. For the acquisition chain, the following aspects are particularly relevant to set up and characterize in order to assess and improve performance: operating point (PMT high voltage), digital integration phasing, noise reduction/rejection and bandwidth characterization.

Optimisation of the Acquisition Operating Point

The detection of the particles shower uses a plastic scintillator (BC-408) coupled to 4 PMTs (R9880U from Hamamatsu) with custom powering board optimised for large pulse mode and fast recharge. Neutral density filters with different attenuation in front of each PMT allows covering a wide range of beam types, The PMT current outputs are pre-amplified to drive long coaxial cables to the surface where another amplifier stage drives 4 parallel high speed digitizers.

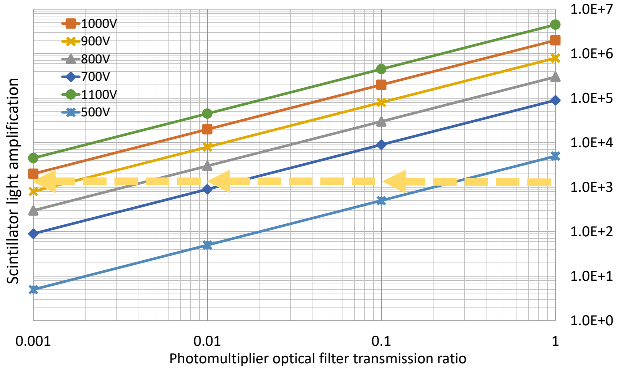

Figure 5: The scintillator light amplification (axis y) combines the 4 PMT optical filters (axis x) and the PMT voltage (colored lines). The dashed line represents an approximation of the amplification set for the measurements in Fig. 6.

Figure 5 shows the scintillator light amplification as function of filter attenuation (i.e. PMT channel) and PMT voltage. The selection of the acquisition working point requires an optimal balance between competing effects. The beam signal needs to be well above the noise level to achieve enough precision without saturating the digitizers. The PMT must also be run in its linear regime. If too many photons are detected, saturation effects appear and degrade the system performance. The visible consequence of PMT's or digitizer's saturation is an artificial growth of the beam size.

Figure 6 shows measurements of LHC type beams in the PSB for different PMT voltages and channels. For each channel, the emittance is stable for a range of voltage, but grows after a certain threshold. This evidences that at least for this beam type different operating points can be found (all leading to about 1.75 µm) but also that particular care has to be taken to avoid operating in saturation.

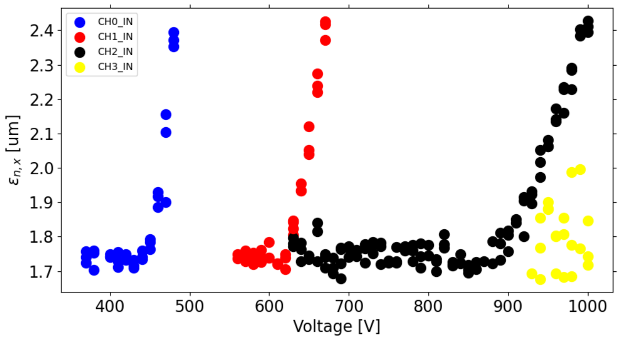

Figure 6: PSB R1V voltage scan, LHCINDIV beam, Intensity: $9.4x10^{10}$ ppb, Energy: 2018 MeV.

Therefore, this type of measurements is very valuable to study linearity, saturation of the analog part of the signal detection and processing (the digital part saturation is easier to detect) and will allow determining if the choice of optical filtera attenuation is adequate to cover all beams, including the ones expected in the future.

Acquisition Integration Adjustment

The PMT signals are captured with a direct-current coupling (DC) digital acquisition system (DAQ) at 500 MHz and 14bit resolution asynchronously to the particle beam. This information is stored into volatile memories with the beam and bunch synchronisation signals. Once the scan is completed, a hardware-based processing integrates the signals to obtain one profile per bunch. This operation requires adjusting the phase between ADC integration windows and beam arrival time. While the phasing is presently performed manually, new FW and SW routines are under development to automatically find the optimal delays for different machines and to be robust against beam phase changes. Figure 7 shows a raw PMT signal of PS-65H (blue), digitally integrated (yellow) using the beam revolution (red) and harmonic reference (green).

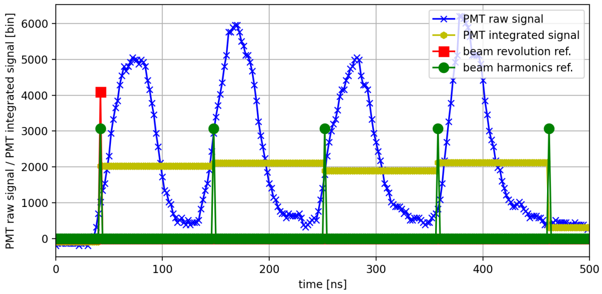

Figure 7: Raw PMT capture of a beam of four bunches with PS.65.H (blue), digitally integrated signal (yellow), beam revolution reference (red) and beam harmonics ref. (green).

Acquisition Noise Characterisation

Noise and electromagnetic interference can heavily affect the wire scanner measurements. In many cases, the data processing and fit filters out most of the stochastic noise when calculating the beam size. Nevertheless, when very small beams are measured, the contribution of low frequency noises is a concern. After inspections, some faulty PMT isolation and ground loops were identified and corrected. The grounding scheme shown in Fig. 1 was finally considered as the optimal.

Figure 8 shows a typical PMT signal power spectrum density without beam (red) and with a common mode noise suppressor based toroid core (green). The main perturbation at 16 kHz has a reproducible phase from scan to scan and is synchronous with the BWS motor driver. It can be attenuated by more than 30 dB with the tested choke, though some resonances between 100-200 kHz are enhanced. This coupling does not take place at the surface, but along the cabling. There is a correlation between noise levels (columns N1, N2) and cable length (column L) visible in Table 1.

Acquisition Bandwidth

The bandwidth of the acquisition system determines the ability of the system to resolve short time structures, in our case the bunch by bunch profiles. Beam measurements on the SPS system show few per-cents cross-talk between bunches spaced by 25 ns. A hardware review has revealed bandwidth and stability limitations of the tunnel pre-amplifier, but the beam tests without it did not show improvement in the machine conditions. A second setup with a smaller scintillator volume from a PS legacy system has been tested showing even worse measurement quality without improving the bandwidth. This is shown in Fig. 9, comparing the LIU type scintillator and amplifier (blue-yellow) to the smaller PS-type without amplifier (green-red). The temporal behavior is similar (bottom) , the PS type shows poor quality (top). Further studies are ongoing to optimize the HW and developing SW based corrections to reduce cross-talk.

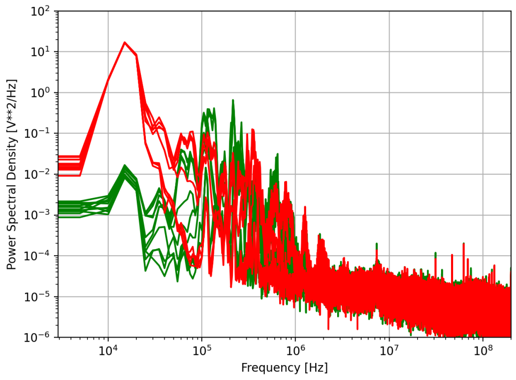

Figure 8: Power Spectral Density of PS-85V PMT signals without beam (9 scans in red) and with a common mode noise suppressor choke (11 scans in green).

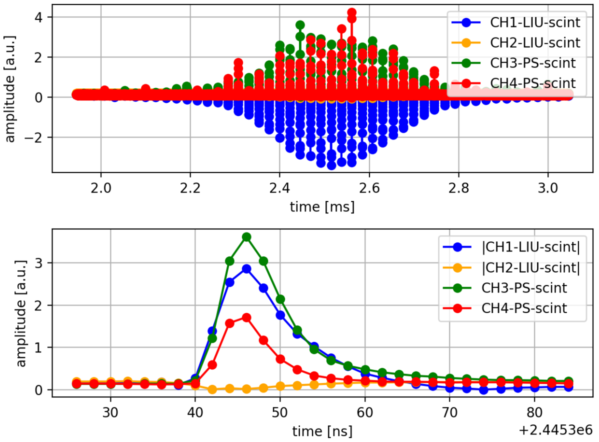

Figure 9: SPS measurements with LIU-type scintillator and pre-amplifier (red, green), and PS-type scintillator without pre-amplifier (blue, yellow). The time structure of a bunch shows similar decay for both systems (bottom) while the PS overall signal is poorer (top).

CONCLUSIONS AND OUTLOOK

The 17 new wire scanners installed in the LHC injectors were all commissioned in a relatively short time given the system complexity. They are daily, extensively used (thousands of scans already in the first few months) by the operation crews, with no major faults. This first operation period already proved the systems' capability to measure 25 ns spaced bunches with few % cross-talk and with a few % statistical error (always difficult to decouple from bunch per bunch and shot by shot beam jitters). More time and dedicated measurements are needed to assess the systems' absolute accuracy and resolution.

Studies are ongoing to tune and optimize PMTs operating ranges, synchronization with the beam, noise and bandwidth. Finally, new features are under development in order to detect PMTs linearity limits, improve the measurement precision by reducing the wire speed, and increase the scan repetition rate up to bursts of several consecutive scans on the same circulating beam.

REFERENCES

[1] M. Koujili *et al.*, "Fast and high accuracy wire scanner," in *Proc. 9th European Workshop on Beam Diagnostics and Instrumentation for Particle Accelerators (DIPAC'09)*, (Basel, Switzerland), JACoW Publishing, May 2009, pp. 188–190.

[2] M. Koujili, Y. Ait-Amirat, B. Dehning, A. Djerdir, J. Emery, and J. H. Alvarez, "Design of an actuator for the fast and high accuracy wire scanner," in *2011 IEEE International Electric Machines Drives Conference (IEMDC)*, May 2011, pp. 1450–1455. DOI: `10.1109/IEMDC.2011.5994822`.

[3] R. Veness *et al.*, "Experience from the Construction of a New Fast Wire Scanner Prototype for the CERN- SPS and its Optimisation for Installation in the CERN-PS Booster," in *Proceedings, 4th International Beam Instrumentation Conference (IBIC2015) , Melbourne, Australia, September 13-17, 2015*, 2016, TUPB061. 4 p. DOI: `10.18429/JACoW-IBIC2015-TUPB061`. `https://cds.cern.ch/record/2263484`

[4] J. H. Alvarez, B. Dehning, and A. B. Condomines, "Minimisation of the wire position uncertainties of the new CERN vacuum wire scanner," Ph.D. dissertation, Jan. 2016. `https://cds.cern.ch/record/2156989`

[5] J. Emery, A. Barjau, B. Dehning, J. H. Alvarez, P. J. Lapray, and M. Macchini, "Design and validation methodology of the control system for a particle beam size measurement instrument at the cern laboratory," in *2017 American Control Conference (ACC)*, May 2017, pp. 4221–4228. DOI: `10.23919/ACC.2017.7963604`.

[6] F. Roncarolo, "Accuracy of the transverse emittance measurements of the CERN large hadron collider," eng, Ph.D. dissertation, SB, Lausanne, 2006. DOI: `10.5075/epfl-thesis-3402`.

[7] J. Emery, P. Andersson, F. Roncarolo, and Y. Thoma, "A low fluctuation control strategy for PMSM direct drive system targeting Particle Beam Instrumentation Application," in *Proceedings, 3rd IEEE Conference on Control Technology and Applications (CCTA2019): Hong Kong, Hong Kong, China, August 19-21, 2019*, 2019, tbd. DOI: `tbd/tbd`.

[8] J. L. Sirvent, J. Emery, and J. M. A. Poveda, *Design of an optical fibre based angular position sensor for wire scanners complying with ultra-high vacuum, high temperature and radiation conditions of the CERN's accelerators*, Presented 2012, 2012. `https://cds.cern.ch/record/1491608`

[9] J. Emery *et al.*, "Laboratory and beam based studies for assessing the performance of the new fast wire scanners for the cern injector complex," in *Proc. 8th Int. Beam Instrumentation Conf. (IBIC'19)*, (Malmö, Sweden), JACoW Publishing, Sep. 2019, pp. 392–396. DOI: `10.18429/JACoW-IBIC2019-TUPP033`.

[10] J. Sirvent, "Beam secondary shower acquisition design for the cern high accuracy wire scanner," Ph.D. dissertation, Barcelona University, Dec. 2018.

[11] J. Sirvent *et al.*, "Performance Assessment of Pre-Series Fast Beam Wire Scanner Prototypes for the Upgrade of the CERN LHC Injector Complex," in *Proceedings, the 6th International Beam Instrumentation Conference (IBIC2017), Grand Rapids, Michigan, USA, August 20-24, 2017*, 2018, WEPCC03. 4 p. DOI: `10.18429/JACoW-IBIC2017-WEPCC03`. `https://cds.cern.ch/record/2661464`

[12] E. Senes *et al.*, "Transverse Emittance Measurement in the CERN Proton Synchrotron in View of Beam Production for the High-Luminosity LHC," in *Proceedings, 10th International Particle Accelerator Conference (IPAC2019): Melbourne, Australia, May 19-24, 2019*, 2019, MOPTS100. DOI: `10.18429/JACoW-IPAC2019-MOPTS100`.

ISBN: 978-3-95450-230-1 ISSN: 2673-5350 doi:10.18429/JACoW-IBIC2021-TUPP19

PROPOSED RESEARCH WITH MICROBUNCHED BEAMS AT LEA*

A. H. Lumpkin†, Argonne Associate, Argonne National Laboratory, Lemont, IL 60439 USA
W. J. Berg, J. Dooling, Y. Sun, K.P. Wootton, Argonne National Laboratory, Lemont, IL 60439 USA
D. W. Rule, Silver Spring, MD, 20904 USA
A. Murokh, RadiaBeam Technologies LLC, Santa Monica, CA 90404 USA
P. Musumeci, UCLA, Los Angeles, CA 90095 USA

Abstract

Significant microbunching of an electron beam at 266 nm is projected with the co-propagation of electrons at 375 MeV and a UV laser pulse through a 3.2-cm period prebuncher undulator. Such microbunched beams will generate coherent optical transition radiation at a metal screen surface boundary or coherent optical diffraction radiation from a nearby metal surface (new model presented). With a 10% microbunching fraction, coherent enhancements of more than 7 million are modelled for a 300-pC charge. Diagnostic plans are described for beam size, divergence, electron microbunching fraction, spectrum, and bunch length on a single shot at the Argonne National Laboratory Linac Extension Area (LEA).

INTRODUCTION

One of the advantages of relativistic electron beams with microbunching at UV to visible wavelengths is the potential to generate coherent optical transition radiation (COTR) at a metal foil for diagnostics purposes. A significant microbunching fraction of at least 10% is expected for the case of a seed laser at 266 nm copropagating with a 375-MeV electron beam through a modulator undulator (3.2 cm period) at the Linac Extension Area (LEA) at Argonne National Laboratory [1,2]. Diagnostic plans have been made for the COTR-based characterization of the microbunched beam size (~100 microns), divergence (sub-mrad), microbunching fraction, spectrum, and bunch length (sub-ps), as well as coalignment of the laser pulse and electron beam as previously described [3]. For that case, COTR enhancements over OTR of more than seven million were calculated, and we expect a similar enhancement of coherent optical diffraction radiation (CODR). Thus, we propose the modification of the microbunching diagnostics station to support initial CODR experiments with beam transit through an aperture in a metal screen or near a metal edge at the second screen position of the interferometer. We would explore whether the coherence function for CODR provides a complementary beam size monitor.

EXPERIMENTAL ASPECTS

The Advanced Photon Source (APS) linac includes options for injection of beam from either a thermionic cathode (TC) rf gun or a photocathode (PC) rf gun into an S-band linac with final beam energies of up to 500 MeV. The schematic of the facility is given in Fig. 1. For operations providing beam to the APS storage ring, beam from one of the two thermionic guns is used. For these proposed experiments, single micropulses from the PC rf gun with Cu cathode irradiated by a quadrupled Nd glass laser at 2 or 6 Hz would be used with electron beam parameters given in Table 1. The chicane is used for bunch compression from 2 ps down to σ_t ~0.5 ps.

At the end of the linac there is an option to transport beam with a bypass of the Particle Accumulator Ring (PAR) to the LEA building where the experiments can be performed. A schematic of the experimental geometry is shown in Fig. 2. After the modulator and dispersive section, there would be the diagnostics chamber which is repurposed from a previous FEL experiment [4]. This chamber has stepper actuators at two locations in z separated by 6.3 cm. The first is a normal imaging station with positions for a YAG:Ce screen plus 45-degree mirror or a metal foil at 45 degrees. When this latter 10-μm thick Al foil is selected, it blocks the seed laser, and it also generates forward COTR as the beam exits from the back surface in the direction of the second mirror at 45 degrees which is 6.3 cm downstream. COTR is also generated at the front surface of this metal mirror. The combination of sources provides the COTR interferometry. By using near field (NF) focusing the microbunched beam size at the first screen can be measured, and by using far-field (FF) focusing the angular distribution pattern of the COTR interferences can be seen and divergences assessed. The expected COTRI patterns have been previously reported [3,5], and an example is provided in the next section.

The YAG:Ce emissions are near 550 nm so a standard digital CMOS camera would be used for initial beam size imaging. The COTR and CODR would be narrowband at the wavelength of the UV seed laser so a UV sensitive imager is needed with a digital capability preferred. Multiple cameras would be used with beam splitters to provide NF, FF, polarized imaging, and spectra on a single shot for

Table 1: Linac Parameters for PC Gun Beam Used in the Proposed Tests

Parameter	Units	Value
Energy	MeV	375
Charge	pC	100-300
Emittance	mm mrad	2-4
Bunch length	ps	0.5-2.0

---

* Work supported in part by UChicago Argonne, LLC under Contract No. DE-AC02-07CH11357 with the U.S. Department of Energy, Office of Science, Office of Basic Energy Sciences.

† lumpkin@anl.gov

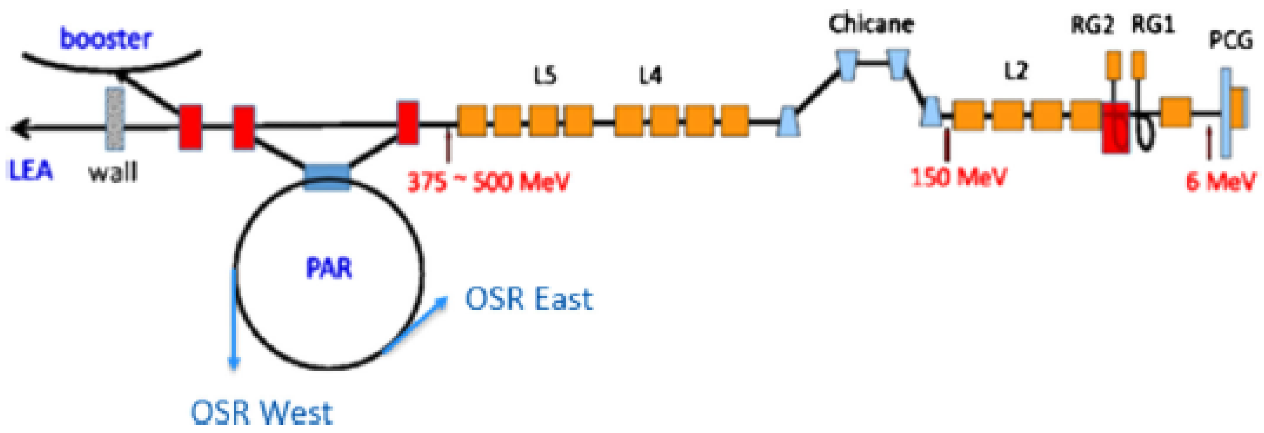

Figure 1: Schematic of the APS linac showing the PC rf gun (PCG), two thermionic cathode rf guns (RG1 and RG2), the accelerating structures (L2, L4, L5), the chicane, PAR, and transport to the LEA. A beam interleaving scheme allows the use of PC gun beam for LEA when the RG2 beam is not needed for the PAR, booster, and storage ring.

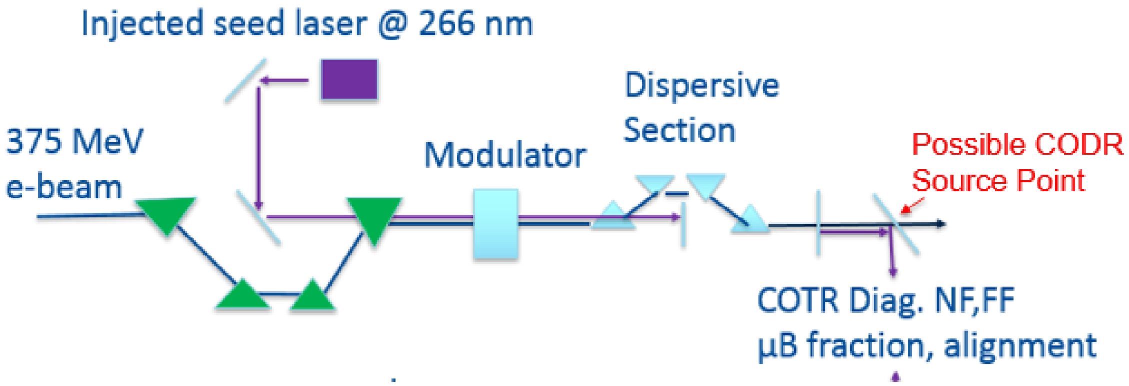

Figure 2: Schematic of the proposed experiment in the LEA showing the seed laser injection point, modulator, dispersive section, and the microbunching diagnostics station for COTR and CODR measurements.

COTR. The spectrometer readout would be done with another UV camera. The microbunching fraction would be assessed by determining the ratio of observed COTR intensity with the seed laser in the modulator to OTR data obtained with the seed laser off as emitted from the back of the first screen. The use of a 450-nm long-pass filter would select the much weaker incoherent OTR for the total beam spot imaging. A UV-sensitive streak camera phase locked to 119 MHz could be used for the bunch length assessment at the sub-ps level. Alignment of the seed laser and electron beam can also be enabled by using the COTR-based transverse, angular, and longitudinal distributions.

The seed laser could be a commercially available Ti:Sapphire oscillator plus amplifier with frequency tripling to ~266 nm and with a nominal 300-fs bunch length after compression. This would be injected onto the beamline axis by mirrors for co-propagation with the electron beam through the modulator as indicated in Fig. 2.

MODELING ASPECTS

The two basic models for COTR and CODR are considered. They are extensions of the FF incoherent OTR Model and the NF ODR model reported previously [6, 7].

COTR Model

The COTR model was described in detail recently [6]. The screen positions act as a two-foil Wartski OTR interferometer [8] having foils at 45° to the beam axis and with spacing *L=63 mm*. The forward directed OTR from the first foil is reflected off the back of the second foil and interferes in the far field. We define the parallel and perpendicular polarizations for a scan along the θ_x axis.

To proceed we start with W_1, the number of OTR photons that a single electron generates per unit frequency ω per unit solid angle Ω from a single foil which is

$$\frac{d^2W_1}{d\omega d\Omega} = \frac{e^2}{\hbar c}\frac{1}{\pi^2\omega}\frac{(\theta_x^2+\theta_y^2)}{(\gamma^{-2}+\theta_x^2+\theta_y^2)^2} \,. \qquad (1)$$

The COTRI model for the two-foil interferometer with the incoherent part $\propto N$ and the coherent part $\propto N_B^2$,

$$\frac{d^2W}{d\omega d\Omega} = \left|r_{\parallel,\perp}\right|^2 \frac{d^2W_1}{d\omega d\Omega}\left[N\boldsymbol{I}(\boldsymbol{k}) + N_B(N_B-1)\boldsymbol{J}(\boldsymbol{k})\right], \qquad (2)$$

where N_B of the total number N are microbunched, i.e., the bunching fraction, bf= N_B/N. Here $\left|r_{\parallel,\perp}\right|^2$is the reflection coefficient for parallel or perpendicularly polarized OTR reflected from the *second* foil. ***I(k)*** is the expression for the interference of the OTR from the first and second foils of the interferometer, given by

$$I(\boldsymbol{k}) = 4\sin^2[\tfrac{kL}{4}\left(\gamma^{-2} + \theta_x^2 + \theta_y^2\right)]\,, \qquad (3)$$

where $k = |\boldsymbol{k}| = 2\pi/\lambda$. Peaks of ***I(k)*** occur at angles ${\theta_x}^2 + {\theta_x}^2 = \frac{2\lambda}{L}(p - p_0)$, where $p = 1/2,\ 3/2\ \ldots$ and $p_0 = L/(2\lambda\gamma^2)$. For good sensitivity to divergence p_0 should be of order unity. The coherence function ***J(k)*** can be defined as

$$J(\boldsymbol{k}) = \left(H_1(\boldsymbol{k}) - H_2(\boldsymbol{k})\right)^2 + H_1(\boldsymbol{k})H_2(\boldsymbol{k})I(\boldsymbol{k})\,, \quad (4)$$

where $H_j(\boldsymbol{k}) = \rho_j(\boldsymbol{k})/Q = g_j(k_x)\, g_j(k_y)\, F_z(k_z)$, for a microbunch of charge distribution $\rho_j(\boldsymbol{x})$ and total charge Q, with j = 1, 2. Here we have introduced two µ-bunch form factors, H_1 and H_2, to account for the increase in bunch radius from the first to the second interferometer foil due to beam divergence. This is important for micron sized beams, but it is a negligible effect for an initial 100-µm beam size with sub-mrad divergence considered here.

One prediction is that the coherence functions for 10 and 100 µm are quite different. As seen in Fig. 3a, only the inner lobes are enhanced for the 100-µm case so the cone angle is about ±1 mrad. The forward COTR will hit the intercepting mirror 63 mm away for COTRI, but it would miss the screen edge when located >200 µm away from the beam trajectory. This potentially allows one to image the CODR from the second screen in the near field. In Fig. 3b we show effects of divergence on COTRI fringe visibility for values of 0.1, 0.3, 0.5, and 0.7 mrad. The larger divergences reduce the modulation. The coherence function provides a 7-million intensity enhancement factor at the smaller angles.

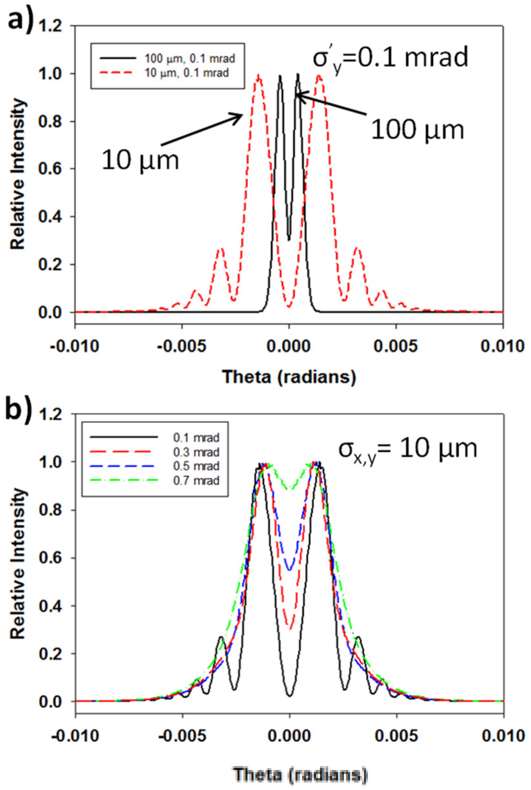

Figure 3: Plots of $I_{total} = I_{\parallel} + I_{\perp}$ for a) two beams with sizes $\sigma_{x,,y}$ =10 µm and 100 µm, both with divergence $\sigma'_{x,,y}$=0.1 mrad, and b) beams all with size $\sigma_{x,y}$ =10 µm and divergences $\sigma'_{x,y}$= 0,1, 0,3, 0,5 and 0.7 mrad. The common parameters used in a) and b) are *E*=375 MeV, 1/γ=1.36 mrad, *L*=63 mm, λ=266 nm, total charge=300 pC, and bunching fraction=10%.

CODR Model

Previously we employed incoherent ODR imaging as a non-intercepting diagnostic. Our initial NF ODR experiments were at 7 GeV on an extraction line from the Booster synchrotron at APS [7]. The high gamma allowed us to have an impact parameter of 4 σ_y above the beam for the horizontal lower edge of a Cu mirror surface. We were able to image the 1300-µm horizontal beam size with a 3 nC bunch charge. In the present case at gamma of ~734 and a beam size of 100 µm, we anticipate the incoherent ODR will be dramatically reduced by 2.6 x 10^{-6} at an impact parameter of 400 µm with λ= 266 nm. However, we estimate an enhancement of CODR to be about 7 x 10^6 for a 10% bunching fraction and micropulse charge of 300 pC as in COTR. We project the NF CODR would be detectable with a low-noise, 12-bit digital UV camera.

The necessity of relying on coherent ODR led us to develop a model for CODR which can be used to predict the enhancement and the effect of the µ-bunch's transverse and longitudinal structure. Our approach is based on the Weizächer-Williams's method of virtual quanta [9] which takes advantage of the similarity of a relativistic particle's field to a photon. The Fourier transform in time, *t* taken at an impact parameter *b* with respect to the particle's trajectory yields the frequency spectrum. Consider Fig. 4, a schematic of a metal screen with its edge at distance of e.g. ~ 4 σ_y, where the beam's vertical size is ~2 σ_y. An electron at $\boldsymbol{r_i}$ with respect to the beam centroid has an impact parameter $\boldsymbol{b_i}$ at point *P* in the screen, located by $\boldsymbol{u_i} = \boldsymbol{b_i} + \boldsymbol{r_i}$, as measured from the beam centroid. The backward ODR is proportional to the field strength squared

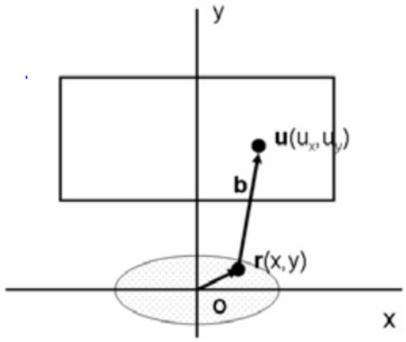

Figure 4: Schematic showing the transverse beam profile, ODR screen and vectors locating a beam particle and point P on the screen relative to the beam centroid [10].

and to the reflectance $\left|r_{\parallel,\perp}(\psi)\right|^2$ for parallel and perpendicular polarizations with the screen at angle ψ relative to the beam axis.

The frequency spectrum is given by [9]

$$\frac{dI(b_i,\omega)}{d\omega}(b_i,\omega) = \frac{c}{2\pi}|E_x(b_i,\omega)|^2 + \frac{c}{2\pi}\left|E_y(b_i,\omega)\right|^2, \quad (5)$$

where the electric field components polarized along the X- and Y-directions are [11]

$$E_{x,y}(b_i,\omega) = \frac{e\alpha}{\pi v}\, e^{-i\frac{\omega z}{v}} \frac{b_{ix,y}}{b_i} K_1(\alpha b_i)\,, \text{and } \omega = \boldsymbol{k}\cdot\boldsymbol{v}\,. \quad (6)$$

Here $\boldsymbol{b_i} = b_{ix}\,\hat{\boldsymbol{x}} + b_{iy}\,\hat{\boldsymbol{y}} = (u_x - x_i)\hat{\boldsymbol{x}} + \left(u_y - y_i\right)\hat{\boldsymbol{y}}$, and $\omega z/v = k_z z_i$, with z_i being parallel to $\boldsymbol{v}$. Also $K_1(\alpha b_i)$ is a modified Bessel function and $\alpha = \omega/v\gamma \approx 2\pi/\gamma\lambda$ for $v{\sim}c$.

If we have a beam which is partially μ-bunched with bunching fraction bf $= N_B/N$ and charge $Q_B = N_B e$, we expect coherent ODR if the transverse beam sizes $\sigma_{x,y} \lesssim 2\pi/\gamma\lambda$ and the longitudinal size σ_z is such that $k_z\sigma_z{\sim}1$.

The total frequency spectrum at point *P,* summing over all the electrons in a single μ-bunch is

$$\frac{dI^T(b_i,\omega)}{d\omega}(b_i,\omega) = \frac{c}{2\pi}|E_x^T(u,\omega)|^2 + \frac{c}{2\pi}\left|E_y^T(u,\omega)\right|^2, \quad (7)$$

where $E_{x,y}^T(u,\omega) = \sum_{i=1}^{N_B} E_{x,y}^i\,(b_i, z_i, \omega)$ and specializing to the y-polarization for simplicity, putting the explicit sums over particles in Eq. (7) above we have

$$\begin{aligned}\left|E_y^T(u,\omega)\right|^2 &= \sum_{i=1}^{N_B}\sum_{j=1}^{N_B} E_y^i\, E_y^{j^*} \\ &= \sum_{i=1}^{N_B}\left|E_y^i\right|^2 + \sum_{j\neq i}^{N_B}\sum_{i=1}^{N_B} E_y^i E_y^{j^*}\,. \end{aligned} \quad (8)$$

The first sum over *i*=*j* gives the incoherent ODR, while the sums over *i*=1-N_B and $i \neq j$ gives the coherent contribution.

This approach was also used for the COTR model, where we treated the μ-bunch as a product of normalized Gaussian forms, assuming that the x-, y-, and z-distributions are separable. The charge density is $\rho(x,y,z) = N_B e F_\parallel(z) F_\perp(x,y)$, with

$$F_\parallel(z) = \frac{1}{\sqrt{2\pi\sigma_z^2}} e^{-z^2/2\sigma_z^2}\,,$$
$$F_\perp(x,y) = \frac{1}{\sqrt{2\pi\sigma_x^2}}\frac{1}{\sqrt{2\pi\sigma_y^2}} e^{-x^2/2\sigma_x^2} e^{-y^2/2\sigma_y^2}. \quad (9)$$

We now replace the incoherent sum over all *N* electrons by the following average of the intensity over the beam profile using Eq.(6):

$$\sum_{i=1}^{N_B}\left|E_y^i\right|^2 \rightarrow \left\langle\left|E_y(u,\omega)\right|^2\right\rangle = N\frac{e^2\alpha^2}{\pi^2 v^2}\iint dxdy\frac{b_y^2}{b^2}K_1^2(\alpha b)F_\perp(x,y), \quad (10)$$

where $b = \left[(u_x - x)^2 + \left(u_y - y\right)^2\right]^{1/2}$. Note that the *z*-dependent phase cancels for the sum over *i*=*j*. This incoherent model was used in Refs. [7, 10], with the integrals done numerically.

Next, we turn to the sums over *i*=1-N_B and $i \neq j$ for which there are $N_B(N_B - 1)$ terms like $E_y^1(b_1, z_1, \omega)E_y^2(b_2, z_2, \omega)^*$. The impact parameters b_1 and b_2 for electrons 1 and 2 are independent variables and we further assume there is no correlation affecting the particles' separation $\boldsymbol{r}_1 - \boldsymbol{r}_2$. Again we proceed with the same Gaussian μ-bunch distribution, but now we average the field strength of each electron independently, rather than the intensity, as in the incoherent part above. We use the same form to do the averaging, given by

$$\langle E_y^i(u,\omega)\rangle = \frac{e\alpha}{\pi v}\iiint dxdydz e^{-ik_z z}F_\parallel(z)\frac{b_y}{b}K_1(\alpha b)F_\perp(x,y). \quad (11)$$

Using the above averaging procedure we replace the sums over discrete electrons in the μ-bunch by

$$N_B(N_B - 1)\langle E_y^1(u,\omega)\rangle\langle E_y^2(u,\omega)\rangle^* = N_B(N_B - 1)\frac{e^2\alpha^2}{\pi^2 v^2}e^{-(\sigma_z k_z)^2}\left|\iint dxdy\frac{b_y}{b}K_1(\alpha b)F_\perp(x,y)\right|^2. \quad (12)$$

Here the integral of $e^{-ik_z z}F_\parallel(z)$ above in Eq. (11) gives the factor $e^{-(\sigma_z k_z)^2}$, the Fourier transform of the μ-bunch's longitudinal profile, indicating that the μ-bunch length should satisfy $k_z\sigma_z{\sim}1$ for coherent ODR. The integral over the beam profile $F_\perp(x,y)$ will be done numerically, similarly to what was done in Refs. [7, 10]. The above Eq. (12) gives the coherent frequency spectrum when used in Eq. (7). The sum over a train of μ-bunches has been discussed in Ref. [4] and is omitted here because of space constraints.

The dependence on N_B^2 is the basis for the large enhancement of CODR expected in the present application, which will dominate the incoherent ODR for sufficiently large bunching fractions.

SUMMARY

In summary, we have described the potential for measuring a comprehensive set of microbunched electron beam properties on a single shot using COTR and potentially extending the basic techniques to CODR imaging. A new NF CODR model is described for the first time which will be used to guide future experiments.

ACKNOWLEDGEMENTS

The ANL-affiliated authors acknowledge the support of J. Byrd and M. Borland of the Accelerator Systems Division at ANL. The submitted manuscript has been created by UChicago Argonne, LLC, Operator of Argonne National Laboratory (Argonne). Argonne, a U.S. Department of Energy Office of Science Laboratory, is operated under Contract No. DE-AC02-06CH11357. The U.S. Government retains for itself, and others acting on its behalf, a paid-up nonexclusive, irrevocable worldwide license in said article to reproduce, prepare derivative works, distribute copies to the public, and perform publicly and display publicly, by or on behalf of the Government.

REFERENCES

[1] W. Berg, J. C. Dooling, S. H. Lee, Y. Sun, and A. Zholents, "Development of the Linac Extension Area 450-MeV Electron Test Beam Line at the Advanced Photon Source", in *Proc. 8th Int. Beam Instrumentation Conf. (IBIC'19)*, Malmö, Sweden, Sep. 2019, pp. 219-221. `doi:10.18429/JACoW-IBIC2019-MOPP048`

[2] Y. Park *et al*., "Tapered helical undulator system for high efficiency energy extraction from a high brightness electron beam", submitted for publication.

[3] A. H. Lumpkin and D. W. Rule, "Feasibility of Single-Shot Microbunching Diagnostics for a Pre-Bunched Beam at 266 nm", in Proc. 39th Int. Free Electron Laser Conf. (FEL'19), Hamburg, Germany, Aug. 2019, pp. 408-411. `doi:10.18429/JACoW-FEL2019-WEP041`

[4] A. H. Lumpkin *et al.*, "Evidence for Microbunching "Sidebands" in a Saturated Free-Electron Laser Using Coherent Optical Transition Radiation," *Phys. Rev. Lett.*, vol. 88, no. 23, p. 234801, Jun. 2002. `doi:10.1103/PhysRevLett.88.234801`

[5] A. H. Lumpkin and D.W. Rule, "Single-shot Diagnostics of Microbunched Electrons in Laser-Driven Plasma Accelerators and Free-electron Lasers", in *Proc. 8th Int. Beam Instrumentation Conf. (IBIC'19)*, Malmö, Sweden, Sep. 2019, pp. 633-636. `doi:10.18429/JACoW-IBIC2019-WEPP039`

[6] A. H. Lumpkin *et al.*, "Coherent Optical Signatures of Electron Microbunching in Laser-Driven Plasma Accelerators," *Phys. Rev. Lett.*, vol. 125, no. 1, p. 014801, Jul. 2020. `doi:10.1103/PhysRevLett.125.014801`

[7] A. H. Lumpkin, W. J. Berg, N. S. Sereno, D. W. Rule, and C.-Y. Yao, "Near-field imaging of optical diffraction radiation generated by a 7-GeV electron beam," *Phys. Rev. ST Accel. Beams*, vol. 10, no. 2, p. 022802, Feb. 2007. `doi:10.1103/PhysRevSTAB.10.022802`

[8] L. Wartski *et al.*, "Interference phenomenon in optical transition radiation and its application to particle beam diagnostics and multiple-scattering measurements, *J. Appl. Phys.* vol. 46, no. 8, p. 3644, Aug.1975. `doi:10.1063/1.322092`

[9] J. D. Jackson, "Bremsstrahlung, Method of Virtual Quanta, Radiative Beta Processes," in *Classical Electrodynamics*, 2nd ed., New York, NY, USA: Wiley, 1975.

[10] C.-Y. Yao, A. H. Lumpkin, and D. W. Rule, "Numerical Simulation of Optical Diffraction Radiation from a 7-GeV Beam", in *Proc. 22nd Particle Accelerator Conf. (PAC'07)*, Albuquerque, NM, USA, Jun. 2007, paper FRPMS001, pp. 3850-3852. `doi:10.1109/PAC.2007.4440020`

[11] M. L. Ter-Mikaelian, Electromagnetic Processes in Condensed Media, New York, NY, USA: Wiley-Interscience, 1972.

ISBN: 978-3-95450-230-1 ISSN: 2673-5350 doi:10.18429/JACoW-IBIC2021-TUPP21

THE HL-LHC BEAM GAS VERTEX MONITOR - PERFORMANCE AND DESIGN OPTIMISATION USING SIMULATIONS

B. Kolbinger*, H. Guerin[1], O. R. Jones, T. Lefevre, J. W. Storey,
A. Salzburger, R. Veness, C. Zamantzas, CERN, Geneva, Switzerland
S. M. Gibson, R. Kieffer, Royal Holloway, University of London, Surrey, UK
[1]also at Royal Holloway, University of London, Surrey, UK

Abstract

The Beam Gas Vertex (BGV) instrument is a novel non-invasive beam profile monitor and part of the High Luminosity Upgrade of the Large Hadron Collider (LHC) at CERN. Its aim is to continuously measure emittance and transverse beam profile throughout the whole LHC cycle, which is currently not possible using a single device. The BGV consists of a gas target and a forward tracking detector to reconstruct tracks and vertices resulting from beam-gas interactions. The beam profile is inferred from the spatial distribution of the vertices, making it essential to achieve a very good vertex resolution. Extensive simulation studies are being performed to provide a basis for the design of the future BGV. The goal of the study is to ascertain the requirements for the tracking detector and the gas target within the boundary conditions provided by the feasibility of integrating them into the LHC. This contribution will focus on the simulations of the forward tracking detector. Based on cutting-edge track and vertex reconstruction methods, key parameter scans and their influence on the vertex resolution will be discussed.

INTRODUCTION

Understanding the evolution of beam profile and size throughout the whole accelerator cycle of the LHC is of great importance for the optimisation of emittance, and hence luminosity. The BGV device is foreseen to provide an independent, continuous, non-invasive, and bunch intensity independent measurement of the beam profile throughout the accelerator cycle. Beam-gas collision products stemming from LHC protons, interacting inelastically with the BGV's gas target installed in the path of each circulating beam, are measured via tracking detectors (Fig. 1 A). The beam profile is determined from the spatial distribution of the reconstructed vertices of the collisions.

A BGV demonstrator device has been successfully installed, commissioned and operated during LHC Run 2 [1]. A vacuum pressure bump of 10^{-7} mbar extending over ≈ 2 m was provided by a gas injection system and acted as the target. The forward tracking detector was composed of several planes of scintillating fibres based on the LHCb SciFi detector modules [2]. It successfully demonstrated the feasibility to use inelastic beam gas interactions for beam monitoring. However, due to poor track quality and limited vertexing capabilities, the demonstrator failed to reconstruct the beam profile. A new design is currently under development based on what has been learned from the BGV demonstrator and the results of detailed and complete simulations.

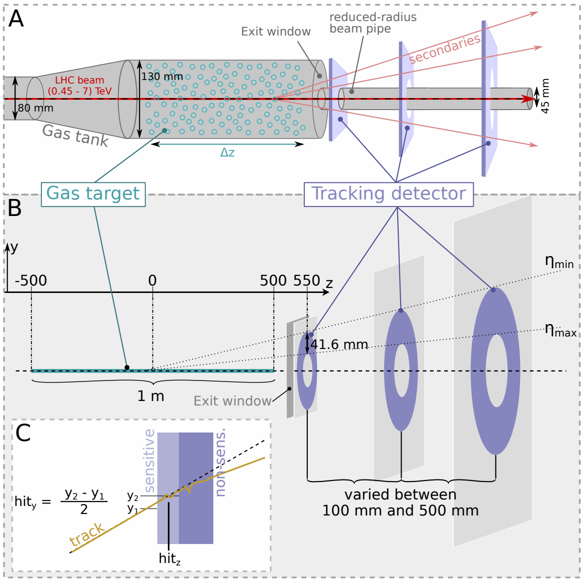

Figure 1: A: Sketch of the BGV. B: Generic simulation setup. The interaction region is shown in turquoise. The detector layers are shown in light grey, their active area in purple. The exit window (dark grey) is placed at z = 545 mm. C: Z-y cross-section of a detector layer.

The true beam profile is extracted from the spatial distribution of reconstructed vertices via deconvolution of the vertex response of the BGV system, making the latter the most important figure of merit for the device's performance. However, a precise knowledge of the vertex response is difficult to achieve. It is therefore desirable to keep its width, i.e. the vertex resolution σ_v, low relative to the true beam width σ_b. At the foreseen location of the BGV, the smallest expected beam size will be $\sigma \approx 200$ µm at 7 TeV. Assuming bunches with Gaussian transverse distributions with standard deviations of σ_b and a Gaussian vertex response with a width of σ_v, the following relation arises via deconvolution, error propagation and assuming negligible measurement uncertainty [3]: $\frac{\delta\sigma_\mathrm{b}}{\sigma_\mathrm{b}} = \frac{\sigma_\mathrm{v}^2}{\sigma_\mathrm{b}^2}\frac{\delta\sigma_\mathrm{v}}{\sigma_\mathrm{v}}$, where $\delta\sigma_\mathrm{b}$ and $\delta\sigma_\mathrm{v}$ denote the absolute beam size and vertex resolution uncertainties. This relation highlights the importance of a small σ_v relative to the beam size and precisely knowing the vertex resolution. Assuming a relative beam size error of ≤ 0.05 (see design specifications listed in Ref. [4]) and $\frac{\delta\sigma_\mathrm{v}}{\sigma_\mathrm{v}} \leq 0.1$, we arrive at an upper limit for the vertex resolution of $\sigma_\mathrm{v} \lesssim 140$ µm.

---

* bernadette.kolbinger@cern.ch, corresponding author

Vertex resolution and interaction/event rate σ_{v} depends on various characteristics of the measured tracks corresponding to an interaction, which will henceforth be called an "event". σ_{v} strongly depends on the number of tracks per event $\sigma_{\mathrm{v}} \propto \frac{1}{\sqrt{N_{\mathrm{tr}}}}$, which in turn depends on beam energy, gas species, detector coverage and the distance from the vertex to the detector. The detector coverage is determined by the exit window of the gas tank (see Fig. 1 A), whose maximum radius has been estimated by impedance simulations [4] to be ≈ 65 mm, and the reduced-radius beam pipe downstream of the tank, whose minimum inner radius is 22.5 mm [4] which is given by the required aperture at injection at the BGV location. Furthermore, σ_{v} is strongly influenced by the track quality, which can be studied via the transverse impact parameter resolution of a single track calculated via [5]:

$$\sigma_{\mathrm{IP}}^2 = \sigma_{\mathrm{int,det}}^2 + \sigma_{\mathrm{MS}}^2 \tag{1}$$

The intrinsic detector contribution $\sigma_{\mathrm{int,det}}$ is calculated via [6] $\sigma_{\mathrm{int,det}}^2 = \frac{\sigma_{\mathrm{res}}^2}{N+1} + \frac{\sigma_{\mathrm{res}}^2}{N+1}\frac{12N}{N+2}\frac{x^2}{L^2}$, where σ_{res} is the spatial resolution, N the number of detector layers, x the distance from the vertex to the centre of the detector and L the detector's total length. This highlights the importance of σ_{res} and the length of the detector for σ_{IP}. The contribution from multiple scattering in the materials is determined via $\sigma_{\mathrm{MS}} = \sqrt{d^2\theta_0^2}$, with the distance d from the scattering plane to the vertex and the multiple scattering angle θ_0 (see Ref. [7] for the formula), which depends on the radiation length of the material and the momentum of the particle. In the calculations discussed later, the multiple scattering contributions of the first detector layer and the exit window are included. The first results of the BGV performance study via simulations using a generic geometry are presented in the next section. The goal is to use this general setup to ease navigation of the BGV's extensive parameter space and to efficiently identify the impact of design parameter and verify that there are no showstoppers. Once the dependence of σ_{v} on BGV and event attributes is known, the rate of events with a sufficiently high vertex resolution can be estimated. The total rate of inelastic beam-gas collisions per proton bunch is calculated via $R_{\mathrm{inel}} = f_{\mathrm{rev}}\ N\ \sigma_{\mathrm{p\text{-}gas}}^{\mathrm{inel}}\ \rho_{\mathrm{gas}}\ \Delta z$, where f_{rev} = 11245 Hz denotes the revolution frequency of the bunches, $N = 2.2 \times 10^{11}$ [8] the nominal number of protons per bunch after the high luminosity upgrade of the LHC, $\sigma_{\mathrm{p\text{-}gas}}^{\mathrm{inel}}$ the inelastic cross-section of the interaction, ρ_{gas} the gas density and Δz the length of the gas in the direction of the beam. Considering gas interactions with protons at the LHC injection energy of 450 GeV (representing the case where the fewest secondaries are created compared to interactions at higher beam energies), a neon gas with a pressure of 10^{-7} mbar and Δz = 1 m, leads to R_{inel} = 147 Hz.

SIMULATION SETUP AND ANALYSIS

The first step in the simulation chain is the creation of the secondaries from beam-gas collisions via CRMC [9], an interface which allows access to several hadronic generators, see Ref. [4]. The resultant HepMC file [10] is read-in by Geant4 [11] which simulates the interaction of the secondaries with the BGV setup. The simulated information such as position, momenta, etc. of secondaries, as well as the simulated detector hits are saved by the Geant4 model. Figure 1 C demonstrates how the hits are determined from the Geant4 particle tracks. Subsequently, tracks and vertices are reconstructed as discussed in the following sections. Finally, the beam profile is determined by deconvolution of the resultant vertex distribution and vertex response, which will not be addressed by this paper.

Simulation geometry and conditions The generic BGV geometry is shown in Fig. 1 B. For the results presented here, 500 000 proton-neon collisions are simulated via the hadronic generator DPMJET 3.06 [12] using a beam energy of 450 GeV. Simulation results with higher beam energies will be discussed in a future and more detailed publication. The longitudinal spread of proton-neon interactions caused by the use of an extended gas volume, is simulated by uniformly distributing the vertices over 1 m along the z direction. Transversely, the vertex distribution is assumed to be Gaussian with a width of 0.5 mm. The exit window is simulated as a square shaped sheet, perpendicular to the z-axis and with a thickness of 0.9 mm (unless otherwise stated). It is entered in the simulation as being made from the same aluminium alloy AA2219 [1] used for the demonstrator tank. This implementation will be updated in future simulations to reflect the actual cone shape of the window with a varying thickness. The current BGV demonstrator has an exit window with a thickness gradient from 0.9 mm (small radii) to 3.2 mm (larger radii). A redesign of the exit window with the goal of lowering its material budget is currently ongoing.

The test setup for the detector consists of three layers of silicon. Each layer is composed of a sensitive material layer, where the hit position is registered for further analysis, and a non-sensitive material behind it, to simulate scattering in the rest of the detector (see Fig. 1 C). The large square shaped detector layers (light grey) allow the use of only one data set by performing subsequent cuts on the pseudo-rapidity η of tracks to simulate different detector sizes, as indicated by the purple discs in Fig. 1 B. In the presented results, the first detector layer covers the entire exit window (23.4 mm $< r <$ 65 mm). The size of the subsequent layers is chosen so that they cover the same solid angle with respect to the centre of the gas volume at (0, 0, 0). The distance between the centre of the gas volume and the first detector layer is 550 mm, which showed the highest N_{tr} for 450 GeV protons in previous studies, see Ref. [4]. In order to investigate the influence of the material budget x/X_0 of the tracker, two different detector layer thicknesses w_{d} are considered: 1 mm (1 % of x/X_0 per layer) of which 300 µm are sensitive, and 0.27 mm (0.29 % of x/X_0 per layer) of which 100 µm are sensitive. Regarding the spatial resolution σ_{res} of the detector, two cases are simulated: (1) σ_{res} = 16 µm, corresponding to a Si pixel detector such as a Timepix [13] detector with a pixel pitch of 55 µm, and (2) a lower resolution of $\sigma_{\mathrm{res}} = 50$ µm, representing e.g. a GEM tracker [14]. Furthermore, the distance between detector layers d_{det} is scanned in 50 mm steps between 100 mm and 500 mm. Note, that increasing d_{det} also increases the area of the second and third detector layers.

Track and vertex reconstruction In order to reconstruct tracks and the associated primary vertices of the beam-gas interactions, the experiment-independent reconstruction toolkit ACTS (A Common Tracking Software) [15, 16] is used. ACTS is intended for charged particle track reconstruction in high energy particle physics experiments for future colliders, and is based on the ATLAS tracking code. A track is defined as a collection of position measurements (hits) recorded by the detector. Only tracks with a hit in each layer are accepted. The process of track finding, i.e. associating which detector hits belong to which track, is initially omitted and a track finding efficiency of 1 is assumed. The low event rate (event pile-up not likely) and low track multiplicity (see Fig. 2) expected are likely to facilitate finding the tracks with high efficiency. The detector resolution is simulated by Gaussian smearing of the real x and y-hit positions with a certain σ_{res}. The tracks are fitted via ACTS's Kalman Fitter [17]. In order to create initial values for the track parameters, the hits of the first and last detector layer of a track are used. For the particle momentum, used by the Kalman fitting to account for multiple scattering effects, the real information is used. The momenta cannot be estimated from the track curvature since they are straight in the absence of a magnetic field. At a later stage, this will be replaced by an estimation via simulations, e.g. using the correlation of momentum with pseudo-rapidity. Afterwards, the fitted tracks are used to determine the vertex via the Billoir fitter [18]. σ_{v} can then be determined by comparing the true vertices to the reconstructed vertices, i.e. the residual distributions of the vertex components $r_i = v_{i,\mathrm{fit}} - v_{i,\mathrm{true}}$ with $i = \{x, y, z\}$. An example residual distribution of r_x is shown in Fig. 3. The vertex resolution is extracted by fitting the residual with a sum of two Gaussians, the so-called core and tail Gaussians [19], that are both centred around zero, but have different widths σ_{c} and σ_{t}. The underlying reason for this is that σ_{v} is impacted by the momenta, opening angles etc. of the tracks stemming from the vertices. The contribution of vertices to core and tail are calculated via the core and tail fractions: $f_{\mathrm{c}} = \frac{p_{\mathrm{c}}\sigma_{\mathrm{c}}}{p_{\mathrm{c}}\sigma_{\mathrm{c}}+p_{\mathrm{t}}\sigma_{\mathrm{t}}}$ and $f_{\mathrm{t}} = \frac{p_{\mathrm{t}}\sigma_{\mathrm{t}}}{p_{\mathrm{c}}\sigma_{\mathrm{c}}+p_{\mathrm{t}}\sigma_{\mathrm{t}}}$, where p denotes the amplitudes and σ the widths of the Gaussians. The vertex resolution can then be calculated as the weighted average $\sigma_{\mathrm{v}} = \sqrt{f_c\sigma_c^2 + f_t\sigma_t^2}$. Since the BGV's main purpose is to measure the transverse profile, the following discussion of the vertex resolution is solely focussed on σ_{x} and σ_{y}, also summarised as $\sigma_{\mathrm{x,y}}$ in the following.

VERTEX RESOLUTION RESULTS

In this section, the simulation results of $\sigma_{\mathrm{x,y}}$ and their dependence on some key parameters are discussed and compared to calculations of σ_{IP} via Eq. (1). A histogram showing the number of tracks per event registered by the detector can be seen in Fig. 2 (left). The percentage of events with a certain N_{tr} or higher are also listed, e.g. 16 % of all collisions show $N_{\mathrm{tr}} \geq 4$. The dependence of $\sigma_{\mathrm{x,y}}$ on N_{tr} can be seen in Fig. 2 (right). Here, d_{det} has been fixed to 250 mm and results for detector resolutions $\sigma_{\mathrm{res}} = \{16, 50\}$ µm and $w_{\mathrm{d}} = \{1, 0.27\}$ mm are shown. As expected, the vertex resolution improves with higher track numbers. The size of the error bars is calculated via error propagation of the fit errors on σ_{c}, σ_{t}, p_{c} and p_{t}. They increase with higher N_{tr} due to the lower statistics for a given number of primary events. The vertex resolution starts converging at $N_{\mathrm{tr}} \approx 5$ to 6. As expected, the detector with the highest resolution and lowest material budget (blue) shows the best $\sigma_{\mathrm{x,y}}$, dropping below 140 µm between 3 and 4 tracks. Furthermore, it can be seen that $\sigma_{\mathrm{x,y}}$ of the detector with higher material budget and higher resolution (red), drops quicker than the detector with lower w_{d} and lower resolution (green).

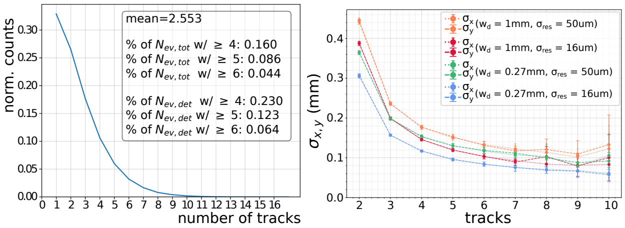

Figure 2: Left: histogram of N_{tr}. The percentage of total events and events registered by the detector are also listed. Right: $\sigma_{\mathrm{x,y}}$ versus N_{tr} for four different detector cases and a fixed number of total events.

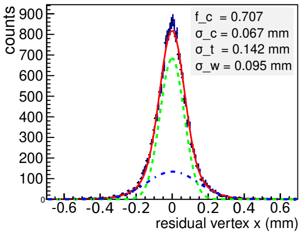

Figure 3: Distribution of r_{x} of vertices stemming from events with 5 tracks. The red line shows the fit of the sum of two Gaussians via ROOT [20], the green and blue dashed lines show the core and tail Gaussians, respectively.

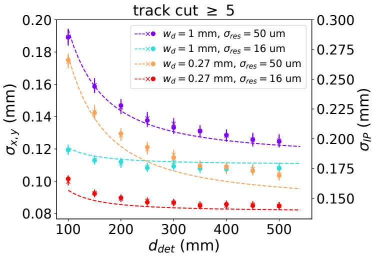

Figure 4: $\sigma_{\mathrm{x,y}}$ as well as σ_{IP} as a function of d_{det}.

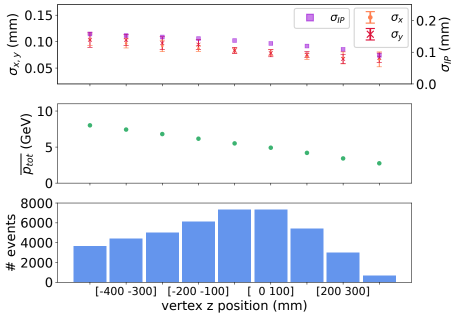

Figure 5: Vertex z position dependence of $\sigma_{x,y}$ and σ_{IP} (top), of the average track momentum (middle), and of the number of events (bottom).

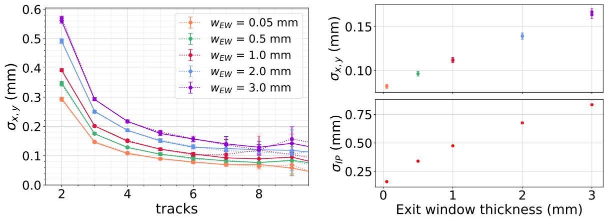

Figure 6: Left: $\sigma_{x,y}$ in dependence of N_{tr} for different window thicknesses. Right: comparison of $\sigma_{x,y}$ (top) and σ_{IP} (bottom) versus w_{EW}.

Figure 4 shows the analysis results of the transverse vertex resolution versus d_{det} for events with $N_{tr} \geq 5$. The calculated results (dashed line) of σ_{IP} (see Eq. (1)), are also presented, for which the average momentum of simulated tracks and a distance of 550 mm between vertices and detector are used. One can see that the behaviour matches the simulation results well. The four colours symbolise detector cases with different material budget and resolution, as noted in the legend of the figure. For $\sigma_{res} = 50$ µm (orange and purple), a significant increase in resolution is observed with d_{det}. On the other hand, for $\sigma_{res} = 16$ µm, the gain in $\sigma_{x,y}$ is less prominent and shows convergence at about 250 mm. These results indicate that a detector with a high spatial resolution such as a Si pixel detector could allow for a more compact detector design.

The dependence of $\sigma_{x,y}$ on the distance between the vertices and the first detector layer, d_{vtx}, is depicted in Fig. 5 (top). A detector with $d_{det} = 250$ mm, $w_d = 0.27$ mm and $\sigma_{res} = 16$ µm is used. The vertices are grouped together in bins with a width of 100 mm, as indicated by the x-axis labels. The data points show the $\sigma_{x,y}$ of events belonging to the same bin and $N_{tr} \geq 5$. As expected from the formulas for σ_{MS} and $\sigma_{int,det}$, the resolution decreases with d_{vtx}. However, this effect is lessened due to the rise of average track momenta with d_{vtx}, see Fig. 5 (middle). Figure 5 (bottom) shows the number of events versus d_{vtx}. Due to the forward nature of the tracks, events closer to the detector are less likely to get registered by the detector. The number of events falls for larger d_{vtx}. Note, that this is dependent on the transverse placement of the detector planes.

Another important parameter is the material budget of the exit window. Figure 6 (left) shows the vertex resolution in dependence of the number of tracks for window thicknesses $w_{EW} = \{0.05, 0.5, 1, 2, 3\}$ mm for a detector with $d_{det} = 250$ mm, $w_d = 1$ mm and $\sigma_{res} = 16$ µm. One can see that the results for $w_{EW} = 1$ mm are fairly close to the idealised case of 0.05 mm for $N_{tr} \geq 5$, and reach $\sigma_{x,y} \leq 140$ µm between 4 and 5 tracks. For $w_{EW} = 2$ and 3 mm, $\sigma_{x,y}$ approaches 140 µm only at 6 and 7 tracks, respectively. The vertex resolution as a function of w_{EW} is shown in Fig. 6 (right). The top plot shows the simulation results ($N_{tr} \geq 5$), the bottom one σ_{IP} for comparison.

The rate of events with sufficient vertex resolution can be calculated as follows. Assuming a tracking detector with $d_{det} = 250$ mm, $w_d = 1$ mm and $\sigma_{res} = 16$ µm, events with $N_{tr} \geq 5$ tracks could be accepted (see Fig. 2 right (red)). Of the 500 000 initial collisions, 69 % have a reconstructable vertex (at least 2 tracks) whereas 7.96% show $N_{tr} \geq 5$. Using the total rate of collisions $R_{inel} = 147$ Hz as calculated in the introduction section, this results in an inelastic rate per bunch of 11.69 Hz of useful events. After an acquisition time of 1 min ($n = 701$ events), the relative statistical error on the bunch width calculated via $\frac{1}{\sqrt{2n-2}}$ [21] would be 2.7 %, which is in the order of magnitude desired by the specifications. However, these first promising estimations are based on an idealised setup and further studies are necessary to incorporate additional effects that impact the vertex resolution, such as a misalignment of the detector. After this first estimation using a generic detector, the next steps will be to add more realism and details to the simulation setup, such as updating the tank exit window, replacing the detector layers by modules based on a chosen technology, etc. In order to increase the rate of useful events, the pressure of the gas target could be increased, however this may be unacceptable for beam operation. A different target gas with a higher atomic number, such as argon, could also be considered to increase the number of tracks per events. Cuts on the z position of the vertex or the track momenta could also increase the resolution or lower the necessary cut on N_{tr}.

SUMMARY & OUTLOOK

The BGV is currently being redesigned for the HL-LHC. First simulation results of an extensive study of the impact of key design parameters on the device's performance have been discussed. Based on the results of the generic BGV setup, design choices of tank shape and detector technology will be made. After a detector technology has been chosen, work on module design and a concrete detector model for the simulation will begin. The first results point towards the possibility of using a compact detector with a high position resolution, like a Si pixel detector.

ACKNOWLEDGEMENTS

This research is supported by the CERN HL-LHC project, and the Royal Holloway University of London. We would like to thank the ACTS team for their invaluable support and discussions, especially Xiaocong Ai, Corentin Allaire and Bastian Schlag.

REFERENCES

[1] A. Alexopoulos *et al.*, “Noninvasive LHC transverse beam size measurement using inelastic beam-gas interactions,” *Physical Review Accelerators and Beams*, vol. 22, no. 4, p. 042 801, Apr. 2019. DOI: `10.1103/PhysRevAccelBeams.22.042801`.

[2] “LHCb Tracker Upgrade Technical Design Report,” Feb. 2014. `https://cds.cern.ch/record/1647400`

[3] P. Hopchev *et al.*, “A beam gas vertex detector for beam size measurement in the LHC,” *IPAC 2014: Proceedings of the 5th International Particle Accelerator Conference*, pp. 3680–3683, 2014. DOI: `10.18429/JACoW-IPAC2014-THPME175`.

[4] H. Guerin *et al.*, “The HL-LHC Beam Gas Vertex Monitor - Simulations for Design Optimisation and Performance Study,” in *presented at the 12th Int. Particle Accelerator Conf. (IPAC’21)*, (Campinas, Brazil), JACoW Publishing, May 2021.

[5] A. Salzburger, “A parametrization for fast simulation of muon tracks in the ATLAS inner detector and muon system,” M.S. thesis, Innsbruck U., 2003.

[6] F. Ragusa and L. Rolandi, “Tracking at LHC,” *New Journal of Physics*, vol. 9, no. 9, pp. 336–336, Sep. 2007. DOI: `10.1088/1367-2630/9/9/336`.

[7] P. Zyla *et al.*, “Review of Particle Physics,” *PTEP*, vol. 2020, no. 8, p. 083C01, 2020. DOI: `10.1093/ptep/ptaa104`.

[8] O. Aberle *et al.*, *High-Luminosity Large Hadron Collider (HL-LHC): Technical design report*, ser. CERN Yellow Reports: Monographs. Geneva: CERN, 2020. DOI: `10.23731/CYRM-2020-0010`.

[9] *CRMC (cosmic ray monte carlo package)*. `https://web.ikp.kit.edu/rulrich/crmc.html`

[10] M. Dobbs and J. B. Hansen, “The HepMC C++ Monte Carlo Event Record for High Energy Physics,” CERN, Geneva, Tech. Rep., Jun. 2000.

[11] S. Agostinelli *et al.*, “Geant4 – a simulation toolkit,” *NIM A*, vol. 506, no. 3, pp. 250–303, 2003. DOI: `10.1016/S0168-9002(03)01368-8`.

[12] F. W. Bopp, J. Ranft, R. Engel, and S. Roesler, “Antiparticle to particle production ratios in hadron-hadron and *d*-au collisions in the dpmjet-iii monte carlo model,” *Phys. Rev. C*, vol. 77, p. 014 904, 1 Jan. 2008. DOI: `10.1103/PhysRevC.77.014904`.

[13] T. Poikela *et al.*, “Timepix3: A 65k channel hybrid pixel readout chip with simultaneous ToA/ToT and sparse readout,” *Journal of Instrumentation*, vol. 9, no. 05, pp. C05013–C05013, May 2014. DOI: `10.1088/1748-0221/9/05/c05013`.

[14] M. Titov and L. Ropelewski, “Micro-pattern gaseous detector technologies and rd51 collaboration,” *Modern Physics Letters A*, vol. 28, no. 13, p. 1 340 022, 2013. DOI: `10.1142/S0217732313400221`.

[15] X. Ai *et al.*, “A common tracking software project,” submitted to *Computing and Software for Big Science* on 25 Jun 2021, 2021. arXiv: `2106.13593 [physics.ins-det]`. `https://arxiv.org/abs/2106.13593`

[16] *Acts on github*, https://github.com/acts-project/acts, Accessed: 2021-08-27.

[17] R. E. Kalman, “A New Approach to Linear Filtering and Prediction Problems,” *Journal of Basic Engineering*, vol. 82, no. 1, pp. 35–45, Mar. 1960. DOI: `10.1115/1.3662552`.

[18] P. Billoir and S. Qian, “Fast vertex fitting with a local parametrization of tracks,” *Nuclear Inst. and Methods in Physics Research, A*, vol. 311, no. 1-2, pp. 139–150, 1992. DOI: `10.1016/0168-9002(92)90859-3`.

[19] “Performance of tracking and vertexing techniques for a disappearing track plus soft track signature with the ATLAS detector,” CERN, Geneva, Tech. Rep., Mar. 2019.

[20] R. Brun and F. Rademakers, “Root – an object oriented data analysis framework,” *Nuclear Instruments and Methods in Physics Research Section A: Accelerators, Spectrometers, Detectors and Associated Equipment*, vol. 389, no. 1, pp. 81–86, 1997, New Computing Techniques in Physics Research V. DOI: `10.1016/S0168-9002(97)00048-X`.

[21] L. Lyons, *A Practical Guide to Data Analysis for Physical Science Students*. Cambridge University Press, 1991. DOI: `10.1017/CBO9781139170321`.

ISBN: 978-3-95450-230-1 ISSN: 2673-5350 doi:10.18429/JACoW-IBIC2021-TUPP22

NEW CERN SPS BEAM DUMP IMAGING SYSTEM

S. Burger*, E. Bravin, A. Churchman, F. Roncarolo, A. Topaloudis, F. Velotti, E. Veyrunes,
CERN, Geneva, Switzerland

Abstract

As part of the LHC injector Upgrade (LIU), the CERN SPS is now equipped with a new Beam Dumping System (SBDS) designed to cope with the high power beams foreseen for the High Luminosity LHC (HL-LHC) era [1, 2]. Before reaching the dump, the proton beam (from 14 to 450 GeV) is vertically kicked and then diluted passing through a series of horizontal and vertical bumps. This prevents the dump damage, by reducing the power density per surface unit. The quality of each dump event must be verified, for which all SBDS parameters are logged and analysed in the so-called Post-Mortem dataset. An essential part of the verification is performed by a beam imaging system based on a Chromox screen imaged on a digital camera. The desired availability level (100%, to protect the dump) and the harsh radiation environment made the design extremely challenging. For example, it implied the need for a 17m long optical line made of high-quality optical elements, a special camera shielding (to minimise single event upsets) and a generally careful design accounting for maintenance aspects, mainly related to expected high activation levels. After giving an overview of the whole imaging system design with details on the chosen layout and hardware, this paper will discuss the DAQ and SW architecture, including the automatic, on-line, image selection for validating every dump event. This will be complemented with experimental results demonstrating the performance and reliability achieved so far.

THE NEW SPS INTERNAL DUMP

The new SPS beam dump is composed of a 5 m long absorber made of several blocks of graphite, Titanium Zirconium Molybdenum (TZM) and pure Tungsten material. It is covered by a 3 layer concrete, cast-iron and concrete/marble shielding. The weight of this assembly is 2 t for the absorber that is impacted by the beam and about 674 t for the shielding. It is located in sector 5 of the SPS machine.

To protect the block against high power density beams, the extracted protons are diluted in order to reach a non-destructive power density. The principle of the beam dumping is sketched in Fig. 1 with a simulated example of a Fixed Target type beam dump dilution shape, as expected at the front plate of the dump.

Instrumentation Specifications

The instrumentation, fundamental to the beam dump quality checks has been requested to fulfill the following main specifications:

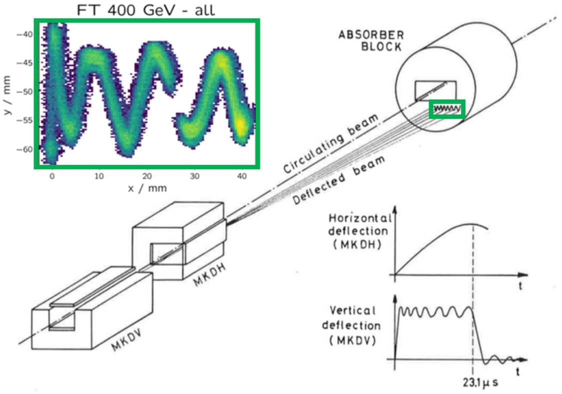

Figure 1: Principle of beam dumping and simulated example of a Fixed Target type beam dump dilution shape.

- All SPS beam dump events must be recorded. This means between $5 \cdot 10^9$ and $8 \cdot 10^{13}$ protons per event, with energy from 14 to 450 GeV.
- The imaging horizontal and vertical spatial resolution must be better than 200 μm.
- The imaging system maintenance must be optimized to cope with high radiation levels.

The design of the new SBDS monitor is based on the so-called Beam TV (BTV) system, exploited in different versions and hundreds of units, throughout the whole CERN facility. A BTV system is based on the use of a screen interacting with the beam and generating photons (i.e. different processes depending on protons energy and screen materials) that are imaged on a camera system, thus providing the proton beam footprint. In the SBDS case, the image acquisition is synchronized with the beam extraction event. After calibration, the digitized images provide an accurate beam position and size to monitor quantitatively the dilution of the beam on the dump surface. As already mentioned above, the high radiation environment has heavily affected the new BTV system design choices, from the layout (i.e. need of a

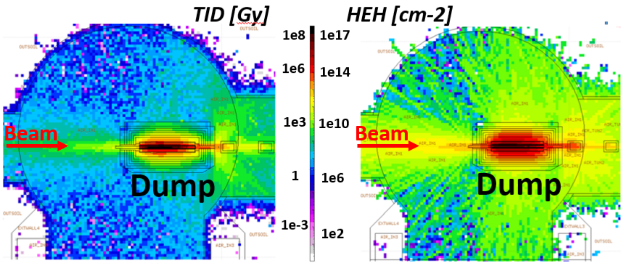

Figure 2: Fluka radiation simulations of the SBDS area showing the top view at the beam level.

---

[*] stephane.burger@cern.ch

long optical line to bring the camera away from the highest radiation zone) to the selection of radiation tolerant or radiation hard components for both the optical line and the camera. Dedicated simulations (see Fig. 2) have allowed predicting up to 10 kGy total ionization dose (TID) and 1×10^{13} cm^{-2} high energy hadron equivalent fluence (HEH) at the location of the screen, about 4m upstream of the dump front plate.

THE SBDS IMAGING SYSTEM

Hardware

As imaging sensor, it was decided to use a digital camera featuring high resolution, sensitivity, gain and adjustable integration time. The harsh radiation environment discussed above yielded to the need for a dedicated optical line and camera shielding to move away and protect the camera itself. In addition, as all extractions and dumps need to be monitored, the screen is fixed, i.e. not removable from the beam trajectory.

Screen and in-Vacuum Mechanics: The worst case failure situation determined the choice of the BTV screen material. As well as the dump, the screen must withstand 100 % of the extracted beams, with a max dump rate of 333 events per hour. The predicted maximum power density of 6.5×10^{12} p/mm^2 at the screen location led to the choice of Al2O3:CrO2 (also known as Chromox [3]) as screen material, see Fig. 3. These type of screens are used at many locations at CERN with up to 1×10^{13} p/mm^2 as limit not to exceed (from heat load calculation, to remain below a temperature of 500 °C and taking some safety margin).

Figure 3: SBDS Al2O3:CrO2 screen mounted on its support, ready for installation.

As the dump line and circulating beam share the same vacuum chamber, the screen support design includes RF fingers in order to minimize the impact on beam impedance. A 3D drawing of the screen support is shown in Fig. 4, where the circulating beam and the vertically dumped beam are represented.

Beam Imaging Optical Line: Digital cameras [4] can be operated only in low radiation areas. Combining the irradiation results of a number of digital cameras at the CERN CHARM facility [5] (max 10 Gy TID and 1.6×10^{9} cm^{-2} HEH) and a set of simulations performed to predict radiation around the SBDS zone, resulted in the decision to design a 17 m long optical line between the screen and the camera. Figure 5 shows a 3D view of the optical line integration, passing through and then around the concrete basement of the SPS dump. The optical line is based on 5 high quality mirrors carefully specified using ZEMAX Optical Studio [6] in order to minimize geometric and chromatic aberrations. Table 1 summarizes the optical line parameters, defined to achieve an optical resolution of 200 μm, horizontal and vertical.

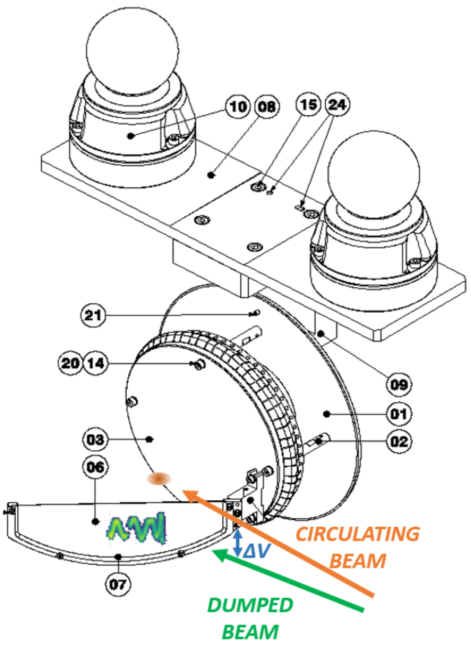

Figure 4: 3D model of the screen instrument equipped with RF fingers for impedance optimization and alignment targets.

The entire optical line volume is enclosed to avoid parasitic light and to protect mirrors from dust and bad manipulations.

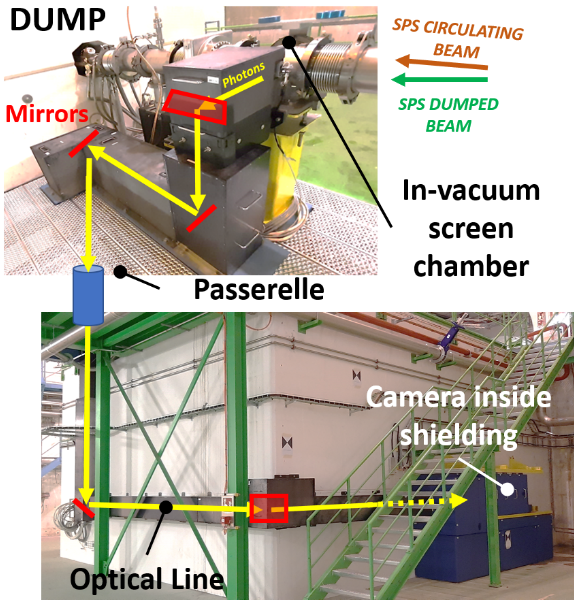

Figure 5: 3D model of the optical line of the imaging system around the new SPS dump infrastructure.

Table 1: Main Parameters of the Optical Elements Composing the Optical Line of the SPS Dump Imaging System

Length	17 m	
3x Mirror	300x200 mm^2	Flatness $\lambda/5$
2x Mirror	200x200 mm^2	Flatness $\lambda/5$
Sigma Camera lens	F600 mm	5.6NA
Basler Camera	Aca2040-35gm	73.4 dB
Spatial resolution	100 µm	
Optical resolution	200 µm	
Visibility (contrast)	35 %	

Camera Shielding: The shielding protecting the camera was dimensioned to exclude the occurrence of single event upsets due to radiation. In addition, as the radiation level imposes quite massive blocks of iron, the shielding was equipped with a movable 'door' allowing quick access for the camera maintenance without the need for transport/handling services. The shielding door is composed of 4 blocks of 900 kg each, which can be handled by a single person thanks to the use of low friction bearings. Figure 6 shows the inside of the shielding, doors open, where the optical elements for the light detection are located.

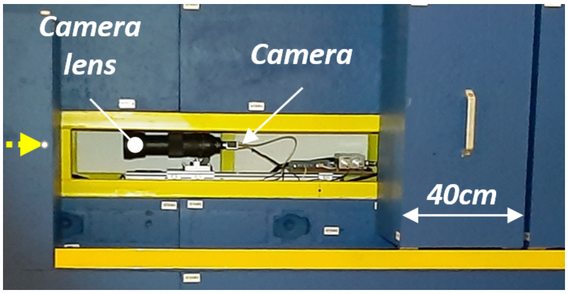

Figure 6: Picture of the shielding while open, showing the camera with its F600mm focal length camera lens.

Software

The light yield of Chromox screen decays relatively slowly (> few 100 ms) and the acquisition system is based on recording several images after each dump event. The on-line SW performs the selection of non-saturated images, with the saturation level depending on beam intensity, size and dilution strength.

Acquisition process: In standard operational mode, the camera is free running with the frame rate set at 35 Hz. All images are continuously feeding a 'rolling' memory buffer of 100 images (number of images can be set). Each dump event, seen as a trigger given by the extraction kicker (synchronous and asynchronous) will start the acquisition process by filling one of the 8 available buffers of 100 images memory space with:

- pre-trigger images from the 'rolling' buffer: used for noise cleaning
- post-trigger following images: saved for online analysis

The online automatic selection of the 1st image not saturated is first of all 'cleaned' by subtracting the pre-trigger image. This minimizes the noise background like remaining light produced by the screen, which can happen if two extractions are too close from each other. Then the image is published and stored in the Post-Mortem Data set. This image is also available for the fixed display operational GUI used by the SPS operator crew. However, all images in the 8 buffers are accessible for any processing, analysis or debugging, but they are overwritten every 8 triggers. An example of image selection is shown in Fig. 7.

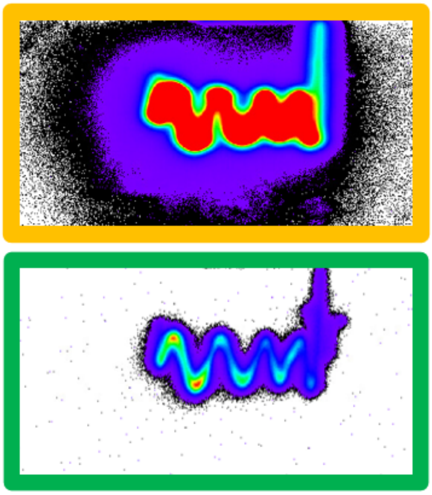

Figure 7: Example of automatic image selection. Top is first image at trigger event. Down is the first non-saturated image corresponding at the ninth image (taken at 35 Hz) after the trigger. This selected image is logged and published.

Internal Watchdog: Several checks are periodically performed to ensure the availability of the acquisition system. In particular, the software looks at:

- status of the camera and the Ethernet switch
- consistency between the settings in Front End Server Architecture (FESA) and the camera

The process includes automatic power reset sequence to recover from any unexpected instability of the system. To minimize the risk of missing beam dump events, the SPS interlock system inhibits any further beam injection, whenever the SBDS BTV system is in fault or down.

Experimental Results

Commissioning with beam: A fundamental part of the SBDS imaging system design was the choice of the camera detector with adequate integration time and gain for covering the range of beams to be measured. This, together with other features of the camera like low noise and intrinsic high dynamic range, allowed the rapid validation of the full system during the beam commissioning period. At first, with the automatic SW mentioned above to discard saturated images, the BTV system was validated with dumped beams ranging from low intensity single bunch to trains of high intensity bunches. The instrument could then be used extensively from day 1 to commission the whole SBDS system, and particularly to measure the kickerś transfer functions, to assess the effect of kicker failures and to check the polarity of the horizontal kicker designed to dilute the particle density onto the dump block. Figure 8 shows few images taken during commissioning, corresponding to dumps with different beam intensities and machine filling schemes.

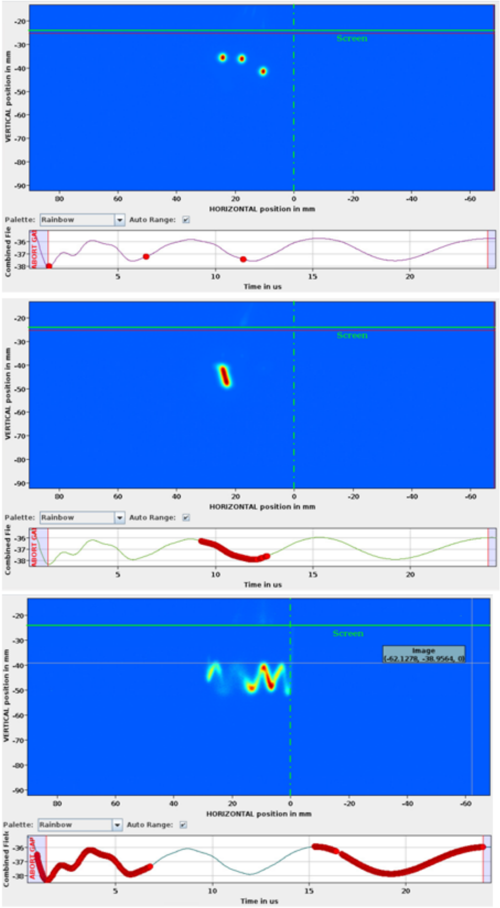

Figure 8: Examples of images taken during SBDS commissioning to confirm the good behavior of the beam extraction system, increasing progressively the number of bunch in the machine from top to bottom plots.

Normal Operation: After the full system validation during commissioning, the SBDS was handed over to the SPS crew as an operational tool to monitor and record any dump event. Figure 9 shows the operational *SBDS Fixed Display*, which includes, apart from the BTV image, a number of status, quality and sanity checks (temperatures, pressure, power, timing, etc...). This particular example refers to an extraction of a beam prepared for fixed target physics. All bunches are also displayed in red in the 'combined field' graph below the image, asserting here the SPS ring was full before extraction (the horizontal axis covers the 23 µs revolution period).

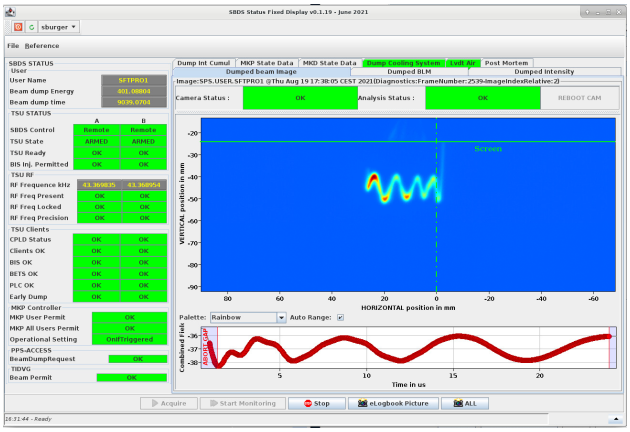

SBDS STATUS

User
User Name: SFTPRO1
Beam dump Energy: 401.08804
Beam dump time: 9039.0704

TSU STATUS

	A	B
SBDS Control	Remote	Remote
TSU State	ARMED	ARMED
TSU Ready	OK	OK
BIS Inj. Permitted	OK	OK
TSU RF		
RF Frequence kHz	43.369835	43.368954
RF Freq Present	OK	OK
RF Freq Locked	OK	OK
RF Freq Precision	OK	OK
TSU Clients		
CPLD Status	OK	OK
Clients OK	OK	OK
BIS OK	OK	OK
BETS OK	OK	OK
PLC OK	OK	OK
Early Dump	OK	OK

MKP Controller
MKP User Permit: OK
MKP All Users Permit: OK
Operational Setting: OnlfTriggered

PPS-ACCESS
BeamDumpRequest: OK

TIDVG
Beam Permit: OK

Image:SPS.USER.SFTPRO1 @Thu Aug 19 17:38:05 CEST 2021(Diagnostics:FrameNumber:2539-ImageIndexRelative:2)
Camera Status : OK
Analysis Status : OK
Palette: Rainbow
Auto Range: ☑
16:31:44 - Ready

Figure 9: SBDS Status Fixed Display showing together with all parameters required for a proper dump extraction the status of the imaging instrument hardware and the selected image of the last event.

OUTLOOK

The new SPS Beam Dump System (SBDS) was equipped with a dedicated beam imaging system, designed to monitor and qualify every single beam dump event. The instrument is based on a fixed scintillating screen in front of the dump and a digital camera as detector. The harsh radiation environment required a challenging design with the integration of a 17 m long optical line composed of 5 high quality mirrors (flatness of $\lambda/5$). The light is thus transported from the dump to a radiation shielded bunker protecting the digital camera from radiation. This monitor is a fundamental device to continuously assess the beam extraction and dump quality as well as the health of the whole system.

A new on-line image selection process was deployed to ensure the published image for *Post-Mortem* analysis is not saturated. The software also includes automatic rebooting from internal hardware and a communication status watchdog, thus minimizing downtime. This watchdog is also part of the global interlock system, ensuring that no injection occurs if the monitoring is off.

The commissioning of the SPS beam dumping system was performed from day one with the full availability of this new beam imaging instrumentation. It was then extensively used to evaluate dump kicker and diluter performance. An operational GUI is available in the control room with data showing the dilution of the beam on the dump, and work is ongoing to extract this information with machine learning methodologies to assess, together with direct kicker monitoring, the occurrence of failures.

REFERENCES

[1] F. M. Velotti *et al.*, "Performance Studies of the SPS Beam Dump System for HL-LHC Beams", in *Proc.*

5th Int. Particle Accelerator Conf. (IPAC'14), Dresden, Germany, Jun. 2014, pp. 3394–3396. `doi:10.18429/JACoW-IPAC2014-THPME069`

[2] F. M. Velotti *et al.*, "Feasibility Study of a New SPS Beam Dump System", in *Proc. 6th Int. Particle Accelerator Conf. (IPAC'15)*, Richmond, VA, USA, May 2015, pp. 3930–3933. `doi:10.18429/JACoW-IPAC2015-THPF097`

[3] S. Burger, B. Biskup, S. Mazzoni, and M. Turner, "Scintillation and OTR Screen Characterization with a 440 GeV/c Proton Beam in Air at the CERN HiRadMat Facility", in *Proc. 5th Int. Beam Instrumentation Conf. (IBIC'16)*, Barcelona, Spain, Sep. 2016, pp. 268–272. `doi:10.18429/JACoW-IBIC2016-MOPG78`

[4] E. Bravin, "Status and plans for beam instrumentation cameras at CERN", Joint ARIES-ADA Workshop on 'Scintillation Screens and Optical Technology for Transverse Profile Measurements', Poland, 2019.

[5] S. Burger *et al.*, "Radiation tests on cameras + tests of different screens in HiRadMat", Joint ARIES-ADA Workshop on 'Scintillation Screens and Optical Technology for Transverse Profile Measurements', Poland, 2019.

[6] ZEMAX OPticStudio®, `https://www.zemax.com/pages/opticstudio`

A BEAM DIAGNOSTICS SYSTEM OF ELECTRON BEAM MELTING FOR ADDITIVE MANUFACTURING*

R. Kavak†, E. Durna, M. G. Sanal, M. M. Sezer, ASELSAN A.S., Ankara, Turkey

Abstract

Electron beam melting has been used recently in additive manufacturing by various researchers. In those electron beam melting applications, the electron energy can be 60 to 100 keV, the beam current can be around 10 mA to 100 mA, and the beam spot size can be as small as 200 µm according to electron energy and beam current. Those parameters can result in very high beam power densities. The diagnostics of this powerful beam can be quite a problematic issue. As the electron beam current required for the application is quite similar to DC current, fast undestructive current measurement techniques for current beam profile and beam position are very limited in performance. Therefore, some destructive techniques to measure current and other beam properties are essential. As part of the beam diagnostics for electron beam melting application for additive manufacturing, the authors proposed a complete beam diagnostics system to measure the electron gun's capabilities and associate electromagnetic lens systems. The following properties have been diagnosed as part of this research work: i) Beam Current, ii) Beam Spot size for enlarged and focused beams, iii) Scanning velocity of the deflected beam, iv) Profile of the beam. The authors proposed methods to measure focused beam spot size and deflected beam scanning velocity using Secondary Emission Grid Sensors. Moreover, the authors proposed a new technique to measure beam profile using consecutively placed several copper plates with beam guiding holes of various diameters. The proposed beam profile measurement method effectively determines the useful beam radius for metal powder melting properties specifically to additive manufacturing applications.

INTRODUCTION

Recent advancements in engineering and material science require complex manufacturing processes [1]. For this reason, Additive Manufacturing (AM) challenges the traditional manufacturing methods in many cases [2]. According to the Additive Manufacturing Trend Report 2021 from HUBS, the global AM market grew 21 percent year-on-year to $12.6 bn in 2020. They also predicted that the AM market will be more than doubled, reaching $37.2 bn in 2026 [3]. The efficient usage of limited resources and the ability to produce complex shapes put AM forward when compared to traditional manufacturing [2, 4].

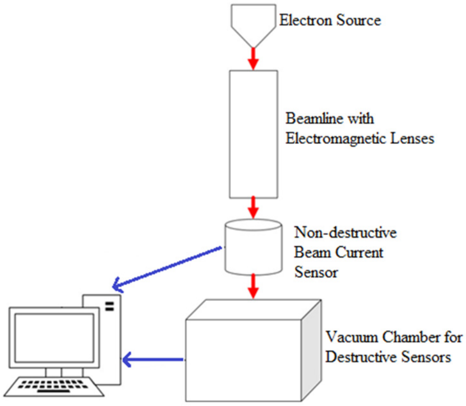

Figure 1: Overview of the EBM test setup and the proposed beam diagnostics system.

As the attention on AM has been dramatically increased among the researchers in the field, Electron Beam Melting (EBM) technique is getting used in the manufacturing process. EBM technique has been preferred to Selective Laser Melting (SLM) because of its advantages. One advantage is on that EBM provides higher beam power and beam scan velocity [5]. Another one is that EBM process occurs under a vacuum, but the SLM process works in an inert atmosphere. Therefore, oxidation of the parts is prevented in most cases for EBM [6].

An EBM system requires controlling several beam parameters in order to ensure the precision during manufacturing process. Some of them are beam power, beam spot size, beam scanning and jumping velocity [6]. The requirements of the EBM system are determined according to desired operating modes, and associated measurement mechanisms should be integrated to the calibration and test processes. Common EBM diagnostics methods are investigated in [7, 8].

In this paper, a beam diagnostics system is proposed for EBM process which diagnoses beam current, beam spot size for enlarged and focused beams, scanning velocity of the deflected beam, and profile of the beam. While proposed system makes use of SEM grid sensors to measure beam spot size and deflected beam scanning velocity, a novel method is put forward to measure the profile of the electron beam. Details of the EBM test system, and the proposed beam diagnostics system is described in the following sections.

SYSTEM DESCRIPTION

The EBM test system under investigation in this paper consists of three main parts, namely electron source, electromagnetic lenses, and test chamber. The source is where the electron beam is generated by Lanthanum Hexaboride (LaB_6) cathode at 60-100 kV. To manipulate the beam, sev-

---

* Work supported by the Scientific and Technological Research Council of Turkey (TUBITAK) under grant number 3170014.
† rafetkavak@protonmail.com

eral electromagnetic lenses are used such as focusing, correction and deflection lenses, which are essential for AM process. Finally, the high-power electron beam hits to the target plate on the test chamber, on which selective metal powders can be used to conduct EBM experiments. The test setup system structure is as shown in Fig. 1.

The EBM test setup is formed such that used electron energy can be 60 to 100 keV, the beam current can be around 10 mA to 100 mA, and the beam spot size can be as small as 200 µm according to electron energy and beam current. Moreover, the beam position on the target plate which is located inside the vacuum chamber can be several tens of centimeters.

PROPOSED BEAM DIAGNOSTICS SYSTEM

The proposed beam diagnostic system, shown in Fig. 1, is intended to measure beam current, beam spot size for enlarged and focused beams, scanning velocity of the deflected beam, and beam profile, which are important specifically to electron beam melting for additive manufacturing. The destructive sensors are located in the vacuum chamber and non-destructive ones are on the beamline as shown in Fig. 1. In this part of the paper, measurements of intended beam properties are described in detail.

Beam Current Measurement

As the electron beam under investigation is a high energy one because of the requirements of additive manufacturing, the current should be measured via non-destructive means. The existing destructive current measurement techniques are either not standard products, hence expensive, or in a very high volume due to dissipated power.

The type of the current, on the other hand, should in a DC form because of the contour tracing, heating, and melting modes of operation of additive manufacturing. In these modes of operation, beam current is required to be constant. Mentioned requirements mandates the proposed beam diagnostic system to use non-destructive DC Current sensors with a microsecond grade fast response type. Authors propose using of DC Transformer type non-destructive current sensors [7, 8] for this purpose.

Beam Spot Size and Scanning Velocity Measurements

Beam spot size is one of most important properties of the electron beam which will precisely melt the metal powders on the target plate for additive manufacturing purposes. Different spot sizes show different melting behaviours with different times that the beam should be directed on to the unit length of metal powder. Besides, the spot size is intended to be kept as small as possible to ensure the precision on the additive manufacturing application.

The proposed beam diagnostic system is intended to measure the spot size of both focused and enlarged beams. When the beam is enlarged, the overall energy of the beam is distributed on a large area, which makes easier to detect the spot size. This enlarged beam spot size measurement can be used to calibrate the electromagnetic lenses along the beamline and to ensure the precise positioning of the beam on the target plate. This diagnostic system proposes the use of SEM Grid Sensors [7, 8], the manufactured grid sensor is as shown in Fig. 2.

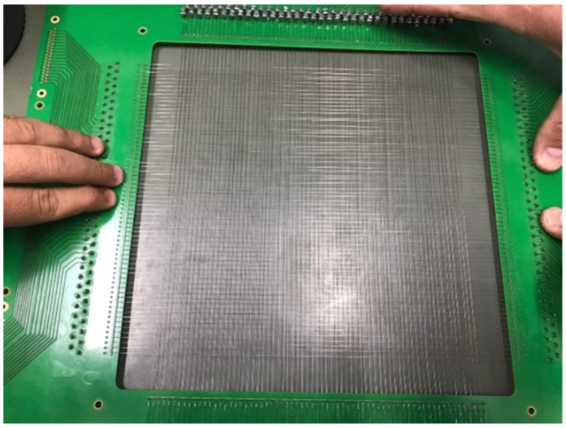

Figure 2: Manufactured SEM Grid Sensor.

On the other hand, the focused beam spot size should also be measured because of the earlier mentioned reasons dictated by additive manufacturing. As the energy density is extremely high, when the high energy electron beam is further focused, either the electron beam should not be directed on a measurement system for a long time, or the measurement system should be extremely large to handle high energy densities. To overcome the high energy density problem, a novel method is used to detect the focused beam spot size. The proposed method uses the SEM Grid readings by deflecting the electron beam as shown in Fig. 3. As shown in Fig. 3, the deflected electron beam passes through wires A and B, and blue and green waveforms are expected in the oscilloscope corresponding to wires A and B, respectively. The scanning velocity of the deflected beam can be measured by using the instants t_A and t_B that beam crosses wires A and B and the distance between them.

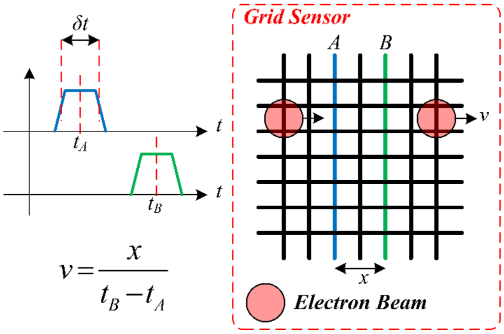

Figure 3: Proposed spot size and beam velocity estimation method using grid sensor.

Proposed Beam Profiler

The beam profiler is an important tool to assess the disturbance of electromagnetic lenses along the beamline. For this reason, a novel destructive beam profiler is proposed in this paper. As the energy is high, measurement of the beam profile with destructive methods is not very easy. Therefore, beam is used in a pulsed mode and it is not focused. The proposed beam profiler is composed of stacked copper plates having openings with various radii on their center as illustrated in Fig. 4. These openings are stacked in a way that the largest opening is on top of all, and the others are put in a descending order in terms of their radii as shown in the top view illustration of the proposed beam profiler in Fig. 5.

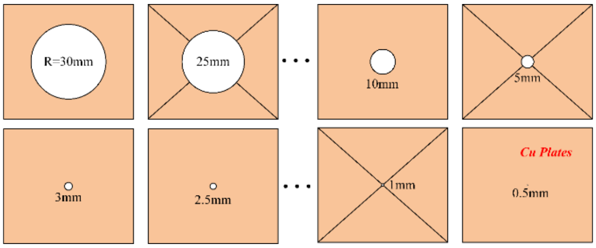

Figure 4: Copper plates of the proposed beam profile detector.

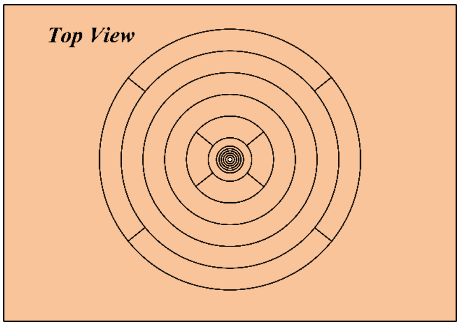

Figure 5: Top view of the proposed beam profile detector.

The proposed beam profiler should be precisely located to the beamline, and this is ensured by using the segmented plates in some layers. This is achieved by measuring the segment currents and making them equal, assuming the beam profile is symmetrical. The operation of the beam profile is such that as the beam hits towards the profiler, its portions smaller than the opening of a plate continue its way, while the others hit to the corresponding plate. The portion of the beam which hits to a plate is measured for each of the plates until the beam is finally hit to a dump plate at the bottom. The current densities are calculated by using the measured current and the corresponding effective area of each copper plate.

The proposed novel beam profiler is put forward first time in the literature and it is mechanically designed as shown in Fig. 6. The designed beam profiler is under manufacturing, only the analytical calculation results of expected beam profiler output is given in the results part of the paper.

Data Collection and Merging

The data which is produced by forementioned beam diagnostic sensors will be collected at a Central Control Unit. Those data will be evaluated, compared, and merged. The non-destructive current sensor will always be attached on top of vacuum chamber and will be sending data online. However, in addition to non-destructive current sensor, only one other sensor will be online since they are destructive/disturbing sensors by their structure and cannot be installed together. Hence all the data will be recorded and will be processed later offline.

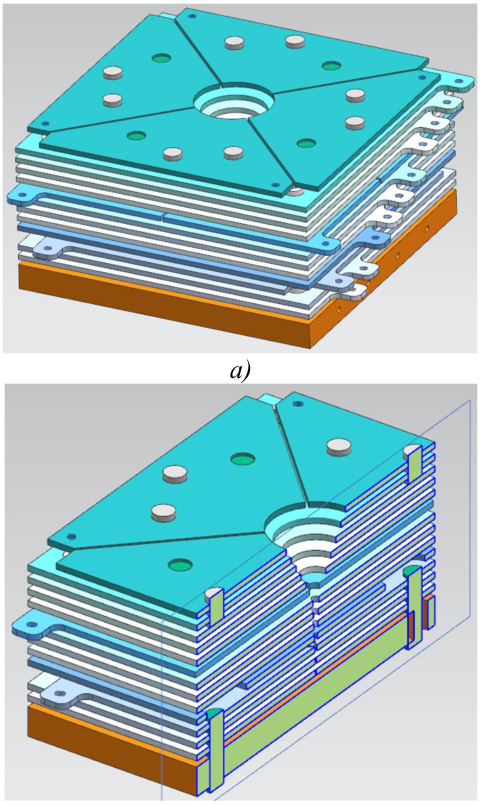

a)

b)

Figure 6: Mechanical design of the proposed novel beam profiler a) isometric, and b) cross-sectional view.

The data coming from non-destructive current sensor and High Voltage Power Supply (HVPS) will be used as a feedback to monitor the beam current. The comparison of those two will also be used for the safety of the system. Considering that the electron beam is not hitting somewhere on the beamline, the current supplied from HVPS should be approximately equal to the current measured by the non-destructive current sensor which is at the end of the beamline.

Offline comparisons and merging algorithms will be used to obtain more precise results. Beam spot size and beam profile for enlarged beams, or beam scan velocity for small angles are examples of those cases. The change at the beam quantities due to a change at system parameters can also be measured with different sensors, recorded, postprocessed offline and merged.

RESULTS

Some parts of the proposed beam diagnostics system are already integrated to the electron beam additive manufacturing test setup, while some others are still in manufacturing or testing phase. For this reason, initial tests are performed only with current measurements, while beam profiler outputs are given as analytical calculations for a synthetic electron beam. The electron beam additive manufacturing test setup is operated to measure the DC current waveforms and it is shown that the readings of the DC current sensor is in a close correlation with the HVPS current output, as expected. Figure 7 shows the interior camera view of the vacuum chamber while electron beam hits a dummy victim copper plate during current measurements and electron gun characterizations.

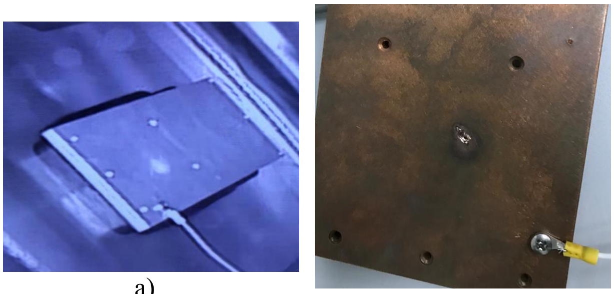
a) b)

Figure 7: Images showing the a) camera recording during experiments on a dummy victim plate, and b) the victim plate after experiments.

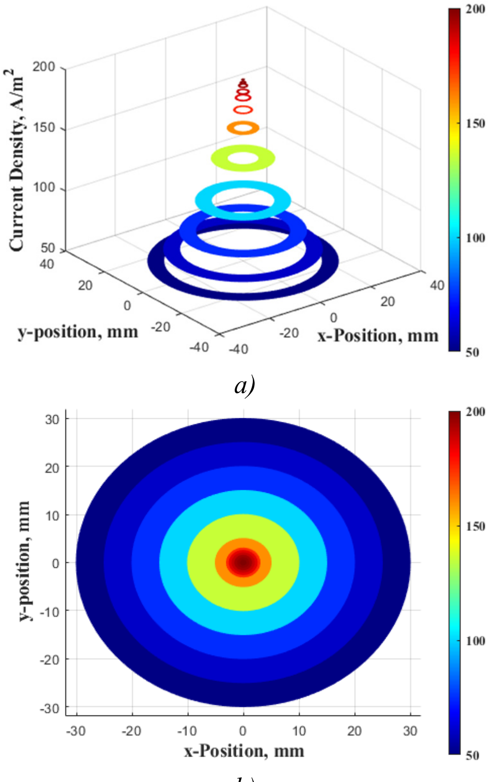

a)

b)

Figure 8: Analytical results of the expected performance for the proposed beam profiler a) 3D view, and b) top view.

As the novel beam profiler proposed in this paper is still under manufacturing, only its theoretical results considering the analytical calculations is illustrated. As the currents that hit to the effective area of each copper plate is measured, its corresponding current density should be calculated by dividing the current value by the area of the effective ring surface that faces the electron beam. Then each of the current densities for corresponding ring areas should be drawn in a 3D graph as illustrated in Fig. 8. The results shown in Fig. 8 is deduced using a synthetic electron beam. The form of the result graph of the beam profiler is in a close correlation with the synthetic electron beam profile. The expected calculations give a hint that the proposed beam profiler is very effective for diagnosing the beam profile of symmetrical electron beams.

CONCLUSION

In this paper, a beam diagnostics system is proposed for EBM process which diagnoses beam current, beam spot size for enlarged and focused beams, scanning velocity of the deflected beam, and profile of the beam. While proposed system makes use of SEM grid sensors to measure beam spot size and deflected beam scanning velocity, a novel method is put forward to measure the profile of the electron beam. As the functional tests of the proposed beam diagnostics system are still in progress, only the initial dummy victim plate tests and analytical results are included in this paper. Nevertheless, the findings of the analytical results show that the novel beam profiler device along with the other components of the beam diagnostics system is a complete tool collect, merge, and evaluate the required data in order to ensure precision in AM processes and provide emergency protection and calibration of electromagnetic lens system along the beamline.

REFERENCES

[1] O. Abdulhameed, A. Al-Ahmari, W. Ameen, and S. H. Mian, “Additive manufacturing: Challenges, trends, and applications”, *Advances in Mechanical Engineering*, vol. 11, no. 2, p. 168781401882288, Feb. 2019. `doi:10.1177/1687814018822880`

[2] M. Attaran, “The rise of 3-D printing: The advantages of additive manufacturing over traditional manufacturing”, *Business Horizons*, vol. 60, no. 5, pp. 677–688, Sep. 2017. `doi:10.1016/j.bushor.2017.05.011`

[3] Additive manufacturing trend report 2021, `https://www.hubs.com/get/trends/`.

[4] H. Paris, H. Mokhtarian, E. Coatanéa, M. Museau, and I. F. Ituarte, “Comparative environmental impacts of additive and subtractive manufacturing technologies”, *CIRP Annals*, vol. 65, no. 1, pp. 29–32, 2016. `doi:10.1016/j.cirp.2016.04.036`

[5] B. Wysocki, P. Maj, R. Sitek, J. Buhagiar, K. Kurzydłowski, and W. Święszkowski, “Laser and Electron Beam Additive Manufacturing Methods of Fabricating Titanium Bone Implants”, *Applied Sciences*, vol. 7, no. 7, p. 657, Jun. 2017. `doi:10.3390/app7070657`

[6] P. K. Gokuldoss, S. Kolla, and J. Eckert, “Additive Manufacturing Processes: Selective Laser Melting, Electron Beam Melting and Binder Jetting—Selection Guidelines”, *Materials*, vol. 10, no. 6, p. 672, Jun. 2017. `doi:10.3390/ma10060672`

[7] P. Strehl, *Beam Instrumentation and Diagnostics*. Springer, 2006.

[8] P. Forck, *Lectures Notes on Beam Instrumentation and Diagnostics*. (GSI, Darmstadt, Germany) Joint University Accelerator School, January-March 2017.

DEVELOPMENT OF A PROFILE MONITOR USING OTR AND FLUORESCENCE FOR INJECTED BEAMS IN J-PARC MAIN RING*

Y. Hashimoto†, Y. Sato, T. Toyama, T. Mitsuhashi, T. Nakamura, M. Tejima, M. Uota,
J-PARC Center, Tokai, Japan
also at Accelerator Laboratory, KEK, Tsukuba, Japan
H. Sakai[1], [1]Mitsubishi Electric System & Service Co., Ltd., Tsukuba, Japan

Abstract

A two-dimensional beam profile monitor having a high dynamic range approximately six digits of magnitude by using of Optical Transition Radiation (OTR) and fluorescence screens, Unit-1, has been operated in the injection-beam transport (3-50BT) line of the J-PARC main ring (MR) [1, 2]. This device contributes to the diagnosis of beam core and halo of intense proton beams before injection to MR, particularly measurement of beam cut effects by beam collimators located in upstream of the device is useful for beam shaping. We have been developing the second device, Unit-2, to be installed into MR for diagnosing on injected beams. By using the both of first and second devices, beam core and halo can be diagnosed in different phases. Property tests of the second device have been conducted at a test bench. But its longitudinal coupling impedance of several ohms (by *Z*/n value) is an issue. Then we have been studying the absorption of the rf power of the resonances up to about 1 GHz using SiC. In this paper, we discuss the characteristics of the developing device, and simulation results of reducing the coupling impedance.

INTRODUCTION

The key to increase beam intensity is how to reduce the beam loss, then the diagnosis of the beam halo with device of Unit-1 in operation has been an advantage. Following the Unit-1, it was planned to put a Unit-2 in MR [3, 4]. At the Unit-2, it will be able to diagnose a halo with a beam core and orbits of about 10 to 20 turns after the injection. Those two-dimensional information on the halo formation at the beginning of the circulation enables us to operate high-intensity beam with reflecting the correlation in the X-Y directions. In addition, by performing measurements synchronized with the Unit-1, it is possible to adjust the collimator balance between 3-50BT and MR, and to diagnose the transverse phase-space distribution of the injection beam including the two-dimensional XY coupling component. Furthermore, by only using the beam halo part of Unit-2 for the measurement of the circulating beam, the beam loss due to the time evolution of the two-dimensional distribution. It is also expected to diagnose resonance condition with such a temporal halo information.

Development as a basic monitor device has been completed, and basic measurements have been made on a test bench. The challenge for the current study is how to reduce the coupling impedance with MR circulating beams. At the beginning of development, the impedance (*Z*/n) was set to almost zero in the frequency range up to 100 MHz. This reason was the MR's basic acceleration frequency of 1.67-1.71 MHz (corresponding to 3-30 GeV) was observed with high-frequency components up to about 100 MHz in the actual beam. However, recently, microwave instabilities have occurred in the region of several hundred MHz at the time of rf de-bunch in a slow extraction. For this reason, a requirement was imposed to reduce the impedance in the region up to around 1 GHz to zero as much as possible.

DEVICE CONFIGURATION

The concept of a high dynamic-range profile monitor is to increase the dynamic range of detection by using two types of screens. The beam core (about 2 digits) is detected by OTR from the titanium screen, and the beam halo (about 4 digits) is detected by the fluorescence from the alumina screen on the outer part [1, 2] (Fig. 1).

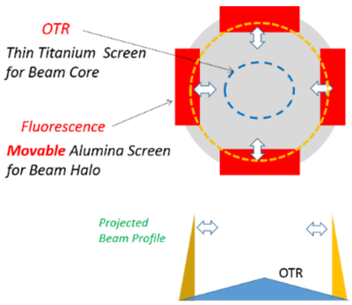

Figure 1: Conceptual screen layout.

In the Unit-2, the following five points were changed from the Unit-1 of 3-50 BT in order to install it in MR.

1. The diameter of the beam hole at the upper concave mirror was increased from 120 mm to 160.
2. Then the diameter of the concave mirror was increased from 300 mm to 350 mm to compensate for the light loss due to the large beam hole as above.
3. The vacuum chambers for the mirror and the target were separated.
4. The imaging point was positioned in the atmosphere to increase the yield of light with close optics.
5. Though conventional mirrors were made by depositing pure aluminium on the entire surface of polished Pyrex glass, considering radiation damage, in Unit-2 pure aluminium (A1050) was used as the base material and machined.

---

* Work supported by Grant-in-Aid for Scientific Research JP16H06288.
† email address: yoshinori.hashimoto@kek.jp

ISBN: 978-3-95450-230-1 ISSN: 2673-5350 doi:10.18429/JACoW-IBIC2021-TUPP24

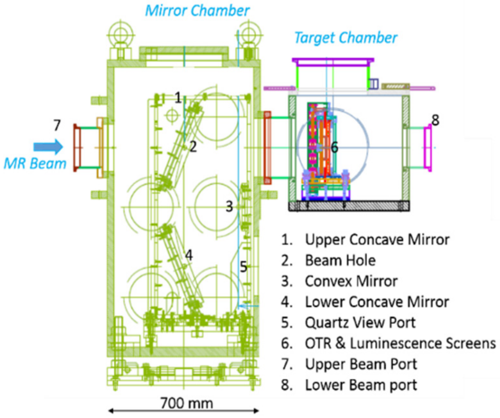

Figure 2: Layout of the device apparatus.

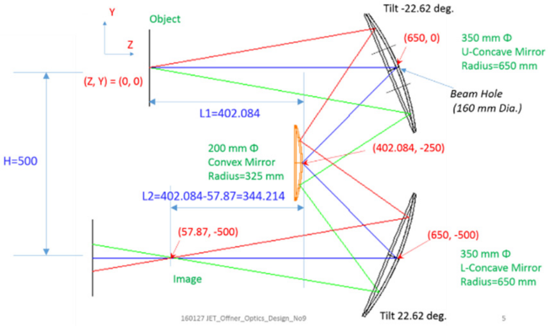

Figure 3: Layout of Offner relay optics.

Figures 2 and 3 show the configurations of the device and the relay optical system, respectively. The optical system transfers the OTR and fluorescence generated at the target to imaging point. The Offner optical system consisting of upper and lower concave mirrors with a diameter of 350 mm and convex mirrors with a diameter of 200 mm [5], and these three surfaces are concentric spheres. The system has a large aperture as that F value is about 0.7. The spread angle of the OTR by the 3 GeV injected proton beam is 27 degrees [1, 2], and the mirror is large enough to cover the solid angle. These spherical mirrors using aluminium (A1050) were made by lathe processing with an air bearing type lathe, then it was possible to achieve a surface accuracy of about 6 to 60 nm in terms of Ra (arithmetic mean roughness) value. The wave surface accuracy was about $\lambda/4$. The optical system was confirmed by a grid pattern test to have a horizontal field of view of 140 mm and a vertical field of view of 100 mm. For the difference in light transmittance depending on the location of the subject, a sensitivity map was created by sweeping the laser spot. It is used to correct the beam measurement data.

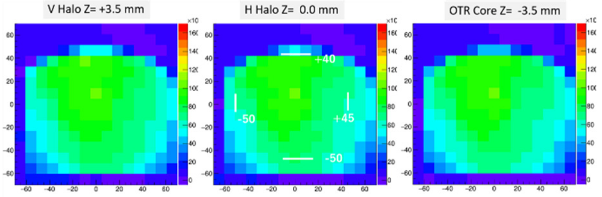

Figure 4: Transmission map by laser swept from 3 types of target positions.

Figure 4 shows uniform transmission area within un-uniformity 15% was 80 mm square. Target position varied ±3.5 mm which amount to actual target differences, the results show almost the same transmission map. They also show that the depth of field can be secured at 7 mm.

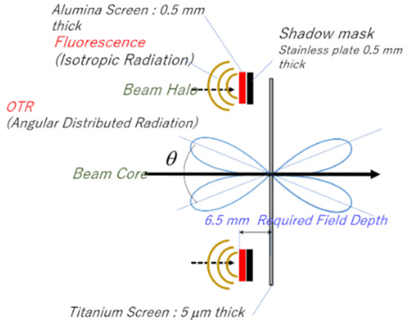

Figure 5: Target configuration.

A target configuration is shown in Fig. 5. A titanium foil screen for beam core with a thickness of 5 μm, and the red rectangles located on the top, bottom, left, and right of alumina screens for beam halo with a thickness of 0.5 mm. Table 1 summarizes the losses in these materials for high intensity beams.

Table 1: Energy Loss in the Screen Materials

	Energy Loss [keV/proton]**	Energy Loss [J/bunch]***
Titanium 5 μm	3.4	4.9e-3
Alumina 0.5 mm	330	4.7e-1

* 3GeV Proton, ** 1e13 proton/bunch

The durability of titanium foil is not a problem even when a high-intensity beam such as 7.6×10^{13} proton / 2bunch was circulated and passed through the foil for about 100 turns (repetition cycle 5.3 μs) at MR [6]. The total energy loss value of alumina in the table is about 100 times larger than that of titanium. However, since the proton density at the alumina target is 10^{-3} or less to the beam center because of beam halo part, the actual total energy loss during use is 1/10 or less of that of titanium, and no problem occurs. Concerning beam spread of these screen materials due to scattering were estimated to be about 1 %/10 turns for the titanium foil in the beam core and 50 %/10 turns for the alumina in the beam halo. Although the alumina screen for the beam halo has the above-mentioned scattering effect, it is also taken into consideration that the beam halo growth exceeding 40 π mm.mrad will be captured by measuring not only the injection time but also during acceleration.

The secondary optical system locates in a lead shield under the target where the radiation exposure dose was about 500-1000 mGy/week by pre-measured using the OSL chip [7] during operation of the high intensity beam. This dose level was almost the same as the value at the Unit-1. The components of the secondary optical system consist of a quartz diffuser plate at the imaging point to convert OTR into scattered light, and a close-range wide-angle optical

ISBN: 978-3-95450-230-1 ISSN: 2673-5350 doi:10.18429/JACoW-IBIC2021-TUPP24

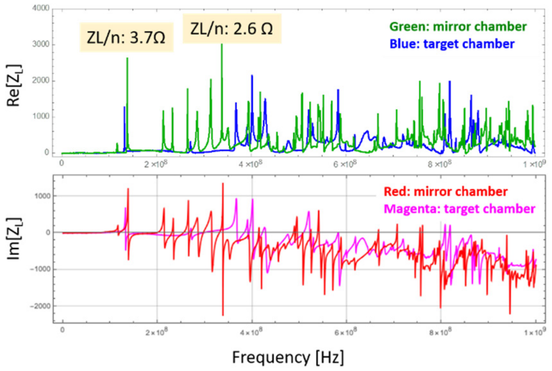

Figure 6: Results of coupling impedance measurement with initial equipment.

system for obtaining beam image. The basic measurement system is a wide dynamic-range CMOS camera with an image intensifier with rise time of 100 ns.

COUPLING IMPEDANCE

Impedance measurements [8] using wire were performed on each of the mirror chamber and the target chamber (Fig. 6). For the impedance value, *Z*/n [Ω] used for the evaluation of instability is used, when n = frequency/revolution frequency. In up to 1 GHz, the mirror chamber had a peak of 3.7 Ω around 150 MHz and a peak of 2.6 Ω near 350 MHz. In the higher frequency region, there were many peaks of about 1.5 Ω or less. In the target chamber, most of the peaks were below about 0.5 Ω.

The slow extraction beam has a high intensity of about 65 kW currently, and microwave instability occurs depending on conditions at the time of de-bunch at 30 GeV. According to the Keil-Schnell criterion [9, 10], which is often used as a measure of the onset of this instability, the MR threshold is estimated to be about several Ω. By a consideration, it was decided to reduce the impedance to about 0.5 Ω or less as much as possible. Therefore, the mirror chamber should be reduced these impedances.

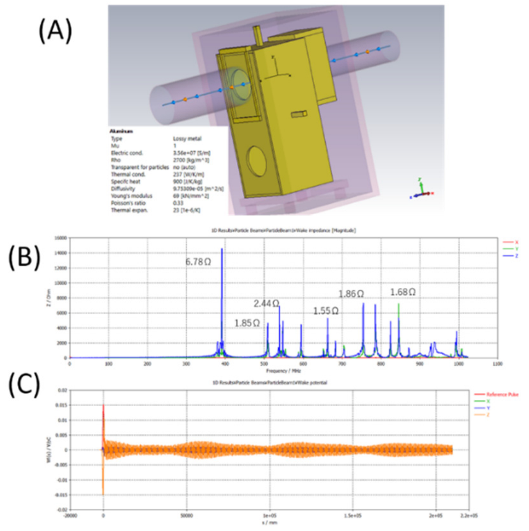

Figure 7: Simulation with a shielded Mirror Unit: (A) Structure, (B) Impedance, (C) Wake potential.

IMPEDANCE REDUCTION

By Structure Modifying

We conducted simulation by wake solver of CST Studio suite [11] to reduce various resonances. However, it is difficult to make *Z*/n sufficiently small, and particularly, the problem was the resonance does not decay by next bunch. For example, Fig. 7 shows an example of a simulation in which the internal mirror unit was covered by an aluminium shield. There was a high resonant peak of 6.78 Ω at 390 MHz, and some resonances remained at higher frequencies (Fig. 7 (B)). Figure 7 (C) shows the wake potential did not decay by the next bunch sufficiently. In Fig. 7, the impedance values(B) are just the lower limits in simulation because of not enough time region(C) to decay them.

Field Absorption Using Silicon Carbide

Therefore, we decided to study a method of absorbing an electric field using a dielectric. For the dielectric, silicon carbide (SiC) [12-14], which has been proven to be used for the purpose of attenuating higher-order modes in accelerating cavities such as KEKB and KEKB DR, was selected. SiC is CoorsTek's CERASIC B [15] (Fig. 8), especially suitable for the frequency above 100 MHz. The absorption power *P* of the high frequency electric field by the dielectric is given by Eq. (1). Here, with K as a constant, ε' is the relative permittivity, tanδ is the dielectric loss angle, *f* is the frequency, and *E* is the electric field strength,

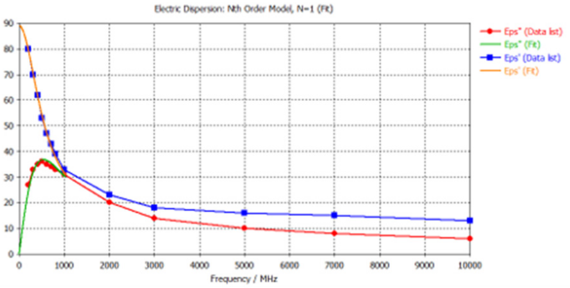

Figure 8: Permittivity of a SiC, ε': blue, and ε'': red.

$$P = K \cdot \varepsilon' \cdot tan\delta \cdot f \cdot E^2 \qquad (1).$$

Simulation with SiC

For the electric field absorption in SiC, it is effective to install it in a place where the normal electric field strength is larger (Eq. (1)). However, in order to remove heat generated by absorption, it is easier to install it at a position facing the atmosphere than inside a vacuum chamber. For this reason, we decided to install SiC on the vacuum side of the inner surface of the port flange of the mirror chamber.

The configuration in which SiC was attached to a total of 9 surfaces, 8 surfaces of the ICF253 flange on the side of the chamber and 1 surface of the ICF406 flange on the top surface. This set had a high effect on impedance

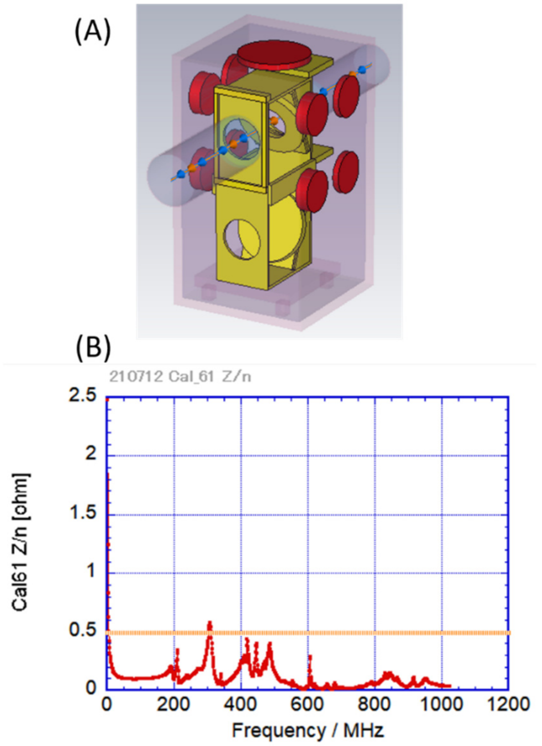

Figure 9: A wake field simulation with SiC, (A) red plates mean SiC, and (B) wake impedances.

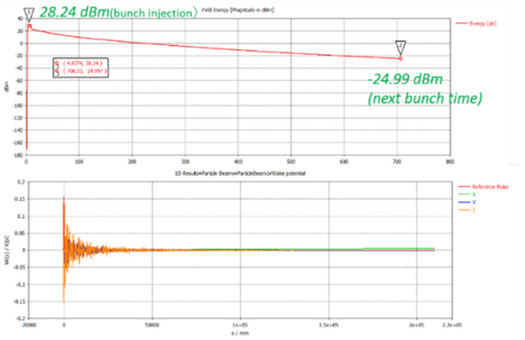

Figure 10: Calculated field energy (A) and wake potential (B) during one-bunch time separation of 700 ns.

reduction (Fig. 9(A)). The position of the SiC plate of ICF253 on the downstream side of the beam level was increased SiC thickness to 60 mm because the viewing space in the cavity was wide, and the others were 30 mm. The longitudinal impedance had the maximum peak of 0.6 Ω at 250 MHz, and the others were below the target of 0.5 Ω (Fig. 9 (B)). Figure 10 shows the varying with time in the field power and in wake potential of one bunch interval. The field is 28.24 dBm (0.66 W) when passing through the bunch and is attenuated gradually by 52 dB during the bunch time. This calculation assumes $3{\times}10^{12}$ protons per bunch and that all power is absorbed by SiC. In a actual case, bunch of $5{\times}10^{13}$ protons, it can be estimated to be about 11 W. In addition, the wake potential decays at about 1/3 of the bunch time interval.

SUMMARY AND PROSPECTS

We have been developing the second profile monitor using OTR and fluorescence in order to increase the intensity of J-PARC MR and to improve the diagnostic equipment for injected beams. The device was completed with the configuration as designed, and the characteristics have been measured on the test bench. For installation on MR, there was a requirement to reduce the coupling impedance with the beam to about 0.5 Ω or less and as small as possible in order to reduce beam instability. By adding SiC as a countermeasure, we obtained simulation results with an impedance of about 0.6 Ω. In the near future, SiC plates will be manufactured and impedance measurement will be performed on the bench.

ACKNOWLEDGEMENTS

We have received a lot of cooperation regarding SiC from KEK Yasunao Takeuchi.

REFERENCES

[1] Y. Hashimoto, T. Toyama, T. M. Mitsuhashi, M. Tejima, and S. Otsu, “A Development of High Sensitive Beam Profile Monitor using Multi-Screen”, in *Proc. 2nd Int. Beam Instrumentation Conf. (IBIC'13)*, Oxford, UK, Sep. 2013, paper TUCL2, pp. 338-341.

[2] Y. Hashimoto *et al.*, “Two-Dimensional and Wide Dynamic Range Profile Monitor Using OTR / Fluorescence Screens for Diagnosing Beam Halo of Intense Proton Beams”, in *Proc. 54th ICFA Advanced Beam Dynamics Workshop on High-Intensity and High-Brightness Hadron Beams (HB'14)*, East Lansing, MI, USA, Nov. 2014, paper TUO2AB04, pp. 187-191.

[3] Yoichi Sato *et al.*, in *Proc. of the 16th Annual Meeting of Particle Accelerator Society of Japan*, July 2019, Kyoto, Japan, pp. 1125-1129. (In Japanese), `https://www.pasj.jp/web_publish/pasj2019/proceedings/PDF/FRPI/FRPI038.pdf`

[4] S. Igarashi *et al.*, “Accelerator design for 1.3-MW beam power operation of the J-PARC Main Ring”, *Prog. Theor. Exp. Phys.*, vol. 2021, p. 033G01, 2021. `doi:10.1093/ptep/ptab011`

[5] A. Offner, “New concepts in projection mask alignment”, *Optical Engineering*, vol. 14, no. 2, p.130-132, 1975.

[6] Y. Hashimoto *et al.*, “Multi-Ribbon Profile Monitor Using Carbon Graphite Foil for J-PARC”, in *Proc. 46th ICFA Advanced Beam Dynamics Workshop on High-Intensity and High-Brightness Hadron Beams (HB'10)*, Morschach, Switzerland, Sep.-Oct. 2010, paper WEO2A01, pp. 429-433.

[7] T. Okazaki *et al.*, in Proc. 15th PASJ annual meeting, Nagaoka, 2018, pp1256-1259, `https://www.pasj.jp/web_publish/pasj2018/proceedings/PDF/THP1/THP137.pdf`

[8] T. Toyama, “Beam Instrument”, OHO 2009 (In Japanese), `http://accwww2.kek.jp/oho/OHOtxt3.html`

[9] K. Keil and W. Schnell, “Concerning longitudinal stability in the ISR”, CERN, Geneva, Switzerland, Rep. CERN-ISR-TH-RF/69-48, Jul. 1969.

[10] Y. H. Chin, “Beam instability on high intensity proton

beam", OHO 2005 (In Japanese), `http://accwww2.kek.jp/oho/OHOtxt3.htm`

[11] CST Studio suite, `https://www.3ds.com/ja/products-services/simulia/products/cst-studio-suite`

[12] Y. Takeuchi, T. Abe, T. Kageyama, and H. Sakai, "RF Dielectric Properties of SiC Ceramics and their Application to Design of HOM Absorbers", in *Proc. 21st Particle Accelerator Conf. (PAC'05)*, Knoxville, TN, USA, May 2005, paper WPAT010, pp. 1195-1197.

[13] T. Kageyama, T. Abe, H. Sakai, and Y. Takeuchi, "HOM Damping of ARES Cavity System for SuperKEKB", in *Proc. 21st Particle Accelerator Conf. (PAC'05)*, Knoxville, TN, USA, May 2005, paper TPPT010, pp. 1186-1188.

[14] Y. Takeuchi, "Design for Microwave Circuit", OHO 2017 (In Japanese), `http://accwww2.kek.jp/oho/OHOtxt4.html`

[15] Coorstek, KK, CERASIC B, `http://www.coorstek.co.jp/jpn/products/detail/detail_19.html`

ISBN: 978-3-95450-230-1 ISSN: 2673-5350 doi:10.18429/JACoW-IBIC2021-TUPP25

BEAM PROFILE MEASUREMENTS UTILIZING AN AMPLITUDE MODULATED PULSED FIBER LASER AT PIP2IT

V. Scarpine, R. Campos, N. Eddy, B. Fellenz, T. Hamerla, J. Ruan, R. Thurman-Keup,
Fermi National Accelerator Laboratory, Batavia, IL USA
M. El Baz, Université Paris Saclay, Orsay, France

Abstract

Fermilab is undertaking the development of a new 800 MeV superconducting RF linac to replace its present normal conducting 400 MeV linac. The PIP-II linac consists of a warm front-end generating 2 mA of 2.1 MeV H- followed immediately by a series of superconducting RF cryomodules to 800 MeV. To limit the potential damage to the superconducting RF cavities, PIP-II will utilize laser-based monitors to obtain beam profiles via photoionization. This paper will present the results of transverse and longitudinal beam profile measurements using a prototype profile monitor that was tested with 2.1 MeV H- beam at the PIP-II Injector Test (PIP2IT) accelerator. This prototype profile monitor utilizes a high repetition rate fiber laser and fiber optic transport into the PIP2IT enclosure. In addition, results will be shown of narrow-band electron detection from amplitude modulated laser pulses

THE PIP-II SUPERCONDUCTING LINAC

The PIP-II project at Fermilab is building a superconducting (SC) Linac to fuel the next generation of intensity frontier experiments [1]. Capitalizing on advances in superconducting radiofrequency (SRF) technology, five families of superconducting cavities will accelerate H− ions to 800 MeV for injection into the Booster. Table 1 shows the main SC Linac beam parameters.

Table 1. PIP-II Linac Beam Parameters

Delivered Beam Energy (kinetic)	800 MeV
Particles per Pulse	6.7×10^{12}
Average Beam Current in the Pulse	2 mA
Pulse Length	550 μs
Pulse Repetition Rate	20 Hz
Bunch Pattern	Programmable

Figure 1 shows the layout of the SC Linac. The β values represent the optimal betas where the corresponding cavity delivers the maximum accelerating voltage. A room temperature (RT) section accelerates the beam to 2.1 MeV and creates the desired bunch structure for injection into the SC Linac. In the SC section of the linac, strict particle-free and high-vacuum requirement place limitation on the design and type of beam instrumentation that can be used [2]. To meet these strict particle-free conditions, invasive beam instrumentation profiling devices, such as wire scanners, are forbidden. Non-invasive laser-based profile monitors will be developed as PIP-II SC Linac beam profiling instruments. Since the PIP-II linac accelerates H- ions, laser induced photoionization ($H^- + \gamma \rightarrow H^o + e^-$) will be used to measurement beam profiles [3] in the region of PIP-II SC linac.

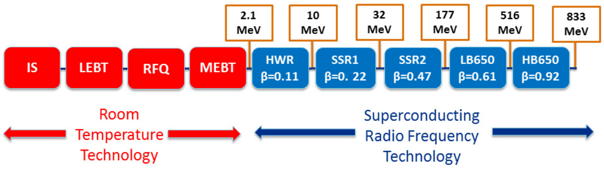

Figure 1: The PIP-II SC Linac technology map.

THE PIP-II INJECTOR TEST FACILITY

As part of the PIP-II R&D strategy, the project has developed and operated the PIP-II Injector Test (PIP2IT) facility. The PIP2IT accelerator covers the first 20 MeV of the PIP-II design [4]. The PIP2IT program performed an integrated system test of the room temperature warm front end (WFE), consisting of the ion source, LEBT, RFQ and MEBT [5], and the first two superconducting cryomodules. Figure 2 shows the layout of the PIP2IT accelerator.

The MEBT operates with 2.1 MeV H- beam up to 5 mA which includes a bunch-by-bunch chopper allowing for any arbitrary beam pattern [6]. For PIP-II beam operations, the MEBT chopper will reduce the beam current from 5 mA to 2 mA before injection into the SC linac.

To test possible laser-based profiling techniques for PIP-II, a prototype laser profile monitor was installed in the PIP2IT MEBT.

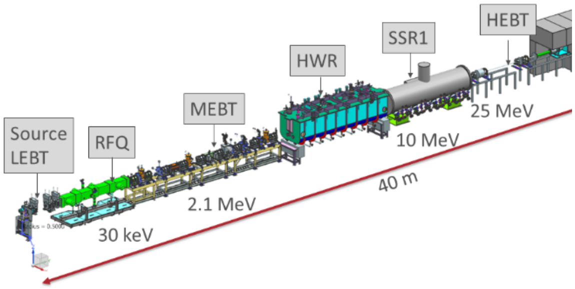

Figure 2: The beamline layout of the PIP-II Injector Test.

PROTOTYEP LASER-BASED BEAM PROFILER FOR PIP2IT

We have developed a prototype laser-based beam profiler to develop techniques that may be used at PIP-II. The prototype profile monitor is based on a low-power fiber laser with all-fiber optical transport through the linac [7]. The fiber laser is an Ytterbium seed laser with amplifier stages from Pritel [8] and operates at the PIP-II bunch repetition rate of 162.5 MHz. The laser light is transported into the beamline via 30m of Nufern PM1060L [9] single-mode polarizing maintaining optical fiber. The laser pulses inducing a small number of photoionization per bunch. Table 2 gives a list of the parameters of the fiber laser system. To improve the signal detection, the laser pulses may be amplitude modulated to allow detection of the photoionized electrons at the same modulation frequency using lock-in amplifier techniques.

Table 2. Fiber Laser Parameters

Laser wavelength	1054 nm
Laser power at beamline	Up to 1 W
Laser pulse frequency	162.5 MHz
Laser pulse width (fwhm)	12 ps

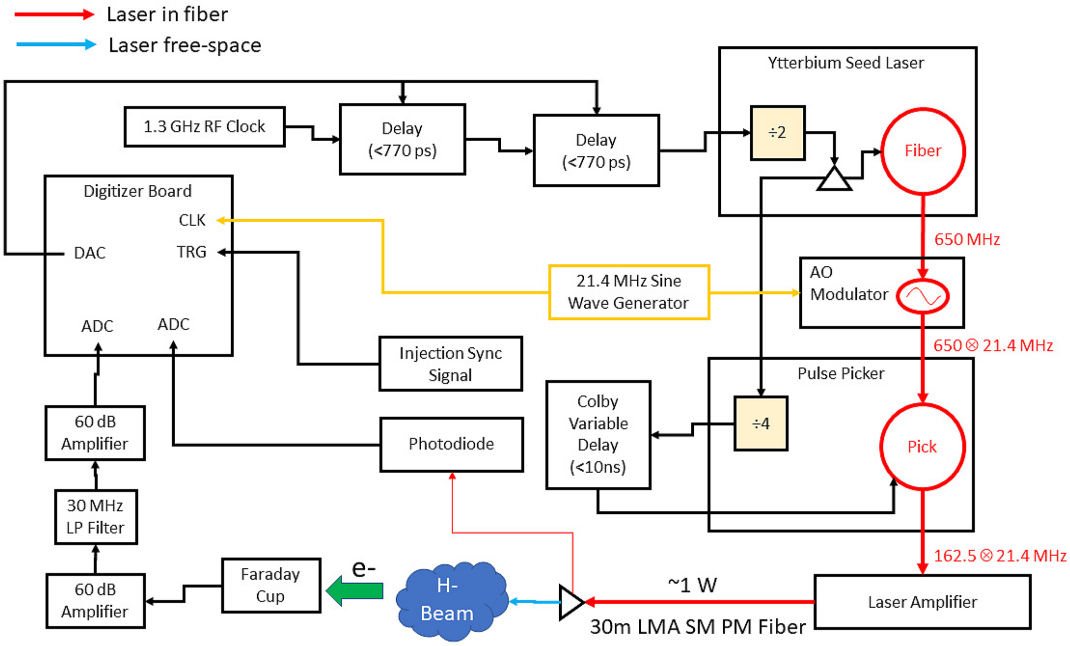

Figure 3: Block diagram of the laser profile monitor system.

Laser Profiler System

Figure 3 shows a block diagram of the laser profile monitor system. The fiber laser is locked to 8th harmonic of the accelerator RF frequency at 1.3 GHz and the laser generates pulses at 162.5 MHz. The laser pulses go through an acousto-optic (AO) modulator which amplitude modulates the laser pulse train at 21.4 MHz. The laser pulses are then amplified. The amplified laser power is limited to ~1W to limit damage to optical fibers and vacuum optical viewports. The laser system and electronics are located outside of the PIP2IT beamline enclosure, and the laser light is transported via a single-mode polarize maintaining fiber into the enclosure to the beamline vacuum chamber. The optical fiber is terminated on a collimator for free-space transport through optical vacuum viewports to the H- beam. To prevent potential damage to the viewports, the laser light is expanded and refocused on to the H- beam. The optical design limits the optical power density at the vacuum viewports to less than 3 W/cm^2. To make transverse H- beam profile measurements the laser is scanned across the beam using a linear motion stage. To make longitudinal H- beam profiles the phase of the RF signal to the laser system is changed. Figure 4 shows the layout of the free-space optics.

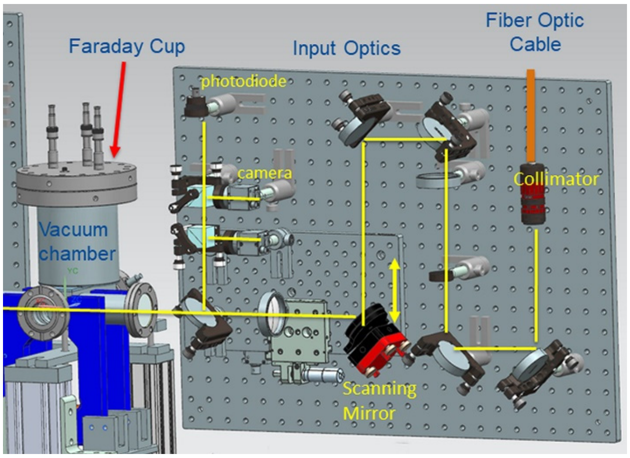

Figure 4: Block diagram of the input optics.

The electrons released from the photoionization are transport by deflection dipole magnets into a Faraday cup. Signal levels from the Faraday cup are expected to be less than a few nA. The signal is amplified by 120 db and filtered before being sampled in by 16-bit ADCs. For amplitude modulated measurements, the digitizing board is locked to modulating frequency. This allows signals from multiple beam pulses to be combined coherently in phase.

BEAM MEASUREMENTS

Initial beamline measurements were made without amplitude modulation of the laser pulses. This allow us to study the background electron signals in the PIP2IT MEBT that are generated by H- beam-beam striping. This effect produces background electrons that have the same kinetic energy as the photoionized electron. The laser profiler was operated with laser off and then on to get an estimate of the background. Figure 5 shows the Faraday cup signal with the laser off and then on. The data shows a 2 nA signal with the laser off and a 6 nA signal with the laser on. This large background signal limits the dynamic range of this broadband direct current profile measurement and hints that a narrowband lock-in amplifier might eliminate this incoherent background.

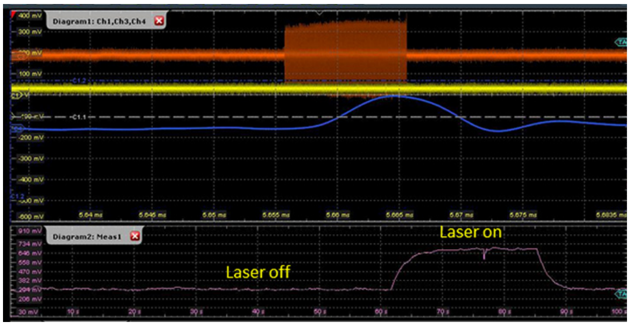

Figure 5: Faraday cup signal with the laser off and then on.

Beam Measurements without Amplitude Modulation

Longitudinal beam profile measurements were made without amplitude modulation. To make the longitudinal profile measurements the phase of the laser pulses was scanned over 360 degrees of the 162.5 MHz beam frequency. The large 120 db gain of the signal amplifiers required many beam pulses to be averaged to reduce the incoherent amplifier noise. Figure 6 shows a longitudinal profile measurement and a Gaussian fit to the data gives a 207 ps RMS bunch length, which is consistent with the expected bunch length.

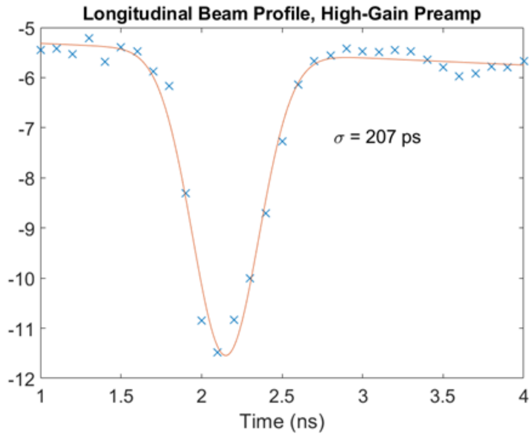

Figure 6: Longitudinal beam profile without amplitude modulation.

Beam Measurements with Amplitude Modulation

Transverse beam profile measurements were made with amplitude modulation of the laser pulses. The laser was scanned transversely across the H- beam using a linear stage. The digitizer board was locked to the 21.4 MHz amplitude modulation frequency and data from multiple beam pulses was added coherently. This allowed for a very narrow bandwidth measurement and a reduction of noise and incoherent background electrons. Figure 7 shows a transverse beam profile measurement and a Gaussian fit to the data gives a 1.8 mm RMS beam size, consistent with expected beam size.

In our initial amplitude modulation measurements at PIP2IT, the reduction in noise was limited due to crosstalk between the modulation signal to the laser and the input signal to our digitizing board. Steps to mitigate this crosstalk, such as better cables and cable layout, will be taken at PIP-II. However, this present measurement gives a proof-of-principle of the amplitude modulation technique.

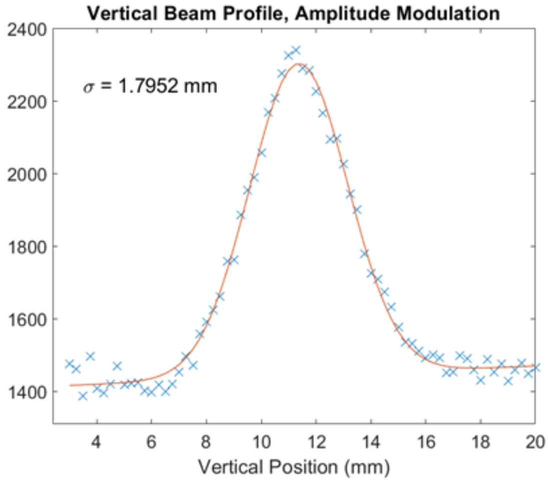

Figure 7: Transverse beam profile with amplitude modulation.

SUMMARY

A prototype H- transverse and longitudinal beam profiler based on an amplitude modulated fiber laser source was constructed and tested at the PIP2IT accelerator. This prototype unit successful demonstrated a lock-in amp technique to make beam profiles from amplitude modulated laser pulses. In addition, locking the DAQ system to the same modulation frequency allowed the lock-in amp technique to be used for pulsed signals.

ACKNOWLEDGEMENTS

The authors would like to thank KV Reddy and the team at Pritel, Inc for their invaluable help in the development and operation of the fiber laser system and Andy Devine and the team at Coastal Connections for their guidance and work on our fiber optic cables.

REFERENCES

[1] PIP-II Conceptual Design Report, 2018, `http://pip2-docdb.fnal.gov/cgi-bin/ShowDocument?docid=113`

[2] V. E. Scarpine *et al.*, “Beam Instrumentation Challenges for the Fermilab PIP-II Accelerator”, in *Proc. 8th Int. Beam Instrumentation Conf. (IBIC'19)*, Malmö, Sweden, Sep. 2019, pp. 181-183. `doi:10.18429/JACoW-IBIC2019-MOPP034`

[3] Y. Liu *et al.*, “Laser Based Diagnostics for Measuring H- Beam Parameters”, in *Proc. 24th Particle Accelerator Conf. (PAC'11)*, New York, NY, USA, Mar.-Apr. 2011, paper WEOCN1, pp. 1433-1437.

[4] P. Derwent *et al.*, “PIP-II Injector Test: Challenges and Status”, in *Proc. 28th Linear Accelerator Conf. (LINAC'16)*, East Lansing, MI, USA, Sep. 2016, pp. 641-645. `doi:10.18429/JACoW-LINAC2016-WE1A01`

[5] L. R. Prost *et al.*, “PIP-II Injector Test Warm Front End: Commissioning Update”, in *Proc. 9th Int. Particle Accelerator Conf. (IPAC'18)*, Vancouver, Canada, Apr.-May 2018, pp. 2943-2946. `doi:10.18429/JACoW-IPAC2018-THYGBF2`

[6] A. V. Shemyakin *et al.*, “Design of 162-MHz CW Bunch-by-Bunch Chopper and Prototype Testing Results”, in *Proc. 61st ICFA Advanced Beam Dynamics Workshop on High-Intensity and High-Brightness Hadron Beams (HB'18)*, Daejeon, Korea, Jun. 2018, pp. 428-433. `doi:10.18429/JACoW-HB2018-THP1WC03`

[7] R. B. Wilcox *et al.*, “A low power laser wire with fiber optic distribution”, in *Proc. of DIPAC* 2011 Hamburg, Germany, TUPD53.

[8] Pritel, Inc, `https://www.pritel.com/`.

[9] Coherent Nufern, `https://content.coherent.com/pdf/pm1060l_fa_spec_202011122143.pdf`

ISBN: 978-3-95450-230-1 ISSN: 2673-5350 doi:10.18429/JACoW-IBIC2021-TUPP28

REAL-TIME BEAM DETECTION AND TRACKING FROM PINHOLE IMAGING SYSTEM BASED ON MACHINE LEARNING

A. A. Nosych, U. Iriso, ALBA Synchrotron, Barcelona, Spain

Abstract

At ALBA Synchrotron each of the two in-air pinhole imaging systems is able to see several beam spots at once due to specific pinhole grid with 3x3 holes placed in the path of the X-ray fan. Each beam image has its own properties, such as source pinhole aperture size, its Point Spread Function (PSF) and copper filter thickness, all of which impact the electron beam size calculation. Until now, these parameters were applied manually to the pinhole device servers for numerical image analysis, so this semi-manual beam size calculator is subject to frequent adjustments and human monitoring.

This study looks at feasibility of training and pointing an Artificial Neural Network (ANN) at image stream coming from pinhole cameras in real time, track all detected beam spots and analyze them, with the end goal to automate the whole pinhole beam image processing.

INTRODUCTION

The ALBA Synchrotron is a 3 GeV third-gen light source located in Cerdanyola del Vallès (Barcelona, Spain). Currently it has 10 operational beamlines, comprising soft and hard X-rays that perform research in fields like material science, condensed matter, nanotechnology, biology and others. The facility provides more than 6000 hours of beam time per year and is available for the academic and the industrial sector, serving several thousand researchers every year.

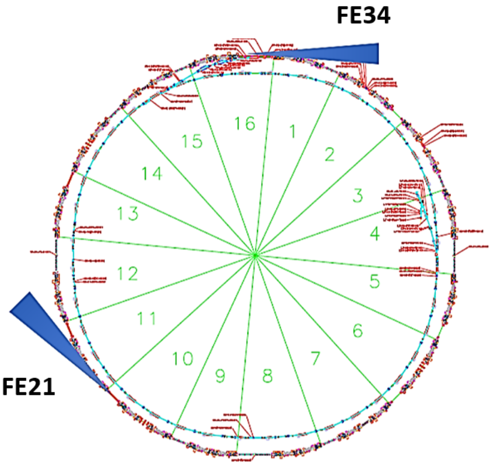

Figure 1: ALBA storage ring layout, and location of both in-air X-ray pinholes in sectors 1 and 11.

Measuring transverse size and emittance [1] of the electron beam at any moment of time is essential to control the machine performance. This measurement is carried out by two in-air X-ray pinhole cameras [2], whose location is shown in Fig. 1 and components laid out in Fig. 2.

Apart from emittance and beam size, the pinholes inevitably monitor beam position and stability. As the simple optics principle of a pinhole, it takes the synchrotron radiation coming from a bending magnet to obtain a magnified transverse image of an electron beam, which is analysed to infer the horizontal and vertical (H and V) electron beam size. Any movement of beam orbit will immediately be seen in the pinholes, and any problematic beam will be observed as blurred, out of shape, or different in size than usual.

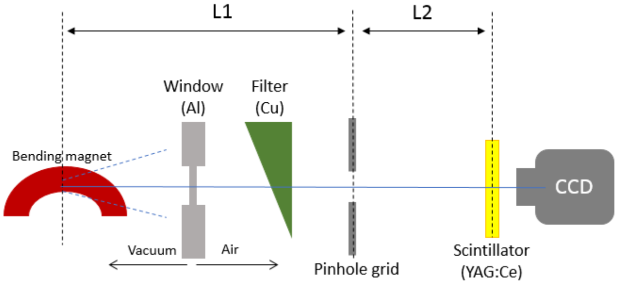

Figure 2: Component schematics of ALBA pinhole system (not to scale).

Since its commissioning in 2011 the storage ring has been operating with only one pinhole located at front-end 34 (FE34) [3], but in 2020 a second pinhole at front-end 21 (FE21) was installed for redundancy. It brings a few improvements with respect to FE34, the main of which is higher magnification. See Table 1 for a list of other differences.

Table 1: ALBA's Pinholes Compared

	FE21	**FE34**
L1	4.111 m	5.936 m
L2	15.357 m	13.828 m
Magnification	3.76	2.31
Visible beam spots	2	6
Al window thickness	1.5 mm	1 mm
Beam size at source	56, 26 μm	53, 23 μm

Both ALBA's X-ray pinhole lines are similar and consist of a chain of elements shown in Fig. 2. This type of pinhole system has previously been described in greater detail [2–4], so we will not focus on its functionality here. The elements important for this work are the copper wedge filter (an X-ray attenuator) and the pinhole grid itself.

The pinhole grid is motorized and has 4 degrees of freedom (lateral, vertical, rotational ad pitch). It consists of apertures made by horizontal and vertical tungsten bars (Fig. 3): in total there are 9 rectangular holes of different size, with 3 squared. FE21 and FE34 share the 50×50 and 10×10 μm hole sizes, while FE34 also has the 100×100 µm and FE21 the 5×5 µm. The values 100, 50, 10 and 5 µm are theoretical: the true apertures were measured in the lab with optical microscopy and diffraction methods and are slightly larger.

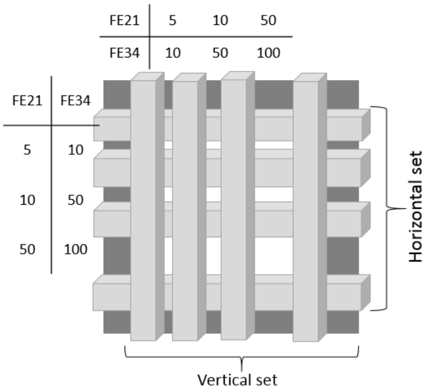

Figure 3: Schematic of a pinhole grid made of 1 mm thick tungsten bars crossing into 9 apertures of different sizes.

PINHOLE IMAGE PROCESSING

The frames stream at 3 Hz rate from both pinhole CCD. For simplicity and speed the frames are cropped around a region of interest (ROI), which is manually fixed to tell the control system where to look, Fig. 4. Device server then does 1D projection Gaussian fits on the fly for beam size estimation. This is sufficient during stable operation of the machine for users. We usually select the ROI around the 10×10 µm pinhole due to its smallest PSF contribution (more on this below). This is reliable and quick, provided the beam does not move.

If the beam or the pinhole grid motors move for some reason, the ROI must be adjusted manually. Moreover, for machine studies and optimization a 2D Gaussian fit must be performed frequently and manually. Here is the part where using machine learning and ANN can come in handy and bring pinhole image analysis on a whole another level.

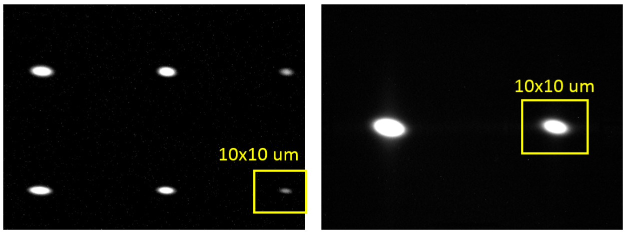

Figure 4: Complete images seen by both pinhole CCDs (FE34 left and FE21 right) while in operation with beam.

Due to grid structure of the pinhole sets, both cameras are able to “see” up to 8 beam spots combined, with FE21 viewing less spots (only 2) due to shorter distances between mechanical elements and larger magnification. So what if we were to look and analyse all of them at once? This becomes a practical *computer vision* application of machine learning algorithms for beam diagnostics!

For fully automated and reliable beam size and emittance monitoring in 2D a computer vision model can be trained to look at the stream of CCD frames, detect all beam spots, and pass their coordinates to mathematical analysis routine. However, one thing must be taken care of.

PSF Calculation

The pinhole image is affected by the system PSF, which is the beam size measured at the camera screen corresponding to a point-like electron beam. Among other characteristics, the PSF strongly depends on the pinhole aperture size and radiation wavelength λ. Here, λ is defined by the Al window thickness (fixed) and the copper filter attenuation (variable).

To emulate a PSF a unit-size electron beam is defined. It is also called a "zero emittance beam" and it combines blurring and diffraction effects [3, 4]:

$$\sigma_{\text{PSF}} = \sqrt{\sigma_{\text{blur}}^2 + \sigma_{\text{diff}}^2 + \sigma_{\text{scr}}^2}, \tag{1}$$

where σ_{diff} is Fraunhofer diffraction

$$\sigma_{\text{diff}} = \frac{\sqrt{12}}{4\pi} \frac{\lambda L_2}{w}, \tag{2}$$

σ_{blur} is blurring due to the finite size of the pinhole

$$\sigma_{\text{blur}} = \frac{w(L_1 + L_2)}{\sqrt{12} L_1}, \tag{3}$$

w is pinhole width or height, and σ_{scr} is the CCD pixel size.

Taking all of this into account, the measured size of a beam spot σ_{YAG} will be larger than the true electron beam size σ_{b}, due to its PSF:

$$\sigma_{\text{YAG}}^2 = (M\sigma_{\text{b}})^2 + (\sigma_{\text{PSF}})^2, \tag{4}$$

where $M = \frac{L_2}{L_1}$ is the pinhole magnification.

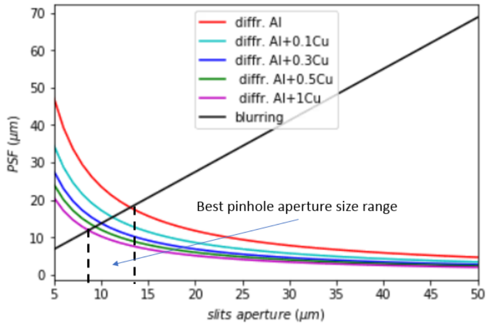

Figure 5: Simulated blurring and diffraction contributions to PSF as functions of pinhole aperture w and Cu thickness. Apertures with sizes 50 µm and larger must be used with care, because they can actually enlarge the beam measurement.

It is always best to build and set up the system mechanically such that PSF is minimal from the start, before any

ISBN: 978-3-95450-230-1 ISSN: 2673-5350 doi:10.18429/JACoW-IBIC2021-TUPP28

numerical analysis. The blurring contribution is independent of the pinhole aperture size in H and V, so by combining blurring with diffraction, Fig. 5, we can estimate analytically the size of pinhole apertures with smallest PSF: 9-14 um. This is why we prefer to work with pinholes of apertures of 10x10 um, and have other aperture sizes for cross-checks.

Accurate characterization of the pinhole PSF is essential for the transverse beam size and emittance calculation. The PSF can be calculated by three different methods: analytically (Eqs. (1-3)), experimentally and by numerical simulations. Until recently, the PSF has only been calculated analytically for pinhole in FE34 [3]. Now with the addition of another pinhole, it became necessary to compare the analytical calculations with the experimental results and simulations.

We have concluded that three methods of PSF calculation are consistent [4], and mapped PSF values against true pinhole apertures and Cu thickness for each pinhole:

$$\mathrm{PSF}(t,w) = \begin{cases} \mathrm{PSF}_{\mathrm{Al}}, & \text{if } t < 0.1\ \mu\mathrm{m} \\ \frac{A(w)}{t} + B(w)t + C(w), & \text{if } t \geq 0.1\ \mu\mathrm{m} \end{cases} \tag{5}$$

where $\mathrm{PSF}_{\mathrm{Al}}$ is PSF of Al window itself without the filter, and t is copper thickness corresponding to the beam spot location on the YAG (see next Section). The fit coefficients A, B, C are different for each w and front-end.

Using this parametric function Eq. (5) we can calculate PSF for any pinhole aperture and Cu filter position, once we know them, and correct our beam size measurements in Eq. (4).

Copper Filter

The copper filter is a wedge-shaped block (a tall right trapezoid) in front of a pinhole grid, Fig. 2. By sliding in/out the block, we are choosing different Cu thickness, and hence control the flux (more Cu – harder X-rays). It also plays several very important roles: 1) reduce heat load on the pinhole grid and renders unnecessary any additional cooling, 2) help avoid CCD image saturation, and 3) produce a monochromatic light to avoid possible chromatic effects.

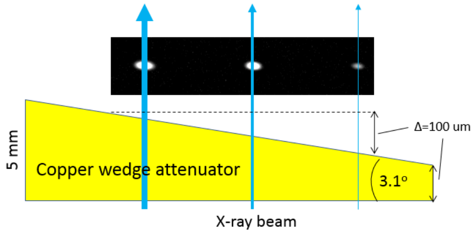

Figure 6: Relation between the Cu filter position and beam spots on the CCD image: each spot receives X-ray flux passed through different Cu thickness (not to scale).

Both the filter and the pinhole grid can move laterally independently of each other. Figure 6 demonstrates that each beam spot receives a different amount of flux depending on mechanical positions of the pinhole grid and Cu filter, so each spot requires a slightly different PSF for correction. The difference in copper thickness between extreme horizontal pixels of the image is around 100 um: comparable to minimum thickness of the filter itself, so it is not negligible.

Since positions of the filter and pinhole grid motors are known, they can be mapped against each other and against the horizontal pixel coordinates of the fixed CCD image (vertical is irrelevant here) to keep track of the pinhole apertures and Cu filter thickness in view of the CCD. This way we can relate any beam spot centroid with w and t.

Now, using w and t for the PSF input, we can move on to actual ANN training and image analysis.

COMPUTER VISION FOR BEAM DIAGNOSTICS

This chapter is is work in progress. It talks about intermediate results obtained after recent pinhole upgrades at ALBA. No other computer vision applications have been developed for Beam Diagnostics at the time of this work.

In order to have automated beam tracking from image stream the software needs to recognise the beam spots, whether Gaussian shapes or any general blobs distinct from the background. It requires supervised learning to classify objects (e.g. beam spots) and must be trained on a set of prepared samples that contain necessary classifiers (i.e. known objects with names). One of the appropriate algorithms at the time of this study appeared to be YOLOv3 [5] with TensorFlow v2.4 [6] backend.

YOLO stands for *You Only Look Once* and it is a handy real-time object detection system based on convolutional ANN which looks at the whole image at once and predicts bounding boxes with classifiers. Its main advantages are speed and model size: a well-trained model is able to detect multiple objects from a live video stream.

For our purposes we train a YOLO model on a single classifier “beam”, since we don’t have other significant objects seen by pinhole CCDs.

In machine learning each model is a hypothesis that predicts a value given a set of input values. The model has a set of weights which are tuned based on a set of training data. A loss function is used to determine how far the predicted values deviate from the actual values in the training data. Training a model is about tuning the model weights by the algorithm to make the loss minimum.

For training a model from scratch a dataset of 300 random 2D Gaussian distributions that resemble beam spots (100×100 px images) is generated along with annotations. Another 50 images are added as a control dataset.

Already with this minimal recommended dataset size, training a working model is feasible without paralleling: on a 3 GHz desktop PC a first "good" model already shows up after 20 learning epochs, with each epoch lasting under 2 hours of CPU time.

Figure 7 shows loss value evolution during iterative training and an average number of detected "beam" objects (6 is

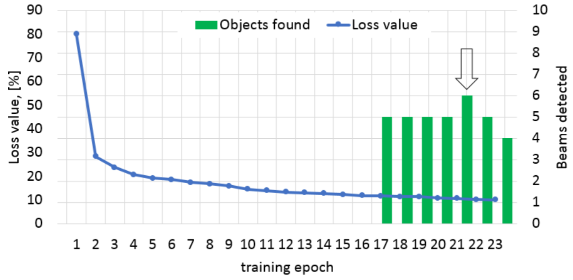

Figure 7: Loss value evolution during iterative YOLO model training vs. max beam objects found by several last models. The "smartest" model of the set is highlighted.

the maximum, Fig. 4). Figure 8 shows the result of using the "smartest" model to detect "beams" on a single CCD frame.

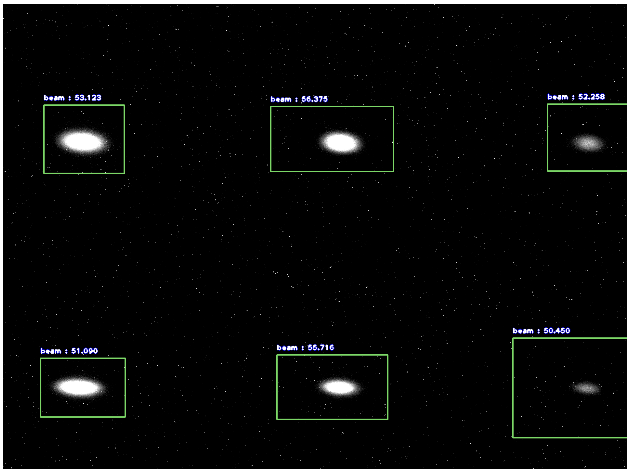

Figure 8: A single pinhole CCD frame with 6 beam spots detected by a trained YOLO model.

Automatic detection of beam spots is half of the desired functionality. Another half is the efficient and robust automatic numerical analysis of those spots. Using dynamic PSF calculator for every detected beam spot we fit them with the 2D Gaussian function and apply corrections: remove PSF contribution, magnification, and finally scale px to mm to get accurate electron beam size, emittance and coupling.

Figure 9 demonstrates very successful results of using the developed system to track beam coupling changes. Here the ANN is looking at the same beam spot (FE34 top row and FE21 bottom row) while the coupling factor changes from small (0.15%), to nominal (0.6%) to high (1.4%). The images are processed at 0.5 fps on a laptop and all output values (beam size, tilt angle, coupling, etc.) are accurate and expected, similar to the ones obtained manually before.

CONCLUSION

We have built a working and accurate real-time beam tracking and image analysis software system based on machine learning. The developed system works at the speed of around 0.5-1 fps on a standard PC, which is already feasible for some machine studies in real-time.

The detection system still has to be studied to deal with several important challenges, e.g. improving the detection score, and speed up to at least 3 Hz. It is also clear, that a "smarter" model can be trained, and it requires better learning data, longer training time, and powerful parallel hardware to learn (CPU->GPU->HPC).

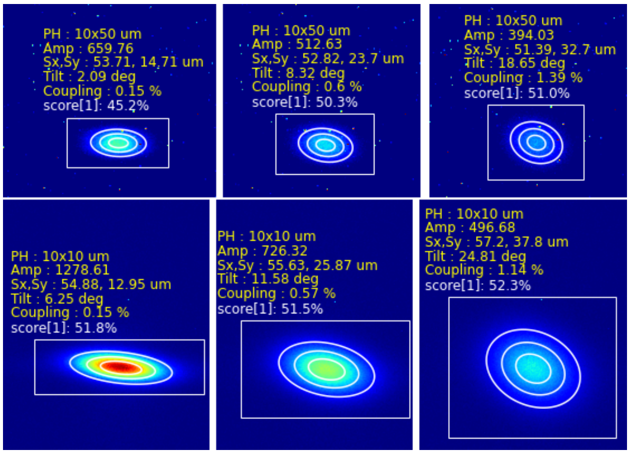

Figure 9: Tracking the same beam spot in both pinholes while changing the coupling factor along the storage ring.

Moreover, the reality and variety of operational conditions, beam experiments and anomalies show that beam spots on the YAG screen can vary a lot in shape, size, position and brightness. Training a model only on artificial 2D Gaussians may not produce clever enough image recognition model.

Alternatively, the model can be reinforced with a real image dataset (»300 samples), but the task of annotating every beam object on hundreds of images is massive, must be done by hand (e.g. with **LabelImg** python tool). However, it may be worth the effort in pursuit of full automation.

ACKNOWLEDGEMENTS

The authors would like to express their thanks to Ingrid Mases Solé and Alba Cazorla for meticulousness and persistence in tackling PSF studies, and Dominique Heinis for priceless help on ANNs.

REFERENCES

[1] A. Wu Chao, M. Tigner, *Handbook of Accelerator Physics and Engineering*. World Scientific. 1998.

[2] V. Suller, “An X-ray Pinhole Camera Design for the ALBA Synchrotron Light Source”, April 2005.

[3] U. Iriso, “Beam Size and Emittance Measurements using the ALBA Pinhole”, Barcelona, Spain, ALBA Internal Note AAD-SR-DI-PINH-01, June 2011.

[4] Ingrid Mases Solé, “Characterization of the PSF for the X-ray pinhole cameras at ALBA Synchrotron”, Treball de Fi de Grau, Facultat de Física, Universitat de Barcelona, 2020.

[5] Redmon Joseph, Farhadi Ali, “YOLOv3: An Incremental Improvement”, arXiv, 2018. `https://pjreddie.com/darknet/yolo`

[6] Martín Abadi *et al.*, “TensorFlow: Large-Scale Machine Learning on Heterogeneous Systems”, 2015. `https://www.tensorflow.org`

FAST SCANNING DIAMOND DETECTOR FOR ELECTRON BEAM PROFILE MONITORING*

V. V. Konovalov†, Applied Diamond, Inc., Wilmington, DE, USA
T. Miller, S. Bellavia, C. Brutus, P. Thieberger, and R. Michnoff,
Brookhaven National Laboratory, Upton, NY, USA

Abstract

The first prototype of a fast scanning diamond beam profile detector (DBPD) suitable for invasive high power CW electron beam core profile measurements in transmittance mode was developed. It consists of a multi-strip solid state diamond detector to scan with high speed (up to 1 m/s) and precision (about 5 μm) through the core of an electron beam. The diamond sensor was made from a thin polycrystalline diamond (PCD) plate with highly B-doped diamond conductive strips both grown by CVD. Transient currents from the multi-strip detector were measured with fast digitizing electrometers. Successful operation of the DBPD was demonstrated for pulsed (5 Hz) and CW (78 kHz) CeC beams, including the detector's ability to withstand a 20 sec insertion into the CW CeC beam core. The X-Y beam spatial profile was measured in one scan. Thermal modelling demonstrated a manageable thermal impact even from a relatively long insertion of the diamond sensor into the CW CeC core and very short (0.2 s) insertion into the CW LEReC beam core. Electrical impedance modelling of the detector and vacuum chamber assembly demonstrated minimal impact on beam line impedance with diamond sensor insertion.

INTRODUCTION

Recently, novel electron cooling systems for ion beams are being developed at Brookhaven National Laboratory, such as the Low Energy electron Cooling (LEReC) system, the first electron cooler without any magnetization, designed to maximize collision rates at the lowest energies available at the Relativistic Ion Collider (RHIC) [1], and the ongoing Coherent electron Cooling (CeC) Proof off Principle (CeC PoP) experiment, currently installed in the RHIC tunnel [2]. LEReC system produces 704 MHz electron bunches, modulated at 9 MHz to overlap Au-ion bunches, with 1.6 - 2.6 MeV electron energies and the beam power ranging from 10 to 140 kW. In the CeC experiment, the electron beam is produced by an electron gun followed by superconducting cavity and a 704 MHz superconducting LINAC producing a 15 MeV electron beam at up to 78 kHz repetition rate.

Efficient electron cooling requires a high quality, high power electron beam with tight parameters (energy and space trajectory). In order to achieve and maintain the required parameters and stability of the electron beam, its parameters have to be continuously monitored and feedback control has to be developed [3]. Interference of beam diagnostic instrumentation with the beam may lead to degradation of beam parameters therefore, invasive and non-interceptive methods of monitoring are preferred. Invasive beam monitoring can be achieved by using highly transparent detectors made from low-Z materials absorbing < 1% of beam energy. However, existing detectors, e.g. wire scanners, are not suitable for invasive profile measurements of powerful continuous wave (CW) electron beams. As a result, the beam profile of these beams is currently monitored in low repetition pulsed mode and assumed to remain the same in CW mode. Common wire scanners have a rather short life-time even when used for pulsed beam monitoring. Their very thin wires are easily overheated and burned, thus contaminating the beam pipe with debris.

Diamond's unique combination of material properties: low energy absorption, tremendous radiation tolerance, ability to dissipate significant heat load, and stability of electronic properties over a wide temperature range, makes it an ideal material for high energy applications. Diamond radiation detectors (DRD) have been used for detection of many types of radiation demonstrating fast time response, high radiation stability, and ability to operate at high temperatures without cooling. DRDs have much longer lifetimes compared to radiation detectors made from other materials like silicon or plastic. Also the signals from gas-filled ion chambers and silicon detectors saturate under high-flux conditions. DRDs are an established technology as beam condition monitors in the highest radiation areas of all Large Hadron Collider experiments [4]. DRDs are used as X-ray beam position monitors for multiple synchrotron radiation and free electron laser sources, including NSLS-II at BNL [5], SOLEIL [6], and CEA at Saclay [7]. DRD was been used with a powerful 90 W/mm^2 white X-ray beam and demonstrated 11 orders of magnitude flux linearity and stable response over an 18 month time period [8]. DRD for electron beam profile and halo monitoring was developed and successfully tested for the XFEL/SPring-8 as a part of a system to protect undulator permanent magnets from radiation damage [9].

The first prototype of a fast scanning diamond beam profile detector (DBPD) suitable for invasive high power CW electron beam core profile measurements in transmittance mode has been developed and fabricated. Its research and development in significant degree was focused on future installation into the high power CeC and LEReC beamlines at BNL and the detector design was tailored to the corresponding BNL requirements. Numerical modeling demonstrated that the DBPD prototype is suitable for direct

---

* Work supported by DOE SBIR under grant No. DE-SC0020498 (AD) and by BSA under DOE contract DE-AC02-98CH10886 (BNL).
† Email address: val@ddk.com.

Table 1: Electron Beam Parameters

Beam	Diamond thickness (µm)	Electron Energy (MeV)	dE/dx (MeV cm^2/g)	Beam Current (µA)	Beam σ_x (mm)	Beam σ_y (mm)	Max absorbed power density (W/cm^2)	Absorbed power (%)
CeC	100	15	1.741	78	3	3	8.38	0.41
LEReC	100	2	1.568	35500	2.64	8.55	95	2.75

core beam profile measurements of the powerful CW mode CeC and LEReC beamlines. The DBPD prototype has been tested at the ATF and CeC electron beamlines at BNL.

DESIGN OF DIAMOND DETECTOR

The mechanical design of the DBPD is shown in Fig. 1 and includes a vacuum chamber and a high speed actuator. Existing pneumatic actuators may provide the required high speed, but they lack speed stability, positioning accuracy and reproducibility. We used the 1 m/s hard shaft motor driven actuator with bellows developed by Ultra High Vacuum Design. Testing of the actuator demonstrated good constant speed over 60 mm travel, only 0.42% speed variation at 1 m/s, and good repeatability. The actuator was equipped with a custom feedthrough with an embedded Cu rod and 12 SMB coaxial connectors. In the initial position the diamond sensor is fully retracted from the beam pipe and at the lowest travel position is fully inserted into the beam core near the center of cube, see Fig. 1.

The diamond sensor consisted of a 48x19x0.15 mm detector-grade PCD plate with embedded 10 vertical and one horizontal conductive strip-lines. Highly B$^+$-doped CVD diamond layers were grown on both sides of the intrinsic PCD plate. Then, on one side the boron layer was masked and RIE/ICP etched to form the strip-lines. The PCD plate was then brazed to a tungsten carbide support attached to the Cu rod (19 mm diameter, 20 cm long). The massive Cu rod provided a good heat sink for the thin diamond sensor.

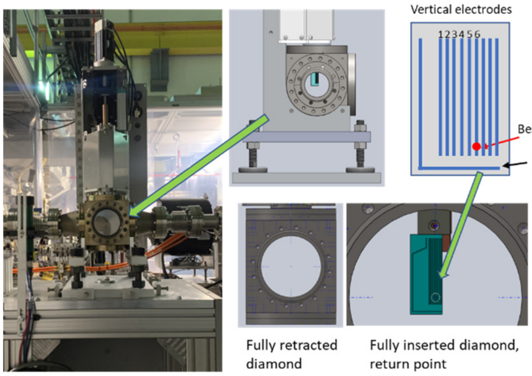

Figure 1: Diamond detector assembly installed at the CeC beam-line and its schematics.

NUMERICAL MODELING

Thermal Impact from High Power CW Electron Beams

Numerical modeling of the thermal impact on the diamond sensor from high power CW beams was performed on a 3D mechanical model, see Fig. 2b, with ANSYS 2020 R1 software. The geometry of the diamond sensor was modeled with a fine element mesh (total 14,728 elements, comprised of 100,856 nodes). The modeling was performed for a number of cases: CeC and LEReC beams, normal and 45° tilted position of the diamond plate to the beam, static position and motion, and two types of metal substrates supporting the diamond sensor. Electron beam parameters and calculated absorbed beam energy are presented in Table 1, and material properties used in modeling are presented in Table 2.

Table 2: Material Properties

Material	Thermal Conductivity (W/m-K)	Density (kg/m^3)	Specific Heat (J/kg-K)
PCD	1200	3515	502
WC-Co	49.6	15600	183
Copper	401	8300	385

CeC Beam

Thermal modeling of a stationary and moving diamond sensor has been performed for CeC beam, see Fig. 2 for geometry and motion profile, corresponding to the maximum 1 m/s actuator speed and the stroke of 45 mm. Ambient temperature (25 C) was placed at the end of the copper rod further from detector. In stationary position sensor doesn't move and beam is turned on at zero time.

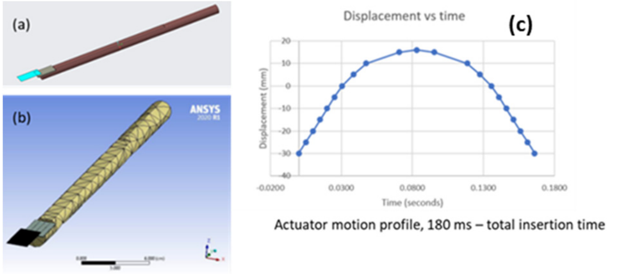

Figure 2: Geometry of diamond sensor brazed to the WC-Co and mounted on Cu rod (a), its fine element mesh (b), and motion profile of diamond sensor (c).

Temperature distribution for stationary sensor position is shown in Fig. 3 at 0.127 s after the beam was turned on and for the achieved steady state. The corresponding time dependence of the maximum temperature on the diamond is shown in Fig. 4. The steady state condition with maximum temperature of about 100 °C is reached at about 10-20 sec. The transient maximum temperature for the motion profile (see Fig. 2c) is shown in Fig. 5. The maximum temperature of 30 °C occurs at about 40 ms and then within several seconds return to the ambient. The maximum steady state temperature for 45° tilted sensor was about 17 °C higher. The replacement of tungsten carbide support substrate to copper substrate, having the higher thermal conductivity, results in a small decrease of temperature by about 10 °C.

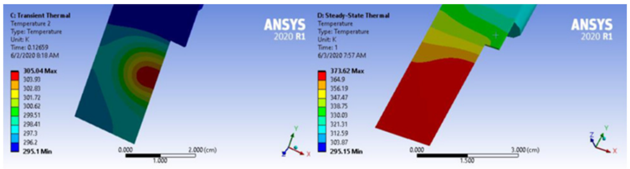

Figure 3: CeC beam, temperature profile at 0.127 s after the beam was turned on (left) and final steady state (right), beam normal orientation.

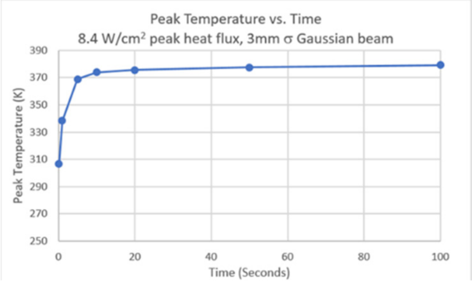

Figure 4: Maximum temperature time dependence after the beam was turned on.

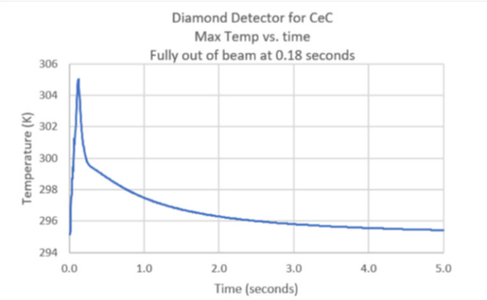

Maximum temperature occurs ~ 40 ms after full insertion

Figure 5: CeC beam, transient state with sensor motion. maximum temperature of diamond for the motion profile on Fig. 2c.

LEReC Beam

The transient temperature profile for much more powerful LEReC beam was also calculated for the motion profile shown in Fig. 2c. The temperature map at short times is shown in Fig. 6 and the time dependence of maximum temperature is shown in Fig. 7. In this case of LEReC beam the maximum temperature of about 370 °C occurs at about 140 ms and then similarly to CeC returns to the ambient within 5 seconds.

Electrical Response and Effect of Ferrite Addition

The vacuum chamber electrical response to the CeC beam was modeled using Particle Studio for the cases with and without additional ferrite installed into the vacuum chamber. The results are shown on Fig. 8 and demonstrate that even one ferrite is very effective in attenuating the oscillations. The oscillations are not the wake field but the electrical oscillations of the sample holder. If the bunch frequency is 78 kHz, there is enough time for these oscillations to decay before the next bunch arrives, even without the ferrite.

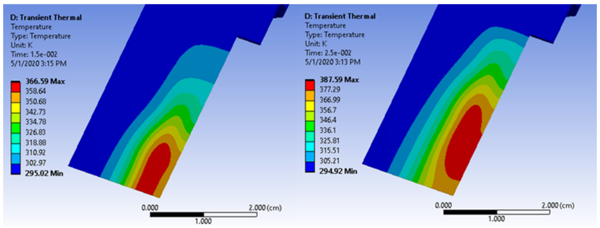

Figure 6: LEReC beam, temperature profile at 15 ms insertion time (left) and 25 ms time (right), beam normal orientation.

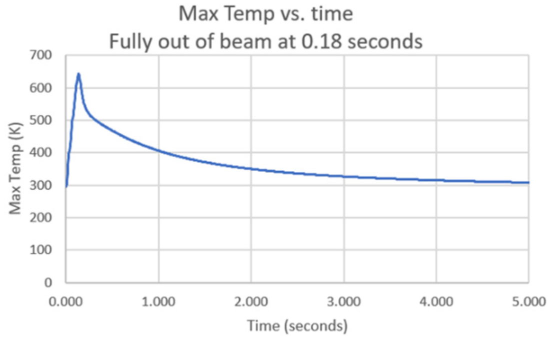

Figure 7: LEReC beam, transient state with sensor motion. Maximum temperature of diamond sensor for the motion profile in Fig. 2c.

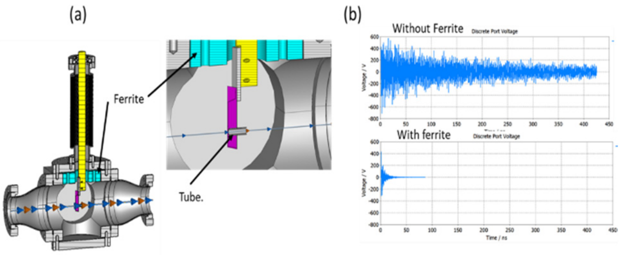

Figure 8: Simulation of the electrical response for the diamond detector system. (a) 3D model of detector system, tube was used to simulate the interaction of the beam with the target; (b) Detector voltage plots with respect to ground for 5 nC, 100 ps FWHM bunches, with and without ferrite.

CeC BEAM TEST

The DBPD was installed close to the beam dump of the CeC diagnostic beam line to minimize radiation from scattered electrons impacting the beam pipe. CeC beam test (about 30 pC per bunch) was performed at 5 and 78 kHz repetition rates. Diamond sensor was moved into the beam pipe line from a fully retracted position, inserted into the beam core for 20 sec, and retracted back. Thus, only half of the beam profile was measured. Digital electrometers used for transient current measurements (2 x F460, 8 total channels, 16 bit, 250 kHz, Pyramid Tech. Cons.) were not

ISBN: 978-3-95450-230-1 ISSN: 2673-5350 doi:10.18429/JACoW-IBIC2021-TUPP30

synchronized with electron beam pulses which resulted in multiple missed pulses. Acquisition time constant of the electrometers was 0.1 s. Electrical bias of the diamond sensor was 0 V, and diamond thickness was 150 µm.

The diamond detector was fully operational under its full insertion into the 78 kHz CW CeC beam core for up to 20 sec. Transient currents (up to 2000 pA) were detected from the horizontal electrode and all six vertical electrodes. The horizontal beam profiles measured by vertical electrodes and vertical beam profile measured by horizontal electrode, are shown in Figs 9 (5 Hz) and 10 (78 kHz). The vertical beam profile at 78 kHz shows an approximately 3 mm wide core well corresponding to the expected the CeC beam width (see Table 1), but it shows very narrow vertical profile at 5 Hz. The horizontal beam profile demonstrates rather unusual double beam cores with second core at channel 4 (5 Hz) and channel 3 (78 kHz). Both observed effects, a narrow vertical beam profile at 5 Hz and double corers, could be the artefacts resulting from low signal intensities at 5 Hz due to the poor signal synchronization, and different strip's sensitivity to the radiation. Thus, the strip's sensitivity to the electron beam must be calibrated before the measurements, e.g. by sweeping the standard narrow radiation beam onto each strip and comparing their responses. Additional tests with higher detector sensitivity (the use of bias voltage will increase the detector signals > 10 times), proper synchronization, and more detector's strips may clarify the observed beam profile data.

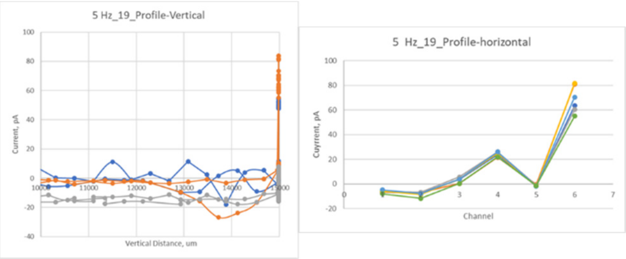

Figure 9: Vertical (left) and horizontal (right) beam profiles for pulsed (5 Hz) CeC beam mode.

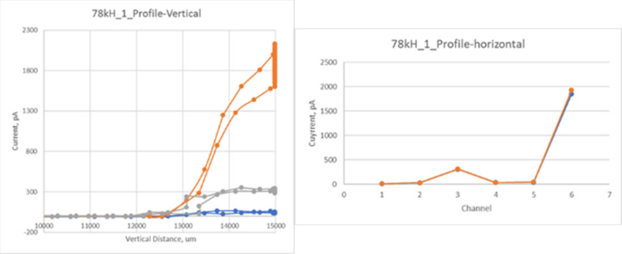

Figure 10: Vertical (left) and horizontal (right) beam profiles for CW (78 kHz) CeC beam mode.

Note, that a 20 s long insertion of diamond sensor into the CeC beam core produced high levels of secondary radiation likely caused by the electron beam interactions with the diamond sensor itself and/or produced by scattered electrons interacting with downstream sections of the beampipe.

CONCLUSIONS

- For the 78 µA CW CeC beam, the steady state condition with a maximum temperature of about 100 °C is reached at about 10-20 sec after the beam is turned on. At the maximum actuator speed, the total insertion/removal time of the sensor could be as small as 180 ms. In this case the maximum temperature of 30 °C occurs at about 40 ms and then returns to the ambient within 5 s.
- For the 35.5 mA CW LEReC beam, at the maximum actuator speed the maximum temperature of about 370 °C occurs at about 140 ms and then, similarly to the CeC, returns to the ambient within 5 seconds.
- The first prototype of a fast scanning diamond beam profile detector suitable for invasive high power CW electron beam core profile measurements in transmittance mode was developed and successfully tested with pulsed (5 Hz) and CW (78 kHz) CeC beams.
- Transient currents from the multi-strip diamond detector were measured with fast digitizing electrometers and XY beam profile can be obtained in one scan.
- The limitation imposed by the diamond detector installation close to the beam dump of the CeC beam line to minimize radiation from scattered electrons impacting the beam pipe needs to be considered for any future applications.
- Scattering of the electrons in the diamond sensor causes most of the beam to be lost on the walls of the beam pipe over a few meters downstream of the detector. The beam interruption and excessive amount of secondary radiation produced could be mitigated in the future by much shorter insertion times or by avoiding full insertion when only beam halo measurements are of interest. The secondary radiation from diamond sensor can be effectively shielded as well.

REFERENCES

[1] A.V. Fedotov *et al.*, "Experimental demonstration of hadron beam cooling using radio-frequency accelerated electron bunches", *Phys. Rev. Lett.*, vol. 124, p. 084801, 2020.

[2] V. Litvinenko *et al.*, "Coherent Electron Cooling Experiment at RHIC: Status and Plans", in *Proc. 12th Workshop on Beam Cooling and Related Topics (COOL'19)*, Novosibirsk, Russia, Sep. 2019, pp. 35-40. doi:10.18429/JACoW-COOL2019-TUZ01

[3] S. Seletskiy *et al.*, "Status of the BNL LEReC Machine Protection System", in *Proc. 7th Int. Beam Instrumentation Conf. (IBIC'18)*, Shanghai, China, Sep. 2018, pp. 249-252. doi:10.18429/JACoW-IBIC2018-TUPA17

[4] W. Trischuk, "Diamond Particle Detectors for High Energy Physics (RD42)", *Nucl. Particle Phys. Proc.*, vol.273–275, pp.1023–1028, 2016.

[5] E. Muller, "Transmission-mode diamond white-beam position monitor at NSLS", *J Synchrotron Radiat.*, vol. 19, pp. 381–387, 2012.

[6] K. Desjardins, M. Bordessoule, and M. Pomorski, "X-ray position-sensitive duo-lateral diamond detectors at SOLEIL", *J. Synchrotron Rad.*, vol. 25, pp. 399-406, 2018.

ISBN: 978-3-95450-230-1 ISSN: 2673-5350 doi:10.18429/JACoW-IBIC2021-TUPP30

[7] P. Bergonzo, D. Tomson, and C. Mer, “CVD diamond-based semi-transparent beam position monitors for synchrotron beamlines: preliminary studies and device developments at CEA/Saclay”, *J. Synchrotron Rad.*, vol. 13, pp. 151-158, 2006.

[8] J. Bohon, E. Miller, and J. Smedley, “Development of diamond-based X-ray detection for high-flux beamline diagnostics”, *J. Synchrotron Rad.*, vol. 17, pp. 711–718, 2010.

[9] H. Aoyagi *et al.*, “Pulse-mode measurement of electron beam halo using diamond-based detector”, *Phys. Rev. ST Accel. Beams,* vol. 15, p. 022801, 2012.

DESIGN AND NUMERICAL INVESTIGATIONS OF SCINTILLATION BEAM LOSS MONITOR FOR PolFEL*

R. Kwiatkowski[†], M. Krakowiak, S. Mianowski, R. Nietubyc, J. Szewinski
National Centre for Nuclear Research, Otwock, Poland
A. Wawrzyniak, National Synchrotron Radiation Centre SOLARIS, Krakow, Poland

Abstract

The Beam Loss Monitor (BLM) system is used mainly for machine protection and is particularly important in the case of high energy density of accelerated beam, when such a beam could lead to serious damages in the case of uncontrolled loss. Operational parameters of PolFEL linear accelerator induced needs to install and operate the BLM system. The BLM concept for PolFEL is based on several scintillation probes placed along the linear accelerator. The paper reports on numerical investigation of electron and X-ray radiation induced during fast electron losses. We also present design of BLM detectors and results of first tests of a prototype on the linear electron accelerator at Solaris research centre.

INTRODUCTION

The main purpose of Beam Loss Monitoring (BLM) system is to detect events of charged particle escaping from its designated path (beam pipe). Such a system, while not being coupled directly with the particle beam, is important from the point of view of machine protection. While above feature is crucial for facilities with high beam current and energy density, ability to detect interaction of particles with accelerator components, could also be used to indirect control of beam position and alignment and fine-tuning these parameters, also for low-power devices.

THE PolFEL PROJECT

The Polish Free Electron Laser, PolFEL, is planned to be operational in the 2024. It is a superconducting FEL, based on the TESLA SRF technology, which could operate in continuous wave (cw) and long pulse (lp) mode. Electron beam, generated in all-superconducting gun will be accelerated by four cavities and then delivered to either THz-undulator, or further accelerated and delivered to VUV-undulator. After passing through undulators, the electron will be used for other experiments (e.g. Inverse Compton Scattering). The maximum electron energies for the beamlines, a THz/IR line and VUV line, are equal to 79 and 154 MeV, respectively. The most important parameters of PolFEL electron accelerator are listed in Table 1 [1, 2].

Table 1: The Parameters of Polfel Electron Beam (Maximal Values, Continues Wave Mode)

	Gun	VUV line	THZ line
Bunch charge [pC]	250	100	250
Repetition rate [kHz]	50	50	50
Bunch length [ps]	10	0.4	10
Beam energy [MeV]	4	154	79
Beam current [μA]	12.5	5	12.5
Beam power [W]	-	770	940

BEAM LOSS AND MACHINE PROTECTION

Beam losses, i.e. deviation of beams from designed path, could be divided into two main classes: regular losses and irregular ones.

Regular Losses

Regular beam loss occurs as a part of normal accelerator operation and are generally unavoidable. However, they are typically localized on the collimator or aperture limits. Such losses could be used for machine diagnostics, e.g. injection studies, tail measurements or lifetime limitations. For further details, see e.g. [3, 4].

Irregular Losses

Irregular or uncontrolled (fast) losses, could happen as a result of misaligned beam, leaks in vacuum system, or other failure of accelerator components. The beam hitting accelerator walls could lead to, e.g.: vacuum lost (in case of melting the vacuum vessel wall), radiation damage of sensitive components (electronics), quench in superconducting circuits (in case of excessive heat deposition by colliding beam). Monitoring of fast losses could also be used to diagnose problems around the machine, like vacuum leaks, obstacles or microparticles in the line.

BEAM LOSS MONITOR TYPES

The Beam Loss Monitor, which in principle is a detector of ionizing radiation, could be built of a different sensor types. The selection of appropriate system is based on several factors, amongst which we can distinguish:

- intrinsic sensitivity
- ease of calibration
- radiation hardness
- reliability, robustness
- dynamic range
- temporal resolution
- shielding properties

---

*The construction of PolFEL received funding from the European Regional Development Fund in the framework of the Smart Growth Operational Programme and Regional Operational Programme for Mazowieckie Voivodeship.

[†] email: Roch.Kwiatkowski@ncbj.gov.pl

- physical size
- cost
- saturation

There exist several different detector types used for beam loss monitoring, e.g.:

- gas ionization chambers (short- and long-ones)
- solid-state ion chamber (PIN diode)
- secondary emission monitor
- scintillation detectors
- Cherenkov detectors.

Each type of detector is characterized by specific properties, and detailed description of them could be found in the literature [3, 4].

BLM SELECTION AND DESIGN FOR PolFEL

Considering the abovementioned factors and taking into account the experience of various NCBJ groups we have decided to use plastic scintillation detector coupled with photomultiplier as a beam loss monitor detector. The features of such system, which made us choose abovementioned configuration are:

- high detection efficiency compared to other detector types
- high dynamic range and possibility to change it by selecting PMT voltage
- possibility of calibration using standard radiation sources
- availability in custom size and shape
- relatively low price
- additional failsafe checking using built-in LED.

Based on the numerical studies and preliminary experimental tests, we have designed BLM detector composed of H11901 miniature photomultiplier [5] and EJ-232 scintillator [6]. The main factors which decided on components choice were small size, fast timing, integrated HV supplier and voltage divider, and relatively low price. The prototype, build using these components, will be constructed and tested thoroughly on the available sources and accelerators at NCBJ and SOLARIS.

NUMERICAL INVESTIGATION

In order to assess the amount of radiation which could be expected during PolFEL operation and/or beam loss event, we have performed numerical studies of chosen design of BLM detector. The studies were performed using FLUKA (version 2021.2.1) Monte Carlo code. During the calculations, we have tested three geometry configurations of the detector vicinity. The detectors (cylinders made of Polyvinyl toluene, 8 mm in diameter and 10 cm in length), parallel to X-axis, were positioned at Z = 0 coordinates. Detectors were placed in Aluminum housing, with 6cm in diameter and 20 cm in length. The steel beam pipe, which represents vacuum pipe, with inner and outer diameters equal to 3.68 and 4.0 cm respectively, was parallel to Z-axis. At chosen position along the beam pipe, we placed solid cylindrical blocks of steel, to imitate magnets put on the beam pipe. The beam interaction point was put 50 cm in front of the magnet

The geometries used during calculations are presented in Fig. 1.

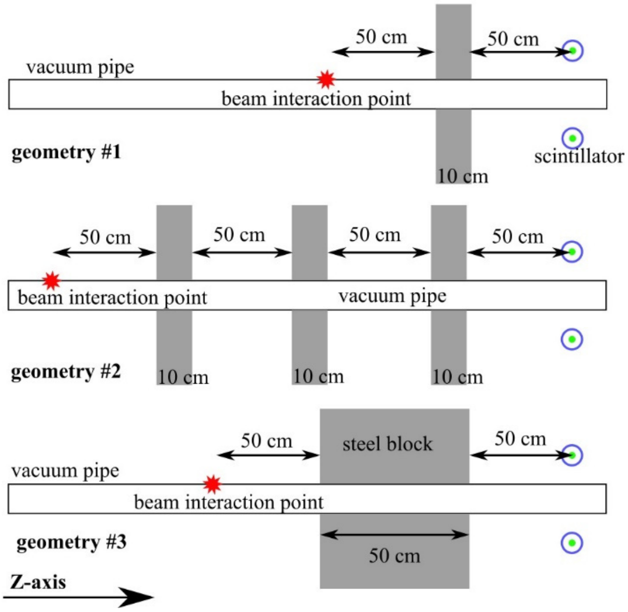

Figure 1: Geometries used during MC calculations. Three configurations of magnets position were used. The detectors, with size according to the design, are placed on the sides of the vacuum tube, parallel to the X-axis. The pipe is parallel with Z-axis. The source is positioned in the position, which ensures hitting the vacuum tube 50 cm in front of the last magnet.

The scored quantity was energy deposition in selected detectors, and energy deposition on the Cartesian grid, around the position of the detectors. The energy deposition spectra, calculated for selected scintillator, are presented in Figs. 2 and 3.

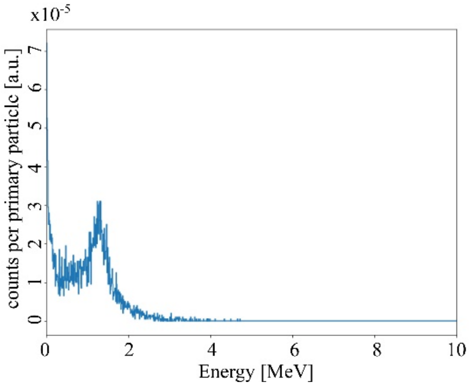

Figure 2: Energy deposition spectrum, calculated for chosen scintillator for geometry #1 and beam angle with respect to Z-axis equal to 10 mrad. Beam interaction point positioned symmetrically between the detectors.

ISBN: 978-3-95450-230-1 ISSN: 2673-5350 doi:10.18429/JACoW-IBIC2021-TUPP31

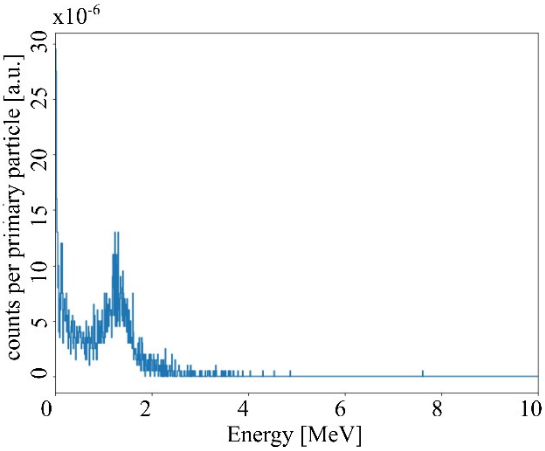

Figure 3: Energy deposition spectrum, calculated for chosen scintillator for geometry #1, beam angle with respect to Z-axis equal to 10mrad. Beam interaction point positioned on the opposite side of the detector.

For better visualization of beam interaction with surrounding, we have calculated energy deposition on Cartesian grid. Results of such calculations are presented on Figs. 4 and 5.

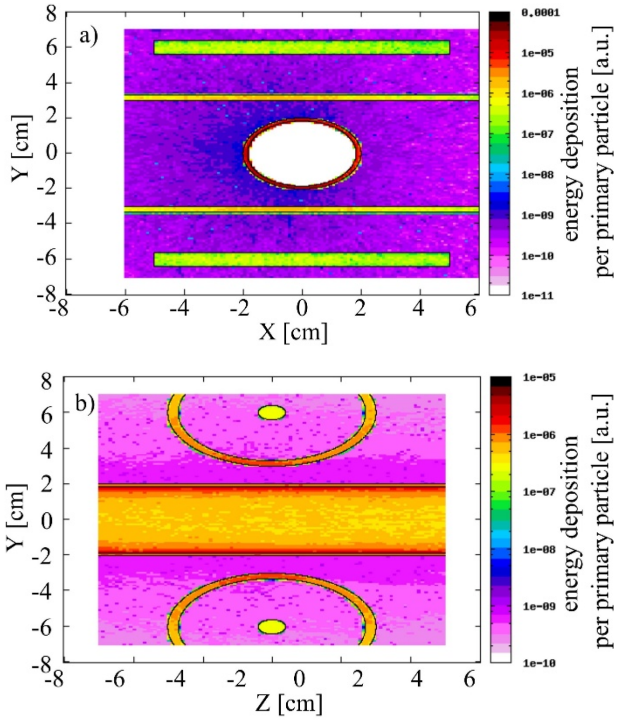

Figure 4: Energy deposition on Cartesian grid (a – XY plane, b – YZ plane). Beam interaction point positioned symmetrically between detectors.

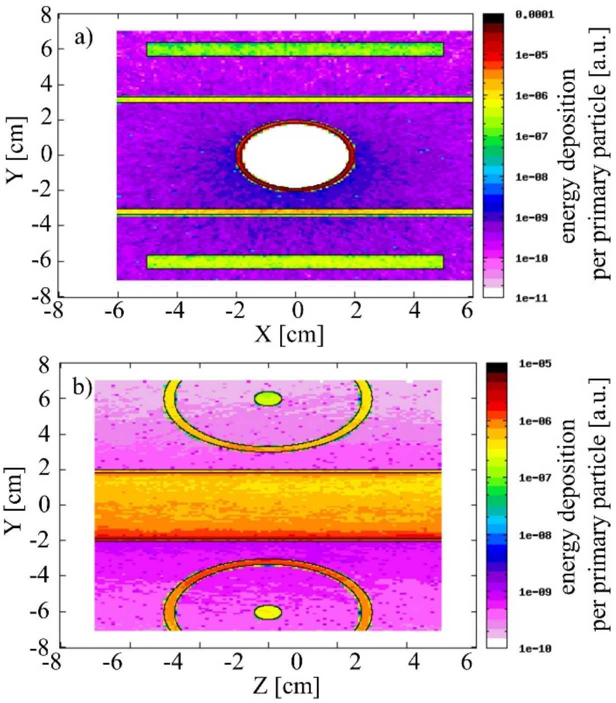

Figure 5: Energy deposition on Cartesian grid (a – XY plane, b – YZ plane). Beam interaction point positioned on the detector side.

PRELIMINARY EXPERIMENTAL TESTS

The first device, a so-called concept-prototype, was built to check the principles and operation of plastic scintillation detector at linear accelerator. The scheme of such detector is presented in Fig. 6.

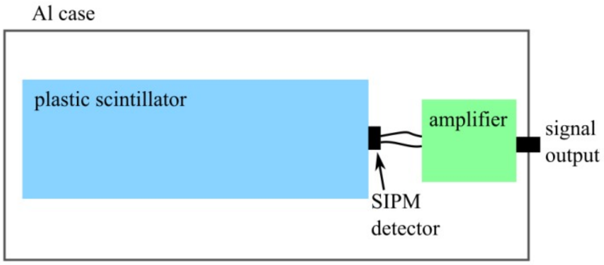

Figure 6: Scheme of concept-prototype version used during first tests at SOLARIS accelerator.

The concept-prototype version was constructed using materials already available in our laboratory, therefore it was considerable different from the prototype design. The device was tested both in our laboratory, using standard radioactive sources, and at SOLARIS linear accelerator. The signals were recorded using digital oscilloscope. Due to the built-in amplifier and fixed operational voltage of the detector, the registered signal was severely clipped. Nevertheless, it was possible to observe changes in signal width, which could be interpreted as an effect of increase in signal amplitude. The exemplary signal, recorded during operation of SOLARIS linear accelerator, is presented on Fig. 7.

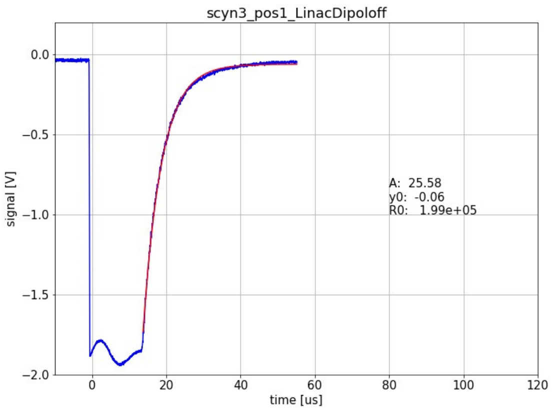

Figure 7: Exemplary signal recorded during tests at SOLARIS accelerator.

Blue line is the recorded signal, and red line represents exponential fitting. Fitting parameters are showed on plot. The results of preliminary tests lead us to conclusions, that we have enough signal and do not need large scintillator for monitoring the beam losses. The high dynamic range of photodetector is also important for the BLMs.

Based on the MC calculations and tests, we decided to build a new prototype, which follow the assumptions:

- small scintillator with length up to about 10 cm
- PMT photosensitive detector with integrated HV supplier
- placement of BLM detectors in several positions along linear accelelator, each of the detector will be calibrated and tested during initial phase of operation.

The new, improved design of BLM detector prototype, based on mentioned in previous section photomultiplier and scintillator (i.e. H11901 and EJ-232), is presented on Fig. 8.

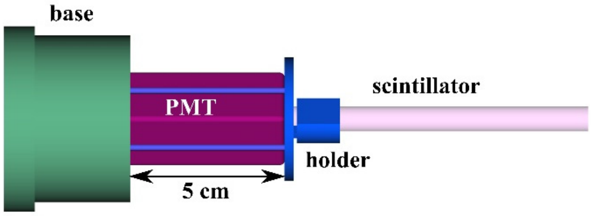

Figure 8: Scheme of new prototype version of BLM detector.

CONCLUSIONS

The Beam Loss Monitor system is important for the machine protection and beam diagnostics and control in large-, as well as small-scale accelerator facilities. The working parameters of PolFEL electron accelerator induce need to install and operate the BLM system. On the basis of numerical (Monte Carlo) calculations and experimental test, we have designed a prototype BLM detector for PolFEL, which uses fast plastic scintillator coupled with miniature photomultiplier. The further investigation, both experimental and numerical, of designed prototype is the next step of BLM system development for PolFEL facility.

REFERENCES

[1] J. Sekutowicz, “PolFEL in context of other FEL facilities”, presented at Wilga 2019 Summer Symposium on Photonics Applications and Web Engineering, Wilga, Poland, May 2019, unpublished.

[2] J. Sekutowicz *et al.*, “Polish free electron laser: short technical description”, in *Proc. SPIE 11054, Superconductivity and Particle Accelerators 2018*, p. 1105405, 2019. `doi:10.1117/12.2526756`

[3] K. Wittenburg, “Beam Loss Monitors”, presented at CAS - CERN Accelerator School: Beam Instrumentation, Tuusula, Finland, June 2018, `https://arxiv.org/abs/2005.06522`

[4] Robert E. Shafer, “A Tutorial on Beam Loss Monitoring”, in *AIP Conference Proceedings*, vol. 648, p. 44, 2002. `doi:10.1063/1.1524391`

[5] `https://www.hamamatsu.com`

[6] `https://scionix.nl`

THE BEAM LOSS MONITORING SYSTEM AFTER LHC INJECTORS UPGRADE AT CERN

M. Saccani*, E. Calvo, W. Viganò, C. Zamantzas, CERN, Geneva, Switzerland

Abstract

The LHC Injector Upgrade (LIU) project aims to increase the available brightness of the beams and improve the efficiency of the whole accelerator chain. The Beam Loss Monitoring (BLM) system is a key element of CERN's accelerator instrumentation for beam optimisation and machine protection by producing continuous and reliable beam loss measurements while ensuring safe operation. The new BLM system for the LHC injectors aimed to provide faster measurements with a higher dynamic range, to install more detectors along the beamlines, and to give the operator more flexible use. A review will be given on the versatility provided by the system to cover requirements from various accelerators and their transfer lines, focusing on the measurements and the operational scenarios.

INTRODUCTION

CERN Accelerator Complex

The High-Luminosity LHC (HL-LHC) upgrade requires the injector chain to produce beams with higher brightness. The LHC Injector Upgrade (LIU) project aims to meet the beam performance in terms of reproducibility, availability, and efficiency [1]. This project consisted of building a new H- linac (i.e. Linac4) and renovating the accelerator chain: The Proton Synchrotron Booster (PSB), the Proton Synchrotron (PS), and the Super Proton Synchrotron (SPS), with all their transfer lines.

The upgrade of the Beam Loss Monitoring (BLM) system in the injectors (i.e. BLMINJ) is an integral part of the LIU program and serves two main purposes: first, to automatically protect the accelerator equipment from damage if it detects excessive losses, and second, to allow operators to observe in real-time losses and adjust machine parameters accordingly. The system development and installation took six years in total and included 322 detectors integrated along the beamlines between the Linac4 source and the SPS injection. This paper first describes the new BLMINJ system recently deployed, before focusing on the commissioning phase and the performance achieved.

BLMINJ SYSTEM ARCHITECTURE

In 2012, an architecture that met the BLMINJ specifications has been proposed [2]. The technical choices resulted in a generic, configurable and high-performance system, in addition to the reliability and availability expectations. The following sections describe the final design, the specification evolution, and the deployment solutions.

The BLMINJ system consists of detectors placed in strategic locations at the tunnel installation and Beam Loss Electronics (BLE) for acquisition & processing located on the surface buildings in a single rack per location, as shown in Fig. 1.

Detectors and Cabling

The BLM detectors are mounted outside the vacuum chamber and measure the secondary shower caused by stray particles interacting with the vacuum chamber walls or magnets. Sensitivity and detection efficiency depend on the size, technology, and positioning of the detector. The BLMINJ system accepts various types of loss monitors as input, all of which were characterised in detail in 2018 [3].

---

* mathieu.saccani@cern.ch

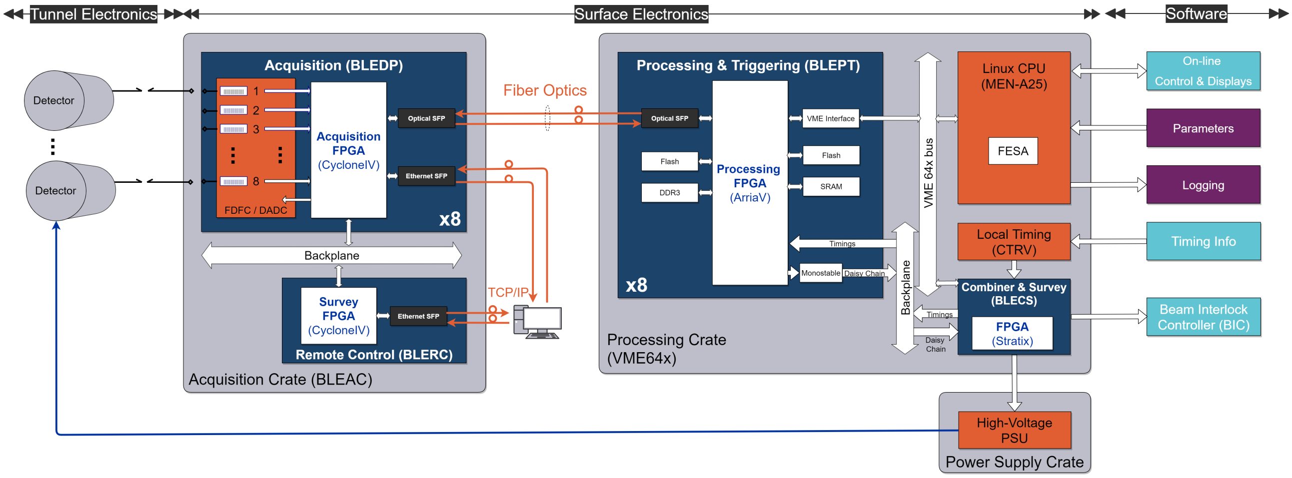

Figure 1: Schematic overview of the BLMINJ system architecture.

Two detector types, shown in Fig. 2, have been deployed:

- The Ionization Chamber (IC) - 50 cm long, 1.5 litres, nitrogen-filled - is already used in the LHC. It is optimised to give an ion collection time of 85 µs and is polarised at 1.5 kV.
- The Flat Ionization Chamber (FIC) is similar to the IC, but with a different geometry for space-constrained locations in the PSB.

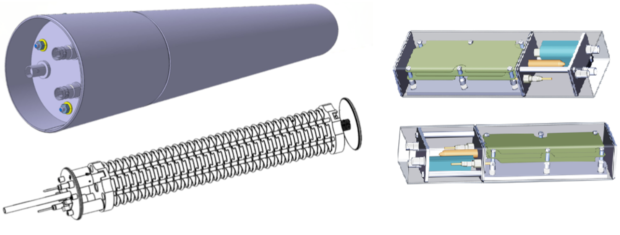

Figure 2: View of an IC (left) and an FIC (right).

A separate high-voltage cable connects the power supply to each detector for additional reliability and testability. Thus, periodic connectivity checks can accurately identify any faulty detectors. This test is currently manual and will be automated in the future.

The implemented cabling schema, shown in Fig. 3, offers the necessary noise immunity by comprising custom coaxial cables and triaxial connectors developed with industry partners.

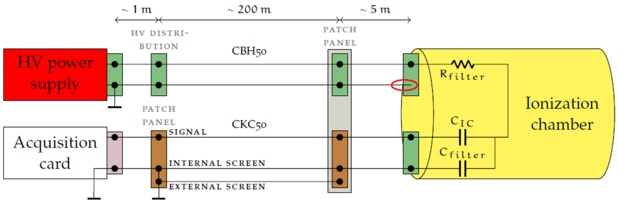

Figure 3: Schematic diagram of the cabling installation.

For the long transfer lines spanning more than one km, a different cabling architecture was deployed to reduce the number of cables in congested areas such as the PS Switchyard (SWY), where the Linac4, PSB, and PS transfer lines cross. A double-shielded multi-wire cable of nine differential pairs and a distribution box chain for nine channels, as shown in Fig. 4, allowed to reduce the installation cost in the long transfer lines while minimizing the number of cables needed.

Acquisition Electronics

The Acquisition Crate (BLEAC) has a custom-designed backplane that can accept up to 64 detector connections. The crate supports up to 8 acquisition modules, one remote-control module (BLERC) [4], and the main panel for system monitoring. The crate also allows to remotely inject a current individually to each channel via an external input or from an internal source via relay contacts. The design foresees the functionality of an automatic calibration sequence, which is planned as a future upgrade.

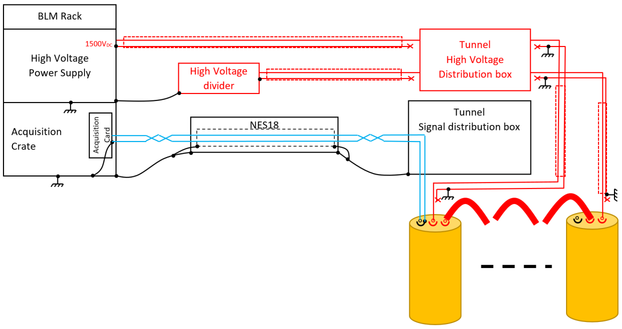

Figure 4: Multi-wire cabling architecture.

The dual polarity acquisition (BLEDP) board acquires, digitises, and transmits the input current from eight BLM detectors in parallel while offering a high level of reliability. The PCB of the board can connect detectors with positive or negative current polarities and ensures the input insulation for low SNR. Its power supply design prevents fault propagation through circuit breakers and current limiters.

Two measurement techniques cover the $2{\cdot}10^{10}$ input range by overlapping [5]:

- The first technique, called the *Fully Differential Frequency Converter* (FDFC), covers the low range from 10 pA to 10 mA. It uses a two-branch differential integrator and comparators to toggle the active branch via a switch. The on-board FPGA keeps count of the toggle pulses, whose frequency is proportional to the input current, and reads the fractional part with an ADC every 2 µs.
- The second technique, called the *Direct ADC* (DADC), covers the high range from 100 µA to 200 mA. Another switch routes the input to the ground, while the FPGA reads the voltage drop across a 3-Ohm resistor via the same ADC.

The FPGA manages the automatic switching between modes and the combination of signals [6]. Figure 5 shows the simplified block diagram of the digitisation circuitry. It generates a 20-bit sample for every 2 µs time period, which represents the beam loss accumulated during this period. A supervision module ensures that the acquisitions are performed correctly, to increase reliability. It allows several hardware parameters of the board, such as temperature, current consumption, and voltage levels, to be periodically monitored and sent to the processing board along with any errors and warnings detected.

Processing Electronics

The Versa Module Europa (VME) crate hosts several modules: a central processing unit (MEN-A25), up to eight Processing & Triggering boards (BLEPT), a timing receiver and a Combiner & Survey module (BLECS). The crate backplane is custom-built for the P0 connector to provide two daisy-chain links between the processing modules, general-purpose I/Os, broadcast lines to distribute timing events, and extra supply voltage outputs.

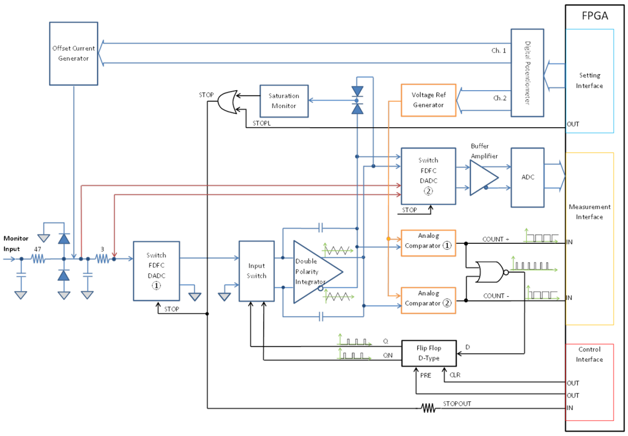

Figure 5: Mixed acquisition circuit.

The BLEPT module uses a new signal processing platform (VFC-HD), which underwent thorough testing and validation [7]. This board also contains an FPGA device that receives the data produced by the BLEDP, calculates different running sums, stores raw data in buffers, and publishes the results and status to the CPU.

The BLEPT keeps track of the user's cycle and the beam presence by using timing triggers and delivers accurate loss measurements to operators, such as the loss integration over beam presence, the evolution of losses along the cycle, one on-demand capture buffer with a resolution of 2 µs, or a global dose value for dosimetry. It can block the beam permit daisy-chain at any time if the measured losses breach a given threshold. This fully redundant hardware interlock function protects the machine by responding within a few µs and is designed to be failsafe.

The Combiner and Survey module (BLECS) is located at the last location of the beam permit daisy chain. If an error is detected in the electronics, the BLECS requests immediately a beam interlock to the Beam Interlock System [8]. In addition, it monitors the various power supplies and distributes timing signals, such as beam cycle or presence events, to each of the processing modules in the crate, as well as initiates the detector connectivity check.

Finally, the FPGA firmware for each of the three module types of the BLMINJ system is common for all machines, which eases debugging and maintenance, with the overhead of additional software configuration parameters. The BLM experts or operators perform and maintain the entire configuration through the CERN operational settings database. This firmware was extensively verified to increase the system reliability by testing individual submodules, including corner cases, random endurance scenarios, covering 100% of the source code, and using the Open Source VHDL Verification Methodology (OSVVM).

Software and Database

Each Front-End Computer (FEC) runs a local server instance, built using the Front-End Software Architecture (FESA) framework, that reads and publishes all the system parameters and diagnostics every 1.2 seconds. Additional functionality provided by the server is used by the operators to limit the radiation levels in the machine by blocking injections on the next cycle using a set of dedicated software thresholds and bad shot counters. This software-generated interlock source is latched until acknowledged and is unique per beam user and channel.

Users can analyse in real-time the data generated by the FESA class through expert applications or fixed displays in the control room. For instance, the PSB BLM vistar shown in Fig. 6 gives the total loss during the beam presence. Operators can also rearrange measurements by assigning detectors to virtual devices and obtain custom plots or scales.

At the PS ring, the system makes use of a concentrator to aggregate data from the two FECs monitoring this location and computes the global sum of losses to trigger a common interlock line.

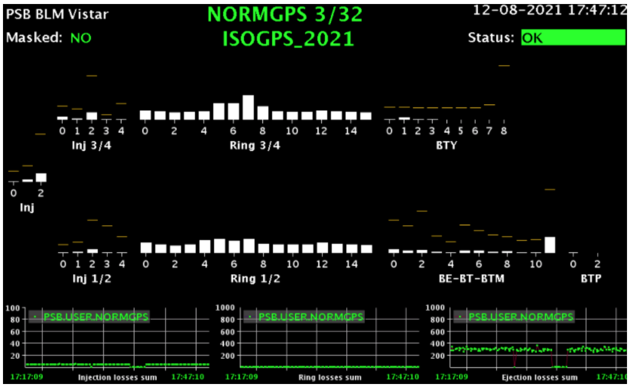

Figure 6: PSB BLM vistar and injection data.

BLMINJ SYSTEM COMMISSIONING

Deployment

The initial request from the CERN LIU management was to install the BLMINJ in Linac4 as a priority to validate this new machine. The BLMs for PSB, PS and their transfer lines have been installed during the long shutdown (LS2). A staged deployment mitigated the risks:

- A prototype with 64 channels was installed in the PSB in 2015.
- In 2016, 15 channels were deployed in Linac4 to start up the new accelerator.
- During the 2016 End-Of-The-Year Technical Stop, the system was fully installed in the PSB and PS rings, representing 164 channels.
- In 2018, 9 channels were added to the Linac4 transfer line to PSB.
- Finally, during LS2, all the remaining detectors were installed, especially in the transfer lines. The legacy BLM system – with 168 channels and 3 racks in PSB and PS – was decommissioned. The processing electronics of the new BLMINJ system were updated together with the firmware and software layers.

By the end of LS2 in early 2021, 322 channels had been deployed and 14 racks installed for a total of 51 pairs of acquisition and processing boards.

On the firmware and software deployment, an overhaul of three FPGAs was performed between the prototype and the final installation, enabling the migration to the new VFC-HD processing module. In addition, the use of common libraries eases maintenance and traceability, reduces development and debugging time, and makes the system more flexible and reliable.

Commissioning after LIU

The commissioning of the system followed three stages: Individual System Tests (IST), dry-runs, and beam tests.

The IST are time-consuming checks that verify the hardware lines from the detector to the electronics: checking each channel connection by modulating the power supply as shown in Fig. 7, and calibrating the acquisition (offset current, analogue threshold) to ensure that all channels have the same offset level, regardless of location and cable lengths.

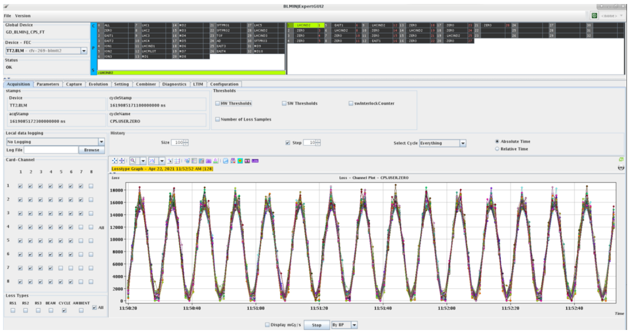

Global Device: GD_BLMINJ_CPS_FT
Device - FEC: TT2.BLM - cfv-269-blmtt2
Status: OK
Device: TT2.BLM
cycleStamp: 1619085171100000000 ns
acqStamp: 1619085172300000000 ns
cycleName: CPS.USER.ZERO
Local data logging: No Logging
Size: 100
Step: 10
Select Cycle: Everything
Losstype Graph - Apr 22, 2021 11:52:52 AM [128]

Figure 7: Modulation test of the detectors belonging to one sub-system visualised by the expert application.

BLM experts and operators performed the dry-run to validate the connection of the system to the controls infrastructure. The first test at this stage consisted in an overall high voltage modulation to ensure that all channels were publishing the acquired data to the operational applications. Then, beam interlocks were intentionally triggered to validate the entire chain from the BLECS to the Beam Interlock System (BIS). The correctness of the data logged in the measurement database was verified and the information shown on the fixed display values in the control room and the different expert applications were compared.

Finally, intentional losses were generated at each detector location to trigger the corresponding interlock and measure the value of the loss. This allowed to detect any remaining channel swap. In the long term, the total dose will be correlated with the dosimetry system installed in the tunnel and compared to previous years of operations.

This three-step commissioning was carried out rapidly during LS2 on each accelerator of the injector complex. First was the Linac4 in 2019, then the PSB and PS in 2020, and finally the SPS injection in early 2021. The focus is now on defining fine threshold values to better protect the machine while increasing beam availability for users.

System Performance

The acquisition resolution of the radiation loss depends on the predefined measurement period: when the time resolution is set to 2 μs, the smallest measurable dose is $1.19 \cdot 10^{-9}$ Gy. The measurement periods depend on the system requirements: 600 μs, 1 ms, and 1.2 s are used in the Injectors and correspond respectively to resolutions of $3.98 \cdot 10^{-12}$ Gy, $2.39 \cdot 10^{-12}$ Gy, and $1.99 \cdot 10^{-15}$ Gy.

RF cavity X-rays affect two detectors in the LINAC4-C section. The disturbance is deterministic; hence the BLM threshold was increased by the same offset.

Noise peaks generating saturation are observed at the PS Switchyard despite precautions against electromagnetic interference. The magnetic field of the nearby injection kicker magnet power cables couples to the BLM signal cables. A second source of disturbance, asynchronous to the beam, comes from the non-coaxial DC power cables of the magnets. An additional grounded metal braid can shield BLM signals from the electric field, but the distance between the cables must be increased to avoid magnetic coupling.

Dosimetry is checked on all machines in the CERN accelerator complex. The Radiation Monitoring and Calculation Working Group regularly cross-checks the deposited energy and the ambient radiation levels measured by BLMs against the simulation results from FLUKA, as well as the radiation monitor records and TIDs from fibre-optic dosimeters. The first outcome is very promising and shows a good correlation. Further measurements in the long term will confirm these results during the next run.

CONCLUSION

The commissioning of the Injectors went remarkably well, from the first beam in Linac4 up to the injection in the SPS. The new BLMINJ system played a key role in this success. All the electronics and most detectors worked from day one so that the protection and monitoring functions were always assured. Since the summer of 2021, the BLM phase has moved from commissioning to optimisation. For example, the effort is put to reduce EM interference in the SWY and transfer lines, refine the synchronisation triggers, and adjust the thresholds. In the future, more functionalities are expected to be added to further improve the flexibility and reliability of the system, with a target of 10^{-7} failures per hour. For instance, continuous functional supervision of the detector connection will be integrated [9]. A redundant optical link will be also added between the acquisition and the processing crates to remove this single point of failure. An Ethernet link will still be available when a suitable SFP module is plugged in, so that the BLEDP can be used in standalone mode, but the main Ethernet interface will be moved to the BLEPT where more SFP connections are available.

REFERENCES

[1] K. Hanke *et al.*, "Status of the LIU Project at CERN", in *Proc. IPAC'14*, Dresden, Germany, June 2014, pp. 3397–3399. `doi:10.18429/JACoW-IPAC2014-THPME070`

[2] C. Zamantzas, M. Alsdorf, B. Dehning, S. Jackson, M. Kwiatkowski, and W. Viganó, "System Architecture for Measuring and Monitoring Beam Losses in the Injector Complex at CERN", in *Proc. IBIC'12*, Tsukuba, Japan, Oct 2012, paper TUPA09, pp. 347–350. `https://jacow.org/IBIC2012/papers/tupa09.pdf`

[3] V. Grishin *et al.*, "A Family of Gas Ionization Chambers and SEM for Beam Loss Monitoring of LHC and Other Accelerators", in *Proc. RuPAC'18*, Protvino, Russia, Oct. 2018, pp. 44–48. `doi:10.18429/JACoW-RUPAC2018-TUZMH03`

[4] E. Calvo Giraldo, W. Viganó, and C. Zamantzas, "Remote Control Unit of the LHC In-jector Complex Beam Loss Monitoring System", *Topical Workshop on Electronics for Particle Physics, TWEPP2018*, Antwerp, Belgium, September 2018, pp.070. `doi:10.22323/1.343.0070`

[5] W. Viganò, M. Alsdorf, B. Dehning, M. Kwiatkowski, G.G. Venturini, and C. Zamantzas, "10 Orders Of Magnitude Current Measurement Digitisers For The CERN Beam Loss Systems", *J. Instrum.*, vol. 9, p. C02011, Feb. 2014. `doi:10.1088/1748-0221/9/02/c02011`

[6] M. Kwiatkowski, M. Alsdorf, B. Dehning, W. Vigano, and C. Zamantzas, "A Real-Time FPGA based Algorithm for the combination of Beam Loss Acquisition Methods used for Measurement Dynamic Range expansion", in *Proc. IBIC'12*, Tsukuba, Japan, Oct 2012, paper TUPA31, pp. 419–423. `https://jacow.org/ibic2012/papers/TUPA31.pdf`

[7] V. Schramm, M. Saccani, W. Viganò, and B. Bertsche, "Combined Testing And Validation Strategy For The New LHC BLM Processing Module", in *Proc. RAMS'19*, Orlando, FL, USA, Jan 2019, pp. 1-7. `doi:10.1109/RAMS.2019.8769268`

[8] B. Mikulec *et al.*, "Engineering Specification: Beam Interlock Specifications For LINAC4, Transfer Lines and PS Booster with LINAC4", Transfer Lines and PS Booster with LINAC4, LHC Project Document No. L4-CIB-ES-0001, v.0.3, 18-01-2011. `https://edms.cern.ch/file/1016233/0.3/L4-CIB-ES-0001-01-30.pdf`

[9] C. F. Hajdu, C. Zamantzas, and T. Dabóczi, "Development of a method for continuous functional Supervision of BLM systems", in *Proc. IBIC'16*, Barcelona, Spain, Sep. 2016, pp. 90–93. `doi:10.18429/JACoW-IBIC2016-MOPG21`

BEAM LOSS SIGNAL CALIBRATION FOR THE LHC DIAMOND DETECTORS DURING RUN 2

S. Morales*[1], B. Salvachua, E. Calvo, E. Effinger, C. Zamantzas, CERN, Geneva, Switzerland
C.P. Welsch, J. Wolfenden, University of Liverpool, Liverpool, United Kingdom
[1] also at University of Liverpool, Liverpool, United Kingdom

Abstract

Chemical Vapour Deposition (CVD) diamond detectors can be used as fast beam loss monitors in particle accelerators. In the Large Hadron Collider (LHC) at CERN, they are installed in the betatron collimation region, a high-radiation environment. In addition to their high-radiation tolerance, their main advantage is a time resolution of 1 ns which makes possible not only turn-by-turn, but also bunch-by-bunch loss measurements. An analysis of the LHC diamond beam loss monitor signals recorded during the last months of Run 2 (September 2018-November 2018) is presented with the aim of obtaining a signal-to-beam-loss calibration.

INTRODUCTION

The Large Hadron Collider (LHC) at CERN is the largest and most powerful accelerator ever built. It has a 27-kilometre long circumference and it is located 100 m underground. The LHC accelerates protons and ions up to a design energy of 7 TeV, with up to 2 556 particle bunches per beam and, on average, 1.15×10^{11} particles per bunch, achieved during Run 2 (2015-2018) [1].

Dipole electromagnets create a field of up to 8.33 T that is used to bend the trajectory of the beam particles along the accelerator. In order to reach and maintain the current of around 11 850 A required to produce this magnetic field, superconducting coils are employed in the LHC magnets [2]. Under these conditions, losses on the level of 30 mJ/cm^3 induced by a local transient beam loss of 4×10^7 protons could provoke a transition from superconducting to normal conducting state (quench) in the magnets and generate an accelerator downtime in the order of hours or even months [3]. Additionally, beam losses could damage the accelerator or detector equipment.

Driven by these concerns, a Beam Loss Monitoring (BLM) system is installed in the LHC. The system includes around 4 000 beam loss detectors placed all around the accelerator ring downstream the most probable loss locations. They measure continuously the beam losses and trigger a beam dump signal when the losses reach certain predetermined thresholds [4]. Even though it is seen mainly as a machine protection system, the signals from the beam loss detectors can also be used to provide a precise number of the lost beam particles and to identify the different loss mechanisms, making it a powerful diagnostics tool to improve the performance of the accelerator. This type of analysis has already been carried out in the past, but only considering the signals from the Ionization Chamber (IC) BLM detectors [5–7]. This work aims at reproducing the same results using the signals from the Diamond BLM (dBLM) detectors that were under test in certain locations in the LHC during Run 2, which offer a bunch-by-bunch loss signal resolution and therefore could provide a more detailed information about the LHC beam loss patterns.

LHC BLM SYSTEM DETECTORS

The LHC BLM system includes four different types of beam loss detectors. The most relevant ones for this analysis are the IC BLMs and the dBLMs.

Ionization Chambers

The IC is the most common beam loss detector type in the LHC BLM system, with around 3 600 installed downstream the most probable loss locations. The IC is made of a stainless steel cylindrical tube which is 50 cm long, with a diameter of 9 cm and filled with nitrogen gas. It contains aluminium plates that are alternatively used as high voltage and signal electrodes. A voltage of 1.5 kV is applied between the electrodes, which generates an electric field of 3 kV/cm inside the chamber. The internal part of an IC BLM detector is shown in Fig. 1. The analog beam loss signal is induced when the lost beam particles or their products traverse the chamber and ionize the gas inside [8]. The signal is then continuously integrated and digitized in the front-end analog electronics using a Current-to-Frequency-Converter card that provides measurements every 40 μs [9]. The read-out electronics then converts the signal bits to Gy/s and keeps a history of the values by producing longer integration windows.

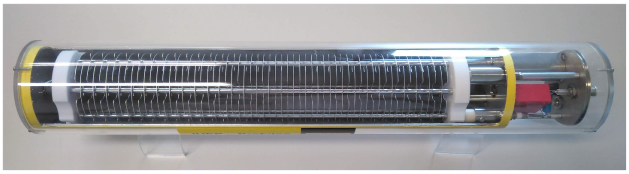

Figure 1: Internal part of an IC BLM detector showing the electrodes. The cables to the read-out electronics are located on the right side.

Diamond Detectors

The dBLM consists of a squared pCVD diamond detector which is 10 mm long and 0.5 mm thick. It offers a time resolution in the order of the ns which allows to record turn-by-turn and bunch-by-bunch beam loss measurements, as the nominal LHC bunches are separated by 25 ns [10]. These

---

* sara.morales.vigo@cern.ch

dBLM detectors were under test during the LHC Run 2 in certain specific locations. A dBLM detector and its analog front-end electronics are shown in Fig. 2. The signal induced in these detectors is digitized; about 57 802 samples per turn (i.e. approximately 89 µs long) are saved. The signals start being processed in the digital back-end, which provides various measurement modes. The one considered for this analysis is the Integral mode, which performs a bunch-by-bunch integration of the measured beam losses for every 11 200 turns (approximately every second) and calculates a baseline reconstruction within bunches that is subtracted from the integrated signal. An example of a dBLM bunch-by-bunch integrated beam loss signal during a Squeeze beam mode from a nominal LHC fill can be seen in Fig. 3.

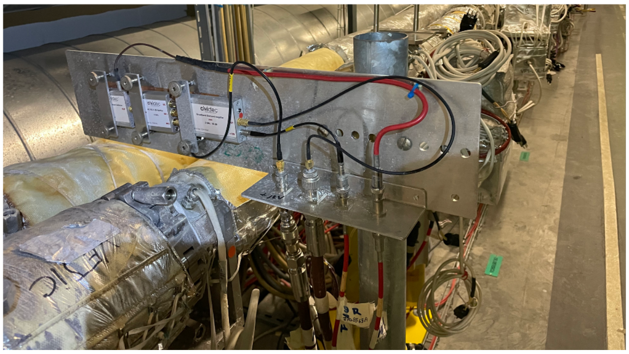

Figure 2: dBLM detector and analog front-end electronics located above the LHC beam pipes. From left to right a detector, AC-DC splitter and signal amplifier can be seen as well as the signal and high voltage cables.

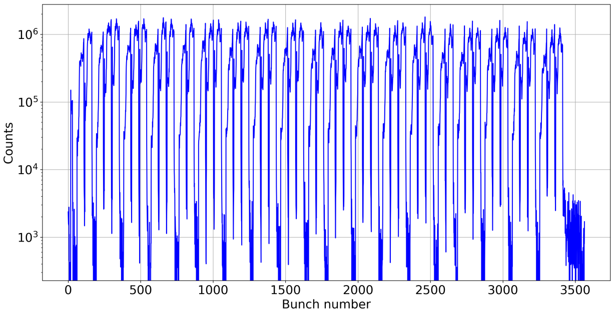

Figure 3: dBLM bunch-by-bunch integrated loss signal during a Squeeze beam mode from a nominal LHC fill.

LHC dBLM DETECTORS LAYOUT

During the LHC Run 2, 6 dBLM detectors were installed in the betatron collimation region, where the collimators which clean the beam from transverse halo particles are located. In Figs. 4 and 5 the dBLM layout in the LHC betatron collimation region is presented respectively for beam 1, which circulates clockwise in the LHC tunnel, and beam 2, which circulates counterclockwise. In both figures, the collimators located upstream the dBLM detectors are indicated with blue horizontal rectangles together with their beam cleaning orientation. The dBLM detectors are indicated with grey vertical rectangles. Additionally, the IC detectors which are located closer to them are indicated with blue vertical rectangles.

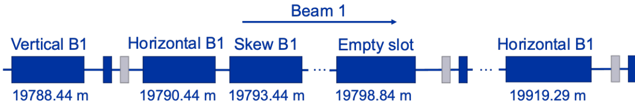

Figure 4: dBLM Layout in the LHC betatron collimation region for beam 1.

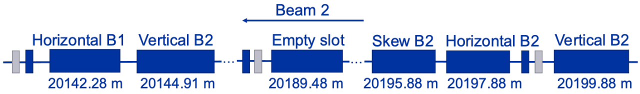

Figure 5: dBLM Layout in the LHC betatron collimation region for beam 2.

As it can be seen in both figures, 3 dBLM detectors were installed per beam. In both beam lines there is a dBLM detector located downstream the primary vertical collimator, which is upstream the rest of the betatron collimation system for each beam. For this reason, the signals from both detectors are expected to be highly sensitive only to the beam particles lost in the respective primary vertical collimators, which is useful to identify whether the beam particles are lost in these collimators or elsewhere in the accelerator. Further downstream the primary collimators in both beam lines there is a dBLM detector located next to an empty slot and a dBLM detector located downstream additional collimators. Based on their positions, the signals from these 4 dBLM detectors are expected to be highly sensitive to the beam particles lost in the betatron collimation region, regardless of the type of the exact collimator where they are lost.

dBLM DETECTOR CALIBRATION

Obtaining a global calibration of the LHC dBLM detectors is key to the development of the loss pattern recognition algorithms that allow to study the LHC beam loss decomposition. These loss pattern recognition algorithms compare measured losses to well defined loss scenarios. Considering the total beam losses as a linear combination of those well studied loss scenarios, it is possible to obtain the loss vector decomposition using linear algebra.

Principle of the Loss Decomposition Algorithm

The signal of a BLM detector, S_i, is proportional to the total number of protons lost by different mechanisms in the LHC, ΔI, so that $S_i = \alpha_i \times \Delta I$. The constant α_i is called the monitor response factor.

For instance, in the case of protons lost in horizontal collimators, the signal of the same BLM detector is related to those lost protons by:

$$S_{i,\mathrm{H}} = \alpha_{i,\mathrm{H}} \times \Delta I_{\mathrm{H}}, \tag{1}$$

where $\alpha_{i,\mathrm{H}}$ is the monitor response factor for horizontal beam losses and ΔI_{H} represents the number of protons lost in the horizontal collimators.

Considering a set of signals from different BLM detectors, $\overrightarrow{S} = (S_1, S_2, S_3, \ldots)$, and protons lost in different loss scenarios, $\overrightarrow{\Delta I} = (\Delta I_{\mathrm{H}}, \Delta I_{\mathrm{V}}, \Delta I_{\mathrm{S}}, \ldots)$, a so-called response matrix, $\boldsymbol{M}$, which includes all the monitor response factors for the different loss scenarios, can be defined as:

$$\overrightarrow{S} = \boldsymbol{M} \times \overrightarrow{\Delta I} \tag{2}$$

In nominal LHC fills it is possible to calculate the protons lost in different loss scenarios by applying the inverse response matrix to the BLM detector signals:

$$\overrightarrow{\Delta I} = \boldsymbol{M}^{-1} \times \overrightarrow{S} \tag{3}$$

Considering the capabilities of the LHC dBLM system to distinguish between particles lost in horizontal and vertical collimators, a preliminary and simplified version of a loss decomposition algorithm including their signals has been developed. Only horizontal and vertical particle loss scenarios are considered.

Data for Calibration: Lossmaps

The data for the calculation of the monitor response factors are collected from the so-called lossmaps. These are periods during which beam losses are generated on purpose with a low-intensity beam by exciting independently bunches with white noise in a selected plane (horizontal or vertical). This makes the beam transverse size to increase in a controlled way. As the beam size grows measurable beam losses start to appear at the collimators. The BLM detector signal and the beam intensity measured with the Beam Current Transformer (BCT) detector are extracted for that lossmap period and the monitor response factor for that loss scenario is calculated using Eq. (1).

For the simplified version of the algorithm, a set of horizontal and vertical lossmaps is required to calculate the monitor response factors. Furthermore, it is preferable to analyze the data from the lossmaps taking place during LHC Squeeze beam modes, as the beams are at top energy but not colliding, so the majority of the beam losses are expected to occur in the betatron collimation region. Therefore, for these lossmaps it is possible to crosscheck the total lost beam intensity calculated from the algorithm with the absolute measurements from the BCT detectors.

The signals of the LHC dBLM detectors were only logged during the last months of the LHC Run 2, from September 2018. For that period of time, a set of horizontal and vertical lossmaps that were performed after the LHC Technical Stop (17-21 September 2018) during a LHC Squeeze beam mode were selected for this analysis.

During that Technical Stop, the setups of some of the LHC dBLM detectors were modified, e.g. the amplified signal gain. Furthermore, the signals from the two LHC dBLM detectors installed downstream the empty slots stopped being logged after the Technical Stop. For that reason, those detectors were not considered in this analysis.

Using the data from the selected lossmaps the monitor response factors for horizontal and vertical loss scenarios were calculated for the 4 remaining LHC dBLM detectors and their closest IC BLM detectors for comparison purposes. As expected, the monitor response factors of the detectors located downstream the primary vertical collimators were much higher in the case of a vertical lossmap. Figure 6 shows the integrated bunch-by-bunch signal of the dBLM detector installed downstream the beam 1 primary vertical collimator during the selected beam 1 horizontal and vertical lossmaps. The signal peak is centered around a single particle bunch (only one particle bunch is excited per lossmap) and the signal during the vertical lossmap is around two orders of magnitude higher than during the horizontal lossmap, even if during both lossmaps the lost beam intensities measured by the BCT detector were around 5 × 10^9 protons. This behavior is expected, as the detected loss for different loss scenarios depends on the location of the detector.

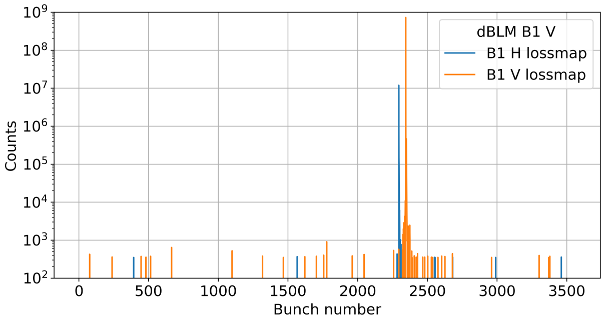

Figure 6: Bunch-by-bunch integrated signal of the beam 1 dBLM detector located downstream the primary vertical collimator for a horizontal and a vertical lossmap.

CALIBRATION VALIDATION

After the calculation of the respective horizontal and vertical monitor response factors, the response matrices of the simplified dBLM and equivalent IC BLM decomposition algorithms were defined as in Eq. (2). The inverse matrices were calculated so that the algorithms could be applied to the dBLM and IC BLM signals as in Eq. (3) for regular LHC fills.

For the validation of the calibration, the decomposition algorithm was applied to the LHC Squeeze beam modes that took place during regular proton Physics periods after the Technical Stop in September 2018. That made a total of 27 Squeeze beam modes considered, each with a duration of around 11 minutes.

Figures 7 and 8 show the total lost beam intensity during each Squeeze period for beam 1 and beam 2 respectively. The red dots indicate the results obtained from the dBLM decomposition algorithm, while the blue stars indicate the results from the IC BLM decomposition algorithm and the green triangles the values measured with the BCT detectors. It can be seen that systematically the results obtained with the IC BLM algorithm show a better agreement with the lost intensity measured with the BCT detector but the dBLM method is able to follow the same trend.

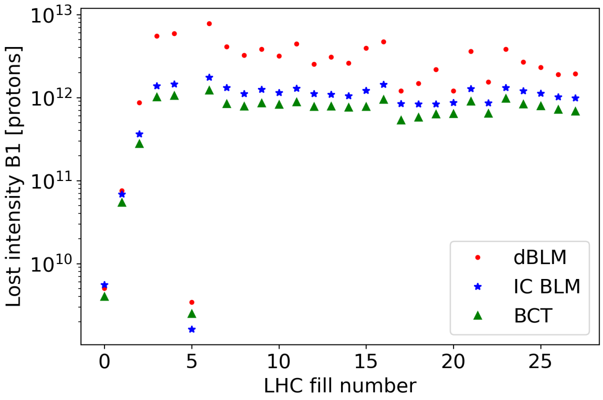

Figure 7: Total lost intensity in beam 1 during LHC Squeeze beam modes as calculated with the dBLM algorithm, the IC BLM algorithm and measured with the BCT detector.

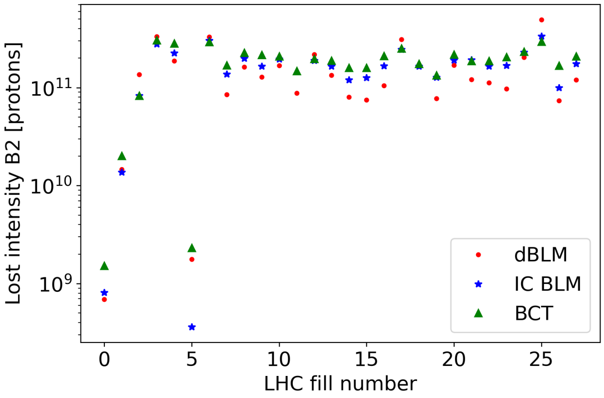

Figure 8: Total lost intensity in beam 2 during LHC Squeeze beam modes as calculated with the dBLM algorithm, the IC BLM algorithm and measured with the BCT detector.

CONCLUSION

Even though the BLM detectors are generally considered as a machine protection device against beam losses, their signals can also be used as a powerful diagnostics tool to improve the performance of the accelerator by providing a precise number of the lost beam intensity and identifying the beam loss mechanisms. In the past, this was only done with the signals from the IC BLM detectors. However, a set of dBLM detectors were installed and under test in the LHC betatron collimation region during the last months of Run 2. Their main advantage with respect to other types of BLM detectors is a time resolution of 1 ns which makes possible not only turn-by-turn, but also bunch-by-bunch loss measurements. A global calibration for the dBLM detectors was carried out. Even if the IC BLMs still show a higher accuracy for this kind of analysis, this paper shows that they can also be calibrated in such a way that the loss measurement is provided in total number of protons lost in the machine. A series of tests at the electron beam facility CLEAR at CERN are foreseen in order to study the response function of the dBLM detectors signals, the mix of signal from multi-bunched beams and the treatment of the signal noise. The aim of these studies is to achieve a better understanding of the dBLM detectors signals and improve their calibration results.

ACKNOWLEDGEMENTS

The authors would like to acknowledge the contribution to these studies to the LHC CERN Beam Instrumentation Beam Loss section.

REFERENCES

[1] J. Wenninger, “Operation and configuration of the LHC in Run 2”, CERN-ACC-NOTE-2019-0007, Mar. 2019. `https://cds.cern.ch/record/2668326`

[2] “Pulling together: superconducting electromagnets”, Aug. 2012. `https://cds.cern.ch/record/1997395`

[3] O. Brunning *et al.*, “LHC design report”, CERN Yellow Reports: Monographs, Geneva, 2004. `https://cds.cern.ch/record/782076`

[4] E.B. Holzer *et al.*, “Beam loss monitoring system for the LHC”, in *2005 IEEE NSS Conf. Record.*, 23-29 Oct. 2005, pp.1052-1056. `https://cds.cern.ch/record/930275`

[5] A. Marsili, “Identification of LHC beam loss mechanism: a deterministic treatment of loss patterns”, CERN-THESIS-2012-316, 2012. `http://cds.cern.ch/record/1541459`

[6] B. Salvachua *et al.*, “Decomposition of beam losses at LHC”, in *Proc. 8th Int. Particle Accelerator Conf. (IPAC’17)*, Copenhagen, Denmark, May 2017, pp. 88-91. `doi:10.18429/JACoW-IPAC2017-MOPAB009`

[7] M. Wyszynski, “Decomposition of beam losses at LHC”, CERN-STUDENTS-Note-2015-219, Geneva, Sep. 2015. `https://cds.cern.ch/record/2054891`

[8] W. Friesenbichler, “Development of the readout electronics for the beam loss monitors of the LHC”, CERN-THESIS-2002-028, 2002. `https://cds.cern.ch/record/570940`

[9] C. Zamantzas, “The real-time data analysis and decision system for particle flux detection in the LHC accelerator at CERN”, CERN-THESIS-2006-037, 2006, `http://cds.cern.ch/record/976628`

[10] LHC dBLM CERN Wiki webpage, `https://wikis.cern.ch/display/BEBI/BLM+Diamonds`

ISBN: 978-3-95450-230-1 ISSN: 2673-5350 doi:10.18429/JACoW-IBIC2021-TUPP34

METHODOLOGY, CHARACTERISATION AND RESULTS FROM THE PROTOTYPE BEAM LOSS MONITORING ASIC AT CERN

F. Martina[1,2,*], C. Zamantzas, L. Giangrande, J. Kaplon, P. V. Leitao, CERN, Geneva, Switzerland
J. W. Bradley[1], C. P. Welsch[1], University of Liverpool, Liverpool, UK
[1]also at Cockcroft Institute, Warrington, UK
[2]also at University of Liverpool, Liverpool, UK

Abstract

The characterisation of novel beam loss monitoring front-end converters, based on radiation-hardened application-specific integrated circuits (ASIC), is undergoing at CERN. An effective performance analysis of the newly developed ASICs plays a key role in their candidacy for the future installation in the HL-LHC complex. This work introduces the latest test-bed architecture, used to characterise such a device, together with the variety of audits involved. Special focus is given on the verification methodology of data acquisition and measurements, in order to allow a detailed study of the conversion capabilities, the evaluation of the device resolution and the linearity response. Finally, the first results of post-irradiation measurements are also reported.

INTRODUCTION

The Beam Loss Monitoring (BLM)[1, 2] is an essential protection system of particle accelerators, since a variety of phenomena cause beam particles to escape from the desired trajectory. These produce secondary particle showers, which lead to unwanted energy deposition in the various machine elements. Thus, the BLM system is mandatory to prevent equipment activation, damage and, like in the case of the LHC, the quench of its superconductive magnets [3–6].

In view of the HL-LHC upgrade [7], a major renovation of the BLM electronics is on-going covering parts both within the accelerator tunnel and in the surface buildings. To cope with the new specifications, the BLM system will be required amongst others to enhance its radiation tolerance to reach 100 MRad of TID (was 50 kRad), and to provide a faster acquisition period of 10 µs in comparison to the currently installed system (was 40 µs) [8–11].

The high radiation tolerance requirements cannot be achieved using only commercial components, and a custom radiation hardened Application Specific Integrated Circuit (ASIC) was necessary to be designed.

The device is able to convert the analogue currents produced by the ionisation chamber detectors [12, 13] into digital data streams. These are serialised [14] and transmitted via optical fibres to the back-ends [15], where the data is further processed to obtain the beam loss measurements.

The measurements are compared in real-time with predefined thresholds [16, 17], unique by location, to decide whether the beam is permitted to circulate or its extraction must be triggered. Since the front-end conversion capabilities relies on the ASIC component, strict validation and performance characterisation on test-beds is required. Later, the post commissioning supervision will be carried on in conformity with the currently installed system [18–20].

In this report we will focus on the second version of the device, the BLMASIC, which implements similar concepts of current-to-frequency converter (CFC) as the currently operational system and an early prototype, studied in [21–24]. The validation has been performed using test-beds specifically designed to qualify the ASIC. In a previous paper [25], we presented a first version of the setup, which has since been significantly improved.

A brief description of the BLMASIC architecture and the methodology for the device validation are described in the following sections. Then, the test-bed assembly architecture, the batch data analysis software, as well as the first post-irradiation results are reported.

CONVERSION ARCHITECTURE

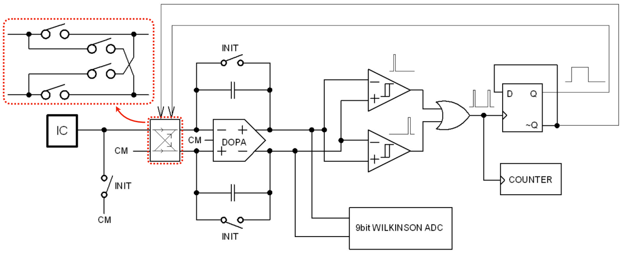

Figure 1: BLMASIC Conversion Architecture. ”IC” represents the ionisation chamber detector (ideally modelled as an independent current source). ”DOPA” is the input fully-differential amplifier configured as a current integrator. Quantisers and the toggling flip-flop are shown on the right.

The schematic architecture of the BLMASIC is shown in Fig. 1. The differential design of the circuit allows to double the internal signal swing and helps to improve the overall linearity response. Because of the configuration symmetry, it is possible to study its behaviour by splitting the complementary signal paths in two equivalent single-ended networks. Finally, the input current to measure is single-ended and the amplifier complementary input is connected to the circuit common-mode node, here considered as a neutral.

After the initialisation of the circuit, i.e. close the ”INIT” switch, any charge injected by the ionisation chamber (IC) will be accumulated in the capacitors, producing a voltage

---

[*] francesco.martina@cern.ch, f.martina@ieee.org

swing at the amplifier outputs. Two quantisers compare the integrated charge with two fixed thresholds. They produce pulses indicating respectively whether an upper or a lower limit has been exceeded. To maximise the swing of the signal, the upper limit is set to a value close to the positive supply voltage and the lower one is close to the ground reference. The produced pulses are then combined with an OR gate and used to feed the clock of a toggling flip-flop. This allows to swap the input connections of the amplifier whenever a limit is reached using the switching circuitry, highlighted in red in Fig. 1.

For example, injecting a continuous current at the input of the circuit, the integrated current will cause a voltage ramp at the amplifier output. As soon as the voltage will reach one of the limits, the switching circuitry will toggle and consequently the ramp slope will be reversed. This mechanism generates an almost triangular waveform at the output of the integrating amplifier. Such an integrator output signal is hereafter referred to as the ”primitive”. The slope magnitude and the waveform frequency are proportional to the input current intensity and to the inverse of the integrating capacitance value. Therefore, knowing the circuit parameters, it is sufficient to track the number of generated pulses in-between the measurement period to obtain a measure of the current intensity.

Finally, at the integrator outputs an auxiliary 9-bit ADC designed following the Wilkinson architecture [26] is connected. It allows to keep track of the ”instantaneous” values of the primitive signal, with a sampling frequency of 100 kHz. For input currents in the range of ~1 µA – 1 mA, the pulse rate (belonging to ~1 – 10 MHz) provides sufficient information to perform the measurements. Whereas, if the device has to measure low currents in the order of ~1 – 100 pA, a longer than 10 µs period would be required to carry out the same procedure, due to the low number of generated pulses. For such cases, the auxiliary ADC is exploited to directly estimate the slope magnitude. The information provided by both methods can be combined in the processing chain, with an algorithm similar to [27], to improve the resolution and reduce the system response time.

METHODOLOGY

Basic Device Functionality Tests

Basic electrical checks are required to prepare the brand new DUT for the characterisation. Initially, it is assembled on a test-bed PCB and connected only to the power supplies. To prevent permanent damages, the current limiter of each power-supply is set to twice the nominal current. Examining the PCB with a thermal camera helps also to detect and to locate excessive power dissipation spots and short circuits.

Three supply rails are used to power the device. The current consumption, measured after initialisation, resulted equal in all the DUTs. Their values were:

- 59 mA on the main (sum of digital & analog) rail (1.2 V)
- 1 mA on the common-mode reference rail (0.6 V)
- <1 mA on the low leakage input stage rail (1.7 V)

At the next step, the communication interfaces were tested. For redundancy, in the DUT both the internal registers access I^2C port and the output differential lane (80 Mbps), used for data transmission and configuration report, are duplicated. A programmable I^2C master terminal has been developed for the test-bed. In parallel, the use of a logic analyser with embeded protocol checker assisted debugging such an interface. Then, the differential lanes were connected to proper 100 Ω termination and probed with an oscilloscope. This includes an 8b/10b decoder that allowed to validate the data frame structure and to decode the first raw measurements. The DUT passed these tests successfully and no data integrity issues or erratic behaviours have been observed.

Finally, reset and power cycle events were tested, verifying the reliability of the device boot. An internal dead-lock state issue has been observed in the DUT for slow power-up ramps. This will be corrected in the next version of the ASIC.

Conversion Performance

The BLMASIC main purpose is the analogue to digital conversion of the input current. The analysis, similar to the one performed for commercial ADCs, characterises the device in terms of integral and differential non-linearity (INL and DNL respectively), conversion noise, settling time and compatibility with the source impedance.

The test-bed has been built to inject calibrated currents into the device and to monitor simultaneously its register contents. Due to the very high dynamic range (up to 180 dB), logarithmic current sweeps are used. The fast output interfaces are connected to an FPGA board, which provides the clock to the DUT and acquires the data. Only one of the lanes has been used during this study; the other lane, meant to provide redundancy, must be tested before the commissioning of the device. Also the two current inputs will be characterised independently.

The test procedure involves configuring the test current, waiting for about a second the output to stabilise and record the DUT memory contents. Such procedure is repeated for all the input current values of interest. The ability to store the entire device memory during the session allows to perform batch data processing directly on the raw values, monitoring the internal configuration. Such a method has the disadvantage of requiring larger storage, but this additional information becomes convenient when evaluating various signal processing methods. Therefore, once the optimal data treatment procedure is found, it can be implemented in the back-end cards to perform the computation in real-time.

During the characterisation of the BLMASIC, these measurement data sets have been collected:

- 50 measurements from 1 pA to 1 nA, of 10 s each
- 500 measurements from 1 nA to 1 mA, of 1 s each

DUT Irradiation

For HL-LHC operation, the BLMASIC must be radiation tolerant. Therefore, tests for the total ionisation dose (TID), the single event latch-up (SEL) and single event upset (SEU)

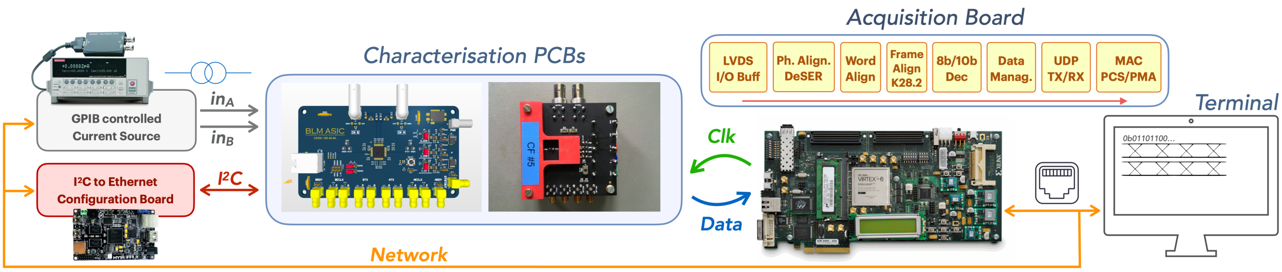

Figure 2: Characterisation Test-Bed Architecture.

must be performed, verifying the correct behaviour of the irradiated circuits and compliance with specifications.

In a preliminary study, a non-irradiated device against five other units irradiated with X-Rays was compared, to monitor any degradation of the conversion performance and validate the main operational functionality of the digital interface. Details of the irradiation sessions (performed at CERN) are reported in Table 1.

Table 1: BLMASIC X-Ray Irradiation Sessions

DUTs	Flux [MRad/h]	Time [h]	TID [MRad]
$CFC_{\#}1$	4.43	23	102
$CFC_{\#}2$	1.54	52	80
$CFC_{\#}3$	4.43	23	102
$CFC_{\#}4$	4.43	23	102
$CFC_{\#}5$	1.54	65	100

As soon as the next version of the device will be manufactured, devices will be subjected to additional irradiation campaigns, that more realistically emulate the final operational environment, such as with high-energy protons at Paul Scherrer Institut (PSI) and with mixed field radiation at CHARM, CERN.

TEST-BED ASSEMBLY

The test-bed makes use of a current source generator and a custom I^2C configuration card to provide the input current and control the device. Two printed circuit board variants, that can accept the DUT, have been developed to support the various activities. The first provided multiple access points and was used in [25]. Later, a more spartan version for the irradiation campaigns was realised. Finally, a supervision acquisition board decodes, collects the data, and transmits all information in real-time to a computer by UDP based packets over a gigabit Ethernet interface. A custom software was developed to perform the measurements and analyse the data. All the test-bed equipment is on the CERN network, allowing the remote control of the characterisation sessions. A block diagram of the test-bed components and connections can be seen in Fig. 2.

DATA ANALYSIS

Data Retrieval

Following the input current sweep runs and the extraction of the relative DUT memory storage, a first treatment was necessary to arrange the measurement registers and produce manageable numeric arrays. This process is computationally expensive because of the necessary bit addressing on the register map of the DUT. Although not usually efficient on CPUs, special functions have been used for bit data management. A possible alternative method would be to expand the results of interest directly on the acquisition board FPGA, but the dump of the entire DUT memory was preferred. Furthermore, to minimise the computation time of the data analysis, all the involved processing steps have been parallelised on separate threads, exploiting the performance of multi-core CPUs.

CFC Counter Data Analysis

The first analysis is focusing on the data provided by the CFC counters, incremented whenever the flip-flop toggles.

The BLMASIC must cover a large dynamic range, and different acquisition times are used for different input ranges, in order to obtain the desired measurement precision. Short times (≤100 µs) are required while performing high losses measurements (currents >10 µA), because a fast response must be guaranteed to protect the accelerator. Response time constraints are further reduced (≤20 µs) when reporting the instrument saturation or currents close to the full scale. On the other hand, longer integration times (up to tens of seconds) are allowed when high precision or low losses measurements (down to ~1 pA) are desired. Exploiting the overall acquired data, it is possible to test the conversion performance with a variety of averaging times. To this aim, a custom software procedure has been developed. For each specified averaging time it performs:

1. the partitioning of the full acquisition samples in clusters of the specified time window;
2. the averaging of the data within each of the cluster, representing an averaged measure;
3. the computation of the standard deviation amongst all averaged measures;
4. the computation of all samples average, representing a reference result.

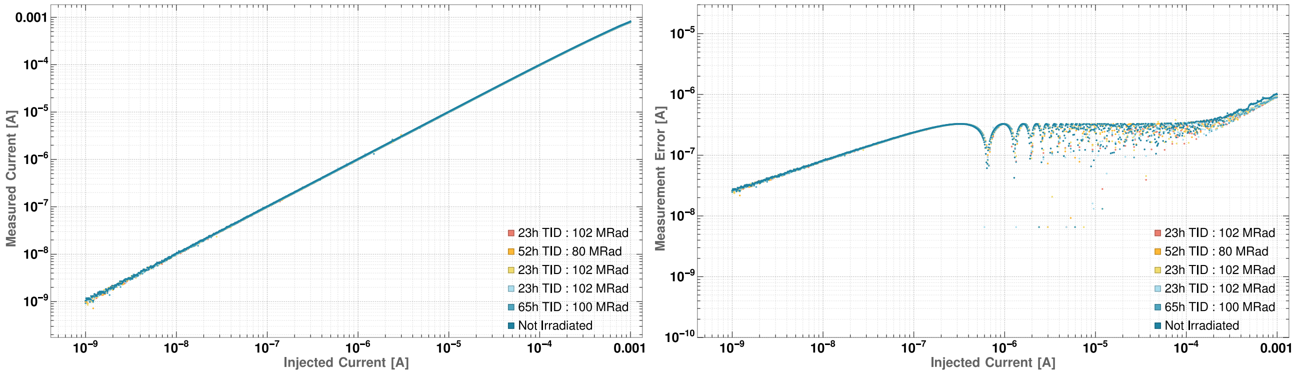

Figure 3: Conversion characteristic (left plot) and absolute errors (right plot) by a logarithmic current sweep of 500 values from 1 nA to 1 mA. The averaging time window is set to 100 µs.

Wilkinson ADC Data Analysis

The procedure used to analyse the Wilkinson ADC data follows similar steps to what was described before. However, a further computation is needed to estimate the slope magnitude of the primitive waveform. To this purpose, the linear regression has been applied on the samples of each cluster. In case this latter includes a slope direction change, detected on the basis of the CFC counter data, it will be discarded. Otherwise, the linear regression result will replace the averaged measures of the procedure step 2.

This analysis has allowed to achieve sub pA precisions for 1 s measurements of low currents (from 1 pA to 1 nA), in conformity with the design specifications. Hovewer, since its FPGA implementation can result resource-intensive, the exploitation of alternative but equally effective methods is under investigation.

POST-IRRADIATION RESULTS

In Fig. 3 it is shown a relevant result example obtained by the presented methodology. In particular, it reports the measured versus the injected current. Configured the test for high currents up to 1 mA, only the CFC counters have been exploited. The averaging time window has been set to 100 µs, corresponding to 10 samples.

No major performance drifts have been observed amongst the DUTs. The ripples in the error plot seem due to the data processing, not reflecting physical phenomena.

To study the conversion precision, relative errors have been computed. It turned out that an error smaller than 10 % is observed in measurements of currents greater than 3 µA, while it stays below the 1 % for currents above 35 µA. This is well inside the design specifications and it can be improved by advanced filtering techniques. Finally, a deviation from the linearity has been observed, which degrades the accuracy for currents in full-scale regime. This is due to a connection bug in the input stage clamping diodes, which has been solved in the third version upgrade. Thus, we will achieve the design value of 2.5 V for the related power rail.

CONCLUSIONS

The work reports on the test-bed architecture, the characterisation methodology and the data analysis aimed to perform the validation of the BLMASIC. Valuable results have been carried out during the tests, showing promising conversion performances and compliance with the design specifications.

The total dose irradiation session did not bring major drifts in the conversion behaviour. In every cases, the devices were able to perform high losses measurements with a precision below the 1% in a range from 35 µA to 1 mA and an integration time of 100 µs.

The presented method does not provide direct information about the INL / DNL factors of our converter, because its bit resolution is not strictly defined by the specifications and it depends on the chosen integration time. However, one could undertake a different approach, compiling a table that includes the equivalent conversion bits, the SNR and the non-linearity factors at various integration time windows. This will be helpful to optimise the device utilisation and eventually develop an auto-tuned methodology for the backends processing.

The consolidation of the gained experience, the procedures standardisation and the design improvement will be crucial for the test on the v3 device, which will begin by Fall 2021.

REFERENCES

[1] B. Dehning *et al.*, "The lhc beam loss measurement system," in *2007 IEEE Particle Accelerator Conference (PAC)*, 2007, pp. 4192–4194. `doi:10.1109/PAC.2007.4439980`

[2] B. Dehning *et al.*, "Overview of LHC beam loss measurements," Tech. Rep., 2011.

[3] C. Kurfuerst, B. Dehning, E. Holzer, A. Nordt, M. Sapinski, and C. Fabjan, "Quench Prevention of the LHC Quadrupole Magnets," 2010, `https://cds.cern.ch/record/1265861`

[4] A. Priebe *et al.*, "Beam-induced Quench Test of a LHC Main Quadrupole," in *Proc. IPAC'11*, San Sebastian, Spain, 2011, paper WEPC172, pp. 2388–2390, `https://jacow.org/IPAC2011/papers/wepc172.pdf`

[5] A. Priebe, B. Dehning, M. Sapinski, M. Q. Tran, and A. Verweij, "Investigations of quench limits of the LHC superconducting magnets," *IEEE Trans. Appl. Supercond.*, vol. 23, no. 3, p. 4 701 205, 2012. `doi:10.1109/TASC.2012.2236378`

[6] M. Sapinski *et al.*, "Beam induced quenches of LHC magnets," in *Proc. IPAC'13*, Shanghai, China, 2013, paper THPEA045, pp. 3243–3245, `https://jacow.org/ipac2013/papers/THPEA045.pdf`

[7] G. Apollinari, I. Béjar Alonso, O. Brüning, M. Lamont, and L. Rossi, "High-luminosity large hadron collider (hl-lhc): Preliminary design report," Fermi National Accelerator Lab.(FNAL), Batavia, IL (United States), Tech. Rep., 2015.

[8] C. Zamantzas, B. Dehning, E. Effinger, G. Ferioli, G. Guaglio, and R. Leitner, "The LHC beam loss monitoring system's real-time data analysis card," in *Proc. DIPAC'05*, Lyon, France, 2005, paper POW019, pp. 280–282, `https://jacow.org/d05/PAPERS/POW019.PDF`

[9] E. Effinger, C. Zamantzas, G. Ferioli, J. Emery, and B. Dehning, "Single gain radiation tolerant LHC beam loss acquisition card," paper WEPC06, pp. 319–321, 2007, `https://jacow.org/d07/papers/wepc06.pdf`

[10] C. Zamantzas, M. Alsdorf, B. Dehning, S. Jackson, M. Kwiatkowski, and W. Vigano, "System Architecture for measuring and monitoring Beam Losses in the Injector Complex at CERN," no. CERN-ACC-2013-0252, 2012, `http://cds.cern.ch/record/1627308`

[11] W. Vigano, M. Alsdorf, B. Dehning, M. Kwiatkowski, G. Venturini, and C. Zamantzas, "10 orders of magnitude current measurement digitisers for the CERN beam loss systems," *J. Instrum.*, vol. 9, no. 02, p. C02011, 2014. `doi:10.1088/1748-0221/9/02/C02011`

[12] M. Stockner, B. Dehning, C. Fabjan, G. Ferioli, and E. B. Holzer, "Measurements and Simulations of Ionization Chamber Signals in Mixed Radiation Fields for the LHC BLM System," in *2006 IEEE Nuclear Science Symposium Conference Record*, vol. 3, 2006, pp. 1342–1345. `doi:10.1109/NSSMIC.2006.354151`

[13] B. Dehning *et al.*, "Lhc beam loss detector design: Simulation and measurements," in *2007 IEEE Particle Accelerator Conference (PAC)*, IEEE, 2007, pp. 4198–4200.

[14] P. Moreira, "The lpgbt project status and overview," in *ACES*, 2016.

[15] A. Boccardi, M. Barros Marin, T. Levens, B. Szuk, W. Viganò, and C. Zamantzas, "A Modular Approach to Acquisition Systems for Future CERN Beam Instrumentation Developments," pp. 1103–1106, 2015. `doi:10.18429/JACoW-ICALEPCS2015-THHB2O02`

[16] C. Zamantzas *et al.*, "Configuration and validation of the LHC beam loss monitoring system," in *Proc. DIPAC'09*, Basel, Switzerland, 2009, paper TUPB31, pp. 240–242, `https://jacow.org/d09/papers/tupb31.pdf`

[17] M. Kalliokoski *et al.*, "BLM threshold evolution and 2016 proposal," pp. 191–196, 2016, `http://cds.cern.ch/record/2294668`

[18] J. Emery, B. Dehning, E. Effinger, A. Nordt, M. Sapinski, and C. Zamantzas, "First experiences with the LHC BLM sanity checks," *J. Instrum.*, vol. 5, no. 12, p. C12044, 2010. `doi:10.1088/1748-0221/5/12/C12044`

[19] C. F. Hajdu, T. Dabóczi, and C. Zamantzas, "On-line system supervision of beam loss monitoring systems with sinusoidal excitation," in *XXI IMEKO World Congress*, 2015, pp. 1176–1180, `https://www.imeko.org/publications/wc-2015/IMEKO-WC-2015-TC10-237.pdf`

[20] C. Hajdu, T. Dabóczi, and C. Zamantzas, "Development of a Method for Continuous Functional Supervision of BLM Systems," in *Proc. IBIC'16*, Barcelona, Spain, 2017, paper MOPG21, pp. 90–93. `doi:10.18429/JACoW-IBIC2016-MOPG21`

[21] G. Venturini, B. Dehning, E. Effinger, and C. Zamantzas, "Design Specifications for a Radiation Tolerant Beam Loss Measurement ASIC," Tech. Rep., 2009.

[22] W. Vigano, E. Effinger, C. Zamantzas, G. Venturini, and B. Dehning, "Comparison of three different concepts of high dynamic range and dependability optimised current measurement digitisers for beam loss systems," 2012.

[23] G. Venturini, F. Anghinolfi, B. Dehning, and M. Kayal, "Characterization of a wide dynamic-range, radiation-tolerant charge-digitizer ASIC for monitoring of beam losses," no. 1, paper MOPA12, pp. 74–78, 2012, `https://jacow.org/IBIC2012/papers/mopa12.pdf`

[24] G. Venturini, F. Anghinolfi, B. Dehning, F. Krummenacher, and M. Kayal, "A 120db dynamic-range radiation-tolerant charge-to-digital converter for radiation monitoring," *Microelectronics Journal*, vol. 44, no. 12, pp. 1302–1308, 2013. `doi:10.1016/j.mejo.2013.08.020`

[25] F. Martina, L. Giangrande, J. Kaplon, P. V. Leitao, and C. Zamantzas, "Testbed Development for the Characterisation of an ASIC for Beam Loss Measurement Systems," in *Proc. IBIC'20*, Santos, Brazil, 2020, paper THPP04, pp. 215–217, `doi:10.18429/JACoW-IBIC2020-THPP04`

[26] T. Vergine, M. De Matteis, A. Baschirotto, and A. Marchioro, "A 32-channel 12-bits 65nm Wilkinson ADC for CMS Central Tracker," *IEEE Nucl. Sci. Symp. Conf. Rec.*, 1–4. 4 p, 2014. `doi:10.1109/PRIME.2014.6872683`

[27] M. Kwiatkowski, C. Zamantzas, M. Alsdorf, B. Dehning, and W. Viganò, "A Real-Time FPGA Based Algorithm for the Combination of Beam Loss Acquisition Methods Used for Measurement Dynamic Range Expansion," in *Proc. IBIC'12*, Tsukuba, Japan, 2012, paper TUPA31, pp. 419–423, `https://jacow.org/IBIC2012/papers/tupa31.pdf`

10th Int. Beam Instrum. Conf. IBIC2021, Pohang, Rep. of Korea JACoW Publishing
ISBN: 978-3-95450-230-1 ISSN: 2673-5350 doi:10.18429/JACoW-IBIC2021-TUPP35

NEW APPLICATIONS AND STUDIES WITH THE ESRF BEAM LOSS MONITORING AT INJECTION

E. Buratin*, N. Benoist, N. Carmignani, F. Ewald, J.-L. Pons, K. Scheidt
European Synchrotron Radiation Facility, Grenoble, France

Abstract

More than one year after the commissioning of the ESRF's new Extremely Brilliant Source (EBS), the Beam Loss Detectors (BLDs) are continuing to be used for extensive applications and studies, notably at injection. A total of 144 BLDs and 36 associated Libera Beam Loss Monitors (BLMs) are distributed in the EBS ring and the Booster. These BLDs allow to measure slow losses during user-mode operation and fast losses at injection, with a sub-orbit-turn time resolution. In this paper these fast beam loss dynamics are presented at injection for different lattice parameters, collimator-settings and beam conditions. We will also show the excellent correlation with results obtained from the injection efficiency diagnostic and the bunch length acquired with the Streak Camera.

INTRODUCTION

The new Extreme Brilliant Source (EBS) ring at the European Synchrotron Radiation Facility (ESRF) has been installed, commissioned and it is now operational since mid-2020. The 6-GeV and 200-mA electron beam has typically horizontal and vertical emittances of 120-pm and 10-pm, respectively, with a typical beam lifetime of above 20 hours. This allows to generate a coherent and bright x-ray beam for the scientific users [1].

One of the useful accelerator diagnostics present in EBS are the Beam Loss Detectors (BLDs), to measure the distribution of the lost electrons around the accelerator [2]. Since the EBS commissioning phase, 128 BLDs have been installed, calibrated, exploited for Machine Dedicated Time (MDTs) studies and USM-mode operation. Additional 8 BLDs have been installed in the Booster, 4 in the injection zone and 4 in the extraction area. And in the Transfer Line from Booster to the EBS ring another 4 extra BLDs had been installed. In March 2021 and for a couple of months other 4 BLDs have been positioned near the Radio Frequency (RF) cavities of cell 25 to study critical events and dynamics. The total of 144 units of BLDs are controlled by 36 Beam Loss Monitors (BLMs) [3, 4].

The BLDs can be used to measure slow losses during operation and fast losses at injection. In User-mode there are about $5 \cdot 10^7$ lost electrons per second around the EBS ring, while at each injection it is about $2 \cdot 10^9$ lost electrons in less than 3 ms. In this paper we concentrate mainly on the injection mode to understand the BLDs fast functionality, behaviour and performance, in order to improve and to optimize the EBS complex, and to correlate and to verify the BLDs signals with other diagnostics.

BLDS AT INJECTION MODE

The measurement of fast losses can be extremely useful to describe the beam dynamics and the quality of the injection process. At injection, the BLDs termination switches automatically to 50 Ω, which is needed for the required time-resolution, thereby allowing these fast loss measurements.

For a standard 200-mA beam and a uniform filling pattern, the typical distribution of the injection losses is displayed on Fig. 1. In y-axis the BLD position is displayed, considering the standard 128 BLDs installed from cell 1 to cell 32. In x-axis the time is plotted up to 2800 µs, equivalent to 1000 turns. The losses are differently distributed depending on BLD position, aperture limitations, machine and beam parameters. An interesting feature visible in Fig. 1 is a periodic recurrence, measured by some the most critical BLDs, such as:

- BLD n.61, after the Insertion Device (ID) of cell 16, that is often one of the smallest gaps,
- BLD n.96, after the collimator of cell 24.

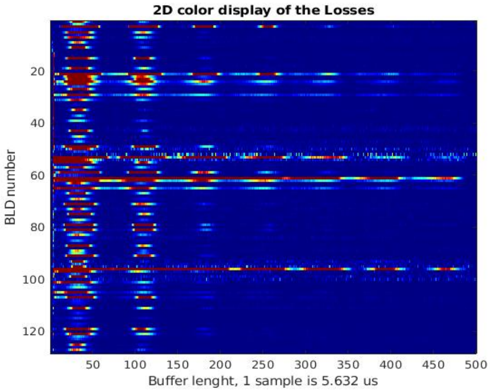

Figure 1: 2D color display of the Losses around EBS, for a 200 mA uniform-filling pattern beam.

The evolution of a single BLD can be analysed to identify the above-mentioned periodicity. In Fig. 2 the so-called Time-Resolved Beam Losses are displayed for the BLD n.96, installed in the middle of the fourth dipole after the collimator of cell 24. A big loss peak is present on the first turns, followed by damped oscillations with a 0.4 ms periodicity. These periodic losses are linked to bunch length oscillations occurring at injection, and presented below.

The evolution in time can also be summed-up so to generate a single value per BLD, the so-called Integrated Injection Losses. The distribution of these losses is reported in Fig. 3. The highest losses are registered on BLDs n.61 and n.96. At each injection, the Integrated

---

* elena.buratin@esrf.fr

Injection Losses are automatically recorded and saved in the ESRF database.

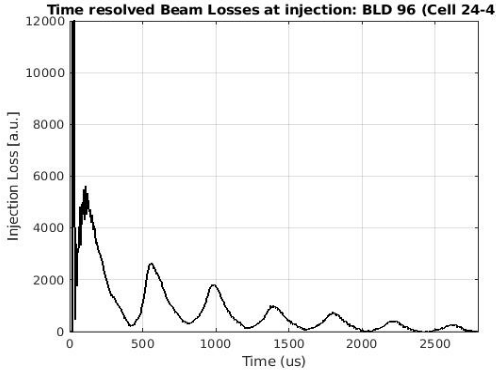

Figure 2: Time-Resolved Beam Losses of BLD n.96, installed down-stream the collimator of cell 24.

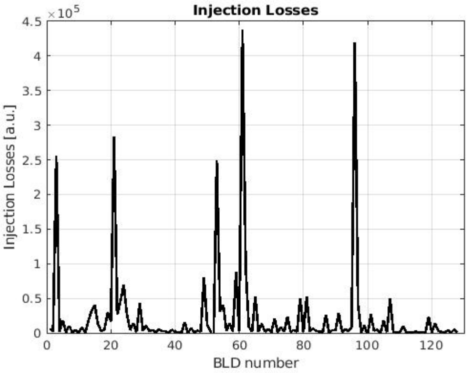

Figure 3: Distribution of the Integrated Injection Losses of the standard 128 BLDs installed in EBS.

As presented above, the 2D-color map, the Time-Resolved Beam Losses, and the Integrated Injection Losses give useful spatial and time informations at injection. In addition, the 2-D color display can be integrated both in time and space, to get a representative value of the losses, called Total Injection Loss, calculated for each injected shot.

MACHINE PARAMETER OPTIMIZATION

One useful application concerns the study of the Time-Resolved Beam Losses as a function of different machine parameters, in order to gain understanding of the BLDs characteristics and to optimize the EBS ring.

The first measurement is about the loss evolution as a function of the aperture of the vertical scraper installed in cell 6, scanned from 4 mm to 10 mm. Fig. 4 shows the fast behaviour of BLD n.24, that sits just after the scraper, as a function of time. The smaller the vertical aperture, the stronger the losses after the scraper, as expected. The losses show a big peak at the first turns, followed by two smaller bumps that appear at around 120 µs and 620 µs, respectively. The losses increase below a 6 mm gap.

The second measurement focuses on the loss evolution as a function of the horizontal collimator apertures (cell 13 and cell 24). The fast losses recorded on BLD n.53 are plotted in Fig. 5. The losses drastically change below a 6 mm gap. Also in this case, the big initial peak corresponds to the losses of the first turns, followed by two additional bumps that appear at the same timestamps as before.

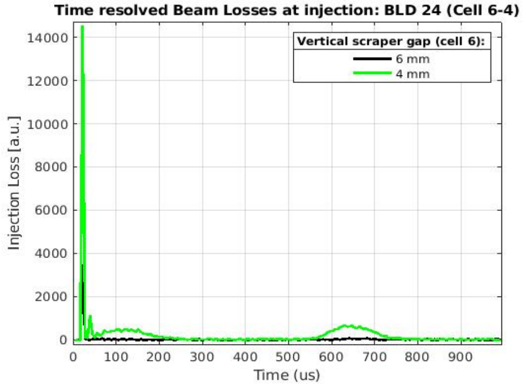

Figure 4: The Time-Resolved Beam Losses of BLD n.24 as a function of the scraper aperture.

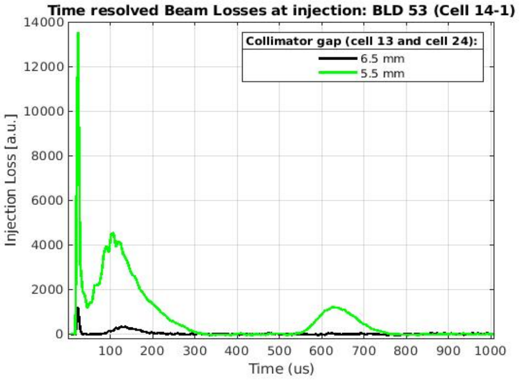

Figure 5: The Time-Resolved Beam Losses of BLD n.53 as a function of the collimator apertures.

The third measurement concerns the sum of all the Time-Resolved Beam Losses as a function of the RF-phase of the Booster with respect to RF-phase of the EBS ring (Fig. 6).

When degrading the optimum phase from -62 to -32 degrees, the losses increase as expected, especially those on the second bump centred at 120 µs. The worst the Booster-to-SR phase matching, the stronger the losses and the weaker the injection efficiency. Therefore, the BLDs fast losses can be an extremely useful measurement to help improving the performance of the injection process.

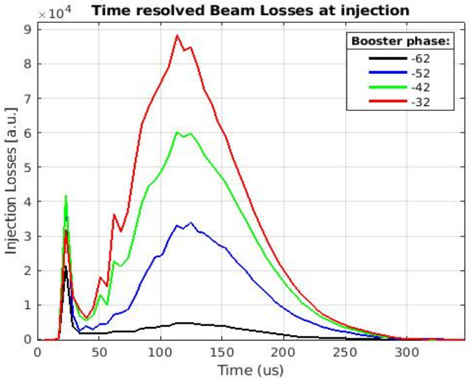

Figure 6: Total sum of the injected Beam Losses as a function of the Booster phase.

BLDS VS OTHER DIAGNOSTICS

In order to verify the proper reliability of the BLDs, the beam loss readings have been compared with two completely different diagnostics. The first comparison concerns the Time-Resolved Beam Losses and the Injected Bunch Length measured with a Streak Camera (Hamamatsu, series C10910) installed in the ID04 lab [5]. The second is about the Total Injection Losses and the Lost Current calculated from the Transfer Efficiency System.

BLDs vs Streak Camera

The dual time-base Streak Camera (SC) installed in the ID04 lab can be used to measure the bunch length of the stored and injected beam, thanks to its installation in the EBS injection zone (cell 4). A typical image acquired with the SC is displayed in Fig. 7, for an injected beam.

The SC fast sweep operates in the so-called synchro-scan mode at 88 MHz (i.e. exactly a fourth of the EBS RF frequency) thereby allowing to repeat that ultra-fast sweep at this 88 MHz, along the y-axis. In addition to that the dual-time axis module provides a 2nd, much slower sweep, along the x-axis. The combination of the above produces images of two visible streaks in the output. In that the (fast) bunch length image is continuously projected along the y-axis, while being repeated along that slower time (x-axis). In these images the injection occurs on the left side and the (slow) time scale runs from left to right. Calculations on these images then provide bunch-length (y-axis) at different moments after the injection (x-axis).

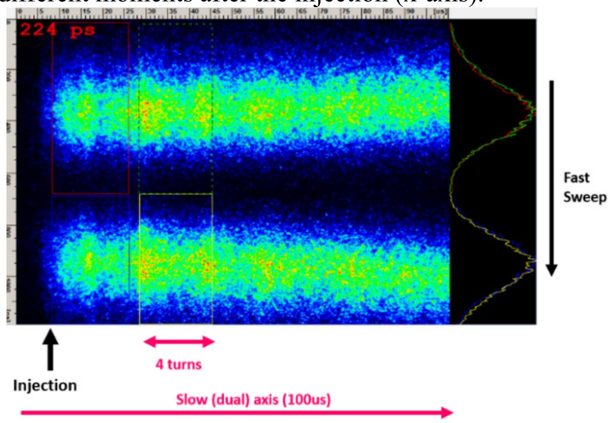

Figure 7: A typical image acquired with the SC, where two streaks of bunches are recorded in parallel for a Booster RF voltage of 7 MV.

An interest study concerned the comparison between the fluctuations of the bunch length (immediately following the injection) of the injected beam on one hand, with the fluctuations of the fast beam losses measured by the BLDs on the other hand. An example of SC measurement is shown in Fig. 8, for a horizontal time scale of 5 ms. The intensity variations in such image correspond to bunch length variations.

This is presented in Fig. 9, for the 1.3 to 2.9 ms after injection. It shows clearly oscillations of the bunch length with a 0.4 ms periodicity. There is also a decrease of bunch length with time as is fully expected.

The periodicity of the bunch length oscillations has a strong resemblance with the Time-Resolved Beam Losses recorded by some BLDs (see Fig. 2). Therefore, we can confirm that the oscillations visible on the injection losses are linked to the bunch length dynamics over the first few milliseconds.

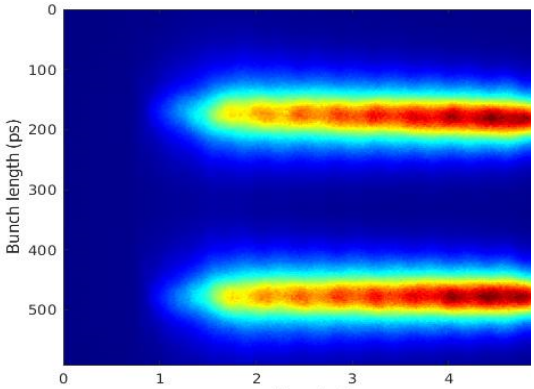

Figure 8: The bunch length fluctuations occurring for a few milliseconds after injection are clearly visible.

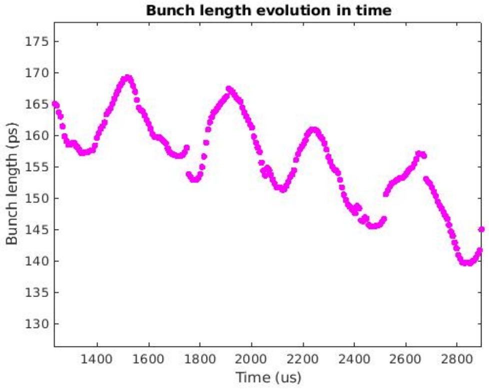

Figure 9: The bunch length evolution is displayed between 1.3 ms and 2.9 ms. The bunch length oscillates and decreases with time.

BLDs vs Injection Efficiency Diagnostic

The injection efficiency between Booster and EBS ring is measured at each injection shot with a fully separate and independent diagnostic called the injection efficiency monitor. It measures both the current (in fact charge, number of electrons) in the Booster (B), and the added current (charge, number of electrons) in the EBS (E). Next to monitoring the injection efficiency (the division of E with B), it can also calculate the Lost Injected Current, which is simply B-E.

The measurement presented below concerns a standard refill during the USM operation, with a filling scheme of 7/8 multibunch and a single bunch. The refill process is composed of three steps, filled respectively with 2 bunches, 4 bunches and one single bunch.

In Fig. 10 the normalised Total Injection Losses (obtained from the BLDs) and this Lost Current (from the injection efficiency monitor) are plotted for more than hundred injection shots. It shows a very good agreement between these two totally independent measurements. The

BLDs signals are fully proportional to the Lost Current so therefore the BLDs in injection mode generate trustful signals also at injection.

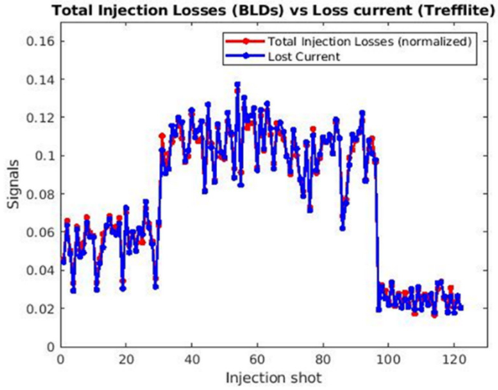

Figure 10: The total Injection Losses from the BLDs and the Lost Current from the injection efficiency monitor.

INJECTION AND EXTRACTION LOSSES IN THE BOOSTER

In the Booster 4 BLDs are positioned in the injection zone and other 4 in the extraction zone, to identify, respectively, the injection and the extraction losses.

The Figure 11 shows the results of the first BLD, positioned at close vicinity to the Transfer Line (Linac to Booster). During a standard refill, two distinct events are visible on this BLD: the injection process and the so-called bunch cleaning that is carried-out about 15 ms after the injection. This cleaning system uses a scraper (in this injection zone) to remove electrons from RF-buckets that are to be fully empty in order to satisfy special requirements of time-resolved experiments with X-rays from EBS.

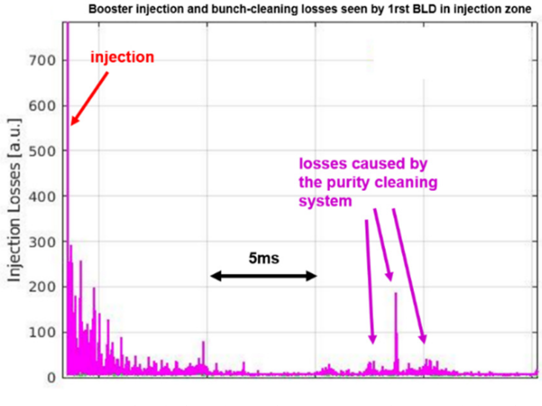

Figure 11: Both injection losses and specific bunch cleaning losses detected in the injection zone of the Booster.

In the extraction zone, interesting losses related to the Booster extraction process are visible on all 4 BLDs (see Fig. 12). The strong rise of these losses starts about 400 us before extraction and shows an oscillatory behaviour that is caused by the complex extraction process itself in which three slow bumpers, one pulse septum magnet and one fast extraction kicker are involved. New tests and studies are planned to further investigate these extraction losses as a function of bumper and kicker parameters.

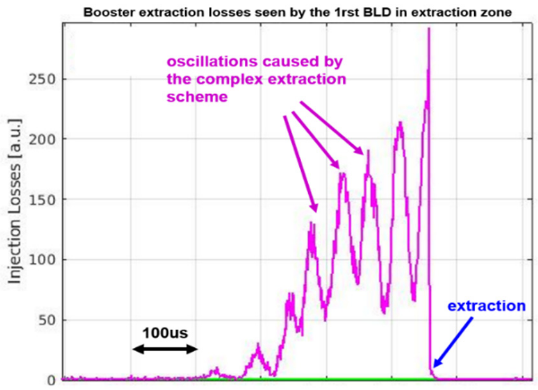

Figure 12: The losses seen in the extraction zone of the Booster. 400 us prior to the extraction moment a strong rise of the losses occurs with an oscillatory behaviour.

CONCLUSION

At ESRF, the BLDs have been intensively and systematically used in EBS, especially now at injection. These time-resolved injection losses have a high potential of helping with the improvement of some of the parameters of both the Injector and the EBS. These fast losses agree very well with other diagnostics, such as the Transfer Efficiency monitor and the Streak Camera. In the Booster, a separate set of BLDs can identify the injection, the bunch cleaning and the extraction processes.

ACKNOWLEDGMENTS

The authors would like to thank F. Taoutaou and G. Denat for the support during installation of the BLDs; P. Colomp and the safety group for the calibration with the Cesium 137 source; the IDs group, the RF group and the operation group for the MDT time and support for the data analysis.

REFERENCES

[1] J. L. Revol *et al.*, "Status of the ESRF-extremely brilliant source project", in *Proc. 9th International Particle Accelerator Conference (IPAC'18)*, Vancouver, BC, Canada, 2018, pp. 2882–2885. doi:10.18429/JACoW-IPAC2018-THXGBD3

[2] K. Wittenburg, "Beam Loss Monitors", presented at CAS - CERN Accelerator School: Beam Instrumentation, Tuusula, Finland, June 2018, https://arxiv.org/abs/2005.06522

[3] L. Torino and K. B. Scheidt, "New Beam Loss Detector System for EBS-ESRF", in *Proc. 7th Int. Beam Instrumentation Conf. (IBIC'18)*, Shanghai, China, Sep. 2018, pp. 346-352. doi:10.18429/JACoW-IBIC2018-WEOB01

[4] BLM: beam loss monitor readout electronics, https://www.i-tech.si/accelerators-instrumentation/liberablm/functionalities

[5] Hamamatsu Universal Streak Camera C10910 series, https://www.hamamatsu.com/resources/pdf/sys/SHSS0016E _C10910s.pdf

APPLICATION OF THE CORIS360 GAMMA RAY IMAGER AT A LIGHT SOURCE

Y. E. Tan *, ANSTO, Clayton, Australia
D. Boardman, L. Chartier, M. Guenette, J. Ilter, G. Watt, ANSTO, Menai, Australia

Abstract

The CORIS360® is a gamma-ray imager developed at Australian Nuclear Science and Technology (ANSTO) for identifying and localising sources of radiation typically from gamma emitting radionuclides. The low EMI and low noise power supply features of the imaging technology have enabled it to have a low energy detection threshold and to detect photons as low as 20 keV. This report shall present the initial measurements performed at the Australian Synchrotron, in the storage ring and beamlines, where the imager is able to detect radiation from all sources of synchrotron radiation (dipole, wiggler and undulator). The radiation imaging results from the injection system and scrapers (to dump the stored beam) will be discussed. Future developments for imaging in pulsed radiation environments and time varying environments will also be discussed.

INTRODUCTION

Synchrotron light sources are a source of radiation with photon energies ranging from milli-eV up to 200 keV. Knowledge of the sources and distribution of ionising radiation is needed to ensure the safety of the people at the facility and also in the protection of equipment susceptible to damage. Simulation of the synchrotron radiation source and its distribution is straight forward however the result of secondary scatter in a complex environment is harder to predict. Therefore we have employed a gamma ray imager to evaluate its effectiveness in diagnosing sources of scattered radiation in the storage ring to detect potential problems and also inform if additional local shielding is required. In this report we present some of the strengths and weaknesses of the CORIS360® gamma ray imager [1] that has been used in this evaluation. In particular the imager is very sensitive and is able to detect sources of hard xray sources from dipole, wiggler and undulator sources. A current drawback of the system is that it requires a constant radiation source intensity. Therefore, the imager will not be suitable for situations with variable source intensities (scraping, transient beam loss) and pulsed sources (injector). The report will conclude with some of the future developments the team at ANSTO are pursuing to address some of these drawbacks.

CORIS360 GAMMA RAY IMAGER

CORIS360® is a novel gamma ray imager developed by ANSTO. Equipped with a 360° × 90° gamma and optical field-of-view (FOV), it can quickly identify and localise gamma-ray and X-ray sources of radiation with energies between 40 keV and >3 MeV. The technology is designed around the theory of compressed sensing and employs two nested cylindrical tungsten masks that independently rotate around a single non-position sensitive detector, which enables a series of quasi-random (incoherent) linear projections of the scene plane to be measured. A compressed sensing approach to gamma-ray imaging had previously been presented in Ref. [2]. The cylindrical mask design provides the 360° × 90° FOV and the compressed sensing approach can localise gamma or X-ray sources of radiation with an order of magnitude fewer samples when compared to traditional imaging techniques, delivering fast results. A modular detector approach means different detectors can ‘plug & play’ into the system. CORIS360® currently uses two different geometry CLLBC detectors that have an energy resolution of ~4 % at 662 keV. A ~44 cm^3 CLLBC detector is used for low to medium dose rate environments and ~ 2 cm^3 detector is used for higher dose rate environments. The CLLBC detector is a dual gamma/neutron scintillator, and for neutron interactions the crystal produces an equivalent gamma energy of 3.1 MeV. During a single image acquisition, these spectroscopic detectors enable any part of the 40 keV to >3 MeV energy range to be imaged over the full system FOV. For this work, the low EMI and low noise power supply features of the imaging technology have enabled the low energy detection threshold to be reduced to 20 keV. A simple to use graphical user interface (GUI) provides the end user with an optical panorama with an overlay of the radiation location, which makes it easy to visualise where the source of radiation is. The GUI also provides the measured spectrum, radionuclide identification and indicates when neutrons have been detected.

MEASUREMENTS

Beamlines

The imager was first used at the beamlines to determine if it were sensitive enough to detect synchrotron radiation from a 1.3 T dipole, 1.9 T wiggler and 22 mm period undulator. In all three cases the imager was placed in the first optical enclosure, where the white beam slits and first optical mirrors were located and was able to detect scattered synchrotron radiation (secondaries that penetrate the vacuum chamber or shielding). Using the observation of the scattered radiation it is possible to identify issues along the optics as was observed on the MX2 beamline. Figure 1 shows how a defunct photon beam position monitor (BPM) appears to still be in the path of the beam. Or it can be used to inform the choice of local shielding that can be used to minimise scattered radiation and improve reliability and longevity of

---

[*] eugene.tan@ansto.gov.au

ISBN: 978-3-95450-230-1 ISSN: 2673-5350 doi:10.18429/JACoW-IBIC2021-TUPP36

any sensitive equipment. For example in Fig. 2 where the first vertical collimating mirror is scattering radiation to the side shield wall then reflecting to the rest of the room, or the wide scattering from the white beam slits as an obvious scattering source. The imager currently does not estimate the potential dose and therefore a direct measurement with a calibrated dosimeter is still required.

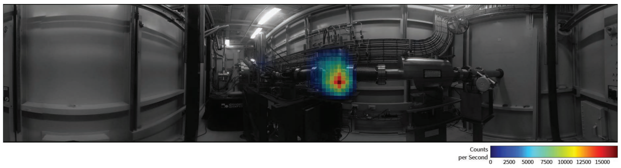

Figure 1: Images taken in the first optical enclosure of the Microfocus Crystallography (MX2) beamline that uses a 22 mm period in-vacuum undulator as its source. A singular source of radiation was identified across the entire spectrum located at an unused beam position monitor, indicating that likely some part of the instrument was intercepting core of the photon beam.

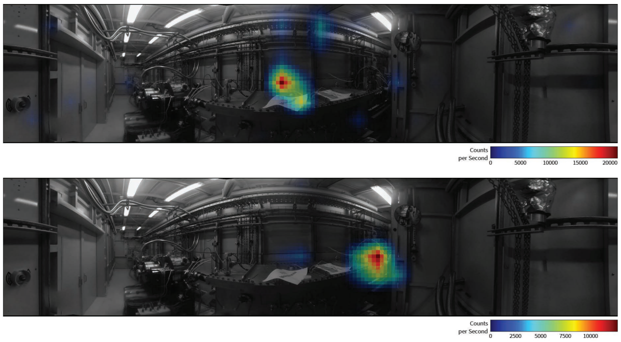

Figure 2: Images taken in the first optical enclosure of the X-ray Absorption Spectroscopy beamline (XAS) that uses a 1.9 T Wiggler as its source. Sources of radiation identified around 40 keV (top) scattered from the hutch wall next to the first vertical collimating mirror and 100 keV (bottom) scattered from the white beam slits. From this beamline the imager could detect photons up to 200 keV.

The spectrum of the scattered radiation measured by the imager from the three different sources is shown in Fig. 3. From the spectrum it is possible to distinguish the broader dipole like spectrum (including wiggler sources) and narrow band undulator spectrum. The imager was also able to capture the transition of the undulator spectrum to a more dipole like spectrum when the K of the in-vacuum undulator (IVU) was greater than 1.5.

Although the photon flux for the undulator beamlines are overwhelmingly at energies below 20 keV which is below the detection of the imager, its sensitivity means that it can still detect minute photons above 30 keV all the way to 300 keV in the case of the XAS wiggler. Therefore the imager can be used as a diagnostic tool for any sources of beam obstruction along the beamline as the higher energy photons will not be generally shielded by the vacuum chamber.

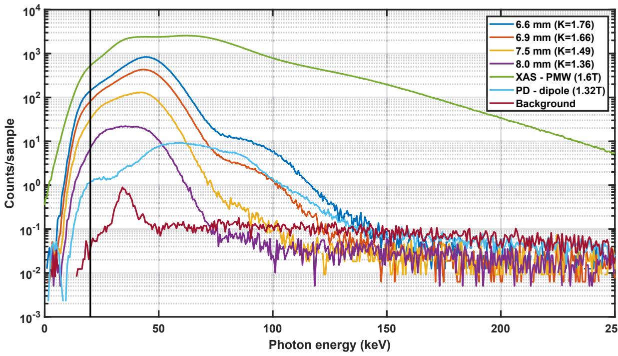

Figure 3: Spectrum measured by the imager in the first optical enclosures of the MX2 beamline (6.6 mm, 6.8 mm, 7.5 mm and 8.0 mm gap of the 22 mm period IVU), XAS beamline (wiggler) and PD beamline (dipole). Both XAS and PD beamline data shows the distinct broadband dipole spectrum while the MX2 beamline shows the undulator spectrum with the enhancement for photons below 70 keV. The spectrum at different IVU gaps clearly show the transition of the undulator to a more dipole like spectrum at higher energies when K is greater than 1.5. Below 40 keV the imager's shielding shows appreciable signal attenuation and exponential roll off below 20 keV (vertical black line).

Storage Ring

Further measurements were taken in the storage ring and we used this opportunity to determine the cause of the discoloration of the clear acrylic protective barriers and hardening of wire insulation around two insertion devices. These insertion devices have been installed with narrow gap Aluminium vacuum chambers with a NEG coating on the inner surface. The cause was believed to be the same as observed at Soleil [3] where synchrotron radiation from the upstream dipole illuminating the chamber wall resulted in secondary scattered synchrotron radiation as well as x-ray fluorescence of elements in the NEG coating. The images as shown in Fig. 4 confirm that the radiation is coming from the upstream dipole as the undulator was fully open. The spectra displays the same dipole like spectrum as seen in Fig. 3. Any effects of the fluorescence could not be clearly determined as it is below the detection limit of the imager.

The imager was also used at the location of a set of vertical beam collimators used to shift losses due to vertical beam scatter and reduce any demagnetisation effects on the IVUs used in the storage ring. The purpose was to see if the imager could be used to identify radiation sources initiated by Bremsstrahlung radiation. This was accomplished by reducing the vertical collimators until the electron beam lifetime was less than 10 hours to instigate a higher than normal rate of Bremsstrahlung radiation in this particular location. The spectrum in Fig. 5 shows the presence of the Bremsstrahlung radiation in the area however it was not

ISBN: 978-3-95450-230-1 ISSN: 2673-5350 doi:10.18429/JACoW-IBIC2021-TUPP36

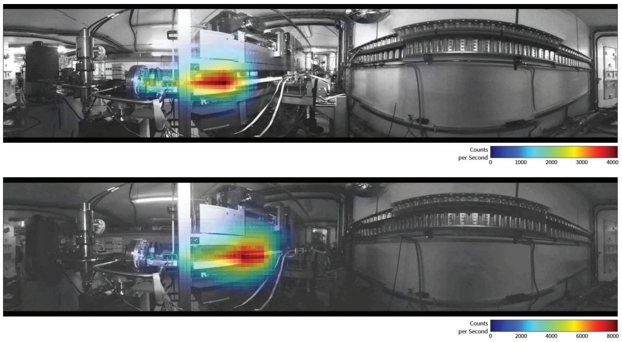

Figure 4: Image of the radiation at 60 keV with the insertion device “open”. Scattered radiation from the upstream dipole penetrating the Aluminium chamber with the beam on axis (top). With a vertical bumped (bottom) the source of the radiation shifts further upstream of the vacuum chamber.

able to define any unique source. Even in this situation the radiation levels are still dominated by scattered dipole radiation making it harder to identify any other sources. The results from the imager indicates that the Bremstrahlung radiation was a broad scatted field and does agree with what one would expect from 3 GeV Bremsstrahlung creating a veritable sea of secondary particles with energies of a few keV up to many MeV.

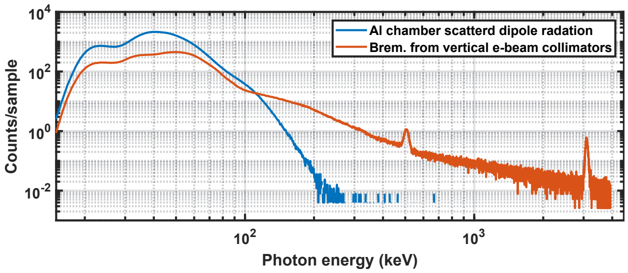

Figure 5: The radiation spectra measured at the vertical collimators (top) indicate the radiation below 100 keV is coming from scattered dipole radiation from a second set of Aluminium chambers that is also captured in this measurement. The source of radiation above 100 keV is from Bremsstrahlung and shows the 511 keV positron-electron annihilation peak as well as a neutron detection peak at 3.1 MeV.

Variable and Pulsed Radiation Sources

To determine the effectiveness across other sources of radiation at the facility the imager was also used to image radiation losses from our injector and from the use of the vertical collimator to remove the stored electron beams. In the first case the imager was not able to identify a source as the imager requires a constant intensity long enough to generate an image. In the second case the dose rate was too high with a very low duty factor where all the is generated radiation in less than 0.2 µs every second (injection rate). There was some evidence that during each pulse the detector was saturating, and future work will investigate if the system could be adapted to pulsed sources. Given the original design parameters of the imager was for the detection of radionuclides with a constant radiation output, it was not surprising that under the two conditions imager could not resolve an image. Despite such a limitation the imager can still be used to identify and characterise the nature of the radiation.

CONCLUSIONS AND FUTURE PLANS

The measurements that has been obtained has shown that the CORIS360® gamma ray imager’s sensitivity is able to resolve and uniquely identify the different types of radiation created at a light source. It was interesting to observe the transition of the undulator spectrum to a dipole like spectrum. The imager will be used in beamlines and storage ring to discover local hot spots and to be used as a diagnostic tool to identify potential obstructions to the synchrotron radiation. The findings from the Aluminium chambers has resulted in a review of the way we design the absorbers that shield the dipole radiation in the straight sections.

We will continue to work with the team that developed the imager to see if it can be modified and optimised for light sources (energies below 1 MeV). This could be achieved by using different detectors and adjusting the thickness of the mask and casing. To address the variable nature of some of the sources of radiation, it may be possible to integrate an external normalisation signal, either in real-time or in post-analysis. Due to the modular design it may be possible to find a combination of detector and MCA that is more suitable for pulsed radiation sources. This is currently under investigation.

Following the measurements in this report, plans are in place to continue to survey the rest of the storage ring to look for anomalies and to determine the scatter pattern from the photon shutter in the front-end of our 4.2 T superconducting wiggler. The data will help inform if additional local shielding is required to help minimise long term damage from radiation.

REFERENCES

[1] Coris360, `https://www.ansto.gov.au/products-services/detection-imaging/coris360/`.

[2] D. Boardman, A. Sarbutt, A. Flynn, and M. Guenette, “Single pixel compressive gamma-ray imaging with randomly encoded masks,” *Journal of Instrumentation*, vol. 15, no. 04, p. P04014, 2020.

[3] N. Hubert *et al.*, “Radiation Damages and Characterization in the SOLEIL Storage Ring”, in *Proc. 2nd Int. Beam Instrumentation Conf. (IBIC’13)*, Oxford, UK, Sep. 2013, paper WECL2, pp. 644–647.

MACHINE-LEARNING BASED TEMPERATURE PREDICTION FOR BEAM-INTERCEPTIVE DEVICES IN THE ESS LINAC

E. M. Donegani*, European Spallation Source ERIC, Lund, Sweden

Abstract

"*Where there is great power [density], there is great responsibility*"[1]. The concept holds true especially for beam-intercepting devices for the ESS linac commissioning. In particular, beam-intercepting devices will be subject to challenging beam power densities, stemming from proton energies up to 2 GeV, beam current up to 62.5 mA, pulses up to few milliseconds long, and repetition rates up to 14 Hz. Dedicated Monte Carlo simulations and thermo-mechanical calculations are necessarily part of the design workflow, but they are too time-consuming when in need of rapid estimates of temperature trends. In this contribution, the usefulness of a Recurrent Neural Network (RNN) was explored in order to forecast (in few minutes) the bulk temperature of beam-interceptive devices. The RNN was trained with the already existing database of MCNPX/ANSYS results from design studies. The feasibility of the method will be exemplified in the case of the Insertable Beam Stop within the Spoke section of the ESS linac.

INTRODUCTION

The European Spallation Source (ESS) in Lund (Sweden) is currently one of the largest science and technology infrastructure projects being built today. The facility will rely on the most powerful linear proton accelerator ever built, a rotating spallation target, 22 state-of-the-art neutron instruments, a suite of laboratories, and a supercomputing data management and software development centre [1].

The ESS accelerator high-level requirements are to provide a 2.86 ms long proton pulse at 2 GeV, with a repetition rate of 14 Hz. This corresponds to 5 MW of average beam power, with a 4% duty cycle on the spallation target [2].

A comprehensive suite of beam instrumentation and diagnostics [3] has started to support the commissioning and operation of the normal-conducting linac (NCL) section of the ESS linac. Additional devices and enabling systems are going to be deployed in the superconducting linac (SCL) section, as well as in the transport line to the tuning dump and to the spallation target.

In particular, the Beam Diagnostics Section is responsible for the design, procurement, test and operation of all the bulkiest beam-interceptive devices in both the NCL and SCL linac sections (see the list in Table 1). The beam instrumentation plays the most important role in the machine protection system by monitoring the beam parameters and stopping the beam operation before damages may occur.

Unfortunately, there is no straightforward expression for anticipating the energy deposition of a beam with high power density within accelerator elements, because the deposited energy depends on many beam properties as well as on the material properties of the beam-interceptive device and the capabilities of its cooling system.

Dedicated Monte Carlo simulations and thermo-mechanical calculations in MCNPX [4] and ANSYS [5], respectively, are part of the standard detector design workflow at ESS. However, many relevant beam- and material-related parameters have to be taken into account for the timing consuming simulations and validation. For instance, on a standard laptop it takes several hours to compute the temperature as a function of the time as shown in Fig. 1, when simulating just 14 proton pulses onto the SPK IBS [6].

Table 1: List of the Bulkiest Beam-interceptive Devices in the ESS Proton Linac. (FC = Faraday cup, IBS = Insertable Beam Stop)

Device	Mean power	Peak Power
LEBT FC	0.005 W	0.0002 MW
MEBT FC	16 W	0.23 MW
DTL2 FC	170 W	2.43 MW
DTL4 FC	323 W	4.63 MW
SPK IBS	411 W	5.88 MW
MBL IBS	1575 W	22.5 MW

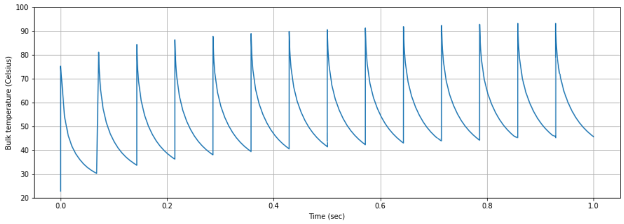

Figure 1: Temperature as a function of the time, calculated in ANSYS for the graphite bulk of the SPK IBS, after 73 MeV protons and 50 µs long pulses, at 6 mA and 14 Hz.

Similarly, dedicated experiments and controlled damage tests are usually expensive and not always an option when the impact(s) of many parameters have to be studied. Therefore, in this contribution a Machine-Learning (ML) based method for the prediction of temperature trends within beam-interceptive devices was developed, not for detector design purposes, but for fast time-series forecasting. In the future, the method described in the next section can be expanded either for standard machine protection purposes or virtual diagnostics.

---

* Corresponding author: elena.donegani@ess.eu

[1] cit. Winston Churchill, 1906

METHOD

In this contribution, the predictions of temperature trends in beam-interceptive devices of the ESS linac rely on the so-called Long Short-Term Memory (LSTM) model [7].

The LSTM is a processing model of an artificial Recurrent Neural Network (RNN) that nowadays is widely used in the field of deep learning for processing not only single data points, but especially sequential data e.g. weather, financial data, audio and text. The LSTM model exploits feedback connections and can store information over a period of time. In fact, the memory capability results from gates that determine whether information is stored or discarded. In this way it is possible to disentangle long-term and short-term memories, as peculiar as human brains.

The method of this contribution is written in python 3; the main library for developing and testing the method is Keras of TensorFlow 2. The training of the RNN is performed on the basis of the MCNPX/ANSYS database, available from past workflow for detector design. The three dimensional energy deposition was in fact previously calculated in MCNPX and then post-processed in ANSYS to compute the temperature as a function of the time.

The MCNPX/ANSYS database includes the temperature trends in the bulk of the beam-interceptive devices, as a result of the seven possible beam modes at ESS (see the list in Table 2). All the MCNPX calculations considered in the present work were performed after 73 MeV protons; the proton beam is assumed to have a Gaussian distribution in both transverse planes and in all the cases the beam dimensions were always the same.

The output MCNPX file has four columns (i.e. the calculated energy deposition value and the three coordinates of the voxel in which the energy deposition is calculated), whereas the ANSYS output has two columns (i.e. the calculated temperature vs. time). The ANSYS data were interpolated and normalized (between 0 and 1).

The method was optimized by means of the Adaptive Moment Estimation optimizer, also known as ADAM [8]. Tests were performed with 20 epochs and the loss was calculated as Mean Square Error (MSE).

Table 2: List of Beam Modes in the MCNPX/ANSYS Database (C = commissioning, T = tuning)

Mode	**Current (mA)**	**Pulse (µs)**	**Rate (Hz)**
Probe	6	5	1
Fast C	6	5	14
RF test	6	50	1
Stability test	6	50	14
Slow C	62.5	5	1
Fast T	62.5	5	14
Slow T	62.5	50	1

RESULTS

Temperature trends in beam-interceptive devices were predicted with an RNN combined with the LSTM model. In this section, the results after 73 MeV protons onto the SPK IBS are reported as representative example. In the following, the proton beam current is 6 mA, the repetition rate is 14 Hz and the pulse duration is 50 µs.

Several tests were performed in order to determine the useful number of training and validation points, in the sense that: the processing time is approximately just one minute (and not hours like for the full ANSYS simulations) and the uncertainty on the temperature is below 20°C. Three test cases are reported in Table 3 to summarize these initial tests. In the case C, one can notice that just three pulses actually calculated in ANSYS were used for the training.

Figure 2 shows the training loss as well as the validation loss, as calculated for the case C with the ADAM optimizer.

Finally, the comparison between the ANSYS results and the results of LSTM-based method is plotted at the top of Fig. 3. The difference between the two datasets is plotted at the bottom of Fig. 3. It is possible to observe that the LSTM model predicts the rising and falling periods with uncertainty less than 2°C, whereas in correspondence of the local maxima, the prediction can be off by up to 16°C. More advanced pre-processing, interpolation and segmentation will be explored with the aim of reducing the discrepancies at local maxima.

Table 3: Summary of tests carried to determine the number of training and validation points. The corresponding number of proton pulses are reported for reference.

	A	**B**	**C**
Training Points	7k	14k	21k
Validation Points	10k	20k	30k
Pulse Number	1	2	3
Processing time	46 sec	58 sec	62 sec
ANSYS/LSTM max diff.	30°C	26°C	16°C

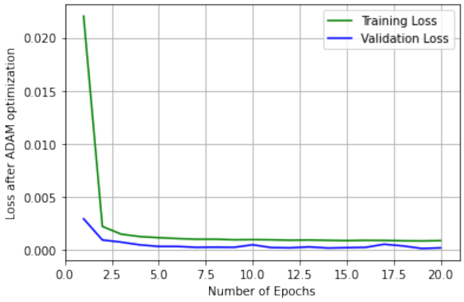

Figure 2: The training and validation loss for the CASE C in Table 3, by means of the ADAM optimizer.

The results are useful for various reasons: firstly, the saturation temperature is obtained within just one minute, so several hours of computational time in ANSYS can be

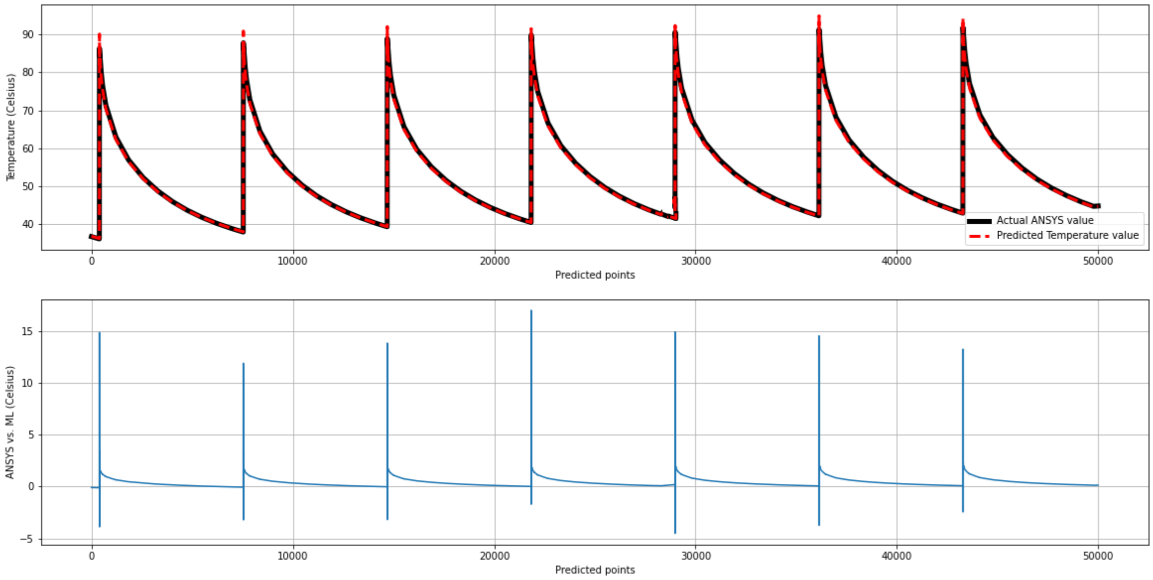

Figure 3: (Top) Comparison between temperature values calculated in ANSYS and those predicted by the Machine-Learning based method presented in this contribution (Bottom) Temperature difference between the ANSYS and the ML-results.

spared. Secondly, the precise temperature values in the rising and falling period can be used for further calculations of temperature trends for pulses shorter than the 50 μs (i.e. the pulse duration hereby considered for the example in Fig. 3) and for anticipating the impact of the temperature rise in materials close to or insulating the detector bulk. Thirdly, the results set also the reference limit after 14 Hz, thus they can be used to infer temperature trends at lower repetition rates.

CONCLUSIONS AND OUTLOOK

The protection of the machine and beam-interceptive diagnostics devices is of paramount importance in high power accelerators. For a quick estimation of temperature trends in beam-interceptive devices, there is no straightforward alternative to the standard simulation tools. Therefore, this paper proposed for the first time at ESS an ML-based model that can predict within few minutes the bulk temperatures in beam-interceptive devices of the ESS proton linac. The predictions are made by means of RNNs and in particular the LSTM processing model [7].

The data training and benchmarking were performed with data available from the MCNPX/ANSYS calculations for the design workflow previously outlined in [6]. The results show that the ML-based method accurately computes the rising and falling temperature trends with an error below 2°C in comparison to the reference ANSYS calculations. Local maxima come with a prediction error up to 16°C, therefore more advanced data pre-processing, interpolation and segmentation techniques will be considered to reduce such discrepancy. The method can be used for further studies at shorter pulse durations and lower repetition rates.

In the future, the method can be further expanded to e.g. build extensive look-up tables for routine checklists, develop a low-latency network for ML-based machine-protection systems or virtual diagnostics.

ACKNOWLEDGMENTS

The author is grateful to the former colleague T. J. Grandsaert for having performed the ANSYS simulations thus having contributed to the establishment of the MCNPX/ANSYS database used in this work.

REFERENCES

[1] ESS website 2020, `https://europeanspallationsource.se/about`

[2] R. Garoby *et al.*, “Corrigendum: The European Spallation Source Design”, *Phys. Scr.*, vol 93, p. 014001, 2018. `https://iopscience.iop.org/article/10.1088/1402-4896/aa9bff/pdf`

[3] T. J. Shea *et al.*,“Overview and Status of Diagnostics for the ESS Project”, in *Proc. 6th Int. Beam Instrumentation Conf. (IBIC’17)*, Grand Rapids, MI, USA, Aug. 2017, pp. 8–15. `doi:10.18429/JACoW-IBIC2017-MO2AB2`

[4] D. B. Pelowitz Ed., “MCNPX Users Manual Version 2.7.0”, LA-CP-11-00438, 2011.

[5] ANSYS Inc., `http://www.ansys.com/`.

[6] E. M. Donegani *et al.*, “The Insertable Beam Stop in the ESS SPK Section”, in *Proc. 9th Int. Beam Instrumentation Conf. (IBIC’20)*, Santos, Brazil, Sep. 2020, pp. 114–116. `doi:10.18429/JACoW-IBIC2020-WEPP07`

[7] S. Hochreiterand and J. Schmidhuber, “Long Short-Term Memory”, *Neural Computation*, vol. 9, no. 8, pp. 1735-80, 1997.

[8] D. P. Kingma and J. Ba, “Adam: A Method for Stochastic Optimization”, `https://arxiv.org/abs/1412.6980`

BEAM EXTINCTION MEASUREMENT AT THE PIP-II INJECTOR TEST FACILITY*

Mathias El Baz†, Université Paris Saclay, Orsay, France
Brian Fellenz, Vic Scarpine, Alexander Shemyakin, Randy Thurman-Keup, Fermilab, Batavia, USA

Abstract

The PIP-II particle accelerator is a new upgrade to the Fermilab accelerator complex, featuring an 800-MeV H^- superconducting linear accelerator that will inject the beam into the present Fermilab Booster. A test accelerator known as PIP-II Injector Test (PIP2IT) has been built to validate the concept of the front-end of such a machine. One of the paramount challenges of PIP2IT was to validate the bunch by bunch chopping system in the Medium Energy Beam Transport (MEBT). For PIP-II beam operations, the chopper will implement an aperiodic “Booster Injection pattern” that will roughly select two-fifth of the bunches, decreasing the beam current from 5 mA to 2 mA before injection into the cryomodules. Beam measurements have been taken by two Resistive Wall Current Monitors (RWCM) and recorded by a high bandwidth oscilloscope in order to validate the complete suppression of the chopped beam. This paper aims to present the beam extinction measurements at PIP2IT and their limitations.

INTRODUCTION

The PIP-II Injector Test facility, also called PIP2IT (see Fig. 1), is a model of what will be the Front End of PIP-II which will accelerate the H^- ion beam up to 25 MeV. The Front End is often divided into three sections: the Low Energy Beam Transport (LEBT), the Medium Energy Beam Transport (MEBT), and the High Energy Beam Transport (HEBT) which contains the superconducting RF Half-Wave Resonator and Single-Spoke Resonator cavities [1].

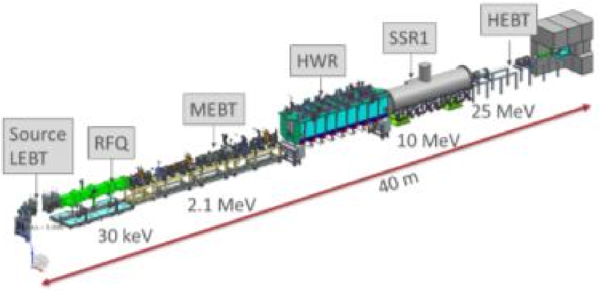

Figure 1: Sketch of PIP2IT.

At the exit of the RFQ, the beam is made of macro-pulses (typically 550 µs), each of them made of short bunches at the frequency of 162.5 MHz.

The bunch-by-bunch chopping system is the heart of the MEBT and one of the most innovative parts of the PIP-II project. The chopper is made of two electric deflectors, called kickers, that kick a pre-programmable set of bunches onto an absorber downstream. The chopper is extremely demanding from a technical perspective, as the kickers voltage reaches 500 V while having the capability to turn on or off in a few nanoseconds [2].

MEASUREMENT SCHEME

Resistive Wall Current Monitor and Cabling

The beam is chopped in the MEBT but the extinction can be measured at any location after the absorber. The data were taken with two identical Resistive Wall Current Monitors (RWCM), one at the end of the MEBT and the other one after the SRF cavities in the HEBT.

A RWCM consists of a resistive gap along a conducting pipe. Charged particles traveling in the vacuum produce a Gaussian shape image current on the surface that has equal magnitude but opposite sign. When this image current passes through the resistive gap, a voltage signal is produced. A ferrite core forces the signal to go through the resistive ring gap made of ceramic rather than allowing it to flow through other conducting paths. The impedance of the ceramic gap is 2.36 Ω (Fig. 2) [3].

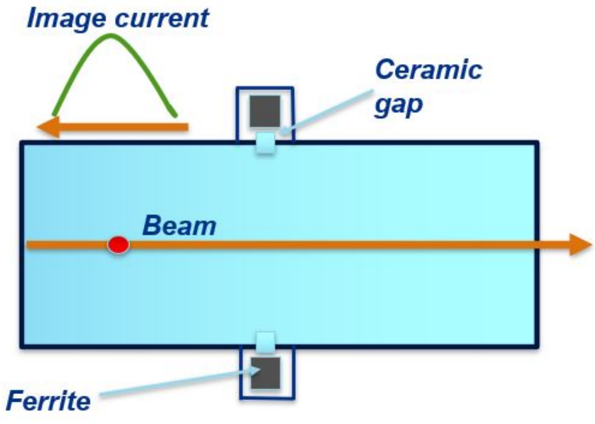

Figure 2: Schematic of the transverse slice of the RWCM.

The RWCM signals are recorded with a Rhode and Schwartz oscilloscope which has an 8 GHz bandwidth.

The same type of cables has been used for the 2 RWCM (but with different cable lengths!), with 4 different cables (including a long Heliax cable) and 5 connectors. The Heliax cable between the MEBT RWCM and the oscilloscope is 30 meters long and is 45 meters long between the HEBT RWCM and the oscilloscope.

---

[*] This work was supported by the U.S. Department of Energy under contract No. DE-AC02-07CH11359

[†] mathias.el-baz@universite-paris-saclay.fr

Extinction Calculation

The extinction measurements aim to give an estimation of the chopping extinction in the specified PIP2IT beam configurations: 550 µs pulse, 2 mA, and most importantly the Booster pattern. Only the bunches that (1) will stay stable and (2) keep an optimum longitudinal distribution at injection into the Booster, are kept in the Booster pattern [4].

Practically, we measure the charge that is left in the chopped beam by groups of successive chopped bunches that we call empty spaces. Likewise, two successive passing bunches will be analyzed together. For example, considering the 2 passing bunches followed by 3 chopped bunches, the extinction will be the ratio of the charge in the cleaned space to the charge of the two passing bunches, and normalized by the factor $\frac{2}{3}$ (Fig. 3) [5].

More generally:

$$\text{Extinction} = \frac{\text{N}_{\text{kicked}}}{\text{N}_{\text{passed}}} \frac{\int_{T_2}^{T_3} s(t)dt}{\int_{T_1}^{T_2} s(t)dt} \qquad (1)$$

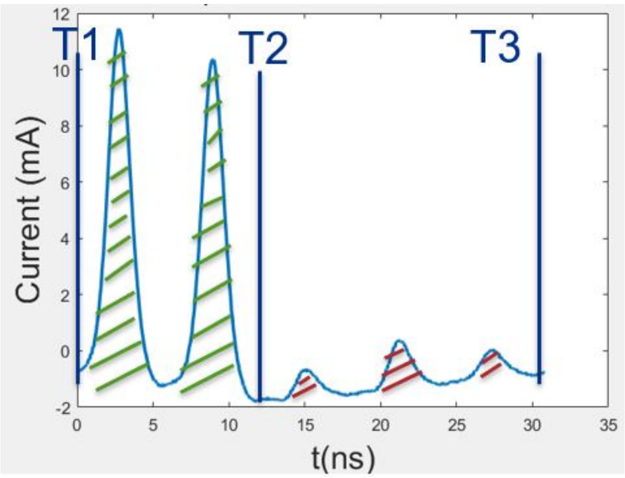

Figure 3: Extinction calculation, non-optimized trajectory (M40CY=−3 A, M50CY=1 A), data taken on March 1st 2021, with the MEBT RWCM (no averaging, 2 passing/3 kicked pattern, 10 µs pulse), Extinction=8% (inspired by D. Frolov's drawing).

ANALYSIS OF THE WAVEFORM DISTORTIONS

Understanding the distortions of the signal (baseline shift, reflections, cable dispersion...) is essential in order to make correct estimations of extinctions. Indeed, the signal left in the cleaned spaces is small (<20 µA) compared to the order of magnitude of the distortions. It is therefore necessary to correct the signal before hand.

Baseline Shift

Measuring beam in the RWCM waveform implies to know its baseline; the remaining charge is the integral of the signal above this baseline. However, knowing the baseline is not obvious in this situation. In Fig. 3 the waveform baseline goes down during the passing bunches and goes up during the cleaned spaces.

This is the consequence of the RWCM frequency response (Fig. 4). The inductance of the cores and the resistance of the gap form a high pass filter with a cutoff frequency of $\frac{R}{2\pi L} = 7$ MHz. As a consequence, the DC component of the signal is cut and the signal needs time to reach the ground voltage when the kickers are on.

Cable Dispersion

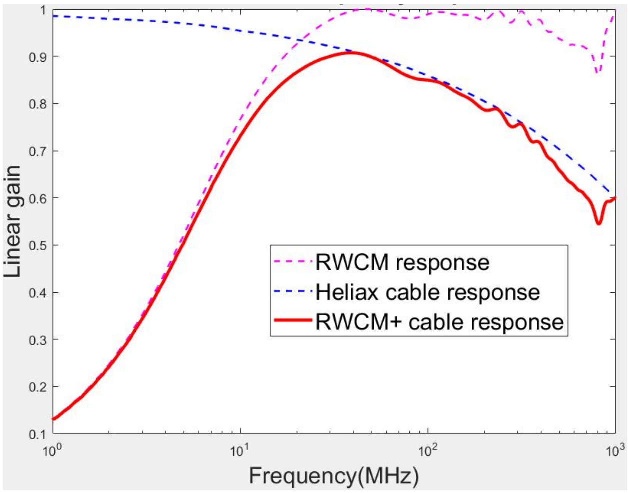

Figure 4: Frequency response of the MEBT Heliax cable (Blue dashed line), the MEBT RWCM (Magenta dashed lines), MEBT cable + RWCM (thick red line).

Dispersion is a signal distortion due to the frequency dependence of the phase velocity of the signal components in coaxial cables. The low frequency components propagate quicker than the high-frequency ones. High frequency components are also more attenuated. Therefore, coaxial cables filter the high frequencies and the beam tails spread in the cleaned spaces.

We use four different cables between the RWCM and the oscilloscope. Only the long Heliax cable significantly distorts the signal and has a cutoff frequency of 1.7 GHz.

Reflections

In addition to the distortions mentioned above, the image current created by the passing bunches is reflected and some of the reflections appear in the cleaned spaces (Fig. 5). At reflection points, a part of the signal power is reflected back to its origin instead of being carried all the way along the cable. This happens where there is an impedance mismatch (between two devices with different impedences for example). The ratio of energy between the reflected bunch and the passing bunch is $\frac{Z_2 - Z_1}{Z_2 + Z_1}$. RWCM waveforms contains several types of reflections: reflections at the connection between two cables, at the oscilloscope input and at the RWCM output (Fig. 6).

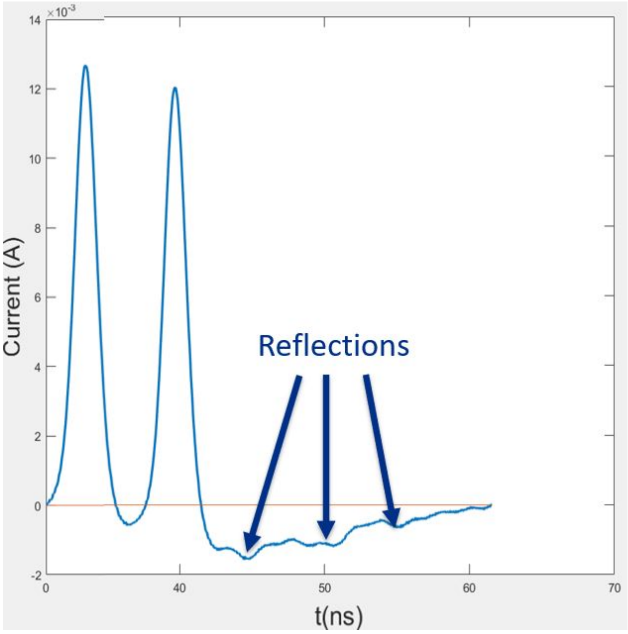

Figure 5: Reflections in the MEBT RWCM waveform with optimum tuning, data taken on March 6th, no averaging, 2 passing/3 chopped pattern, 10 µs pulse, end of pulse.

One of the principal sources of reflection is the connection between the RWCM (2.36 Ω) and the Heliax cable (50 Ω). As the evolution of the impedance between the RWCM and the oscilloscope is not monotonous, we expect both positive and negative reflections.

Figure 6: Cabling between the HEBT RWCM and the oscilloscope (inspired by D. Frolov's drawing).

In order to locate reflections, an instrument called an electrical time-domain reflectometer (ETDR) can be used to locate the points of impedance mismatch. This instrument works by sending a short pulsed signal into the cable and measuring how much time the reflection takes to return. TDR measurements have been performed on April 30th and May 3rd 2021 to locate the sources of reflection between the two RWCM and the oscilloscope. These measurements seem coherent with the set of RWCM waveforms taken during the last week of the PIP2IT run. Although the ETDR is useful to locate the reflections, it could not be used to know accurately the amplitudes of reflections that changed from a shift to another.

The reflections close to the RWCM (with longer round trip time, according to Fig. 7) arrive early in the waveform (3 and 11ns after the passing bunch for the HEBT RWCM) and the reflections close to the scope arrive later in the pulse, after a few hundreds of nanoseconds. Consequently, the beginning of the pulse is always cleaner with fewer reflections, and therefore, easier to analyze.

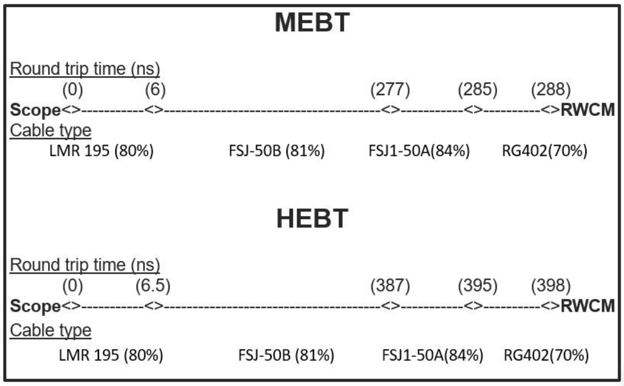

Figure 7: TDR measurements taken on May 3rd for both RWCM.

Not Explained Distortions

Despite the previous analysis, some distortions are still not explained by the day this article is written. These distortions are located right after the passing bunch and the first reflections and look like oscillations of the baseline in the HEBT waveform. Bunches in the MEBT RWCM waveforms are too wide for us to notice these oscillations. Most of these oscillations are not where the suppressed bunches are supposed to be and are likely not remaining beam. In Fig. 8, the ”predicted” waveform corresponds to a simulation of the image current including only the RWCM+cable frequency response and the explained reflections [6].

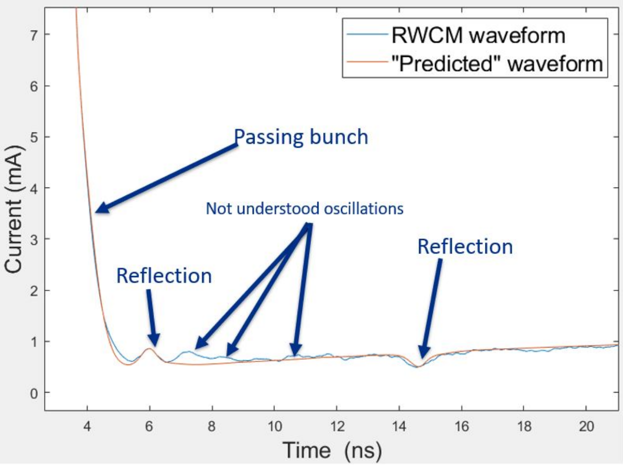

Figure 8: Close up of the not explained oscillations in the data taken on April 15th with the HEBT RWCM, averaging set at 1000, 1 passing/9 chopped pattern, beginning of pulse.

These oscillations are not due to the performance of the chopper since the bumps are not where we could expect remaining beam. The proximity of these bumps to the passing bunch and their orientation leads to the hypothesis of resonances due to the features of the pickup. Multiple reflections likely happen inside the RWCM, between the ceramic gaps or at the connectors. However, the TDR measurements and MicroWave studios simulations could not prove this hypothesis.

These oscillations are dominant over the oscilloscope noise during the first 6–8 ns after the passing bunch. The oscillations are damped and have a maximum amplitude of 250 µA. The precision of the extinction measurements is consequently limited during the 6-8 first nanoseconds of the cleaned spaces.

CONCLUSION

Understanding the RWCM waveform distortions is necessary in order to measure extinctions at PIP2IT since no chopped beam is visible at optimum tuning of the chopping system. In all cases, the measured extinction is consistent with zero, and the results differ by the value of the upper boundary of the uncertainty which depends on the quality of the distortions analysis. A calculation of the extinction and its uncertainty has been done in [6].

However, the estimates for the cleaned space immediately following the passing bunch have a significantly larger uncertainty. Partially it comes from the model approximation of the bunch-induced RWCM signal as Gaussian, while the actual shape is more complicated and the tail spills into the following bucket. The accurate shape has been presented in [4]. This effect is small at high energies, but can still explain the deviation between the expected baseline and the waveform in Fig. 8. In addition, there are after-pulse oscillations clearly not associated with the beam remnants but not properly explained.

ACKNOWLEDGEMENTS

I want to thank the team members for their expertise and assistance on all the aspects of our study and for their help in writing this note. Daniil Frolov's work from 2018 on the extinction measurements with the old setup was extremely useful for the extinction analysis based on RWCM waveforms. I also thank Greg Saewert for giving me his knowledge of his chopping system.

REFERENCES

[1] Valeri Lebedev, "The PIP-II Reference Design Report", FERMILAB-DESIGN-2015-01 `https://inspirehep.net/literature/1607162`

[2] A.V. Shemyakin *et al.*, "Design of 162-MHz CW Bunch-by-Bunch Chopper and Prototype Testing Results", in *Proc. HB'18*, Daejeon, Korea, Jun. 2018, pp. 428–433. `doi:10.18429/JACoW-HB2018-THP1WC03`

[3] J. Crisp and B. Fellenz, "Tevatron Resistive Wall Current Monitor", *J. Instrum.*, vol. 6, p. T11001, 2011. `doi:10.1088/1748-0221/6/11/T11001`

[4] A.V. Shemyakin, "Analysis of BPM harmonics at PIP2IT MEBT", PIP-II Document 2187-v3, 2018.

[5] Daniil Frolov, "Extinction measurement in MEBT", PIP-II Document 1567-v1, 2018.

[6] Mathias El Baz, "Technical note on the extinction meausrements", PIP-II Document 5514-v2, 2021.

ISBN: 978-3-95450-230-1 ISSN: 2673-5350 doi:10.18429/JACoW-IBIC2021-TUPP41

MACHINE LEARNING METHODS FOR SINGLE SHOT RF TUNING

J. S. Lundquist*, S. Werin, Lund University, Lund, Sweden
N. Milas, ESS, Lund, Sweden

Abstract

The European Spallation Source, currently under construction in Lund, Sweden, will be the world's most powerful neutron source. It is driven by a proton linac with a current of 62.5 mA, 2.86 ms long pulses at 14 Hz. The final section of its normal-conducting front-end consists of a 39 m long drift tube linac (DTL) divided into five tanks, designed to accelerate the proton beam from 3.6 MeV to 90 MeV. The high beam current and power impose challenges to the design and tuning of the machine and the RF amplitude and phase have to be set within 1% and 1° of the design values. The usual method used to define the RF set-point is signature matching, which can be a challenging process, and new techniques to meet the growing complexity of accelerator facilities are highly desirable. In this paper we study the use of ML to determine the RF optimum amplitude and phase, using a single pass of the beam through the ESS DTL1 tank. This novel method is compared with the more established methods using scans over RF phase, providing similar results in terms of accuracy for simulated data with errors. We also discuss the results and future extension of the method to the whole ESS DTL.

INTRODUCTION

The European Spallation Source (ESS) is a state of the art neutron science facility under construction in Lund, Sweden [1]. The basic process used by the facility is spallation, wherein one impinges a high neutron material, in this case Tungsten, with high energy protons, causing the target to shed excess neutrons. The high energy protons are provided by the ESS linear accelerator (linac), a 600 m long accelerator consisting of many different sections utilizing varied accelerator technologies in order to raise the proton energy from the 75 keV source output to the final 2.0 GeV arriving on the target. A crucial part of this machine is the 39 m long drift tube linac (DTL) divided into five tanks, designed to accelerate the proton beam from 3.6 MeV to 90 MeV. As the machine is expected to deliver beam of high current and power, a primary concern is to avoid slow beam losses, as these lead to radiation activation of surrounding equipment. In order to avoid such losses, proper and careful tuning of the RF fields is crucial. As a result the requirement for accuracy of the RF set point is to be within 1% in RF amplitude and 1° in phase [1]. In order to achieve this type of accuracy, much work has been performed in the last decades to develop new techniques to meet the growing scale and complexity of facilities [2–4]. Within this paper we will investigate how Machine Learning (ML) may serve this purpose. This paper presents our current strides in the development of a tuning technique using ML, with simulated data used in such a way that a single pass through the untuned cavity could be sufficient for setting it up.

RF TUNING

RF Phase Scan

In order to be able to quantify how the beam responds to changes to the RF set-point, a diagnostic sensitive to the beam time of flight through the cavity must be used. For those cases a Beam Position Monitor (BPM) can be used. As the beam passes a BPM both the amplitude and phase of the fields excited on the BPM sensor by the passing beam are recorded. Although this phase alone doesn't hold much usable information for cavity tuning, by comparing two BPM phases we can get a fast measurement which is proportional to the time-of-flight, or looking with respect to acceleration in a RF cavity, the energy gain between the two devices. It is important to stress that this measurement is relative and that extracting the absolute values of the energy is not an easy task. For this technique, using only the relative phase changes has proven to be enough [2–4].

The BPMs are used to measure the energy gain (or time-of flight) as a function of the set points in the accelerating cavity. As the BPM's measured phase is closely dependent on the energy of the beam, scanning RF amplitude and phase in a cavity and plotting out the resulting phase differences will give rise to different curves depending on the proximity to the ideal set point for the cavity. A few of these signature curves can be seen in Fig. 1, where the ideal set point can be found from the signature for the ideal amplitude $A_0 = 6.89$ kV, the ideal input beam energy $E_0 = 3.62$ MeV and the -35° phase set point.

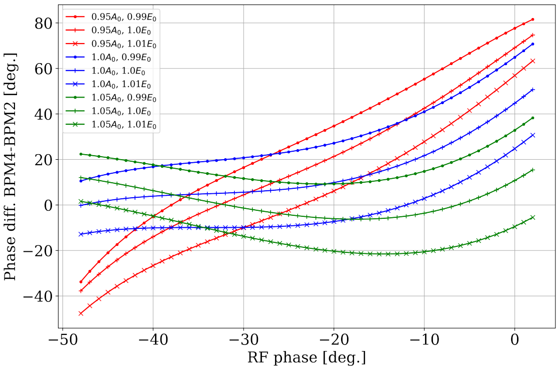

Figure 1: The phase curves for different RF amplitude and input energy set points. BPM phases simulated as comparison between two BPMs in the first DTL tank in the ESS linac.

---

[*] johan.lundquist@ess.eu

Identifying these types of signatures is the basis of most established techniques for cavity tuning [2–4]. We are suggesting a new type of identifiable signature for this type of tuning, which could be measured in a single pass through the cavity, rather than requiring scanning over a parameter, described in more detail in the following section.

Single Shot Measurement

RF phase scans are an established and reliable method for extracting the information needed to achieve good tuning, and with a more limited diagnostic output it is the only option available for now. However, with the large number of BPMs within the ESS DTL section, a restructuring of the data can be done such that we can see distinct signatures for each cavity setpoint in amplitude, phase and beam input energy. We look at BPM phase differences, not against RF phase, but against each diagnostic output, the pairing of BPMs. Figure 2 shows an example of this type of plot, where each line represents a cavity set point and is measured in a single pass through the machine, without scanning any parameter. From here we encounter the same problem to be solved as with the phase scan data, needing to accurately identify these new signatures. The nature of the signatures in this data format leaves ML uniquely equipped for the task.

If accurate predictions can be made with this data format, a few new advantages manifest. Being able to tune the machine acceptably with a single shot could cut down set up times. One would also not require to determine a range for the scanned parameters as in more traditional RF tuning [2, 3] but would in principle reload the last machine state with good settings and run a single verification pulse.

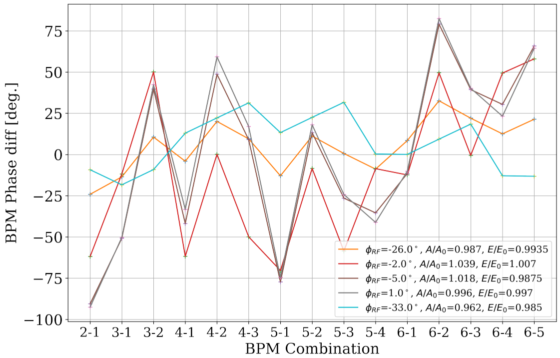

Figure 2: BPM phase differences for each possible BPM coupling, with the different plots each corresponding to a single cavity set point.

Simulations

OpenXAL was used to simulate the first tank of the ESS DTL during acceleration and to reproduce the signals from the six BPMs inside the DTL tank 1 [5, 6]. As phase difference is the data of interest, this results in 15 different BPM combinations, each combination producing one data point for each cavity set point, in RF amplitude and phase and input beam energy. ML requires large amounts of data for training networks and for this purpose an error free dataset was used. This consisted of 110 different amplitude set points, with a variation of ±5.5% around the design RF cavity amplitude A_0, 60 different input beam energy set points, with a variation of ±1.5% around the design input energy E_0, and 55 different phase set points, spread evenly around the -35° design set point.

To this perfect machine four different types of errors were then applied. BPM longitudinal position within the machine was adjusted, potentially caused by installation and construction, as well as the phase readout from these BPMs, produced by electronic limitations. There are also errors arising from production limitations when constructing the cavities. Such limitations could give rise to errors in both RF amplitude and phase gap-to-gap. The different types of errors and their magnitudes are summarized in Table 1.

Table 1: The Different Types of Errors Used in Simulations and Their Corresponding Magnitude

Error Type	Magnitude
BPM Δs	$\pm 100\,\mu$m
BPM $\Delta\phi$	$\pm 1^\circ$
RF Amplitude	$\pm 2\%$
RF Phase	$\pm 0.5^\circ$

MACHINE LEARNING

Machine learning algorithms come in many forms and can solve many distinct problems using varying network structures, definitions of loss and optimization algorithms [7]. The problem we are looking at in this project involves reducing larger scans of data down to three dependent variables, RF amplitude, RF phase and input beam energy. We compare two types of network, a traditional linear regression structure, and a newer decision tree boosting model called XGBoost.

Linear Regression Network

This network was defined using the python library Keras [8]. The library comes with predefined versions of our loss function, mean squared error, and our optimization algorithm, ADAM. ADAM has different coefficients which may be tuned to improve the networks performance, although the learning rate is most relevant [9]. Optimization of the network structure and training parameters was done iteratively, looking at generalized performance as the figure of merit. This was quantified as the loss on a subset of data separated during training. Through this process we arrived at a 10-layer structure with an 160-160-80-80-40 symmetrical neural layout, and a final output layer of three neurons. This was trained for 20 000 epochs with a learning rate of 0.00001. This network was used to produce the results presented in the following section.

Table 2: Three standard deviations in difference between predicted and correct values for the RF Amplitude and phase and the input energy. Results shown for both linear regression (LR) and XGBoost (XGB) network structures.

Data Set		$3\sigma_A$ [%]	$3\sigma_\phi$ [°]	$3\sigma_E$ [%]	μ_A [%]	μ_ϕ [°]	μ_E [%]
No Errors	LR	0.075	0.051	0.045	0.002	0.000	0.002
	XGB	0.891	1.755	0.153	0.025	-0.013	0.002
All Errors	LR	4.002	5.568	0.804	-0.013	-0.068	-0.009
	XGB	3.171	5.217	0.750	0.022	0.038	0.016

XGBoost

The modern ML system of XGBoost (eXtreme Gradient Boosting) is an open source gradient boosting model, which has proven extremely powerful for solving varied, nonlinear problems [10]. Gradient boosting tree models such as this are based on the decision tree model of network structures, with a regularized objective function. In a decision tree ML system, the parameters adjusted in training are not the weighted connections within a network of nodes, but rather the branching criteria in a large decision tree. A gradient boosting ML system uses an ensemble of many decision trees in order to improve the final predictions, and commonly a regularized loss function which penalises increasing complexity of the model as well as the usual error of predictions. This regularized loss is then applied to the ensemble of trees iteratively to improve the output by training the branching criteria.

For the results produced here an ensemble of 10000 trees was used, each with a max allowed depth, the amount of branching criteria, of 20. A learning rate factor of 0.0001 was applied and an early stopping system was also used during training, forcing the training to halt if the generalized performance of the ensemble network did not improve over a period of 500 iterations.

RESULTS

Table 2 shows three standard deviations (3σ) and the mean (μ) of the difference between the predicted and expected value for the RF Amplitude (A) and phase (ϕ), as well as for the input energy (E). The low mean in all rows shows there is little to no systematic offset to the predictions. We see both types of network performing within the given limits on the training data set, although we do see higher standard deviation from the XGBoost training. However, it is generalized performance on the realistic error data set which presents the more relevant figure of merit. Here we see good performance in the energy predictions, but both methods fail to produce the sought results in both phase and amplitude. XGBoost only slightly outperforms the more traditional linear regressor, but remains far outside the limit in the phase prediction. The variation in the single shot signatures as a function of phase is quite small, so networks struggling to distinguish between these is understandable.

OUTLOOK

While both methods may fail the limits for operation at this stage of investigation, there are still many factors which could prove this method more reliable than suggested by these results. The error data set produced may have been pessimistic in the predictions of one or many of the factors included. Further optimization of the meta parameters for the training of the networks could reveal better results in the future. New data sets could be produced with more distinguished patterns arising from difference in RF phase.

Furthermore, even if this technique would prove unable to produce the sought results for initial cavity tuning, the 1° and 1% error in RF phase and amplitude predictions, it does not render it useless. The single shot nature of the data could allow for updated tuning information during operation of the machine, as well as long term tracking of drifts on the RF parameters. Also, the data available for each set point increases rapidly with added diagnostics. Applying this single shot data to the full ESS DTL section would include more BPM combinations, and the increase in available data could perhaps be sufficient to improve the method to within the restrictions. Further applications of this online tuning information could be developed in the future, for use in the ESS control room or elsewhere.

ACKNOWLEDGEMENTS

This study has only been possible with the help of the entire Beam Physics team at ESS, as well as that of other teams at the facility.

REFERENCES

[1] R. Garoby *et. al.*,“The European Spallation Source Design”, *Physica Scripta*, vol 93, p. 014001, 2018.

[2] G. Shen and M. Ikegami, “Tuning of RF amplitude and phase for the drift tube linac in J-PARC”, *Chin. Phys C*, vol. 33, p. 577, 2009.

[3] T.L. Owens, M. B. Popovic, E. S. McCrory, C. W. Schmidt and L.J. Allen, “Phase Scan Signature Matching for Linac Tuning”, *Particle Accelerators*, vol. 8, no 1, pp. 169-179, 1994.

[4] G. B. Shen, H. Sako, and S. Sato, “RF Amplitude and Phase Tuning of J-PARC SDTL”, in *Proc. 22nd Particle Accelerator Conf. (PAC’07)*, Albuquerque, NM, USA, Jun. 2007, paper TUPAN062, pp. 1529–1531.

[5] J. Galambos, A. V. Aleksandrov, C. Deibele, and S. Henderson, “PASTA An RF Phase and Amplitude Scan and Tun-

ing Application”, in *Proc. 21st Particle Accelerator Conf. (PAC’05)*, Knoxville, TN, USA, May 2005, paper FPAT016, pp. 1529-1531.

[6] OpenXAL, `https://openxal.github.io/`.

[7] A. Edelen *et al.*, “Opportunities in Machine Learning for Particle Accelerators”, **1811.03172**, arXiv, 2018.

[8] Keras, `https://keras.io/`.

[9] D. P. Kingma and J. Ba, “Adam: A Method for Stochastic Optimization”, **1412.6980**, arXiv, 2017.

[10] T. Chen and C. Guestrin, “XGBoost: A Scalable Tree Boosting System”, **1603.02754**, arXiv, 2016.

ISBN: 978-3-95450-230-1 ISSN: 2673-5350 doi:10.18429/JACoW-IBIC2021-TUPP42

GOUBAU-LINE SET UP FOR BENCH TESTING IMPEDANCE OF IVUE32 COMPONENTS

Paul Volz[*], A. Meseck, M. Huck, S. Grimmer
Helmholtz-Zentrum Berlin für Materialien und Energie (HZB), Berlin, Germany

Abstract

IVUE32 is the world first elliptical in-vacuum undulator, being developed at HZB. With a period length of 32 mm and a minimum gap of 7 mm, the 2.5 m long insertion device (ID) will be installed in the BESSY II storage ring, delivering soft X-rays to several beam lines. In-vacuum undulators put complex structures in close proximity of the particle beam which makes them susceptible to wake field effects. These effects can cause beam instabilities and unwanted heating of undulator components, possibly damaging them. Therefore understanding the impedance characteristics of the device prior to installation is paramount. Numerical studies, e.g. CST simulations of such complex structures become very resource intensive for high frequencies, making the ability to bench test such a device invaluable. A Goubau line is a single wire transmission line for high frequency surface waves that can mimic the transverse electric field of a charged particle beam out to a certain distance, allowing for impedance measurements of IDs outside of the working accelerator. The status of a Goubau-line set up, optimized for measuring IVUE32-components, will be presented.

INTRODUCTION

BESSY II is a third generation synchrotron light source with an electron beam energy of 1.7 GeV. There are 32 dipole magnets and 13 undulators supplying 48 beam lines with radiation ranging from infrared to soft X-ray. In September of 2018 the first in-vacuum undulator (IVU) CPMU17 [1] was installed in BESSY II to provide hard X-rays for the Energy Materials In-Situ Laboratory (EMIL) [2]. As previously described in [3] IVUs require shielding foils between their magnets and the accelerator beam. The second IVU for BESSY II, IVUE32 [4], is currently under developement. The APPLE II configuartion poses even greater design challenges than the planar CPMU17. IVUE32 features four individually movable magnet rows which requires a longitudinal slit in the shielding foils. The split shielding foils further complicate the design of the transition taper between the beam pipe and the undulator magnets.

Motivation

Without a vacuum chamber wall between the beam and the undulator magnets, both CPMU17 and IVUE32 change their geometry from a collimator to a cavity over the entire gap range. This has an impact on wakefield characteristics and beam dynamics. The impact on beam stability is dificault to simulate. Beam based impedance measurements using orbit bump and tune shift methods have been done for the already installed CPMU17 with different gap settings [5]. Grow-damp and drive-damp methods have been utilized as well by M. Huck *et al.* [6]. The novel design of IVUE32 brings even more challenges as the shielding foil is split in the middle longitudinally to accommodate the different polarization settings. Therefore the impact on beam stability and accelerator operation are difficult tu simulate and predict. Beeing able to measure impedance outside of the running accelerator is desirable to avoid complicated down time. As introduced in [3] a Goubau-line test stand is a possible way to measure impedance of insertion devices. Designed by Georg Goubau in 1950 [7] based on the work of Sommerfeld from 1899 [8], a Goubau-line is a transmission line that uses a single wire to transmit surface waves. Its transverse electric field can be used to mimic that of a charged particle beam. Goubau-line set ups have been successfully used to measure the impedance of accelerator components, for example at Argonne APS [9] or at Bergoz Instrumentation [10]. Studies of CPMU17s impedance suggest that the fill pattern at BESSY II induces effects up to a frequency of 20 GHz which is significantly higher than the aforementioned test stand examples.

The following sections will discuss the design parameters of a Goubau-line test stand, capable of measuring up to frequencies of 20 GHz.

THEORETICAL CONSIDERATIONS

The main parts making up a Goubau-line are a transmitter, a receiver and a dielectrically coated wire. Horn antennas are usually used as transmitter and receiver shown in Fig. 1. The transmitted waves are guided as transverse magnetic modes the coated wire. Figure 2 shows the orientation of electric and magnetic fields along the coated wire. The electric and magnetic Fields are described by cylinder functions. These formulars are derived in Goubau's original paper [7] and in a revision considering modern computational advances by B. Vaughn *et al.* [11]. Three distinct regions can be considered: inside of the conductor, inside of the dielectric coating, and outside of the wire. The continuity of the fields accross the interfaces of these regions can be used to numerically calculate the guided wave propagation constant [11] and

Figure 1: Schematic of a Goubau-line consisting of two conical horn antennas and a dielectrically coated wire similar to the design at Argonne APS [9].

---

[*] paul.volz@helmholtz-berlin.de

ISBN: 978-3-95450-230-1 ISSN: 2673-5350 doi:10.18429/JACoW-IBIC2021-TUPP42

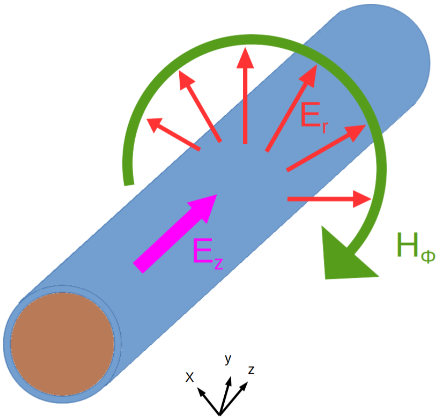

Figure 2: Schematic of field orientation of a Goubau-line. The copper conductor is shown with a dielectric coating in blue.

the transverse electric field of the Goubau-line. The fields outside of the wire are described by Hankel functions

$$E_r = iA\frac{h}{\gamma_0}H_1^{(1)}(\gamma_0 r)e^{i(\omega t - hz)} \tag{1}$$

$$E_z = AH_0^{(1)}(\gamma_0 r)e^{i(\omega t - hz)} \tag{2}$$

$$H_\phi = iA\frac{k_0^2}{\omega\mu\gamma_0}H_1^{(1)}(\gamma_0 r)e^{i(\omega t - hz)} \tag{3}$$

with

$$\gamma_i^2 = k_i^2 - h^2 \tag{4}$$

where h is the guided wave propagation constant, k_0 is the free wave propagation constant, and A is a complex amplitude. The radial electric field (1) is proportional to $1/r$ close to the wire. Therefore it can be used to emulate a charged particle beam before falling off exponentially at greater distances from the wire. The usable region is determined by the radial wave number γ_0 [11]. The frequency of the guided wave, the thickness of the conductor and dielectric insulation, as well as the dielectric constant of the insulation determine γ_0. Minimizing γ_0 extends the distance from the wire at wich the Goubau-line can emulate the fields of a charged particle beam. In order to conduct meaningful measurements, the electric field needs to extend further than the aperture of the device under test.

Wire Properties

IVUE32 has a maximum aperture of around 22 mm. A Goubau-line with a transverse electric field extending out to about 30 mm at a frequency of 20 GHz is needed to survey IVUE32. As shown in [3] a 1 mm diameter copper wire coated with 500 nm of Cerablak™ [12] produces the desired field parameters. Figure 3 shows the amplitude of the radial electric field for a 1 mm diameter copper wire with different coats of Cerablak™ [12].

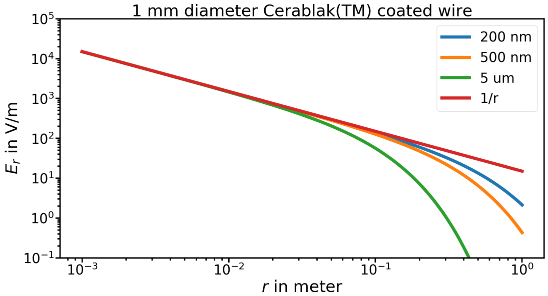

Figure 3: Amplitude of transverse electric field of a Goubau-line using a 1 mm diameter copper wire with several thicknesses of Cerablak™ [12] coating at 20 GHz.

Characteristic Impedance

In order to impart the surface waves onto the Goubau-line, the characteristic impedance needs to be calculated. The characteristic impedance of the Goubau-line depends on the wire parameters and also the frequency of the guided waves. It can be calculated with an equvalent TEM expression as shown by B. Vaughn *et al.* [11].

$$Z_{GB} = \frac{Z_0 \ln\left(\frac{b}{r_c}\right)}{2\pi} \tag{5}$$

where $Z_0 = 377\ \Omega$ is the intrinsic impedance of free space, r_c is the radius of the Goubau-line conductor, and b is the radius of the outer conductor of an equivalent coaxial cable. This equivalent radius is obtained by equating the power flow through the Goubau-line to an equivalent coaxial cable

$$P_{eq} = \frac{1}{2}\mathrm{Re}(V_g I_z^*) = \frac{4A^2\omega\epsilon_0\mathrm{Re}(h)}{\pi\,|\gamma_0|^4}\ln\left(\frac{b}{r_c}\right) \tag{6}$$

$$V_g \approx \frac{iAh}{\gamma_0^2}\left(H_0^{(1)}(\gamma_0 r_c) - H_0^{(1)}(\gamma_0 b)\right) \tag{7}$$

$$I_z = \frac{2\pi\sigma A r_c}{\gamma_0}H_1^{(1)}(\gamma_0 r_c)\left(\frac{k_0}{k_c}\right)^2 \tag{8}$$

with

$$k_c = \omega\sqrt{\mu_0\left(\frac{\sigma}{i\omega} + \epsilon_0\right)}$$

where σ is the conductivity of the Goubau-line wire. Equation (6) is solved numerically for b and the characteristic impedance is then obtained via Eq. (5). Figure 4 shows how the characteristic impedance of a Goubau-line using a 1 mm diameter copper wire coated with 500 nm of Cerablak™ [12] changes with the frequency of the guided wave.

Transmitter and Receiver

To excite the surface waves on the insulated wire a transmitter or launcher is needed. Cone or horn antennas are mainly used for that task. These consist of the outside cone and a center conductor which together act as a coaxial transmission line taper. Its main purpose is to match the impedance of the Goubau-line with that of the signal source,

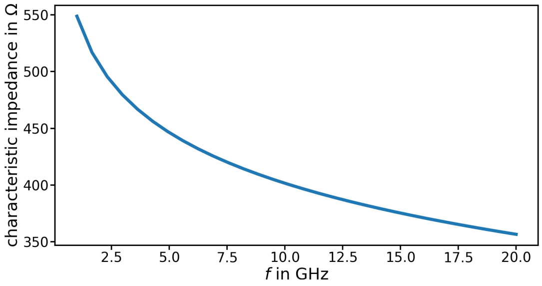

Figure 4: Characteristic impedance of a Goubau-line using a 1 mm diameter copper wire coated with 500 nm of Cerablak™ [12] as a function of frequency.

most likely a 50 Ω coaxial cable. To ensure the quality of the measurements, the impedance transition should be as smooth as possible in order to minimize reflections. As shown in Fig. 4 the charcteristic impedance of a Goubau-line depends on the frequency of the guided wave. For the fill pattern at BESSY II we expect an impedance response from the IVUs between 10 and 20 GHz. Over that frequency range the characteristic impedance of the Goubau-line varies between 350 and 400 Ω. Therefore a perfectly smooth impedance transition is not possible over the measuered frequency band.

There are several possible designs for the transmission line taper. For example at the Argonne Advanced Photon Source a conical antenna was used together with a six-section matching transformer as a taper [9]. Another example would be an antenna with a Gaussian profile together with a Klopfenstein taper used by Bergoz Instrumentation [10]. The optimal design depends on the frequency band, the maximum accepted reflection coefficient and the space available.

The design and characterization of the antennas for the BESSY II test stand are still in progress.

CONCLUSION

In order to extend the frequency range of a Goubau-line test stand to 20 GHz a new design from the ground up is necessary. The presented calculation results show, which type of wire and dielectric coating can achieve the required frequency range necessary for the IVU measurements at BESSY II. The characteristic impedance of the Goubau-line has been calculated over the desired frequency range. The design of the horn antennas and tapers still needs to be finalized.

As a next step, coated wire for the Goubau-line will be ordered and first reflection coefficient measurements will be set up.

ACKNOWLEDGEMENTS

I would like to thank Günther Rehm for his discussions and advice regarding high frequency instrumentation and Frank Stulle for sharing his experience regarding Goubau-Lines.

REFERENCES

[1] J. Bahrdt *et al.*, “Characterization and Implementation of the Cryogenic Permanent Magnet Undulator CPMU17 at Bessy II”, in *Proc. 10th Int. Particle Accelerator Conf. (IPAC’19)*, Melbourne, Australia, May 2019, pp. 1415–1418. `doi:10.18429/JACoW-IPAC2019-TUPGW014`

[2] K. Lips *et al.*, “EMIL: the Energy Materials in-Situ Laboratory Berlin – a Novel Characterization Facility for Photovoltaic and Energy Materials”, Sep. 2015

[3] P. I. Volz, S. Grimmer, M. Huck, and A. Meseck, “Goubau-Line Set Up for Bench Testing Impedance of In-Vacuum Undulator Components”, presented at the 12th Int. Particle Accelerator Conf. (IPAC’21), Campinas, Brazil, May 2021, paper THPAB057.

[4] J. Bahrdt, W. Frentrup, S. Grimmer, C. Kuhn, C. Rethfeldt, M. Scheer, and *et al.*, “In-Vacuum APPLE II Undulator”, in *Proc. IPAC’18*, Vancouver, Canada, Apr.-May 2018, pp. 4114–4116. `doi:10.18429/JACoW-IPAC2018-THPMF031`

[5] M. Huck, J. Bahrdt, H. Huck, A. Meseck, and M. Ries, “Transverse Broad-band Impedance Studies of the New In-vacuum Cryogenic Undulator at Bessy II Storage Ring”, in *Proc. IBIC’20*, Santos, Brazil, Sep. 2020, pp. 263–267. `doi:10.18429/JACoW-IBIC2020-THPP26`

[6] M. Huck, J. Bahrdt, A. Meseck, G. Rehm, M. Ries, and A. Schaelicke, “Experimental Studies of the In-Vacuum-Cryogenic Undulator Effect on Beam Instabilities at BESSY II”, presented at the 12th Int. Particle Accelerator Conf. (IPAC’21), Campinas, Brazil, May 2021, paper WEPAB134.

[7] G. Goubau, “Surface Waves and Their Application to Transmission Lines”, *Journal of Applied Physics*, vol. 21, pp. 1119-1128, 1950. `doi:10.1063/1.1699553`

[8] A. Sommerfeld, “Ueber die Fortpflanzung elektrodynamischer Wellen längs eines Drahtes”, *Ann. Phys.*, vol. 303, pp. 233-290, 1899. `doi:10.1002/andp.18993030202`

[9] M. P. Sangroula, R. R. Lindberg, R. M. Lill, and R. Zabel, “Measuring vacuum component impedance for the Argonne Advanced Photon Source upgrade”, *Phys. Rev. Accel. Beams*, vol 23, p. 082803, 2020. `doi:10.1103/PhysRevAccelBeams.23.082803`

[10] S. Y. Kim, F. Stulle, C. K. Sung, K. H. Yoo, J. Seok, K. J. Moon, *et al.*,“Characterization of the Goubau line for testing beam diagnostic instruments”, *J. Instrum.*, vol. 12, p. P12016, 2017. `doi:10.1088/1748-0221/12/12/p12016`

[11] B. Vaughn and D. Peroulis, “An updated applied formulation for the Goubau transmission line”, Journal of Applied Physics, vol. 126, p. 194902, 2019, `doi:10.1063/1.5125141`

[12] Applied Thin Films Inc., `https://www.atfinet.com`

ISBN: 978-3-95450-230-1 ISSN: 2673-5350 doi:10.18429/JACoW-IBIC2021-TUPP43

DESIGN OF A MULTI-LAYER FARADAY CUP FOR CARBON THERAPY BEAM MONITORING*

K. Tang†, R. S. Mao, Z. G. Xu, T. C. Zhao, Z. L. Zhao, K. Zhou
Institute of Modern Physics, Chinese Academy of Sciences (IMP/CAS), Lanzhou, China

Abstract

Because of determining the depth of Bragg Peak, range and energy of carbon beam are very important parameters in therapy. In order to measure those parameters rapidly, we design a multi-layer Faraday cup (MLFC). Simulation of proton beam and carbon beam are given in this paper. A prototype has 128 channels have been developed. Each consists of a 40 µm copper foil and 600 µm FR4 plate. A 128 channels electronics was used to measurement the deposited ions in each copper foil.

INTRODUCTION

China's first Heavy Ion Medical Machine (HIMM) developed by the Institute of Modern Physics (IMP) was approved to be registered at January 10, 2020. The main parameters at treatment place are listed in Table 1.

Table 1: Main Beam Parameters of HIMM

Parameters	Value
Ion	$^{12}C^{6+}$
Beam energy	80~430 MeV/u
Intensity at treatment room	(2 pA ~ 0.4 nA) 2e6 ~ 4e8 pps
Extraction time	2 s
Extraction cycle	8 s

It is very crucial that the difference between the radiation field achieved by patient and given by prescription is as small as possible. Two of most importance beam parameters which decide the radiation field are beam energy and beam energy distribution. Therefore, these parameters should be checked or calibrated before treating.

Overview of range verification of proton and light-ion beams have been given by W. T. Chu [1]. It involves ex vivo or off-line measurement method [2] and in vivo or online measurement method. MLFC (Multi Layer Faraday Cup) was proposed for testing Monte Carlo models [3]. And then it was first applied to verify proton range by Bernard Gottschalk at NPTC [4]. Now it has become a conventional tool and has been used in numerous proton therapy research center [5-13]. However, MLFC can only used for proton beam so far. Because, in proton therapy most of the primary particles will stop near Bragg Peak with no secondary fragments creation. But for carbon particles, there will be several charged secondary fragments such as H, He ,Li ,Be and B created. Those charged particles will be collected by charge meter as well as primary carbon particles.

After carefully analyzing the affection by secondary fragments and with Fluka simulation, the author find that the peak of beam charge collection curve was near Bragg Peak. So, we propose that use MLFC to measure carbon beam range and energy. In this paper, the measurement theory will be described firstly. And then, Fluka simulation result will be given. Finally, a prototype of MLFC are also given.

EXPERIMENT METHODS

Measurement Theory

The theory of MLFC is well-documented. A MLFC is a stack of metal collecting plates which separated from each other by thin insulating plates. MLFC is connected to a multi channel charge meter so that each active sheet of the MLFC is connected to one channel. Take proton beam for example, if a proton beam (for a therapy beam, beam energy are usually from 70 MeV to 250 MeV) inject into a MLFC, most proton particles will pass through several metal plates and insulating plate and stop near Bragg peak position in the last. When particles stop, each layer plate can collect the deposited charge. In other words, the MLFC can measure beam differential fluence as a function of depth [4].

As a result of statistical fluctuations, the effect of range straggling give a charge distribution. For a therapy proton beam, range straggling can be modelled by a Gaussian distribution [14-16]. Because proton is the lightest ion so no nuclear fragments created. Therefore, no extra charged particles or charged fragments affect the charge collection. So, we can use MLFC to measure the proton range and energy.

But for carbon beam, the situation is different. High energy charged fragment occur along the beam penetration path in materials. These charged fragments include H, He ,Li ,Be and B. Those fragments will continue move forward and will also be collected by charge meter as well as primary carbon particle. Its will have an affection on charge collection. Fortunately, the peak of these charged fragments are near the Bragg peak.

Differential Fluence v. Depth of Proton Beam

For proton therapy beam, the range distribution can be described by Gaussian function [14-16]

$$R_0(x) = I_0 \exp\left(-\frac{(x-R_0)^2}{2\sigma_0^2}\right) \tag{1}$$

Where I_0 is beam total charge, R_0 is beam range and σ_0 is the sigma of the Gaussian range straggling. The differential charge distribution as a function of depth in copper of a 70 MeV proton beam is simulated by Fluka (Fig. 1). The

---

* Work supported by the Young scientists Fund Grant NO.11905075
† email address: tangkai@impcas.ac.cn

ISBN: 978-3-95450-230-1 ISSN: 2673-5350 doi:10.18429/JACoW-IBIC2021-TUPP43

basic parameters and process is described below. The density of the copper is 8.9 g/cm^3 and the total thickness of the copper plate is 10 mm. Beam fluence at each depth are calculated by USRTRACK card and the differential charge (deposited charge in each layer) can be derived by subtraction. Gaussian fitting of the differential fluence curve shows a good fitting. This point confirmed the hypothesis. Beam range given by the fitting result is 7.04 mm, which is consistent with NIST result 7.09 mm. In another words, we can use the maximum position of the differential fluence distribution or deposited charge distribution as the beam range. We also can derive beam energy form beam range.

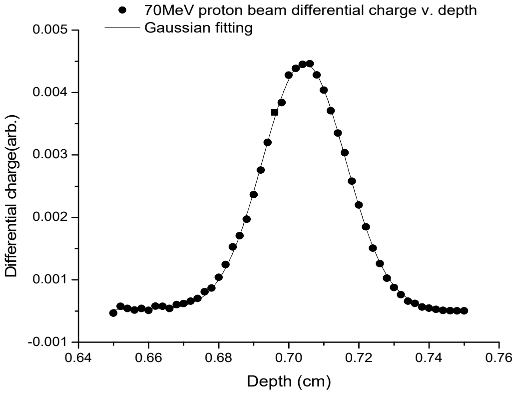

Figure 1: The differential charge distribution as a function of depth of 70 MeV proton beam in copper (points) and Gaussian fitting (solid line).

We also simulated the deposited charge by 250 MeV with 0.5% Gaussian distribution energy spread proton beam in each copper plate of a MLFC (Fig. 2). The MLFC have 64 layer copper plates with 1 mm thickness and 64 layer Kapton insulting films with 50 µm thickness.

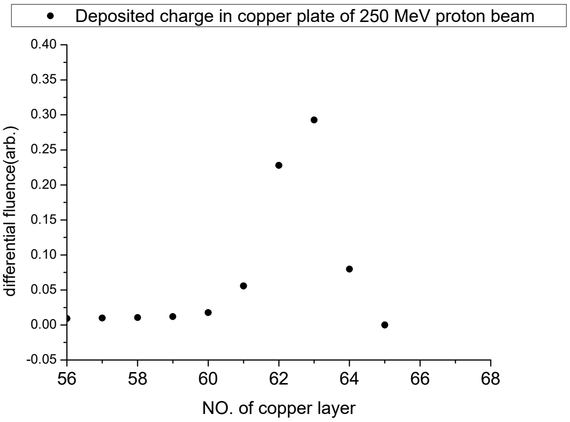

Figure 2: The deposited charge in each layer of 250 MeV 0.5% Gaussian distribution energy spread proton beam.

Deposited Charge v. Depth of Carbon Beam

As analyzed before, there will be many kinds of charged segments produced when carbon beam penetrating material. E. Haettner and H. Iwase et al have studied nuclear fragmentation of 200 and 400 MeV/u ^{12}C ions in water through experiment [17-18]. According their experiments, the amount of charged fragments increase with depth and a maximum is reached around the Bragg peak. Behind the Bragg peak the amount of fragments drops down sharply. As a result, we still can use the maximum position of the deposited charge distribution as beam range. The problem is how large the error introduced.

According their experiment's result, H and He are produced most frequently while the production of heavier fragments (B, Be and Li) is much smaller. For example, the Bragg peak is 25.8 cm for carbon in water. At this depth the yields of production are about 0.76 (H), 0.55 (He), 0.06(Li), 0.03 (Be) and 0.07 (B). Because a H^+ ion and a Li^+ ion contains 1 unit charge. A He^{2+} ion and a Be^{2+} ion contains 2 units charge, and a B^{3+} ion contains 3 units charge. From the perspective of the quantity of electric charge, the yields of production of these five fragment are 0.126 (H), 0.183 (He), 0.01 (Li), 0.01 (Be) and 0.035 (B). In total, the electric charge of fragments is 31 percent of the carbon particles.

Simulation of Deposited charge of Carbon Beam

Firstly, Bragg peak curve of 400 MeV/u carbon beam in water was simulated by Fluka. The simulation result show that the Bragg peak is at 27.35 mm. Deposited charge as a function of depth was also simulated. The maximum of the curve is at 27.34 mm which is equal to the Bragg peak.

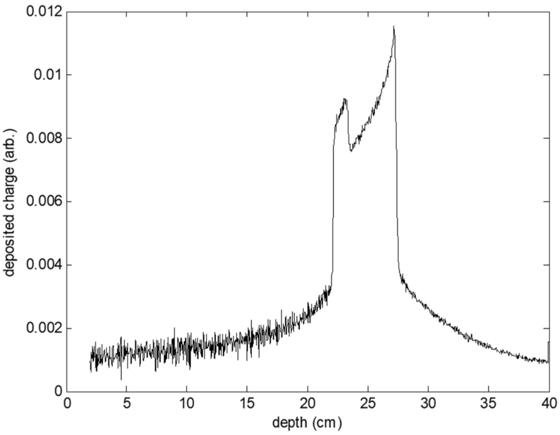

Figure 3: The deposited charge in water of 400 MeV/u carbon beam.

Prototype Design

Our goal is design a MLFC which can cover 80 – 430 MeV/u carbon beam range measurement. Our MLFC (see Fig. 4) consist of 128 layer sheets which include a 29 µm copper foil and a 600 µm FR4 plate which corresponds to approximately 177 µm copper. The diagram of sheet is 90 mm. One sheet is correspond to 206 µm copper. In total, 128 layers sheet are approximately 26.368 mm which equals to the beam range of 286.7 MeV/u carbon beam.

In order to fulfill measurement of 286.7 ~430 MeV/u carbon beam, an absorber system also be designed. The absorber system consists of 2 thick copper whose thickness are 10 mm and 30 mm.

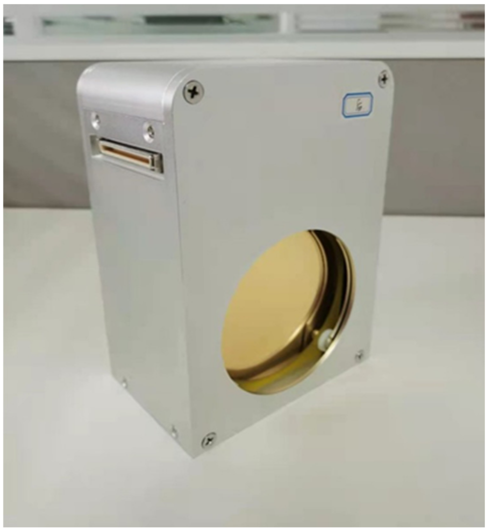

Figure 4: A MLFC prototype consists of 128 layers sheet.

The beam diagnostic system consists of a 128 channel electronics (Fig. 5), a high speed digital I/O module NI 9402, a digital acquisition card NI 9215 and a controller NI cRIO 9064 (Fig. 6). The 128 channel electronics is developed by IMP Electronics Group.

Figure 5: 128 channels electronics.

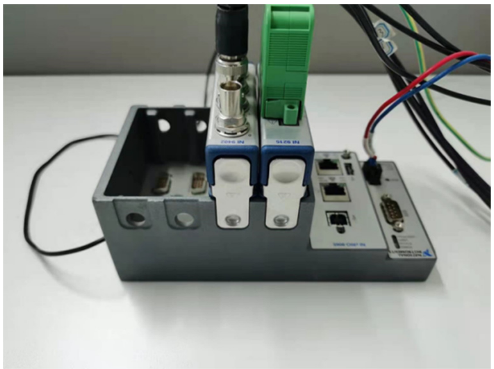

Figure 6: NI 9402, NI 9215 and NI cRIO 9064.

A LabVIEW program was written for controlling and data analysis. And a calibration program is also written. By using Keithley 6221 current source, we calibrate the electronics response at 0.2 nA ~ 2 nA with step 0.2 nA. The calibration coefficient was obtained.

Outlook

Next stage, we plan to do some experiment. And experiment data will be compare with water tank. We find 2 peaks occur in deposited charge distribution curve (see Fig. 3). It will be analyzed by simulation and experiment.

REFERENCES

[1] W. T. Chu, Ludewigt B-A, and Renner T-R, “Instrumentation for treatment of cancer using proton and light-ion beams”, *Review of Scientific Instruments*, vol. 64(8), pp. 2055-2122, 1993.

[2] A.C. Knopf, and L. Antony, “In vivo proton range verification: a review”, *Physics in Medicine and Biology*, vol. 58(15), pp. R131-R160, 2013.

[3] Bernard Gottschalk, Platais Rachel, and Paganetti Harald, “Nuclear interactions of 160 MeV protons stopping in copper: A test of Monte Carlo nuclear models”, *Medical Physics*, vol. 26(12), pp. 2597-2601, 1999.

[4] B Gottschalk. “Calibration of the NPTC range verifier”, 2001, `http://users.physics.harvard.edu/~gottschalk`

[5] M. R. Nchodu. “Determination of energy spectra of proton therapy beams”, Ph.D. thesis, Phys. Dept., University of Cape Town, Western Cape, South Africa, 2002.

[6] H. Berkhoff *et al.*, “Test of a Multi-layer Faraday cup for quick beam energy measurement at PROSCAN”, PSI Scientific and Technical Report Volume VI. 2003, unpublished.

[7] B. Przewoski *et al.*, “Beam Properties of the new Radiation Effects Research Stations at Indiana University Cyclotron Facility”, *2004 IEEE Radiation Effects Data Workshop*, pp 145-150, 2004.

[8] R. Dölling, “Profile, Current, and Halo Monitors of the PROSCAN Beam Lines”, in *AIP Conference Proceedings*, vol. 732, p. 244, 2004.

[9] J-W Kwon *et al.*, “Development of a CCD-scintillator device and a multi-layer Faraday cup for therapeutic proton beam monitoring”, *Journal of Korean Physical Society*, vol. 48(4), pp. 759-762, 2006.

[10] M. A. Mcmahan *et al.*, “Standard Practice for Dosimetry of Proton Beams for use in Radiation Effects Testing of Electronics”, `https://www.osti.gov/servlets/purl/937497`

[11] C. H. Wen, *et al.*, “Energy spectrum control for modulated proton beams”, *Medical Physics*, vol. 36(6), pp. 2297-2308, 2009.

[12] J Kim and K. Dogyun, “Development of dosimetry tools for proton therapy research”, *Radiation Measurements*, vol. 45(10), pp. 1417-1421, 2010.

[13] C. S. G. Kunert, J. Bundesmann, T. Damerow, A. Denker, and A. Weber, “A Multi-leaf Faraday Cup Especially for the Therapy of Ocular Tumors with Protons”, *in Proc. 5th Int. Particle Accelerator Conf. (IPAC'14)*, Dresden, Germany, Jun. 2014, pp. 2149-2152. `doi:10.18429/JACoW-IPAC2014-WEPRO082`

[14] T Bortfeld and W. Schlegel, “An analytical approximation of depth-dose distributions for therapeutic proton beams”,

Physics in Medicine & Biology, vol. 41(8), pp. 1331-1339, 1996.

[15] T. Bortfeld, “An analytical approximation of the Bragg curve for therapeutic proton beams”, *Medical Physics*, vol. 24(12), p. 2024, 1997.

[16] Anwar Kamal, *Passage of Radiation Through Matter*, Heidelberg, Berlin, Germany: Springer, 2014.

[17] E Haettner, H. Iwase, and D. Schardt, “Experimental fragmentation studies with 12C therapy beams”. *Radiation Protection Dosimetry*, vol. 122(1-4), pp. 485-487, 2006.

[18] E Haettner *et al.*, “Experimental study of nuclear fragmentation of 200 and 400 MeV/u12C ions in water for applications in particle therapy”, *Physics in medicine & biology*, vol. 58(23), pp. 8265-8279, 2013.

10th Int. Beam Instrum. Conf. IBIC2021, Pohang, Rep. of Korea JACoW Publishing
ISBN: 978-3-95450-230-1 ISSN: 2673-5350 doi:10.18429/JACoW-IBIC2021-TUPP44

DESIGN OF HYDROSTATIC LEVEL SYSTEM FOR THE APS-U STORAGE RING*

W. Cheng[#], D. Karas, G. Wang
Argonne National Laboratory, Lemont, IL, USA

Abstract

A Hydrostatic Leveling System (HLS) has been designed for the Advanced Photon Source Upgrade (APS-U) storage ring (SR) to characterize the relative floor motion along each Insertion Device Front End (IDFE) and the global floor motion of the SR tunnel. 3 HLS sensors will be installed alongside each IDFE. Two sensors will be mounted near the ID Beam Position Monitors (BPMs), which are located at either end of the ID. The 3rd HLS sensor will be mounted near the Grazing-Incidence Insertion Device X-Ray BPM (GRID xBPM), about 20 meters away from the source point. In addition, there will be 1 sensor installed in each of the 5 sectors in Zone-F where there are no ID beamlines. The HLS water network along each of the 35 IDFEs and 5 sectors in Zone-F are connected via valves to form a global network around the 1.1 km SR tunnel. The HLS will measure the vertical floor displacement at a total of 110 locations. Combined with the highly stable BPM/xBPM stands, the HLS can better characterize the electron and photon beam long-term stability. The HLS design is based on a two-pipe system for easy installation in tight spaces. In this paper, we present the design of the HLS system and preliminary performance of the first article units.

INTRODUCTION

Modern light sources have tight requirements of the beam stability. For example, the Advanced Photon Source Upgrade (APS-U) machine asks for an orbit stability [1] of 0.4 µm for short term (0.01 Hz – 1 kHz) and 1 µm for long-term (7 days). With careful design of the magnets, the supporting structure, Beam Position Monitor (BPM) electronics and the orbit feedback system, the short-term orbit stability can normally be achieved. However, the long-term stability is not obviously achievable even with the best modern electronics and feedback algorithms. The situation is even more complicated by comparing the stability of electron beam and photon beam. Long-term stability is affected by many factors including the mechanical/thermal stability of BPM/xBPM stands, BPM electronics long-term stability, utility system stability, ground motion, etc.

To achieve the long-term beam stability goals, all sources of mechanical motion of critical in-tunnel beam position monitoring devices must be carefully evaluated and appropriately addressed. This includes the effects of water and air temperature, as well as earth tides and diffusive ground motion. A Hydrostatic Leveling System (HLS) is designed to quantify this floor motion.

The fundamental principle of the HLS is that any fluid seeks its own level. Given two reservoirs set at the same height and connected by a pipe or tube, the fluid level in each reservoir will be at the same absolute elevation. This is determined by the balance between gravity and air pressure. For small systems, the absolute elevation can be relative to some reference such as mean sea level. For larger systems, the curvature of the earth and other gravitational effects need to be considered. Given a reference point, the relative level of the fluid will vary as the sensor is moved up or down with respect to all the other sensors. While any fluid can be used, water has the advantages of a low viscosity (allowing for relatively rapid movement between reservoirs), it is non-toxic, is easily obtained, and if treated with sufficient care there will be no growth of biota in the reservoirs or tubing [2]. Specifically, the HLS requires that the system use demineralized water treated with fungicide.

3 HLS sensors per Insertion Device Front End (IDFE) will provide the necessary ground motion measurement. There will be a total of 105 HLS sensors to cover the 35 IDFEs. An additional sensor will be installed in each sector in Zone-F where there are no ID beamlines. This allows a global HLS network to be formed with a total of 110 sensors around the Storge Ring (SR).

Figure 1 illustrates the current HLS design for a generic sector in the APS-U SR. The B:P0 and A:P0 BPMs are mounted on invar stands on either side of the ID. The Grazing-Incidence Insertion Device (GRID) X-Ray BPM [3] in the IDFE is mounted on a granite table. 3 HLS sensors are mounted on the floor near the B:P0, A:P0 and GRID X-ray BPM stands. Water and air pipes will connect the sensors at each location. The invar stands and granite table will exhibit very good thermal stability given the tunnel ambient temperature will be stabilized within 0.1° C. Thus, we can assume that any ground motion measured by the HLS will be directly related to the change in position of the BPM sensors and any relative height differences between the BPMs can be characterized.

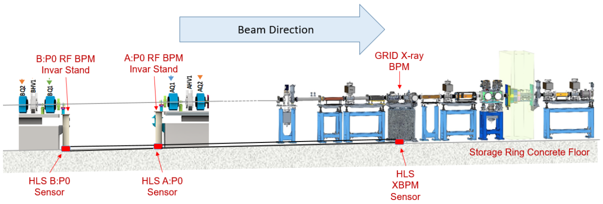

Figure 1: Hydrostatic Leveling System (HLS) for one of the APS-U IDFEs.

---

*Work supported by DOE contract No: DE-AC02-06CH11357

[#] wcheng@anl.gov

The HLS that will be implemented for the APS-U will be a completely closed 2-pipe system in which there are two pipes connecting the reservoirs: 1 pipe filled with air and the other filled with water. In a two-pipe system, the piping can be flexible as long as the sensors are placed at the same absolute height. A 1-pipe HLS prototype system has been installed and tested at the existing APS tunnel [4-6]. It has been demonstrated that the 1-pipe HLS meets the technical specifications (50 nm resolution @0.01Hz, and stability of 500 nm for 1 week period). However, the 1-pipe configuration poses trip hazard especially at the duck-under locations (see more information in the mechanical design). The 2-pipe configuration is selected as the performance will be similar to a 1-pipe system, and they are widely used at other accelerator facilities [7-11].

HLS MECHANICAL DESIGN

HLS Sensor and Stand

Each sensor will be mounted to a reservoir and will require its own stand as depicted in Fig. 2. The reservoir will be filled with water and connects to the nearby reservoirs through the two bottom pipe fittings. The top pipe fittings will be connected to the air pipes. The capacitive sensor measures the water surface distance, this way relative water height difference, caused by floor movement, can be measured. The sensor shall have a minimum measurement range of 3 mm.

The stands consist of four drop-in anchors, 4 Invar 36 support rods, a SS platform, 3 tuning bolts, a central PEEK bolt, and fasteners. The Invar 36 threaded rods will be mounted to the ground using drop-in anchors for concrete. The platform will slide over the four threaded rods and be held in place using jam nuts as fasteners. This approach allows the HLS reservoirs/sensors to be mounted on the same level, even though the floor settled differently around the ring. The reservoir will be held in place by the central PEEK bolt. The bolt screws into a tapped hole on the bottom surface of the reservoir and a nut on the bolt is torqued against the platform. This creates a compression force against the tuning bolts holding thus holding the sensor in place. The 3 tuning bolts allow for accurate adjustment of the position of the sensor as there is some height variation of the SR concrete floor. To protect the sensor, a cover which encloses the sensor will also be mounted to the platform.

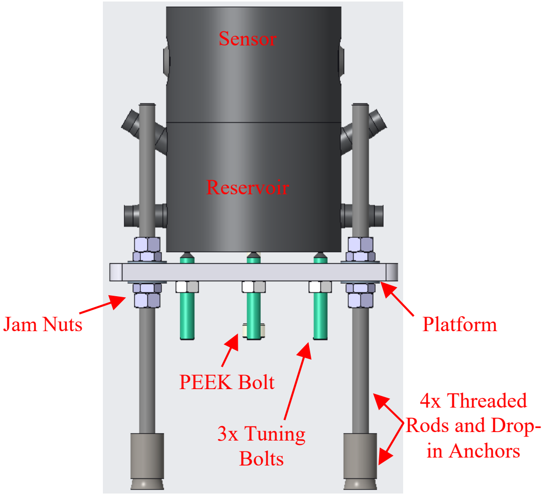

Figure 2: HLS sensor/reservoir and its stand.

It is understood that even in a near constant temperature in the SR tunnel, the stand will experience some thermal expansion which may impact the measurements by the sensors. To reduce the potential of thermal expansion influencing the measurements, Invar 36 was chosen for the threaded rods because of its strong thermal stability.

HLS Piping and Duck-Under Ramp

The piping for the HLS will route along the floor inside of a standard slotted hole aluminum Unistrut backed with plastic bars to keep the piping relatively level throughout the network. The Unistrut will be mounted to the concrete floor.

The open spaces underneath the QMQ bridges (QMQ is a module formed with two quadrupole magnets and on dipole M2 magnet) along each IDFE will be used as a duck-under and allow people to pass underneath the SR girders to gain access to the FEs (see Fig. 3). Because the pipe channel will route directly along these openings, a ramp will be installed to protect the pipes while mitigating the risk of someone tripping over the channel. The low angled ramp will have an opening through the center for the pipes to pass horizontally through. There will also be a polyurethane foam backing through the center of the ramp to any absorb any disturbances that might occur when someone steps on the ramp. The foam will be held in place using a polyurethane glue such as Gorilla Glue or equivalent. The surfaces of the ramp will have anti-slip tape on them for extra grip. The ramp will mount to the ground.

Generally speaking, the HLS water network along the IDFEs will be connected to the HLS water network of the following sector using a straight valve. The straight valves can be opened to form a global network or closed to divide the global network into isolated local networks.

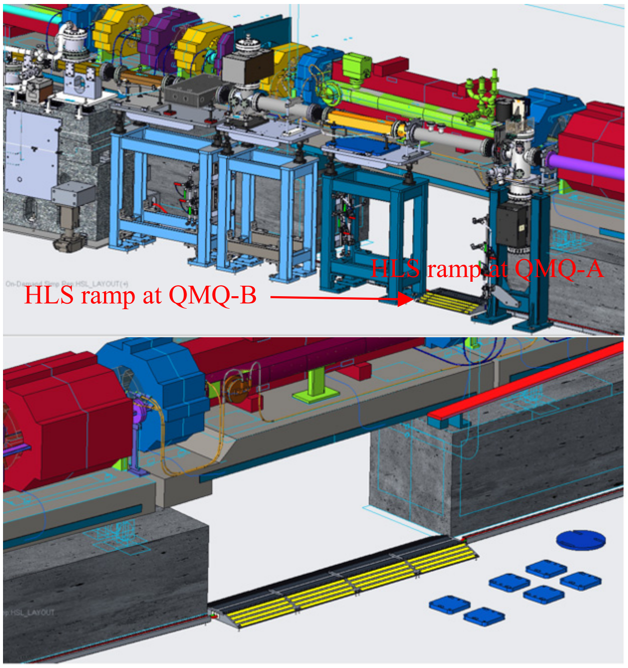

Figure 3: Duck-under at QMQ-B (top) and QMQ-A (bottom). HLS ramp mounted on the floor beneath the duck-under allows water and air pipes to pass through.

To form a complete loop around the SR, 1 additional sensor will be in each of the 5 Zone-F sectors. Ramps will also be used in these sectors in the same manner described above.

Because the water pipe will be completely filled with water in the 2-pipe system, ambient temperature and pressure changes will impact the water volume inside the network. This will impact the water level measurements inside the reservoirs. Therefore, the reservoirs should be equipped with a temperature sensor to measure the temperature of the water.

HLS Water Refill

Although the system will be completely closed, there is still some evaporation and/or micro leakage that will occur and overtime the water level will decrease inside the reservoir. Before the water level falls below the measurement range of the sensors, the system will need to be refilled. Therefore, a refilling/purging station must be implemented to refill the water inside of the networks. To achieve this for a general sector containing an IDFE, the GRID X-Ray BPM HLS sensor from each sector will be connected to the B:P0 BPM HLS sensor of the following sector by a T-valve (or similar) as depicted in the valve schematic below (see Fig. 4). All valves will be opened during the manual refilling process and can be closed after that to have isolated HLS measurements for each IDFE.

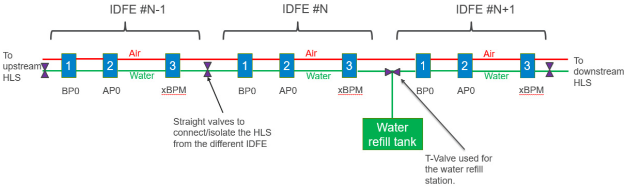

Figure 4: Gneral valve schematic for the HLS for sectors 1-35 containing IDFEs.

HLS ELECTRONICS DESIGN

The HLS electronics shall be close to the pickups. Like other electrical systems in the APSU, the HLS electronics will be configured organized in double sectors: 6 HLS sensors (from two sectors) will have signals run to an electronics rack. The digitizer shall sample the HLS distance and temperature at 0.01 Hz rate or faster. The digitized HLS signal shall be integrated into the APS-U control system. The interface is RS232/RS485. The whole HLS system, with the electronics, shall be demonstrated with the required resolution and stability.

Signal cables and power supply cables connect the HLS sensor and mezzanine electronics. The cable length varies depending on the HLS sensor locations, and the maximum cable length can be more than 30 meters long. Figure 5 depicts the HLS electronics schematics.

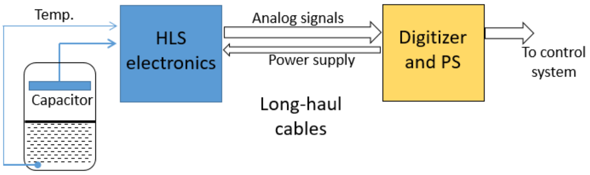

Figure 5: HLS electronics schematics.

HLS PROCUREMENT STATUS

The HLS sensor/reservoir and electronics contract has been awarded to Fogale Nanotech [12] in April 2021. The first article units, including 5 HLS sensors and 1 electronics box has been fabricated and tested at the factory. Test results show that the resolution and stability both meet the requirements [13]. The first article units will be shipped to Argonne in September 2021.

EPICS drivers have been developed for the HLS electronics. These drivers have been tested with the first article units.

The HLS sensor stand has also been purchased and will be delivered in late Fall 2021. The refill station is currently being designed and its components will be ordered soon.

SUMMARY

A hydrostatic level system (HLS) has been designed for APS-U SR to characterize the relative floor motion along each IDFE and the global floor motion of the storage ring tunnel. A 2-pipe system has been selected for ease of installation in tight spaces and to mitigate trip hazards. The HLS sensors and electronics have been ordered, and the first article units have been tested to be within the APS-U specification.

Components related to the HLS system, such as the sensor stand, have been purchased. Other components such as the refilling station are still being designed. All other components are being ordered or will be ordered soon.

The author acknowledges Fogale colleagues for fruitful discussion. Discussion with other accelerator facilities (Diamond, ESRF, SOLEIL, CERN) have been beneficial for the design.

The work is supported by the U.S. Department of Energy, Office of Science, Office of Basic Energy Sciences, under Contract No. DE-AC02-06CH11357.

REFERENCES

[1] "Advanced Photon Source Upgrade Project – Final Design Report", APSU-2.01-RPT-003, May 2019.

[2] J. Volk *et. al.*, "Hydrostatic Level Sensors as High Precision Ground Motion Instrumentation for Tevatron and Other Energy Frontier Accelerators", *Journal of Instrumentation*, vol. 7, p. 01004, Jan. 2012.

[3] B. Yang, "Next Generation X-ray BPM Development for the Advanced Photon Source Upgrade", Future Light Source Workshop 2018.

[4] R. M. Lill, G. Decker, N. Sereno, and B. X. Yang, "Design and Development of a Beam Stablity Mechanical Motion System Diagnostic for the APS MBA Upgrade", in *Proc. 6th Int. Particle Accelerator Conf. (IPAC'15)*, Richmond, VA, USA, May 2015, pp. 1164-1166. `doi:10.18429/JACoW-IPAC2015-MOPWI010`

[5] R. M. Lill, N. Sereno, and B. X. Yang, "BPM Stabiltiy Studies for the APS MBA Upgrade", in *Proc. 5th Int. Beam Instrumentation Conf. (IBIC'16)*, Barcelona, Spain, Sep. 2016, pp. 55-58. `doi:10.18429/JACoW-IBIC2016-MOPG10`

[6] N. Sereno, "APS-U Beam Stability Requirements and R&D in Sector27", APS-U Forum, March 2016.

[7] J. Kay, K. A. R. Baker, W. J. Hoffman, and I. P. S. Martin, "Stability of the Floor Slab at Diamond Light Source", in *Proc. 2nd Int. Particle Accelerator Conf. (IPAC'11)*, San Sebastian, Spain, Sep. 2011, paper MOPO035, pp. 562-564.

[8] A. Lestrade, "An Estimation of Vertical Slow Drift Between Storage Ring and Nanoscopium Long Beamline with HLS & Beam Diagnostics at Synchrotron SOLEIL", in *Proc. IWAA'2016*, Grenoble, France, Oct. 2016.

[9] C. Zhang, "From the HLS Measurement for Ground Movement at the Spring-8", in *Proc. IWAA'2004*, Geneva, Switzerland, Oct. 2004.

[10] D. Martin, "HLS and WPS used at the ESRF", presented at CERN-PRAL Workshop, Apr. 2009.

[11] D. Martin *et al.*, "The European Synchrotron Radiation Facility Hydrostatic Leveling System – Twelve Years' Experience with a Large Scale Hydrostatic Leveling System", in *Proc. IWAA'2002*, Japan, 2002.

[12] `https://www.fogale.fr/`.

[13] Fogale Nanotech, private communication.

REAL-TIME LONGITUDINAL PROFILE MEASUREMENT OF OPERATIONAL H$^-$ BEAM AT THE SNS LINAC USING LASER COMB*

Y. Liu†, C. Long, and A. Aleksandrov
Spallation Neutron Source, Oak Ridge National Laboratory, Oak Ridge, TN 37831, USA

Abstract

We demonstrate a novel technique to measure the longitudinal profile of an operational hydrogen ion (H$^-$) beam in a nonintrusive, real-time fashion. The measurement is based on the photoionization of the ion beam with a phase modulated laser comb – pico-second laser pulses with controllable temporal structure. The measurement technique has been applied to a 1-GeV, 1.4-MW H$^-$ beam at the Spallation Neutron Source (SNS) high energy beam transport (HEBT). A stroboscopic photograph of the H$^-$ beam micro bunch can be obtained by using a phase modulated laser comb. The entire measurement takes only 700 μs.

INTRODUCTION

Short-pulsed laser beam has been proposed to measure the longitudinal H$^-$ beam profiles in the particle accelerators [1, 2]. The measurement is based on the photo neutralization of the ion beam where the electrons are detached from the ions by a focused laser beam, often named as laser wire, and the number or density of the detached electrons leads to the determination of the original ion density. The measurement is generally nonintrusive and can be conducted on operational particle beams. So far, laser wire based longitudinal profile measurements have been conducted on relatively low energy beams. One reason is that for the short-pulsed, high repetition rate lasers, the available peak power is in the range of 1-10 kW, which produces photodetachment yield below 10^{-4}. Detection of such weak signals requires high sensitivity detectors such as photomultiplier tube (PMT) and suffers from the large background noise in the low/medium-energy beam line.

In this paper, we describe the longitudinal profile measurement of 1-GeV H$^-$ beam using a customized light source, referred to as a laser comb, which has multi-layer pulse structure with a peak power of more than 100 MW. The laser pulses can be phase modulated so that each comb tooth has a different phase delay with respect to the ion beam micro-bunches. When a phase modulated laser comb is applied to the ion beam, the photo-detached electrons are detected with a Faraday cup (FC). A stroboscopic photograph of the H$^-$ beam micro-bunch can be obtained from the FC output with the measurement time of only 700 μs. This real-time measurement causes negligible beam loss and therefore was conducted at different locations of the 1.4-MW neutron production H$^-$ beam line.

LIGHT SOURCE DEVELOPMENT

Estimation of Laser Power Requirement

Photo neutralization is a non-resonant process with a very small cross section (~3×10^{-17} cm^2). In laser-based H$^-$ beam diagnostics, the photo-detached electrons are directly proportional to the product between photon and ion beam densities as expressed by

$$n_{det} = c\sigma n_b n_l \tag{1}$$

where c is the light speed, σ the photon-ion interaction cross-section, and n_b and n_l represent density functions of ion and photon beams, respectively.

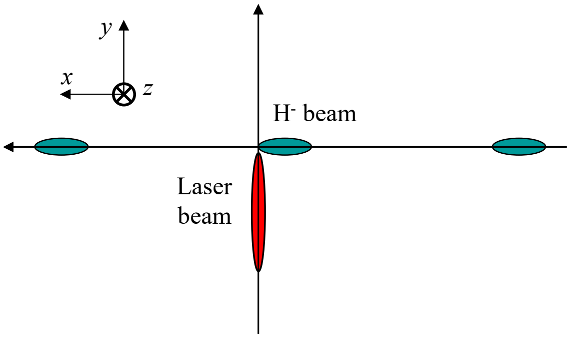

Figure 1: Schematic of laser-H$^-$ beam interaction.

A typical laser-ion interaction scheme is shown in Fig. 1. Both n_b and n_l are assumed to have a Gaussian function distribution as

$$n_b = \frac{N_b}{(2\pi)^{3/2}\sigma_{bx}\sigma_{by}\sigma_{bz}} \exp\left[-\frac{(x-\beta ct)^2}{2\sigma_{bx}^2} - \frac{y^2}{2\sigma_{by}^2} - \frac{z^2}{2\sigma_{bz}^2}\right], \tag{2}$$

$$n_l = \frac{N_l}{(2\pi)^{3/2}\sigma_{lx}\sigma_{ly}\sigma_{lz}} \exp\left[-\frac{x^2}{2\sigma_{lx}^2} - \frac{(y-c(t-s))^2}{2\sigma_{ly}^2} - \frac{z^2}{2\sigma_{lz}^2}\right]. \tag{3}$$

Here N_b and N_l are ion and photon numbers, respectively, $\sigma_{bx,y,z}$ ($\sigma_{lx,y,z}$) represents the RMS size of the ion (photon) beam along the ion beam propagation, photon beam propagation, and vertical direction, respectively, and s denotes the phase delay in longitudinal profile scan. For pulsed beam with low duty factor, the overall photodetachment yield over one micro bunch of the ion beam can be calculated by integrating n_{det} over an entire space and time as

$$\eta = \frac{c\sigma}{N_b} \iiint_{-\infty}^{+\infty} n_b n_l \, dx dy dz dt$$

---

* This manuscript has been authored by UT-Battelle, LLC, under contract DE-AC05-00OR22725 with the US Department of Energy (DOE). The US government retains and the publisher, by accepting the article for publication, acknowledges that the US government retains a nonexclusive, paid-up, irrevocable, worldwide license to publish or reproduce the published form of this manuscript, or allow others to do so, for US government purposes. DOE will provide public access to these results of federally sponsored research in accordance with the DOE Public Access Plan (http://energy.gov/downloads/doe-public-access-plan).”

† liuy2@ornl.gov

$$= \eta_{max}\exp\left[-\frac{s^2}{2\left[\tau_{bx}^2+(\sigma_{lx}/\beta c)^2+\tau_{ly}^2+\left(\sigma_{by}/c\right)^2\right]}\right]. \quad (4)$$

with

$$\eta_{max} \cong \frac{\sigma\lambda E_l}{2\pi h\beta c\sigma_{bz}\sqrt{(\tau_b^2+\tau_l^2)c^2+\sigma_{by}^2}} \quad (5)$$

where λ and E_l are laser wavelength and pulse energy, h is the Planck constant, βc is the ion beam speed, τ_b ($=\sigma_{bx}/\beta c$) and τ_l ($=\sigma_{ly}/c$) are ion and laser pulse width. For typical H$^-$ beam parameters in the SNS linac for neutron production, $\eta_{max} \sim 0.01$ is required to achieve sufficient dynamic range in the measurement, which leads to a laser pulse energy of ~ 10 µJ.

Laser Comb

To measure the longitudinal profile of H$^-$ beam micro bunches, laser pulse width needs to be at the picosecond order. Such laser pulses are normally generated from mode-locked lasers with typical pulse energy at a 10 nJ order. Therefore, a power amplification with a gain of at least three orders of magnitude is required.

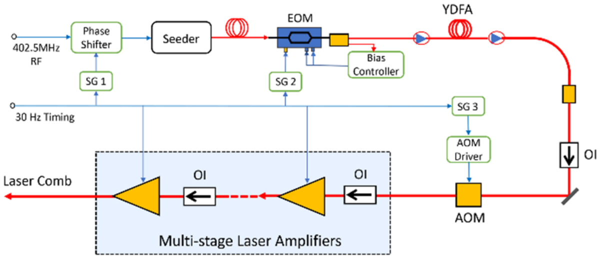

Figure 2: Laser system schematic. EOM: electro-optic modulator, AOM: acousto-optic modulator, YDFA: ytterbium-doped fiber amplifier, OI: optical isolator, SG: signal generator.

Recently, we developed a laser system that has a multi-layer pulse structure [3]. The system has been modified in this work by including a new mode-locked seed laser with the RMS pulse width of ~5 ps. Figure 2 shows a schematic of the laser system that consists of a mode-locked seed laser, pulse picking components, and multi-stage amplifiers. Each macropulse of the laser is referred to as a laser comb as it contains multiple mini-pulses (comb teeth). The comb parameters, i.e., comb duration, width and spacing of individual comb teeth, are produced by a combination of high-bandwidth, high-extinction-ratio EOM, a fiber-based pre-amplifier, and an AOM. The laser combs are amplified by three stages of double-pass, diode-pumped Nd:YAG amplification modules with a total gain greater than 10^6. The seed laser and the control electronics of the EOM have been properly conditioned to achieve high quality pulse generation and efficient power amplification.

An example of the laser output is plotted in Fig. 3. A laser comb used in this measurement contains 75 comb teeth and the width and spacing of comb teeth are 30 ns and 9.45 µs, respectively. The laser comb repeats at 30 Hz. As shown in Fig. 3(b), each comb tooth further contains certain number of micro-pulses generated form the mode-locked seed laser. Such a micro-pulse structure of the laser comb minimizes the required laser average power. For example, the peak power of the micro-pulse in Fig. 3 is 20 MW while the average power is only about 6 W in this case.

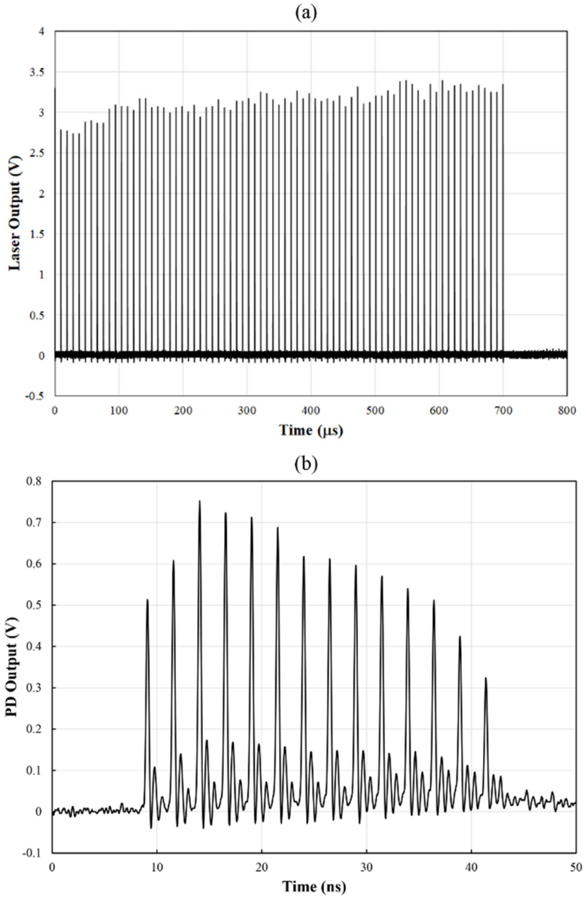

Figure 3: (a) A laser macro-pulse (laser comb) consisting of 75 mini-pulses (comb teeth). (b) Micro-pulses inside a single laser comb tooth.

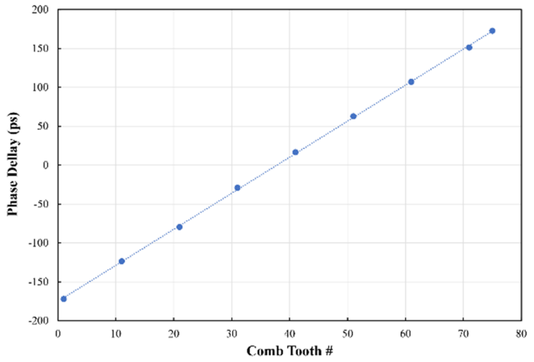

Figure 4: Phase delay vs. individual comb tooth as a result of phase modulation.

As illustrated in Fig. 2, the phase of individual micro pulses can be controlled with a phase shifter. In this work, we controlled the phase shifter with a 30-Hz sawtooth signal so that each comb tooth has a different phase delay with respect to the H$^-$ beam bunches. An excellent linearity between the phase delay and comb teeth has been measured as shown in Fig. 4.

LONGITUDINAL PROFILE MEASUREMENT

Measurement Results

The longitudinal profile measurement was conducted at the end of the SNS linac as shown in Fig. 5. The laser was placed outside the accelerator tunnel and the laser beam was delivered to the measurement station through a free-space laser transport line. The laser beam had an RMS pulse width of about 5 ps with a peak power of ~10 MW. The electrons detached by the laser comb are detected by the FC. Although there were multiple micro-pulses within an individual laser comb tooth as shown in Fig. 3, due to the bandwidth limitation of the detectors, all electrons generated from one laser comb tooth were detected as one pulse. During the profile measurement, individual laser comb teeth interacted with different time sheets of the H$^-$ beam micro-bunch. The FC output signals were gated to the laser comb so that the electrons from individual temporal slices of the H$^-$ beam were properly processed to reconstruct the profile.

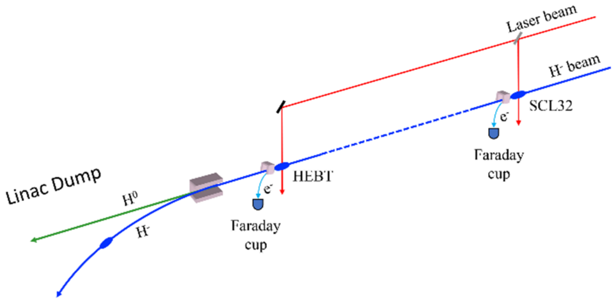

Figure 5: Longitudinal profile measurement locations. First measurement is conducted before the linac dump and second measurement is conducted at the end of SNS superconducting linac (SCL).

As a result of the phase modulation, each laser comb tooth interacts with the ion beam bunch at a different phase. The FC output of all 75 comb teeth can be visualized in a two-dimensional graph as shown in Fig. 6. Since each laser comb tooth corresponds to a different phase delay, the graph represents a stroboscopic photograph of the H$^-$ beam bunch. It is noted that the entire photograph was taken within a time period of 700 μs. By integrating the FC output and plot it as a function of the phase delay, we obtain the longitudinal profile the H$^-$ beam as shown in Fig. 6(b). The estimated RMS bunch width is about 50 ps.

Another longitudinal profile measurement was conducted at the end of SCL which is about 45 metres upstream of the first measurement location. The measurement is shown in Fig. 7. The RMS bunch width is ~30 ps from the Gaussian fit.

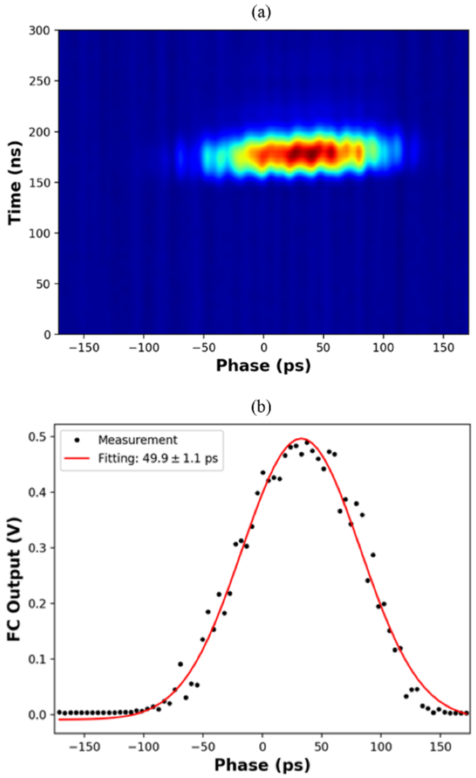

Figure 6: (a) Stroboscopic photograph of H$^-$ beam bunch and (b) longitudinal profile before the linac dump.

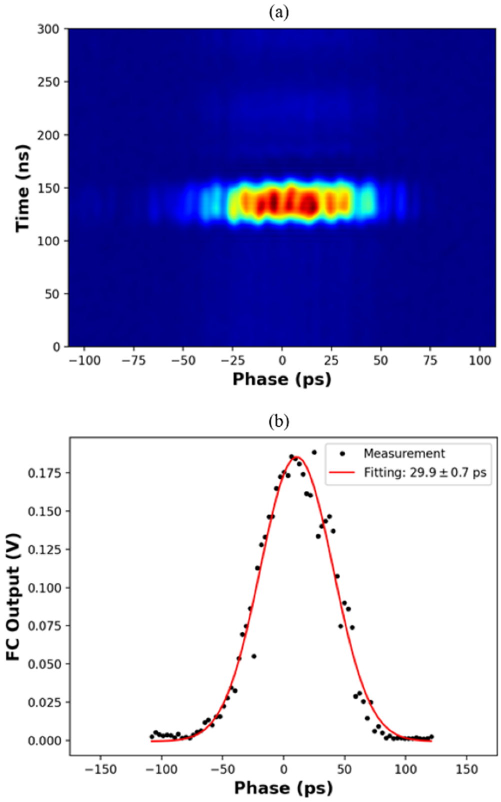

Figure 7: (a) Stroboscopic photograph of H$^-$ beam bunch and (b) longitudinal profile at the end of SCL.

Discussions

As shown in Eq. (4), the measured bunch width is a convolution of the actual value with the contributions from the transverse beam width of the H$^-$ beam, the longitudinal and transverse beam widths of the laser beam. In the above measurement locations, those parameters are measured to be σ_{by}/c = 4~8 ps, $\tau_l \approx$ 5 ps, $\sigma_{lx}/\beta c \approx$ 0.4 ps. Based on that, the actual RMS bunch width are estimated to be about 49 ps and 29 ps for the two measurement locations. Obviously, the effect of those parameters is negligible for large RMS bunch widths. On the other hand, for the measurement of longitudinal profiles in the SCL where typical RMS bunch width is around 10 ps, precise ion beam size and laser pulse width are important to achieve accurate measurement results. It is noted that the ion beam size at SCL can be measured by our laser wire profile monitors. The measurement accuracy will also be affected by the laser pulse intensity jitter and laser beam pointing stability.

If we assume the pulse broadening is homogeneous between the two measurement locations described above, the energy spread can be estimated from the pulse broadening as

$$\frac{\Delta E}{E} = \gamma(\gamma + 1)\frac{\Delta t_0}{t_0}, \qquad (6)$$

where γ is the Lorentz factor of the H$^-$ beam, t_0 is the propagation time between the two measurement locations, and Δt_0 is the growth of the bunch width. For γ = 2.07, Δt_0 = 20 ps, t_0 = 170.85 ns, we calculated $\Delta E/E \approx 7.5 \times 10^{-4}$. Both the measured RMS bunch width and estimated energy spread are close to the design values.

A number of new beam instrumentation systems could be conceived at the SNS accelerator by employing the laser comb based longitudinal profile measurement technique. First, the current longitudinal profile measurement can be applied to 8 cryomodules along the SCL beam line. The longitudinal phase space can be reconstructed from the measurement at different cavity phases. The measurement can only be performed on low-repetition-rate, narrow-pulsed ion beam in this case. Measurement of longitudinal phase space of an operational beam could be realized if the energy spread of each longitudinal slice of the neutralized hydrogen beam can be measured in the linac dump. The longitudinal phase space could also be measured by taking advantage of the large beam dispersion in the end of the HEBT and measuring longitudinal profiles of different transverse portions (corresponding to different energy segments) using a laser comb.

Finally, a nonintrusive high-dimensional beam diagnostics can be realized by combining the longitudinal profile scan with the existing laser wire transverse emittance measurement. This capability was recently demonstrated in a time-resolved emittance measurement [3]. Using the current laser comb system with pico-second laser pulses, we can perform more investigations about the emittance variations within a bunch on the neutron production ion beam.

CONCLUSION

We have described a novel technique of longitudinal profile measurement of the H$^-$ beam by using a laser comb. The proposed technique has been applied to the emittance measurement on the 1-GeV, 1.4-MW neutron production H$^-$ beam at the SNS high energy beam transport. We have experimentally demonstrated that a stroboscopic photograph of micro-bunch can be obtained within a time period of 700 µs. Our experiment strongly supports that the laser-based nonintrusive beam diagnostics can provide unique information about the high-energy, high-power particle beam.

REFERENCES

[1] V.W. Yuan *et al.*, “Measurement of longitudinal phase space in an accelerated H beam using a laser-induced neutralized method”, *Nucl. Instrum. Methods Phys. Res., Sect. A*, vol. 329, p. 381, 1993.

[2] A. P. Zhukov, A. V. Aleksandrov, and Y. Liu, “Longitudinal Laser Wire at SNS”, in *Proc. 3rd Int. Beam Instrumentation Conf. (IBIC'14)*, Monterey, CA, USA, Sep. 2014, paper MOCYB3, pp. 12-15.

[3] Y. Liu, C. Long, and A. Aleksandrov, “Nonintrusive measurement of time-resolved emittances of 1-GeV operational hydrogen ion beam using a laser comb”, *Phys. Rev. ST Accel. Beams*, vol. 23, p. 102806, 2020.

BUNCH-RESOLVED 2D DIAGNOSTICS – STREAKING COMBINED WITH INTERFEROMETRY*

M. Koopmans†[1], J.-G. Hwang, A. Jankowiak[1], M. Ries, G. Schiwietz
Helmholtz-Zentrum Berlin für Materialien und Energie GmbH (HZB), Berlin, Germany
[1]also at Humboldt-Universität zu Berlin, Berlin, Germany

Abstract

Due to the complexity of the fill pattern in the BESSY II electron-storage ring, bunch-resolved diagnostics are required for machine commissioning and to ensure the long-term quality and stability of operation. In addition, low-α operation and a possible VSR upgrade demand bunch-length measurements with picosecond resolution. Therefore, a dedicated beamline equipped with a fast streak camera was set up and successfully commissioned. Couplings between time- and space-coordinates also call for bunch-selective and correlated multi-parameter detection methods. Thus, the beamline and the streak camera have been made capable of direct beam-profile imaging and interferometry of the vertical beam size using the X-ray blocking baffle method. The horizontal or vertical dimension can additionally be imaged with the streak camera and bunch-resolved 2D measurements are possible. Imaging the vertical direction, the characteristic dip in the center of the interference pattern from the π-polarized synchrotron radiation can be observed and is used to extract bunch resolved information about the vertical beam size. The streak camera measurements are validated with direct imaging measurements with a regular CCD camera at the beamline and compared to model calculations. The results are converted into absolute values by a calibration with the BESSY II pinhole monitors.

INTRODUCTION

The BESSY II electron storage ring provides synchrotron radiation (SR) to a very diverse user community. In standard user operation a complex fill pattern features multiple bunch types for dedicated applications. Special operation modes like single bunch or low-α operation for short pulses are offered for few weeks a year [1, 2]. In addition, a new operation with a second orbit is tested and developed [3] and a possible upgrade to a variable pulse length storage ring (VSR) is envisioned [1].

Non-invasive bunch resolved diagnostics are needed for maintaining and improving of existing as well as for commissioning and development of new operation modes. For this purpose dedicated diagnostic beamlines have been installed. A new beamline dedicated for bunch resolved longitudinal diagnostics equipped with a fast streak camera has been commissioned and is in full operation since mid 2020 [4]. Although this beamline is optimized for maximum photon flux, it has extremely good transverse imaging capabilities. Furthermore, the streak camera features an entrance aperture with a horizontal slit. Depending on the beamline settings, it is possible to image either a slice corresponding to the horizontal or the vertical direction of the initial electron beam in the horizontal direction of the streak camera. In combination with the streak camera an RMS resolution down to 120 µm was reached for direct imaging in the transverse direction. It was also shown that bunch position fluctuations below 10 µm (RMS) can be measured applying a statistical analysis method to single shot streak camera images [5].

To overcome the resolution limit of direct imaging, a combination of interferometry with the streak camera is investigated to become sensitive to bunch sizes below 120 µm [6]. For this goal the interference in the vertical direction originating from the X-ray blocking baffle using π-polarized SR turned out to be very promising. This method is similar to the obstacle diffractometer method introduced in Ref. [7, 8].

VERTICAL BEAMLINE IMAGING

A simplified schematic of the longitudinal diagnostics beamline at BESSY II, which contains the components relevant for the vertical imaging, is shown in Fig. 1. The SR beam first passes the X-ray blocking baffle and is then collimated through an intermediate focus with the M1 ellipsoid and the M2 toroid mirrors, which are replaced by lenses in the schematic. Then a polarisation filter, followed by a 90° rotation of the SR beam with a periscope (not shown in Fig. 1) and a 700 nm bandpass filter (10 nm FWHM bandwidth) are used to obtain a clear interference pattern, which is finally detected with a regular CCD or the streak camera. Additionally, a slit with an opening aperture of 2 mm is used to cut out approximately an eighth of the collimated beam for improved coherence due to the varying quality along the beam profile. The region with a minimal wavefront error was chosen by adjusting the slit position to optimize the

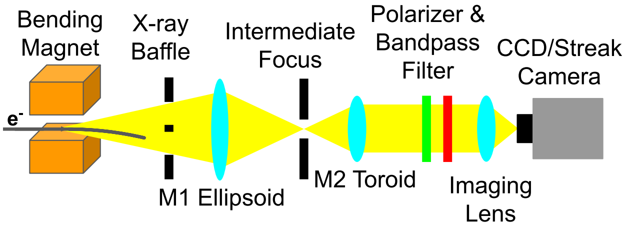

Figure 1: Schematic of the relevant objects for vertical imaging at the longitudinal diagnostics beamline at BESSY II. The two mirrors are replaced by lenses in this linearized drawing by keeping the main optical properties (M1 for point-to-point focussing and M2 for collimation).

---

* Work supported by the German Bundesministerium für Bildung und Forschung, Land Berlin and grants of the Helmholtz Association

† marten.koopmans@helmholtz-berlin.de

interference pattern at the CCD camera.

An example image of the interference pattern for π-polarized SR, measured with the CCD camera at the focus of a 75 cm focal length achromat lens, can be found in Fig. 2. Note that all data presented in this paper are taken with the rotated beamline configuration. This enables measuring the vertical interference pattern also in the horizontal direction of the streak camera. Therefore, the directions corresponding to the electron beam are switched in the CCD camera image. Two separate peaks for π-polarized SR are observed due to a destructive interference in the center. The interference fringes extend to large distances and are still visible 250 Pixel away from the center. Within this paper only the projection corresponding to the vertical beam direction (imaged in horizontal CCD or streak camera direction) will be analyzed and discussed.

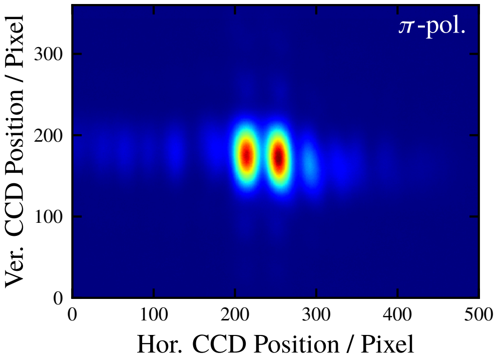

Figure 2: CCD camera interference image taken with π-polarized SR using a 700 nm bandpass filter. The horizontal axis in the image corresponds to the initial vertical beam direction and vice-versa.

MEASUREMENTS WITH VARIABLE VERTICAL BEAM SIZE

A measurement series with variable beam size was conducted to further verify the method and show that it is in principle possible to obtain high resolution bunch-resolved quantitative results for the vertical bunch size with the streak camera. For this purpose the BESSY II feature for a blow-up of the vertical beam size by a white noise excitation is used, with which the vertical beam size can be increased by up to a factor of 6 at maximum excitation. Variation of the vertical beam size by this excitation is a very useful tool for lifetime studies or to obtain resolution limits in combination with beam loss monitor measurements as presented in Refs. [6,9]. Here the excitation is also used to vary the vertical beam size, while observing the interference pattern with the CCD and the streak camera. Finally the properties of the measured interference patterns are correlated with the beam size at the source point of the beamline and accurate quantitative results can be given.

CCD Camera Measurements

First the interference patterns obtained from bunch averaged measurements with the regular CCD camera are presented. The measurements were performed in the same setup as described above. The obtained projections of the interference patterns corresponding to the vertical beam size at different white noise excitation amplitudes applied to the beam are shown for both polarisations in Fig. 3.

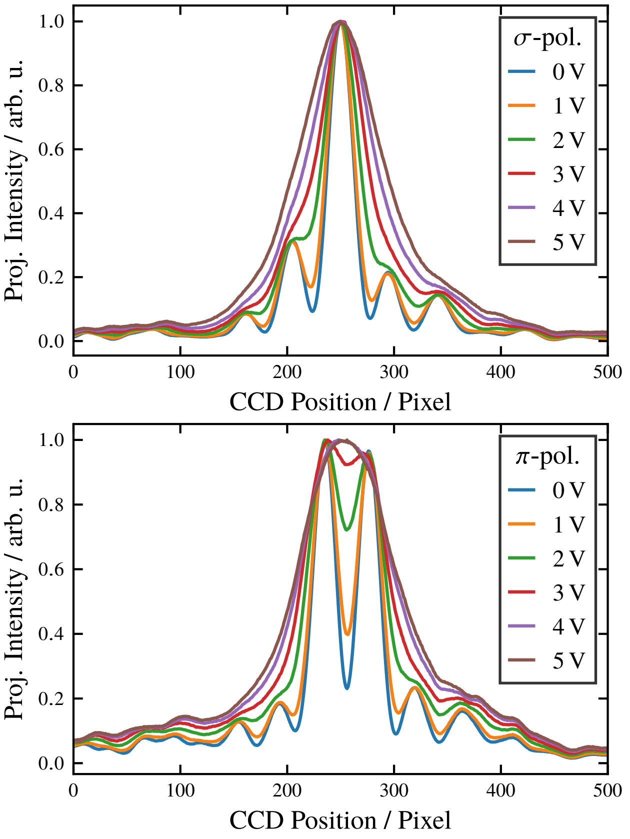

Figure 3: Projections of the interference pattern corresponding to the vertical beam direction for σ (top) and π-polarized SR (bottom) from measured CCD camera images at a wavelength of 700 nm for different white noise excitation settings to manipulate the vertical beam size.

The averaged distance between the different interference maxima at the CCD camera is about 41 pixels (with a pixel size of 4.54 µm). This includes both polarisations settings and also the distance between the two main peaks for π-polarized SR. The effect of changing the beam size can be nicely observed in the projection of the interference pattern. For increasing beam sizes the visibility decreases and the interference pattern is smoothed out for both polarisations until only the envelope remains at high excitations. For the interference pattern of σ-polarized SR this results mainly in a broadening of the central peak. For π-polarized SR the central dip in the interference pattern is visible, but vanishes when beam excitations corresponding to a set value above 3 volt are applied.

Streak Camera Measurements

It was now attempted to image the vertical interference in the horizontal direction of the streak camera. Measurement images taken during the manipulation of the vertical beam size with the white excitation are shown without and with maximum excitation for π-polarized SR in Fig. 4. The fill pattern was modified to include a separated bunch with the same current as the train bunches (slightly below 1 mA).

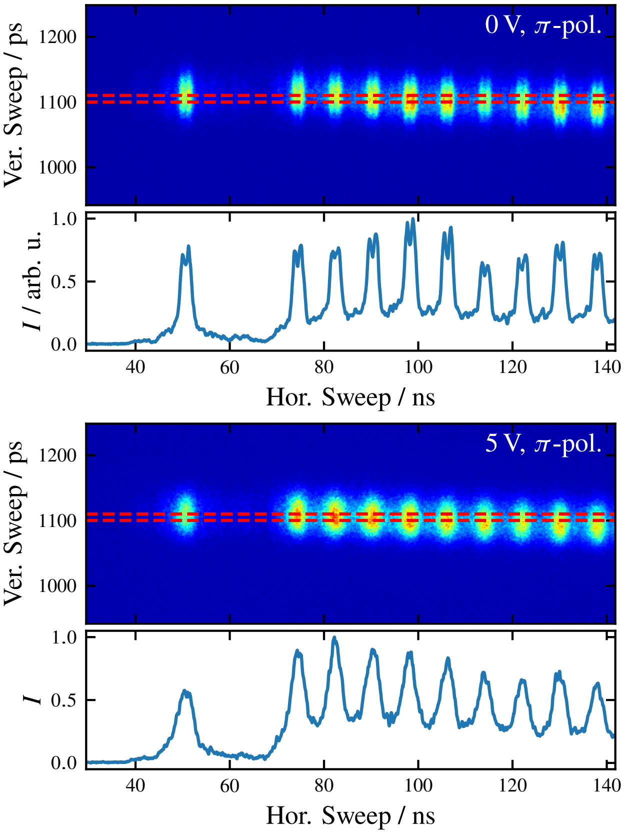

Figure 4: Streak camera images taken with π-polarized SR using a 700 nm bandpass filter imaging the vertical interference in the horizontal direction streak camera direction for minimal vertical bunch sizes (top, 0 V excitation) and maximal vertical bunch sizes (bottom, 5 V excitation).

In the vertical direction a fast sweep is applied and the bunch length can be obtained from this direction in the streak camera image. In the horizontal direction a slow sweep is used to separate the bunch spots corresponding to the fill pattern in the horizontal direction in the streak camera image. In addition, for each single bunch the interference pattern similar as measured with the CCD camera can be recognized. Due to the smaller magnification and the conversion processes in the streak camera, the resolution of the streak camera is worsened compared to the CCD camera. It is also clearly visible that the interference patterns smooth out, the intensity spots get broader and the central dips in the interference patterns vanish with increasing excitation. Note that due to the limited intensity from collimation and the used filters quite long integration times are required. For the displayed streak camera images analog integrations of 1000 continuous acquisitions with exposure times of 120 ms were used.

For comparison of the properties of the projected interference patterns measured with the CCD camera, an average train bunch projection is calculated from all train bunches detected in the streak camera images. The average train bunch projections from the streak camera measurements are shown for different excitation settings and for both polarisations in Fig. 5.

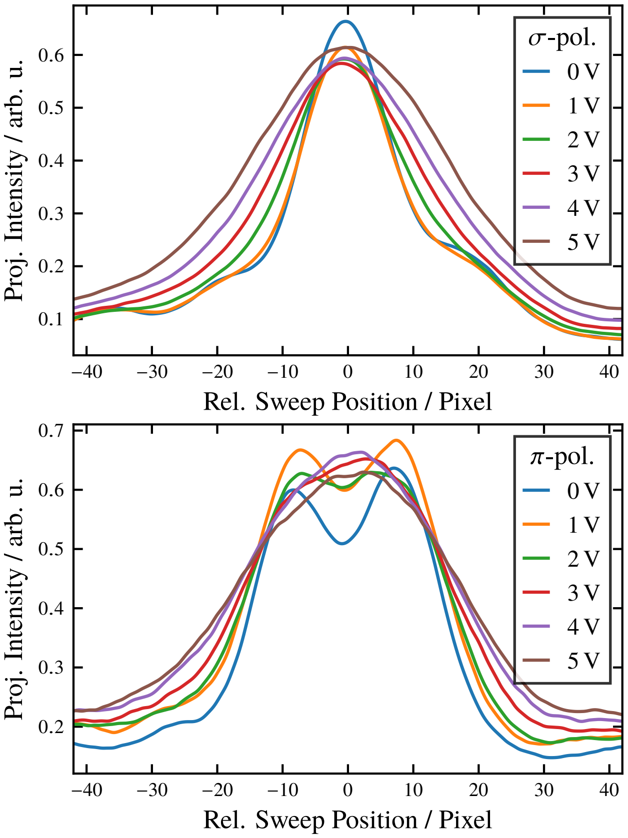

Figure 5: Average train bunch projections of the interference pattern corresponding to the vertical beam direction for σ (top) and π-polarized SR (bottom) from measured streak camera images at a wavelength of 700 nm for different white noise excitation settings to manipulate the vertical beam size.

One can recognize the slight broadening of the central peaks for both polarisations and the central dip of the π-polarized SR disappears for larger vertical beam sizes with increasing excitation. In comparison to the CCD camera measurements the central dip of the interference pattern for π-polarized SR is only visible for an excitation setting up to about 2 V. Note that the intensity between the train bunches in the streak images does not drop to 0 and the effect of overlapping interference patterns in the streak camera (Fig. 4) increases for larger beam sizes.

Quantitative Results

For direct comparison of the CCD and the streak camera measurements, the respective pixel values of both systems are converted into absolute source-point positions using the known image magnifications. As a reference value the pinhole monitors [10] for transverse beam size measurements were used and a calibration as presented in Ref. [6] was performed. Using the measured resolution of the pinhole systems the true beam sizes at the respective source points are estimated as function of the excitation set value. The expected beam size at the source point of longitudinal diagnostics beamline is then calculated via the vertical β-functions from the standard BESSY II lattice model.

The FWHM widths of the central peak or the two central peaks depending on the selected polarisation in the interference pattern measured at the CCD and the streak camera are shown as a function of the estimated FWHM beam size in Fig. 6. The measured FWHM widths in the interference patterns for both polarisations and both devices increase monotonously. With the CCD camera a FWHM width of the central peak down to about 120 µm (50 µm RMS) and for the streak camera an improved FWHM resolution below 220 µm (93 µm RMS) is reached. The details functional dependencies can be understood considering the ideal interference patterns, the true beam size and the resolution of the systems.

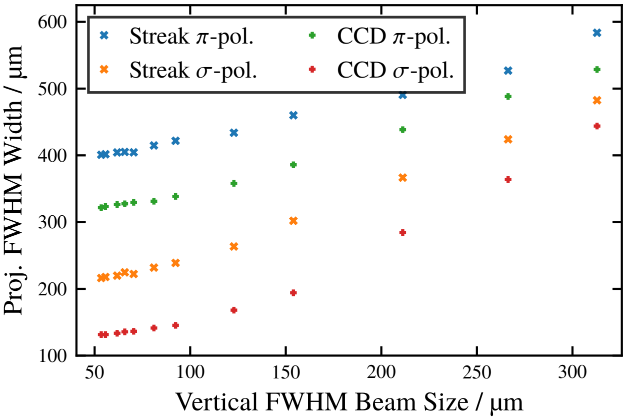

Figure 6: FWHM widths obtained from the central interference maxima for σ and π-polarized SR of the projections from CCD camera images and average train bunch projections of streak camera measurements converted to dimensions corresponding to the source points as a function of the estimated vertical FWHM bunch size.

Even more interesting is the central dip for π-polarized SR. The peak-dip ratio R is calculated as the ratio of the intensity at the central dip divided by the averaged intensity at the two surrounding peaks. The obtained peak-dip ratios from the CCD and streak camera measurements are shown as a function of the vertical beam size in Fig. 7.

The peak-dip ratios obtained from the CCD camera images range between about 0.23 for the minimum beam size and 1 (no dip) for vertical beam sizes above 100 µm. The variation of R is significantly reduced for the streak camera. Here the minimum measured peak-dip ratio is about 0.75 and a value of 1 is reached already below a vertical RMS beam size of 90 µm. Nevertheless, a region were the peak-dip ratio has a clear dependency on the vertical beam size is observed and the RMS resolution is estimated to be about 10 µm. The results are again consistent considering the resolution of the streak camera and the image magnifications of both systems. In addition the peak dip ratios obtained from CCD camera measurements are compared with 1D model calculations. The general behavior is similar, but the deviations are not negligible. Investigation are ongoing, so that the model can also be used as a reference to obtain the beam size from measurements of R.

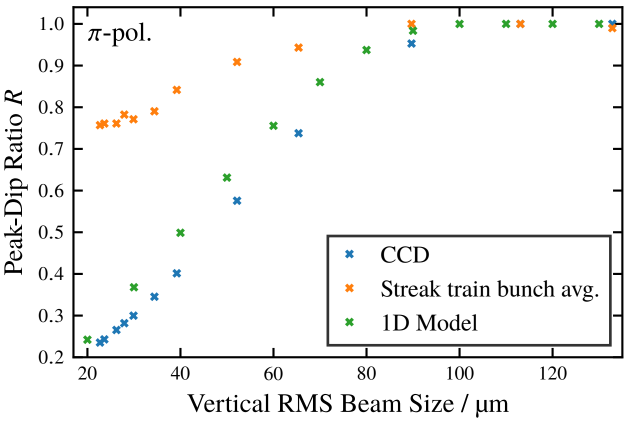

Figure 7: Peak-dip ratio as a function of the vertical RMS beam size obtained from the central minima of the interference patterns of π-polarized SR from measurements of CCD and streak camera projections for the average train bunch, and from 1D model calculations.

CONCLUSION

Together with the standard longitudinal bunch length measurements, it is possible to image interference patterns with a streak camera corresponding to the vertical beam direction at our beamline. Vertical bunch sizes below 90 µm (RMS) can be resolved with the method and quantitative results with an accuracy of about 10 µm (RMS) can be obtained using a calibration. Further improvements for higher resolution are tested. The outer interference fringes can be blocked with the slit at the intermediate focus. Therefore, the spots of individual bunches are well separated at the streak camera and the focal length of the final lens may be increased to enlarge the interference patterns.

REFERENCES

[1] A. Jankowiak *et al.*, Eds., “BESSY VSR – Technical Design Study”, Helmholtz-Zentrum Berlin für Materialien und Energie GmbH, Germany, 2015. `doi:10.5442/R0001`

[2] R. Müller *et al.*, “BESSY II Supports an Extensive Suite of Timing Experiments”, in *Proc. 7th Int. Particle Accelerator*

Conf. (IPAC'16), Busan, Korea, May 2016, pp. 2840–2843. `doi:10.18429/JACoW-IPAC2016-WEPOW011`

[3] P. Goslawski *et al.*, "Two Orbit Operation at Bessy II - During a User Test Week", in *Proc. 10th Int. Particle Accelerator Conf. (IPAC'19)*, Melbourne, Australia, May 2019, pp. 3419–3422. `doi:10.18429/JACoW-IPAC2019-THYYPLM2`

[4] G. Schiwietz *et al.*, "Bunch-resolved diagnostics for a future electron-storage ring", *Nuclear Instruments and Methods in Physics Research Section A: Accelerators, Spectrometers, Detectors and Associated Equipment*, vol. 990, p. 164992, 2021. `doi:10.1016/j.nima.2020.164992`

[5] M. Koopmans *et al.*, "Statistical Analysis of 2D Single-Shot PPRE Bunch Measurements", presented at the 12th Int. Particle Accelerator Conf. (IPAC'21), Campinas, Brazil, May 2021, paper MOPAB296.

[6] M. Koopmans *et al.*, "Vertical Beam Size Measurement Methods at the BESSY II Storage Ring and their Resolution Limits", in *Proc. 10th Int. Particle Accelerator Conf. (IPAC'19)*, Melbourne, Australia, May 2019, pp. 2491–2494. `doi:10.18429/JACoW-IPAC2019-WEPGW012`

[7] J. Breunlin et al., "Methods for measuring sub-pmrad vertical emittance at the Swiss Light Source", *Nuclear Instruments and Methods in Physics Research Section A: Accelerators, Spectrometers, Detectors and Associated Equipment*, vol. 803, pp. 55–64, 2015. `doi:10.1016/j.nima.2015.09.032`

[8] Å. Anderson *et al.*, "Diagnostics at the Max IV 3 GeV Storage Ring During Commissioning", in *Proc. 5th Int. Beam Instrumentation Conf. (IBIC'16)*, Barcelona, Spain, Sep. 2016, pp. 1–5. `doi:10.18429/JACoW-IBIC2016-MOAL02`

[9] M. Koopmans, "Interferometric Beam Size Monitor for BESSY II", Master thesis, Humboldt-Universität zu Berlin, Berlin, Germany, 2017.

[10] K. Holldack, J. Feikes and W. B. Peatman, "Source size and emittance monitoring on BESSY II", *Nuclear Instruments and Methods in Physics Research Section A: Accelerators, Spectrometers, Detectors and Associated Equipment*, vol. 467, pp. 235–238, 2001.

ABSOLUTE BUNCH LENGTH MEASUREMENTS OF LOW ENERGY BEAMS USING ACCELERATING RF CAVITY

Ji-Gwang Hwang*, Helmholtz-Zentrum Berlin, Berlin, Germany
Tsukasa Miyajima, Yosuke Honda,
High Energy Accelerator Research Organization (KEK), Ibaraki, Japan
Eun-San Kim, Korea University Sejong Campus, Sejong, Republic of Korea

Abstract

The experimental technique has been proposed and demonstrated by authors for measuring the temporal distribution and absolute bunch length of picosecond-level low-energy electron bunch generated by an electron gun using radial electric and azimuthal magnetic fields of an accelerating (TM_{01} mode) radio frequency cavity. In this scheme, an accelerating RF cavity provides a phase-dependent transverse kick to the electrons, resulting in the linear coupling of the trajectory angle with the longitudinal position inside the bunch like a transverse deflecting cavity. In this paper, we show a detailed estimation of various aspects of the temporal resolution of this method with feasible parameters and deconvolution of the Gaussian distribution for accurate reconstruction of the temporal distribution.

INTRODUCTION

Energy Recovery Linac (ERL) demonstrators [1–3] are established to demonstrate physical challenges and key technologies of the generation, acceleration, transport, and energy recovery of high brilliance and high average current beams in superconducting cavities. The beam quality assurance in those high-brightness and high-current injectors is crucial. Therefore, a diagnostics beamline is mostly installed at the end of the injector to gauge beam quality in six-dimensional phase spaces [4, 5]. A transverse deflecting cavity that has a dipole mode to imprint the temporal information into transverse momentum is widely adopted [6–8] to measure a temporal distribution as well as absolute bunch length. This is a space-charge-free method but it has a technical difficulty to transport low-energy beams without the deterioration of beam qualities to the cavity where is typically located far downstream of the injector due to the limited space in low-energy injectors. As a complementary way to measure longitudinal beam properties near the electron gun, the zero-phase method [9] is also used. This method yields a linear RF chirp in the longitudinal phase space by using an accelerating cavity with a zero-crossing phase and transforms the longitudinal phase-space distribution to the transverse direction by dispersion function originated by a dipole magnet. However, it is not suitable for high current beams because the longitudinal phase space is strongly distorted at higher bunch charge by longitudinal space charge forces [10] while the beam is transported to the dipole magnet located far downstream of the gun. We have been proposed and demonstrated [11, 12] a new method that uses radial EM fields of an accelerating cavity to measure the temporal distribution and absolute bunch length using existing instruments in the beamline such as a corrector magnet and a screen monitor.

RESOLUTION OF THE METHOD

To utilize the method, it demands a corrector magnet for adjusting the initial beam offset and angle, an accelerating cavity (TM_{01} mode), and a screen monitor located downstream of the cavity. The schematic layout is shown in Fig. 1.

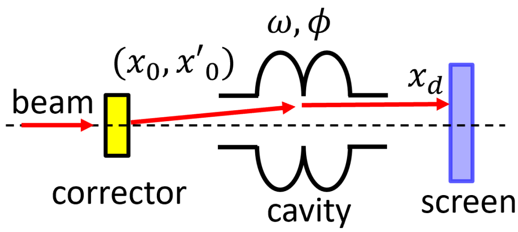

Figure 1: Schematic layout for the proposed method.

The initial beam offset x_0 and angle x_0' are defined at the position of the corrector magnet. The beam passes the center of the cavity when the offset is vanished at the corrector position, i.e. $x_0 = 0$. With an on-axis beam, the temporal resolution R_t of the method is given by [12]

$$R_t = \frac{\sqrt{\sigma_c^2 + 2\sigma_{x0}\sigma_c}}{\left|d_{12}x_0'\right| \omega}, \quad (1)$$

where σ_c is the spatial resolution of the screen monitor, σ_{x0} is the initial beam size at the screen monitor without the offset and angle, d_{12} is the deflection coefficient associated with an initial angle, and $\omega = 360 \text{ deg} \times f$, where f is the frequency of the cavity. With a state-of-the-art technique for the screen monitor [13] that has been proven measurements of a beam size of 1.44 μm using a 200 μm thick LYSO:Ce scintillator, the temporal resolution of our method can be improved enormously. Assuming that the initial beam angle is 16 mrad which is equivalent to 1/3 of the cavity radius for a 1.3 GHz superconducting cavity and d_{12} of -0.0324 mm/deg/mrad measured at a beam energy of 390 keV, the temporal resolution is calculated as a function of the spatial resolution of the screen monitor at various initial beam sizes.

As shown in Fig. 2, the method with a spatial resolution of the screen monitor of 1.44 μm yields temporal resolutions of 32 fs, 50 fs, and 70 fs for initial beam sizes of 20 μm, 50 μm,

---

* ji-gwang.hwang@helmholtz-berlin.de

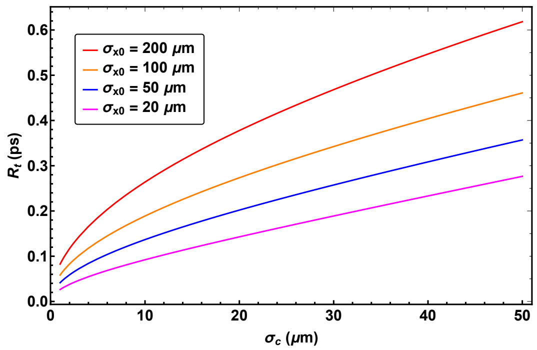

Figure 2: Temporal resolution as a function of the spatial resolution of the screen monitor at various initial beam sizes. The calculation is performed with an initial angle of 16 mrad and d_{12} = -0.0324 mm/deg/mrad measured at a beam energy of 390 keV.

and 100 µm. From Eq. (1), the temporal resolution depends not only on the spatial resolution of the screen monitor and the initial beam size but also on the deflection coefficient d_{12} which is determined by a peak on-axis accelerating field, a distance between the cavity and the screen monitor, and the beam energy. By numerical simulations using General Particle Tracer code [14], the d_{12} is investigated as a function of the initial beam energy at a peak on-axis accelerating field of 7.21 MV/m. The coefficient is rescaled with the experimentally measured value of -0.0324 mm/deg/mrad at a beam energy of 390 keV. The d_{12} as a function of the beam energy is fitted by the formula of

$$d_{12}(x) = a_1 \left(\frac{1}{1 + e^{a_2 (x^{a_3} + a_4)}} - 1 \right), \tag{2}$$

where a_1, a_2, a_3, and a_4 are fitting parameters. The fitted parameters are given in Tab. 1 and the result is shown in Fig. 3.

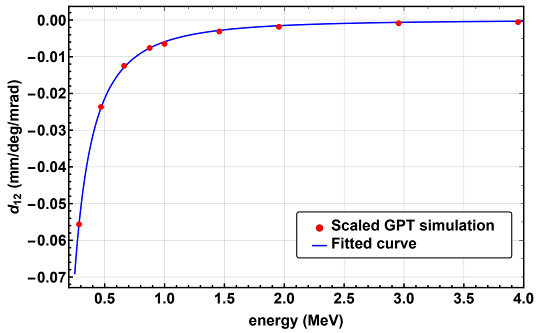

Figure 3: Rescaled d_{12} value as a function of the initial energy. This is simulated using General Particle Tracer and rescaled by the measured value.

The resolution as a function of the initial beam energy can be estimated by substituting the fitting coefficients and Eq. (2) into Eq. (1). With a fixed initial angle of 16 mrad and a spatial resolution of the monitor of 1.44 µm, the temporal resolution as a function of the initial beam energy is shown in Fig. 4.

Table 1: Fitting Parameters for the Estimation of d_{12} Value at the Specific Beam Energy

Coefficient	**Value**	**Coefficient**	**Value**
a_1	2.77	a_2	-17.1
a_3	0.11	a_4	-0.64

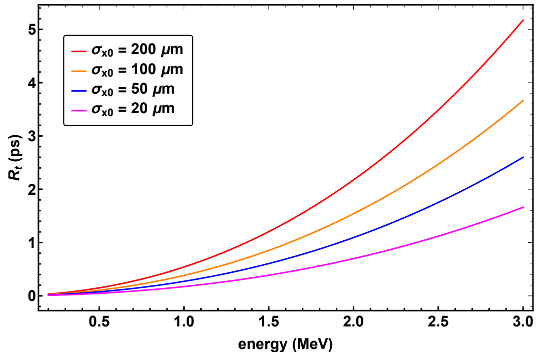

Figure 4: Temporal resolution of the method as a function of the initial beam energy with various initial beam sizes.

The temporal resolution is 76 fs, 272 fs, and 1.1 ps for beam energies of 0.5, 1, and 2 MeV with an initial beam size of 50 µm. This indicates that the method can measure about 100 fs bunch for photo-cathode DC guns that has a beam energy of about 0.5 MeV and about 1 ps bunch for photo-cathode SRF guns which has the initial energy of about 2 MeV.

RECONSTRUCTION OF TEMPORAL DISTRIBUTION

The method enables single-shot measurements of the temporal distribution of the beam that is imprinted into the horizontal direction through coupling generated by the cavity. However, the horizontal profile at the screen monitor not directly reveals the temporal distribution since the horizontal distribution at the screen monitor $H(x)$ can be interpreted by a convolution of the initial temporal distribution $f(\tau)$ and horizontal distribution with the deflecting term $g(x)$. This is given by [12]

$$H(x) = \int f(\tau) g\left(x - d_{12} x'_0 \omega \tau\right) d\tau. \tag{3}$$

Therefore, a deconvolution of the initial profile measured with $x' = 0$ is necessary. Assuming a Gaussian distribution in both horizontal $Ae^{-x^2/(2\sigma_x^2)}$ and longitudinal $Be^{-\tau^2/(2\sigma_t^2)}$ planes, the beam distribution at the screen monitor can be represented by performing the integration in Eq. (3). This is given by

$$H(x) = AB \frac{\sqrt{2\pi}\sigma_t \sigma_x}{\sqrt{\sigma_x^2 + k^2 \sigma_t^2}} \; e^{-\frac{x^2}{2(\sigma_x^2 + k^2 \sigma_t^2)}}, \tag{4}$$

where $k = d_{12}x'_0\omega$. The convoluted profile is also Gaussian distribution with a standard deviation of $\sqrt{\sigma_x^2 + k^2\sigma_t^2}$ since the Gaussian profiles have been taken into account. For the deconvolution of the initial horizontal beam size, this can be achieved by performing renormalization of the measured profile with several parameters defined in the beam experiment as

$$T(x) = e^{-\left(\frac{x^2}{2k^2\sigma_t^2}\right)} = H(x)/H\left(\frac{\sigma_x}{k\sigma_t}x\right). \qquad (5)$$

With the horizontal beam size estimated from an image measured with $x' = 0$, bunch length and machine parameters such as frequency and deflecting coefficient, the Gaussian deconvolution is applied. In addition to the Gaussian deconvolution (Eq. (5)), the Wiener filter and the Richardson-Lucy algorithm are also tested. The Wiener filter is the most popular deconvolution algorithm and it uses a closed analytic formula for estimating the object function. The Richardson-Lucy algorithm, also known as the expectation maximization method, is an iterative scheme that computes successive improved images from the starting point [15]. For both filters, a Gaussian Point Spread Function (PSF) with the width determined by fitting on the initial profile measured with $x' = 0$ is applied. The results are shown in Fig. 5.

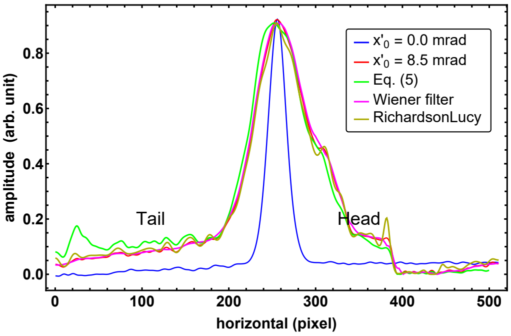

Figure 5: Deconvolution of temporal distribution using analytical formula (Eq. (5) for Gaussian beams and various algorithms.

Since the beam size measured with an angle of 7.3 mrad is a noticeably larger than the initial profile, the modification of the distribution by the deconvolution using two algorithms is negligible. Further studies on the deconvolution algorithm with non-Gaussian filters are necessary.

SUMMARY

We proposed a new method for measuring a temporal profile and absolute bunch length at contemporary high brightness injectors without special instruments. This opens a new possibility of the precise tuning of longitudinal beam properties at low-energy photo-cathode guns. A state-of-the-art screen monitor enables the bunch length measurement in the range of tens of femtoseconds at 0.5 MeV and one picosecond at 2 MeV with a peak on-axis accelerating field of about 7 MV/m. For the precise reconstruction of the temporal distribution, several methods for the deconvolution of the initial beam distribution, also well known as PSF, are tested. The result shows that the deconvolution is not crucial when the beam enlargement by the cavity field is large enough.

REFERENCES

[1] N. Nakamura *et al.*, “Present Status of the Compact ERL at KEK”, in *Proc. 5th Int. Particle Accelerator Conf. (IPAC’14)*, Dresden, Germany, Jun. 2014, pp. 353–355. `doi:10.18429/JACoW-IPAC2014-MOPRO110`

[2] S. Sakanaka *et al.*, “Recent Progress and Operational Status of the Compact ERL at KEK”, in *Proc. 6th Int. Particle Accelerator Conf. (IPAC’15)*, Richmond, VA, USA, May 2015, pp. 1359–1362. `doi:10.18429/JACoW-IPAC2015-TUBC1`

[3] M. Abo-Bakr *et al.*, “The Berlin Energy Recovery Linac Project BERLinPro - Status, Plans and Future Opportunities”, in *Proc. 63rd Advanced ICFA Beam Dynamics Workshop on Energy Recovery Linacs (ERL’19)*, Berlin, Germany, Sep. 2019, pp. 8–13. `doi:10.18429/JACoW-ERL2019-MOCOXBS04`

[4] S. Sakanaka *et al.*, “Construction and Commissioning of Compact-ERL Injector at KEK”, in *Proc. 53th Advanced ICFA Beam Dynamics Workshop on Energy Recovery Linacs (ERL’13)*, Novosibirsk, Russia, Sep. 2013, paper WG102, pp. 16–21.

[5] B. C. Kuske *et al.*, “The Injector Layout of BERLinPro”, in *Proc. 4th Int. Particle Accelerator Conf. (IPAC’13)*, Shanghai, China, May 2013, paper MOPFI004, pp. 288–290.

[6] S. Matsuba, Y. Honda, and T. Miyajima, “Deflecting Cavity for Bunch Length Diagnostics at Compact ERL Injector”, in *Proc. 1st Int. Particle Accelerator Conf. (IPAC’10)*, Kyoto, Japan, May 2010, paper MOPE002, pp. 951–953.

[7] S. Belomestnykh *et al.*, “Deflecting cavity for beam diagnostics at Cornell ERL injector”, *Nuclear Instruments and Methods in Physics Research A*, vol. 614, pp. 179-183, 2010.

[8] G. Kourkafas, T. Kamps, A. Neumann, and B. Keune, “Transverse Deflecting Cavity for Longitudinal Beam Diagnostics at BERLinPro”, in *Proc. 29th Linear Accelerator Conf. (LINAC’18)*, Beijing, China, Sep. 2018, pp. 875–878. `doi:10.18429/JACoW-LINAC2018-THPO083`

[9] D. X. Wang, G. A. Krafft, and C. K. Sinclair, “Measurement of femtosecond electron bunches using a rf zero-phasing method”, *Physical Review E*, vol. 57, pp. 2283, 1998.

[10] J.-G. Hwang, E.-S. Kim, and T. Miyajima, “Effects of space charge in a compact superconducting energy recovery linac with a low energy”, *Nuclear Instruments and Methods in Physics Research A*, vol. 684, pp. 18-26, 2012.

[11] J.-G. Hwang, E.-S. Kim, and T. Miyajima, “Bunch Length Measurement by Using a 2-Cell Superconducting RF Cavity in cERL Injector at KEK”, in *Proc. 5th Int. Particle Accelerator Conf. (IPAC’14)*, Dresden, Germany, Jun. 2014, pp. 3596–3598. `doi:10.18429/JACoW-IPAC2014-THPME146`

[12] J.-G. Hwang, T. Miyajima, Y. Honda, and Eun-San Kim, “Measurement of bunch length and temporal distribution using accelerating radio frequency cavity in low-emittance injector”, *Scientific Reports*, vol. 10, pp. 18905, 2020.

[13] G. Kube *et al.*, "Transverse Beam Profile Imaging of Few-Micrometer Beam Sizes Based on a Scintillator Screen", in *Proc. 4th Int. Beam Instrumentation Conf. (IBIC'15)*, Melbourne, Australia, Sep. 2015, pp. 330–334. `doi:10.18429/JACoW-IBIC2015-TUPB012`

[14] Pulsar Physics, General Particle Tracer. `http://www.pulsar.nl/gpt`

[15] Christoph Dalitz, Regina Pohle-Frohlich, and Thorsten Michalk "Point Spread Functions and Deconvolution of Ultrasonic Images", *IEEE Transactions on Ultrasonics, Ferroelectrics, and Frequency control*, vol. 62, pp. 531, 2015.

ISBN: 978-3-95450-230-1 ISSN: 2673-5350 doi:10.18429/JACoW-IBIC2021-WEOB01

CHARGE MEASUREMENTS IN SwissFEL AND RESULTS OF AN ABSOLUTE CHARGE MEASUREMENT METHOD

G. L. Orlandi*, P. Craievich, M. M. Dehler, R. Ischebeck, F. Marcellini, D. Stäger
Paul Scherrer Institut, 5232 Villigen PSI, Switzerland

Abstract

A comparative measurement campaign of the beam charge was carried out at SwissFEL using the following instruments: Faraday-Cup (FC), Wall-Current-Monitor (WCM), Integrating-Current-Transformer (Bergoz Turbo-ICT-2) and the reference cavity of the Beam-Position-Monitor (BPM). The goal of the measurement campaign was to determine an absolute charge measurement method for a general purpose of instrument calibration and machine routine operation. Results of the absolute charge calibration method proposed for SwissFEL will be presented.

INTRODUCTION

In the electron linac driven SwissFEL – the X-ray laser facility of Paul Scherrer Institut (PSI, www.psi.ch) – two undulator lines can be simultaneously supplied at a maximum repetition rate of 100 Hz by electron bunches with a charge in the range 10-200 pC and energy of 6.2 GeV and 3.3 GeV, respectively. A 2-bunch train of charge is emitted by a photocathode with a time duration of a few ps for the single bunch and a time macro-structure of 28 ns, accelerated by a 3 GHz RF booster and 6 GHz RF linac and compressed up to a few fs by two magnetic chicanes. The two bunches are split apart by a RF kicker into a magnetic switchyard to be finally injected into the ARAMIS and ATHOS undulator lines [1, 2], respectively.

The measurement of the bunch charge at the different acceleration stages of a linac driven Free-Electron-Laser (FEL) is relevant for characterizing the beam features such as the tranverse emittance and peak current, for monitoring the correct transport of the beam through all the acceleration and compression stages, for protecting the machine from possible accidental beam losses and for a legal certification of the charge-per-hour accelerated by the machine.

In SwissFEL, the charge of each single bunch of the 28 ns long macro-structure can be measured at different position of the machine. Just downstream of the gun, a standard Bergoz ICT and a Bergoz Turbo-ICT-2 [3] can measure the integrated charge of the bunch train and the charge of the single bunch, respectively. At the gun, a Faraday-Cup (FC) and a Wall-Current-Monitor (WCM) are also available. The FC was initially installed just downstream of the SwissFEL gun to measure the dark current. The WCM is used in SwissFEL to measure the electron bunch charge and mainly to synchronize the photocathode laser and the radio frequency of the RF gun. In addition to the Turbo-ICT in the gun, three more Turbo-ICTs are available along the ARAMIS electron beam line as well as two Turbo-ICTs can provide the charge readout at the beginning and at the end of the ATHOS electron beam line. A further monitor of the beam charge is represented by the cavity-BPM. The charge dependent signal of the monopole RF cavity of the BPM is used to normalize the dipole signal of the adjacent RF cavity which instead depends on the product of the charge and position of the bunch. The normalized dipole signal is hence processed to determine the bunch position in the horizontal and vertical directions. In SwissFEL, about two hundred cavity-BPMs are distributed all along the machine. The monopole RF signal of the cavity-BPMs has been so far calibrated against the charge readout of a reference Turbo-ICT-2 in order to provide an additional and a quite densely localized charge readout of the single bunch at 100 Hz.

The absolute calibration of the charge monitor is a crucial and sensitive issue in all the particle accelerators and, in that sense, SwissFEL does not makes an exception. The determination of an absolute method of charge calibration is even more stringent and necessary in linac facility where different charge monitors designed, realized and calibrated by distinct manufactures – quite often by a third party – are all together integrated in the machine as in the SwissFEL.

At the beginning of the SwissFEL project an agreement was signed between PSI and Bergoz for the realization of a fast Integrating-Current-Transformer (ICT) able to discriminate the 28 ns macro-structure of the SwissFEL beam in the charge range 10-200 pC. The company provided PSI with Turbo-ICT-2 sensors equipped with a factory calibration certification and a native front-end readout electronics. In order to perform a correct integration of the Turbo-ICT with the most general machine environment of the signal control and timing system of SwissFEL, the Turbo-ICT native electronics was interfaced with the standard back-end readout electronics in use at PSI.

Manufacturer company and PSI share a distinct role and action domain in the ICT set-up and operation. The company is responsible for the sensor calibration and front-end readout electronics while PSI is responsible for the back-end readout electronics and opeartions. Consequently, a clear recognition of the actions for bug-fixing and system improvements as well as every possible intervention of recalibration of a Turbo-ICT or correction of a charge readout discrepancy between different ICTs requires a complex formal procedure with possible local breaks of the machine operations as well as a large investment of beam time and manpower resources.

In order to ensure to PSI an absolute calibration procedure to be applied to all the charge monitors in operation at SwissFEL, the decision to develop in-house an independent charge measurement and calibration method was taken and realized as in the following described.

---

* gianluca.orlandi@psi.ch

ISBN: 978-3-95450-230-1 ISSN: 2673-5350 doi:10.18429/JACoW-IBIC2021-WEOB01

THE SwissFEL CHARGE MONITORS

An overview of the charge monitor used in SwissFEL will be given in this section: Faraday-Cup (FC), Wall Current Monitor (WCM), cavity Beam Position Monitor (BPM). With the exception of the FC, all the other instruments are non destructive and can be used as online monitors during machine operations.

Integrating-Current-Transformer

In SwissFEL two type of Integrating Current Transformers (ICTs) produced by Bergoz [3] are in use: one standard ICT with BCM-IHR readout electronics and six Turbo-ICT-2s with BCM-RF electronics. The conventional ICT is installed just in front of the gun together with a Turbo-ICT-2. Three more Turbo-ICT-2s are installed all along the main branch of the ARAMIS linac; two Turbo-ICT-2s are installed in the linac of ATHOS.

In a standard ICT [3] the measurement of the beam charge results from the time integral of the beam induced current in the transformer. The proportionality between the time integral of the transformer current and the beam charge in a conventional ICT is ensured by the large spectral band of the frequency response from the near-DC (kHz) to the ten MHz regions [10, 11]. In SwissFEL, because of the large band of the frequency response and the relatively long integration time 5 µs [12], the dual bunch structure of the electron beam cannot be resolved by the standard ICT. Only the total charge with included the dark current contribution from the gun can be measured with a resolution ~pC.

The Turbo-ICT-2 produced by Bergoz for SwissFEL is instead able to discriminate the 28 ns time structure of the two bunches and to provide a measurement of the single bunch charge in the range 10-200 pC. The Turbo-ICT-2 is indeed equipped with a high frequency transformer ensuring a bandwidth up to several hundred MHz and with a narrow band-pass filter centered at around 180 MHz [3, 9, 13]. The output signal of the Turbo-ICT-2 is not a pulse but a resonance at the filter central frequency with an amplitude which is proportional to the bunch charge. The Turbo-ICT-2 output signal is practically insensitive to the dark current and, thanks to the short time length of the SwissFEL electron bunch, it is also insensitive to the electron bunch shape. The beam charge readout of the Turbo-ICT-2 is finally determined by the apex of the resonance that is measured by the sample-and-hold electronics of the BCM-RF. Charge resolution (rms) of the Turbo-ICT-2 is 0.1 pC (1%) within the range 10-200 pC. In order to meet the design constraint to discriminate the 28 ns spaced dual bunch structure, the native front-end filter amplifier has been modified by reducing the filter quality factor and hence decreasing the single bunch resonance duration [14].

Faraday-Cup

Based on the design of an analogous instrument already in use in the SLS linac, a Faraday-Cup (FC) is installed in SwissFEL in front of the 2.5 cell S-band gun of the 7 MeV photoinjector [4]. The FC sensor and the signal transmission line are designed as a 50 Ω coaxial structure with a bandwidth of more than 4 GHz, see Fig. 1. The FC can be inserted into the beam line by means of a pneumatic feedthrough. The FC was installed in SwissFEL to measure the dark current from the gun. Examples of FC waveforms acquired during machine operations at 200 pC are shown in Fig. 2.

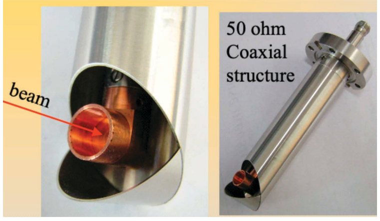

Figure 1: Details of the SwissFEL FC sensor and transmission line.

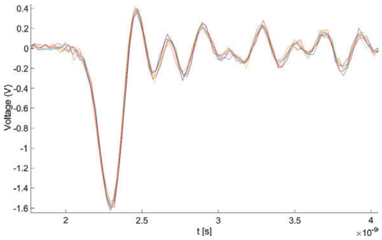

Figure 2: FC waveforms acquired at SwissFEL during machine operations at 200 pC. A 30 dB attenuator was used to protect the oscilloscope during the measurements.

Wall-Current-Monitor

A Wall-Current-Monitor (WCM) is installed downstream of the SwissFEL gun. The signal induced by the electron beam on the WCM is used as a time reference for a coarse synchronization of the timing of the photocathode laser and the RF bucket in the gun. The time integration of the WCM output signal also allows the charge of the 2-bunch train structure to be determined.

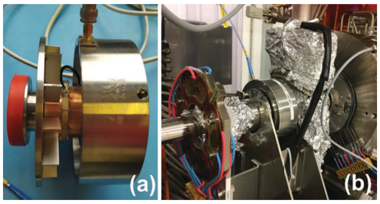

Figure 3: Images of the spare WCM (a) and SwissFEL WCM (b): nominal R_{gap} = 3.0±0.05 Ω (12 x 36 Ohm gap resistors) and NiZn ferrite ring.

A spare WCM – identical to the one installed in SwissFEL – is shown in the photo of Fig. 3. In the photo it is visible a set of 12 equally spaced 36 Ω resistors which bridge in parallel a gap in the beam pipe where a ceramic ring ensures the electrical insulation and the vacuum seal. A NiZn ferrite ring enclosed in the external metallic cylinder surrounds the

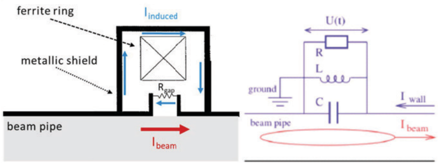

Figure 4: schematic sketch of the WCM and equivalent circuit model of the WCM as a parallel of an inductance L, gap resistor R and gap capacitor C.

resistor crown and the gap in the beam pipe, see Fig. 4. The external metallic cylinder constitutes a Faraday cage for the resistors. It also ensures a confinement of the electromagnetic field travelling with the electron beam as well as of the current induced into the metallic shielding by the fast time variation of the magnetic field trapped by the ferrite core [5]. The time integration of the voltage drop (V_{gap}) across the parallel of the resistors (R_{gap}) permits to determine the beam charge (Q):

$$Q = \frac{1}{R_{gap}} \int_{t_0}^{t_1} V_{gap}(t)\, dt \ . \tag{1}$$

Typical time windowing of the WCM signal readout at SwissFEL is in the order of ten nanoseconds. With reference to the equivalent circuit model in Fig. 4 it is possible to estimate the bandwidth of the WCM response in the frequency domain as well as to better understand the limitation of this instrument in determining a precise measurement of the beam charge. The inductance L represented by the ferrite and the metallic shield affects the low frequency response of the WCM with a cutoff frequency f_{low} that prevents to measure the DC component of the current input signal of the WCM:

$$f_{low} = \frac{R_{gap}}{2\pi L}. \tag{2}$$

The gap in the vacuum pipe filled with the ceramic ring acts as a capacitor (C) which is responsible for a high frequency cutoff of the WCM frequency response (tipically in the GHz region):

$$f_{high} = \frac{1}{2\pi R_{gap} C}. \tag{3}$$

A correct determination of the gap resistance R_{gap} is crucial for a precise measurement of the absolute charge from the WCM. The SwissFEL WCM was the result of an adaptation to the specific case of a former instrument already developed for SLS [4]. With respect to the former SLS model, the resistance of the resistor parallel in the SwissFEL WCM was increased from the nominal value of 1 Ω to 3 Ω to improve the sensitivity.

Both the WCM installed in SwissFEL and the spare WCM prototype have been experimentally characterized. The achieved experimental results have been compared with results of numerical simulations of a model of the SwissFEL WCM developed by means of the codes *CST Studio Suite* [6] and *ANSYS HFSS* [7]. Details on the work of experimental characterization and numerical modelling of the WCM will be presented in a dedicated article [8]. In the present paper, the main results and conclusions will be summarized.

Gap resistance and inductance of both the SwissFEL and the spare WCM were determined by measuring the reflection coefficient S_{11} at the WCM output port by means of a Vector Network Analyzer (VNA). For the spare WCM, the measurement results of the reflection coefficient S_{11} confirmed the expected nominal value of the gap resistance ($R_{gap} = 3\,\Omega$) and permitted to determine the inductance driven low frequency cutoff of the WCM bandwidth $f_{low} \simeq 200$ kHz. A gap resistance ($R_{gap} = 3.55\,\Omega$) larger than the nominal value 3.0 Ω was instead measured in the SwissFEL WCM. Since the SwissFEL WCM cannot be inspected, possible explanation of this mismatch is the accidental failure or damage of 2 of the 12 resistors bridging the ceramic gap.

A deeper insight into the question of the gap resistance of the SwissFEL WCM and of the value of the gap resistance to be used for the charge calculation in Eq. (1) was obtained thanks to a complete characterization with a VNA of the transfer function of the spare WCM prototype and a comparison with the numerical predictions from the CST model of the WCM.

For the VNA measurement of the transfer function of the spare WCM

$$Z(\omega) = \frac{V_{out}(\omega)}{I_{beam}(\omega)}\,[\Omega] \tag{4}$$

a dedicated testing workbench based on the coaxial wire method was set up in the laboratory, see Fig. 5. According to the VNA measurements, the transfer function shows the expected low frequency cutoff and a constant value in the frequency region up to several MHz where it is possible to evaluate the value of the impedance $Z(\omega) \simeq R_{gap}$ to be used for the charge calculation in Eq. (1). The estimated value of the gap impedance underestimates of about 5 – 6% the expected nominal value of 2.83 Ω resulting from the parallel of the 3.0 Ω of the resistor crown across the gap and the 50 Ω load of the VNA [8].

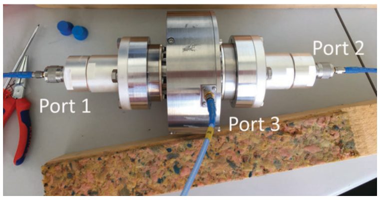

Figure 5: Laboratory setup for the measurement with a VNA of the WCM transfer function by means of the coaxial wire method.

In order to better investigate the discrepancy observed in the spare WCM between the low frequency measurement of the transfer impedance and the expected nominal value of the gap resitance, CST numerical simulations were performed. Numerical simulation from CST of the voltage signal across the resistor parallel and the related frequency spectrum for a Gaussian electron bunch with a rms pulse width of $\sigma = 25$ ps are shown in Fig. 6. The size of the 3D mesh defining the CST computing grid as well as the electron bunch length of 25 ps – corresponding to a sampling frequency up to 13 GHz

ISBN: 978-3-95450-230-1 ISSN: 2673-5350 doi:10.18429/JACoW-IBIC2021-WEOB01

– were optimized in order to ensure the required asymptotic convergence of the numerical predictions in a reasonable and affordable computing time. As shown in Fig. 6, the CST frequency spectrum of the WCM voltage is characterized by the expected constant amplitude in a frequency region from the near-DC up to a few hundreds MHz. In correspondence of this frequency region the time integration of the WCM output signal via Eq. (1) can be performed with respect to a well defined value of the gap resistance. At higher frequencies, the spectral distribution of the WCM voltage also shows a broadband peak around 1.5 GHz and a sharp peak at about 4.7 GHz. The origin of the 1.5 GHz broad band peak in the frequency spectrum of the WCM output voltage – Fig. 6(b) – can be explained [5] as the result of the mismatch of the gap resistance with the impedance of a parallel transmission line represented by the ceramic gap. CST numerical simulations of the frequency spectrum of the WCM voltage as a function of the gap resistance confirmed such hypothesis [8]. About the origin of the 4.7 GHz sharp peak in the voltage frequency spectrum, which is responsible of the fast oscillation characterizing the quenching tail of the voltage signal in Fig. 6(a), this is due to a spurious resonance occurring in the WCM beam pipe. Such a resonance is caused by the step transition from the outer beam pipe into the inner part of the WCM as demonstrated in [8] by means of an eigenmode simulation of the WCM performed with the code *ANSYS HFSS*.

About the aforementioned discrepancy of the nominal value of the gap resistance of the spare WCM with respect to the result of the VNA characterization, numerical simulations with the CST code allowed us to better understand the origin of this mismatch. It was indeed observed [8] that the outcome of the time integration of the WCM gap voltage in CST via Eq. (1) depends on the model assumed for the permeability μ of the NiZn ferrite. According to an ideal model of the ferrite with a constant value of the permeability $\mu = const$ in the considered integration frequency band, the result of the time integration of the gap voltage fits with the 200 pC input charge of the CST simulation. Conversely, if a more realistic and frequency dependent model for the ferrite permeability $\mu(\omega) = \mu'(\omega) - i\mu''(\omega)$ is implemented in CST, the time integration of the resulting gap voltage underestimates the input value of the beam charge. Explanation of this beahaviour is the presence of ohmic losses inside the ferrite core due to the imaginary part of the complex expression of the ferrite inductance L when a dispersive model for the permeability μ is considered. According to a more realistic dispersive model of the ferrite, in the circuital model of the WCM sketched in Fig. 4, an additional ohmic resistance $R_L(\omega)$ should be added in series with the inductance L(ω). The presence of ohmic losses in the ferrite can explain hence the observed mismatch of the gap resistance measured during the transfer function characterization of the spare WCM with respect to the expected nominal value.

In conclusion, on the basis of the experimental results of the transfer impedance measurements of the spare WCM we can estimate that the gap impedance is 5–6% less than the expected nominal value 2.83 Ω (parallel of 3.0 Ω and 50 Ω) because of the ohmic losses from the ferrite. Since it is practically impossible to repeat the same measurement of the transfer impedance in the SwissFEL WCM, we assume that the same estimate of the ohmic losses of the spare WCM ferrite can be also applied to the SwissFEL WCM since the two WCMs are in principle identical. On the basis of this assumption on the ohmic losses of the SwissFEL WCM, the low-frequency value of the transfer impedance $Z_L(\omega)$ to be used in Eq. (1) instead of the nominal gap resistance $R_{gap} = 3.31\,\Omega$ (parallel of 3.55 and 50 Ω) should be $Z_{L,exp}(\omega) = 3.11\,\Omega$. CST numerical simulations of the WCM transfer impedance based on the best up to date available dispersion model of the ferrite situate the value of the transfer impedance at $Z_{L,theo}(\omega) = 3.26\,\Omega$. Finally, to the best of our up to date experimental and theoretical knowledge of the SwissFEL WCM we can estimate a low-frequency transfer impedance of $Z_L(\omega) = 3.11 - 3.26\,\Omega$ (parallel with 50 Ω already included).

In Fig. 7, the measured output waveform of the SwissFEL WCM (upper plot) as well as the time integration of the output signal via Eq. (1) as a function of the integration time (lower plot) are shown for a nominal charge of the single bunch of 200 pC (Bunch-2, when Bunch-1 is OFF). In the plot of the time integral of the WCM waveform, the negative slope before time=0 is due to the integration of a background (most likely a RF environment background coming from the gun); the negative slope after time=0 is instead due to the combined effect of the background and of the absence of the DC component in the frequency distribution of the signal acquired by the WCM. The determination of the beam charge from the plot of the time integration of the waveform – Fig. 7 lower plot – can be performed by applying a suitable fitting procedure to the curve slopes around time=0 as more diffusely described in [8].

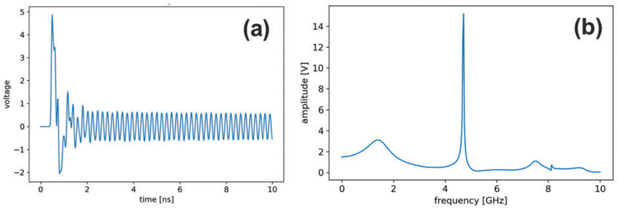

Figure 6: CST numerical simulation of the WCM output signal for an electron bunch length of 25 ps in the time domain (a) and in the related frequency domain (b).

Cavity-Beam-Position-Monitor and Method for Measuring the Beam Charge

The method for determining the beam charge from the analysis of the charge excited monopole signal in the cavity BPM has been proposed and implemented at SwissFEL by one of the authors (F.M.).

About 200 cavity BPMs are distributed along the SwissFEL linacs, transfer and undulator lines. They consists of

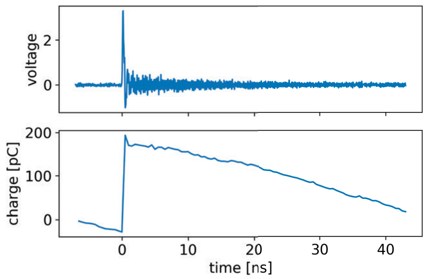

Figure 7: SwissFEL WCM signal readout of the single bunch with nominal charge 200 pC: (upper plot) measured output waveform; (lower plot) time integration of the WCM waveform via Eq. (1) as a function of the integration time.

two cavities: a so called position cavity resonating at the TM_{110} mode (dipole) and a reference cavity designed to resonate at the TM_{010} mode (monopole) [17]. Cavity BPMs ensure at SwissFEL the tracking of the beam orbit of the 2-bunch beam structure in the horizontal and vertical direction and the monitoring of the single bunch charge. The BPM sensitivity largely covers the 10-200 pC range ensuring a beam centroid positioning with a spatial resolution up to the sub-micrometer scale. More details on the cavity BPM performance and application as position monitor in [15, 16]. In the present context, our attention will be focused on the BPMs as charge monitors. During normal machine operation at SwissFEL, the monopole cavity signal of the BPMs provides a shot-to-shot estimate of the beam charge to the users. For normal machine operations, the calibration of the BPM monopole signal is performed against a reference Turbo-ICT-2: i.e., the BPM monopole ADC signal – as processed by the front-end electronics – is converted into a charge dimensional signal thanks to the comparison with the absolute charge readout of a reference Turbo-ICT-2. It should be noted that, in the application of the method of the cavity BPM for absolute charge measurements as below described, the monopole signal is directly acquired by an external oscilloscope and not from the standard BPM ADC.

Depending on the beam pipe aperture, four different types of cavity BPM are installed in SwissFEL. Furthermore, they can be classified in two types according to the working frequency: 3.284 GHz and low quality factor and 4.926 GHz and high quality factor. Each BPM is a double cavity device, where one cavity (usually called reference cavity) is used to normalize the signal detected by the other cavity to the beam charge. The output of the reference cavity comes from the energy that the beam releases on the TM_{010} cavity mode, and, since its sensitivity to beam position is negligible, it depends on the beam charge only. For our estimate of the SwissFEL bunch charges, we measured the output signal of several BPMs along the machine. The measurements setup simply consisted of a 16 GHz, 40 GS/s oscilloscope, connected to the cable that brings the BPM reference cavity signal to the technical gallery and a low pass filter, with cut-off frequency between the TM_{010} mode and the first HOM frequencies, to isolate the contribution of the TM_{010} mode to the measured waveform. A number of waveforms have been grabbed for each BPM, at the bunch repetition rate (see Fig. 8). From the theory the signal $V_{out}(t)$ at the cavity output is:

$$V_{out}(t) = q\omega\sqrt{\frac{Z}{Q_e}R/Q}\,e^{-\frac{\omega t}{2Q_L}}\cos(\omega t), \tag{5}$$

where q is the bunch charge; ω is the angular frequency of the cavity TM_{010} mode; Z is the characteristic impedance of the cavity output line (50 Ohms in our case); R/Q is a RF parameter depending on the cavity geometry; $Q_e = \omega U/P_{out}$ is the cavity external quality factor (U is the cavity stored energy and P_{out} the power coupled out of the cavity); $Q_L = \omega U/(P_{wall} + P_{out})$ is the cavity loaded quality factor, which takes into account also the power lost P_{wall} in the cavity walls.

Every single BPM has been measured to determine its individual values of ω, Q_L and Q_e. There are also quite complicate techniques to measure R/Q, but we believe that numerical simulations can estimate its value even with larger precision. So, we assumed that all the BPMs of the same type have the same R/Q, and this was obtained by simulations with two different codes (HFSS and CST). Therefore, the bunch charge can be measured fitting the oscilloscope waveforms with the formula in Eq. (5), where the only free parameter is q. The attenuation of all the cables used in the measurements has also been measured and the amplitude of $V_{out}(t)$ scaled accordingly. The low-pass filter employed in the measurement has also been considered in the final expression used in the fit (see Fig. 9).

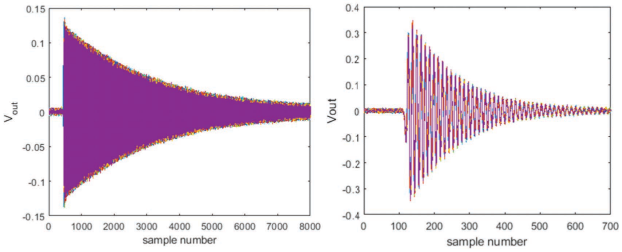

Figure 8: Waveforms measured with the oscilloscope for one high Q (left) and one low Q (right) BPM.

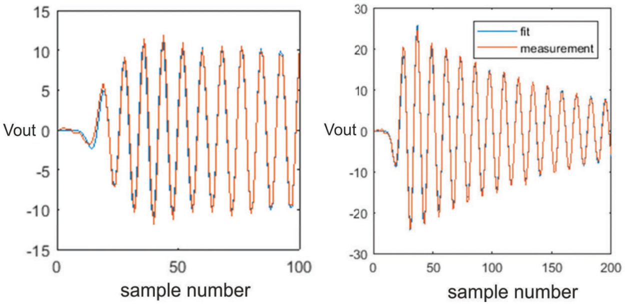

Figure 9: Examples of fittings for a high Q (left) and one low Q (right) BPM.

ABSOLUTE CHARGE MEASUREMENTS AT SwissFEL

The Method

In the last couple of years several sessions of beam charge measurements were carried out at SwissFEL. Goal of this campaign of measurements was the definition of an univocal method for the absolute calibration of the non-descructive charge monitors of SwissFEL.

As mentioned above, the procedure so far adopted for calibrating the amplitude of the reference cavity signal of the BPMs involves using the reading of a reference Turbo-ICT-2 in the linac. As it is evident from the plot in Fig. 10 (red lines), the Turbo-ICT-2 readings along the linac are not constant and the choice of the reference Turbo-ICT-2 for the calibration is made in an arbitrary way. The question that raised a few years ago was whether it was possible to make absolute charge measurements using signals from the BPM reference cavities. In addition, to validate the charge measurements from the BPM, before using them as a comparison and subsequent calibration of the ICT, the charge values obtained from the cavity BPMs were compared with the readings from the WCM and the FC.

For such a purpose, the WCM of SwissFEL was the object of a careful work of experimental characterization and numerical modelling as described in previous section. About the cavity BPMs, all the knowledge of the characterization parameters was already available since they have been designed and experimentally characterized at PSI. Furthermore, the attenuation of the RF cables used for the cavity BPMs was also very precisely measured exactly at the frequency of resonance of the cavity. Charge measurements with FC were also performed. With respect to cavity BPM results we observed the FC underestimates of about 7% the beam charge.

In conclusion, behind the work carried out in the last couple of years on the subject of the charge measurements at SwissFEL, there were the following objectives: (1) check the reliability of the WCM and cavity BPM as absolute charge calibration tools; (2) on the basis of the charge calibration reference established by means of the WCM and cavity BPMs, proceed with the alignment of all the charge monitor in operation at SwissFEL in order to verify the long term stability and the possible time drift of the intrinsic calibration of each system. In the following paragraph, the results obtained in the definition of an absolute calibration method for the charge monitors of SwissFEL will be presented.

The Results

Results of the measurements of beam charge carried out in SwissFEL by acquiring the signal from the monopole RF cavity of several BPMs all along the machine are shown in Figs. 10. The BPM charge measurements of the electron beam charge plotted in Figs. 10 were obtained by applying the analysis method of the cavity BPM monopole signal as described in a dedicated paragraph. The cavity BPM results of the beam charge for bunch-1 and bunch-2 are compared in Figs. 10 with analogous measurement results from the closest Turbo-ICT-2s. The acquisition of the measured data shown in Figs. 10 was not simultaneous but carried out individually for single device over a time interval of several hours. The corresponding Turbo-ICT-2s measurements were not synchronous but simultaneous to the cavity BPM measurements. The analysis of the data reported in Figs. 10 for bunch-1 (same considerations apply to the bunch-2 case) shows a relative systematic offset of the Turbo-ICT-2s along the machine and a substantial alignment of the cavity BPM measurements within the statistical error bars. Furthermore, it can be observed that some of the Turbo-ICT-2s provide a charge readout very close to the cavity BPM results. With respect to the charge measurements of the first Turbo-ICT, the average of the cavity BPM measurements in Fig. 10 is about 20 pC smaller: with respect to the bunch-1 charge readout of the first Turbo-ICT-2, the mean value of the charge measured by the cavity BPM is indeed 10% ± 2% smaller. In a further dedicated measurement session carried out in the high energy part of ARAMIS, a similar percentage offset of 10% ± 3% was observed in the mean value of the cavity BPM charge readouts for bunch-1 with respect to the first Turbo-ICT-2 (which is our reference ICT in this comparison). It should be noted that the dispersion affecting the measurements results of the different cavity BPMs in Fig. 10 may have a statistical and systematic origin. A statistical dispersion of the cavity BPM data can be expected since the measurement acquisition is not simultaneous (several hours needed for the acquisition of the complete set of measurements) and passing from a device to the other fluctuation of the beam charge can occur. The possible systematic error in the cavity BPM measurements can be instead explained by the incertitude in the attenuation measured for each RF cable.

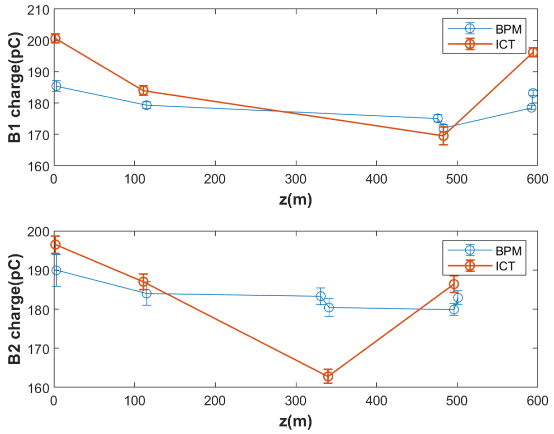

Figure 10: Comparison of charge measurements from Turbo-ICT-2 and cavity BPM all along the ARAMIS and ATHOS electron beam lines: bunch-1 (B1) (upper plot); bunch-2 (B2) (lower plot).

In addition to the Turbo-ICT-2 and cavity BPM measurements carried out for bunch-1 and bunch-2 at a constant charge of 200 pC all along the ARAMIS and ATHOS elec-

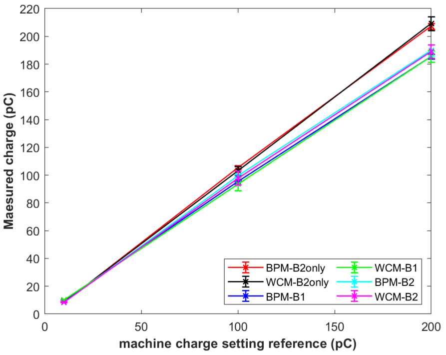

Figure 11: Comparison of the charge readout from the WCM and cavity BPM charge readout vs machine setting charge. The WCM and the cavity BPM are placed at coordinate z=0.58 m and z=3.01 m from the gun cathode, respectively.

tron beam line, simultaneous measurements were performed for a variable beam charge (10, 100 and 200 pC) by means of the first Turbo-ICT-2 placed at a distance of z=1.86 m from the gun cathode, the first cavity BPM placed at z=3.0 m and the WCM placed at z=0.58 m for three different acquisition settings, see Fig. 11: measurement of bunch-2 only (no bunch-1 emitted by the gun); measurement of bunch-1 in presence of bunch-2; measurement of bunch-2 in presence of bunch-1. Under the hypothesis of a transfer impedance $Z_L(\omega) = 3.26\,\Omega$ for the SwissFEL WCM the ratio of the WCM readout over the cavity BPM readouts for the different charge values are reported in Table 1. Taking into account the incertitude on the value of the transfer impedance of the WCM as above described ($Z_L(\omega) = 3.11 - 3.26\,\Omega$), we can very optimistically guess that the reliability of the WCM compared to the cavity BPM is within ±5%. Moreover, with respect to the bunch-1 charge readout of the first Turbo-ICT-2 at 200 pC – see Fig. 11 – the charge readout of the first cavity BPM at the gun is about $(8 \pm 1)\%$ smaller.

In conclusion, on the basis of the comparative study of the experimental results of the charge measurements for bunch-1 from the first Turbo-ICT-2 at the gun and from the cavity BPMs at the gun and all along the machine, the criterion that we can assume in a procedure of alignment of all the charge monitors in SwissFEL under the hypothesis of full transmission of the machine is the following: for a charge readout of 200 pC of the very first Turbo-ICT-2, the correct alignment value of all the charge monitors in SwissFEL – included the first Turbo-ICT-2 – should be about $(9 \pm 2\%)$ less, i.e., the aggregate outcome from the correction factors so far obtained $(10\% \pm 2\%, 10\% \pm 3\%, 8 \pm 1\%)$.

Presently, the evaluation of the aforementioned charge alignment factor of the charge monitor in SwissFEL is only based on the absolute charge measurements of the cavity BPM which cannot be corroborate by the WCM which is affected by an incertitude that can be optimistically estimated in ±5%. Further numerical studies and experimental characterization will be needed to better characterize the SwissFEL WCM; the present impossibility to remove it from the beam line makes this goal quite hard to achieve. Further cavity BPM measurements in a simultaneous acquisition with the Turbo-ICT-2s are necessary to better quantify the aforementioned percentage calibration factor of the charge readout of the SwissFEL charge monitors as well.

Table 1 shows the ratio of the WCM over cavity BPM charge readout measured in SwissFEL for different acquisition settings and for different nominal values of the charge 10, 100 and 200 pC (see Fig. 11). Measurement of bunch-2 only (no bunch-1 emitted by the gun), measurement of bunch-1 in presence of bunch-2, and measurement of bunch-2 in presence of bunch-1. In the WCM calculation of the charge by means of Eq. (1) an impedance of $Z_t = 3.26\,\Omega$ (parallel of the estimated transfer impedance with the $50\,\Omega$ load of the scope) was assumed in agreement with the results of the CST characterization of the SwissFEL WCM (see related paragraph).

Table 1: Ratio of the WCM over Cavity BPM Charge Readout Measured in SwissFEL for Different Charge Values

Nominal charge	200 pC	100 pC	10 pC
WCM/BPM bunch-2 only	1.0092	0.9773	1.0361
WCM/BPM bunch-1	1.0011	0.9770	1.0204
WCM/BPM bunch-2	0.9953	0.9819	1.0341

CONCLUSIONS AND OUTLOOK

In the present paper a review of the charge monitors in operation at SwissFEL is presented. Results of a recent characterization of the SwissFEL WCM based on experimental measurements and code aided modelling are also presented. The numerical and experimental characterization of the SwissFEL WCM did not dissolve an incertitude in the WCM calibration parameters that we optimistically estimate in ±5%. A new method for determining the beam charge from the monopole RF signal of the cavity BPM is presented as well as the experimental results of its practical implementation at SwissFEL. Cavity BPMs showed a more robust and statistically consistent reliability in the measurement of the beam charge in SwissFEL. They demonstrated to be an useful tool to determine an absolute measurement of the beam charge in SwissFEL.

ACKNOWLEDGEMENTS

The authors wish to thank the SwissFEL operation crew for the valuable support during the measurements. The authors are particularly grateful to Markus Baldinger for his valuable support in the design and set up of the test-bench equipment.

REFERENCES

[1] E. Prat *et al.*, “A compact and cost-effective hard X-ray free-electron laser driven by a high-brightness and low-energy

electron beam”, *Nature Photonics*, vol. 14, pp. 748–754, 2020. `doi:10.1038/s41566-020-00712-8`

[2] R. Ganter *et al.*, “The SwissFEL soft X-ray free-electron laser beamline: Athos”, *J. Synchrotron Rad.*, vol. 26, pp. 1073–1084, 2019. `doi:10.1107/S1600577519003928`

[3] Bergoz Instrumentation, *Integrating Current Transformer and Beam Charge Monitor*. `https://www.bergoz.com/en/ict-bcm-ihr`

[4] M. Dach, M. Dehler, A. Jaggi, P. Kramert, M. Pedrozzi, V. Schlott, and A. Streun, “SLS linac diagnostics-commissioning results”, *AIP Conference Proceedings*, vol. 546, p. 563, 2000. `doi:10.1063/1.1342631`

[5] R. Webber, “Longitudinal emittance: An introduction to the concept and survey of measurement techniques including design of a wall current monitor”, *AIP Conference Proceedings*, vol. 212, p. 85, 1990. `doi:10.1063/1.39712`

[6] *CST Studio Suite*, Dassault Systemes. `https://www.3ds.com/products-services/simulia/products/cst-studio-suite/`

[7] *ANSYS HFSS*, `https://www.ansys.com/products/electronics/ansys-hfss`

[8] D. Stäger *et al.*, “Characterization of the SwissFEL Wall Current Monitor: experimental and numerical simulation results”, to be submitted for publication.

[9] S. Artinian, J. F. Bergoz, F. Stulle, P. Pollet, and V. Schlott, “Development and First Tests of a High Sensitivity Charge Monitor for SwissFEL”, in *Proc. IBIC’12*, Tsukuba, Japan, Oct. 2012, paper MOPB87, pp. 287–290. `https://jacow.org/IBIC2012/papers/mopb87.pdf`

[10] K. Nakamura, D. E. Mittelberger, A. J. Gonsalves, J. Daniels, H.-S. Mao, F. Stulle, J. Bergoz, and W. P. Leemans, “Picocoulomb charge measured at BELLA to percent-level precision using a Turbo-ICT”, *Plasma Phys. Control. Fusion*, vol. 58, p. 034010, 2016. `doi:10.1088/0741-3335/58/3/034010`

[11] F. Stulle, J. Bergoz, W.P. Leemans, and K. Nakamura, “Single Pulse Sub-Picocoulomb Charge Measured by a Turbo-ICT in a Laser Plasma Accelerator”, in *Proc. IBIC’16*, Barcelona, Spain, Sep. 2016, pp. 119–122. `doi:10.18429/JACoW-IBIC2016-MOPG35`

[12] R. Ischebeck *et al.*, “Overview of Beam Instrumentation Activities for SwissFEL”, in *Proc. IBIC’14*, Monterey, CA, USA, paper MOPF31, pp. 119–123, 2014. `https://jacow.org/IBIC2014/papers/mopf31.pdf`

[13] F. Stulle and J.F. Bergoz, “Turbo-ICT Pico-Coulomb Calibration to Percent-level Accuracy”, in *Proc. FEL’15*, Daejeon, Korea, pp. 118–121, 2015. `doi:10.18429/JACoW-FEL2015-MOP041`

[14] S. Artinian, J. Bergoz, F. Stulle, P. Pollet, and V. Schlott, “Goubau Line and Beam Characterization of TURBO-ICT for SwissFEL”, in *Proc. IPAC’13*, Shanghai, China, p. 476, paper MOPME005, 2013. `https://jacow.org/ipac2013/papers/mopme005.pdf`

[15] B. Keil, R. Baldinger, R. Ditter, W. Koprek, R. Kramert, G. Marinkovic, M. Roggli, M. Stadler, and D. M. Treyer, “A Generic BPM Electronics Platform for European XFEL, SwissFEL and SLS”, in *Proc. IBIC’12*, Tsukuba, Japan, Oct. 2012, paper MOCB02, pp. 11–15. `https://jacow.org/IBIC2012/papers/MOCB02.pdf`

[16] T. Schietinger *et al.*, “Commissioning experience and beam physics measurements at the SwissFEL Injector Test Facility”, *Phys. Rev. Accel. Beams*, vol. 19, p. 100702, 2016. `doi:10.1103/PhysRevAccelBeams.19.100702`

[17] F. Marcellini, B. Keil, M. Rohrer, M. Stadler, J. Stettler, D.M. Treyer, D. Lipka, D. Noelle, M. Pelzer, and S. Vilcins, “Design of Cavity BPM Pickups for SwissFEL”, in *Proc. IBIC’12*, Tsukuba, Japan, Oct. 2012, paper TUPA24, pp. 390–393. `https://jacow.org/IBIC2012/papers/TUPA24.pdf`

ISBN: 978-3-95450-230-1 ISSN: 2673-5350 doi:10.18429/JACoW-IBIC2021-WEOB02

COMMISSIONING OF THE CRYOGENIC CURRENT COMPARATOR (CCC) AT CRYRING*

D. M. Haider†, A. Reiter, M. Schwickert, T. Sieber, F. Ucar,
GSI Helmholtz Centre for Heavy Ion Research, Darmstadt, Germany
H. De Gersem, N. Marsic, W. F. O. Mueller, TU Darmstadt, Darmstadt, Germany
M. Schmelz, R. Stolz, V. Zakosarenko[3], Leibniz IPHT, Jena, Germany
M. Stapelfeld, Friedrich-Schiller-University Jena, Jena, Germany
T. Stoehlker[1,2], V. Tympel, Helmholtz Institute Jena, Jena, Germany
[1]also at GSI Helmholtz Centre for Heavy Ion Research, Darmstadt, Germany
[2]also at Institute for Optics and Quantum Electronics, Jena, Germany
[3]also at Supracon AG, Jena, Germany

Abstract

Accurate non-destructive measurement of the absolute intensity of weak ion beams (< 1 µA) in storage rings is often restricted to special beam conditions and, even then, is associated with large uncertainties and tedious calibration procedures. However, experiments with rare ions in particular depend on excellent current resolution. In order to make these beams accessible, the Cryogenic Current Comparator (CCC) monitors deviations of the DC beam current on a scale of nA and compares the signal to a calibrated reference current. At the heavy-ion storage ring CRYRING at GSI a CCC prototype for FAIR was installed and first results of the commissioning are reported here. Preceding the operation with beam, a careful design of the beamline helium cryostat was required to provide the stable cryogenic environment needed for CCC operation. Mechanical and electro-magnetic perturbations that interfere with measurement of the beam's faint magnetic field are suppressed by the internal structure of the system and a superconducting magnetic shield, while the remaining interference can be filtered with adequate signal processing. In this way, a current resolution in the nA range was demonstrated.

INTRODUCTION

In the second half of 2020, a Cryogenic Current Comparator (CCC) was installed at the heavy-ion storage ring CRYRING at GSI to serve as the prototype for a total of up to five CCC installations at FAIR. A CCC monitor consists of a cryogenic system supporting the stable operation of the sensing unit and a CCC detector as developed within the CCC collaboration at the FSU Jena [1] and the Leibniz IPHT [2]. The FAIR prototype consists of a newly manufactured beamline cryostat that has been developed with ILK Dresden§ at GSI specifically for the needs at FAIR [3]. The particular CCC detector (FAIR-Nb-CCC-XD [1]) that is installed is part of the same design family (CCC-XD) as the one developed for the use at the Antiproton Decelerator at CERN [4] with extended dimensions to accommodate the FAIR beamlines with a diameter of 150 mm. Both, the cryostat and the CCC detector, were tested separately in a laboratory environment.

Herein, we will introduce the first results of the commissioning of the assembled setup in an accelerator setting. In the following, the configuration of the detector setup at the CRYRING is presented and the effect of the environment on the performance of the CCC is discussed.

BEAMLINE SETUP

The CCC beamline setup (see Fig. 1) is based on a helium bath cryostat with a volume of 80 l, a gas-cooled heat shield with a nominal throughput of 15 l/day and a local cryocooler-based liquefier from Cryomech¶ with a performance of up to 19.4 l/day. At the moment, the cold operating time is limited to 7 days due to an excessive heat load and an oscillating gas flow to the liquefier. The additional heat input that leads to an increased evaporation rate of 22 l/day is most likely due to the installation of heating foils for the bake-out of the UHV beamline which is surrounded by the cryostat (c.f. Fig. 2). In this area, the cryogenic CCC detector and the heat shield is placed as close to the beamline as possible and the additional material from

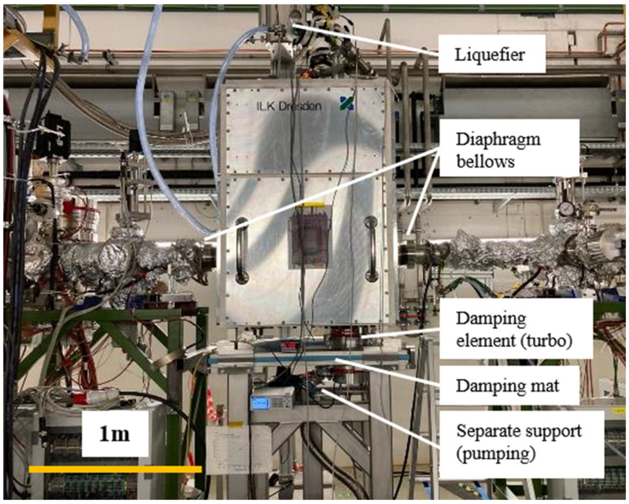

Figure 1: CCC beamline setup at the CRYRING.

---

*Work supported by AVA – Accelerators Validating Antimatter the EU H2020 Marie-Curie Action No. 721559 and by the BMBF under contract No. 5P18SJRB1.

†d.haider@gsi.de

§ILK Dresden gGmbH, Dresden, Germany

¶Model PT415 from Cryomech Inc, Syracuse, NY, USA

‡Datasheet, Sylomer SR28, Getzner Spring Solutions GmbH, Germany

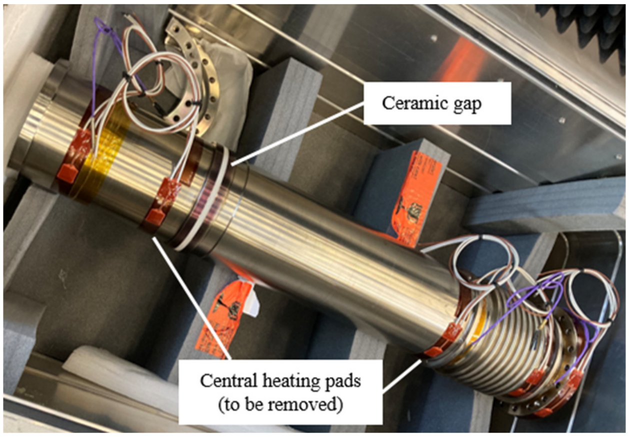

Figure 2: UHV beamline with Kapton heating foil for bake-out and a ceramic gap. In the final assembly it is closely surrounded by the cryogenic helium vessel of the cryostat.

the heating pads increase the heat transfer to the helium vessel. However, the bake-out at CRYRING has shown that it is sufficient to passively heat the section of the beamline that is surrounded by the helium vessel by heating pads right before and after the section to reach a beamline vacuum of better than $1 \cdot 10^{-10}$ mbar. Therefore, at the next opportunity the heating foils will be removed to restore the nominal evaporation rate of 15 l/day. Unfortunately, no reliable solution to stabilize the helium flow was found so far. However, a detailed investigation of the flow resistances is ongoing and has already resulted in several modifications to promote the gas flow along the cooling line and suppress the gas intake through the liquid helium return nozzle of the liquefier.

The UHV beam line, the heat shield and the helium tube as part of the helium vessel each need to incorporate an electrical insulator along the beam tube at the position of the CCC detector such that mirror currents do not shield magnetic field components of the ion beam. In general, ceramic gaps are used for this purpose. However, no ceramic gap could be produced in time which can withstand the mechanical stress on the helium vessel during the cooldown. Therefore, the helium tube features a gap made from polyimide that was glued to the stainless steel tube and is currently in use with a leakage rate smaller than $1 \cdot 10^{8}$ mbar·l/s.

Mitigation of External Perturbations

An accelerator environment is far from an ideal operating condition for the CCC which, in fact, is also a highly sensitive magnetometer. External magnetic field disturbances, mechanical vibrations and small temperature/pressure fluctuations all affect the measurement significantly. Therefore, an effective electromagnetic and mechanical decoupling of the CCC from the environment is important (see Fig. 1). The setup at the beamline is supported by a massive sand-filled stainless steel stand. The two are isolated by a Sylomer SR28 damping mat that attenuates mechanical vibrations above a cut-off frequency of 26.8 Hz[‡]. The beamline and the liquefier are mechanically decoupled from the cryostat by diaphragm bellows while the turbo pump is connected via a dedicated damping element. Due to these measures, the signal quality was not noticeably deteriorated by mechanical perturbations during this measurement campaign.

All external magnetic fields are attenuated by the superconducting shield of the CCC detector with a damping factor of 85 dB [5]. To minimize local magnetic perturbations as few permeable materials as possible are used in the construction of the cryostat. Finally, the cryostat provides a very stable operating temperature and pressure. Any such changes are gradual and their effect on the measurement is small and can often be neglected.

COMMISSIONING

After the installation at the beamline the CCC was calibrated using an electric reference current that simulates the ion beam. This calibration current is sent through the detector via a wire that runs parallel to the beamline. During the subsequent commissioning all major components of the storage ring (dipoles, HF cavity, vacuum pumps, etc.) were active in order to establish realistic operating conditions. Apart from the dipoles no other accelerator component had a significant effect on the signal of the CCC. Figure 3 shows the response of the CCC to an electric calibration signal in the shape of a square wave with an amplitude of 21.2 nA and a frequency of 1 kHz. One can see that currents in the tens of nA can be resolved very well, but also that there are fluctuations of the baseline on the scale of individual nA that produce a small error on the absolute measurement at these bandwidths. At frequencies from ~1 kHz up to the maximum bandwidth of 200 kHz deviations of the current by individual nA can be resolved. At lower frequencies down to DC and in order to convert the

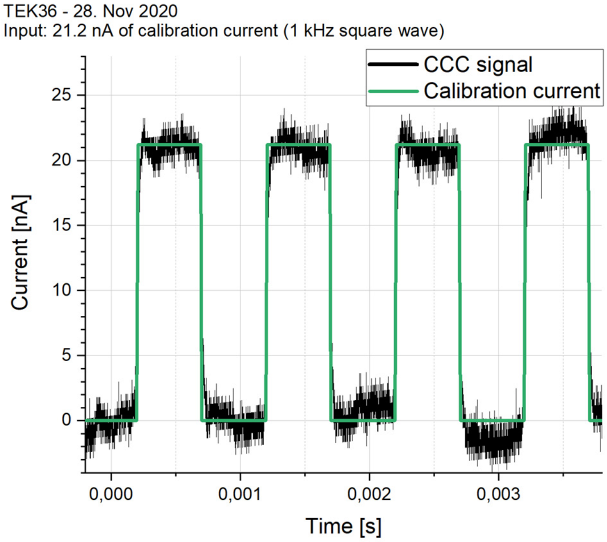

Figure 3: CCC signal (black) of an electric calibration current with amplitude of 21.2 nA and a frequency of 1 kHz (green). The measurement is performed with the CCC installed at the CRYRING and with all major accelerator component running.

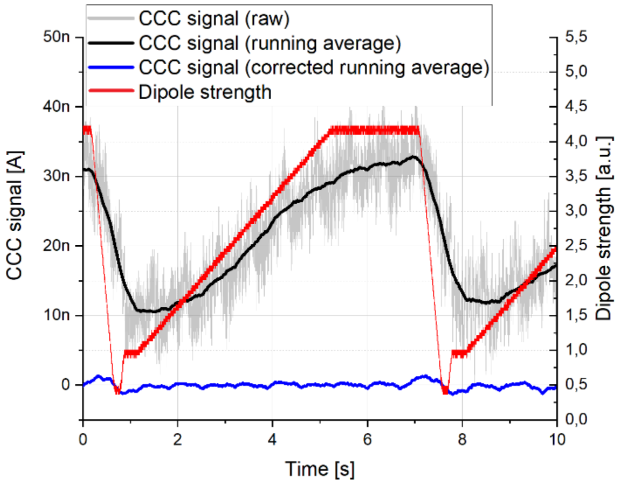

Figure 4: Magnetic field strength of the dipole (red) during one accelerator cycle. The resulting signal of the CCC before the dipole correction (black & grey) and the corrected CCC signal in which the effect of the dipole is subtracted by using the recorded CCC response for this ramp (blue).

signal from a relative measurement to an absolute current reading, additional signal-processing is necessary to determine the signal baseline and to remove the two main sources of perturbations, the dipole ramp and the helium liquefier. Finally, also the much smaller error caused by slow temperature or pressure drifts of the helium vessel (generally < 0.7 nA/s) can be corrected by using the temperature data from the cryostat.

Despite the field attenuation of the superconducting shield a small magnetic stray field from the neighbouring dipoles reaches the CCC and produces a signal with a maximum amplitude of ~23 nA that follows the dipole ramp (see Fig. 4). Since the ramp of the dipole is strongly deterministic, the response of the CCC to the dipole ramp can be measured in a dry run before there is any beam current in the storage ring. This data can then be used to subtract the effect of the dipole on the CCC in order to get the true current data. The blue line in Fig. 4 shows the CCC signal during a background measurement after the elimination of the dipole using the recorded response of the CCC. After this correction the remaining current noise due to the dipole is generally below 2 nA and is concentrated at the fast ramp down of the magnets at the end of the accelerator cycle. An attempt to determine a single response function that predicts the reaction of the CCC to the dipole strength for arbitrary dipole ramps was not yet successful. Therefore, a dedicated measurement of the dipole response function is necessary whenever a new dipole ramp is implemented.

The perturbation originating from the liquefier is created by the periodic pumping of the pulse-tube cryo-cooler at a fixed frequency of 1.4 Hz. Measurements with an accelerometer have shown that mechanical vibrations of the liquefier are strongly attenuated before they reach the cryostat. However, there is evidence that the coupling is based on the pressure fluctuations created by the periodic refrigeration at the cryo-cooler. While the operating frequency is stable, the phase of the cryo-cooler is fluctuating and the exact shape of the resulting signal at the CCC depends on the system state (e.g. remaining liquid helium level). This makes it difficult to use background measurements to directly subtract this noise source. Therefore, a digital FFT-based band-block filter is used to eliminate signals with a frequency between 1 and 3 Hz. The effect of this filtering can be seen in Fig. 5. The graph shows the response of the CCC to a calibration signal in the form of a square wave, again with an amplitude of 21.2 nA but with a much slower frequency of 200 mHz. At this timescales the perturbation by the liquefier at 1.4 Hz is visible and makes it difficult to extract the beam current. Figure 5 shows that after the application of the band-block filter the perturbation by the liquefier is strongly attenuated and the applied calibration current can be observed. Alternative means to suppress the pressure fluctuations before they can reach the CCC detector are in preparation. The resulting current resolution of the CCC system depends strongly on the successful elimination of noise signals, the errors of the initial calibration and on the desired measurement range. The first results of the commissioning have shown that at measurement ranges below 1 µA, current resolutions better than 10 nA are feasible.

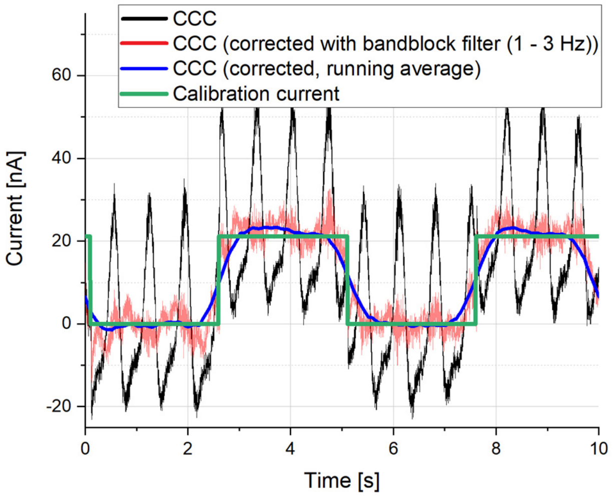

Figure 5: Signal perturbation induced by the helium liquefier (1.4 Hz) visible in the CCC signal (black), resulting signal after band-block filter (red), running average (blue) and the applied calibration current of 21.2 nA (green).

While the results of the commissioning are very promising and not too far from the optimal current resolution achieved in the laboratory [1], a significant reduction of the SQUID performance parameter was observed when moving the setup to the accelerator environment. More specifically, the modulation swing of the SQUID voltage in the flux to voltage characteristics was reduced. This is most likely due to a substantial increase of rf interference that reaches the detector through the enclosed beam tube. Such a phenomenon which could be reproduced in a lab experiment. Moreover, the critical current of the SQUID was reduced by up to 70 % which implies that the superconductor experiences additional strain imposed by the environment. At the moment, there is no conclusive explanation to this phenomenon but the presence of static or dynamic magnetic fields during the transition to the superconducting state might lead to such an effect. It is planned to incorporate a small local soft-iron shield to protect the SQUID and its housing from external fields during the cooldown.

CONCLUSION

A Cryogenic Current Comparator was installed and commissioned at CRYRING and shows excellent absolute current resolution better than 10 nA in a noisy accelerator environment. The dominant sources of perturbation are the dipole magnets and the helium liquefier which both can be filtered with adequate signal-processing. The beamline setup successfully decouples the CCC from mechanical vibrations of the surrounding and reduces the influence of temperature fluctuations to a minimum. However, the limited cryogenic operating time of up to 7 days due to an oscillation of the helium gas flow is still to be improved. Further investigations are planned to stabilize the SQUID performance under the influence of the high level of electromagnetic interference in the accelerator environment. The demonstrated accuracy makes the CCC an excellent tool for diagnostics of low ion beam intensities when an absolute non-destructive current monitor with a current resolution of nA is required.

REFERENCES

[1] P. Seidel *et al.*, “Cryogenic current comparators for larger beamlines”, *IEEE Trans. Appl. Supercond.*, vol. 28, no. 4, p. 1601205, Jun. 2018. `doi:10.1109/TASC.2018.2815647`

[2] V. Zakosarenko *et al.*, “Coreless SQUID-based cryogenic current comparator for non-destructive intensity diagnostics of charged particle beams”, *Supercond. Sci. Technol.*, vol. 32, p. 014002, Dec 2018. `doi:10.1088/1361-6668/aaf206`

[3] D.M. Haider *et al.*, “Versatile beamline cryostat for the Cryogenic Current Comparator (CCC) for FAIR”, *in Proc. 8th Int. Beam Instrumentation Conf. (IBIC’19)*, Malmö, Sweden, pp. 78-81, Sep. 2019.

[4] M. Fernandes *et al.*, “Non-perturbative measurement of low-intensity charged particle beams”, *Supercond. Sci. Technol.*, vol. 30, p. 015001, Nov 2016. `doi:10.1088/0953-2048/30/1/015001`

[5] F. Kurian, “Cryogenic Current Comparator for Precise Ion Beam Current Measurements”, Ph.D. thesis, Goethe University, Frankfurt am Main, Germany, 2015.

10th Int. Beam Instrum. Conf. IBIC2021, Pohang, Rep. of Korea JACoW Publishing
ISBN: 978-3-95450-230-1 ISSN: 2673-5350 doi:10.18429/JACoW-IBIC2021-WEPP01

LONGITUDINAL IMPEDANCE MEASUREMENTS WITH STREAK CAMERA AT BEPC II ELECTRON STORAGE RING*

D. C. Zhu [†], W. Zhang, Y. F. Sui, J. H. Yue, J. S. Cao, J. Q. Wang
Institute of High Energy Physics, Chinese Academy of Sciences, Beijing, China

Abstract

We measure the bunch length at BEPC II electron storage ring using a dual sweep streak camera at visible light diagnostic beamline. The impedances estimated by a series *R*+*L* impedance model. Resistive impedance of R=446±21 Ω is obtained by measuring loss factor from measured synchronous phase advancing with streak camera. An inductance impedance of L=23.3±1.8 nH has been estimated by measuring single bunch lengthening with beam current. Both loss factor and inductance are close to the impedance budget. Besides, the streak camera is also used to measure synchronous phase at low current as RF voltage changing from 0.85 MV to 1.65 MV.

INTRODUCTION

BEPC II is a double-ring e+e- collider that operates in the τ and charm region. The energy reached to 2.474 GeV, the highest collision energy by far in Feb. 2021. Beam-based experiments are made to determine the longitudinal impedance. Some parameters are shown in Table 1.

Table 1: Main Parameters of BEPCII

Parameters	Value	unit
Energy	2.474	GeV
Revolution frequency	1.2421	MHz
RF frequency	499.8	MHz
RF voltage	1.65	MV
Momentum compaction factor	0.0189	--
Synchrotron tune	0.02767	--
Energy spread	$6.9*10^{-4}$	--

LONGITUDINAL IMPEDANCE

The longitudinal broadband coupling impedance of the storage ring can be divided into real and imaginary parts. The real part is a resistance, can be characterized by the loss factor as an energy loss of the bunch. The imaginary part does not cause energy loss, but it leads to energy transfer inside the bunch, and results in bunch lengthening and energy spread growth. We measure the impedance with streak camera, the real part resistance from synchronous phase shift measurement, and the imaginary part from bunch lengthening measurement.

Synchronous Phase Shift

The parasitic energy loss induced by real part resistance is dependent on charge in the bunch as $\Delta E = -k_l q^2$. In terms of voltage it becomes $\Delta V = -k_l q$ or $\Delta V = -k_l \frac{I_b}{f_0}$,where I_b is the bunch current and f_0 is the revolution frequency. For the reason of energy balance of the bunch, the current-dependence synchronous phase shift $\Delta\varphi_s$ can be derived from the equation as follows:

$$V_0 cos(\varphi_s)\Delta\varphi_s = k_l \frac{I_b}{f_0} \quad (1)$$

where V_0 is the RF voltage, φ_s is the synchronous phase at zero current. The time shift is:

$$\Delta\tau = \frac{k_l I_b}{\omega_{RF} V_0 cos(\varphi_s) f_0} \quad (2)$$

Streak camera at BEPC II is OptoScope SC-10 from Optronis. For synchronous phase shift measurement, it works at synchroscan sweep mode with the frequency of 249.9 MHz (1/2 RF frequency). Ten reference bunches are injected in adjacent even buckets with 0.1 mA per bunch and a total current of 1mA. The reference bunches have fixed low intensity so that have long beam lifetime. The main bunch is injected in an odd bucket, its current changes from 0.5 mA to 10 mA with a step of 0.5 mA. Since just synchroscan sweep plate is applied, the image has two profiles in the central part, the left profile is main bunch while the right profile is reference bunch, as in Fig. 1.

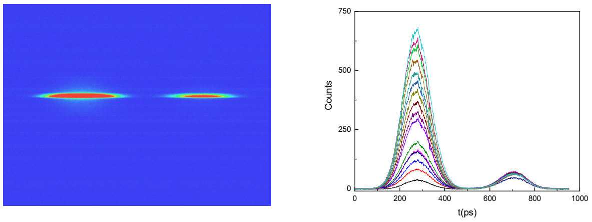

Figure 1. Left: Bunch image captured by streak camera. Right: Bunch profile with main bunch current from 0.5 mA to 10 mA.

The profile data are fitted with asymmetric Gaussian distribution [1, 2]:

$$I(z) = I_0 + I_1 exp\left\{-\frac{1}{2}\left(\frac{(z-\bar{z})}{[1+\mathrm{sgn}(z-\bar{z})A]\sigma_Z}\right)^2\right\} \quad (3)$$

I_0 is the initial pedestal, $I_1$is the maximum value of the distribution, σ_Z the longitudinal rms size, $\bar{z}$ the center of the distribution, and *A* the asymmetric coefficient.

Time jitter of main bunch profile can be reduced by subtracting the reference bunch profile's center time. By linear fitting the corrected profile center time data with current, the time shift $\Delta\tau = 0.32 \pm 0.02$ ps/mA is obtained, as in Fig. 2. The loss factor is calculated with Eq. (2) as $k_l =$

---

* email address : zhudc@ihep.ac.cn

2.04 ± 0.10 V/pc, while the k_l budget is 1.76 V/pc. Resistance is $R = k_l \times 2\sqrt{\pi} \times \sigma_Z = 445.6 \pm 21.0\ \Omega$.

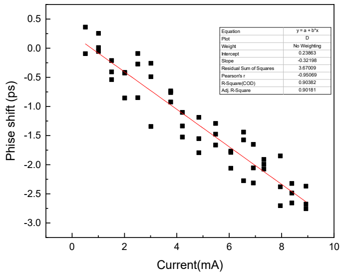

Figure 2. Phase shift with different bunch current.

Bunch Lengthening

Potential-well distortion (PWD) and microwave instability are two major factors result in bunch lengthening. Since the beam current in BEPC II design is 910 mA with the single bunch current of 9.8 mA, a strict impedance budget [3] with $(Z/n)_0$=0.23 Ω was designed in order to control the bunch lengthening. The microwave instability threshold would be more than 30 mA of single bunch.

Streak camera is applied to measure bunch length. It works at synchroscan sweep mode in order to detect the low current beam. Bunch length is measured with single bunch current changing from 0.1 mA to 11 mA, which is below the microwave instability threshold, so that bunch lengthening is caused by PWD. All IDs are moved out. Zotter's formula [4] for PWD is applied to calculate longitudinal coupling impedance as follows:

$$\left(\frac{\sigma_l}{\sigma_{l0}}\right)^3 - \left(\frac{\sigma_l}{\sigma_{l0}}\right) + I_b \frac{e\alpha_p \mathrm{Im}\left[\left(\frac{Z_\parallel}{n}\right)_{eff}\right]}{\sqrt{2\pi}\nu_{s0}^2 E}\left(\frac{R}{\sigma_{l0}}\right)^3 = 0 \qquad (4)$$

where σ_l is the rms bunch length, σ_{l0} the natural rms bunch length, I_b the average beam current, e the electron charge, α_p the momentum compaction factor, E the beam energy, ν_{s0} the synchrotron tune.

Figure 3 shows the bunch lengthening data and fitting results. The measured $Im\left[\left(\frac{Z_\parallel}{n}\right)_{eff}\right]$ is 0.185 Ω, the inductance L is 23.3±1.8 nH. While the budget of $Im\left[\left(\frac{Z_\parallel}{n}\right)_{eff}\right]$ is 0.23 Ω.

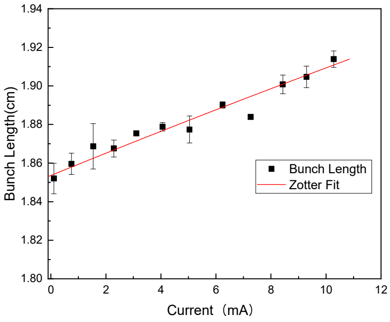

Figure 3. Measured bunch length as function with beam current.

SYNCHRONOUS PHASE MEASUREMENT

At low bunch current, phase shift due to parasitic energy loss can be neglected. The synchronous phase φ_s is determined by RF voltage V_{rf} and synchrotron radiation energy loss per turn U_0 as the followed formula:

$$\varphi_s = \varphi_m + \varphi_0 = \pi\text{-}\ arcsin\left(U_0/eV_{rf}\right) \qquad (5)$$

where φ_m is the measured phase, and φ_0 is the relative phase which is a constant.

Streak camera is applied to measure beam profile at low current (<0.1 mA), the mass center phase can be obtained after fitting the beam profile with Gaussian. As the RF voltage changes from 0.85 MV to 1.65 MV, different mass center phases are obtained. By fitting the data with the formula, φ_0=75.2° can be measured, as in Fig. 4. φ_s at different RF voltage can be calculated and shown in Table 2.

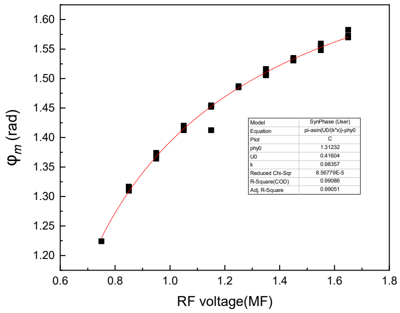

Figure 4. Bunch phase as function with RF voltage.

Table 2: Synchronous Phase at Different RF Voltage

V_{RF}(MV)	φ_s
0.75	144.8°
0.85	150.0°
0.95	153.2°
1.05	155.8°
1.15	157.2°
1.25	159.9°
1.35	161.2°
1.45	162.5°
1.55	163.8°
1.65	164.9°

CONCLUSION

BEPC II operated at its highest collision energy of 2.474 GeV. Some beam-based experiences are applied to determine the longitudinal impedance and synchronous phase with streak camera. Resistive impedance of R=446±21 Ω is obtained by measuring loss factor from measured synchronous phase advancing. An inductance impedance of L=23.3±1.8 nH has been estimated by measuring single bunch lengthening with beam current. Both loss factor and inductance are close to the impedance budget. Synchronous phases at different RF voltage are measured at low current with streak camera.

REFERENCES

[1] Q. Qin *et al.,* "Studies of bunch lengthening at the BEPC",*Nuclear Instruments and Methods in Physics Research Section A: Accelerators, Spectrometers, Detectors and Associated Equipment,* vol. 463, pp. 77-85, 2001.

[2] Garg, A. D. *et al.*, "Studies of longitudinal profile of electron bunches and impedance measurements at Indus-2 synchrotron radiation source", *Nuclear Instruments and Methods in Physics Research Section A: Accelerators, Spectrometers, Detectors and Associated Equipment*, vol. 814, pp. 66-72, 2016.

[3] J. Q. Wang, Z. Y. Guo, Q. Qin, and J. Xing, "Collective Effects Study for BEPCII", in *Proc. 8th European Particle Accelerator Conf. (EPAC'02)*, Paris, France, Jun. 2002, paper WEPRI017.

[4] B. Zotter, "Potential-Well Bunch Lengthening", Rep. CERN-SPS/81-14 (DI), Geneva, Switzerland, 1981.

ISBN: 978-3-95450-230-1 ISSN: 2673-5350 doi:10.18429/JACoW-IBIC2021-WEPP02

TIME DOMAIN PHOTON DIAGNOSTICS FOR THE ADVANCED PHOTON SOURCE UPGRADE*

K. P. Wootton†, W. Cheng, G. Decker, S.-H. Lee, N. S. Sereno, B. X. Yang
Argonne National Laboratory, Lemont, IL 60439, USA

Abstract

With swap-out injection and a third-harmonic bunch lengthening cavity, time domain diagnostics will be beneficial tools for optimisation of the Advanced Photon Source Upgrade electron storage ring. In the present work, we present plans for time-domain X-ray and visible photon diagnostics for the Advanced Photon Source Upgrade. Particular emphasis is given to implementation of visible light streak cameras and X-ray bunch purity monitors as time domain photon diagnostics.

INTRODUCTION

The Advanced Photon Source (APS) storage ring presently provides beams to user X-ray beamlines. The Advanced Photon Source Upgrade (APS-U) project is currently underway to increase the brilliance of photon beams to user beamlines [1–3]. Several user programs take advantage of the pulsed time-of-arrival of X-rays corresponding to the storage ring fill pattern. As these user programs are anticipated to continue during Advanced Photon Source Upgrade (APS-U) operations, we plan to provide temporal photon beam diagnostics for the optimisation and diagnostics of accelerator operations.

In the present work, we motivate time-domain photon diagnostics for the APS-U storage ring. We outline the time distribution of photons for beamlines at APS-U. Proposed techniques for time-domain photon diagnostics are summarised. Finally, we describe the proposed changes to the existing beamline configuration to employ these diagnostics.

FILL PATTERN AND BUNCH PROFILE

Fill patterns of the APS are controlled by the radiofrequency (rf) of the main rf cavities (352 MHz), and the storage ring circumference (1104 m). This accommodates 1296 buckets.

At present, the APS operates three fill patterns for routine user operations. Essentially, these are either bunches equally-spaced, or a camshaft fill (‘hybrid mode’, 1 + 8×7), with 1 bunch, and 8 trains of 7 bunches spaced at 2.84 ns [4]. For APS-U operations, a 48-bunch mode and 324-bunch mode are foreseen, with 324 bunches operating in bunch trains with ion-clearing gaps and guard bunches [5]. A camshaft fill pattern is not envisaged for future APS-U operations. These fill patterns and bunch lengths are summarised in Table 1 below.

Table 1: Temporal Structure Corresponding to Fill Patterns of APS and APS-U Storage Rings

Description	Bunch Spacing (ns)	Bunch Length (ps)	Ref.
APS Fill Patterns:			
324 bunches	11.4	25	[6]
24 bunches	153	40	[6]
Hybrid (1, 8×7)	2.84	50, 32	[4]
APS-U Fill Patterns:			
324 bunches	11.4	88	[2]
48 bunches	77	104	[2]

So for APS-U, the proposed bunch lengths to be measured are of the order ∼100 ps, with a minimum bunch spacing of 11.4 ns. We propose to use bunch length measurements sensitive on the picosecond time scale [7].

TIME DOMAIN PHOTON DIAGNOSTICS

At present, the APS operates temporal diagnostics at the 35-BM bending magnet diagnostic beamline [8–11]. Specifically, this includes bunch length measurement and bunch purity monitoring. These two temporal diagnostics are outlined below.

Bunch Length Measurement

For the existing APS, the bunch lengths can be reasonably approximated as Gaussian in profile. However, for bunches in the future APS-U storage ring, the operation of the higher harmonic cavity to lengthen the bunch results in a bunch distribution that potentially departs significantly from a Gaussian approximation [12]. This motivates experimental techniques to measure the bunch temporal profile without assumption about the bunch shape.

For APS-U, bunch length measurements will be performed using a visible light streak camera [13]. Visible light streak cameras have been employed as a bunch length diagnostic at APS since its commissioning [14–18]. Synchronising the vertical (fast) sweep with the storage ring rf (‘synchroscan’) has been usefully employed in studies of longitudinal dynamics in the storage ring [19–23]. The streak camera can be synchronised with the third subharmonic of the storage ring main rf frequency (117 MHz), derived from the APS-U timing and synchronisation system [24].

Bunch Purity Monitor

Ensuring bunch purity in the fill pattern is essential to the operation of some user X-ray experiments at APS. At the

---

* Work supported by the U.S. Department of Energy, Office of Science, Office of Basic Energy Sciences, under Contract No. DE-AC02-06CH11357.

† kwootton@anl.gov

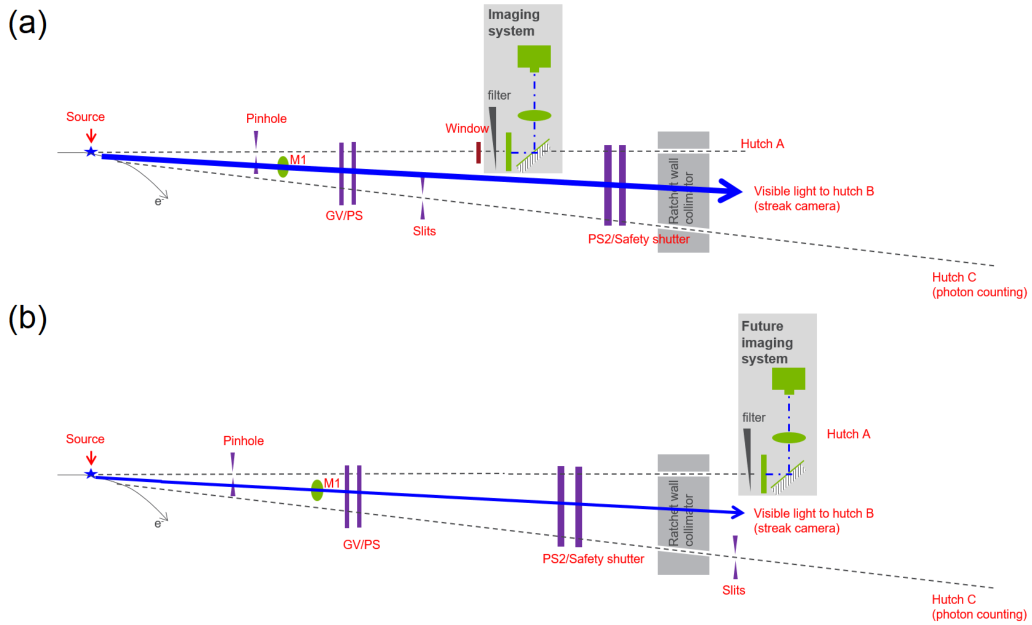

Figure 1: Schematic illustration of 35-BM beamline in plan view [25]. (a) Most common configuration of 35-BM beamline for APS operations. For daily operations, the outboard branch line serves a pinhole camera for imaging, with the pinhole located in the beamline front end, and the X-ray camera physically located within the storage ring tunnel. The placement of the M1 mirror allows visible synchrotron radiation to be present within hutch B independent of shutter status. Time-correlated single photon counting is performed in hutch C using the inboard X-ray branchline when storage ring photon shutters can be opened. (b) Proposed configuration of 35-BM for APS-U operations. Future capability for a pinhole camera will be allowed for on the outboard branch line in hutch A, visible light transport will be reconfigured to connect to hutch B, and the capability of photon counting for bunch purity monitoring will be preserved in hutch C.

APS, the electron bunch is cleaned in the Particle Accumulator Ring (PAR) to provide a single electron bunch, which is accelerated and accumulated in the storage ring [26]. A bunch purity monitor can provide a real-time diagnostic of the storage ring fill pattern, and at the APS the operation of bunch cleaning [27].

At the APS, time-correlated single photon counting of X-rays is employed to measure bunch purity [28–33]. This capability will be preserved in order to measure bunch purity of the APS-U storage ring. Clocks for the data acquisition system will be synchronised with the APS-U timing and synchronisation system [24].

BEAMLINE GEOMETRY

The principal features of the bending magnet radiation beamline at 35-BM are outlined. As illustrated schematically in Fig. 1 [25], in routine operation three photon beams are provided to three experimental areas, separated horizontally in angle. During APS operations, X-ray beams can be provided to either hutch A or hutch C (through a radiation-shielded transport pipe passing through hutch B), and visible light is provided via an optical transport line to hutch B.

For daily operations, the outboard branch line typically serves a pinhole camera, with the pinhole located in the beamline front end, and the X-ray camera physically located within the storage ring tunnel. For routine beam size monitoring, locating the pinhole camera detector within the storage ring tunnel is convenient because the electron beam dimensions can be observed independent while keeping X-ray (photon) and bremsstrahlung shutters closed.

An elevation view of the proposed changes to the beamline front end is illustrated in Fig. 2 [34]. An existing in-tunnel X-ray pinhole camera assembly is removed, as the principal emittance diagnostic for APS-U will be the 38-AM diagnostic beamline [35].

Visible Light

Calculations of the angular distribution of synchrotron radiation in the vertical plane for polarisations in both the horizontal (σ) and vertical (π) is illustrated in Fig. 3 [25]. The parameters used in the calculation of visible synchrotron radiation flux as presented in Fig. 3 are summarised in Table 2 [25].

Table 2: Parameters Used in Calculation of Visible Synchrotron Radiation Flux [25]

Parameter	Units	APS	APS-U
Beam energy	GeV	7	6
Electron beam current	mA	100	100
Bending magnet field	T	0.60	0.68

ISBN: 978-3-95450-230-1 ISSN: 2673-5350 doi:10.18429/JACoW-IBIC2021-WEPP02

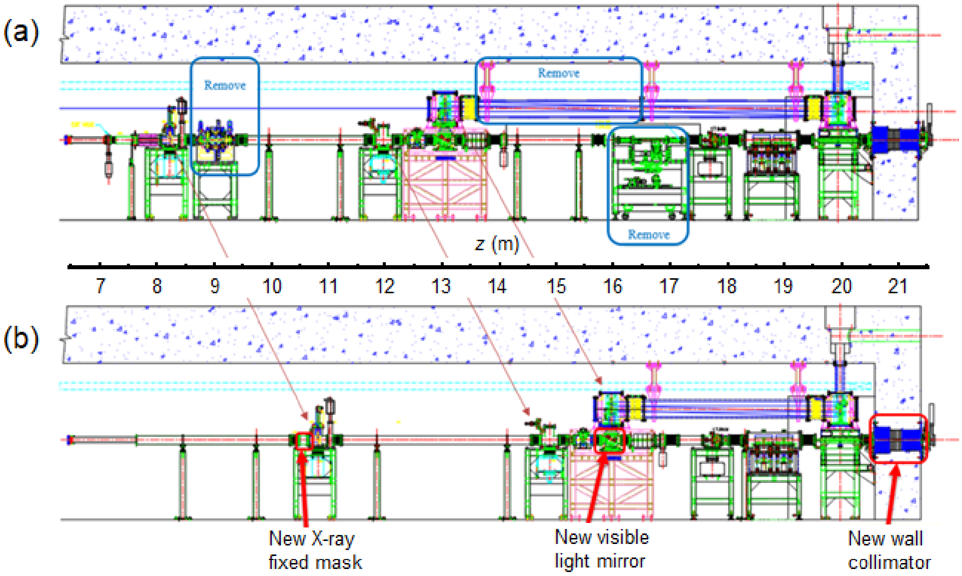

Figure 2: Profile of components in 35-BM front end [34]. The longitudinal coordinate z is with respect to the bending nominal bending magnet photon source point. (a) Existing components and assemblies in the 35-BM front end for APS storage ring operations. A section of the visible light telescope, the pinhole aperture assembly and pinhole camera will be removed. (b) Proposed configuration of beamline front end for APS-U storage ring operations.

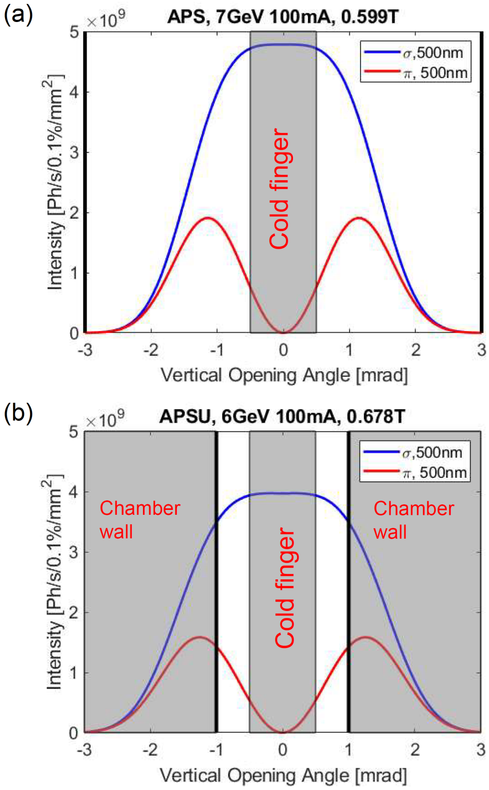

Figure 3: Calculated angular distribution of visible synchrotron radiation and angular apertures in the beamline in the vertical plane [25]. Beam parameters are summarised in Table 2. (a) Calculated flux at 500 nm for APS. (b) Calculated flux at 500 nm for APS-U. Implementation of a cold finger for the APS-U storage ring would significantly reduce the visible photon flux.

As illustrated in Fig. 2, the first visible light mirror will be relocated downstream, and a section of the visible light telescope will be removed from the beamline. Principally, the table supporting the mirror and telescope (beginning at z = 12.5 m in Fig. 2(a)) overlaps laterally with the anticipated footprint of a full-length insertion device in the adjacent 35-ID insertion straight. Furthermore, since it is not planned to use the visible light beamline to spatially image the electron beam size, the optical magnification of the existing telescope does not need to be preserved.

Vertical apertures in the vacuum system are shown in Fig. 3. The vertical aperture of the bending magnet vacuum chamber is ±1 mrad. The inclusion of a cold finger in the visible light photon transport (masking the central ±0.5 mrad core of the photon fan) for the APS-U configuration of the beamline would significantly further reduce the available photon flux at the beamline. To maximise visible photon flux, we are considering the use of a gold-coated diamond mirror, rather than a cold finger and metallic mirror as used in the present configuration.

Hard X-ray

The lateral shift of bending magnet source points 42.3 mm inboard between the APS and APS-U storage rings necessitates changes to the existing X-ray beamline [1]. The proposed X-ray beamline geometry is outlined in Fig. 1.

Initially, we envisage adapting the inboard-most branchline to provide X-ray beams to hutch C. As illustrated in Fig. 2, this necessitates the design of a new X-ray fixed mask, and a new wall collimator.

In the future, we envisage implementing a pinhole camera to image the electron beam source size. Owing to the horizontal dispersion at the location of the bending magnet front ends, the horizontal electron beam size in APS-U is dominated by the electron beam energy spread. Hence a pinhole camera at this location is anticipated to provide a complementary measurement capability to the proposed emittance monitor at 38-AM [35].

SUMMARY

Time domain diagnostics will be beneficial tools for optimisation of the APS-U electron storage ring. In the present work, we have presented plans for time-domain X-ray and visible photon diagnostics for the APS-U storage ring commissioning and operations. To the maximum extent possible, existing components are re-used.

ACKNOWLEDGEMENTS

The submitted manuscript has been created by UChicago Argonne, LLC, Operator of Argonne National Laboratory (“Argonne”). Argonne, a U.S. Department of Energy Office of Science Laboratory, is operated under Contract No. DE-AC02-06CH11357. The U.S. Government retains for itself, and others acting on its behalf, a paid-up nonexclusive, irrevocable worldwide license in said article to reproduce, prepare derivative works, distribute copies to the public, and perform publicly and display publicly, by or on behalf of the Government. The Department of Energy will provide public access to these results of federally sponsored research in accordance with the DOE Public Access Plan. `http://energy.gov/downloads/doe-public-access-plan`

REFERENCES

[1] T. E. Fornek, “Advanced Photon Source Upgrade Project Final Design Report”, Argonne National Laboratory, Lemont, IL, USA, Rep. APSU-2.01-RPT-003, May 2019. `doi:10.2172/1543138`

[2] T. E. Fornek, “Advanced Photon Source Upgrade Project Preliminary Design Report”, Argonne National Laboratory, Lemont, IL, USA, Rep. APSU-2.01-RPT-002, Sep. 2017. `doi:10.2172/1423830`

[3] M. Borland *et al.*, “The Upgrade of the Advanced Photon Source”, in *Proc. 9th Int. Particle Accelerator Conf. (IPAC’18)*, Vancouver, Canada, Apr.-May 2018, pp. 2872–2877. `doi:10.18429/JACoW-IPAC2018-THXGBD1`

[4] L. Emery, K. C. Harkay, and V. Sajaev, “Alternate Hybrid Mode Bunch Patterns for the Advanced Photon Source”, in *Proc. 23rd Particle Accelerator Conf. (PAC’09)*, Vancouver, Canada, May 2009, paper TU5RFP002, pp. 1084–1086.

[5] J. Calvey, and M. Borland, “Modeling ion effects for the Argonne Advanced Photon Source upgrade”, *Phys. Rev. Accel. Beams*, vol. 22, p. 114403, 2019. `doi:10.1103/PhysRevAccelBeams.22.114403`

[6] A. H. Lumpkin, F. Sakamoto, and B. X. Yang, “Dual-Sweep Streak Camera Measurements of the APS User Beams”, in *Proc. 21st Particle Accelerator Conf. (PAC’05)*, Knoxville, TN, USA, May 2005, paper RPAT086, pp. 4185–4187. `doi:10.1109/PAC.2005.1591759`

[7] A. H. Lumpkin, “Time-domain diagnostics in the picosecond regime”, *AIP Conf. Proc.*, vol. 367, pp. 327–340, 1996. `doi:10.1063/1.50317`

[8] A. Lumpkin, B. Yang, W. Gai, and W. Cieslik, “Initial Tests of the Dual-Sweep Streak Camera System Planned for APS Particle-Beam Diagnostics”, in *Proc. 16th Particle Accelerator Conf. (PAC’95)*, Dallas, TX, USA, May 1995, paper MPQ11, pp. 2476–2478. `doi:10.1109/PAC.1995.505589`

[9] B. Yang and A. H. Lumpkin, “The Planned Photon Diagnostics Beamlines at the Advanced Photon Source”, *AIP Conf. Proc.*, vol. 333, pp. 252–258, 1995. `doi:10.1063/1.48048`

[10] A. Lumpkin, and B. Yang, “Status of the synchrotron radiation monitors for the APS facility rings”, in *Proc. 16th Particle Accelerator Conf. (PAC’95)*, Dallas, TX, USA, May 1995, paper MPQ09, pp. 2470–2472. `doi:10.1109/PAC.1995.505587`

[11] A. H. Lumpkin, “Commissioning results of the APS storage ring diagnostics systems”, *AIP Conf. Proc.*, vol. 390, pp. 152-172, 1997. `doi:10.1063/1.52314`

[12] M. Borland, T. Berenc, R. Lindberg, and A. Xiao, “Tracking Studies of a Higher-Harmonic Bunch-Lengthening Cavity for the Advanced Photon Source Upgrade”, in *Proc. 6th Int. Particle Accelerator Conf. (IPAC’15)*, Richmond, VA, USA, May 2015, pp. 543–545. `doi:10.18429/JACoW-IPAC2015-MOPMA007`

[13] A. H. Lumpkin, “Advanced, time-resolved imaging techniques for electron-beam characterizations”, *AIP Conf. Proc.*, vol. 229, pp. 151–179, 1991. `doi:10.1063/1.40746`

[14] A. H. Lumpkin, “RF-Synchronized Imaging for Particle and Photon Beam Characterizations”, in *Proc. 15th Particle Accelerator Conf. (PAC’93)*, Washington D.C., USA, Mar. 1993, pp. 2086–2091. `doi:10.1109/PAC.1993.309230`

[15] A. H. Lumpkin, W. Sellyey, and B. Yang, “Proposed Time-Resolved Photon/Imaging Diagnostics for the APS”, in *Proc. 4th European Particle Accelerator Conf. (EPAC’94)*, London, UK, Jun.-Jul. 1994, pp. 1687–1690.

[16] B. X. Yang and A. H. Lumpkin, “Initial time-resolved particle beam profile measurements at the Advanced Photon Source”, *Rev. Sci. Instrum.*, vol. 67, p. 3367, 1996. `doi:10.1063/1.1147368`

[17] B. X. Yang, A. H. Lumpkin, M. Borland, K. Harkay, and A. Nassiri, “Characterization of Beam Dynamics in the APS Injector Rings Using Time-Resolved Imaging Techniques”, in *Proc. 17th Particle Accelerator Conf. (PAC’97)*, Vancouver, Canada, May 1997, paper 5P040, pp. 2052–2054. `doi:10.1109/PAC.1997.751104`

[18] A. H. Lumpkin and B. X. Yang, “First multi-GeV particle-beam measurements using a synchroscan and dual-sweep x-ray streak camera”, *AIP Conf. Proc.*, vol. 451, pp. 214–221, 1998. `doi:10.1063/1.57001`

[19] B. Yang, A. H. Lumpkin, K. Harkay, L. Emery, M. Borland, and F. Lenkszus, “Characterizing transverse beam dynamics at the APS storage ring using a dual-sweep streak camera”, *AIP Conf. Proc.*, vol. 451, pp. 229–236, 1998. `doi:10.1063/1.57002`

[20] A. H. Lumpkin, B. X. Yang, and L. Emery, "Observations of Effective Transverse Beam-Size Instabilities for a High Current Per Bunch Fill Pattern in the APS Storage Ring", in *Proc. 18th Particle Accelerator Conf. (PAC'99)*, New York, NY, USA, Mar. 1999, paper WEA111, pp. 2137–2139. `doi:10.1109/PAC.1999.794398`

[21] B. X. Yang, M. Borland, W. Guo, K. C. Harkay, and V. Sajaev, "Streak Camera Studies of Vertical Synchro-Betatron-Coupled Electron Beam Motion in the APS Storage Ring", in *Proc. 21st Particle Accelerator Conf. (PAC'05)*, Knoxville, TN, USA, May 2005, paper MPPE066, pp. 3694–3696. `doi:10.1109/PAC.2005.1591584`

[22] B. Yang, "Streak Camera 101: Visualizing Charged-Particle Beam Dynamics", *AIP Conf. Proc.*, vol. 868, pp. 124–137, 2006. `doi:10.1063/1.2401398`

[23] K. C. Harkay, V. Sajaev, and B. X. Yang, "Transverse Multi-bunch Bursting Instability in the APS Storage Ring", in *Proc. 22nd Particle Accelerator Conf. (PAC'07)*, Albuquerque, NM, USA, Jun. 2007, paper FRPMN110, pp. 4360–4362. `doi:10.1109/PAC.2007.4440009`

[24] U. Wienands, T. Berenc, T. Fors, F. Lenkszus, N. Sereno, and G. Waldschmidt, "A Scheme for Asynchronous Operation of the APS-U Booster Synchrotron", in *Proc. 9th Int. Particle Accelerator Conf. (IPAC'18)*, Vancouver, Canada, Apr.-May 2018, pp. 1823–1825. `doi:10.18429/JACoW-IPAC2018-WEPAF007`

[25] W. Cheng, private communication, Jan. 2020.

[26] N. S. Sereno, "Bunch Cleaning Strategies and Experiments at the Advanced Photon Source", in *Proc. 18th Particle Accelerator Conf. (PAC'99)*, New York, NY, USA, Mar. 1999, paper WEP27, pp. 2322–2324. `doi:10.1109/PAC.1999.792678`

[27] A. H. Lumpkin, T. Toellner, B. X. Yang, and C. Y. Yao, "Bunch Purity Evolution during APS Storage Ring Top-up Operations", in *Proc. 20th Particle Accelerator Conf. (PAC'03)*, Portland, OR, USA, May 2003, paper WPPB002, pp. 2411–2413. `doi:10.1109/PAC.2003.1289137`

[28] S. Kishimoto, "High time resolution x-ray measurements with an avalanche photodiode detector ", *Rev. Sci. Instrum.*, vol. 63, pp. 824, 1992. `doi:10.1063/1.1142619`

[29] S. Kishimoto, "Bunch-purity measurements of synchrotron X-ray beams with an avalanche photodiode detector", *Nucl. Instrum. Methods Phys. Res. Sect. A*, vol. 351, pp. 554–558, 1994. `doi:10.1016/0168-9002(94)91385-4`

[30] T. S. Toellner, W. Sturhahn, E. E. Alp, P. A. Montano, and M. Ramanathan, "Avalanche photodiodes as large dynamic range detectors for synchrotron radiation", *Nucl. Instrum. Methods Phys. Res. Sect. A*, vol. 350, pp. 595–600, 1994. `doi:0168-9002(94)91262-9`

[31] W. E. Norum and B. X. Yang, "A Novel FPGA-Based Bunch Purity Monitor System at the APS Storage Ring", in *Proc. 22nd Particle Accelerator Conf. (PAC'07)*, Albuquerque, NM, USA, Jun. 2007, paper FRPMN115, pp. 4384–4386. `doi:10.1109/PAC.2007.4440014`

[32] B. X. Yang, W. E. Norum, S. E. Shoaf, and J. B. Stevens, "Bunch-by-Bunch Diagnostics at the APS Using Time-Correlated Single-Photon Counting Techniques", in *Proc. 14th Beam Instrumentation Workshop (BIW'10)*, Santa Fe, NM, USA, May 2010, paper TUPSM044, pp. 238–242.

[33] T. Obina, T. Kasuga, M. Tobiyama, T. Katsura, and K. Tamura, "Measurement of the longitudinal bunch structure in the Photon Factory positron storage ring with a photon counting method", *Nucl. Instrum. Methods Phys. Res. Sect. A*, vol. 354, pp. 204–214, 1995. `doi:10.1016/0168-9002(94)01047-1`

[34] B.-X. Yang, private communication, Jan. 2020.

[35] K. P. Wootton *et al.*, "Design of the X-Ray Beam Size Monitor for the Advanced Photon Source Upgrade", presented at the 12th Int. Particle Accelerator Conf. (IPAC'21), Campinas, Brazil, May 2021, paper MOPAB303.

TERAHERTZ DIAGNOSTIC FOR THE ADVANCED PHOTON SOURCE PARTICLE ACCUMULATOR RING*

K. P. Wootton†, W. J. Berg, S.-H. Lee, N. S. Sereno, J. L. Steinmann[1]
Argonne National Laboratory, Lemont, IL 60439, USA
[1]also at Karlsruhe Institute of Technology, Karlsruhe, Germany

Abstract

Electron beam microbunching instabilities can present operational limits on the practical operation of storage ring accelerators. In the present work, we outline components of a synchrotron radiation diagnostic beamline for the Advanced Photon Source Particle Accumulator Ring operating at frequencies up to approximately 1 THz.

INTRODUCTION

The Particle Accumulator Ring (PAR) is an electron storage ring at the Advanced Photon Source (APS). The principal function of the ring is an accumulator ring, damping multiple (<30) injections from the linac into a single bunch [1]. For the Advanced Photon Source Upgrade (APS-U), we require accumulation of charge in a single bunch up to 20 nC [2]. At such high charges, measurement and control of electron beam instabilities may be important [3].

The intensity of coherent synchrotron radiation (CSR) is dependent on the longitudinal bunch profile. Observation of CSR can provide a sensitive diagnostic tool to detect instabilities. We propose an extension of the optical synchrotron radiation diagnostics port to support the detection of long wavelengths of incoherent synchrotron radiation (ISR) and CSR in the terahertz range, without installing a new beam port and without disturbing existing optical synchrotron radiation diagnostics.

In the present work, we outline the design of the PAR terahertz diagnostic beamline. Performance requirements of the beamline are outlined. The operating principles of the proposed instruments are summarised. Implementation of the beamline subsystems is outlined.

THEORY

We have chosen a spatial separation of the terahertz and optical frequencies because of the different opening angles of synchrotron radiation. For bending magnet radiation, an approximation to the vertical opening angle Θ_{vert} is [4]:

$$\Theta_{\mathrm{vert}} = 1.66188 \times \left(\frac{c}{fR}\right)^{(1/3)} [\mathrm{rad}] , \quad (1)$$

where c is the speed of light in vacuum, f is the frequency of synchrotron radiation (much less than the frequency corresponding to the critical photon energy), and R is the bending radius.

The waveguide cutoff frequency of a rectangular chamber describes the frequency limit for waves that can propagate in the beam pipe: whether or not they are directly emitted by the bunch. The low-frequency cutoff is limited by the cutoff frequency of the synchrotron light monitor port acting as a waveguide. For a waveguide with rectangular profile, the cutoff frequency f_c is defined as:

$$f_c = \frac{c}{2a}, \quad (2)$$

where a is the larger dimension of the waveguide. The bending magnet vacuum chamber defines the input aperture to the beamline, and is rectangular in profile. For a waveguide of dimension 100 × 40 mm [5], the low-frequency cutoff frequency is 3 GHz.

Rather than synchrotron radiation, waves propagating at frequencies above cutoff could be wakefields from the beam pipe, cavities, or other components. This can distort the measurement at lower frequencies. Hence, we must also consider the formation length of the (bending magnet) synchrotron radiation which is at significantly higher frequency. A cutoff frequency f_{cutoff} incorporating the formation length of synchrotron radiation is given by [6–9]:

$$f_{\mathrm{cutoff}} = \sqrt{\frac{\pi}{6}} c \sqrt{\frac{R}{h_c^3}}, \quad (3)$$

where h_c is the chamber gap height. For a bending radius of $R = 1$ m, and chamber gap height of $h_c = 0.04$ m, $f_{\mathrm{cutoff}} = 27$ GHz. The detector should therefore be sensitive at frequency ranges higher than 27 GHz. The high frequency limit is bound by the length scale of longitudinal bunch substructure that may produce CSR (extending up to a few hundred GHz).

The longitudinal impedance due to synchrotron radiation for the PAR at an electron beam energy of 470 MeV is illustrated in Fig. 1 [5]. Additionally, the minimum focus point size is reduced at higher frequencies. A good compromise seems to be 100 GHz to approximately centre on this frequency range, and where the focus point size matches the detector acceptance.

A problem is that the timescale of electron bunch instability substructures in the PAR is undetermined. Simulations have been performed of the longitudinal impedance due to the PAR vacuum components [10], and there are also measurements of the loss factor [11]. We suspect that the bunch may be far above the microbunching instability threshold, with potentially <10 ps substructures.

---

* Work supported by the U.S. Department of Energy, Office of Science, Office of Basic Energy Sciences, under Contract No. DE-AC02-06CH11357. Partial support of J.L.S. by "Matter and Technologies" of Helmholtz Association.

† kwootton@anl.gov

ISBN: 978-3-95450-230-1 ISSN: 2673-5350 doi:10.18429/JACoW-IBIC2021-WEPP03

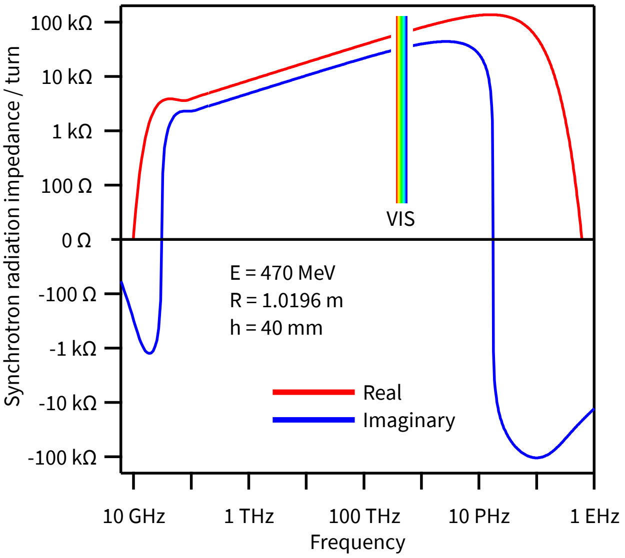

Figure 1: Simulated longitudinal impedance due to synchrotron radiation for an electron between two infinite, conducting, parallel plates in a PAR dipole [5]. The real component corresponds to the emitted radiation and thus describes the synchrotron radiation spectrum emitted in the PAR.

APPARATUS

The terahertz diagnostic provides for an in-vacuum mirror assembly and transmission viewport to direct terahertz radiation to a suitable terahertz detector system. The apparatus is illustrated schematically in Fig. 2.

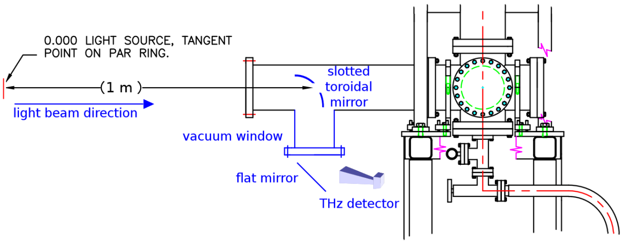

Figure 2: Schematic of terahertz diagnostic apparatus in the APS PAR [5]. Implementation is limited to the replacement of a single spool piece that is part of the existing PAR photon monitor vacuum transport line [12].

The design is required to retain the original visible synchrotron radiation transport function for the photon monitor which is located outside of the accelerator enclosure [12, 13]. The proposed terahertz diagnostic mechanical assembly is illustrated in Fig. 3 [14].

In order to accommodate alignment adjustments to the mirror without breaking vacuum, the mirror is supported by a translatable mechanical assembly. The principal components of the mirror assembly are illustrated in Fig. 4 [14].

As illustrated in Fig. 5, the toroidal mirror focusses and reflects the terahertz beam 90° out of the vacuum chamber while the visible synchrotron radiation passes through the slot. No water cooling is required for the mirror because the total energy deposition is negligible.

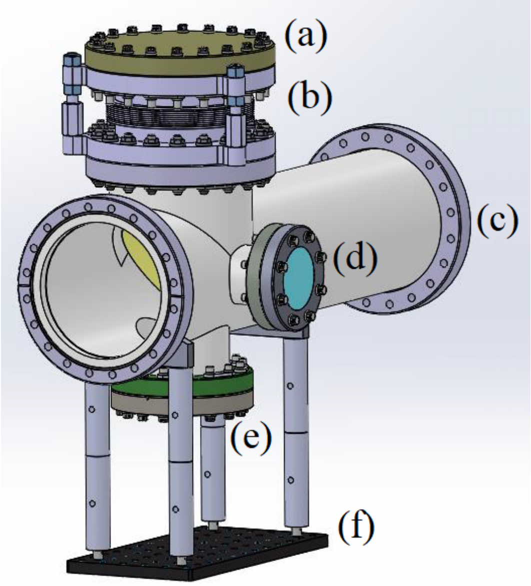

Figure 3: Overview of terahertz diagnostic principal components [14]. The chamber replaces a spool piece on the optical photon monitor of the PAR. (a) Mirror assembly. A toroidal mirror is used to reflect terahertz radiation out of the quartz crystal mirror, where a detector is positioned. The fixed toroidal mirror has a clear aperture centered on the axis of the optical path to allow simultaneous transmission of the visible SR light through the chamber to the existing PAR photon monitor. (b) Bellows. (c) Stainless steel chamber weldment. (d) Optical viewport. (e) Quartz crystal window. (f) Aluminium breadboard and optical posts.

FEATURES

We denote two frequency ranges of interest. The existing optical synchrotron light monitor beamlines are served by synchrotron radiation at optical wavelengths (‘optical’), and the radiation collected by the terahertz diagnostic, extending to sub-terahertz frequencies (‘terahertz’).

Focussing of Terahertz Radiation at Detector

For the present application, we have chosen not to make use of the transverse profile of the terahertz photon beam, and there is not sufficient space for a telescope setup or similar. Focussing of the terahertz beam inside the vacuum chamber serves two purposes: first, the beam size should be reduced to fit through the vacuum window (63 mm aperture) and, second, it should maximize the flux at the detector. To meet these requirements, a single focussing element is sufficient.

A magnification of 0.3 leads to a focus point 0.3 m after the mirror. This is achieved by a focal length of 231 mm. The focal length requires a horizontal radius $R_h = 653$ mm and vertical radius of $R_v = 326$ mm. Different radii for the

ISBN: 978-3-95450-230-1 ISSN: 2673-5350 doi:10.18429/JACoW-IBIC2021-WEPP03

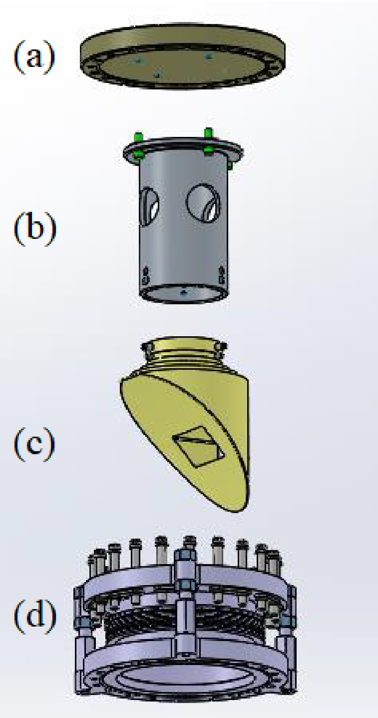

Figure 4: Exploded view of mirror assembly principal components [14]. (a) Mirror holder flange. (b) Mirror holder. (c) Toroidal mirror with rectangular clear aperture. (d) Vacuum bellows.

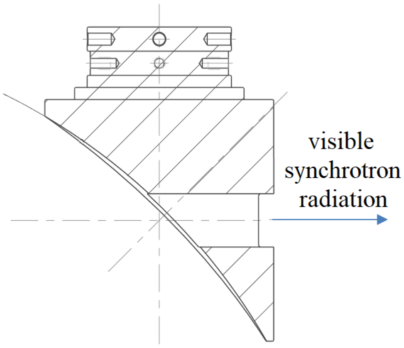

Figure 5: Cross section view of the toroidal mirror.

horizontal and vertical plane are needed because the radiation is reflected at a 90° angle, leading to a toroidal shaped mirror [15]. A toroidal shape is easier to manufacture than an off-axis paraboloid mirror and introduces less spherical aberrations.

The diameter of the waist in terahertz radiation at the focus is dependent on the radiation wavelength and is ~6 mm for frequencies >300 GHz, and extending up to 11 mm at 100 GHz. A Schottky diode detector with a horn antenna is proposed [5], with an aperture of 13.6 mm transverse extent [16].

Optical Light Beamline Optical Stay Clear

The existing photon beamline has a finite acceptance angle of 49 mrad in the horizontal plane [17], which corresponds to requiring a clear aperture of full width 49 mm at the mirror position. In both the horizontal and vertical planes, this is limited by the transverse diameter of the lens 145 mm, and the longitudinal position of the lens from the source (2.985 m) [17].

However the opening angle of the fan of optical synchrotron radiation in the vertical plane is significantly narrower than this. Simulations in Synchrotron Radiation Workshop (SRW) [18] indicate that allowing a clear full aperture of 23 mrad in the vertical plane will obscure less than 10^{-6} of the optical light [5]. This corresponds to requiring a full aperture larger than 23 mm height at the position of the toroidal mirror. To achieve this, optical wavelength synchrotron radiation and terahertz radiation are separated in angle using a slotted mirror. The spatial distribution of synchrotron radiation is illustrated in Fig. 6.

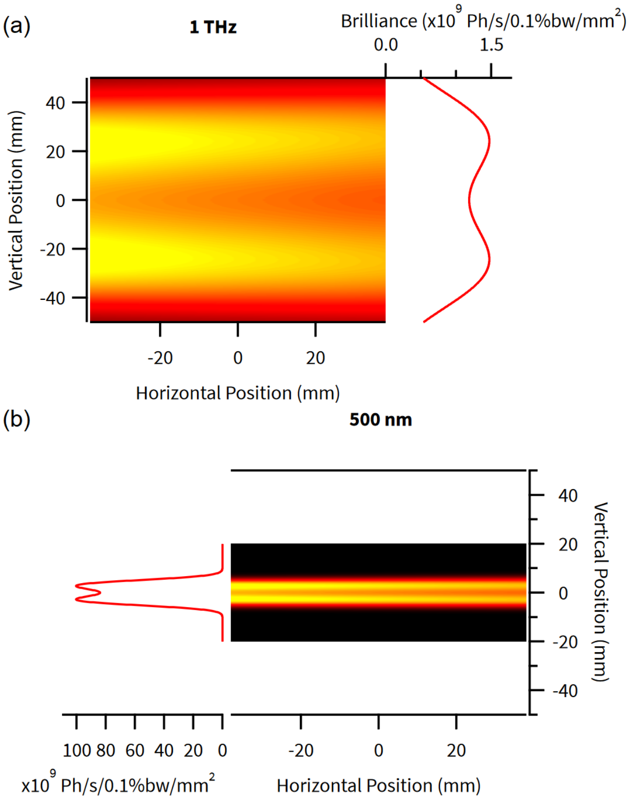

Figure 6: Simulations in SRW [18] of the beam profile from a single electron (point-like source) [5]. (a) Spatial distribution of synchrotron radiation at 1 THz frequency. (b) Spatial distribution of optical synchrotron radiation at 500 nm wavelength.

Hence for the terahertz diagnostic, we require a clear aperture for optical synchrotron radiation of no less than 49 mrad in the horizontal and 23 mrad in the vertical.

Transparency of Terahertz Window

At the frequency range of interest (50–2000 GHz), the window needs to be transparent to terahertz radiation. At these frequencies, the window material should be single crystal SiO_2 (quartz). Future terahertz detectors might be polarization dependent. To maintain the polarization of the beam in the presence of a birefringent quartz window, a z-cut orientation is used so that the optical axis of the crystal is perpendicular to the flat surfaces.

Detector

The terahertz detection bandwidth should match the experimental needs. At this initial proof-of-principle stage, the bandwidth of the detector system should be at the frequency where the highest flux is expected. While the emitted power at the lower frequencies is expected to be higher, terahertz beam transport is more efficient for higher frequencies. We consider a detector system broadly similar to previous systems at other laboratories [19–21]. The detector architecture is summarised schematically in Fig. 7 below.

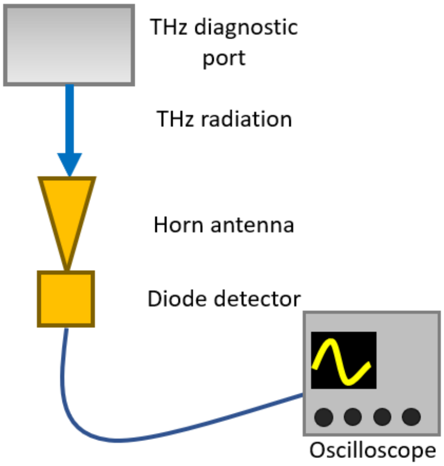

Figure 7: Schematic of detector arrangement for the PAR terahertz diagnostic during the initial phase.

The system outlined in Fig. 7 is composed of several key components: a horn antenna, a diode detector, and an oscilloscope.

By way of example, we consider a Schottky diode and horn antenna as a potential RF detector [22]. These diodes have a fast response time (<100 ps), and so are capable of resolving single bunches. We would propose operating at the 100 GHz frequency range for the PAR, able to observe microbunching distributions on the timescale of 10 ps.

Fast data acquisition systems have been developed for bunch instability measurements [23]. For an initial phase of measurements, we plan to read out the diode signal using an oscilloscope.

In order to observe the electron beam in the PAR at turn-by-turn or bunch-by-bunch, we require bandwidth at minimum equal to the revolution frequency of the PAR (9.77 MHz). To observe individual bunchlets injected from the linac (which operates at 2.856 GHz), the analog bandwidth of the detector should exceed 3 GHz. To avoid a pile-up of the detector signal by consecutive bunchlets, an even higher frequency is needed to ensure the detector signal is completely decayed before the next bunchlet signal arrives.

Detector Signal Amplification

The detector amplifier should not degrade the analog performance of the detector and should be sufficiently fast to observe the bunchlets from the linac. That requires at minimum a frequency of 3 GHz. However, if the amplifier is much faster than the following readout electronics, additional noise is introduced. A low-noise amplifier is needed to ensure a sufficient signal-to-noise ratio. Since this equipment is to be installed outside of the tunnel, adjustments can be made without beam intervention.

SUMMARY

A sub-terahertz beamline has been designed, and is in the process of fabrication and installation in the PAR ring at the APS. This beamline could be used as a diagnostic for beam instabilities in the PAR ring.

Beyond the use of CSR for the detection of microbunching instabilities, CSR is also a useful source of infrared radiation. Other laboratories have proposed compact storage rings as sources of CSR [24,25], and at APS, the PAR could potentially serve as a useful source of CSR.

ACKNOWLEDGEMENTS

J.L.S. acknowledges partial support by the programme “Matter and Technologies” of the Helmholtz Association.

The submitted manuscript has been created by UChicago Argonne, LLC, Operator of Argonne National Laboratory (“Argonne”). Argonne, a U.S. Department of Energy Office of Science Laboratory, is operated under Contract No. DE-AC02-06CH11357. The U.S. Government retains for itself, and others acting on its behalf, a paid-up nonexclusive, irrevocable worldwide license in said article to reproduce, prepare derivative works, distribute copies to the public, and perform publicly and display publicly, by or on behalf of the Government. The Department of Energy will provide public access to these results of federally sponsored research in accordance with the DOE Public Access Plan. `http://energy.gov/downloads/doe-public-access-plan`

REFERENCES

[1] E. A. Crosbie, “The Positron Accumulator Ring for the APS”, in *Proc. 13th Particle Accelerator Conf. (PAC’89)*, Chicago, IL, USA, Mar. 1989, pp. 1707–1709. `doi:10.1109/PAC.1989.72901`

[2] T. E. Fornek, “Advanced Photon Source Upgrade Project Final Design Report”, Argonne National Laboratory, Lemont, IL, USA, Rep. APSU-2.01-RPT-003, May 2019. `doi:10.2172/1543138`

[3] K. C. Harkay *et al.*, “High-Charge Injector for on-Axis Injection Into A High-Performance Storage Ring Light Source”,

in *Proc. 10th Int. Particle Accelerator Conf. (IPAC'19)*, Melbourne, Australia, May 2019, pp. 3423–3426. `doi:10.18429/JACoW-IPAC2019-THYYPLM3`

[4] W. D. Duncan, G. P. Williams, "Infrared synchrotron radiation from electron storage rings", *Appl. Opt.*, vol. 22, pp. 2914–2923. 1983. `doi:10.1364/AO.22.002914`

[5] J. L. Steinmann, private communication, Sep. 2020.

[6] J. L. Steinmann, "Diagnostics of Short Electron Bunches with THz Detectors in Particle Accelerators", Ph.D. Thesis, Karlsruhe Institute of Technology, Karlsruhe, Germany, 2019. `doi:10.5445/KSP/1000090017`

[7] S. Heifets and A. Michailichenko, "On the impedance due to synchrotron radiation", in *Conference Record of the 1991 IEEE Particle Accelerator Conference 1991*, San Francisco, CA, USA, May 1991, vol. 1, pp. 458-–460. `doi:10.1109/PAC.1991.164333`

[8] D. Sagan, G. Hofstaetter, C. Mayes, and U. Sae-Ueng, "Extended one-dimensional method for coherent synchrotron radiation including shielding", *Phys. Rev. ST Accel. Beams*, vol. 12, p. 040703. 2009. `doi:10.1103/PhysRevSTAB.12.040703`

[9] D. J. Wingham, "Electron synchrotron radiation in the far infrared", *Phys. Rev. D*, vol. 35, pp. 2584-–2594, 1987. `doi:10.1103/PhysRevD.35.2584`

[10] C. Yao, J. Carvelli, K. C. Harkay, L. H. Morrison, J. S. Wang, D. Hui, "Longitudinal Impedance Modeling of APS Particle Accumulator Ring with CST", in *Proc. 4th North American Particle Accelerator Conf. (NAPAC'19)*, East Lansing, MI, USA, Sep. 2019, pp. 140–143. `doi:10.18429/JACoW-NAPAC2019-MOPLM17`

[11] J. Calvey, T. Berenc, private communication, Sep. 2019.

[12] W. Berg, B. Yang, A. Lumpkin, J. Jones, "Design and Commissioning of the Photon Monitors and Optical Transport Lines for the Advanced Photon Source Positron Accumulator Ring", *AIP Conf. Proc.*, vol. 390, pp. 483–490, 1997. `doi:10.1063/1.52325`

[13] A. Lumpkin, and B. Yang, "Status of the synchrotron radiation monitors for the APS facility rings", in *Proc. 16th Particle Accelerator Conf. (PAC'95)*, Dallas, TX, USA, May 1995, paper MPQ09, pp. 2470–2472. `doi:10.1109/PAC.1995.505587`

[14] S.-H. Lee, private communication, Sep. 2020.

[15] M. R. Howells, "Mirrors for Synchrotron-Radiation Beamlines", in A. S. Schlachter, F. J Wuilleumier (eds) *New Directions in Research with Third-Generation Soft X-Ray Synchrotron Radiation Sources*, NATO ASI Series (Series E: Applied Sciences), vol. 254, Springer, Dordrecht, 1994. `doi:10.1007/978-94-011-0868-3_14`

[16] *Nominal Horn Specifications*, Virginia Diodes, Inc., Charlottesville, VA, USA, May 2020; `https://www.vadiodes.com/images/AppNotes/VDI_Feedhorn_Summary_2020.05.04.pdf`

[17] B.-X. Yang, private communication, Aug. 2017.

[18] O. Chubar and P. Elleaume, "Accurate and Efficient Computation of Synchrotron Radiation in the Near Field Region", in *Proc. 6th European Particle Accelerator Conf. (EPAC'98)*, Stockholm, Sweden, Jun. 1998, paper THP01G, pp. 1177–1179.

[19] U. Arp, G. T. Fraser, A. R. Hight Walker, T. B. Lucatorto, K. K. Lehmann, K. Harkay, N. Sereno, and K.-J. Kim, "Spontaneous coherent microwave emission and the sawtooth instability in a compact storage ring", *Phys. Rev. Spec. Top. Accel. Beams*, vol. 4, p. 054401, 2001. `doi:10.1103/PhysRevSTAB.4.054401`

[20] J. L. Steinmann, *et al.*, "Continuous bunch-by-bunch spectroscopic investigation of the microbunching instability", *Phys. Rev. Accel. Beams*, vol. 21, p. 110705, 2018. `doi:10.1103/PhysRevAccelBeams.21.110705`

[21] J. L. Steinmann, *et al.*, "Non-interferometric Spectral Analysis of Synchrotron Radiation in the THz regime at ANKA", in *Proc. 6th Int. Particle Accelerator Conf. (IPAC'15)*, Richmond, VA, USA, May 2015, pp. 1509–1511. `doi:10.18429/JACoW-IPAC2015-TUPWA043`

[22] J. L. Hesler and T. W. Crowe, "Responsivity and Noise Measurements of Zero-Bias Schottky Diode Detectors", in *Proceedings of 18th International Symposium on Space Terahertz Technology*, Pasadena, CA, USA, 21-23 Mar. 2007, pp. 89–92.

[23] C. M. Caselle, *et al.*, "Commissioning of an Ultra-fast Data Acquisition System for Coherent Synchrotron Radiation Detection", in *Proc. 5th Int. Particle Accelerator Conf. (IPAC'14)*, Dresden, Germany, Jun. 2014, pp. 3497–3499. `doi:10.18429/JACoW-IPAC2014-THPME113`

[24] J. M. Byrd, Z. Hao, M. C. Martin, D. S. Robin, F. Sannibale, R. W. Schoenlein, A. A. Zholents, and M. S. Zolotorev, "Laser Seeding of the Storage-Ring Microbunching Instability for High-Power Coherent Terahertz Radiation", *Phys. Rev. Lett.*, vol. 97, p. 074802, 2006. `doi:10.1103/PhysRevLett.97.074802`

[25] J. M. Byrd, F. Sannibale, and M. C. Martin, "Coherent synchrotron radiation in storage rings as a broadband high power terahertz source", in *2006 Joint 31st International Conference on Infrared Millimeter Waves and 14th International Conference on Teraherz Electronics*, Shanghai, China, 18-22 Sep. 2006, p. 160. `doi:10.1109/ICIMW.2006.368368`

SCHOTTKY SIGNAL FROM DISTRIBUTED ORBIT PICK-UPs

O. Marqversen†, Steen Jensen, CERN-SY-BI, Geneve, Switzerland

Abstract

In the CERN Extra Low ENergy Anti-proton (ELENA) ring, intended for the deceleration of antiprotons, the longitudinal Schottky signal is obtained by summing the multiple electrostatic pick-up (PU) signals that are also used to measure the closed orbit. The signals from the individual PUs are phase-compensated to a single, common longitudinal location in the machine and added in the time domain. In this contribution, the related theoretical phase compensation is calculated and compared to measurements. We show how the cross correlation between the Schottky noise from the individual PUs can be used to find the correct phase-compensation for an optimal signal-to-noise ratio (SNR). This improvement in terms of SNR is, as expected, proportional to the square root of the number of PUs. The capability of the system to measure both, the bunched and the un-bunched low intensity ($\sim 3\cdot 10^7$ H$^-$ @ 100 keV / 144 kHz) beams is confirmed by the experimental results presented. Furthermore, the inter-bunch phase correlation is briefly addressed and, for the case of bunched beams, the Schottky signal levels once down converted to different harmonics of the revolution frequency (f_{rev}) are presented. In applications where the coherent beam signal dominates the spectrum and limits the dynamic range of the signal processing system, a down-conversation to a non-integer multiple of the RF harmonic is proposed as a way to reduce the coherent signal level.

THE MEASUREMENT SYSTEM

The digital part of the CERN ELENA orbit measurement system is implemented on in-house designed VME Bus Switched Serial - Digital Signal Processor – Field Programmable Gate Array Mezzanine Card (VXS-DSP-FMC) carrier boards, carrying FPGAs, FMCs and DSPs with the possibility to transmit data between them via the VXS bus [1]. The key features of the VXS-DSP-FMC carrier, used in this extension of the ELENA orbit system [2], is the possibility to synchronize local oscillators across cards for all down-converters and pass real-time data between DSPs.

The orbit system already uses the sum and the delta signals from all PUs, as these analog signals are connected to inputs of the ADCs. To extract the longitudinal Schottky signal only the sum signals are used. Each PU sum signal is individually down-converted by a configurable harmonic of the revolution frequency. In ELENA, the Schottky system functionality is typically used for unbunched beam, whereas the orbit system functionality is used for bunched beam. Using the same down-mixers, the two functions can operate on different harmonics while sharing the same hardware in a time-multiplexed fashion or operate simultaneously if using the same harmonic. The relative phase difference between the individual local oscillators (LOs) used in the down-converters must be kept minimal for a successful phase compensation, otherwise it would introduce an unwanted phase shift between the various down-converted signals. The zero phase between LOs is obtained by a simultaneous reset of the phase accumulators in the Direct Digital Synthesis (DDS) used as local oscillators.

The expected bandwidth of the longitudinal Schottky signal in ELENA dependents on the beam energy and the cooling status and is 50 Hz – 200 Hz times the chosen Schottky harmonic. The sampling time, and hereby the bin width of the resulting Fast Fourier Transformation (FFT), can be chosen from 20 ms to 650 ms per spectrum, resulting in a bin width range of 48 Hz to 1.5 Hz. Up to a total of 128 spectra can be sampled on one or two energy levels during the ELENA cycle where beam cooling is performed.

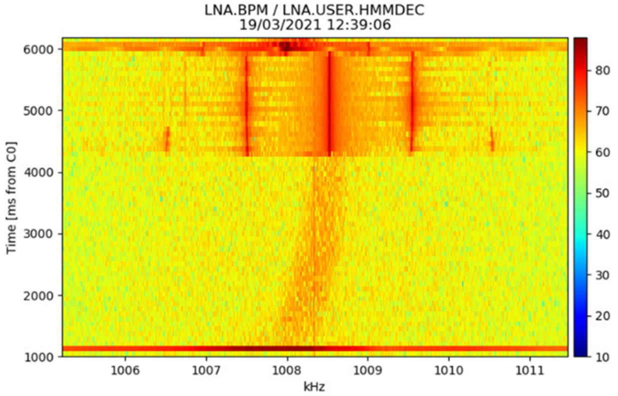

Figure 1: The measurement shows longitudinal Schottky in ELENA [3] as a function of time i.e. for both un-bunched and bunched beam.

The measurement shown in Fig. 1 is performed, on a flat 100 keV energy level in the ELENA deceleration cycle, using the phase compensating technique i.e. phase-compensating and adding 16 PUs down-converted from the 7th harmonic of the revolution frequency, with $f_{RF} = 4\, f_{rev}$ in the bunched part. The beam is injected at approximately 1080 ms relative to machine cycle start (C0), it is then debunched, slightly changed in energy using the electron cooler and re-bunched at approx. 4250 ms.

LONGITUDINAL SCHOTTKY SIGNALS

A single particle circulating in an accelerator will, on a sum PU, generate a series of Dirac pulses spaced in time by the revolution time τ_{rev}, i.e. a Dirac comb. The Fourier series of this signal is given by:

$$s(t) = \frac{1}{\tau_{rev}} \sum_{n=-\infty}^{\infty} e^{j\cdot n 2\pi \frac{t}{\tau_{rev}}}. \qquad (1)$$

For beam diagnostics purposes typically, a particular harmonic is selected for the Schottky signal observation. The

---

† Ole.Marqversen@cern.ch.

Schottky signal around any harmonic of the revolution frequency is a superposition of the Dirac pulses from all particles in the ring. If the beam is un-bunched beam, the spectrum will be continuous around each harmonic of the revolution frequency. If the beam is bunched, i.e., RF voltage is applied to the de-accelerating cavities, the revolution frequency of the individual particles will continuously be changed around a nominal value of the synchronous particle. This results in a frequency modulation and the signal spectra peaks at every harmonic of the revolution frequency, surrounded by synchrotron sidebands [4].

THE PHASE COMPENSATION

To constructively add the signals from different PUs distributed around an accelerator ring, their theoretical phase difference can be calculated either from the known physical location of each PU, or by performing a cross correlation between the down-converted PU sum signals from a reference PU and the PU to be phase compensated.

Physical Pickup Location

The phase difference, not including cable lengths ($\Delta\varphi_{nc}$), between two PU sum signals of a particular revolution frequency harmonic is given by the observation frequency ($f_{Schottky}$) and the time of flight (Δt) of the particle between the two PU locations. βc being the speed of the particles. l_{ELENA} the circumference of the accelerator and l_{Δ_PUs} the distance between the two PU.

$$\Delta\varphi_{nc} = 2\pi f_{Schottky}\Delta t = 2\pi \cdot h_{Schottky} \cdot f_{rev} \cdot \Delta t,$$

where

$$f_{rev} = \frac{\beta c}{l_{ELENA}} \; and \; \Delta t = \frac{l_{\Delta\_PUs}}{\beta c}.$$

It follows, that

$$\Delta\varphi_{nc} = 2\pi h_{Schottky} \frac{l_{\Delta\_PUs}}{l_{ELENA}}. \qquad (2)$$

As Eq. (2) shows, $\Delta\varphi_{nc}$ only depends on the physical distance between the PUs and the chosen observation harmonic ($h_{Schottky}$) of $f_{rev}, i.e.$ all the frequencies in the spectra at that harmonic can be compensated by the same $\Delta\varphi_{nc}$ correction. By applying a phase delay in the complex plane to the sampled quadrature (IQ) data from a particular pickup location ($IQ_{PUposition2}$), using the calculated $\Delta\varphi_{nc}$ correction, we can transform the IQ data to the location of another (reference) PU:

$$IQ_{PUposition1} = IQ_{PUposition2} \cdot e^{-j\Delta\varphi} \qquad (3)$$

One particular PU is chosen as reference location and all other PU signals are phase shifted to this reference location, before all the PU signals are added, followed by a Fast Fourier Transformation (FFT) to evaluate the longitudinal Schottky spectra. In the CERN ELENA system this phase compensation is performed on the down-converted, decimated data.

Equation (2) assumes an equal length of the signal cable between each PU and the signal acquisition system. In the case of different cable lengths an additional cable phase compensation term is required to find the needed phase $\Delta\varphi_{cld}$:

$$\Delta\varphi_{cld} = \Delta\varphi_{nc} - 2\pi h_{Schottky} \cdot f_{particle} \cdot \frac{l_{cld}}{c \cdot \beta_{cable}} \qquad (4)$$

with l_{cld} being the cable length difference between the two PUs of interest to the acquisition system, $c \cdot \beta_{cable}$ the signal speed on the cable and $f_{particle}$ the revolution frequency of an individual particle. Now the $\Delta\varphi_{cld}$ correction depends on the revolution frequency of each individual particle, i.e. phase compensation is different over the measurement frequency band. However, in case of ELENA the bandwidth of the Schottky signals at, e.g. the 14th harmonic of f_{rev} is expected to be approximate 700Hz. The difference in $\Delta\varphi$ calculated at the 14th harmonic of f_{rev}, for a cable length difference of 10m and f_{rev} – 350 Hz vs. f_{rev} + 350 Hz is negligible. Equation (4) can therefore be used with $f_{particle} = f_{rev}$ giving the needed phase, $\Delta\varphi_{cld}$ for correction including the phase change caused by cable length differences, but not including phase difference across the bandwidth of the Schottky signal.

Cross-correlation

Performing a cross-correlation on sampled IQ data from two different PUs will also reveal the $\Delta\varphi$ required for the phase compensation for an optimum constructive summing of these two PU signals. A high SNR is needed as the input to the cross-correlation to get a precise phase i.e., the $\Delta\varphi$ is best found from bunched beam signals, but can following be used also on un-bunched beam data. Any spurious signals in the data will disturb the result of the cross-correlation.

The $\Delta\varphi$ calculated from the physical location Eq. (4) of the PUs is used in the ELENA Schottky system, while the cross-correlation method is used as validation of the optimum $\Delta\varphi$ correction value.

Phase Sweep

As a sanity check we applied a $\Delta\varphi$ sweep 0° – 360° on the IQ data, from a bunched beam signal, from one particular PU and added this term following Eq. (3) to the IQ data from another PU (simultaneously sampled and down mixed with both local oscillators in phase and on the same harmonic of f_{rev}), followed by an FFT. The spectrum shows the expected bunched beam Schottky signal pattern, similar as shown in the upper part of Fig. 1 (where the beam is bunched after 4250ms). In Fig. 2 we plot the amplitude of the central harmonic line, the first lower and the first upper satellites of the Schottky spectrum. For this data the constructive / destructive interference is clearly observed at $\Delta\varphi = 40°$ and 220° respectively. The peak and dip of the signal amplitudes coincide at the same phase for all three traces, and the sum at the destructive phase approaches the noise floor, indicating a high correlation between the two signals.

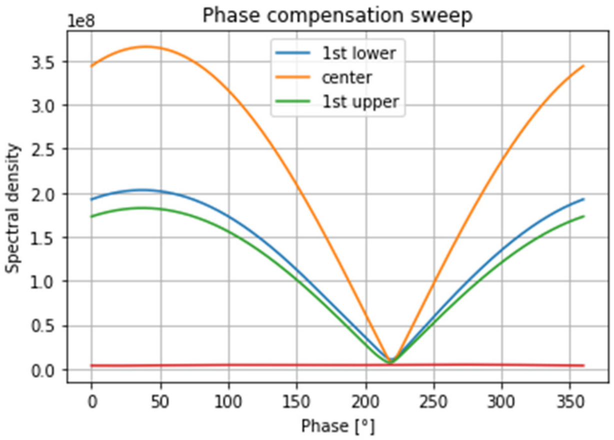

Figure 2: The amplitude of the three main spectral peaks in the bunched beam spectrum found from adding two PUs (one PU being phase shifted), as a function of the phase compensation.

The constructive peak phase agrees with the $\Delta\varphi$ found by both methods, the cross-correlation on IQ data between the two PUs and from the physical location including the cable length compensation (Eq. (4)).

SNR IMPROVEMENT

Acquiring and analysing low-level Schottky signals near the equivalent thermal noise level, averaging of the spectra data is a common method to improve the SNR. If the averaged Schottky signal data is correlated and the thermal related noise signal contribution is uncorrelated, the theoretical SNR improvement is 3dB for each doubling of the number of signal sources.

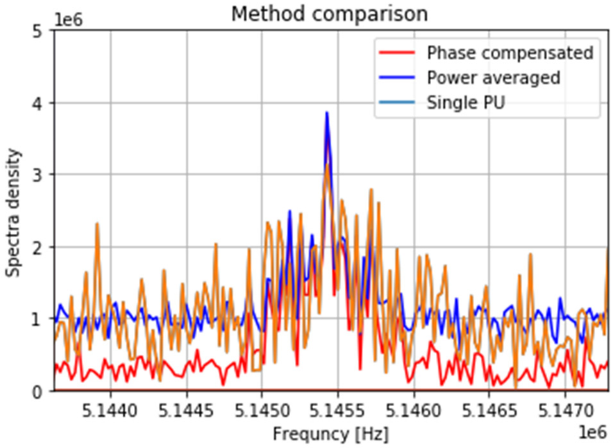

Figure 3: Comparison of noise reduction methods: Single PU vs. power average of spectra vs. presented phase compensated method. The beam is un-bunched and observed at 14th harmonic of f_{rev}.

In Fig. 3 the longitudinal Schottky spectrum from a single PU is compared with the spectrum generated by the same beam, but taking the average of 13 consecutive spectra. The noise amplitude decreases for the averaged spectra compared to single PU spectrum. Furthermore, under the same beam condition, the combined spectra of 13 phase-compensated PUs is shown, with the signals normalized to the number of PUs. The latter shows the substantial improvement on the SNR, compared to simple averaging of a single PU data, which is basically limited to average out the noise contribution, whereas the presented phase compensating method on top lowers the background noise, thus improves the SNR. The SNR improvement has been evaluated for 2, 4, 8 and 13 PUs. The results are shown in Fig. 4 and they follow well the expected $\sqrt{number\ of\ PUs}$ dependency. The result clearly indicates the benefit of a constructive signal summing, when using phase-compensated signals from BPMs in different locations of an accelerator.

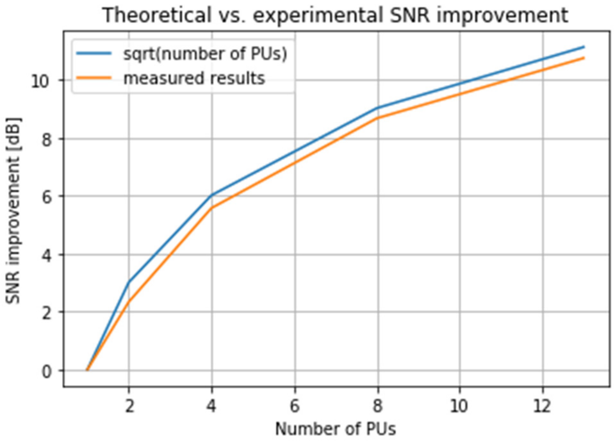

Figure 4: Theoretical and experimental SNR improvements vs. number of PUs used.

INTER BUNCH PHASE CORRELATION

The $\Delta\varphi$ correction calculated from the physical PU location should not be confused with the longitudinal phase relationship between particles in bunched beams: With a single particle in a ring and two PUs 180° in circumference apart, given by their relative physical location, the two sum signals added would cancel for the 1st harmonic of f_{rev} (unless phase compensated), whereas for the 2nd harmonic of f_{rev} the summing will be constructive. The same holds for any number of particles in the ring, as the Schottky signal is a superposition of signals generated by all individual particles. Limiting our considerations only to the central revolution harmonic: With two particles in a ring 180° apart (like a beam bunched with $f_{RF} = 2\ f_{rev}$) and a *single* PU, the sum signal of the 1st harmonic would also cancel. Analysing the 2nd harmonic, the signals would add up constructively (the phase difference would be given by $h_{Schottky} \cdot 180° = 360°$). In the multi-particle case, due to the bunch intensity differences and the lack of perfect symmetries of the longitudinal particle distribution the discussed constructive and destructive effects are reduced. The signals will add up constructively on all $n \cdot h_{RF}$-harmonics (n is integer), but destructively only to some extent on all others. It is worth to note that the beam bunched at e.g., $f_{RF} = 4\ f_{rev}$ will have strong coherent signals at 4th, 8th, 12th, … harmonics of the revolution frequency, and low, still non-zero signal at other harmonics. Figure 5 shows the relative amplitude of the central satellites for a beam bunched at $f_{RF} = 4\ f_{rev}$ measured in the CERN

ELENA ring. In Schottky monitoring systems with large coherent signal contribution (like LHC Schottky Monitor [5]) the dynamic range of the measurement system may limit the observation of the non-coherent Schottky sidebands and exploiting this effect as a mitigation technique might be considered.

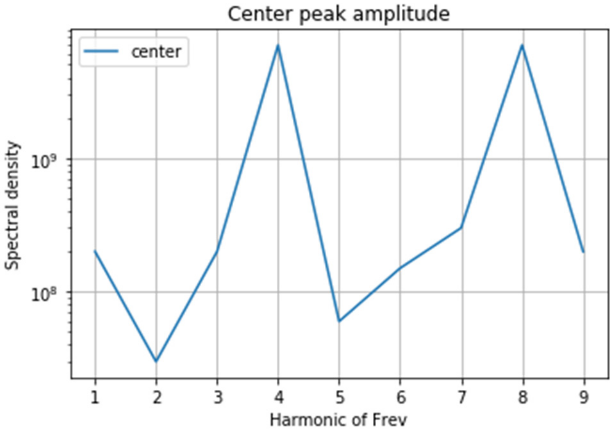

Figure 5: Relative amplitude of the central satellite in a bunched ($f_{RF} = 4\ f_{rev}$) longitudinal Schottky spectrum as a function on the observed Schottky harmonic.

CONCLUSION

A substantial SNR improvement of the longitudinal Schottky signal has been implemented and successfully achieved on the ELENA ring. The technique uses signals from several distributed PUs in a ring that are phase-compensated before being summed and presented as frequency domain Schottky spectrum. It provides, as expected, superior performance compared to the power-spectral density (PSD) averaging of a single beam pickup. The values required for the phase compensation were calculated from the knowledge of the relative physical location of the PUs in the ring, and validated by cross correlation between sampled data from individual PUs. Cable lengths between PUs and the acquisition system were included as necessary and cable length differences minimized. Unwanted interference/spur if uncorrelated will be reduced. The presented method is implemented as an extension to the existing CERN ELENA orbit measurement system. It uses the same PUs and acquisition system, and can operates as follows: Measuring the orbit when the beam is bunched and performing the longitudinal Schottky analysis when the beam is un-bunched during cooling at fixed energy or operating on the same harmonic of f_{rev} for orbit and Schottky monitoring.

ACKNOWLEDGEMENTS

Thanks to F. Pedersen for ideas and inspiration on the summing of Schottky signals and to J. Molendijk for support on the VXS-DSP-FMC carrier.

REFERENCES

[1] M. E. Angoletta *et al.*, “A Leading-Edge Hardware Family for Diagnostics Applications and Low-Level RF in CERN's ELENA Ring”, in *Proc. 2nd Int. Beam Instrumentation Conf. (IBIC'13)*, Oxford, UK, Sep. 2013, paper TUPF28, pp. 575-578.

[2] O. Marqversen *et al.*, “The Orbit Measurement System for the CERN Extra Low Energy Antiproton Ring”, in *Proc. 6th Int. Beam Instrumentation Conf. (IBIC'17)*, Grand Rapids, MI, USA, Aug. 2017, pp. 206-208. `doi:10.18429/JACoW-IBIC2017-TUPCF05`

[3] C. Carli *et al.*, “ELENA Commissioning and Status”, presented at the 12th Int. Particle Accelerator Conf. (IPAC'21), Campinas, Brazil, May 2021, paper MOPAB177.

[4] K. Lasocha *et al.*, “Estimation of longitudinal bunch characteristics in the LHC using Schottky-based diagnostics”, *Phys. Rev. Accel. Beams*, vol. 23, p. 062803, 2020.

[5] M. Betz *et al.*, ”Bunched-beam Schottky monitoring in the LHC”, *Nuclear Instruments and Methods in Physics Research Section A.*, vol. 874, pp. 113-126, 2017.

ISBN: 978-3-95450-230-1 ISSN: 2673-5350 doi:10.18429/JACoW-IBIC2021-WEPP05

TWO COLOR BALANCED OPTICAL CROSS CORRELATOR TO SYNCHRONIZE DISTRIBUTED LASERS FOR SHINE PROJECT*

Chunlei Li, Lie Feng, Jinguo Wang, Wenyan Zhang, Xingtao Wang, Bo Liu†
Shanghai Advanced Research Institute, Chinese Academy of Science, Shanghai, China

Abstract

The planned Shanghai high repetition rate XFEL and extreme light facility (SHINE) generate X-ray light pulses in femtosecond range. For photoinjector drive laser, seed laser, and time resolved pump-probe experiments it is crucial to synchronize various slave laser oscillator to the master reference laser with a long term stability of better than 10 fs. For this purpose two color balanced optical cross correlator for locking slave laser to master laser is under developing.

In this paper, we report on the progress of the development of a background free two color balanced cross correlator (TCBOC) to synchronize 800 nm slave laser to 1550 nm master laser. The synchronization system is being tested by linking a commercial Ti:sapphire oscillator to a locally installed timing reference source.

INTRODUCTION

At present, FELs are the only facilities that can generate bright, coherent hard X-ray pulse with temporal durations below 100 fs and up to 10^{13}photon per pulse [1]. High precision timing synchronization systems are critical for FELs because X-ray temporal duration is highly sensitive to the overall synchronization between the injector laser, the Linacs, and the bunch compressors. Moreover, for the seeded FELs, timing jitter between the seed laser and the electron bunch must be minimized. Finally, the relative timing jitter between the FEL output and the pump laser must be controlled with a precision better than the FEL pulse duration for pump probe experiments aiming high temporal resolution [2].

The optical synchronization system for SXFEL and under consideration for the SHINE is based on an ultra-stable mode locked master laser locked to a low noise RF oscillator generating hundreds of fs light pulse of 1550 nm. The master laser is phase locked to the low noise RF master oscillator of the accelerator to ensure stable operation and small jitter. The timing information is contained in the precise repetition frequency of 238 MHz of the pulse train and distributed via actively length stabilized fiber links to remoted locations.

Recently, one scheme has been demonstrated that pulsed-optical timing stability distribution system using polarization maintaining fibers can deliver sub femtosecond timing stability over kilometer-scale distances [2]. One of the key components of the synchronization system is the two color balanced cross correlator (TCBOC) which provides a method to lock slave laser systems to the timing reference with less than 10 fs accuracy [3]. This balanced optical cross correlation scheme was firstly suggested by Franz X. Kärtner group to perform pure timing measurements in the optical domain [4], and have been developed to achieve sub femtosecond precision [5-7].

PRINCIPLE OF TWO COLOR BALANCED CROSS CORRELATOR

FH: Fundamental harmonics of input pulses; DM: Dichroic mirror; HM: high reflective mirror; GVD: Silica slab for group velocity delay.V1 and V2: output voltage from photodetector.

The principle of two color balanced cross correlator is shown in Fig. 1. Two optical pulses with different central wavelength are input to a BBO crystal in a forward pass and reverse pass configuration, where one pulse is from the master laser and the other pulse is from slave laser. A third light pulse of their sum frequency will be created when they overlap spatially and temporally. As they propagate through the BBO crystal, they walk through each other due to different group velocity. Therefore, different amount of sum frequency light is generated depending on their temporal overlap in the forward and reverse pass. The generated sum frequency pulses are separated from input pulses by dichroic mirror and measured by two identical channels of a balanced photodetector. Therefore, the difference of the sum frequency pulse cancels the intensity fluctuations of input pulses, and the generated voltage signal is only proportional to the time separation of input pulses. Base on this principle, one can detect timing fluctuations significantly smaller than the pulse duration itself. Another advantage it that this method is immune to temperature variations due to the timing detection is performed directly in the optical domain.

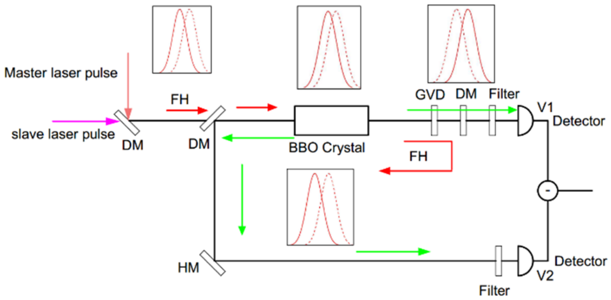

Figure 1: Principle of timing detection using TCBOC.

Supposing two Gaussian-shaped input pulses with their intensities $I_1(t)$ and $I_2(t)$, the intensity of generated sum frequency light is expressed by the convolution of the two input pulses:

$$I_{sum}(t) \propto \int_{-\infty}^{\infty} I_1(\tau) I_2(t-\tau) d\tau \tag{1}$$

---

* Work supported by Shanghai Municipal Science and Technology Major Project (Grant No. 2017SHZDZX02)
† email address liubo@zjlab.org.cn

ISBN: 978-3-95450-230-1 ISSN: 2673-5350 doi:10.18429/JACoW-IBIC2021-WEPP05

Where τ is the time delay between the two input pulses. Eq. (1) can be described by

$$I_{sum}(t) = \frac{1}{\sqrt{2\pi(\sigma_1^2+\sigma_2^2)}} exp\left\{-\frac{(t-\Delta t)^2}{2(\sigma_1^2+\sigma_2^2)}\right\}, \qquad (2)$$

where $I_{sum}(t)$ is highly sensitive to variation of relative timing Δt between the two input pulses. Therefore, intensity changes of sum frequency pulse is a measure for the timing changes.

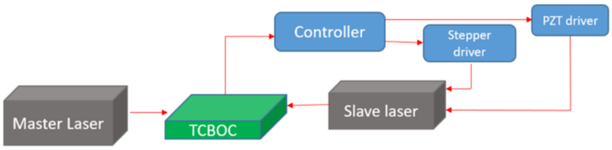

Figure 2: Schematic of TCBOC feedback control system to synchronize the pulse trains of two ultrafast laser at different wavelength.

In order to synchronize Ti:sapphire laser oscillator to the master laser, an feedback control loop is developed as described in Fig. 2. The TCBOC is used as high precision timing detectors. The voltage signal generated from the TCBOC is used as a feedback signal to control the frequency of the slave laser oscillator via its step motor and intra-cavity PZT shown in Fig. 3. Once the feedback control is running, it will pull the frequency of the slave laser f_S oscillator closer to that of the master laser f_M which will stretch the period response curve in time. As shown in Fig. 3, once frequency difference Δf is sufficiently small ($\Delta f \ll f_M$), the phase lock loop will operate in the linear region of the detector output and lock the slave oscillator's frequency by suppressing the error voltage as tightly as possible to zero. Once a stable locking is achieved, the TCBOC output will be a DC voltage.

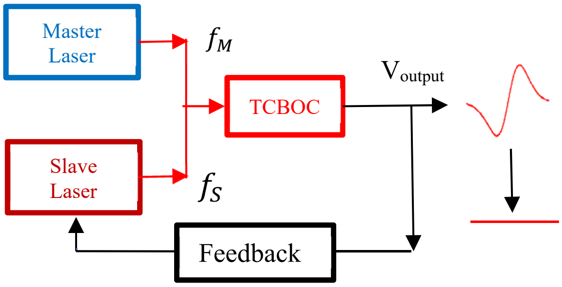

Figure 3: Operating principle of frequency synchronization using TCBOC.

As shown in Fig. 3, pulse trains from the master laser and slave laser with small repetition rate difference ($\Delta f \ll f_M$) are sent to the TCBOC to measure their relative timing error. The repetition period difference ΔT between the two pulse trains can be expressed as

$$\Delta T = \frac{1}{f_M} - \frac{1}{f_M+\Delta f} = \frac{\Delta f}{{f_M}^2+f_M\Delta f} \approx \frac{\Delta f}{{f_M}^2} \qquad (3)$$

Eq. (3) shows that the pulse trains temporally move with respect to each other by ΔT in every time period T_M of Master pulse [2]. As a result of this temporal pulse "sliding", the TCBOC generates a cross correlation signal every time the pulses coincide. Therefore, the output signal of TCBOC can be recorded by an oscilloscope and measure the slope of the cross correlation at the zero crossing point with unit mV/s. However, the recorded time scale has to be converted to the relative time scale between the pulses, which can be expressed as

$$\xi = \frac{\Delta f}{f_M} \qquad (4)$$

EXPERIMENT SETUP

As shown in Fig. 4, the 1550 nm ± 10 nm pulses with a repetition rate of 238 MHz and power of 17.7 mW is from a stabilized polarization maintaining fiber link, which is provided by Cycle company. The 800 nm ± 40 nm pulse is from Ti:sapphire laser oscillator(Micra, Coherent) which has a repetition rate of 79.33 MHz and 45 mW power. In order to reduce the fiber dispersion influence, 800 nm pulses is reflected into the TCBOC system through free space. Beta barium borate (BBO) with a thickness 5 mm was chosen for the generation of 527 nm sum frequency signal. The phase match angle is calculated to be 22.2° according to Sellmeier equation for the used collinear type-I configuration(ooe) [8]. A free space balanced amplified photodetector (PDB210A/M, Thorlabs) with gain of 500×10^3 V/A was chosen for measure the sum frequency signal and corresponding signal difference. This detector acts as balanced receivers by subtracting the two optical input signals from each other, resulting in the cancellation of common mode noise, which allows small changes in the signal path to be extracted from the interfering noise floor.

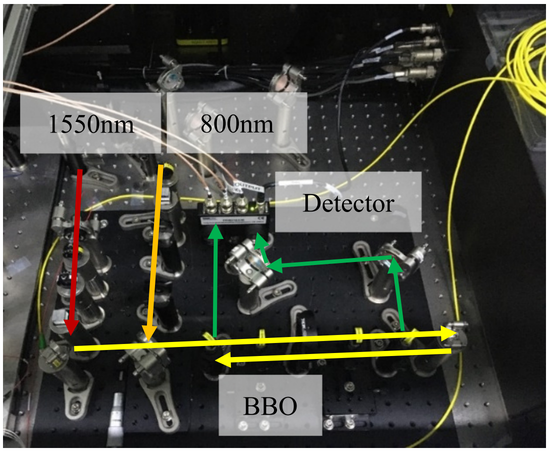

Figure 4: Experimental setup of two color balanced cross correlator.

MEASUREMENT RESULTS AND DISCUSSIONS

When two input pulses are combined and propagate through the BBO crystal in forward direction, 527 nm sum frequency signal is produced shown in Fig. 5 red curve. As the two pulses are reflected back and propagate through the

BBO crystal again, 527 nm sum frequency signal is generated shown in Fig. 5 blue curve. The real time scale in Fig. 5 is obtained by multiplying the time scale of the oscilloscope by a ratio of the repetition rate difference 3.3 Hz to the repetition rate of the master laser 238 MHz.

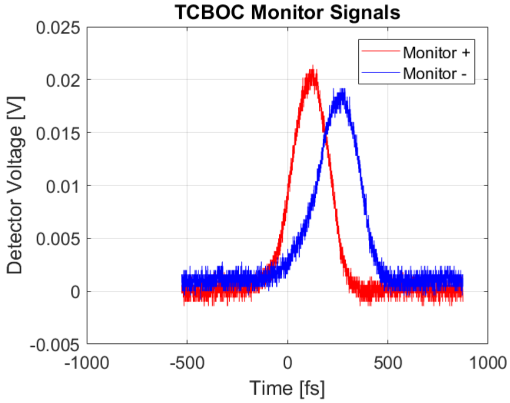

Figure 5: Measured 527 nm sum frequency signal intensity on a balanced detector.

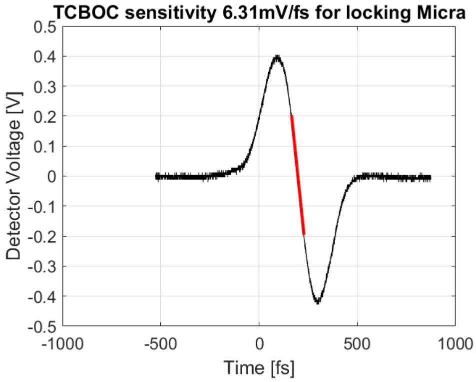

Figure 6: Measured difference signal by two color balanced optical cross correlator. The slope of red part curve is 6.31 mV/fs around zero crossing.

Figure 6 shows the difference signal generated from TCBOC. The sensitivity of the curve is calculated by selecting the red part of the curve, which given a voltage difference 0.4 V and time difference 63.3 fs. Therefore, we extract a slope around the zero crossing of 6.31 mV/fs, which is sufficient for the feedback control loop.

Further investigation of this will include careful characterization of all the input pulse length in the setup and changing the group delay glass accordingly.

CONCLUSION

An two color balanced cross correlator was developed and tested, which will be used to phase lock two individual laser systems operating at different center wavelength and different repetition rates. The repetition rate between the master laser and the slave laser has to be a harmonic of the other's. At present, difference signal of sum frequency have been obtained, which shows a sufficient slope around zero crossing for phase locking. The next step is to make short and long term stability measurements with an identical out of loop TCBOC.

In the future, this TCBOC system will be reassembled and upgraded from breadboard setups to a professionally engineered version, which promises long term stability, user friendly operation and low maintenance.

The same type of two color balanced cross correlator can be used for laser system of SHINE project, such as drive laser, seed laser as well as pump probe laser, which presumably only requires BBO crystal with different cutting angle.

ACKNOWLEDGEMENTS

This work was supported by Shanghai Municipal Science and Technology Major Project (Grant No. 2017SHZDZX02).

REFERENCES

[1] Kemal Safak *et al.*, "A pulsed-optical timing distribution system for LCLS-II", in *Proc. Conference on Lasers and Electro-Optics (CLEO'20)*, Washington, DC, United States, May, 2020. `doi:10.1364/CLEO_SI.2020.SM2N.5`

[2] Kemal Shafak, "Large-scale laser microwave synchronization for attosecond photon science facilities", Ph.D. thesis, Universität Hamburg, Hamburg, Germany, 2017.

[3] S. Schulz *et al.*, "An optical cross correlation scheme to synchronize distributed laser systems at FLASH", in *Proc. 11th European Particle Accelerator Conf. (EPAC'08)*, Genoa, Italy, June, 2008, paper THPC160, pp. 3366-3368.

[4] T. R. Schibli *et al.*, "Attosecond active synchronization of passively mode-locked lasers by balanced cross correlation", *Opt. Lett.*, vol. 28, no.11, pp. 947-949, 2003.

[5] J. Müller *et al.*, "Large-scale optical synchronization system of the European XFEL", in *Proc. 29th Linear Accelerator Conf. (LINAC'18)*, Beijing, China, September, 2008, paper MOPO121, pp. 253-256.

[6] Ming Xin *et al.*, "Sub femtosecond precision timing synchronization systems", *Nuclear Inst. and Methods in Physics Research, A*, vol. 907, pp. 169-181, 2018.

[7] Kemal Safak *et al.*, "Large-scale turkey timing distribution system for attosecond photon science facilities", in *Proc. Conference on Lasers and Electro-Optics (CLEO'17)*, San Jose, CA, United States, May, 2017. `doi:10.1364/CLEO_AT.2017.JTu4L.3`

[8] C. L. Li, L. Feng, B. Liu, X. T. Wang, and W. Y. Zhang, "Measurements of Ultraviolet FEL Seed Laser Pulse Width Broading in Thin ß-BBO Crystals", in *Proc. 9th Int. Beam Instrumentation Conf. (IBIC'20)*, Santos, Brazil, Sep. 2020, pp. 140-144. `doi:10.18429/JACoW-IBIC2020-WEPP20`

OBSERVATION AND ANALYSIS OF ISLAND PHENOMENON IN THE STORAGE RING LIGHT SOURCE*

Yunkun Zhao, Sanshuang Jin, Jigang Wang[†], Baogen Sun[‡], Fangfang Wu, Tianyu Zhou,
Ping Lu, Leilei Tang,
National Synchrotron Radiation Laboratory (NSRL),
University of Science and Technology of China (USTC), Hefei, China

Abstract

In the previous experimental investigations and measurements using the radio-frequency (RF) phase modulation method to study the longitudinal beam characteristics of the Hefei Light Source-II (HLS-II), we found that the longitudinal bunch distributions under different modulation frequencies and amplitudes have great difference. In order to further explore island phenomenon and better understand beam motion associated with external RF phase modulation, the streak camera is exploited to effectively observe the longitudinal bunch profile and distribution in single-bunch filling mode. In addition, the dependence between island size, bunch dilution effect and modulation frequency are also discussed in detail. This is meaningful for researching the impact of RF noise on longitudinal beam dynamics, beam manipulation, and machine maintenance and debugging.

INTRODUCTION

In accelerators, the investigation of the nonlinear longitudinal beam dynamics [1,2] is of great physical significance and engineering value. This is particularly important for studying and exploring the mechanism of beam instability, analysis of beam evolution, observation of longitudinal bunch characteristics, and beam manipulation. In the actual operation of accelerators and synchrotron radiation light sources, particle motion is generally disturbed by RF noise, wakefields, power supply ripple, vibration, etc. There is no doubt that these disturbances will cause changes in beam motion and machine performance due to RF phase and voltage modulations. A part of the theoretical analysis and experimental measurements have been demonstrated that this RF modulation has significant advantages as that of suppressing the coupled bunch instability, improving the beam lifetime, and performing beam manipulation in phase space. Therefore, the RF phase modulation (RFPM) technique was preferred introduced into the HLS-II storage ring to deeply research longitudinal beam characteristics and effectively improve beam lifetime in recent research work [3,4]. However, it is a pity that the exploration of the nonlinear longitudinal beam dynamics is not comprehensive and ambiguous in the presence of the RFPM error noise. Moreover, some clerical errors need to be corrected in reference [3]. As a consequence, the motivation of this article is to further investigate the nonlinear beam dynamics in HLS-II based on the RFPM approach. The main research contents include the observation of resonance island phenomenon, characterization of island size, and study of transient beam response.

THEORETICAL MODELLING AND ANALYSIS

In the synchrotron radiation light sources, when charged particles are suffered from RFPM, the effective parametric resonance Hamiltonian equation can be expressed as [1,2]

$$\begin{aligned} H(\delta,\phi) = {} & \frac{\omega_s\delta^2}{2} + \omega_s \tan\phi_{s0}\left[\sin\phi\cos\left(a_m\sin\omega_m t\right)\right. \\ & \left. + \cos\phi\sin\left(a_m\sin\omega_m t\right)\right] \\ & - \omega_s\cos\phi\cos\left(a_m\sin\omega_m t\right) \\ & + \omega_s\sin\phi\sin\left(a_m\sin\omega_m t\right) - \omega_s\sin\phi\tan\phi_{s0} \end{aligned} \tag{1}$$

In Eq. (1), ω_s denotes the synchronous oscillation angular frequency with $\omega_s = 2\pi f_s$, in which f_s denotes the synchrotron oscillation frequency. It is noted that ϕ_{s0} is determined by the synchrotron phase ϕ_s, namely equivalent to $\phi_{s0} = \pi - \phi_s$. a_m indicates the modulation amplitude, and ω_m indicates the angular frequency of RFPM that is satisfied with $\omega_m = 2\pi f_m$ where f_m is the modulation frequency. δ and ϕ are the energy deviation and the phase, respectively.

In the case that the RFPM frequency is close to the synchrotron frequency, for which the violent first-order parametric resonance can be produced at this time. After through coordinate transformation (J,ψ) and a series of simplifications and ignoring non-parametric resonance terms, the time-averaged Hamiltonian can be described by [5]

$$\langle H\rangle_t = \left(\omega_s - \omega_m\right)J - \frac{\omega_s J^2}{16} - \frac{\omega_s a_m}{2}\left(2J\right)^{\frac{1}{2}}\cos\psi \tag{2}$$

By introducing the feature function g, the solution of the above Eq. (2) can be written as

$$\begin{cases} g_1(x) = -\frac{8}{\sqrt{3}}\sqrt{x}\cos\frac{\xi}{3}, & (\text{SFP}, \psi = \pi) \\ g_2(x) = \frac{8}{\sqrt{3}}\sqrt{x}\cos\left(\frac{\pi}{3} + \frac{\xi}{3}\right), & (\text{SFP}, \psi = 0) \\ g_3(x) = \frac{8}{\sqrt{3}}\sqrt{x}\cos\left(\frac{\pi}{3} - \frac{\xi}{3}\right), & (\text{UFP}, \psi = 0) \end{cases} \tag{3}$$

---

* Work supported by the National Natural Science Foundation of China under Grant 12075236, Grant 12005223, Grant 51627901, and Grant 11705203, the Anhui Provincial Natural Science Foundation under Grant 1808085QA24, and the Fundamental Research Funds for the Central Universities under Grant WK2310000080.

[†] wangjg@ustc.edu.cn

[‡] bgsun@ustc.edu.cn

ISBN: 978-3-95450-230-1 ISSN: 2673-5350 doi:10.18429/JACoW-IBIC2021-WEPP06

where $x = 1 - \omega_m/\omega_s$, $x_{\mathrm{bif}} = 1 - \omega_{\mathrm{bif}}/\omega_s$, $\xi = \arctan(\sqrt{\left(\frac{x}{x_{\mathrm{bif}}}\right)^3 - 1})$, and the bifurcation angular frequency is $\omega_{\mathrm{bif}} = \omega_s \left[1 - \frac{3}{16}(4a_m)^{\frac{2}{3}}\right]$. Here, it is especially emphasized that g_1 and g_2 stand for the outer and the inner stable fixed points (SFPs), whereas g_3 for the unstable fixed point (UFP). These fixed points act as the attractors whose role are to draw and capture the charged particles to move in the longitudinal phase space, for which leads to the formation of the resonant islands or beamlets. Of course, the particle distribution and bunch density can be effectively manipulated by means of RFPM. According to the aforementioned theoretical model Eqs. (2)– (3), numerical simulations are carried out based on the core parameters of HLS-II [3], as shown in Fig. 1.

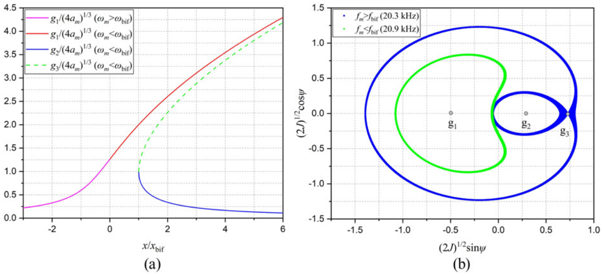

(a) (b)

Figure 1: The phase amplitudes of fixed points and Hamiltonian tori in phase space (the simulated parameters are: $a_m = 0.02$ rad, $f_s = 21.3$ kHz, and $f_{\mathrm{bif}} = 20.6$ kHz).

In Fig. 1, it can be seen that the phase amplitude of the fixed point and the Hamiltonian torus are significantly different with the variation of the modulation frequency. As the modulation frequency is smaller than the bifurcation frequency, two SFPs and one UFP appear. This means that there are at least two resonant islands in the beam manipulation and bunch intensity dilution process. However, when the modulation frequency is larger than the bifurcation frequency, there is only one real solution to Eq. (3), yields

$$g_1(x) = -(4a_m)^{1/3}\left[\left(\sqrt{1-\left(\frac{x}{x_{\mathrm{bif}}}\right)^3}+1\right)^{1/3} - \left(\sqrt{1-\left(\frac{x}{x_{\mathrm{bif}}}\right)^3}-1\right)^{1/3}\right] \tag{4}$$

From Eq. (4), it is indicated that there is an island generated in the presence of RFPM. It is necessary to especially note that the resonance islands can be generated or annihilated owning to the transient and unstable beam response for the case that the modulation frequency is close to bifurcation frequency. For simplicity and convenience, it is straightforward to take advantage of the mixture of multi-Gaussian equation for analyzing the size of the resonant islands and beam dilution rate in the practical experimental measurements.

$$I(\tau) = I_0 + \sum_{i=1}^{n} I_i \exp\left[-\frac{(\tau-\overline{\tau_i})^2}{2\sigma_i^2}\right] \tag{5}$$

Here, I_0 is the initial beam intensity, I_i is the peak value of the distribution, i is the number of islands, and σ_i is the width of i-th island. In this way, the island phenomenon caused by RFPM can be effectively quantitatively described and analyzed. According to Eq. (5), the simulated longitudinal bunch profiles of bi-Gaussian and multi-Gaussian cases are distinctly shown in Fig. 2.

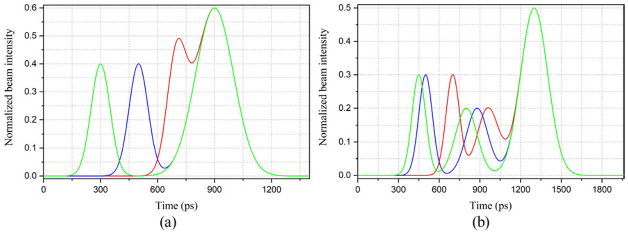

(a) (b)

Figure 2: Longitudinal bunch profiles of bi-Gaussian and multi-Gaussian models.

EXPERIMENTAL SETUP AND RESULTS

In terms of the above-mentioned theoretical analysis, the RFPM is applied onto the RF system to observe the longitudinal bunch distribution and explore the island phenomenon. The experimental measurement system is clearly depicted in Fig. 3.

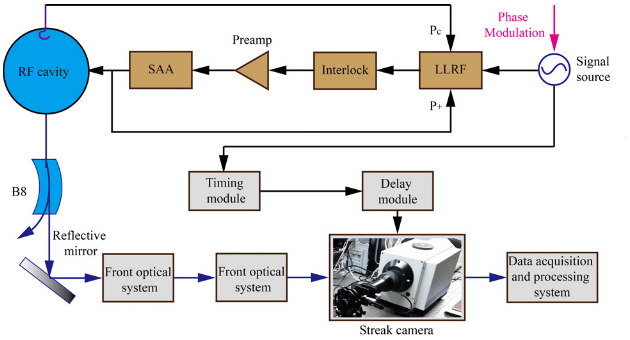

Figure 3: Diagram of the experimental measurement system for RFPM (the beam current is in the range of 11–13 mA with top-off mode).

As shown in Fig. 3, the RFPM experimental measurement system mainly consists of a RF cavity system and a streak camera measurement system. In the RF system, the 204 MHz RF signal output by the signal source is transmitted into the interlock module after the digital low-level RF (LLRF) system. And then it is fed into the solid-state amplifier (SSA) system after passing through the pre-amplifier, and finally 9.3 kW of power output from SSA propagated onto the RF cavity. Furthermore, the power signal coupled from the SSA and RF cavity is sent to the LLRF system as a feedback signal, of which is further delivered into the Free Programmable

Gate Array (FPGA) board for control calculation after down-conversion and analog-to-digital conversion in the digital LLRF system. Notice that the interlock module is connected with three protection signals that is used to ensure the safety of personnel and machine.

It should be pointed out that the RFPM is applied to the signal source, and then affects the bunch motion in HLS-II. At the same time, the longitudinal bunch distribution and island effect subjected to RFPM are measured and observed by the streak camera measurement system installed downstream at the diagnostic beamline B8. Further, we obtained the longitudinal bunch intensity images and distributions without and with RFPM as shown in Figs. 4 and 5, respectively.

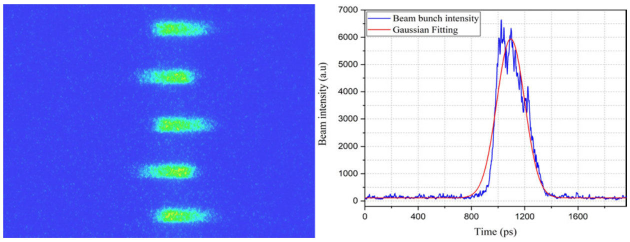

Figure 4: Longitudinal bunch intensity image and profile in the absence of RFPM.

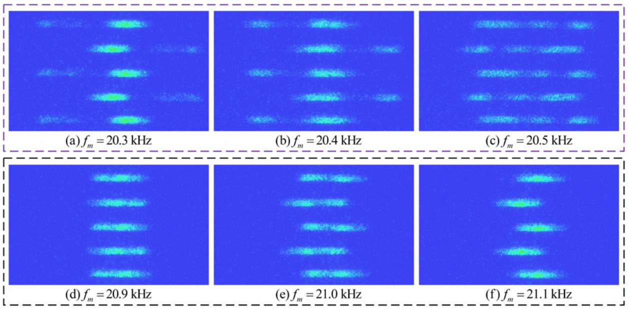
(a) $f_m = 20.3$ kHz (b) $f_m = 20.4$ kHz (c) $f_m = 20.5$ kHz
(d) $f_m = 20.9$ kHz (e) $f_m = 21.0$ kHz (f) $f_m = 21.1$ kHz

Figure 5: Longitudinal bunch intensity image versus RFPM frequency.

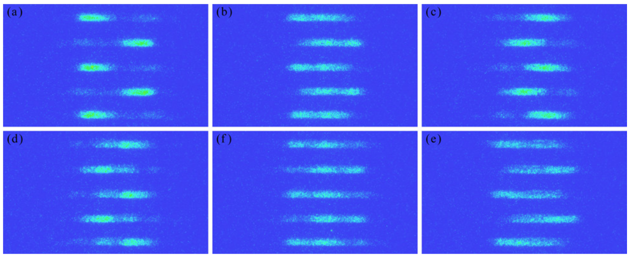

Figure 6: Observations of the longitudinal bunch structures in transient response under the modulation frequency of 20.6 kHz.

Figure 4 shows the bunch intensity and distribution without RFPM, and the blue and red lines are the longitudinal bunch profile and corresponding fitting curve, respectively. Through in-depth data-analysis, the root-mean-square (rms) bunch length can be acquired as 104.3 ps. In Fig. 5, the upper trace reveals the longitudinal bunch intensity images when the RFPM frequency is 20.3, 20.4, and 20.5 kHz, respectively, near the bifurcation frequency of 20.6 kHz. Nevertheless, the lower trace reveals the longitudinal bunch intensity images as that of the modulation frequency of 20.9, 21.0, and 21.1 kHz, individually, exceeding the bifurcation frequency. It is observed from Fig. 5 that the introduced RFPM can effectively manipulate the beam intensity and elongate bunch length. Additionally, it can be clearly seen that the RF phase error noise can produce the dramatic island phenomena. This main reason is that when the nonlinear parametric resonance will occur when the modulation frequency approaches to the synchrotron frequency, of which results in the dilution of bunch density, and simultaneously to stretch the bunch length and form the resonant islands. Here, it is emphasized that this island effect is the transient response of beam, with which the island can be generated or annihilated as the case that the modulation frequency is close to the bifurcation frequency, as shown in Fig. 6. As a result, the island phenomenon can be utilized for roughly analysing and evaluating the impact of the existed RF noise on beam characteristics in the storage ring light source. Indeed, this has certain reference and application value for machine study and beam evolution exploration in the actual accelerator operation.

In order to further analyze and discuss the island phenomenon, the mixed multi-Gaussian model is exploited to quantize the width of island and the beam dilution effect at various RFPM frequencies, as shown in Figs. 7 and 8, respectively.

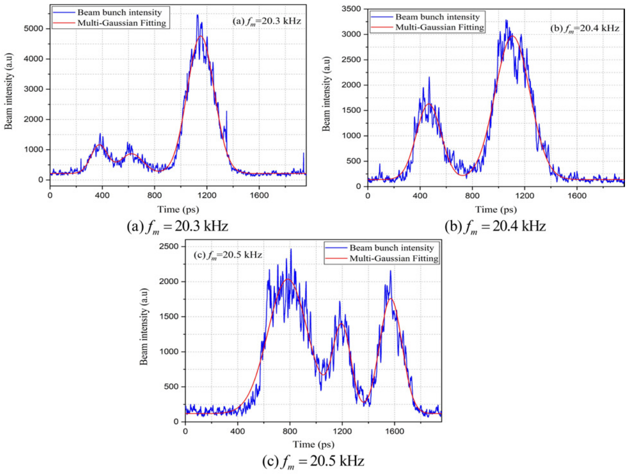

(a) $f_m = 20.3$ kHz (b) $f_m = 20.4$ kHz
(c) $f_m = 20.5$ kHz

Figure 7: Longitudinal bunch distributions and data-analysis below the bifurcation frequency.

Figure 7 expresses the longitudinal bunch distributions and according fitting curves corresponding to the RFPM frequency of 20.3, 20.4, and 20.5 kHz, respectively, below the bifurcation frequency. Nevertheless Fig. 8 depicts the longitudinal bunch distributions and according fitting curves in the case of the RFPM frequency exceeding the bifurcation frequency of 20.9, 21.0, and 21.1 kHz, respectively. From detailed data analysis, the rms widths of the formed reso-

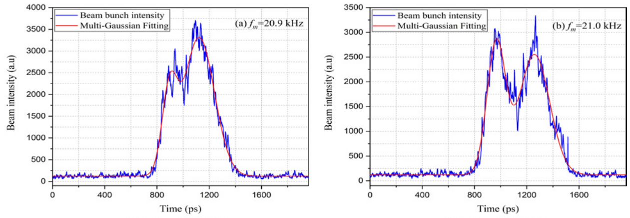

(a) $f_m = 20.9$ kHz (b) $f_m = 21.0$ kHz

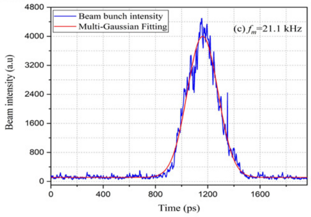

(c) $f_m = 21.1$ kHz

Figure 8: Longitudinal bunch distributions and data-analysis above the bifurcation frequency.

nance islands are obtained to be 62.5 ps/45.1 ps/72.9 ps, 66.9 ps/94.6 ps, and 108.3 ps/50.0 ps/60.7 ps, which correspond to the RFPM frequencies are 20.3, 20.4, and 20.5 kHz, respectively. And the island widths are 41.0 ps/83.4 ps, 50.2 ps/82.9 ps, and 117.5 ps when the RFPM frequencies are finely adjusted to be 20.9, 21.0, and 21.1 kHz, respectively. It is apparent that the beam dilution effect becomes more significant as the width of the island increases as a result of RFPM.

CONCLUSION

In this paper, the RFPM method is used for researching the longitudinal bunch distribution and nonlinear island phenomenon on HLS-II. It has shown that the generation of the resonant island and the beam dilution effect are dependent on the RFPM frequencies and amplitudes. In addition, the mixed multi-Gaussian theoretical model is developed to analyze the size of the resonance island and effectiveness of beam manipulation. This is useful and meaningful for the analysis of the influence of RF noise, investigation of the longitudinal beam dynamics, exploration of the nonlinear island phenomena, maintenance and debugging of machine.

ACKNOWLEDGEMENTS

This work was supported in part by the National Natural Science Foundation of China under Grant 12075236, Grant 12005223, Grant 51627901, and Grant 11705203, the Anhui Provincial Natural Science Foundation under Grant 1808085QA24, and the Fundamental Research Funds for the Central Universities under Grant WK2310000080.

REFERENCES

[1] H. Huang *et al.*, "Experimental determination of the Hamiltonian for synchrotron motion with rf phase modulation", *Phys. Rev. E*, vol. 48, no. 6, pp. 4678–4688, 1993. `doi:10.1103/PhysRevE.48.4678`

[2] N. P. Abreu *et al.*, "Longitudinal dynamics with rf phase modulation in the Brazilian electron storage ring", *Phys. Rev. ST Accel. Beams*, vol. 9, no. 12, p. 124401, 2006. `doi:10.1103/PhysRevSTAB.9.124401`

[3] Y. Zhao *et al.*, "Experimental research on HLS-II performance by means of the RF phase modulation technique", *IEEE T. Nucl. Sci.*, vol. 68, no. 2, pp. 92–100, 2021. `doi:10.1109/TNS.2020.3040266`

[4] Y. Zhao *et al.*, "Effect of phase modulation on the transverse beam size and emittance of the HLS-II ring", in *Proc. 9th Int. Beam Instrumentation Conf. (IBIC'20)*, Santos, Brazil, Sep. 2020, paper WEPP26, pp. 158–161. `doi:10.18429/JACoW-IBIC2020-WEPP26`

[5] S. Y. Lee, "Synchrotron motion", in *Accelerator Physics*, Singapore: World Scientific, 2018, pp. 260–264.

DESIGN AND SIMULATION OF THE COUPLING STRUCTURE FOR SINGLE RESONANT CAVITY BUNCH LENGTH MONITOR*

Huanxiang Tuo, Qing Luo, Fangfang Wu, Tianyu Zhou, Ping Lu, Baogen Sun†
National Synchrotron Radiation Laboratory (NSRL),
University of Science and Technology of China (USTC), Hefei, China

Abstract

The measurement of the bunch length can better realize the monitoring of the beam, because the bunch length is one of the important longitudinal parameters of the beam. In this paper, a new single-cavity bunch length monitor is proposed, whose coupling structures consist of two kinds of filters. One is a low pass filter, the other is a band pass filter. The coaxial low-pass filter is used to couple out low-frequency signals, and the band-pass filter is used to couple higher-frequency signals. According to the beam characteristics of the National Synchrotron Radiation Laboratory (NSRL)based on the tunable infrared laser energy chemistry research large-scale experimental device (FELiChEM), we perform simulation in CST. The simulation results show that the monitor can measure the bunch length of the FELiChEM device very well, and the simulation measurement error is less than 2%.

INTRODUCTION

FELiChEM is a large-scale experimental device built by the National Synchrotron Radiation Laboratory of the University of Science and Technology of China. The device has high pulse intensity, continuously adjustable wavelength, and the bunch length is on the order of ps [1]. The bunch length monitor based on the resonant cavity is a non-intercepting measurement and has little effect on beam. Therefore, this measurement method is suitable for measuring the bunch length of FELiChEM. When the beam moves from the beam tube through the resonant cavity, several characteristic modes will be excited in the cavity [2–4]. We extract the desired electromagnetic field, and then process it electronically to get the bunch length information. Compared to conventional double-cavity bunch length monitor, the single-cavity bunch length monitor more compact [5]. In this paper, we designed a single-cavity beam bunch length monitor and its coupling structure based on the beam current parameters of FELiChEM.

THEORETICAL ANALYSIS

In the resonant cavity, for the Gaussian distributed beam, the Fourier expansion is performed, and the n-th harmonic amplitude is obtained [6] as shown in Eq. (1).

$$I_{\mathrm{n}} = 2I_0 \exp\left(-\frac{n^2\omega_0^2\sigma_\tau^2}{2}\right) \tag{1}$$

In Eq. (1), I_0 denotes the beam fundamental wave amplitude. ω_0 represents the fundamental angular frequency. n denotes the harmonic order and σ_τ is the bunch length.

According to Eq. (1), we can get Eq. (2).

$$V_n = I_n \times Z_n = 2I_0 \exp\left(-\frac{n^2\omega_0^2\sigma_\tau^2}{2}\right) \times Z_n \tag{2}$$

Where V_n represents the voltage value obtained by harmonic detection, and Zn is the shunt impedance of the cavity that can be obtained through actual measurement.

Let $\omega_1 = n_1\omega_0$, $\omega_2 = n_2\omega_0$, then

$$\begin{cases} V_1 = I_1 \times Z_1 = 2I_0 \exp\left(-\frac{\omega_1^2\sigma_\tau^2}{2}\right) \times Z_1 \\ V_2 = I_2 \times Z_2 = 2I_0 \exp\left(-\frac{\omega_2^2\sigma_\tau^2}{2}\right) \times Z_2 \end{cases} \tag{3}$$

where ω_1 and ω_2 are the angular frequencies of multiple harmonics, and V_1 and V_2 are the corresponding measured harmonic voltage values respectively.

The above term in Eq. (3) is divided by the following term to get Eq. (4).

$$\frac{V_1}{V_2} = \frac{Z_1}{Z_2} \exp\left[\frac{\left(\omega_2^2 - \omega_1^2\right)\sigma_\tau^2}{2}\right] \tag{4}$$

Let $K = \frac{Z_2}{Z_1}$, which can be obtained by actual measurement, then

$$\exp\left[\frac{\left(\omega_2^2 - \omega_1^2\right)\sigma_\tau^2}{2}\right] = K\frac{V_1}{V_2} \tag{5}$$

$$\sigma_\tau = \sqrt{\frac{2}{\left(\omega_2^2 - \omega_1^2\right)} \ln\left(K\frac{V_1}{V_2}\right)} \tag{6}$$

It can be seen from Eq. (6) that is necessary to measure the harmonic voltage values of two different frequency modes to obtain the bunch length.

The beam current parameters of FELiChEM are shown in Table 1. According to Table 1, the designed single-cylindrical resonant cavity needs to resonantly output an electromagnetic field with a multiple frequency mode of 0.476 GHz. Equation (7) represents the resonant frequency formulas of cylindrical resonators [7].

$$\begin{cases} f = \frac{c}{2}\sqrt{\left(\frac{p}{l}\right)^2 + \left(\frac{v_{nm}}{\pi r}\right)^2}, & (TM) \\ f = \frac{c}{2}\sqrt{\left(\frac{p}{l}\right)^2 + \left(\frac{\mu_{mm}}{\pi r}\right)^2}, & (TE) \end{cases} \tag{7}$$

---

* Work supported by the National Key Research and Development Program-X-ray free electron laser principle and key technology research Grant 2016YFA0401900, and Grant 2016YFA0401903, the Natural Science Foundation Grant 12075236.

† bgsun@ustc.edu.cn

ISBN: 978-3-95450-230-1 ISSN: 2673-5350 doi:10.18429/JACoW-IBIC2021-WEPP07

Where v_{nm} is the root of the Bessel function and μ_{nm} is the root of the Neumann function. r denotes the radius of the cylindrical cavity.

Table 1: Electron Beam Parameters of FELiChEM

Parameter	**Specification**
Energy	60 MeV
Energy spread	<240 KeV
Bunch charge	1.0 nC
Bunch length	5 ps
Micro-pulse repetition rate	0.476 GHz

In an accelerator, charged particles passing through the center of the cavity will generate an electric field in the longitudinal direction, so it is usually desirable to establish a TM mode in the cavity. In order to make full use of microwave power, TM_{010} mode is generally used [8]. According to Eq. (7), when the radius is same, the modes of two frequencies must be different to couple out two kinds of frequencies, so we choose the other mode as TM_{030}. The final mode and frequency are TM_{010} mode resonating at 2.38 GHz, the 5th harmonic of 0.476 GHz, and the TM_{030} mode which resonates at the 18th harmonic of 0.476 GHz at 8.568 GHz. After the mode and frequency are determined, the radius of the resonant cavity is also determined. By adjusting the structure of the single resonant cavity bunch length monitor, the required two modes can be coupled separately at the same time.

MODEL CONSTRUCTION

Coaxial Low-pass Filter Design

In order to reduce the interference of other modes on the TM_{010} mode, a coaxial line low-pass filter is designed. High-impedance lines are used to simulate series inductance, and low-impedance lines are used to simulate parallel capacitors. Several high- and low-impedance lines are alternately cascaded to form a low-pass filter [9].

Let l_0=l_6=5 mm, l_1=l_5=6.124 mm, l_2=l_4=5.235 mm, and l_3=11.664 mm. l is used to indicate the length, and the subscript indicates the position of the transmission line. The inner diameter of the outer conductor is taken as 10 mm. Look up the table (refer to [9] for details) to get the diameter of each section of transmission line d_0=d_6=4.343 mm, d_1=d_3=d_5=1.351 mm, d_2=d_4=8.464 mm. d is used to indicate the diameter, and the subscript indicates the position of the transmission line.

The structure diagram of the filter is shown in Fig. 1. Figure 1(a) is a three-dimensional model diagram, and Fig. 1(b) is a cross-sectional view thereof. In the CST Microwave Studio, the designed model is simulated, and the S parameters of the filter obtained by the simulation are shown in Fig. 2.

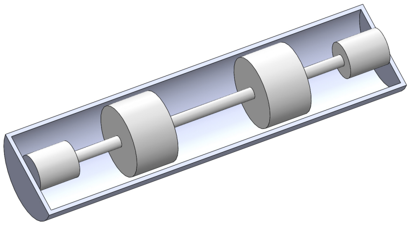

(a) 3D model of low pass filter

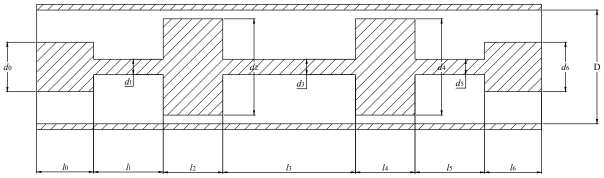

(b) cutaway view of low pass filter

Figure 1: Structure of low pass filter.

Figure 2 shows that the cut-off frequency of the filter obtained by simulation is about 2.62 GHz, which is between TM_{010} mode and TM_{110} mode. By using this filter, the interference of other modes on the TM_{010} mode can be removed, and a single mode can be extracted.

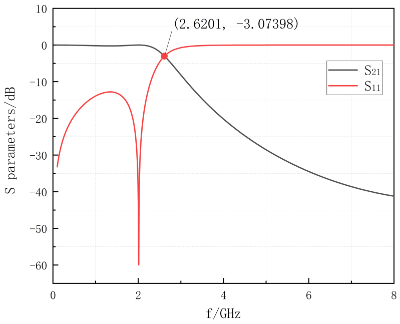

Figure 2: S parameters of low pass filter.

Diaphragm Loaded Waveguide Bandpass Filter Design

From the previous analysis, it can be seen that the measurement of the bunch length requires the simultaneous coupling of two signals of different frequency modes. In order to better couple out the TM_{030} mode, it is proposed to use a diaphragm-loaded waveguide bandpass filter as a coupler for the TM_{030} mode. In high-frequency communications, bandpass filters composed of rectangular waveguides are very common [10] and the diaphragm-loaded waveguide bandpass filter is a typical application. The waveguide section is used as a series resonator, and the parallel inductance formed by the diaphragm is used as the coupling structure between the resonators [11]. The designed filter should be able to conduct and output signal at 8.568 GHz, so the rectangular waveguide model R84 is selected whose main mode frequency range is from 6.57 GHz to 9.99 GHz, and size is a=28.499 mm and b=12.624 mm [12].

The three-dimensional structure of the waveguide band-pass filter is shown in Figs 3 and 4 is its cross-sectional view. The filter structure is adjusted according to the simulation results in the CST studio, and the final optimized size is shown in Table 2.

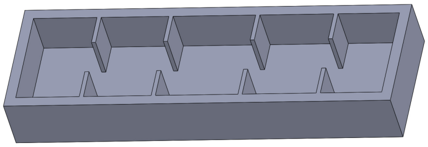

Figure 3: 3D model of band pass filter.

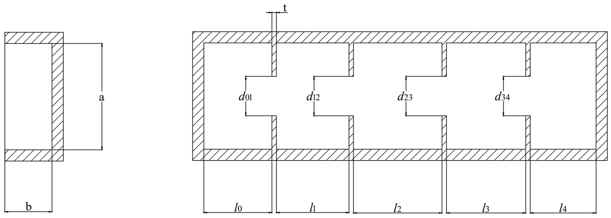

Figure 4: Cutaway view of band pass filter.

Table 2: Parameters of Band Pass Filter

Parameters	**Value/mm**
d_{01}	10.54463
d_{12}	6.26978
l_0	104.85
l_1	21.19
l_2	22.47
t	1.2

The S parameters of the band-pass filter obtained by simulation in CST Microwave Studio are shown in Fig. 5. S_{11} is the return loss of the filter and S_{21} is the insertion loss of the filter. It can be seen from Fig. 5 that the passband bandwidth of the filter is narrow and the return loss is less than -3 dB at 8.568 GHz frequency, which meets the design requirements.

Single Resonant Cavity Bunch Length Monitor Design

When the mode and frequency of the resonant cavity are determined, the radius of the resonant cavity can be calculated by using Eq. (8).

$$r = \frac{cv_{mn}}{2\pi f} \tag{8}$$

Where r denotes the radius of the resonant cavity. c is the speed of light. μ_{nm} represents the root of the Bessel function, and f is the frequency.

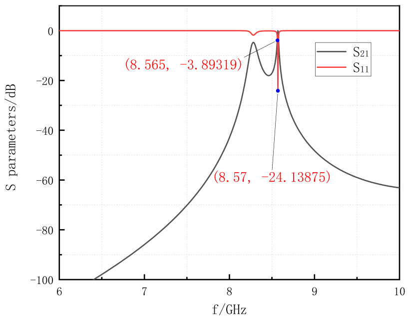

Figure 5: S parameters of band pass filter.

The structure of the finally optimized design of the bunch length monitor is shown in Fig. 6. The center of cylindrical cavity coincides with the center of the beam pipe. The radius of cylindrical cavity is 51.8 mm and the radius of the beam pipe is 17.5 mm. The size in the longitudinal direction has no obvious effect on the frequency of the coupling mode, so the longitudinal length of the resonant cavity is taken as 12 mm. Similarly, the longitudinal length of the beam pipe is taken as 110 mm. The size of the coupling hole is 10.5 mm×0.4 mm×12 mm. The center of the coaxial low-pass filter is offset by 24 mm from the center of the beam pipe and installed symmetrically. At the same time, the waveguide filters are installed symmetrically on the upper and lower coupling holes of the single cylindrical resonant cavity.

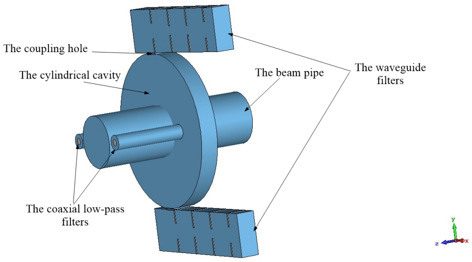

Figure 6: Structure of bunch length monitor.

SIMULATION

In the CST particle studio, the simulated electron beam is set according to the parameters in Table 1, and the bunch length is set to 5 ps. The simulated electric field mode excited by the monitor is shown in Fig. 7. The field distribution of TM_{010} mode is shown in Fig. 7(a), and the field distribution of TM_{030} mode is shown in Fig. 7(b). The output signal of the port is shown in Fig. 8. Figure 8(a) shows the signal that output from the low-pass filter port, and Fig. 8(b) shows the signal which output from the band-pass filter port.

It can be seen from Fig. 8 that the use of filter to couple the signal can well remove the interference of other modes signals to the desired signal. In the CST particle studio,

ISBN: 978-3-95450-230-1 ISSN: 2673-5350 doi:10.18429/JACoW-IBIC2021-WEPP07

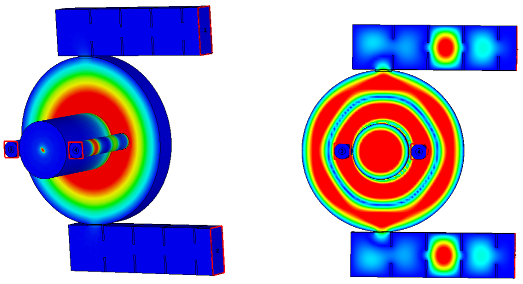

(a) electric field distribution of TM_{010} mode

(b) electric field distribution of TM_{030} mode

Figure 7: Electric field distribution of coupling mode.

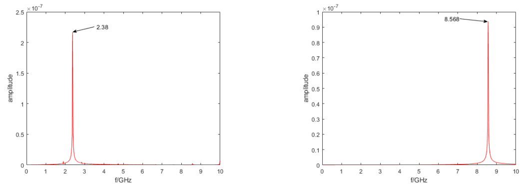

(a) output signal of low pass filter

(b) output signal of band pass filter

Figure 8: Port output signal.

the beam is loaded and the beam length is changed multiple times. The simulation results are shown in Table 3. V_{TM010} represents the spectral amplitude of TM_{010} mode, and V_{TM030} represents the spectral amplitude of TM_{030} mode.

Table 3: Parameters of Band Pass Filter

Bunch length/(ps)	$\frac{V_{TM010}}{V_{TM030}}$	Measurements of bunch length/(ps)	Relative error/(%)
2	2.251	2.03	1.50
3	2.266	2.99	0.33
4	2.287	3.97	0.75
5	2.313	4.91	1.80
10	2.557	9.93	0.70
15	3.024	14.94	0.40
20	3.828	19.97	0.15

CONCLUSION

This paper combines the filters with a single cavity based on the bunch length measurement theory and the filter design principle. By simulation with CST Microwave Studio and Particle Studio, bunch length monitor is designed that can couple output TM_{010} and TM_{030} modes at the same time. The simulation results show that the measurement error of the single-cavity bunch length monitor from 2 to 20 ps is less than 2%, which meet the measurement requirements of FELiChEM bunch length. Compared with a single cavity directly coupled with a probe, the signal interference of the output coupled with the filter is significantly reduced.

ACKNOWLEDGEMENTS

This work was supported by the National Key Research and Development Program-X-ray free electron laser principle and key technology research Grant 2016YFA0401900, and Grant 2016YFA0401903, the Natural Science Foundation Grant 12075236.

REFERENCES

[1] Heting Li, Qika Jia, Shangcai Zhang *et al.*, “Design of FELiChEM, the first infrared free-electron laser user facility in China”, *Chinese Physics C*, vol. 41, no. 01, pp. 199–205, 2017.

[2] Qian Wang, “Study of the Cavity-based Bunch Length Diagnostic Tech-nology for Linac”, University of Science and Technology of China, 2020.

[3] Jian Chen, Yongbin Leng *et al.*, “Beam test results of high Q CBPM prototype for SXFEL”, *Nuclear Science and Techniques*, vo. 28, no 04, pp. 3-10, 2017.

[4] Shanshan Cao, Yongbin Leng, Renxian Yuan *et al.*, “Study on precise bunch current measurement based on dual cavity monitor”, *Nuclear Techniques*, vol 42, no 04, pp. 5-10, 2019.

[5] Qian Wang, Qing Luo, Baogen Sun *et al.*, “Design and simulation of a bunch length monitor for linac based on single cavity”. *High Power Laser and Particle Beams*, vol. 29, no 11, pp. 125-129, 2017.

[6] Jiang Guo, Zeran Zhou, Qing Luo, “Design and simulation of TM_{020} cavity bunch length monitor”, *High Power Laser and Particle Beams*, vol. 28, no. 9, p. 095104, 2016.

[7] Yuanji Pei, “Basics of Electron Linear Accelerator Design”, Science Press, 2013.

[8] Roberts B, Mammei R R, Poelker M *et al.*, “Compact noninvasive electron bunch-length monitor”. *Physical Review Accelerators and Beams*, vol. 15, p.122802, 2012.

[9] Benfu Gan, Wanchun Wu, “The structure and design of modern microwave filter”, Science Press, 1973.

[10] Jarry P, Pham J M, Roquebrun O *et al.*, “A new class of dual - mode asymmetric microwave rectangular filter”, *IEEE International Symposium on Circuits & Systems*, pp. 859–862, 2002. `doi:10.1109/ISCAS.2002.1010360`

[11] Chen T S, “Characteristics of Waveguide Resonant-Iris Filters (Correspondence)”, *IEEE Transactions on Microwave Theory & Techniques*, vol. 15, no. 4, pp. 260-262, 2003.

[12] Ruimin Xu, Pu Tang, Zhenghui Xue *et al.*, “Fundamentals of Microwave Technology ”, Science Press, 2009.

ISBN: 978-3-95450-230-1 ISSN: 2673-5350 doi:10.18429/JACoW-IBIC2021-WEPP08

FEMTOSECOND FIBER LINK STABILIZATION TO TIMING SYNCHRONIZATION SYSTEM FOR SHINE PROJECT*

Lie Feng, Jinguo Wang, Chunlei Li, Wenyan Zhang, Xingtao Wang, Bo Liu†
Shanghai Advanced Research Institute, Chinese Academy of Science, Shanghai, China

Abstract

The under-construction Shanghai high repetition rate XFEL and Extreme light facility (SHINE) project has a high precision requirement for the timing synchronization system on femtosecond timescale over than more than 3-km long optical fiber links, therefor, an ultra –low noise reference signals from the optical master oscillator (OMO) transmission is play an important role. For this purpose, a fiber link stabilization units based on balanced optical cross-correlators to stable the long-distance fiber link is under developing.

In this paper, the latest progress of the fiber link stabilization experiment and measured results for the performance will be reported.

INTRODUCTION

FELs facilities can generate bright, coherent X-ray pulses with temporal duration below 100 fs and up to 10^{13} photon per pulse [1]. Such high brightness and ultra-short pulses light source facilities put forward higher requirements for the accuracy of timing synchronization system. The traditional RF method cannot meet the XFEL's femtosecond precision synchronization requirements on femtosecond timescale. According to the timing synchronization schemes of several major FELs facilities under operation all over the world, such as FLASH, the European XFEL, and FERMI FEL [2-5], we have conducted research on femtosecond synchronization system as is shown in Fig. 1. For such a timing system, it is essential to stabilize the long-distance fiber link to provide the drift and jitter-free reference pulsed optical signals to multiple terminals, including photo-injector laser, seed laser, RF system, user experiment stations, bunch arrival time monitors and so on.

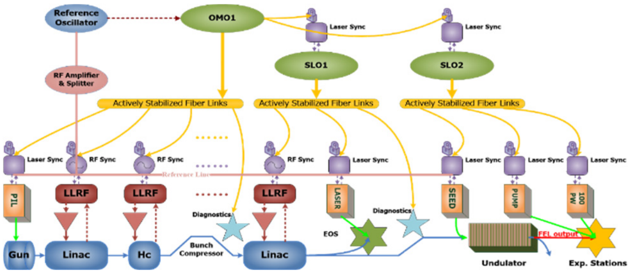

Figure 1: Schematic of typical femtosecond synchronization system.

Fiber link stabilization system based on a mode-locked fiber laser (OMO), which locked on a RF master oscillator (RMO), using the a phase detector called balanced optical cross-correlators (BOC) due to its attosecond timing resolution, long-term stability, amplitude invariance and robustness against environmental fluctuations.

PRINCIPLE OF FIBER LINK STABILAZAION

BOCs is a highly sensitive method to measure timing fluctuations between optical pulses and it can be also employed to detect time of flight fluctuations of pulses circulating in a fiber link [5]. Figure 2 shows the timing detection principle of BOC, the relative timing of both input optical pulse is to be measured by the double-pass configuration. BOC is based on the second-harmonic generation (SHG) between two orthogonal polarizations pulses in a non-linear crystal PPKTP [6, 7]. The forward two pulses with a time delay Δt transmitted through the dichroic mirror (DBS1), overlap in the crystal and generate the SH1. The residue fundamental pulse is reflected by the DBS2, and backward into the crystal second time, generate another second harmonic signal SH2. A balanced photodetector receives the both SHG signals separately, and the output indicates the time delay of both input pulses.

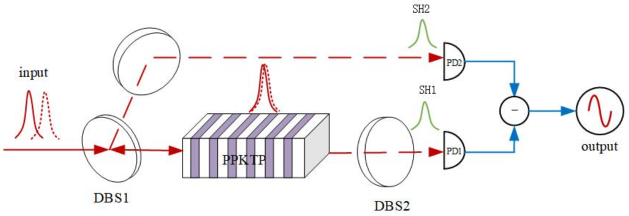

Figure 2: Principle of BOC.

Figure 3 illustrates the operation principle of fiber link stabilization using a BOC. Since the mode-locked laser can provide ultra-low noise optical and microwave signals in the form of optical pulse trains, it has great advantage as the optical master oscillator (OMO) for the high precision timing synchronization system.

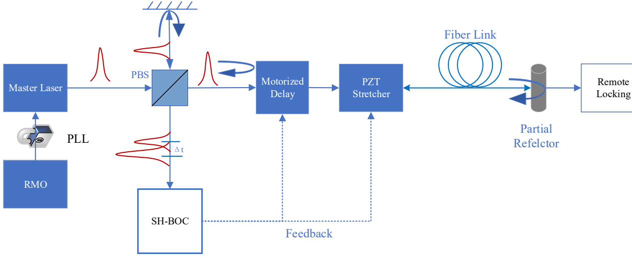

Figure 3: Operation principle of fiber link stabilization.

---

* Work supported by Shanghai Municipal Science and Technology Major Project (Grant No. 2017SHZDZX02)
† Email address liubo@zjlab.org.cn

OMO is locked in a RF master oscillator with low jitter using phase-locked-loop method. The pulse from OMO is divide into two paths: one is for reference pulses and the other for fiber link pulses. Fiber link pulses go through the long distance to the remote site. There is a partially reflector at the end of the link, and the pulses back to the fiber link will be combined with the reference pulses going through into the BOC. The output time delay between the two pulses will be used as a feedback to control the motorized delay and PZT stretcher to stabilize the long-distance fiber link.

EXPERIMENT SETUP

The experiment schematic of fiber link stabilization unit in laboratory is shown in Fig. 4. The OMO is manufactured by Menhir, which provide the optical pulse with centre wavelength at 1550 nm, FWHW pulse duration of 150 fs, and repetition rate of 216.77 MHz. The pulse train from the master laser is divided by a 1×4 fiber splitter into four parts with different power. One part is for in-loop BOC and anther one is for out-of-loop BOC.

For in-loop BOC, optical pulse train is divided into two paths by PBS: the reference path and the fiber link path. To avoid the instability caused by the environment, the reference optical path should be as short as possible [8, 9]. The laser pulses in the free space go through a fiber collimator (Throlabs TC12APC-1550) into the fiber link, which including a motorized optical delay line (ODL), fiber stretcher, aerbium-doped fiber amplifier (EDFA), a 40-m fiber link, and a 90/10 transmission/reflection fiber-coupled Faraday rotator (FC-FR). The 40-m fiber link is comprised of 10-m of dispersion-compensating fiber (DCF) and 30-m of standard single-mode fiber (SMF). The FC-FR is placed at the end of the fiber link in order to simultaneously turn the polarization of the pulse by 90° and reflect the pulse train into the in-loop BOC1 detector for timing stabilization. In order to guarantee that the polarization state of the backward pulse from the SMF link exactly turn 90°, a half-wave plate and a quarter-wave plate aligned in front of the collimator is necessary.

To evaluate the performance of the link stabilization unit, a out-of-loop BOC2 is necessary. The output laser pulse from the link and fresh pulse from OMO are combined into out-of-loop BOC2. Once the in-loop section is locked with the feedback system, the output signals is used for the measurements of short-term timing jitter and long-term drift.

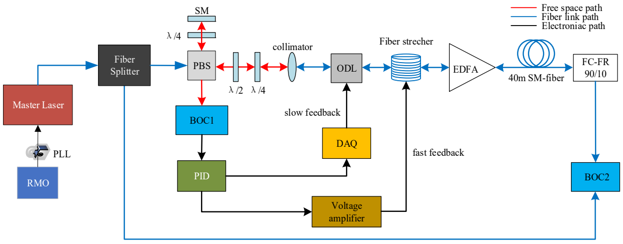

Figure 4: Schematic diagram of experimental setup.

The BOC mainly consists of a dichroic mirror, a single periodically-poled KTiOPO4 (PPKTP) crystal (1 mm×2 mm×4 mm), and a balanced photodetector (Thorlabs PDB210A). The combined reference and fiber link pulses with orthogonal polarization states are transmitted through a dichroic mirror, which transmits the input pulse (1550 nm) and reflects the second harmonic pulse (775 nm). The back surface of the crystal is dichroic coated, which transmits the second harmonic pulse and reflects the input pulse. The output from the balanced photodetector is processed by a PID controller and divided into two paths: fast feedback and slow feedback. The fast feedback path is amplified by a voltage amplifier to control fiber stretcher, and the slow feedback path sampled by a data acquisition card and to control the motorized optical delay line with a turning range of 560 ps.

EXPERIMENTAL RESULTS

First, we measured the sensitivity of both in-loop and out-of-loop BOCs. The time delay curves of both BOCs are showed in Fig. 5(a) and Fig. 5 (b). The highest sensitivity of in-loop BOC is up to 6.4 mV/fs with the input power about +14.6dbm, and the out-of-loop sensitivity is about 2 mV/fs, with +11dbm reference power and +10dbm link output power.

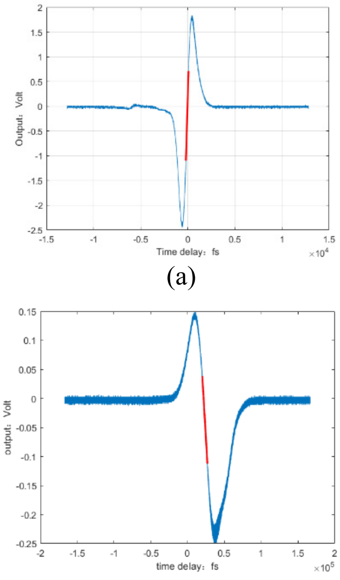

(a)

(b)

Figure 5: Error out from in-loop and out-of-loop BOCs.

After stabilized the fiber link using the feedback system, the voltage noise spectral density has been measured by the baseband analyzer E5052B, and the analysed timing jitter result is RMS=3.17 fs from 1 Hz to 1 MHz, as is shown in Fig. 6.

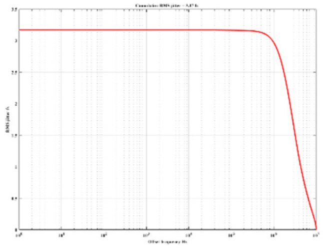

Figure 6: Analysed results of timing jitter.

CONCLUSION

We have setup a fiber link stabilization unit in laboratory to femtosecond timing synchronization system for SHINE project, and the performance have been measured. But considering our present system performed with the single mode fibers (SMF) maybe not reach the long-term stabilization requirements because of the polarization-mode-dispersion, we will update the SMF to polarization maintaining fiber (PMF) to improve the whole system performance to stabilize the kilometers-long fiber for SHINE project in the future.

ACKNOWLEDGEMENTS

This work was supported by Shanghai Municipal Science and Technology Major Project (Grant No. 2017SHZDZX02).

REFERENCES

[1] Kemal Safak *et al.*, “A pulsed-optical timing distribution system for LCLS-II”, in *Proc. Conference on Lasers and Electro-Optics (CLEO’20)*, Washington, DC, United States, May, 2020.

[2] M. Y. Peng *et al.,* “Balanced optical-microwave phase detector for subfemtosecond optical-RF synchronization”, *Opt. Express*, vol. 22, pp. 27102-27111, 2014.

[3] C. Sydlo *et al.*, “Femtosecond Timing Distribution at the European XFEL”, in *Proc. 37th Int. Free Electron Laser Conf. (FEL'15)*, Daejeon, Korea, Aug. 2015, pp. 669-671. `doi:10.18429/JACoW-FEL2015-WEP047`

[4] F. Zummack *et al.*, “Status of the Fiber Link Stabilization Units at FLASH”, *in Proc. 2nd Int. Beam Instrumentation Conf. (IBIC'13)*, Oxford, UK, Sep. 2013, paper MOPC33, pp. 139-142.

[5] M. Ferianis *et al.*, “Generation and Distribution of Stable Timing Signals to Synchronize RF and Lasers at the FERMI FEL Facility”, in *Proc. 27th Int. Free Electron Laser Conf. (FEL'05)*, Palo Alto, CA, USA, Aug. 2005, paper MOPP041, pp. 134-137.

[6] M. Xin *et al.,* “One-femtosecond, long-term stable remote laser synchronization over a 3.5-km fiber link”, *Opt. Express*, vol. 22, pp. 14904-14912, 2014.

[7] M. Y. Peng *et al.,* “Long-term stable, sub-femtosecond timing distribution via a 1.2-km polarization-maintaining fiber link: approaching 10^{-21} link stability”, *Opt. Express* vol. 21, pp. 19982-19989, 2013.

[8] J. Kim *et al.,* “Long-term femtosecond timing link stabilization using a single- crystal balanced cross-correlator”, *Opt. Letters*, vol 32(9), pp. 1044-1046, 2007.

[9] J. Kim *et al.,* “Drift free femtosecond timing synchronization of remote optical and microwave sources”, *Nature Photonics*, vol. 2, pp. 733-736, 2008.

DEVELOPMENT OF AN ON-LINE BUNCH LENGTH MONITORING SYSTEM AT PLS-II USING AN ULTRAFAST PHOTODIODE

W. Song, Pohang University of Science and Technology, Pohang, Korea
G. Hahn†, D. Kim, Y. Joo, Y. Lee and T. Ha, Pohang Accelerator Laboratory, Pohang, Korea
J. Hwang, Helmholtz-Zentrum Berlin, Berlin, Germany

Abstract

Users of time-resolving experiments at 3rd generation synchrotron light sources deem online bunch length and filling pattern monitoring as an important real-time diagnostic. We developed an on-line monitoring system that can measure bunch lengths and filling pattern using a photodiode, a wideband pre-amplifier, and a sampling digitizer. Two different methods were evaluated to reconstruct the bunch lengths: Gaussian deconvolution method as an approximation scheme and Fourier analysis as a method to restore the original signal by using the power transmission characteristics of the electronic devices in the system, including a bias-tee, a wide band amplifier and cables, as well as the photodiode. A bunch lengthening experiment has been conducted to compare and verify the results of those two methods of the photodiode and the result of the streak camera images by changing the overall gap voltage of the superconducting RF cavities. In this paper, we elaborate upon the said photodiode-based measurement techniques, and present the experimental results.

INTRODUCTION

Pohang Light Source (PLS-II) is a 3rd generation light source and is designed to form a bunch train with 470 RF buckets placed 2 ns apart in a synchrotron of 281.82 m (accelerated RF frequency of 500 MHz, harmonic number of 470). Since 2019, to support time-resolving experiments, PLS-II has applied filling-pattern profiling to operation by selectively injecting electron beams into each bucket to control the amount of charge for each bunch. The 1B diagnostic beamline uses a streak camera to observe longitudinal properties of the beam, such as electron beam filling pattern and bunch length. The streak camera has a high temporal resolution and sensitivity, and so is appropriate for fine longitudinal beam measurements; however, it can only manually monitor specific events due to its incapability of making continuous measurements.

Filling pattern measurement mainly uses a beam position monitor (BPM). However, BPM has low resolution, and the signal sum value from 4 pickups makes signal analysis difficult. To solve this problem, at the 2008 Australian Synchrotron, D. J. Peake measured the filling pattern using a photodiode [1]. During normal operation (250~400 mA) of the PLS-II storage ring, the average RMS bunch length is about 19~21 ps. A high-speed readout system is required to measure the single bunch length. Therefore, we built and tested a diagnostic device that continuously measures bunch length and filling pattern information using an ultrafast MSM (Metal-Silicon-Metal) photodiode.

EXPERIMENTAL SETUP

The simple schematic diagram in Fig.1 (a) presents the filling pattern and bunch length monitoring system with the photodiode. An MSM photodiode (Hamamatsu G4176-03) with a rise time of 30 ps always observes the radiation produced by the bunch train. The optical signal is converted to an electric signal by the photodiode and passes through the Picosecond 5541A 26 GHz bandwidth bias tee and a wide bandwidth amplifier (Mini-Circuits ZX60-14012L) to amplify the low photocurrent. A Pico Technology Picoscope 9404-16, a sampling digitizer, was used as the readout device. Picoscope 9404-16 has a maximum 2.5 TS/s random sampling and 500 MS/s real-time sampling, and 16 GHz analog input bandwidth is suitable for filling pattern and bunch length measurement.

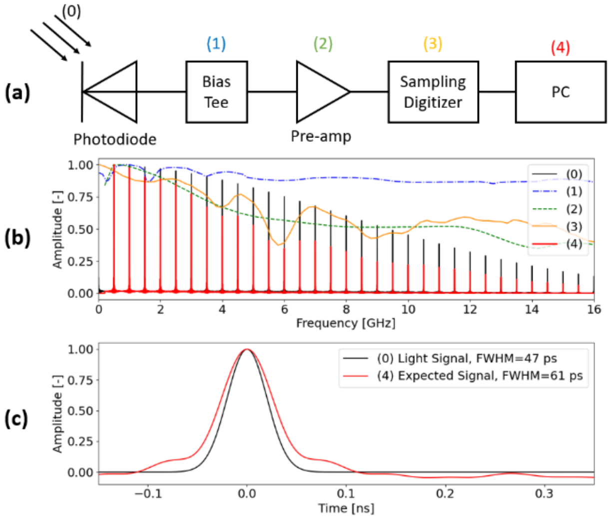

Figure 1: Experimental configuration and signal flow. Synchrotron radiation(0) is incident on the photodiode. The signal passed through the bias tee(1) and amplifier(2) is sampled by the sampling digitizer(3) then, the signal measured by the PC(4) is read. (b) When a Gaussian signal (0) with a standard deviation of 20 ps is input, the spectrum of the signal in (0), (4) and the gain of (1), (2), (3) electronics. (c) The original signal is distorted as it passes through the electronics.

ANALYSIS METHOD

Single bunch length is about 20 ps, and when converted to a frequency band, the bandwidth (-3 dB) is about 10 GHz. The high frequency broadband signal is difficult to accurately measure bunch length because the bandwidth and time constant of electronics are distorting the original

---

† garam@postech.ac.kr

ISBN: 978-3-95450-230-1 ISSN: 2673-5350 doi:10.18429/JACoW-IBIC2021-WEPP10

signal. Figure 1(b) shows the signal distortion process by bandwidth in a bunch length monitoring system. The length and waveform of the gaussian signal change as in (c) due to the gain of bias tee, amplifier, scope, and cable.

The impulse response function was used as the deconvolution kernel for original signal restoration. Assume an input signal(synchrotron radiation) is x(t) and the readout signal is y(t), y(t) can be expressed as a convolution of x(t) and the system response function h(t):

$$y(t) = x(t) * h(t) = \int x(\tau)h(t-\tau)d\tau \; . \qquad (1)$$

Assuming that both the input signal and the system response function are Gaussian pulses since Gaussian has semigroup properties, the standard deviation of each signal in Eq. (1) is,

$$\sigma_y^2 = \sigma_x^2 + \sigma_h^2, \qquad (2)$$

where σ_y^2, σ_x^2, and σ_h^2 is standard deviation of y, x, and h, respectively.

System response function h(t) consists of the response of N electronics by

$$h(t) = \sqrt{\sum_{i=1}^{N} h_i^2(t)}.$$

However, since information on $h_i(t)$ of each electronics is not required, we can obtain the basis function from the overall system response. If x(t) is a delta function, Eq. (1) is

$$y(t) = x(t) * h(t) = \delta(t) * h(t) = h(t). \qquad (3)$$

Therefore, we measured the RMS length of the basis function h(t) to be 29 ps using a femtosecond laser. It means that if we measure an electron beam length with 20 ps, a scope shows a bunch length with 35 ps by Eq. (2).

As a method of correcting signal distortion due to the gain characteristics of electronics shown in Fig. 1(b), the loss due to attenuation was compensated for using the scattering parameter. In this method, the necessary information is the forward voltage gain in the circuit, so S_{21} of each part was measured using a vector network analyser. The analog bandwidth of the sampling digitizer was estimated by inputting a constant input power using a signal generator and converting the output voltage measured by the digitizer to calculate the attenuation. Fig. 1(b) shows the gain measurement of each electronic including sampling digitizer. Here, we can see attenuation is large at a specific frequency. This underestimates the input power at some frequencies of the broadband signal, resulting in a distorted signal.

Next, a streak camera was used to verify the deconvolution method and to calibrate the results measured by the photodiode. In PLS-II storage ring, jitter of the main RF is about 70 fs, jitter of ¼ rf divider is 465 fs, and Fig. 2(a) shows that 1 sigma length of point spread function of the streak camera is about 3.75 ps. These values were used to find the basis function of the streak camera. Fig. 2(b) is an image taken by accumulating bunch trains under the RF gap voltage of 3 MV and 200 mA operating conditions in the PLS-II storage ring, and the average bunch length is 22 ps.

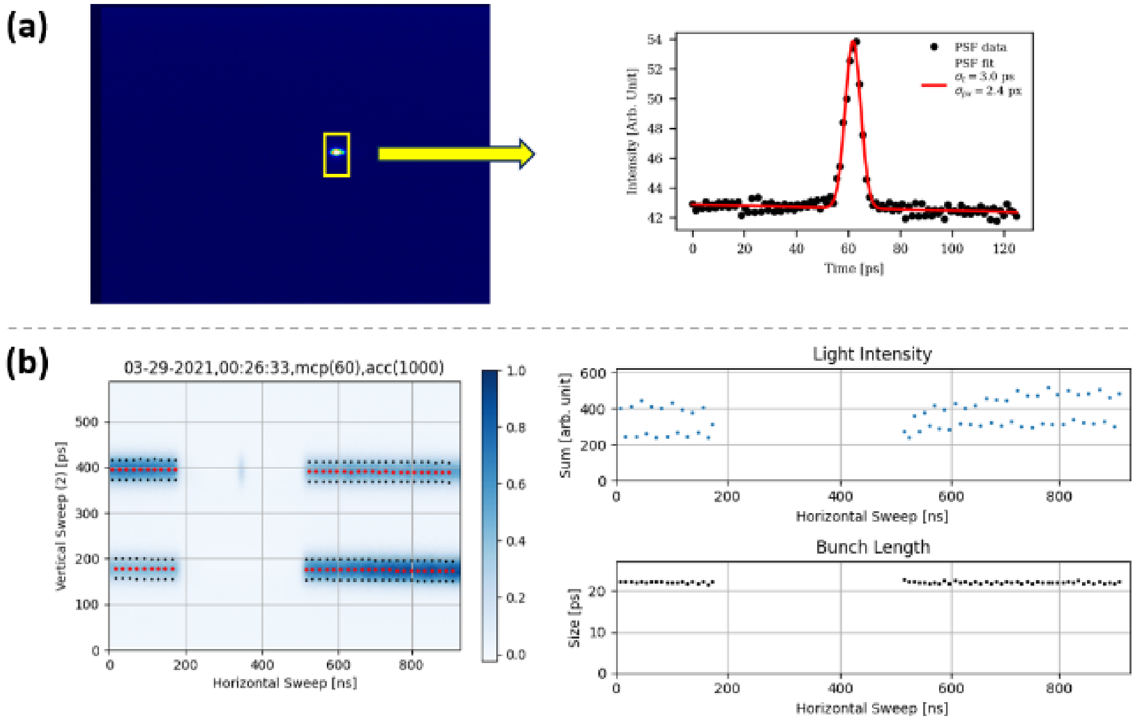

Figure 2: (a) Streak camera focus mode image (left) and PSF obtained by fitting the data (right). (b) Data obtained by accumulating 1000 images of synchrotron radiation by a bunch train with a total length of 1us (left) and each electron bunch length (right).

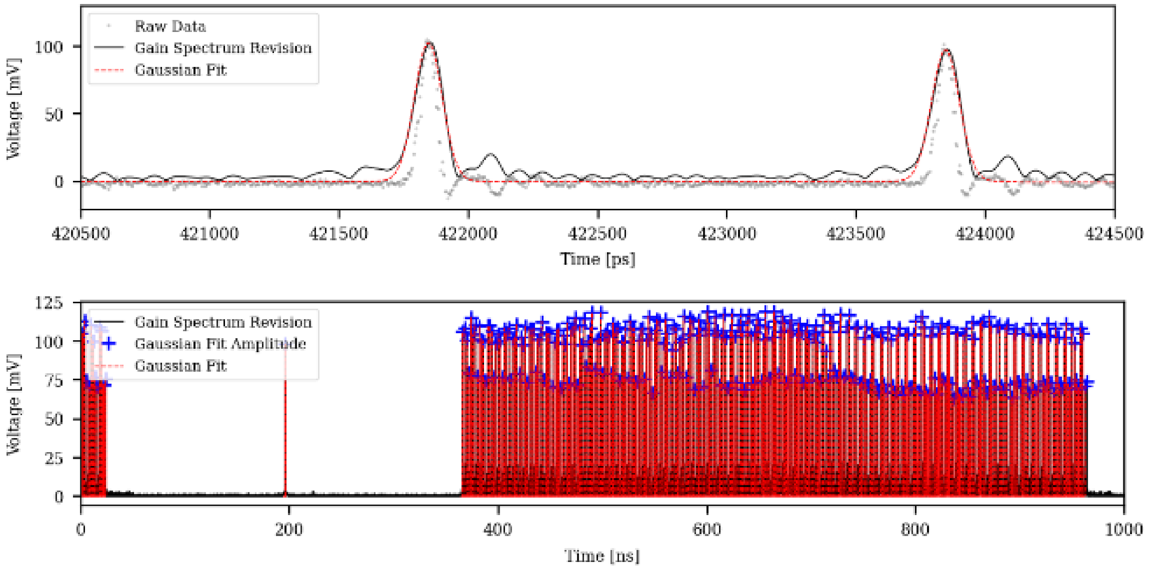

Figure 3: A picture of measuring the filling pattern (above) of a 1us-long bunch train under the 3 MV, 200 mA operating condition using a photodiode and an enlarged part of the filling pattern (below). The gain is compensated (black line) for the data sampled at 250 kS/se (gray dot) and then processed through Gaussian fitting (red dash line).

EXPERIMENTAL VERIFICATION

The signal measured by the photodiode is restored to the original signal using signal analysis, and the result is shown in Fig. 3. The sampling digitizer data do not show a Gaussian distribution as expected. Therefore, the gain (see Fig. 1(b)) compensates for the measured signal, and the resulting profile is Gaussian-fitted. The processed signal shows the filling pattern well in the graph below in Fig. 3.

We conducted experiments to verify and calibrate the analysis method by changing the electron beam bunch length in the PLS-II storage ring. Two parameters were varied in order to change the bunch length: the main RF cavity gap voltage and the beam current [2][3]. In normal operation, when the gap voltage decreases, the bunch length becomes longer [4], so we measured the bunch length by changing the total gap voltage from 3 MV to 2.2 MV at 200 kV intervals. Figure 4 shows the bunch length measured with a streak camera, and the bunch length increases when the gap voltage is lower.

The bunch length measurement result obtained without signal processing is shown in Fig. 5 (a). The fitting curve meets on the y-axis because when the bunch length decreases, it is predicted to saturate to a constant value due to the basis function h(t) of Eq. (3). The y-intercept is 25 ps, which is shorter than the length of the basis function of 29 ps. On the other hand, the distribution of the measured values in the normal operation section with a bunch length of 20-25 ps is dense, and when the length measured with a streak camera is 22 ps, the measured value of the photodiode is 29.90±0.15 ps. Fig. 5 (b) shows the result of applying the deconvolution method to the raw data in Fig. 5 (a). Here, the distortion was corrected with a basis function and the resultant data points were fitted with a linear curve, whose y-intercept was found to be about -15 ps. After gain and basis function correction, the distribution of the measured values becomes wider and the error range is also larger than (a) image one. However, the bunch length of the photodiode is 22.05±0.96 ps in the bunch length 22 ps measured with a streak camera, which is a good prediction value.

We explore the discrepancy in the two graphs and y-intercept mismatching. The gain was measured separately for each component and used for a bunch lengthening experiment and basis function measurement, so there is a possibility that the spectrum can be changed. For example, the result of compensating the gain by FFT of the filling pattern shown in Fig. 3 increased excessively in the vicinity of 6 GHz, and the attenuation was relatively large above 11 GHz. Another cause is that the optical gain of the photodiode, which has the longest rise time in the circuit and is expected to have a large effect on signal distortion, is not considered. We expected that the basis function measurement would show the characteristics of the photodiode well, but the predicted values did not fit well as shown in Fig. 5. Therefore, a more accurate method of correcting the characteristics of the photodiode should be considered.

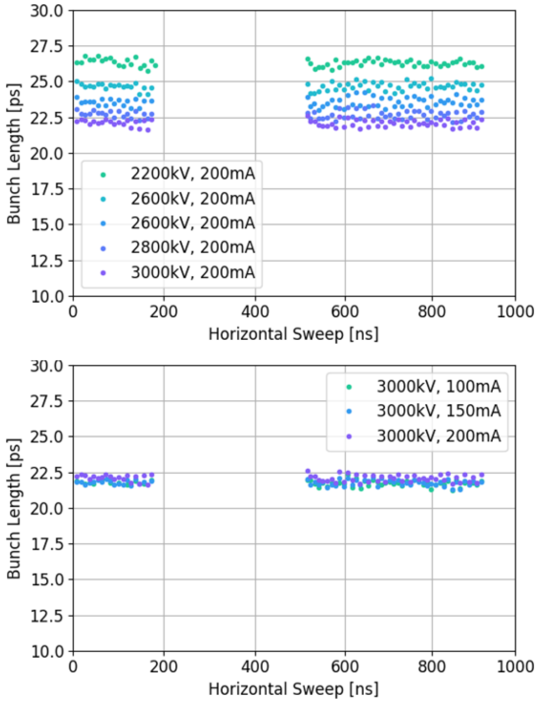

Figure 4: Changes in bunch length according to varying RF gap voltage (above) and beam current (below) measured with a Streak camera. When the total RF gap voltage is increased from 2.2 MV to 3 MV, the average bunch length in each condition decreases to 26.3, 24.7, 23.6, 22.7, and 22.1 ps.

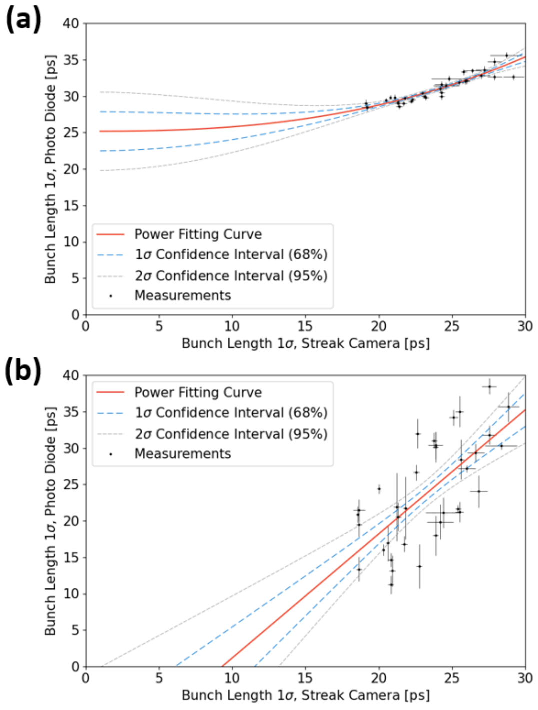

Figure 5: Bunch length measured by a photodiode and streak camera when RF gap voltage and beam current are changed. (a) Bunch length obtained directly from raw data without signal processing. (b) Bunch length calculated by applying the deconvolution method (gain and basis function correction).

CONCLUSION

In this paper, we design and test a system that can continuously measure filling patterns and bunch lengths in PLS-II storage rings. Several methods were used to recover the original signal to measure the exact bunch length. Bunch length measurement using a photodiode is an inexpensive and simple method. Since the calibration results were well measured up to the operating range, on-line measurement results will be provided to beamline users.

REFERENCES

[1] D. J. Peake, M. J. Boland, G. S. LeBlanc, and R. P. Rassool, “Measurement of the real time fill-pattern at the Australian Synchrotron”, *Nucl. Instrum. Meth. A*, vol. 589, pp. 143-149, 2008, `doi:10.1016/j.nima.2008.01.072`

[2] Y. Joo, I. Yu, I. Park, M.H. Chun, and Y. Sohn, “Reduction of RF accelerating voltage of Pohang Light Source-II superconducting RF cavity for stable top-up mode operation”, *Journal of Instrumentation*, vol. 12, p. P03025, 2017.

[3] Youngdo Jo *et al.*, “Studies and optimization of Pohang Light Source-II superconducting radio frequency system at stable top-up operation with beam current of 400 mA”, *Journal of Applied Physics*, vol. 116, p. 233301, 2014. `doi:10.1063/1.4904188`

[4] A. Wolski, “Low emittance machines,” Lecture at CAS September 2007, Daresbury, UK, 2007.

BROADBAND CHARACTERIZATION OF A COMPACT ZERO-BIAS SCHOTTKY DIODE DETECTOR WITH A CONTINUOUS WAVE THz SYSTEM*

R. Yadav†,1, S. Preu, Terahertz Devices and Systems, TU Darmstadt, Darmstadt, Germany
A. Penirschke, High Frequency Tech., Mittelhessen Univ. of Applied Sciences, Friedberg, Germany
1also at High Frequency Tech., Mittelhessen Univ. of Applied Sciences, Friedberg, Germany

Abstract

Over the last few decades several types of Terahertz (THz) detectors have been developed to maturity, paving the way for various potential applications such as diagnostics of THz generation at particle accelerators. An important class are zero-biased Schottky diode THz detectors that are frequently applied at accelerator facilities for operation at room temperature. Zero-biased Schottky diode THz detectors are having lower noise compared to biased ones due to the absence of shot noise. Here we demonstrate the sensitivity of Schottky detectors using a commercial continuous wave photomixing THz system as source. Both, a commercially available as well as a research-grade compact quasi-optical detector with improved video bandwidth are compared from 0.05 to 1.2 THz in terms of sensitivity. At 1 THz, the research grade quasi optical detector shows 7 dB higher dynamic range than the commercial one.

INTRODUCTION

Terahertz (THz) radiation generated either from Free Electron Lasers (FELs) or by Coherent Synchrotron Radiation (CSR) sources with high brilliance and power open doors for research and applications(low and high power) in THz domain [1]. Ultra-short pulses with picosecond length are available at several FELs have higher power compared to other table top THz sources and provide the opportunity for characterizing targets at atomic scale and beyond [2, 3]. Optical pump-probe THz (or vice versa) experiments are frequently applied to study matter and materials. These experiments are affected from time jitter as there is no natural phase locking, so that electro-optical sampling is not optimized to use in such cases. This means direct detectors have to be used. For studying the transient behavior, however, the detectors have to be sufficiently fast, with a time constant of the order of a few ps at least. Bolometers and hot-electron detectors [4] are not suitable for such studies. Also, Bolometers need to operate at cryogenic conditions which make the whole setup big, bulky and expensive. Schottky diode- [5,6] and Field Effect Transistors (FETs)-based [2, 3] are handy, easy to use, plug-play and less expensive operating costs compared to their cryogenic counterparts with reported time constants in the range of 6-20 ps [3, 5].

Continuous wave (CW) sources are such as FEL, photomixers and p-i-n diode can be used as THz sources [7] for various experiments such as spectroscopy, medical imaging, communication etc. The available Schottky diodes and FETs THz detectors can be used for these applications. Schottky diodes can rectified the signal upto the cut-off frequencies, while FETs can be used far beyond their cut-off frequencies in higher THz domain. Both are faster and sensitive compared to other counterparts available to the date. In this work, we characterize the zero-bias Schottky diode detectors: Both commercial available and modified research graded [5, 8]. The dynamic range of both are detectors is compared. This is part of the ongoing work for optimizing the Schottky diode and FETs THz detectors for applications at Particle accelerators and in future in other domains too.

THEORY

The Schottky barrier diode consists of metal-semiconductor junction. Quasi-vertical schottky barrier diodes [9] developed by ACST GmbH has been used in both, the commercial and the research grade THz detectors. The cross section is shown in Fig. 1.

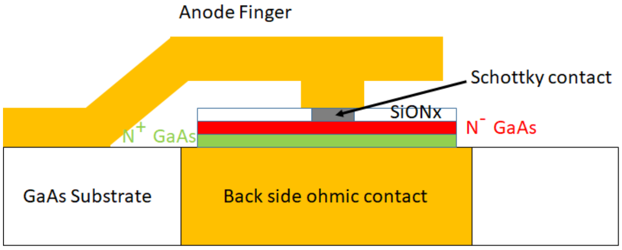

Figure 1: Cross section schematic of a qausi-vertical Schottky diode [9].

The diode is fabricated on a Gallium Arsenide (GaAs) substrate. The Anode and cathode are vertically fabricated, in contrast to the traditional horizontal contacting. This reduces the parasitic capacitance and series resistance. The quasi-vertical structure helps to keep the field distribution uniform across the anode finger and prevents current overloading when the ohmic contact is small, opposite to what' there in case of Whisker-contacted Schottky diodes. Also, quasi-vertical structures help to keep the noise level low compared to Whisker-contacted as the anode and ohmic contact are not located on the same plane, reducing the cross link of the fields. The modified Schottky diode reduces

---

* We are grateful to the Hesse ministry of science and culture (HMWK) for funding the position of Mr. Rahul Yadav. Thankful to ACST GmbH for providing the Schottky diode and commercial detector.

† yadav@imp.tu-darmstadt.de

the heating of the device which ultimately improved the power performance. The first version of quasi-vertical type Schottky diode was developed at Technical University of Darmstadt, Germany in 2004 [10]. The back side ohmic contact provides as opportunity for flip chip mounting of the diode using up-side-up concept, instead of up-side-down as in case if both electrodes are located in the same plane. The fabricated Schottky diode is shown in Fig. 2.

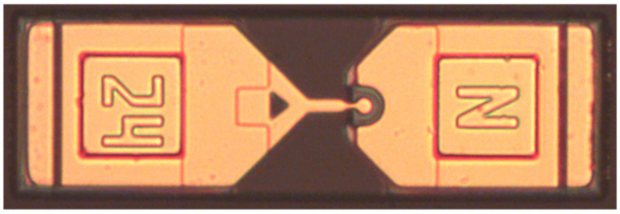

Figure 2: Fabricated quasi-vertical Schottky diode [9].

Theoretically, the majority charges (electrons) are responsible for the conduction of current in metal-semiconductor junction.

In the conduction mode, the Schottky model thermionic current is given by [11]:

$$I = I_s[\exp(\frac{q \cdot V_F}{n \cdot K \cdot T}) - 1] \qquad (1)$$

where, I_s is the saturation current, q is electronic charge, V_F is forward bias, K is Boltzmann's constant, T is absolute temperature. In the ideal case n is equal to 1. Due to the quasi-vertical structure of Schottky diode these limitations has been rectified by improving the heat sink and field distribution uniformly over the anode finger and the ohmic contact located on the back plane. The cross link of fields between meta-semiconductor is decreased by using the quasi-vertical structure. The non-linearity of Eq. 1 is used for THz detection.

CHARACTERIZED DEVICES

In this paper we characterized two types of packaged devices: one with lower video bandwidth (SMA connector) and a research grade detector with improved Bandwidth (K connector) as the output from the Schottky diode. In Fig. 3, the block diagram of SMA connector mounted THz detector is shown. A collimated lens with 12 mm diameter is used to couple the THz radiation and focus onto the silicon substrate mounted (of 500 µm thick) log spiral antenna coupled Schottky diode that is mounted on the back of the lens. The rectified signal is taken out from the pads of log spiral antenna and connected to the video path. The research grade detector has a video path using 25mil rogers substrate for transition from antenna contact pads to K connector. The block diagram is otherwise identical to the commercial device.

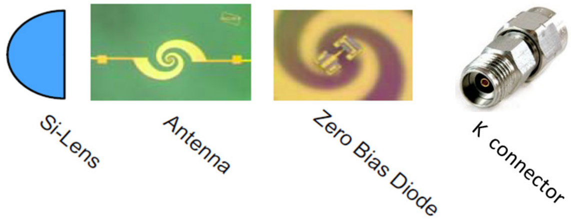

Figure 3: Block diagram of the research grade K connector-mounted THz detector.

One optimization criterion is the maximum IF frequency. The higher the video bandwidth, the shorter pulses can be detected. The commercial available one has 18 GHz of video bandwidth (limited by SMA connector), while the K mounted research graded one has 40 GHz of video bandwidth. The THz bandwidth of both is 50 GHz to 2 THz.

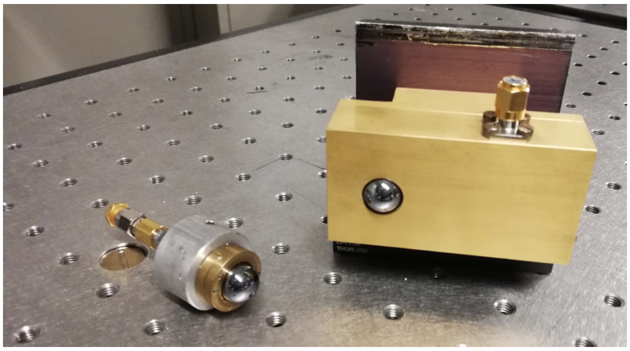

Figure 4: Left: K mounted Schottky diode THz detector, Right: SMA mounted Schottky diode THz detector.

In Fig. 4, the photo of both THz detectors is shown. A further optimization criterion was compactness: the research grade device is strongly reduced in size as compared to the commercial device. The smaller size of detector gives the flexibility for handy use at room temperature without needing much space in the experimental setup.

EXPERIMENTAL SETUP

A commercially available Continuous wave (CW) THz photomixer source from Toptica Photonics AG was used to characterize the detectors. The experimental setup is shown in Fig. 5.

A commercial pin-diode transmitter was used as source, shown by the yellow tag in Fig. 5. Parabolic mirrors and TPX THz lenses are used to align the THz beam and focus it onto the Schottky diode receivers. This setup also helps to get rid of unwanted RF signal which sometimes can couple in through the Silicon lens at THz detector. The recified signal of the THz detector is connected to a Transimpedance amplifier (TIA) to amplify the signal with a transimpedance gain of $10^6 \frac{V}{A}$, which was read out by the lock-in amplifier afterwards. The pin-diode-based transmitter shows a strong roll-off towards 1 THz, with about 20 dB lower power at 1 THz as compared to 200 GHz.

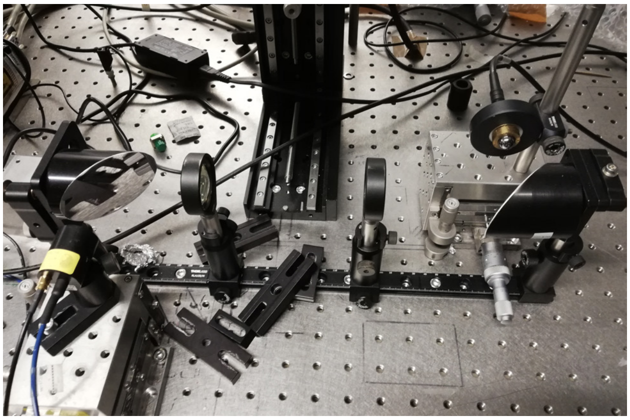

Figure 5: Experimental setup for the THz detectors characterization with Continuous Wave (CW) source.

RESULTS AND DISCUSSIONS

The rectified signal using both detectors is shown in Fig. 6.

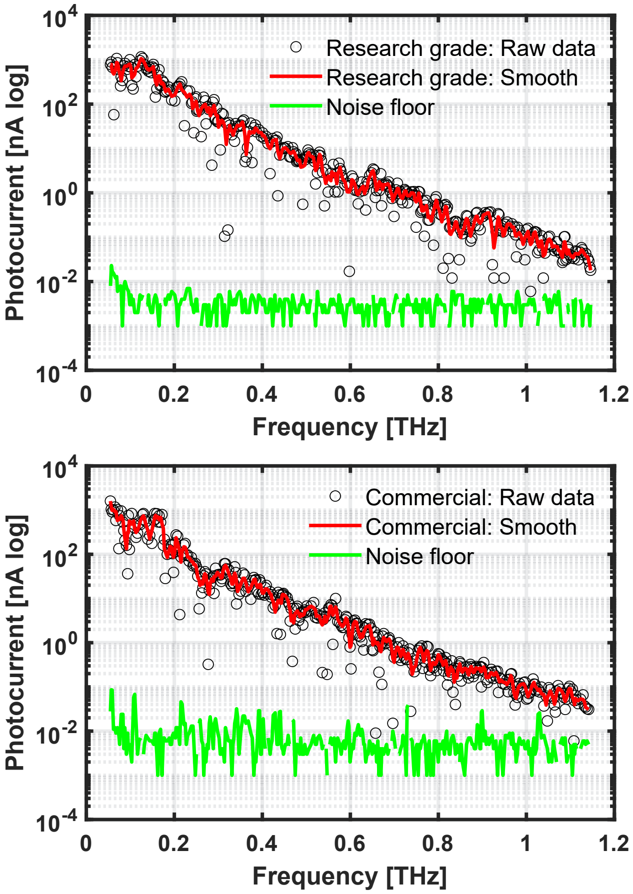

Figure 6: Top: Rectified signal from the research grade detector, Bottom: Rectified signal from the commercial detector.

The research grade (K mounted) detector features a slightly higher rectified signal over the whole frequency range compared to commercial (SMA mounted) one. Its main advantage, however, is reduced noise floor. The dynamic range (DR) is defined as follows:

$$DR\ [dB] = 20 \cdot log_{10}\left(\frac{Rectified\ signal}{Noise\ floor}\right) \tag{2}$$

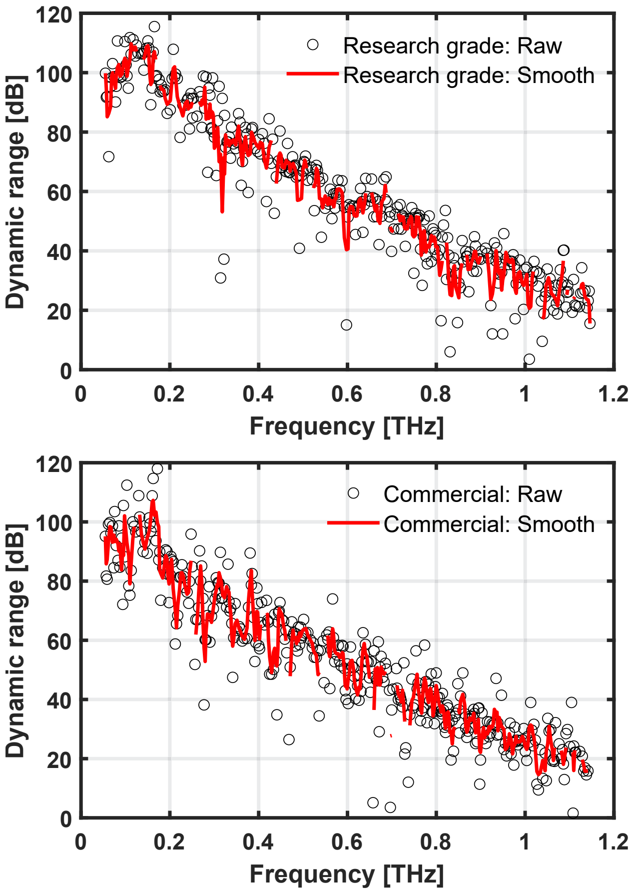

Figure 7: Top: Dynamic range of research grade detector, Bottom: Dynamic range of commercial detector.

In Fig. 7, dynamic range of both the connectors is shown. For the K connectorized device, 111 dB at 110 GHz is obtained compared to 105 dB for the SMA connectorized detector. In General in range of 50 to 180 GHz, the smoothed dynamic range just touches 100 dB fort the SMA device and slightly above 100 dB for the K-connectorized device. At 1 THz, research grade device offers 33 dB of dynamic range as compared to 26 dB by commercial one.

Phase versus frequency response for K mounted detector is shown in Fig. 8. Over the course from 0.1 THz to 1 THz, the maximum phase change is only three degrees. It is almost constant between 0.5 and 0.9 THz.

The characterized detectors in this paper along with the modified video chain detector was used to detect the pulse at FELBE HZDR, Dresden, Germany. The results were published in [5] as shown in Fig. 9. The K mounted (compact housing) research grade detector records a 16.8 ps pulse width very close to the expected pulse widht , whereas the SMA mounted (commercial) showed a severely broadened pulse with a width of 39.2 ps, proving the improved IF bandwidth of the research-grade device.

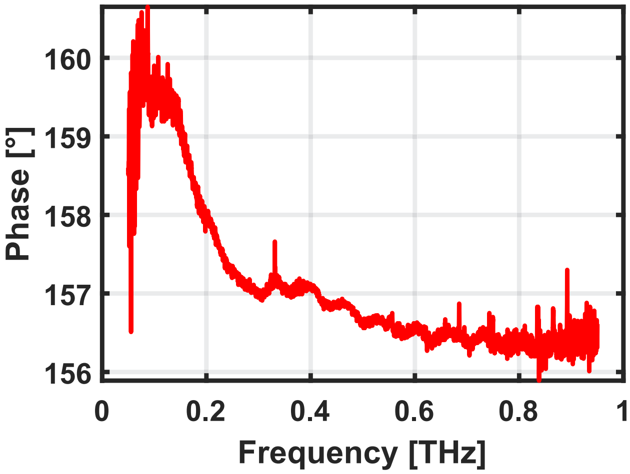

Figure 8: Phase of rectified signal from research grade detector.

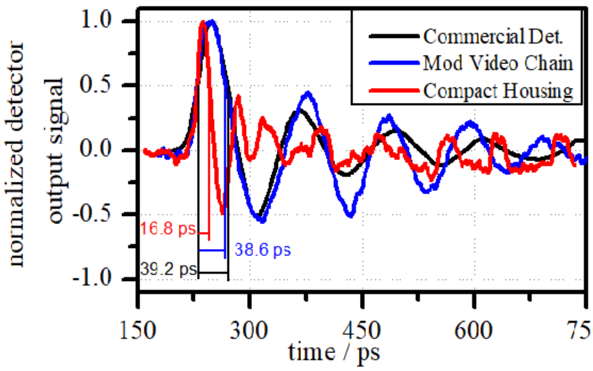

Figure 9: Detector characterization at 1.3 THz at FELBE, HZDR, ©2014 IEEE reprinted with permission from [5].

CONCLUSIONS

In this paper, we showed the broadband characterization of commercial and research grade zero-bias Schottky diode THz detectors using a CW source. The K-connectorized device with improved IF path features a slightly higher dynamic range at 1 THz. With higher power at FELBE, we can detect much shorter pulses and higher video-bandwidth with the research grade device as compared to the commercial detector.

REFERENCES

[1] E. J. Jaeschke, S. Khan, J. R. Schneider and J. B. Hastings, *Synchrotron light sources and free-electron lasers: Accelerator physics, instrumentation and science applications*, 2nd Edition, Cham: Springer International Publishing, 2020. `doi:10.1007/978-3-030-23201-6`

[2] S. Preu, M. Mittendorff, S. Winnerl, O. Cojocari and A. Penirschke, "THz Autocorrelators for ps Pulse Characterization Based on Schottky Diodes and Rectifying Field-Effect Transistors", *IEEE Transactions on Terahertz Science and Technology*, vol. 5, no. 6, pp. 922-929, Nov. 2015. `doi:10.1109/TTHZ.2015.2482943`

[3] S. Regensburger, S. Winnerl, J. M. Klopf, H. Lu, A. C. Gossard and S. Preu, "Picosecond-Scale Terahertz Pulse Characterization With Field-Effect Transistors", *IEEE Transactions on Terahertz Science and Technology*, vol. 9, no. 3, pp. 262-271, May 2019 `doi:10.1109/TTHZ.2019.2903630`

[4] A. D. Semenov, H. Hubers, K. S. Il'in, M. Siegel, V. Judin and A. Muller, "Monitoring coherent THz-synchrotron radiation with superconducting NbN hot-electron detector", in Proc. *2009 34th International Conference on Infrared, Millimeter, and Terahertz Waves*, 2009, pp. 1-2. `doi:10.1109/ICIMW.2009.5324688`

[5] A. Penirschke, M. Soboryntskyy, S. Preu, M. Mittendorff, S. Winnerl, M. Hoefle, O. Cojocari and R. Jakoby, "Compact quasi-optical Schottky detector with fast voltage response", in Proc. *2014 39th International Conference on Infrared, Millimeter, and Terahertz waves (IRMMW-THz)*, 2014, pp. 1-2. `doi:10.1109/IRMMW-THz.2014.6956027`

[6] A. Semenov, H.-W. Hübers, A. Pohl, O. Cojocari, M. Sobornytskyy,A. Hoehl, R. Müller,M. Ries, G. Wüstefeld, "Schottky Diode Detectors for Monitoring Coherent THz Synchrotron Radiation Pulses", in *Proc. 5th Int. Particle Accelerator Conf. (IPAC'14)*, Dresden, Germany, Jun. 2014, pp. 3465–3467. `doi:10.18429/JACoW-IPAC2014-THPME097`

[7] S. Preu, G. H. Döhler, S. Malzer, L. J. Wang, and A. C. Gossard , "Tunable, continuous-wave Terahertz photomixer sources and applications", *Journal of Applied Physics*, vol. 109, p. 061301, 2011. `doi.org/10.1063/1.3552291`

[8] M. Hoefle, A. Penirschke, O. Cojocari and R. Jakoby, "Broadband zero-bias Schottky detector for E-field measurements up to 100 GHz and beyond", in Proc, *2013 38th International Conference on Infrared, Millimeter, and Terahertz Waves (IRMMW-THz)*, 2013, pp. 1-2, `doi:10.1109/IRMMW-THz.2013.6665893`

[9] I. Mehdi, J. V. Siles, C. Lee and E. Schlecht, "THz Diode Technology: Status, Prospects, and Applications", in *Proceedings of the IEEE*, vol. 105, no. 6, pp. 990-1007, June 2017. `doi:10.1109/JPROC.2017.2650235`

[10] O. Cojocari, C. Sydlo, H.-L. Hartnagel, S. Biber, J. Schur, and L.-P. Schmidt, "Schottky–structures for THz-application based on quasi-vertical design-concept", in Proc. *16th Int. Symp. Space THz Technol.*, pp. 490–495, May2005.

[11] A. Y. C. Yu, "The metal-semiconductor contact: an old device with a new future", *IEEE Spectrum*, vol. 7, no. 3, pp. 83–89.,March 1970.

ISBN: 978-3-95450-230-1 ISSN: 2673-5350 doi:10.18429/JACoW-IBIC2021-WEPP12

MODAL ANALYSIS OF ELECTROMAGNETIC COUPLING BETWEEN SMA-FEEDTHROUGH ELECTRODE AND BEAM FOR WIDEBAND BEAM MONITOR

T. Suwada*, High Energy Accelerator Research Organization (KEK),
also at SOKENDAI (The Graduate University for Advanced Studies), Tsukuba, Japan

Abstract

The direct simultaneous detection of electron (e^-) and positron (e^+) bunch signals was successfully performed for the first time by a wideband beam monitor at the e^+ capture section of the SuperKEKB factory. This monitor can measure a time interval between the e^- and e^+ bunches, their bunch lengths, bunch intensities, and transverse beam positions, depending on the phase of accelerating structures. For this purpose, a new beam monitor with wideband pickups simply using SMA feedthroughs and a wideband detection system based on a real-time oscilloscope was developed to investigate their capture process at the capture section and to maximally optimize the e^+ intensity. The required specification for the new monitor is to simultaneously detect the e^+ and e^- bunches generated in the capture section within the resolution of pico-second level with a sufficient dynamic range in the time-interval and bunch-length measurements. In this report, the basic design and numerical results based on a modal analysis of electromagnetic couplings between SMA-feedthrough and beam are in detail given.

INTRODUCTION

The SuperKEKB B-factory [1] (SKEKB) is a next-generation B-factory that is currently in operation at KEK, after the KEK B-factory [2] (KEKB) was discontinued in 2010. The SKEKB is a e^+e^- collider with asymmetric energies; it comprises 4 GeV e^+ (LER) and 7 GeV e^- (HER) rings. The target luminosity (8×10^{35} cm^{-2}s^{-1}) of the SKEKB, that is, the rate of e^- and e^+ collisions, is 40 times the peak luminosity of the KEKB. To improve the collision rate, the development of a powerful and stable e^+ source is one of the key elements in this experiment. The SKEKB injector linac [3] is an e^-/e^+ linear accelerator for the SKEKB; the KEKB injector linac [4] was upgraded for the abovementioned purpose. The requirements for the injector linac are full energy injection into the SKEKB rings with the e^- and e^+ bunch charges of 5 and 4 nC, respectively. The injector linac should deliver high-current e^+ beams to the SKEKB. The e^+ production and capture section are described in detail elsewhere [3].

Since both the electrons and positrons with approximately equivalent amounts of bunch charges are generated at the target, not only the positrons but also the electrons are simultaneously captured and accelerated (or decelerated) in the capture section with a certain time interval that is dependent on the operational condition of the capture section. The time interval between the e^- and e^+ bunches is very short with a time range from 135 to 265 ps.

The time interval between the e^- and e^+ bunches, their bunch lengths and intensities for each e^- and e^+ bunch are very important parameters that can be fundamentally investigated on the basis of detailed beam dynamics at the capture section. However, they have never been measured because the time interval is too short to detect them independently, while they are generally simulated on the basis of beam dynamics in multidimensional transverse and longitudinal phase spaces. Thus, it is a challenging to experimentally verify and elucidate complicated beam dynamics for both positrons and electrons in the capture section in order to fully understand them and to maximize the e^+ intensity under an optimized operation condition.

For this purpose, new beam monitors with not only wideband pickups but also a wideband detection system were installed at the capture section to simultaneously detect e^- and e^+ signals during the summer shutdown of 2019. They are essential diagnostic instruments to fully investigate the e^- and e^+ capture process and to maximally optimize the e^+ intensity. Both the electrons and positrons generated at the target are formed into their steady bunched beams through their phase slip process in accelerating structures of the capture section. Thus, the experimental tests were successfully carried out at the e^+ capture section of the injector linac [5].

In this report a very wideband beam monitor with SMA-feedthroughs has been designed, and the modal analysis of electromagnetic coupling between SMA-feedthrough and beam is described on the basis of analytical methods with electromagnetic couplings between two coaxial structures.

WIDEBAND BEAM MONITOR SYSTEM

Mechanical Structure

A photo picture of the wideband beam monitor is shown in Fig. 1.

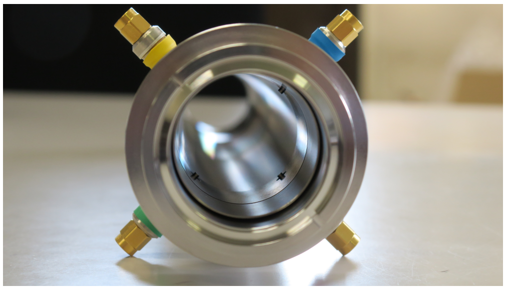

Figure 1: Photograph of the new beam monitor.

---

[*] tsuyoshi.suwada@kek.jp

The total length of the monitor including two bellows and quick-release flange couplings (KFS-NW40, EVAC AG) at both ends is 431 mm, and the inner diameter is 38 mm. The inner surface of the front bellows is covered with a cylindrical pipe to remove the irregularity in order to suppress any wakefield effects caused at the monitor front as much as possible. The pickups of the monitor are made of SMA-type vacuum feedthroughs composed of a central conductor pin made of Kovar and a dielectric substance made of ceramic. The pickups have good frequency characteristics, which were tested in the frequency region greater than 10 GHz. The four pickups, two horizontal and two vertical, are mounted on the upstream of the monitor with $\pi/2$ rotational symmetry. Thus, this monitor can also work as beam position monitor (BPM). The tips of the center pins protrude for a length of 1 mm toward the monitor center from the inner surface of the monitor in order to have its good frequency response.

Signal Detection System

A schematic drawing of the signal detection system is shown in Fig. 2.

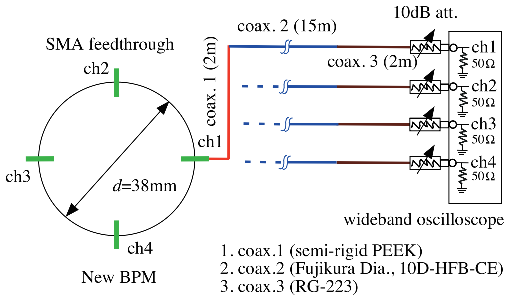

Figure 2: Signal detection system of the new monitor.

The beam signal can be detected with four SMA feedthrough electrodes and the four signals are sent directly to a wideband oscilloscope with four channels through 10-dB attenuator in front of each channel. One coaxial cable comprises 2m-long semirigid coaxial with its insulator of polyether ether ketone ($\epsilon_r = 3.5$), 15m-long 10D coaxial cable, and 2m-long RG223 cable. The total length of the coaxial is 19 m. The maximum operating frequency is limited at 10 GHz, which is the cutoff frequency of lowest TE mode for the 10D cable.

ELECTROMAGNETIC COUPLING ANALYSIS

Detection Principle

It may be instructive to describe fundamental electromagnetic couplings between two coaxial structures before the coupling between beam and SMA feedthrough. We consider SMA and another coaxial structure as shown in Fig. 3 (*a*).

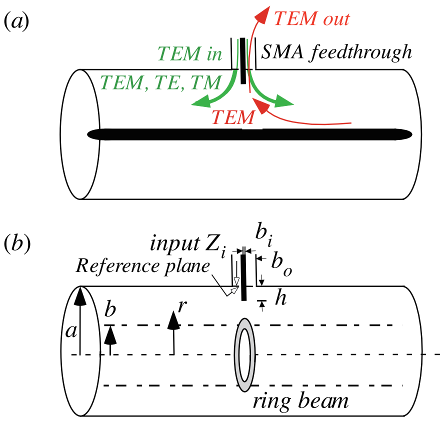

Figure 3: (*a*) Schematic drawing of electromagnetic couplings between SMA feedthrough and coaxial structure. (*b*) Electromagnetic couplings between SMA feedthrough and a thin ring beam. Inner radius of the coaxial structure: $a = 19$ mm, ring-beam radius: b, radii of the SMA inner and outer conductor: $b_i = 0.9$ mm, $b_o = 2.05$ mm, and the characteristic impedance of the SMA is $Z_0 = 50\ \Omega$.

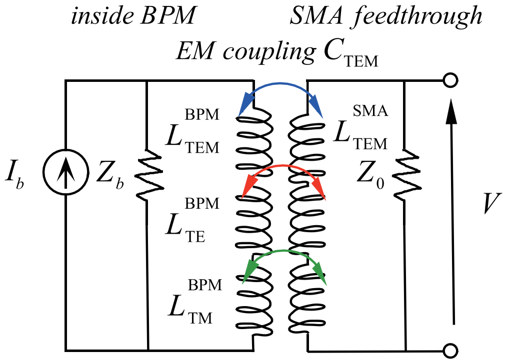

Figure 4: Equivalent circuit of electromagnetic couplings between SMA feedthrough and coaxial structure. The arrows indicate the couplings between TEMs (blue), TE and TEM (red), and TM and TEM (green).

If the SMA is excited by an external rf source, the coaxial tube is excited through electromagnetic coupling, which can be in detail described based on a coupling scheme between two coaxial structures [6]. The fundamental TEM and also higher-order TE and TM modes are excited in the coaxial tube at a reference plane defined as a boundary surface between the SMA and coaxial tube, if the excited electromagnetic fields are viewed at the reference plane to the direction of rf transmission from the SMA to the coaxial tube. If the coaxial tube is excited, it can be understood that these higher-order modes are excited at the reference plane in the time reversal process. However, the higher-order modes cannot transmit directly to the SMA due to its higher cut-off frequency. It is thus enough to take into account only the TEM couplings between two coaxial structures, while slight parts of the higher-order modes may be transformed to fundamental TEM at the reference plane. Thus, a scheme is shown by an equivalent circuit with taking into account electromagnetic couplings as shown in Fig. 4.

Based on such a coupling scheme, the coaxial tube may be replaced by a sufficiently thin ring beam, because the equivalent current flow in the coaxial tube is limited on the outer surface of the inner rod. Thus, the coupling between two coaxial structures is equivalent to that between SMA feedthrough and beam. If a gaussian beam in the transverse directions is taken into account, by appropriate integration in the transverse directions, the coupling strength can be numerically calculated.

ANALYTICAL FORMULATION

If SMA feedthrough is excited by an external rf source, TEM excited in a coaxial tube is represented by

$$E_{r_0}(r) = \frac{1}{\sqrt{\ln(a/b)}}\frac{1}{r},\ \ E_{\phi_0}(r) = 0. \tag{1}$$

The higher-order TEs are represented by

$$E_{r_{mn}}(r) = \\ \frac{\sqrt{\pi}(m/r)[J_m(kc_{mn}r)N'_m(kc_{mn}b)-N_m(kc_{mn}r)J'_m(kc_{mn}b)]}{\sqrt{\left(J'_m(kc_{mn}b)/J'_m(kc_{mn}a)\right)^2[1-(m/kc_{mn}a)^2]-[1-(m/kc_{mn}b)^2]}}, \tag{2}$$

$$E_{\phi_{mn}} = \\ \frac{\sqrt{\pi}(kc_{mn})[J'_m(kc_{mn}r)N'_m(kc_{mn}b)-N'_m(kc_{mn}r)J'_m(kc_{mn}b)]}{\sqrt{\left(J'_m(kc_{mn}b)/J'_m(kc_{mn}a)\right)^2[1-(m/kc_{mn}a)^2]-[1-(m/kc_{mn}b)^2]}}, \tag{3}$$

$$E_{r_{mn}}(\phi) = \sin(m\phi),\ \ E_{\phi_{mn}}(\phi) = \cos(m\phi). \tag{4}$$

Here, E_r and E_ϕ are the excited electric fields in the radial and angular directions, respectively. The subscripts 0 and mn mean those for TEM and TE modes, respectively. $f_c(m,n)$ and kc_{mn} are the cutoff frequency and wave length for TE modes, respectively. $J_m(z)$ and $N_m(z)$ are Bessel and Neumann functions, respectively. $J'_m(z)$ and $N'_m(z)$ are derivatives on z for Bessel and Neumann functions, respectively. X'_{mn} are roots of Bessel-Nuemann combined function [7]. This relation is given by

$$af_c(m,n) = \frac{c_0 X'_{mn}}{2\pi(b/a)},\ \ X'_{mn} = kc_{mn}b. \tag{5}$$

By applying these formulation, the impedances for TEM, TE and TM modes are given by

$$Z^{TEM} = \frac{\eta_0}{2\pi}\left[\int_{a-h}^{a} I(r)E_{r_0}(r)dr\right]^2, \tag{6}$$

$$Z_{mn}^{TE} = \frac{\eta_{mn}}{2\pi\sigma\int_a^b [E_{r_{mn}}^2(r) + E_{\phi_{mn}}^2(r)]rdr}\left[\int_{a-h}^{a} I(r)E_{r_{mn}}(r)dr\right. \\ \left.\times \int_{a-h}^{a} I(r)E_{r_{mn}}(r)F_{mn}(r,b_i)dr\right], \tag{7}$$

$$Z_{mn}^{TM} = \frac{-jm^2\eta_{mn}}{2\pi\sigma\int_b^a r^3 E_{\phi_{mn}}^2(r)dr}\left[\int_{a-h}^{a} I(r)E_{r_{mn}}(r)dr\right. \\ \left.\times \int_{a-h}^{a} I(r)E_{r_{mn}}(r)F_{mn}(r,b_i)dr\right]. \tag{8}$$

$$\eta_{mn} = \frac{\eta_0}{\sqrt{1-(kc_{mn}/\beta_0)^2}},\ \ \eta_0 = \sqrt{\frac{\mu_0}{\epsilon_0}} = 376.7\ (\Omega), \tag{9}$$

$$I(r) = \frac{\sin[\beta_0(h+r-a)]}{\sin(\beta_0 h)}, \tag{10}$$

$$F_{mn}(r) = \frac{1}{2\pi}\int_0^{2\pi} e^{-\gamma_{mn}b_i|\sin\theta|}\cos\left[m\cdot\tan^{-1}\left(\frac{b_i\cos\theta}{r}\right)\right]d\theta. \tag{11}$$

Here, h is the extruding length of the SMA feedthrough from the inner surface of BPM, η_0 the wave impedance in vacuum, η_{mn} the intrinsic impedance transmitted in BPM, β_0 the phase constant in vacuum, γ_{mn} the propagation constant of TE and TM modes, σ a constant by $\sigma = 1/2$ for $m > 0$ and $\sigma = 1$ for $m = 0$, ϵ_0 and μ_0 are permittivity and permeability in vacuum, respectively. $I(r)$ a normalized current excited in BPM, which is a function of the radius r of BPM. F_{mn} is the attenuation function of the excited electromagnetic fields in BPM as a function of r with taking into account the geometrical structure of the SMA feedthrough.

Based on these formulation, the input (output) impedance Z_{in} (Z_{out}) viewed the reference plane from the SMA (BPM) side to the BPM (SMA) side can be represented by

$$Z_{in} = \frac{1}{2}\left[Z_{TEM} + \sum_{m=1}^{\infty}\sum_{n=1}^{\infty} Z_{TE_{mn}} + \sum_{m=0}^{\infty}\sum_{n=1}^{\infty} Z_{TM_{mn}}\right], \tag{12}$$

$$Z_{out} = Z_{TEM}. \tag{13}$$

Here, in Eq. (12), the factor 1/2 corresponds to a junction of the excited current at the reference plane in the directions of both upstream and downstream of BPM. On the other hand, when BPM is excited in one-way direction, this factor does not need to be taken into account.

If a gaussian beam in the transverse directions is taken into account, based on appropriate integration in the transverse directions, the input impedance can be numerically calculated. In the calculations, the integration region is taken into account $3\sigma_b$ ($r \le a$) or the limit a ($r > a$), where σ_b is one sigma of the gaussian beam. Figure 5 shows the results of the input impedance calculation. Fig. 5 (a) ((b)) indicates the variation in the input impedance (TEM and TE (TM) modes) as a function of frequency and the beam size. Gaussian function is assumed in the transverse charge distribution. It is easily understood that Z_{TEM} does not depend on frequency, and the higher-order modes arise in order at their corresponding cutoff frequencies starting from their lowest order. Note that the input impedances of TE (TM) modes are $7\times10^{-3} \sim 5\times10^{-2}\ \Omega$ ($7\times10^{-3} \sim 2\times10^{-2}\ \Omega$) depending on frequency and beam size. It is easily understood that the input impedance of TE mode is larger than those of TM mode.

Coupling Strength Between SMA Feedthrough and Beam

If the BPM is excited by a beam with an unit current, the coupling strength C_{TEM} between a beam and SMA feedthrough with taking into account only fundamental TEMs is given by

$$C_{TEM} = \frac{Z_{out}}{Z_{BPM}},\ \ Z_{BPM} = \frac{\eta_0}{2\pi}\ln(a/b). \tag{14}$$

Figure 6 shows the variations in the coupling strength as a function of frequency and the beam size with taking into account a gaussian beam in the transverse direction. It is expected $C_{TEM} \sim 7\times10^{-4}$ in a case of $\sigma_b = 6$ mm. The result shows that in a case of bunch currents of ~ 1 kA, which corresponds to beam charges of 1 nC for a single bunch, ~ 0.7 A is expected to be excited at the reference plane of SMA feedthrough. The amplitude of ~ 35 V is expected to be detected in a 50 Ω transmission system. This amplitude is sufficiently detectable in the SKEKB e^+ capture section.

Figure 7 shows the variations in the coupling strength as a function of frequency and the extruding length h at the beam

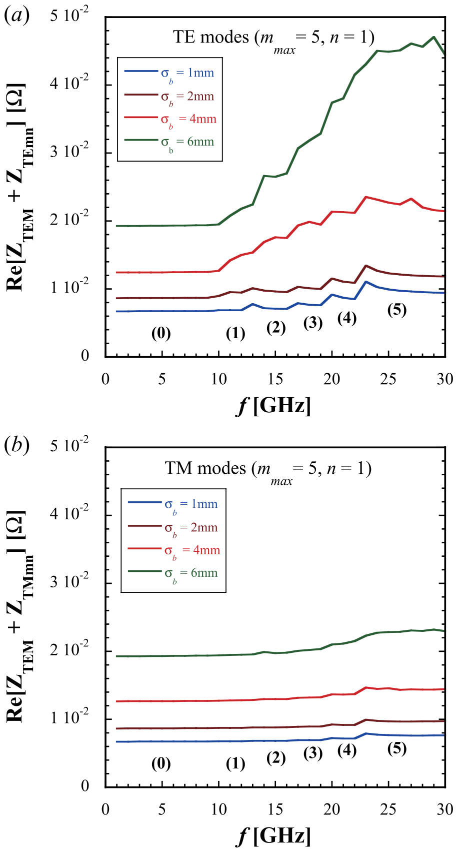

Figure 5: (a) Variations in the input impedance (TEM and TE modes) as a function of frequency and the beam size, (b) Variations in that (TEM and TM modes) as a function of frequency and the beam size. The subscripts n and maximum m are fixed to 1 and 5, respectively. The extruding length h is fixed to 1 mm.

size of σ_b = 4 mm. Note that with increasing the extruding length, the coupling strength increases as a function of frequency and also beam size, while the frequency dependence of the coupling strength increases. In our present design, the length is h = 1 mm, and thus, the variation of it is ~ 0.7% in the frequency region up to 10 GHz. It is understood that the variation of the coupling strength is negligibly small.

CONCLUSION

The basic design and numerical results based on a modal analysis for electromagnetic couplings between SMA-feedthrough electrode and a beam are successfully investigated. Based on the design parameters, it was verified that the wideband monitor system can work well in the direct simultaneous detection of e^- and e^+ bunches.

REFERENCES

[1] Y. Ohnishi *et al.*, "Accelerator design at SuperKEKB ", *Prog. Theor. Exp. Phys.*, vol. 2013, p.03A011, 2013. `doi:10.1093/ptep/pts083`

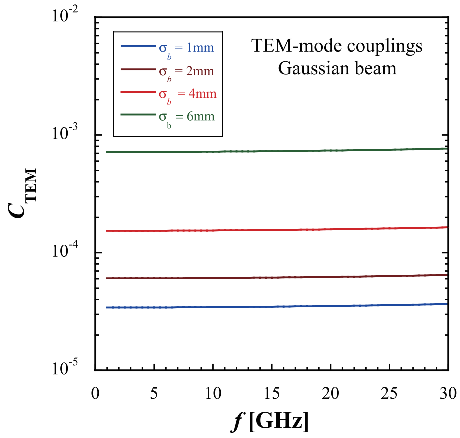

Figure 6: Variations in the coupling strengths between the TEM modes as a function of frequency and the beam size.

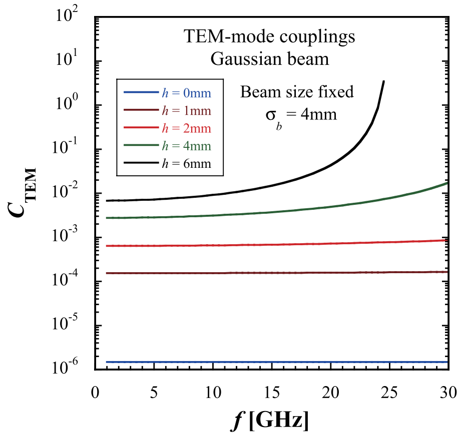

Figure 7: Variations in the coupling strengths between the TEM modes as functions of frequency and the length h. The transverse charge distribution of σ_b = 4 mm is fixed.

[2] T. Abe *et al.*, "Achievements of KEKB", *Prog. Theor. Exp. Phys.*, vol. 2013, p. 03A001, 2013. `doi:10.1093/ptep/pts102`

[3] M. Akemoto *et al.*, "The KEKB injector linac", *Prog. Theor. Exp. Phys.*, vol 2013, p. 03A002, 2013. `doi:10.1093/ptep/ptt011`

[4] I. Abe *et al.*, "The KEKB injector linac", *Nucl. Instrum. Methods Phys. Res. A*, vol. 499, p. 167, 2003. `doi:10.1016/S0168-9002(02)01787-4`

[5] T. Suwada, M. A. Rehman, and F. Miyahara, "First simultaneous detection of electron and positron bunches at the positron capture section of the SuperKEKB factory", *Sci. Rep.*, vol. 11, p. 12751, 2021. `doi:10.1038/s41598-021-91707-0`

[6] J. G.Davis and A. A. P. Gibson, "Higher order mode impedances and cut-off frequencies of overmoded coaxial waveguides", *Int. J. Electron.*, vol. 93, no. 5, pp. 335–346, 2006. `doi:10.1080/00207210500429077`

[7] N. Marcuvitz, *Waveguide Handbook*, Peter Peregrinus Ltd., UK, 1986, p. 74.

10th Int. Beam Instrum. Conf. IBIC2021, Pohang, Rep. of Korea JACoW Publishing
ISBN: 978-3-95450-230-1 ISSN: 2673-5350 doi:10.18429/JACoW-IBIC2021-WEPP13

BUNCH ARRIVAL TIME MEASUREMENT SYSTEM TEST FOR SHINE*

Y. M. Zhou†, S. S. Cao, J. Chen, Y. B. Leng#
Shanghai Advanced Research Institute, CAS, Shanghai, China

Abstract

To achieve high-precision synchronization between electron bunches and seeded lasers, a femtosecond resolution bunch arrival time measurement system (BAM) is required at SHINE (Shanghai High repetition rate XFEL aNd Extreme light facility). The bunch signal from a GHz-bandwidth cavity monitor is mixed with a reference signal from the device synchronization clock in the RF front-end. Then, the generated IF signal is collected by the digital acquisition system. In the pre-research stage, four sets of cavity monitors with different frequencies and load quality factors and three sets of analog front-ends with different schemes were performed, but now only one monitor with the attenuation time constant of 200 ns was installed for beam experiment testing. The system can measure the bunch charge, bunch arrival time, and bunch flight time. The first results will be presented in this paper.

INTRODUCTION

Shanghai High repetition rate XFEL aNd Extreme light facility (SHINE) is the first hard X-ray FEL facility in China, which started construction in April 2018 [1]. It will be used to generate brilliant X-rays between 0.4 and 25 keV at pulse repetition rates of up to 1MHz. Some important parameters are shown in Table 1.

Table 1: Main Parameters of the SHINE

Parameter	Value
Beam energy/ GeV	8.0
Bunch charge/ pC	100
Max repetition rate/ MHz	1
Pulse length/ fs	20-50
Photon energy/ keV	0.4-25
Total facility length/ km	3.1

The high-precision synchronization between the electron beam and the seed laser is of great significance to the debugging and operation of the accelerator. The SHINE project has very high requirements for the bunch arrival time measurement. The cavity probe has the characteristics of high resolution and high sensitivity. Therefore, the bunch arrival time monitor (BAM) system based on the radio frequency (RF) resonant cavity method can be used as an auxiliary measurement tool for the beam distribution area and the FEL section. It is hoped to accurately measure each bunch with a resolution better than 25 fs @100 pC.

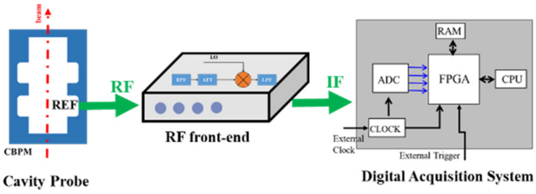

Figure 1: System block diagram.

Figure 2: Photos of CBPM 200.

SYSTEM STRUCTURE

The BAM system is mainly composed of three modules, as shown in Fig 1. The cavity probe is used to couple beam electromagnetic fields, including beam charge, beam arrival time, and position information. The function of the RF front-end is to filter, amplify, and down-convert the high-frequency signal into an intermediate frequency (IF) signal. A real-time online digital IQ demodulation algorithm is implemented in FPGA to extract beam position and phase information. All signal processing will be completed in the tunnel.

Cavity Probe

In general, the design of the reference cavity is relatively simple compared to the position cavity. Therefore, the two will be designed jointly, but the reference cavity is mainly used for bunch arrival time measurement. We have designed four sets of cavity probes with different frequencies and load quality factors. The detailed design parameters and test results can be found in Ref [2]. So far, the manufacturing and laboratory testing of three CBPM200 probes have been completed, as shown in Fig.2. The cold tests with a network analyzer have been performed, the results are presented in Table 2. The S-parameter spectrum of the reference cavity is relatively close to the simulation result. The frequency of the three sets of cavities is within ±6 MHz of the design value, and the bandwidth is within ±0.2 MHz of the design value, which meets the design requirements. The three CBPM200 probes have been installed on the beam test platform of the SHINE. The experimental beam mainly comes from the Shanghai soft X-ray FEL (SXFEL) facility.

---

*Work supported by Ten Thousand Talent Program and Chinese Academy of Sciences Key Technology Talent Program
†zhouyimei@zjlab.org.cn
#lengyongbin@sinap.ac.cn

Table 2: Cold Test Results of CBPM 200 Reference Cavity

Parameter	Cavity 1	Cavity 2	Cavity 3
Frequency/ GHz	5.769	5.773	5.776
BW/ MHz	1.54	1.49	1.56
Qload	3755	3877	3720
Amplitude/ dB	-37	-47	-32

RF Front-end

The BAM system shares a set of RF front-end with the beam position monitor (BPM) system during the testing process [3, 4]. The basic schematic diagram is shown in Fig. 3, which is made up of filters, adjustable attenuators, amplifiers, and mixers. To get a small noise figure (NF), three prototypes with different architectures were designed. The pictures are shown in Fig. 4. The main differences between them are RF units (coaxial or PCB), dynamic range control (cascade or switching), and gain control (numerical or voltage). The noise floor of the three prototypes has been evaluated, and the results show that prototype #3 is the best.

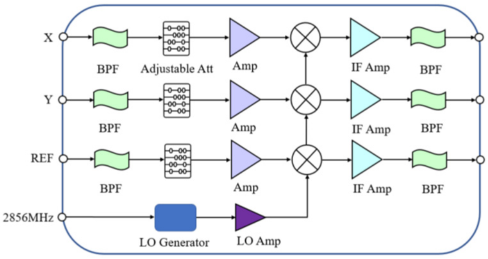

Figure 3: Schematic diagram of the RF front-end.

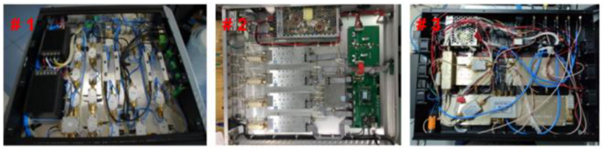

Figure 4: Photos of RF front-end.

Signal Acquisition System

We are developing a dedicated digital BPM signal processor that can meet the high repetition frequency of 1 MHz, which can realize real-time processing of beam position and phase information extraction in the SHINE. The technical requirements include:

a) The number of channels >3;
b) The analog input bandwidth >60 MHz;
c) The sampling rate >500 MSPS;
d) The ENOB > 9 bits;
e) The SNR >60 dB.

Figure 5 shows the main data acquisition board used for testing at this stage. It includes the zcu102 evaluation board based on Zynq UltraScale and MPSoC from Xilinx and the ADC daughterboard (QT7135) developed by Queentest. The ADC sampling rate is 1GSPS, the analog bandwidth is 1.2 GHz, and the ENOB is better than 10bits, which fully meets the design requirements.

Figure 5: Photo of data acquisition board.

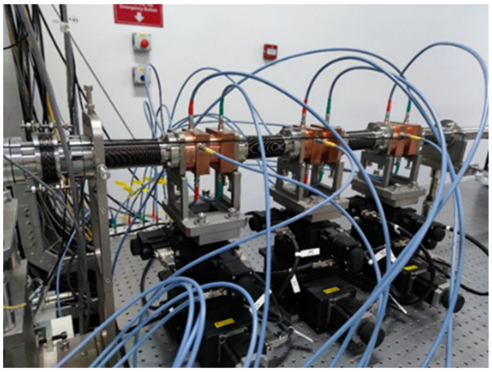

Figure 6: Photo of CBPM200 layout in the tunnel.

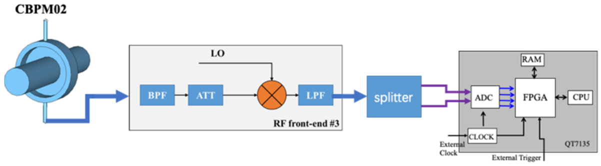

Figure 7: The scheme of evaluating the digitizer (QT7135).

EXPERIMENTS AND RESULTS

Figure 6 shows the layout of three CBPM 200 installed in the tunnel. They were placed on a three-dimensional movable platform. So far, we have conducted three experiments: 1) evaluating the digitizer (QT7135); 2) evaluating the RF front-end; 3) measuring the bunch arrival time and bunch flight time. The following will introduce the experimental design scheme and test results.

Evaluating the Digitizer (QT7135)

What we mainly used in this experiment is CBPM02 and RF front-end #3, the design scheme is shown as in Fig. 7. Only the digitizer was evaluated, so the front end and the probe need to be configured the same. The probe signal was filtered and mixed by the RF front-end to output an IF signal. Then, the IF signal was divided into two parts by a power divider. The data were obtained by four existing digitizers (SP ADQ14AC-4C, DAQ by USTC, QT7135, QT7126). We compared the performance of digitizers by evaluating the signal amplitude extraction uncertainty. The test results are shown in Table 3, indicating the QT7135 is currently the best (see Fig. 8).

Table 3: Performance Comparison of Different Digitizers

DAQ	SP ADQ14A C-4C	DAQ by USTC	QT7135	QT7126
Resolution/ bits	14	16	16	12
Sampling rate/ MHz	1004.8	833	952	2380
Range/ V	±0.95	±1	±1	±0.6
Uncertainty/ ‰	0.116	0.15	0.071	0.33

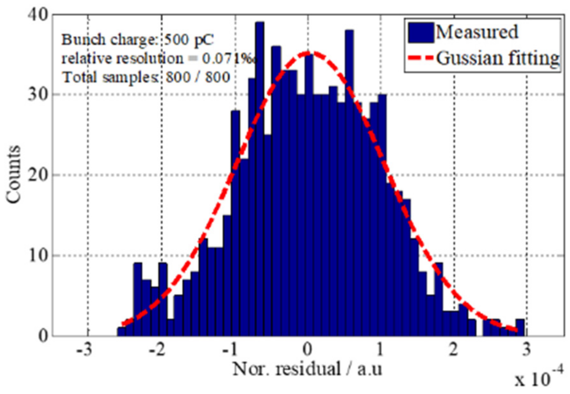

Figure 8: Signal amplitude extraction uncertainty of QT7135.

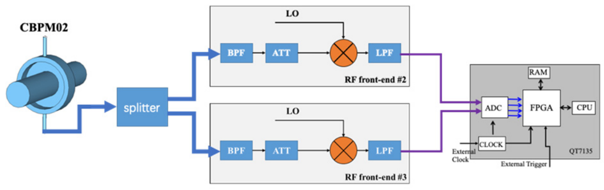

Figure 9: The scheme of evaluating the RF front-end.

Evaluating the RF Front-end

The purpose of this experiment is to evaluate the consistency of different front-ends. The laboratory test results of the noise floor of each front-ends are shown in Table 4. In the beam experiment, the amplitude extraction uncertainty of prototype #2 and prototype #3 is 0.032% (Fig. 10), which is consistent with the lab test results. The design scheme is shown in Fig. 9. The probe signal was directly divided into two parts by a power divider in the tunnel, and the two signals were respectively connected to prototype #2 and prototype #3. The data was sampled by the QT7135.

Table 4: Noise Test Results of RF Front-ends REF Channel

Parameter	Prototype #1	Prototype #2	Prototype #3
Adjustable gain dB/step	1	1	0.25
Crosstalk/ dB	<-61	<-62	<-66
Noise Figure/ %	0.059	0.056	0.037
Local oscillator phase noise / fs	36	20	7

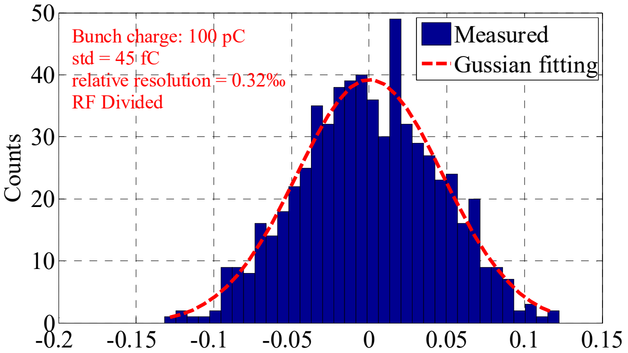

Figure 10: Signal amplitude extraction uncertainty between prototype #2 and prototype #3.

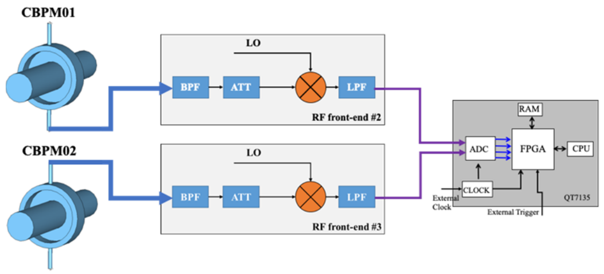

Figure 11: The scheme of measuring the bunch arrival time and bunch flight time.

Measuring the Bunch Arrival Time and Bunch Flight Time

Two adjacent probes can measure the bunch arrival time and bunch flight time. The probes used in this experiment are CBPM01 and CBPM02, the RF front-ends are prototype #2 and prototype #3. The data acquisition system is QT7135. The design scheme is shown in Fig. 11. The output waveforms of the IF signals from the two BAM systems are shown in Fig. 12, which indicates that the main error comes from the inconsistency of the two probes. The phase difference between them represents the bunch flight time, as shown in Fig. 13. After multiple acquisitions, the best resolution can reach 6.9 fs (shown in Fig. 14), which meets the design specifications.

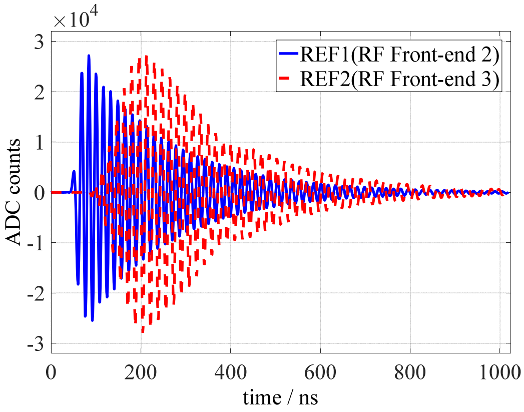

Figure 12: The output waveforms of the IF signals from the two BAM systems.

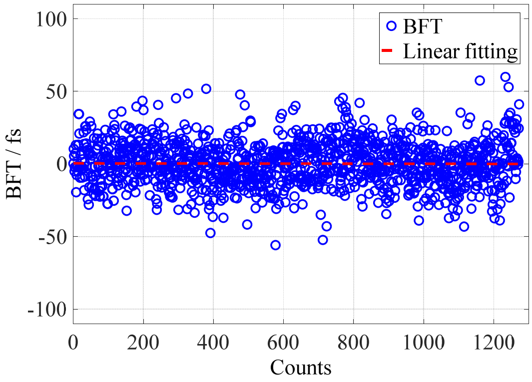

Figure 13: Bunch flight time measurement in scheme #3.

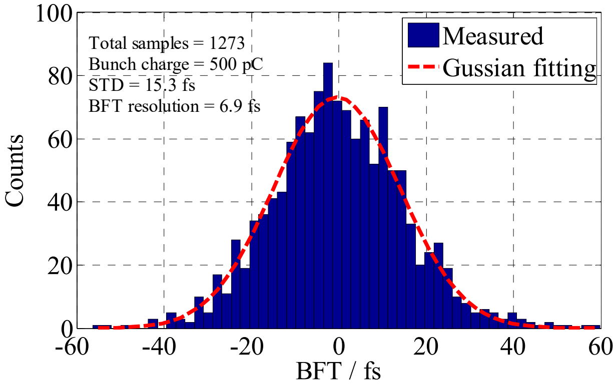

Figure 14: Bunch flight time resolution in scheme #3.

CONCLUSIONS

As an important beam diagnostic tool for FEL facilities, the BAM system is of great significance to beam adjustment and operation. The BAM prototypes for the SHINE have been designed and installed on the test platform. In this article, each sub-module was tested and evaluated, and bunch arrival time and flight time were measured. The best resolution of BFT reaches 6.9 fs, which meets the BAM system design specification of the SHINE.

REFERENCES

[1] C. Feng and H.J. Deng, "Review of fully coherent free-electron lasers", *Nuclear Science and Techniques*, vol. 29(160), pp. 1-15, 2018. `doi:10.1007/s41365-018-0490-1`

[2] S. S. Cao, R. Jiang, Y. B. Leng, and R. X. Yuan, "Design and Test of CBPM Prototypes for SHINE", in *Proc. 9th Int. Beam Instrumentation Conf. (IBIC'20)*, Santos, Brazil, Sep. 2020, pp. 124-127. `doi:10.18429/JACoW-IBIC2020-WEPP13`

[3] J. Chen, Y. B. Leng, R. X. Yuan, L. W. Lai, and S. S. Cao, "Development of the Prototype of the Cavity BPM System for SHINE", presented at *the 12th Int. Particle Accelerator Conf. (IPAC'21)*, Campinas, Brazil, May 2021, paper FRXC06.

[4] Y. M. Zhou, S. S. Cao, J. Chen, and Y. B. Leng, "Prototype Design of Bunch Arrival Time Measurement System Based on Cavity Monitor for SHINE", in *Proc. 9th Int. Beam Instrumentation Conf. (IBIC'20)*, Santos, Brazil, Sep. 2020, pp. 154-157. `doi:10.18429/JACoW-IBIC2020-WEPP24`

ISBN: 978-3-95450-230-1 ISSN: 2673-5350 doi:10.18429/JACoW-IBIC2021-WEPP14

BUNCH COMPRESSION MONITOR BASED ON COHERENT DIFFRACTION RADIATION AT EUROPEAN XFEL AND FLASH

Ch. Gerth* and N. M. Lockmann
Deutsches Elektronen-Synchrotron, Hamburg, Germany, EU

Abstract

Bunch compression monitors (BCMs) based on the detection of coherent diffraction radiation have been installed at the European XFEL for a beam-based stabilisation of the accelerating phases as well as monitoring of bunch lengths. The monitor systems comprise zero-bias Schottky and pyro-electric detectors in combination with low and high pass filters. The detector responses and filters are matched to the spectral ranges of the coherent part of the emitted diffraction radiation which is given by the particular beam energy and bunch lengths after each bunch compression stage. In this paper, we describe in detail the experimental setup of the BCMs. The last BCM has been calibrated with the help of a transverse deflecting structure to establish a (rms) bunch length monitor in the range of a few tens of femtoseconds, and results from compression scans are presented. To enable operation at megahertz repetition rates of the superconducting accelerator, a correction method for the signal pileup of the pyro-electric detectors has been applied. Installation of the same BCMs is foreseen at FLASH within the FLASH2020+ upgrade project.

EUROPEAN XFEL

High-gain, single-pass free-electron lasers (FELs) require high-brightness electron bunches with kiloampere peak currents, which are longitudinally compressed in several stages by off-crest acceleration in combination with magnetic dipole chicanes. Figure 1 depicts schematically an overview of the European XFEL accelerator [1] with three radio-frequency (RF) accelerating sections (L_1,L_2,L_3) followed by bunch compression chicanes (BC_1,BC_2,BC_3). The settings of the compression stages were optimised for various bunch charges [2] as the electron bunches can be affected by collective, non-linear effects at these high peak currents. To establish the correct compression settings and ensure stable, long-term FEL operation, monitoring of the bunch compression is mandatory.

Bunch compression monitors (BCM) based on the detection of coherent diffraction radiation (CDR) have been installed after each of the three BC chicanes as is indicated in Fig. 1. CDR is generated by an electron bunch passing through an aperture in a screen and, therefore, is non-invasive to the electron beam. BCM1 has been installed after L_2 at higher beam energies, as this leads to a smaller emittance and, therewith, beam size and reduces the risk of beam losses at the aperture.

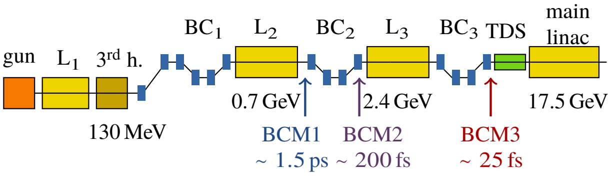

Figure 1: Schematic overview of the European XFEL accelerator. The positions of the BCMs and nominal rms bunch lengths for a bunch charge of 250 pC are indicated.

BCM SETUP

A BCM consists of a screen station mounted in the electron beamline for the generation of CDR as well as an optics and detector unit for transport and detection of the CDR.

Screen Station

Figure 2 shows a CAD image of the screen station and CDR screen which is mounted on a remotely-controllable vacuum feed-through (screen mover). The screen consists of solid aluminum, and the screen normal has an angle of 45° with respect to the electron beam axis. The radiator area at the bottom (32 mm × 80 mm, 1 mm-thick) is depicted enlarged in the right part of Fig. 2 and comprises two apertures with effective diameters of 5 mm and 7 mm in the projection of the electron beam axis. The surface of the CDR screen has been machined with a diamond milling cutter and has a roughness < 1 µm. Backward CDR is emitted perpendicular to the electron beam axis and enters the optics and detector unit through a fused silica vacuum window at BCM1 and BCM2 and a diamond vacuum window at BCM3.

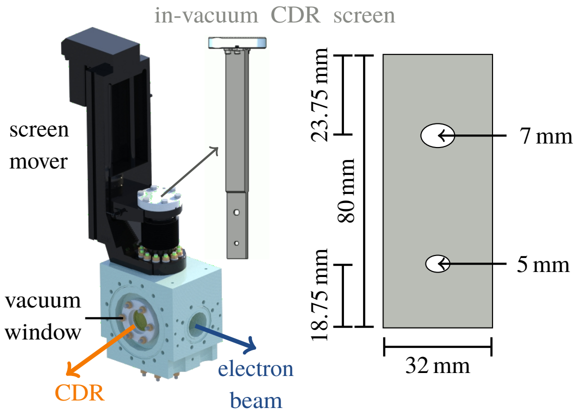

Figure 2: (Left) CAD model of the screen station and CDR screen. (Right) The radiator area enlarged with dimension.

---

* chirstopher.gerth@desy.de

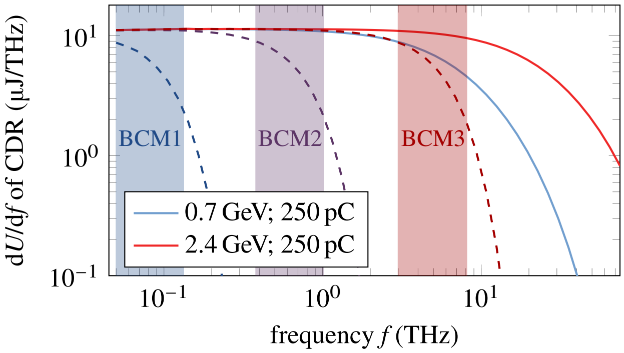

Figure 3: Spectral energy density emitted by the CDR screen (aperture Ø = 7 mm) at beam energies of 0.7 GeV (solid blue) and 2.4 GeV (solid red). The dashed lines include the form factor term $|F(f)|^2$ of Eq. (1) and are calculated for Gaussian longitudinal profiles with rms bunch lengths as given in Fig. 1. The coloured areas mark the regions where the form factor term decreases from 0.8 to 0.2.

The spectral energy density of CDR emitted at the screen station scales quadratically with the bunch charge Q and can be expressed by

$$\left[\frac{\mathrm{d}U}{\mathrm{d}f}\right]_{\mathrm{CDR}} = \left[\frac{\mathrm{d}U}{\mathrm{d}f}\right]_1 \cdot \left(\frac{Q}{e}\right)^2 \cdot |F(f)|^2 , \tag{1}$$

where $[\mathrm{d}U/\mathrm{d}f]_1$ is the spectral energy density emitted by a single electron and $F(f)$ the complex form factor which is described by the 3D-particle distribution of the electron bunch. Transverse beam size effects are strongly suppressed for the frequency ranges and electron beam energies considered here, and $F(f)$ can be approximated by the longitudinal form factor $F_l(f)$ which is given by the Fourier transform of the normalised longitudinal current profile $\rho(t)$:

$$F_l(f) = \int_{-\infty}^{+\infty} \rho(t)\, \exp(-i\, 2\pi f t)\, \mathrm{d}t\,. \tag{2}$$

The spectral energy density has been calculated with the help of the generalised Ginzburg-Frank equation for DR given in Ref. [3] for infinitesimally short electron bunches at a beam energy of 0.7 GeV (solid blue line, BCM1 and BCM2) and 2.4 GeV (solid red line, BCM3) and is depicted in Fig. 3. CDR has the advantage of being non-invasive, however, the spectral energy density exhibits a cut-off towards high frequencies depending on the beam energy. The dashed lines include the longitudinal form factor $F_l(f)$ for electron bunches that have a Gaussian current profile with rms bunch lengths as indicated in Fig. 1. The coloured areas mark the frequency regions where the form factor term $|F(f)|^2$ in Eq. (1) decreases from 0.8 to 0.2. The latter are of interest for the BCM, as bunch length changes lead to strong variations of the radiated energy in these frequency bands, while radiated energies at lower (DC content) or higher (substructures) frequencies do not contain any information on changes of the rms bunch length.

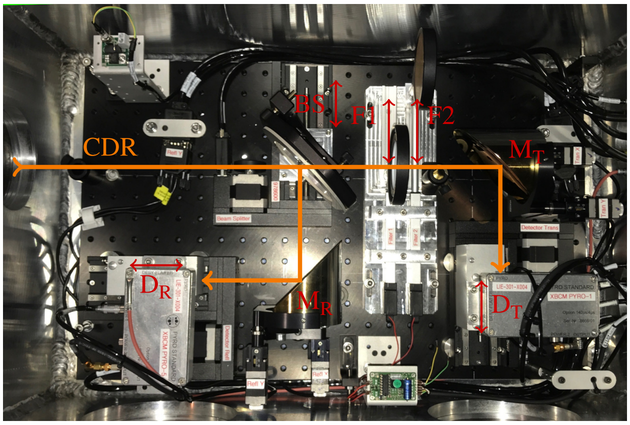

Figure 4: Photograph showing a top view of the optics and detector unit. The beam path and components are marked (BS: beamplitter, F: filter, M: mirror, D: detetcor).

Optics and Detector Unit

A photograph showing a top view of the compact optics and detector unit is depicted in Fig. 4. All components are enclosed in a sealed aluminum housing to be insensitive to humidity changes inside the accelerator tunnel. The housing can be attached directly to the supports of the electron beamline, which is suspended at a height of 2.25 m. All optical components are mounted with commercially available supports onto a solid aluminum breadboard with a footprint of 600 x 400 mm^2.

The first optical element is a thin film polarizer used as beamsplitter (BS, Ø = 4”, Microtech Instruments, F15-L) that separates the radial polarised CDR into a transmitted (vertically polarised) and reflected (horizontally polarised) beam path. By retracting the beamsplitter out of the beam path, the full CDR intensity is transported into the transmitted beam path. The transmitted beam path is equipped with two filter holders (F1 and F2, Ø = 3”, angle = 90°) which can be moved independently. The CDR is then focused by gold-coated toroidal mirrors ($\mathrm{M_T}$ and $\mathrm{M_R}$, Ø = 3”, LT Ultra) with a focal length of 101.6 mm onto the detectors ($\mathrm{D_T}$ and $\mathrm{D_R}$). The mirrors are adjustable to compensate misalignments of the experimental setup, and the detectors are mounted on linear stages to be able to move longitudinally through the focus. In order to match the respective frequency range (see Fig. 3), zero-bias Schottky diodes (75 - 100 GHz, DET-10-RPFWO, Millitech) are used at BCM1 and pyro-electric detectors (DESY in-house) at BCM2 and BCM3. The detector signals are transmitted by coaxial cables of several meters length to a digitizer board (SIS8300-L2D, Struck Innovative Systeme) in MicroTCA.4 standard, which is the common front-end electronics of the European XFEL accelerator.

BCM CALIBRATION

A cross-calibration of the BCM signal to rms bunch lengths has been established with the help of a TDS [4] for the last BCM (see Fig. 1) where the electron bunches are fully compressed. As was demonstrated in Ref. [5],

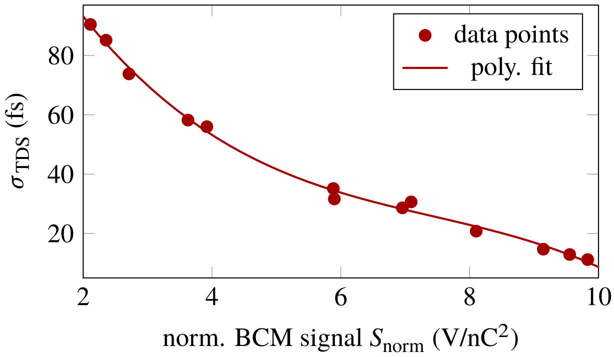

Figure 5: Third-order polynomial fit (solid line) as a cross-calibration of the charge-normalised BCM signal S_{norm} to the rms bunch lengths σ_{TDS} measured with a TDS.

the particular shape of the longitudinal profiles of electron bunches with the same rms bunch length leads to differences in the form factor $F(f)$ at high frequencies. Therefore, a low-pass filter with a cut-off frequency of 6 THz was applied (see Fig. 3). Furthermore, as the CDR intensity and thereby BCM signal S_{BCM} scales quadratically with the bunch charge Q (see Eq. (1)), the normalised BCM signal $S_{\text{norm}} = S_{\text{BCM}}/Q^2$ has to be considered.

The cross-calibration has been obtained for a bunch charge $Q = 250\,\text{pC}$ by varying compression settings of the accelerator modules L_2 and L_3 (see Fig. 1) and, therewith, the bunch lengths between 6 fs and 90 fs. The result is shown in Fig. 5 where the rms bunch lengths measured with the TDS (red dots) are plotted vs. the charge-normalised BCM signal together with a third-order polynomial fit (solid line). For the determination of the rms bunch lengths, the temporal resolution R_{TDS} of the TDS has been subtracted quadratically according to

$$\sigma_{\text{TDS}} = \sqrt{\sigma^2_{\text{mess}} - R^2_{\text{TDS}}} \,. \tag{3}$$

The same set of data is plotted in Fig. 6 for the independent compression scans of L_2 (top) and L_3 (bottom), for which the RF amplitude and phase of the accelerating fields were varied such that the mean beam energy remained constant. The rms bunch lengths measured with BCM3 were determined with the use of the third-order polynomial fit in Fig. 5. The relative difference between the rms bunch lengths measured with the TDS (green dots) and determined from BCM data (red line) is less than 10 %. However, the long-term validity of the BCM3 calibration with the third-order polynomial fit needs to be confirmed in further comparative measurements and probably established separately for operation at different bunch charges.

MEGAHERTZ OPERATION

The superconducting accelerator of European XFEL delivers bunch trains of up to 600 µs at a repetition rate of 10 Hz with an intra-train rate of up to 4.5 MHz. By using non-invasive CDR and fast detection systems in combination

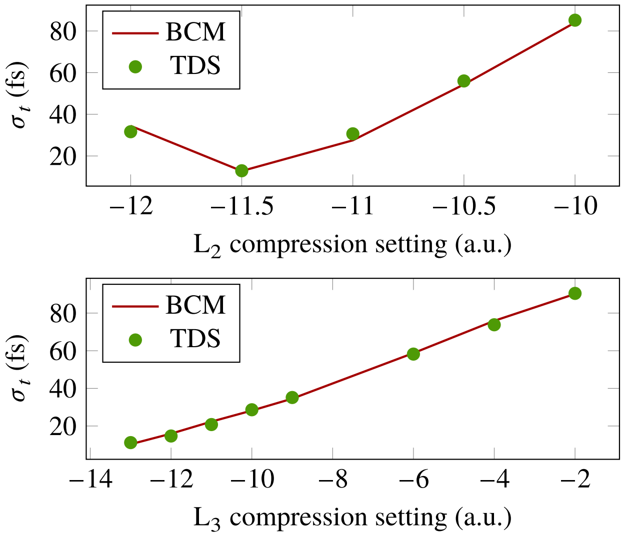

Figure 6: Comparison of rms bunch lengths measured with the TDS and obtained from the BCM data with the calibration presented in Fig. 5.

with the BCM calibration described above, determination of the rms bunch lengths along the bunch trains can be realised in parallel to FEL user operation. However, mechanical oscillations of the pyro-electric detectors with characteristic frequencies in the vicinity of the bunch repetition rate lead to signal pileup which needs to be corrected.

Signal Pileup Correction

The influence of the pileup effect on the BCM signals is demonstrated in Fig. 7 for a bunch train that was sampled with the ADC (blue curve) at a bunch repetition rate of 4.5 MHz. For the first ≈ 50 bunches a signal slope is induced, while for later bunches the signal pileup evolves into a constant contribution. After the last bunch there is no CDR emitted, however, pileup results in a non-zero signal. An algorithm to correct the pileup in the signal processing

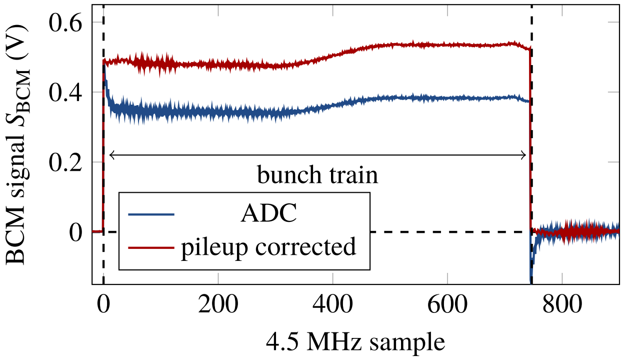

Figure 7: Example of signal pileup (blue) sampled with the ADC at a bunch repetition rate of 4.5 MHz. The bunch train begins at sample #0 and ends at #750. Pileup leads to artificial signal slopes at the beginning and after the bunch train, which are removed by applying pileup correction (red).

has been presented in Ref. [6] and is applied routinely to the BCMs equipped with pyro-electric detectors. In comparison to the raw ADC signal, for the pileup corrected signal (red curve) the slope of the first bunches is removed and the baseline after the bunch train is zero within the noise level.

Comparative Measurements with TDS

Compression data has been recorded with BCM3 during operation with 1.1 MHz bunch repetition rate. The signals have been pileup corrected and converted into rms bunch lengths σ_t by applying the calibration with the TDS as described above. The resulting mean of the rms bunch lengths for 30 bunch trains (red curve) is presented in Fig. 8 together with the rms fluctuations as an error band (light red).

The measured rms bunch lengths increase continuously along the first 90 bunches with a steep slope beginning at bunch #60. Afterwards, the BCM signal remains approximately constant until the end of the bunch train at bunch #390. During this measurement, the RF accelerating parameters for bunch compression were divided into two different settings along the bunch train, and these so-called RF flattops are marked as FT1 and FT2 in Fig. 8. This operation mode enables operation of two FEL beamlines in parallel with independently optimised compression settings. The transition time between the RF flattops is required for adjustment of the RF parameters in the superconducting accelerator.

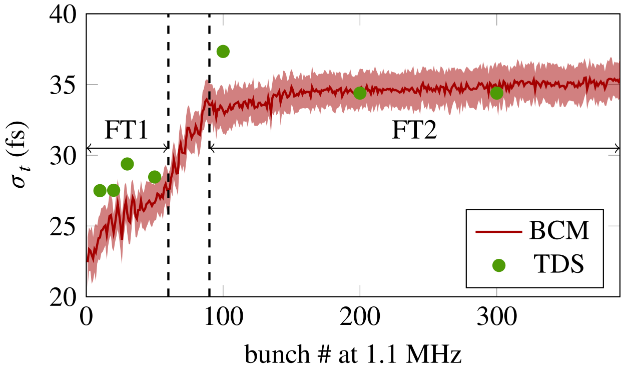

Figure 8: Bunch lengths (rms) measured for all bunches in the bunch train with BCM3 (red curve) by applying the calibration presented in Fig. 5 and for a few selected bunch numbers with the TDS (green dots). The solid red line represents the mean of 30 consecutive bunch trains.

The difference in bunch compression for both RF flattops is clearly detected by the BCM, and the transition between both RF flattops at bunch numbers #60 to #90 exhibits a steep increase of the rms bunch length by about 7 fs. This behaviour of the rms bunch lengths is confirmed by comparative measurements with the TDS in combination with a fast kicker magnet and off-axis screen [4]. The rms bunch lengths have been measured successively for a few selected bunch numbers, and the temporal resolution of about 15 fs has been corrected according to Eq. (3). The TDS results (green dots) are compared to the BCM data in Fig. 8 and show good overall agreement and corroborate the increase in bunch length in RF flattop FT1 and constant behaviour in flattop FT2. The relative deviations for the rms bunch lengths obtained with BCM and TDS are less than 15%.

CONCLUSIONS

BCMs have been installed after each bunch compressor at European XFEL to measure the bunch compression non-invasively during FEL operation for optimisation and stabilisation of the superconducting linear accelerator. A signal pileup correction has been implemented for the pyro-electric detectors to enable bunch-resolved measurements at intra-train repetition rates of up to 4.5 MHz. Based on a successful calibration with a TDS, the signals of the BCM after the last bunch compressor are converted to rms bunch lengths which allows monitoring of entire bunch trains. BCMs with the same layout will be installed at FLASH within the framework of the FLASH2020+ Upgrade Project [7].

AKNOWLEDGEMENTS

The authors would like to thank O. Hensler and R. Kammering for their support with BCM control software and B. Beutner for his assistance with the TDS measurements.

REFERENCES

[1] W. Decking *et al.*, “A MHz-repetition-rate hard X-ray free-electron laser driven by a superconducting linear accelerator,” *Nature Photonics*, vol. 14, no. 6, pp. 391–397, 2020. DOI: `10.1038/s41566-020-0607-z`.

[2] I. Zagorodnov, M. Dohlus, and S. Tomin, “Accelerator beam dynamics at the european x-ray free electron laser,” *Phys. Rev. Accel. Beams*, vol. 22, p. 024 401, 2 2019. DOI: `10.1103/PhysRevAccelBeams.22.024401`.

[3] S. Casalbuoni, B. Schmidt, and P. Schmüser, “Far-infrared transition and diffraction radiation, part I: Production, diffraction effects and optical propagation,” DESY, Hamburg Germany, Report 2005-15, 2005.

[4] C. Gerth, B. Beutner, O. Hensler, F. Obier, M. Scholz, and M. Yan, “Online longitudinal bunch profile and slice emittance diagnostics at the European XFEL,” 2017, pp. 153–156. DOI: `10.18429/JACoW-IBIC2017-TUPCC03`.

[5] M. Veronese, R. Appio, P. Craievich, and G. Penco, “Absolute bunch length measurement using coherent diffraction radiation,” *Phys. Rev. Lett.*, vol. 110, p. 074 802, 7 2013. DOI: `10.1103/PhysRevLett.110.074802`.

[6] N. M. Lockmann, C. Gerth, B. Schmidt, and S. Wesch, “Noninvasive THz spectroscopy for bunch current profile reconstructions at MHz repetition rates,” *Phys. Rev. Accel. Beams*, vol. 23, p. 112 801, 11 2020. DOI: `10.1103/PhysRevAccelBeams.23.112801`.

[7] E. Allaria *et al.*, “FLASH2020+ plans for a new coherent source at DESY,” in *Proc. IPAC’21*, TUPAB086, Campinas, SP, Brazil, 2021.

PROPOSED LONGITUDINAL PROFILE DIAGNOSTICS FOR OPTICAL STOCHASTIC COOLING OF STORED ELECTRONS IN THE IOTA RING*

A. H. Lumpkin†, Fermi National Accelerator Laboratory, Batavia, IL 60510 USA

Abstract

The Fermilab Integrable Optics Test Accelerator (IOTA) ring optical stochastic cooling (OSC) experiment is designed for a low nominal beam current (~0.1 microAmps of 100-MeV electrons) to reduce intrabeam scattering (IBS), and during cooling, OSC is expected to reduce the bunch length from ~200 ps to ~130 ps. These equilibrium bunch lengths can be measured using a streak camera and the optical synchrotron radiation (OSR) generated in a ring dipole by the circulating beam as demonstrated on a small ring elsewhere recently. The same model streak camera has been installed on IOTA, and one expects the integrated system will have sufficient sensitivity and resolution for measuring the evolution and equilibrium values of the bunch length during OSC experiments.

INTRODUCTION

Optical stochastic cooling (OSC) experiments [1] are an extension to optical frequencies of stochastic cooling experiments for particle beams performed previously in the microwave regime [2]. They are motivated by an increase in the cooling bandwidth by up to 3 orders of magnitude in principle. Complementary experiments on OSC for electrons are being implemented at 1 GeV at the Cornell Electron Storage Ring (CESR) in an arc bypass [3] and at 100 MeV at the Fermilab Integrable Optics Test Accelerator (IOTA) ring [4]. This latter experiment will use two undulators (with resonant wavelength of 0.95 μm) in a straight section of the ring for the "pickup undulator" (PU) and the "kicker undulator" (KU). An optical delay path is used to match the transit time of the photon emitted in the PU with the same electron that emitted it (after the transit of a magnetic chicane) in the KU. Small longitudinal kicks to the electrons can result in a cooling effect on the momentum offset with appropriate delay tuning.

One of the predicted signatures of successful optical stochastic cooling in the Fermilab IOTA ring is reduction of the bunch length. The IOTA OSC experiment is designed for a low nominal beam current (~0.1 microAmps of 100-MeV electrons) to reduce intrabeam scattering (IBS), and during cooling, OSC is expected to reduce the bunch length from ~200 ps to ~130 ps [4]. These equilibrium bunch lengths can be measured using a streak camera and the optical synchrotron radiation (OSR) generated in a ring dipole by the circulating beam. A similar measurement was previously performed at the Advanced Photon Source with a Hamamatsu C5680 synchroscan streak camera operating at 117.3 MHz [5]. In this case, synchronous summing of OSR resulted in a bunch length measurement of 354 ± 12 ps using only 389 electrons circulating at 425 MeV. At IOTA, an existing streak camera has been modified to operate at the 11th harmonic of the ring's revolution frequency of 7.50 MHz and has been installed on an OSR port in support of the OSC experiments. The integrated system will have sufficient sensitivity and resolution for measuring the evolution and equilibrium values of the bunch length during OSC.

EXPERIMENTAL ASPECTS

A brief description of the FAST/IOTA facility is given in this section plus that of the streak camera system being implemented to support OSC experiments.

The FAST Electron Injector Linac

The Integrable Optics Test Accelerator (IOTA) electron injector at the FAST facility (Fig. 1) begins with an L-band rf photoinjector gun built around a Cs_2Te photocathode (PC [6]). When the UV component of the drive laser, described elsewhere [7] is incident on the PC, the resulting electron bunch train with a 3-MHz micropulse repetition rate exits the gun at <5 MeV. Following a short transport section with a pair of trim dipole magnet sets, the beam passes through two superconducting rf (SCRF) capture cavities denoted CC1 and CC2, and then a transport section to the low-energy electron spectrometer. In this case this dipole is off so 25-MeV beam is transported to and through the cryomodule (CM2) with an exit energy of 100 MeV. Generally, a single bunch of ~100 pC is transported to the IOTA ring for injection into it.

The IOTA Ring

The IOTA ring is a multipurpose research accelerator which normally circulates electrons injected from the linac at 100 or 150 MeV and with a 7.50-MHz revolution frequency. Currents have been stored from a few mA to a single electron. The target area for the OSC experiments is 83,000 e^-, or 0.1 μA and lower. There are 8 dipoles in the ring lattice as shown in Fig. 2, and the streak camera was installed on the M3R OSR port. Signal is shared with one of the standard FLIR CMOS digital cameras used for e-beam transverse size measurements via OSR.

Streak Camera

A C5680 Hamamatsu streak camera with an S20 PC operating with the M5675 synchroscan vertical deflection unit will be phase locked to 82.50 MHz as shown in Fig. 3. The synchroscan unit was selected over the slow sweep unit plugin with a trigger rate of 500 kHz at 2-ns sweep and

---

* Work supported by Fermi Research Alliance, LLC under Contract No. DE-AC02-07CH11359 with the U.S. Department of Energy, Office of Science, Office of High Energy Physics.

† Lumpkin@fnal.gov

ISBN: 978-3-95450-230-1 ISSN: 2673-5350 doi:10.18429/JACoW-IBIC2021-WEPP15

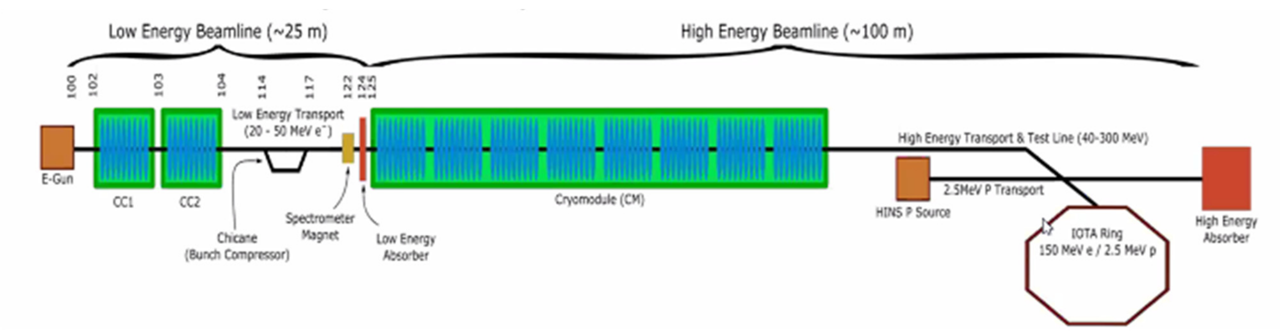

Figure 1: Schematic of the FAST linac with PC rf gun, capture cavities (CCn), low energy transport line, the cryomodule (CM), high-energy transport line, and the IOTA ring.

trigger jitter of 50 ps and the fast sweep unit with a limited trigger rate of 10 kHz compared to the 7.50-MHz revolution frequency of the IOTA ring. In addition, we use a phase-locked-loop C6878 delay box that stabilizes the streak image positions to about 1 ps temporal jitter over 10 s of minutes. These steps enable the synchronous summing of millions of OSR pulses/s generated by the circulating beam or the offline summing of 10-100 images to improve statistics in the sum images.

One can apply the principle to the OSR generated by transit of the beam through one of the IOTA dipoles, M3R. Commissioning of the streak camera system was facilitated through a suite of controls centered around ACNET. This suite includes operational drivers to control and monitor the streak camera as well as Synoptic displays to facilitate interface with the driver. Images were captured from the streak camera using the readout camera, a FLIR 1.5-Mpixel digital CMOS camera with 2/3" format. These can be analyzed both online and with an offline MATLAB-based ImageTool processing program [8]. Adjustable chip integration times 0.1-10 s will support OSR imaging at ultra-low charges. Bunch-length measurements using these techniques previously were done most relevantly on ultra-low charge at the Advanced Photon Source (APS) particle accumulator ring (PAR) [5].

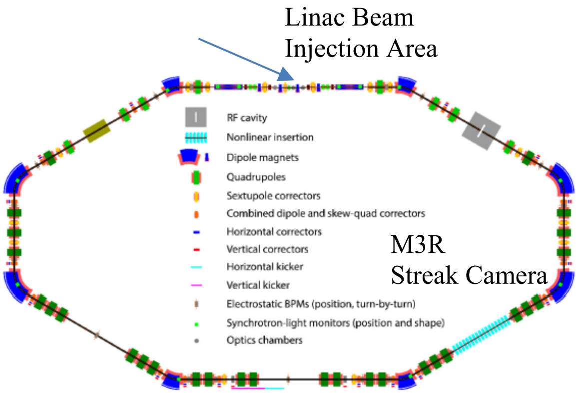

Figure 2: IOTA ring schematic showing the lattice with 8 dipoles. The M3R location for the streak camera is indicated.

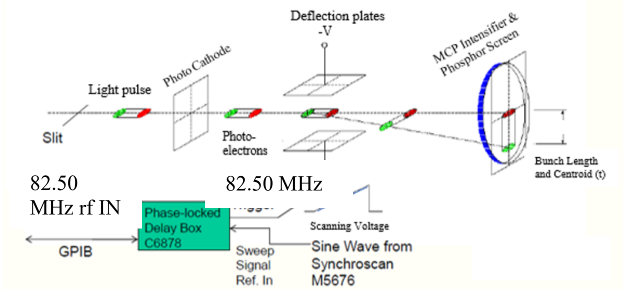

Figure 3: Schematic of the C5680 synchroscan streak camera with phase locking at 82.50 MHz.

SIMULATIONS OF THE OSC EFFECT ON THE LONGITUDINAL PROFILE

A comprehensive set of simulations that assess the IOTA OSC experiment has been provided in reference [4]. These address intrabeam scattering (IBS) as a factor in choosing a parameter space to use to minimize that competing factor in detecting the changes in transverse size due to OSC. These considerations lead to the operating target of 0.1 μA (83,000 e-) in the ring. However, the simulations also show that the longitudinal profile and rms bunch length should show reduction with OSC at all currents considered as shown in Fig. 4. The streak camera measurements will address these effects with potentially a temporal resolution 10 times smaller than the minimum bunch length anticipated. This will result in high sensitivity to parameter changes, more so than expected in the transverse size imaging with OSR.

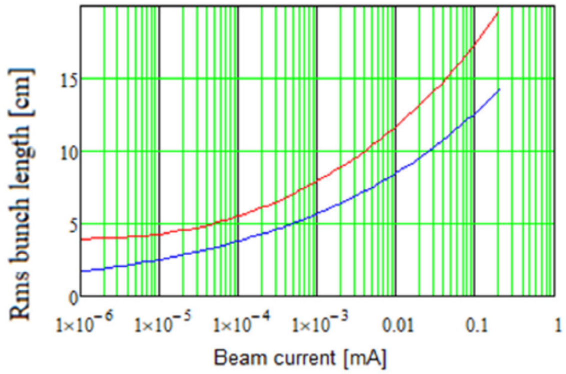

Figure 4: Dependence of rms bunch length on the beam current with (blue) and without (red) OSC [4].

EXPERIMENTAL RESULTS

Proof-of-Principle Example at APS

An example of the x-t streak camera image from the APS PAR experiment is provided in Fig, 5 [5]. This is a 200-image sum from the camera with only 389 electrons stored. With 33 ms per frame for the 8-bit analogue camera, the sum of the digitized images was used to provide a useful image with effectively 6.6 s of integration time. The single Gaussian fit was for 354 ± 12 ps with sampling at about 10-ps resolution. This is a proof-of-principle for the application to OSC experiments starting at 83,000 e^-. With the shorter bunches anticipated in the IOTA OSC cases and with a 12-bit digital camera for readout with integration times of 1-10 s, we expect useful images to be obtainable at ultra-low charges. We note the x-t imaging could provide additional insight into the OSC process as a function of x if proper spatial imaging of the OSR source point to the streak camera entrance slit were done. Dual-sweep operations to track OSC effect evolution at the 100-ms level would be subject to statistical considerations, but successive 1-s chip integrations and 1-Hz readout should be viable at the target current. Shorter integrations would be possible at higher charges with the purpose of looking at the cooling rate of OSC [5].

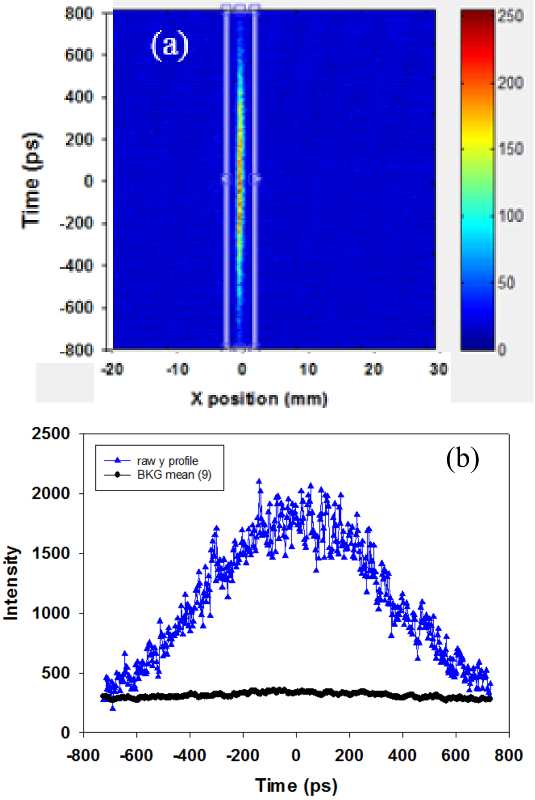

Figure 5: (a) Streak camera sum image from the APS PAR OSR source with 389 electrons stored and (b) the projected temporal profile for the image. A bunch length of 354 ± 12 ps at 425 MeV was determined with a single Gaussian fit [5].

Preliminary Results from IOTA

Preliminary data have recently been reported on the equilibrium bunch length at ~1 μA stored. The 20-30% reduction of bunch length with OSC cooling was visible in the comparison of the vertical/time extent of streak camera images [9].

SUMMARY

In summary, we have described a technique using a synchroscan streak camera and OSR to measure the electron-beam equilibrium longitudinal distributions in the IOTA ring as a function of stored beam current and under the OSC process. A proof-of-principle result for 389 electrons stored was shown from another small ring. An extensive set of experiments has been done with this technique to support OSC studies at IOTA in the past months which will be reported elsewhere.

ACKNOWLEDGEMENTS

The author acknowledges the support of C. Drennan, A. Valishev, G. Stancari, D. Broemmelsiek, and M. Lindgren of the Accelerator Division of Fermilab. He specifically acknowledges J. Jarvis and V. Lebedev for discussions on OSC and J. Santucci for coordinating the relocation of the laser lab streak camera to IOTA.

REFERENCES

[1] M. S. Zolotorev and A. A Zholents, "Transit-time method of optical stochastic cooling", *Phys. Rev. E*, vol. 50, no. 4, p. 3087, 1994.

[2] D. Moehl, G.Petrucci, L.Thorndale, and S.van der Meer, "Physics and Technique of Stochastic Cooling", *Phys. Rep.*, vol. 58, p. 73, 1980.

[3] M.B. Andorf *et al.*, "Optical Stochastic Cooling with an arc bypass in the Cornell Electron Storage Ring", *Phys. Rev. Accel. and Beams,* vol. 23, p. 102801, 2020.

[4] V. Lebedev, J. Jarvis, H. Piekarz, A. Romanov, J. Ruan, M. Andorf, "Conceptual Design Report: Optical Stochastic Cooling at IOTA", `https://arxiv.org/abs/2012.09967`

[5] A.H. Lumpkin and K. P. Wootton, "High-Resolution Longitudinal Profile Diagnostics for Ultralow Charges Stored in a Ring", *Phys. Rev. Accel. and Beams*, vol. 24, p. 072806, 2021.

[6] The ASTA User Facility Proposal, Fermilab-TM-2568, October 2013.

[7] J. Ruan, M. D. Church, D. R. Edstrom, T. R. Johnson, and J. K. Santucci, "Commission of the Drive Laser System for Advanced Superconducting Test Accelerator", in *Proc. 4th Int. Particle Accelerator Conf. (IPAC'13)*, Shanghai, China, May 2013, paper WEPME057, pp. 3061-3063.

[8] R. Thurman-Keup, FNAL, off-line MATLAB-based Image-Tool, 2011.

[9] Jonathan Jarvis and Valeri Lebedev, "OSC at IOTA: The World's First Experimental Demonstration of Optical Stochastic Cooling", Accelerator Physics and Technology Seminar, May 11, 2021, Fermilab.

ISBN: 978-3-95450-230-1 ISSN: 2673-5350 doi:10.18429/JACoW-IBIC2021-WEPP16

COMPARISON OF FESCHENKO BSM AND FAST FARADAY CUP WITH LOW ENERGY ION BEAMS

R. Singh*[1], S. Lauber[1,2,3], W. Barth [1,2,3], P. Forck [1], M. Miski-Oglu [1,2], T. Reichert [1], V. Scarpine [4], T. Sieber [1], D. Sun [4]
[1]GSI Helmholtz Center for Heavy Ion Research, Darmstadt, Germany
[2]Helmholtz Institute Mainz, Mainz, Germany
[3]Johannes Gutenberg-University, Mainz, Germany
[4]Fermilab, Batavia, IL, USA

Abstract

A comparison between Fast Faraday Cup and Feschenko longitudinal bunch shape detectors was recently performed at HELIAC Advanced Demonstrator beamline at GSI. Feschenko bunch shape monitor (BSM) uses the time to space conversion by means of secondary electrons emitted from a wire correlated to a rf deflector [1], while the fast Faraday cup (FFC) measures the deposited charge in a cup geometry matched to 50 Ω. The FFC design aims to minimize the bunch shape dilution due to field polarization and secondary electrons produced on irradiation [2]. An He^{1+} with 100 µA average current and 1.4 MeV/u kinetic energy is utilized for this comparison. A buncher upstream of the detectors was operated to focus the beam longitudinally. The results are discussed in this contribution.

INTRODUCTION

Longitudinal charge distribution measurements are essential for the commissioning and optimization of linear accelerators. The emergence of new nonlinear beam dynamics concepts employing a variation of particle synchronous phases different from the traditional -30 deg resonance acceleration pattern, e.g. KONUS [3], EQUUS [4] has called for better understanding of longitudinal phase space and relevant instrumentation. Charge distribution measurements of non relativistic heavy ions beams are not feasible with electromagnetic-field sensing devices like capacitive pickups because the field distribution is elongated in comparison to charge distribution. A commonly used instrument for longitudinal beam profile measurements is the Feschenko bunch shape monitor (BSM), which relies on the time-to-space conversion of electrons emitted when the beam interacts with a wire [5]. Alternatively, there has been several designs for a Fast Faraday Cup (FFC), which intend to avoid the induction of image charges on the cup before the charges are deposited on the cup while maintaining a 50 Ω geometry [6–8]. Recently, longitudinal charge distribution measurement using coherent transition radiation in GHz regime has been investigated [9]. Although BSMs and FFCs are widely used, no benchmarking of these devices among each other is known to us. In this contribution, we compare both of these monitors under similar beam and machine conditions and the experimental results are discussed.

The tests were performed at the Helmholtz Linear Accelerator (HELIAC) *Advanced Demonstrator* beam line at GSI [10]. The HELIAC components marked in grey were not installed. Various charge states and ion species were delivered to the test setup by the GSI High Charge State (HLI) injector with an kinetic beam energy of 1.4 MeV/u and a duty cycle of up to 25 % in the regime of some 30-100 µA average current. The beam line is equipped with phase probe sensors, a slit-grid emittance measurement device, beam position monitors, beam profile grids as well as Feschenko BSMs. Recently a test Fast Faraday Cup was made available on loan from Fermilab for comparison with Feschenko BSMs, which was installed to the preliminary line setup with a beam pipe substituting the cavities. The test beamline (with the cavities to be installed) is shown in Fig. 1.

BUNCH SHAPE MONITOR

The bunch shape monitor of Feschenko type provides for precise measurements of heavy ion beams with an accuracy of up to ±0.5 deg at an rf frequency of 108 MHz [5]. It consists of three main parts: a thin filament in the beam line, an optical system and an electron multiplier. The thin filament is irradiated by the heavy ion beam, and thus emits secondary electrons in all directions. The optical system, which is entered by the secondary electrons through a pinhole at the border of the beam pipe, provides for the suppression of noise and translates the time dependent electron current $I(t)$ to a spatially resolved signal $I(z)$, primarily with use of an deflecting electric field. A narrow part of the spatial signal is steered to enter the secondary electron multiplier, where it is measured. Thus, $I(z)$ is scanned successively by steering and subsequently available for readout. The installed version of the Feschenko BSMs optical system features additional bending magnets for further noise reduction [1].

A measurement series with the Feschenko-BSMs has been successfully used to calculate the longitudinal phase portrait of the bunch with use of an advanced tomographic reconstruction technique at the HELIAC *Advanced Demonstrator* beam line [11]. Although a useful device, there are couple of shortcomings of the BSM, first of which is the averaged nature of the measurement, i.e. measurement at each phase is a different macropulse which does not allow resolving the bunch length variations between consecutive macropulses.

---

* r.singh@gsi.de

ISBN: 978-3-95450-230-1 ISSN: 2673-5350 doi:10.18429/JACoW-IBIC2021-WEPP16

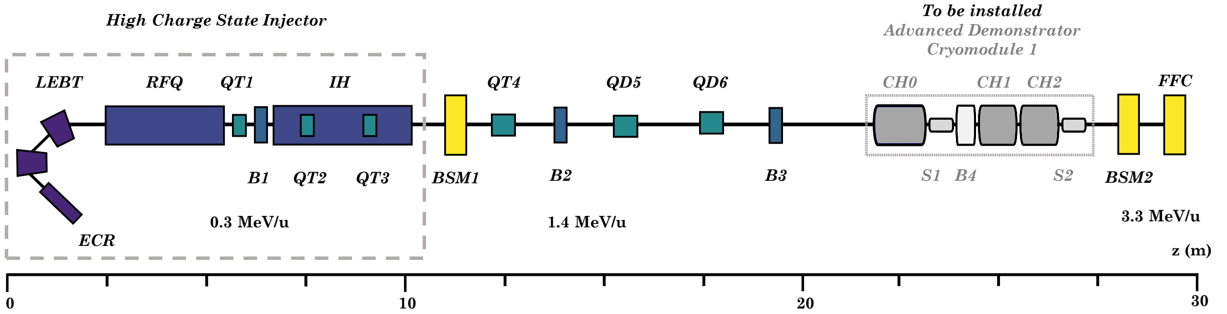

Figure 1: Relevant beamline and its components: Quadrupole Triplet (QT), Buncher (B), Interdigital H-Mode Cavity (IH), Feschenko Bunch Shape Monitor (BSM), Quadrupole Doublet (QD), superconducting Crossbar H-Mode Cavity (CH), superconducting Solenoid (S), Fast Faraday Cup (FFC). The greyed out components were not installed during these tests.

Thus, bunch-by-bunch longitudinal profile measurements which are required for countering intensity effects or any other fast changes using a low level rf feedback are outside the scope of BSM. Secondly, careful tuning is required for many parameters in order to align the beam with the wire and obtaining appropriate secondary electron statistics at the final detector. In context of phase space reconstruction, there is a limitation given by the measuring time of the BSM. A typical measurement time of 1-2 min per profile is experienced for high resolution measurements. At least 10 measurements at different buncher rf-amplitudes are necessary for the reconstruction, which makes this analysis time-consuming. The usage of Fast Faraday Cup is being investigated in these contexts.

FAST FARADAY CUP

The Fast Faraday Cup used in this work was obtained on loan from Fermilab with details discussed here [12]. Its design consists of a ground plate with an oriface diameter of 0.8 mm which allows a small part of the beam to reach the collector plate at a "gap distance" of 1.7 mm from the oriface. The collector is basically a hole in the central conductor of a coaxial cable terminated into two symmetric 50 Ω outputs to avoid reflections. The depth of collector hole is chosen to avoid secondary particles leaving the collector. The choice of gap distance and oriface aperture is dependent on the beam velocity and is chosen to avoid dilution or widening of the measured charged distribution with respect to actual charge distribution for the HLI beam parameters. Further details of these design considerations for certain simplified geometries can be found here [13]. The scattering parameters of the device were measured up to 20 GHz and the terminations were found to be well matched. The S21 parameter is shown in Fig. 2. The relevant region is upto 8 GHz until which the frequency response is rather constant. A wideband amplifier with 10 GHz bandwidth (0.01-10 GHz) was used [14] as the termination followed with semi-rigid cables. The signal was digitized with a Lecroy wavemaster WaveMaster 830Zi-B^{TM} with the maximum sampling rate of 80 GSa/s and an analog bandwidth 22 GHz. Challenges associated with FFC measurements are discussed later in this report.

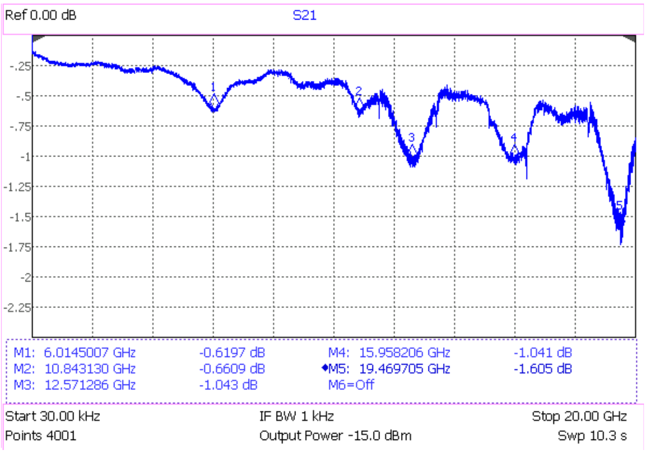

```
M1:  6.0145007 GHz    -0.6197 dB     M4:  15.958206 GHz    -1.041 dB
M2:  10.843130 GHz    -0.6609 dB    ◆M5:  19.469705 GHz    -1.605 dB
M3:  12.571286 GHz    -1.043 dB      M6=Off
Start 30.00 kHz                IF BW 1 kHz                  Stop 20.00 GHz
Points 4001                    Output Power -15.0 dBm           Swp 10.3 s
```

Figure 2: S21 measurement of the FFC from 30 kHz to 20 GHz.

MEASUREMENTS

Figure 1 shows the schematic of the test set-up. The bunchers B2 and B3 were manipulated to change the longitudinal orientation and phase profile of the He^{1+} ion beam. Figure 3 (top) shows the initial section of the overlaid measured signals from the FFC and an immediately preceding pick-up (PU) for a single 100 µs macro-pulse. Figure 3 (bottom) shows the enlarged view showing three rf periods at the peak around 20 µs from the start of signal recording. The beam was transversely focused onto the FFC opening in order to concentrate all the charges on the FFC collector plate and obtain this single-shot FFC measurement. The average beam current was 102 µA for this specific macropulse. Signal amplitude fluctuations within the macro-pulse are evident both on FFC and PU signals. The cause of these rather large beam current fluctuations is not clear, but was consistently observed on FFC, pick-up as well as BSM signal in the reported measurements. Figure 4 (top) shows the same FFC

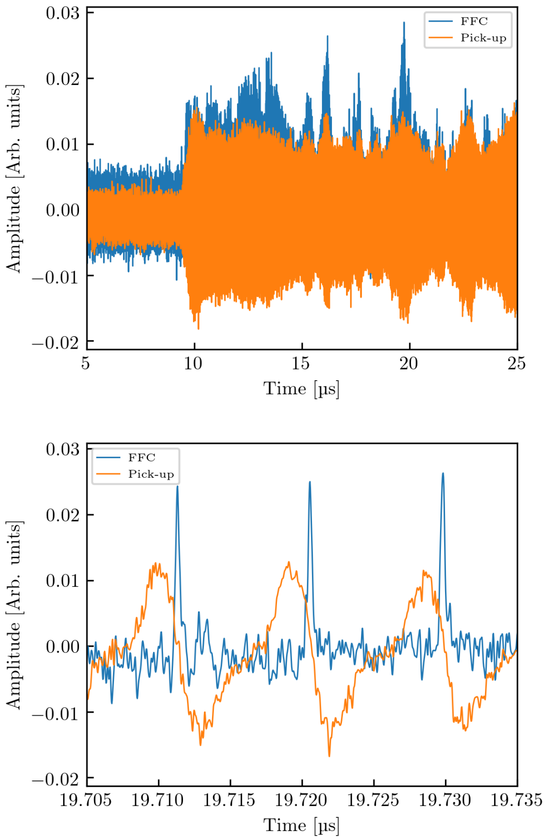

Figure 3: (Top) Direct digitized signals from a single macro-pulse from FFC and pick-up, the fluctuations are similar and visible in both pick up and the FFC. (Bottom) Enlarged view at 19.72 µs for three consecutive rf periods.

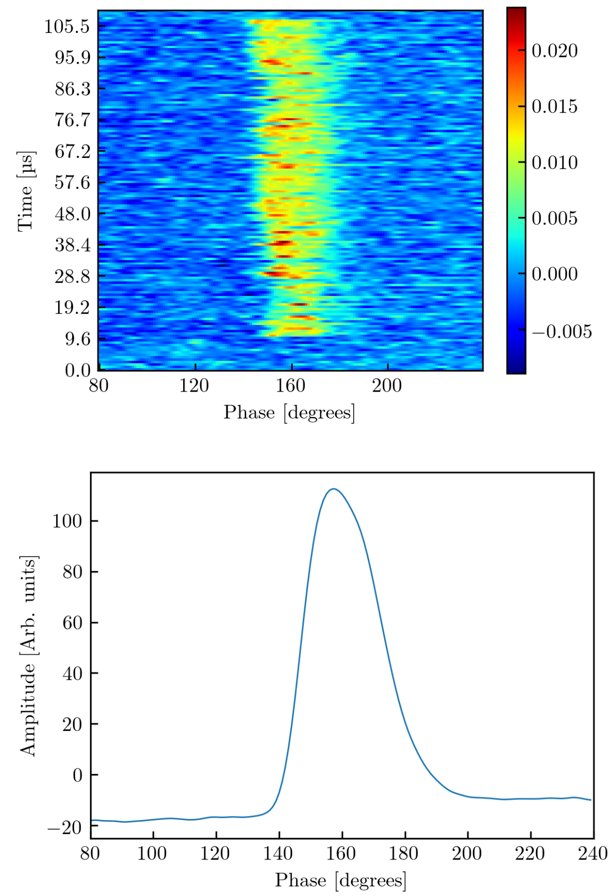

Figure 4: (Top) Time domain signal sorted per rf period over the macro-pulse for FFC. (Bottom) Integration along y-axis resulting in an averaged longitudinal profile over the full macro-pulse.

signal as in Fig. 3, but splitted and stacked per rf period in units of µs and degrees. The plot shows the evolution of bunch length and signal strength during the macro-pulse. There are <10% fluctuations in the bunch length over the macropulse. Figure 4 (bottom) shows an integrated bunch shape measurement over the macro-pulse. Such an integrated pulse is used for comparison with the bunch shape monitor (BSM) discussed next.

Figure 5 shows the FFC and BSM signals for three machine settings. The profiles are normalized to the area under the profiles. The Feschenko BSM is installed ≈ 1 m upstream of the FFC. The BSM scans with 1 deg per macro-pulse with a temporal resolution of 1 µs. Thus one BSM measurement covering 200 deg phase requires 200 macro-pulses. The FFC measurement is performed within a single macro-pulse with the same procedure as mentioned for Fig. 4 (bottom). One has to note that the transverse beam alignment was performed in order to irradiate the FFC oriface by the core of the beam. In hindsight, it appears that the BSM wire was not irradiated by the core of the beam, which is potentially the reason behind large "noise" observed on the bunch shape measured by the BSM. The bunch shape results are consistent with each other and agreement is rather good given that both the measurement techniques are fundamentally different. An additional measurement was performed for FFC to observe the dependence of longitudinal profile on the transverse measurement location of the sampled beam, e.g. coupling on longitudinal and transverse planes. Figure 6 (top) shows the measured charge distribution when the FFC was displaced upto 5 mm vertically. The plots are not normalized to charge in this case in order to highlight the change in obtained signal as a function of FFC position. No significant change in the measured charge distribution is seen as a function of transverse position. Interestingly, for certain offsets ($\Delta x = -2$ mm in this case) of FFC, a fixed frequency close to third harmonic of rf in this case is picked up. The exact cause is not clear yet and will be investigated further.

CONCLUSION AND OUTLOOK

The first results comparing the devices look promising, and some further test measurements need to be performed to fully characterize the measured charge distribution from the FFC.

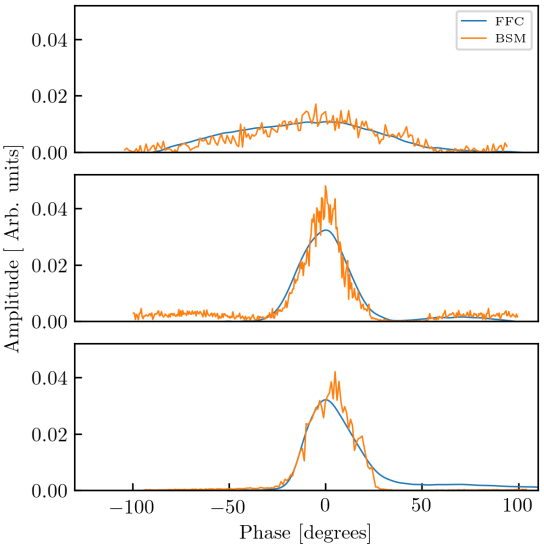

Figure 5: Comparison of the normalized longitudinal profiles of FFC and BSM for three machine settings, (Top) B2 = 0 V, (Middle) B2 = 2.35 V, (Bottom) B2 = 2.35 V with additional transversal beam focus onto FFC input.

1. Investigatation of interferences observed on the FFCs at some transverse location with respect to beam is required. Further, transition radiation generated when charges cross the oriface also needs to be simulated.
2. Measurement of the potential effect of secondary emissions on the measured profile. This effect can be investigated by applying a bias either on the collector or ground plate in line with [6].
3. Further thermal simulations in order to determine the intensity thresholds which the non-cooled FFC can withstand.

Finally, the potential increase in oriface radius need to be evaluated for improved signal to noise ratio as well as easier alignment with the beam. Therefore, widening the oriface diameter and all consequent changes in the FFC design are under consideration.

ACKNOWLEDGMENTS

We thank the mechanical workshop colleagues from beam diagnostics for timely installations of the set-up. Alexander Shemyakin is acknowledged for helpful discussions on the FFC design.

REFERENCES

[1] S. Gavrilov, A. Feschenko, D. Chermoshentsev, "Bunch shape monitors for modern ion linacs", *Journal of Instrumentation*, vol. 12, p. P12014, 2017. `doi:10.1088/1748-0221/12/12/P12014`

[2] A. V. Shemyakin *et al.*, "Experimental Study of Beam Dynamics in the PIP-II MEBT Prototype", in *Proc. 61st ICFA Advanced Beam Dynamics Workshop on High-Intensity and High-Brightness Hadron Beams (HB'18)*, Daejeon, Korea, Jun. 2018, pp. 54–59. `doi:10.18429/JACoW-HB2018-MOP1WB03`

[3] R. Tiede *et al.*, "KONUS Beam Dynamics Designs Using H-Mode Cavities", in *Proc. 42nd ICFA Advanced Beam Dynamics Workshop on High-Intensity and High-Brightness Hadron Beams (HB'08)*, Nashville, TN, USA, Aug. 2008, paper WGB11, pp. 223–230.

[4] S. Minaev *et al.*, "Superconducting, energy variable heavy ion linac with constant β, multicell cavities of CH-type", *Phys. Rev. ST Accel. Beams*, vol. 12, p. 120101, 2009.

[5] A. V. Feschenko, "Methods and Instrumentation for Bunch Shape Measurements (Invited)", in *Proc. 19th Particle Accelerator Conf. (PAC'01)*, Chicago, IL, USA, Jun. 2001, paper ROAB002, pp. 517-521. `doi:10.1109/PAC.2001.987557`

[6] W. R. Rawnsley *et al.*, "Bunch measurements using Fast Faraday cups and an oscilloscope operated by LabVIEW over ethernet", *AIP Conference Proceedings*, vol. 546, p. 547, 2000. `doi:10.1063/1.1342629`

[7] F. Marcellini and M. Poggi, "Design of a Tapered Stripline Fast Faraday Cup for Measurements on Heavy Ion Beams: Problems and Solutions", *AIP Conference Proceedings*, vol. 451, p. 522, 1998. `doi:10.1063/1.57056`

[8] M. Ferianis *et al.*, "Characterisation of Fast Faraday Cups at the ELETTRA Linac", in *Proc. 6th European Workshop on Beam Diagnostics and Instrumentation for Particle Accelerators (DIPAC'03)*, Mainz, Germany, May 2003, paper PM10, pp. 113–115. `http://accelconf.web.cern.ch/d03/papers/PM10.pdf`

[9] R. Singh and T. Reichert, "Longitudinal charge distribution measurement of non-relativistic ion beams using coherent transition radiation", `https://arxiv.org/abs/2107.08689`

[10] W. Barth *et al.*, "First heavy ion beam tests with a superconducting multigap CH cavity", *Phys. Rev. Accel. Beams*, vol. 21, p. 020102, 2018.

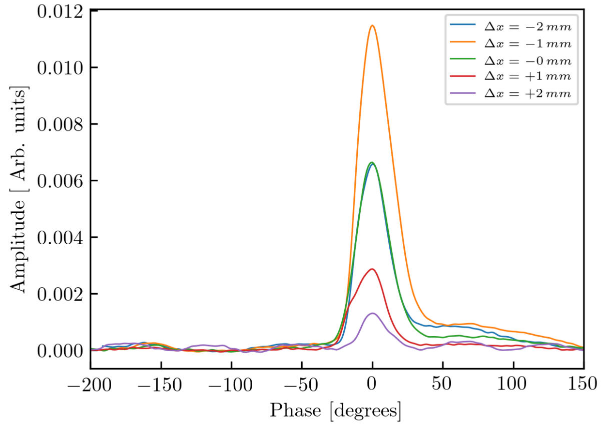

Figure 6: FFC is moved by ±2 mm and the profile is measured at each step.

[11] S. Lauber *et al.*, “Longitudinal phase space reconstruction for a heavy ion accelerator”, *Phys. Rev. Accel. Beams*, vol. 23, p. 114201, 2020.

[12] J.-P. Carneiro, B. Hanna, L. Prost, A. Saini, A. Shemyakin and D. Sun, “Longitudinal beam dynamics studies at the PIP-II injector test facility”, *Int. J. Mod. Phys. A*, vol. 34, no. 36, p. 1942013, 2019. `doi:10.1142/S0217751X19420132`

[13] A. Shemyakin, “Estimation of dilution of a Fast Faraday Cup response due to the finite particles speed”, `https://arxiv.org/abs/1612.09539`

[14] Evaluation board EVAL-HMC8410; `https://www.analog.com/en/design-center/evaluation-hardware-and-software/evaluation-boards-kits/EVAL-HMC8410.html`

NEW X-BAND RF DEFLECTOR FOR FEMTOSECOND DIAGNOSTICS OF LCLS-II BEAMS[*]

V. A. Dolgashev[†], H. Bassan, S. Condamoor, A. Haase, P. Krejcik, T. Maxwell, J. Wang,
SLAC National Accelerator Laboratory, Menlo Park, CA, USA

Abstract

An X-band Transverse deflector CAVity (XTCAV) has been successfully developed for femtosecond electron and X-ray pulse temporal diagnostic at the Linear Coherent Light Source (LCLS). The working frequency for the deflector is 11.424 GHz. New free electron laser LCLS-II has two undulator beamlines, one Soft-X-Ray (SXR) and another Hard-X-Ray (HXR). The HXR line deflector is made of two one-meter long XTCAVs. We have designed, built, installed and commissioned another, 1.5 meter long X-band deflector in the Soft-X-Ray beam line. Both HXR and SXR deflectors share one klystron. RF power is transmitted from a 50 MW klystron to a tunnel in an overmoded circular waveguide and then directed to either of the deflectors using a remotely controlled variable RF power splitter. The power split ratio can be changed arbitrarily, and both deflectors can work simultaneously. The system is successfully commissioned and operational. In this article, we provide details on the development and commissioning of the new deflector.

INTRODUCTION

LCLS is the world's first hard X-ray free electron laser. It allows for X-ray snapshots of atoms and molecules at work, providing atomic resolution detail on ultrafast timescales to reveal fundamental processes in materials, technology and living things [1]. One of the most important tools for electron beam diagnostics in LCLS is X-band transverse deflecting structures [2,3]. XTCAVs are used in the LCLS accelerator for bunch length and beam longitudinal phase space measurements. The high frequency time variation of the deflecting fields streaks the electron bunch while the resulting transverse beam shape measured on a profile monitor represents the absolute bunch length [2,3]. The LCLS-II is an evolution of the original LCLS with a much higher pulse repetition rate, it is also will benefit from the diagnostic capabilities of the XTCAVs. In LCLS-II there are two X-ray beam lines: HXR line and SXR line. To achieve femtosecond resolution, the XTCAVs are driven by a SLAC 50 MW XL-4 klystron. The klystron and its high voltage modulator are the most expensive components of the system. Rather than purchase a second XL-4 klystron and modulator we chose to use one klystron with a power splitter [4]. This paper will provide details of upgrading the original HXR system with its original two-cavity-deflector, and the addition of a new, simultaneously operated single-cavity deflector on the SXR beamline. The new layout is shown in Fig. 1.

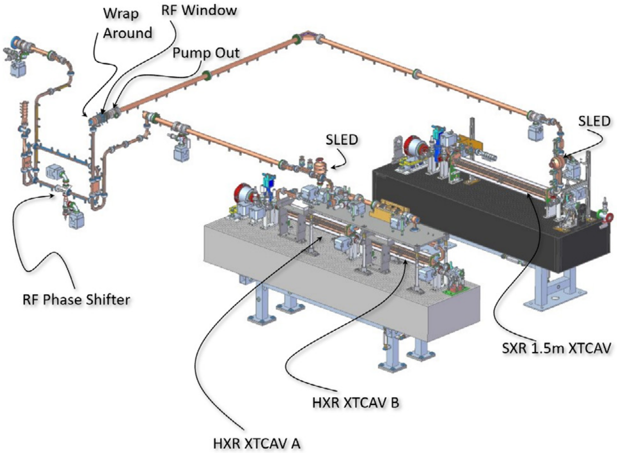

Figure 1: System layout showing the rf deflectors (XTCAVs) of HXR and SXR beam lines. RF power from klystron is coming from the left. LCLS electron beam direction is from the left to right.

Upgrade Goals and Approach

The aim of the modernization was to create a system for measuring the longitudinal phase space of electron beams with a femtosecond resolution, which allows reconstructing the temporal structure of an X-ray pulse in an FEL for alternating operation in two X-ray beams. The goal of the upgrade was to build a system for measuring the longitudinal phase space of electron beams with a femtosecond resolution, which allows reconstructing the temporal structure of FEL X-ray pulse for interleaved operation in two X-ray beamlines, HXR and SXR, at LCLS repetition rate of 120 Hz. To achieve this, we proposed following:

- Build, tune and install a new, longer RF deflector in the Soft X-Ray beamline.
- Build, tune, install a new SLED rf-pulse compressor for operation with new 1.5 m deflector.
- Build, and install a multi-megawatt RF variable power splitter based on a remotely controlled phase shifter.
- Move HXR SLED closer to HXR deflector, install both HXR and SXR SLEDs downstream after the rf power splitter.
- Upgrade the control system for operation with the copper linac, then upgrade it for superconducting linac of LCLS-II.

---

[*] Work supported by the U.S. Department of Energy Contract No. DE-AC02-76SF00515.

[†] dolgash@slac.stanford.edu

NEW HARDWARE

1.5 m Long RF Deflector

The HXR line uses two 1 m long XTCAVs [2] fed from a power divider. The performance of a deflector is ultimately limited by rf breakdowns, which in turn limit input rf power into the deflector. The two-cavity system achieves higher deflecting voltage required for diagnostics of higher energy HXR beams, but is more costly to fabricate. The electron beam in the SXR line has lower energy, so the same temporal resolution as the HXR can be achieved with a single deflector. To compensate some of the lost voltage, we increased the length of the deflector from 1 m to 1.5 m. The deflectors are constant impedance structures and share identical electrical design, with added regular cells for longer deflector. The parameters common for both deflectors are shown in Table 1. The parameters which depend on lengths of the deflectors are shown in Table 2.

Table 1: Common Parameters of both 1 m and 1.5 m 11.424 GHz XTCAVs

Parameter	**Value**
Frequency	11.424 GHz
Beam pipe diameter	10 mm
Phase advance per cell	$2\pi/3$
Kick/m in one cell@20 MW	31 MeV/m
Max. el. field (inp. coupler)	100 MV/m
Max. mag. field (inp. coupler)	405 kA/m
Max. el. field in first cell	115 MV/m
Max. mag. field in first cell	340 kA/m
Peak pulse heating in first cell@110 ns	16 °C@20 MW
Peak pulse heating in coupler@110 ns	23 °C@20 MW
Cell quality factor	6300
Dipole mode frequency separation	100 MHz
Group velocity/speed of light	3.2 %

Table 2: Parameters of 1 m and 1.5 m XTCAVs

Parameter	**1 m**	**1.5 m**
# cells	117	171
Total structure kick@20MW	24 MeV	30 MeV
Total attenuation	0.62 Np	0.90 Np
Dissipated power@20MW	14 MW	16.7 MW
Structure length (with beam pipes)	1.185 m	1.657 m
Fill time	~ 110 ns	~ 160 ns

Variable RF Power Splitter

We have developed an adjustable RF power splitter to enable one klystron to power two RF deflectors with an arbitrary power ratio. Our splitter must meet the following requirements: reliably and reproducibly direct a pre-set power to any of the deflectors, operate at a power of 40-50 MW without faults, and allow a transition to an operating mode in which all the power of the klystron is supplied to any of the deflectors pulse to pulse. The splitter consists of two waveguide hybrids, a remotely controlled phase shifter and auxiliary components such as pumpouts and rf loads. When we started the project we had two previously developed phase-shifters, one designed by Chris Nantista, and more recent one developed by Sami Tantawi and based on a compact high power polarizer [5]. The former was well tested at high power, but the latter is more compact. We adopted the polarizer-based phase-shifter after extensive high-power testing.

MANUFACTURING AND TUNING

1.5 m Deflector

This 1.5 meter long X-band rf deflector is currently the longest of its kind built at SLAC or elsewhere. All cell machining was done at the SLAC Advanced Prototype Fabrication machine shop. Fabrication was completed by diffusion bonding the cells in two half-length structures then joining these and the couplers together with specially designed center coupling cells with high temperature brazing. The bonding and brazing were done in an atmospheric pressure hydrogen retort furnace. Before tuning the completed assembly was straightened to within 200 μm. For preliminary tuning and post-tuning characterization we used the nonresonant perturbation technique, the so-called beadpull [6, 7]. Setup of the final beadpull is shown in Fig. 2. For the tuning of the deflector we used the nodal shift method [8] with a reflective plunger. During the measurements and tuning, the deflector was filled with pure dry nitrogen and its temperature was stabilized to 20 °C ± 0.05 °C.

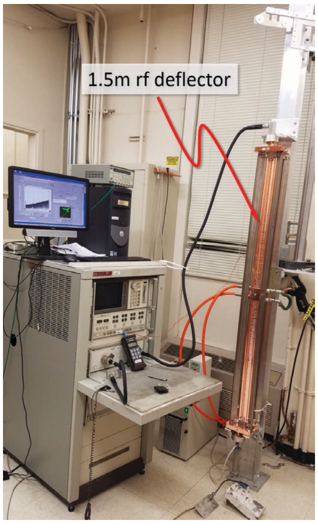

Figure 2: Final beadpull measurements of new 1.5 m rf deflector.

The amplitude and phase of electrical field were obtained by analyzing the reflection from a small ceramic bead moving along the central axis of the deflector. Figure 3(a) shows the measured electrical field amplitude along the central axis.

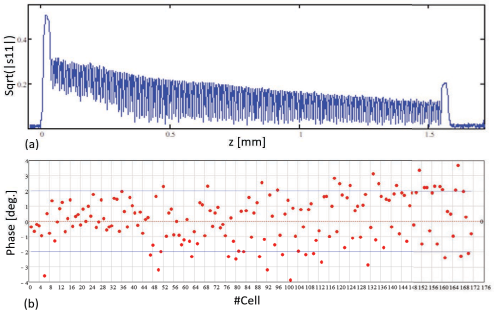

Figure 3: Results of beadpull measurements for the new 1.5 m rf deflector: (a) RF electric field amplitude along the central axis ; (b) Difference between beam synchronous phase and rf phase along the central axis.

This data shows that there is no internal standing wave, this means that the tuning was successful. Figure 3(a) shows the measured rf phase variation from beam-synchronous phase along the central axis of the deflector *vs.* cell number. Random phase variation of ±3 ° has no appreciable effect on deflector operation.

New SLED

The second SLED had the same design as one already feeding HXR XTCAVs [9]. It consists of a compact polarizer [5] and a spherical cavity. The tuning of the cavity was done in two steps. The cavity is build in with a ridge-to-be-cut and a post for deforming the cavity top. The ridge was cut after "before final brazing" cold test to put the frequency in the range of the deformation tuner. The final cold test of the cavity is shown in Fig. 4. The final parameters of the cavity were a good fit for feeding the new deflector.

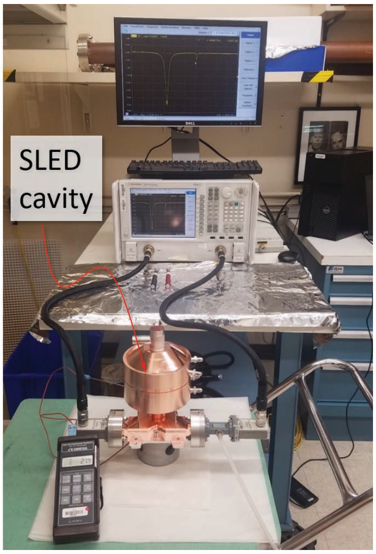

Figure 4: Cold test of new SLED rf pulse compressor.

Variable RF Power Splitter

The rf power splitter was built out of previously developed components such as waveguide hybrids, bends, dry high power rf loads, etc. Again, most of the components were built at SLAC Advanced Prototype Fabrication machine shop. Before installation the splitter was successfully cold tested. The cold test setup is shown in Fig. 5.

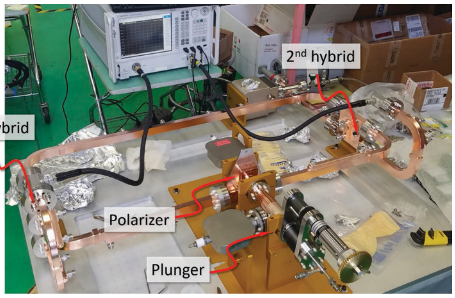

Figure 5: Cold test of variable RF power splitter.

CONTROLS UPGRADES

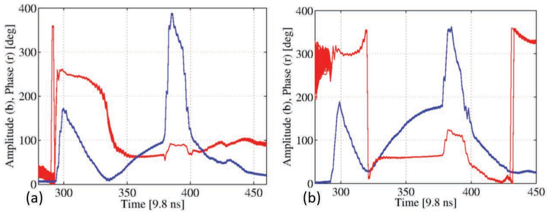

Figure 6: Typical output signals of (a) SXR and (b) HXR SLED RF pulse compressors. Red curves are amplitudes in arbitrary units and blue curves are phases in degrees. The resonant frequencies of the SLED cavities are controlled independently from each other with cooling water temperature.

With the addition of the new SLED and XTCAV in the SXR beamline, several controls upgrades were completed to support the independent and simultaneous operation of two SLEDs and both the XTCAVs in the HXR and SXR beamlines. Some of these upgrades are summarized below with brief notes on the main LLRF software upgrades.

- A second *phase and amplitude detector* (PAD) was added to read in the LLRF signals from the SXR XTCAV and the SXR SLED cavity. An example of SLED output signals measured with the PADs is shown in Fig. 6.
- Vacuum controls were upgraded to precisely monitor and control the vacuum in the new RF waveguides and waveguide components.
- As second remotely controlled water chiller for the new SLED and additional temperature sensors were added for temperature monitoring and feedbacks.
- The LLRF Feedback Controls Software was upgraded to support the SXR XTCAV operation.

Table 3: Summary of Practically Achieved Parameters for HXR and SXR RF Deflectors

Parameter	**HXR**	**SXR**	**Units**
Beam Energy	4-14	4-10	GeV
Beam emittance	0.5	0.5	µm
Structure length (with beam pipes)	2×1.185	1.657	m
Number of regular cells (including joining ring)	2×113	171	
Input power	$70 + 70$	70	MW
On-crest deflecting voltage	80	60	MeV
Resolution achieved	0.5-2	1-4	rms fs
Distance deflector-screen	32	32	m
Beta functions at RF deflector	80@8 GeV	80@8 GeV	m
Beta functions at the screen	63@8 GeV	55@8 Gev	m

The original Software Multiplexer (MUX) for the HXR was split into two virtual MUX-es for independent LLRF Feedback Controls of the two deflectors. This was based on the allocation of the Data Slots corresponding to the two beamlines wherein the two feedbacks are regulated independently of each other. Two different timeslots are used to manage and detect the beam arrival time into HXR and SXR beamlines. The XTCAV LLRF Software is able to support independent LLRF Feedback Controls for the two cavities by setting up and managing two different configurations of these timeslots corresponding to two pairs of data slots. The two data slots have independent settings and read-backs thus allowing the user to configure both the cavities for different rf phase and amplitude values of the klystron output. With these upgrades to the LLRF Feedback Software, deflectors in both beamlines could operative simultaneously, at LCLS rate of 120 Hz, in spite of coupling of the deflectors though the klystron and common rf distribution. This simultaneous operation was a significant milestone for LLRF feedback controls in the LCLS two-beamline (HXR and SXR) operations, and a predecessor for other LLRF stations' feedback controls that are yet to come for future operation with LCLS-II superconducting linac.

OPERATION

The system was installed at the beginning of October 2020 and we started high power processing and commissioning of controls system. A photo of 1.5 m deflector in SXR beamline is shown in Fig. 7. First successful streaking of the SXR beam was done on November 7th 2020. Since then the deflectors are routinely used by LCLS operators to tune the linac and FEL. As an example we show images of the streaked beams in Fig. 8. Typical working parameters of the system are shown in Table 3.

ACKNOWLEDGMENTS

This work is an excellent example of successful and coherent work of multiple SLAC departments: Accelerator Directorate, Technology-Innovation-Directorate, Mechanical Fabrication Department, Facilities and Operation, etc. Together they maintain SLAC competence in high gradient normal conducting accelerators.

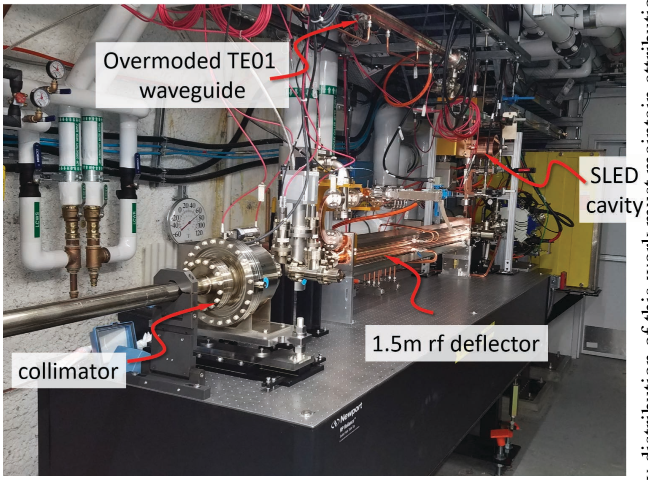

Figure 7: New 1.5 m rf deflector installed in Soft-X-Ray beamline. LCLS beam is coming from the left.

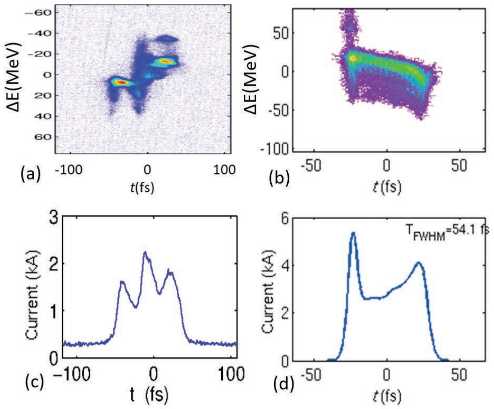

Figure 8: Measurement of lasing LCLS beam's longitudinal phase space using SXR and HXR rf deflectors: (a) image on SXR screen with it current profile in (c); (b) image on HXR screen with it current profile in (d).

REFERENCES

[1] LCLS-II Project Team, "LCLS-II Final Design Report," SLAC, Menlo Park, CA, USA, 2014, p. 554.

ISBN: 978-3-95450-230-1 ISSN: 2673-5350 doi:10.18429/JACoW-IBIC2021-WEPP18

[2] V. A. Dolgashev *et al.*, "Design and application of multi-megawatt X -band deflectors for femtosecond electron beam diagnostics," P*hys. Rev. Spec. Top.-Accel. Beams*, vol. 17, no. 10, p. 102801, Oct. 2014. `doi:10.1103/PhysRevSTAB.17.102801`

[3] C. Behrens *et al.*, "Few-femtosecond time-resolved measurements of X-ray free-electron lasers," *Nat. Commun.*, vol. 5, no. 1, pp. 1–7, Apr. 2014. `doi:10.1038/ncomms4762`

[4] Y. Ding *et al.*, "X-band RF Transverse deflectors for the LCLS-II", SLAC LCLS-II Tech. Note, vol. 15, no. 21, 2015.

[5] Matthew Franzi *et al.*, "Compact rf polarizer and its application to pulse compression systems", *Phys. Rev. Accel. Beams*, vol 19, p. 062002, 2016.

[6] C. W. Steele, "A Nonresonant Perturbation Theory,", *IEEE Trans. Microwave Theory Tech.*, vol 14, p. 70, 1966.

[7] K. B. Mallory and R. H. Miller, "On Nonresonant Perturbation Measurements (Correspondence)", *IEEE Trans. Microwave Theory Tech.*, vol. 14, p. 99, 1966.

[8] E. L. Ginzton, *Microwave Measurements*, NY, USA:McGraw-Hill, 1957.

[9] Juwen W. Wang *et al.*, "Development for a supercompact X -band pulse compression system and its application at SLAC", *Phys. Rev. Accel. Beams*, vol. 20, p. 110401, 2017.

ISBN: 978-3-95450-230-1 ISSN: 2673-5350 doi:10.18429/JACoW-IBIC2021-WEPP19

BUNCH ARRIVAL-TIME MEASUREMENT WITH ROD-SHAPED PICKUPS ON A PRINTED CIRCUIT BOARD FOR X-RAY FREE-ELECTRON LASERS*

B. E. J. Scheible†, S. Mattiello, A. Penirschke, TH Mittelhessen, Friedberg, Germany
M. K. Czwalinna, H. Schlarb, Deutsches Elektronen-Synchrotron, Hamburg, Germany
W. Ackermann, H. De Gersem, TU Darmstadt, Darmstadt, Germany

Abstract

The all-optical synchronization system implemented in the European X-ray free-electron laser (EuXFEL) is to receive an upgrade. The modifications are intended to allow operation with consistently high accuracy in a 1 pC mode, which is required for various user experiments. The lower charges, e.g. a factor of 20, lead to a reduced signal strength at the pickups and thus to a decreased resolution. A significant potential for improvement has been identified in a modified pickup structure and transmission network, which provide the transient voltage signal to subsequent parts of the synchronization system. One solution for a broadband pickup structure with short signal paths, large active surfaces and minimum aperture diameter could be achieved by connecting rod-shaped pickups to a combination network on a printed circuit board, which will be mounted in the beamline. In this contribution the proposed design is introduced and analyzed by electromagnetic field simulations.

INTRODUCTION

A stable high-resolution synchronization system is indispensable in fourth generation light sources, specifically linac-based free-electron lasers (FELs). To exploit their potential, it is necessary to synchronize various subsystems, distributed in the km-long facilities, with fs precision [1, 2].

There are two commonly used approaches for synchronization systems in FELs. The first is based on resonant cavities synchronized to the low-level rf, for example implemented at the LCLS [3]. In contrast the second uses a train of laser pulses, synchronized to the main rf clock, as an optical reference, which is correlated to the transient signal induced by the coasting bunch [4]. Though the additional installation of an optical distribution as well as a laser oscillator with sufficient rate, timing stability and short pulse duration is costly, these systems have advantages for high resolution synchronization in large facilities [2, 4]. The European X-ray free-electron laser (EuXFEL) [5], FERMI@Elettra [6] and the SwissFEL [7] are some of the notable examples, where the optical scheme is in operation. Furthermore, such a synchronization system will be used for SHINE [8].

One substantial criterion for the classification of light-sources is the pulse duration [9]. For many experiments it is favorable to have short pulses in atomic time scales, which can be achieved when the bunch charges are reduced [10]. Yet the non-invasive electro-optical arrival-time measurement, a key challenge in synchronization, depends on transient fields of the electron beam [1, 4] and thus is a limiting factor for a reliable low charge operation of current FELs.

To extend the EuXFEL parameter range towards low charges, the bunch arrival-time monitors (BAMs) need to be improved. Following a former design upgrade, the EuXFEL's operating synchronization system is capable to operate with 20 pC bunches and with resolution well below 6 fs r.m.s. for higher charges [11, 12]. After the successful completion of the ongoing design update, the BAM is planned to achieve a consistently high accuracy with 1 pC bunches.

In this paper a possible design and intermediate stages are presented after a brief introduction to the current BAMs.

ELECTRO-OPTICAL BAM

The arrival time of a single bunch is measured relative to an optical reference in the BAM, which is one end-station of the all-optical synchronization system. As a reference, 1 ps short laser pulses [13] are emitted from an optical laser oscillator synchronized to the master rf oscillator [2]. The laser pulse distribution system is actively stabilized by piezo fibre stretchers and free-space delay stations [2, 5].

The operation principle of electro-optical BAM, introduced in [4], can be divided into the rf part and the electro-optical correlation to the reference laser pulse.

In the rf part, the transient electric fields of coasting bunches couple with button-type pickups and induce a bipolar voltage signal [4]. State-of-the-art BAMs are equipped with four cone-shaped pickups [14] evenly distributed around the beam pipe. The signals are transmitted via coaxial cables [14] while each pair of opposite pickups is combined to compensate for the beam position [13].

Afterwards, the voltage signal is applied to a Mach-Zehnder-type electro-optical modulator (EOM), where the signal is probed by the optical reference [4]. By another free-space delay station the working point is set exactly to the voltage signal's zero crossing (ZC) for a perfectly timed bunch [4, 13]. Any temporal deviation causes a modulation voltage that effects the amplitude of the probing reference pulse [4]. In the operating range the amplitude difference is proportional to the arrival time [5] and therefore the relative timing can be determined by comparing the modulated pulse to unaltered reference pulses [4]. The information is retrieved and digitized in the data acquisition and the results are used to stabilize the operation by a feedback-loop [4, 5, 13].

---

* This work is supported by the German Federal Ministry of Education and Research (BMBF) under contract no. 05K19RO1

† bernhard.scheible@iem.thm.de

Design Upgrade

A low charge mode with 1 pC bunches is demanded for the EuXFEL. To achieve the desired resolution, the BAM must receive an upgrade, increasing the sensitivity approximately by a factor of 20. Out of potential candidates for improvement, it is foreseen to update the EOMs and the rf part, aiming for at least a factor of 10 in the latter. By the function principle of the electro-optical BAM the sensitivity is directly proportional to the signal slope at ZC, which is depending on the signal yield and the bandwidth. The targeted slope normalized to the bunch charge is $150\,\mathrm{mV\,ps^{-1}\,pC^{-1}}$.

To accomplish these improvements by decrease of the distance to the bunch or reduction of losses in the rf path, two designs were proposed in [15] and compared with a scaled version of the cone-shaped pickups. Despite some advantages, both did not meet the required signal strength and further development is necessary. In the following section an alternative is presented, which afterwards is combined with the printed circuit board (PCB) approach from [15].

ROD-SHAPED PICKUPS

A small protrusion of the pickup into the beamline was introduced in the second generation of cone-shaped pickups presented in [14]. The authors of [14] expected that the positive effect would be limited to a small protrusion. In this contribution a rod inserted into the beamline is adopted as a possible design basis, because a preliminary series of simulations with increasing protrusion showed a consistent rise of the signal slope at ZC. In the CST model, pictured in Fig. 1, the tapering was omitted for simplicity of the manufacturing process and for mechanical stability, but a small tapering of the tip might be beneficial if the radius does not significantly exceed the bunch length [14–16].

The resulting pickup is similar to an open coax-line electrode BAM as presented in [17] and an antenna on coaxial high power coupler [18], which is an open coaxial with substantial penetration depth of the inner conductor. The adopted BAM design is less complex, since the subsequent transmission line is likewise coaxial and not waveguide based as in the high power coupling case.

The rod-shaped pickup design allows for a reduced distance to the beam with minimal coverage of the transverse plane, which in turn reduces the cross-section for beam incidents and the potential halo disturbance. Furthermore the beamline wall needs a hole considerably smaller than that of the second generation pickup, thus desired wall currents are expected to be less disturbed.

Ideally the vacuum feedthroughs are placed flush with the beamline surface to reduce the number of transitions.

The greatest advantage of a rod-shaped pickup is the large active area. While the interaction is mainly limited to the circular top of the cone-shaped pickup, a protruding rod senses electric fields at its top as well as on a substantial part of the lateral surface.

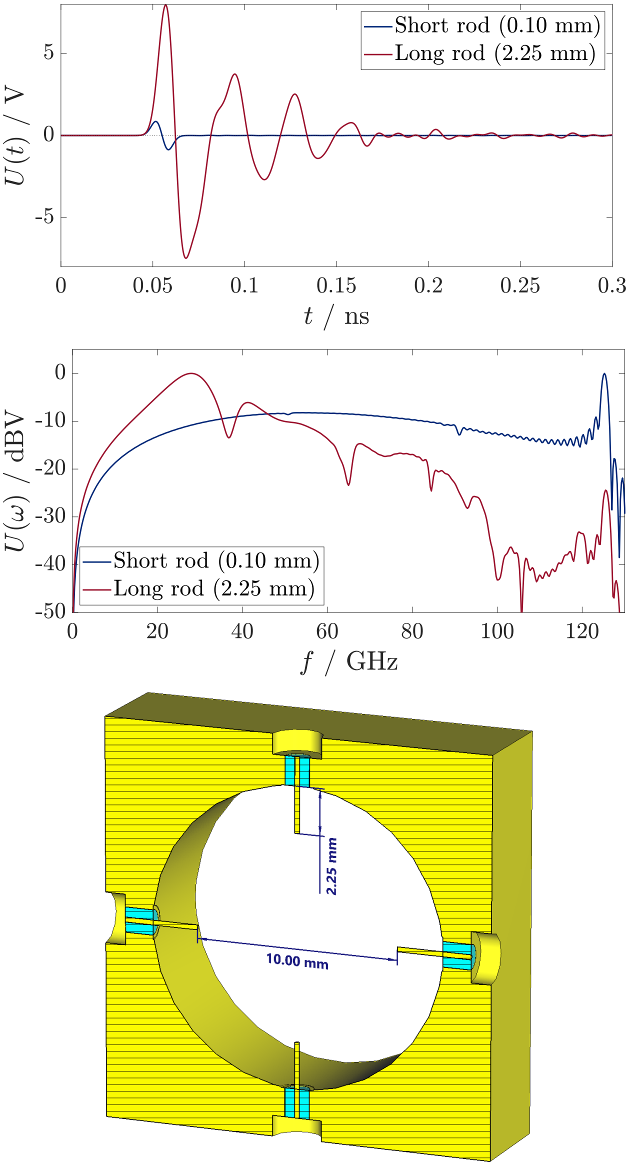

Figure 1: Simulated signal after the feedthrough in time domain (top) and its normalized shifted spectrum (bottom) with two different pickup lengths and constant tip-to-tip distance (10 mm) as well as a cross-section of the CST model of the simulated BAM structure containing four 2.25 mm long rod-shaped pickups with 10 mm tip-to-tip distance on v-type feedthroughs. The bunch is simulated as a Gaussian line charge with $Q_\mathrm{b} = 20$ pC and $\sigma_\mathrm{b} = 1$ mm.

A low stray capacity may ensure bipolarity of the signal as determined for the so called inductive limit [15, 16], though some assumptions of these analytic solutions are violated.

Negative aspects, like cross-talk and strong resonances, have to be investigated. The latter are caused by reflections at the feedthrough and the open end of the rod, hence the signal travels back and forth. The pickup will act as a dipole antenna, radiating part of the energy back into the beamline. Both problems must be addressed regarding long-range wakefields and head-tail instabilities.

Simulation Results

First simulations of the rod-shaped design with the wakefield solver of CST PARTICLE STUDIO™ using a Gaussian current distribution with charge $Q_\mathrm{b} = 20\,\mathrm{pC}$ and standard deviation $\sigma_\mathrm{b} = 1\,\mathrm{mm}$ are promising. The influence of the rod length, a crucial parameter, was analyzed in two series of simulations. To assess the optimal length maximizing the signal slope at ZC, the first series used a fixed beamline diameter of 41 mm and the second a fixed distance between opposite pickup tips of 10 mm.

The second series gave an optimum length of approximately 2.25 mm while the first showed a non-linear relation. For short stubs the slope strongly depends on the length, but after about 2 mm a saturation effect is observed, which holds until an exponential growth is seen for unfeasibly long rods.

A design in accordance to the EuXFEL facility parameters achieved $120\,\mathrm{mV\,ps^{-1}\,pC^{-1}}$, which is 80 % of the objective. Further optimization, e.g. by using other feedthroughs and tapering or widening the rod, have not been fully exploited.

Non-hermetic Demonstrator

The simulation model was adapted to allow machining of a non-hermetic normal conducting demonstrator with short rods as pictured in Fig. 2. The brass body with 7.5 mm inner diameter was manufactured in-house by a turn and mill complete machining center DMC CTX alpha 300. A glass bead has been inserted in each of four milling pockets angular separated by 90°. The beads are fixed by pressure using Anritsu V102F connectors screwed into the brass body.

The scattering parameters were measured with a 40 GHz vector network analyzer (VNA) in free space under room conditions. While two ports have been attached to the VNA the other were terminated with 50 Ω.

All ports are highly reflective and in good agreement indicating that there are no significant variations due to production errors. Differences occur between port 1 and 2 of the VNA, furthermore some values are surpassing 0 dB and the reflective parameters do not match the simulation. Supposedly this is caused by calibration uncertainties.

The high reflection indicates low cross talk between the pickups and therefore the reflections occurring downstream of the rf path will have a minor influence on the other ports or the beamline.

Measured transmission spectra are shown in Fig. 3 alongside the corresponding simulation results. Common peaks indicate transmission between neighboring or opposite pickups. By evaluating the simulated fields they have been attributed to different TE-modes excited in the circular waveguide. This is confirmed by calculation of the related analytical frequencies of TE_{11}, TE_{21}, TE_{31} and TE_{41}.

It is planned to measure a demonstrator with elongated pins with a 67 GHz VNA in order to analyze the complete spectrum. Afterwards the response to a bunch will be measured by sending a short pulse through the beamline on a central wire or by building a hermetic body for tests, e.g. at the Accelerator Research Experiment at SINBAD (ARES).

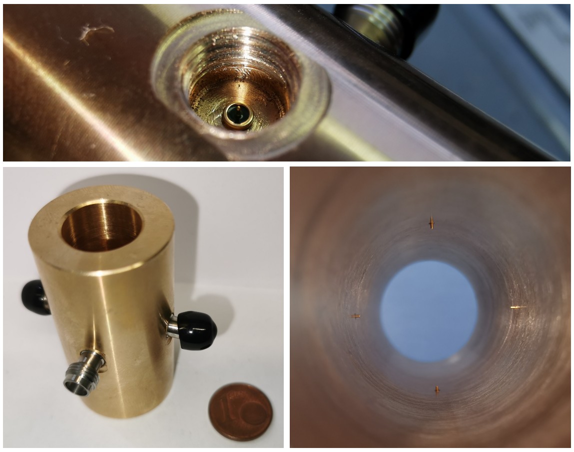

Figure 2: Photographs of the non-hermetic brass demonstrator. The images show a glass bead before final assembly of the v-type connector (top), the finished demonstrator (bottom left) and the protruding pins (bottom right).

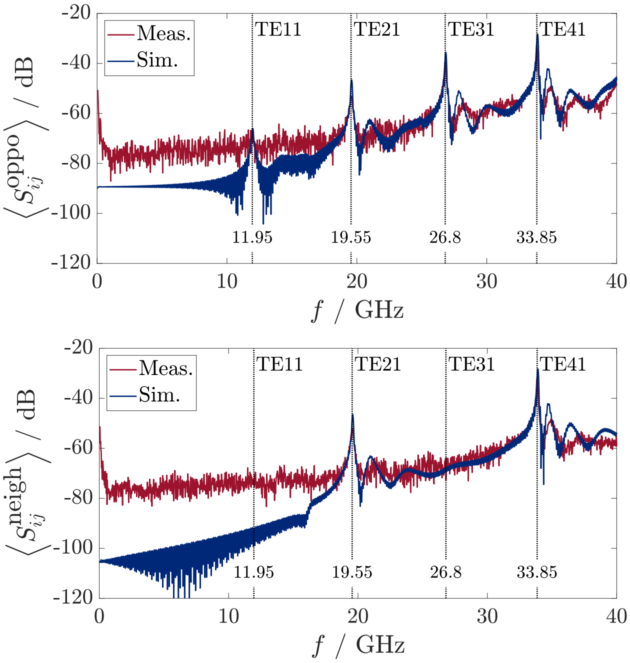

Figure 3: Measured (red) and simulated (blue) transmission parameters between opposite (top) and neighboring (bottom) pickups. The spectra are the mean of according S_{ij} parameter (note that only $j = 1$ was simulated). Dashed vertical lines mark resonances in the filtered measurement data.

ROD-SHAPED PICKUPS ON A PCB

A stripline pickup had been proposed in [15]. Though it achieved promising results and potential for optimization is left, the rod-shape yields a stronger signal and has been adopted. Nonetheless, the PCB could fulfil the requirements for a short high bandwidth combination network and offer the opportunity to get close to the beam without a reduction of the beampipe radius. For this purpose, the PCB is mounted inside the beamline vacuum.

A PCB equipped with four rod-shaped pickups is expected to merge the benefits of both approaches. The rods couple to the electric field of the coasting bunch and a microstrip line joins the four channels to a common exit. The combined signal is coupled out of the beamline through a single v-type connector.

The first draft and the simulation result are pictured in Fig. 4. It achieved a normalized signal slope at ZC of $171.6\,\mathrm{mV\,ps^{-1}\,pC^{-1}}$, which exceeds 114 % of the required design value. With a 20 pC bunch the peak-to-peak voltage is 27.9 V, presumably leaving only 1.4 V for 1 pC operation at the end of the combination network. A duration of 13.5 ps peak-to-peak is the upper limit of the dynamic range.

Optimization can be achieved by reducing the angle between each of the pickup pairs. This reduces the lossy transition line, but the BAM capability to compensate for beam position will be narrowed in one direction. Furthermore the junctions offer little signal enhancement, mainly compensating for losses on the path. Rod diameter, length and tapering are less constrained by the proposed design, thus leaving additional room for optimization.

Wakefields and Ringing

The design contains various sources for wakefields and ringing, which have to be addressed. The coasting beam inside the substrate aperture is a source of Cherenkov diffraction radiation (ChDR) as well as transition diffraction radiation (TDR) [19] and the PCB ground plate also causes TDR. Furthermore the transmission line includes many transitions which cause field reflections. Part of the energy is lost in the transmission line and part will be radiated from the rod-shaped pickup antenna.

It is necessary to prevent an effect on the bunch tail, to subsequent bunches and to the voltage signal. A potential solution to reduce the effect of radiation on the signal is the use of a shielded quasi-coaxial transmission line. According to simulations, TDR contributes most to the perturbative fields. Supposedly it could be limited at expense of the cylindrical symmetry by clipping the ground to the significant area which would be efficiently restricted by using a quasi-coaxial design.

CONCLUSION

In simulations the use of rod-shaped pickups showed clear advantages compared to the cone-shape and became the basis for further developments. In addition, measurements on a non-hermetic demonstrator were in accordance with the simulation, but further measurements are necessary to prove viability of the concept in a use-case scenario.

A set of four rod-shaped pickups on a PCB is a promising design for a low charge BAM. In simulations the signal slope after combination surpassed the project goal about 14 %. The design offers a good starting point for optimization, with many variable geometry parameters and a preliminary combination network. Another demonstration experiment and a manufacturable design for the pickups on a PCB are foreseen after the optimization phase.

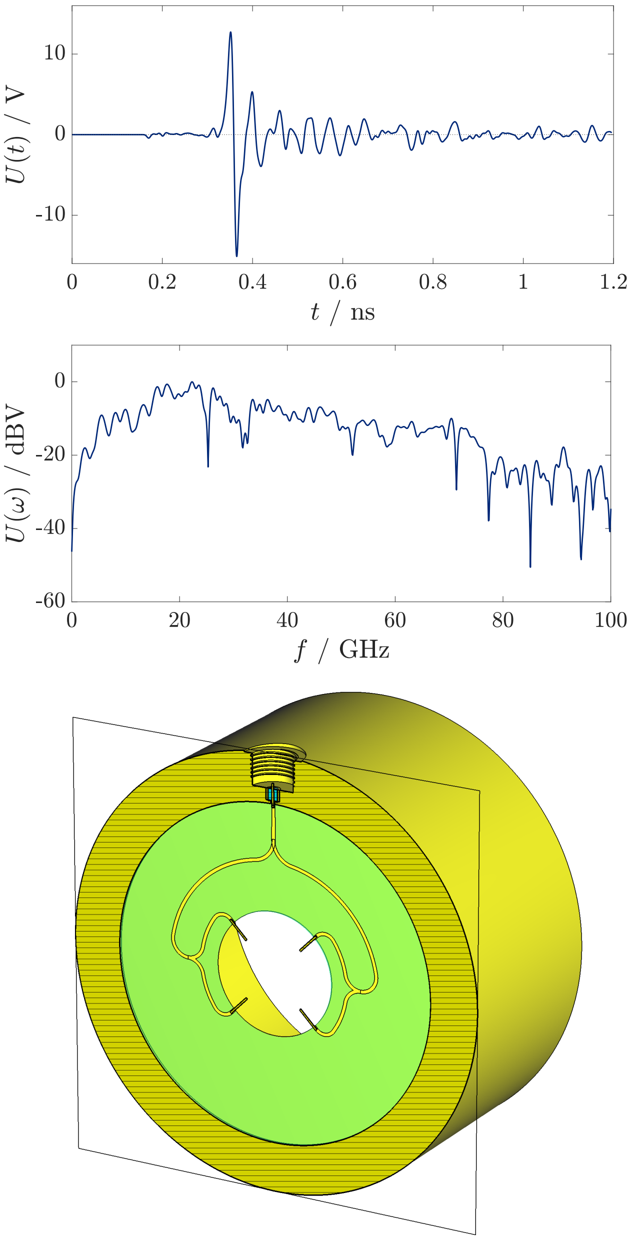

Figure 4: Simulated signal in time domain (top) and its normalized spectrum shifted to max(U) = 0 (center) taken at the end of the vacuum feedthrough (v-type) as well as the simulation model of rod-shaped pickups on a PCB (bottom) cut at the center of the feedthrough. The bunch is simulated as a Gaussian line charge with $Q_b = 20$ pC and $\sigma_b = 1$ mm.

ACKNOWLEDGEMENTS

Our thanks go to the laboratory of production engineering under the lead of Prof. Udo Fiedler associated to the faculty of *Engineering Management - Industry* at *Technische Hochschule Mittelhessen* (Friedberg, Germany) for the manufacturing of the demonstrator's brass body and in particular to Harald Jung for his dedication and excellent work.

REFERENCES

[1] E. J. Jaeschke, S. Khan, J. R. Schneider, and J. B. Hastings, "Synchrotron light sources and free-electron lasers: Accelerator physics, instrumentation and science applications", 2nd Edition, Cham: Springer International Publishing, 2020. `doi:10.1007/978-3-030-23201-6`

[2] S. Schulz *et al.*, "Femtosecond all-optical synchronization of an X-ray free-electron laser", *Nat. Commun.*, vol. 6, pp. 5938, 2015. `doi:/10.1038/ncomms6938`

[3] J. M. Byrd *et al.*, "Femtosecond synchronization of laser systems for the LCLS"in *Proc. 14th Beam Instrum. Workshop (BIW'10)*, Santa Fe, NM, USA, May 2010, paper MOCNB04, pp. 58-62.

[4] F. Löhl *et al.*, "Electron bunch timing with femtosecond precision in a superconducting free-electron laser", *Phys. Rev. Lett.*, vol. 104, no. 14, p. 144801, Apr. 2010. `doi:10.1103/PhysRevLett.104.144801`

[5] T. Lamb *et al.*, "Large-scale optical synchronization system of the European XFEL with femtosecond precision"in *Proc. 10th Int. Particle Accelerator Conf. (IPAC'19)*, Melbourne, Australia, May 2019, pp. 3835-3838. `doi:10.18429/JACoW-IPAC2019-THPRB018`

[6] M. Ferianis *et al.*, "How the optical timing system, the longitudinal diagnostics and the associated feedback systems provide femtosecond stable operation at the FERMI free electron laser", *High Power Laser Sci. Eng.*, vol. 4, p. e13, 2016. `doi:10.1017/hpl.2016.6`

[7] V. Arsov *et al.*, "Design and commissioning of the bunch arrival-time monitor for SwissFEL"in *Proc. 6th Int. Beam Instrumentation Conf. (IBIC'17)*, Grand Rapids, MI, USA, Aug. 2017, pp. 182-185. `doi:10.18429/JACoW-IBIC2017-TUPCC15`

[8] X. Q. Liu, L. W. Lai, Y. B. Leng, R. X. Yuan, N. Zhang, and Y. M. Zhou, "Prototype of the bunch arrival time monitor for SHINE"presented at the IPAC'21, Campinas, Brazil, May 2021, paper MOPAB278.

[9] H. Winick, "Fourth generation light sources"in *Proc. 17th Particle Accel. Conf. (PAC'97)*, Vancouver, Canada, May 1997, pp. 37–41.

[10] J. B. Rosenzweig *et al.*, "Generation of ultra-short, high brightness electron beams for single-spike SASE FEL operation", *Nucl. Instrum. Methods Phys. Res., Sect. A*, vol. 593, no. 1-2, pp. 39-44, Aug. 2008. `doi:10.1016/j.nima.2008.04.083`

[11] W. Decking and T. Limberg, "Technical note: European XFEL post TDR description", European XFEL GmbH, Hamburg (Germany), XFEL.EU TN-2013-004-01, 2013.

[12] S. Schulz *et al.*, "Few-Femtosecond Facility-Wide Synchronization of the European XFEL", in *Proc. 39th Int. Free Electron Laser Conf. (FEL'19)*, Hamburg, Germany, Aug. 2019, pp. 318–321. `doi:10.18429/JACoW-FEL2019-WEB04`

[13] M. Viti *et al.*, "Recent upgrades of the bunch arrival time monitors at FLASH and European XFEL"in *Proc. IPAC'17*, Copenhagen, Denmark, May 2017, pp. 695-698. doi:`10.18429/JACoW-IPAC2017-MOPIK072`

[14] A. Angelovski *et al.*, "Pickup signal improvement for high bandwidth BAMs for FLASH and European - XFEL"in *Proc. 2nd Int. Beam Instrum. Conf. (IBIC'13)*, Oxford, UK, Sep. 2013, paper WEPC40, pp. 778-781.

[15] B. E. J. Scheible *et al.*, "Pickup development for short low-charge bunches in x-ray free-electron lasers", *Phys. Rev. Accel. Beams*, vol. 24, iss. 7, pp. 072803, Jul. 2021, American Physical Society. `doi:10.1103/PhysRevAccelBeams.24.072803`

[16] J. Y. Huang, I. H. Yu, W. H. Hwang, M. H. Chun, and S. C. Kim, "Analysis of pickup signals in the time domain and the frequency domain for the beam position monitor at the Pohang Light Source", *J. Korean Phys. Soc.*, vol. 48, no. 94, Apr. 2006, pp. 768-771.

[17] L. Pavlovic, A. O. Borga, M. Ferianis, M. Predonzani, and F. Rossi, "Bunch arrival monitor at FERMI@Elettra"in *Proc. 14th Beam Instrum. Workshop (BIW'10)*, Santa Fe, NM, USA, May 2010, paper TUPSM086, pp. 394-397.

[18] D. Alesini, "Power coupling"in Proceedings of *CERN Accelerator School, RF for accelerators*, Ebeltoft, Denmark, June 2010, pp. 125 - 147. `doi:10.5170/CERN-2011-007`

[19] V. L. Ginzburg, "Transition radiation and transition scattering", *Phys. Scr.*, vol. T2A, pp. 182-191, 1982. `doi:10.1088/0031-8949/1982/T2A/024`

ISBN: 978-3-95450-230-1 ISSN: 2673-5350 doi:10.18429/JACoW-IBIC2021-WEPP20

DESIGN OF THE BUNCH-LENGTH MONITORS FOR THE NEW SUPERCONDUCTING LCLS LINAC

E. Aneke†, T. Maxwell, A. Fisher, L. Sapozhnikov, B. Jacobson
SLAC National Accelerator Laboratory, Menlo Park, CA 94025, USA

Abstract

The LCLS x-ray free-electron laser at SLAC uses the third km of the original 3-km copper linac. We are now installing LCLS-II, a superconducting linac that replaces the first km. Two undulators, for hard and soft x rays, will be driven by bunches from either linac. One of the solutions developed at SLAC involves a pyroelectric detector, which converts the infrared emitted by the electron bunch into voltage by measuring fast changes in the temperature of the detecting crystal. Not only are the pyrodetectors used at SLAC but also a method with gap diodes. The radial electric field produced by the bunches leaks through a ceramic gap in the beampipe and is collected by a horn antenna and conveyed through a one millimeter waveguide. The waveguides act as a filter, only passing shorter wavelengths and a zero-bias Schottky diode measures the power. In both methods, a portion of the spectral energy emitted by the bunch is intercepted. After normalizing to differentiate between bunches of the same length with different charge, the detected signal is sensitive to only changes in bunch length. This poster discusses the mechanics and optics behind the LCLS-II bunch length monitors' operations and plans for collaboration.

BACKGROUND

This paper describes the physics requirements and implications for instrumenting the single-shot relative bunch length monitors (BLM) based on coherent edge radiation (CER) at the end of the LCLS-II bunch compressor chicanes. It also describes the physics requirements and implications for instrumenting single-shot, diode-based relative bunch-length monitors (BLEN) based on radiation picked up from a ceramic break in the vacuum pipe and coupled to a GHz detection diode [1, 2].

PYROELECTRIC DETECTOR

The superconducting linac will have two stages of bunch length compression with off-crest RF phasing to energy-chirp the bunch. Afterwards, compression is then achieved in 4-dipole bunch compressor chicanes named: BC1 and BC2. The critical final peak current of 1 kA is generated after these stages, with a nominal 100 pC charge per bunch. The final peak current, which is directly related to the final bunch length, must be stable to < 10% rms from pulse to pulse. The goal is to also have the peak current stable over much longer time periods (e.g., one week), until manual intervention is eventually required [1].

The compression system, and in turn, the final peak current, will be very sensitive to time-dependent variations in things such as: RF phasing, accelerator gradient, bunch charge, and laser timing from the gun. Maintaining the peak current over longer time scales will require a longitudinal feedback system based on continual single-shot electron beam measurements. Such a system has already been described for the LCLS and requires at least one single-shot relative bunch length monitor located immediately after each chicane. A measurement of the absolute bunch length is not necessary for feedback purposes. It is sufficient to produce a relative signal which is approximately proportional (inversely proportional) to the peak current (electron bunch length) over a reasonable dynamic range [1].

Bunch length monitors in the injector and immediately prior to the undulators will also be of great importance, but are not necessary of the critical longitudinal feedback system. The pyroelectric detector diagnostic method as a BLM is the only the single-shot monitors needed for the critical longitudinal feedback system integrated in the BC chicanes. This is crucial to the integrity of LCLS-II operations [1].

A mirror with a long, vertical slot for the electron beam will be insertable into the beamline to reflect the upstream CER from the fourth bend magnet (B4) out of the vacuum chamber. The CER will then be sent up into the optics box containing the diagnostic. See Fig. 1 [3].

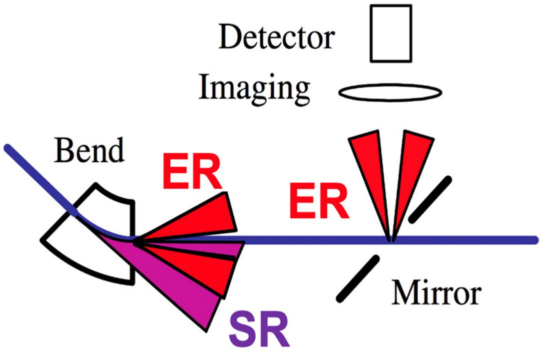

Figure 1: Diagram of the capture of edge radiation.

Once in the optics box, the CER will be guided by a couple of off-axis parabolic mirrors. Then it will pass 4 insertable filters followed by a beam splitter. It is meant to image the CER onto two identical pyroelectric detector elements. There are two pyroelectric detectors for redundancy in the event of a single element failure. Detectors will include preamplifiers with remotely selectable gain [1]. See Figs. 2 and 3.

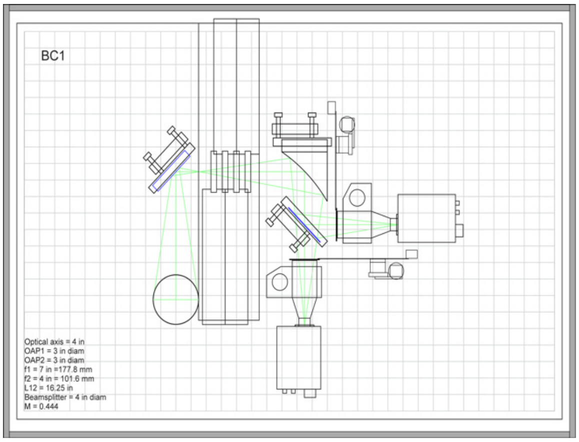

Figure 2: Diagram of the optical breadboard.

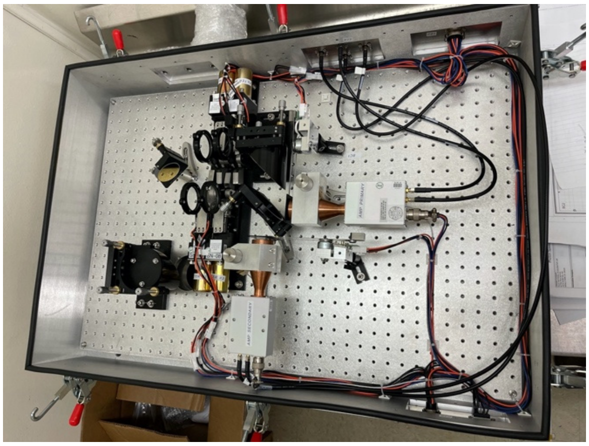

Figure 3: Picture of the completed optics box.

GAP DIODE

Like stated earlier, bunch compression for the LCLS-II beam has two stages of compression that uses off-crest RF phasing to energy-chirp the bunch followed by compression in the 4- dipole bunch-compressor chicanes BC1 and BC2. These stages achieve the critical final peak current of 1 kA with a nominal 100 pC charge per bunch. The stability of the final peak current, which yields the final bunch length, is integral to the operation of the LCLS-II. What's more, those beam parameters must be stable for time periods around one week until things like invasive machine tuning is eventually required. The beam's sensitivity to time-dependent variations makes the need for feedback crucial [2].

Another method being used at the LCLS-II that tackles the same issues as the pyroelectric detectors diagnostic. It is another single-shot monitor needed for longitudinal feedback at two locations where the bunch length is expected to be ≥ 0.1 mm RMS or longer: after the injector capture cavity and, in some cases, immediately after BC1 [2].

As the electron travels in the +z direction along the beamline, it radial emits an electric field in the r direction for all theta. The beam then traverses a ceramic break in the vacuum pipe. The ceramic gap is covered in circular apertures in a metal shield. Two sets of diametrically opposed, pyramidal, high-frequency (GHz-THz) RF horns are placed outside the ceramic gap in the vacuum pipe. These horns pick up signal from the electron bunches by shrinking to the size of the waveguide. The waveguides elongate and attenuate pulses, filters out wavelengths of RF that are unsatisfactory, and are finally measured by high-frequency, Schottky-diode detectors. The diode measures the power and the power can be interpreted as a bunch length. Lastly, like the pyroelectric detector method, the power readings must be normalized so as to differentiate between bunches of the same length but different charge. See Fig. 4.

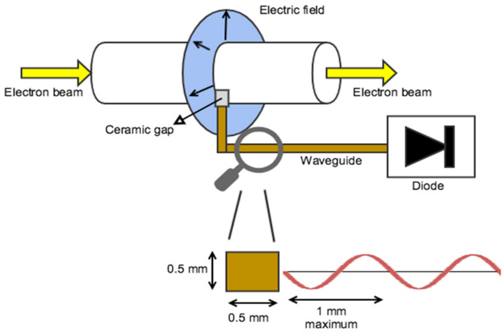

Figure 4: Diagram of gap diode BLM mechanism.

Summing the two opposing horns reduces sensitivity to an off-axis beam. With proper selection of the frequency of the diodes and waveguides, this sum is inversely proportional to the electron bunch duration [2]. See Fig. 5.

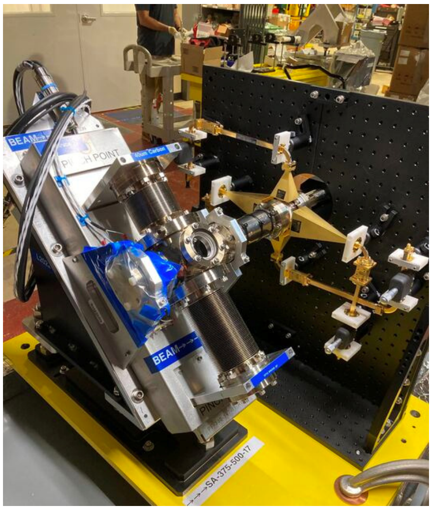

Figure 5: Picture of Gap Diode BLM Mechanism on optical breadboard.

CONCLUSION

Both pyroelectric detector method and the ceramic gap-diode method for the superconducting LCLS-II solve the problem of needing a single-shot monitor with longitudinal feedback. Both have already been constructed and await use when the LCLS-II is commissioned.

ISBN: 978-3-95450-230-1 ISSN: 2673-5350 doi:10.18429/JACoW-IBIC2021-WEPP20

REFERENCES

[1] T. Maxwell, J. Chan, T. Raubenheimer, and D. Schultz, "Single-shot CSR Relative Bunch Length Monitor Requirements", unpublished.

[2] A. Fisher, T. Maxwell, J. Chan, P. Emma, and D. Schultz, "Gap Diode Bunch Length Monitor Requirements", unpublished.

[3] H. Loos, T. Borden, P. Emma, J. C. Frisch, and J. Wu, "Relative Bunch Length Monitor for the Linac Coherent Light Source (LCLS) using Coherent Edge Radiation", in *Proc. 22nd Particle Accelerator Conf. (PAC'07)*, Albuquerque, NM, USA, Jun. 2007, paper FRPMS071, pp. 4189-4191.

ISBN: 978-3-95450-230-1 ISSN: 2673-5350 doi:10.18429/JACoW-IBIC2021-WEPP23

DESIGN OF WALL CURRENT MONITOR IN BRing AT HIAF

Peilin He[†], Yongliang Yang, Xincai Kang, Xiaotao Liu, Zhiguo Xu, Ruishi Mao
Institute of Modern Physics, Chinese Academy of Sciences, Lanzhou, China

Abstract

The Wall Current Monitor (WCM) can monitor the longitudinal beam shape, beam stability, beam longitudinal emittance and intensity, which has been applied widely in the laboratories of high-current proton accelerators. Many accelerators such as CERN-PS, CERN-CLIC, J-PARC and CSNS-RCS have designed different WCMs according to their respective accelerator beam parameters. In order to provide the high-intensity heavy-ion accelerator facility (HIAF)-BRing high-frequency system of with the intensity of each harmonic beam to compensate for wake field; and to observe the changes of the bundle length during the injection, acceleration, and extraction of the bundle, it is planned to place a WCM in HIAF-BRing. According to physical requirements, the lower limit of the WCM working bandwidth is expected to reach 10 kHz, and the upper limit can reach 100 MHz. According to this bandwidth requirement, a WCM structure is designed, and its theoretical bandwidth is 2 kHz~400 MHz, which fully meets the demand. This article gives a detailed and comprehensive introduction to the overall design of this WCM, the selection of various components, design calculations and related simulation calculations. At present, the WCM has completed the procurement and processing of various components, while offline and online testing has not been carried out owing to time constraints. It is expected to be installed on the Heavy Ion Research Facility in Lanzhou-Cooling Storage Ring (HIRFL-CSR) for online testing in August.

PRINCIPLE OF WCM

When the beam passes through the vacuum pipe, its AC component will produce a constant-amplitude and inverse-phase mirror current on the wall of the vacuum pipe. The WCM uses this principle to measure the longitudinal information of the beam. Its schematic diagram and the corresponding equivalent circuit are shown in Fig. 1.

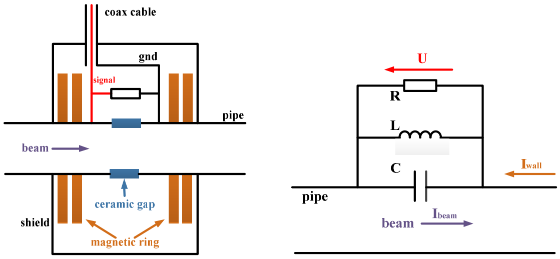

Figure 1: the schematic diagram and the corresponding equivalent circuit of WCM.

Cut the vacuum pipe and install a section of ceramic ring, connecting a resistor across the two ends of the ceramic ring, the induced wall current(mirror current) will produce a voltage which is proportional to the beam current on this resistor. By directly measuring the voltage signal, the intensity signal of the beam pulse can be measured [1].

Ceramic Gap

The main purpose of adding a ceramic ring is to isolate the vacuum pipe, making the induced wall current flow to the resistance. In addition, after welding with the vacuum pipe, it can also make the magnetic ring, shield and other parts outside the vacuum, which makes it easy to control the vacuum performance index of the whole device.

Its equivalent capacitance value is:

$$C_{gap} = (\varepsilon_0 \varepsilon_r S)/t \tag{1}$$

The characteristic impedance of the ceramic ring is:

$$Z = 377 \frac{t}{2\pi r_0} \frac{1}{\sqrt{\varepsilon_r}} \tag{2}$$

Where ε_0 is the vacuum dielectric constant, ε_r is the relative dielectric constant, S and t are the side area and thickness of the ceramic ring. $r_0 = (r_{in} + r_{out})/2$, r_{in} and r_{out} are the inner and outer radius of the ceramic ring.

Magnetic Ring

The magnetic ring is filled outside the vacuum pipe and inside the shielding shell, acting as a role to increase the inductance. Its equivalent inductance value is:

$$L = \frac{\mu_0 \mu_r}{2\pi} h \ln(\frac{b}{a}) \tag{3}$$

Where μ_0 is the vacuum permeability, μ_r is the relative permeability，h is the thickness of the magnetic ring，a and b are the inner and outer diameter of the magnetic ring.

Signal Pick-up Resistance

Because resistors have certain inductance and capacitance characteristics under high frequency, the signal pickup resistor of WCM uses multiple non-inductive resistors connected across the ceramic gap in parallel, and in order to achieve matching, the equivalent resistance value R must be equal to the characteristic impedance Z of the ceramic ring.

Working Bandwidth

Upper cutoff frequency:

$$f_{\mathrm{H}} = \frac{1}{2\pi R C_{gap}} = \frac{r_0}{377 S \varepsilon_0 \sqrt{\varepsilon_r}} \tag{4}$$

Lower cutoff frequency:

[†] hpl@impcas.ac.cn

ISBN: 978-3-95450-230-1 ISSN: 2673-5350 doi:10.18429/JACoW-IBIC2021-WEPP23

$$f_L = \frac{R}{2\pi L} = \frac{R}{\mu_0 \mu_r h \ln(\frac{b}{a})} \qquad (5)$$

DESIGN OF WCM

Ceramic Ring Size Calculation

The ceramic ring material is 97 ceramic, ε_r=9.5 , din (inner diameter) is equal to the diameter of the vacuum pipe, 200 mm. The various indicators of the ceramic ring are analyzed as shown in Fig. 2. Figure 2(a) shows that when t is constant, the influence of dout/din on f_H and Z; Fig. 2(b) shows that when the inner and outer diameters are constant , the influence of t on f_H and Z.

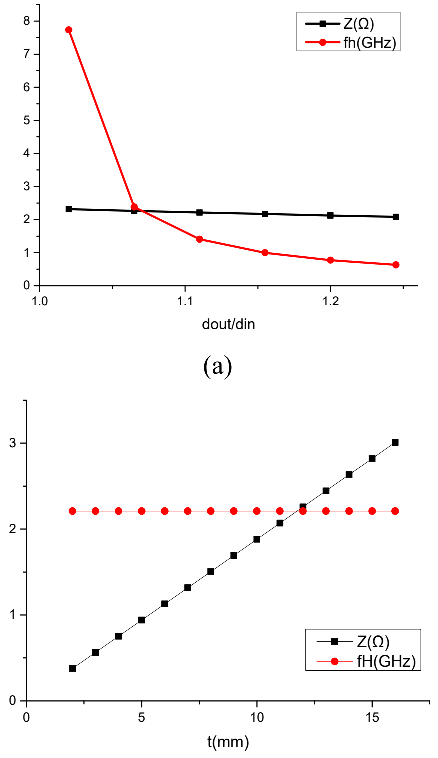

(a)

(b)

Figure 2: Analysis of different parameters of ceramic ring on its performance. (a) When t fixed, the influence of dout/din on f_H and characteristic impedance Z; (b) When din and dout fixed, the influence of t on f_H and Z.

Combining the din, dout and t on f_H and Z, the final ceramic ring size parameters are: din=200 mm, dout=225 mm, t=12 mm, at this time, corresponding to f_H =1.2375 GHz, C_{gap} =58.494 pF, Z=2.1986 Ω

Magnetic Ring Design

The design of magnetic materials mainly includes material selection, size calculation, and reasonable combination design of different material rings.

According to the investigation, 1K101 and 1K502A are selected. The size of the magnetic ring is 220*280*30 mm. Meanwhile, Since the permeability of magnetic materials changes with frequency, choosing a suitable combination of magnetic materials can greatly improve the working bandwidth of WCM. Considering the ceramic ring, signal pick-up resistance, magnetic ring and other factors,

First, a total of 4 magnetic rings are used, and the system impedance vs. frequency curve is analyzed under different combinations of magnetic rings, as shown in Fig. 3. It can be seen that when all four magnetic rings use nanocrystalline magnetic materials, WCM low-frequency response is particularly excellent; when all four magnetic rings use amorphous magnetic materials, WCM high-frequency response is particularly excellent; while combination two nanocrystalline and two amorphous magnetic materials, the bandwidth of the WCM is significantly improved. Obviously, the combination of two materials is better.

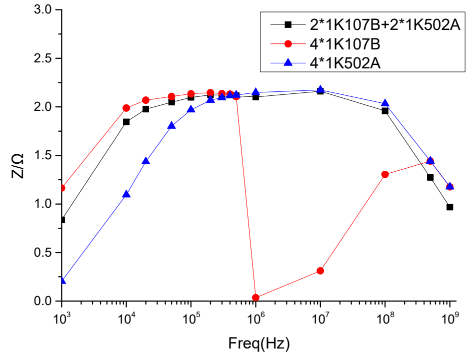

Figure 3: The impedance vs. frequency under different combinations of four magnetic rings.

In order to further broaden the WCM bandwidth, it is necessary to increase the inductance, which can only be achieved by increasing the volume of the magnetic ring or increasing the number of magnetic rings. Here, we choose to increase the number of magnetic rings to six and eight combinations. The WCM system impedance vs. frequency curve is shown in Fig. 4.

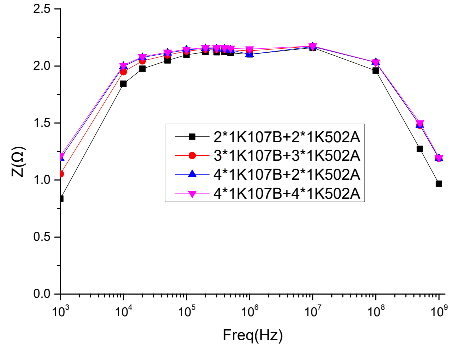

Figure 4: The impedance vs. frequency under combinations of four/six/eight magnetic rings.

It can be seen that the more the number of magnetic rings, the broaden the frequency band, but the total number is no longer improved significantly after the total number is increased from 6 to 8. And the system bandwidth of the combination of 4 nanocrystals and 2 amorphous magnetic materials is best. Therefore, finally choose 4*1K107B and

2*1K502A magnetic ring combination, the theoretical 3dB working bandwidth of this WCM is 2 kHz~400 MHz.

Figure 5 shows the actual processed magnetic ring and the magnetic permeability test results of the magnetic ring.

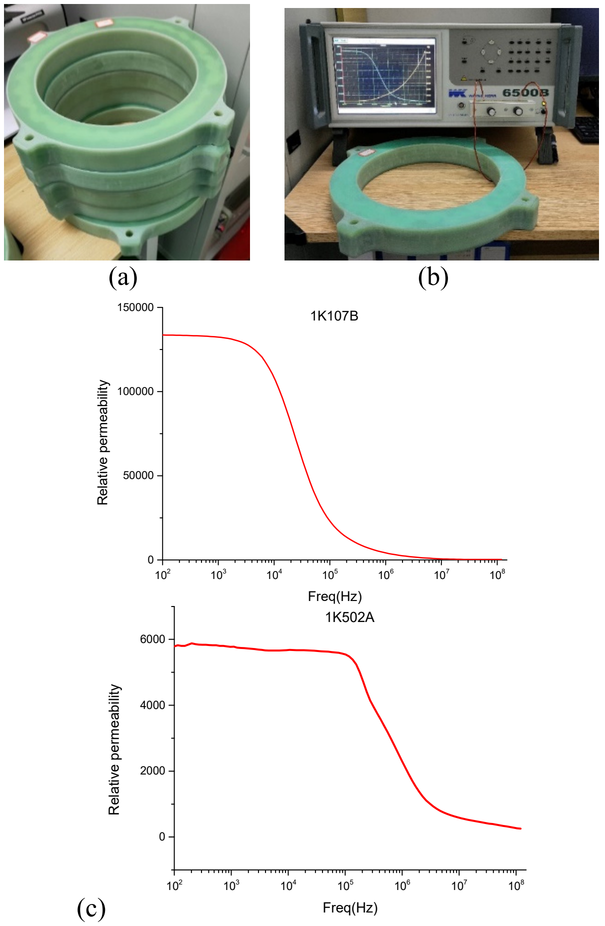
(a) (b)

(c)

Figure 5: The actual magnetic ring processing and the magnetic permeability test results of the magnetic ring. (a) Magnetic ring finished product; (b) L-f performance test scenario; (c) The magnetic permeability of the two cores and the magnetic ring change curve with frequency.

Signal Pick-up Resistor Design

This part of the design directly affects the accuracy of the final extracted signal. Here, we choose a flexible circuit board to design a flexible resistance band for signal pickup.

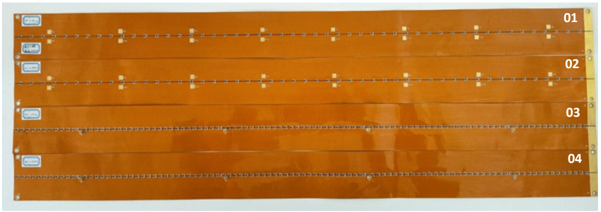

Figure 6: Physical picture of flexible resistance band.

The flexible resistance board material used Panasonic R-F777, and its equivalent resistance is 2.2 Ω. Two versions of the resistance board are designed, as shown in Fig. 6. 50 110 Ω resistors are used in parallel for circuit boards 01 and 02; the signal is led out by pads. 100 220 Ω resistors are used in parallel for circuit boards 03 and 04, the signal is led out by a patch-type SSMP connector, using a patch-type SSMP connector can effectively reduce the signal reflection at the connection compared with direct pad welding. The upper and lower copper-clad parts of the circuit board are connected by a number of metallized vias to ensure good electrical conduction between the resistance band and the vacuum pipeline.

Table 1: Measured Value of Equivalent Resistance Value of Flexible Resistance Band

Number	Test resistance(Ω)	Inherent error(Ω)	Actual resistance(Ω)
01	2.35	0.151	2.199
02	2.353	0.151	2.202
03	2.35	0.151	2.199
04	2.353	0.151	2.202

The theoretical design value of the equivalent resistance of the flexible resistance band is 2.2 Ω, the actual measured value is 2.2±0.002 Ω as shown in Table 1. The accuracy is controlled within one thousandth, which meets the design requirements.

WCM Mechanical Structure Design

Figure 7 shows the WCM mechanical structure, mainly considering from the aspects of mechanical processing and assembly, such as: strict control of the brazing process between the ceramic ring and the vacuum pipe, the fixing of the magnetic ring structure, the good conductive contact between the flexible resistance band and the stainless steel pipe, the reasonable installation position of each connector and the filling of the wave absorbing material, etc.

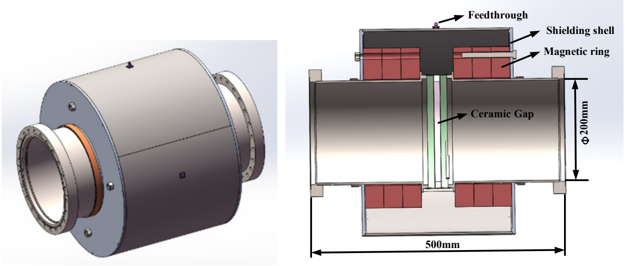

Figure 7: Three-dimensional drawing and cross-sectional view of the mechanical structure of WCM.

SIMULATION OF WCM

Calibration Platform Designer and Simulation

A calibration platform is needed to calibrating and testing for W

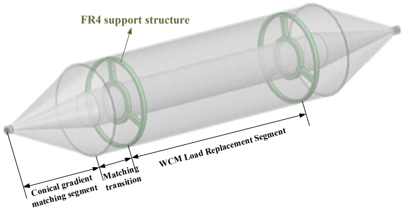

Figure 8: Simulation modal of calibration structure.

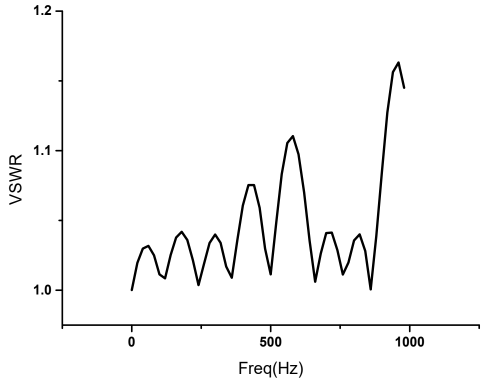

Figure 9: VSWR vs. frequency curve.

From the perspective of microwave transmission, a tapered gradual coaxial conversion structure is designed for offline calibration of the WCM, and the electromagnetic simulation software ANSYS HFSS software is used for design simulation calculations. The model structure is shown in Figs. 8 and 9 shows the VSWR vs. frequency curve of this coaxial in 0~1 GHz. The result shows that in the range of 0~400 MHz, VSWR⩽1.05, the matching is excellent, which can be used for the calibration of WCM of this design.

WCM simulation analysis

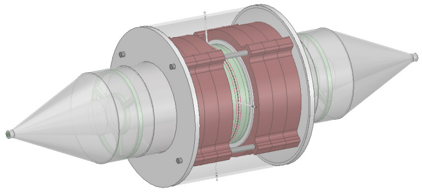

Figure 10: simulation model of WCM.

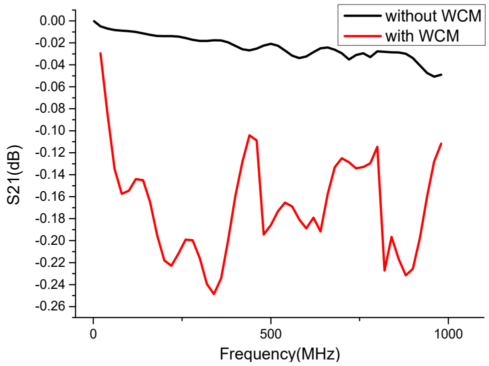

Figure 11: Frequency response curve.

The simulation model of WCM is shown in Fig. 10, its working bandwidth is analyzed. The result is shown in Fig. 11, the coaxial conversion structure (shown in Fig. 8), the transmission coefficient S21⩾-0.05dB in the frequency range of 0~1 GHz. After loading the WCM structure (shown in Fig. 10), S21 drops slightly in the frequency range of 10 kHz to 1 GHz, but does not exceed 0.25 dB, which proves that the high energy transmission efficiency is in line with expectations.

DISCUSSION

There is still room for optimization in this solution [2]. For example, the flexible circuit board designed to bridge the signal pickup resistance can be integrated the function of microstrip power combiner, which can improve the reliability of the structure; The test verifies the current absorbing performance of the absorbing material in the range of 2 k~400 MHz. If it does not have a significant absorbing effect, we need to consider reducing the size of the cavity without adding absorbing materials or using a ferrite absorbing array solution [3].

CONCLUSION

This article comprehensively introduces the detailed design process of WCM for HIAF [4]. According to current theoretical calculations and simulation results, the working bandwidth of this WCM is 2 kHz~400 MHz. However, according to other WCM designs and test results investigated [1, 5, 6], compared with the design results, the measured working bandwidth will be better than the design bandwidth. At present, the WCM has completed the procurement and processing of various components, but due to time constraints, offline and online testing have not yet been carried out. It is expected to be installed at the Heavy Ion Research Facility in Lanzhou-Cooling Storage Ring (HIRFL-CSR) for online testing in August.

ACKNOWLEDGEMENT

Special thanks to Jilei Sun from Institute of High Energy Physics for his guidance and help in this design.

REFERENCES

[1] Sun Jilei *et al.*, "Design of the wall current monitor system at CSNS rapid cycling synchrotron[J]", *High Power Laser and Particle Beams*, vol. 30, p. 125103, 2018. `doi:10.11884/HPLPB201830.180224`

[2] A. D'Elia, R. Fandos, and L. Søby, "High bandwidth Wall Current Monitor for CTF3", in *Proc. 7th. European Particle Accelerator Conference. (EPAC'08)*, Genoa, Italy, June. 2008, pp. 1092-1094. `doi:10.18429/JACoW-EPAC08-TUPC021`

[3] B. Fellenz and J. Crisp, "An improved resistive wall monitor", *American Institute of Physics*, vol. 451, pp. 446-453, 1998. `doi:10.1063/1.57030`

[4] Yang J C *et al.*, "High Intensity heavy ion Accelerator Facility (HIAF) in China", *Nuclear Instruments and Methods in Physics Research Section B Beam Interactions with Materials and Atoms*, vol. 317, pp. 263-265, 2013. `doi:10.1016/j.nimb.2013.08.046`

[5] J.M. Belleman and W. Andreazza, "A New Wall Current Monitor for the CERN Proton Synchrotron", in *Proc.5th. International Beam Instrumentation Conference. (IBIC'16)*, Barcelona, Spain, Sept. 2016, pp. 143-146. `doi:10.18429/JACoW-IBIC2016-MOPG41`

[6] P.Odier, "A New wide band Wall Current Monitor", in *Proc. 6th. Beam Diagnostics and Instrumentation for Particle Accelerators. (DIPAC'03)*, Mainz, Germany, May. 2003, pp. 216-218. `doi:10.18429/JACoW-DIPAC 2003-PT20`

PSB H^0-H^- MONITOR CALIBRATION AND COMMISSIONING

A. Navarro*, S. Bart, D. Belohrad, C. Bracco, E. Renner, F. Roncarolo, J. Tassan-Viol,
CERN, Geneva, Switzerland

Abstract

During the LHC Long Shutdown 2 (LS2), the H^- LINAC4 replaced the proton LINAC2 as Proton Synchrotron Booster (PSB) injector. In each of the four PSB rings, the injection region was upgraded to accommodate the necessary elements for a proper H^- charge exchange injection system. Four beam dumps (one per ring), installed downstream the stripping foil, prevent the unstripped H^- particles from being injected in the ring. The H^0 H^- monitors, consist of four titanium plates placed a few centimetres upstream of the dump, intercept partially stripped H^0 or not stripped H^- ions and allow a continuous monitoring of the stripping efficiency, providing an interlock signal to block the injection process in the case of severe degradation or breakage of the foil, which would heavily damage the dumps.

This contribution focuses on the commissioning and operation of these new systems. It describes the results from the calibration campaigns, performed by comparison to beam current transformer measurements during special periods with low intensity beams and no stripping foil, and during normal operation, when it was already possible to monitor stripping inefficiencies below 1% and compare different beams and stripping foil types.

INTRODUCTION

The LHC high luminosity programme (HL-LHC) [1] calls for the production and acceleration of brighter beams from the injectors [2]. During the Long Shutdown 2 (LS2) at CERN, the new LINAC4 accelerator [3] was connected to the Proton Synchrotron Booster (PSB). It provides a 160 MeV H^- particle beam. With respect to the LINAC2, the increase of injection energy from 50 to 160 MeV doubles the relativistic factor $\beta\gamma^2$ at PSB injection allowing the beam brightness to be doubled. The beam from LINAC4 consists of four individual pulses, separated by a 1 µs particle-free gap and a pulse length that depends on the number of turns injected per ring. The pulses are then distributed to the corresponding booster rings for injection.

To inject the H^- beam in the PSB, a new charge exchange injection system [4] was installed in each ring. This new system reduces injection losses which were unavoidable in the previously used multi-turn injection. Figure 1 shows a schematic representation of the new injection system which comprises a stripping foil, a set of four pulsed dipole magnets (BSW) [5] and four horizontal kickers (KSW) [6] (Not indicated in the picture).

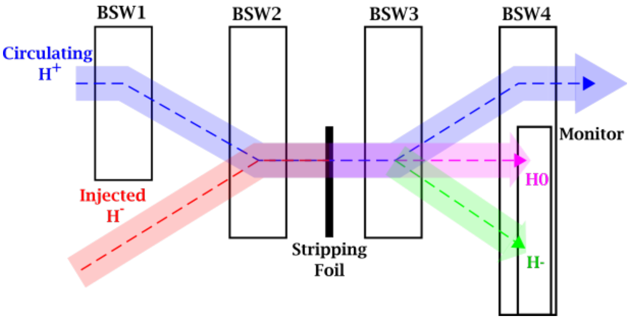

Figure 1: Schematic representation of PSB H- Charge injection system.

The first magnet (BSW1) acts as a septum generating a high-field region for the circulating beam and a field-free region for the injected H^- beam. It is followed by 3 bumper magnets (BSW2-4) that help merging the injected beam with the circulating beam. The stripping foil (about 20 mm wide and 20 mm high) is made of carbon with a density around 200 µgcm^{-2}. It strips electrons from the incident H^- particles. The characteristics of the used stripping foil have been optimized to provide sufficient stripping efficiency (> 99%) while minimizing emittance blow-up. After the stripping foil, fully-stripped protons are injected into the circulating beam while the partially-stripped and unstripped ions are collected by a dedicated dump.

PSB H0H- BEAM CURRENT MONITOR

The injection region geometry and the very limited space available preclude extraction of the unstripped or partially stripped ions. For that reason, four internal Ti_6Al_4V dumps, one per ring, were installed downstream of the stripping foil, within the vacuum chamber of the chicane magnet BSW4, as shown in Figs. 2 and 3. The geometry of the dump provides an unobstructed passage for the circulating beam during injection as well as for the injected proton beam, whilst providing optimal protection of the downstream elements by absorbing a few percent of the unstripped beam during regular operation, and also by absorbing the full beam in the event of a foil failure. In Figs. 2 and 3 the dump is represented in black.

The H^0H^- monitors (represented in red in Figs. 2 and 3) are installed 4 cm upstream from the face of the dump. The dump is far enough from the detectors to prevent secondary electrons coming from the dump affecting the signal of the monitors. The H^0H^- monitors consist of four titanium plates: two 22 mm wide central plates and two 18 mm wide external plates with around 1 mm separation between the plates which allows to supplement the intensity measurements with some beam positioning information. The two outer plates are expected to measure H^- particles while

---

* araceli.navarro.fernandez@cern.ch

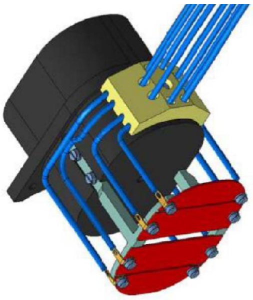

Figure 2: Mechanical design of the H^0H^- current monitors (red) and Ti_6Al_4V dump (black).

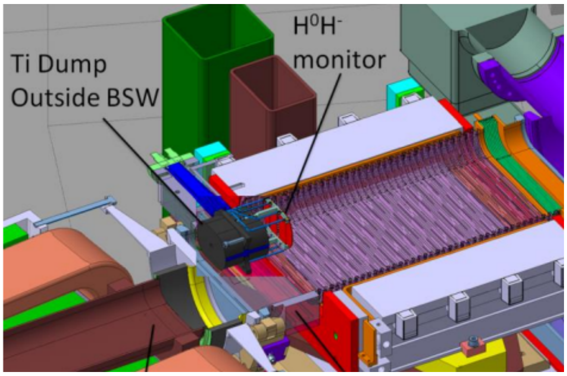

Figure 3: Integration of the H^0 H^- dump (black) and intensity monitor (red plates) in a PSB ring. The purple element is the BSW4 magnet.

the two inner plates are expected to measure the partially stripped H^0 particles.

The plates are made of titanium chosen for its low Z (i.e. low activation) and moderate conductivity ($2.34 \cdot 10^6\ \Omega^{-1}\mathrm{m}^{-1}$), which is a good compromise between the high conductivity needed for reading out the deposited charge and the low conductivity required due to the presence of a pulsed magnetic field in the BSW4 chamber. The thickness of 1 mm guarantees stopping all the stripped electrons and is compatible with the presence of a vertical B-field. No thermal problem is expected even if the stripping foil fails as the temperature at the center of the beam spot does not exceed 90 K.

As shown in Figs. 2 and 3, each monitor plate has two read-out cables (represented in blue). This duplication has been implemented only for hardware redundancy: in the case of cable damage, a second one will be immediately available. During operation only one signal cable per plate is connected to the acquisition system, as reading out both outputs simultaneously would heavily reduce the monitor's sensitivity.

EXPECTED SIGNALS

The electrical signal generated in the plates allows determining the number of H^0 and H^- particles reaching the dump, and thus the stripping inefficiency. Several effects contribute to the charge formation in the plates. The most relevant ones are charge deposition (Q_{dep}) and Secondary Emission (SE) charge generation (Q_{SE}):

$$Q\left(\frac{e}{Proj}\right) = Q_{dep} + Q_{SE} \tag{1}$$

For an accelerated ion with N_p protons in the nucleus and N_e electrons we can estimate the deposited charge as:

$$Q_{dep} = N_p \cdot \eta - N_e \cdot \mu \tag{2}$$

where η and μ represent the ratios of protons and electrons that remain in the material. In our particular case (160 MeV H^0 or H^- particles, 1 mm thick titanium plate) the values of these parameters were calculated using Geant4 10.07 as $\eta \approx 0.003$ and $\mu \approx 0.463$.

The SE charge (Q_{SE}) is generated when a particle passes through the interfaces of a material. The particle transfers energy to the electrons in the medium and if this energy is high enough they can escape the material. Such an emission process is known as Secondary Electron Emission (SEE) [7]. The main parameter describing the SEE is the Secondary Emission Yield (SEY) which is the average number of electrons emitted when an incident projectile enters or exits a surface. Q_{SE} can be estimated as:

$$\begin{aligned} Q_{SE} = 2 \cdot (N_p \cdot \eta \cdot SEY_p + N_e \cdot \mu \cdot SEY_e) \\ BS_p \cdot SEY_p + BS_e \cdot SEY_e \end{aligned} \tag{3}$$

where BS_e and BS_p are the ratios of backscattered particles with the indices p and e indicating protons and electrons, respectively. Their values were also calculated with Geant4 and in our particular case yield $BS_p \approx 0$ and $BS_p \approx 0.5369$. Table 1 presents the expected signals per an incident H^0 and H^- particle. The SE reduces the current measured by the intensity monitors. With the small energy of the SE, the magnetic field of BSW4 is large enough to suppress the SE. Thus, the expected charge per incident particle does not comprise the Q_{SE} term.

Table 1: Expected Net Charges per Incident H^0 and H^- Particle for a Titanium Detector, 1 mm Thickness, with (w. SE) and without (w.o. SE) Secondary Emission

	w. SE	**w.o. SE**
$Q\left(e/H^0\right)$	-0.2169	-0.463
$Q\left(e/H^-\right)$	-0.375	-0.975

The number of H^0 and H^- particles depends on the stripping efficiency. In normal operational conditions, during injection, the expected ratio of H^0 particles should be $< 2\%$ of the entire Linac4 pulse. The total ratio of H^- particles is expected to be very low $\approx 10^{-4}\%$. Stripping foil degradation is tolerated until the beam dump load reaches a safety limit. Currents larger than 10% of the Linac4 beam pulse generate an interlock signal that stops the particle beam.

ISBN: 978-3-95450-230-1 ISSN: 2673-5350 doi:10.18429/JACoW-IBIC2021-WEPP24

MEASUREMENT PROCEDURE

The main goal of the measurements was to obtain a calibration factor (R_{tot}) which, independently of the intensity or type of beam, relates the signal in the plates to the total number of particles reaching the dump. Several tests were performed with different configurations. In order to obtain a calibration factor independent of the stripping foil, all tests were performed with an H^- particle beam. This also allowed us to reach all the plates in the different detectors by properly adjusting some correctors and magnets.

The electronics of the H^0 H^- monitors are designed for accurately measuring a maximum of 10 % of the Linac4 beam pulse. For obtaining a non-saturated signal during the measurements, the calibration factor was calculated with a LINAC4 beam of reduced intensity (I_{beam} < 4 mA). The final calibration factor is independent of the beam intensity measured in each ring with Beam Current Transformers (BCTs) placed before the injection bump. The calibration factors were calculated for all plates in the rings, by comparing the signal measured in the plates with the signal measured by the BCTs:

$$R_i \left[\frac{Charge}{ADCcounts}\right] = \frac{SignalBCT}{SignalPlate} \quad (4)$$

In the above formula, the index i refers to the name of the plate. For convenience we will use H_{00}, H_{01}, H_{M0}, and H_{M1} to refer to the four different plates.

CALIBRATION FACTOR RESULTS

Figure 4 shows analog signals (boosted by a fast amplifier) measured by the H^0H^- monitors in Ring 4, for a beam pulse length of around 500 ns. Different colors represent signals measured by different plates. The particle beam was fully focused on the the plate closest to the beam pipe center (H_{00}). The signal measured by the plate has a negative amplitude as it is generated by charge deposition (Q_{dep}). The red curve shows the so-called integrating windows. Plate signals are integrated when the integration signal is positive. The length of this window can be modified but during the measurements it was set to integrate 720 ns over a 1 µs period, which captures the full length of the beam pulse.

Figure 5 shows the signals registered by the H_{00} plate in Ring4 after the full chain of electronics (filtering, amplifications, digitalization) for different beam conditions. Each point corresponds to the integral of one beam pulse. For longer beam pulses a larger number of particles reach the plates leading to a higher output current. On the other hand, a larger number of turns injected in that PSB ring results in a current observed for a longer time. These integrated signals are the ones that the user constantly monitors. The calibration factor was thus calculated by comparing these integrated signals and the intensities measured by the closest downstream BCTs. This comparison is also subjected to a correction factor that accounts for tail/head beam effects, beam placement, etc.

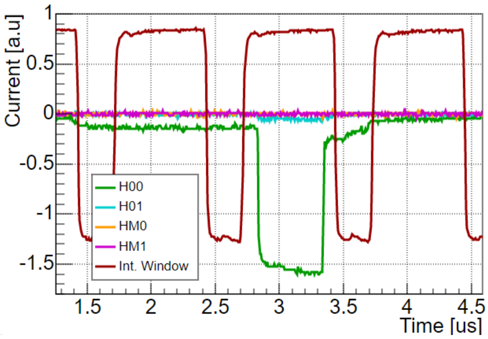

Figure 4: Signals from H^0H^- monitors in Ring4. Every color represents the signal generated in a different plate. The red curve shows the integration windows.

Figure 6 shows the calibration factors calculated for the H^0H^- intensity monitors in Ring1. One can distinguish two sets of points. The blue points were measured with BSW4 on i.e. when the H^0H^- intensity monitors were exposed to a constant magnetic field of around 0.18 T. Under such conditions, the obtained calibration factors were very similar for all the plates (R = 1.31(2) $\cdot 10^{-8}$ [Charges/ADC count]). For the H_{00} and H_{01} plates, it was also possible to take measurements without the magnetic field (green points). In this case the calibration factor obtained was R = 1.67(2) $\cdot 10^{-8}$ [Charges/ADC count]. The magnetic field of BSW4 is strong enough to suppress the low energy secondary electrons. This translates to an overall smaller signal measured in the plates and thus a higher calibration factor.

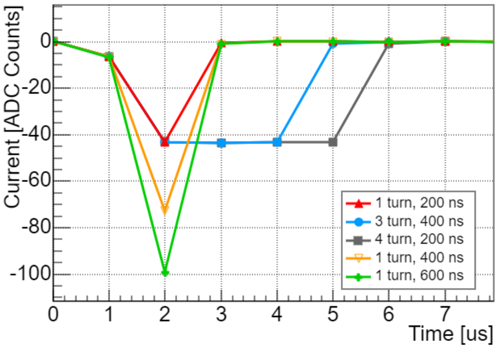

Figure 5: Signal of the H_{00} plate (Ring1) after the electronics chain, for several beam conditions.

Since during normal operation BSW4 remains turned on, the final value of the calibration factor was calculated in the presence of the BSW4 magnetic field. Figure 7 shows the calibration factors measured for all the plates, in all the PSB rings. The average calibration factor for all plates is R = 1.53 $\cdot 10^{-8}$ [Charges/ADC counts] and it remains stable within 1.5 % for all plates under different beam conditions. Using this calibration factor, the total number of particles reaching the dump can be calculated as:

$$N_{Part} = R_{TOT} \cdot (2 \cdot H_{00} + 2 \cdot H_{01} + H_{M0} + H_{M1}) \quad (5)$$

ISBN: 978-3-95450-230-1 ISSN: 2673-5350 doi:10.18429/JACoW-IBIC2021-WEPP24

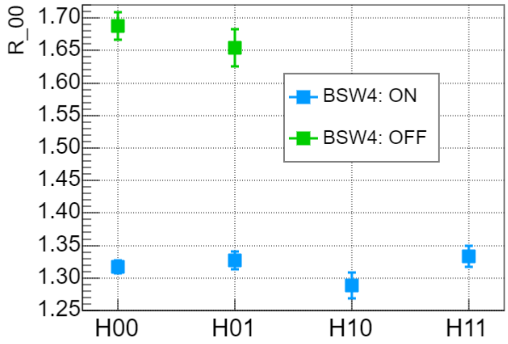

Figure 6: Calibration factor of the H0H- monitors in Ring 1, with BSW4 on and off. This factor is always measured in units of $10^{-8}[Charges/ADCCount]$.

where H_{00}, H_{01}, H_{M0}, and H_{M1} refer to the ADC counts measured by each plate. Doubling the H_{00} and H_{01} signal is necessary as during regular operation these plates are expected to measure uniquely H^0 particles. As it was previously shown, the net charge generated in H^0 is more or less half of what is generated in the H^- plates, due to H^0 only having one electrons. Nevertheless, the number of protons reaching the dump is the same in both cases.

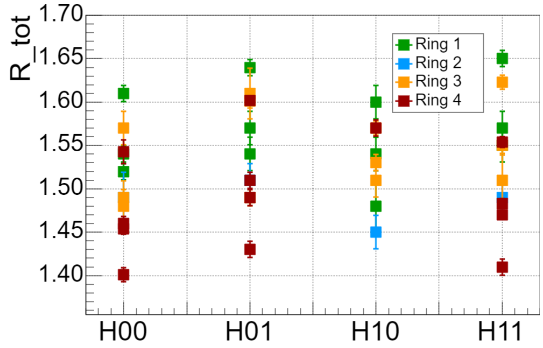

Figure 7: Calibration factors calculated for the different plates in the different rings, for different beam pulse lengths and number of turns. This factor is always measured in units of $10^{-8}[Charges/ADCCount]$.

STRIPPING INEFFICIENCY CALCULATIONS

Following the calibration phase, the H^0H^- monitors were used to measure the stripping efficiency from six different stripping foils (see Table 2 for their details). Figure 8 shows the distribution of the stripping inefficiency as measured by the H^0H^- monitors for this six foils. In all the cases, the measured stripping inefficiency was smaller than 1%.

CONCLUSIONS

During the Long Shutdown 2, LINAC4 replaced LINAC2 as PSB injector. The newly installed H^0H^- intensity monitors are indispensable for ensuring a proper charge exchange injection. They continuously measure the number of unstripped H^0 and H^- particles. The monitors are connected to an interlock system that blocks the injection process in the case of heavy degradation or breakage of the foil.

Table 2: Characteristics of the Measured Stripping Foils

Type	Weight	Description
XCF-200	200 µgcm^2	Arc evaporated amorphous Carbon
MLG-250	240 µgcm^2	Multilayer Graphene
GSI-200	200 µgcm^2	Arc evaporated amorphous Carbon

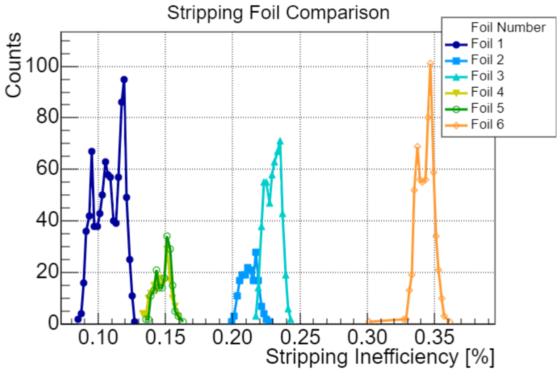

Figure 8: Stripping inefficiency as measured by the H^0H^- monitor in the PSB Ring 3 during dedicated studies with different foil types (preliminary results).

As presented in this paper, the H^0H^- intensity monitors have been fully commissioned. Due to the complexity of their electronics, a calibration factor was necessary to correlate the ADC signals with the number of particles reaching the dump. This factor was calculated by comparing the signals measured by the monitors and the closest upstream BCTs. A calibration factor R = 1.53·10^{-8} [Charges/ADC Counts] was obtained. It remains stable within 1.5 % error for all plates in all PSB rings and for various beam conditions. It allows us to relate the signal provided by the monitors to the total number of particles reaching the dump.

The monitors are now in continuous operation to measure stripping inefficiencies smaller than 1% as well as to test stripping foils.

REFERENCES

[1] High Luminosity LHC Project, `https://hilumilhc.web.cern.ch`

[2] J. Coupard *et al.*, “LHC Injectors Upgrade, Technical Design Report, Vol. I: Protons”, CERN, Geneva, Switzerland, Rep. CERN-ACC-2014-0337, 2014.

[3] L. Arnaudon *et al.*, “Linac4 Technical Design Report”, CERN, Geneva, Switzerland, Rep. CERN-AB-2006-084, 2006.

[4] Dudnikov V G “Charge exchange injection into accelerators and storage rings”, *Phys. Usp.*, vol 62, pp. 405–412, 2019.

[5] B. Balhan, C. Baud, C. C. M. Borburgh, and M. Hourican, “Design and Construction of the CERN PS Booster

Charge Exchange Injection Chicane Bumpers", in *Proc. 9th Int. Particle Accelerator Conf. (IPAC'18)*, Vancouver, Canada, Apr.-May 2018, pp. 2575–2577. `doi:10.18429/JACoW-IPAC2018-WEPMF082`

[6] L. M. C. Feliciano *et al.*, "A New Hardware Design for PSB Kicker Magnets (KSW) for the 35 mm Transverse Painting in the Horizontal Plane", in *Proc. 6th Int. Particle Accelerator Conf. (IPAC'15)*, Richmond, VA, USA, May 2015, pp. 3890–3892. `doi:10.18429/JACoW-IPAC2015-THPF086`

[7] E. J. Sternglass, "Theory of Secondary Electron Emission by High-Speed Ions", *Phys. Rev.*, vol. 108, p. 1, 1957.

ISBN: 978-3-95450-230-1 ISSN: 2673-5350 doi:10.18429/JACoW-IBIC2021-WEPP27

HIGH SPEED PARALLEL DIGITAL SIGNAL PROCESSING STRUCTURE IN BUNCH-BY-BUNCH POSITION MEASUREMENT BASED ON FPGA*

Ruizhe Wu, Leilei Tang†, Ping Lu, Bao-gen Sun, National Synchrotron Radiation Lab. (NSRL),
University of Science and Technology of China (USTC), Hefei, Anhui, China

Abstract

In storage ring, the measurement of bunch-by-bunch positions can help to obtain abundant beam dynamics characteristic information, diagnose the instability of beam motion and provide a basis for the suppression of instability. However, the measurement of bunch-by-bunch requires one analog-to-digital converter (ADC) with high sampling rate and one processor with fast digital signal processing (DSP) ability. With the development of electronics, high sampling rate ADCs are no longer a problem. Therefore, high-speed DSP has become the key. In this paper, a parallel digital signal processing architecture based on polyphase decomposition is proposed. This architecture realizes the GHz DSP speed on the programmable gate array (FPGA), which can be used as the infrastructure of high-speed DSP in the bunch-by-bunch position measurement system.

INTRODUCTION

Beam diagnostics is an indispensable part of synchrotron light source to ensure its stability in operation. In beam diagnostics, the beam position monitor (BPM) used to monitor electron beam can obtain the position and current intensity information of the beam, then shows the running state of the synchrotron light source. In recent years, with the improvements of digital devices in terms of working frequency, DSP is of interest in the field of BPM.

With different DSP dealing rates, different types of beam information can be obtained by BPM:

- Closed Orbit: Sample at 10 Hz for high precision position measurement. The average value of multi turn beam position in the storage ring can be obtained.
- Fast Orbit: Sample at 10 kHz for fast orbit feedback. The average value of multi turn beam position in the storage ring can be obtained.
- Turn-By-Turn: Sample at the time for the bunch to move one turn in the storage ring. The average position data of all bunches in the storage ring can be obtained.
- Bunch-By-Bunch: Sample at the time interval between adjacent bunches. The position of each bunch in the storage ring can be obtained.

At present, BPM can obtain the beam information from closed orbit to turn-by-turn through the development of digital devices [1]. However, the obtain of bunch-by-bunch beam information usually imposes higher requirements on DSP dealing capacity. Hence the BPM of bunch-by-bunch, limited by the DSP part, is still in its initial stage.

The DSP part of BPM is usually implemented with FPGA. By coding, digital logic can be mapped to FPGA, so as to achieve various digital logic functions. This great programming flexibility of FPGA is provided by its internal interconnect bus architecture, but this architecture also limits its processing speed to about 500 MHz. Therefore, the DSP speed of BPM is basically at 500 MHz, and then it is difficult to realize the DSP work of bunch-by-bunch.

In FPGA, static timing analysis technology [2] can verify the correctness of digital circuit timing and predict the working frequency of digital system implemented by FPGA.

$$F_{max} \leq \frac{1}{T_{co} + T_{logic} + T_{routing} + T_{su} - T_{skew}} \qquad (1)$$

As shown in the Eq. (1), the highest DSP speed F_{max} depends on T_{co}, T_{logic}, $T_{routing}$, T_{su} and T_{skew} parameters. Among them, T_{co} and T_{su} are intrinsic parameters of FPGA that cannot be changed. $T_{routing}$ and T_{skew} are dynamic parameters in FPGA implementation process optimized by Tcl timing constraints, but its change is quite limited. Therefore, only the code logic T_{logic} can be modified to achieve the high speed DSP structure meeting the requirements of bunch-by-bunch.

The high speed parallel DSP structure proposed in this paper will be described in five parts: selection of DSP form, analysis of DSP structure, implementation of DSP structure, data parallelization and performance of parallelization implementation.

SELECTION OF DSP FORM

Generally, in DSP digital filters has two forms, finite impulse response FIR and infinite impulse response IIR.

FIR is a stable all zero structure with linear response characteristics. While IIR, a structure with both poles and zeros, has no linear phase response. If IIR needs to realize linear phase response, it needs to use all-pass filter for correction, which consumes additional digital logic resources. Moreover, due to the nonlinear influence caused by the quantization effect in hardware implementation, the poles of IIR will change and even become unstable [3].

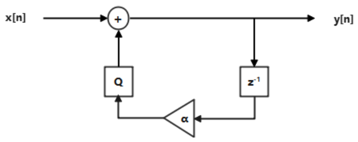

Figure 1: IIR transfer function.

As shown in Fig. 1, the IIR transfer function $\frac{1}{1-\alpha z^{-1}}$ has been transformed into the block design form of state-space

---

* National Synchrotron Radiation Laboratory

† tanglei@ustc.edu.cn

equation $y[n] = Q[\alpha y[n-1]] + x[n]$ in time domain, the nonlinear part quantization Q in the equation can be clearly seen. Therefore, FIR is usually selected for DSP.

ANALYSIS OF DSP STRUCTURE

For FIR, the key of structure optimization is to find out the critical path in the delay line of the signal and then transform the critical path.

$$y[n] = \sum_{n=0}^{N-1} h[n]z^{-n} \tag{2}$$

$$y[n] = h[0]z^{-0} + h[1]z^{-1} + \cdots + h[N-1]z^{-N+1} \tag{3}$$

Expand the transfer function equation Eq. (2) of FIR into equation Eq. (3). Then the addition chain direct structure of FIR shown in Fig. 2 can be obtained from Eq. (3), in which the path shown by the hollow arrow is the key path in the structure. Assuming T_S is the latency of the system, T_M is the time to complete a multiplication, T_A is the time to complete an addition, and N is the length of the impulse response function $H[n]$, then the latency of the addition chain direct structure is $T_S = T_M + (N-1)T_A$.

If the addition chain in the addition chain direct structure is modified to the form of addition tree, then the addition tree direct structure can be generated, as shown in Fig. 3. Its lantency is $T_S = T_M + \log_2(n-1)T_A$. Compared to the addition chain direct structure, the tree structure has been time optimized in addition calculation.

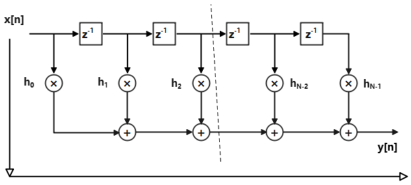

Figure 2: FIR Addition Chain Direct Structure.

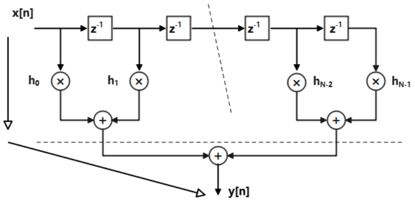

Figure 3: FIR Addition Tree Direct Structure.

The transpose structure can be generated by tranposing each stage in the addition chain direct structure. The transposition process of transpose structure is shown in Fig. 4.

Figure 4(a) shows the addition chain direct structure, the vertical dotted line indicates that there are multiple repeated structural units in the middle, and the part between the oblique dotted line and the vertical dotted line indicates the structural unit to be transposed. Figure 4(b) shows the transposed structure unit compared to Fig. 4(a). The transposed structure in Fig. 4(c) can be obtained by repeatedly transposing the structural units. In this structure, the latency is $T_S = T_M + T_A$.

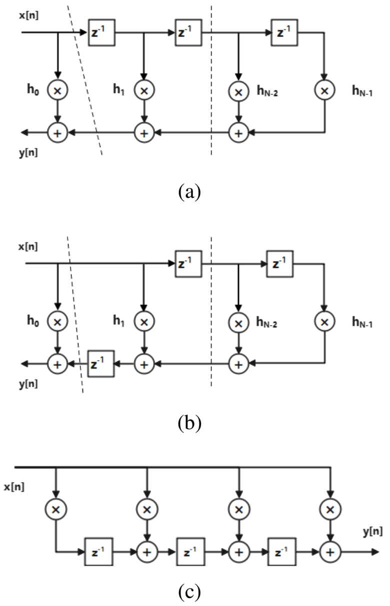

(a)

(b)

(c)

Figure 4: Transpose Process of the Transposed Structure.

FIR structures are usually the above three structures: addition chain direct structure, addition tree direct structure and transpose structure. Table 1 shows the differences in the three structures.

Table 1: Comparison of FIR Structures

Structure	Latency	Multiplier	Adder
Addition Chain	$T_M + (N-1)T_A$	N	$N-1$
Addition Tree	$T_M + \log_2(N-1)T_A$	N	$2N-3$
Transpose	$T_M + T_A$	N	$N-1$

IMPLEMENTATION OF DSP STRUCTURE

Compared with similar products, Xilinx's FPGA board has higher performance and meets the needs of bunch-by-bunch position measurement better. Therefore, all the following structures are designed and implemented based on the FPGA of Xilinx company.

In order to archieve high performance DSP, Xilinx integrates DSP48E2 slice in FPGA. DSP48E2 slice includes one 27-bit preadder, one 27×18 multiplier and one 48-bit ALU to support multiple calculation functions [4]. Moreover, with dedicated clock lines, DSP48E2 slice has much higher performance compared to the conventional logic implemented by configurable logic block.

In most cases, DSP48E2 is in reuse mode for DSP. While to realize high speed DSP, DSP48E2 slices need to be completely used. With the dedicated clock lines of DSP48E2, the DSP speed can reach the clock limit of the board F_{clk}.

By mapping the transposed structure to DSP48E2 slice, the implementation as shown in Fig. 5 can be obtained [5].

As shown in Table 1, its transpose latency is $T_M + T_A$, which means one processing can be completed only by one multiplication and one addition in DSP48E2. However, its fan-out is large, due to the same signal input in transpose structure. Besides, in FPGA implementation stage, large fan-outs will occupy a lot of wiring resources, resulting in signal congestion and timing deterioration, even timing fail. Therefore, the length N of the impulse response function $H[n]$ is limited by fan-outs, and then the transpose structure with multiple multiplication coefficients cannot be implemented.

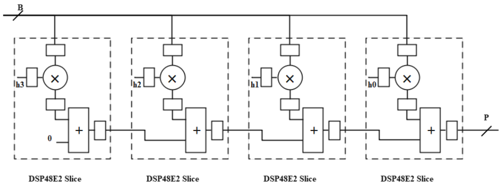

Figure 5: Transpose Structure Implemented by DSP48E2.

By mapping the addition chain direct structure to DSP48E2 slice, the implementation as shown in Fig. 6 can be obtained [5]. This implementation is called systolic, which solves the problem of fan-out at the cost of latency increasement. As shown in Table 1, assuming that the coefficient of DSP is N, the corresponding latency is $T_M + (n-1)T_A$.

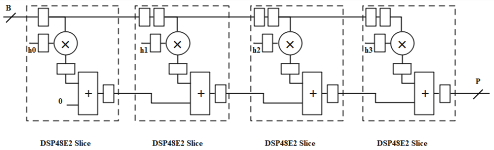

Figure 6: Systolic structure implemented by DSP48E2.

The addition tree direct structure can also be mapped to DSP48E2 slice, but requires more DSP48E2 slices. Due to the valuableness of DSP48E2 slices in FPGA, this structure does not have much implementation value.

Owing to the ultrafast speed and short data interval of DSP48E2 slice, the addition chain direct structure and transpose structure can achieve a speed close to the F_{clk}. Table 2 below shows their implementation.

Table 2: Comparison of Implementations

Structure	**Interval**	**Latency**	**DSP48E2**	**N Limited**
Addition Chain	$1/F_{clk}$	$T_M + (N-1)T_A$	N	No
Addition Tree	$1/F_{clk}$	$T_M + \log_2(N-1)T_A$	$2N-3$	No
Transpose	$1/F_{clk}$	$T_M + T_A$	N	Yes

However, in FPGA, the number of DSP48E2 slices is limited, so it is impossible to fully use DSP48E2 to implement all DSP functions, and the maximum working frequency of DSP48E2 is also limited to F_{clk}. Therefore, in order to achieve the speed of GHz DSP, one parallel structure is needed.

DATA PARALLELIZATION

Polyphase decomposition is a common technology in multi-rate DSP [6]. Equation (4) is the form of polyphase decomposition.

$$H(z) = \sum_{k=0}^{M-1} z^{-k} E_k(z^M), E_k(z) = \sum_{i=0}^{\frac{L}{M}-1} z^{-i} h(iM+k) \tag{4}$$

Polyphase decomposition transforms the transfer function $H(z)$ of DSP into multiple sub filter structures, archieve the data shunting of each sub filter path, and reduces the amount of data on one data path. The multi-input single-output (MISO) DSP system will be obtained if the left delay line of polyphase decomposition is removed, as shown in Fig. 7. In this DSP system, the speed reduction is realized.

$$H(z) = \sum_{k=0}^{M-1} \sum_{i=0}^{\frac{L}{M}-1} z^{-k} z^{-iM} h(iM+k) \tag{5}$$

$$Y(z) = H(z)X(z) = \sum_{k=0}^{M-1} \sum_{i=0}^{\frac{L}{M}-1} z^{-k} z^{-iM} h(iM+k) X(z) \tag{6}$$

If the two equations in Eq. (4) are combined, the Eq. (5) can be obtained, and then the Eq. (6) of the output $y(n)$ in the z domain is also obtained.

By transforming Eq. (6) from z domain to time domain, the Eq. (7) between input $x(n)$ and output $y(n)$ in time domain can be obtained, where $H_k(n)$ is the pulse response function of sub transfer function $E_k(n)$.

$$\begin{aligned} y(n) &= \sum_{k=0}^{M-1} \sum_{i=0}^{\frac{L}{M}-1} h(iM+k) x(n-(k+iM)) \\ &= h_0(n) * x(n) + \cdots + h_k(n) * x(n) \\ &= \sum_{k=0}^{M-1} h_k(n) * x(n-k) \end{aligned} \tag{7}$$

According to the linear time invariant property of DSP, the output $y(n-(L-1))$ Eq. (8) can be obtained.

$$\begin{aligned} & y(n-(L-1)) \\ &= \sum_{k=0}^{M-1} \sum_{i=0}^{\frac{L}{M}-1} h(iM+k) x(n-(k+iM+L-1)) \\ &= \sum_{k=0}^{M-1} h_k(n) * x(n-k-(L-1)) \end{aligned} \tag{8}$$

Transform the output $y(n-(L-1))$ into the z domain again, Eq. (9) can be obtained.

$$\begin{aligned} & Y(z-(L-1)) \\ &= H(z)X(z-(L-1)) \\ &= z^{-(L-1)} [\sum_{k=0}^{M-1} \sum_{i=0}^{\frac{L}{M}-1} z^{-k} z^{-iM} h(iM+k) X(z)] \end{aligned} \tag{9}$$

Equation (9) has only one more time shift unit $z^{-(L-1)}$ compared with Eq. (6), so the M-Input L-Output structure (MILO) can be obtained, as shown in Fig. 8. Obviously, L times of resources are required for data parallelization.

ISBN: 978-3-95450-230-1 ISSN: 2673-5350 doi:10.18429/JACoW-IBIC2021-WEPP27

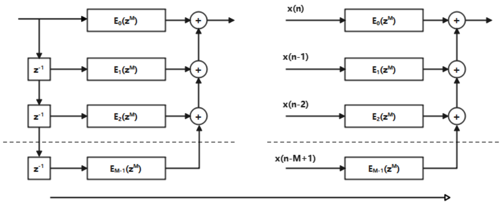

Figure 7: MISO.

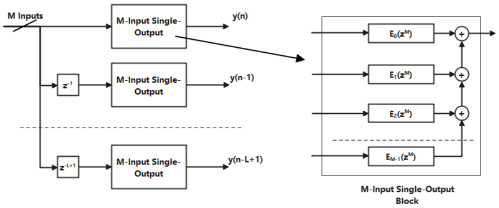

Figure 8: MILO.

During high-speed signal processing, with the help of the MILO, the data stream can be shunted, so that the signal processing frequency on the data input branch path can be reduced to $1/M$, and the GHz signal processing can be easily realized. At the same time, the L outputs can match the parallel input transfer function of the next stage and fully implement the parallel processing of data.

PERFORMANCE OF PARALLEL DSP STRUCTURE

In order to improve the implementation efficiency of parallelized digital signal processing logic, the high-level synthesis tool HLS provided by Xilinx is used here. HLS can convert C\C++ language code that meets certain hardware rules into finite state machine logic in hardware description language, which helps to quickly realize the hardware logic related to the algorithm. In HLS, the parallelized digital signal processing logic implemented in C\C++ language is described in the form of time domain, so the code can be written with the help of Eqs. (7) and (8).

When the HLS sets the target clock cycle as 5 ns, the performance comparison between common FIR and the 5-Input 5-Output ParallelFIR is shown in Table 3. The target period setten as 5 ns represents the system is expected to work at 200 MHz and above; the estimated period 3.42 ns shows the system's maximum operating frequency is 209 MHz; the two cycles latency indicates that the time required for the data from input to output is 6.84 ns; the one cycle interval indicates that the data input is the same as the working speed of the system.

Table 3: HLS implementation Performance Comparison

Type	Target	Estimated	Latency	Interval	Data Deal Rate
FIR	5 ns	3.42 ns	2 cycles	1 cycle	209 Msps
ParallelFIR	5 ns	3.42 ns	2 cycles	1 cycle	1045 Msps

In Table 3, the performance of the two systems are the same. It is found that the performance of common FIR determines the performance of MILO system, but there are differences in data deal rate between the two systems. For common FIR, the data deal rate is 209 Msps; for the ParallelFIR, the data deal rate is 209 Msps×5 = 1045 Msps. As a result, if the parallelism of the MILO structure is increased, higher signal processing speed can be achieved and the needs of bunch-by-bunch can be meeted.

Cite an instance for Hefei Light Source II. Its storage ring operates at 204 MHz. In the case of N points sampling for one bunch in storage ring, the bunch-by-bunch signal processing speed should be 204 MHz×N. Based on MILO system, if the N parallellization is carried out for bunch-by-bunch signal processing, the DSP implemented by FPGA only needs to work at 204 MHz. For FPGA, the frequency of 204 MHz can be easily achieved. Therefore, this MILO structure can meet the requirements of bunch-by-bunch BPM simply.

CONCLUSION

The parallel data processing structure based on polyphase decomposition is a method of exchanging resources for processing performance. When the degree of parallelism is L, L times resource consumption is needed, but there is an M-fold improvement in data processing rate requirement.

At present, the conventional bunch-by-bunch BPM mostly uses simple time-domain algorithms, such as difference-ratio-sum algorithm, interpolation algorithm and look-up table matching algorithm, but there are very few algorithms in digital frequency domain. The main reason is that the digital frequency domain algorithm is limited by its implementation structure, and it is difficult to realize the frequency domain processing under the condition of high data input rate. The parallel data processing method based on polyphase decomposition breaks through this limitation, can easily deal with the data with GHz input rate, and makes a variety of frequency domain processing methods possible in bunch-by-bunch BPM.

REFERENCES

[1] X. Zhang, “Development of Bunch-by-bunch Beam Position Measurement Electronics for High Energy Photon Source”, University of Chinese Academy of Sciences, 2020.

[2] Gangadharan, S. and S. Churiwala, *Constraining Designs for Synthesis and Timing Analysis - A Practical Guide to Synopsys Design Constraints (SDC)*, New York, USA: Springer, 2013, p. 226.

[3] Mitra, S. K., *Digital Signal Processing, Computer-Based Approach*, NY, USA, McGraw-Hill Companies, 2011.

[4] Xilinx, *UltraScale Architecture DSP Slice User Guide*, 2020.

[5] Hawkes, G.C., *DSP: Designing for Optimal Results*,. Xilinx Advanced Product Division, 2005.

[6] P, Vaidyanathan., *Multirate Systems And Filter Banks*, Upper Saddle River, NJ, USA, Prentice-Hall, 1993.

ISBN: 978-3-95450-230-1 ISSN: 2673-5350 doi:10.18429/JACoW-IBIC2021-WEPP28

SUB-ns SINGLE-PARTICLE SPILL CHARACTERIZATION FOR SLOW EXTRACTION

T. Milosic*, R. Singh, P. Forck
GSI Helmholtz Centre for Heavy Ion Research, Darmstadt, Germany

Abstract

With the recent developments on improving spill quality at GSI/FAIR, appropriate measurement devices have come into focus again. In contrast to commonly used scaler-based approaches where events at a certain sample frequency are counted, we present a measurement concept resolving single-event detector timestamps in the sub-ns regime leveraging a well-established off-the-shelf TDC VMEbus module. This allows for high-resolution time structure information with respect to the ring RF as well as evaluation of inter-particle separation distributions. This yields insightful information for specific experiments at GSI whose efficiencies are heavily limited by pile-ups and detector dead times. We will present the concept of the measurement setup and exemplary data taken in recent campaigns in context of spill microstructure improvements for slow extraction.

INTRODUCTION

Recent experiments measuring and optimizing slow-extraction spills at GSI/FAIR led to promising results [1]. The focus on spill quality introduced the demand to complement traditional counter-based approaches with single-particle detection at higher time resolution. Ideally, this would allow to resolve bunches and directly access the particle-interval information. Both is not possible with scalers even at high latching rates.

This goal can be achieved by fast time-to-digital converters (TDCs). They turn logic input signals, such as discriminated detector signals, into precise timestamps. Figure 1 schematically depicts timing events derived from two input signals and recorded by a TDC. Time-structure information is extracted from the detector event by correlating it with the SIS18 cavity RF or, alternatively, with a custom clock. The red arrows TS_n mark the difference between a detector event and the preceding slope-sensitive zero-crossing of the RF reference. This data is histogrammed at a user-definable bin size and time slice, providing a reconstruction of the time structure confined to the RF period range.

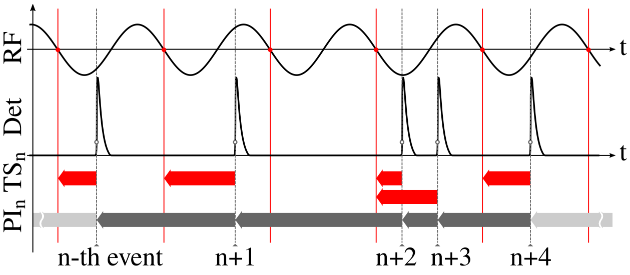

Figure 1: Single-particle events used to characterize spills.

Similarly, the particle-interval (also *separation*) information PI_n is retrieved as the difference between consecutive detector timestamps as represented by gray arrows. Event data grouped in time slices is histogrammed with user-definable bin sizes and total range. The particle-interval distribution is useful to evaluate and optimize reduced efficiencies as a consequence of dead times of specific experiments.

Two application targets are considered. An online tool allows to asses spill characterization for operating and experiments. Furthermore, offline analysis preserving full information of the raw data is available. The TDC module comes with some limitations for which, in particular high-performance, online analysis is a challenge. However, the setup presented is capable to make use of the TDC ASICs performance to its fullest even in online mode.

HARDWARE SETUP

A system leveraging a high-precision TDC already existed as part of the ABLAX suite [2]. It is based on a RIO3 VMEbus controller, a CAEN V1290N TDC module and a custom software stack on top of LynxOS. Being limited to a net detection rate of ≪ 100 kEvents/s and the increasing challenge to maintain the environment this gave rise to a new development from scratch but using the same TDC module.

Constrained to the VMEbus, the new system uses a x86-64 MEN A25 controller [3] paired with a PMC White Rabbit FAIR timing receiver node (FTRN) [4] (Fig. 2). The controller is based on the Intel(R) Pentium(R) CPU D1519 with 4 cores supporting 2 threads per core through hyper-threading at 1.50 to 2.10 GHz and 8 GiB of RAM. It has been equipped with a 1 TB mSATA SSD to store data locally.

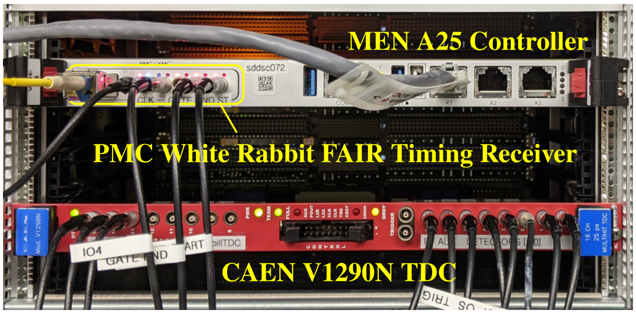

Figure 2: VMEbus mainframe configuration.

Time-to-Digital Converter

The V1290N TDC VMEbus module is build around CERN's HPTDC ASIC [5] and is still available from CAEN.

---

* t.milosic@gsi.de

Featuring two HPTDC ASICs, each serving 8 NIM inputs, 16 channels are available in total. A single ASIC is expected to be able to process a total maximum event rate of 4 MEvents/s at a double-hit resolution of 5 ns. Events are recorded with a native 21-bit timestamp counter. The TDC is operated in *Continuous Storage Mode* interleaving all recorded events in a sequential data stream. An RMS time resolution of 35 ps per input channel is achieved.

IMPLEMENTATION

The software stack implements a C++ FESA [6] class and a JavaFX GUI application. Additionally, an exporter is available to convert recorded binary data for offline data analysis. In the following, an overview on the most important aspects of the FESA class implementation is given.

Having an online mode for the DAQ was an essential requirement for operating and experiments. This complements the option to dump stream data containing full event information for in-depth offline analysis. However, online processing of data while being able to exploit the full event rate of the HPTDCs is challenging. The V1290N TDC module comes with some limitations that need to be considered carefully. With a 32-bit data word only 21 bits represent the timestamp to additionally accommodate headers and state flags. The counter value is mapped to time by a calibration factor, also called *least significant bit* (LSB) in this context. By applying a precise regular clock and a subsequent linear fit this yields a calibrated LSB time value of 24.414 ps. Consequently, the resulting dynamic range is only $2^{21} \cdot 24.414\,\text{ps} = 51.2\,\mu\text{s}$. Hence, manual overflow correction is mandatory with spill lengths up to several tens of seconds. At the same time, strict chronological order of TDC events is not guaranteed in the sequential stream of data. Unfortunately, this rules out the trivial approach to overflow correction by checking if $t_{n+1} < t_n$ for any consecutive recorded events. Just following that rule, without correcting ordering mismatches first, would lead to severe inconsistencies. This, among other compute-intensive tasks like prefetching the rate-divided RF timestamps, suggests to parallelize the data processing in order to leverage full performance of the HPTDC ASICs and avoid stalling of the acquisition and processing pipeline.

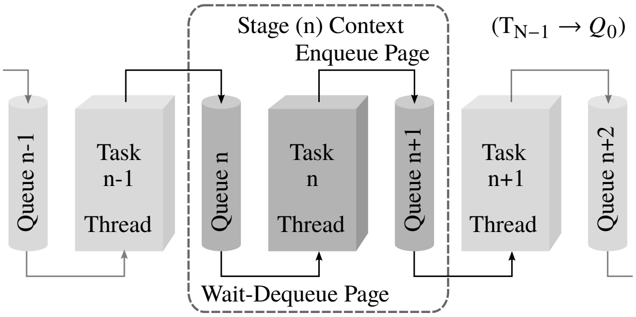

Figure 3: Pipeline concept with chained stages. Closed cycle: Last task N-1 outputs to queue 0 again.

Pipeline

The processing cycle is divided into sequential tasks representing separate stages of a pipeline. This is depicted schematically in Fig. 3. Each stage context consists of at least one input and one output queue (FIFO) accompanied by a thread processing a dedicated task along the pipeline. The thread dequeues a pointer to a page from the input queue, processes it and enqueues it to the output queue. A page, in this context, is defined as the data read from the TDC output buffer per acquisition cycle. By allocating a block of memory on the heap once and segment it into contiguous pages no further dynamic allocation will be required which avoids object creation and copy overhead. Flow control within the pipeline is provided by means of queues holding pointers to pages. At program initialization all pages are enqueued into the first queue of the pipeline maintaining their order. Moreover, synchronization is implicitly provided by the queue concept running as single-consumer single-producer at all stages. The pipeline is running in a closed cycle with the last stage outputting/enqueueing to the first queue again.

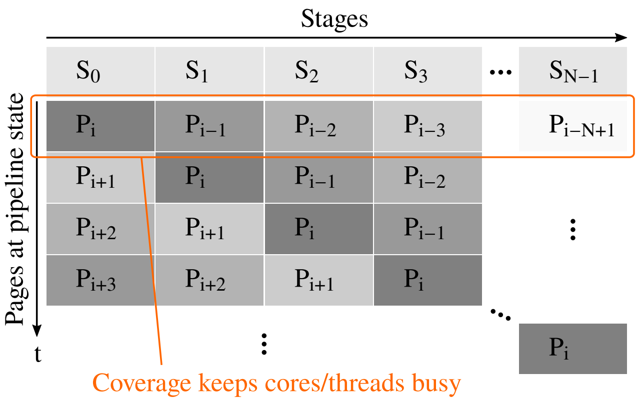

Figure 4: Coverage diagram for a pipeline with N stages.

Thread coverage is shown in Fig. 4. As processing progresses pages are transferred through the pipeline. Each stage is busy with a dedicated task but operates on a different page. This targets modern multi-core systems to distribute workloads.

The implementation features two coupled pipelines operating on pages of different word sizes. This is necessary to account for a larger dynamic range after manual overflow correction. With the longer word size of the second pipeline, 48 bits are used for the extended counter holding overflow-corrected timestamp values instead of the native 21 bits of the TDC. Thereby, the dynamic range is increased from 51.2 µs to more than 114 minutes while accuracy and precision is still preserved at the original LSB of 24.414 ps.

Figure 5 lists the stages, eight in total, for the two pipelines. Data flow starts at a tight acquisition loop on the TDC, reading data once a fill threshold of the output FIFO is met. The further stages will restore the chronological ordering and prefetch RF events. Overflow correction is the last stage of the first pipeline and provides coupling. It is also the first stage of the second pipeline at the same time and, thus, the

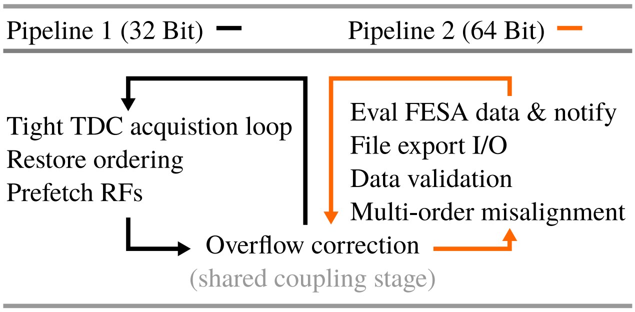

Figure 5: Data flow and tasks.

only stage reading and writing from two queues. Data flow in the second pipeline continues by checking for multi-order misalignments (occurs rarely at high rates) followed by a validation stage for data consistency. After passing the I/O stage, FESA data is prepared and properties are notified.

USER INTERFACE

A Java application, which is the typical interface for FESA classes at GSI, allows to view TDC data online. Common users are operators, experts from beam instrumentation and accelerator physics. The GUI application is depicted in Fig. 6. Configuration items are related to detector selectors, timing configuration and RF reference (SIS18 native or AUX clock). Furthermore, bin sizes, ranges and global time slice duration can be configured but have no effect on stored data. Dumped data is based on single-event timestamps and, thus, preserves full detector information acquired in the first place. Time slices define the size of the time window within which data is evaluated.

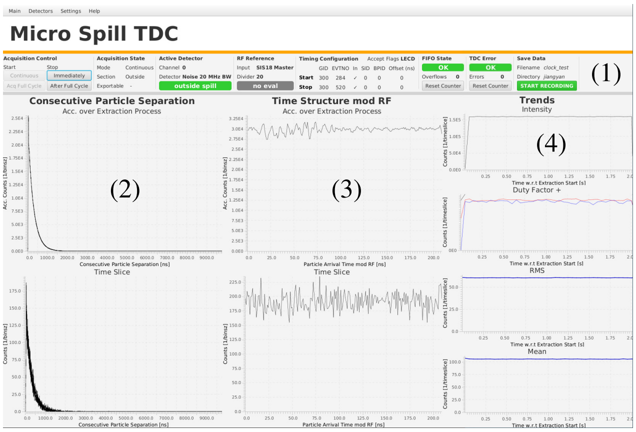

Figure 6: Remote Java GUI interfacing the FESA class.

The top row (1) features some configuration items, but also information about the current detector rate and acquisition status (output FIFO overflows and TDC errors).

Users can track particle-interval distributions in the left column (2). Time-structure information is presented to the user in the middle column (3). In both cases, the bottom row shows data of a single time slice. The top row is the accumulated information w.r.t. the current spill. For the screenshot a noise generator was attached providing a Poisson-like particle-interval distribution (left column). At the same time, events are not correlated with the RF, thus, the time structure is flat (middle column).

The right column (4) features a time series of parameters evaluated for each time slice along the spill. From top to bottom: intensity (current), duty factor [7] as well as mean and RMS of the time structure.

MEASUREMENTS

In the following, typical data analysis will be presented using the aforementioned exporter. Three targets are supported: time structures, particle-interval distributions and a high-res intensity/current mode. In all cases it is possible to superimpose spills with the high precision of the White-Rabbit timing [4] and, thus, enhance statistics. This is accomplished by injecting the spill start and end timing events into the data stream as TDC inputs generated by the FTRN. Beyond file information, the exporter supports filtering and selections of spills. This is handy in case of accidental timing settings recording different spills shared on the beam line. Filtering works on the basis of counts per spill and spill length. Additionally, the exporter supports selecting spills by range or index cherry-picking.

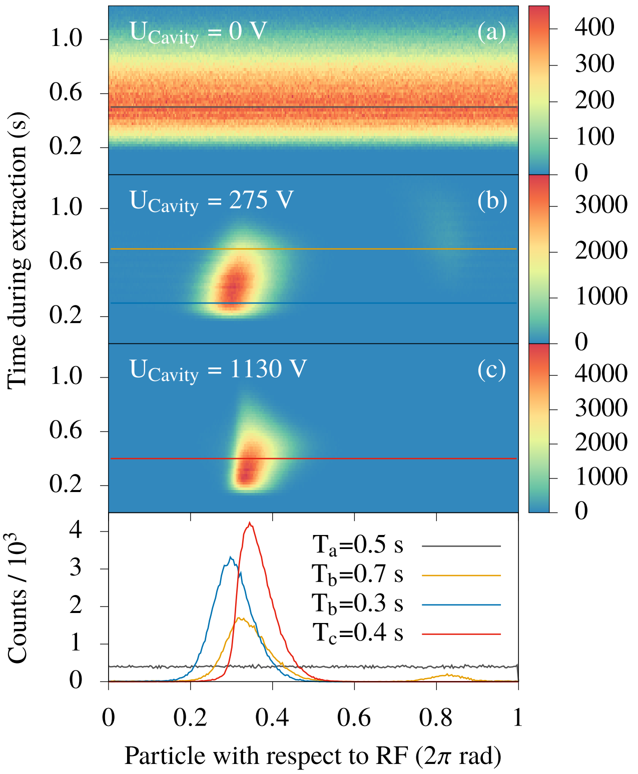

Figure 7: Time-structure information for Bi^{68+} beam.

Time Structure

A Bi^{68+} beam at 300 MeV/u recorded with a plastic scintillator is plotted in Fig. 7. Data is shown within a full RF period on the x axis and the time during extraction w.r.t. spill start on the y axis. Each row represents a time slice exported with 20 ms. The top data at a cavity voltage of 0 V clearly hints an unbunched beam with no correlation w.r.t. the RF. The time slice at $T_a = 0.5$ s confirms this with a flat time structure. At a cavity voltage of 275 V the beam is bunched but a second bunch emerges during extraction as can be seen in the bottom window for time slices at $T_b = 0.3$ s and 0.7 s. With a cavity voltage of 1130 V only one bunch is present but position and shape varies during extraction. Further interpretation of data is outside the scope of this paper.

Particle Intervals

Based on the same recorded data used for the time-structure before, Fig. 8 depicts particle-interval information for three different cavity voltages. The bottom window shows the projection onto the x axis given in units of RF periods. For 0 V cavity amplitude, the particle arrival interval is governed by a Poisson process. The resulting exponential interval distribution is apparent from the projection. At a cavity voltage of 275 V a pattern is visible with distinct accumulation regions evenly spaced by the RF. The projection reveals a second accumulation in between the prominent regions. At 1130 V only the prominent regions remain.

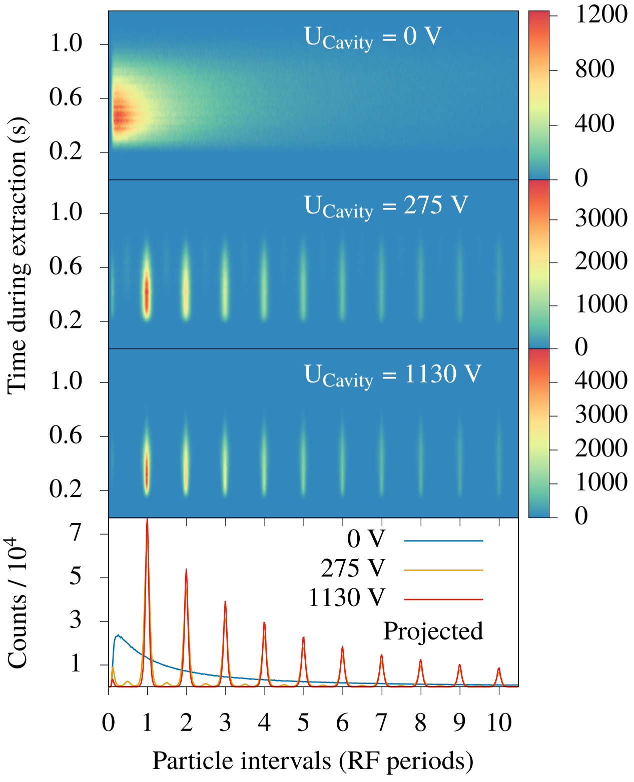

Figure 8: Particle-interval distribution for Bi^{68+} beam.

Spill Characterization

The slow extraction spill characterization using scaler data is discussed in [7]. Although the duty factor and maximum-to-mean ratio give a measure of the smoothness of the spill, it is not a direct quantification of the potential events and triggers seen by the experimental detectors. The time of arrival measured at the TDC provides a more direct measure of the usable part of a spill for a given detector response. Figure 9 shows a cumulative density function (CDF) of the particle intervals for a coasting slow extraction spill and bunched beam spill along with the hypothetical Poisson and uniform spills at the same extraction rate. The rate for the spills shown was $1.2 \cdot 10^6$/s and extraction duration was 10 s. The jumps in the bunched beam extraction correspond to the 205 ns and its multiples i.e. RF period, which represents the temporal separation between particles maintained by the RF cavities. Bunched beam is known to mitigate the spill modulation caused by low frequency power supply ripples due to synchrotron motion at the cost of introducing high frequency structures at RF frequency [8]. It is evident, that there is a higher proportion of particles with larger time intervals for the bunched beam in comparison to coasting beam extraction. For some detector dead times, the correlations at RF periods can even be advantageous. An example of such a case is visible in Fig. 9; if a hypothetical detector has a dead time of 250 ns after arrival of every particle or event, bunched beam extraction provides potentially larger event rates in comparison to purely random Poisson statistics for the given extraction rate. Thus, the extraction rate and RF period has to be carefully chosen to benefit from bunched beam extraction.

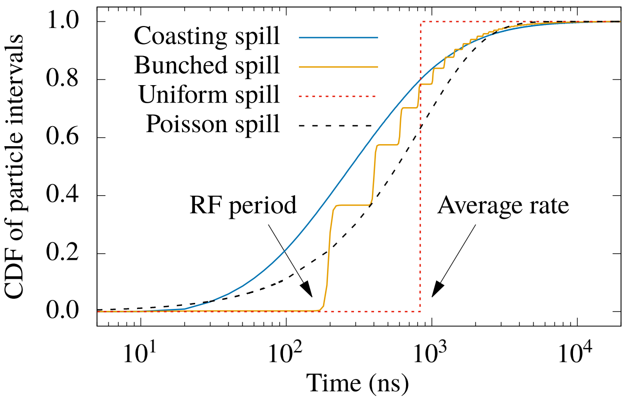

Figure 9: Cumulative distribution of the spills.

SUMMARY

We presented a newly developed measurement setup for spill characterization based on an off-the-shelf TDC. Its implementation concept to leverage full TDC performance even in online mode was outlined. Experimental data highlights the additional and relevant information beyond what scalers can provide. The setup is used in regular operations providing a GUI application targeting different user groups. A feature-rich exporter is available to transform stored data streams for in-depth data analysis.

ACKNOWLEDGEMENT

We thank P. Boutachkov for helpful discussions on experimental detector dead times.

REFERENCES

[1] R. Singh, P. Forck, and S. Sorge, "Reducing fluctuations in slow-extraction beam spill using transit-time-dependent tune modulation," *Phys. Rev. Applied*, vol. 13, p. 044 076, 4 Apr. 2020. DOI: `10.1103/PhysRevApplied.13.044076`. `https://link.aps.org/doi/10.1103/PhysRevApplied.13.044076`

[2] T. Hoffmann, P. Forck, and D. A. Liakin, "New spill structure analysis tools for the vme based data acquisition system ablass at gsi," *AIP Conference Proceedings*, vol. 868, no. 1, pp. 343–350, 2006. DOI: `10.1063/1.2401422`. `https://aip.scitation.org/doi/abs/10.1063/1.2401422`

[3] A. Wujek, D. Cobas, G. Daniluk, and M. Suminski. "Status and plans for the men-a25 vme cpu." BI/TB on uTCA, LIU wire-scanner results and AWAKE status. (Sep. 2017), `https://indico.cern.ch/event/659372/contributions/2703686/attachments/1523293/2380688/A25_BI-TB.pdf`

[4] C. Prados *et al.*, "Fair timing system developments based on white rabbit," in *Proc. 14th Int. Conf. on Accelerator and Large Experimental Physics Control Systems (ICALEPCS'13)*, (San Francisco, CA, USA), Oct. 2013, pp. 1288–1291. `https://accelconf.web.cern.ch/ICALEPCS2013/papers/thppc092.pdf`

[5] J. Christiansen, "Hptdc high performance time to digital converter," CERN, Geneva, Tech. Rep., 2004, Version 2.2 for HPTDC version 1.3. `https://cds.cern.ch/record/1067476`

[6] M. Arruat *et al.*, "Front-end software architecture," in *Proc. 11th Int. Conf. on Accelerator and Large Experimental Physics Control Systems (ICALEPCS'07)*, Knoxville, TN, USA, 2007, p. 310. `http://cds.cern.ch/record/1093646`

[7] R. Singh, P. Boutachkov, P. Forck, S. Sorge, and H. Welker, "Slow Extraction Spill Characterization From Micro to Milli-Second Scale," in *Proc. 9th International Particle Accelerator Conference (IPAC'18), Vancouver, BC, Canada, April 29-May 4, 2018*, (Vancouver, BC, Canada), ser. International Particle Accelerator Conference, https://doi.org/10.18429/JACoW-IPAC2018-WEPAK007, Geneva, Switzerland: JACoW Publishing, Jun. 2018, pp. 2095–2098, ISBN: 978-3-95450-184-7. DOI: `doi:10.18429/JACoW-IPAC2018-WEPAK007`. `http://jacow.org/ipac2018/papers/wepak007.pdf`

[8] S. Sorge, P. Forck, and R. Singh, "Measurements and Simulations of the Spill Quality of Slowly Extracted Beams from the SIS-18 Synchrotron," in *Proc. 9th International Particle Accelerator Conference (IPAC'18), Vancouver, BC, Canada, April 29-May 4, 2018*, (Vancouver, BC, Canada), ser. International Particle Accelerator Conference, https://doi.org/10.18429/JACoW-IPAC2018-TUPAF081, Geneva, Switzerland: JACoW Publishing, Jun. 2018, pp. 924–926, ISBN: 978-3-95450-184-7. DOI: `doi:10.18429/JACoW-IPAC2018-TUPAF081`. `http://jacow.org/ipac2018/papers/tupaf081.pdf`

TESTS OF DIGITAL BPM SIGNAL PROCESSORS FOR SHINE*

L.W. Lai[†], Y.B. Leng, Y.M. Zhou, W.M. Zhou, X. Yang, J. Wan, H.S. Wang,
SSRF, Shanghai Advanced Research Institute, Chinese Academy of Sciences, Shanghai, China

Abstract

Digital signal processors that can handle 1 MHz bunch rate BPM signal processing is under development for SHINE. At the same time, two general purpose processor prototypes for all BPM signal sampling and processing have been developed. One uses 14bits ADC, the other uses 16bits ADC. Both processors have been completed. This paper will introduce the tests of the processors and the related performance evaluations.

INTRODUCTION

Shanghai HIgh repetitioN rate XFEL and Extreme light facility (SHINE) is a 3 km long hard X-ray FEL facility built underground in Shanghai. The designed beam repetition rate is 1 MHz. The project was initiated at the end of 2018. Now the research of key technologies has entered the final stage. There will be three types of BPMs located in different parts of the machine, including stripline BPM, cold button BPMs, and cavity BPM. The required BPM system resolution is 10 µm, 50 µm and 200 nm at 100 pC respectively.

BPM electronics will use independent RF front-end modules and digital signal processors. Different RF front-end modules will be designed to meet the signal characteristics requirements of different BPM types. The design of the RF front-end modules will not be introduced here. All three types of BPM will use unified digital signal processor hardware. The processor will be used for signal processing of different BPMs through the development of corresponding FPGA firmware and software [1]. The processor mainly contains 4 channels ADCs for sampling, FPGA for signal processing and ARM for system control and communication. Considering the beam dynamic range and the required system performance, the relative resolution of the processor should be better than 0.1%.

The processor is designed as a 1U height standalone instrument. The processor consists of a FPGA carrier board and an ADC daughter board. The boards are connected through FMC connector. The sampled data from ADCs are transmitted to FPGA through the JESD204B protocol. Another FMC connector is reserved for a WRN timing board. Figure 1 is the structure of the processor. Other interfaces including a Ethernet port, serial port, JTAG, SD slot, et al. Table 1 lists the specification of the processor. Except for the generic BPM processor, another direct RF sampling processor for cavity BPM also has being developed, the hardware is completed but firmware is still in progress, it will not be introduced here.

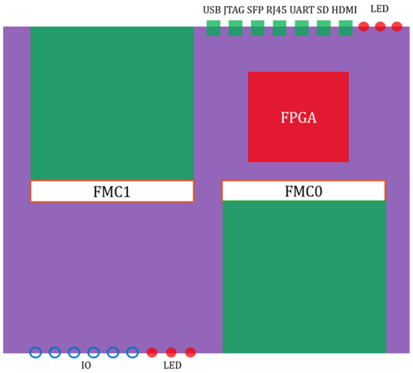

Figure 1: Processor structure.

Table 1: DBPM Specifications

Parameter	Value
Channels	4
Bandwidth	≥ 1 GHz
ADC bits	≥ 14
Max ADC rate	≥ 500 MSPS
FPGA	Xilinx Zynq Ultra+MPSoC
Clock	External
Trigger	Ext./Self/Period
SFP	≥ 2
Interlock	Lemo
DDR	≥ 512 MB
Software	Arm-Linux/EPICS
Relative resolution	≤ 0.100%

In order to cultivate qualified vendors for SHINE, two processor prototypes were developed at the same time. One processor uses 14 bits ADCs, the other two uses 16 bits ADCs. The maximum sampling rate of all ADCs is 1 GSPS. The development of the processors has been introduced in previous conference paper [2]. Recently, all the two processor prototypes come to the final stage. The tests of the processors will be introduced here.

---

*Work supported by Youth Innovation Promotion Association, CAS (Grant No. 2019290); The National Key Research and Development Program of China (Grant No. 2016YFA0401903).

[†] Corresponding author: lailongwei@zjlab.org.cn

ISBN: 978-3-95450-230-1 ISSN: 2673-5350 doi:10.18429/JACoW-IBIC2021-WEPP32

TESTS OF PROCESSOR A

Processor A uses 14bits ADCs and Xilinx FPGA XCZU9EG. 8V19N490 is used to provide low jitter clock for ADCs and the system. Figure 2 is the PCB of the ADC card and FPGA card. The ADC card is designed according to FMC standard.

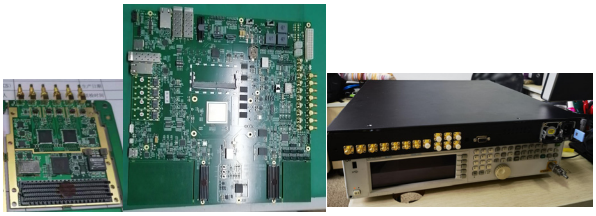

Figure 2: Processor A.

The processor has been tested in lab with a vector RF signal generator. A 29.75 MHz RF signal was divided into 4 channels and fed into the processor. At the same time, a 119 MHz signal from the generator was used as synchronized external clock of the processor. The clock was multiplied to 595 MHz with PLL 8V19N490, and then used as ADC sampling clock. Figure 3 is the spectrum of sampled data. The 2nd, 3rd and 4th harmonics were higher than -60dB. The relative position was calculated with Δ/Σ algorithm like orthogonal stripline BPM. The calculated relative position resolution is 3.47e^{-5}. Beam tests have not yet been done.

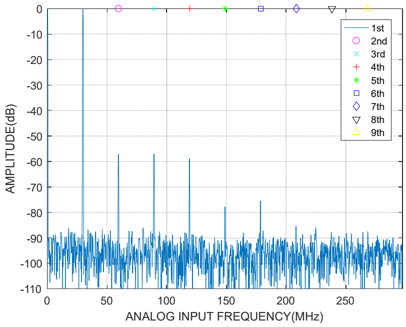

Figure 3: Spectrum of processor A sampled data.

TESTS OF PROCESSOR B

Processor B using 16 bits ADCs and Xilinx FPGA XCZU9EG. LMK04832 is used to provide low jitter clock for ADC and the system. Figure 4 is the PCB of the processor. The ADC board is wider than the FMC standard. Lab test conditions were the same as the processor A test, but the sampling clock was multiplied to 833 MHz.

Figure 4: Processor B.

Lab Test

Figure 5 is the spectrum of sampled data. The 2nd harmonic was lower than -60dB, and 3rd harmonic were lower than -70dB. The relative position resolution is 1.74e^{-5}. The performance of processor B shows better than processor A.

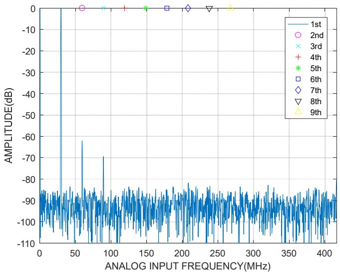

Figure 5: Spectrum of processor B sampled data.

Beam Tests on SXFEL

The processor has been used to sample the signal from stripline BPM and cavity pickup on SXFEL. Figure 6 is the block diagram of the test on stripline BPM. The output signals of pickup B and D were filtered with 20 MHz band pass filters firstly, then adjusted to proper range with amplifiers and attenuators, and then divided and fed into processor. 119 MHz signal from timing system is used as synchronized external clock.

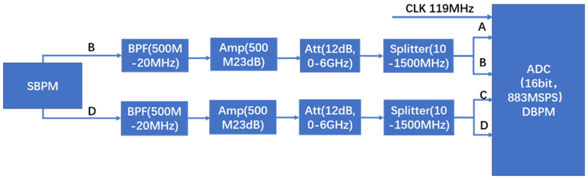

Figure 6: Block diagram of stripline BPM test.

Two unified positions can be obtained from the test. Figure 7 shows the relative position resolution is 1.80e^{-4}.

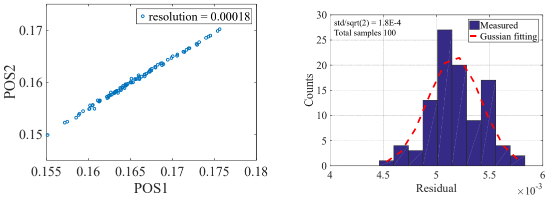

Figure 7: Relative position resolution of test with stripline BPM.

During the test, there was no available cavity BPM nearby. Fortunately, two cavity pickups IN_BAM01 and LA_BAM01 for beam arrival time measurement (BAM) can be used. The output signals of the two cavities were treated as the signals from position cavity and reference cavity of a BPM. Figure 8 is the block diagram of the test. The output signal from the cavities were down converted to 34 MHz IF signal with front-end module, and then attenuated and divided to feed into the processor.

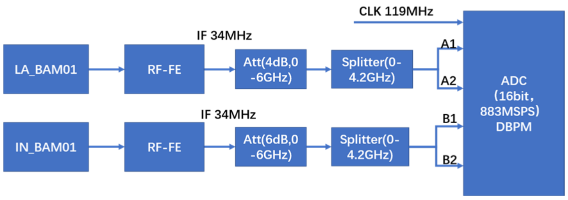

Figure 8: Block diagram of cavity BPM test.

The relative position resolution is 1.24e^{-4} as in Figure 9 (left). The beam flight time (BFT) between IN_BAM01 and LA_BAM01 also can be obtained from the same data. The relative BFT resolution is 3.9 fs shown in Figure 9 (right).

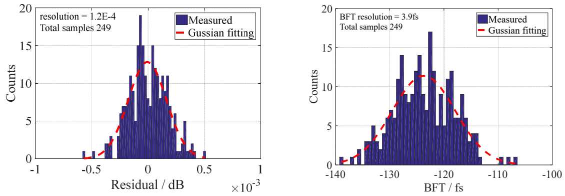

Figure 9: Relative resolution of measured position (left) and BFT (right).

SUMMARY

Two general processor prototypes for stripline BPM, cold button BPM and cavity BPM have been developed for SHINE. The ADCs are 14bits and 16bits respectively. The lab tests with RF signal generator shown the performance of processor B is better than processor A. The beam tests on SXFEL show that the relative position resolution of processor B is better than 1.80e^{-4}, which is far better than the 0.1% requirement of the BPM system.

Next we will focus on developing firmware and software to make the processor a fully functional equipment for SHINE.

REFERENCES

[1] L.W.Lai, Y.B.Leng, "High-Speed Beam Signal Processor for SHINE", in *Proc. 8th Int. Beam Instrumentation Conf. (IBIC'19),* Malmo, Sweden. Sep. 2019, pp. 283-284, `doi: 10.18429/JACoW-IBIC2019-TUPP004`

[2] L.W.Lai, Y.B.Leng, Y.M.Zhou, J.Wan, F.Z.Chen, T.Wu, "Status of Digital BPM Signal Processor for SHINE", in *Proc. 12th Int. Particle Accelerator Conf. (IPAC'21, virtual conference)*, Campinas, Brazil, May, 2021, WEPAB322.

THE FACET-II DATA ACQUISITION SYSTEM*

S. J. Gessner†, SLAC National Accelerator Laboratory, Menlo Park, CA, USA

Abstract

The Data Acquisition System (DAQ) at FACET-II is designed to address the challenge of collecting synchronized, time-stamped data from a variety of diagnostics spread throughout the kilometer-long linac and experimental area. The EPICS control system is used to read out data from devices at FACET-II via Channel Access (CA) over the network. This poses a problem for collecting image data at the 30 Hz beam rate. With image sizes ranging from 0.3-10 Megapixels, the data rate from a single camera can be as high as 0.6 Gbps and there are nearly 100 cameras deployed at FACET-II. Simultaneous image acquisition from just a few of these cameras would overwhelm the network. The FACET-II DAQ solves this problem by coordinating the camera IOCs to write their image data to network-attached storage (NAS) and then validating time-stamps to confirm synchronization.

INTRODUCTION

FACET-II [1] at SLAC uses EPICS [2] to control and retrieve data from diagnostics and devices spread throughout the kilometer-long accelerator and experimental area. The principle diagnostics for experiments at FACET-II are digital cameras. FACET-II hosts nearly 100 digital cameras and more than half of them are dedicated to the experimental area. Communication with the cameras is handled by the Channel Access (CA) network protocol. CA is the appropriate tool for monitoring and managing devices, but data rates are limited by the network. This poses a challenge for data acquisition (DAQ) because we require simultaneous images from multiple cameras corresponding to a single shot. The beam rate at FACET is 30 Hz and the average image size is over 1 Megapixel, equal to 2 MB/frame. FACET users commonly request datasets utilizing ten or more cameras, which yields a data rate of ≈ 5 Gbps. This rate can easily overwhelm the network, which utilizes both 1 GbE and 10 GbE switches, and may disrupt accelerator applications.

The FACET-II DAQ avoids the problem of acquiring data over the network by coordinating camera Input-Output Controllers (IOC) to save their data to a Network Attached Storage (NAS) drive located on the same switch as the camera servers. With this approach, the camera data never leaves the switch and network traffic is maintained at an acceptable level.

HARDWARE, LAYOUT, AND TOPOLOGY

The majority of cameras at FACET are AVT Manta and Mako GigE-interface devices running on Advantech Sky 8201 servers. Each server can host up to 12 cameras. FACET also uses scientific-CMOS cameras in the experimental area. All servers run areaDetector [3] IOCs. There are 7 camera servers along the linac and 9 camera servers located in Sector 20 (S20), the experimental area. The camera servers in S20 collect the majority of the data requested by users via the DAQ. A control server called facet-srv20 and NAS drive are also located in S20 and connected to the same switch as the camera servers. The NAS uses bonded ports to maximize data rate onto the drive. The topology of the network in S20 is shown in Fig. 1. The layout of the machine is shown in Fig. 2 and the distribution of the cameras is shown in Table 1.

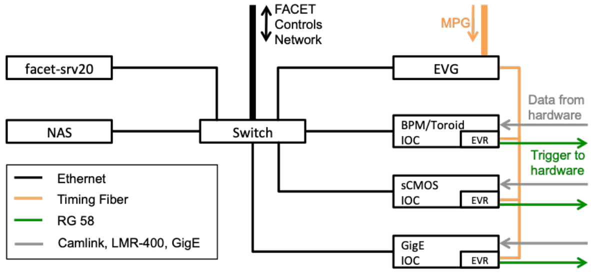

Figure 1: Network topology in FACET Sector 20. Note that the EVG has been relocated to the FACET injector in Sector 10.

DATA SOURCES AND SYNCHRONIZATION

In addition to camera images, the FACET-II DAQ also collects data from a variety of sources. This includes devices that update at the beam rate, such as beam position monitors (BPM), toroids, and photo-multiplier tubes (PMT), as well as devices that update asynchronously, such as magnet currents, motor positions, and temperatures. The beam-synchronous devices produce scalar data and are included in SLAC's beam-synchronous acquisition (BSA) infrastructure [4]. BSA devices store data in a rolling buffer with 2800 events. The length of the buffer was chosen for compatibility with the legacy SLC Control Program (SCP) [5]. The buffer exists on the IOC hosting the device, and each IOC can support multiple buffers with unique event definitions. For example, if the nominal beam rate at FACET is 30 Hz, an event code (EC) may be used to specify a lower rate (e.g. 10 Hz) or a rate subject to conditions (e.g. beam destination). Events are timestamped and tagged with a pulse ID number. The pulse ID is a rolling value that updates at 360 Hz. The maximum pulse ID is 131040, which is also a legacy of the SCP. This implies that the pulse IDs are not unique, but a buffer of length 2800 will not contain duplicate pulse IDs. BSA buffers are centrally managed by the Event Generator

---

* This work performed under DOE Contract DE-AC02-76SF00515.

† sgess@slac.stanford.edu

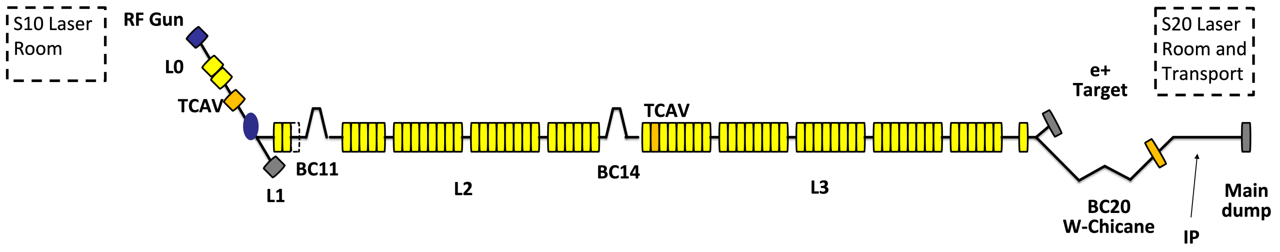

Figure 2: Layout of the FACET-II accelerator and experimental area.

Region	S10 Laser	Injector	L1	L2	BC20	S20 Laser	IP Area	Spectrometer	Total
Cameras Deployed	7	3	6	2	2	21	18	12	76
Cameras Planned	10	5	10	6	2	21	24	16	94

Table 1: Distribution of Digital Cameras at FACET-II

(EVG). Configuring an event buffer on the EVG configures the event buffer on all BSA devices at FACET.

The camera IOCs are not part of the BSA infrastructure because they cannot hold 2800 images in RAM. However, each IOC has an Event Receiver (EVR) which receives timing information from the EVG [6]. The IOC tags the camera image with pulse ID. The timestamp and pulse ID are included with the image when requested over CA and are embedded in the image metadata when written to disk. The pulse ID is used to compare and temporally align images across different cameras and with the BSA data.

DAQ SOFTWARE

The DAQ software is written in MATLAB R2020A and includes a GUI interface created with MATLAB's App Designer tool. The GUI allows users to interact with the FACET DAQ API [7]. The GUI prompts users to select the desired data rate (Event Code) and number of shots. The maximum number of shots is determined by the amount of RAM required store images on the camera servers with a cap set at 2800 (same as the BSA buffer). Users select cameras to include in the DAQ, organized by their region in the accelerator and experimental area. The user can include BSA and non-BSA devices, also organized by region. The BSA and non-BSA device lists are easily edited by users, so new devices can be included in the DAQ as needed. The DAQ has a single-step mode which acquires data for the given number of shots. It also has scan modes in which a parameter is varied and data is acquired for each parameter setting. The GUI interface allows the user to select one or two dimensional scans, but API is written such that n-dimensional scans are possible by flattening the scan region into a 1D array indexed by a single step number.

The DAQ contains various validation and "safe-fail" methods. At the start of a DAQ run, CA is used to verify the PVs in the BSA and non-BSA lists. If a CA call to a PV in the list does not return a value (either because it is mis-specified or the IOC is offline), it is removed from the list. The DAQ checks the connection status of the cameras before proceeding. Temporary camera failures are common due to the high-radiation environment. The DAQ identifies these failures when present and attempts to reboot the affected cameras. An "Abort" method exists so that the user can preemptively end the DAQ run.

The DAQ is run from the control server (facet-srv20). The control server and all camera servers mount the NAS drive. At the start of a DAQ step, the control server creates a folder on the NAS for the new dataset, and subdirectories for each of the cameras. Next, the DAQ configues the NDFileTIFF areaDetector plugin with the desired number of shots and the location to save the data. At this point, the camera triggers are disabled before data taking starts. The DAQ then configures the BSA buffer with the desired EC to match the cameras. The data taking begins when a command is sent via CA to the EVG to open the buffer and camera triggers are re-enabled. The DAQ starts a timer based on the number of images requested and the event rate. The camera IOCs start writing data to disk as soon as they start receiving frames. At the same time, the BSA buffers fill with data. Both processes are local to the IOCs and do not pass data over the network. During this time, the DAQ acquires non-BSA data at 1 Hz using CA. The DAQ also checks for user aborts during this time.

When the timer ends, a command is sent to the EVG to close the BSA buffer. The DAQ waits for all image data to be written disk. Writing data to disk may continue after data taking has ended if the image buffers are backed up. The DAQ also checks for camera failures that may have occurred during the DAQ step. Once image writing is complete, the DAQ retrieves the BSA buffers via CA and stores them in a MATLAB data structure. If the DAQ is running a scan, it sets the next parameter value and the process repeats.

When the scan or single-step is complete, the DAQ performs synchronization and quality control. The DAQ loops through all of the camera images and extracts the pulse IDs which are compared across cameras and to the pulse IDs in the BSA buffers. The DAQ assigns a timestamp and unique ID (the pulse IDs are not unique) to all data, and compiles

ISBN: 978-3-95450-230-1 ISSN: 2673-5350 doi:10.18429/JACoW-IBIC2021-WEPP33

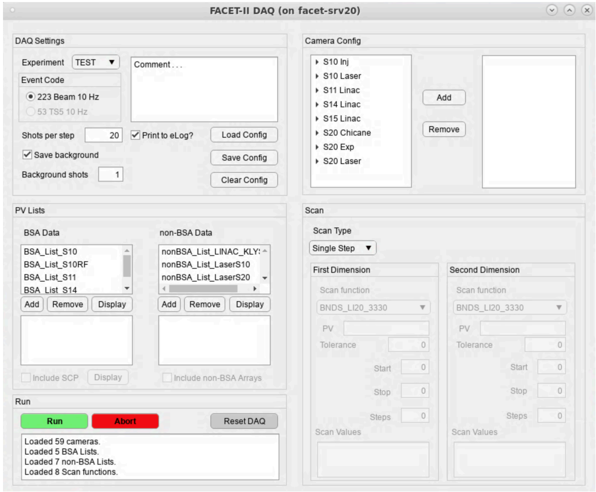
FACET-II DAQ (on facet-srv20)

Experiment: TEST
Event Code: ● 223 Beam 10 Hz ○ 53 TS5 10 Hz
Shots per step: 20
☑ Print to eLog?
☑ Save background
Background shots: 1

BSA_List_S10
BSA_List_S10RF
BSA_List_S11
BSA_List_S14

nonBSA_List_LINAC_KLY
nonBSA_List_LaserS10
nonBSA_List_LaserS20

☐ Include SCP
☐ Include non-BSA Arrays

Loaded 59 cameras.
Loaded 5 BSA Lists.
Loaded 7 non-BSA Lists.
Loaded 8 Scan functions.

S10 Inj
S10 Laser
S11 Linac
S14 Linac
S15 Linac
S20 Chicane
S20 Exp
S20 Laser

Scan Type: Single Step

First Dimension: Scan function: BNDS_LI20_3330; PV: ; Tolerance: 0; Start: 0; Stop: 0; Steps: 0

Second Dimension: Scan function: BNDS_LI20_3330; PV: ; Tolerance: 0; Start: 0; Stop: 0; Steps: 0

Figure 3: The FACET-II DAQ interface.

a list of common shots. In a typical DAQ with no camera failures, 90-100% of shots from all devices will be matched. The list of matched is added to the data structure, along with the paths to the image data on the NAS. The image data itself is not stored in the data structure. The DAQ ends by writing the data structure to the NAS as a MATLAB file and as an HDF5 file. The HDF5 format is convenient for analyzing data in Python, which is a popular language amongst FACET users. Finally, the DAQ writes a message to the FACET eLog which includes the location of the data and the success rate of the matching process.

Users perform online analysis of the data using the Data Analysis Tool (DAN). The DAN is a separate MATLAB GUI and API. The DAN includes image analysis, correlation plots, and a motivation indicator. For offline analysis, the data is transferred from the NAS to SLAC Central Computing by a daily cron job. We expect to collect roughly 25 TB of data per year with the FACET-II DAQ.

IMPROVEMENTS TO THE DAQ

There are several improvements planned for the DAQ, mostly related to the synchronization procedure. At present the DAQ sequentially starts the BSA buffer and then enables the trigger for each of the cameras with CA commands. The time required to send these command to the IOC is a few milliseconds at worst, and usually the cameras all start and stop taking data on the same event. A more efficient process is to create an EC that is used by both the BSA buffers and the cameras. This EC will be identical to the usual ECs that specify data rate, but can be globally enabled or disabled on the EVG. With this approach all devices participating in the DAQ will receive and identical set of triggers and see the same events.

Another improvement to synchronization is the planned switch to the event2 module which will provide more robust timestamping. The event2 module is aware of both trigger delay and camera exposure. This helps eliminate off-by-one errors and flags events when the frame was returned outside of the expected window. In addition, the event2 module returns the camera pulse IDs as an array and eliminates the time-consuming process of extracting pulse IDs one-by-one from image metadata.

Additional improvements to the DAQ include the capability to acquire BSA and non-BSA waveforms, as well as legacy SCP data. A number of devices such as linac BPMs, klystrons, and magnets are controlled by the SCP and are not available through EPICS. We plan to install a dedicated server in S20 for running the DAN.

CONCLUSION

We have developed a data acquisition system capable of recording synchronized from multiple cameras at high data rates. The DAQ enables plasma wakefield accelerator science at FACET, as well as machine learning studies and general accelerator R&D. The FACET-II DAQ will continue to evolve in order to meet the needs of the users.

REFERENCES

[1] V. Yakimenko *et al.*, “FACET-II facility for advanced accelerator experimental tests”, *Phys. Rev. Accel. Beams*, vol. 22, no. 10, p. 101301, 2019.

[2] EPICS, `https://epics-controls.org`

[3] areaDetector, M. Rivers, ANL. `https://areadetector.github.io/master/index.html`

[4] K. H. Kim, S. Allison, T. Straumann, and E. Williams, “Real-Time Performance Improvements and Consideration of Parallel Processing for Beam Synchronous Acquisition (BSA)”, in *Proc. ICALEPCS’15*, Melbourne, Australia, Oct. 2015, pp. 992–994.

[5] N. Phinney, “Report on the SLC Control System”, in *Proc. PAC’85*, Vancouver, Canada, May 1985, pp. 2117–2120.

[6] J. E. Dusatko, S. Allison, J. Browne, and P. Krejcik, “The LCLS Timing Event System”, in *Proc. BIW’10*, Santa Fe, NM, USA, May 2010, paper TUPSM083, pp. 379–383.

[7] FACET DAQ, S. Gessner, SLAC. `https://github.com/slaclab/facet-matlabTNG/tree/master/F2_DAQ`

[8] FACET DAN, H. Ekerfelt, SLAC. `https://github.com/slaclab/facet-matlabTNG/tree/master/F2_DAN`

[9] event2, B. Hill, SLAC. `https://github.com/slac-epics/event2`

ISBN: 978-3-95450-230-1 ISSN: 2673-5350 doi:10.18429/JACoW-IBIC2021-WEPP35

EPICS CONTROL SYSTEM FOR RAON DIAGNOSTICS

Eun Hoon Lim[1], Y. S. Chung, H. J. Woo, G. D. Kim, J. W. Kwon
Institute for Basic Science, Daejeon, Korea
E. S. Kim, Department of Accelerator Science, Korea University, Sejong, Korea
[1]also at Department of Accelerator Science, Korea University, Sejong, Korea

Abstract

RAON has a variety of diagnostic devices for measuring beam characteristics, such as FC, WS, and BV, etc. Each device is driven through a PLC and acquires data with a DAQ. The whole system is controlled through EPICS and is displayed OPI of CSS. PV created in PLC, DAQ are aliased according to the naming convention. EPICS SEQUENCER are written in FSM code to step through the operation of each device sequentially. Below we show the working principle of the device and its algorithm and measurement results.

INTRODUCTION

RAON is a heavy ion accelerator facility to accelerate both stable and rare isotope (RI) beams up to the power of 400 kW with an energy higher than 200 MeV/u [1]. For this purpose, RAON has a variety of diagnostic devices such as Faraday Cup(FC), Wire Scanner(WS), and Beam Viewer(BV). Experimental Physics and Industrial Control System(EPICS) is adopted to efficiently control many devices. Device is managed through EPICS PV and sequential operation is performed through SEQUENCER. microTCA has two Single Board Computer(SBC), Data Acquisition(DAQ) that acquires data, and a Control board that controls DAQ. SBC and Control board are connected to the main system through Ethernet and the EPICS IOC is running. One SBC is used as Programmable Logic Controller(PLC) IOC and PLC is used to controlled Servo Motor of WS and Air Cylinder of FC and BV and E-relay. In DAQ, current of WS and FC is obtained, and it is connected to the main system through Control board. Another SBC IOC has a SEQUENCER module, which is used to operate devices in sequence. CS-Studio(CSS) Operator Interface(OPI) provides a display of control system. A schematic diagram of this is shown in Fig. 1.

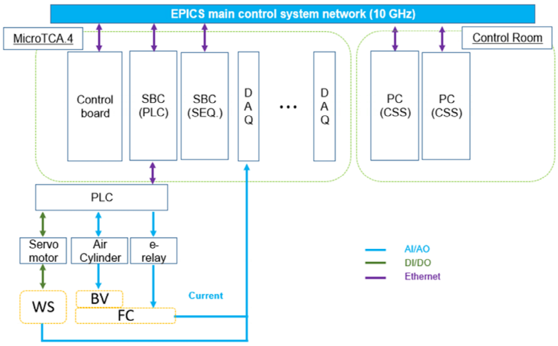

Figure 1: Schematic diagram of diagnostics control system.

EPICS

EPICS is used to implement distributed control systems for large-scale experiments [2]. It uses a server/client based SCADA architecture. EPICS consists of IOC that transmits and receives data of device, OPI to display data and control experiments, Protocol Channel Access (CA) used for data distribution and PV to which data is transferred item. The structure for this is shown in the Fig. 2.

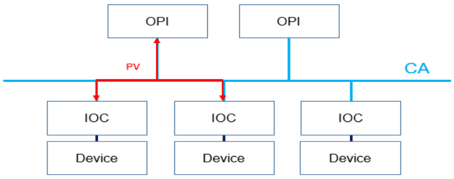

Figure 2: EPICS system.

PV is the name given when creating a record in Database and represents a single value within the EPICS host. PV are shared between IOCs through CA. Therefore, the same PV must not exist. Record can be written directly in the EPICS database or using Visual Database Configuration Tool(VDCT). Record sets types such as analog input(ai) or analog output(ao) and has a PV name. Fields represent the action of the record, and we can set initial values, calculations, scan rates, and so on. It can easily create many records by using the macro function of PV.

Typically, each record value is initialized when the IOC is rebooted. This can be problematic for experiments if all PV values are reset every time a reboot for an IOC change or shuts down due to some issue. To avoid this, we use the autosave module. Autosave module assign the PV and time interval to save, and it's make a saving file during IOC running Then, when the IOC is run, the PV value is loaded from the saved file.

The SEQUENCER module is used for sequential operation of each device. SEQUENCER is a Finite State Machine (FSM) and has a structure and syntax similar to that of C language. FSM have multiple states and drives the program to states based on events. When an event occurs in one state, it performs action and transitions to the next state. PV can be assigned to a variable in a Sequencer. Therefore, it can operate sequentially according to the change of PV.

RAON DIAGNOSIC CONTROL SYSTEM

PV is managed according to the RAON Naming Convention so that it does not overlap with other groups. Figure 3. shows the rules for naming conventions. Naming Convention is largely divided into elements such as system

ISBN: 978-3-95450-230-1 ISSN: 2673-5350 doi:10.18429/JACoW-IBIC2021-WEPP35

elements, device elements and signal element. System elements indicates section such as LEBT/MEBT and SUBSYS such as ECRIS/DIAG. Device elements indicates the devices and number such as FC001, WS001. Signal elements indicates such as current/position.

$$\underbrace{\textbf{SEC/SYS} - \textbf{SUBSYS}}_{\text{a system element}} : \overbrace{\text{DEVXXX}(-\text{SUBDEVXXX})}^{\text{a device element}} : \underbrace{\mathit{SignalName}.\text{Field}}_{\text{a signal element}}$$

Figure 3: Naming convention.

Autosave module was introduced to maintain PV values such as FC calibration values, WS center position. Autosave module saves the value every 5 seconds and the stored value is entered when the IOC is turned on.

Control board has PV for local use. Such PVs are inconvenient to use in the main system. Perform alias according with Naming Convention to merge into main system. Figure 4 shows an example of Alias. It was written in python using a separate diagnostic device management list.

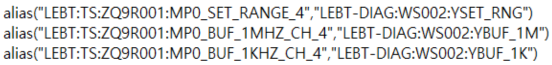

```
alias("LEBT:TS:ZQ9R001:MP0_SET_RANGE_4","LEBT-DIAG:WS002:YSET_RNG")
alias("LEBT:TS:ZQ9R001:MP0_BUF_1MHZ_CH_4","LEBT-DIAG:WS002:YBUF_1M")
alias("LEBT:TS:ZQ9R001:MP0_BUF_1KHZ_CH_4","LEBT-DIAG:WS002:YBUF_1K")
```

Figure 4: PV alias.

Sequential operation and interlock system of devices were configured using SEQUENCER. SEQUENCER is effectively used when performing sequential operations of FC or repetitive operations of WS.

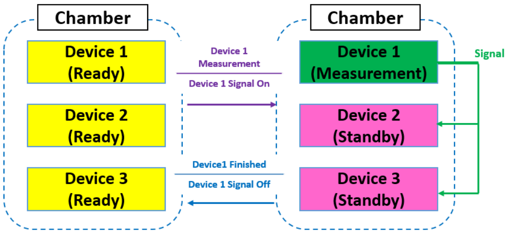

Figure 5: Interlock system for diagnostic chamber.

Several diagnostic devices are installed in single chamber. Interlock system was prepared to prevent a possibility of failure such as broken wire in WS, Conflicts between devices. The procedure of the interlock system is shown in Fig. 5. If there are no problems, all devices are Ready state. When Device 1 starts measuring, it sends a signal and other devices transitions to a Standby state. Measurement cannot be started in the Standby state. When the measurement of Device 1 is completely finished, the status of all devices is transitioned to Ready state.

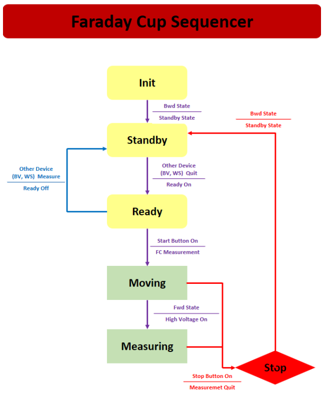

Figure 6: Faraday cup sequence.

Figure 6 shows the action sequence of the Faraday Cup. Initial state is the step to check the device state when IOC operation. When the device is in the backward position, it transitions from the initial state to the standby state. Standby/Ready status is determined by the interlock. In Ready state, pressing the start button on the OPI moves the Faraday Cup to the inside of the chamber. When FC moving inside, it can also exit by pressing the stop button. When the Faraday Cup goes to the measurement position, the high voltage turns on and starts the measurement. The measured value is the value obtained by calibrating the current read from DAQ. Measurements are displayed in the monitoring OPI. when the end button is pressed, the high voltage is turned off, the cylinder is pulled back, and it enters the standby state.

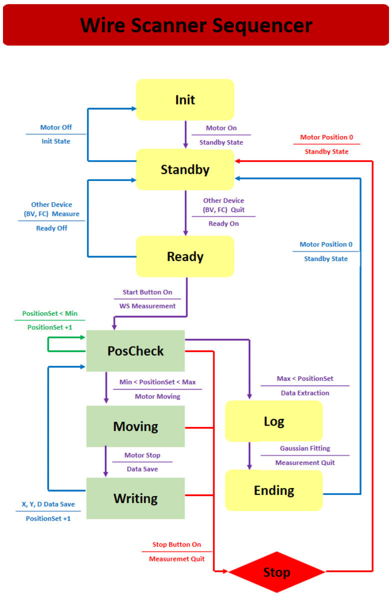

Figure 7: Wire scanner sequence.

Figure 7 shows the action sequence of the Wire Scanner. When the motor is powered on, it transitions from initial state to the standby state. Similar to FC, Standby/Ready status is determined by interlock. We can set the measurement condition such as range, interval of WS in Ready state. When the start button is pressed, the position to be measured is checked first. When the measurement range is confirmed, servo motor moves to that position. Then stops and records current and position. Since the WS is inserted at a 45 degree angle, the X and Y axes have a compensation between the motor position and the recording position. Execute these corrections in the writing state. Diagonal (D) is recorded as the motor position. Measures are displayed in OPI in real time. Repeat positioning and measurement until all set ranges have been measured. After the measurement, the center position and sigma value are calculated through Gaussian fitting in the python EPICS module and the Gaussian graph is displayed in the OPI. After all measurements are completed, it returns to the position and enters the standby state.

INSTALLATION AND REMOTE TESTING

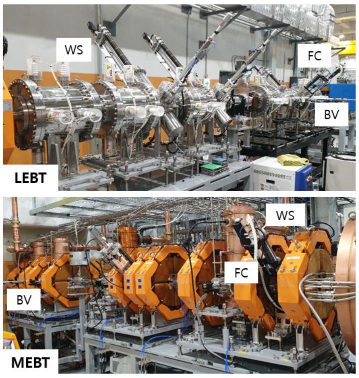

Figure 8: LEBT/MEBT section.

The injector section consists of ECR-IS and LEBT, RFQ, MEBT. The LEBT section has 4 WS, 2 BV and 3 FC. MEBT section has 4 WS, 1 BV and 2 FC. All installed as shown in Fig. 8.

Figure 9: Control room.

Figure 9 shows the RAON Control Room. The operation and measurement of the diagnostic device were performed in the control room.

Control System Studio is a collection of tools and applications to monitor and operate large scale control systems [3].

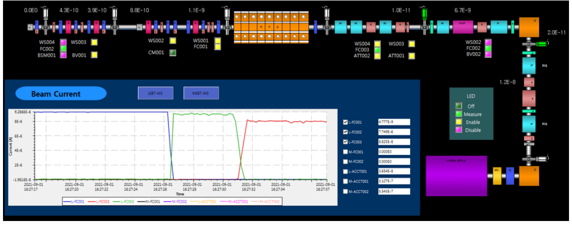

Figure 10: Monitoring OPI.

Figure 10 shows the monitoring OPI of the injector. We can check the vacuum level of the beam line and whether the gate valve is open or closed. Real-time display of current from FC and ACCT so we can see only what we need. In addition, the current status of each diagnostic device can be checked through the LED. The LED state depends on the state of the sequencer. Dark green is OFF, green is measuring, yellow is Ready, and pink is standby.

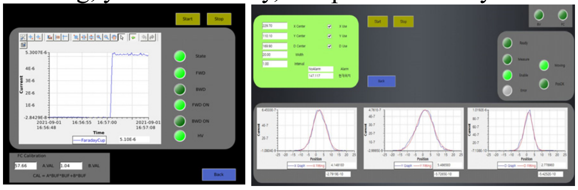

Figure 11: Control OPI, (a)left : Faraday cup OPI, (b)right : Wire scanner OPI.

Figure 11 shows each device Control OPI. The Faraday Cup OPI displays the measured current and the status of the pneumatic cylinder. It can input a calibration value to compensate for the current loss in the cable. Since the operation sequence is written in the SEQUENCER, it can use by pressing just the Start/Stop button. In the Fig. 11(a), FC is in the forward position and the current is measured after HV is turned on.

The Wire scanner OPI displays the measured current and position. And it can set the measurement options for WS. Options include whether the axis is measured or not, the center position, the measurement range and interval. When pressing the start button, it follows the sequencer to measure. It can stop at any time during the measurement. In Fig. 11(b), after the X, Y, D measurements of the WS are completed, Gaussian fitting is performed.

CONCLUSTION

Beam diagnostic device was installed in the injector section, and control and measurement were performed using EPICS/CSS. Sequential operation and interlock system based on SEQUENCER also confirmed no problem. Whenever an error occurs in SEQUENCER, it is being fixed. Research is underway to measure the beam of the injector and make an optimized beam for the acceleration part. The installation and control of diagnostic devices in the SCL3 and P2DT sections are also being prepared.

ACKNOWLEDGMENT

This work was supported by the Rare Isotope Science Project of the Institute for Basic Science, funded by the Ministry of Science, ICT, and NRF of Korea (2013M7A1A1075764).

REFERENCES

[1] D. Jeon *et al.*, “Design of the RAON accelerator systems”, *J. Korean Phys. Soc.*, vol. 65, pp. 1010-1019, 2014.

[2] EPICS, `https://epics.anl.gov/`.

[3] CS-Studio, `https://controlsystemstudio.org/`.

10th Int. Beam Instrum. Conf. IBIC2021, Pohang, Rep. of Korea JACoW Publishing
ISBN: 978-3-95450-230-1 ISSN: 2673-5350 doi:10.18429/JACoW-IBIC2021-WEPP36

STUDY OF SOLUTIONS FOR INTERFACING ILSF BEAM DIAGNOSTICS TOOLS TO CONTROL SYSTEM

P. Navidpour, F. A. Mehrabi, S. Mohammadi Alamouti
Iranian Light Source Facility, Institute for Research in Fundamental Sciences, Tehran, Iran

Abstract

There is an ongoing study at Iranian Light Source Facility (ILSF) aims to determine control solutions for a variety of diagnostics tools that will be placed at various locations around the facility. In this paper, an overview of the possible control solutions with a focus mostly on the low-level part of the control system is reported.

INTRUDUCTION

The ILSF synchrotron light source is under design and construction and now that the basic design phase of the diagnostics subsystems is finished, our job in the control and diagnostics group is to study and document the possible control solutions for each diagnostics tools. However, the study is still in progress and our choices are not finalized yet. The diagnostics tools we will discuss in this paper are Fluorescent Screen (FS) and Optical Transition Radiation (OTR) systems, Beam Loss Monitors (BLM), Fast Current Transformer (FCT), Integrating Current Transformer (ICT), Faraday Cup (FC), and Direct Current Transformer (DCCT). These tools are categorized into three sections and the control solution is discussed for each one.

CAMERA BASED DIAGNOSTICS TOOLS

Camera based diagnostics tools have applications in measuring the size and profile of the beam. There are several FS/OTR and SRM stations at various locations around the facility. Table 1 summarizes the location and controllable components for each of these tools.

Table 1: Camera Based Diagnostics Tools and their Controllable Components

Tool	Location	Qty.	Controllable Component
FS/ OTR	Linac Diagnostics line, LTB, Booster, BTS, Storage ring	20	Stepper Motors, CCD Cameras, Single-Board Computers
SRM	LTB, Booster, BTS, Storage ring, Diagnostics beamline	9	Streak Camera, CCD Cameras

The standard we choose to transfer the image data from the camera to the IOC depends on the required frame rate and the image quality. For a typical 2-4-megapixel camera that we will use in FS/OTR systems, we presume that the required speed demand will not exceed 1000 Mbps. This makes the GigE solution a good choice in terms of much longer cable it supports compared to the Firewire, and also, its simplicity and much lower cost compared to other non-Ethernet based standards.

For the Streak camera, with a high bandwidth demand of about 2 Gbps, we will use CoaXPress (CXP) interface to send data from the camera to a frame grabber that is installed on a PC workstation. In the future, depending on the community support and commercial availability of the required equipment, other network-based solutions like 10 GigE might be used as well. Table 2 gives a summary of camera based diagnostics tools control specification and its IOC platform.

Table 2: Control Requirements and IOC Platform for the Camera Systems

Camera	Interface	Data Rate	Frame Grabber	IOC
CCD Camera	GigE	320 Mbps	No	PC
Streak Camera	CXP	2000 Mbps	Yes	PC

All camera systems have PC-based IOCs. This PC runs the camera EPICS IOC, areaDetector modules [1], and applications such as ImageJ to calculate some parameters and visualize the image data.

A simplified layout of the control interface of the camera based diagnostics tools at ILSF is shown in Fig. 1. There will be one workstation PC in the instrumentation area that is used as the EPICS IOC for FS/OTR and SRM cameras. Another workstation PC that hosts the CXP frame grabber is used as the EPICS IOC of the streak camera and SRMs that are located in the diagnostics beamline. The latest one will be located somewhere near the beamline instrumentation area to ease the access of the engineers to it.

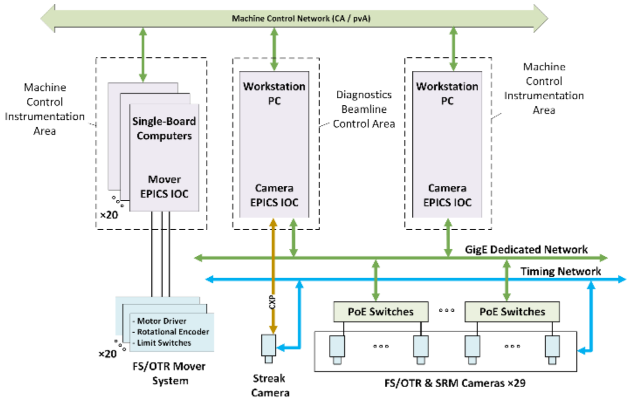

Figure 1: An example of the possible control solution for camera based diagnostics tools.

Each FS/OTR stations has a mover system that is controlled by a single-board computer (e.g. BeagleBone Black). The board runs soft IOCs to interface the mover system with the EPICS channel Access. Similar solution is proposed for the scraper mover system.

BEAM LOSS MONITORS

Bergoz single-ended type BLMs will be installed outside of the BR and SR vacuum chambers, mostly near the possible loss locations (e.g. near dipole magnets, insertion devices, scrapers, collimators, and downstream of RF cavities; see Table 3). The output of each sensor is a 50-ohm positive TTL pulse which can be sent through a coaxial cable to a counter unit.

A complete solution to interface BLM sensors to the control system is presented by Cosylab [2]; in which, a central unit runs the EPICS IOC and the BLM sensors can be connected to the central unit, either directly, or in a daisy chain, through signal conditioner (BSC) units. Another option for us is to use MTCA based solution, in which, the existing MicroTCA crates of the BPM system hosts the scaler AMC boards in order to receive BLM signals. This way, the timing AMC as well as other resources in the MTCA crate can be shared between multiple diagnostics systems and it might bring us better performance.

Table 3: Location of BLM Sensors and Their IOC Platform

Location	Qty.	IOC
Near to the booster dipole magnets	55	MTCA
Near the storage ring dipole magnets	100	MTCA
Downstream of the RF cavities	6	MTCA
Near to the insertion devices	7	MTCA
Next to the collimators and scrapers	4	MTCA

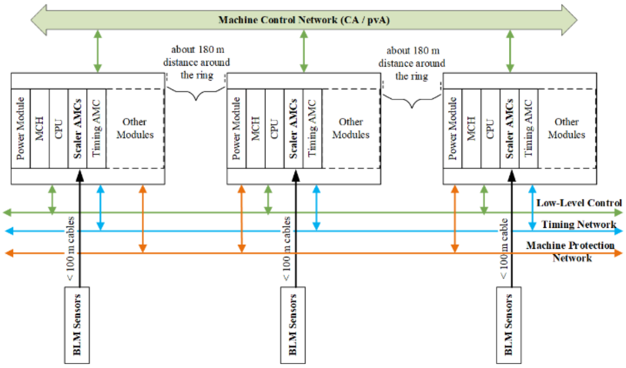

Figure 2: An example of the possible solution for interfacing the BLM system to the control system.

The circumference of the ILSF storage ring is 528 m and the crates will be placed in the control instrumentation areas around the storage ring. As shown in Fig. 2, BLM signals will be distributed between three MTCA crates in a way that the length of the cabling between a particular sensor and its associated AMC does not exceed 100 m. This way we do not have to amplify the sensors signal.

ANALOG DIAGNOSTICS TOOLS

Some diagnostics tools like FCTs, ICTs, and the Faraday Cups have analog output signals. For now, it is not decided to use these signals as input for feedback system. However, we need to visualize the signal, calculate some parameters, and send the data in form of PVs to the EPICS control network. For the sake of simplicity and ease of signal visualization, we employ a couple of oscilloscopes to view and digitize the output signal of these diagnostics tools (see Table 4).

Most modern oscilloscopes have USB or Ethernet port to communicate with a PC. This can PC host a proper EPICS hardware supports for the oscilloscopes and runs the EPICS IOC to interface oscilloscopes to the channel access or pvA network (see Fig. 3). It also runs applications such as Matlab, LabVIEW, etc. to calculate the required parameters and send them over the control network so that other EPICS clients can access or monitor them. Depending on the control demand in the future, we might use PXI or PCI digitizer cards for this purpose as well.

Table 4: Analog Diagnostics Tools and Their Controllable Components and IOC Platform

Tool	Location	Qty.	Controllable Component	IOC
FCT	Linac, LTB, BTS,Storage Ring	9	Oscilloscope 4GSa/s, 1GHz	PC
ICT	LTB	2	Oscilloscope 2GSa/s, 1GHz	PC
FC	Linac Diagnostics line	1	Oscilloscope 2GSa/s, 200MHz	PC
DCCT	Booster, Storage Ring	2	18bit Digital Multimeter	PC

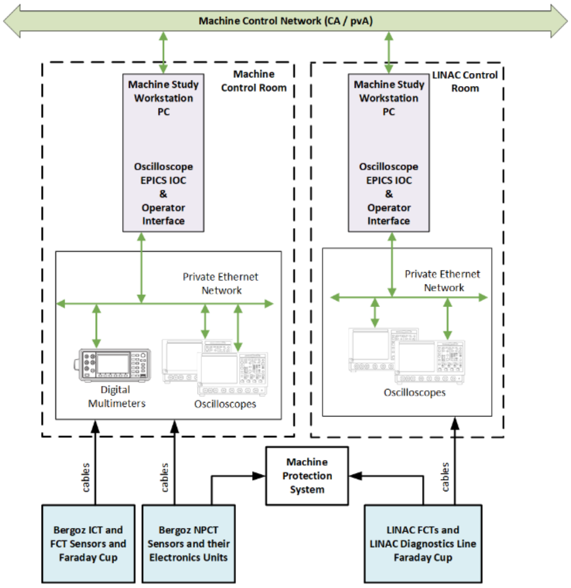

Figure 3: An example of the possible solution for interfacing analog diagnostics tools to the control system.

DCCTs are other diagnostic tools with analog output signal. Both of the storage ring and the booster ring will be equipped with a DCCT (Bergoz NPCT) together with its

ISBN: 978-3-95450-230-1 ISSN: 2673-5350 doi:10.18429/JACoW-IBIC2021-WEPP36

associated electronics that provide the analog output proportional to the average beam current that flow through it. Similarly, the output signals of DCCTs can be connected to digital Multimeters that communicates with the EPICS IOC PC via Ethernet. The digital Multimeters may have at least 18-bit resolution in order to have good accuracy in calculating the beam lifetime. As it is shown in the Fig. 3, the same PC as the one used for FCTs, ICTs, and Faraday Cup will be used for this purpose. This PC is responsible for calculating machine parameters and serving the EPICS clients too. To check the interlock thresholds related to the beam current, the output signals of the Faraday Cup and the DCCTs will be delivered to the machine protection system as well.

SUMMARY

We presented our progress in the ongoing phase of the study of possible control solutions for some of the ILSF diagnostics tools. We presented simplified layouts of control solutions for camera based diagnostics tools, mover systems of FS/OTR and scrapers, BLM system, and analog diagnostics tools. The next step is to choose between the solutions studied, and build prototypes and test benches accordingly.

REFERENCES

[1] `https://epics-controls.org/resources-and-support/modules/soft-support/.`

[2] M. Kobal, J. F. Bergoz, J. Dedic, and R. Stefanic, “A Complete Solution for Beam Loss Monitoring”, in *Proc. 11th European Particle Accelerator Conf. (EPAC'08)*, Genoa, Italy, Jun. 2008, paper TUPC050, pp. 1170-1172.

BUNCH-BY-BUNCH 3D MEASUREMENT SYSTEM IN HLS-II[*]

Ruizhe Wu, Leilei Tang, Bao-gen Sun, Fangfang Wu, Jiang Wang, Zeran Zhou, Ping Lu[†]
National Synchrotron Radiation Laboratory (NSRL),
University of Science and Technology of China (USTC), Hefei, Anhui, China

Abstract

In order to improve the performance of Hefei Light Source (HLS-II) , it is necessary to study various problems of nonlinear beam dynamics in the storage ring, so as to optimize the beam filling mode and injection mode, and then improve the intensity and brightness of HLS-II. In beam dynamics, bunch-by-bunch can provide detailed information of beam bunches and help beam researchers to study the problems of beam bunches deeper. Therefore, HLS-II diagnostics group has developed an on-line bunch-by-bunch three-dimensional measurement system based on high bandwidth and high speed oscilloscope.

SYSTEM STRUCTURE AND FUNCTION OVERVIEW

The measurement system uses SDS6204 H12 Pro oscilloscope of Siglent company [1] as the front end of signal processing to collect bunch-by-bunch signal. The front-end oscilloscope uses the 0.1Hz trigger signal provided by HLS-II timing system. The signal processing back-end of the system is the win10 virtual machine created by Zstack IAAs platform [2]. In the back-end, all signal processing programs are written with LabVIEW. In these programs, calab writes the PV variable of EPICS into the IOC of CentOS system, and then displays the results of back-end signal processing through OPI, as Fig. 1.

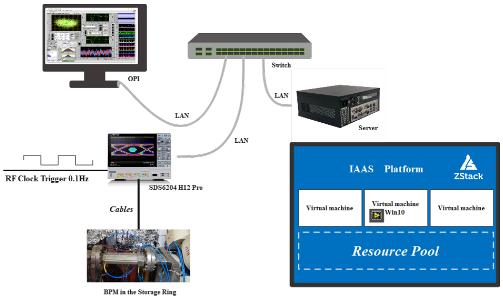

Figure 1: Overall structure of the system in HLS-II.

Driven by the 0.1 Hz trigger signal, the system updates every 10 seconds. Each time it is triggered, the back-end program will collect waveform data from four channels of BPM for 500 µs. The waveform data records 2266 circles of bunch-by-bunch. Through these data, various information of bunch-by-bunch can be calculated, such as time, amplitude, intensity and transverse information. Moreover, the system can obtain turn-by-turn information and the tune of each bunch through the waveform data.

OPI INTERFACE

Templates are provided for recommended software and authors are advised to use them. Please consult the individual conference help pages if questions arise.

After obtaining the three-dimensional information of bunch-by-bunch, the 3D position information of 2266 circles of bunch-by-bunch can be displayed through the three views function of OPI interface to clarify the distribution of the bunch-by-bunch centroid. As shown in Fig. 2, the OPI interface shows the bunch-by-bunch three-dimensional centroid distribution under the normal state, while in Fig. 3 it shows the bunch-by-bunch three-dimensional centroid distribution under the injection state. In the three views on the left are measured by stripline BPM and the three views on the right are measured by button BPM. And different colors in three views represent the average results of different numbers of bunch-by-bunch bunches.

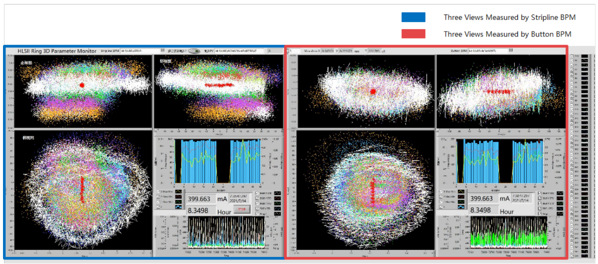

Figure 2: Three views under the normal state.

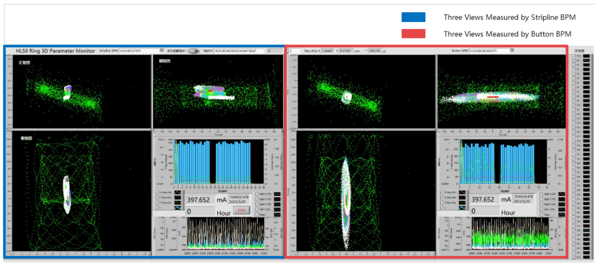

Figure 3: Three views under the injection state.

Moreover, the OPI interface also provides bunch-by-bunch tracking interfaces to track a specific bunch, as shown in Fig. 4. In Fig. 4(a), the upper left part is a two-dimensional diagram of the bunch-by-bunch current intensity. For this part, the abscissa is the number of 45 bunches in one circle, and the ordinate is the number of cycles of bunches running in the storage ring, while its colors indicate different current intensities. The lower left part shows the average current intensity of 2266 cycles for each bunch in

---

[*] National Synchrotron Radiation Laboratory

[†] lup@ustc.edu.cn

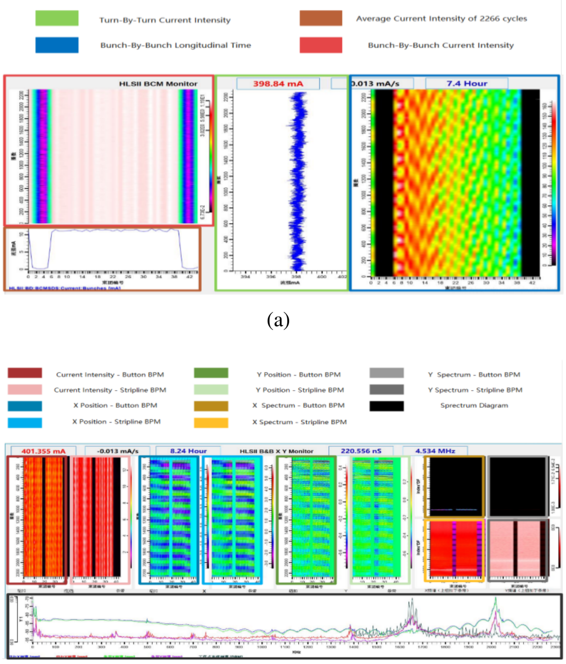

(a)

(b)

Figure 4: Bunch-By-Bunch tracking interface.

the storage ring. The middle part is the turn-by-turn current intensity curve, in which the abscissa is the current intensity and the ordinate is the number of cycles. The right part is a two-dimensional diagram of longitudinal time, its abscissa and ordinate is the same as the upper left part, while its colors represents different longitudinal times. In Fig. 4(b), all the diagrams except the "Spectrum Diagram" below has the same abscissa and ordinate as bunch-by-bunch current intensity diagram in Fig. 4(a). And their colors represent their corresponding bunch-by-bunch information shown in Fig. 4(b) legend. At the end, the spectrum diagram of the interface shows the transverse spectrum information. In this part, the tune can be clearly found.

SYSTEM ERROR ANALYSIS

Due to the couple of longitudinal oscillation to transverse direction, gyration can be observed in bunch-by-bunch three-dimensional centroid distribution OPI interface. After removing the low frequency part "gyration", the measurement error can be analyzed by calculating the standard deviation STD. The following figure Fig. 5 shows the distribution of the measurement of one bunch after excluding its low frequency part, corresponding to x, y and z. The STD of x, y and z are respectively 3.8 µm, 4.2 µm and 0.4 ps, their corresponding round up is 5 µm, 5 µm and 0.5 ps.

In order to further analyze the measurement error, the bunch-by-bunch three-dimensional system needs to be compared with Libera B+ commercial system. For three-dimensional system, the transverse information of each bunch obtained at trigger time can obtain the information of turn-by-turn, fast acquisition (FA) at 44 kHz and medium speed acquisition (MA) at 2kHz. While Libera B + commercial system measures slow acquisition (SA) at 10 Hz only. For comparison between three-dimensional system and Libera B+ commercial system, 200 points extracted from MA in three-dimensional system need to be averaged and then compared to Libera B+ commercial system's SA results. As in Fig. 6, it shows the STD results of one bunch measured by the three-dimensional bunch-by-bunch system. While Fig. 7 shows the measurement results of one bunch in close orbit diagnostics (COD) measured by Libera B+ commercial system.

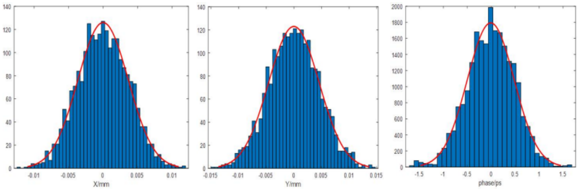

(a) (b) (c)

Figure 5: Three dimensional error analysis diagram.

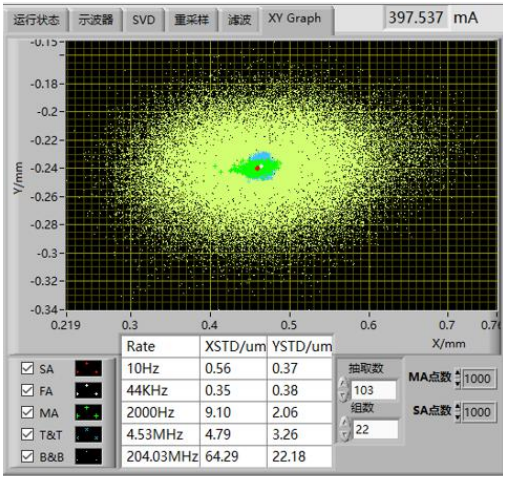

	Rate	XSTD/um	YSTD/um
☑ SA	10Hz	0.56	0.37
☑ FA	44KHz	0.35	0.38
☑ MA	2000Hz	9.10	2.06
☑ T&T	4.53MHz	4.79	3.26
☑ B&B	204.03MHz	64.29	22.18

抽取数 103
组数 22
MA点数 1000
SA点数 1000

Figure 6: STD in three-dimensional system

395.0 mA HLS II Storage Ring BPM Manager 8.37 Hour

	X [mm]	Y [mm]	stdX[um]	stdY[um]	DSC	AGC	Att
SR-BD-BPM01	0.576	−0.609	0.624	0.312	ON	ON	31
SR-BD-BPM02	−1.437	0.801	0.729	0.485	ON	ON	31
SR-BD-BPM03	0.871	−1.687	0.473	0.576	ON	ON	31
SR-BD-BPM04	0.315	−2.018	0.415	0.787	ON	ON	31
SR-BD-BPM05	1.282	0.147	0.643	0.262	ON	ON	31
SR-BD-BPM06	0.530	−0.010	0.479	0.486	ON	ON	31
SR-BD-BPM07	−0.724	−0.229	0.204	0.576	ON	ON	31
SR-BD-BPM08	0.062	0.449	0.348	0.255	ON	ON	31
SR-BD-BPM09	−0.148	0.302	0.593	0.549	ON	ON	31
SR-BD-BPM10	0.316	0.687	0.435	1.687	ON	ON	31
SR-BD-BPM11	0.269	−0.319	0.328	0.213	ON	ON	31
SR-BD-BPM12	0.139	−0.396	0.769	0.278	ON	ON	31
SR-BD-BPM13	−0.627	−0.277	0.556	0.279	ON	ON	31
SR-BD-BPM14	0.573	0.111	0.253	0.194	ON	ON	31
SR-BD-BPM15	0.442	0.419	0.263	0.213	ON	ON	31
SR-BD-BPM16	0.015	−0.299	0.398	0.140	ON	ON	31

	X [mm]	Y [mm]	stdX[um]	stdY[um]	DSC	AGC	Att
SR-BD-BPM17	0.221	0.490	0.408	0.254	ON	ON	31
SR-BD-BPM18	1.242	0.091	0.555	0.380	ON	ON	31
SR-BD-BPM19	0.458	−0.240	0.311	0.611	ON	ON	31
SR-BD-BPM20	−0.071	0.454	0.183	0.410	ON	ON	31
SR-BD-BPM21	0.466	−0.031	0.237	0.206	ON	ON	31
SR-BD-BPM22	1.461	−0.050	0.578	0.202	ON	ON	31
SR-BD-BPM23	1.729	0.182	0.453	0.333	ON	ON	31
SR-BD-BPM24	−0.463	0.458	0.373	0.298	ON	ON	31
SR-BD-BPM25	0.051	0.056	0.184	0.343	ON	ON	31
SR-BD-BPM26	0.477	0.051	0.186	0.236	ON	ON	31
SR-BD-BPM27	0.396	0.121	0.307	0.354	ON	ON	31
SR-BD-BPM28	0.837	0.072	0.816	0.615	ON	ON	31
SR-BD-BPM29	0.301	0.115	0.565	0.199	ON	ON	31
SR-BD-BPM30	1.054	−0.074	0.515	0.276	ON	ON	31
SR-BD-BPM31	0.135	0.581	0.473	0.336	ON	ON	31
SR-BD-BPM32	−0.337	0.458	0.328	0.716	ON	ON	31

SR-BD-DBPM

Figure 7: Measurement results of Libera B+.

For short time measurements in Figs. 6 and 7, the STD of SA transverse data of 32 BPMs in COD system measured by Libera B+ is within 1 µm, while the STD of SA

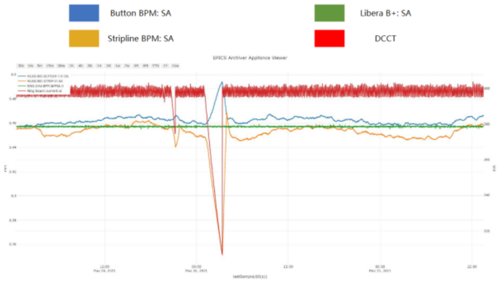

(a) X Direction Measurements with COD

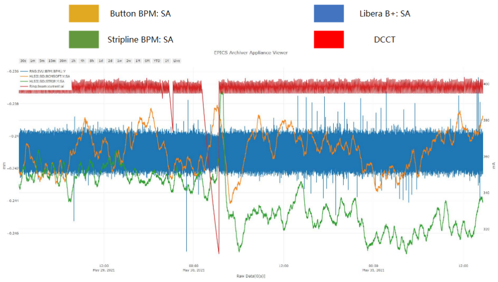

(b) Y Direction Measurements with COD

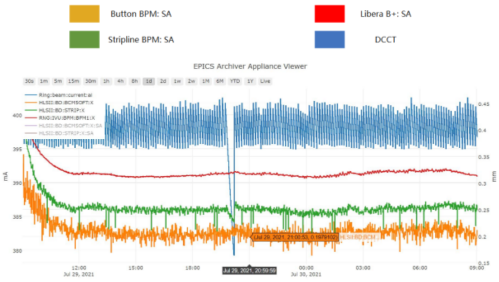

(c) X Direction Measurements without COD

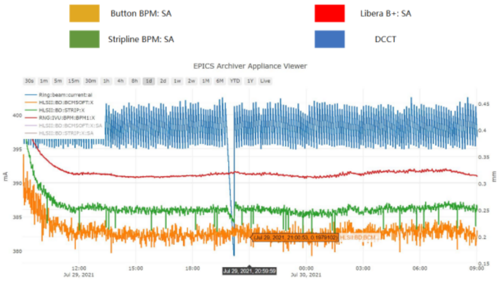

(d) Y Direction Measurements without COD

Figure 8: The measurements for long time.

transverse data averaged by oscilloscope is equivalent to it. Obviously, the performance of the two systems is equivalent in the short time measurements. Therefore, long time measurement comparison is required. The following Fig. 8 shows the measurements of three-dimensional system and Libera B+ commercial system for 2.5 days.

For long time measurements in Fig. 8, the SA STD of Libera B+ is stable within the range from 3 µm to 4 µm. However, for three-dimensional system, the SA STD of X direction fluctuates at 20 µm and the SA STD of Y direction fluctuates at 10 µm. This fluctuation is supposedly related to the temperature control mechanism of front-end oscilloscope and the signal channel inconsistency for long-term operation. At the same time, the measurement results of the three-dimensional system are strongly dependent on the current intensity. Further study is needed for all these phenomenon.

CONCLUSION

The bunch-by-bunch three-dimensional system has been working online in HLS-II. Based on the data generated by this system, a variety of bunch-by-bunch information can be easily obtained. Further, the version 1.0.X of this bunch-by-bunch three-dimensional system, now is open source on gitee [3], can easily set parameters to fit all light sources. And the next version system in plan will focus on the six-dimensional bunch-by-bunch centroid.

REFERENCES

[1] SDS6204 H12 Pro oscilloscope, `https://www.siglent.com/products-model/sds6000-pro/#navs`

[2] Zstack IAAS Platform Website, `https://www.zstack.io`

[3] Gitee Open Source Archives, `https://gitee.com/lup9304/Ring3D`

HIGH-RESOLUTION, LOW-LATENCY, BUNCH-BY-BUNCH FEEDBACK SYSTEMS FOR NANOBEAM PRODUCTION AND STABILISATION

P. N. Burrows, D. R. Bett, N. Blaskovic Kraljevic, T. Bromwich, G. B. Christian, C. Perry, R. Ramjiawan,
John Adams Institute, Oxford, UK

Abstract

High-precision intra-bunch-train beam orbit feedback correction systems have been developed and tested in the ATF2 beamline of the Accelerator Test Facility at the High Energy Accelerator Research Organization in Japan. Two systems are presented: 1) The vertical position of the bunch measured at two stripline beam position monitors (BPMs) is used to calculate a pair of kicks which are applied to the next bunch using two upstream kickers, thereby correcting both the vertical position and trajectory angle. This system was optimised so as to stabilize the beam offset at the feedback BPMs to better than 350 nm, yielding a local trajectory angle correction to within 250 nrad. Measurements with a beam size monitor at the focal point (IP) demonstrate that reducing the trajectory jitter of the beam by a factor of 4 also reduces the observed wakefield-induced increase in the measured beam size as a function of beam charge by a factor of c. 1.6. 2) High-resolution cavity BPMs were used to provide local beam stabilization in the IP region. The BPMs were demonstrated to achieve an operational resolution of ~20 nm. With the application of single-BPM and two-BPM feedback, beam stabilization of below 50 nm and 41 nm respectively has been achieved with a closed-loop latency of 232 ns.

INTRODUCTION

A number of in-construction and proposed future particle accelerator designs feature trains of particle bunches with bunch-separation intervals in the ranges of nanoseconds to tens or hundreds of nanoseconds. For example, the International Linear Collider (ILC) design [1] calls for bunch trains comprising thousands of bunches separated in time by around 500 ns with a train repetition frequency of 5 Hz; the Compact Linear Collider (CLIC) design [2] specifies bunch trains comprising several hundred bunches separated in time by around 0.5 ns, with a train repetition frequency of 50 Hz. Free-electron lasers based on similar accelerating technologies as ILC and CLIC, such as the European XFEL [3], have respectively similar bunch-train time structures. Beam control at such facilities calls for beam position monitors (BPMs) that can resolve bunches on an intra-train (ideally bunch-by-bunch) timescale, with submicron position resolution in single-pass mode. The designs of such BPM and feedback systems are presented here.

STRIPLINE BPM SYSTEM AT ATF2

The system was developed by the Feedback on Nanosecond Timescales (FONT) group [4] and it was deployed, commissioned and tested at the Accelerator Test Facility (ATF) [5] at KEK. The layout of the BPMs is shown in more detail in Fig. 1. The design goal for the FONT5 system is to stabilize the vertical beam position to the 1 μm level at the entrance to the final-focus system. This requires BPMs capable of resolving bunches separated in time by around 100 ns, and with a position resolution at the submicron level. For tests of the FONT system the ATF is operated in a mode whereby a train of two or three bunches is extracted from the damping ring and sent down the ATF2 beam line. The bunch separation is determined by the damping ring fill pattern and typically is chosen to be between 140 ns and either 154 ns (3-bunch mode) or 300 ns (2-bunch mode).

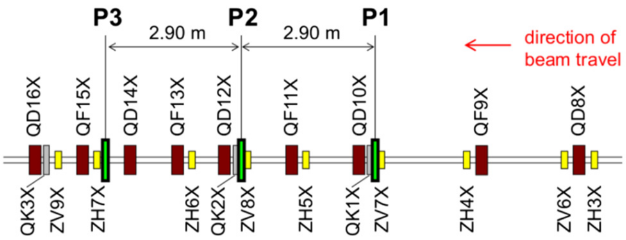

Figure 1: Layout of the FONT BPMs (P1, P2 and P3) in the ATF2 extraction line; quadrupole ("Q") and dipole corrector ('Z') magnets are indicated.

The FONT5 BPM system (Fig. 2) consists of three stripline BPMs (Fig. 3) each of which is instrumented with an analogue processor, and a custom multichannel digitizer. Stripline BPMs were used due to their inherently fast, broadband response and capability to resolve bunches with the required time resolution. In the FONT5 system, only the vertical plane of the BPMs is routinely instrumented.

The FONT5 analogue processors' (Fig. 4) function [6] is to deliver the stripline pickoff-pair difference and sum signals in a form that can be easily recorded by the digitizer for calculation of the position-dependent, beam charge-independent ratio of the two. Ten processors were built and are used in beam operations at ATF2. A single BPM processor can be used to process the beam position data in either the horizontal or vertical plane; from here on only the vertical plane is considered. The BPM processor outputs are digitised by a custom digital feedback processor board (Fig. 5). The board has nine analogue signal input channels digitised using ADCs with a maximum conversion rate of 400 MS/s, and two analogue output channels formed using DACs, which can be clocked at up to 210 MHz. The digital signal processing is based on a Xilinx Virtex5 FPGA. The FPGA is clocked with a 357 MHz source derived from the ATF master oscillator and hence locked to the beam. The ADCs are clocked at 357 MHz.

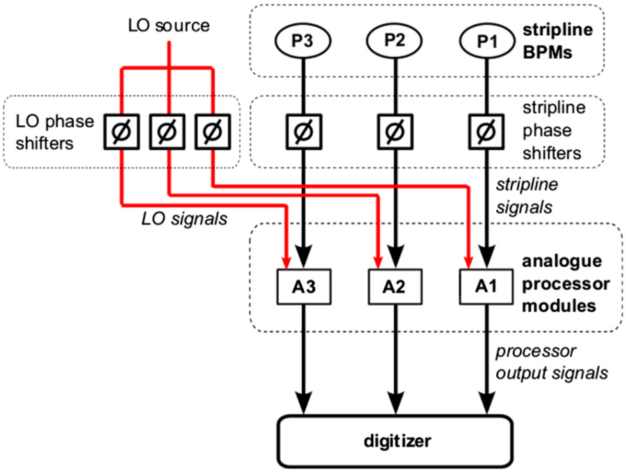

Figure 2: Schematic of the FONT5 BPM system. For each BPM, a phase shifter is used on one of the stripline signals to adjust the relative path lengths of the two input signals at the BPM processor, and another phase shifter is used to adjust the phase of the LO signal at each processor.

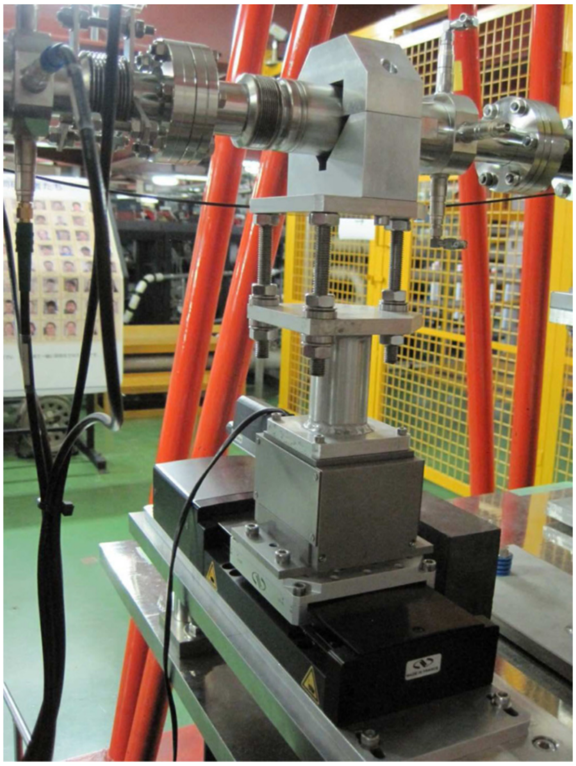

Figure 3: Photograph of FONT5 stripline BPM P3 and its mover in the ATF2 beam line.

The BPM resolution achieved [7, 8] is summarised in Fig. 6. For a bunch charge of 1.3 nC a resolution of c. 157 nm was obtained [8].

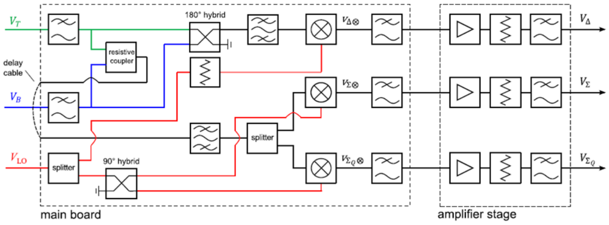

Figure 4: Schematic diagram illustrating the structure of the FONT5 analogue processor.

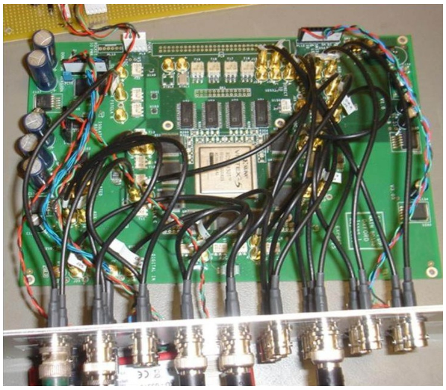

Figure 5: FONT5 digital feedback board.

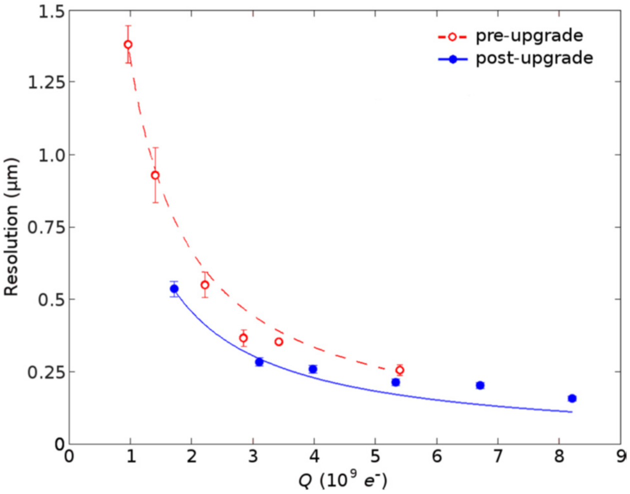

Figure 6: BPM resolution vs. beam bunch charge (Q) [8]. The filled and unfilled data points correspond to measurements with the upgraded and original systems respectively. In each case the line shows the result of extrapolating the lowest-charge data point to higher charges with a $1/Q$ dependence.

ILC IP FEEDBACK SYSTEM

An intra-train position feedback system has been designed to achieve and maintain collisions at the ILC, and a prototype has been developed, commissioned, and tested at the ATF; full details are reported in [9]. The beam position is measured using a stripline BPM with analogue signal-processing electronics as just described. The outputs are processed on the FPGA-based digital

ISBN: 978-3-95450-230-1 ISSN: 2673-5350 doi:10.18429/JACoW-IBIC2021-THOB02

board used to calculate and deliver a correction signal, which is amplified by a high-current drive amplifier and applied to a stripline kicker. All components have been designed for minimum latency, with an overall feedback latency of 148 ns, allowing bunch-to-bunch feedback at the ILC. The stripline BPM has a position resolution of 291 +- 10 nm and a linear range of 500 µm and satisfies the ILC requirements. The kicker response is linear over a correction range of over 60 µm measured at the feedback BPM which satisfies the ILC requirements. The feedback system has been used to successfully stabilize the second and third bunches in a three-bunch train with 154 ns bunch spacing, where the first bunch is used as a pilot bunch. The propagation of the correction has been verified by using an independent stripline BPM located downstream of the feedback system. The system has been demonstrated to meet the BPM resolution, beam kick, and latency requirements for the ILC [9].

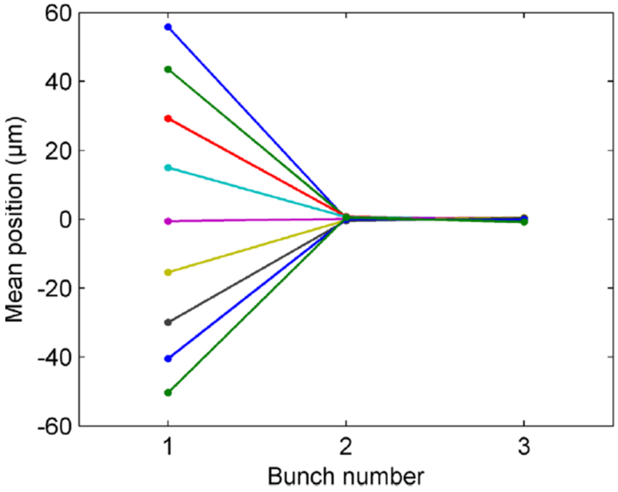

Figure 7: Mean position measured at P3 with feedback on versus the bunch number for nine incoming beam orbit settings (colour coded). Standard errors are given.

The performance is illustrated in Figs. 7-9. In order to assess the feedback operation over a wide correction range, the vertical position of the beam arriving at P3 was swept through a range of approximately 60 µm by varying an upstream corrector magnet. The results show that the mean positions (Fig. 7) of the second and third bunches are zeroed and the spread of positions (Fig. 8) is consistently reduced to around 500 nm, which is limited by the BPM resolution. As an additional test, two vertical steering magnets were used to enhance the incoming beam jitter. The magnets were set up so as to apply a random kick conforming to a predefined distribution with the kick updated successively at the train repetition frequency. The feedback was observed (Fig. 9) to successfully centre and stabilize the beam, even when the full spread of uncorrected positions reaches +-100 µm.

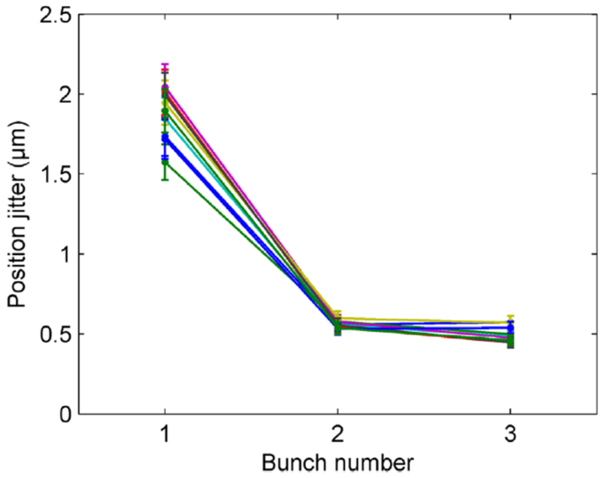

Figure 8: Mean jitter measured at P3 with feedback on versus the bunch number for nine incoming beam orbit settings (colour coded). Standard errors are given.

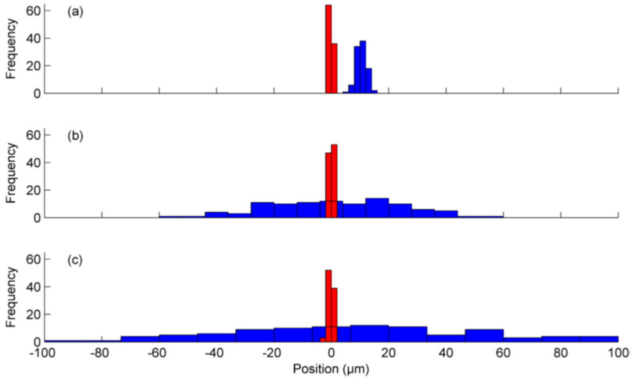

Figure 9: Distributions of positions with feedback off (blue) and feedback on (red) for bunch 2 at P3 with incoming, uncorrected r.m.s position jitters of (a) ~2 µm, (b) ~22 µm, and (c) ~45 µm.

ATF2 Y-Y' FEEDBACK SYSTEM

We report the results of a feedback system based on this technology to stabilize both the beam position and the trajectory angle in the ATF2. The corrections were applied in the vertical plane locally in the early part of the ATF2 beamline so as to deliver a stable beam to the entrance of the final focus system. Figure 10 shows the overall beamline layout of the components used here.

The hardware of the y-y' feedback system is depicted schematically in Fig. 11. P2 and P3 are the stripline BPMs; the upgraded analogue signal processor system (see Fig. 6) was used for the results reported here. For each train of two bunches extracted from the ATF damping ring, the feedback calculation converts the measured position of the first bunch at the feedback BPMs P2 and P3 into a pair of kicker drive signals to be applied to the second bunch at the kickers K1 and K2.

ISBN: 978-3-95450-230-1 ISSN: 2673-5350 doi:10.18429/JACoW-IBIC2021-THOB02

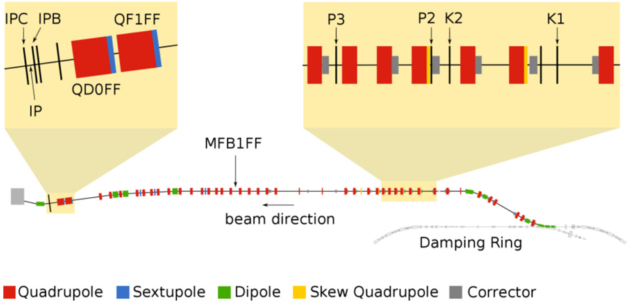

Figure 10: Schematic of the ATF2 beamline showing the layout of components (used here) in the upstream region and at the IP.

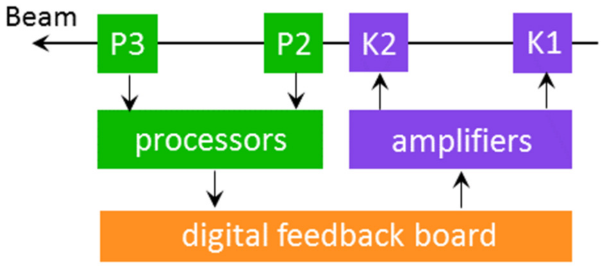

Figure 11: Schematic of the y-y' feedback system using BPMs P2 and P3 and kickers K1 and K2.

The beam stability study was performed using trains of two bunches extracted from the Damping Ring with a bunch spacing of 187.6 ns, a train repetition rate of 1.56 Hz and a bunch population of $0.45\mathrm{x}10^{10}$ electrons. The stripline BPM MFB1FF (Fig. 10) is located about 25m downstream of the feedback system and was instrumented with an analogue processor of the same type as used for P2 and P3. The outputs of this processor were monitored using a second FONT5 board operating purely as a digitizer. The cavity BPMs IPB and IPC (see later) are located either side of the focal point. These BPMs were instrumented with a completely distinct set of processing electronics, the outputs of which were monitored by a third FONT5 board.

Distributions of the vertical beam position recorded at each BPM are shown in Fig. 12 [8] for a typical run comprising 200 beam pulses. The feedback was toggled on and off for alternate beam pulses and the distributions are shown separately for the feedback-off and feedback-on sets of pulses. The feedback BPMs themselves are mounted on translatable mover stages and, at the start of a period of data taking, are normally aligned so as to approximately zero the mean of the readout position of bunch 1. It is clear from the feedback-off data that there is a difference of c. 35 µm in the orbits of the two bunches, suggesting a non-uniformity of the extraction kicker pulse that removed the bunch train from the damping ring. The relative timing of the extraction kicker pulse can be adjusted to ensure that neither bunch is close to the pulse edges, but the goal of this scan is to maximize the bunch-to-bunch correlation rather than match the mean orbits. The higher the correlation between the pulse-by-pulse positions of the two bunches, the more stable the position of the corrected bunch is. Kick offset parameters are available to eliminate the residual offset of the mean position at each BPM.

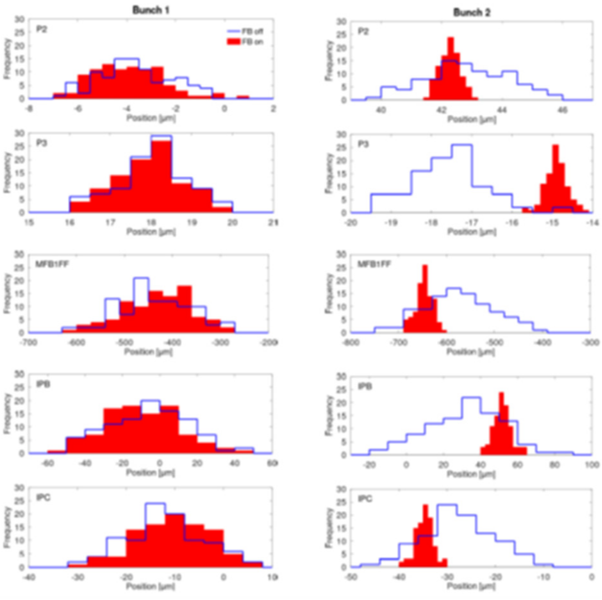

Figure 12: Distribution of position measured at each BPM (rows) for bunch 1 (left column) and bunch 2 (right column) with feedback off (outline) and on (filled). Where necessary a reduced bin width is used to display the feedback-on data so as to limit the maximum frequency of a single bin for display purposes.

The performance of the feedback system in terms of the beam stability is shown in Fig. 12. Bunch 1 provides the feedback input and its position is not corrected. Bunch 2 is well corrected by the feedback as shown by the substantial reduction in the position jitter seen at the two feedback BPMs. The correction is limited by the resolution of BPMs P2 and P3, which was approximately 200 nm for the bunch charge used. The correction factor at all three witness BPMs is consistent with the in-loop correction of roughly a factor of 4. The predictions of a linear beam transport model of theATF2 beamline based on MAD are in good agreement with the direct measurements [8], implying that there are no major sources of additional beam jitter between the feedback kickers and the ATF2 final focus.

As the system is dual-phase, the effect of the feedback on the angular jitter of the beam is also of interest. The angular jitter of the bunch is calculated using the position measured at two BPMs and knowledge of how the beam propagates from one BPM to the other; the MAD model is used for the transfer matrix from P2 to P3. The measured position and angle can then be propagated downstream using additional transfer matrices from the model in order to give the predicted distributions of the beam angle at each witness BPM. In the IP region the transfer matrix is trivially obtained as the beam propagates in a ballistic fashion from IPA to IPB to IPC. The angles at P3 and in the IP region are shown in Fig. 13. The results show that the angular jitter of bunch 2 is also corrected by the feedback by about a factor of 4, consistent with the position correction

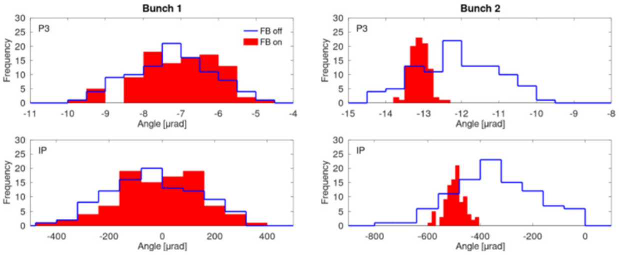

Figure 13: Distribution of angle at P3 (calculated from the position at P2 and P3) and in the IP region (calculated from the position at IPB and IPC) with feedback off (outline) and feedback on (filled). A reduced bin width is used for the feedback on data where necessary to limit the maximum frequency of a single bin for display purposes.

ATF2 is known to be particularly sensitive to wakefields due to the long bunch length and the relatively low beam energy. The primary sources of wakefields in the ATF2 beamline are C-band cavity BPMs, bellows and vacuum flanges. The orbit change caused by wakefields at ATF2 has been reported and several of the cavity BPMs were removed in order to reduce it. As the magnitude of the wakefield kick is proportional to the position offset between bunch and wakefield source (for small offsets), a position feedback that reduces the offset between bunch and wakefield source would be expected to mitigate the increase in beam size due to wakefields.

The ATF was set up to provide trains consisting of two bunches separated by 302.4 ns. Figure 14 shows the measured size of the second bunch as a function of beam charge, both with and without operation of the y-y' feedback. It can be seen that stabilizing the position and angle of the second bunch with the FONT feedback system also reduced the charge dependence of the beam size measured at the IP by a factor of 1.6 +- 0.2, from 27.4 +-1.9 nm/$10^9 e$ to 16.9 +- 1.6 nm/$10^9 e$. The magnitude of this reduction is in line with what would be expected from a detailed model of beam transport in the ATF2 beamline including explicitly the known wakefield sources [8]; full details are reported in [10].

ATF2 'IP' FEEDBACK SYSTEM

We report the design and performance of a high-resolution, high-precision, low-latency, beam position feedback system located around the ATF2 IP (Fig. 10), which is aimed at stabilizing directly the IP vertical beam position to the nanometer level. This system incorporates (Fig. 15) five cavity BPMs similar to those reported in [11], but with a much lower `quality factor'. The cavities are fabricated from aluminium and were designed [12] to have ultra-low quality-factor values so as to be suitable for resolving in time individual particle bunches in multi-bunch trains with bunch separation of order 100 ns. The signals from the BPMs are digitised on a `FONT5A' board [9] and the feedback calculation is performed on the FPGA mounted on the board. An analogue correction signal is output from the board, amplified using a custom power amplifier, and used to drive a dedicated stripline kicker, IPK.

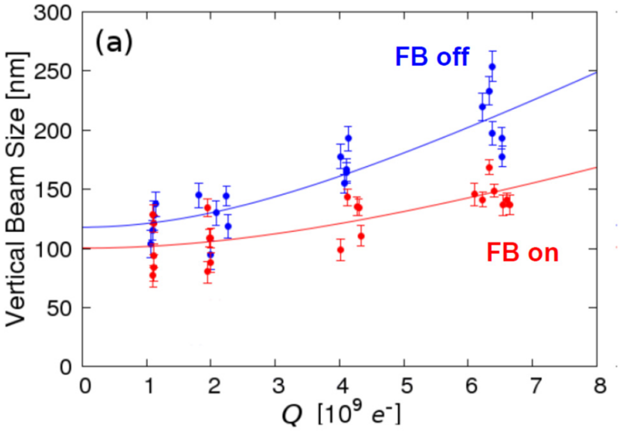

Figure 14: Beam size as a function of beam charge for two-bunch operation with feedback on (unfilled points) and feedback off (filled points). Each point represents a single beam size measurement.

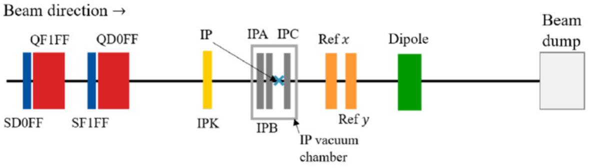

Figure 15: Schematic of the ATF2 IP region, showing the final-focus magnets and the elements of the FONT IP feedback system including dipole cavity BPMs IPA, IPB and IPC, reference cavity BPMs Ref x and Ref y, and the stripline kicker IPK.

The cavity BPM signals undergo two stages of frequency down-mixing (see Fig. 16) so as to produce baseband signals that can be digitized with the FONT5A board. In the first stage, both the reference and dipole cavity signals are down-mixed to an intermediate frequency (IF) centred at 714 MHz using a common Local Oscillator (LO) signal so as to retain the phase relation between the signals. The 5.712 GHz LO signal is derived by frequency up-mixing the DR master oscillator signal and hence is phase-locked to the beam. In the second stage, the reference and dipole signals are mixed in-phase and in-quadrature to produce I and Q signals, respectively. These signals are orthogonal components that together include the full amplitude and phase information of the BPM waveform. Before digitization these signals are amplified so as to reduce the effect of quantization noise.

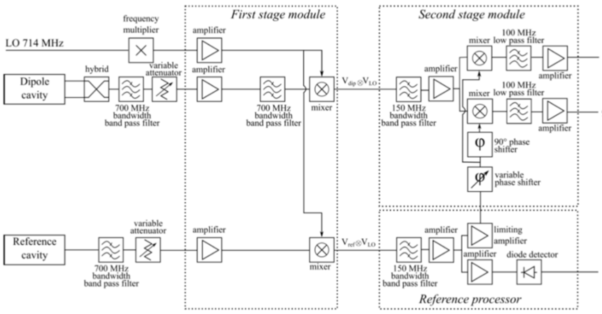

Figure 16: Simplified block diagram of the two-stage down-mixing process of the dipole and reference cavity signals from GHz-level to baseband.

The FONT5A board contains nine 14-bit analogue-to-digital converters (ADCs) grouped into separately-clocked banks of three. Seven ADCs are used to digitize the I and Q waveforms from IPA, IPB and IPC, and the q waveform from the Ref y cavity, at 357 MHz. Representative digitized waveforms for 2-bunch-train operation are shown in Fig. 17. A linear combination of I and Q can be chosen to produce a signal, I', with an amplitude proportional to the bunch position [11]. A signal orthogonal to I' can also be generated, Q', that is proportional to the beam pitch.

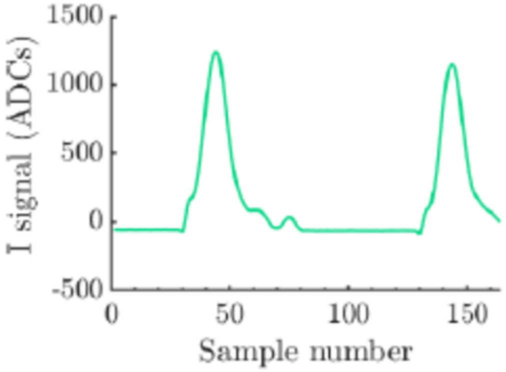

Figure 17: Representative digitized I waveform from IPC, for two-bunch-train operation with a bunch spacing of 280 ns. The waveform was sampled at intervals of 2.8 ns.

Each dipole BPM is calibrated w.r.t. position by vertically scanning the beam across a known range and measuring the corresponding BPM response. For each measured bunch in the beam, the calibration calculation can be performed using either single or multiple samples of the I and Q waveforms. The position resolution can be significantly improved by integrating over multiple samples of the I and Q signals as this both increases the signal level and averages over thermal and electronic noise. The integration range is chosen around the peak of the I and Q signals, as samples significantly in advance of the peak may contain transient effects from unwanted modes and samples late in the waveform have a poorer signal-to-noise ratio. This integration is performed in real time on the FONT5A board.

The resolution of the BPM system was evaluated using measurements of the bunch trajectory at all three dipole BPMs. Since the bunch follows a straight-line trajectory which can be characterized with measurements from only two BPMs, measurements from the third BPM can be used to estimate the resolution of the system. For a representative data set with bunch charge $0.5\text{x}10^{10}$ e, Fig. 18 shows the resolution as a function of the number of I and Q samples integrated in real time for the position calculation. It can be seen that the resolution improves from 41 nm (single sample) to an optimal value of 19 nm with 11 samples. No improvement is seen by integrating additional later samples as the BPM waveforms have decayed and the signal levels are low (see Fig. 17).

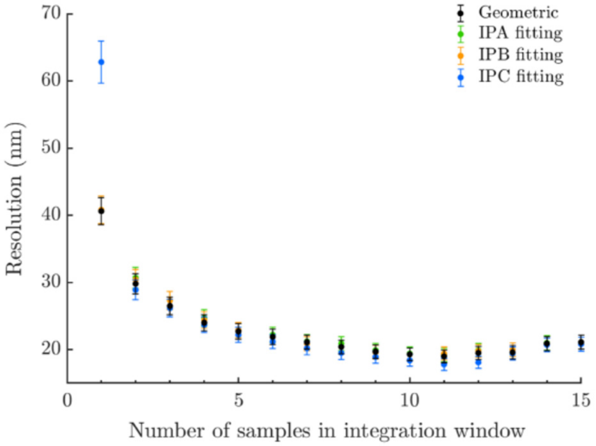

Figure 18: Resolution vs. number of samples integrated. The error bars show the statistical uncertainty.

The high-resolution real-time vertical beam position information from the cavity BPM system was used as input to a closed-loop feedback. In extracted two-bunch trains the position of the first bunch was measured and used to correct the position of the second bunch. Two feedback operating modes were used, represented functionally in Fig. 19. In single-BPM mode the position signal from one BPM was input to the FONT5A board and the derived correction signal was supplied to the kicker IPK such that the vertical beam position was stabilised at the chosen BPM. For this mode the IP was moved longitudinally from the nominal IP to the centre of the chosen BPM so as to stabilise directly the nanobeam vertical position there. In two-BPM mode the IP was placed longitudinally at one BPM; the position signals from the other two BPMs were used to derive a correction signal such that the nanobeam was stabilised vertically at the chosen BPM, which hence served as an independent witness of both the corrected and uncorrected beam positions. For both modes the correction signal to the kicker is output from the FONT5A board via a 14-bit digital-to analogue converter (DAC).

The correction signal from the FONT5A board requires amplifying before it can be used to drive the kicker. The amplifiers are capable of a drive current of +-30 A. The stripline kicker consists of two conducting strips, 12.5 cm in length and separated by 24 mm. The closed-loop feedback latency is defined as the time interval between bunch 1 passing through the longitudinal centre of IPK and the derived kicker correction pulse (for bunch 2) reaching 90% of its final output value. The latency was measured directly with the beam to be 83 samples, i.e. 232 ns.

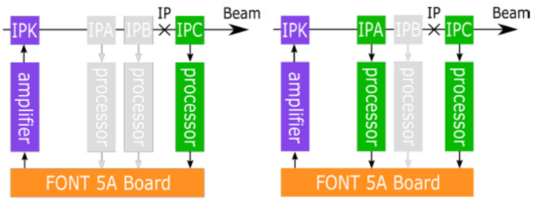

Figure 19: Diagrams of feedback loops showing dipole cavity BPMs (IPA, IPB and IPC) and stripline kicker (IPK). (a) Single-BPM feedback with beam measurement and stabilization illustrated at IPC. (b) Two-BPM feedback, illustrated for position measurements at IPA and IPC with beam stabilization at IPB.

For the operation of the IP bunch-by-bunch feedback system the ATF DR was configured to deliver two-bunch trains to ATF2 with a bunch separation of 280 ns. The train repetition rate was 1.56 Hz. The feedback was operated in the two complementary modes to stabilise the vertical position of the ultra-small beam produced at the focal point of the ATF2. In single-BPM feedback mode, beam stabilization to 50 +- 5 nm was demonstrated. Two-BPM feedback was operated with the IP set at IPB and with IPA and IPC used as inputs to the feedback; hence IPB was used as an independent witness of the feedback performance. The feedback performance is illustrated in Fig. 20. Since bunch-1 provides the input to the feedback its position is unaffected by the correction. By contrast the bunch-2 jitter is substantially reduced, from 96 nm to 41 nm, in good agreement with the predicted value, given the incoming beam conditions, of 40 nm.

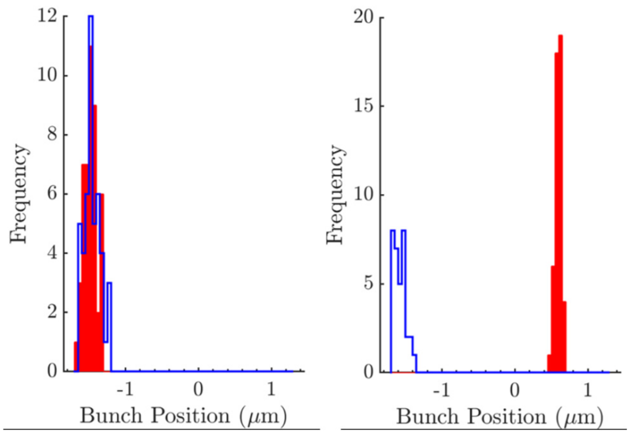

Figure 20: Distributions of bunch-1 (left) and bunch-2 (right) positions measured at IPB, with feedback off (blue) and feedback on (red).

Some margin remains to improve the feedback performance by optimising the gain, as well as by increasing the degree of bunch-to-bunch position correlation in the incoming beam. For the best achieved position resolution to date, and for 100% bunch-to-bunch correlation, an ultimate beam stabilisation to about 24 nm is in principle achievable with the current hardware. Should ATF/ATF2 beam operations resume, this will be the subject of future feedback studies.

ACKNOWLEDGMENTS

We thank the KEK ATF staff for their outstanding logistical support and for providing the beam time and the necessary stable operating conditions for this research. In addition, we thank our colleagues from the ATF2 collaboration for their help and support. In particular, we thank the KNU group for fabricating the low-quality-factor BPMs, the LAL group from the Paris-Saclay University for providing the BPM mover system, and the KEK group for making available the analogue signal-processing down-mixing electronics. We acknowledge financial support for this research from the United Kingdom Science and Technology Facilities Council via the John Adams Institute, University of Oxford, and CERN, CLIC-UK Collaboration, Contract No. KE1869/DG/CLIC. The research leading to these results has received funding from the European Commission under the Horizon 2020/Marie Sklodowska-Curie Research and Innovation Staff Exchange (RISE) project E-JADE, Grant Agreement No. 645479.

REFERENCES

[1] C. Adolphsen *et al.*, The ILC technical design report, volume 3: Accelerator, JAI-2013-001, 2013.

[2] M. Aicheler *et al*, CLIC conceptual design report, CERN-2012-007, 2012.

[3] M. Altarelli *et al.*, The European X-Ray Free-Electron Laser: Technical Design Report, DESY 2006-097, 2006.

[4] `http://groups.physics.ox.ac.uk/font/`.

[5] G. R. White *et al.*, "Experimental Validation of a Novel Compact Focusing Scheme for Future Energy-Frontier Linear Lepton Colliders", *Phys. Rev. Lett.*, vol. 112, p. 034802, 2014.

[6] R. J. Apsimon, D. Phil. thesis, University of Oxford, 2011.

[7] R. J. Apsimon *et al.*, "Design and performance of a high resolution, low latency stripline beam position monitor system", *Phys. Rev. ST Accel. Beams*, vol. 18, p. 032803, 2015.

[8] D. R. Bett *et al.*, "A sub-micron resolution, bunch-by-bunch beam trajectory feedback system and its application to reducing wakefield effects in single-pass beamlines", *JINST*, vol. 16, P01005, 2021.

[9] R. J. Apsimon *et al.*, "Design and operation of a prototype interaction point beam collision feedback system for the International Linear Collider", *Phys. Rev. Accel. Beams*, vol. 21, p. 122802, 2018.

[10] P. Korysko *et al.*, "Wakefield effects and mitigation techniques for nanobeam production at the KEK

Accelerator Test Facility 2”, *Phys. Rev. Accel. Beams*, vol. 23, p. 121004, 2020.

[11] Y. Inoue *et al.*, “Development of a high-resolution cavity-beam position monitor”, *Phys. Rev. ST Accel. Beams*, vol. 11, p. 062801, 2008.

[12] S. W. Jang, E.-S. Kim, Y. Honda, T. Tauchi, and N. Terunuma, “Development of a cavity-type beam position monitors with high resolution for ATF2”, in *Proc. 4th Int. Particle Accelerator Conf. (IPAC'13)*, Shanghai, China, May 2013, paper MOPME058, pp. 604-606.

ADAPTIVE CONTROL AND MACHINE LEARNING FOR PARTICLE ACCELERATOR BEAM CONTROL AND DIAGNOSTICS*

A. Scheinker†, Los Alamos National Laboratory, Los Alamos, USA

Abstract

In this tutorial, we start by reviewing some topics in control theory, including adaptive and model-independent feedback control algorithms that are robust to uncertain and time-varying systems, and provide some examples of their application for particle accelerator beams at both hadron and electron machines. We then discuss recent developments in machine learning (ML) and show some examples of how ML methods are being developed for accelerator controls and diagnostics, such as online surrogate models that act as virtual observers of beam properties. Then we give an overview of adaptive machine learning (AML) in which adaptive model-independent methods are combined with ML-based methods so that they are robust for and applicable to time-varying systems. Finally, we present some recent applications of AML for accelerator controls and diagnostics. In particular we present recently developed adaptive latent space tuning methods and show how they can be used as virtual adaptive predictors of an accelerator beam's longitudinal phase space as well as all of the other 2D projections of a beam's 6D phase space. Throughout the tutorial we will present recent results of various algorithms which have been applied at the LANSCE ion accelerator, the EuXFEL and LCLS FELs, the FACET plasma wakefield accelerator facility, the NDCXII ion accelerator, and the HiRES compact UED.

INTRODUCTION

The control of charged particle beams in particle accelerator facilities is a very challenging task due to the time variation and complexity of the beams and of the machines. Accelerators are typically composed of hundreds-thousands of coupled components which include radio frequency (RF) resonant cavities used for acceleration as well as magnets for focusing of the beams. The performance of large RF systems is known to drift with time due to external disturbances such as vibrations in the case of superconducting cavities and temperature fluctuations for normal conducting cavities which perturb their resonant frequencies. On slower time scales environmental temperature changes result in slight variation of RF cables or analog RF components such as mixers or local oscillators which also introduces phase and amplitude shifts in the highly sensitive high frequency RF systems. The performance of magnets is also perturbed and uncertain due to issues such as power source ripple, hysteresis, and misalignments.

Charged particle beams themselves are also highly complex and time-varying objects which live in a 6 dimensional phase space (x, y, z, p_x, p_y, p_z) which is impossible to measure directly or quickly. While newer electron machines are able to measure 2D longitudinal phase space projections (z, E) hadron machines are many times limited to scalar beam position or current monitor-based measurements online. More detailed measurements are possible but typically rely on slow emittance scans or wire scanners, which cannot be performed online in real-time without disrupting operations. Furthermore, both hadron and electron machines suffer from time-varying initial phase space distributions at their sources and undergo complex collective effects such as space charge forces. In the case of highly relativistic intense electron beams collective effects such as coherent synchrotron radiation are also an issue.

Because of all of the complexities and uncertainties described above, advanced controls and diagnostics are of great importance in the accelerator community. Control theory methods, including adaptive and model-independent feedback control algorithms exist which are robust to uncertain and time-varying systems and we provide some examples of their application for particle accelerator beams at both hadron and electron machines. We also discuss recent developments in machine learning (ML) and show some examples of how ML methods are being developed for accelerator controls and diagnostics, such as online surrogate models that act as virtual observers of beam properties. Then we give an overview of adaptive machine learning (AML) in which adaptive model-independent methods are combined with ML-based methods which are used to train surrogate models directly from raw data.

ADAPTIVE CONTROL

Model-independent feedback methods have been developed by the control theory community with an emphasis of robustness to un-modeled disturbances and changes to system dynamics. One classic adaptive control result is given for a scalar linear system of the form

$$\dot{x}(t) = ax(t) + bu(t), \tag{1}$$

where the values of a and b are unknown. Such a system cannot be stabilized with simple proportional integral derivative (PID)-type feedback, but if the sign of b is known, for example if $b > 0$, a stable equilibrium of (1) can be established at $x = 0$ by the following nonlinear controller

$$u(t) = \theta(t)x(t), \quad \dot{\theta}(t) = -kx^2(t), \quad k > 0. \tag{2}$$

This approach does not depend on a detailed knowledge of system dynamics, but has major limitations which are: 1). The sign of the unknown term b must be known and cannot be time-varying. 2). The presence of an arbitrarily small

---

[*] Work supported by Los Alamos National Laboratory

[†] ascheink@lanl.gov

un-modeled disturbance in the dynamics (1) can destabilize the closed loop nonlinear system [1–3].

For a long time, the main limitation of nonlinear and adaptive control approaches was an inability to handle a sign-changing time varying coefficient $b(t)$ in system (1) which multiplies the control input $u(t)$, such as $b(t) = \cos(2\pi f t)$ which changes sign repeatedly thereby changing the effect of control input $u(t)$. For particle accelerators such variation comes from the fact that the beam at a certain location is influenced by many upstream components, such as magnet settings as well as the initial phase space distribution of the beam entering into the particle accelerator. Changes in input beams and accelerator components upstream have an influence on the response of quantities such as beam loss relative to downstream components. For example, consider a state $x(t)$ which describes beam loss in a particle accelerator, whose minimization is desired, which is influenced by a large collection of quadrupole magnets $\mathbf{u} = (u_1, \dots, u_m)$. The effect of a single magnet, u_m, depends on the initial beam's phase space as it enters the accelerator from the source and also on the settings of all of the other quadrupole magnets that are upstream, $u_{i<m}$ and changes with time as the upstream magnets are adjusted and as the initial beam conditions change. One day decreasing x may require decreasing the current of magnet u_m and another day it might have to be increased.

The control and stabilization of time-varying systems is notoriously difficult, even simple linear time-varying systems are difficult to analyze in general because standard eigenvalue techniques break down and stability can only be proven by using Lyapunov theory [1]. Recently, a nonlinear extremum seeking (ES) feedback control method was developed which could stabilize and minimize the analytically unknown outputs of a wide range of dynamics systems, scalar and vector-valued which can be time-varying, nonlinear and open loop unstable with unknown control directions [4–6]. The ES method is applicable to a wide range of nonlinear and time-varying systems of the form

$$\begin{aligned} \dot{x} &= a(t)x(t) + b(t)u(\hat{y}(t)), \\ \dot{\mathbf{x}} &= A(t)\mathbf{x}(t) + B(t)\mathbf{u}(\hat{y}(t)), \\ \dot{\mathbf{x}} &= \mathbf{f}(\mathbf{x}(t), \mathbf{u}(\hat{y}(t)), t), \\ \hat{y}(\mathbf{x}, t) &= y(\mathbf{x}, t) + n(t), \end{aligned} \tag{3}$$

which include scalar time-varying linear systems, vector-valued time-varying linear systems, and vector-valued nonlinear time-varying systems, where in each case the feedback control u is based only on a noise-corrupted measurement $\hat{y}(t)$ of an analytically unknown cost function $y(\mathbf{x}, t)$. For example, a measurable but analytically unknown cost function an be the sum of beam loss along a many kilometer long particle accelerator, which depends on all accelerator parameters and on the initial 6D phase space of the beam being accelerated.

For accelerator applications, the ES method can tune groups of parameters, $\mathbf{p} = (p_1, \dots, p_m)$. For example, tuned parameters might include RF cavity amplitude and phase set points as well as magnet power supply voltages or currents. The adaptive ES algorithm dynamically tunes parameters according to

$$\dot{p}_j = \psi_j \left(\omega_j t + k\hat{y}(\mathbf{x}, t) \right), \tag{4}$$

where ω_i are distinct dithering frequencies defined as $\omega_i = \omega r_i$ with $r_i \neq r_j$ for $i \neq j$, k is a feedback gain. The ψ_j may be chosen from a large class of functions which may be non-differentiable and not even continuous, such as square waves which are easily implemented in digital systems [6]. The only requirements on the ψ_j are that for a given time interval $[0, t]$ they are measurable with respect to the L^2 norm and that they are mutually orthogonal in Hilbert space in the weak sense relative to all measurable functions $f(t) \in L^2[0, t]$ in the limit as $\omega \to \infty$, which can be written as

$$\begin{aligned} \lim_{\omega\to\infty} \int_0^t \psi_i(\tau)\psi_j(\tau)d\tau &= 0, \ \forall i \neq j, \\ \lim_{\omega\to\infty} \int_0^t \psi_i(\tau)f(\tau)d\tau &= 0, \ \forall i, \ \forall f(t) \in L^2[0,t], \\ \lim_{\omega\to\infty} \int_0^t \psi_i^2(\tau)f(\tau)d\tau &= \int_0^t c_i f(\tau)d\tau, \end{aligned}$$

$\forall i, \forall f(t) \in L^2[0, t], \ c_i > 0.$

One particular implementation of the ES method is especially convenient for particle accelerator applications because the tuning functions ψ_i have analytically guaranteed bounds despite acting on analytically unknown and noisy functions, which guaranteed known update rates and limits on all tuned parameters [5]:

$$u_i = \sqrt{\alpha_i \omega_i} \cos\left(\omega_i t + k\hat{y}(\mathbf{x}, t)\right). \tag{5}$$

The utility of this approach is clearly demonstrated by considering a system of the form

$$\dot{\mathbf{x}} = \mathbf{f}(\mathbf{x}(t), \mathbf{u}(\hat{y}(t)), t), \quad \dot{p}_i = \sqrt{\alpha\omega_i} \cos\left(\omega_i t + k\hat{y}(\mathbf{x}, t)\right), \tag{6}$$

which results in average dynamics that minimize the noise-corrupted unknown function $y(\mathbf{x}, t)$:

$$\dot{\bar{p}}_i = -\frac{k\alpha}{2} \frac{\partial y(\mathbf{x}, t)}{\partial p_i}. \tag{7}$$

This method has been utilized for various particle accelerator applications including real-time betatron oscillation minimization in a time-varying magnetic lattice at the SPEAR3 synchrotron [7], for maximization of the output power of the Linac Coherent Light Source (LCLS) free electron laser (FEL) and of the European X-ray FEL [8], for real-time multi-objective optimization for simultaneous trajectory control and emittance growth minimization at the AWAKE plasma wakefield acceleration facility at CERN [9], and for beam loss minimization by automatically tuning the amplitude and phase set points of multiple RF cavities at the Los Alamos Neutron Science Center (LANSCE) linear ion accelerator. One limitation of adaptive methods such as the ES approach is that they are local feedback-based methods and it is possible for them to get stuck in a local minimum when optimizing for an analytically unknown output function.

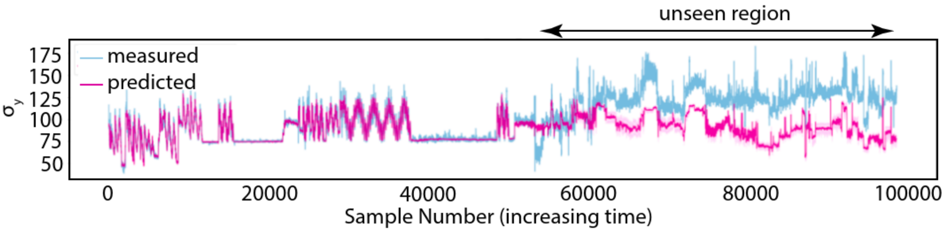

Figure 1: The accuracy of the σ_y prediction quickly degrades once the system has had time to evolve and leaves the span of the collected training data set. Such an approach would have to be continuously and repeatedly re-trained to maintain accuracy, which is infeasible and defeats the purpose of the ML-based diagnostic [16].

LIMITATIONS OF ML FOR TIME-VARYING SYSTEMS

Machine learning (ML) tools are being developed that can learn representations of complex accelerator dynamics directly from data. ML methods have been utilized to develop surrogate models to act as virtual diagnostics [10], powerful polynomial chaos expansion-based surrogate models have been used for uncertainty quantification [11], convolutional neural networks have been used for time-series classification and forecasting in accelerators [12], Bayesian Gaussian processes utilize learned correlations in data/physics-informed kernels [13], surrogate models can help speed up simulation-based optimization [14], and various ML methods have been used for beam dynamics studies at CERN [15].

A major limitation of ML methods, and an active area of research in the ML community, is the problem of time-varying systems, known as distribution shift. If a system changes with time then the data that was used to train an ML-based tool will no longer provide an accurate representation of the system of interest, and the accuracy of the ML tool will degrade. Distribution drift is a challenge for all ML methods including neural networks for surrogate models, the use of neural networks to represent cost functions or optimal policies in reinforcement learning, and even for methods such as Gaussian processes which utilize learned correlations in their kernels. Incorporating methods to deal with distribution shift is a major need for the accelerator community because accelerators and their beams change unpredictably with time. This challenge is illustrated by Fig. 1 which demonstrates that an ML-based prediction quickly degrades in accuracy as the system changes over time, which in this case is the σ_y beam prediction for the LCLS [16]. Such an approach would have to be continuously and repeatedly re-trained to maintain accuracy, which is infeasible and defeats the purpose of the ML-based diagnostic.

ADAPTIVE ML FOR TIME-VARYING SYSTEMS

Efforts have begun to combine the robustness of adaptive feedback with the global representations that can be learned with ML methods to develop adaptive machine learning (AML) for time-varying systems. The first such result combined neural networks and model-independent feedback to provide fast, robust, and automatic control over the energy vs time phase space of electron bunches in the LCLS [17]. Recently, AML methods have been studied in more generality for adaptive tuning of the inputs and outputs of ML tools such as neural networks for time-varying systems [18].

Some of the most powerful ML tools are encoder-decoder generative convolutional neural networks (CNN) which can be used to find highly efficient nonlinear functions that can project incredibly high dimensional input spaces, which may be combinations of images and vectors, down to a very low dimensional latent space, before generating back up to a high dimensional representation [19, 20]. Encoder-decoder networks have been used for anomaly detection [21], time-series data [22], and for optimization of deep generative models [23].

A novel approach to AML for time-varying systems is now being developed which utilizes such generative CNN-based encoder-decoders to adaptively tune directly the low-dimensional latent space representation (as small as 2 dimensions), for incredibly high dimensional systems (hundreds of thousands - millions of parameters) [24–26]. The setup of such an encoder-decoder generative CNN is shown in Figure 2. The network takes inputs that are 2D images of beam phase space distributions together with vectors of accelerator parameter settings such as magnets and RF systems. The high dimensional inputs are squeezed down to a low-dimensional latent space representation from which a collection of distributions is then generated, as shown in Figure 3 for a 2-dimensional latent space representation.

The method works by first performing a supervised learning-based training in which we have access to input-output pairs of the form $(\mathbf{x}_{\text{in}}, \mathbf{X}_{\text{in}}, \hat{\mathbf{Y}}_{\text{out}})$ where $\mathbf{x}_{\text{in}}$ are vectors of accelerator parameter inputs, $\mathbf{X}_{\text{in}}$ are stacks of 2D phase space image inputs. The generative half of the encoder-decoder CNN builds back up to a high dimensional output $\hat{\mathbf{Y}}_{\text{out}}$ which is a $752,640 = 224 \times 224 \times 15$ dimensional output with the 15 channels representing the 15 2D projections of the 6D phase space: (x, y), (x, z), (x, x'), (x, y'), (x, E), (x', y), (x', z), (x', y'), (x', E), (y, z), (y, y'), (y, E), (y', z), (y', E), (z, E) in the HiRES UED as shown in Figure 2 and in a similar setup the output is a $1,228,800 = 128 \times 128 \times 75$ dimensional object with the 75 channels representing the 15 2D projections of the 6D phase at 5 different locations in FACET-II, shown in 3. By

ISBN: 978-3-95450-230-1 ISSN: 2673-5350 doi:10.18429/JACoW-IBIC2021-THOB03

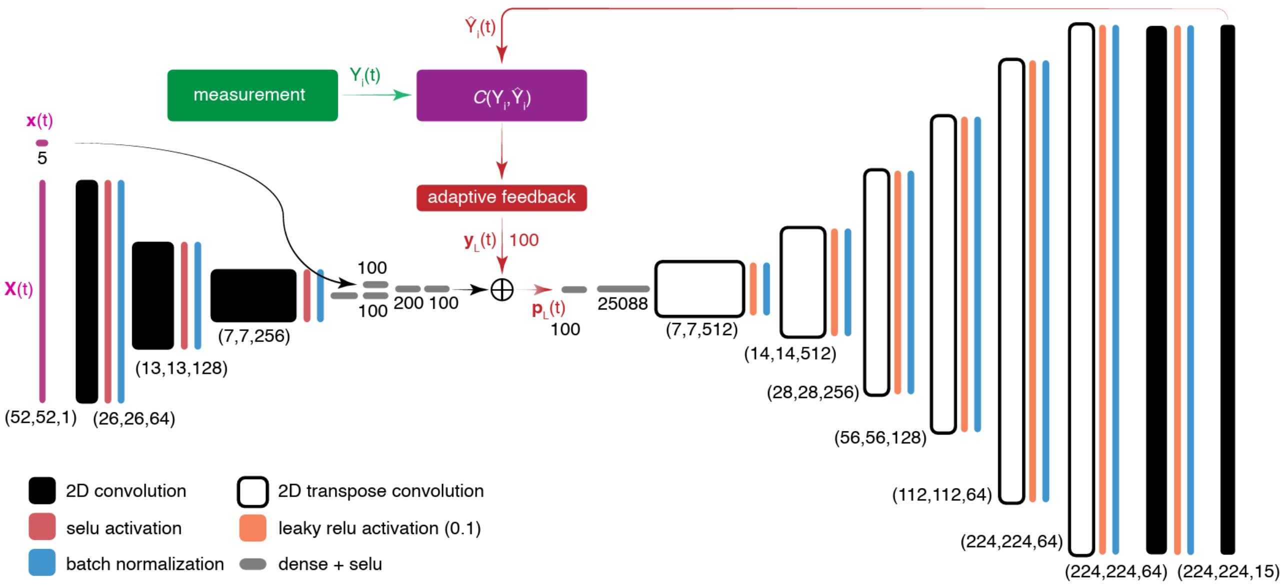

Figure 2: The HiRES encoder-decoder CNN structure for the AML setup is shown with layer sizes such as (224, 224, 15) representing an output of 15 filters of image size 214 × 214 each. The dense layer widths shown as single numbers.

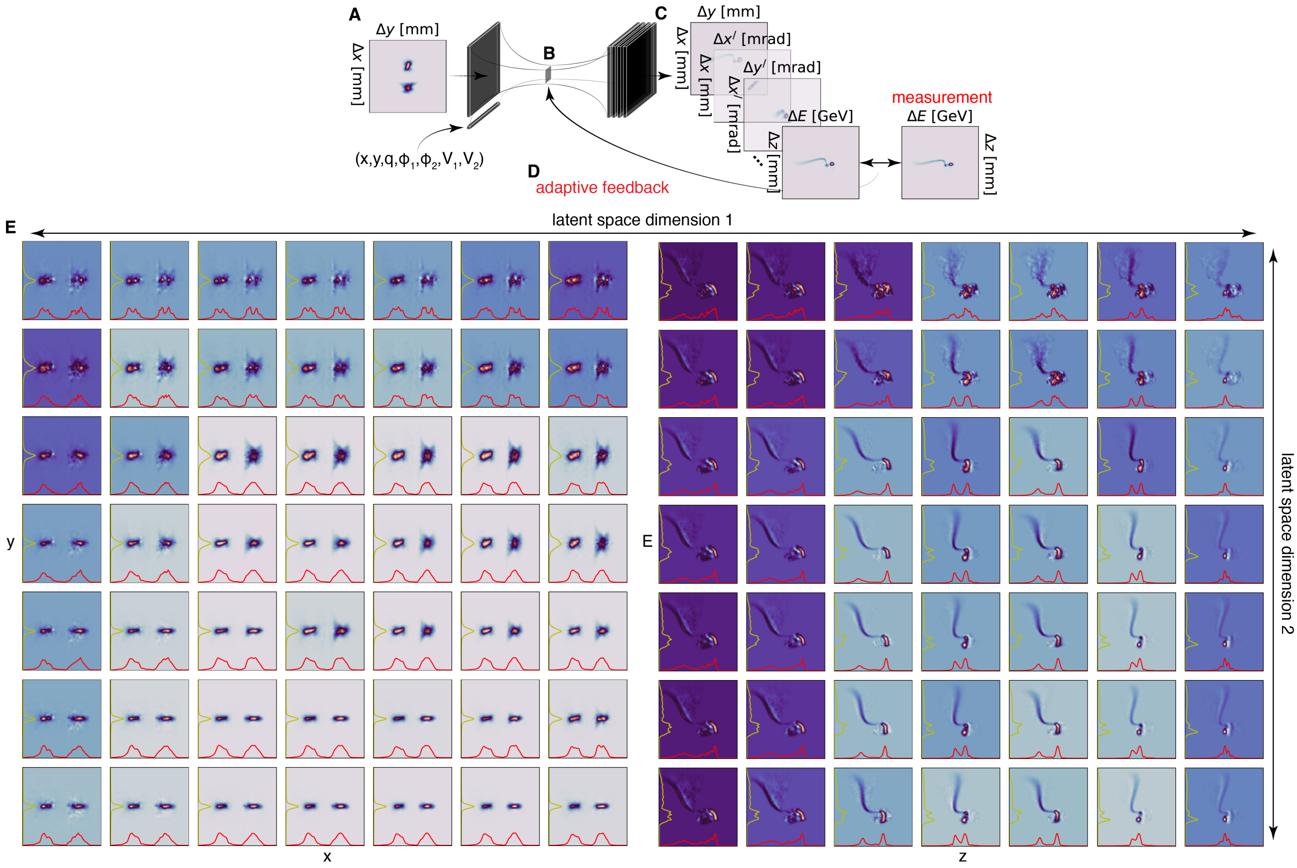

Figure 3: An encoder-decoder convolutional neural network setup is shown which takes an image of an electron beam's (x, y) phase space distribution as an input together with a vector of accelerator parameters (A). The high dimensional inputs are squeezed down to a 2 dimensional latent space (B), from which 75 2D distributions are then generated which are all 15 2D projections of the beam's 6D phase space at 5 different particle accelerator locations (C). Some of the projections, such as the (z, E) longitudinal phase space distributions can be compared to TCAV-based measurements to guide adaptive feedback which takes place in the low dimension latent space to compensate for unknown changes in both the accelerator parameters and in the initial beam distribution (D). The variation of the (x', y') and (z, E) 2D phase space projections is shown as one moves through the 2D latent space learned by the network and adaptively tuned (E) [25].

forcing the generative half of the CNN to predict such high dimensional outputs which contain all of the projections of the beam's 6D phase space simultaneously, we are forcing the CNN to learn the relationships between various phase space projections as well as their correlations and physics constraints within the particle accelerator system for which the network is being trained.

In both the HiRES and the FACET-II setup we are considering a mapping of inputs to outputs of the form

$$\hat{\mathbf{Y}}_{\text{out}}(t) = \mathbf{F}\left(\mathbf{x}_{\text{in}}(t), \mathbf{X}_{\text{in}}(t)\right), \tag{8}$$

where both the accelerator parameters $\mathbf{x}_{\text{in}}(t)$ and the input beam $\mathbf{X}_{\text{in}}(t)$ are expected to change unpredictably with time and furthermore we assume that we will not have access to non-invasive and accurate measurements of these changes. Furthermore, once the accelerator is operational, we lose access to most of the true measurements of the beam's phase space $\mathbf{Y}_{\text{out}}(t)$ which could be compared to their predictions from the generative CNN $\hat{\mathbf{Y}}_{\text{out}}(t)$. However, most advanced accelerators do have access to non-invasive measurements of some subset of the beam's phase space, for example transverse deflective cavities together with dipole magnets can be used to measure the beam's longitudinal phase space (LPS) 2D (z, E) distribution as is routinely done at the LCLS.

In order to accurately predict $\hat{\mathbf{Y}}_{\text{out}}(t)$ without knowledge of the time-varying accelerator beam and component measurements $(\mathbf{x}_{\text{in}}(t), \mathbf{X}_{\text{in}}(t))$, we rely on the fact that the generative CNN has learned the correlations within the system and respects the physics constraints in the data and therefore we use just the available measurements, such as the LPS distribution or energy spread spectrum measurements, which we denote as $\hat{\mathbf{Y}}_i(t) \in \hat{\mathbf{Y}}_{\text{out}}(t)$.

We compare just these predictions to their measurements and operate the trained generative CNN in a un-supervised adaptive manner in which we apply feedback directly on the low-dimensional latent space representation in order to track the time-varying measurements by actively minimizing a cost function in real time, of the form:

$$C(\mathbf{Y}_i(t), \hat{\mathbf{Y}}_i(t)) = \iint \left|\mathbf{Y}_i(t) - \hat{\mathbf{Y}}_i(t)\right| dY_i, \tag{9}$$

which is minimized by adaptively tuning the latent space parameters $\mathbf{y}_L = (y_1, \ldots, y_n)$, according to the model-independent ES algorithm described above, according to:

$$\frac{dy_j(t)}{dt} = \sqrt{\alpha_i \omega_i} \cos\left(\omega_j t + k_j C(\mathbf{Y}_i(t), \hat{\mathbf{Y}}_i(t))\right), \tag{10}$$

as shown in Figure 2.

Note that with this implementation, the relationship in Equation (8) is now being approximated by

$$\hat{\mathbf{Y}}_{\text{out}}(t) \approx \hat{\mathbf{F}}\left(\mathbf{y}_L(t)\right), \tag{11}$$

where $\hat{\mathbf{F}}$ is the generative half of the CNN and $\hat{\mathbf{Y}}_{\text{out}}(t)$ is now parameterized by the low dimensional latent space vector $\mathbf{y}_L(t)$ without needing access to measurements of $(\mathbf{x}_{\text{in}}(t), \mathbf{X}_{\text{in}}(t))$.

One example of such convergence for the FACET-II setup with a 7-dimensional latent space is shown in Figure 4, which shows the trajectory taken by ES in the latent space from a starting point very far from the correct input distribution and accelerator parameters $(\mathbf{x}_{\text{in}}(t), \mathbf{X}_{\text{in}}(t))$ as it converges to the global minimum, with the components (y_1, y_n) for $n \in \{2, 3, 4, 5, 6, 7\}$ shown overlaid on top of the cost function surface. Figure 5 shows the results of the convergence

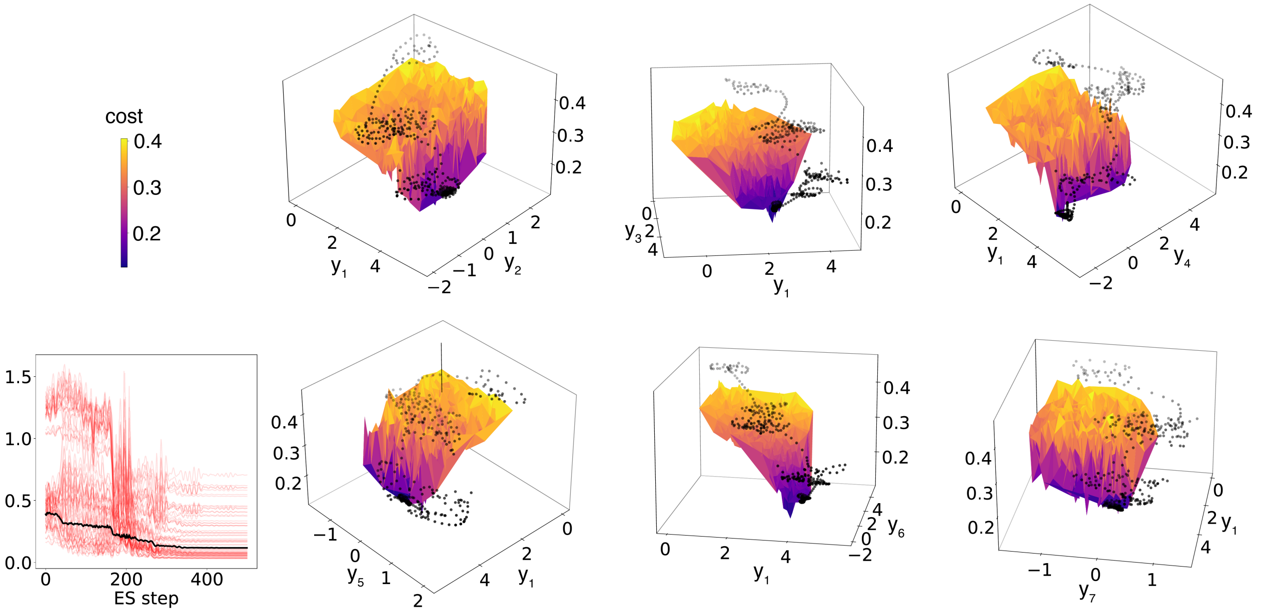

Figure 4: Several 3D projections (y_1, y_n) for $n \in \{2, 3, 4, 5, 6, 7\}$ of convergence within the 7D latent space are shown with the adaptively tuned trajectory shown as black dots lifted slightly above the surface of the cost function. The cost convergence is also shown and seen to take approximately 400 steps to converge.

ISBN: 978-3-95450-230-1 ISSN: 2673-5350 doi:10.18429/JACoW-IBIC2021-THOB03

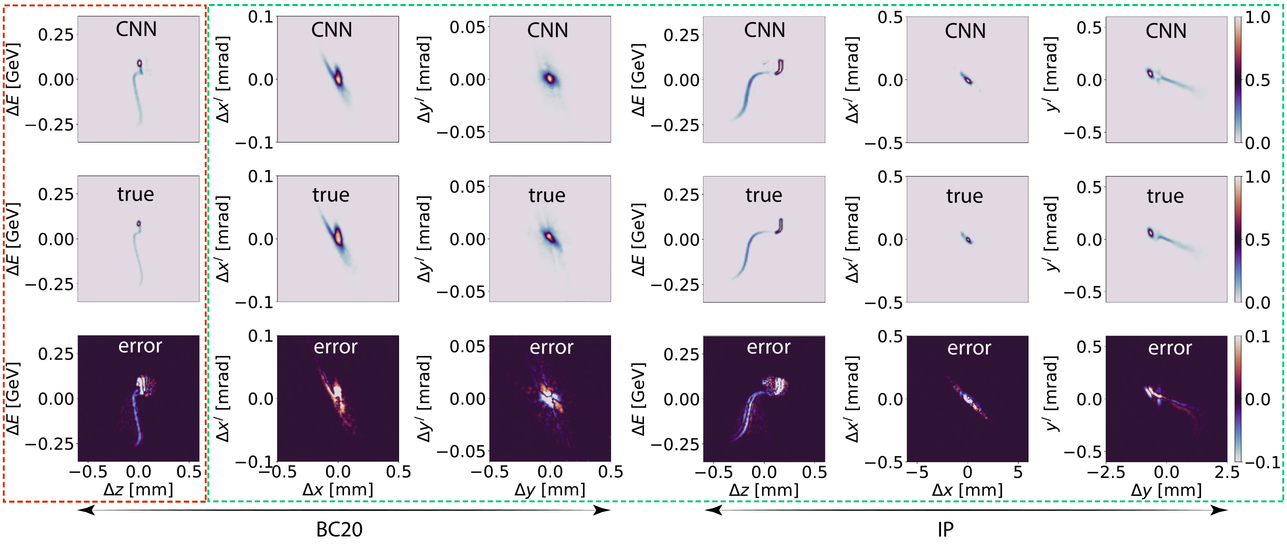

Figure 5: Predictions of the 7D latent space model of the phase space at bunch compressor 20 of FACAT-II (BC20) and at the interaction point (IP). The red dashed box shows a LPS diagnostic that was used as part of the cost function while the other 2D phase space projections in the green dashed box were unseen by the CNN which is correctly predicting projections of the beam's 2D phase space not only at BC20, but also at the unseen IP location.

which gives a close match of various 2D phase space projections throughout the accelerator despite feedback acting only based on a single LPS measurement.

CONCLUSION

This work demonstrates an adaptive ML approach to high dimensional time-varying systems in general and in particular for particle accelerator applications in which both the accelerator components and the input beams change unpredictably with time due to various external disturbances. By training a deep convolutional encoder-decoder style generative neural network and forcing it to predict all 2D projections of the beam's 6D phase space simultaneously this physics-informed approach gives accurate predictions for unseen phase space projections by adaptively matching only a measurable distribution.

REFERENCES

[1] H. K. Khalil, *Nonlinear Systems*, Prentice Hall, 2002.

[2] P. Ioannou and B. Fidan, *Adaptive control tutorial,* Society for Industrial and Applied Mathematics, 2006.

[3] P. A. Ioannou and J. Sun, *Robust adaptive control,* Courier Corporation, 2012.

[4] A. Scheinker, "Model Independent Beam Tuning", in *Proc. IPAC'13*, Shanghai, China, May 2013, paper TUPWA068, pp. 1862–1864.

[5] A. Scheinker, "Simultaneous stabilization and optimization of unknown, time-varying systems," 2013 American Control Conference, IEEE, 2013. `https://ieeexplore.ieee.org/document/6580232`

[6] A. Scheinker and D. Scheinker, "Bounded extremum seeking with discontinuous dithers," *Automatica*, vol. 69, pp. 250-257, 2016. `doi:10.1016/j.automatica.2016.02.023`

[7] A. Scheinker, X. Huang, and J. Wu, "Minimization of betatron oscillations of electron beam injected into a time-varying lattice via extremum seeking," *IEEE Transactions on Control Systems Technology*, vol 26, no .1, pp. 336-343, 2017. `doi:10.1109/TCST.2017.2664728`

[8] A. Scheinker *et al.*, "Model-independent tuning for maximizing free electron laser pulse energy," *Physical Review Accelerators and Beams*, vol. 22, no .8, p. 082802, 2019. `doi:10.1103/PhysRevAccelBeams.22.082802`

[9] A. Scheinker *et al.*, "Online multi-objective particle accelerator optimization of the AWAKE electron beam line for simultaneous emittance and orbit control," *AIP Advances*, vol. 10, no .5, p. 055320, 2020. `doi:10.1063/5.0003423`

[10] C. Emma *et al.*, "Machine learning-based longitudinal phase space prediction of particle accelerators," *Physical Review Accelerators and Beams*, vol. 21, no .11, p. 112802, 2018. `doi:10.1103/PhysRevAccelBeams.21.112802`

[11] A. Adelmann, "On nonintrusive uncertainty quantification and surrogate model construction in particle accelerator modeling," *SIAM/ASA Journal on Uncertainty Quantification*, vol. 7, pp.383–416, 2019. `doi:10.1137/16M1061928`

[12] S. Li *et al.*, "A Novel Approach for Classification and Forecasting of Time Series in Particle Accelerators," *Information*, vol. 12, no .3, p. 121, 2021. `doi:10.3390/info12030121`

[13] J. Duris *et al.*, "Bayesian optimization of a free-electron laser," *Physical review letters*, vol. 124, no. 12, p. 124801, 2020. `doi:10.1103/PhysRevLett.124.124801`

[14] A. Edelen *et al.*, "Machine learning for orders of magnitude speed up in multiobjective optimization of particle accelerator systems," *Physical Review Accelerators and Beams*, vol. 23, p .4, p. 044601, 2020. `doi:10.1103/PhysRevAccelBeams.23.044601`

[15] E. Fol *et al.*, "Supervised learning-based reconstruction of magnet errors in circular accelerators," *The European Phys-*

ical Journal Plus, vol. 136, no .4, pp. 1-19, 2021. `doi:10.1140/epjp/s13360-021-01348-5`

[16] Figure shared by collaborators at SLAC National Accelerator Laboratory.

[17] A. Scheinker *et al.*, “Demonstration of model-independent control of the longitudinal phase space of electron beams in the linac-coherent light source with femtosecond resolution,” *Physical review letters*, vol. 121, no .4, p. 044801, 2018. `doi:10.1103/PhysRevLett.121.044801`

[18] A. Scheinker, “Adaptive Machine Learning for Robust Diagnostics and Control of Time-Varying Particle Accelerator Components and Beams,” *Information*, vol. 12, no .4, p. 161, 2021. `doi:10.3390/info12040161`

[19] A. L. Caterini, A. Doucet, and D. Sejdinovic. “Hamiltonian variational auto-encoder." arXivpreprint arXiv:1805.11328, 2018. `https://arxiv.org/abs/1805.11328`

[20] Y. Pu, Z. Gan, R. Henao, X. Yuan, C. Li, C. A. Stevens, and L. Carin, “Variational autoencoder for deep learning of images, labels and captions," *Advances in neural information processing systems*, vol. 29, pp. 2352-2360, 2016. `https://proceedings.neurips.cc/paper/2016/file/eb86d510361fc23b59f18c1bc9802cc6-Paper.pdf`

[21] J. An and S. Cho, “Variational autoencoder based anomaly detection using reconstruction probability,” Special lecture on IE., vol. 2, no .1, pp. 1-18, 2015. `http://dm.snu.ac.kr/static/docs/TR/SNUDM-TR-2015-03.pdf`

[22] R. Maulik, A. Mohan, B. Lusch, S. Madireddy, P. Balaprakash, and D. Livescu, “Time-series learning of latent-space dynamics for reduced-order model closure,” *Physica D: Nonlinear Phenomena*, vol. 405, p. 132368, 2020. `doi:10.1016/j.physd.2020.132368`

[23] A. Tripp, E. Daxberger, and J. M. Hernández-Lobato. “Sample-efficient optimization in the latent space of deep generative models via weighted retraining,” *Advances in Neural Information Processing Systems*, 33, 2020. `https://proceedings.neurips.cc/paper/2020/file/81e3225c6ad49623167a4309eb4b2e75-Paper.pdf`

[24] A. Scheinker, F. Cropp, S. Paiagua, and D. Filippetto, “Adaptive deep learning for time-varying systems with hidden parameters: Predicting changing input beam distributions of compact particle accelerators,” arXiv preprint arXiv:2102.10510, 2021. `https://arxiv.org/abs/2102.10510`

[25] A. Scheinker, F. Cropp, S. Paiagua, and D. Filippetto, “Adaptive Latent Space Tuning for Non-Stationary Distributions,” arXiv preprint arXiv:2105.03584, 2021. `https://arxiv.org/abs/2105.03584`

[26] A. Scheinker, “Adaptive Machine Learning for Time-Varying Systems: Low Dimensional Latent Space Tuning,” arXiv preprint arXiv:2107.06207, 2021. `https://arxiv.org/abs/2107.06207`

IDENTIFICATION OF THE INTER-BUNCH AND INTRA-BUNCH BEAM DYNAMICS BASED ON DYNAMIC MODAL DECOMPOSITION (DMD)*

C. Rivetta[†][1], SLAC National Accelerator Laboratory, Menlo Park, USA
T. Mastoridis, Physics Dept. California Polytechnic State University, San Luis Obispo, CA, USA
J. Fox, Physics Dept. Stanford University, Palo Alto, USA
[1]also at Nadeval LLC, Palo Alto, USA

Abstract

The beam dynamics in circular and linear particle accelerators have been studied defining physics-driven / model-driven models that have been used for operation of the machine, diagnostics and feedback system designs. In this paper, a data-driven technique is evaluated to characterize the inter-bunch / intra-bunch beam dynamics in particle accelerators. The dynamic modal decomposition (DMD) is an equation-free, data-driven method capable of providing an accurate decomposition of a complex system into spatiotemporal coherent structures that can be used for short-time future state prediction and control. It does not require knowledge of the underlying governing equations and only uses snapshots in time of observables from historical, experimental, or black-box simulations. The application of the DMD algorithm to particle accelerator cases is illustrated by examples of the collective longitudinal motion of the bunches in a circular storage ring and the transverse motion of a bunch circulating in an accelerator.

INTRODUCTION

The beam dynamics in circular and linear particle accelerators have been studied defining a framework for design and operation of machines as well as the background for future research in the topic [1]. Based on this framework, multiple studies were conducted in order to delineate models of the beam dynamics to create diagnostic tools and design feedback systems to stabilize the beam and improve the machine performance [2]. These physics-driven / model-driven models are commonly used during the operation of the machine and their parameters are obtained via measurements to provide both diagnostic tools to the control room operators and design tools to set the feedback systems.

There is another option to create models for dynamic systems that does not requires the previous knowledge of the physical system. Data-driven modeling and control of complex systems is a field that is having a large impact in engineering and physical sciences. Those complex systems generally evolve on a low-dimensional attractor that can be characterized by spatiotemporal coherent structures. In this paper, we present the dynamic mode decomposition (DMD), and apply it to characterize the intra-bunch and inter-bunch beam dynamics. As example, the analysis of the coupled longitudinal beam dynamics of bunches in a circular accelerator is presented. Results from simulation are compared with results using traditional methods based on model-driven analysis. The analysis of the transverse dynamic of a single bunch is used as an example to show the application of the DMD algorithm to characterize the intra-bunch motion.

DYNAMIC MODAL DECOMPOSITION

Generalities

The DMD method originated in the fluid dynamics community as a method to decompose complex flows into a simple representation based on spatiotemporal coherent structures [3]. The particular characteristic of DMD is that it is an equation-free, data-driven method capable of providing an accurate decomposition of a complex system into spatiotemporal coherent structures that can be used for short-time future state prediction and control. DMD has a number of uses, classified in three primary tasks:

- **Diagnostics.** In particular, the algorithm extracts key low-rank spatiotemporal features of many high-dimensional systems, allowing for physically interpretable results in terms of spatial structures and their associated temporal responses.
- **State estimation, future-state prediction, and system identification.** Another application of the DMD algorithm is associated with using the spatiotemporal structures that are dominant in the data to construct dynamical models of the underlying processes observed.
- **Control.** The ultimate goal of the algorithm is to define viable and robust control strategies directly from the data sampling or the models identified by the algorithm. This is the most challenging task due to the dynamics associated is nonlinear and the DMD creates a linear model based on the data taken.

Background

The main objective is to characterize the intra-bunch / inter-bunch dynamics of the beam based on measurements. The beam dynamics can be represented by a set of ordinary differential equations (ODE),

$$\frac{dx(t)}{dt} = f(x(t)) \qquad \text{with } x \in R^{2n} \text{or } x \in C^n$$

ODEs in general are used to describe the inter-bunch dynamics. Partial differential equation (PDF) are used to represent

---

* Work supported by the DOE contract #DE-AC02-76SF00515.

[†] chrivetta@nadeval.com

the intra-bunch dynamics of a bunch in the accelerator,

$$\frac{\partial x(z,t)}{\partial t} = g(\frac{\partial x(z,t)}{\partial z}, x(z,t))$$

with $x \in R^{2n}$or $x \in C^n$, and $z \in R^m$. If due to the measurements, the state variables $x(z,t)$ are not evaluated continuously in the space variable z, otherwise at discrete locations in z, then the PDE becomes an ODE. If the data is collected by sampling the state variables at $t = k\Delta T$, with $k = 1, ..., N$ for a total of N measurement times, the ODEs in continuous time domain is transformed in a discrete equation $x_{k+1} = F(x_k)$, with $x_k = x(t)\big|_{t=k\Delta T}$. The beam dynamics can be simplified more if the analysis is conducted around the operation point, then by linearizing $F(x_k)$, the equation can be approximated by $x_{k+1} = Ax_k$. All the information about the beam dynamics is represented by the matrix A. This matrix defines a mapping between the subsequent samples x_k and x_{k+1}.

The DMD algorithm estimates the matrix A and produces a low-rank eigendecomposition of the matrix A that optimally fits the measured trajectory x_k for $k = 1, 2, \ldots, N$ in the least-square sense so that

$$\|x_{k+1} - Ax_k\|_2$$

is minimized across all the points for $k = 1, 2, \ldots, N - 1$ [3]. To minimize the approximation error across all the snapshots from $k = 1, 2, \ldots, N$, it is possible to arrange the N snapshots into two large data matrices:

$$X = \begin{bmatrix} | & | & & | \\ x_1 & x_2 & \ldots & x_{N-1} \\ | & | & & | \end{bmatrix}$$

$$X' = \begin{bmatrix} | & | & & | \\ x_2 & x_3 & \ldots & x_N \\ | & | & & | \end{bmatrix}$$

The local linear approximation $x_{k+1} = Ax_k$ may be written in terms of these data matrices as $X' = AX$. The best fit A matrix is given by

$$A = X'X^{\dagger}$$

where $X^{\dagger}$ is the Moore-Penrose pseudoinverse.

To solve the pseudo inverse in case the state dimension n is large, the DMD algorithm circumvents the eigendecomposition of A by considering a rank-reduced representation in terms of a *Proper Order Decomposition*-projected matrix $\tilde{A}$. The algorithm takes the singular value decomposition (SVD) of X, $X = U\Sigma V^*$, where $*$ denotes the conjugate transpose, $U \in C^{n\times n}, \Sigma \in C^{n\times N-1}, V \in C^{N-1\times N-1}$ (In case $x_k \in C^n$ and $X \in C^{n\times N-1}$). The matrices U and V are unitary and the singular values of X are, in descendent order, located in the diagonal of Σ. If the data presents a low order structure, the singular values will decrease sharply to zero defining a limited number of dominant modes. In this case, it is possible to truncate the singular values of X and reduce the system taking into account only those r dominant modes. The decomposition of the matrix X can be approximated by defining $U \in C^{n\times r}, \Sigma \in C^{r\times r}, V \in C^{N-1\times r}$. Thus, the matrix A can be obtained by using the pseudoinverse of X obtained via the SVD:

$$A = X'V\Sigma^{-1}U^*$$

In practice, it is more efficient computationally to estimate $\tilde{A}$, the $r \times r$ projection of the full matrix A onto the *Proper Order Decomposition* modes:

$$\tilde{A} = U^*AU = U^*X'V\Sigma^{-1}.$$

The matrix $\tilde{A}$ defines a low-dimensional linear model of the dynamical system:

$$\tilde{x}_{k+1} = \tilde{A}\tilde{x}_k$$

where the low- and high-dimensional states are related by $x_k = U\tilde{x}_k$.

The matrix $\tilde{A}$ can be eigendecomposed by

$$\tilde{A}W = W\Lambda$$

where the columns of W are the eigenvectors and Λ is a diagonal matrix containing the corresponding eigenvalues λ_i, with $i = 1, \ldots, r$. It is possible to reconstruct the eigendecomposition of A from W and Λ. The eigenvalues of A are given by Λ and the eigenvectors of A are given by the columns of $\mathbf{\Phi}$

$$\mathbf{\Phi} = X'V\Sigma^{-1}W$$

Based on the low-rank approximation of both the eigenvalues and the eigenvectors, the solution of the states can be estimated for all time in the future. The estimation is given by

$$x_k \approx \sum_{i=1}^{r} \phi_i e^{\lambda_i k\Delta T} b_i = \mathbf{\Phi} e^{\Lambda k\Delta T} b \tag{1}$$

where b_i is the initial condition of each mode, $\mathbf{\Phi}$ is the matrix whose columns are the eigenvectors ϕ_i and b is a vector of the coefficients b_i.

ANALYSIS OF INTER-BUNCH DYNAMICS

To apply the DMD algorithm to characterize the inter-bunch dynamics, the collective effects of the longitudinal bunch dynamics of a full circular accelerator is analyzed. The example corresponds to the electron ring of the Electron Ion Collider (EIC) under design at Brookhaven National Laboratory. The ring operates at E = 10 GeV and the beam current is $I_{b_{DC}}$ = 2.5 A and there are 17 RF stations operating at 1.27 MV.

The longitudinal inter-bunch dynamic is defined by the coupling between the individual bunches in the ring through the total machine impedance distributed along the ring. In particular if the analysis is focused on the low-order longitudinal modes of the beam dynamics, the main source of coupling among bunches is the RF station impedance. Results from simulations consider the RF station configured with the LLRF feedback system optimally setup for impedance minimization but it does not include any one-turn delay (comb) filter. Additionally, there is no longitudinal feedback to stabilize the beam. In this example the beam motion is unstable.

Given the analysis is focused on the low-order longitudinal mode dynamics of the beam, the bunches are represented by a reduced number of macrobunches to reduce the complexity in the simulation. They represent the charge of several bunches, keeping the total current in the ring equal to nominal. In the simulations, the full ring is represented by 20 macrobunches.

Figure 1 shows the unstable longitudinal motion of all the macrobunches. To compare the DMD technique with the traditional model-driven analysis used to study the bean motion and stability, the data is also processed by transforming the longitudinal beam motion into the modal domain using the *n even-filled bunch* base [2]. The motion in the modal domain is

$$\varphi_m(t) = \frac{1}{n}\sum_{\ell=1}^{n}\phi_{B_\ell}(t)e^{-j2\pi\frac{m\ell}{n}}$$

with $\varphi_m(t)$ motion for the m-mode, $\phi_{B_\ell}(t)$ longitudinal motion around the synchronous phase of the ℓ-bunch and n the total number of macrobunches. Figure 2 depicts the beam motion in the modal domain, where a slow growing mode 0 and dominant unstable modes -3, -2, and -4 can be observed.

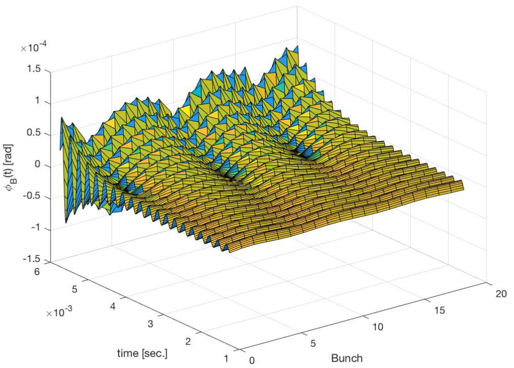

Figure 1: Longitudinal motion of the bunches.

Applying the DMD algorithm described in the previous section to the data, it is possible to extract the dominant modes of the beam dynamics. These modes are characterized by the eigenvalues

$$\lambda_{-3} = 1198 + j2\pi 4.674e3\ sec^{-1}$$
$$\lambda_{-2} = 818 + j2\pi 4.389e3\ sec^{-1}$$
$$\lambda_{-4} = 106 + j2\pi 4.611e3\ sec^{-1}$$

To validate the model obtained by the DMD algorithm, the time evolution of the longitudinal displacement obtained by the estimation defined by Eq. (1) is compared with the original data displayed in Fig.1. Figure 3 depicts the estimated phase angle for all the macrobunches, matching the time evolution of the original data shown in Fig.1.

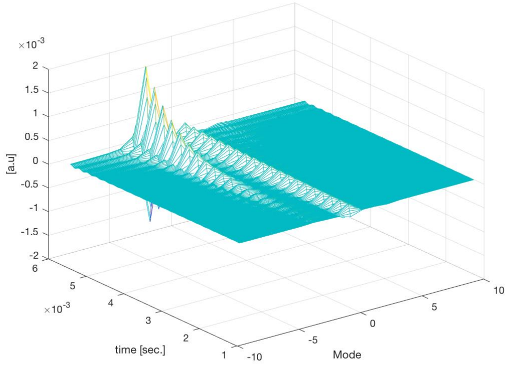

Figure 2: Motion in the modal domain.

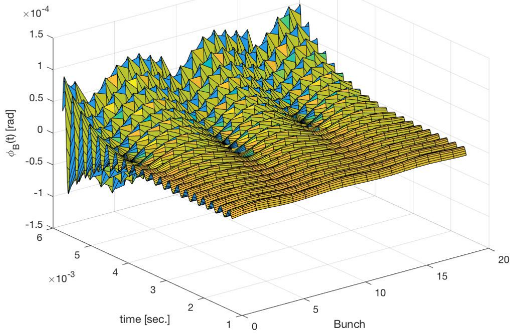

Figure 3: Estimated longitudinal motion of the bunches.

ANALYSIS OF INTRA-BUNCH DYNAMICS

The application of the DMD technique to analyze the intra-bunch dynamics is based on measurements of the transverse bunch motion in the SPS ring at CERN. To measure the vertical motion along the bunch, the acquisition stage of a 3.2 GSamp/sec processing system [4–6] is synchronized with the bunch and able to acquire 16 samples along the 5 nsec bucket. The signal from the exponential pick-up installed in the ring is processed to equalize the cable attenuation and determine the dipole motion of the bunch. This acquired signal corresponds to the product of the vertical motion $y(z)$, at each particular location in the longitudinal dimension z of the bunch, and the bunch charge $Q(z)$ at that particular coordinate.

During these tests, three different lattices have been used the $Q20$, $Q22$, and $Q26$, in particular for this measurement the $Q22$ was set in the machine. Some characteristic parameters of the bunch motion due to this lattice are, vertical fractional tune ≈ 0.185 and longitudinal fractional tune ≈ 0.011.

The motion of the bunch measured is unstable and the transverse displacement in time is depicted in Fig. 4. The data shows the motion for the 16 samples acquired, where sample 0 corresponds to the head of the bunch and sample 16 to the tail. The bunch exhibits an unstable 'head-tail' motion.

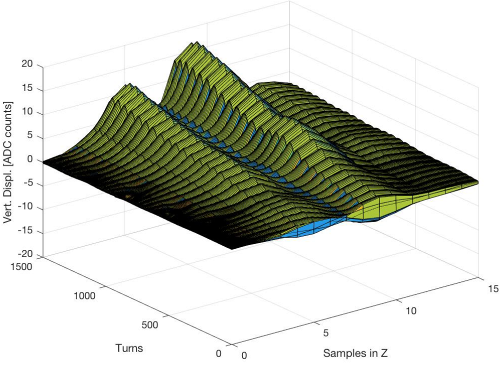

Figure 4: Transverse motion along the bunch.

Applying DMD to characterize and reduce the bunch dynamics, the estimated vertical motion using Eq. (1) for the same initial condition defined in Fig. 4, is depicted in Fig. 5. Comparing both figures, the measurements and the estimated motions match showing that the model extracted by the DMD algorithm defines the characteristics of the bunch for that motion.

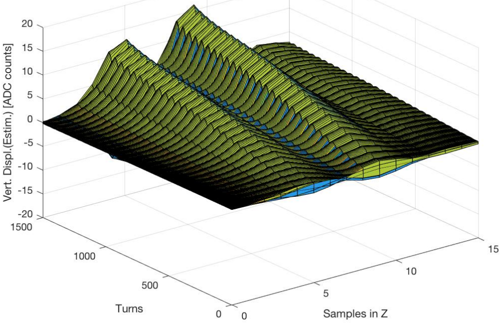

Figure 5: Estimated transverse motion along the bunch.

Further details of this analysis can be presented. Figure 6 depicts the n singular values of the matrix X (or matrix Σ) showing only $r = 2$ dominant modes to characterize this motion. The data displayed in Fig. 6 includes only the 2 dominant modes to approximate the representation. These modes have the following eigenvalues:

$$\lambda_a = 0.0013 + j2\pi 0.196\, 1/rev$$
$$\lambda_b = 0.0001 + j2\pi 0.1965\, 1/rev$$

The associated eigenvectors (or discrete eigenfunctions) for each mode are depicted in Fig. 7. They all have similar shapes. Observing the real part of the eigenvalues, it is possible to conclude that the growth rate of λ_a is dominant with respect to the one of λ_b. If the bunch motion is free of noise, the analysis will define only one dominant mode characterized by the eigenvalue λ_a. Due to noise and perturbations in the components settling the transverse motion of the bunch, this motion has a modulation that is captured and approximated by the mode defined by the eigenvalue λ_b.

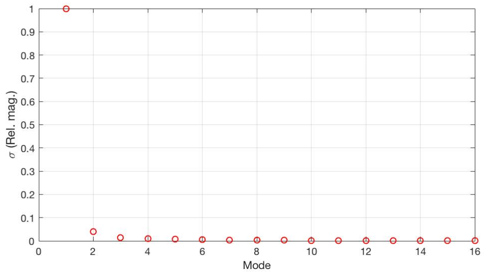

Figure 6: Singular Values of matrix X.

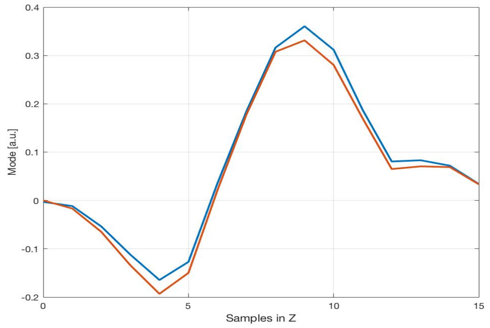

Figure 7: Eigenvectors (discrete eigenfunctions) for the dominant modes.

CONCLUSIONS

The dynamic modal decomposition is applied in this work to identify the inter-bunch / intra-bunch dynamics of the beam in particle accelerators. The method can be applied to create analysis and diagnostic tools and could be extended to identify the beam model to design feedback systems to stabilize the beam motion.

The advantage of this technique is that it is model-free, the characterization of the dynamics does not require the knowledge of the eigenstructure of the system dynamics. Based on measurements or simulation results the eigenvalues - eigenvectors (or discrete eigenfunctions) can be estimated for the dominant modes of the motion.

This technique has been applied successfully in other fields dealing with ordinary or partial differential equations to describe the system dynamics.

Further research is necessary to improve the method and create diagnostic tools and beam model identification.

ACKNOWLEDGEMENTS

The authors would like to thank the collaborators of Brookhaven National Laboratory, CERN and past members of SLAC LARP Collaboration for the useful discussions and support with collecting data during the Machine Development sessions.

REFERENCES

[1] A. Chao, *Physics of Collective Beam Instabilities in High Energy Accelerators*, New York, USA:Wiley, 1993.

[2] S. Prabhakar, “New Diagnostics and Cures for Coupled-Bunch Instabilities”, Ph.D. thesis, Stanford University, Stanford, CA, USA, 2000.

[3] N. Kutz, S. Brunton, B. Brunton, J. Proctor, *Dynamic Mode Decomposition: Data-Driven Modeling of Complex Systems*, USA:SIAM, 2016.

[4] J. E. Dusatko, J. D. Fox, C. H. Rivetta, W. Höfle, and O. Turgut, “Recent Upgrades to the CERN SPS Wideband Intra-bunch Transverse Feedback Processor”, in *Proc. IPAC’16*, Busan, Korea, May 2016, pp. 2687–2689. `doi:10.18429/JACoW-IPAC2016-WEPOR010`

[5] J.E. Dusatko *et al.*, “Upgrade Development Progress for the CERN SPS High Bandwidth Transverse Feedback Demonstrator System”, in *Proc. IBIC’14*, Monterey, CA, USA, Sep. 2014, paper WEPD25, pp. 700–702.

[6] J.E. Dusatko *et al.*, “The Hardware Implementation of the CERN SPS Ultrafast Feedback Processor Demonstrator”, in *Proc. IBIC’13*, Oxford, UK, Sep. 2013, paper MOPC28, pp. 124–127.

List of Authors

Bold papercodes indicate primary authors; ~~crossed out~~ papercodes indicate 'no submission'

Institutes List

AEC
Bern, Switzerland

- Braccini, S.
- Casolaro, P.
- Dellepiane, G.
- Häffner, P.
- Mateu, I.
- Scampoli, P.
- Voeten, N.
- Zyaee, E.

ALBA-CELLS Synchrotron
Cerdanyola del Vallès, Spain

- Benedetti, G.
- Günzel, T.F.
- Iriso, U.
- Martí, Z.
- Morales, E.
- Nosych, A.A.
- Solano, E.
- Torino, L.

ANL
Lemont, Illinois, USA

- Berg, W.
- Brill, A.R.
- Cheng, W.X.
- Decker, G.
- Dooling, J.C.
- Karas, C.N.
- Kim, K.
- Lee, S.H.
- Lumpkin, A.H.
- Power, J.G.
- Sereno, N.
- Shao, J.H.
- Steinmann, J.L.
- Sun, Y.
- Wang, S.G.
- Wootton, K.P.
- Yang, B.X.

ANSL
Yerevan, Armenia

- Arutunian, S.G.
- Harutyunyan, G.S.
- Lazareva, E.G.
- Margaryan, A.V.

ANSTO
Menai, New South Wales, Australia

- Boardman, D.
- Chartier, L.
- Guenette, M.C.
- Ilter, J.K.
- Watt, G.

Applied Diamond, Inc.
Wilmington, Delaware, USA

- Konovalov, V.V.

AS - ANSTO
Clayton, Australia

- Tan, Y.E.

ASELSAN A.S.
Ankara, Turkey

- Durna, E.
- Kavak, R.
- Sanal, M.G.
- Sezer, M.M.

BNL
Upton, New York, USA

- Bellavia, S.
- Blaskiewicz, M.
- Brutus, J.C.
- Drees, K.A.
- Gassner, D.M.
- Hayes, T.
- Hetzel, C.
- Holmes, D.
- Hulsart, R.L.
- Inacker, P.
- Liu, C.
- Michnoff, R.J.
- Miller, T.A.
- Minty, M.G.
- Montag, C.
- Padrazo Jr, D.
- Paniccia, M.C.
- Ptitsyn, V.
- Ranjbar, V.H.
- Sangroula, M.P.
- Seletskiy, S.
- Shaftan, T.V.
- Thieberger, P.
- Wang, E.
- Willeke, F.J.

BPT
Madrid, Spain

- Berdascas JuliÃ¡n, F.
- García-Tabarés Valdivieso, A.

Brookhaven National Laboratory (BNL), Electron-Ion Collider
Upton, New York, USA

- Bellon, J.R.
- Blednykh, A.

CalPoly
San Luis Obispo, California, USA

- Mastoridis, T.

CEA-DRF-IRFU
France

- Farabolini, W.

CERN
Meyrin, Switzerland

- Albertone, J.

ISBN: 978-3-95450-230-1 ISSN: 2673-5350

- Andreazza, W.
- Bantemits, G.
- Barros Marin, M.B.M.
- Belohrad, D.
- Boccardi, A.
- Bodart, D.
- Bogey, T.B.
- Bozzolan, M.
- Bracco, C.
- Bravin, E.
- Burger, S.
- Butti, D.
- Calvo Giraldo, E.
- Cenede, J.
- Corsini, R.
- Degl'Innocenti, I.
- Di Carlo, S.
- Effinger, E.
- Emery, J.
- Esteban Felipe, J.C.
- Farabolini, W.
- Gąsior, M.
- Giangrande, L.
- Gilardi, A.
- Goetz, A.
- Goldblatt, A.
- Gudkov, D.
- Guerin, H.
- Guerrero, A.
- Jackson, S.
- Jensen, S.
- Jones, O.R.
- Kain, V.
- Kaplon, J.
- Kieffer, R.
- Kolbinger, B.
- Krupa, M.
- Lacarrere, G.O.
- Lefèvre, T.
- Leitao, P.V.
- Levasseur, S.
- Li, K.S.B.
- Malinowska, P.A.
- Marqversen, O.
- Martin Nieto, M.
- Martina, F.
- Mazzoni, S.
- McLean, M.
- Morales Vigo, S.
- Navarro Fernandez, A.
- Renner, E.
- Rinaldi, A.T.
- Roncarolo, F.
- Rossi, A.
- Saccani, M.
- Salvachua, B.
- Salzburger, A.
- Sandberg, H.S.
- Schillinger, C.
- Schneider, G.
- Senes, E.
- Storey, J.W.
- Tassan-Viol, J.
- Topaloudis, A.
- Trad, G.
- Tranquille, G.
- Velotti, F.M.
- Veness, R.
- Veyrunes, E.
- Viganò, W.
- Wendt, M.
- Zamantzas, C.

Cockcroft Institute
Warrington, Cheshire, United Kingdom

- Martina, F.
- Welsch, C.P.

DESY
Hamburg, Germany

- Czwalinna, M.K.
- D'Arcy, R.T.P.
- Gerth, C.
- Gonzalez-Caminal, P.
- Kube, G.
- Lipka, D.
- Lockmann, N.M.
- Osterhoff, J.
- Schlarb, H.
- Schmidt-Föhre, F.
- Wittenburg, K.

DLS
Oxfordshire, United Kingdom

- Bloomer, C.
- Bobb, L.
- Houghton, C.E.
- Howling, E.R.

DNSC
Dongguan, People's Republic of China

- Wang, D.Y.

Doshisha University, Graduate School of Engineering
Kyoto, Japan

- Wada, M.
- Yamada, I.

Elettra-Sincrotrone Trieste S.C.p.A.
Basovizza, Italy

- Brajnik, G.
- De Monte, R.

ESRF
Grenoble, France

- Benoist, N.
- Buratin, E.
- Carmignani, N.
- Ewald, F.
- Franchi, A.
- Pons, J.L.
- Scheidt, K.B.

ESS
Lund, Sweden
- Donegani, E.M.
- Lundquist, J.S.
- Milas, N.

Euclid TechLabs
Solon, Ohio, USA
- Antipov, S.P.
- Avrakhov, P.V.
- Callahan, J.R.
- Knight, E.W.
- Kuzikov, S.V.
- Liu, A.

EuXFEL
Schenefeld, Germany
- Milne, C.J.

Fermilab
Batavia, Illinois, USA
- Campos, R.
- Diamond, J.S.
- Eddy, N.
- Fellenz, B.J.
- Hamerla, T.W.
- Lebedev, V.A.
- Lumpkin, A.H.
- Nagaitsev, S.
- Romanov, A.L.
- Ruan, J.
- Santucci, R.R.
- Scarpine, V.E.
- Semenov, A.
- Shemyakin, A.V.
- Shiltsev, V.D.
- Slimmer, D.
- Stancari, G.
- Sun, D.
- Thurman-Keup, R.M.
- Valishev, A.
- Voy, D.C.

FSU Jena
Jena, Germany
- Stapelfeld, M.

GANIL
Caen, France
- Jamet, C.
- Legallois, P.

GSI
Darmstadt, Germany
- Barth, W.A.
- Dorn, C.
- Forck, P.
- Haider, D.M.
- Lauber, S.
- Milosic, T.
- Miski-Oglu, M.
- Reichert, T.
- Reiter, A.
- Schwickert, M.
- Sieber, T.
- Singh, R.
- Stöhlker, T.
- Ucar, F.

HIJ
Jena, Germany
- Stöhlker, T.
- Tympel, V.

HIT
Heidelberg, Germany
- Cee, R.
- Feldmeier, E.
- Haberer, Th.
- Peters, A.
- Schreiner, J.
- Winkelmann, T.W.

Huazhong University of Science and Technology, State Key Laboratory of Advanced Electromagnetic Engineering and Technology,
Hubei, People's Republic of China
- Fan, K.

HUST
Wuhan, People's Republic of China
- Chen, Q.S.
- Li, J.Q.

HZB
Berlin, Germany
- Grimmer, S.
- Huck, M.
- Hwang, J.-G.
- Jankowiak, A.
- Koopmans, M.
- Meseck, A.
- Ries, M.
- Schiwietz, G.
- Volz, P.I.

HZDR
Dresden, Germany
- Arnold, A.
- Ma, S.
- Ryzhov, A.A.
- Schaber, J.
- Teichert, J.
- Xiang, R.

I-Tech
Solkan, Slovenia
- Bardorfer, A.
- Bogataj, L.
- Cargnelutti, M.
- Leban, P.
- Paglovec, P.
- Repič, B.

IAP
Frankfurt am Main, Germany

- Ateș, A.
- Blank, G.
- Ratzinger, U.
- Wagner, C.

IBS
Daejeon, Republic of Korea
- Chung, Y.S.
- Kim, G.D.
- Kwon, J.W.
- Woo, H.J.

IHEP
Beijing, People's Republic of China
- Cao, J.S.
- Jin, D.P.
- Liu, M.Y.
- Liu, X.Y.
- Meng, M.
- Sui, Y.F.
- Tian, J.M.
- Wang, J.Q.
- Yue, J.H.
- Zeng, L.
- Zhang, W.
- Zhang, Y.L.
- Zhu, D.C.
- Zhu, P.

IHEP CSNS
Guangdong Province, People's Republic of China
- Huang, W.L.
- Kang, M.T.
- Li, F.
- Mu, Z.C.
- Nie, X.J.
- Qiu, R.Y.
- Sun, J.L.
- Wang, A.X.
- Xie, Z.X.
- Xu, T.G.
- Xu, Zh.H.
- Yang, T.

ILSF
Tehran, Iran
- Ahmad Mehrabi, F.
- Mohammadi Alamouti, S.
- Navidpour, P.

IMP, TU Darmstadt
Darmstadt, Germany
- Preu, S.
- Yadav, R.

IMP/CAS
Lanzhou, People's Republic of China
- Du, Z.
- Feng, Y.C.
- Gu, K.
- He, P.L.
- Jing, L.
- Kang, X.C.
- Li, L.L.
- Li, Z.X.
- Liu, X.T.
- Mao, R.S.
- Tang, K.
- Tian, R.X.
- Wei, X.J.
- Wei, Y.
- Wu, J.X.
- Xie, H.M.
- Xu, Z.G.
- Yang, Y.L.
- Yin, J.
- Zhang, Y.
- Zhao, T.C.
- Zhao, Z.L.
- Zhou, K.
- Zhu, G.

INFN/LNF
Frascati, Italy
- Buonomo, B.
- Cardelli, F.
- Di Giovenale, D.
- Di Giulio, C.
- Foggetta, L.G.

IOQ
Jena, Germany
- Seidel, A.
- Stöhlker, T.

IPHT
Jena, Germany
- Schmelz, M.
- Stolz, R.
- Zakosarenko, V.

IPM
Tehran, Iran
- Sanaye Hajari, S.

J-PARC, KEK & JAEA
Ibaraki-ken, Japan
- Sato, Y.
- Tejima, M.

JAEA/J-PARC
Tokai-mura, Japan
- Kamiya, J.
- Kinsho, M.
- Moriya, K.

JAI
Oxford, United Kingdom
- Bett, D.R.
- Blaskovic Kraljevic, N.
- Bromwich, T.
- Burrows, P.
- Christian, G.B.
- Pakuza, C.
- Perry, C.
- Ramjiawan, R.L.

KBSI
Gangseo-gu, Busan, Republic of Korea
- Hong, J.G.

KEK
Ibaraki, Japan
- Aryshev, A.
- Hashimoto, Y.
- Honda, Y.
- Mitsuhashi, T.M.
- Miyajima, T.
- Nakamura, T.
- Rehman, M.A.
- Satou, K.
- Suwada, T.
- Terunuma, N.
- Toyama, T.
- Uota, M.
- Urakawa, J.

KIRAMS
Seoul, Republic of Korea
- An, D.H.
- Choi, S.H.
- Hong, H.B.
- Kang, K.U.
- Kim, G.B.
- Kim, J.H.
- Park, C.W.
- Yang, T.K.

KIRAMS/KHIMA
Seoul, Republic of Korea
- Jang, H.S.

KIT
Karlsruhe, Germany
- Bründermann, E.
- Caselle, M.
- Chilingaryan, S.A.
- Dritschler, T.
- Ebersoldt, A.
- Funkner, S.
- Kopmann, A.
- Müller, A.-S.
- Nasse, M.J.
- Niehues, G.
- Patil, M.M.
- Reissig, M.
- Steinmann, J.L.
- Weber, M.
- Widmann, C.

Korea Basic Science Institute
Busan, Republic of Korea
- Kim, S.J.
- Ok, J.W.
- Park, J.Y.

Korea University Sejong Campus
Sejong, Republic of Korea
- Lim, E.H.

KUS
Sejong, Republic of Korea
- Kim, E.-S.

LANL
Los Alamos, New Mexico, USA
- Bohon, J.
- Kim, D.
- Scheinker, A.
- Smedley, J.

LBNL
Berkeley, California, USA
- Norum, W.E.

Lund University
Lund, Sweden
- Werin, S.

Mitsubishi Electric System & Service Co., Ltd
Tsukuba, Japan
- Sakai, H.

MPQ
Garching, Munich, Germany
- Hori, M.

Naples University Federico II
Napoli, Italy
- Scampoli, P.

NCBJ
Świerk/Otwock, Poland
- Krakówiak, M.
- Kwiatkowski, R.
- Mianowski, S.
- Nietubyc, R.
- Szewiński, J.

NSRC SOLARIS
Kraków, Poland
- Wawrzyniak, A.I.

NSTRI
Tehran, Iran
- Ghasemi, F.

ORNL
Oak Ridge, Tennessee, USA
- Aleksandrov, A.V.
- Liu, Y.
- Long, C.D.

Osprey DCS LLC
Ocean City, USA
- Dalesio, L.R.

Oxford University Press (Oxford Electronic Publishing)
Oxford, United Kingdom
- Gal, Y.
- Smith, L.

Oxford University, Physics Department
Oxford, Oxon, United Kingdom
- Burrows, P.
- Pakuza, C.

PAL
Pohang, Republic of Korea
- Ha, T.
- Hahn, G.
- Joo, Y.D.
- Kim, C.
- Kim, D.
- Ko, J.
- Lee, Y.S.
- Nam, I.H.
- Shin, S.

PhLAM/CERLA
Villeneuve d'Ascq, France
- Bielawski, S.
- Evain, C.

POSTECH
Pohang, Republic of Korea
- Song, W.J.

Private Address
Silver Spring, USA
- Rule, D.W.

PSI
Villigen PSI, Switzerland
- Arbelo, Y.P.
- Bacellar Cases da Silveira, C.
- Bougiatioti, P.
- Cirelli, C.
- Craievich, P.
- David, Ch.
- Dehler, M.M.
- Ischebeck, R.
- Juranič, P.N.
- Knopp, G.
- Marcellini, F.
- Nass, K.J.
- Orlandi, G.L.
- Ozkan Loch, C.
- Reiche, S.
- Schlott, V.
- Staeger, D.
- Stampfli, A.M.M.
- Uemura, Y.
- Vila Comamala, J.

RadiaBeam
Santa Monica, California, USA
- Murokh, A.Y.

Royal Holloway, University of London
Surrey, United Kingdom
- Gibson, S.M.
- Guerin, H.

Sandia National Laboratories
Albuquerque, New Mexico, USA
- Harris, C.T.

SARI-CAS
Pudong, Shanghai, People's Republic of China
- Cao, S.S.
- Feng, L.
- Gao, B.
- Lai, L.W.
- Li, C.L.
- Liu, B.
- Wang, J.G.
- Wang, X.T.
- Zhang, W.Y.
- Zhou, Y.M.

SCIPP
Santa Cruz, California, USA
- Gonzalez, E.
- Kachiguine, S.
- Martinez-Mckinney, F.
- Mazza, S.M.
- Nizam, M.
- Padilla, R.
- Potter, E.K.
- Ryan, E.
- Schumm, B.A.
- Tarka, M.
- Wilder, M.

Shahid Beheshti University
Tehran, Iran
- Abbasi, F.
- Najafiyan, A.R.

SINAP
Shanghai, People's Republic of China
- Deng, Y.M.
- Wan, J.
- Xu, X.Y.
- Yang, X.

SLAC
Menlo Park, California, USA
- Aneke, E.C.
- Bassan, H.
- Condamoor, S.
- Convery, O.R.
- Dolgashev, V.A.
- Edelen, A.L.
- Emma, C.
- Fisher, A.S.
- Gessner, S.J.
- Haase, A.A.
- Halavanau, A.
- Hanuka, A.
- Hogan, M.J.
- Hoobler, S.L.
- Huang, Z.
- Jacobson, B.T.
- Krejcik, P.
- Li, S.
- MacArthur, J.P.
- Martinez-Galarce, D.S.
- Maxwell, T.J.
- McKee, B.D.
- Nantista, C.D.
- Othman, M.A.K.
- Rivetta, C.H.

- Rowen, M.
- Sapozhnikov, L.
- Silva Torrecilla, I.
- Storey, D.W.
- Wang, J.W.
- Young, A.
- Zhu, D.

SLRI
Nakhon Ratchasima, Thailand
- Sudmuang, P.

Sokendai
Ibaraki, Japan
- Popov, K.

SOLEIL
Gif-sur-Yvette, France
- Alves, F.
- Bence, A.
- Broucquart, R.
- El Ajjouri, M.
- Gamelin, A.
- Hubert, N.
- Labat, M.
- Pédeau, D.
- Ricaud, J.P.

SSRF
Shanghai, People's Republic of China
- Chen, F.Z.
- Chen, J.
- Gao, B.
- Hua, L.F.
- Jiang, R.
- Leng, Y.B.
- Wu, T.
- Xu, X.Y.
- Yuan, R.X.
- Zhang, N.
- Zhou, W.M.
- Zhou, Y.M.

Stanford University
Stanford, California, USA
- Fox, J.D.

Supracon AG
Jena, Germany
- Zakosarenko, V.

Synchrotron Light Research Institute (SLRI)
Muang District, Thailand
- Naeosuphap, S.

TEMF, TU Darmstadt
Darmstadt, Germany
- Ackermann, W.
- De Gersem, H.
- Marsic, N.
- Müller, W.F.O.

The University of Liverpool
Liverpool, United Kingdom
- Bradley, J.W.
- Martina, F.
- Welsch, C.P.
- Wolfenden, J.

THM
Friedberg, Germany
- Mattiello, S.
- Penirschke, A.
- Scheible, B.E.J.

Tongmyong University
Busan, Republic of Korea
- Jung, H.W.

TU Dresden
Dresden, Germany
- Schaber, J.

UCLA
Los Angeles, USA
- Denham, P.E.
- Guo, V.
- Musumeci, P.
- Ody, A.
- Park, Y.

UCSC
Santa Cruz, California, USA
- Norvell, N.P.

UMAN
Manchester, United Kingdom
- Bertsche, W.

UNIST
Ulsan, Republic of Korea
- Chung, M.
- Kim, S.Y.
- Kwak, D.H.
- Shin, B.K.
- Sung, C.K.

Universita' degli Studi di Milano & INFN
Milano, Italy
- Paroli, B.
- Potenza, M.A.C.

University of Chicago
Chicago, Illinois, USA
- Lobach, I.

University of Chinese Academy of Sciences
Beijing, People's Republic of China
- Xu, X.Y.

University of Oxford
Oxford, United Kingdom
- Eakins, D.

University of Warwick
Coventry, United Kingdom
- Newton, M.E.

Università degli Studi di Milano
Milano, Italy

- Siano, M.
- Teruzzi, L.

Université Paris-Saclay, CNRS/IN2P3, IJCLab
Orsay, France

- Ben Abdillah, M.
- El Baz, M.
- Fournier, F.

USTC/NSRL
Hefei, Anhui, People's Republic of China

- Jin, S.S.
- Li, Y.L.
- Lu, P.
- Luo, Q.
- Sun, B.G.
- Sun, L.W.
- Tang, L.L.
- Tuo, H.X.
- Wang, C.H.
- Wang, J.G.
- Wang, Y.G.
- Wu, F.F.
- Wu, R.Z.
- Zhao, Y.K.
- Zhou, T.Y.
- Zhou, Z.R.

Participants List

— A —

Alberdi, Benat
HZB

Alves, Diogo
CERN

An, Seohyeon
NCC, Korea

Aneke, Emmanuel
SLAC

Ateș, Adem
IAP

— B —

Bantemits, Georgios
CERN

Ben Abdillah, Mohammed
CNRS/IN2P3 ※ IJCLab

Benedetti, Gabriele
ALBA-CELLS

Bett, Douglas Robert
JAI

Blokland, Willem
ORNL

Bloomer, Christopher
DLS

Bobb, Lorraine
DLS

Boccardi, Andrea
CERN

Boehme, Christian
FZJ ※ DELTA ※ ESS-ERIC

Bozzolan, Michele
CERN

Bründermann, Erik
KIT

Braisz, Lukas
GSI

Brajnik, Gabriele
Elettra

Broucquart, Romain
SOLEIL

Buratin, Elena
ESRF

Burger, Stephane
CERN

Burrows, Philip
JAI

— C —

Cao, Shanshan
SARI-CAS

Cargnelutti, Manuel
I-Tech

Carlà, Michele
ALBA-CELLS ※ CERN

Casolaro, Pierluigi
AEC

Cee, Rainer
HIT

Cenede, Jean
CERN

Chen, Fangzhou
SSRF

Cheng, Weixing
ANL

Choi, Sang Hyoun
KIRAMS

Chubunov, Pavel
JSC URSC-ISDE

Chung, Moses
UNIST ※ Fermilab ※ PPPL

Chung, Yeonsei
IBS

Cleva, Stefano
Elettra

— D —

De Franco, Andrea
QST

De Monte, Raffaele
Elettra

Degl'Innocenti, Irene
CERN ※ Università di Pisa

Di Giulio, Claudio
INFN/LNF

Diete, Wolfgang
AXILON AG

Dinter, Hannes
DESY

Dolgashev, Valery
SLAC

Donegani, Elena Maria
ESS-ERIC

— E —

Eddy, Nathan
Fermilab

El Ajjouri, Moussa
SOLEIL

El Baz, Mathias
CNRS/IN2P3 ※ IJCLab

El Khechen, Dima
KIT

Emery, Jonathan
CERN

Emma, Claudio
SLAC

Evain, Clement
PhLAM/CERLA

Evtushenko, Pavel
HZDR-ELBE

— F —

Feng, Lie
SARI-CAS

Feng, Yongchun
IMP/CAS

Ferianis, Mario
Elettra

Fisher, Alan Stephen
SLAC

Forck, Peter
GSI ※ IAP

Frank, Joyce
MiTeGen

Frassier, Alexandre
CERN

— G —

Gao, Bo
SARI-CAS

Gassner, David
BNL

Gerth, Christopher
DESY

Gonzalez-Caminal, Pau
DESY ※ University Hamburg

Grimm, Oliver
MAX IV

Grulja, Sandi
Elettra

Guo, Veronica
PBPL-UCLA

— H —

Hahn, Garam
PAL

Haider, David Manuel
GSI

Hashimoto, Yoshinori
KEK-J-PARC

He, Peilin
IMP/CAS

Hong, Jonggi
KBSI

Houghton, Claire
DLS

Howling, Emily
Royal Holloway, University of London ※ DLS

Hubert, Nicolas
SOLEIL

Hulsart, Robert
BNL

Hwang, Ji-Gwang
HZB

— I —

Iriso, Ubaldo
ALBA-CELLS

— J —

Jacobson, Bryce
SLAC ※ RadiaBeam ※ University of Hawaii

Jamet, Christophe
GANIL

Jansson, Andreas
ESS-ERIC

Jaster-Merz, Sonja
DESY ※ University Hamburg

Jiang, Ruitao
SSRF

Jin, Sanshuang
USTC/NSRL

Jones, Peter John
AS-ANSTO

Jordan, Kevin
Jlab

— K —

Kim, Changbum
PAL

Kim, Gyujin
PAL

Kim, Yunwon
ITS Co

Kirsch, Matthias
Struck Innovative Systems

Klemz, Guido
HZB

Ko, Jinjoo
PAL

Ko, Jun Ho
PAL ※ POSTECH

Kolbinger, Bernadette
CERN

Konovalov, Valeriy
Applied Diamond, Inc.

Koopmans, Marten
HZB

Kowalski, Grzegorz Wawrzyniec
NSRC SOLARIS ※ S2Innovation

Krejcik, Patrick
SLAC

Krupa, Michal
CERN

Kube, Gero
DESY

Kwiatkowski, Roch
NCBJ

Kwon, Jangwon
IBS ※ KUS

— L —

Labat, Marie
SOLEIL

Lai, Longwei
SARI-CAS

Lan, Jinkai
USTC/NSRL

Lasocha, Kacper
CERN ※ Jagiellonian University

Leban, Peter
I-Tech

Lee, Justin
Conveyi@CN

Lee, Yohan
Kyoto University

Lefevre, Thibaut
CERN

Leng, Yongbin
SSRF

Li, Chunlei
SARI-CAS

Li, Siqi
SLAC ※ Stanford University

Lidia, Steven Michael
FRIB

Lim, Eunhoon
KUS

Lipka, Dirk
DESY

Liu, Ao
Euclid TechLabs

Liu, Mengyu
IHEP

Liu, Yun
ORNL

Liu, Zhengzheng
HUST

Lobach, Ihar
University of Chicago

Lockmann, Nils Maris
DESY

Lumpkin, Alex
Fermilab ※ ANL ※
Natural Science LLC

Lundquist, Johan Sven
MAX IV ※ ESS-ERIC

— M —

Ma, Shuai
HZDR-ELBE

Maesaka, Hirokazu
SPring-8 XFEL

Marques, Sergio Rodrigo
LNLS

Marqversen, Ole
CERN

Martí, Zeus
ALBA-CELLS

Martina, Francesco
Cockcroft Inst. ※ University
of Liverpool ※ CERN

McLean, Mark
CERN

Michnoff, Robert
BNL

Milosic, Timo
GSI

Min, Chang-Ki
PAL

Mirza, Sajjad Hussain
GSI ※ TEMF, TU Darmstadt

Morgan, Alun
DLS

— N —

Naeosuphap, Sakdinan
SLRI

Najafiyan, Ali Řeža
Shahid Beheshti University

Nantista, Christopher Dennis
SLAC

Navarro Fernandez, Araceli
CERN ※ UPC

Navidpour, Pedram
ILSF ※ IPM

Norum, Eric
LBNL

Nosych, Andriy
ALBA-CELLS

— O —

Orlandi, Gian Luca
PSI

Ortega Ruiz, Inaki
CERN

Othman, Mohamed
SLAC

Ozkan Loch, Cigdem
PSI

— P —

Pakuza, Collette
JAI ※ Oxford University

Patil, Meghana Mahaveer
KIT

Penirschke, Andreas
THM

Perez, Francis
ALBA-CELLS

Pertica, Alex
STFC/RAL/ISIS

Popov, Konstantin
Sokendai

— R —

Rajan, Keerthana Rajan
University of Kerala

Rehman, Muhammad Abdul
KEK ※ Sokendai

Ricaud, Jean-Paul
SOLEIL

Rivetta, Claudio Hector
SLAC

Roche, Benoit
ESRF

Roncarolo, Federico
CERN

Rossi, Adriana
CERN

— S —

Saccani, Mathieu
CERN

Saifulin, Maxim
GSI

Salvachua, Belen
CERN

Sandberg, Hampus
CERN

Sanfelici, Lucas
LNLS

Scarpine, Victor
Fermilab

Scheible, Bernhard E.J.
THM

Scheinker, Alexander
LANL

Schiwietz, Gregor
HZB

Schlott, Volker
PSI

Schmidt-Föhre, Frank
DESY

Seidel, Andreas
IOQ

Senes, Eugenio
CERN

Sezer, Mustafa Murat
ASELSAN A.S.

Shea, Thomas
ESS-ERIC

Shiltsev, Vladimir
Fermilab

Shim, Chi Hyun
PAL

Shin, Seunghwan
PAL

Siano, Mirko
University of Milano ※ INFN

Silva Torrecilla, Isleydys
SLAC

Singh, Rahul
GSI

Song, Woojin
POSTECH

Stampfli, Anna Maria Magdalena
PSI

Steinmann, Johannes Leonhard
ANL ※ KIT

Storey, Douglas W
SLAC

Storey, James William
CERN

Sun, Xiang
ANL

Sung, Chang-Kyu
KUS ※ UNIST

Suwada, Tsuyoshi
KEK

Swann, Levasseur Louis
CERN

— T —

Tan, Jocelyn
CERN

Tan, Yaw-Ren Eugene
AS-ANSTO

Tang, Kai
IMP/CAS

Tavares, Daniel de Oliveira
LNLS

Teytelman, Dmitry
Dimtel

Thurman-Keup, Randy Michael
Fermilab

Tipper, Alan
DLS

Torino, Laura
ALBA-CELLS

Tortora, Mattia
CAEN

Touzain, Etienne
BERGOZ

Tuo, H.X.
USTC/NSRL

— V —

Veness, Raymond
CERN

Veronese, Marco
Elettra

Vitoratou, Niki
DLS

Voelker, Jens
HZB

Volz, Paul Ignatius
HZB ※ KPH Mainz

— W —

Wang, Chuhan
USTC/NSRL

Wawrzyniak, Adriana Izabela
NSRC SOLARIS

Weber, Jonah
LBNL

Wendt, Manfred
CERN

Wittenburg, Kay
DESY

Wootton, Kent Peter
ANL

Wu, Ruizhe
USTC/NSRL

— X —

Xu, Xingyi
SSRF ※ CAS

— Y —

Yadav, Rahul
IMP, TU Darmstadt

Yamada, Ippei
Doshisha University

Yamakawa, Emi
JAI

Yang, Jiangyan
GSI

Yang, Tao
IHEP-CSNS

Yepez, David
ALBA-CELLS

Young, Andrew
SLAC

Yue, Junhui
IHEP

— Z —

Zamantzas, Christos
CERN

Zhao, Yunkun
USTC/NSRL

Zhou, Yimei
SARI-CAS ※ SSRF

Zhu, Dechong
IHEP